TRANSACTIONS
American Society for Metals
VOL. XLVII 1955

TECHNICAL PROGRAM AND REPORTS OF OFFICERS AMERICAN SOCIETY FOR METALS—36th ANNUAL CONVENTION, CHICAGO, NOVEMBER 1 to 5, 1954

FOR purposes of record and for the benefit of members who were not in attendance at the Thirty-sixth Annual Convention of the Society, held in Chicago, November 1 to 5, 1954, the Programs of the Technical Papers and Educational Lectures together with the Reports of Officers for 1954 are herewith published in full.

ASM Seminar on Impurities and Imperfections

Saturday, October 30

Ballroom, Palmer House, 9:30 A.M.

Presiding Officer
A. S. Nowick, Yale University

Lattice Vacancies and Interstitials, by H. Brooks. Cruft Laboratory. Harvard University, Cambridge, Mass.

Dislocations, by J. C. Fisher, Metallurgy Research Department, General Electric Co., Schenectady, N. Y.

Grain Boundaries, Substructure and Impurities, by R. W. Cahn, University of Birmingham, England. (Visiting lecturer, Johns Hopkins University, Baltimore, Md.)

Ballroom, Palmer House, 2:00 P.M.

Presiding Officer
E. S. Machlin, Columbia University

Effects on Crystal Growth, by Bruce Chalmers, Head of the Department of Metallurgy, Harvard University, Cambridge, Mass.

Impurities and Imperfections in Metallic Diffusion, by D. Lazarus, Department of Metallurgy, University of Illinois, Urbana, Ill.

Role of Structural Impurities on Phase Transformations, by David Turnbull, Research Laboratories, General Electric Co., Schenectady.

Sunday, October 31

Ballroom, Palmer House, 9:30 A.M.

Presiding Officer
L. K. Jetter, Oak Ridge National Laboratory

Effects on Mechanical Properties, by E. R. Parker, Chairman, Department of Minerals Technology, University of California, Berkeley, Calif.

Effects on Electrical Properties, by J. S. Koehler, Department of Metallurgy, University of Illinois, Urbana, Ill.

Effects on Chemical Properties, by W. D. Robertson, Associate, Metallurgical Laboratory, Yale University, New Haven, Conn.

Ballroom, Palmer House, 2:00 P.M.

Presiding Officer

P. A. Beck, University of Illinois

Impurity Phenomena in Semiconductors, by J. A. Burton, Bell Telephone Laboratory, Murray Hill, N. J.

Effects on Dielectrics and Ionic Crystals, by R. J. Maurer, Department of Metallurgy, University of Illinois, Urbana, Ill.

Radiation Damage, by Frederick Seitz, Research Professor, University of Illinois, Urbana, Ill.

Technical Program of the American Society for Metals

Monday, November 1

Ballroom, Palmer House, 9:30 A.M.

Constitutional Diagrams

Presiding Officers

B. W. Gonser, Battelle Memorial Institute

J. E. Burke, General Electric Co.

Aluminum-Vanadium Alloy System, by O. N. Carlson, D. J. Kenney and H. A. Wilhelm, Institute for Atomic Research and Department of Chemistry, Iowa State College, Ames, Iowa.

Partial Phase Diagram of the Iron-Cerium System, by James O. Jepson, Research Engineer, Jet Propulsion Laboratory, and Pol Duwez, Professor of Mechanical Engineering and Chief of Materials Section, Jet Propulsion Laboratory, California Institute of Technology, Pasadena, Calif.

Titanium-Cobalt System, by F. L. Orrell, Jr., Dow Chemical Co., Midland, Mich., and M. G. Fontana, Head, Department of Metallurgy, Ohio State University, Columbus, Ohio.

System Titanium-Aluminum-Manganese, by R. F. Domagala, Associate Metallurgist, and W. Rostoker, Senior Metallurgist, Research Department, Armour Research Foundation of Illinois Institute of Technology, Chicago, Ill.

Constitution of Ordering Alloys of the System Copper-Gold, by F. N. Rhines, Professor of Metallurgy, W. E. Bond, Research Assistant, and R. A. Rummel, Laboratory Assistant, Metals Research Laboratory, Carnegie Institute of Technology, Pittsburgh, Pa.

Special Session

Laboratory Instruction in Process Metallurgy

(Conducted by the ASM Advisory Committee on Metallurgical Education)

Red Lacquer Room, Palmer House, 9:30 A.M.

Development of Laboratory Experiments for the Unit Process Approach to Extractive Metallurgy, by R. Schuhmann, Jr., Purdue University, Lafayette, Ind.

Role of Metallurgical and Thermodynamic Problems in the Metallurgical Engineering Laboratory, by C. S. Samis, University of British Columbia, Vancouver, B. C., Canada.

Unit Process Experiments in Fluid Flow, Combustion and Heat Transfer for Metallurgical Engineering Students, by W. O. Philbrook, Carnegie Institute of Technology, Pittsburgh, Pa.

Special Problems for Experiments in Process Metallurgy Laboratory, by A. W. Schlecten, Missouri School of Mines, Rolla, Mo.

Role of Electrochemical Experiments in Process Metallurgy Instruction, by Herbert H. Kellogg, Columbia University, New York, N. Y.

Ballroom, Palmer House, 2:00 P.M.

Mechanical Metallurgy

Presiding Officers
R. B. Johnson, General Electric Co.
W. T. Lankford, United States Steel Corp.

Effect of Prestraining Under Different Stress States on the Fracture and Flow Properties of 2S-O Aluminum, by I. Rozalsky, Shell Oil Co., Wood River Research Laboratory, Wood River, Ill.

Deformation Mechanisms in Polycrystalline Aggregates of Magnesium, by F. E. Hauser, C. D. Starr, L. S. Tietz and J. E. Dorn, Professors of Metallurgy, Minerals Research Laboratory, University of California, Berkeley, Calif.

Tensile and Impact Properties of Low-Carbon Martensites, by C. C. Busby and H. W. Paxton, Metals Research Laboratory, Carnegie Institute of Technology, Pittsburgh, Pa., and M. F. Hawkes, Head of Metallurgical Section, Quality Evaluation Laboratory, U. S. Naval Ammunition Depot, Oahu, Hawaii.

Tensile Characteristics of Unalloyed Zirconium at Low and Moderate Temperatures, by J. H. Keeler, Research Laboratory, General Electric Co., Schenectady, N. Y.

Red Lacquer Room, Palmer House, 2:00 P.M.

Processing Steels

Presiding Officers
W. M. Baldwin, Case Institute of Technology
L. P. Tarasov, Norton Co.

Influence of Chemical Composition on the Machinability of Rephosphorized Openhearth Screw Steel, by E. J. Paliwoda, Research Engineer, Jones & Laughlin Steel Corp., Pittsburgh, Pa.

Influence of the Grinding Process on the Structure of Hardened Steel, by W. E. Littmann, Research Metallurgist, Timken Roller Bearing Co., Canton, Ohio, and John Wulff, Professor of Metallurgy, Massachusetts Institute of Technology, Cambridge, Mass.

Zonal Rolling Texture of Low Carbon Steel Cold Rolled at Various Temperatures, by C. Nusbaum, Associate Professor of Physics, Case Institute of Technology, Cleveland, Ohio, and Consultant, Cold Metal Products Co., and W. Brenner, Jr., Metallurgist, Cold Metal Products Co., Canfield, Ohio.

Tuesday, November 2

Hardenability

Ballroom, Palmer House, 9:30 A.M.

Presiding Officers
R. D. Chapman, Chrysler Corp.
F. T. McGuire, Deere & Co.

An Electron Metallographic Study of the Dependence of Microstructure on Hardenability, by S. T. Ross, Project Engineer, R. P. Sernka, Research Metallurgist, and W. E. Jominy, Chief of Metallurgical Research, Chrysler Corp., Detroit, Mich.

Calculation of Hardenability in High Carbon Alloy Steels, by C. F. Jatczak and R. W. Devine, Jr., Research Metallurgists, Timken Roller Bearing Co., Canton, Ohio.

Hardenability of Carbon Tool Steel, by N. J. Culp, Metallurgical Department, Carpenter Steel Co., Reading, Pa.

Effect of Carbon and Nitrogen on the Attainable Hardness of Martensitic Steels, by A. E. Nehrenberg, P. Payson and P. Lillys, Research Laboratory, Crucible Steel Co. of America, Harrison, N. J.

Industrial Heating Panel Session I

Presented by the Industrial Heating Equipment Association
Under the Auspices of the American Society for Metals
Red Lacquer Room, Palmer House, 9:30 A.M.

Atmospheres

Theory of Gases, by Allen G. Hotchkiss, General Electric Co.
Exothermic Atmosphere, by W. H. Boyd, Gas Atmospheres, Inc.
Endothermic Atmosphere, by Ralph J. Perrine, Electric Furnace Co.
Dry Nitrogen-Base Prepared Atmosphere, by Donald Beggs, Surface Combustion Corp.
Dissociated Ammonia, by M. R. Ogle, Drever Co.
Atmospheres, Their Control and Safety, by W. L. Besselman, Leeds & Northrup Co.

Ballroom, Palmer House, 2:00 P.M.

Physical Metallurgy

Presiding Officers
M. J. Day, Armour Research Foundation
V. H. Patterson, Climax Molybdenum Co.

Conditions for Dendritic Growth in Alloys, by W. Morris, W. A. Tiller, J. W. Rutter and W. C. Winegard, Department of Metallurgical Engineering, University of Toronto, Toronto, Canada.
Stress-Corrosion Mechanism in a Magnesium-Base Alloy, by D. K. Priest, Pfaudler Co., F. H. Beck, Assistant Professor of Research, and M. G. Fontana, Professor, Department of Metallurgy, Ohio State University, Columbus, Ohio.
Thermodynamics of Binary Interstitial Solid Solutions, by R. Speiser and J. W. Spretnak, Associate Professors, Department of Metallurgy, Ohio State University, Columbus, Ohio.
Influence of Substructure on the Shape of the Creep Curve, by T. Hazlett and R. D. Hansen, Research Engineering Department, University of California, Berkeley, Calif.

Industrial Heating Panel Session II

International Amphitheatre, 2:00 P.M.

Atmosphere Applications

Carburizing, by Walter Holcroft, Holcroft & Co.
Equilibrium Relationships for Dew Point Measurement and Control, by N. K. Koebel, Lindberg Engineering Co.
Practical Applications of Dew Point Measuring and Control, by O. E. Cullen, Surface Combustion Corp.
Brazing, a movie by LeRoy B. Thompson, Westinghouse Electric Corp.
Carbonitriding, by Harold Ipsen, Ipsen Industries.
Neutral Heat Treating, by A. W. Frank, Hevi Duty Electric Co.
Sintering, by Carl G. Paulson, C. I. Hayes, Inc.

Wednesday, November 3

Ballroom, Palmer House, 9:30 A.M.

ASM Annual Meeting

Edward DeMille Campbell Memorial Lecture

James P. Gill, Vanadium-Alloys Steel Co., Chairman

Factors Affecting Directional Properties in Aluminum Wrought Products, by Kent R. Van Horn, Director of Research, Aluminum Co. of America, New Kensington, Pa.

Ballroom, Palmer House, 2:00 P.M.

Mechanical Properties

Presiding Officers
A. H. Geisler, General Electric Co.
M. F. Judkins, Firth Sterling, Inc.

Elastic Limit and Yield Behavior of Hardened Steels, by H. Muir, Senior Lecturer, Otago University, Dunedin, New Zealand, B. L. Averbach, Associate Professor, and Morris Cohen, Professor, Department of Metallurgy, Massachusetts Institute of Technology, Cambridge, Mass.

Effect of Composition on Transverse Properties of Slack-Quenched Steel, by J. Vajda and P. E. Busby, Metals Research Laboratory, Carnegie Institute of Technology, Pittsburgh, Pa.

Statistical Fatigue Properties of Lamellar and Spheroidal Eutectoid Steel, by G. E. Dieter, Ordnance Corps, R. F. Mehl, Director of Metals Research Laboratory, and G. T. Horne, Metals Research Laboratory, Carnegie Institute of Technology, Pittsburgh, Pa.

Effect of Static Stress on the Damping of Some Engineering Alloys, by A. W. Cochardt, Metallurgy Department, Westinghouse Electric Corp., East Pittsburgh, Pa.

Red Lacquer Room, Palmer House, 2:00 P.M.

Ferrous Physical Metallurgy

Presiding Officers
J. A. Berger, University of Pittsburgh
R. A. Grange, United States Steel Corp.

Further Study of Microstructural Changes on Tempering Iron-Carbon Alloys, by B. S. Lement, Research Staff, Division of Industrial Co-Operation, B. L. Averbach, Associate Professor, and Morris Cohen, Professor of Physical Metallurgy, Massachusetts Institute of Technology, Cambridge, Mass.

Effects of Cold Work on Cementite in Steel, by D. V. Wilson, Lecturer, Department of Industrial Metallurgy, Birmingham University, Edgbaston, Birmingham, England.

Isothermal Transformation of Austenite Under Externally Applied Tensile Stress, by S. Bhattacharyya and G. L. Kehl, Associate Professor of Metallurgy, Columbia University, New York, N. Y.

Industrial Heating Panel Session III

International Amphitheatre, 2:00 P.M.

Induction Heating

Induction Melting, by G. W. Holz, Lindberg Engineering Co.

Induction Brazing, by E. S. Goodridge, Induction Heating Corp.

Induction Heat Treating, by H. B. Osborn, Jr., Ohio Crankshaft Co.

Sixty-Cycle Induction Heating for Forming and Extrusion, by John A. Logan, Magnethermic Corp.

High-Frequency Induction Heating for Hot Forging, by Frank T. Chesnut, Ajax Electrothermic Corp.

Dual-Frequency Heating for Hot Forging, by Carl P. Bernhardt, Westinghouse Electric Corp.

Thursday, November 4

Ballroom, Palmer House, 9:30 A.M.

Stainless

Presiding Officers
D. J. Carney, United States Steel Corp.
Peter Payson, Crucible Steel Co. of America

Effect of Cold Work and Recrystallization on the Formation of the Sigma Phase in Highly Stable Austenitic Stainless Steels, by A. J. Lena, Associate Director of Research, and W. E. Curry, Chief Metallographer, Allegheny Ludlum Steel Corp., Brackenridge, Pa.

Laves and Chi Phases in a Modified 15Cr Stainless Alloy, by F. L. VerSnyder and H. J. Beattie, Jr., Thomson Laboratory, General Electric Co., West Lynn, Mass.

Austenitic Chromium-Manganese-Nickel Steels Containing Nitrogen, by R. Franks, Manager, W. O. Binder and J. Thompson, Technical Service and Development Department, Electro Metallurgical Co., Niagara Falls, N. Y.

Effect of Deformation on the Martensitic Transformation in Austenitic Stainless Steels, by H. C. Fiedler, Research Laboratory, General Electric Co., Schenectady, N. Y., B. L. Averbach, Associate Professor, and Morris Cohen, Professor, Department of Metallurgy, Massachusetts Institute of Technology, Cambridge, Mass.

Red Lacquer Room, Palmer House, 9:30 A.M.

Heat Treatment

Presiding Officers

G. V. Smith, United States Steel Corp.
R. D. Chapman, Chrysler Corporation

Role of Water Vapor and Ammonia in Case Hardening Atmospheres, by P. A. Clarkin and M. B. Bever, Department of Metallurgy, Massachusetts Institute of Technology, Cambridge, Mass.

Effect of Heat Treatment Upon Microstructures, Microconstituents and Hardness of a Wrought Cobalt-Base Alloy, by J. W. Weeton and R. A. Signorelli, Lewis Flight Propulsion Laboratory, National Advisory Committee for Aeronautics, Cleveland, Ohio.

Secondary Graphitization of Quenched and Tempered Ductile Cast Iron, by J. C. Danko and J. F. Libsch, Department of Metallurgy, Lehigh University, Bethlehem, Pa.

Method for Determining the Continuous Cooling Transformations in Steel, by R. D. Chapman, Research Metallurgist, and W. E. Jominy, Chief Metallurgist, Engineering Division, Chrysler Corp., Detroit, Mich.

Red Lacquer Room, Palmer House, 2:00 P.M.

High Temperature

Presiding Officers

W. O. Binder, Electro Metallurgical Co.
W. D. Manly, Oak Ridge National Laboratory

Elevated Temperature Properties of Ductile Cast Irons, by C. R. Wilks, Metallurgist, N. A. Matthews, Assistant Chief Metallurgist, and R. Wayne Kraft, Jr., Metallurgist, American Brake Shoe Co., Mahwah, N. J.

Effect of Cold Work on the High-Temperature Creep Properties of Dilute Aluminum Alloys, by R. E. Frenkel, Research Engineer, Oleg D. Sherby, Research Engineer, and John E. Dorn, Professor of Physical Metallurgy, University of California, Berkeley, Calif.

Creep-Tempering Relationships in Hardened 4.5% Chromium Steels, by E. C. Roberts, Assistant Professor of Metallurgy, Montana School of Mines, Butte, Mont., N. J. Grant, Associate Professor of Metallurgy, and Morris Cohen, Professor of Metallurgy, Massachusetts Institute of Technology, Cambridge, Mass.

Strength of Wrought Zirconium-Base Binary Alloys at 1800–2200 °F., by H. A. Saller, J. T. Stacy and S. W. Porembka, Battelle Memorial Institute, Columbus, Ohio.

ASM—LECTURE COURSE

Monday, November 1, 4:30 P.M.

All Sessions in Red Lacquer Room, Palmer House

Temperature Measurement

Presiding Officers
F. G. Tatnall, Baldwin Locomotive Works
W. J. Buechling, Copperweld Steel Co.

Industrial Temperature Measurement With Thermocouple Pyrometers, by W. E. Belcher, Jr., Products and Application Engineer, Minneapolis-Honeywell Regulator Co., Brown Instruments Division, Philadelphia, Pa.

Tuesday, November 2, 4:30 P.M.

Industrial Temperature Measurement With Total Radiation and Optical Pyrometers, by Donald Robertson, Head, Pyrometer Section, Engineering Department, Leeds and Northrup Co., Philadelphia, Pa.

Wednesday, November 3, 4:30 P.M.

Industrial Temperature Measurement With Resistance Thermometers and Filled Systems, by W. F. Hickes, Assistant to Chief Engineer, Foxboro Co., Foxboro, Mass.

ANNUAL MEETING OF AMERICAN SOCIETY FOR METALS

Ballroom, Palmer House, 9:00 A.M.

Wednesday, November 3, 1954

The annual meeting was called to order by President James B. Austin. The order of business was:

1. President's address
   Printed in this volume of TRANSACTIONS, page 8.
2. Report of the Treasurer
   Printed in this volume of TRANSACTIONS, page 11.
3. Report of the Secretary
   Printed in this volume of TRANSACTIONS, page 15.
4. Report of ASM Foundation for Education and Research
   Printed in this volume of TRANSACTIONS, page 29.
5. Presentation of President's Medal and Certificate to Ralph L. Wilson
6. Presentation of Henry Marion Howe Medal to:
   F. L. VerSnyder and H. J. Beattie, Jr. for their paper entitled "Microconstituents in High Temperature Alloys" adjudged the paper of highest merit published in the ASM TRANSACTIONS in 1953.
7. Presentation of ASM Teaching Awards to:
   Joseph F. Libsch, Lehigh University
   Maurice J. Sinnott, University of Michigan
   Ele E. Stansbury, University of Tennessee
8. Election of Officers
   The report of the election of officers appears on page 31.
9. Campbell Lecture
   Printed in this volume of TRANSACTIONS, beginning on page 38.

ANNUAL ADDRESS OF THE PRESIDENT

JAMES B. AUSTIN, *President*

Thirty-sixth Annual Meeting, Chicago, November 3, 1954

THE experience of serving as President of the American Society for Metals is one of the most pleasant and rewarding privileges which can come to any man in our profession. I wish that each of you could share the greater appreciation of the scope of our Society and its activities which I have gained in visiting chapters and regional meetings, and in sitting in on various Committee meetings at National Headquarters. It is truly impressive.

Before summarizing the principal events of the past year, I should like to express my gratitude for the whole-hearted support which I have received from the chapter officers and from my colleagues on the Board of Trustees. Their splendid cooperation is typical of the spirit which characterizes our membership and which has enabled our Society to flourish. I should also like to express to the two retiring Trustees, Harry B. Knowlton and Ralph L. Wilson, the thanks of the Society for their many efforts on our behalf.

The Society's objectives in the fields of education and local chapter activities have remained essentially unchanged in character, though expanded in scope and progress in achieving these aims has been gratifying. At the same time, as I believe you will gather from the Treasurer's report, our finances have been maintained in satisfactory condition.

During the year, the Trustees held four meetings. Your President visited thirty-five chapters and participated in three regional meetings. Other Trustees visited an additional twenty-four chapters and two regional meetings, thus bringing the total to fifty-nine chapters and five regional meetings,—a sizeable fraction of our eighty-nine chapters. This close relationship between the National officers and the local sections is not only one of the sources of the strength of our Society but is an inspiration to those entrusted with the management of the Society's affairs.

It should also be noted that charters have been granted to four new chapters—Alberta, Albuquerque, Northeast Pennsylvania and Savannah River.

Last November, your President made a quick trip to England to represent you at the opening of the new Laboratories of the British Iron and Steel Research Association in Sheffield and to meet with the European Committee which is making plans for the Joint Meeting to be held next June.

To facilitate planning for this meeting on this side of the Atlantic, an American Committee comprising five members of our Society and five representatives of the American Institute of Mining and Metallur-

gical Engineers was set up last March. It has held two meetings and I can report that plans are now well-advanced. A detailed program is now in the press and will be available in the very near future.

As a brief summary, however, this conference is to convene in London on June 1, 1955 and will continue in England for seven days. There will then be a visit of five days to Germany, with activities centering in Dusseldorf. The meeting then moves to France for five days with an optional visit of one day to Liege in Belgium. The main conferences terminate in Paris on June 18 but additional meetings in Italy, Austria and possibly Spain are being planned. This joint conference will include informal discussions on a variety of subjects of interest to both the ferrous and nonferrous industries, as well as a number of plant inspections. Conditions in Europe make it necessary, regrettably, to limit attendance at many features of the program to a total of three hundred and fifty, including ladies.

The Society held a midwinter meeting in Boston in March which featured four sessions on the subject of beryllium, all of which were well attended. There were also four other sessions covering a variety of metallurgical subjects.

The Publications Committee has, in addition to its regular duties, studied certain aspects of our publication policies and has made recommendations which will improve this important part of our activities.

The Committee for Vocational Education, under its able and enthusiastic chairman, William F. Collins, made substantial progress during the year. Courses in "Metals Technology" for teachers in vocational schools were given in New York, Connecticut, Pennsylvania, Michigan, Illinois and Kansas. Interest in this work has also been expressed by educational authorities in about fifteen other states. This is a forward-looking program which will be of great benefit to the metals industries during the years ahead.

For some time it has been evident that there is a lack of metallurgical text material suitable for educational courses, correspondence courses and in-plant training. The Society has now taken initial steps toward filling this need. At our request, Professor Louis Haller of Penn State has prepared a list of some forty topics and has asked an outstanding man in each field to draw up a detailed outline covering material pertinent to his subject. These outlines will serve as the basis for preparation of the several texts. This is another example of our expanding activity in the educational field about which you will hear more in the Secretary's report.

To cover some other activities very briefly, the series of regional conferences for chapter officers, which was inaugurated several years ago, has been continued with gratifying results. In the program of visiting lectureships, arrangements were completed with eleven colleges and universities. The Society continues as the sole sponsoring member of

ACTA METALLURGICA, which has now nearly completed its second year. The program of Science Achievement Awards, which is administered for us by the National Science Teachers Association, has grown appreciably and is attracting increased attention and participation.

You have heard at recent Annual Meetings of the growing difficulties with regard to the present location of National Headquarters. The Trustees have, as you will see from the Treasurer's report, been making provision financially for a new site and building. A few months ago, Bill Eisenman made some imaginative and extensive suggestions for a long-range program covering improved facilities for the National Office. I believe he will outline these for you today. At his request, a Committee, headed by Dr. Kent Van Horn, has been appointed to study this matter and to make recommendations to the Trustees.

It is customary for the President's report to record the awards and outstanding events of the previous National Metals Congress. In Cleveland in 1953 the President's Medal was given to John Chipman. The ASM Medal for the Advancement of Research was awarded to Hiland G. Batcheller, Chairman of the Board of the Allegheny Ludlum Steel Corporation, and the Gold Medal of the Society was presented to George F. Sachs, Director of Metallurgical Research, Syracuse University. The Albert Sauveur Award was given to William T. Ennor, Assistant Director of Research of the Aluminum Company of America. The Henry Marion Howe Medal was awarded to Lew F. Porter and Philip C. Rosenthal of the University of Wisconsin. The Campbell Memorial Lecture was presented by Donald S. Clark, Professor of Mechanical Engineering, California Institute of Technology. Honorary Membership was conferred upon Founder Member A. E. White of the University of Michigan. ASM Teaching Awards were given to William M. Armstrong, University of British Columbia, Albert W. Schlechten, University of Missouri School of Mines and Metallurgy, and Otto Zmeskal, University of Florida.

On behalf of the American Society for Metals, I wish to express our thanks to those societies which have joined with us in this National Metals Congress for their fine cooperation. The programs of the Institute of Metals Division of the American Institute of Mining and Metallurgical Engineers, of the American Welding Society, and of the Society for Non-Destructive Testing have made a significant contribution to the success of this unique gathering.

In closing, I should like to repeat that it has been both pleasant and instructive to serve the Society. One of the most pleasant and most instructive of my experiences has been a better acquaintance with our remarkable Secretary, Bill Eisenman, and with his efficient and loyal staff. So, to Bill and all his associates, I express my gratitude for their invaluable assistance throughout this year.

TREASURER'S REPORT

WILLIAM A. PENNINGTON, *Treasurer*

AGAIN, your Society has had a good financial year. At the close of the fiscal year, August 31, 1954, the net assets were $2,756,298.90, being increased $366,015.85 during the period. The eighty-eight chapters have also reflected good management in increasing their combined assets by $18,000.00 to a total of $290,000.00.

The carrying value of all securities including accrued interest was $1,701,967.87, an increase of $58,950.39. The estimated market value was $2,030,851.55, an increase of $237,645.61 for the year. This increase is 13.2 per cent of the estimated market value at the beginning of the period. The increase resulted not only from interest and dividends reinvested, but also from an upturn in the market.

Dividends and interest amounted to $73,969.52, which is 4.35 per cent based on the carrying value of the total securities; last year the value was 3.82 per cent.

The cash account was increased during the year by $58,284.27 to $200,093.58.

There has been no change in the investment policy during the year.

Total income and expenses for the year are shown in Table I.

Table I

Income and Expenses—Fiscal Year Ended August 31, 1954

Income	$ 1,813,516.71	
Expenses	1,514,300.37	
Net Income		$ 299,216.34
Appropriations:		
Educational purposes	$ 41,000.00	
Building site and building	258,216.34	
Total appropriations		$ 299,216.34
Unappropriated net income		0,000,000.00

The relative income and expense for various items are shown in Table II, where the values are expressed in percentage of total income. About 75% of the income came from Metal Progress and the Metal Exposition. The net dues from membership amounted to approximately 9 per cent. Metal Progress and the Metal Exposition also accounted for the greater part of the outgo, amounting to some 55 per cent; general administration required about 10 per cent. The net income at 16.5 per cent was appropriated for educational purposes and the building site and building.

Transactions and Metals Review represent services performed at a net cost of $49,358.04 and $43,979.22, respectively.

Appropriations for educational projects for 1954 are shown in Table III and a history of the appropriations over the past four years is shown in Table IV. In the latter table, the identification by Item Number is the same as that in the preceding Table.

Table II

ASM Income and Its Disposition—Fiscal Year Ended August 31, 1953

	Income (%)	*Outgo (%)*
Metal Progress (Incl. special issue)	49.0	39.1
Metal exposition	25.7	14.6
Membership (Net)	8.8	3.5
Books published (Excl. Handbook)	4.6	5.0
Dividends and interest earned	4.1	—
Metals Handbook	3.0	2.4
Metals Review (Incl. Literature Review)	2.1	4.0
Sale of Securities	1.1	—
Transactions	0.6	3.4
General Administrative	—	10.1
Miscellaneous	1.0	1.4
	100.0	83.5
Appropriations	—	16.5
	100.0	100.0

Table III

Appropriation for Educational Projects (1954)

No.	*Designation*	*Amount*
1.	Acta Metallurgica (Journal of Science)	$ 10,000.00
2.	Teaching Awards	2,500.00
3.	Chapter Educational Activities	15,000.00
4.	World Metallurgical Congress	—
5.	Program with National Science Teachers Association	10,000.00
6.	Visiting Lectureships	—
7.	New Headquarters' Site	50,000.00
8.	New building	208,216.34
9.	Metals Handbook Revision	—
10.	Cooperative Activities with Defense Agencies	—
11.	Grant to American Society for Metals Foundation for Education and Research	3,500.00
	TOTAL	$299,216.34

Table IV

History of Appropriations for Educational Projects (1951–54 Incl.)

No.	*Appropriated*	*Expended*	*Balance (8-31-54)*
1.	$ 70,521.50	$55,521.50	$ 15,000.00
2.	22,500.00	13,531.63	8,968.37
3.	45,000.00	28,963.12	16,036.88
4.	90,000.00	36,071.14	53,928.86
5.	40,000.00	24,480.76	15,519.24
6.	18,000.00	7,901.12	10,098.88
7.	150,000.00	-0-	150,000.00*
8.	258,216.34	-0-	258,216.34*
9.	30,000.00	-0-	30,000.00
10.	10,000.00	2,985.27	7,014.73
11.	3,500.00	-0-	3,500.00**
TOTAL			$160,066.96
	(Excluding Items 7 and 8)*		

Again, the American Society has marched forward. In the words of our Secretary, Mr. William H. Eisenman, "We must go forward."

*Separate Investment Funds have been set up in the Cleveland Trust Company for the building site and for the building. The returns from these investments now supplement the balances shown.

**Previous appropriations have been transferred to the Foundation.

Under his diligent leadership, the Society has done just that. It is with a great deal of satisfaction that your Treasurer makes this acknowledgement. Attention should also be called to the cooperation and assistance offered by Assistant Treasurer, A. A. Hess, Trust Officers, A. W. Marten and W. W. Horner of the Cleveland Trust Company, the Finance Committee, and the Officers and Members of the Board of Trustees of the Society.

BALANCE SHEET

AMERICAN SOCIETY FOR METALS—August 31, 1954

ASSETS

CASH			$ 200,093.58
SECURITIES (approximate market or redemption prices aggregate $2,030,851.55)			
Bonds, stocks, and land trust certificates—at cost		$1,693,268.29	
Accrued interest		8,699.58	1,701,967.87
CASH SURRENDER VALUE OF LIFE INSURANCE			80,938.37
ACCOUNTS RECEIVABLE			
Advertising accounts	$41,122.29		
National Metal Exposition—Chicago—November, 1954	40,452.50		
Western Metal Show—Los Angeles—March, 1955	66,106.25		
Miscellaneous	19,119.92	$ 166,800.96	
Less allowance for doubtful accounts		2,000.00	164,800.96
INVENTORIES—at cost or lower			
Bound and unbound publications, books, paper stock, etc.		$ 188,281.93	
Less allowance for obsolescence		6,000.00	182,281.93
OTHER ASSETS			
Officers, employees, and sundry accounts and deposits			19,346.11
FUND FOR BUILDING SITE AND BUILDING			
Principal cash		$ 1,458.12	
Bonds—at cost (approximate redemption prices $144,998.90)		151,000.00	
Accrued interest		1,256.90	153,715.02
REAL ESTATE (at cost less allowances for depreciation)			44,250.00
OFFICE FURNITURE, FIXTURES, AND EQUIPMENT (at cost less allowances for depreciation)			102,555.62
DEFERRED CHARGES			
Prepaid exposition expenses:			
National Metal Exposition—Chicago—November, 1954	$72,160.61		
Western Metal Show—Los Angeles—March, 1955	8,934.70	$ 81,095.31	
Prepaid sundry expenses		20,440.00	
Prepaid insurance		4,814.13	106,349.44
			$2,756,298.90

LIABILITIES, RESERVES, AND SURPLUS

LIABILITIES			
Accounts payable:			
For purchases, expenses, etc.		$ 76,288.77	
Payroll taxes and taxes withheld from employees		5,733.85	
For apportionment of dues to local chapters		4,127.57	$ 86,150.19
INCOME APPROPRIATED FOR EDUCATIONAL PURPOSES			160,066.96
INCOME APPROPRIATED FOR BUILDING SITE AND BUILDING			258,216.34
RESERVES			
For METALS HANDBOOK		$ 82,130.22	
For conventions		60,000.00	

For dues paid in advance	50,000.00	
Campbell Memorial lecture fund	15,000.00	
H. M. Howe medal fund	5,000.00	
Sauveur achievement award	5,000.00	217,130.22
FUND FOR BUILDING SITE AND BUILDING		
Reserve		153,715.02
DEFERRED INCOME		
National Metal Exposition—Chicago—November, 1954	$424,350.00	
Western Metal Show—Los Angeles—March, 1955	153,725.00	
Advance receipts on publications	336.60	578,411.60
SURPLUS		
Balance at September 1, 1953, and August 31, 1954 (no change during the year)		1,302,608.57
		$2,756,298.90

STATEMENT OF APPROPRIATED INCOME

AMERICAN SOCIETY FOR METALS
Year ended August 31, 1954

INCOME APPROPRIATED FOR BUILDING SITE AND BUILDING			
Balance September 1, 1953			$150,000.00
Less amount transferred to fund for building site and building			150,000.00
			$ —0—
Add amount appropriated during year			258,216.34
BALANCE AUGUST 31, 1954			$258,216.34
INCOME APPROPRIATED FOR EDUCATIONAL PURPOSES			
Balance September 1, 1953			$176,353.05
Less expenditures during year:			
International Journal of Science		$20,000.00	
Chapter educational courses		14,106.72	
A.S.M. Science Achievement Award		10,060.00	
Teaching award		6,473.39	
Visiting lectureships		4,343.88	
World Metallurgical Congress		3,264.63	
A.S.M. Foundation for Education and Research		1,846.10	
Metallurgical Advisory Board		903.74	
Metals Handbook revision	$19,806.23		
Less allocation from reserve	23,518.60*	3,712.37*	57,286.09
			$119,066.96
Add amount appropriated during year			41,000.00
BALANCE AUGUST 31, 1954			$160,066.96

* Indicates red figures.

STATEMENT OF INCOME AND EXPENSES

AMERICAN SOCIETY FOR METALS
Year ended August 31, 1954

INCOME		
METAL PROGRESS—Monthly publication		$ 808,520.79
Metal Exposition		466,263.68
Memberships		158,963.38
Book sales		83,755.12
METAL PROGRESS—special issue		80,727.50
Dividends and interest earned		73,969.52
A.S.M. METALS HANDBOOK Sales		55,378.00
The METALS REVIEW—monthly publication		37,407.89
Net gain on sales of securities		18,975.28
TRANSACTIONS sales		11,559.53
General reprints		7,828.22
Discount earned		4,001.86
Sundry sales, etc.		3,686.37
Increment in cash value and dividends on life insurance		2,157.53
Sale of purchased books		322.04
TOTAL INCOME		$1,813,516.71
EXPENSES		
METAL PROGRESS—monthly publication	$650,467.50	
National Metal Exposition—Cleveland—October, 1953	265,187.06	
Books published	91,418.36	
General expenses	85,980.25	
The METALS REVIEW—monthly publication	71,751.99	

Memberships	63,542.44	
TRANSACTIONS	60,917.57	
METAL PROGRESS—special issue	59,721.14	
A.S.M. METALS HANDBOOK	43,476.67	
Secretary's office	36,984.78	
Accounting department	23,993.63	
Headquarters	18,027.24	
Warehouse	13,454.83	
National committees	8,572.32	
Trustees	5,051.42	
President's office	4,067.07	
Transfer of net income to fund for building site and building	3,715.02	
Winter meeting—Boston	2,642.14	
Medals awards and lectures	2,062.72	
Technical books	1,304.15	
Research and educational contributions	900.00	
Miscellaneous merchandise	541.50	
Library	520.57	
TOTAL EXPENSES		1,514,300.37
NET INCOME—Note A		$ 299,216.34
Income appropriated as authorized by the Board of Trustees:		
For educational purposes	$ 41,000.00	
For building site and building	258,216.34	299,216.34
UNAPPROPRIATED NET INCOME		$ —0—

Note A—In addition to expenses shown above, expenditures in the amount of $57,286.09 were made during the year from prior years' appropriations (see accompanying statement).

Cleveland, Ohio
September 24, 1954

Board of Trustees,
American Society for Metals, Cleveland, Ohio.

We have examined the balance sheet of American Society for Metals as of August 31, 1954, and the related statements of income and expenses and surplus for the year then ended. Our examination was made in accordance with generally accepted auditing standards, and accordingly included such tests of the accounting records and such other auditing procedures as we considered necessary in the circumstances.

In our opinion, the accompanying balance sheet and statement of income and expenses present fairly the financial position of American Society for Metals at August 31, 1954, and the results of its operations for the year then ended, in conformity with generally accepted accounting principles applied on a basis consistent with that of the preceding year.

ERNST & ERNST
Certified Public Accountants

ANNUAL REPORT OF THE SECRETARY

WILLIAM H. EISENMAN, *Secretary*

THE ASM OF TOMORROW

I AM deeply grateful for the distinguished honor the members of the ASM have bestowed upon me in electing me for the 19th consecutive two-year term as your secretary. The 36 years already served have prepared me, I feel, to take a look into the metallurgical world of tomorrow—and, from my experience and my faith in the future of the ASM, to present to the Board of Trustees and to the Membership a plan of progressive, dynamic expansion and progress safely within ASM's splendid economic capacities.

So, if I may have your indulgence for a few moments, I will unfold to you the new fields of activity the ASM is prepared to, and, in my humble judgment should, enter. Here is a forward look towards the:

American Society for Metals of Tomorrow.

One may state there are two paths of future action open to the ASM. Here they are:—

1) To continue and improve if possible (and it undoubtedly is) the services that are at present provided for its 24,000 members. While such an operation may seem satisfactory at the present time, and, in some places, the present services of the ASM have called forth commendations, nevertheless, such a path presents an uninspiring program. It will never fire the members of the Society to great zeal in its behalf but will create, I believe, a contented staff of employees who will be satisfied to carry on in the same old manner, in the same old channels.

If such a complacent scheme of action were established, the members would undoubtedly soon see the ASM fall into a cut-and-dried rut so frequently observed in other groups, that of being happily satisfied, and, even with a feeling of pride, doing the same old things in the same old way, year in and year out.

2) The other possible path of action for the ASM would lead with vigor and dynamic progress to new and increased activities to service and serve the engineering field of the great metal industry. The ASM would then soon take its place as the greatest engineering and educational force of its time. It would again show and lead the way to progress.

As I view the ASM of Tomorrow, I cannot imagine a decline or leveling off of its activities. The ASM has never been, and I'm sure never could be, a "status quo" organization, but it will be and should be an "ASM On The March."

To me there seems to be but one choice: "LET US HAVE FAITH —LET US MOVE FORWARD!"

However, the final decision does not rest with me, but with all my colleagues of the Board of Trustees of the ASM. I grant it is my privilege and duty to present for their consideration and final decision the broad field of possible future activities of the society as I see them.

The Board of Trustees and all the Past Presidents of the ASM have quite some time ago been given my views on the future of the ASM. They received my recommendations quite cordially and have unanimously approved the first two, and are giving study and consideration to the other three. Plans for placing the first two proposals in operation are under way.

We all know that tomorrow comes very quickly. Therefore, it is important that any progress and advancement planned for now and in the near future must have the reserve capacity for the ASM's future needs.

So, here begins my word picture of:

THE ASM OF TOMORROW

One should not be so busy and occupied with present activities that

he fails to recognize the dawn of a new day with new possibilities for increased service and the need for an alert and forward look.

I would not for a moment have you feel that the thoughts expressed on the projected activity here unfolded represent the last word in just how and when they might be placed in operation. The real purpose I have in mind now is to present the broad picture of great possible future usefulness of the ASM, not to give minute details of its operation but to show how all the projected activities dovetail into an ASM picture of tomorrow.

The ASM of Tomorrow, as I foresee it, will be a gradual progression from one phase of accomplishment to the next. An evolution springing from the present firm and substantial base of service, a base created through 36 years of growth and advancing preparation for the tremendous opportunities that should now be attacked with vigor and comprehension.

And here are the phases of the recommendations and proposals I make, with a fuller discussion of each to follow:

1. The erection of an adequate new headquarters building (within 2 years)
2. The creation of a division of the ASM to be known as the Metal Engineering Institute (in operation within 2 years)
3. The creation of a division of the ASM to be known as ASM Metallurgical Seminars (within 3 years)
4. The creation of a division of the ASM to be known as the ASM Metal Research Laboratory (as soon as practical!)
5. The creation of a division of the ASM to be known as the Metal Science University (to follow the Research Laboratory)

I wish to present a few facts about a new headquarters building.

1) The necessity for a new headquarters building, as well as a new location, has already been recognized and approved by the Board of Trustees. The present quarters at 7301 Euclid Avenue are externally and internally attractive but inadequate in size and undesirable as to location, due to business neighbors, the surroundings, and also the personal safety of employees and property. Also, the present site and buildings are economically unsound.

The site and headquarters building fund, including the appropriations already made, and exclusive of all other assets of the Society, now total $500,000, and it is expected that by the time the building location and plans have been approved, the fund will total more than one million dollars. A committee is now actively searching for a site, either within city limits or in a suburban area which would be easily accessible and where the value of the land has not been inflated, but has every prospect of a very substantial increase in value.

2) The second step in the March of Metallurgical Progress is the

creation of a division of the ASM to be known as the ASM Metal Engineering Institute. I am pleased to report that this forward moving activity has already received the unanimous approval of the Board of Trustees.

Metal Engineering Institute is the tentative name that has been assigned to that division of the Society that will have control of the preparation, manufacturing, presentation and administration of the Educational Courses now being written by carefully selected high authorities on the 41 metallurgical and metals engineering subjects so far scheduled for production.

Work on these Educational Courses has been in progress for about a year, during which time the invited authors prepared extended outlines of each of the fifteen chapters of their course, and after a conference with each author in Cleveland to discuss his outline and the general form for presentation of the subject material, 38 of the 41 subjects are now in process of completion within a 12-months' period. The authors have been enthusiastic about the entire plan and have been most happy to cooperate in this outstanding educational activity. Consequently, it is hoped that within 18 months, the Metal Engineering Institute should be ready for presentation of the 41 Education Courses to be used for:—

1. ASM Chapter Educational Courses
2. In-plant Training
3. Correspondence (Home Study) Courses

1. *The ASM Chapter Educational Courses:* A chapter will be able to select the number of lessons desired (3 to 6 or more) of greatest interest to its members. This will give a chapter greater flexibility in the selection of subjects since it relieves the lecturer of the necessity of preparing lesson material. The committee could select a group of lecturers from one ASM Educational Course, or (since each of the 15 lessons in a course is a complete unit), the committee could select individual lectures (lessons) from a number of courses. The availability of these Educational Courses will greatly increase the educational activities of the ASM Chapters, give them an opportunity for greater service, and enhance the chapters' local stature in many ways.

2. *In-plant Training:* We are all aware of the great extent to which this type of training is being sponsored and the importance attached to it by the metals-producing and fabricating industry. While some of the larger companies are staffed to do this in-plant training, there are literally thousands of plants that either do without it or must depend on an outside source for this service. And where, one might ask, would they be most apt to turn, but to the ASM, the Engineering Society of the Metals Industry.

3. *The Correspondence (Home Study) Course:* The "typical" student will be a young man possibly between the ages of 24 to 31,

married, a high-school graduate who went into Service, then to work, and is at present employed in the metals industry, either in production, fabrication, testing or in some specialized investigation (such as corrosion, high-temperature and so on). The type of metal industry in which he is engaged will vary from the manufacture of earth-moving machinery to airplanes, from transportation to construction, from steel mills to automobiles. This individual may be a young man in any type of manufacture using metal who wants to and should know more about the material or process with which he is working, and why it performs the way it does. The ASM courses will supply that information.

The great number of individuals employed in all branches of the metals industry represents a large percentage of the total number employed in the national economy. (The metals industry is 50% of the present economy). Consequently, the field for home study courses is large—almost unlimited. The opportunity to engage in self-study and self-improvement will undoubtedly have a great appeal for those young men whose ambition and education will play a very important part in their future.

It is reported that some two million Americans are now paying more than $40,000,000 each year to study everything from budgetary control to blue print reading. Enrollment is up 15% over 1952. Today there are more than 40 accredited institutions belonging to the National Home Study Council, only two of which together offer 4 courses in Metallurgy. These courses are broad and all-inclusive, and will have no similarity at all to the ASM courses that break down the general course they offer into over 40 different special subjects (divisions).

Training supervisors for large corporations generally recognize the value of home study. Some firms have contracted with training institutions to take over part of their load.

Today, educators in most schools of the country recognize the need for such off-campus training, since there are currently more students enrolled in home study courses than in all the universities, colleges, professional and vocational schools *combined*.

The Metal Engineering Institute will be self-supporting and should in a very limited time of operation, return many times the modest cost incurred in the preparation, production and presentation of the courses.

Because of the outstanding reputation of the authors, their grasp of the aims, ideals and purposes of each Educational Course, their knowledge of the vast group in the metal industry these courses are to serve, I am more than safe in predicting that this division of the ASM will soon grow into the most widely known, recognized and appreciated activity of the Society, fulfilling an important function in and for the metals industry, a service that will become the most valuable and continuing asset the ASM has.

The third step in the program is the ASM Metallurgical Sem-

inars. These Seminars will present continuously throughout the year intensive one-and two-week institutes for discussion and study at an advanced educational level of important and current phases of metallurgy and metals engineering.

For these Seminars will be assembled the top scientists and specialists in the field under discussion—an opportunity for informal discussion groups devoted to individual metallurgical problems as well as refresher courses in metallurgical procedure.

Seminars are becoming increasingly important in providing opportunities for members of organizations to meet together to exchange information, solve common problems, make decisions, bring to participants the results of study and experience in the field under consideration, together with practical application to specific problems. Attendance at these seminars will be limited to insure maximum attention to individual needs.

The ASM Metallurgical Seminars will be in session throughout the year, not confined to the few summer months, and will thus afford a gathering center or forum where metallurgical problems and new information on metals engineering will always be the prime topic for conversation and study.

4. *ASM Metal Research Laboratory:* The next new project for the American Society for Metals, in line with a policy of dynamic expansion, should be the establishment of a metals research laboratory. Properly organized and directed, it would fill an area now unoccupied and perform important functions now neglected, yet of great importance to America's metallurgical advance.

At present, laboratories in and for the metals industry may be roughly subdivided as follows:

(1) Laboratories in the individual plant or in a central location of a single corporation.

(2) Governmental laboratories, such as Bureau of Mines, Bureau of Standards, Atomic Energy Commission, Army Arsenals. Essentially these are the same as category No. 1 above.

(3) Commercial Testing Laboratories. Many are doing some development work. However, in metallurgy these are largely confined to inspection and representation.

(4) University and Endowed (or Self-Supporting) Research Institutes. Their work is principally an extension of that listed in Categories No. 1 and 2 upon well-defined problems beyond the man power or instrumentation available in the sponsor's own laboratory.

(5) Laboratories for Fundamental Research, of which there are not very many, although there is a very good example here in the University of Chicago's Institute for the Study of Metals.

Such a review even though very brief indicates one important field

now all but completely neglected. Categories No. 1, 2, 3, and 4 work on "ad hoc, practical" problems, of limited scope, designed to benefit a limited public.

Category No. 5 is working at the advanced frontiers of knowledge.

The gap between these two represents the field for the American Society for Metals Research Laboratory—namely, industrial problems in metals of widest generality, useful either to the whole metals refining industry, or to the whole heat treating industry, to the whole superpower industry, and so on. Since there is nothing like it in America now, one would have to go abroad to find parallels of laboratories studying the main problems of whole industries, such as the British Non-Ferrous Metals Research Association, the French Iron and Steel Research Institute (IRSID), Centre Technique des Industries de la Fonderie, or the Swiss Watch Industry's Central Laboratory. In the United States we might have to go back as far as the 1920's and cite ASM's Past President Charles Herty's study of openhearth steelmaking processes at the Pittsburgh Station of the Bureau of Mines, financed by practically all the firms in the steel industry. Much work is done in the cooperating plants, thus avoiding installation of heavy equipment of mill type.

In brief, an American Society for Metals Research Laboratory with the objective of solving general problems concerning the use, and improvement and application of metals in American industry would not be competing with existing effort, but would in fact fill a great gap in American metallurgical research.

When such an American Society for Metals Research Laboratory becomes a working organization it would naturally attract the type of problems it is equipped to handle. Undoubtedly it would be called upon, not only to serve the metals industry, but in case of emergency, may well serve the nation.

While the scale of activities in the ASM Metals Research Laboratory would largely depend on the number of research programs devised by the laboratory director, it could also receive direct support from the American Society for Metals Foundation for Education and Research and the American Society for Metals itself.

5. With the ASM Engineering Institute, the Metallurgical Seminars and the Metal Research Laboratory in operation, the fifth phase of my proposal follows as a natural sequence:

The creation of a division of the ASM to be known as the Metal Science University.

The top metal scientists, engineers and researchers will be attracted to and become a fixed part of this great assembly of metal men. Their teaching talents and instructional abilities will be fully made use of in the classrooms and laboratories of the university.

Differing from other institutions, it will offer courses in metal science only beginning with the third year students and continuing

through the post graduate studies. Special care will be given to the training of research workers so the graduates may help fill a void that is now developing. The graduates should also be capable of going immediately into industry and head a research department having had training in management and research planning.

I have unfolded my view of the ASM of Tomorrow. It is not a hastily conceived plan, but one towards which the ASM has been moving for many years. This forward looking program is no small plan, yet it is logical and can readily be carried to full fruition if only you have the will and faith to go forward.

While I am pleased to be the author of this expansion program, it is by no means a one-man operation, nor is any one man essential to its gradual accomplishment. There are hundreds of live, energetic and capable individuals who recognize that the ASM should not rest on its reputation, however good it is, but must look and advance forward—and who can easily take the formula presented here, and with the assistance of all ASM members—the world's largest group of metal scientists and engineers—reach the highest peak of usefulness and service to the metals industry.

If I have expressed my thoughts clearly, you have recognized how this Metal Science Center has grown and expanded in a logical progression—each activity an advance on the frontier of increased educational activities—each one a new service for a great primary industry.

You have already visioned with me the extensive acreage necessary to comfortably accommodate and house the extensive buildings which this progressive expansion of the society will require.

You have recognized, I am sure, that as the present ASM has been successful in giving extensive service to its members at a minimum cost and has, at the same time, created a firm financial structure, the ASM of tomorrow, as I have outlined it, will continue as a successful, self-sustaining organization, with all divisions helping one another so that in a smooth operating society the net result can only be a continuous and increasing service by all of the divisions of the ASM of Tomorrow.

I commend this program to you—it is no little plan. I hope you believe, as I do, with Daniel H. Burnham who says:

> "Make no little plans; they have no magic to stir one's blood and probably themselves will not be realized. Make big plans; aim high in hope and work, remembering that a noble, logical diagram once recorded will never die, but long after we are gone will be a living thing, asserting itself with ever growing insistency."

Remember, let ASM make no little plans! Let ASM make only big plans, realizing that vision is indispensable to progress. I have pre-

sented this diagram of the ASM of Tomorrow so that it may be recorded and made a part of the official record.

You, the members and the Board of Trustees and all of us can fill out that diagram in every phase—and when it is completed, it will be a more finished and successful achievement than could possibly be created by a word picture of the most glowing eloquence. But to create and accomplish, we must have Faith in the ASM as an instrumentality through which all of us, recognizing that the security and welfare of our civilization depend increasingly on the advancement of scientific knowledge, will have an opportunity to serve humanity—our industry —and our country.

Hear ASM's call to greater service.
If we listen and hear the Call,
And answer with a will and determination,
No barrier can halt the progress of the ASM of Tomorrow.

1954—Annual Report of the Secretary

The American Society for Metals on October 1, 1954 had a total membership of 24,300, a gain of 5.6% since last October.

Of this number, 20,865 are regular members, 1099 are junior members, and 2211 are sustaining members.

There are 52 honorary and life members, and 73 are in the armed forces.

Publications Committee

Seventeen persons constitute the membership of the Publications Committee for 1954, under the chairmanship of F. T. McGuire, Manager, Materials Engineering Department, Deere & Co., Moline, Ill. The members of the Committee and their Chapter affiliation are: W. W. Austin, Carolinas; B. L. Averbach, Boston; H. S. Avery, New York; J. A. Berger, Pittsburgh; W. O. Binder, Buffalo; D. J. Carney, Chicago; R. D. Chapman, Detroit; K. L. Fetters, Mahoning Valley; A. H. Geisler, Eastern New York; J. L. Gregg, Southern Tier; W. D. Manly, Oak Ridge; Peter Payson, New York; G. V. Smith, New Jersey; J. W. Spretnak, Columbus; J. L. Wyatt, Cleveland; and Ray T. Bayless, Secretary, Cleveland.

During the year the Committee has reviewed 63 papers. Of this number 41 papers were approved for publication in Transactions, 39 of which were selected for presentation at the October National Metal Congress and two for publication in Transactions only. 22 papers were not approved for publication and returned to authors and a few of these may be revised according to Committee suggestions and returned to the Society for re-review. Thirteen papers are now in the process of review.

The Publications Committee held one formal meeting on June 22

and 23, 1954, at which time the final arrangements for the technical program at this Convention were made.

Educational Committee

The Educational Committee for the year 1954 was composed of the following personnel: F. G. Tatnall, Philadelphia, Chairman; A. M. Bounds, Philadelphia; W. J. Buechling, Warren; J. M. Edge, Birmingham; R. S. Guinan, Rochester; N. C. Jessen, Akron; C. H. Lorig, Columbus; H. J. Smith, Louisville; Otto Zmeskal, Chicago; and Ray T. Bayless, Secretary, Cleveland.

This Committee held one formal meeting on December 8, 1953 at which time the educational lectures for this Convention were discussed and the lectures for the 1955 Convention were also arranged. These lectures are:

1954

1. "Furnace Atmospheres"
2. "Temperature Measurement"
   W. E. Belcher, Jr., Minneapolis-Honeywell Regulator
   Donald Robertson, Leeds & Northrup Co.
   W. F. Hickes, The Foxboro Co.

Due to factors beyond the control of the Committee, it was found necessary to abandon the series on "Furnace Atmospheres."

1955

1. "Embrittlement Phenomenon"
   by B. R. Queneau, U. S. Steel Corp.
2. "Deep Hardening Steels"
   by C. M. Carmen, Pitman-Dunn Labs., Frankford Arsenal

The new motion picture film entitled "Heat Treatment of Steel" which was sponsored by the Educational Committee and produced by the Photographic Department of Ohio State University under the supervision of Professor J. O. Lord, is now available to ASM Chapters and others.

ASM Metals Handbook Committee

The Handbook Committee has made substantial progress. During the past year, 22 author committees have submitted reports. These have been reviewed by hundreds of ASM members, then revised, approved by the Handbook Committee and published as the first Supplement to the ASM Metals Handbook. All members received this Supplement as a 13th issue of Metal Progress, dated July 15, 1954.

Work continues toward the next full edition of the Handbook. Forty-two additional committees are being formed. To assist in this expanding program of technical committee work, Mr. James P. Hontas has been employed as ASM Staff Metallurgist, bringing the profession staff of the Handbook to three.

Sales of the 1948 edition outside the membership continue at a high level; during the past year sales were greater than for the year preceding.

Special Libraries Association

The Metals Division of the Special Libraries Association is again holding its fall meeting in conjunction with the National Metal Congress on Wednesday, Thursday, and Friday, November 3, 4, and 5. The program includes field trips to John Crerar Library on Wednesday, and to Inland Steel Co. on Friday, a morning technical session Thursday on "The Small Metallurgical Library" and an afternoon session on "Economics and Marketing in the Metallurgical Field."

Through the courtesy of the American Society for Metals, the Division is again sponsoring a library booth at the National Metal Exposition. Periodicals and government publications, new technical books, ASM and SLA publications are on display, and a competent staff of technical librarians is on hand to provide a working reference service for visitors.

Transactions

Since the last National Metal Congress, Vol. 46 and Vol. 46A of the Transactions were published and distributed to the membership in March 1954. Vol. 46 totals 1659 pages and constitutes 72 articles with their discussions. It contains all of the papers presented at the October 1953 Convention held in Cleveland, together with some of the papers presented at the Eighth Western Metal Congress held in Los Angeles, March 1953, all of the papers presented at the midwinter meeting held in Boston in March 1954, and also the interim papers received during the year. The president, secretary and treasurer's reports for 1953 and other current items of record were included in Vol. 46 together with a report of the Convention.

Vol. 46A contains 12 papers (270 pages) presented at the Seminar on "Relation of Properties to Microstructures" held on Saturday and Sunday, October 17 and 18, 1953, during the National Metal Congress and Exposition, Cleveland. This seminar was sponsored by the American Society for Metals, the subject being selected by a committee appointed by the Board of Trustees. The personnel of this committee was: Morris Cohen, Chairman; David Turnbull, A. D. Schwope, R. Smoluchowski, E. R. Parker, Bruce Chalmers, L. K. Jetter, Harvey Brooks, Frederick Seitz, O. T. Marzke, E. S. Machlin and Paul Beck. The preparation and coordination of the series of subjects and solicitation of speakers were carried on by David Turnbull.

Preprints

Thirty-nine papers were prepared in preprint form for presentation at this Convention. These preprints were distributed to those members of the Society who requested them. The total number of pages is 753 and a total of 45,000 preprint copies was distributed free to the membership.

Metal Progress

This report concerns the 12 regular monthly issues of Metal Progress, prepared by the editorial staff. The 13th issue in mid-July will be noted in the report of the Metals Handbook Committee.

1954 proved to be the most successful year. Advertising volume (1946 ½ pages in the 12 issues) again practically matched the highest totals of the mid 1940's. Editorial volume of 826 pages in the 12 issues represented an 18½% increase over the average for the preceding 10 years. Circulation increased about 6%, accompanying the increased membership in the Society (averaging 22,300 in fiscal '53 and 23,560 in fiscal '54). Consequently it can be seen that a record-breaking amount of information was also distributed to ASMembers.

Some notable series of articles have been presented. First may be mentioned the second Review of International Progress in Metallurgy (January 1954) wherein 14 eminent engineers in foreign countries described important advances in their respective countries. A new department for critical and descriptive book reviews of notable publications has appeared in almost every issue. A series on the use of statistical control in the metals industry appeared during the fall of 1953. Several articles on fabrication and use of beryllium metal were printed in April 1954, reporting the symposium held at the Boston midwinter meeting in cooperation with the U.S. Atomic Energy Commission. Other exclusive articles about atomic energy and the metallurgical work at various A.E.C. installations have been presented. Peter Kosting of Watertown Arsenal is writing a history of large cannon, and chapters in this work are appearing at intervals. Several important articles on new heat treatments and devices to control surface composition of steel have been printed.

To enlarge the editorial coverage, 137 critical digests of timely articles appearing in other American and foreign journals have been printed. Each of these extended abstracts is prepared by some ASMember, expert in the field under discussion. The periodic "surveys of reader performance", made by the R. O. Eastman research organization, indicate that this department in Metal Progress has unexpectedly high ratings in reader interest, attention and value.

The Editor of Metal Progress, as for several years past, has given a considerable amount of time to the Atomic Energy Commission as a member of its Advisory Committee on Industrial Information, particularly as chairman of working groups appraising operations and documents at the various facilities.

Metals Review

During the 12 months from October 1953 through September 1954, Metals Review published a total of 696 pages—96 pages more than in

the preceding 12 months, an increase registering greater response than ever before of chapter reporters to home office solicitation of material. Of the 696 pages, 53% were devoted to news of chapter activities, doings of members and headquarters actions; and 47% were devoted to ASM Review of Metal Literature.

Continuing the special issue inaugurated in 1951, the February issue of METALS REVIEW published the biographies and photographs of junior members to assist them in obtaining employment during the coming year. The feature "Meet Your Chapter Chairman" was continued during the year, and a new feature "Metallurgical News and Developments" was started.

The 10th volume of the ASM Review of Metal Literature, containing 714 pages and 8033 annotations, was published.

BOOKS

During the past year, a total of 27,116 books published by the Society was sold to members and others. This figure includes 2714 ASM Metals Handbooks and 1266 Handbook Supplements.

During this period 11 titles were added to the publication list. They are:

Revision of "Engineering Alloys" by N. E. Woldman
Transactions of ASM—Vol. 46
Relation of Properties to Microstructures—Seminar by 12 authors
Metals Technology, edited by Alfred Bornemann
Surface Protection Against Wear and Corrosion—by 17 authors
ASM—1954 Handbook supplement
Review of Metal Literature—Vol. 10
Basic Metallurgy—Prepared by members of Philadelphia Chapter, ASM
Behavior of Metals Under Impulsive Loads—by J. S. Rinehart & John Pearson
Fatigue—by 3 authors
Utilization of Heat Resistant Alloys—by 17 authors

The following titles are now in preparation:

Vol. 47—ASM Transactions
The Metal Beryllium

SEMINAR ON IMPERFECTIONS AND IMPURITIES

The Seminar on Imperfections and Impurities this year was an outstanding success. It was divided into four important and interesting sessions with the meeting room filled to capacity. This interest is a great compliment to the Committee and the seminar speakers and assures a continuance of this important annual event.

The Committee on arrangements consisted of the following personnel: David Turnbull, Chairman, Schenectady; P. A. Beck, Peoria; Harvey Brooks, Boston; Bruce Chalmers, Boston; R. L. Cunningham, Ottawa Valley; Eric Jette, Los Alamos; L. K. Jetter, Oak Ridge; E. S. Machlin, New York; R. Maddin, Baltimore; A. S. Nowick, New Haven; Frederick Seitz, Urbana; and O. T. Marzke, Washington, Coordinator of the Seminar.

ASM Science Achievement Awards

The ASM Science Achievement awards were held again under the auspices of the National Science Teachers' Association.

There was a large increase in the number of students in the program this year, with approximately 2000 participating in this activity to increase the interest of junior and senior high school pupils in the sciences.

Young Engineers' Day

Over 200 student members of the ASM were the guests of the Society at luncheon at the Saddle and Sirloin Club on Friday, November 5th. The students came from Notre Dame, Purdue, University of Illinois, University of Wisconsin and Illinois Institute of Technology.

An added feature of Young Engineers' Day, besides visiting the Exposition, was the privilege of meeting the 25-year members of the Society who have contributed so much to the present stature of the Society. There was present over 160 members with a record of 25 years or more. They also were the guests of the Society at this luncheon.

National Metal Exposition

The National Metal Exposition occupied the full facilities of the International Amphitheatre and again was considered both by visitors and exhibitors as having achieved an outstanding high mark of excellence.

There were 450 exhibitors occupying 150,000 square feet of space. The exhibits were witnessed by 65,000 visitors.

The new booth backgrounds, the spreading of the royal red carpet and the festive decorations all added to the creation of the spirit of the Metal Show.

The National Metal Congress

The National Metal Congress again had the cooperation of the Institute of Metals Division of the American Institute of Mining and Metallurgical Engineers, the American Welding Society, the Society for Non-Destructive Testing, and the Metals Division of the Special Libraries Association.

This year a new cooperator was added, The Industrial Heating Equipment Association, presenting three programs.

All of the technical sessions of the cooperating societies as well as the ASM were of outstanding interest and created a great Metal Congress. The three sessions offered by the Industrial Heating Equipment Association in cooperation with the ASM were particularly well attended and convinced the participants that a continuation of this type of program in cooperation with the Congress was quite desirable.

American Society For Metals
Foundation For Education And Research
Annual Report Of The President

RALPH L. WILSON, *President*

THE ASM Foundation for Education and Research has nearly completed its second full year of operations. In this report are combined a statement of the activities and the financial standing of the Foundation to August 31, 1954.

The Trustees have continued to emphasize educational rather than research programs for the near future. In keeping with this policy, the $400 awards for undergraduate scholarships in metallurgy have been renewed at the eligible colleges on the original list and a few more schools were added by extending participation to all institutions giving day-school courses leading to a degree in metallurgy. There are now 42 schools in the United States and 6 in Canada sharing in the scholarship plan.

A new feature of the educational work of the Foundation is the establishment of the ASM Graduate Fellowship in Metallurgy. This Fellowship is intended to encourage qualified persons who are engaged in industrial or non-academic research to return to college to resume studies in their field of interest. The amount of the Fellowship for one year will be $2,400 for a single person or $3,000 for a married person. Also, the school will receive a grant of $1,200 for tuition and research expenses. The first award will be made for the academic year 1955–56.

In the year ending August 31, 1954 the total assets of the Foundation were $663,464.04 as compared to $654,768.64 the year before. In the following tables are shown the position of the Foundation with respect to Endowment Principal and Unexpended Income on August 31, 1954 based on an unaudited report.

Endowment Principal

Amount on August 31, 1953		$650,000.00
Grant from ASM August 31, 1953		1,846.10
Gain on Disposal of Securities		2,497.51
Amount on August 31, 1954		$654,343.61

Unexpended Income

Balance August 31, 1953		$ 4,749.07
Income Sept. 1, 1953 to Aug. 31, 1954	$28,100.18	
Expense Sept. 1, 1953 to Aug. 31, 1954	4,528.82	23,571.36
		28,320.43
Awarded 48—$400 Scholarships		19,200.00
Balance August 31, 1954		$ 9,120.43

Treasurer Walter E. Jominy will submit a complete audited financial statement for the entire fiscal year ending November 30, 1954, which will be incorporated in the Foundation annual report as it will appear in the ASM Transactions. (Audit published on page 30)

AUDITED BALANCE SHEET

AMERICAN SOCIETY FOR METALS FOUNDATION FOR EDUCATION AND RESEARCH—November 30, 1954

ASSETS

CASH ON DEPOSIT		
The Cleveland Trust Company:		
Income cash	$ 16,168.14	
Principal cash	$ 1,389.82	$ 17,557.96
SECURITIES (approximate market prices aggregate $754,683.48)		
Bonds and stocks—Note A		656,397.68
OTHER INCOME ASSET		
Accrued bond interest		3,091.64
		$677,047.28

FUNDS

PRINCIPAL OF ENDOWMENT FUND		
Grants from American Society for Metals	$655,346.10	
Profit on disposal of securities	2,441.40	$657,787.50
UNAPPROPRIATED NET INCOME		19,259.78
		$677,047.28

Note A—Securities obtained by grant from American Society for Metals are stated at market price at July 15, 1952. Subsequent additions are at cost.

STATEMENT OF INCOME AND EXPENSES AND UNAPPROPRIATED NET INCOME

AMERICAN SOCIETY FOR METALS FOUNDATION FOR EDUCATION AND RESEARCH—For the year ended November 30, 1954

INCOME		
Dividends, interest and discount earned		$ 28,377.61
EXPENSES		
Professional services	$ 1,713.82	
Fiscal agents' fees and expense	1,427.56	
Board of Trustees	919.99	
Stationery and supplies	310.90	4,372.27
NET INCOME		$ 24,005.34
Unappropriated net income, November 30, 1953		14,454.44
		$ 38,459.78
Scholarships awarded during the year		19,200.00
UNAPPROPRIATED NET INCOME NOVEMBER 30, 1954		$ 19,259.78

Board of Trustees,
American Society for Metals Foundation
for Education and Research, Cleveland, Ohio.

Cleveland, Ohio
December 17, 1954

We have examined the balance sheet of American Society for Metals Foundation for Education and Research as of November 30, 1954, and the related statement of income and expenses and unappropriated net income for the year then ended. Our examination was made in accordance with generally accepted auditing standards, and accordingly included such tests of the accounting records, and such other auditing procedures as we considered necessary in the circumstances.

Securities were confirmed to us by The Cleveland Trust Company, agent.

In our opinion, the accompanying balance sheet and statement of income and expenses and unappropriated net income present fairly the financial position of American Society for Metals Foundation for Education and Research, at November 30, 1954, and the results of its operations for the year then ended, in conformity with generally accepted accounting principles applied on a basis consistent with that of the preceding year.

ERNST & ERNST
Certified Public Accountants

The Trustees of the Foundation wish to thank the Society for permission to present this report at the annual meeting and to publish the final version in the ASM Transactions.

ELECTION OF OFFICERS

PRESIDENT AUSTIN: We will now proceed with the election of officers, complying with the Constitution. I appointed in March, 1954, the following Nominating Committee, selected from a list of candidates suggested by the eligible chapters prior to March 1, 1954.

Chairman: M. J. Day—Chicago

Ardrey M. Bounds—Philadelphia
E. E. Stansbury—Oak Ridge
S. F. Urban—Buffalo
W. E. Bancroft—Hartford
E. S. Rowland—Canton-Massillon
Eldon Van Meter—Wichita
C. B. Carpenter—Rocky Mountains
J. C. Thompson—San Diego

The Nominating Committee met in Chicago on May 20, 1954 and made the following nominations:

FOR PRESIDENT

George A. Roberts, Vice President, Technology,
Vanadium-Alloys Steel Company, Latrobe, Pa.—1 year

FOR VICE-PRESIDENT

A. O. Schaefer, Vice President,
Engineering & Manufacturing, The Midvale Company, Nicetown, Pa.—1 year

FOR TRUSTEES

Walter Crafts—Associate Director of Research,
Electro Metallurgical Division, Union Carbide and Carbon Research
Laboratory, Niagara Falls, New York.—2 years
Karl L. Fetters—Assistant to the Vice President in Charge of Operations,
Youngstown Sheet & Tube Company, Youngstown, Ohio—2 years

Complying with the Constitution, a quorum of the immediate Past Presidents met in New York on May 26th and nominated for *Secretary,* William H. Eisenman.

I have been informed by the Secretary that no additional nominations were received prior to July 15, 1954 for any of the vacancies appearing on the Board of Trustees. Consequently, the nominations were closed. I now call upon the Secretary to carry out the provisions of the Constitution with respect to the election of officers:

SECRETARY EISENMAN: Conforming to the provisions and requirements of the Constitution of the American Society for Metals, I hereby cast the unanimous vote of the members for the election of the aforenamed candidates who were nominated on May 20th and 26th, 1954.

The President introduced the newly elected officers and called upon the President-elect, George A. Roberts, to say a few words.

PRESIDENT AUSTIN: Has anyone present anything to bring before the meeting for the good of the Society?—If not, then a motion to adjourn is in order.

At 10:30 President Austin reconvened the meeting by introducing Past President James P. Gill, the chairman of the Edward DeMille Campbell Memorial Lecture, who introduced Dr. Kent R. Van Horn who presented the twenty-ninth Edward DeMille Campbell Memorial Lecture entitled "Factors Affecting Directional Properties in Aluminum Wrought Products." The lecture is printed in full in this volume of TRANSACTIONS.

ASM ANNUAL DINNER

On Thursday evening, November 4, members and guests assembled in the Ballroom of the Palmer House for the Annual Dinner of the Society. The attendance was in excess of 400.

Those persons seated at the speakers' table were: Walter Crafts, Union Carbide and Carbon Corp.—Trustee-Elect, ASM; Karl L. Fetters, Youngstown Sheet and Tube Co.—Trustee-Elect, ASM; Harry B. Knowlton, International Harvester Co.—Trustee, ASM; W. A. Pennington, University of Maryland—Treasurer, ASM; Ralph L. Wilson, Timken Roller Bearing Co.—Past-President-Trustee, ASM; Gerold H. Tenney, Los Alamos Scientific Laboratory—President, Society for Nondestructive Testing; Irwin H. Such, Editor—*Steel;* F. L. Plummer, Hammond Iron Works—President, American Welding Society; A. O. Schaefer, The Midvale Co.—Trustee and Vice-President-Elect, ASM; Francis B. Foley, International Nickel Co.—Past-President, ASM; Alexander Feild, Armco Steel Corp.—Recipient of 1954 Sauveur Achievement Award; A. E. White, Ann Arbor—First President and Founder Member, ASM; Lawrence Kimpton, Chancellor of University of Chicago—Principal Speaker; James B. Austin, United States Steel Corp.—President, ASM; William E. Umstattd, Timken Roller Bearing Co.—Recipient of 1954 ASM Medal for Advancement of Research; James P. Gill, Vanadium-Alloys Steel Co.—Past-President, ASM; George A. Roberts, Vanadium-Alloys Steel Co.—Vice-President and President-Elect, ASM; Edgar C. Bain, United States Steel Corp.—Past-President, ASM; Bradley Stoughton, Lehigh University, Past-President, ASM; Kent R. VanHorn, Aluminum Company of America—Past-President, ASM; Robert F. Mehl, Carnegie Institute of Technology; George T. Hook, publisher *The Iron Age;* G. M. Young, Aluminum Company of Canada, Ltd.—Trustee, ASM; F. L. VerSnyder, General Electric Co.—Recipient of 1954 Henry Marion Howe Medal; H. J. Beattie, Jr., General Electric Co.—Recipient of 1954 Henry Marion Howe Medal; R. J. Raudebaugh, International Nickel Co.—Trustee, ASM; W. H. Eisenman—Secretary and Founder Member, ASM.

ALBERT SAUVEUR ACHIEVEMENT AWARD

In 1934 the Board of Trustees established an award consisting of

a metal plaque and certificate in honor of Dr. Albert Sauveur, distinguished metallurgist and for many years an honorary member of the ASM. The purpose of this award is to recognize a metallurgical achievement which has stood the test of time and stimulated others along similar lines to the extent that a marked basic advance has been made in the metal arts and sciences. The 1954 candidate was Alexander L. Feild, associate director, Research Division, Armco Steel Corporation. In presenting Dr. Feild, Past-President Francis B. Foley read the citation of Dr. Feild's accomplishments. President Austin then conferred the award. The citation is:

> The Award is made in recognition of his pioneering in the application of physical chemistry to steelmaking, culminating in the scientific control of the reduction of chromium oxide into stainless steel on a practical commercial basis.
>
> Achievements in American industry, while the result of cooperative effort on the part of many individuals, usually becomes successful through the efforts of an interested, capable person who persists in the drive towards a goal that he alone sees clearly. Usually the history of the persistent one upon whose shoulders the burden always rested carries many incidents that mark his outstanding character.
>
> A glance at the background of Dr. Alexander Littlejohn Feild shows that brilliance was evident early in his career receiving awards and medals for his work in blast furnace studies and for his work on welding of armor.
>
> A pioneer in the applications of the science of physical chemistry to aid in solving the problems of iron and steelmaking, he has been working on the problems associated with smelting of chromium and its use in commercial products for more than 25 years. The success of his full-scale operating process to produce stainless steels directly from chromium ores in furnaces lined with chromium oxide opened up the utilization of the scrap incidental to production and usage of those metals. Until that scrap utilization problem was solved, the whole economy of stainless steel was in doubt.
>
> For a lifetime in metal work, as a student, a teacher, an experimenter, a developer of practical methods and, above all, a searching director of fundamental scientific studies, his reward in part has been the satisfaction of knowing that industry has builded on the solid foundations of his sound thinking.
>
> For the reduction to practice of a process that combines the raw materials and the utilization of the scrap in the production of alloys of iron and chromium on a sound economic basis, I have the honor, Mr. President, to present Dr. Alexander Littlejohn Feild, the Associate Director of the Research Laboratories of the

Armco Steel Corporation to receive the American Society for Metals' Albert Sauveur Achievement Award.

Honorary Memberships

Honorary memberships in the Society were conferred on Bradley Stoughton, Past-President of the Society, and Albert Portevin, distinguished French metallurgist. In conferring this membership on Dr. Stoughton, Past-President Edgar C. Bain read the following citation:

> It was just fifty-seven years ago that Bradley Stoughton, having completed his studies at Yale and at Massachusetts Institute of Technology, came to Columbia as assistant to Henry Marion Howe. Since then he has never been far from the academic field. In 1923, he became Head of the Department of Metallurgy at Lehigh, a position he occupied with distinction until his retirement. His counsel was highly valued by his students, many of whom continued to seek his advice long after graduation. During his later years at Lehigh he also served as Dean of the College of Engineering. Today, he can be justly regarded as the Dean of Teachers of Metallurgy and Metallurgical Engineering in the United States. Throughout his long career he has, through his writings and through his personal influence, played a significant role in the development of metallurgical education in this country.
>
> Bradley Stoughton is also a man of affairs. He was President of the Electrochemical Society in 1931. In 1939, he was elected Treasurer of the American Society for Metals, becoming Vice-President in 1940 and President in 1941. In 1951 he conducted one of the study tours for the World Metallurgical Congress. He has been active on many Committees of our Society and his endeavors for the Lehigh Valley Chapter have been recognized by it in an annual Bradley Stoughton Night.
>
> He has also been ever ready to serve his country. From 1917 to 1920 he was associated with the National Research Council as Head of the Division of Metallurgy and Vice-Chairman of the Division of Engineering. From 1941 to 1945 he served as Head of the Heat Treating Equipment Section of the War Production Board, and in 1945 he was Deputy Representative in London of the Technical Industrial Intelligence Committee of the Foreign Economic Administration.
>
> In recognition of his many contributions to his students, to this Society, to his profession and to his country, the Board of Trustees has unanimously elected him an Honorary Member of our Society. Mr. President, it is with great pride and pleasure that I present Dean Bradley Stoughton.

In conferring this membership on Dr. Portevin, Robert F. Mehl,

director of the Metals Research Laboratory, Carnegie Institute of Technology, read the following citation:

> The American Society for Metals recognizes metallurgy's indebtedness to a French scientist and engineer Professor Albert Portevin whose conscientious studies of metal properties, metallography, and heat treatment began when these were almost mysteries in the early years of the century; through them he was able to formulate industrial applications basic to contemporary techniques. His work has brought him many high honors in his own country and also abroad, including the Osmond, the Bessemer, the Carnegie, the Seaman and the Trasenster medals.
>
> In bestowing this honorary membership, an educational society thus recognizes a great teacher. Professor in several French technical schools, he has inspired his students with the orderliness, clarity, precision and concision that typifies a French intellectual alloy at its best, and an alloy highly resistant to the corrosion of these recent critical years of French history. The purpose of the ASM, to keep metallurgists informed of scientific and technical advance, has also been one of his aims; he has publicized foreign work widely in France, where he heads the editorial committees of various other technical magazines; he is the author of some 350 papers describing his own and others' research; for upwards of 25 years he has been a contributor to our own engineering magazine, "Metal Progress."
>
> We are especially pleased to have as honorary member a gentleman whose charm, simplicity and sense of humor have made him universally liked as well as admired; a man neither hypocritically modest or inordinately proud; and an artist, whether in enriching his writing with literary references or in decorating porcelain.
>
> Mr. President: I have the honor to present Mr. Albert Marcel Germain Rene Portevin, scientist of world renown, publicist, cultered gentleman for Honorary Membership in the American Society for Metals.

Conferring of the ASM Medal for the Advancement of Research

The 1954 ASM Medal for the Advancement of Research was awarded to William E. Umstattd, President of Timken Roller Bearing Company, in recognition of his consistent sponsorship, foresight and influence in financing and prosecuting metallurgical research, which have helped substantially to advance the arts and sciences relating to metals.

In presenting Mr. Umstattd, Past-President James P. Gill read the citation engrossed on the scroll which accompanies the medal. President Austin then conferred the award. The citation is:

> When research was still a new tool of American industry and when metallurgy was mostly associated with mining, Timken Roller Bearing Company under the leadership of William E. Umstattd began its endeavor in the field of metallurgical research. This effort was continued with ever-increasing energy through periods of depression as well as periods of expansion and so many developments came forth that it is impossible to elaborate on them here or even to mention all of them. There is time to name only a few of the more important ones.
>
> A fundamental development came as early as 1920 in the McQuaid-Ehn carburizing test for determining the "normality" of carburizing steels—that is, the ability to harden without soft spots. This test has endured thirty-odd years of scrutiny and is still used in practically all specifications for constructional alloy steel.
>
> It was natural that this test should be followed by work aimed to control grain size in steel, the principal contribution here being the ability to make fine-grained steels of high coarsening temperatures consistently.
>
> A series of graphitic steels were developed for wear resistance, and established themselves with excellent performance in many tool and die applications.
>
> A search for steel that would exhibit improved strength at the high temperatures was started by Timken at the University of Michigan in 1927. Many new products came from this work. Among the early ones were the intermediate series of chromium-molybdenum alloy steels and the "Sicromo" series of silicon-chromium-molybdenum steels.
>
> This was followed by a number of high temperature "super alloys" such as the 16–25–6 chromium-nickel-molybdenum alloy used so extensively in jet engines, gas turbines, superchargers and the like.
>
> A contribution which has been of tremendous value to high temperature research has been the test known as the "rupture-strength" test, in which a constant load is applied at elevated temperatures and the time measured to produce rupture. This test today is the most popular means for determining strength of materials above 1000 °F.
>
> Another important development involved large fatigue testing machines capable of testing full-size parts as large as railroad locomotive and car axles. A great amount of data, on which some

radical and successful designs have been based, has thus been made available to engineers.

Under Mr. Umstattd's guiding influence many more scientific advances were made. He has continuously and consistently supported the cause of research. It can be truly said that, by his foresight and influence in making available financial support, he has helped substantially to advance the arts and sciences relating to metals.

Address of the Evening

President Austin then presented Lawrence A. Kimpton, Chancellor of the University of Chicago, who was the main speaker of the evening. The title of his talk was "Business and Education."

FACTORS AFFECTING DIRECTIONAL PROPERTIES IN ALUMINUM WROUGHT PRODUCTS

(1954 Edward DeMille Campbell Memorial Lecture)

By Kent R. Van Horn

WE are assembled to honor and perpetuate the memory of Edward DeMille Campbell. Some of your earlier lecturers were acquainted with Professor Campbell and were able to introduce the lecture by citing an interesting personal experience. Unfortunately, I am among the group of recent lecturers who have known Professor Campbell only from his numerous distinguished contributions to technical literature, and by conversation with some of his former associates. It is hoped that the younger members of our Society have read some of his works and are aware of his outstanding exhibition of courage and fortitude, rarely exampled in professional circles. At the age of 28, he lost his sight in an explosion during a laboratory examination of steel. Instead of accepting defeat and obscurity, he continued his work with such perseverance and success that at the time of his death he was Head Professor of Chemistry and Metallurgy and Director of the Chemical Laboratory at the University of Michigan. He contributed seventy-five research papers to the scientific literature, yet all but three were published after he lost his sight. He was able to follow the literature with the aid of five part-time assistants, who read the technical articles to him and led him around the campus at Ann Arbor. His investigations gained worldwide acceptance and he was honored both at home and abroad.

About sixty-five of his papers were concerned with the chemical constitution or heat treatment of steel and the nature of the iron carbides. During the final three years of Professor Campbell's life, one of his assistants was Dr. William L. Fink, now Chief of the Physical Metallurgy Division of Aluminum Research Laboratories. In 1921–1922, Professor Campbell became intrigued with a new metallurgical tool, X-ray diffraction, then in its swaddling clothes. Campbell attended lectures at Ann Arbor, given by the pioneers Bragg and Davey. He had Fink explain the atomic space models after the lectures and construct diffraction patterns by employing cord, string and thread to represent the different line intensities. Campbell suggested to Fink that X-ray diffraction might be used to investigate the structure of hardened

---

This is the Twenty-ninth Edward DeMille Campbell Memorial Lecture, presented by Kent R. Van Horn, director of research, Aluminum Research Laboratories, Aluminum Company of America, New Kensington, Pa. The lecture was presented November 3, 1954, during the Thirty-sixth Annual Convention of the Society, held in Chicago.

steel. Starting with a homemade apparatus in the Physics Department, and later employing one of the first General Electric multiple diffraction units, Fink designed the unique wedge reflection camera for the work. Fink and Campbell were the first to discover tetragonal or body-centered iron in martensite; i.e., the transition stage from face-centered cubic austenite to body-centered cubic ferrite. It is interesting to note that Campbell, shortly before his death, approved each detail of Fink's thesis, which later was an ASM paper. Even in his final years, Campbell recognized the possibilities of X-ray diffraction.

I must humbly admit that, after an interval of thirty years, one of the principal implements of investigation utilized for this Campbell Memorial Lecture is the X-ray diffraction method. I do wish, however, to express my appreciation to the Board of Trustees of the American Society for Metals for the invitation to give this lecture. I realize that this honor is more a recognition of the work of Alcoa's Aluminum Research Laboratories than myself, and therefore accept on behalf of my associates, some of whom it will be possible to acknowledge for specific contributions to this lecture.

Grain Orientation and Directional Properties

The correlation between grain orientation and the resulting directional properties in polycrystalline metals has received little attention. This lecture presents the structures or textures that were observed in cold-rolled and annealed high purity and commercial aluminum sheet, and in a heat treated high strength aluminum alloy extrusion, and correlates these textures with directional mechanical properties. First, before attempting to explain these behaviors, it seems advisable to briefly review some of the fundamental mechanisms causing the variations in directionality of grain arrangement, working characteristics and mechanical properties in wrought and annealed products.

The crystals that compose a metal or alloy actually deform in a very complicated manner. Their external appearance does not disclose the internal rearrangement that occurs. Etching, however, often reveals that the crystals of a wrought metal or alloy do not have the random orientation that would be expected in a completely disordered structure. A large proportion of the etched crystals reflect in nearly the same manner, suggesting that a more or less parallel or preferred orientation of the grains exists. This is the result of a so-called crystallographic fiber structure.

Preferred orientation of cold-worked metals is produced by the following mechanism: the orientation of a single crystal in the form of a rod may be characterized in a simple way by the angles between the directions of the principal stresses and some important crystal planes or directions, such as the active slip plane and slip direction. During deformation in tension, the slip planes and slip direction gradually

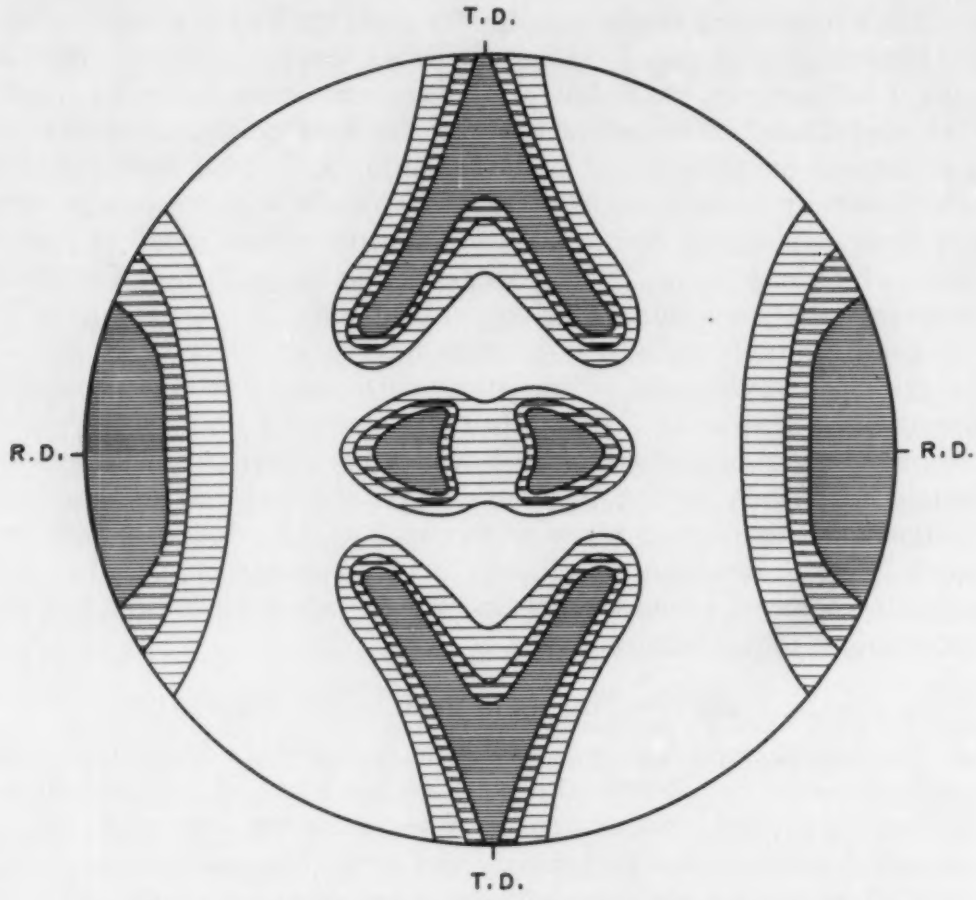


Fig. 1—{111} Pole Figure Showing Preferred Orientations of Grains in High Purity Aluminum Sheet Cold-rolled 98% Reduction (rolling texture).

approach the rod axis or direction of tension, disregarding the original orientation. Thus, differently oriented crystals tend to assume a common orientation during drastic working in a specific direction. A similar though more complex process occurs in any grain of a polycrystalline metal during cold deformation.

The result is a more or less completely preferred orientation of the crystals in any deformed crystalline material. The type of orientation depends mainly on the type of the crystal lattice of the metal and the deformation or working process. Most types of preferred orientation are derived from deformation by tension or by compression, or by a combination of the two. An example of the latter is the rolling texture in aluminum sheet, the pole figure of which is illustrated in Fig. 1. The orientation is determined exclusively by the type and degree of the strain and the resulting grain flow. The numerous investigations on this subject, however, have shown that the preferred orientation of each metal varies considerably with the specific conditions of working.

Industrial annealing processes usually destroy a preferred grain arrangement (deformation texture) in most metals and alloys. How-

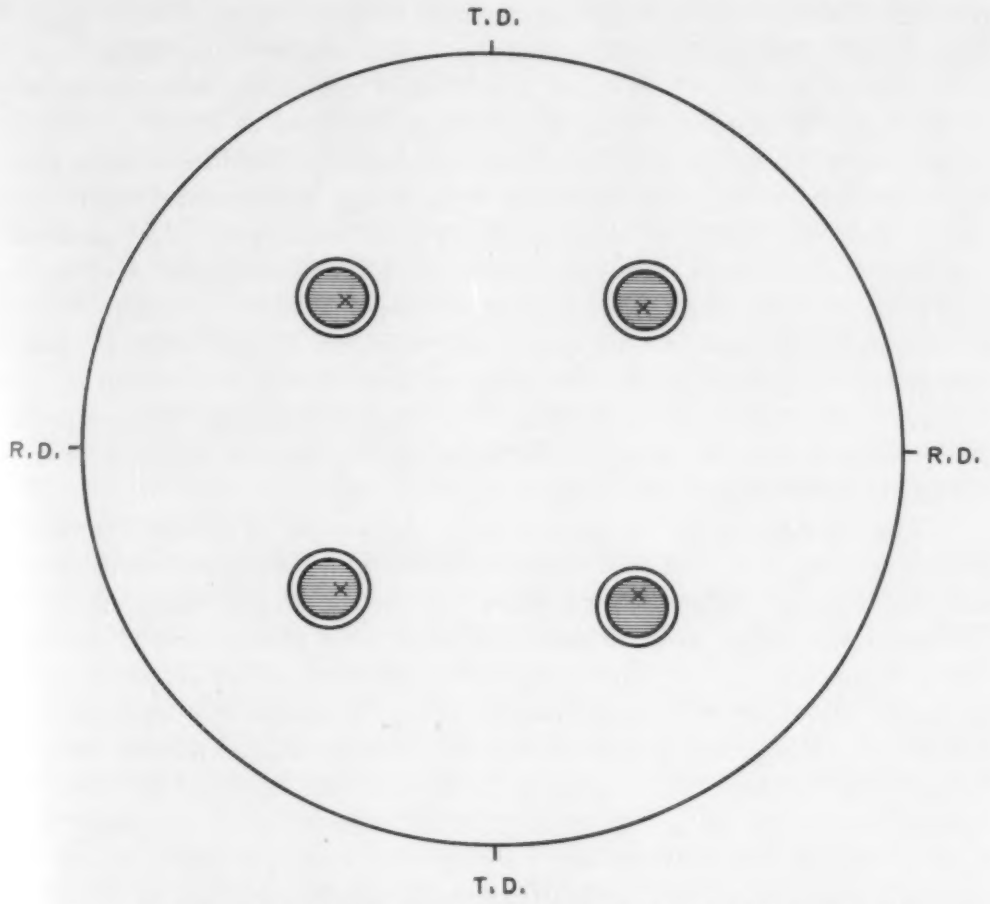


Fig. 2—{111} Pole Figure Representing Preferred Orientations of Grains in High Purity Aluminum Sheet Cold-rolled 98% Reduction and Annealed 1 hour at 1200 °F (650 °C) (recrystallization texture).

ever, in some cases a combination of drastic reductions and high annealing temperatures results in a more perfected preferred orientation (recrystallization texture) that can be produced by any working process. The pole figure of the recrystallization texture characteristic of cold-rolled heavily reduced aluminum sheet that has been annealed is represented in Fig. 2.

Under certain manufacturing conditions, wrought products of pure metals and alloys are obtained with pronounced directional characteristics in tensile strength, elongation and other properties. Generally a sheet is desired with uniform properties in all directions, but there are applications where the presence of preferred orientation or directional properties is a distinct advantage. It has been demonstrated, for example, that certain preferred orientations are of definite benefit in accomplishing difficult deep draws of steel sheet in the automobile industry. In the case of longitudinally stressed members, such as rod, bar and wire, it is desirable to obtain maximum strength in the longitudinal di-

rection. The existence of a preferred orientation which imparts desired directionality to the strength of the metal is obviously beneficial.

The most marked effect of directionality in sheet is the formation of ears during deep drawing. Ears are projections of metal at specific locations on the flange of a drawn cup, caused by nonuniform metal flow. The occurrence of ears increases trim scrap, and a sheet with pronounced directionality is more liable to crack or wrinkle during drawing than a sheet with random properties. Excessive earing may interfere with smooth operation in a complex multiple draw operation where provision for trimming is normally not required. Even today, when the conditions conducive to ear formation and methods of prevention are known, difficulties of this type are frequent. Consequently, a number of investigations have been conducted to determine the relation of earing to manufacturing conditions.

The directionality in mechanical properties of sheet originates from the characteristics of the individual crystals, which possess different properties in different directions. The properties of sheet, as-rolled or annealed, appear to be determined mainly by the preferred orientation of the grains or crystallographic fibering. Furthermore, in a wrought metal certain constituents and inclusions are aligned and cavities are elongated in the direction of the principal strain, thereby constituting a mechanical fibering. This condition may persist after recrystallization and may influence to some extent the directional properties of sheet. The directionality in bending characteristics, which increases considerably with progressive strain hardening, is probably caused mainly by the mechanical fibering. Annealed strips generally can be bent equally well in all directions; whereas hard-rolled metals fracture more readily when the bending axis is parallel to the direction of rolling. Also, the properties of forgings in different directions depend more on the mechanical than the crystallographic fibering. The properties of magnesium alloy forgings are, however, appreciably affected by the preferred orientation.

Other physical properties of commercial metal sheet, such as the elastic modulus, may also vary with the direction of testing, as has been observed for copper and iron. All properties of noncubic metals, such as zinc, even when fine-grained, show considerable variation in different directions.

Preferred Orientation and Directional Properties in Aluminum Sheet

Two grades of aluminum were used in this investigation. One was high purity aluminum (99.986) containing 0.004% silicon, 0.004% iron, and 0.006% copper. The other was commercial aluminum (99.29) containing 0.7% iron, 0.11% silicon, and 0.01% copper. Both contained spectroscopic traces of other elements.

In investigating the effects of plastic deformation and recrystallization on grain orientation, it is, of course, desirable to start with metal having a random orientation of the grains, i.e., isotropic slab. Inasmuch as slab produced by ordinary commercial operations is usually not entirely isotropic, a method was developed for the high purity aluminum which would produce 0.5 inch thick isotropic slab from 1.0 thick cold-rolled plate. The procedure used was as follows: the 1.0 inch thick cold-rolled slab was annealed two hours at 1110 °F (600 °C) and then given a series of three reductions (approximately 20% each) in thickness with two intermediate anneals and a final anneal of two hours at 750 °F (400 °C). The rolling direction during each of the 20% reductions was perpendicular to the preceding rolling direction. This procedure yielded 0.5 inch thick annealed slab which was shown to be isotropic by structure integrating X-ray diffraction patterns and mechanical property tests.

In the case of the commercial purity aluminum it was sufficient to anneal the 1.0 inch thick cold-rolled slab 2 hours at 750 °F (400 °C) to obtain an essentially random orientation as determined by structure integrating patterns. However, in order to have a direct comparison between high purity and commercial purity sheet, some of this commercial purity 1.0 inch thick slab was rolled and annealed in exactly the same manner as was the high purity slab, and comparable 0.5 inch thick isotropic slab was produced.

A description of the fabrication of the various lots of sheet aluminum included in this investigation follows:

1. High purity sheet 0.01 inch thick, cold-rolled directly from 0.5 inch thick isotropic slab (98% reduction).
2. High purity sheet 0.01 inch thick, cold-rolled directly from 0.5 inch thick isotropic slab (98% reduction) and annealed 1 hour at 1200 °F (650 °C).
3. High purity sheet 0.01 inch thick, cold-rolled from 0.5 inch thick isotropic slab, in a series of four approximately 60% reductions (all in same direction) with intermediate anneals of 16 hours at 570 °F (300 °C) between each reduction, and a final anneal of 71 hours at 525 °F (275 °C).
4. Commercial purity sheet 0.032 inch thick, cold-rolled directly from 1.0 inch thick isotropic slab (96.8% reduction). This sheet was used for the mechanical property tests.
5. Commercial purity sheet 0.01 inch thick, cold-rolled directly from 0.5 inch thick isotropic slab (98% reduction).
6. Commercial purity sheet 0.01 inch thick, cold-rolled from 0.5 inch thick isotropic slab in a series of four approximately 60% reductions (all in the same direction) with intermediate anneals of 2 hours at 570 °F (300 °C) between each reduction and a final anneal of 2 hours at 570 °F (300 °C).
7. Commercial purity sheet 0.009 inch thick, cold-rolled from

0.4 inch thick, hot-rolled slab with one intermediate anneal at 750 °F (400 °C).

8. Commercial purity sheet 0.009 inch thick, cold-rolled from 0.4 inch thick, hot-rolled slab with two intermediate anneals at 750 °F (400 °C).
9. Commercial sheet 0.009 inch thick, cold-rolled from 0.4 inch thick hot-rolled slab with three intermediate anneals at 750 °F (400 °C). Items 7, 8 and 9 were used for the deep drawing or earing tests.

A "structure integrating" X-ray diffraction camera (1)[1] designed to average out local differences and to determine the preferred orientation in coarse-grained as well as fine-grained metal, was used in the investigation. A large specimen (2.0 x 6.0 x 0.006 inches) is mounted in a holder between the pinhole and the film cassette. The specimen holder is moved horizontally across the ways. At each end of the horizontal path of the specimen holder, wedge-shaped stops are provided which index the specimen up approximately the width of the X-ray beam and at the same time throw a toggle switch which reverses the motor to move the specimen holder in the opposite direction. In this manner the entire specimen contributes to the pattern: therefore, a good average of the distribution of grain orientations is obtained. The specimen holder can also be set at various angles. The total angular movement about the vertical axis is 30 degrees (15 degrees each side of center), while about the horizontal axis the rotation can be as much as 70 degrees one side of center. At angular settings of the specimen greater than 15 degrees about the horizontal axis, the specimen frame interferes with the film cassette: therefore, a smaller specimen (0.75 x 6.0 x 0.006 inches) was utilized. The small specimen frame was not capable of mechanical indexing, so that scanning was accomplished by occasional manual adjustment.

For the construction of pole figures, X-ray diffraction patterns were prepared at 5 degree intervals up to 15 degrees about the vertical axis and up to 70 degrees about the horizontal axis. All the X-ray patterns were made with unfiltered copper K-radiation and a specimen-film distance of 3 centimeters. The pole figures were constructed with a Wever (2) chart. Four degrees of darkening in the Debye-Scherrer circles were identified visually and are indicated on the pole figures by characteristic shading. It is, of course, recognized that the spectrometer method of determining preferred orientation is more quantitative than that employed in this work, where the objective is the qualitative relationship between type of grain orientation, directional properties and applied deformation stress.

For the tensile tests on the 0.032 inch thick commercial purity sheet (Item 4) standard specimens (3) were tested in an Amsler machine equipped with self-aligning grips (4). The yield strength was

[1] The figures appearing in parentheses pertain to the references appended to this lecture.

determined from the stress-strain curve drawn by an electrically recording extensometer (5).

Cups 0.38 inch high by 0.70 inch in diameter were deep drawn from blanks 1.34 inch in diameter of the 0.009 inch thick sheet of commercial purity (Items 7, 8, 9) and the earing characteristics of the samples determined.

Pole Figures

The preferred orientations, developed in severely cold-rolled (98% reduction) high purity aluminum sheet 0.01 inch thick, are shown in Fig. 1. This pole figure is not entirely explained by any single or combination of ideal textures which have been published. However, it duplicates the original pole figure of as-rolled 99.5% purity aluminum sheet presented by Wever (6) and subsequently confirmed by other investigators (7).

Complete pole figures were not constructed for the as-rolled commercial purity aluminum sheet 0.032 inch and 0.01 inch thick (Items 4 and 5). However, a sufficient number of structure integrating X-ray diffraction patterns were prepared to establish that the preferred orientations in these two lots of sheet were essentially identical with those in the as-rolled high purity sheet (Fig. 1).

The high purity aluminum sheet 0.01 inch thick, which was cold-rolled (98% reduction) and then annealed 1 hour at 1200 °F (650 °C), was characterized by a preferred orientation illustrated in Fig. 2. This pole figure shows an almost perfect cube texture with {001} in the plane of rolling and <001> in the direction of rolling. This texture was predicted by Schmid and Wasserman (8) on the basis of a structure similar to that which is to be described in the next paragraph, and has since been observed by numerous investigators (9). The perfection of this texture is as high as was developed in the case of annealed copper (10).

A less perfect recrystallization texture, reproduced in Fig. 3, was obtained from the high purity aluminum sheet which was cold-rolled through a series of four approximately 60% reductions with intermediate annealing treatments of sixteen hours at 570 °F (300 °C) between each reduction, and a final anneal of seventy-one hours at 525 °F (275 °C). Essentially identical results were obtained from this metal when the final annealing treatment was performed at various temperatures up to and including 930 °F (500 °C). Furthermore, the commercial purity sheet (Item 6), fabricated in the same way, also possessed the same final preferred orientation.

The commercial purity sheet, which was cold-rolled from 0.4 inch thick, hot-rolled slab to 0.009 inch thick sheet with one intermediate anneal at 750 °F (400 °C) (Item 7) had a structure represented by Fig. 4. This pole figure exhibits a definite predominance of the rolling texture type of preferred orientation.

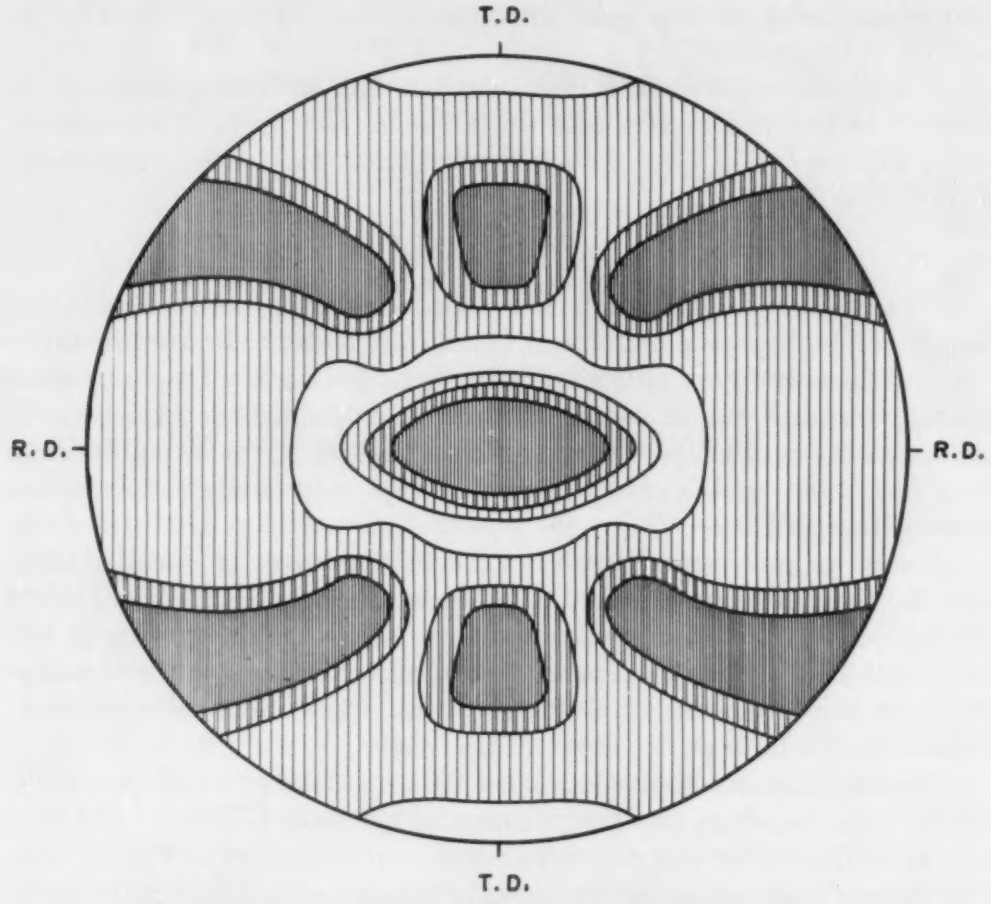


Fig. 3—{111} Pole Figure Showing Preferred Orientations of Grains in High Purity Aluminum Sheet Cold-rolled Through a Series of Four Approximately 60% Reductions with Intermediate Anneals of 16 hours at 570 °F (300 °C) Between Each Reduction and a Final Anneal of 71 Hours at 525 °F (275 °C) (recrystallization texture).

The preferred orientations developed in commercial purity sheet which was cold rolled from 0.4 inch thick, hot-rolled slab to 0.009 inch thick sheet with two intermediate anneals at 750 °F (400 °C) (Item 8) are illustrated in Fig. 5. This pole figure reveals a mixture of both rolling and recrystallization textures, both types being fairly well developed.

The commercial purity sheet cold-rolled from 0.4 inch thick hot-rolled slab to 0.009 inch thick sheet with three intermediate anneals at 750 °F (400 °C) (Item 9) had preferred orientations represented by Fig. 6. This pole figure also shows a mixture of the two types of textures. However, the recrystallization texture definitely predominates.

Tensile Tests

Tensile properties were determined of the commercial purity sheet which was cold-rolled directly from 1.0 inch thick isotropic slab to 0.032 inch sheet (96.8% reduction) using specimens machined with their longitudinal axes parallel, perpendicular and at 45 degrees to the direction of rolling. The results are plotted in the polar diagram of

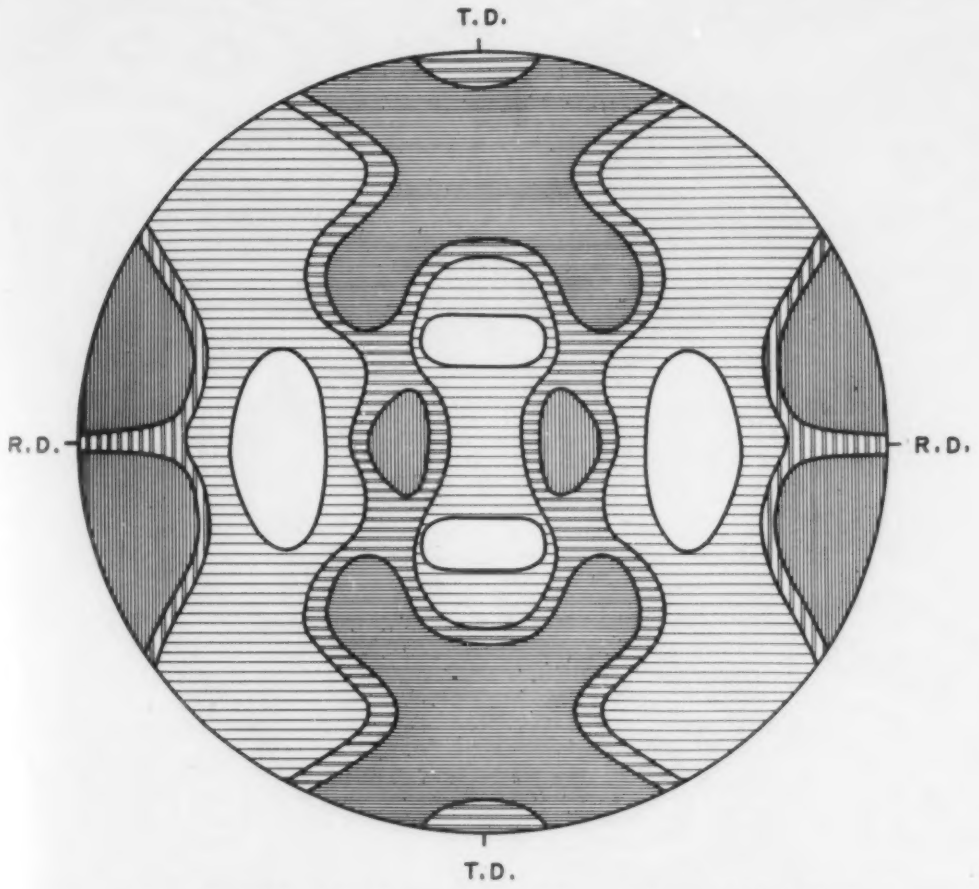


Fig. 4—{111} Pole Figure Representing Preferred Orientations of Grains in Commercial Purity Aluminum Sheet Cold-rolled from 0.4 Inch Thick Hot-rolled Slab to 0.009 Inch Thickness With One Intermediate Anneal at 750 °F (400 °C) (rolling texture predominant).

Fig. 7. As previously described, this material possessed a high degree of preferred orientation of the rolling texture type (Fig. 1). Although the tensile tests reflect the highly preferred orientations present in this sheet, preferred orientations of low degrees are not clearly indicated by tensile tests.

Deep Drawing Tests

Deep drawing tests are a sensitive mechanical test of the existence and degree of preferred orientation. Consequently, small cups were deep drawn from samples of the commercial purity 0.009 inch aluminum sheet, the preferred orientations of which are represented in Figs. 4, 5 and 6. Photographs of these cups are reproduced in Fig. 8. It is apparent that the earing tendencies of these three lots of aluminum sheet are related to the preferred orientations. The sheet, which had a high degree of rolling texture type of preferred orientation (Fig. 4), developed ears at 45 degrees to the rolling direction. The metal, which possessed a mixture of the two types of textures, rolling and recrystallization (Fig. 5), developed ears parallel, normal, and at 45 degrees to

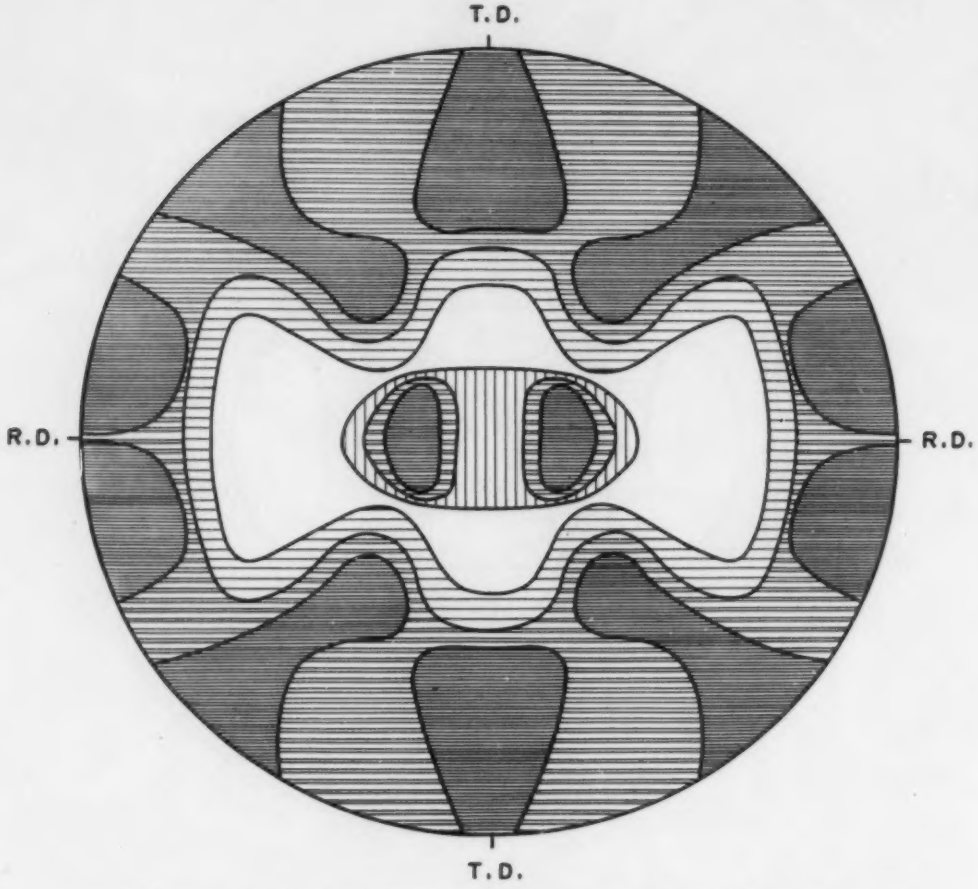


Fig. 5—{111} Pole Figure Showing the Preferred Orientations of Grains in Commercial Purity Aluminum Sheet Cold-rolled from 0.4 Inch Thick Hot-rolled Slab to 0.009 Inch Thickness With Two Intermediate Anneals at 750 °F (400 °C) (mixture of rolling and recrystallization textures).

the direction of rolling. Finally, the sheet which showed a predominance of the recrystallization texture (Fig. 6), developed ears parallel and perpendicular to the direction of rolling. These relations between preferred orientation and earing tendencies of sheet have been previously recognized. However, no complete explanation of these relationships has been developed.

Correlation of Preferred Orientation with Directional Properties

It is generally recognized that plastic deformation in metal crystals is primarily accomplished by means of slip along specific crystallographic planes and in certain crystallographic directions. There have been many publications correlating the resolved shear stresses on slip planes and in slip directions with the mechanical behaviors of single crystals. However, similar relations for polycrystalline metals and alloys have received little attention. It is the objective of this section to make these correlations and to explain, in a qualitative manner, the

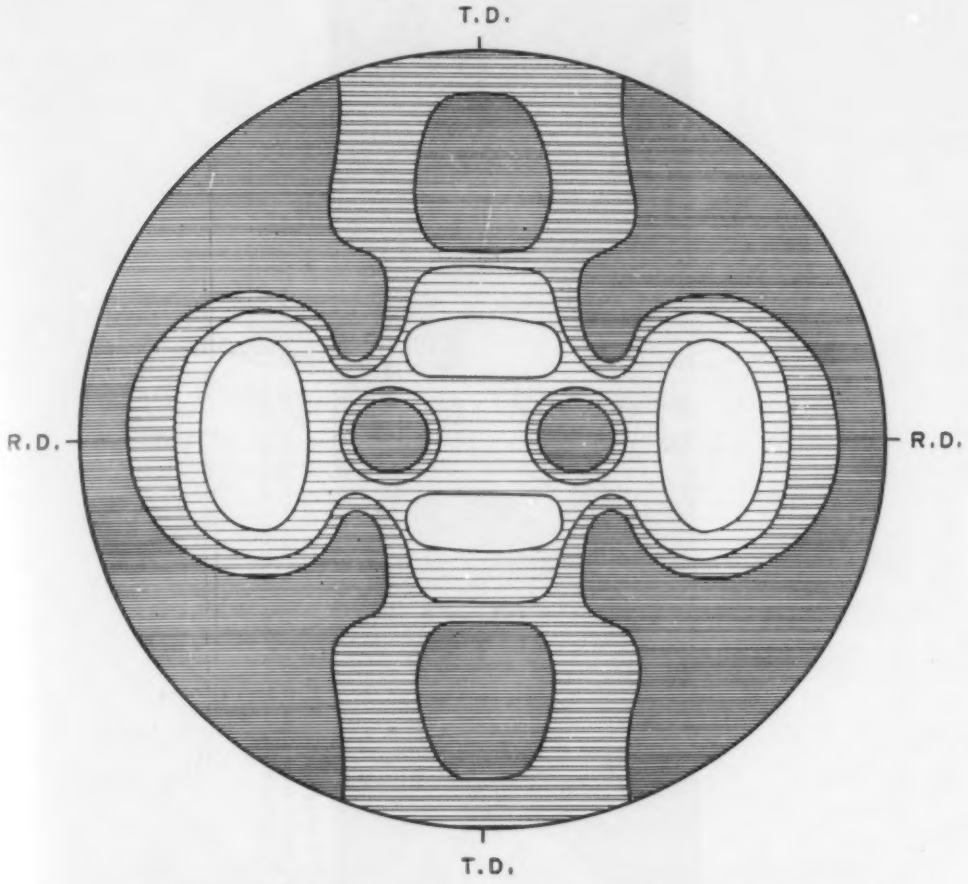


Fig. 6—{111} Pole Figure Representing the Preferred Orientations of Grains in Commercial Purity Aluminum Sheet Cold-rolled from 0.4 Inch Thick Hot-rolled Slab to 0.009 Inch Thickness With Three Intermediate Anneals at 750 °F (400 °C) (recrystallization texture predominant).

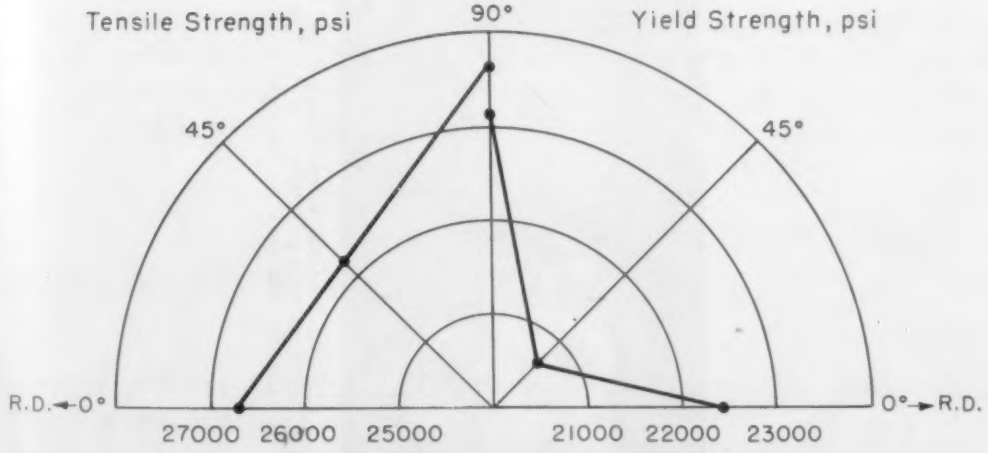


Fig. 7—Results of Tensile Tests on Commercial Purity Sheet Cold-rolled Directly from 1 Inch Thick Isotropic Slab to 0.032 Inch Thickness (96.8% reduction). Specimens were selected with longitudinal axes parallel, at 45 degrees and normal to the rolling direction.

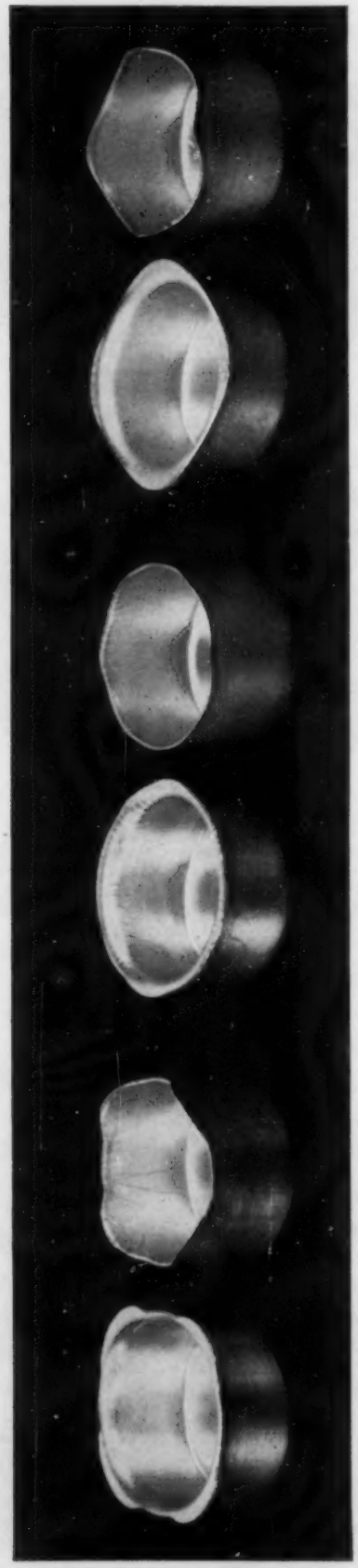


Fig. 8—Cups Deep Drawn From Three Lots of Commercial Purity Sheet. The cups on the left are from the lot which had a high degree of rolling texture (Fig. 4). The middle cups are from the sheet which possessed a mixture of rolling and recrystallization textures (Fig. 5). The cups on the right are from the lot which showed a predominance of the recrystallization type (Fig. 6).

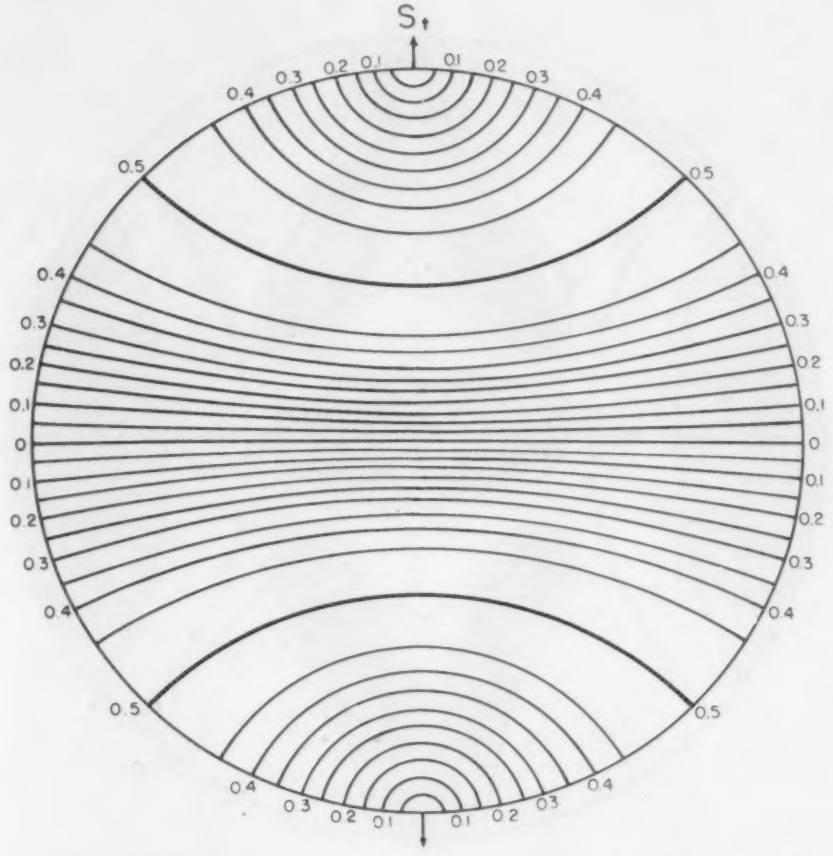


Fig. 9—Stereographic Projection Illustrating the Orientation Dependence of Magnitude of Resolved Shear Stress in Planes Inclined at Various Angles to the Axis of a Principal Stress.

directional properties and earing tendencies observed in aluminum sheet.

A tensile force applied in a specific direction to any material may be resolved into two components—one, a shearing force parallel to a plane inclined to the direction of the externally applied force, and the other, a tensile force normal to the same plane. If F_t is the externally applied tensile force, F_s the shearing force parallel to a plane forming an angle α with the direction of the applied tensile force, and F_n the force normal to this same plane, then the following relations obtain:

$$(F_t)^2 = (F_s)^2 + (F_n)^2 \qquad \text{Equation 1}$$

$$F_s = F_t \cos \alpha \qquad \text{Equation 2}$$

$$F_n = F_t \sin \alpha \qquad \text{Equation 3}$$

The applied tensile stress

$$S_t = \frac{F_t}{A} \qquad \text{Equation 4}$$

where A is the cross sectional area subjected to the tensile stress. Likewise, the shear stress

$$S_s = \frac{F_s}{A'} \qquad \text{Equation 5}$$

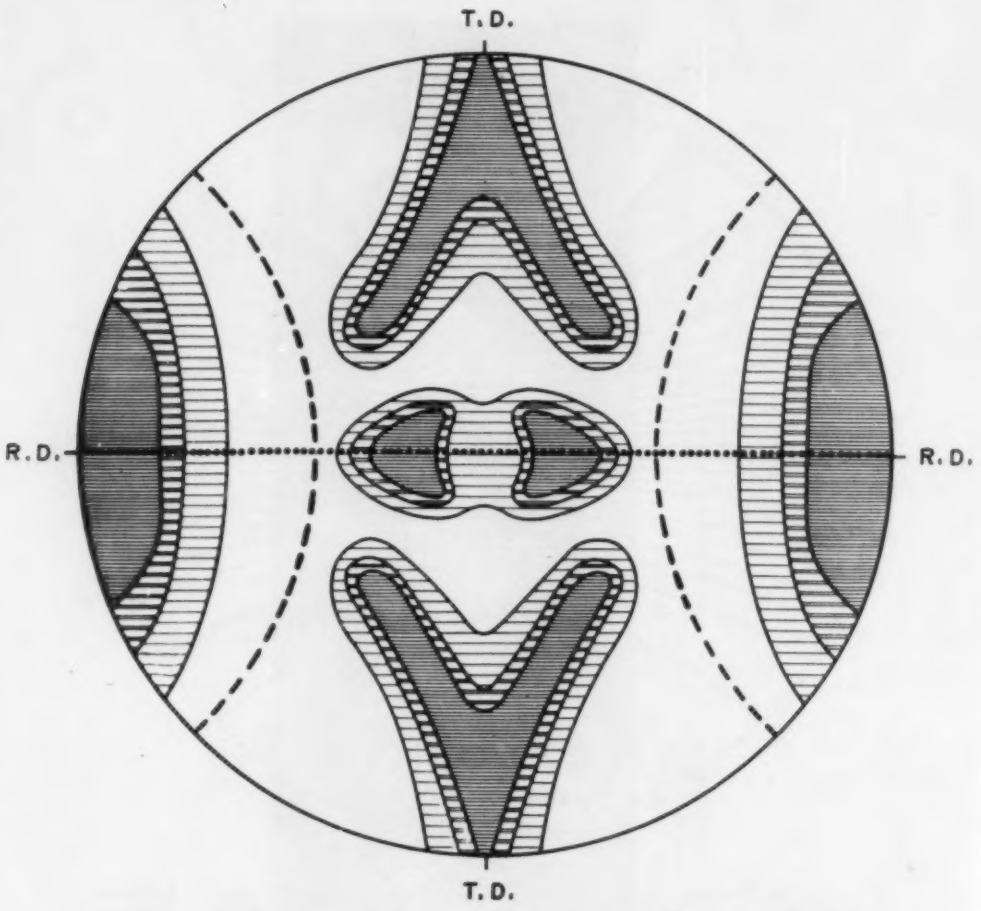


Fig. 10—The Superposition of the {111} Pole Figure Typical of the Rolling Texture (Fig. 1) and the Pole Figure of Maximum Resolved Shear Stress Planes When the Principal Stress is Applied Parallel to the Rolling Direction (R.D.). Loci of poles of maximum resolved shear stress planes are dashed and tension stress or axis dotted.

where A′ is the area of the plane to which the shear stress is parallel. The relation between these two areas is as follows:

$$A' = \frac{A}{\sin \alpha} \qquad \text{Equation 6}$$

Substituting Equations 4, 5 and 6 in Equation 2 results in the equation:

$$\frac{S_s A}{\sin \alpha} = S_t A \cos \alpha \qquad \text{Equation 7}$$

or $$S_s = S_t \sin \alpha \cos \alpha \qquad \text{Equation 8}$$

or $$S_s = S_t \frac{\sin 2\alpha}{2} \qquad \text{Equation 9}$$

From this latter equation, it may be seen that the shear stress is maximum when the angle α is equal to 45 degrees. Under these conditions, the shear stress is equal to one-half of the tensile stress.

Stereographic projection can be utilized to represent the distribution of shear stresses on all planes located in space. In Fig. 9, the latitude lines represent contours of maximum shear stress, i.e., all planes whose

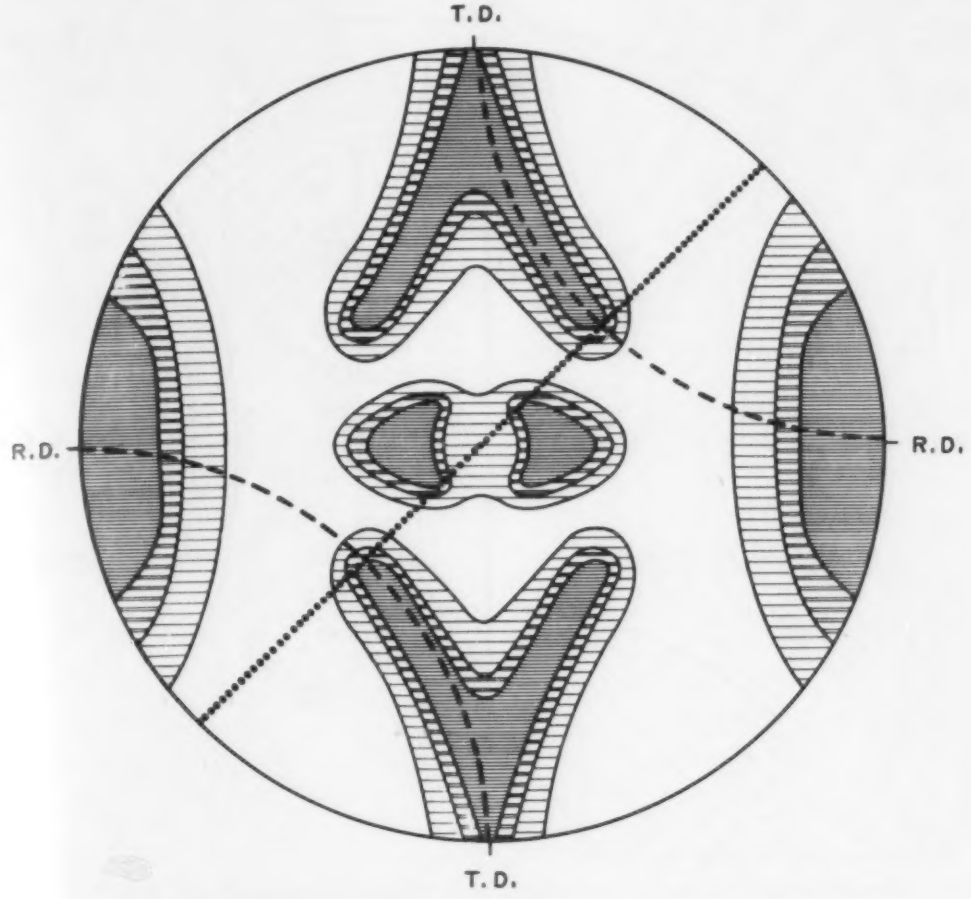


Fig. 11—Similar to Fig. 10 Except That the Principal Stress is Applied at 45 degrees to the Rolling Direction.

poles lie on the same latitude line have the same maximum shear stress.

By analogy with the behavior of single crystals, it would seem that when in a polycrystalline metal a large number of grains are so oriented that slip planes are parallel to maximum resolved shear stresses, plastic flow would occur with a relatively low applied tensile stress; and as the number of grains so oriented decreases, the tensile stress required to cause plastic flow would increase. The relative number of grains oriented with slip planes parallel to maximum resolved shear stresses, in tensile specimens selected at various angles to some reference line in a sheet, may be qualitatively estimated by superimposing the pole figures of maximum resolved shear stresses and slip planes so that the tensile axes coincide.

In Figs. 10, 11 and 12, the superpositions were made so that the tensile axis of that specimen was oriented, respectively, parallel at 45 degrees and perpendicular to the rolling direction for heavily cold-rolled aluminum sheet exhibiting a high degree of rolling texture (Fig. 1). The tensile specimen oriented with its longitudinal axis parallel to the rolling direction (Fig. 10) exhibits a low degree of

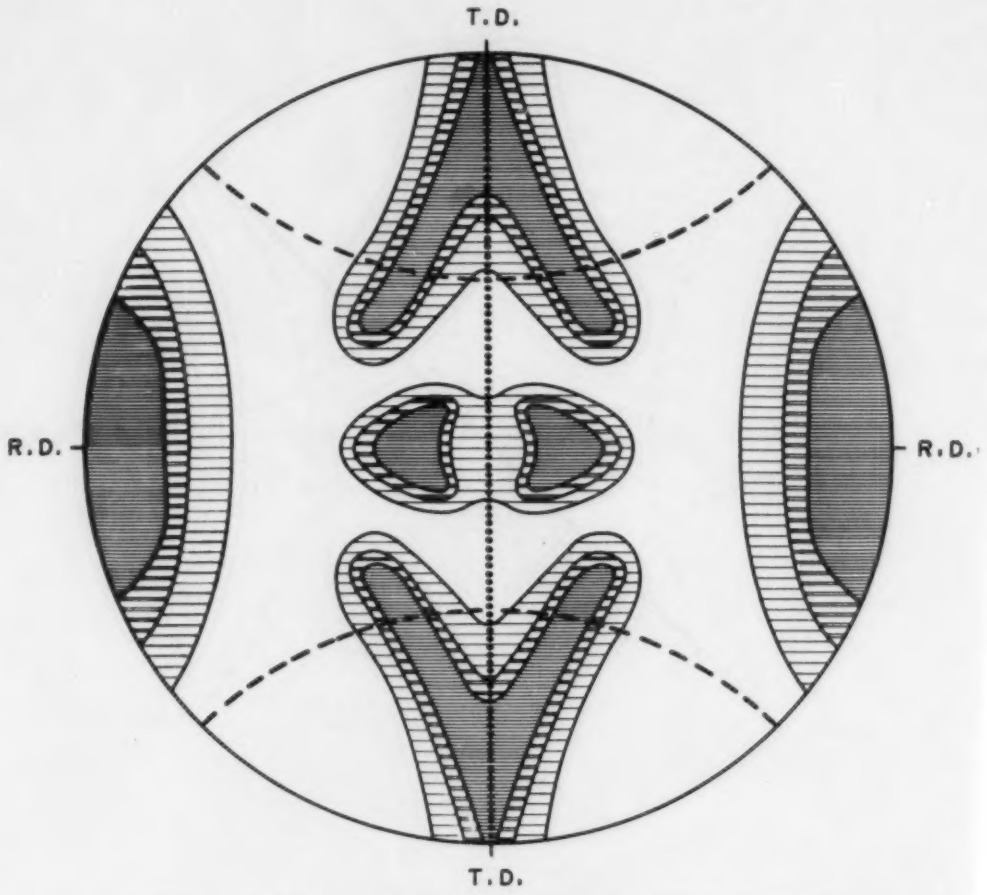


Fig. 12—Similar to Figs. 10 and 11 Except That the Principal Stress is Applied Perpendicular to the Rolling Direction.

coincidence between maximum resolved shear stresses and {111} slip planes. As a result, this specimen would have a relatively high yield strength. For the case where the tensile specimen axis is at 45 degrees to the rolling direction (Fig. 11), a very high degree of coincidence is obtained and, therefore, such a specimen would have a relatively low yield strength. Finally, in the case where the tensile specimen axis is perpendicular to the rolling direction (Fig. 12) the degree of coincidence is again low and a relatively high yield strength would be expected.

It may be observed that the expected results of this correlation are in good agreement with the experimental results of Fig. 7, for the specimens machined from the 0.032 inch thick cold-rolled (96.8% reduction) commercial purity aluminum sheet which had a high degree of rolling texture. The only apparent discrepancy seems to be that the correlation would indicate a somewhat higher yield strength for the specimens parallel to the rolling direction than for those perpendicular to the rolling direction. However, the test results were in the reverse order. This difference is probably attributable to mechanical fibering

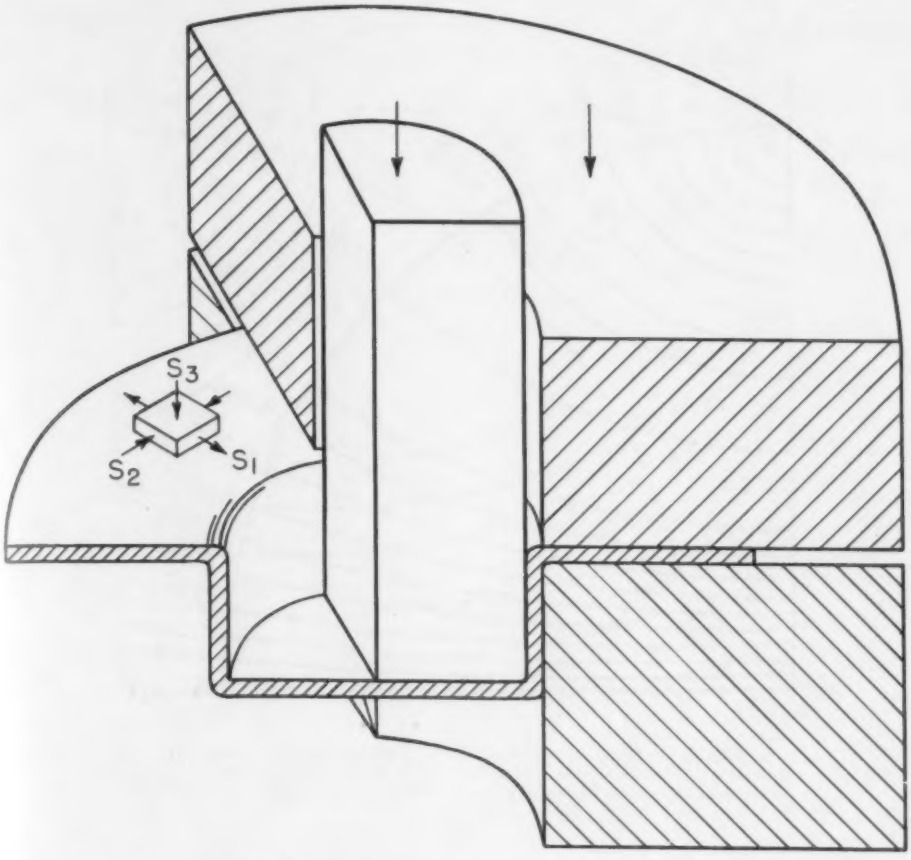


Fig. 13—Schematic Representation of Deep Drawing of Cylindrical cup:
S_1 = radial tensile stress
S_2 = tangential compressive stress
S_3 = normal compressive stress

(i.e., lined-up insoluble constituents, grain elongation, etc.), which would tend to produce a higher yield strength in the transverse direction rather than parallel to the rolling direction.

During deep drawing of a cup from sheet, a more complex stress system is encountered. Fig. 13 represents schematically a cup partially drawn from a circular blank. The directions of the three principal stresses on a small element in the outer rim are indicated. These principal stresses are: S_1—radial tensile stress, S_2—tangential compressive stress, and S_3—normal compressive stress. In the general case, where a plane is inclined to the axes of the three principal stresses, the maximum resolved shear stress in this plane can be calculated from the equation (11):

$$S_s^2 = S_1^2l^2 + S_2^2m^2 + S_3^2n^2 - (S_1l^2 + S_2m^2 + S_3n^2)^2$$

S_s = maximum shear stress on a plane,

S_1, S_2 and S_3 = principal stresses (tensile stress has positive sign and compressive stress has negative sign),

l, m and n are direction cosines, i.e., the cosines of the angles between the normal to the plane and the respective directions of the principal stresses.

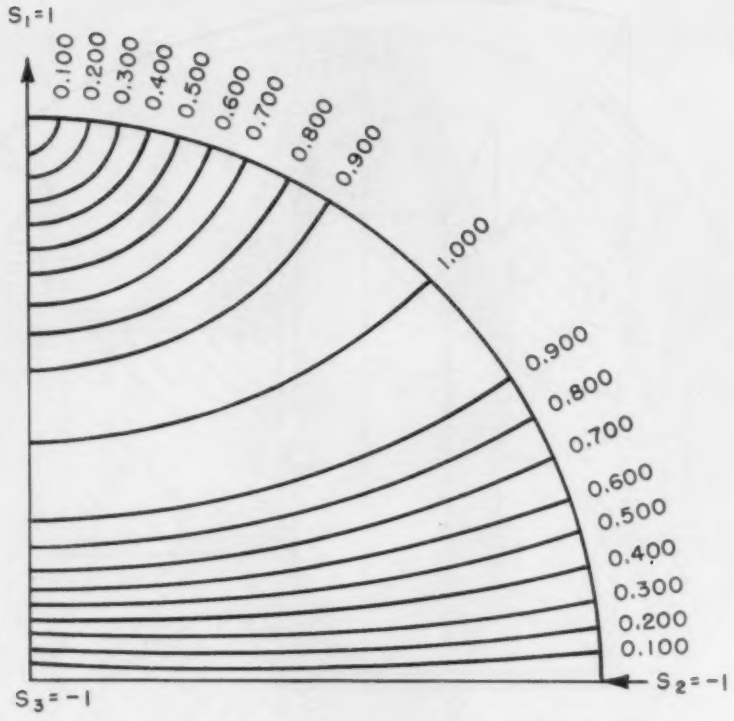


Fig. 14—One Quadrant of a Stereographic Projection of Resolved Shear Stress Contours in a Metal Subjected to Three Principal Stresses Mutually Perpendicular to Each Other, Where $S_1 = 1$ and $S_2 = S_3 = -1$.

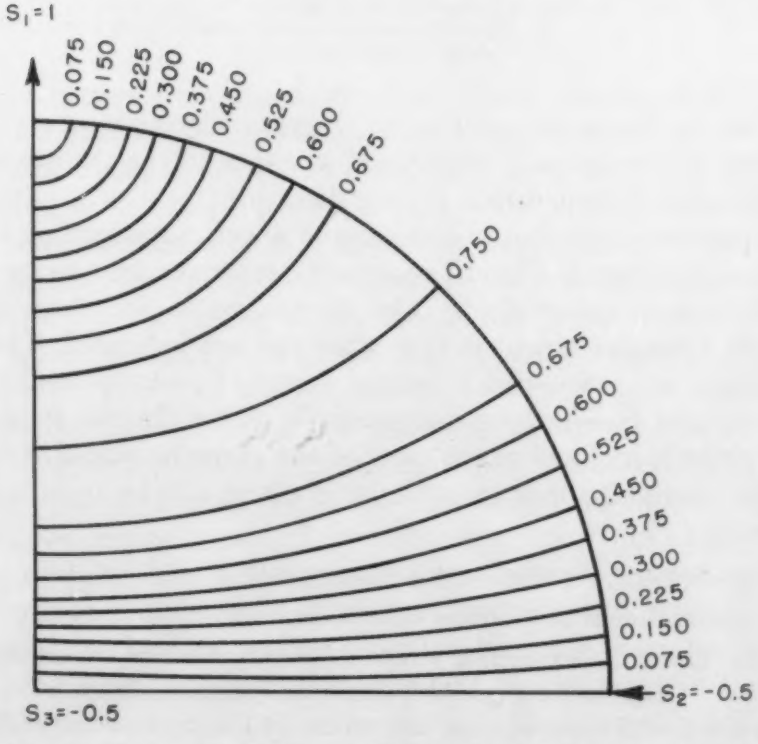


Fig. 15—Same as Fig. 14 Except That $S_1 = 1$ and $S_2 = S_3 = -0.5$.

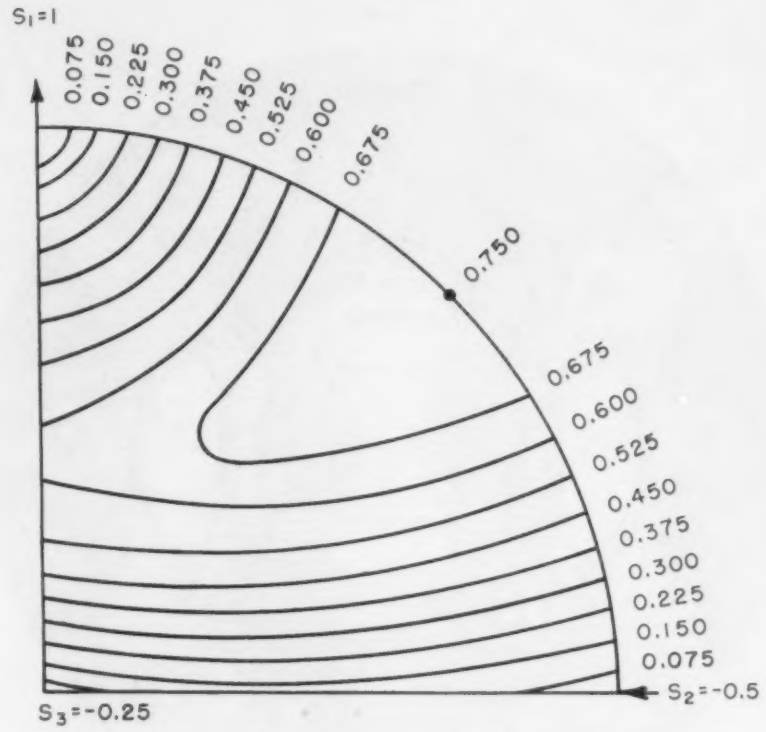


Fig. 16—Same as Figs. 14 and 15 Except That $S_1 = 1$, $S_2 = -0.5$ and $S_3 = -0.25$.

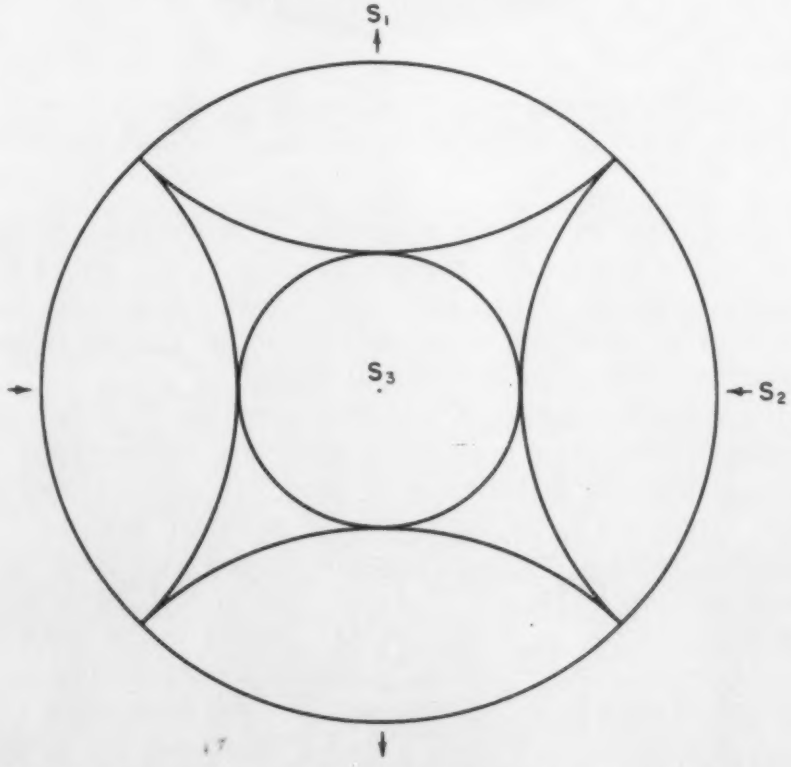


Fig. 17—Stereographic Projection of the Loci of Poles of Planes on Which Are Resolved the Maximum Shear Stresses from Three Individual Principal Stresses.

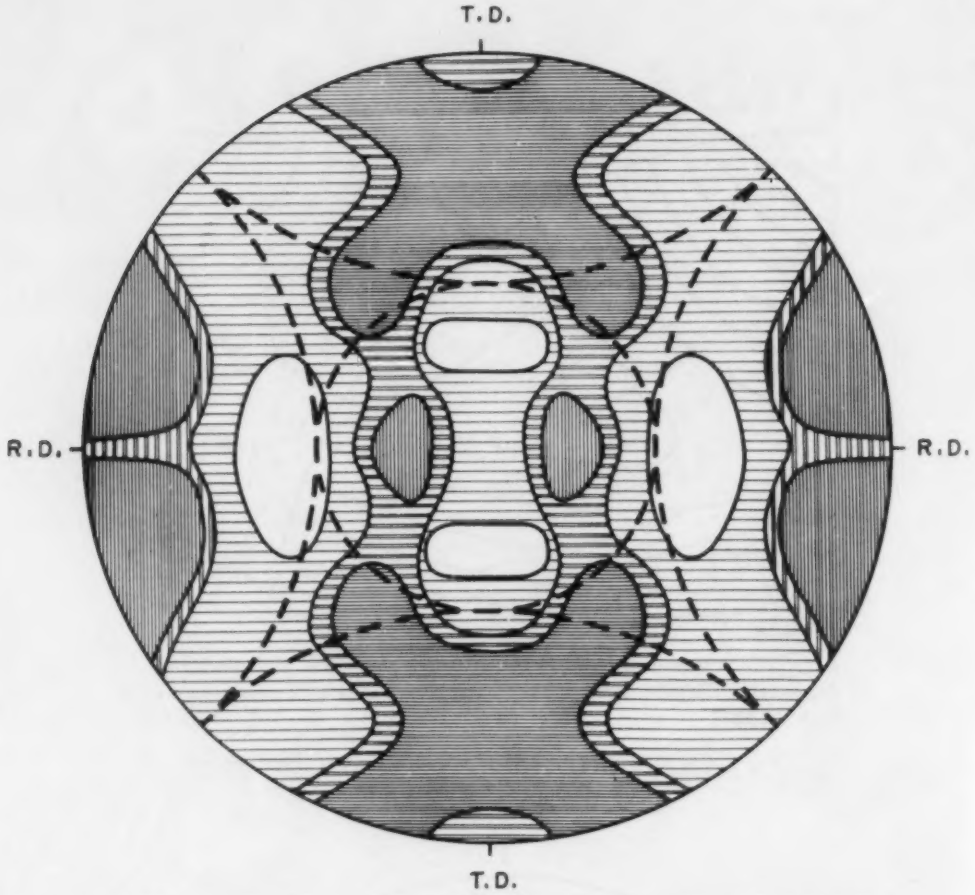


Fig. 18—The Superposition of Figs. 4 and 17 Such That for S_1 (or S_2) of Fig. 17 is Parallel to the Rolling Direction (R.D.) of Fig. 4 (rolling texture). Loci of poles of maximum resolved shear stress planes are dashed.

This equation assumes that the maximum shear stress in any plane resolved from the individual principal stresses is not collinear except in the case where the plane under consideration is parallel to one of the directions of principal stress and, therefore, normal to the plane of the other two directions of principal stress.

If the relative magnitude and the signs of the three principal stresses are known, it is possible to construct stereographic projections, representing the distribution of shear stresses on planes oriented in various directions to the three axes of principal stresses. To illustrate this, quadrants of stereographic projections were constructed and reproduced in Figs. 14,15, and 16. In the first $S_1 = 1$, $S_2 = S_3 = -1$; in the second $S_1 = 1$, $S_2 = S_3 = -0.5$; finally in the third $S_1 = 1$, $S_2 = -0.5$, and $S_3 = -0.25$. It is observed that as long as two of the principal stresses have the same sign and the same value (Figs. 14 and 15) a plot similar to that of Fig. 9 is produced. However, if the three principal stresses differ, a more complex configuration is obtained (Fig. 16).

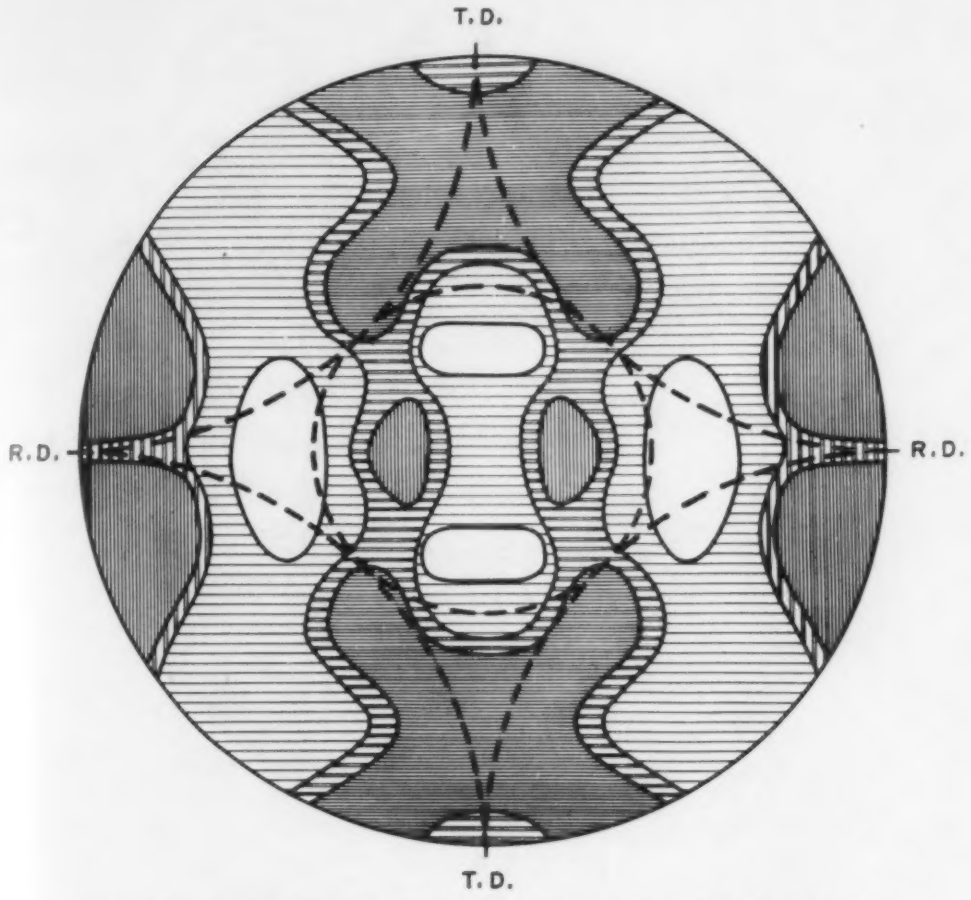


Fig. 19—The Superposition of Figs. 4 and 17 Such That S_1 of Fig. 17 Is At 45 degrees to Rolling Direction of Fig. 4 (rolling texture).

A superposition of pole figures, one representing the distribution of crystallographic slip planes in a metal, and others showing the distribution of planes having various relative values of resolved shear stress, should yield a correlation between preferred orientation and earing tendencies during deep drawing, similar to that presented for directional tensile properties.

Consider now cold-rolled aluminum sheet of commercial purity with a rolling type of preferred orientation predominant (Fig. 4). Lacking quantitative information concerning the relative values of the three principal stresses, a simplified plot of shear stresses is employed that contains only the loci of poles of planes upon which are resolved the maximum shear stresses from the individual principal stresses (Fig. 17). Further, consider only the elements near the outside of the circular blank and in positions such that their radial directions are parallel, perpendicular, and at 45 degrees to the direction of rolling.

By the superposition of Figs. 4 and 17, such that the radial tensile stress S_1 of Fig. 17 is parallel to the rolling direction (R.D.) of Fig. 4, the condition existing in an element of a circular blank parallel to the

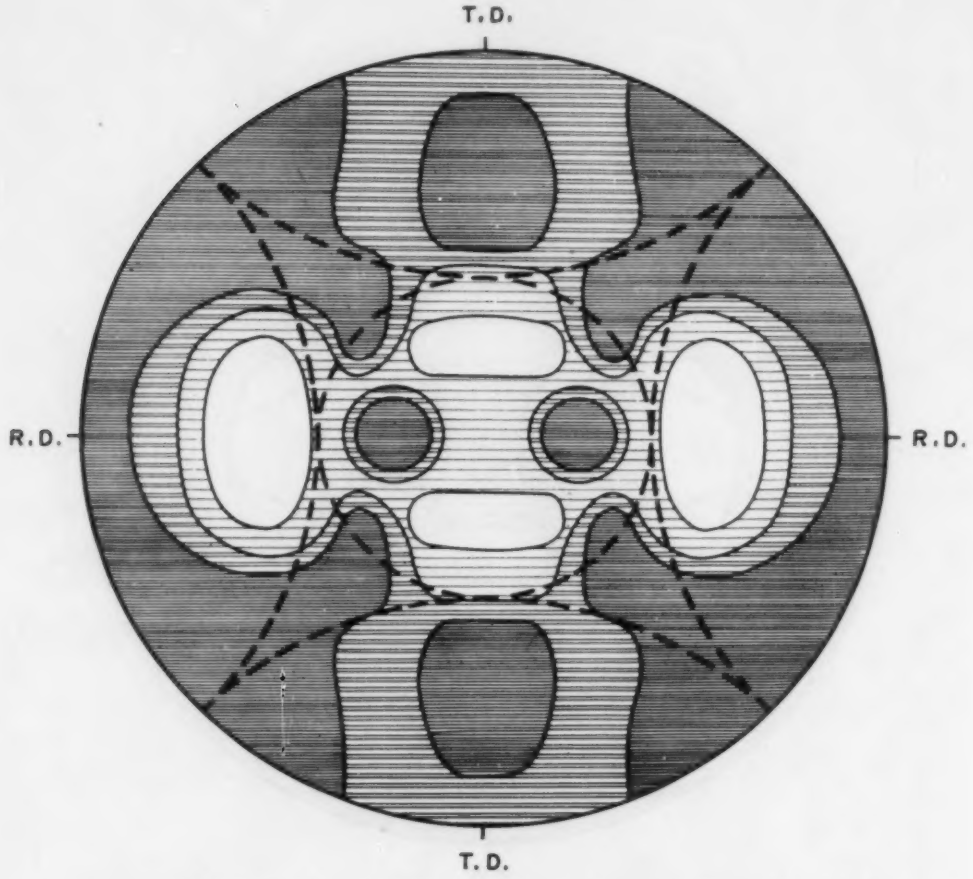


Fig. 20—The Superposition of Figs. 6 and 17 Such That S_1 (or S_2) of Fig. 17 is Parallel to Rolling Direction of Fig. 6 (recrystallization texture). Loci of poles of maximum resolved shear stress planes are dashed.

rolling direction is obtained (Fig. 18). Few crystallographic slip planes coincide with planes having maximum resolved shear stresses. Consequently, the metal in this location would be relatively resistant to plastic deformation during deep drawing.

The conditions existing in an element with its radial direction normal to the rolling direction are identical with the preceding except that the positions of S_1 and S_2 are interchanged. Again, few crystallographic slip planes coincide with planes having maximum resolved shear stresses and the metal in this location would also have a relatively high resistance to plastic deformation.

The superposition of Figs. 4 and 17, such that the radial tensile stress S_1 of Fig. 17 is at 45 degrees to the rolling direction of Fig. 4, produces the conditions occurring in an element of a cup with its radial direction 45 degrees to the rolling direction (Fig. 19). Many crystallographic slip planes coincide with planes having relatively high resolved shear stresses and, as a result, metal in these locations would have a relatively low resistance to plastic deformation during deep drawing.

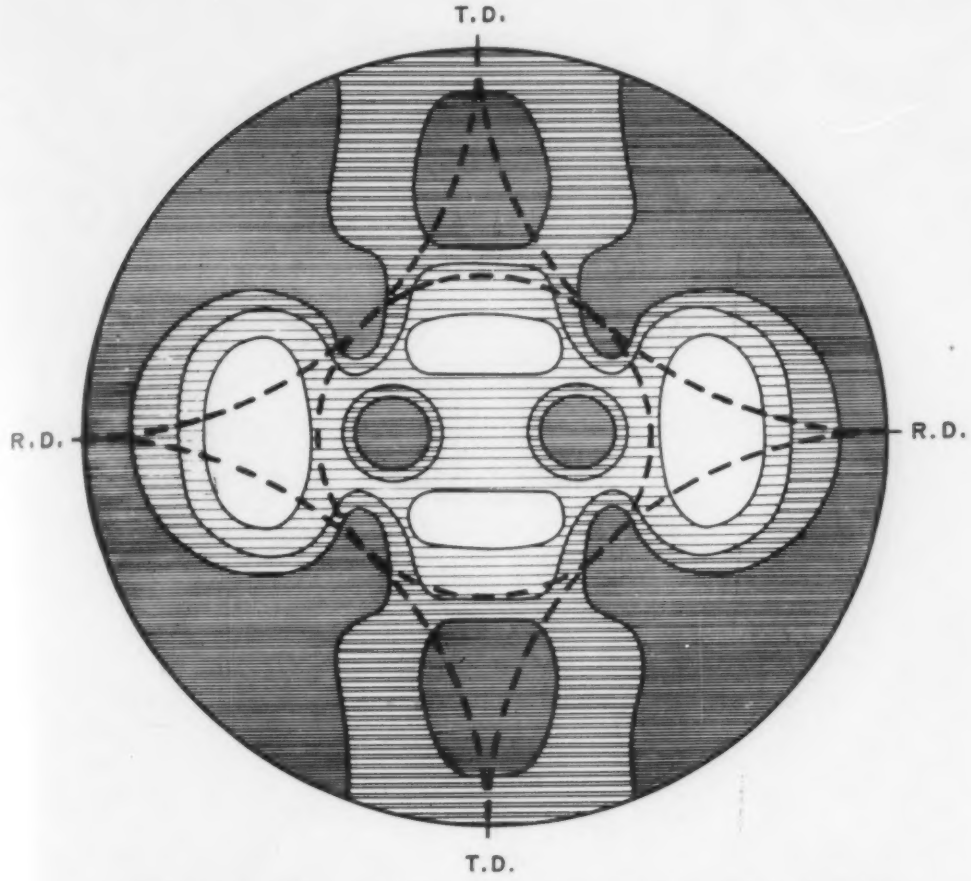


Fig. 21—The Superposition of Figs. 6 and 17 Such That S_1 of Fig. 17 is at 45 degrees to Rolling Direction of Fig. 6 (recrystallization texture).

The relations developed demonstrate that metal in the rim of a cup being deep drawn and with its radial direction either parallel or normal to the rolling direction will be relatively rigid compared to similar metal with its radial direction at 45 degrees to the rolling direction. As a consequence, the more plastic metal at 45 degrees to the rolling direction will deform more, causing ear formation in these four locations. This is consistent with the results of actual earing tests with sheet having a predominant rolling texture (Fig. 8).

The origin of ear formation in sheet with a predominant recrystallization texture can be explained in a similar manner. Figs. 20 and 21 show superpositions of the pole figure of planes having maximum resolved shear stresses (Fig. 17) on a pole figure of crystallographic slip planes in sheet of this type (Fig. 6). These figures respectively represent conditions existing in elements in the outer part of the circular blank having radial directions parallel or perpendicular, and at 45 degrees to the rolling direction. It is apparent that good coincidence between poles of slip planes and poles of planes of maximum resolved shear stress is obtained for metal in locations parallel and normal to the rolling direction. The metal at 45 degrees to the rolling direction has

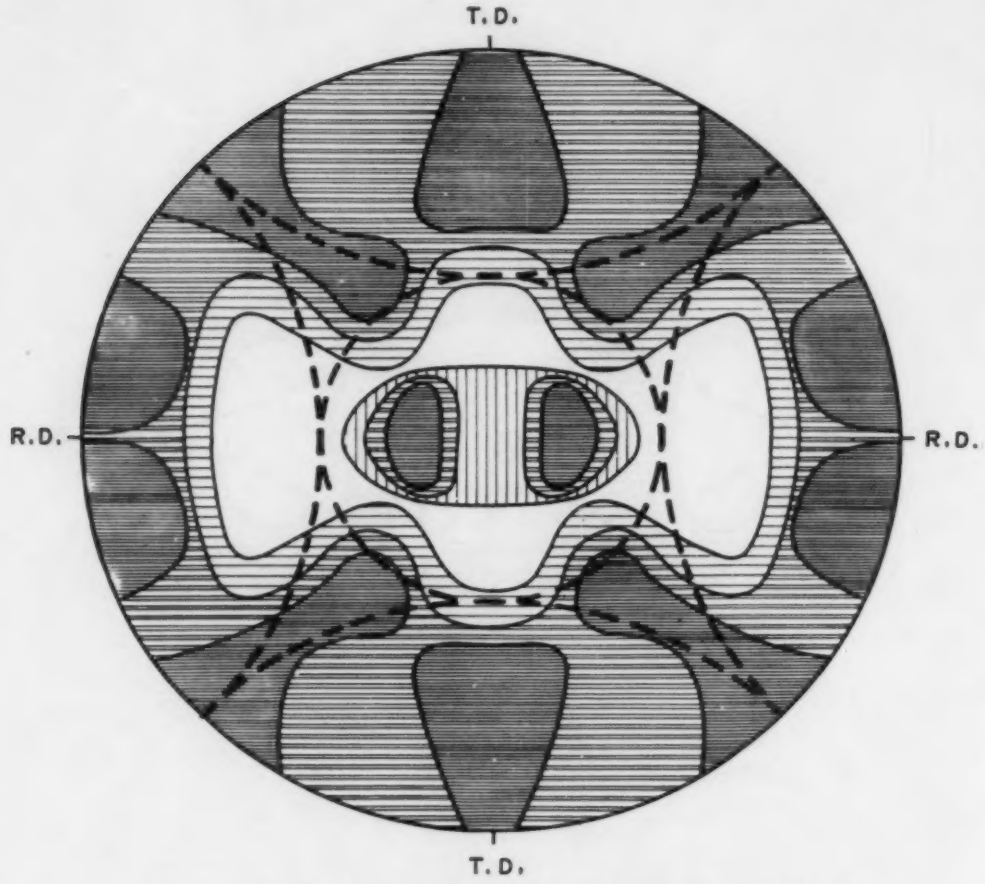


Fig. 22—The Superposition of Figs. 5 and 17 Such That S_1 (or S_2) of Fig. 17 is Parallel to Rolling Direction of Fig. 5 (mixture of rolling and recrystallization textures). Loci of poles of maximum resolved shear stress planes are dashed.

relatively poor coincidence. Following the same reasoning, this metal with a prevailing recrystallization texture will form ears in locations parallel and at right angles to the direction of rolling.

When pronounced rolling and recrystallization textures exist in sheet simultaneously and in approximately equivalent quantities (Fig. 5) directional flow occurs during deep drawing such that eight ears will form—two parallel, two normal, and four at 45 degrees to the rolling direction. The correlation between the preferred grain orientations and the resolved shear stresses is represented in Figs. 22, 23 and 24. Employing the coincidence principle of maximum stress and slip planes, it is apparent why the ears are formed in these locations in practice.

The Effects of Preferred Orientation on Drawing Capacity of Aluminum Alloy Sheet

Little is known regarding the effects of preferred orientation on the relative drawing capacity of the aluminum alloys. Recently, however, it was demonstrated that certain preferred grain orientations are

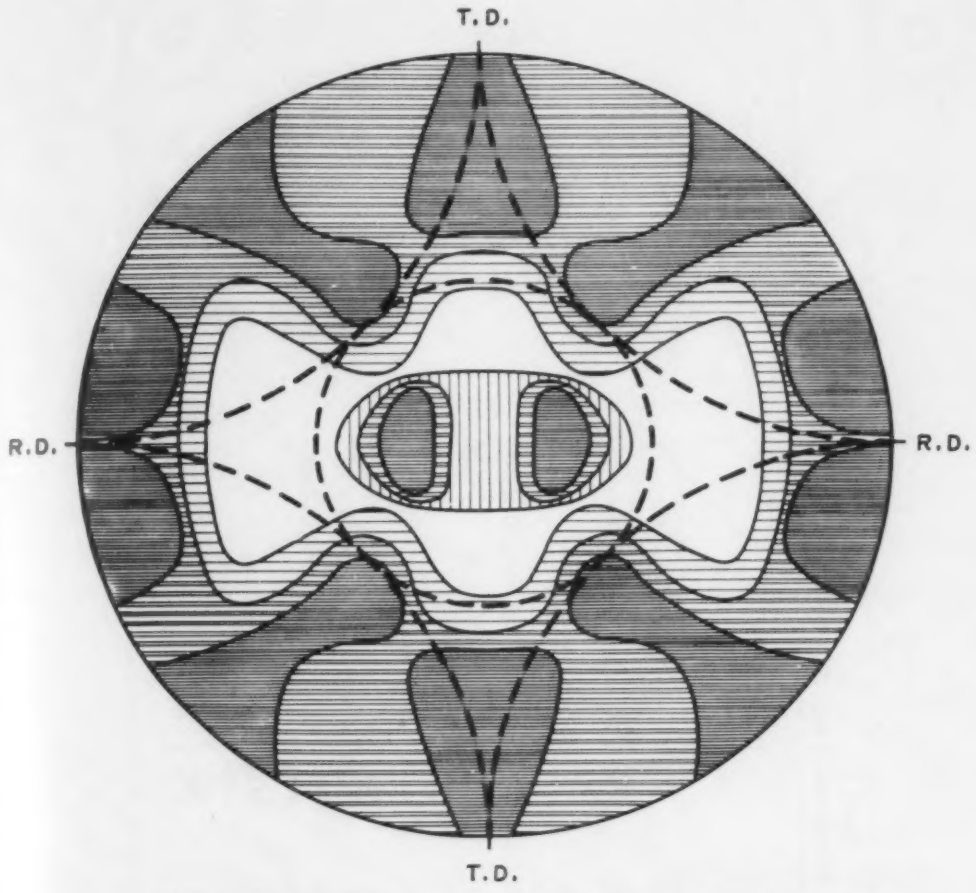


Fig. 23—The Superposition of Figs. 5 and 17 Such That S_1 of Fig. 17 is at 45 degrees to Rolling Direction of Fig. 5 (mixture of rolling and recrystallization textures).

of definite benefit in producing difficult deep draws of steel sheet in the automotive industry. It would seem that the drawing capacities of some aluminum alloys might also be affected by preferred orientation.

In the present test, indications of the degree of preferred orientation were obtained from determination of the earing characteristics of the sheet and by X-ray diffraction analysis. The drawing was performed on a 75-ton double action hydraulic press made by the Clearing Machine Corporation. The press has a variable speed inner slide and independent controls for the holddown and the cushion. The formability test consisted of drawing circular blanks from 0.064 inch sheet of several aluminum alloys into 3.0 inch square shells (Fig. 25) with the rolling direction in the sheet oriented parallel to the sides, or 45 degrees to the sides, of the die. The maximum diameter of blank that could be drawn into a shell served as a measure of formability. The earing characteristics (% height of ears) of the alloys were determined by drawing 4.0 inch diameter cups from the same 0.064 inch sheet.

An examination of the data in Table I reveals that the X-ray diffraction and drawing tests were in good agreement and that pre-

Table I
Comparison of Drawing Characteristics of Aluminum Alloy Sheet—Effect of Preferred Orientation

Alloy Designation	3-inch Square Cup: R.D. 45° to Sides — Max. Blank Diameter Inches	3-inch Square Cup: R.D. 45° to Sides — Reduction by Drawing Per Cent	3-inch Square Cup: R.D. Parallel to Sides — Max. Blank Diameter Inches	3-inch Square Cup: R.D. Parallel to Sides — Reduction by Drawing Per Cent	X-Ray Preferred Orientation — Degree	X-Ray Preferred Orientation — Predominant type	*Earing Characteristics — Location Degrees	*Earing Characteristics — Height Percent
2S-0	7.25	58.6	7.62	60.6	Med.High	Rolling	45	5
2S-0	7.37	59.3	7.62	60.6	Med.High	Recrystallization	45	5
3S-0	7.37	59.3	7.62	60.6	Med.Low	Unbalanced texture	45	5
3S-0	7.50	60.0	7.37	59.3	Low	Rolling	45	3
B50S-0	7.50	60.0	7.12	57.8	Med.	Recrystallization	0-90	7
4S-0	7.37	59.3	7.50	60.0	Low	Rolling	45	3
4S-0	7.37	59.3	7.37	59.3	Low	None	No ears	
52S-0	7.50	60.0	7.62	60.6	Low	Rolling	45	5
52S-0	7.50	60.0	7.50	60.0	Low	None	0-90	3
52S-0	7.37	59.3	7.25	58.6	Med.	Recrystallization	0-90	5
52S-0	7.50	60.0	7.37	59.3	Med.	Recrystallization	0-90	5
2S-H14	7.50	60.0	6.75	55.5		Recrystallization	0-90	10
2S-H24	7.12	57.8	7.87	61.8	High	Rolling	45	15
3S-H14	7.25	58.6	7.37	59.3	Med.	Rolling	45	3
3S-H24	7.25	58.6	7.75	61.2	Med.High	Rolling	45	15
B50S-H34	7.37	59.3	7.25	58.6	Med.		0-45-90	4

* Based on drawing 4-inch diameter cup.

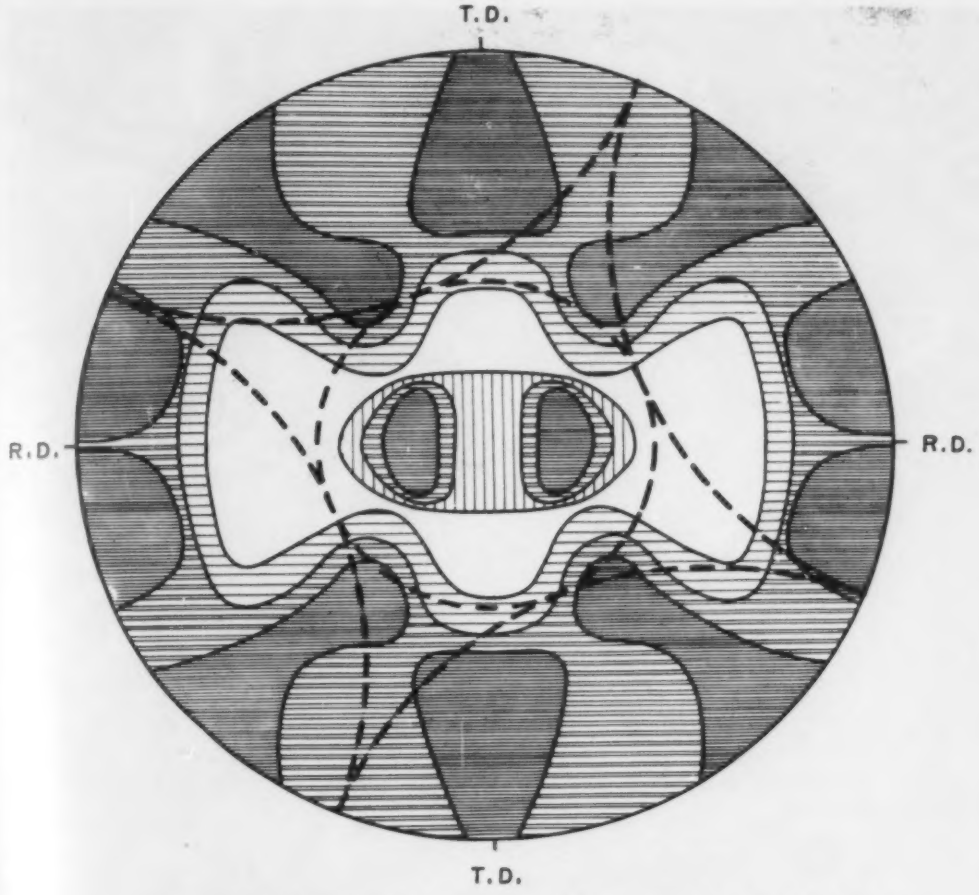


Fig. 24—The Superposition of Figs. 5 and 17 such that S_1 of Fig. 17 is at 22.5 degrees to rolling direction of Fig. 5 (mixture of rolling and recrystallization textures).

ferred grain orientation or types of texture had a definite effect on the drawability of the various alloys. With but few exceptions, sheet with a predominant rolling type of texture (ears at 45 degrees) drew best when oriented with the rolling direction parallel to the sides of the die. Sheet with a predominant recrystallization type of texture (ears at 0 and 90 degrees) drew best when oriented with the rolling direction of the sheet at 45 degrees to the sides; i.e., parallel to diagonals passing through the corners. In both cases, the best drawability was obtained when the sheet was oriented with respect to the die in such a manner that the ears formed at the corners of the shell. Moreover, the difference in drawability between sheets oriented parallel or at 45 degrees to the sides of the cup was roughly proportional to the height of the ears. The greater the earing tendency or degree of preferred orientation, the greater was the difference in drawability in either of two directions. This is an example where preferred grain orientation can be utilized to advantage and can facilitate the drawing of a shell.

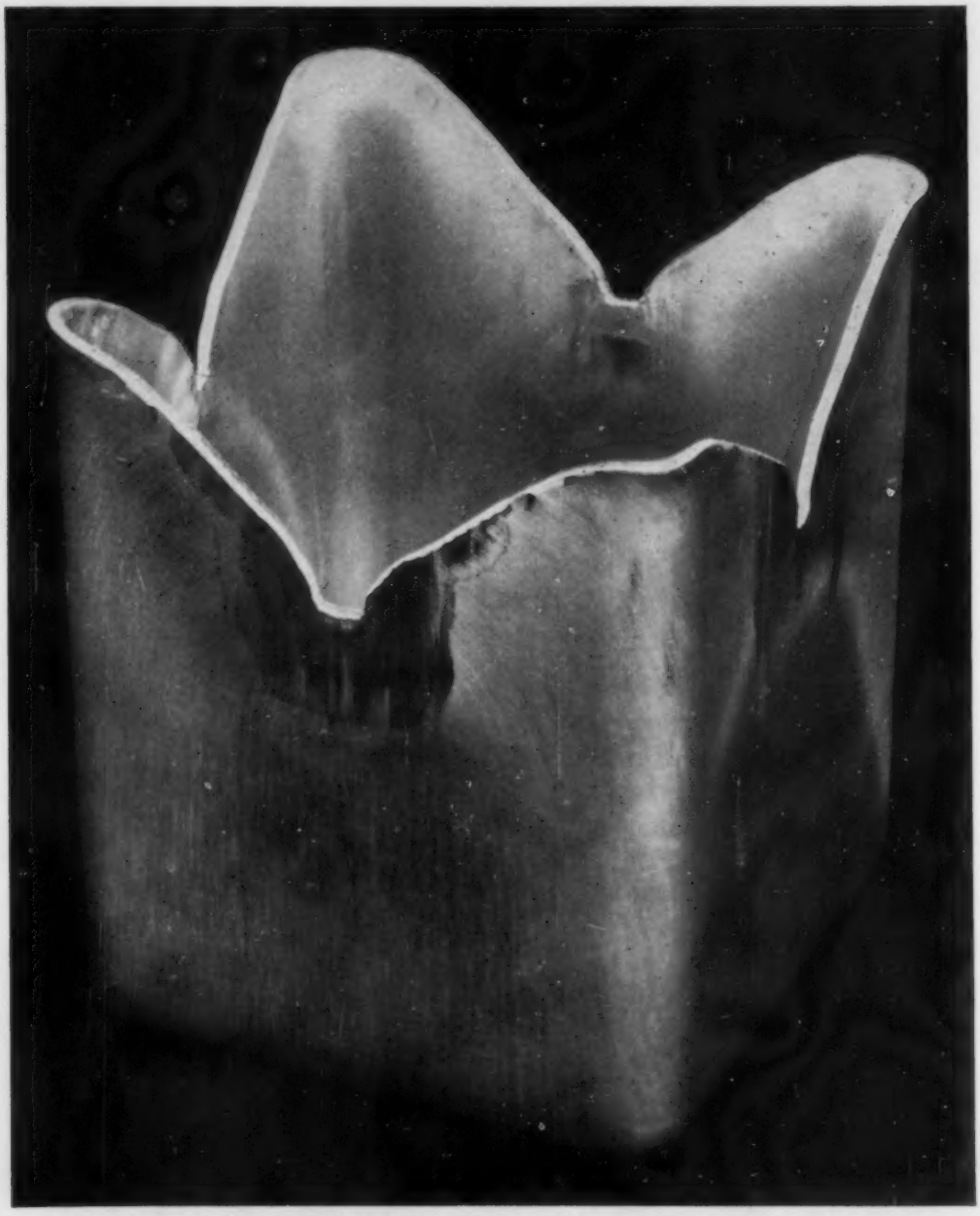


Fig. 25—Photograph of 3-inch Square Cup Drawn from 8-inch Diameter Blank of 0.064 Inch Sheet on Clearing Machine Press.

Preferred Orientation and Directional Properties in an Extruded Aluminum Alloy Bar

A high strength aluminum alloy of the following composition: 4.48% copper, 1.49% magnesium, 0.66% manganese, 0.18% silicon, and 0.23% iron was selected for the investigation. A rectangular bar approximately 3.0 x 3.0 inches was extruded at a temperature of 750 °F (400 °C) from an 11.0 inch diameter ingot. The extruded bar was given a solution heat treatment of 2 hours at 930 °F (500° C) quenched in cold water, and aged at room temperature.

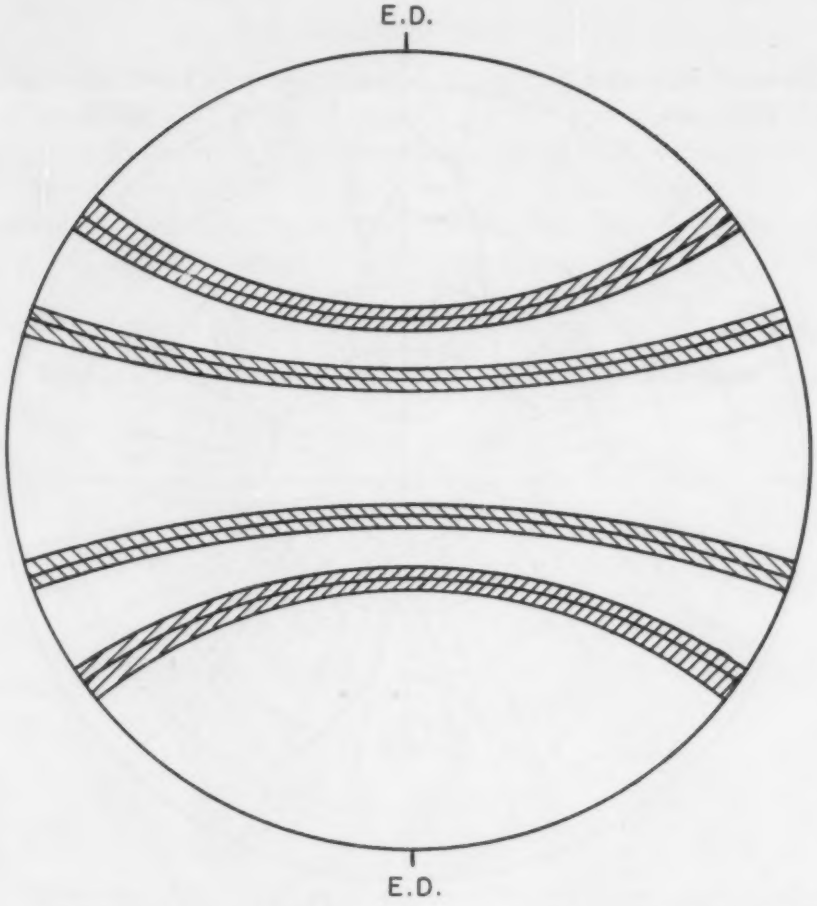


Fig. 26—{111} Pole Figure Illustrating a Duplex <111> and <001> Type of Preferred Orientation in a Heat Treated Extruded Bar of a High Strength Aluminum-copper-magnesium Alloy.

The type of preferred orientation in the high strength extruded aluminum alloy bar was determined from X-ray diffraction photograms prepared by the structure-integrating method (1). A flat specimen 6.0 x 1.5 x 0.006 inches, machined diagonally from the central portion of the extrusion, so that its long direction was parallel to the extrusion direction, was employed for this purpose. Diffraction patterns were prepared with the X-ray beam normal and inclined at various angles to the flat surface of the specimen. Unfiltered copper K-radiation was used. A {111} pole figure was constructed from the data obtained by this method of X-ray diffraction analysis.

The tensile properties were determined from A.S.T.M. standard 0.5 and 0.316 inch diameter specimens, with threaded ends (3), removed from the extruded sections so that the gauge length was included in that part of the section which was examined for preferred grain orientation. The longitudinal axes of the specimens were at angles of 0,10,17.5, 25,45,65,72.5,80 and 90 degrees to the extrusion direction. The speci-

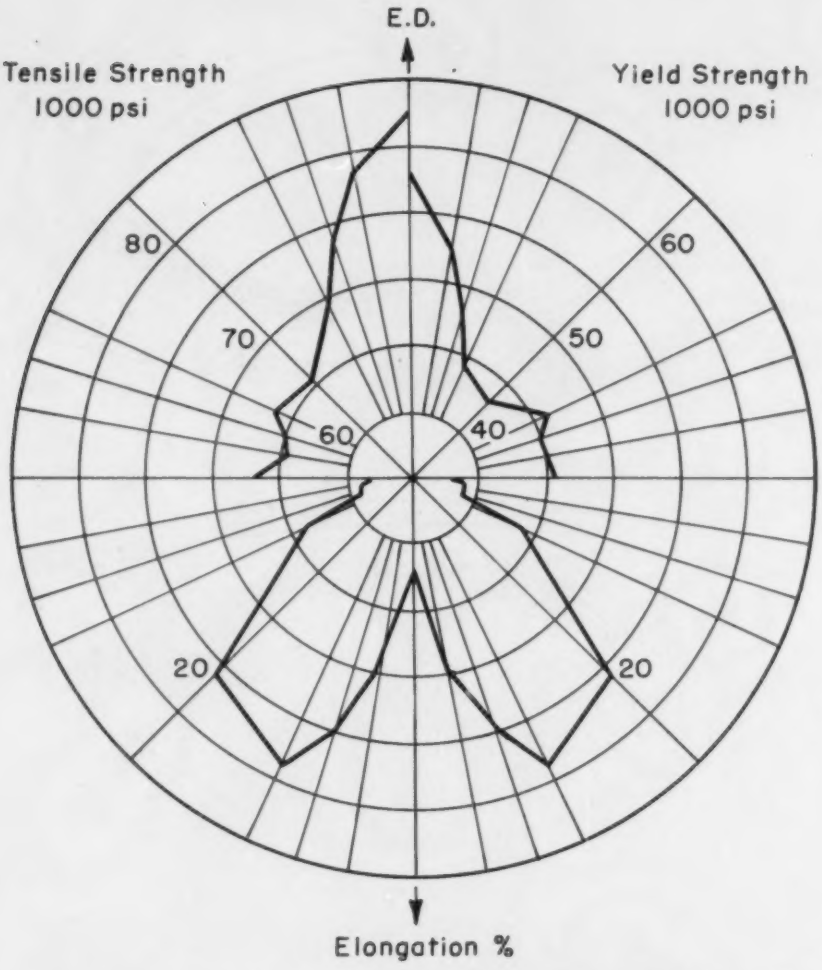


Fig. 27—Polar Graph of Tensile Test Results Obtained for a Heat Treated Extruded Bar of a High Strength Aluminum-copper-magnesium Alloy Having a High Degree of a Duplex <111> and <001> Texture.

mens at angles of 10,17.5 and 25 degrees to the extrusion axis were cut as pairs with opposite directions of inclination to determine whether this affected the results. The specimens were held in self-aligning grips (4) and the yield strengths were determined from stress-strain curves drawn by an electrically recording extensometer (5). Duplicate specimens were tested in all cases and the results averaged.

Preferred Orientation

The type of preferred orientation in this high strength extruded aluminum alloy bar is represented in Fig. 26. It is evident that a highly developed duplex extrusion texture exists in the bar with <111> and <001> axes parallel to the extrusion direction. Although both types of preferred orientation are highly developed, the <111> type appears to be slightly predominant. This type of duplex texture has been previously reported in the case of some of the other face-centered cubic metals, such as silver and copper.

Mechanical Properties

The results of the mechanical property tests are assembled in Table II and Fig. 27. Table II reveals that all specimens with the same degree of inclination to the extrusion axis exhibit substantially identical properties regardless of the direction of inclination. Fig. 27 is a polar graph in which the vertical direction corresponds to the direction of extrusion, and the azimuth angles represent the angles of the axes

Table II
Tensile Tests of a Heat Treated Extruded Aluminum-Copper-Magnesium Alloy Bar

Angle Between Tension Axis and Extrusion Direction Degrees	Direction of Inclination to Extrusion Direction	Yield Strength (Permanent set = 0.2%) Psi	Tensile Strength Psi	Elongation Per Cent in 4D
0	—	57,550	82,200	13.3
10	Right	52,900	79,250	18.0
	Left	51,800	77,500	16.0
	(Average)	52,350	78,400	17.0
17.5	Right	48,300	73,900	20.0
	Left	47,200	72,800	19.5
	(Average)	47,750	73,350	19.8
25	Right	44,700	69,550	22.0
	Left	43,800	68,600	21.5
	(Average)	44,250	69,100	21.8
45	Right	43,100	65,850	20.4
65	Right	45,600	66,500	14.4
72.5	Right	44,750	64,750	12.0
80	Right	44,750	64,450	12.0
90	—	45,250	66,800	11.2

of the test specimens with the extrusion axis. Quantitative representation of the magnitude of the properties is given on a linear scale in a radial direction from the center of the graph. The yield strength is plotted in the upper right-hand quadrant, the tensile strength in the upper left-hand quadrant, and the elongation in the lower two quadrants. The existing symmetry elements indicate that the same relationship between direction and properties exist in each quadrant.

The tensile properties exhibited a marked directional dependence. The yield strength was at a maximum in the longitudinal direction. As the angle of the tension axis with the extrusion axis increased, the yield strength value decreased sharply to a minimum at 45 degrees. As the angle increased beyond 45 degrees and approached 90 degrees, the yield strength again increased slightly. The tensile strength varied in a similar manner. The elongation was low in both the longitudinal and the transverse directions, the latter having the minimum value, and reached a maximum between 25 and 45 degrees.

Correlation of Preferred Orientation with Directional Properties

In a preceding section of the lecture, a detailed discussion was

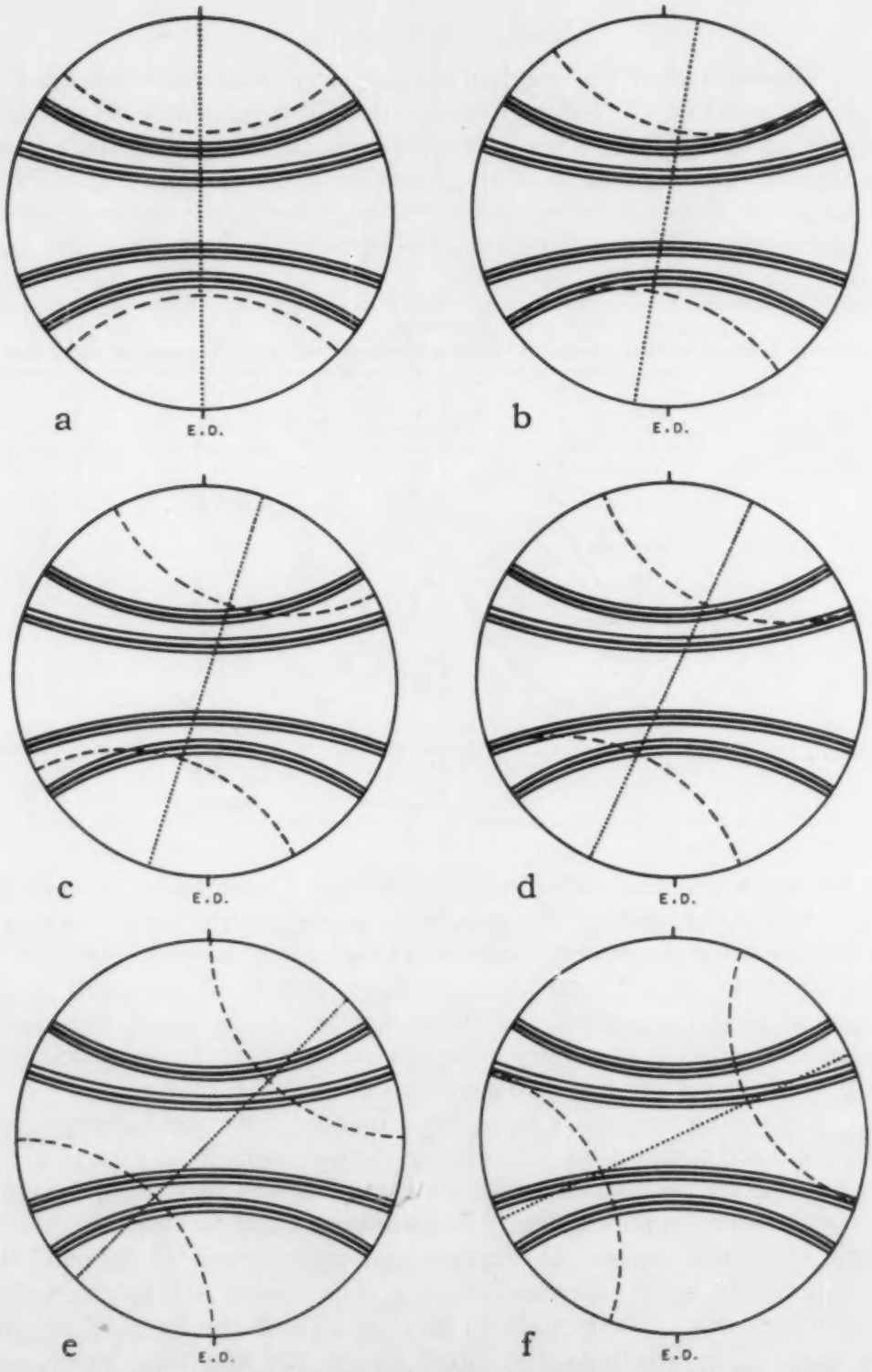


Fig. 28—A Series of Stereographic Projections Representing the Conditions Existing in Tensile Specimens Removed From a Large Heat Treated 24S Extrusion Having a Duplex <111> and <001> Type of Preferred Orientation. The tension axis is inclined to the extrusion axis as follows:

a = 0° b = 10° c = 17.5° d = 25° e = 45° f = 65°

Loci of poles of maximum resolved shear stress are dashed and tension stress or axis dotted.

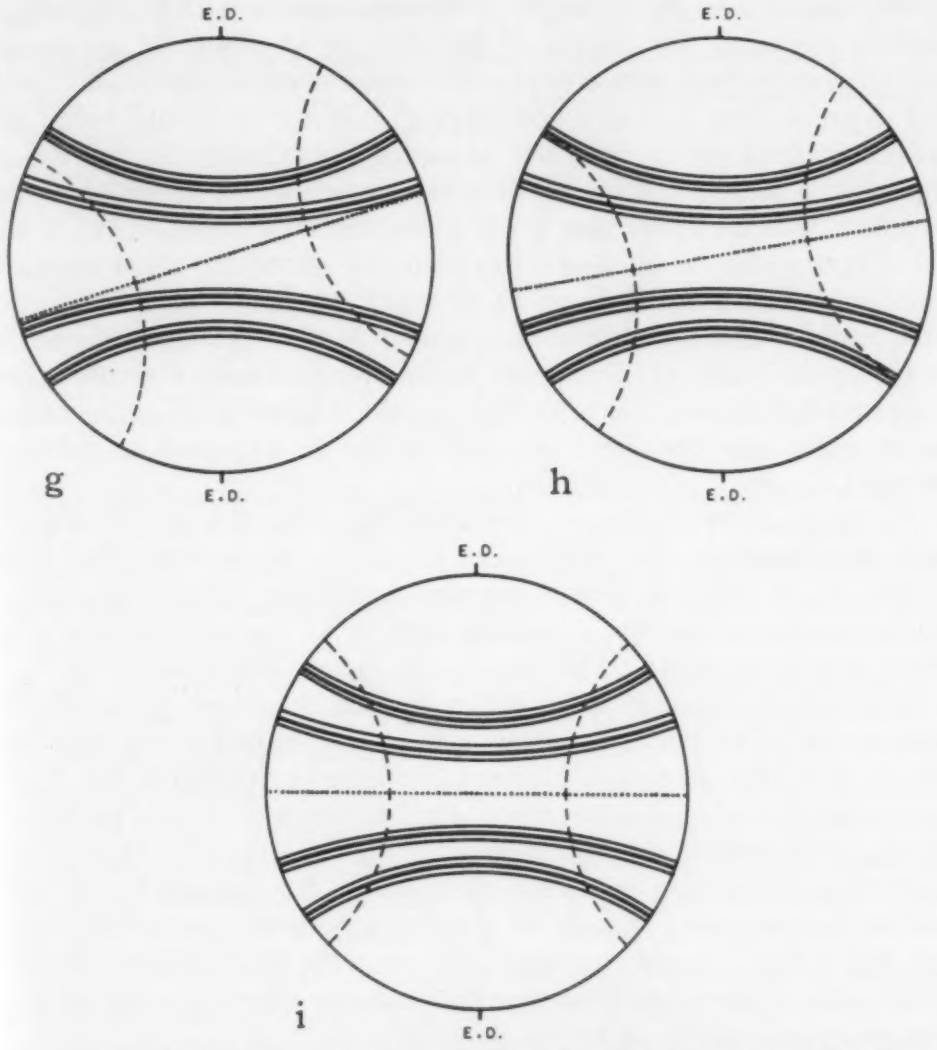


Fig. 28 (cont.)—A Series of Stereographic Projections Representing the Conditions Existing in Tensile Specimens Removed from a Large Heat Treated 24S Extrusion Having a Duplex <111> and <001> Type of Preferred Orientation. The tension axis is inclined to the extrusion axis as follows:

g = 72.5° h = 80° i = 90°

Loci of poles of maximum resolved shear stress are dashed and tension stress or axis dotted.

given of the principle involved in correlating preferred grain orientation with the directional properties of aluminum sheet. Figs. 28a to 28i represent the superposition of the {111} pole figure for the extrusion and the pole figures of the planes of maximum resolved shear stress for tensile specimens selected at different directions to the extrusion axis of the bar. Fig. 28 reveals that when the tensile axis of the specimens is parallel to the extrusion direction, there is no coincidence of planes of maximum resolved shear stress with {111} slip planes. Therefore, no grains are so oriented that the resolved shear stress on their slip planes is at a maximum, and accordingly the yield strength would be expected to be higher than in other directions in which there

is some coincidence. As the angle of the tension axis with the extrusion direction increases, the degree of coincidence of planes of maximum resolved shear stress with slip planes increases rapidly to a maximum of 45 degrees; that is, more and more grains are so oriented that the resolved shear stress on their slip planes is a maximum. At this orientation of the tensile specimen, there is coincidence at the poles of the projection, which implies that every grain involved in the <111> extrusion texture has at least one slip plane on which the shear stress is maximum. Accordingly, the yield strength would be expected to decrease rapidly from a maximum parallel to the extrusion direction to a minimum value at 45 degrees inclination. At angles greater than 45 degrees and approaching 90 degrees, the degree of coincidence decreases again, and the yield strength would be expected to increase somewhat.

A comparison of these considerations with the yield strength values illustrated in Fig. 27 shows excellent agreement. The yield strength was a maximum at 0 degrees inclination, decreased rapidly with increasing inclination to a minimum at 45 degrees, and then increased slightly from 45 to 90 degrees to the extrusion direction.

The tensile strength exhibited a similar relationship. It did not correspond in all respects, however, and, in fact, would not be expected to do so, for this correlation between preferred orientation and directional properties is applicable only to the beginning of plastic deformation; that is, it is valid only up to about the yield strength. At any later time during the tension test, the conditions as represented by the pole figure no longer exist, because of the changes in structure introduced by the deformation during testing. Only when the tension axis coincides with the crystallographic fiber direction can the effect of original preferred grain orientation be the vital factor.

The elongation presents a still more complicated relationship. It was low in both directions parallel and perpendicular to the extrusion axis, and increased to a maximum at some intermediate inclination. Although undoubtedly the original preferred orientation of the grains is a factor affecting this relationship, it appears that it is not the only one. A metallographic examination revealed an alignment of the insoluble constituents in the extrusion direction. Mechanical fibering probably contributed to the lower elongation in the transverse direction. The elongation is also affected by the change in grain orientation produced by the plastic deformation occurring during the tensile test.

Structure and Tensile Properties of the Extruded Bar after Recrystallization

A four-foot length was cut, before heat treatment, from the same extruded bar that was examined for tensile properties and preferred orientation. This length was stretched 6.9% and then heat treated

Table III
Tensile Tests of Extruded Aluminum-Copper-Magnesium Alloy Bar Stretched 6.9 Per Cent Before Solution Heat Treatment

Angle Between Tension Axis and Extrusion Direction Degrees	Yield Strength (Permanent set = 0.2%) Psi	Tensile Strength Psi	Elongation Per Cent in 4D
0	42,150	68,000	21.7
10	43,200	69,300	21.5
17.5	43,950	69,850	21.5
25	44,400	69,950	21.7
45	42,900	67,800	18.0
65	44,050	66,600	14.0
72.5	44,200	66,600	12.8
80	44,000	65,650	12.4
90	43,250	64,900	10.8

along with the extruded bar previously described; i.e., 2 hours at 930 °F (500 °C), followed by quenching in cold water. The mechanical properties of the stretched and heat treated bar were determined from standard tensile specimens cut with their longitudinal axes at the same angles to the direction of extrusion as with the first bar. Structure integrating X-ray diffraction patterns were prepared, and revealed that the extruded section, which was stretched before heat treatment, had completely recrystallized and possessed a very low degree, if any, of preferred orientation. This change was caused by the cold work introduced by the stretching operation. The extrusion texture type of preferred orientation (Fig 26) which previously existed disappeared completely during recrystallization and no new texture formed. Metallographic examination revealed that the stretched section had a normal recrystallized structure. As was the case with the bar with a high degree of preferred orientation, the insoluble constituents were aligned in the extrusion direction, indicating no decrease in mechanical fibering.

The results of the tensile tests are assembled in Table III and are represented in the polar diagram in Fig. 29. If a statistical or random distribution of the slip planes exists, the tensile properties would be expected to be the same in all directions. If this were true, the curve representing the relationship between tensile properties and direction of extrusion in the polar diagram would be a concentric arc. The yield strength and the tensile strength approximate this condition. The elongation, however, shows a distinct dependence on direction, being a maximum parallel to the extrusion direction and decreasing with increasing inclination angle to a minimum (about one-half the maximum value) in the transverse direction. Obviously, this is caused by some factor other than grain orientation. Metallographic examination revealed that alignment of insoluble constituents in the extrusion direction still existed after stretching and heat treatment. It is safe to assume that mechanical fibering caused the low elongation in the transverse direction. The mechanical fibering also contributed to the low transverse

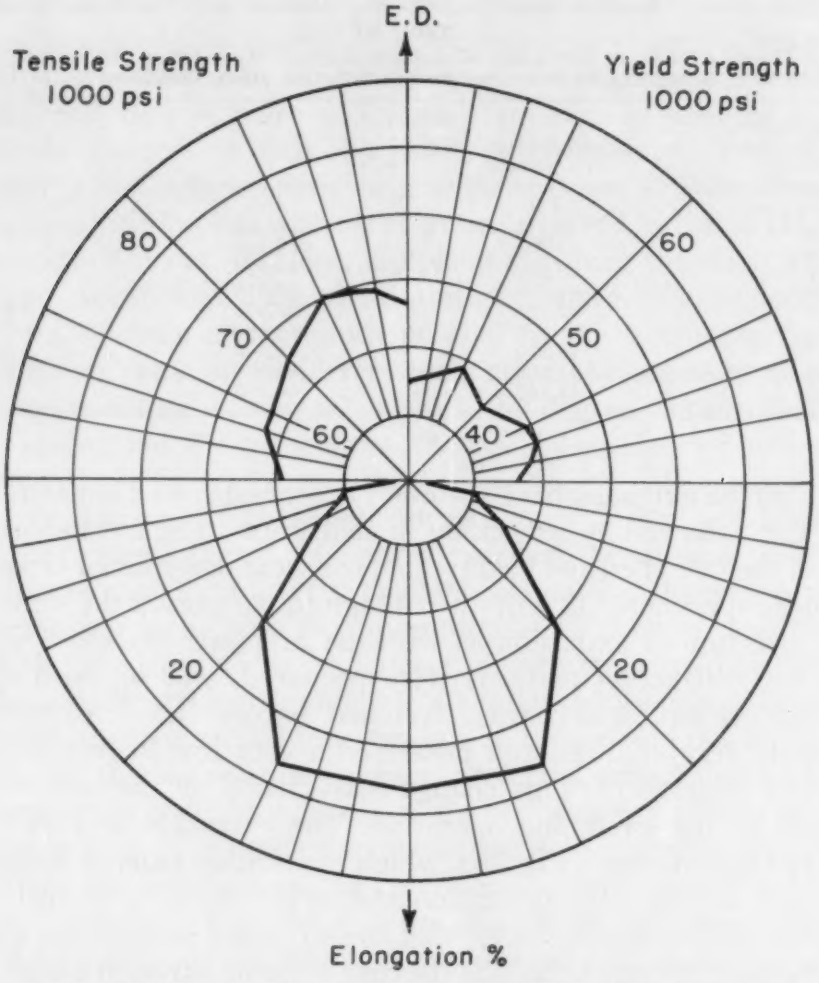


Fig. 29—Polar Graph of Tensile Test Results Obtained From an Extruded Bar of a High Strength Aluminum-copper-magnesium Alloy That Was Stretched 6.9% Before Solution Heat Treatment. The bar possessed a very low degree, if any, of preferred orientation.

elongation in the portion of the extruded bar that possessed the high degree of preferred orientation.

A most interesting point (12) in comparing the properties of the two sections of the extruded bar is that the highest values of yield strength and tensile strength are obtained parallel to the extrusion direction, when preferred orientation exists. Stretching before heat treatment caused recrystallization to occur during heat treatment with loss of the preferred orientation and with reversion to the normal tensile properties of the alloy.

In the case of longitudinally stressed members or structures, made from extruded rod or bar, it is often desirable to obtain maximum strength in the longitudinal direction. The existence of a preferred orientation which imparts desired directionality to the strength of the alloy in such cases is beneficial.

Summary

Two distinct types of preferred orientation may exist in aluminum sheet, the rolling and recrystallization types. Furthermore, these textures may exist simultaneously in various relative quantities. The earing tendencies of sheet aluminum having preferred orientation depend on the type and degree of preference. The location of the ears on drawn cups is related to the type of grain orientation, and the size of the ears to the degree of preference. With the rolling type of preferred orientation, ears form at 45 degrees to the direction of rolling; and with the recrystallization type texture prevalent, the ears form parallel and perpendicular to the direction of rolling. When the two types of preferred orientation coexist, eight ears are formed in locations parallel, normal and at 45 degrees to the direction of rolling. These earing characteristics and the directional variation in tensile properties of the sheet are explained by the degree of coincidence between the crystallographic planes of slip and planes of maximum resolved shear stress. The slip directions on the slip planes apparently have a negligible influence.

It was established that a large heat treated aluminum-copper-magnesium alloy extrusion had a highly developed duplex texture (extrusion) with <111> and <001> axes parallel to the direction of extrusion. This bar exhibited pronounced directional properties. The maximum yield strength, which occurred parallel to the extrusion direction, was 32.5% greater than the minimum yield strength, which was 45 degrees to the direction of extrusion. The directional variation in mechanical properties was explained on the basis of the degree of coincidence between planes of maximum resolved shear stress and crystallographic planes of slip.

Deformation by stretching of an extruded bar caused recrystallization during heat treatment with consequent loss of the extrusion texture. The tensile and yield strengths of this extrusion reverted to normal values for the alloy and exhibited little directional dependence. In the case of longitudinally stressed members, a high degree of preference would be advantageous if the direction of principal stress were parallel to the extrusion direction. Improvement in longitudinal strength was approximately 35% when the extrusion texture type of preferred orientation was present.

Acknowledgments

The majority of the experimental work was performed by W. L. Fink, D. W. Smith, H. R. Freche and L. K. Jetter when the latter three were associated with the Aluminum Research Laboratories. The data on formability of aluminum sheet alloys were determined by W. A. Anderson. R. G. Sturm assisted in the calculation of the maximum

shear stress values. The author also gratefully acknowledges the help of T. W. Bossert, E. H. Dix, Jr., M. W. Daugherty, W. L. Fink, F. C. Frary, E. C. Hartmann, F. Keller, and R. L. Templin for constructive suggestions offered during the review of the manuscript, and George Wilcox for the preparation of the illustrative material.

References

1. C. S. Barrett (Contribution by W. L. Fink and D. W. Smith), "X-Ray Diffraction Equipment and Methods," *Symposium on Radiography and X-Ray Diffraction,* American Society for Testing Materials, 1936, p. 194.
2. F. Wever, "Texture of Metals after Cold Deformation, "*Transactions,* American Institute of Mining and Metallurgical Engineers, Institute of Metals Division, Vol. 93, 1931, p. 51.
3. Standard Methods of Tension Testing of Metallic Materials, American Society for Testing Materials, Standard No. E-8-52T, Part 1, 1952, p. 1389.
4. R. L. Templin, "Effects of Size and Shape of Test Specimens on the Tensile Properties of Sheet Metals," *Proceedings,* American Society for Testing Materials, Vol. 26, Part 11, 1926, p. 378; Methods for Determining the Tensile Properties of Thin Sheet Metals," *Proceedings,* American Society for Testing Materials, Vol. 27, Part 11, 1932, p. 235.
5. R. L. Templin, "An Autographic Extensometer for Use in Tension Tests of Materials," *Proceedings,* American Society for Testing Materials, vol. 32, Part 11, 1932, p. 783.
6. F. Wever, "Structure of Cubically Crystalline Metals after Rolling," Zeitschrift fur Physik, Vol. 28, 1924, p. 69.
7. G. V. Vargha and G. Wasserman, "On the Relation of Crystalline Orientation in Rolled Aluminum Sheet and the Thickness of the Sheet," Metallwirtschaft, Vol. 12, 1933, p. 511; H. Hu, P. R. Sperry and P. H. Beck, "Rolling Textures in Face-Centered Cubic Metals, *Transactions,* American Institute of Mining and Metallurgical Engineers, Institute of Metals Division, Vol. 194, 1952, p. 76.
8. E. Schmid and G. Wasserman, "The Recrystallization of Aluminum Sheet," Metallwirtschaft, Vol. 10, 1931, p. 409.
9. P. A. Beck and H. Hu, "Annealing Textures in Face-Centered Cubic Metals," *Transactions,* American Institute of Mining and Metallurgical Engineers, Institute of Metals Division, Vol. 194, 1952, p. 83.
10. M. Cook and T. L. Richards, "The Structural Changes in Copper Effected by Cold Rolling and Annealing," *Journal,* Institute of Metals, Vol. 66, 1940, p. 1.
11. S. Timoshenko, *Theory of Elasticity,* McGraw-Hill Book Co., Inc., 1934.
12. E. H. Dix, Jr., THE PHYSICAL METALLURGY OF ALUMINUM ALLOYS, American Society for Metals, 1949, p. 200.

THE EFFECT OF PRESTRAINING UNDER DIFFERENT STRESS STATES ON THE FRACTURE AND FLOW PROPERTIES OF 2S-O ALUMINUM

By I. Rozalsky

Abstract

The effects of prestrain under conditions of different stress states but identical strain states upon the fracture and flow properties in tension were obtained for commercially pure (2S-O) aluminum.

For prestrains of the same magnitude a prestrain stress state of simple compression results in a higher retained tensile ductility than does a prestrain stress state of biaxial tension. Also a change in prestrain stress state from simple compression to biaxial tension influences the shape of the fracture stress versus prestrain curve but does not affect the shape of the yield strength versus prestrain curve.

Introduction

THE object of this investigation was a correlation of the prestrain effects produced under conditions of different stress states but identical strain states upon the tensile fracture and flow properties of 2S-O aluminum.

Fig. 1 [1] summarizes some of the possible types of plastic strains or prestrains that may be followed by a tensile test.

Tensile prestrain in the same direction as that of the subsequent tensile test may be produced under prestrain conditions of different stress states but identical strain states.

The conditions represented by Fig. 1a, the prestrain stress state of simple tension, have been studied by Liu and Sachs (1)[2] for 24ST aluminum and by Ripling and Baldwin (2) and McAdam and his associates (3) for steel.

Bridgman (4) considered the conditions represented by Fig. 1b,

[1] The subscripts a, b, and c for each stress (s) and strain (ϵ) may apply interchangeably to any of the three principal directions.

[2] The figures appearing in parentheses pertain to the references appended to this paper.

This paper is based upon a portion of a research program conducted in the Metals Research Laboratory, Department of Metallurgical Engineering, Case Institute of Technology, Cleveland, Ohio in cooperation with the Office of Naval Research, U. S. Navy.

A paper presented before the Thirty-sixth Annual Convention of the Society, held in Chicago, November 1 to 5, 1954. The author, I. Rozalsky, is metallurgist, Shell Oil Co., Wood River Research Laboratory, Wood River, Ill., formerly research associate, Metals Research Laboratory, Case Institute of Technology, Manuscript received November 3, 1953.

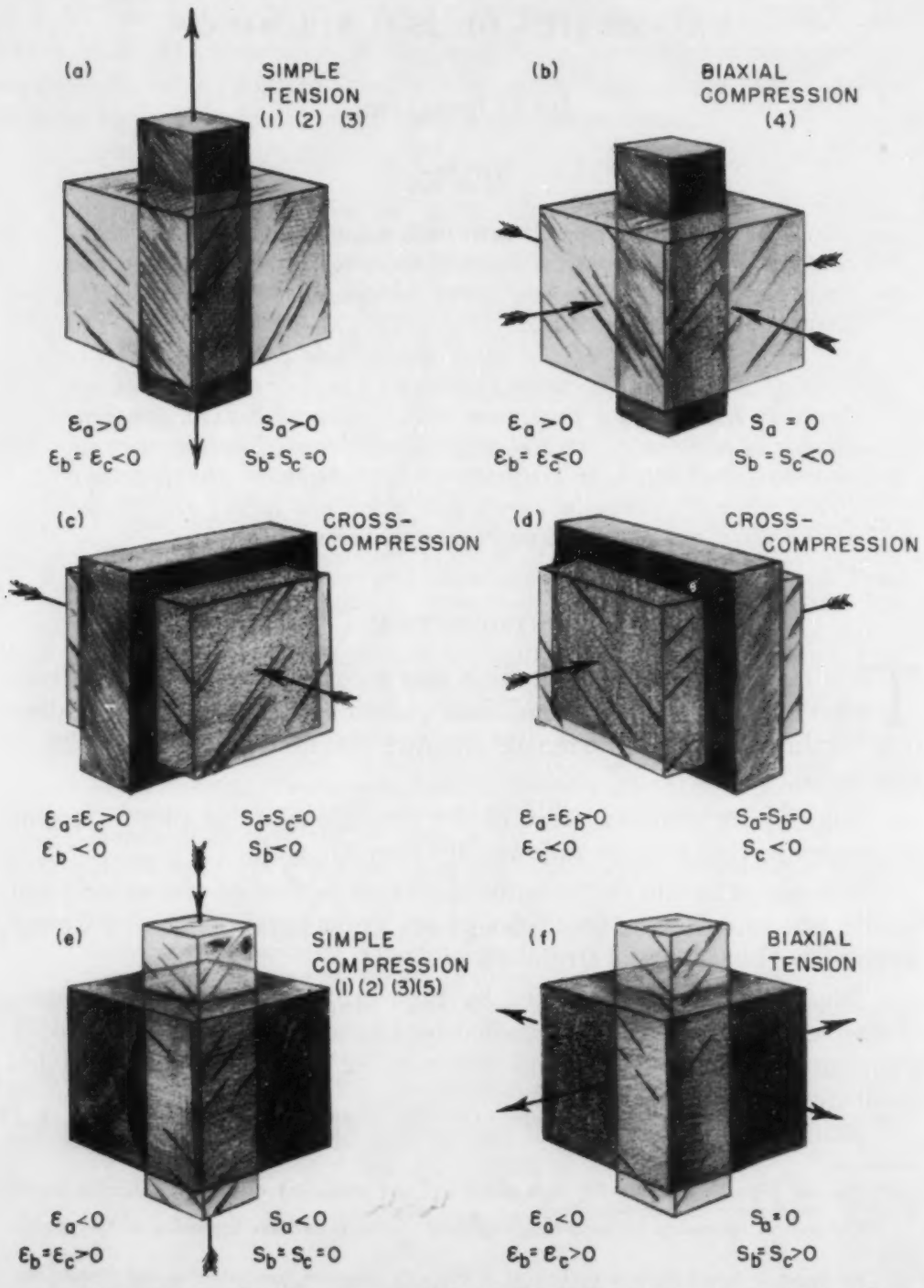


Fig. 1—Various Prestrain Stress and Strain States Under Isotropic Conditions. Clear blocks indicate shape before prestraining.

the prestrain stress state of biaxial compression, in his studies of a number of alloys.

The prestrain stress state of "cross-compression" [3] represented by Fig. 1c and 1d was considered in this paper as another possible means of obtaining tensile prestrain.

Compressive prestrain in the same direction as that of the subsequent tensile test may also be produced under conditions of different stress states but identical strain states.

The conditions represented by Fig. 1e, the prestrain stress state of simple compression, were studied by Liu and Sachs for 24ST aluminum (1), Ripling and Baldwin (2), McAdam (3) and Koerber and his coworkers (5) for steel.

The prestrain stress state of biaxial tension represented by Fig. 1f was considered in this research as another means of obtaining compressive prestrain in the same direction as that of the subsequent tensile test.

This paper represents an attempt to gain insight into the subject of the mechanical behavior of metals.

Material and Procedure

The different prestraining conditions were carried out on specimens cut from a 10 foot by 4 foot by ¾ inch 2S aluminum plate and annealed at 650 °F for 30 minutes.[4] The methods by which the tests were conducted are described below:

Final Tensile Test—These specimens were of the dimensions shown in Fig. 2 except for specimens taken in the normal direction of the plate after compressive prestrain in the normal direction. Under

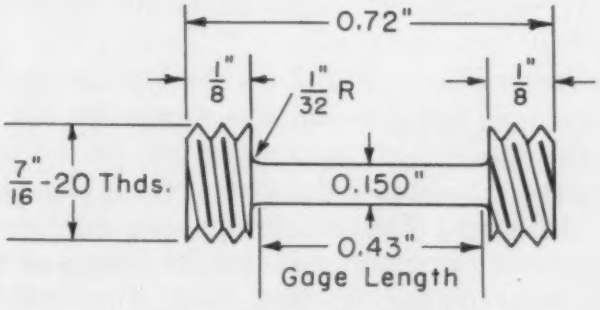


Fig. 2—Tensile Test Specimen.

these conditions, see Fig. 1e and 1f, the total length of the tensile test specimen was necessarily decreased; however, the specimen diameter of 0.150 inch was retained.

---

[3] Compressive prestrain in one principal direction followed by testing in one of the other principal directions (90 degrees removed from the prestrain direction). The "cross-compression" results in a tensile prestrain in the test direction.

[4] In the fully annealed condition the 2S aluminum is designated as 2S-O aluminum.

Each tensile test was made with a crosshead speed of approximately 0.04 inch per minute, with all tests including the prestrains being made at room temperature. Concentricity of loading during the tensile testing operation was ensured by the use of a specially constructed fixture (6).

Prestrain According to Fig. 1a—The type of specimen used for simple tensile prestrain was of the shape shown in Fig. 2. It was not considered necessary to re-machine these specimens prior to their being tested in tension. Prestrains of this type and subsequent tensile tests were made for each of the three principal directions, i.e., the longitudinal (rolling), transverse, and normal directions of the aluminum plate. The direction of the tensile prestrain was the same as the direction of the subsequent tensile test.

Prestrain According to Figs. 1c and 1d—The type of specimen used for cross-compressive prestrain was a rectangular parallelepiped of the dimensions 0.72 inch by 0.50 inch by 0.50 inch or 0.72 inch by 2.00 inch by 2.00 inch. The 0.72 inch dimension was in the normal direction of the plate, the dimensions in the longitudinal and transverse directions being determined by the direction of the subsequent tensile test and the magnitude of prestrain.

Specimens were prestrained by compressing them between two flat parallel plates in a tensile test machine. A commercial preparation of molybdenum sulphide was used as a lubricant on the plates to decrease friction between the plates and the specimen bases. This technique was also used for simple compressive prestrain, see Fig. 1e.

For each of the three test directions two sets of data were obtained by means of cross-compressive prestrain, e.g., for tests in the normal direction, it was possible to prestrain by compression in either the longitudinal or transverse direction to obtain a tensile prestrain in the normal direction.

Prestrain According to Fig. 1e—The type of specimen used for prestraining in simple compression was a cylinder, the axis of which was parallel to the direction of compression and the test direction. Those taken in the normal direction of the plate were 0.72 inch in height and 0.50 inch in diameter. The maximum amount of prestrain was ϵ_p[5] $= -0.60$; greater prestrains reduced the length of the subsequent tensile test specimens to an impractical point. Those taken in the longitudinal and transverse directions were of two sizes:

0.75 inch in height and 0.50 inch in diameter for compressive prestrains less than $\epsilon_p = -0.60$, and
2.00 inch in height and 0.75 inch[6] in diameter for compressive prestrains greater than $\epsilon_p = -0.60$.

---

[5] $\epsilon_p = \ln \frac{\text{Original Area}}{\text{Area after Prestrain}}$

[6] Narrow flats were left on the cylindrical surfaces of these specimens for the plate thickness was only 0.72 inch, see Fig. 4.

The maximum length of the tensile test specimen taken in the normal direction that could be machined from the plate after heavy compressive prestrain in the normal direction, according to Fig. 1e or 1f, was shorter the greater the prestrain. It was observed that the effect of variation in gage length upon the fracture and flow properties of the 2S-O aluminum was not significant, except for the yield strength of specimens of exceedingly short gage length.

The aluminum plate used in this investigation was anisotropic as may be seen in Fig. 3 and 4 by the oval cross section which originally circular specimens assumed when compressed.

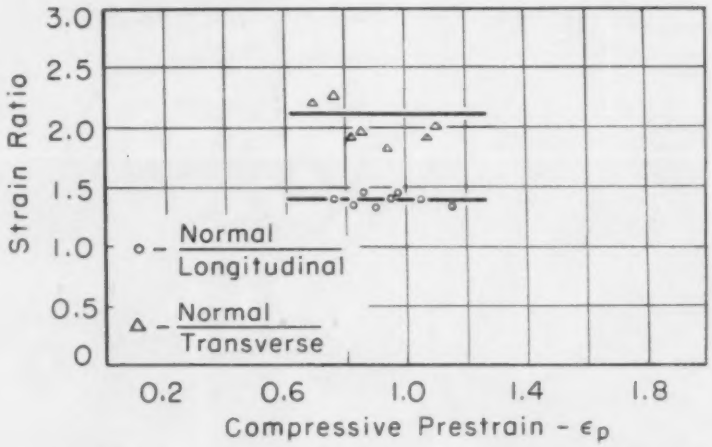


Fig. 3—Dependence of Strain Anisotropy Upon Compressive Prestrain in ¾ Inch Thick 2S-O Aluminum Plate.

Prestrain According to Fig. 1f—Prestraining in biaxial tension was effected by bulging the 2S-O aluminum plate by hydraulic means on a 1,000,000 pound hold-down press. While thin sheet has previously been bulged in such presses (7,8), the bulging of thick sheet or plate introduces two difficulties:

(a) The bend stresses at the periphery of the bulge are such as to destroy a simple biaxial stress state for some distance in from the edge. Consequently, as large a diameter die (6 inch diameter with a specimen of 10 inch by 10 inch surface dimensions) as could be handled by the press was used. Tensile test specimens were taken from the center (pole) of each dome (bulge) normal to the surface of the plate.[7]

(b) Even at the pole of the dome a uniform biaxial strain state did not exist from the inside surface to the outside surface as was evidenced by strains measured from 20-lines-to-the-inch grids photographically applied (9) to both the outside and inside surfaces.

[7] Actually a simple biaxial stress state (stresses in the plane of the sheet only) is not achieved in the case of bulging thick plate since here the hydraulic pressure develops some slight stress normal to the plane of the sheet.

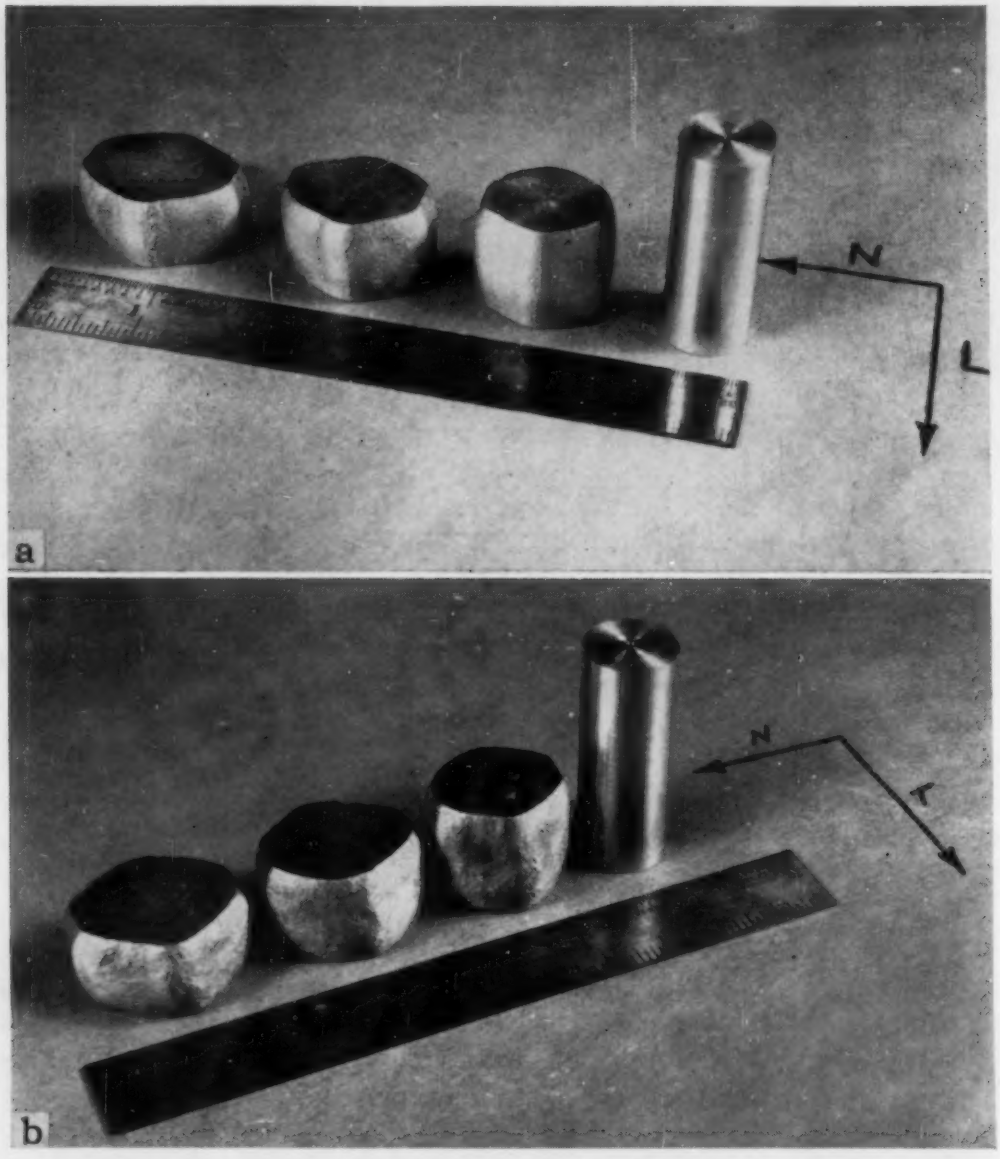


Fig. 4—Plate Anistropy as Evidenced by Specimens Prestrained in Simple Compression. (a) Cylindrical specimens of 2S-O Aluminum compressed various amounts in the transverse direction of the plate. The normal (N) and longitudinal (L) directions of the plate are shown. (b) Cylindrical specimens of 2S-O aluminum compressed various amounts in the longitudinal (rolling) direction of the plate. The normal (N) and transverse (T) directions are shown.

After bulging, strain distributions on the top and bottom surfaces of each bulge were plotted, Figs. 5,6 and 7, for the portion of the bulge in the vicinity of the pole.

The strains were measured from the pole, see Fig. 5, in the longitudinal direction of the plate at the top and bottom surfaces (e_{LT} and e_{LB}, respectively) and in the transverse direction of the plate at the top and bottom surfaces (e_{TT} and e_{TB}, respectively) of the bulge. The bot-

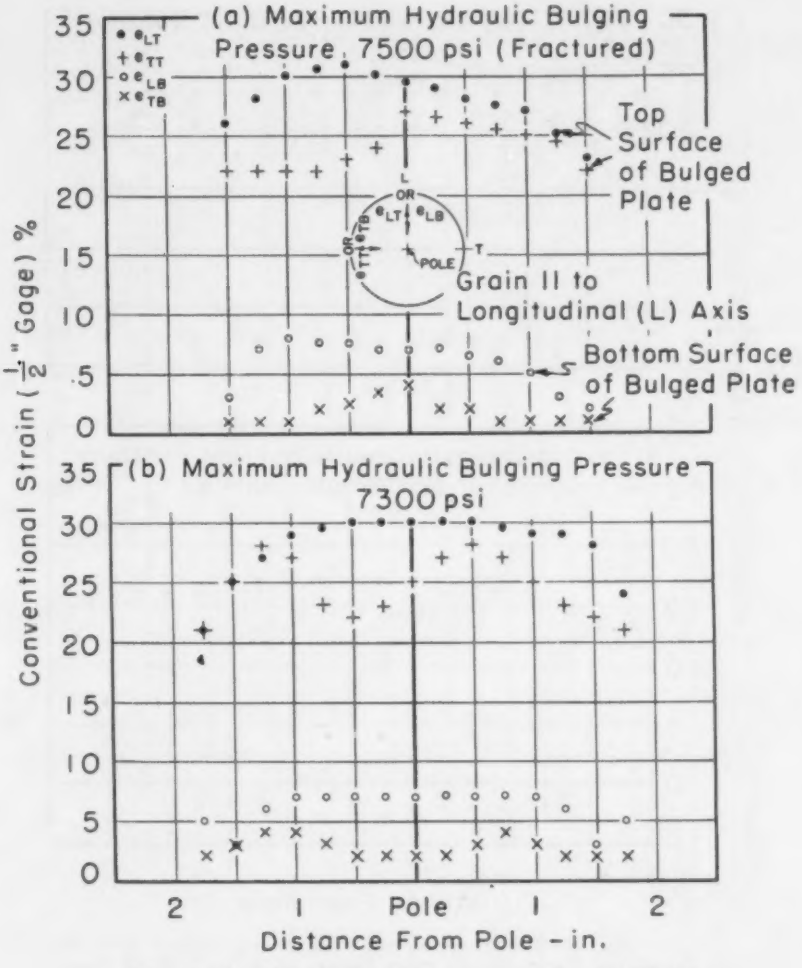


Fig. 5—Longitudinal and Transverse Strain Distributions for Hydraulic Circular Bulges of ¾ Inch 2S-O Aluminum Plate.

tom surface of the bulge was denoted to be the surface in contact with the oil during the bulging operation.

The first plate was bulged until fracture occurred. By extrapolation of Thielsch's data for the hydraulic pressure required for fracture versus thickness of sheet for 2S-O aluminum (10), it was determined that an approximate pressure of 6500 psi would be required to fracture ¾ inch plate under conditions of balanced [8] biaxial tension by means of hydraulic bulging. Actually, it was experimentally determined that a pressure of 7500 psi was required. The difference in hydraulic pressure was perhaps due in part to the slight triaxiality in stress state involved in the bulging of the plate.

No tensile test specimens were taken from this bulge which fractured under hydraulic pressure, because of the excessive nonuniformity of strain distribution. More aluminum plates were bulged

[8] Using circular bulging die.

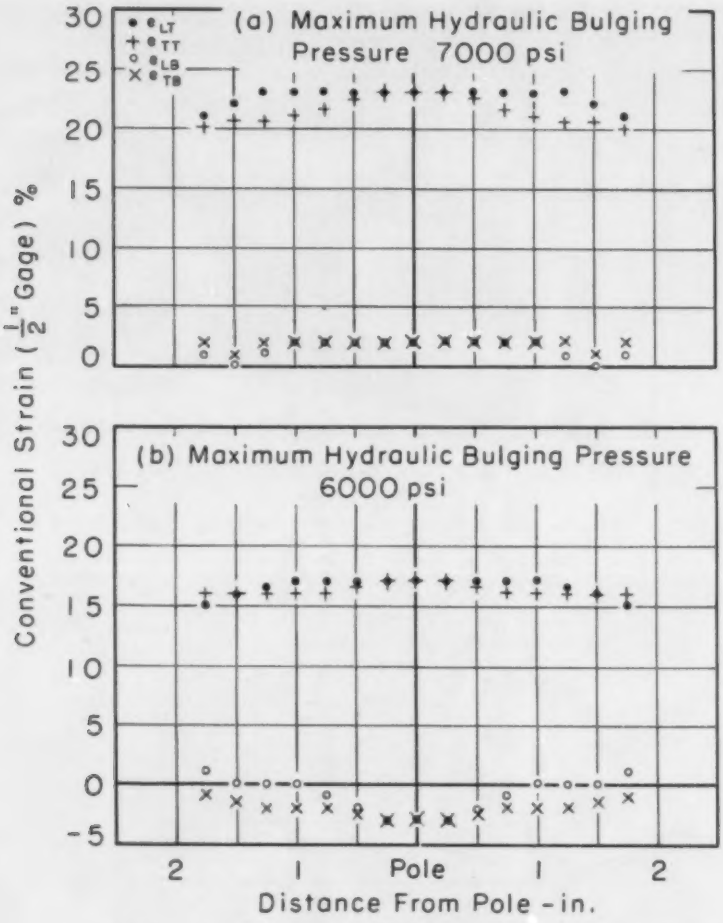


Fig. 6—Longitudinal and Transverse Strain Distributions for Hydraulic Circular Bulges of ¾ Inch 2S-O Aluminum Plate.

at successively lower pressures, and from one specimen, see Fig. 5a, to nine specimens, see Fig. 7b, were taken from the pole of each bulge, the number of specimens depending upon the uniformity of strain in the vicinity of the pole. Each specimen was cut from the bulge so that its axis was perpendicular to the top bulge surface.

Compressive prestrain in each of these specimens was computed (a) from thickness measurements made with pointed micrometers and (b) from the average strains in the plane of the plate taken on both the inside and outside surfaces by the assumption of constancy of volume,

$$\epsilon_1 + \epsilon_2 + \epsilon_3 = 0$$

ϵ_1 being the longitudinal strain, ϵ_2 the transverse strain and ϵ_3 the normal strain. The results obtained by both methods for each specimen were almost identical.

A considerable strain gradient existed between the top and bottom surfaces of each bulge, see Figs. 5,6 and 7, and concomitantly, between

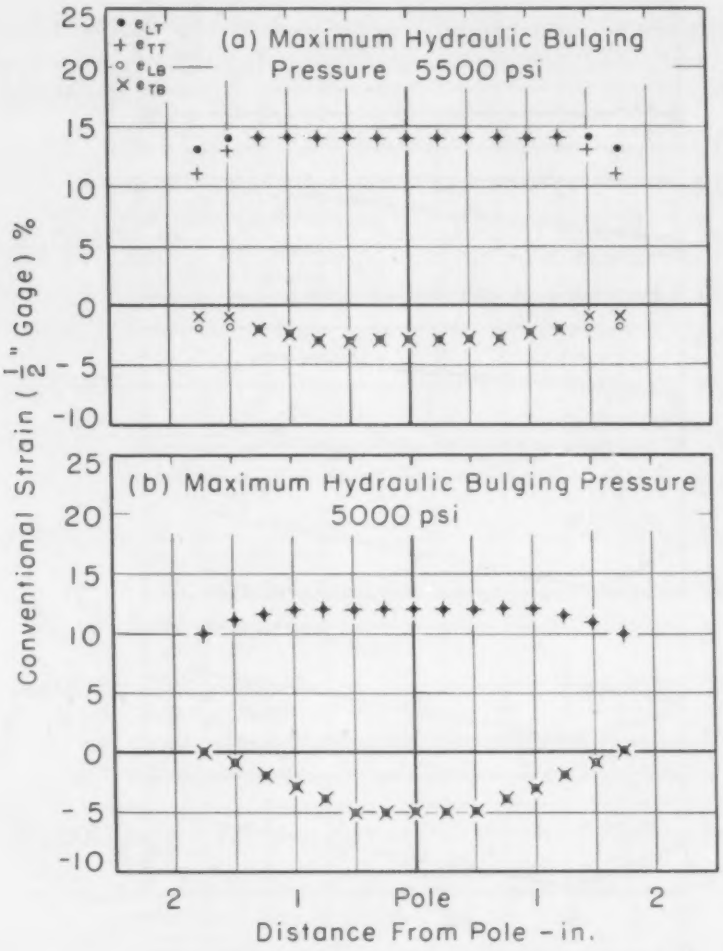


Fig. 7—Longitudinal and Transverse Strain Distributions for Hydraulic Circular Bulges of ¾ Inch 2S-O Aluminum Plate.

the bases of the tensile test specimens cut from the pole of each bulge. For low hydraulic bulging pressures, the strains in the longitudinal and transverse directions were compressive [9] at the bottom surface and tensile at the top surface of the bulge, however, for high pressures, the strains at the top and bottom surfaces were both tensile but varied greatly in magnitude.

To determine the strain gradient throughout the thickness, Knoop hardness traverses were made on specimens cut from the poles of the bulges, Fig. 8. The variation in Knoop hardness was essentially linear with respect to thickness, even after taking into account the minima in these curves where a transition from compressive to tensile strains occurred at some distance from the bottom surface of the bulge. The hardness was assumed proportional to the strain, thus the strain at any depth could be obtained. Hence, although some of the tensile test speci-

[9] The apparently anamalous compressive strains cannot be explained by the author at this time; however, their explanation may lie in the realm of bulge mechanics.

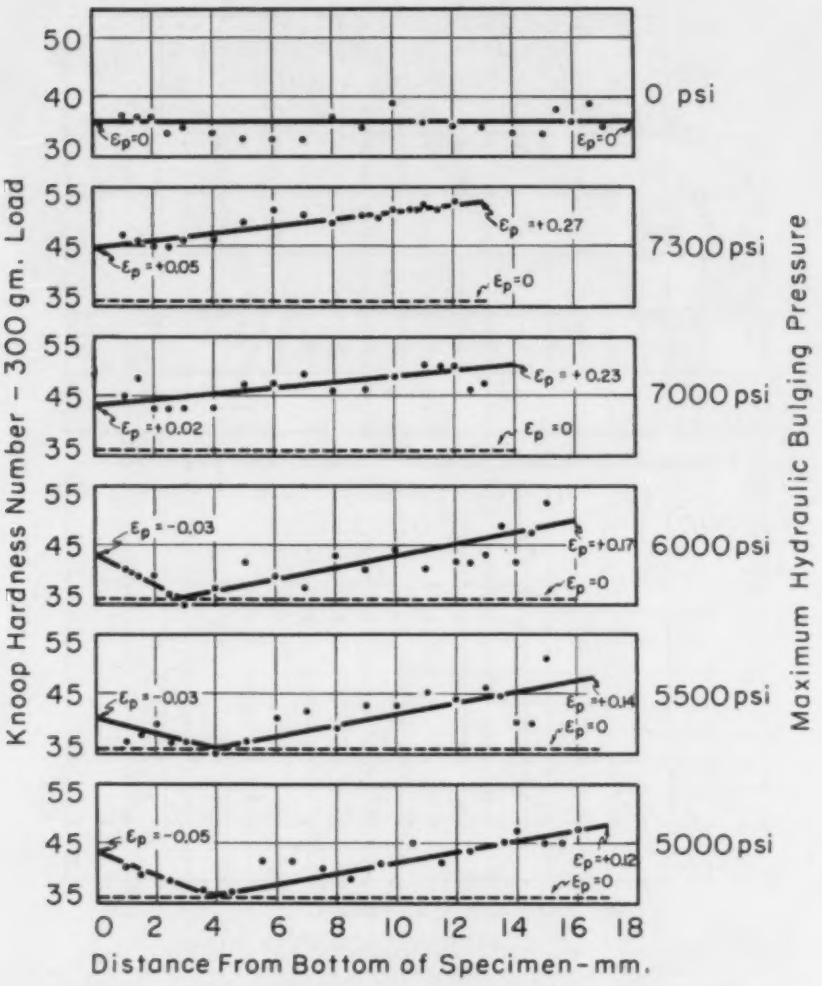


Fig. 8—Knoop Hardness Traverses Along the Axes of 2S-O Aluminum Tensile Test Specimens Prestrained in Biaxial Tension.

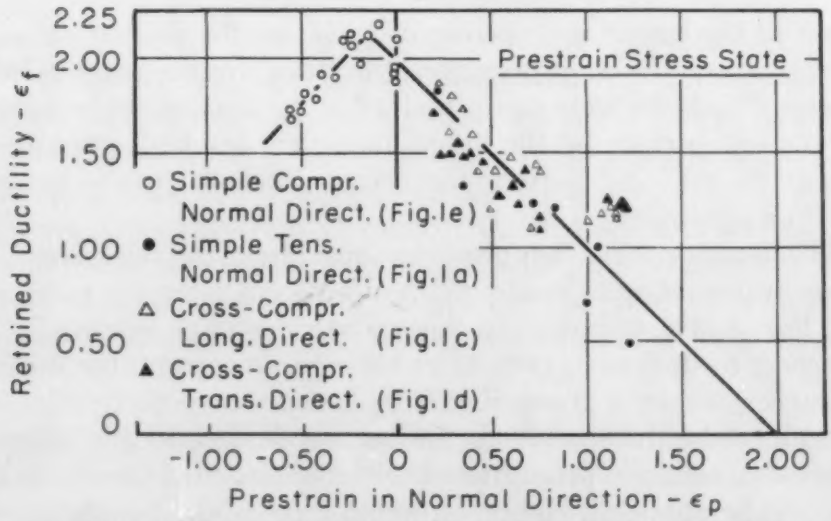


Fig. 9—Effect of Tensile ($\epsilon p > O$) and Compressive ($\epsilon p < O$) Prestrain in the Normal Direction of ¼ Inch Thick 2S-O Aluminum Plate Upon the Retained Tensile Ductility in the Normal Direction for Various Prestrain States.

mens did not fracture at the exact center of the gage length, the magnitude of the prestrain at the point of fracture in the tensile test specimen could be determined.

Results

The effect of prestrain (ϵ_p) upon various fracture and flow properties of 2S-O aluminum in tension are represented in Figs. 9 to 24. The fracture properties determined were the retained ductility (ϵ_f)[10] and the fracture stress (S_f)[11]. The only flow property investigated was the yield strength (0.2% offset).

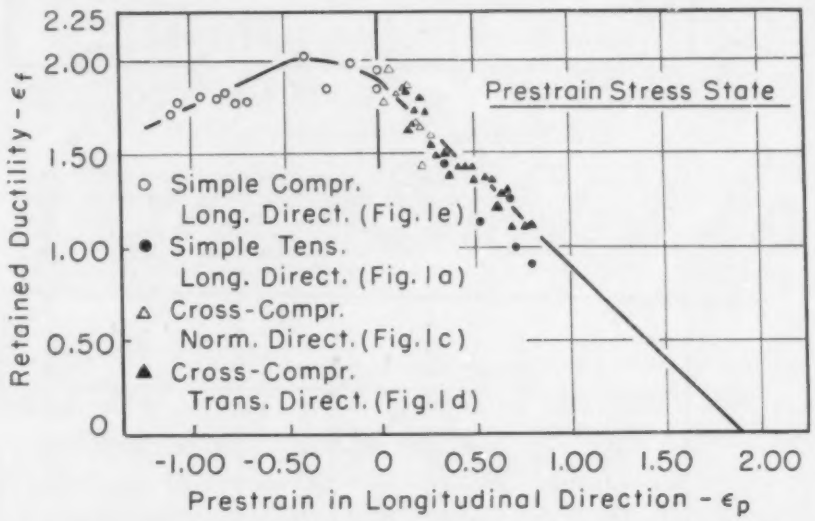


Fig. 10—Effect of Tensile ($\epsilon_p>0$) and Compressive ($\epsilon_p<0$) Prestrain in the Longitudinal Direction of ¾ Inch Thick 2S-O Aluminum Plate upon the Retained Tensile Ductility in the Longitudinal Direction for Various Prestrain Stress States.

Fracture Properties

Retained Ductility—Plots of retained tensile ductility versus prestrain for prestrain stress states of simple compression ($\epsilon_p<0$), simple tension ($\epsilon_p>0$), and cross-compression ($\epsilon_p>0$) are shown in Fig. 9, 10 and 11 for specimens prestrained and tested in the normal, longitudinal and transverse directions, respectively.

For each of the three test directions the curves for the prestrain stress states of simple tension and cross-compression appear to coincide in a straight line of 45 degree slope.

However, for tests taken in the normal direction, Fig. 9, for large cross-compressive prestrains in the longitudinal and transverse directions, there appears to be a tendency for deviation from the 45 degree line in a manner analagous to the curve for biaxial compression, see

[10] $\epsilon_f = \ln \frac{\text{Area After Prestrain}}{\text{Final Area}} = \frac{A_p}{A_f}$

[11] $S_f = \frac{\text{Load at Fracture}}{\text{Area at Fracture}}$

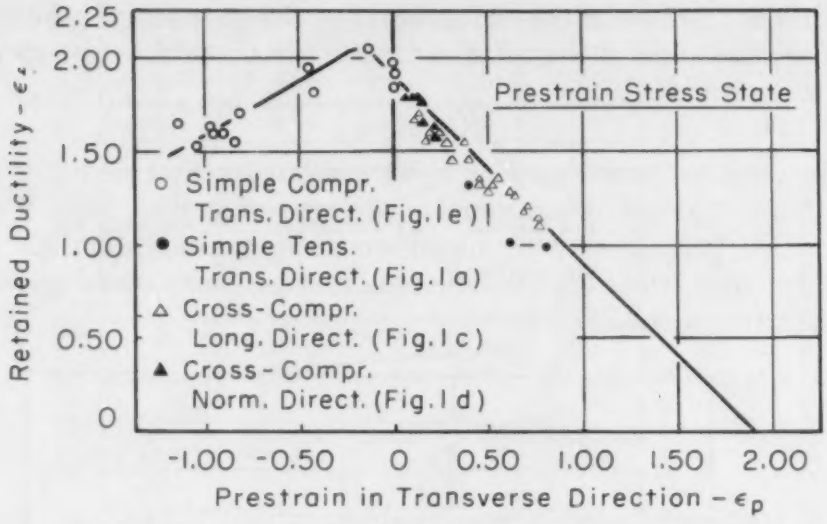


Fig. 11—Effect of Tensile (ϵp>O) and Compressive (ϵp<O) Prestrain in the Transverse Direction of ¾ Inch Thick 2S-O Aluminum Plate Upon the Retained Tensile Ductility in the Transverse Direction for Various Prestrain Stress States.

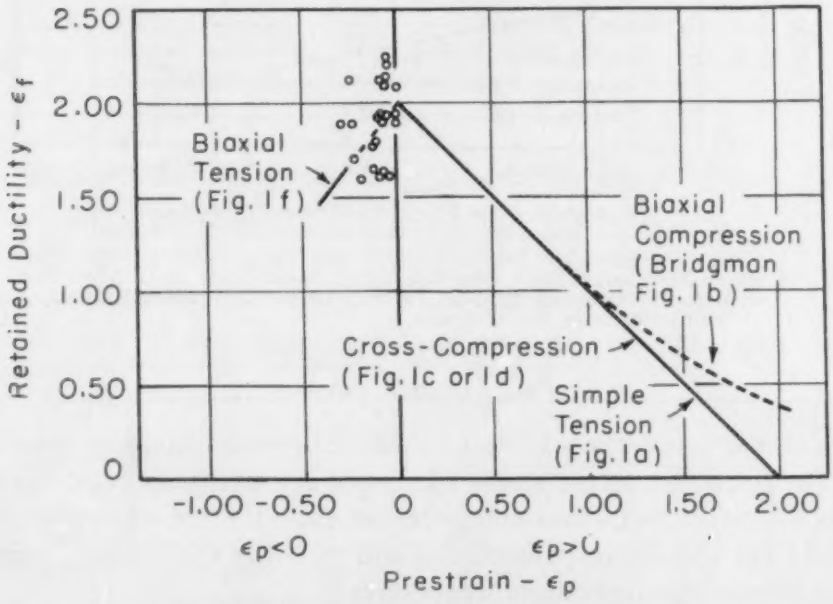


Fig. 12—The Effect of Prestrain in Biaxial Tension (ϵp<O) and in Biaxial Compression (ϵp>O) (Schematic after Bridgman) upon the Retained Tensile Ductility in the Normal Direction of ¾ Inch Thick 2S-O Aluminum Plate.

Fig. 12. It was not possible to justify this tendency for deviation from the 45 degree line, because of experimental difficulties, e.g., prestrain specimen size limitation in the normal direction and buckling tendencies in prestraining restricted the magnitude of the prestrains to those shown in Fig. 9. In this paper the curves for cross-compressive prestrain will be assumed to lie along a line of 45 degree slope for all three test directions as shown in Figs. 9,10 and 11.

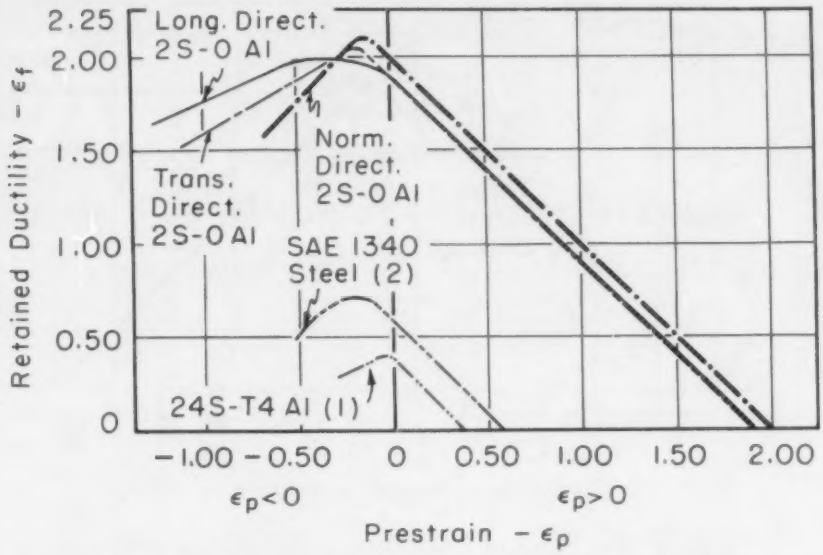


Fig. 13—The Effect of Prestrain in Simple Compression ($\epsilon\rho<0$) or in Simple Tension ($\epsilon\rho>0$) upon the Retained Tensile Ductility for ¼ Inch Thick 2S-O Aluminum Plate for Each of the Three Principal Directions. The prestrain direction was the same as the direction of the subsequent tensile test.

In these plots the following should be noted for each test direction: The continuous nature of each of the curves from the tensile prestrains ($\epsilon_p>0$) through zero prestrain ($\epsilon_p=0$) to compressive prestrains ($\epsilon_p<0$); the maximum in the curve at a simple compressive prestrain of small magnitude; and the subsequent decrease in retained tensile ductility (ϵ_f) at larger compressive prestrains. These features have also been observed in other investigations (1, 2).

A plot of the retained tensile ductility versus prestrain under a prestrain stress state of biaxial tension and a schematic curve of the expected retained tensile ductility (4) versus prestrain under the stress state of biaxial compression are shown in Fig. 12. For compressive prestrain (biaxial tension), the curve is a straight line of very steep slope, i.e., the retained ductility decreases very rapidly with increasing compressive prestrain. For tensile prestrain (biaxial compression), the curve has a smaller slope than the curve for simple tension (45 degrees) after exceeding some critical magnitude of prestrain (4).

The curves in Figs. 9,10 and 11 were combined with similar curves for 24S-T4 aluminum (1) and SAE 1340 steel[12] (2) in Fig. 13.

A comparison of the unworked ductilities of 2S-O aluminum in each of the three directions of the plate shows that the ductility in the normal direction is somewhat greater than that in either the longitudinal or transverse direction. At large compressive prestrains, however, the retained ductility is greater for the longitudinal and transverse directions than for the normal direction. Of course, for the tensile

[12] For specimens taken in the longitudinal direction of round bar stock.

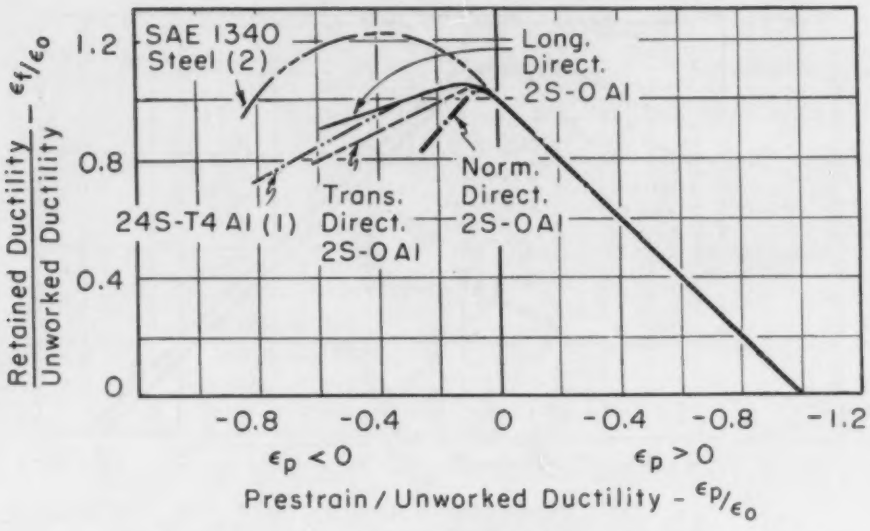


Fig. 14—The Effect of Prestrain in Simple Compression ($\epsilon\rho<O$) or in Simple Tension ($\epsilon\rho>O$) upon the Retained Tensile Ductility for ¾ Inch Thick 2S-O Aluminum Plate for Each of the Three Principal Directions. The prestrain direction was the same as the direction of the subsequent tensile test.

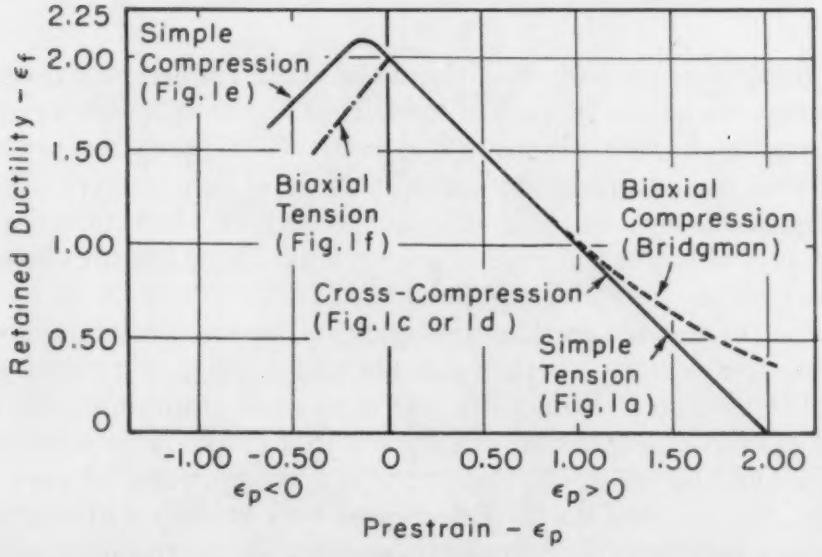


Fig. 15—The Effect of Prestrain Stress State upon the Retained Tensile Ductility in the Normal Direction of ¾ Inch Thick 2S-O Aluminum Plate. The curve for biaxial compressive prestrain is schematic after Bridgman (4).

prestrains, the ductility in the normal direction for any magnitude of prestrain is greater than that in the longitudinal or transverse direction because of the relationship between the unworked ductilities ($\epsilon_p = 0$) in the three directions.

The general shapes of the curves for 24S-T4 aluminum and SAE 1340 steel are similar to those for simple tensile or compressive prestrain for 2S-O aluminum.

Because of the much lower unworked ductilities of 24S-T4 alu-

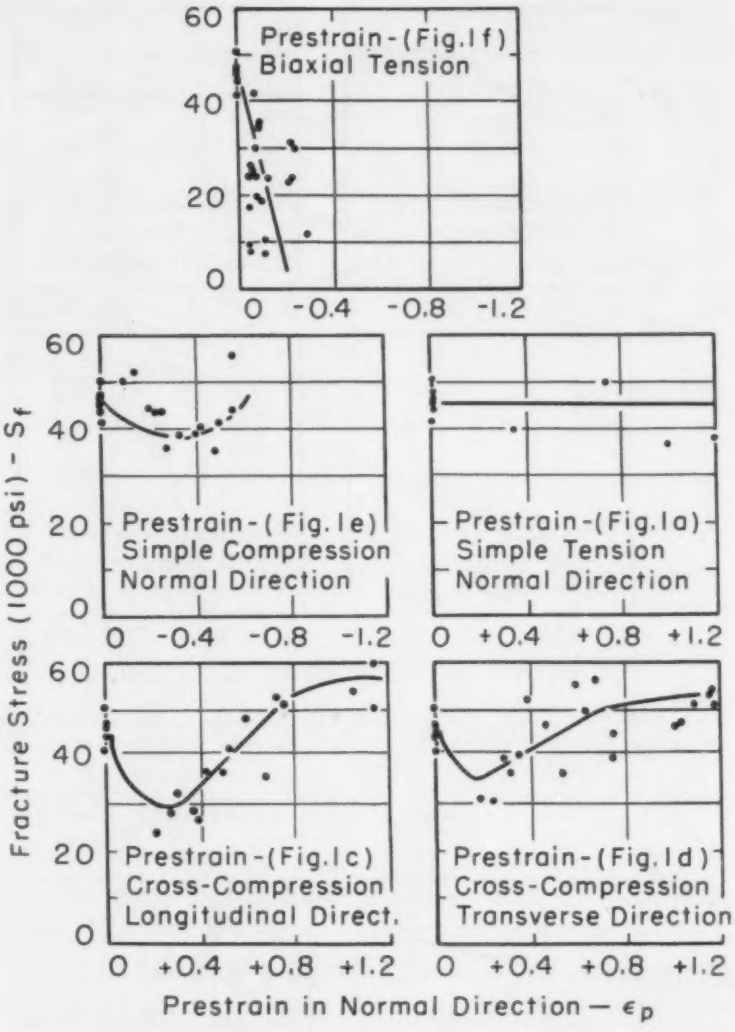


Fig. 16—Effect of Various Prestrain Stress States upon the Tensile Fracture Stress in the Normal Direction of ¾ Inch Thick 2S-O Aluminum Plate.

minum and SAE 1340 steel in comparison with that of 2S-O aluminum, the plots in Fig. 13 are transposed to Fig. 14 where the ratio of retained ductility to unworked ductility is plotted versus the ratio of prestrain to unworked ductility.

The curve for SAE 1340 steel is considerably higher than the other curves, whereas the curve for 24S-T4 aluminum approximates somewhat the curve for 2S-O aluminum prestrained and tested in the longitudinal direction.

For comparison purposes Fig. 15 was obtained by combining the curves in Fig. 12 with the curve for the prestrain stress state of simple compression in the normal direction in Fig. 9.

Fracture Stress—Plots of tensile fracture stress versus prestrain under conditions of different stress states are shown for the normal di-

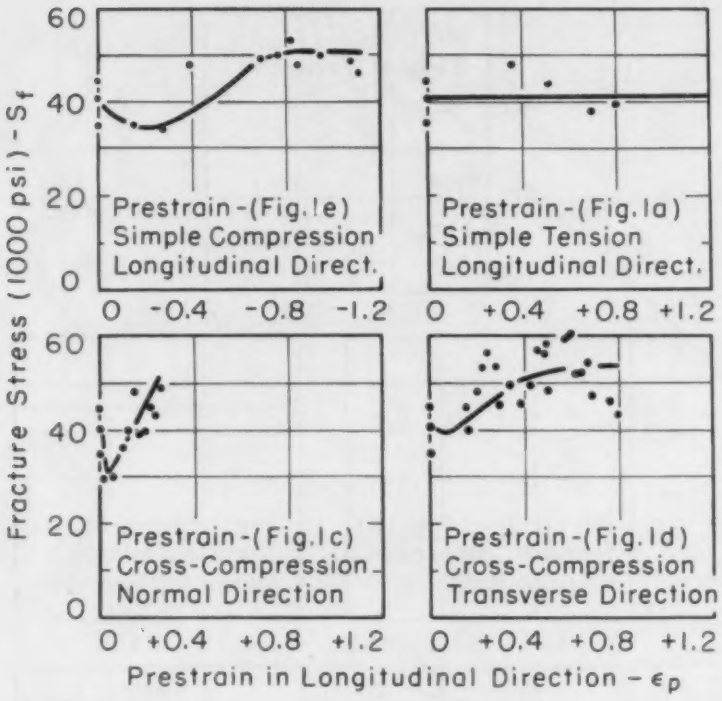


Fig. 17—Effect of Various Prestrain Stress States upon the Tensile Fracture Stress in the Longitudinal Direction of ¾ Inch Thick 2S-O Aluminum Plate.

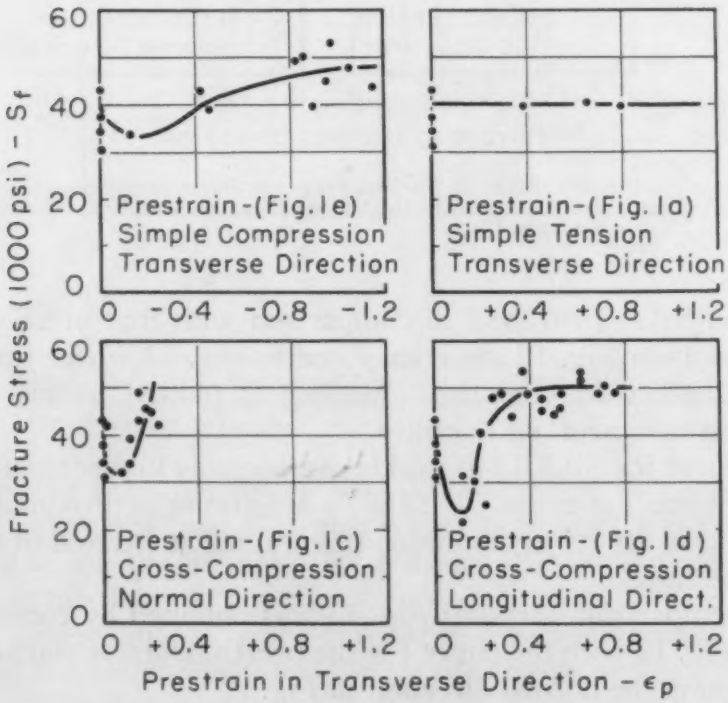


Fig. 18—Effect of Various Prestrain Stress States upon the Tensile Fracture Stress in the Transverse Direction of ¾ Inch Thick 2S-O Aluminum Plate.

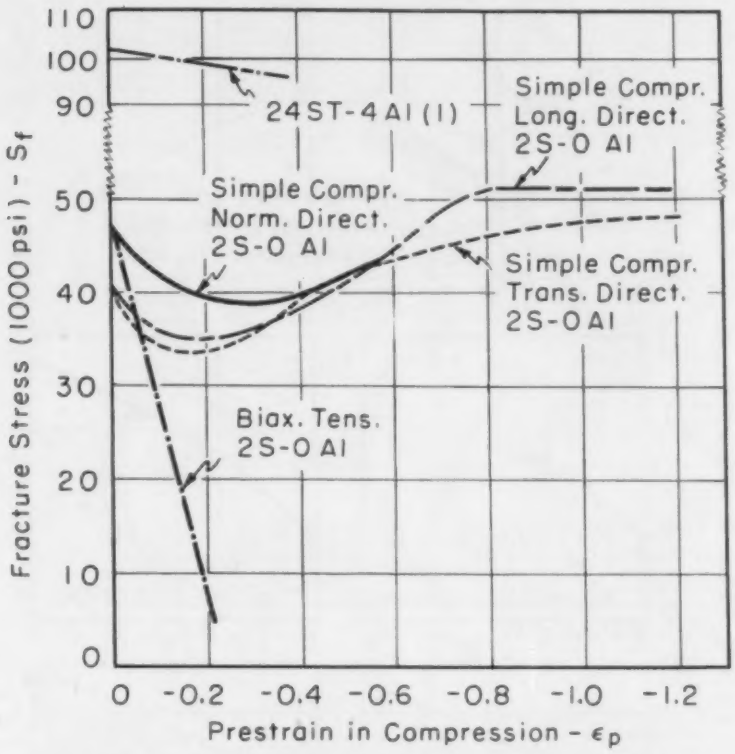


Fig. 19—Comparison of Compressive Prestrain Effects Upon the Fracture Stress in Tension of 2S-O Aluminum for Various Prestrain States and Prestrain Directions.

rection, Fig. 16, the longitudinal direction, Fig. 17, and the transverse direction, Fig. 18.

For each of the three principal directions for prestrain in simple tension, the curve appears to be a horizontal line; however, for prestrain stress states of simple compression and "cross-compression," each of the tensile fracture stress curves exhibits a minimum for each of the three test directions.

Fig. 19 shows plots of tensile fracture stress versus compressive prestrain for the prestrain stress state of simple compression in each of the three principal directions and for the prestrain stress state of biaxial tension in the normal direction. Also included is the curve for 24S-T4 aluminum (1). The curves for simple compressive prestrain for each of three directions in the 2S-O aluminum plate are similar in that each exhibits a minimum at a relatively low magnitude of prestrain and then rises; however, the curves for the longitudinal and transverse directions do show a tendency to flatten out at higher prestrains at a fracture stress of the order of magnitude of 50,000 psi. The curve for the prestrain stress state of biaxial tension for 2S-O aluminum differs in that it is a straight line of steep slope with no minimum and no propensity towards flattening out. The curve for 24S-T4 aluminum is a straight line of gentle slope.

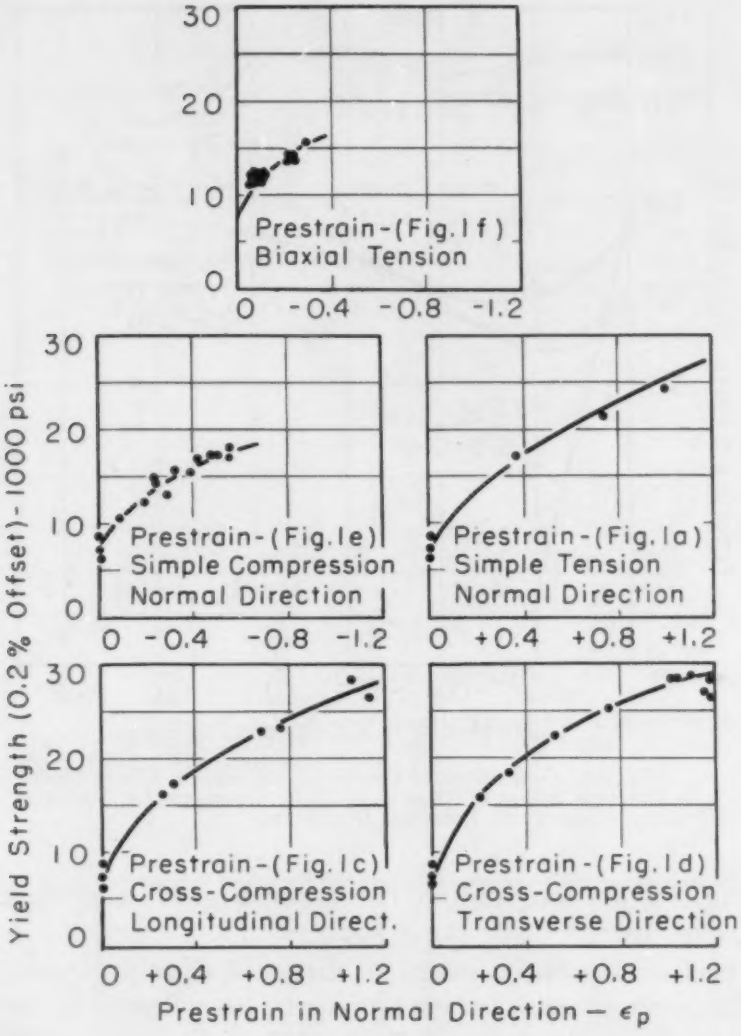


Fig. 20—Effect of Various Prestrain Stress States upon the Yield Strength (0.2% Offset) in Tension in the Normal Direction of ¼ Inch Thick 2S-O Aluminum Plate.

The Effect of Prestrain Upon Flow Properties

Yield Strength—Plots of yield strength in tension versus prestrain for different prestrain stress states are shown for the normal direction, Fig. 20; the longitudinal direction Fig. 21; and the transverse direction, Fig. 22. For a given principal direction, there are but slight differences in the yield strength curves for the various prestrain stress states.

Plots of yield strength in tension versus compressive prestrain for the prestrain stress state of simple compression in each of the three principal directions and for the prestrain stress state of biaxial tension in the normal direction are shown in Fig. 23. Also included is the curve for 24S-T4 aluminum (1). The curves for 2S-O aluminum for simple

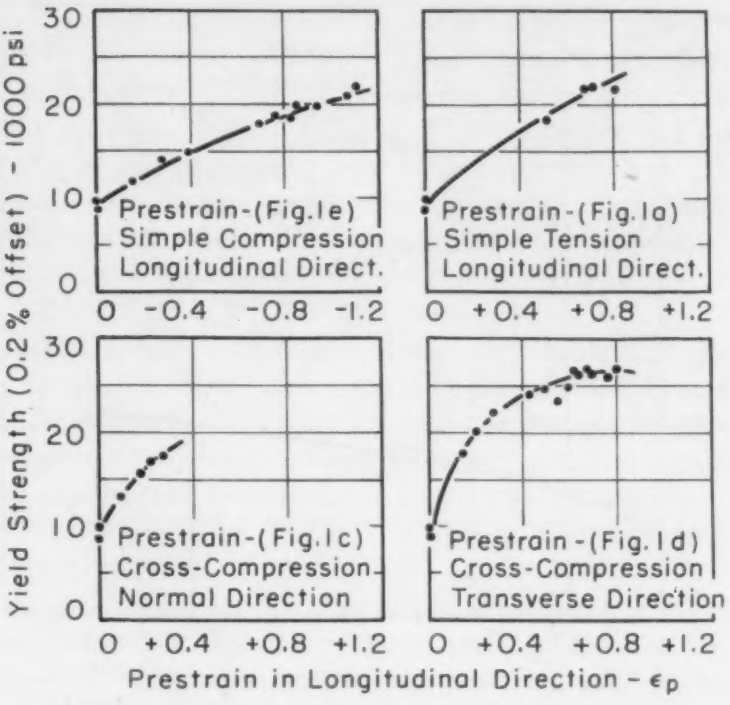


Fig. 21—Effect of Various Prestrain Stress States upon the Yield Strength (0.2% Offset) in Tension in the Longitudinal Direction of ¾ Inch Thick 2S-O Aluminum Plate.

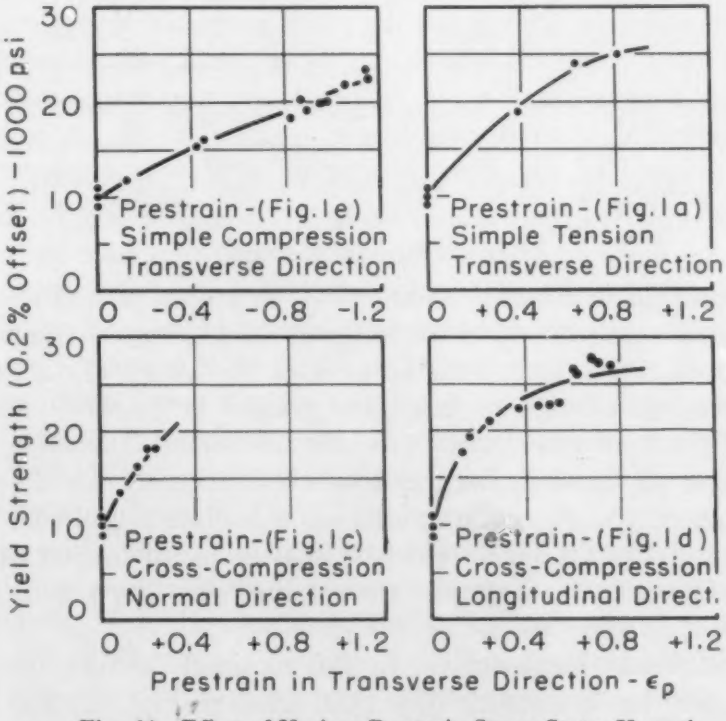


Fig. 22—Effect of Various Prestrain Stress States Upon the Yield Strength (0.2% Offset) in Tension in the Transverse Direction of ¾ Inch Thick 2S-O Aluminum Plate.

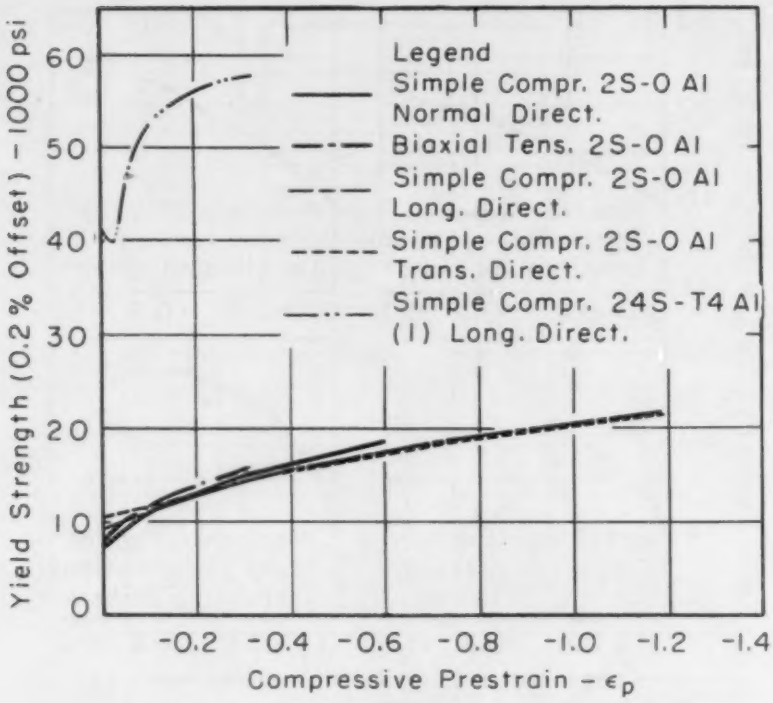


Fig. 23—Comparison of Compressive Prestrain Effects upon the Yield Strength (0.2% Offset) in Tension for ¾ Inch Thick 2S-O Aluminum Plate and 24S-T4 Aluminum (1) for Various Prestrain Stress States and Directions. The prestrain direction was the same as the direction of the subsequent tensile test.

compression in the three principal directions are all quite similar. This similarity can also be shown for the other prestrain stress states. Liu's curve is of course much higher than those for 2S-O aluminum, has a minimum at a very small value of prestrain, and has a much steeper slope at prestrains of small magnitude.

No evidence of the Bauschinger effect[13] was apparent for the work in this paper.

Discussion of Results

Prestraining in Biaxial Tension—It is apparent in Figs. 5,6 and 7 that the strain anisotropy in the bulge at the vicinity of the pole of the bulge is strain dependent; i.e., the greater the longitudinal and transverse strains in the bulge surfaces, the greater is the strain anisotropy.

The Effect of Prestrain upon the Retained Ductility—The inherent scatter of the data for the unworked ductility for 2S-O aluminum in each of the three directions of the plate should be noted in Figs. 9,10 and 11. This characteristic scatter in unworked ductility is an implicit factor in the scatter of the retained ductility versus prestrain data for the above curves.

The relatively large scatter in the retained ductility versus prestrain data for the stress state of biaxial tension, Fig. 12, was probably

[13] Lowering of the yield strength by a difference in stress state between the prestrain and the test.

caused by a combination of variations in the previously mentioned bend stresses and by the plate anisotropy. The trend of the data might have been more apparent if it had been possible to obtain larger compressive prestrains by means of biaxial tension. This condition was not possible with the material and equipment used in this investigation.

The greater unworked ductility in the normal direction than in the longitudinal direction of the 2S-O aluminum plate appears anomalous when compared with the results in the published literature (11). The discrepancy cannot be explained at this time.

The differences between the curves for retained tensile ductility versus prestrain in simple compression in the normal direction and in biaxial tension, Fig. 15, seem to be of fundamental significance. The unknown mechanism which causes an increase in retained tensile ductility for small compressive prestrains for a prestrain stress state of simple compression appears to be inoperative for a prestrain stress state of balanced biaxial tension.

The absence of a discontinuity in the prestrain curve from simple compressive to simple tensile prestrain in Fig. 13 possibly indicates that the small increase in retained ductility for small values of compressive prestrain has only a slight effect upon the fracture mechanism in tension.

A change in prestrain stress state from simple tension to "cross-compression" does not affect the retained tensile ductility, see Fig. 9, 10 and 11, but a change in prestrain stress state to simple compression or biaxial tension, Fig. 15, modifies the retained tensile ductility curve.

From Fig. 1 the prestrain stress state of cross-compression is apparently intermediate between simple tension and biaxial compression. The results, however, indicate that for each of the three test directions the curve for retained tensile ductility versus prestrain in cross-compression, Figs. 9,10 and 11, coincides with the curve for simple tension, rather than lying somewhere between the curves for prestrain in simple tension and biaxial compression, Fig. 15.

Fracture Stress—Although the retained ductility and fracture stress are both considered to be fracture properties, the change in prestrain stress state from simple tension to "cross-compression" (for both, $\epsilon_p > 0$) caused no change in the retained tensile ductility curve, Figs. 9,10 and 11, but caused a change in the shape of the tensile fracture stress curve, Figs. 16,17 and 18.

These results should be considered from the point of view that the fracture stress is not a simple phenomenon. The fracture stress of a metal depends upon the ductility, the strain hardening rate and the yield strength of the metal. The interrelations between the above variables and considerations of their relative magnitudes could certainly produce minima in those curves for tensile fracture ductility when the prestrain stress state is changed from one of simple tension to simple

compression or "cross-compression," see Figs. 16,17 and 18, or change the slope of the fracture stress curve from a horizontal line for a prestrain stress state of simple tension to a straight line of steep slope for a prestrain stress state of biaxial tension, see Fig. 16.

The curves for prestrain in simple compression for the three directions of the 2S-O aluminum plate exhibit certain similarities, see Fig. 19. There is a minimum in each of these curves at a small value of compressive prestrain. Then the curves for the longitudinal and transverse directions rise, flattening out at larger prestrains at fracture stress values of about 50,000 psi. It seems possible to expect that the curve for the normal direction would also have flattened out after rising from the minimum, had it been possible to obtain larger prestrains in the normal direction.

Liu's curve for 24S-T4 aluminum is of different shape from the above curves for 2S-O aluminum. The difference may be explained by the large difference in ductility between 2S-O and 24S-T4 aluminum. Koerber (5) found that the tensile fracture stress for a mild steel consistently decreased with increasing compressive prestrain. But McAdam (3) reported that with increasing compressive prestrain, the tensile fracture stress of an annealed chromium steel first decreased to a minimum and then increased continuously. Complex curves for fracture stress versus prestrain were obtained by Backofen and his associates (12) under conditions of prestrain in torsion and testing in tension. It is possible that a difference between the stress state in prestraining and in testing tends to complicate the horizontal curve expected when the stress states for prestrain and testing are of the same type.

The curve for fracture stress versus prestrain in balanced biaxial tension is significantly different from that for simple compressive prestrain in the normal direction, Fig. 19. Apparently, the effect of the balanced biaxial tensile prestrain is to mask completely those characteristics present in the curve for simple compressive prestrain and to cause only a rapid linear decrease in fracture stress with increasing compressive prestrain.

Yield Strength—The evident proximity of the curves for all prestrain stress states, see Figs. 20 to 23, indicates that a difference in prestrain stress state has no significant influence upon the effect of prestrain on the yield strength in tension.

Conclusions

The fracture properties (stress and strain) of 2S-O aluminum depend not only upon the nature and magnitude of the prestrain, but also upon the stress state under which a given prestrain is effected, see Fig. 24.

Thus, for example, for each test direction for compressive pre-

strains of the same magnitude, a prestrain stress state of simple compression resulted in a higher retained tensile ductility than did a prestrain stress state of biaxial tension.

For tensile prestrains of the same magnitude (after a critical amount of prestrain) a prestrain stress state of biaxial compression resulted in a higher retained tensile ductility than did a prestrain stress state of simple tension.

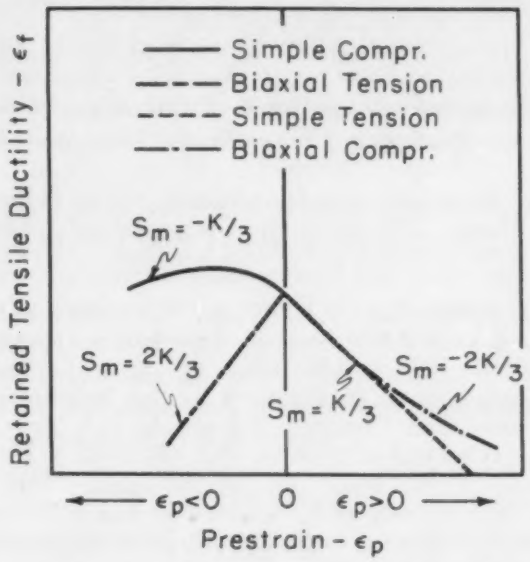


Fig. 24—Schematic Representation of Retained Tensile Ductility Versus Prestrain for Various Prestrain Stress States for 2S-O Aluminum Plate. The prestrain direction is the same as that of the subsequent tensile test. The mean stress (S_m) is given for each prestrain stress state in terms of the yield strength in tension.

However, for tensile prestrains of the same magnitude, a prestrain stress state of simple tension resulted in the same retained tensile ductility as did a prestrain stress state of cross-compression.

For compressive prestrains of the same magnitude, a prestrain stress state of simple compression resulted in a higher tensile fracture stress than did a prestrain stress state of biaxial tension.

The shapes of the curves obtained for tensile fracture stress versus prestrain differed considerably when the prestrain stress state was varied.

No significant changes in the tensile yield strength versus prestrain curves were obtained by variations in the prestrain stress states.

Acknowledgments

This work was conducted in cooperation with the Office of Naval Research, U. S. Navy. The aid and advice of Dr. W. M. Baldwin, Jr., Dr. L. J. Ebert, Dr. E. J. Ripling and other members of the Metals Research Laboratory are greatly appreciated.

References

1. S. I. Liu and G. Sachs, "The Flow and Fracture Characteristics of the Aluminum Alloy 24ST after Alternating Tension and Compression," *Metals Technology,* Vol. 15, June, 1948, TP2392.
2. E. J. Ripling and W. M. Baldwin, Jr., "Overcoming Rheotropic Brittleness: Precompression Versus Pretension," TRANSACTIONS, American Society for Metals, Vol. 44, 1952, p. 1047–1054.
3. D. J. McAdam, Jr., G. W. Geil and W. D. Jenkins, "Influence of Plastic Extension and Compression on the Fracture Stress of Metals," *Transactions,* American Society for Testing Materials, Vol. 47, 1947, p. 554–574.
4. P. W. Bridgman, Studies in Large Plastic Flow and Fracture, McGraw-Hill, 1952, p. 293–310.
5. F. Koerber, A. Eichinger and R. Moeller, "The Behavior under Tensile Stress of Metals Deformed by Compression," *Mitteilungen aus dem Kaiser-Wilhelm-Institut für Eisenforschung zu Dusseldorf,* Vol. 26, 1943, p. 71–88.
6. G. Sachs, J. D. Lubahn and L. J. Ebert, "Notched Bar Tensile Tests on Heat Treated Low Alloy Steels," TRANSACTIONS, American Society for Metals, Vol. 31, 1943, p. 136–160.
7. G. Sachs, G. Espey, and G. B. Kasik, "Circular Bulging of Aluminum Alloy Sheet at Room and Elevated Temperatures," *Transactions,* American Society of Mechanical Engineers, Vol. 68, 1946, p. 161–173.
8. W. T. Lankford, A. R. Low and M. Gensamer, "The Plastic Flow of Aluminum Alloy Sheet under Combined Loads," *Transactions,* American Institute of Mining and Metallurgical Engineers, Vol. 171, 1947, p. 574–604.
9. W. F. Brown, Jr. and M. H. Jones, "Strain Analysis by Photogrid Method," *Iron Age,* Vol. 153, September 12, 1946, p. 50–55.
10. H. Thielsch, "Bulge Testing of Sheet Metal," METAL PROGRESS, Vol. 56, July, 1949, p. 86–88.
11. L. J. Klingler and G. Sachs, "Fracturing Characteristics of Aluminum-Alloy Plate," *Journal of the Aeronautical Sciences,* Vol. 15, No. 12, December 1948, p. 731–734.
12. W. A. Backofen, B. B. Hundy and J. Wulff, "The Ductile Fracture of Metals," Tech. Report No. 3, O.N.R. Contr. N5ori-07841, Project No. NR 031-356, July 30, 1951, p. 7–8.

DISCUSSION

Written Discussion: By B. B. Hundy, British Iron and Steel Research Association, Sheffield, England.

The problem of the fracture of metals is very complicated and, as yet, is little understood. This paper by Dr. Rozalsky is a very interesting contribution to our meager knowledge of this subject and may, one day, help toward a fuller understanding of the factors governing fracture.

It is perhaps fortunate that 2S aluminum was chosen as the subject for this thorough investigation; our work at Massachusetts Institute of Technology[14, 15] on mechanical anisotropy showed that, of the 6 or 7 different metals tested, only 2S aluminum exhibited no mechanical anisotropy due to previous processing. Our

[14] W. A. Backofen, A. J. Shaler and B. B. Hundy, "Mechanical Anisotropy in Copper," TRANSACTIONS, American Society for Metals, Vol. 46, 1954, p. 655.

[15] W. A. Backofen and B. B. Hundy, "Mechanical Anisotropy in some Ductile Metals," *Journal,* Institute of Metals, Vol. 81, 1952–53, p. 433.

work suggested that most wrought metals contain an oriented system of minute flaws or microcracks which are aligned by the processing to give maximum ductility in the direction of working and minimum ductility transverse to this direction. Thus, in most cases, when a metal is prestrained by cold working, reorientation of the microcracks (due to the change in shape of the specimen) may possibly affect the fracture behavior and it is difficult to decide on the essential effect of the cold work only. As the ductility in the normal direction of the 2S plate used in this present work was, if anything, higher than in the longitudinal or transverse directions, it seems, in agreement with our own work, that the influence of microcracks (if present) was negligible and that in this case we can probably consider the effects of prestraining as being due only to the cold work.

On the other hand, however, there is one other factor which complicates the results and which has not been eliminated in this work: this is the crystallographic anisotropy. It is generally recognized that preferred orientation affects fracture as well as the flow properties and it is to be expected that prestraining would modify the annealing texture so as to affect the mechanical properties to some extent. It is not impossible, of course, that this is only a minor effect and can be ignored. I do feel, however, that the modification of the texture by the cold work of prestraining should not be overlooked.

Were the true stress-strain curves recorded during the final tensile test? Dr. Rozalsky makes no mention of this and only quotes the fracture properties and the yield strength. The shape of the stress-strain curve and the rate of work hardening are also of very great interest and I would welcome any information that the author might have on the effects of the various methods of prestraining on these.

Authors' Reply

The author appreciates the constructive criticisms and comments offered by Dr. Hundy.

The primary purpose of this investigation was to determine the effect of prestraining under different stress states on the fracture properties of 2S-O aluminum; the only flow property investigated was the yield strength (0.2% offset). In order to determine the yield strength a true stress-true strain curve was recorded for each prestrained aluminum specimen during the final tensile test operation. However, no rigid analysis has as yet been made to determine the effect of the various methods of prestraining on the rate of work hardening and the shape of the stress-strain curve.

DEFORMATION MECHANISMS IN POLYCRYSTALLINE AGGREGATES OF MAGNESIUM

By F. E. Hauser, C. D. Starr, L. Tietz and J. E. Dorn

Abstract

Deformation mechanisms in polycrystalline magnesium at atmospheric temperature were investigated by metallographic and X-ray techniques. Basal slip and twinning on $(10\bar{1}2)$ planes were observed. In addition deformation took place by kinking and grain boundary shearing. Fracturing occurred on various crystallographic planes of high index as well as by an intergranular mechanism.

Introduction

SCIENTIFIC and technical interest have stimulated detailed and extensive investigations directed toward uncovering the fundamental processes involved in the plastic deformation of metals. The majority of such investigations have been concerned with simple stressing of single metal crystals with the objective in mind to simplify the analyses by eliminating many of the variables inherent in the more complex problem of deformation in polycrystalline aggregates; and the virtue of thus controlling and reducing the variables has been substantiated by the definitive correlations that have matured among the crystal structure, laws of deformation and the deformation mechanisms. But the ultimate objective of all such investigations has been the complete rationalization of the plastic behavior of polycrystalline aggregates. Whether the plastic behavior of polycrystalline aggregates might be completely deduced from singular knowledge of deformation mechanisms in single crystals has not yet been fully established. Undoubtedly the auxiliary knowledge gained from investigations on polycrystalline aggregates concerning the more general conditions of stressing encountered by each grain and concerning interactions at their mutual boundaries will be required before any extrapolation of the plastic properties of single metal crystals to those of the polycrystalline aggregate can be made with confidence.

The investigations described in this report were initiated as preliminary studies of deformation and fracture mechanisms in polycrystalline aggregates. It was thought that the polycrystalline aggregate would exhibit all of the mechanisms of deformation that could be de-

A paper presented before the Thirty-sixth Annual Convention of the Society, held in Chicago, November 1 to 5, 1954. Of the authors, F. E. Hauser and C. D. Starr are research engineers, L. Tietz is laboratory technician and J. E. Dorn is professor of physical metallurgy, University of California, Berkeley, Cal. Manuscript received April 30, 1954.

tected in single metal crystals and that it might also reveal new mechanisms or new details of deformation processes fundamental to polycrystalline behavior. High purity magnesium was chosen for this study not only because of the extensive interest in this light-weight metal but particularly because of the limited number of deformation mechanisms single crystals of magnesium are known to exhibit at atmospheric temperature. For this reason it appeared that polycrystalline magnesium would more readily exhibit new mechanisms of deformation and perhaps new details of deformation when deformed as a polycrystalline aggregate than metals from other systems that exhibit a greater number of deformation mechanisms.

The known fact that polycrystalline aggregates of magnesium undertake general plastic deformations suggests that each grain should exhibit at least five independent mechanisms of deformation. This conclusion follows from the argument that a general deformation involves six strain components; but the sum of the three normal components of the strain equals zero due to the fact that the volume remains constant; consequently only five independent mechanisms of deformation are required to account for the five independently variable components of the strain. The three mechanisms of basal slip can account for only two of the five required mechanisms, since all three are coplanar. The deformations arising from twinning in magnesium are negligible in view of its almost theoretical axial ratio for close packing. This suggests the possible introduction of pyramidal slip, which has been announced for single crystals particularly at elevated temperatures as necessary to account for the so-called three missing mechanisms of deformation; but, if pyramidal slip or other slip mechanisms are not found, yet other mechanisms of deformation will have to be uncovered to account for the facts.

Experimental Procedure

The preliminary objective of this investigation was to observe and evaluate the metallographic evidence following tensile straining of polycrystalline magnesium. A high purity magnesium extrusion was selected in preference to a casting in order to ensure better reproducibility of results and to provide for easier grain size control. It was recognized that this selection would not provide the most general observations since the extrusion would exhibit preferred grain orientations. Furthermore, by necessity, the observations would be limited to the surface grains. But it was hoped that such observations as could be made would nevertheless be somewhat indicative of the general behavior of internal grains as well.

High purity (99.97% magnesium) magnesium was supplied by courtesy of The Dow Chemical Company in the form of extruded bars 0.100 inches thick and 0.75 inches wide. The bars were carefully machined into parallel gage section tension specimens 0.375 inches wide,

having a gage length of 1.00 inch. The surface of each specimen was hand polished to remove the die markings and then given a grain coarsening anneal for 6 hours at 600 °C (1110 °F) in an SO_2 atmosphere. Following this each specimen was electrolytically polished in an ethyl alcohol solution containing 37.5% of orthophosphoric acid using 1.5 volts and 20 ma per dm^2. Etching to reveal the grain boundaries was conducted in an aqueous solution containing 10% citric acid. The specimens exhibited a mean grain diameter of about 0.05 inches, deemed large enough to facilitate this initial study.

Five specimens were investigated in this study. Specimens 1, 2 and 5 were tested in the as-etched condition in order to review the general characteristics of deformation. In order to provide a basis of local strain measurements and to assist in relocating interesting grains during interrupted tensile testing specimens 3 and 4 were lightly scribed with a ruling machine to produce a fine 0.0200 inch square grid over the gage section. Although some very small mechanical twins were produced in the immediate vicinity of the scribed lines by this procedure, the deformation observations were identical with those obtained on the ungridded specimens. Furthermore the orientations of 39 contiguous grains were determined in specimen 4 by microbeam back-reflection Laue X-ray technique, using Greninger's method of analysis, for the purpose of facilitating identifications of slip band markings, twin plane traces, crystallographically oriented low angle boundaries, fracture planes and mutual orientation effects in the vicinity of the grain boundaries.

Thirty-nine contiguous grains of specimen 4 were identified by the numbering scheme presented in Fig. 1. Fig. 2a illustrates the relative orientation of the tension axis of the specimen in each grain as viewed in terms of a standard projection. For the purpose of revealing more rapidly the type of preferred orientation encountered here, these same orientation data were plotted as a pole figure for the [0001] and the $[11\bar{2}0]$ axes respectively as viewed with the net oriented parallel to the flat surface of the extruded bar (Fig. 2b). These data reveal that the predominating texture is one in which the basal plane lies in or near the extrusion plane with nearly equal scattering in all directions from this position while the $[11\bar{2}0]$ slip directions are randomly oriented with respect to the extrusion direction. For purpose of discussion the orientation of each of the thirty nine grains was identified in terms of the angle χ between the tension axis and the [0001] direction and the angle λ between the tension axis and the most favorably oriented $[11\bar{2}0]$ axis for basal slip as recorded in Table I. Thus the average shear stress σ on the basal plane in the slip direction is

$$\sigma = s \sin \chi \cos \lambda \qquad \text{Equation 1}$$

where s is the average tensile stress. Basal slip will therefore be facile

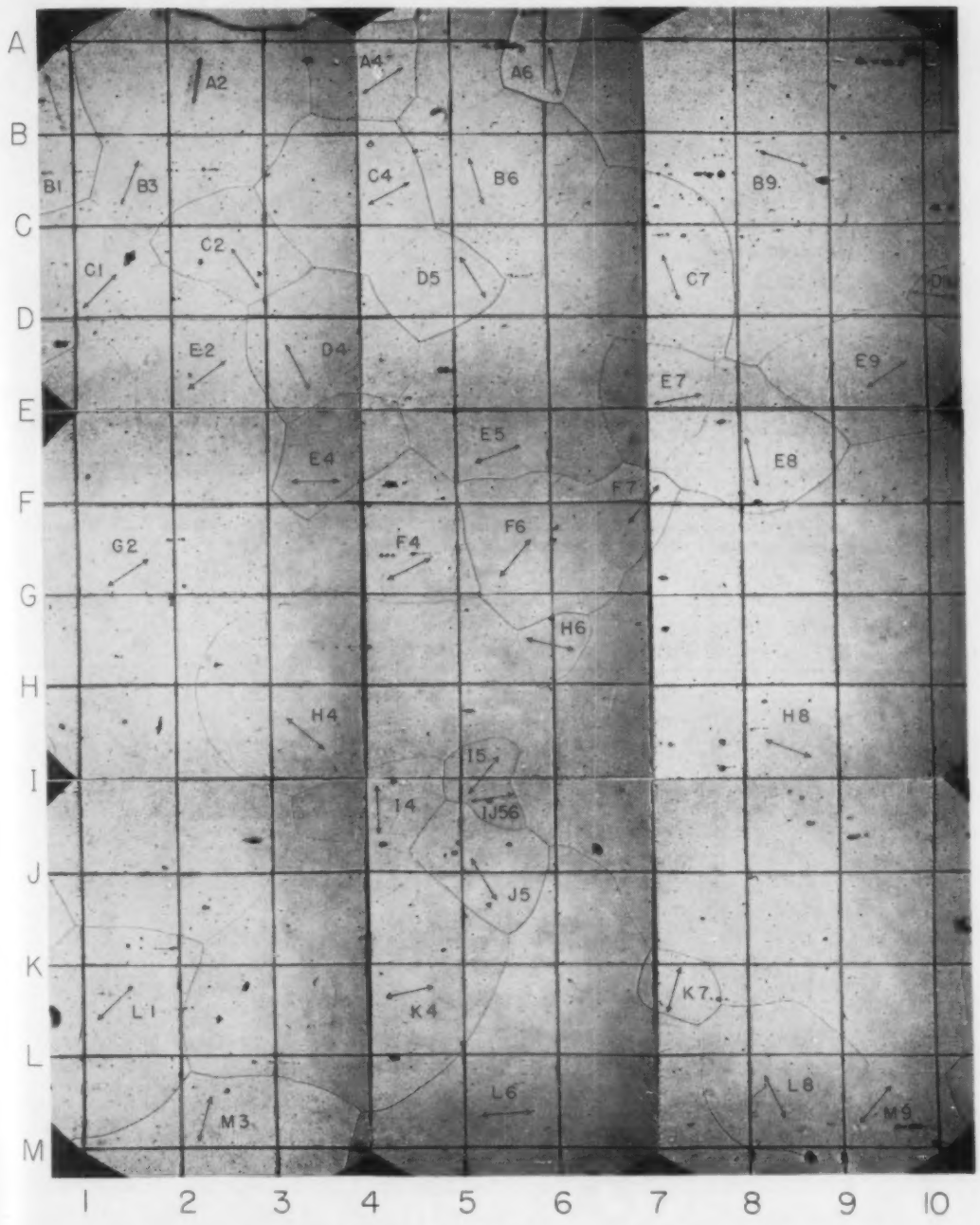


Fig. 1—Method of Identification of Grains in Specimen 4. Lines represent slip directions calculated from X-ray Orientations. Specimen 4 at 0%ϵ. (X 100 reduced to 1/5 size).

on those grains having the largest values of sin χ cos λ. The data recorded in Table I reveal an extensive range of values of sin χ cos λ suggesting that the specimen contained grains of widely differing orientations.

Results and Discussion

As shown in Fig. 3, the tensile properties of the five specimens appeared to exhibit rather large scatter from each other. This, however,

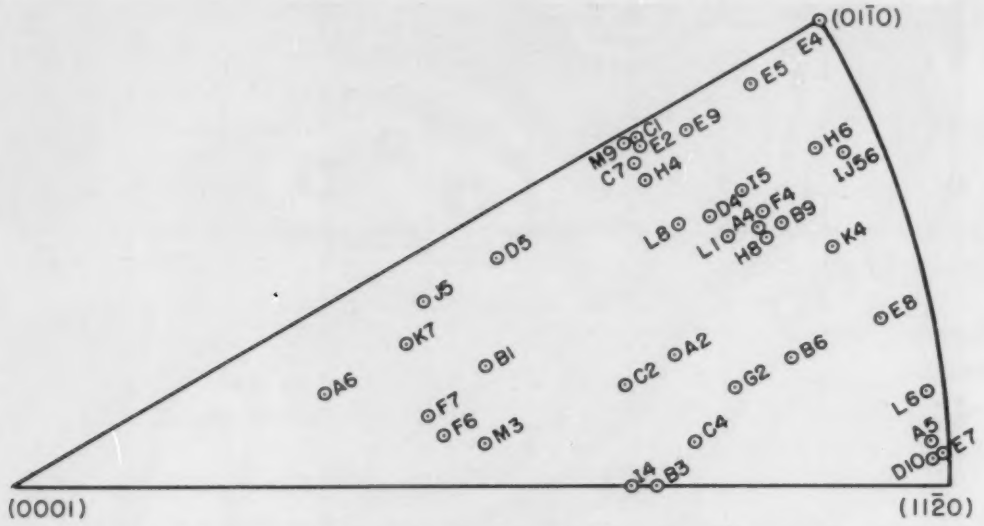


Fig. 2a—Orientation of Grains in Specimen 4. Poles of tension axis of each grain represented on standard stereographic projection.

Table I
Orientation of Grains in Specimen 4

Grain	χ	λ	Sin χ / Cos λ
A2	18	21.5	0.287
A4	9.5	21.5	0.154
A5	1	3	0.017
A6	51	53	0.465
B1	34.5	37	0.452
B3	21	21	0.334
B6	9.5	13.5	0.160
B9	8	20.5	0.130
C1	15	53.5	0.218
C2	22.5	24.5	0.348
C4	17.5	18	0.286
C7	17	36	0.249
D4	13.5	21.5	0.212
D5	30	38.5	0.392
D10	1	2	0.017
E2	15	34	0.219
E4	0	12	0.000
E5	6	32	0.092
E7	0.5	2	0.009
E8	3.5	11.5	0.060
E9	11.5	34	0.172
F4	8.5	22	0.137
F6	40	40.5	0.489
F7	41	42	0.407
G2	14	16	0.233
H4	16	30	0.239
H6	4	23	0.064
H8	9	21.5	0.145
I4	23	23	0.360
I5	9.5	24	0.151
IJ56	2.5	22	0.041
J5	38	44	0.443
K4	5	17	0.083
K7	41	45	0.464
L1	12	22.5	0.192
L6	1	6	0.017
L8	15	26	0.233
M3	36	36.5	0.473
M9	16	34	0.232

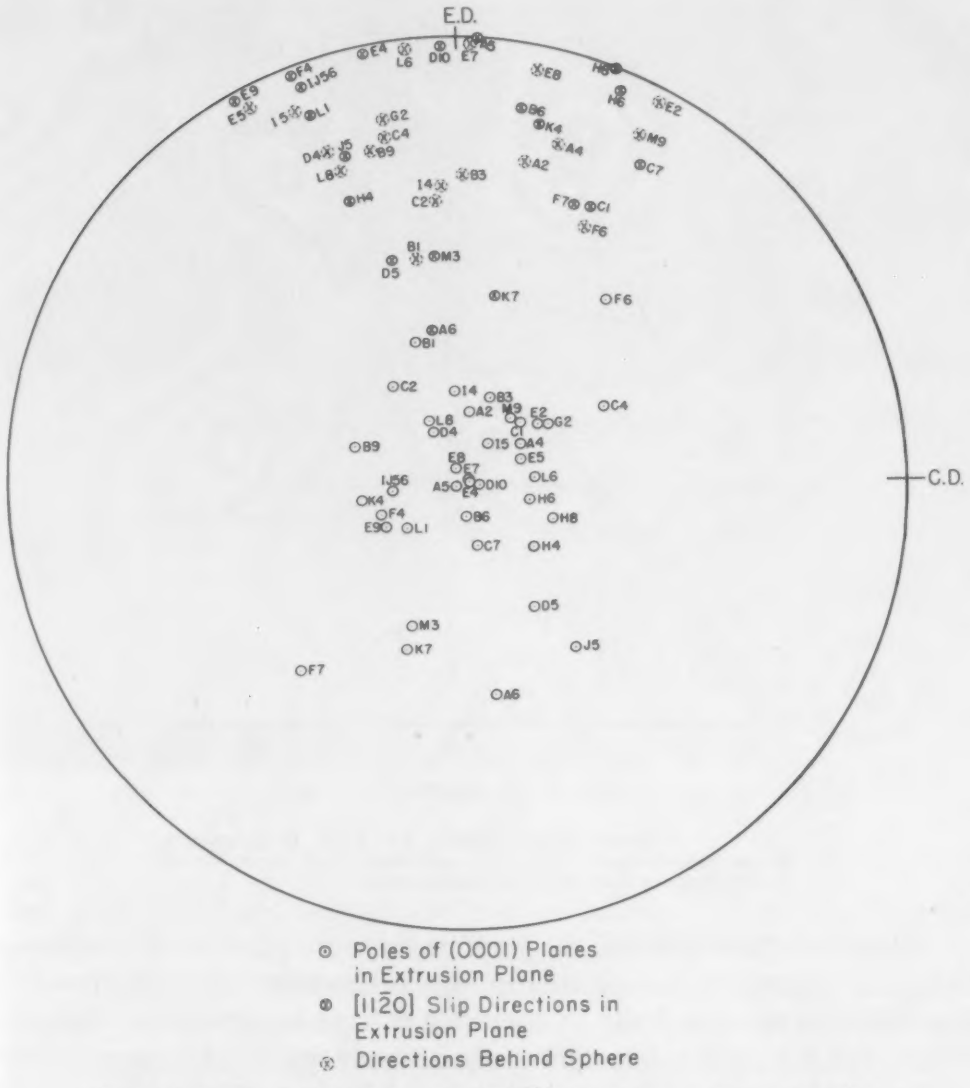


Fig. 2b—Poles of (0001) Axes and [11$\bar{2}$0] Directions in Extrusion Plane.

might partly be attributed to the limited number of grains in the section and occasional clustering, as shown by review of the data in Table I and Fig. 1, of grains of similar orientation. In addition specimens 1 and 5 were tested without interruption whereas specimens 2,3 and 4 were unloaded periodically for removal from the tension testing machine for metallographic examination. As will be described more fully later, some twinning occurred during loading, but additional twinning was also observed to take place on unloading. Consequently both the interrupted testing and the resulting twinning might also have contributed to the scatter in the stress-strain curves for the various specimens. During the metallographic study on the tensile specimens the following observations were made.

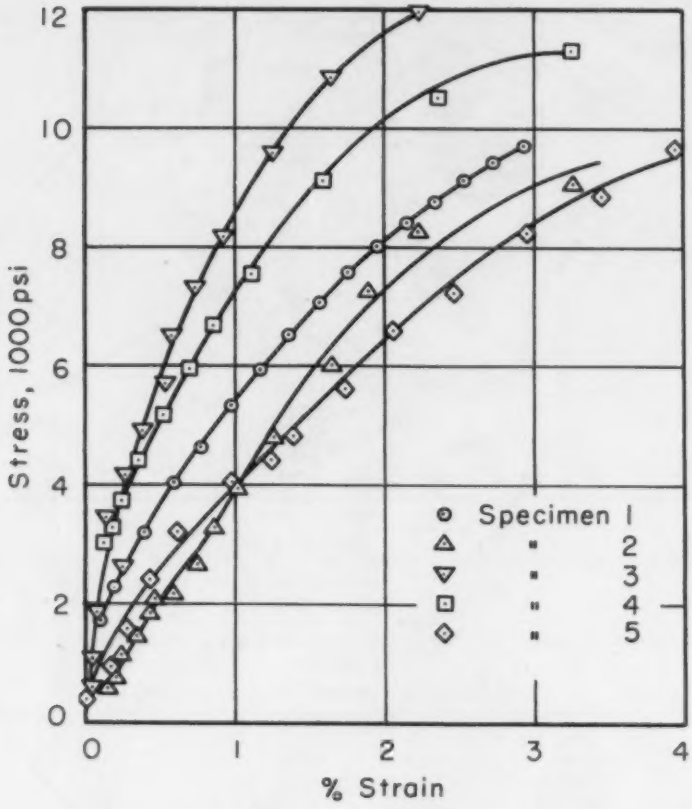


Fig. 3—Stress-Strain Curves for Pure Magnesium at Room Temperature. Curves for specimens, 2, 3, 4 periodically interrupted for microscopical examination.

Slip: All the slip-bands in each grain were parallel as shown by the typical photomicrograph in Fig. 4. Furthermore, the slip traces in all grains that exhibited slip in specimen 4 were in agreement with the (0001) [1$\bar{1}$2$\bar{0}$] mechanisms given for single crystals of magnesium at low temperatures (1).[1] In specimens 2 and 3 where traces of twins and slip bands permitted an estimate of crystal orientation, slip was also observed to be consistent with the basal mechanisms (0001) [11$\bar{2}$0]. Basal slip was also evident in reoriented twin material. There was no evidence of duplex slip on two alternate sets of slip planes.

Grains A-5, D-10, E-4, E-5, E-7, H-6, IJ-56, and L-6 in specimen 4 (see Fig. 1) all had the basal plane almost parallel to stress direction. Since the resolved shear stress on the basal plane is very small, these grains were examined very closely for evidence of slip on pyramidal planes of the first type, (10$\bar{1}$1). Although striations were observed on E-7 as shown in Fig. 5, they were identified as noncrystallographic cracks. No evidence was found that could be attributed to pyramidal slip. This is difficult to reconcile with the observation by Burke and Hibbard on single crystals of magnesium where faint stria-

[1] The figures appearing in parentheses pertain to the references appended to this paper.



Fig. 4—Basal Slip in Pure Magnesium. Specimen 2 at 0.75%ϵ. X 100.

tions were identified as traces of pyramidal slip planes (2). They rationalized the advent of pyramidal slip at ambient temperature on the basis of grip constraint. Their observations seemed confirmed by additional data obtained by Dow Chemical Company during rolling of single crystals of magnesium (3), wherein cross slip was observed in locally constrained areas. Additional investigations on compression type specimens in which the basal planes were parallel to the stress direction, and which correspondingly produced a relatively high resolved shear stress on the $(10\bar{1}1)$ planes, failed to exhibit pyramidal slip (4).

Jillson (5) has questioned the interpretation of similar striations as evidence of pyramidal slip. Examination of basally cleaved surfaces of zinc single crystals which had been subjected to stretching and bending revealed, in addition to three sets of $(10\bar{1}2)$ twin markings, three sets of striations, two of which were essentially normal and one parallel to the twin traces. Although the set of striations parallel to the twins might be ascribed to pyramidal slip, the two sets of striations normal to the twin traces cannot be accounted for by first order pyramidal slip. Instead it was suggested that all three sets of striations were the result of bending of the basal plane.

Examination of Grains E-5 and L-6 in specimen 4 reveals the pres-

Table II
Critical Stress for Slip in Specimen 4

Grain	sin χ cos λ	Tensile Stress for Slip	Shear Stress for Slip
A2	0.287	3,716	1066
A4	0.154	7,544	1160
A5	0.017	>11,300	—
A6	0.465	3,013	1401
B1	0.452	3,013	1362
B3	0.334	3,013	1006
B6	0.160	>11,300	—
B9	0.130	5,952	774
C1	0.218	3,261	711
C2	0.348	3,716	1293
C4	0.286	3,013	862
C7	0.249	5,952	1482
D4	0.212	5,952	1262
D5	0.392	5,952	2333
D10	0.017	>11,300	—
E2	0.219	5,160	1130
E4	0.000	>11,300	—
E5	0.092	>11,300	—
E7	0.009	>11,300	—
E8	0.060	>11,300	—
E9	0.172	5,952	1024
F4	0.137	9,114	1250
F6	0.489	5,160	2523
F7	0.487	5,160	2510
G2	0.233	3,261	760
H4	0.239	3,261	779
H6	0.064	3,261	209
H8	0.145	5,160	748
I4	0.360	5,160	1860
I5	0.151	7,544	1140
IJ56	0.041	9,114	374
J5	0.443	3,013	1335
K4	0.085	3,716	316
K7	0.464	3,261	1513
L1	0.192	5,160	991
L6	0.017	>11,360	—
L8	0.233	9,114	2120
M9	0.232	5,160	1200
M3	0.473	3,013	1425

ence of bend planes (Fig. 6). The markings appear to correspond to traces from $(10\bar{1}0)$ planes. These will be considered in more detail in a later section.

The advent of basal slip in single crystals has been shown to be stress dependent according to the relationship given in Equation 1. The critical shear stress law for basal slip in magnesium is well established. Deviations from this law in polycrystalline aggregates might therefore be attributed to interactions between conjugate grains. The average resolved shear stress at which each grain was first observed to exhibit basal slip bands was estimated as recorded in Table II. Several factors, however, were involved in the accuracy of these estimations: First the observation of slip bands was done following each increment of tensile stressing (about 1000 psi). Secondly slip bands were detected by metallographic examination at 100 diameters. And thirdly slip was recorded only when several major slip bands were noted over the central section of the grain. This criterion was adopted because on occa-



Fig. 5—Fine Cracks in Specimen 4 on Grain E7 at 3.3%ϵ. X 100.

sions only one corner of a grain would exhibit a few early slip bands due to facile slip in the adjoining grains. The general trends of the data recorded in Table II support the thesis that favorably oriented grains begin to slip at lower tensile stresses than unfavorably oriented grains. On the other hand the resolved shear stress at which slip first became prominent exhibits considerable scatter from grain to grain. And although suspicion is prevalent that this scatter might arise from interactions between contiguous grains, a review of the data given in Tables I and II with the grain position identified in Fig. 1 suggests that the scatter is random.

Twinning: Mechanical twinning occurs in single crystals of magnesium on $(10\bar{1}2)$ planes and is assumed to be the result of a simple shear in the $[10\bar{1}1]$ direction plus minor atomic readjustments (6). In the present investigation all twins formed on the $(10\bar{1}2)$ planes. No evidence was found to corroborate twin formation on $(10\bar{1}1)$ planes as reported on one occasion (7).



Fig. 6a—$(10\bar{1}0)$ Bend Planes Indicated by Arrows. Specimen 4, grain L6 at 2.4%ϵ. X 100.

Microscopic examination revealed that twins grow in a uniform manner; bilaterally if no constraints are present or unilaterally in the presence of constraints as shown in Figs. 7a and b.

Magnesium may be detwinned by the application of a reverse stress as well as by residual stresses as postulated some years ago (8). For example, the large twin present in Fig. 8 at an elongation of 0.52% has partially detwinned by subsequent straining to an elongation of 0.71%. Detwinning can also occur in cases where the twinned material has undertaken slip as shown in Fig. 9. Thus the original lattice is not necessarily restored to its initial conditions since visible microscopic features remain on the surface.

In some grains, such as M-3 as many as 5 different pyramidal planes eventually became active twin planes. Although it is possible for all six pyramidal planes to be active, only select orientations as shown in Fig. 10 (8) might exhibit these mechanisms for uniaxial tensile stresses. But as shown in Fig. 10, Grain M-3 lies in region C and should therefore exhibit only 2 mechanisms of twinning during tensile straining



Fig. 6b—$(10\bar{1}0)$ Bend Planes Indicated by Arrows. Specimen 4, grain E5 at 2.4%ϵ. X 100.

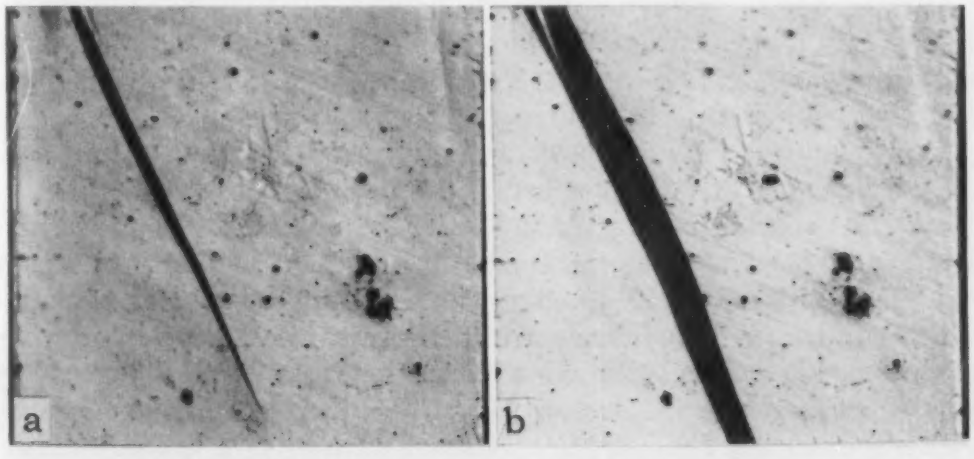


Fig. 7a—Bilateral Twin Growth Specimen 4. X 100. (a)—1.1%ϵ. (b)—1.6%ϵ.

instead of the 5 observed. Furthermore all grains oriented in region D would exhibit contraction in the direction of tensile straining if twins were formed. The large number of twins present in grains such as

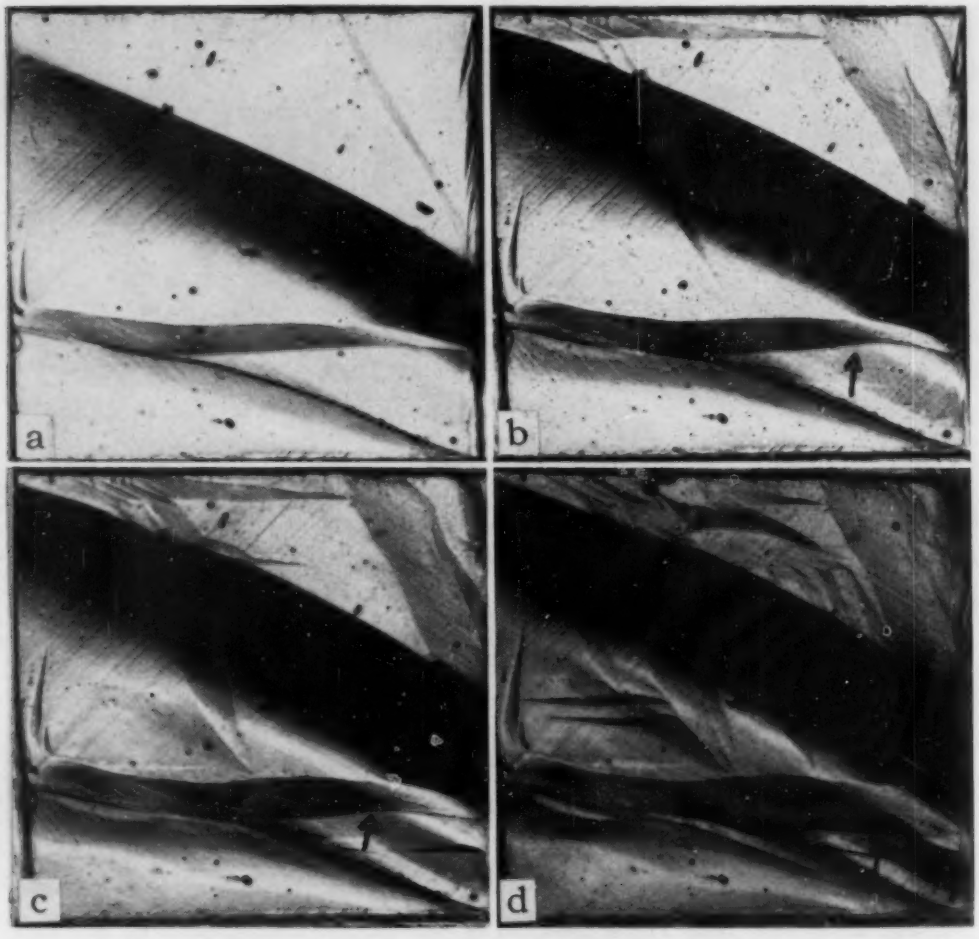


Fig. 7b—Unilateral Twin Growth in Presence of Constraints. Specimen 4. X 100. (a)—0.25%ϵ. (b)—0.52%ϵ. (c)—0.71%ϵ. (d)—1.1%ϵ.

H-8 in Fig. 17b which should not exhibit twinning during tensile straining suggest that either the operative stress direction in polycrystalline aggregates must be vastly altered or twins were formed during the periodic unloading of the specimen for metallographic examination. Measurement of the distance between grid lines also revealed that the grains had actually contracted in the tensile direction. Subsequent uninterrupted tensile stressing of specimen 5 revealed 33 twins in 29 grains of known orientation at 3.3% elongation. During the tensile test at constant strain rate 10 twins caused extension while 23 twins produced contraction in the stress direction. Thus the overall strain due to twinning in this specimen is actually negative, a fact not easily reconciled with strain energy considerations.

It has been suggested that twinning is a shear stress dependent phenomenon although the evidence is not at all conclusive (9–10). Instead, numerous observations suggest that twinning is the result of a more complex mode of deformation arising from concurrent bending and stressing (2,7,11). For example, irrespective of crystal orientation,



Fig. 8—Detwinning During Tensile Straining of Magnesium. Note that low angle boundary also disappears. Specimen 4. X 100. (a)—0.52%ϵ. (b)—0.71%ϵ.

Burke and Hibbard (2) observed that twins were formed in single crystals of magnesium only near the grips or adjacent to cemented wire strain gages where external constraints were present. Since both the grips and strain gages restrain the rotation of the slip plane during tensile straining, it was suggested that some phenomenon such as bending existed in conformity with the applied stress to produce twinning. This suggestion appeared justified by the observation that the size and number of twins decreased as the amount of bending decreased. Additional corroboration is afforded by the observations of Bakarian (12) that magnesium, regardless of initial orientation, will twin readily when suddenly twisted or bent.



Fig. 9—Slip Traces Remaining on Surface After Detwinning. Specimen 4 at 0.52%ϵ. X 100.

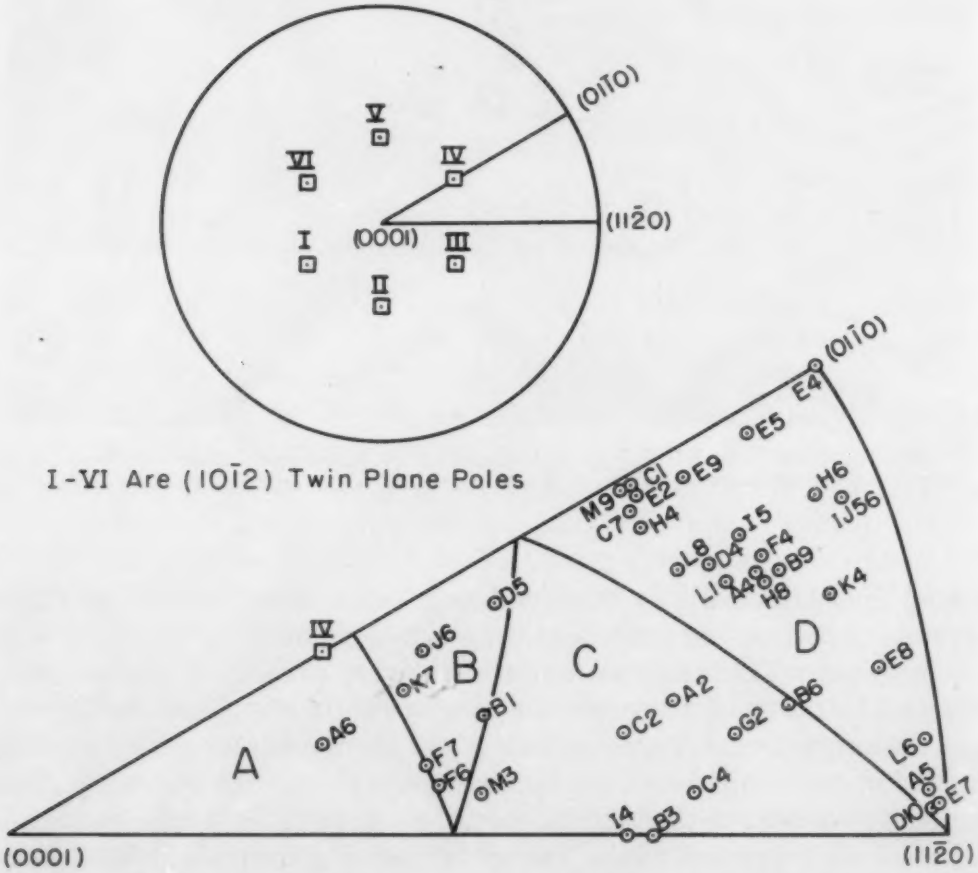


Fig. 10—Location of Tensile Stress Axes Governing Extension or Contraction on Twinning in Pure Magnesium. Stress axes of grains in specimen 4 plotted. Area A twinning on planes I—VI causes extension. Area B twinning on planes II, III, V, VI causes extension. Area C twinning on planes I, IV causes contraction. Area D twinning on planes I—VI causes contraction.

Bending Planes Associated with Twinning

The process of twinning also results in a decided bending of the basal plane as shown by Jillson's schematic diagram given in Fig. 11. This phenomenon has been termed an accommodation plane or band (5), accommodation kink (13), and crystallographic low angle boundary (14). Numerous such boundaries were observed in twinned areas as shown by the typical photomicrograph in Fig. 12. In some cases these

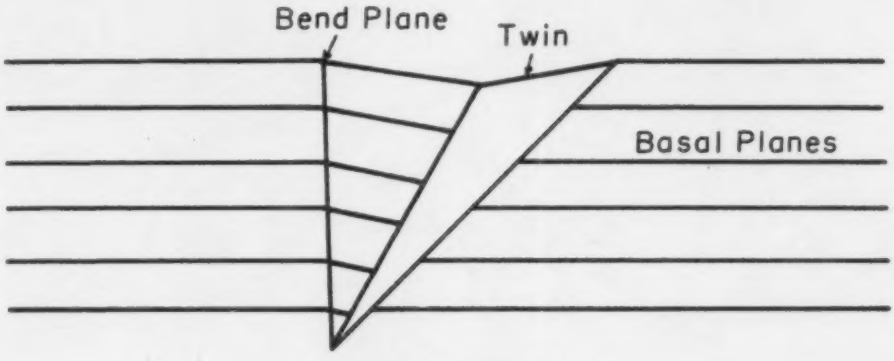


Fig. 11—Schematic Illustration of Bend Plane Associated with Formation of a Twin. (After Jillson, ref. 5).

boundaries were evident at both ends of the twin. In all cases, the boundary followed the trace of a $(10\bar{1}0)$ plane. Similar boundaries have been reported to occur in $(11\bar{2}0)$ planes in single crystals of magnesium (3). In that instance however it appears that the crystal under observation was so oriented that the boundary could be attributed to either $(10\bar{1}0)$ or $(11\bar{2}0)$ planes. Since numerous boundaries were evaluated here and since in basally cleaved zinc specimens these boundaries are observed to be parallel to twin traces, it appears that this bending of the basal plane is about a $(10\bar{1}0)$ plane.

Metallographic observations reveal that these low angle boundaries move in conjunction with twin growth. Thus as the twin extends, the accommodation band likewise appears to grow. During bilateral growth the accommodation band increases in width and in angular tilt (13). The reverse mechanisms occurred during detwinning (See Fig. 8). Thus the existing evidence clearly shows that these low angle boundaries are mobile under stress at atmospheric temperature.

Noncrystallographic Low Angle Boundaries

Another manifestation of the deformation process in hexagonal metals has been the occurrence of forked or curved traces on the surface of grains which have been variously termed rumpling (5), buckling (5), cell formation (15), kinking (5), mosaic walls (3,13), and non-

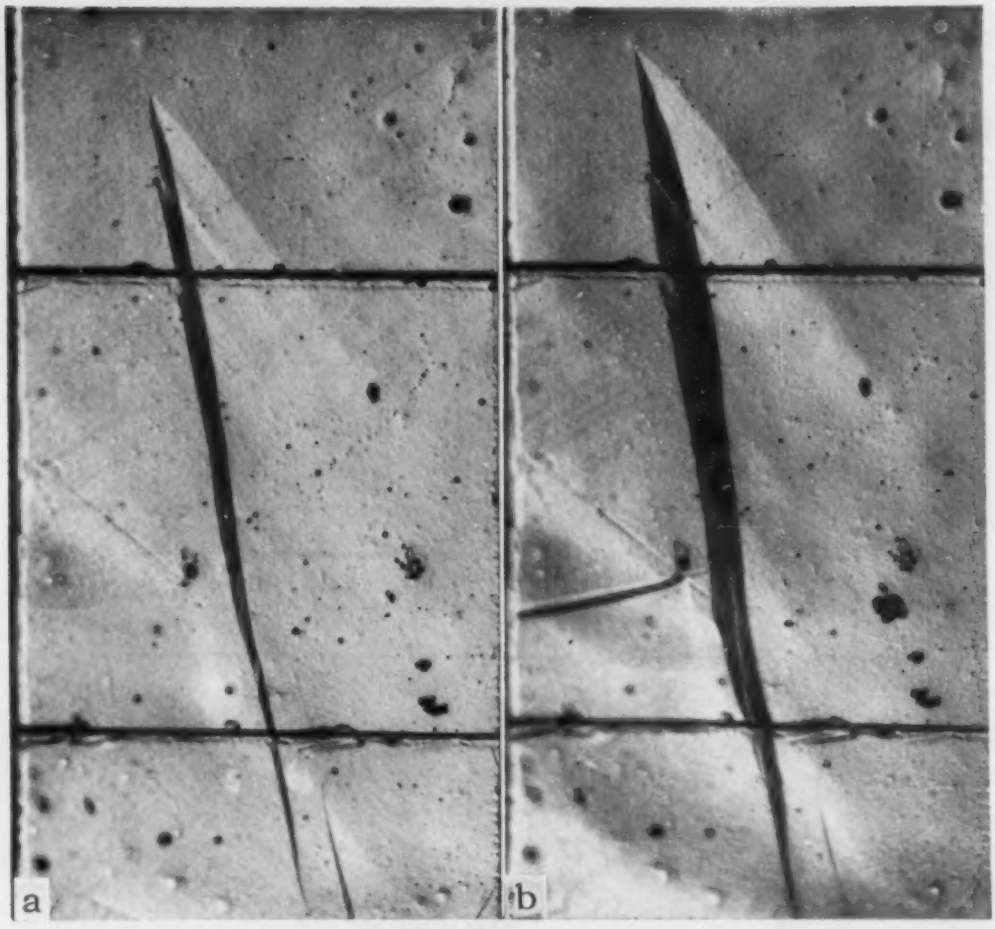


Fig. 12—Low Angle Accommodation Boundary Accompanying Growing Twin. Specimen 4. X 100. (a) 1.1%ϵ. (b) 1.6%ϵ.

crystallographic low angle boundaries (14). The principal distinction between these low angle boundaries and accommodation boundaries is that the former do not follow well delineated crystallographic planes, are not associated with twinning, and exhibit greater angles of tilt than the accommodation boundaries (13). The genesis of one such boundary (marked A) is shown in Fig. 13. In these figures the stress direction is vertical. On initial straining a general undulation is formed with one terminus at the junction of three grains. On further straining, a sharp noncrystallographic boundary is formed which moves toward the grain boundary as shown by the last three micrographs in Fig. 13. It will also be observed that increased tilting occurs during successive periods of straining. Additional low angle boundaries, B and C, are also formed during straining. Although boundary C appears quite mobile, boundary B does not advance through the accommodation kink emanating from the twin adjacent to the grain boundary. Similar boundaries have been observed in zinc at elevated temperatures (15) and it has been suggested that these boundaries are introduced by "drag" during

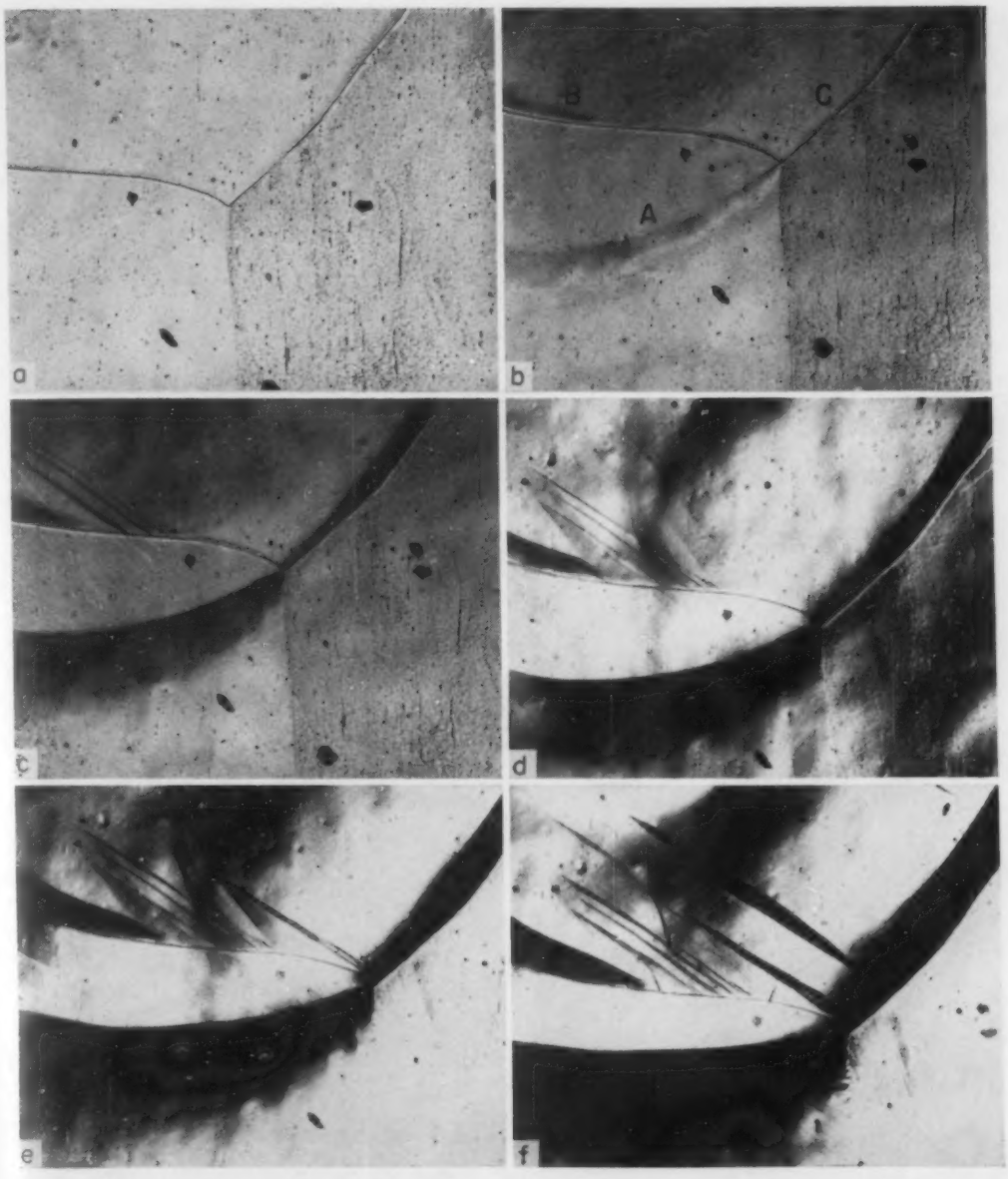


Fig. 13—The Formation and Movement of a Noncrystallographic Low Angle Boundary. Specimen 2. (X 100 reduced by 50%). (a) 0%ϵ. (b) 0.14%ϵ. (c) 0.35%ϵ. (d) 0.47%ϵ. (e) 0.75%ϵ. (f) 1.06%ϵ.

the relative motion of the two adjacent grains. Such a process suggests that the slope of the undulation would be a maximum near the boundary. Although this is consistent with the observation for boundaries B and C, the postulate is not representative for boundary A. It is possible that this boundary might be produced by the nonhomogeneous deformation of grains below the surface. In order to maintain continuity across the grain boundary under the surface, the surface grain is bent and a noncrystallographic boundary is subsequently generated by the appropriate entrapment of like dislocations. Subsequent slip in the grain could cause an increase in the number of trapped dislocations in the



Fig. 14—Noncrystallographic Low Angle Boundary of Fig. 15 Crossing Grain Boundary with no Apparent Discontinuity. Specimen 2 at 0.47%ϵ. (X 100 reduced to ½ size).

vicinity of the boundary thereby not only causing it to move but also to increase the angle of tilt of the boundary. The successive cuts in Fig. 13 reveal that these boundaries are mobile and the angle of tilt does increase with increased straining. This hypothesis is substantiated by such observations as that shown in Fig. 14 where the low angle boundary crosses a grain boundary.

Occasionally low angle boundaries appear to originate in the interior of a grain as shown by Fig. 14, or to start near a grain boundary and traverse from one grain to another with no apparent discontinuity at the grain boundary. Again it appears that the formation of a non-

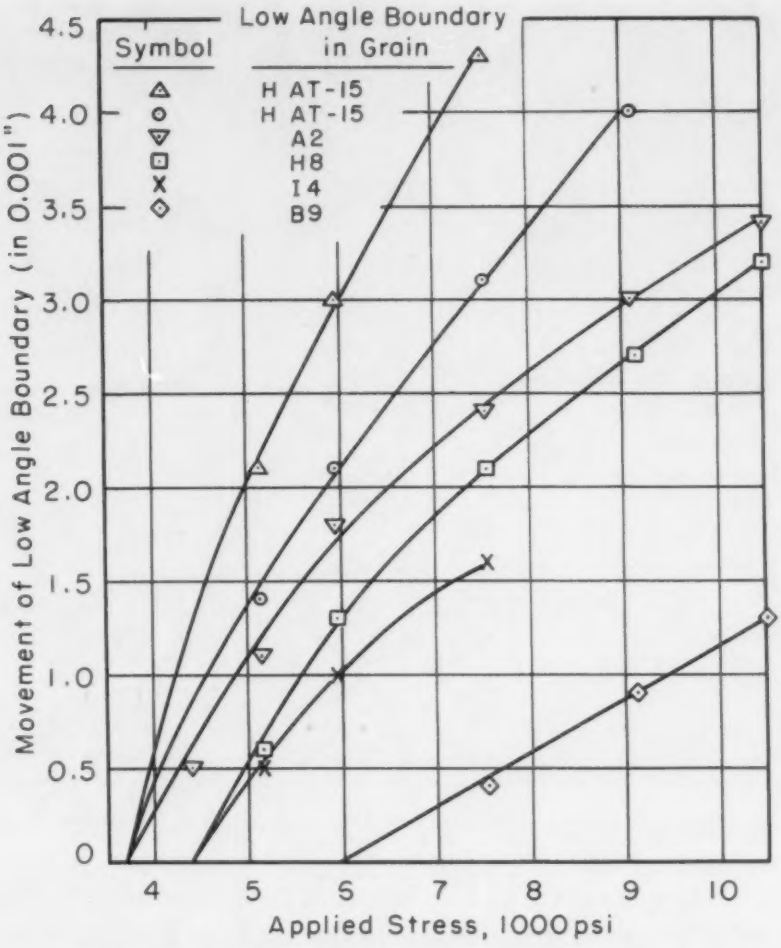


Fig. 15—The Effect of Stress on the Displacement of Noncrystallographic Low Angle Boundaries in Magnesium.

crystallographic boundary might on occasion be caused by nonhomogeneous deformation of underlying grains.

The postulate of bending as a criterion for the formation of a noncrystallographic low angle boundary is consistent with the observations of Pratt and Pugh (13), Jillson (5), and Washburn (16), etc. wherein slight bending readily induces the formation of low angle boundaries. The formation of such boundaries has also been shown to occur on the opposite faces of specimens subjected to mild indentations. Thus the bending can propagate through rather large distances with comparative ease. Indirect evidence is also noted from investigations on single crystals subjected to uniaxial stressing where bending is minimized and the existence of noncrystallographic boundaries is quite rare.

Investigations on the effect of temperature on similar noncrystallographic boundaries in zinc have shown that even prolonged heating in the vicinity of the melting temperature does not cause a change in the shape of these boundaries (13). Although these boundaries are ther-

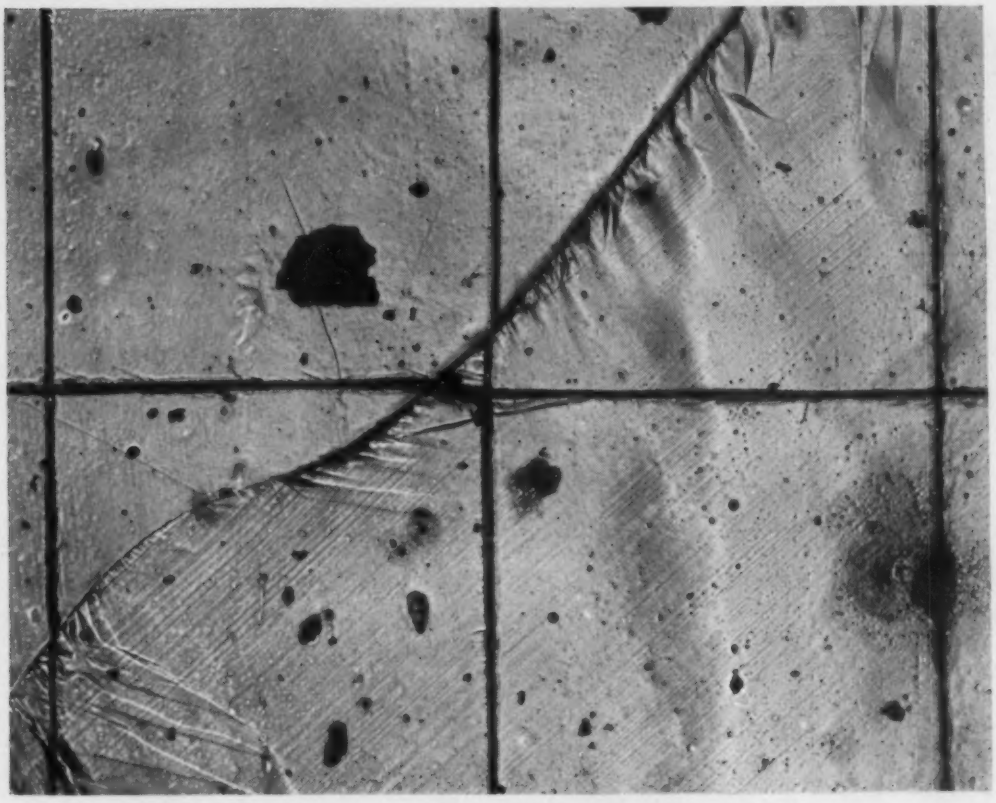


Fig. 16a—Grain Boundary Shear, Stress Direction Vertical, Specimen 3 at 0.93%ϵ. X 100.

mally stable, they are quite mobile in stress fields as shown in Fig. 13 for all three noncrystallographic boundaries. In Fig. 15 are recorded the displacements of a number of noncrystallographic boundaries as a function of the applied stress. The displacements were measured approximately normal to the low angle boundary by utilizing etch pits located on each side of the boundary as a traverse for measurement of displacement after successive amounts of strain. Within the limits of experimental accuracy, the boundaries move linearly with the applied stress.

Grain Boundary Shearing

Although grain boundary shearing is quite common in polycrystalline alloys at elevated temperatures, its occurrence at low temperatures, as far as the present authors are aware, has been suggested on only one occasion. Gross (17), during an investigation on the elastic straining of pure iron and silicon iron, observed a rotation of spots on an X-ray pattern during stressing. It could not be deduced, however, whether the slight rotation was attributable to grains or to mosaic subgrains.

In the present investigation, extensive evidence of the existence of grain boundary shearing was observed. At strains as low as 0.16%, shear displacements were observed across the grain boundary between grains L-6 and K-4 in specimen 4 (see Fig. 17). Continued straining

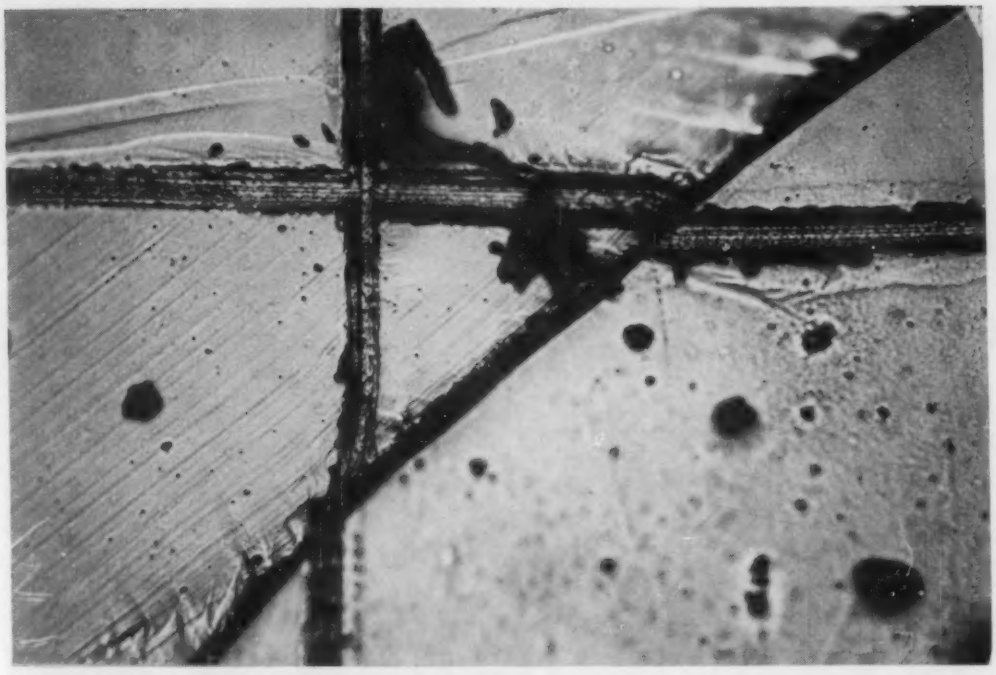


Fig. 16b—Grain Boundary Shear, Stress Direction Vertical, Specimen 3 at 0.93%ϵ. X 500.

caused an increase in the amount of grain boundary shearing in this region as well as the introduction of grain boundary shears in other regions of the specimen. Typical examples of shear are recorded in Fig. 16.

Comparison of the crystal orientations of grains L-6 and K-4 where grain boundary shearing was first observed reveals that both grains have their basal planes essentially parallel to the stress direction and are therefore not suitably oriented for slip. The respective orientations of the two contiguous grains alone, therefore do not appear to offer an explanation for the initiation of grain boundary shear. Examination of other contiguous grains in Figs. 17a, b and c reveals that both M-3 and J-5 are suitably oriented for slip (see Table II) and do exhibit visible slip at 0.16% strain. During stressing, the stress is relieved in these two grains by plastic deformation, and, perhaps, concentrated in grains K-4 and L-6. The stress concentration thus imposed and the requirement for continuity across the grain boundaries of all grains could lead to the shearing observed. In most cases where grain boundary shearing was evident, fracture was also evident. Thus it is possible that fracture precedes grain boundary shearing. In this event, it may be that stress concentration causes premature fracturing which subsequently induces grain boundary shearing to occur. Because of deformation occurring in underlying grains, it is as yet unknown which phenomenon occurs first. The preceding comments are accordingly, apropos for both phenomena.



Fig. 17a—Specimen 4 at 0.36%ϵ. (X 100 reduced to 1/5 size).

The total strain contribution from grain boundary shearing was estimated by measuring the displacement across all grain boundaries. The mean displacement per boundary is simple $\bar{d}_{g.b.}$ If n grain boundaries are encountered per unit distance, the strain contribution from grain boundary shearing is

$$\epsilon_{g.b.} = n\bar{d}_{g.b.} \qquad \text{Equation 2}$$

Evaluation of $\epsilon_{g.b.}$ on specimen 4 at a total strain of 2.4% gave a

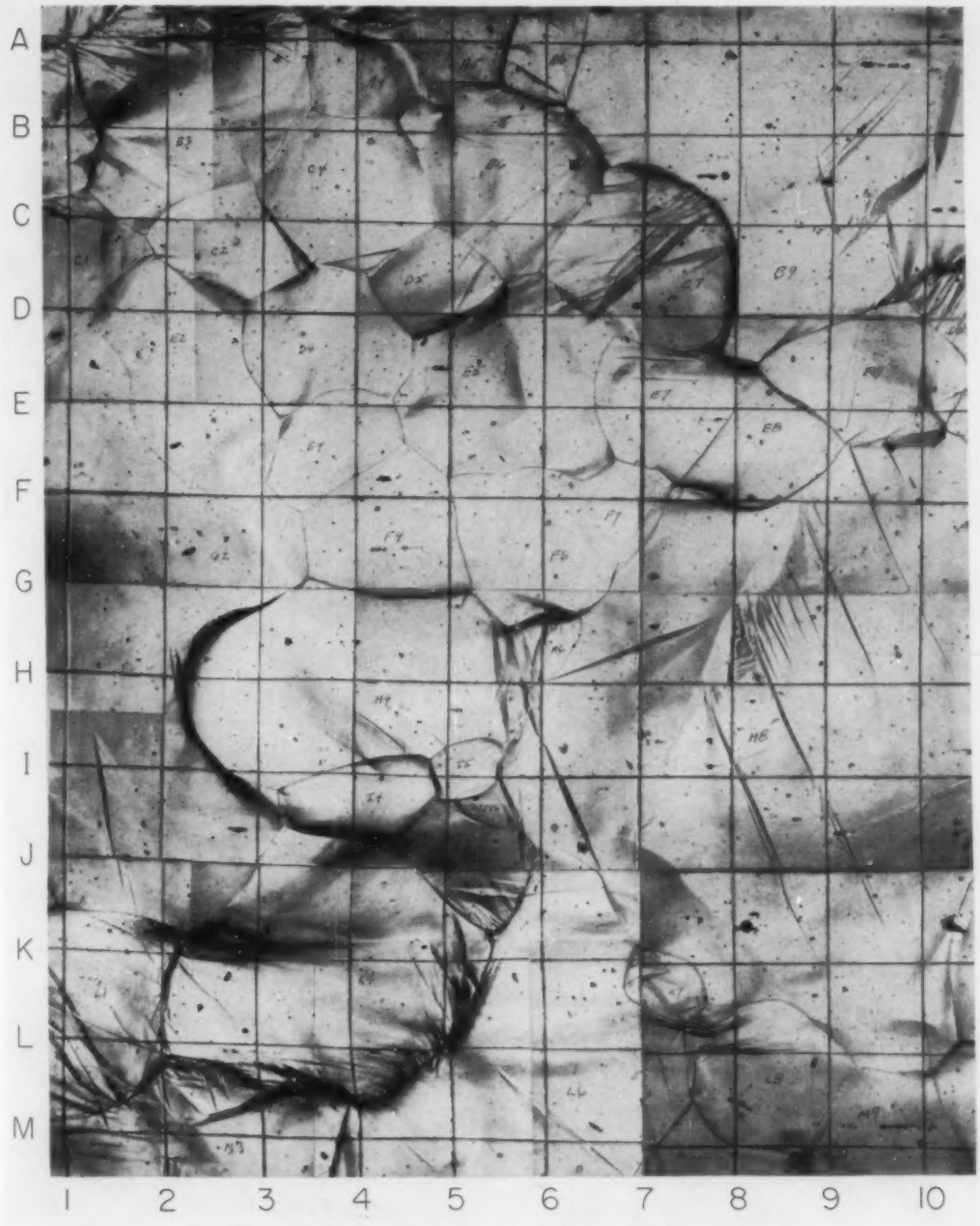


Fig. 17b—Specimen 4 at 1.1%ϵ. (X 100 reduced to 1/5 size).

strain of 0.1%. Thus the strain contribution from grain boundary shearing is small. But the effect of grain boundary shearing on subsequent deformation appears large.

Rupturing: In grain K-4 of specimen 4, cracks were first observed at strains as low as 0.16%. The cracks appeared to originate at the grain boundary and grow towards the interior of the grain. Continued straining resulted in additional cracks forming in the same grain which were essentially parallel to the initial ones. Fig. 18, taken at 0.53% strain,

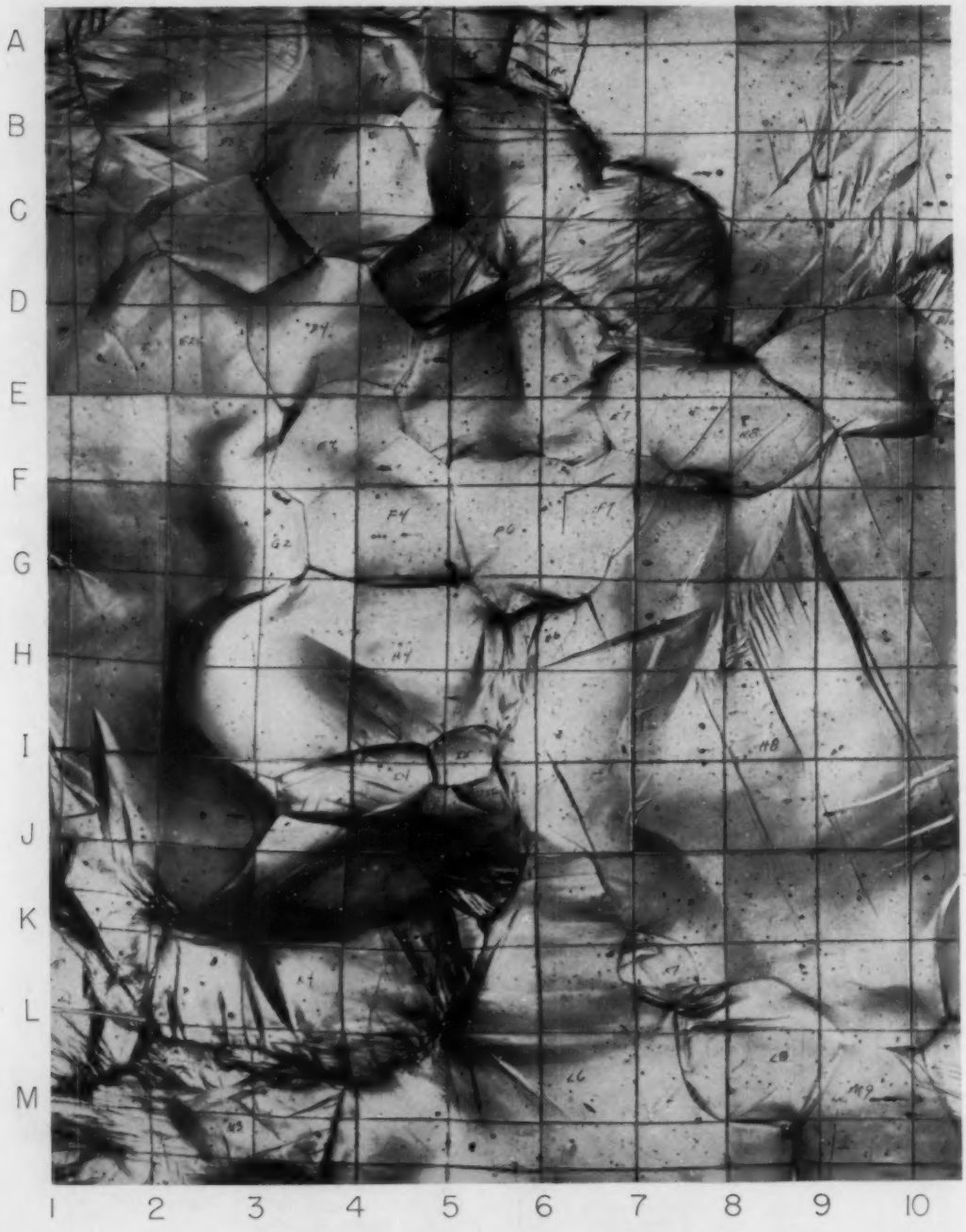


Fig. 17c—Specimen 4 at 3.3%ε. (X 100 reduced to 1/5 size).

reveals 10 of these cracks at an angle of 60 degrees to the stress direction. Subsequent straining produced a second set of major cracks almost normal to the stress direction and a series of finer branched cracks within grain K-4. Concurrently, cracks appeared in both those grains favorably oriented for slip, F-6 and G-2, and those unfavorably oriented —E-7, E-8, B-9, H-8 and L-1.

Orientation determinations of the cracks observed at x100 indi-

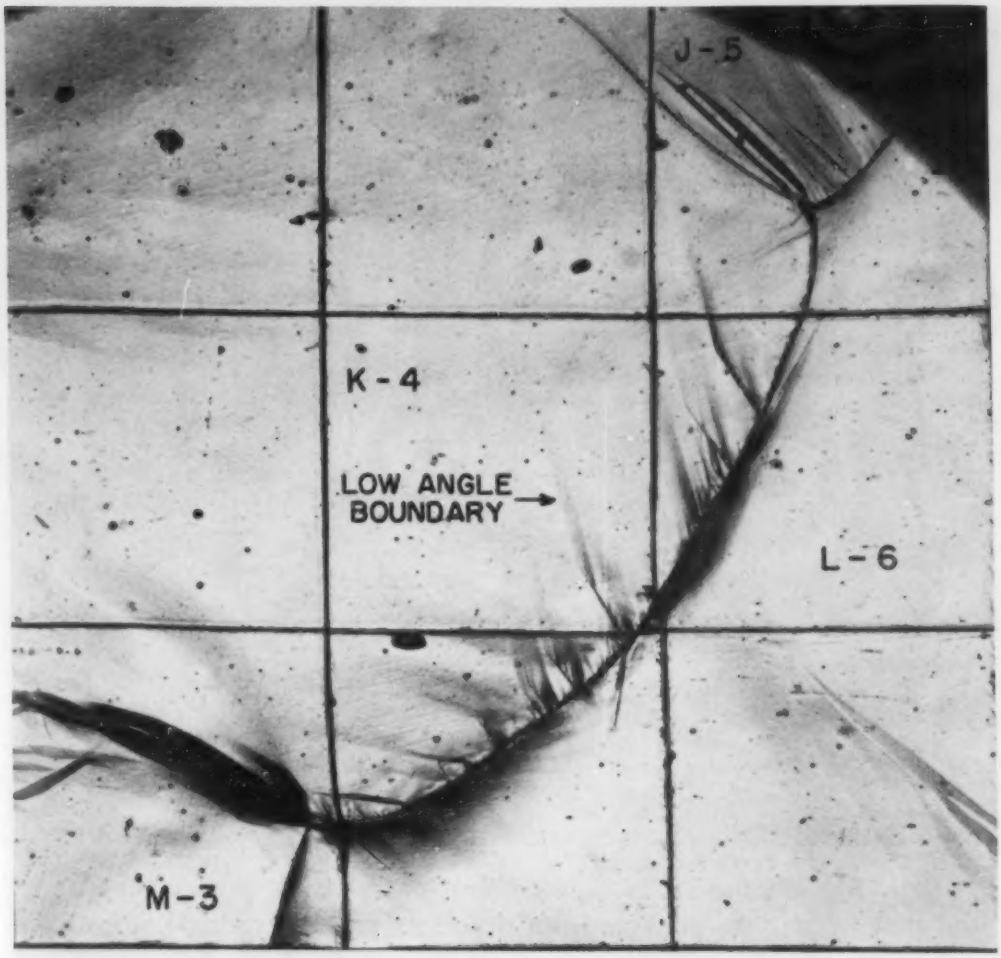


Fig. 18—Crack Formation at 60 Degrees to Stress Direction in Grain K4 of Specimen 4 at 0.53%ϵ. Stress direction horizontal. X 100 reduced to ¾ size.

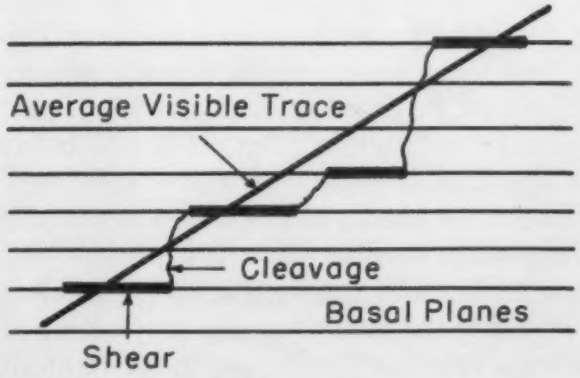


Fig. 19—Alternate Shear on Basal Plane and Cleavage or Tearing which Results in Noncrystallographic Microcracks in Specimen. (Specimen surface in plane of paper).



Fig. 20—Parallel Cliffs on Face of Cracks in Grain K4. Specimen 4 at 0.71%ϵ. X 500.

cated that the cracks occurred on a number of high index planes such as $(10\bar{1}9)$, $(20\bar{2}7)$, etc. But no common orientation of cracks could be obtained for all the cracks visible in specimen 4. The parallelism of the cracks in K-4 shown in Fig. 18 however suggests an orientation dependence of the cracks. Perhaps alternate shear and cleavage could produce apparent noncrystallographic traces on the surface as shown schematically in Fig. 19. Various combinations of shear displacements and cleavage would thus yield noncrystallographic surface traces. Moreover, these traces would be more or less parallel in any one grain but could alter appreciably from grain to grain due to interaction between conjugate grains. Qualitative validity for this postulate is given in Fig. 20 which shows one of the cracks in grain K-4 at x500. Here it is noted that parallel, sharp, cleavage-like cliffs are present in the crack. Between these cleavage-like cliffs appears the rough dull surface indicative of shear fractures. Since the surface of the crack is inclined to the surface of the specimen, a true orientation of the facets on the crack cannot be obtained. It was estimated, however, that they correspond to $(10\bar{1}1)$ traces.

It is interesting to note that crystallographic low angle boundaries are evident at the tip of the cracks and have the same orientation $(10\bar{1}0)$

as the accommodation boundaries associated with twinning. Qualitative evaluation of the surface contour on both sides of the cracks revealed that the low angle boundaries always occurred on the depressed side of the crack. Typical examples are shown in Fig. 18 for the cracks in grain K-4. The shear displacement along the crack and downward in the grain, as shown in Fig. 20, gives rise to the same geometrical relationship shown for twinning in Fig. 11. In this case the twin can be replaced by the crack. Thus, it appears that the basal plane is bent by the formation of cracks in much the same manner as in the formation of a twin.

The final rupture of specimen 4 occurred primarily by intergranular fracture of grains whose boundaries were approximately at 45 degrees to the direction of stressing in such a manner that a macroscopic "saw tooth" rupture normal to the stress direction was obtained. This region was outside of the section selected a priori for study. But it was interesting to note that a second intergranular rupture started in grain L-1 and followed the grain boundary of grain G-2 (just off the diagram shown in Fig. 17). This failure extended across approximately ¾ of the specimen.

Conclusions

1. Polycrystalline magnesium was observed to slip exclusively by the mechanism (0001) $[10\bar{1}0]$ at room temperature.
2. Twinning occurred exclusively along the $(10\bar{1}2)$ planes.
3. Low angle kink boundaries issuing from the spurs of mechanical twins were found to agree with the hypothesis that they consist of a series of edge dislocations on $(10\bar{1}0)$ planes.
4. Grain boundary shearing was observed at room temperature.
5. Noncrystallographically oriented low angle boundaries were produced during deformation of polycrystalline aggregates of magnesium.
6. Rupturing occurred on a number of high order crystallographic planes as well as along the grain boundaries.

Acknowledgment

This investigation was conducted under sponsorship of the Office of Ordnance Research. The authors express their sincere appreciation to the O.O.R. for their wholehearted support of this investigation.

References

1. E. Schmid, "Bertrage Zur Physik und Metallographie des Magnesium," *Zeitschrift für Electrochemie,* Vol. 37, 1931, p. 447.
2. E. C. Burke and W. R. Hibbard, Jr., "Plastic Deformation of Magnesium Single Crystals," *Transactions,* American Institute of Mining and Metallurgical Engineers, Vol. 194, 1953, p. 295.
3. Dow Chemical Co., "Plasticity of Magnesium Alloy Single Crystals and Origin of Secondary Maxima (002) Pole Figures for Rolled Magnesium Alloys," Final Report No. 15960, Part 2, 1953, pp. 10–11.

4. Dow Chemical Co., Part 3, p. 18, *ibid.*
5. D. C. Jillson, "An Experimental Survey of Deformation and Annealing Processes in Zinc," *Transactions,* American Institute of Mining and Metallurgical Engineers, Vol. 188, 1950, p. 1009.
6. C. H. Mathewson and A. J. Phillips, "Twinning in Be, Mg, Zn, and Cd," Trans. AIME, 1928, p. 445.
7. E. Schiebold and G. Siebel, "Studien an Magnesium und Magnesium Legierungen," *Zeitschrift für Physik,* Vol. 69, 1931, p. 458.
8. J. E. Dorn and E. Thomsen, "Magnesium, Notes on the Modulus of Elasticity," *Light Metal Age,* Vol. 1, 1943, p. 10.
9. N. Thompson and D. J. Millard, "Twin Formation in Cd," *Philosophical Magazine,* Vol. 43, 1952, p. 422.
10. N. N. Davidsen, A. F. Kolesnikov, and K. V. Fedoriv, *Journal of Experimental and Theoretical Physics,* USSR 3, 1933, p. 350.
11. R. F. Miller, "Creep and Twinning in Zinc Single Crystals," *Transactions,* American Institute of Mining and Metallurgical Engineers, Vol. 122, 1936, p. 176.
12. P. A. Bakarian and C. H. Mathewson, "Slip and Twinning of Magnesium Single Crystals at Elevated Temperatures," *Transactions,* American Institute of Mining and Metallurgical Engineers, Vol. 152, 1943, p. 226.
13. P. L. Pratt and S. F. Pugh, "The Movement of Twins, Kinks and Mosaic Walls in Zinc," ACTA METALLURGICA, Vol. 1, No. 2, March 1953, p. 218.
14. F. E. Hauser, C. D. Starr, L. Tietz, and J. E. Dorn, "Deformation of Polycrystalline Magnesium Alloy," First Status Report, University of California, Inst. of Engineering Research, Report Series No. 73, Issue No. 1, Sept. 15, 1953.
15. R. C. Gifkins and J. W. Kelley, "Note on the Formation and Development of Cells in Polycrystalline Zinc," ACTA METALLURGICA, Vol. 1, May 1953, p. 320.
16. C. H. Li, E. H. Edwards, J. Washburn, and E. R. Parker, "Stress Induced Movement of Crystal Boundaries," ACTA METALLURGICA, Vol. 1, No. 2, March 1953, p. 223.
17. N. P. Gross, "Grain Displacement in Metal Stressed below Elastic Limit," METALS PROGRESS, Vol. 61, 1952, p. 87.
18. A. B. Greninger, "Determination of Orientations of Metallic Crystals by Means of Back-Reflection Laue Photographs," *Transactions,* American Institute of Mining and Metallurgical Engineers, Vol. 117, 1935, p. 61.
19. E. I. Salkovitz, "Crystallographic Angles for Magnesium, Zinc and Cadmium," *Transactions,* American Institute of Mining and Metallurgical Engineers, Vol. 189, 1951, p. 64.
20. C. S. Barrett, *Structure of Metals,* McGraw-Hill Co., N.Y., 1943.

DISCUSSION

Written Discussion: By C. S. Roberts, The Dow Chemical Co., Midland, Mich.

I am indeed appreciative of the task which the authors set for themselves and carried out in such a splendidly systematic way. The results are of considerable value to those of us who are especially concerned with the deformation of magnesium. It seems appropriate to summarize briefly the results of similar research in our laboratories. Our work is in the process of completion after which it will be prepared for publication. The magnesium was of comparable purity to that used by the authors and the grains were coarsened by the same treatment. The resulting grain size was about twice as large as obtained by them.

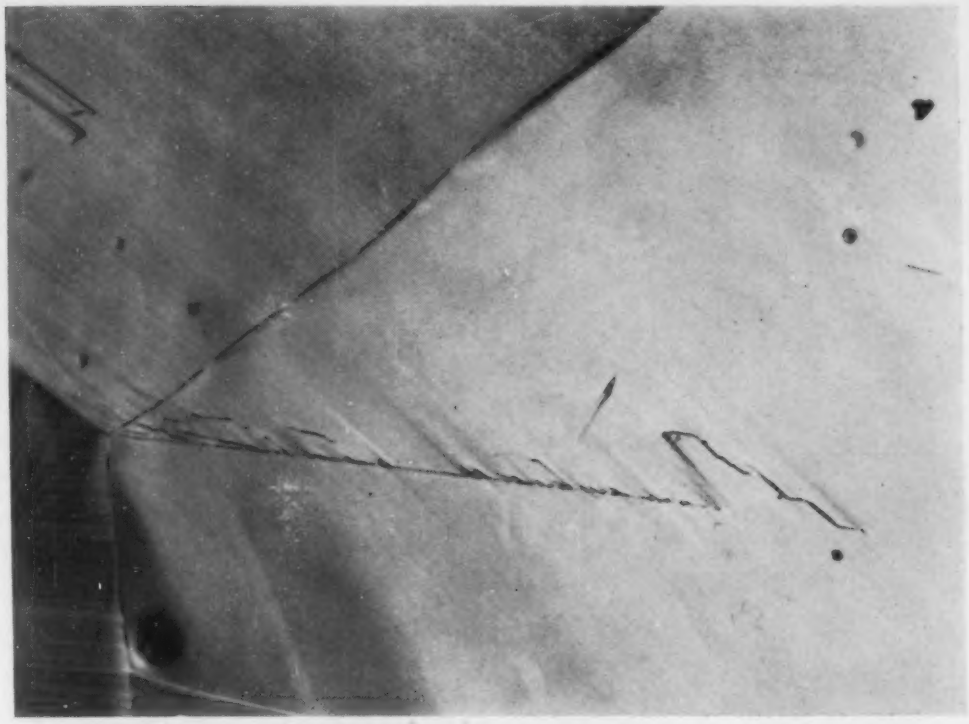


Fig. 21—High-Purity Magnesium After 0.85% Plastic Strain at Room Temperature. Stress axis vertical. × 150.

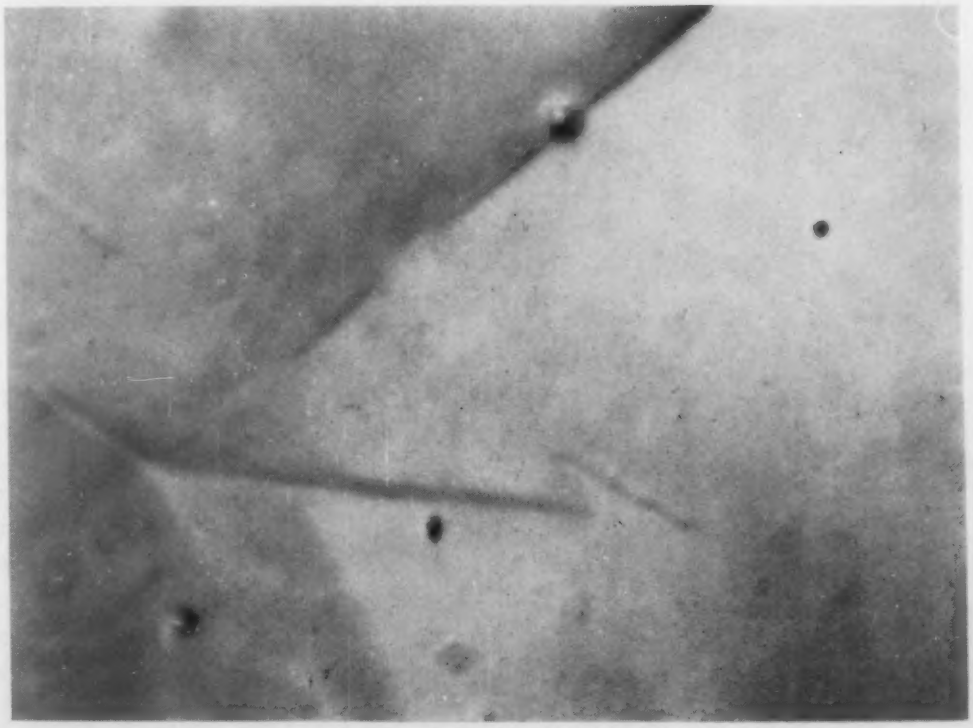


Fig. 22—Field of Fig. 21 After Electrolytic Repolishing for 30 Minutes. × 100.

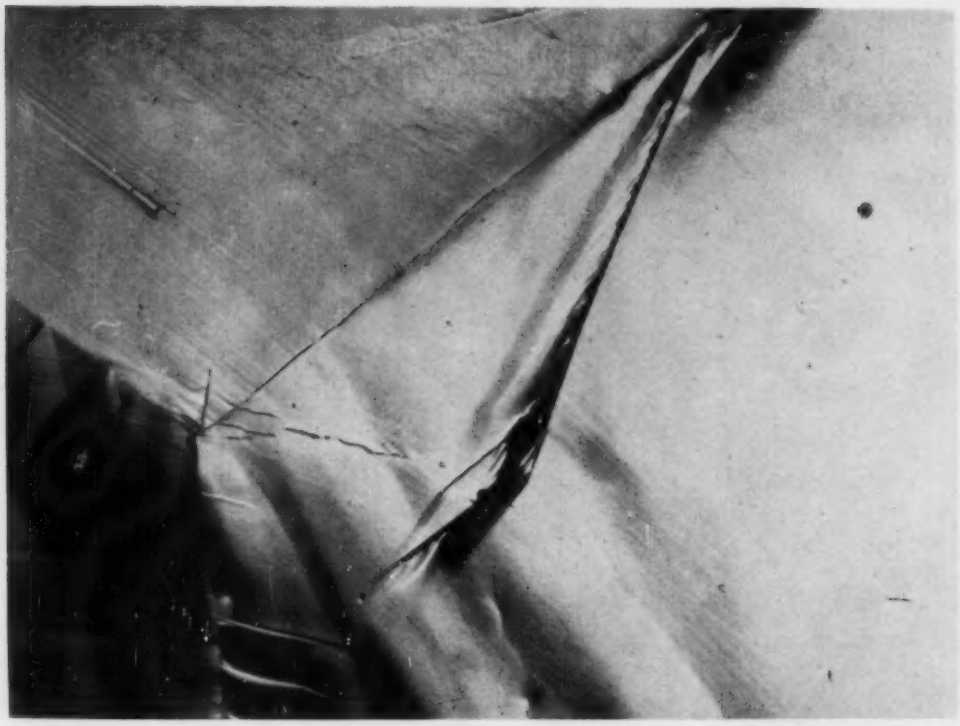


Fig. 23—Field of Fig. 21 After Straining Further to 2.0% Total Plastic Strain. × 100.

Metallographic observations were made on surfaces electropolished by the same Jacquet technique. The specimens were strained in tension parallel to the original extrusion axis at room temperature.

The importance of basal slip, twinning and low angle boundaries as observed by the authors was confirmed. However, these differences from their results were obtained:

1. Non-basal slip was detectable at about 1% plastic strain and became widespread before fracture occurred (5–6% plastic strain).
2. Cracks were not detectable until plastic strains greater than 3% were attained.
3. Although structural details very similar to those in Fig. 20 were observed, it was not possible to identify them as cracks.

My conclusions are based on examination at magnifications up to × 1000 supplemented by an additional test which has been found sensitive in our plastic deformation studies. This is the use of a light electrolytic repolishing. A suspected surface feature will be cavitated if it is a crack and smoothed if it is not. A light etch will assist in identifying twins. I should like to know more about the procedure which the authors used to identify their cracks.

The micrograph in Fig. 21 shows a line which proved to be non-basal slip at 0.85% plastic strain. X-ray orientation of the grain in conjunction with trace analysis showed it to be consistent with slip on a $\{10\bar{1}0\}$ or type I prism plane. Electrolytic polishing smooths it as shown in Fig. 22. Although the detail was removed completely with a few more minutes of polishing, some of these slip lines reappeared after strain to 2.0%, Fig. 23. The upper left corners of Figs. 21 and 23 show a feature which elongated on further straining. Trace analysis

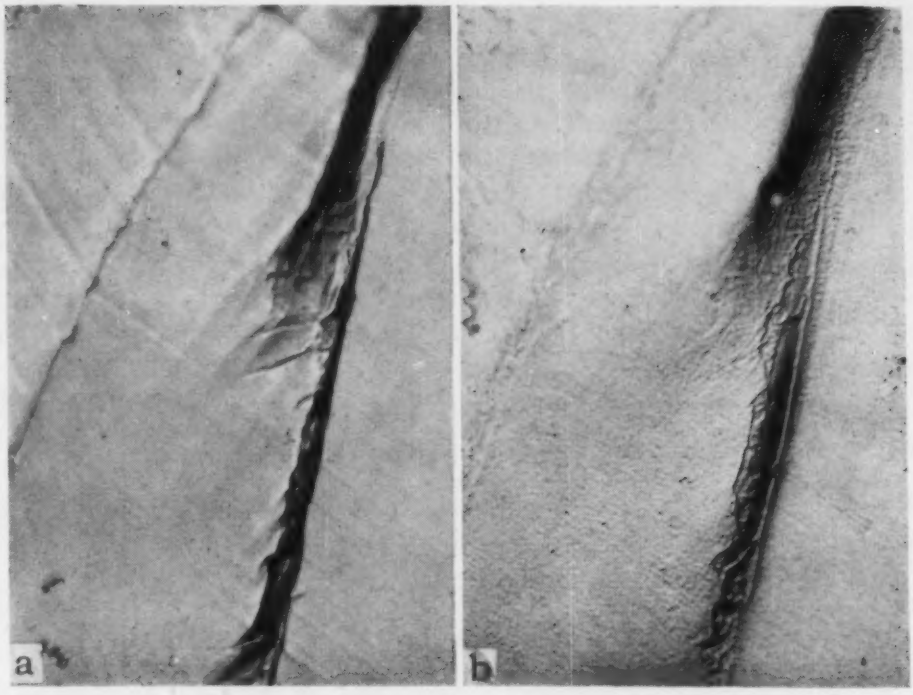


Fig. 24—(a) Strained as in Fig. 23. Stress Axis vertical. × 500. (b) Repolished 10 minutes and etched in acetic glycol.

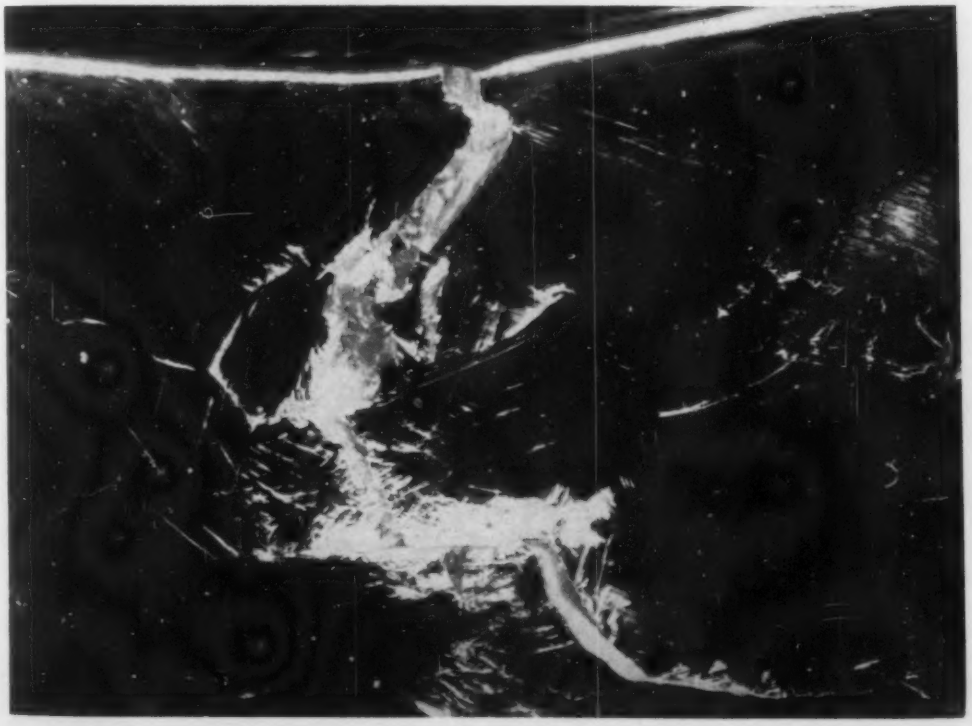


Fig. 25—Grain Boundary and Crystallographic Cracking at Fracture (>3% Plastic Strain). Stress axis horizontal. Approximately × 9.

showed that it could be interpreted ambiguously as either $\{10\bar{1}0\}$ or $\{10\bar{1}1\}$ slip.

The surface features in Fig. 24a are similar to those in the authors' Fig. 20 and are typical of many which were observed at 0.85% plastic strain. High magnification revealed no surface separation and repolishing followed by light etching, Fig. 24b, is confirmatory. The resulting appearance could be explained in terms of twins which have been severely deformed and which are fringed with distorted subgrains. However, in agreement with the authors, it has not been possible to prove these features as $\{10\bar{1}2\}$ twins by trace analyses. It is believed that the symmetry of the networks formed by these elements as shown in Fig. 23, for example, argues for crystallographic orientation. A search for a systematic interpretation is being continued but at present the authors' failure to find it can not be questioned. In agreement with them, the accommodation kinks were found to be on $\{10\bar{1}0\}$ planes.

When cracks did appear just prior to fracture (5–6% plastic strain) they were sharp enough to be seen directly or with low magnification. The cracks preferred to follow grain boundaries and major twin interfaces. As can be seen in Fig. 25, the overall fracture appearance conforms to the description given by the authors.

Authors' Reply

The contributions and comments made by Mr. Roberts are appreciated and the authors are looking forward to the forthcoming publication of his results on similar research.

Since the writing of this paper the occurrence of nonbasal slip has been observed by the authors on many occasions at subatmospheric temperatures. The secondary slip system at low temperatures was also found to be consistent with slip on a first order prism plane $(10\bar{1}0)$ as found by Mr. Roberts. Still other investigators have reported slip on first order pyramidal planes $(10\bar{1}1)$ particularly at elevated temperatures. Thus the occurrence of duplex slip in magnesium seems to be dependent on temperature in a systematic way. At low temperature both basal and prismatic slip occur. Near ambient temperature slip is almost exclusively basal and at elevated temperatures pyramidal slip takes place in addition to basal slip. But other as yet undetermined variables such as strain rate and grain size probably also govern the initiation of the secondary slip system and thus tend to mask the temperature effects noted by different investigators.

The identification of the surface features in Fig. 18 as cracks was done by microscopic observation at high magnification. It was noted that most cracks had sloping sides and since the deepest part of the fissure could not be brought into focus, the depth of the cracks could not be determined. The repolishing method employed by Mr. Roberts might serve as a useful tool in future investigations into the nature of these cracks.

TENSILE AND IMPACT PROPERTIES OF LOW CARBON MARTENSITES

By C. C. Busby, M. F. Hawkes, and H. W. Paxton

Abstract

The mechanical properties of thirty-eight low carbon martensites (0.11 to 0. 28% carbon) in the as-quenched and quenched and tempered condition have been examined. All tempering was done at 212°F (100°C). It was found that the ductility as measured by reduction of area and elongation was greater at all tensile strengths from 180,000 to 260,000 psi than the average of higher carbon steels (0.3 to 0.5% carbon) quenched and tempered to comparable strengths. Brine quenching gave better properties than oil quenching. The yield strength was comparatively low. The yield tensile ratio was about 0.7 in the quenched and tempered condition; this could be increased to any value up to 1.0 by a suitable strain aging treatment. The several alloying elements added to obtain the requisite hardenability had no appreciable effect on tensile properties. They did, however, markedly change the impact behavior of the material. Strain aging adversely affected the impact properties.

Introduction

THE purpose of this study of the mechanical properties of low carbon martensites was primarily to obtain new basic information about such martensites and to utilize this information in the development of high strength steels having better ductility and toughness at each of several tensile strength levels. Qualitatively, it has been known for many years that untempered martensites are tougher the lower the carbon; however, the quantitative effect of carbon on ductility and toughness in both untempered and tempered martensites had not been determined with the precision desired, and, for this reason, as well as that of developing better quality steels for high strength aircraft applications, the present investigation was made.

This study forms a part of a larger program sponsored by the Aeronautical Research Laboratory, Department of the Air Force, Wright Air Development Center, Wright-Patterson Air Force Base, Ohio, under Contract AF 33(038)-10218.

A paper presented before the Thirty-sixth Annual Convention of the Society, held in Chicago, November 1 to 5, 1954. Of the authors, C. C. Busby and H. W. Paxton are associated with the Metals Research Laboratory, Carnegie Institute of Technology, Pittsburgh, and M. F. Hawkes, formerly with the Metals Research Laboratory, is now Head, Metallurgical Section, Quality Evaluation Laboratory, U. S. Naval Ammunition Depot, Oahu, Hawaii. Manuscript received April 26, 1954.

Material

The chemical compositions of the thirty-eight steels used in this investigation are given in Table I; all steels were fine-grained and aluminum-killed. The chemical analyses were made on billets rolled from the ingots.

The C and D steels are from two different 15-ton basic electric heats, and five different compositions were obtained from each heat by

Table I
Chemical Composition of Steels

Steel	Per Cent of Element C	Mn	P	S	Si	Ni	Cr	Mo	V
1C	0.16	0.77	0.010	0.015	0.30	0.85	0.70	0.51	0.10
3C	0.18	0.77	0.010	0.015	0.29	0.85	0.69	0.51	0.09
*4C	0.14	0.77	0.010	0.015	0.29	0.84	0.69	0.49	0.09
5C	0.11	0.80	0.009	0.015	0.30	2.63	1.04	0.51	0.10
6C	0.14	0.80	0.005	0.015	0.30	2.29	1.01	0.51	0.10
1D	0.20	0.79	0.008	0.014	0.26	2.36	1.07	0.47	0.10
2D	0.24	0.80	0.010	0.015	0.28	2.35	1.09	0.48	0.10
3D	0.15	0.81	0.009	0.015	0.26	2.35	1.73	0.49	0.10
4D	0.19	0.78	0.009	0.014	0.26	2.35	1.85	0.49	0.10
5D	0.28	0.80	0.010	0.015	0.28	2.36	1.85	0.49	0.10
V1	0.17	0.82			0.27	—	2.85	—	—
V2	0.19	0.84	0.012	0.025	0.28	—	2.86	—	—
V3	0.23	0.82	0.012	0.025	0.24	—	3.08	—	—
V4	0.24	0.81			0.21	—	3.08	—	—
V5	0.18	1.55	0.013	0.026	0.26	—	1.02	—	—
V6	0.19	1.54			0.27	—	1.03	—	—
V7	0.22	1.62	0.011	0.018	0.26	—	1.02	—	—
V8	0.25	1.59			0.25	—	1.03	—	—
V9	0.15	3.01	0.014	0.019	0.31	—	1.04	—	—
V10	0.22	2.98			0.33	—	1.04	—	—
V11	0.22	0.84	0.011	0.025	0.32	—	1.03	—	—
V12	0.25	0.84			0.35	—	1.07	—	—
V13	0.16	0.79	0.014	0.020	0.25	—	2.10	—	—
V14	0.21	0.79			0.28	—	2.08	—	—
V15	0.23	0.86	0.015	0.010	0.19	—	2.08	—	—
V16	0.26	0.80			0.19	—	2.08	—	—
V17	0.18	0.74	0.016	0.012	0.25	1.57	1.05	—	—
V18	0.21	0.73			0.24	1.68	1.01	—	—
V19	0.19	0.78	0.011	0.015	0.31	3.19	1.01	—	—
V20	0.21	0.76			0.31	3.14	0.99	—	—
V21	0.23	0.81	0.011	0.014	0.28	3.19	1.07	—	—
V22	0.25	0.78			0.28	3.22	1.07	—	—
V23	0.23	0.84	0.011	0.009	0.24	5.46	1.04	—	—
V24	0.27	0.88			0.25	5.37	1.04	—	—
6	SAE 2320								
7	SAE 4615								
8	0.26	0.65				3.41	1.28	0.25	—
9	0.14	0.55				5.47	1.51	0.05	—

* 0.0005 boron added as Grainal #79

making alloying additions to the mold during teeming. The ingots were hot-rolled into 7-inch rounds.

The V steels were made as 300-pound heats in an induction furnace. Two compositions were made from each heat by pouring one ingot at a desired carbon content and then recarburizing to a higher carbon content before pouring the second ingot. The ingots thus ob-

tained differed essentially only in carbon content. These steels were hot-rolled into 1¼-inch square bars.

Steels 6, 7, 8, and 9 were used in preliminary work and their history is not known; they were in the form of ⅝-inch, 1-inch, and 1 3/16-inch round bars, respectively.

Unless otherwise noted, the following conditions apply to all tests reported:

1. Tensile tests were 0.252 inch in diameter and in the longitudinal direction of the billet
2. Impact tests were made on V-notch Charpy specimens also cut in the longitudinal direction
3. All specimens were finish-machined and then heat treated
4. The specimens were austenitized for one hour at 1600 °F (870 °C) in a controlled atmosphere furnace to minimize composition changes.

Tensile Properties of the Steels

Quenched in Iced Brine—Tensile specimens from thirty-four steels were given a standard austenitizing treatment; those from Steels 6, 7, 8, and 9 were austenitized for one hour at 1700 °F (925 °C), and all specimens were quenched in iced brine. The results of tests in both the as-quenched and quenched and tempered conditions were obtained.

The majority of the steels showed very small amounts of ductility as measured by elongation and reduction of area in the as-quenched condition. Steels 3D, V5, V6, all of the C steels, and the four steels used in preliminary work developed appreciable ductility and, with the exception of 5C which contained only 0.11% carbon, had tensile strengths of approximately 200,000 psi or more. However, it should be noted that the yield strength of these latter steels (where obtained) was low, giving yield-tensile ratios of 0.61 to 0.68 at 0.1% offset.

It was observed that a relatively short tempering treatment at 212 °F (100 °C) improved all of the mechanical properties of the steels except the tensile strength of the specimens containing lower percentages of carbon. Essentially maximum tensile strength (on a basis of carbon content) was obtained on the lower carbon steels in the as-quenched condition and this was not improved by tempering. To obtain maximum improvement, it was found that four hours at 212 °F (100 °C) was sufficient for the lower carbon steels, but the higher carbon steels required up to twelve hours in some cases. Tempering times greater than this produced no noticeable change in mechanical properties. The hardness at the surface and center of specimens was essentially alike both before and after tempering and, as shown in Fig. 1, fell, within experimental error, between the curves of Burns, Moore, and Archer (1)[1] and Hodge and Orehoski (2).

All the properties are reported in Table II for as-quenched and

[1] The figures appearing in parentheses pertain to the references appended to this paper.

Table II
Tensile Properties of As-Quenched and Quenched and Tempered Specimens

Steel	Heat Treatment	TS	YS (0.1%)	YS (0.2%)	RAL	Elong.	YS (0.1%)	YS (0.2%)	R_c
		psi/1000			%	%	TS	TS	
1C	AQ	202	128	147	50	14	0.63	0.73	
	T	197	144	159	58	14	0.73	0.81	
3C	AQ	221	150	167	44	12	0.68	0.76	
	T	217	158	174	55	14	0.73	0.80	
4C	AQ	200	129	159	44	12	0.65	0.80	
	T	199	141	156	57	14	0.71	0.78	
5C	AQ	184	—	140	58	15	—	0.76	
	T	189	130	147	59	14	0.69	0.78	
6C	AQ	205	—	—	47	13	—	—	
	T	212	155	170	57	15	0.73	0.80	
1D	AQ	232	—	—	10	5	—	—	48
	T	233	164	180	51	13	0.70	0.77	48
2D	AQ	230	—	—	4	2	—	—	
	T	250	175	194	48	12	0.70	0.78	50
3D	AQ	209	133	155	50	14	0.64	0.74	
	T	210	145	162	59	15	0.69	0.77	
4D	AQ	220	—	—	16	4	—	—	
	T	230	157	174	55	15	0.69	0.77	
5D	AQ	201	—	—	3	1	—	—	49
	T	255	176	194	52	13	0.69	0.76	50
V1	AQ	203	142	160	11	4	0.70	0.79	
	T	215	155	171	61	16	0.72	0.80	
V2	AQ	203	149	165	7	2	0.73	0.81	
	T	229	164	181	58	14	0.72	0.79	
V3	AQ	172	—	—	5	1	—	—	
	T	244	169	187	53	13	0.69	0.77	
V4	AQ	145	—	—	3	1	—	—	
	T	263	181	200	41	11	0.69	0.76	
V5	AQ	216	134	158	42	12	0.62	0.73	
	T	213	145	163	61	15	0.68	0.77	
V6	AQ	227	139	164	52	13	0.61	0.72	
	T	221	152	169	57	15	0.69	0.76	
V7	AQ	234	—	—	24	8	—	—	
	T	236	167	188	55	14	0.71	0.80	
V8	AQ	213	—	—	4	2	—	—	
	T	247	162	181	51	14	0.66	0.74	
V9	AQ	144	—	—	—	—	—	—	
	T	216	148	164	55	15	0.69	0.76	45
V10	AQ	93	—	—	—	—	—	—	50
	T	245	165	185	53	15	0.67	0.76	50
V11	AQ	211	—	—	9	3	—	—	—
	T	233	159	177	55	14	0.68	0.76	48
V12	AQ	194	—	—	5	—	—	—	50
	T	246	160	180	54	14	0.67	0.73	50

quenched and tempered specimens. The values for tempered specimens represent the average of the results of several tempering times after the change in properties had occurred, and the as-quenched values are the average of two specimens. Yield strengths were not measured on many specimens because of the possibility of damage to the extensometer as a result of premature fracture in specimens of lower ductility.

It will be observed that for those specimens for which yield strength data are available in the as-quenched condition, the yield-tensile ratio increases considerably after the tempering treatment. It is, however, still not as high as is desired. The reduction of area and elongation is markedly improved, especially in the higher carbon steels, and the tensile strength of these steels is significantly increased, probably because their better ductility leads to the avoidance of premature fracture. The fact that tensile strength does not increase in the lower carbon steels

Table II (Continued)

Steel	Heat Treatment	TS	YS (0.1%)	YS (0.2%)	RAL	Elong.	YS (0.1%)	YS (0.2%)	Rc
		psi/1000			%	%	TS	TS	
V13	AQ	205	141	157	16	6	0.69	0.77	
	T	209	144	163	61	15	0.69	0.77	
V14	AQ	217	—	—	10	5	—	—	
	T	225	159	173	59	15	0.71	0.77	48
V15	AQ	205	—	—	6	2	—	—	
	T	236	168	185	54	14	0.71	0.78	
V16	AQ	176	—	—	5	2	—	—	
	T	254	177	194	53	13	0.70	0.76	51
V17	AQ	207	—	—	16	6	—	—	43
	T	205	139	157	61	14	0.68	0.77	43
V18	AQ	199	—	—	4	4	—	—	45
	T	231	157	177	56	14	0.68	0.77	48
V19	AQ	198	—	—	3	4	—	—	44
	T	221	149	167	59	15	0.67	0.76	46
V20	AQ	176	—	—	—	—	—	—	49
	T	233	150	171	57	15	0.64	0.73	48
V21	AQ	172	—	—	—	—	—	—	45
	T	237	163	181	58	15	0.69	0.76	49
V22	AQ	—	—	—	—	—	—	—	—
	T	249	166	182	52	14	0.64	0.70	51
V23	AQ	Broke at thread							
	T	249	162	185	54	15	0.65	0.74	49
V24	AQ	Broke at thread							
	T	266	167	189	51	13	0.63	0.71	51
6	AQ	210	—	—	58	15	—	—	47
7	AQ	207	—	—	60	15	—	—	47
8	AQ	244	—	—	49	14	—	—	53
9	AQ	197	—	—	58	15	—	—	45

RAL — reduction of area in the longitudinal direction
Rc — hardness on Rockwell "C" scale
AQ — as-quenched
T — quenched and tempered at 212 °F (100 °C)

AQ yield strength values are single tests; all other values are averages of two tests.
Tempered yield strength values are averages of three to five tests; all other values are averages of six to ten tests.

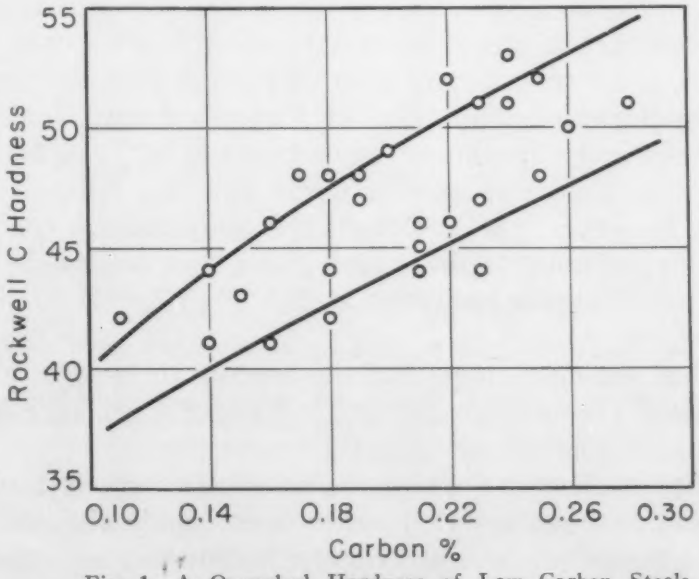


Fig. 1—As-Quenched Hardness of Low Carbon Steels. Upper curve—Burns, Moore, and Archer; lower curve—Hodge and Orehoski

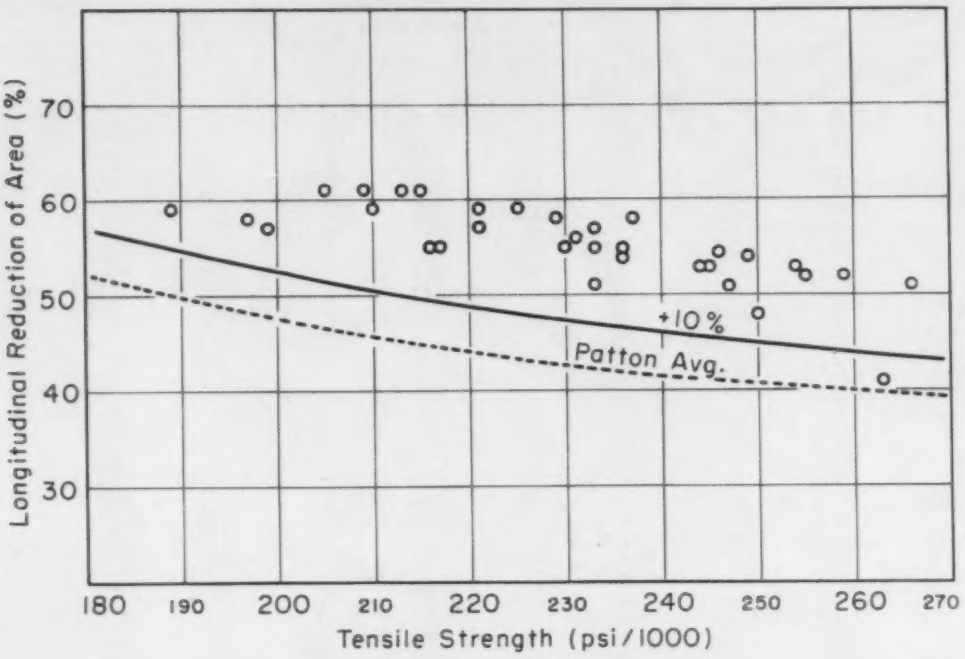


Fig. 2—Shows That All Plotted Reduction of Area Averages, Except One, for the Low Carbon Steels (0.11 to 0.28% Carbon) Fall Above the Solid Curve. Most of the large number of averages for Patton's 0.30 to 0.50% carbon steels fall below it.

after tempering could well be also connected with their better ductility in the as-quenched condition.

All plotted reduction of area averages, except one, for the low carbon steels (0.11 to 0.28% carbon) fall above the solid curve in Fig. 2 while most of the large number of averages for Patton's (3) higher carbon steels (0.30 to 0.50% carbon) fall below it. On the average, the reduction of area value at a given tensile strength is 13% higher for the lower carbon steels. Steel V4, which has a tensile strength of 263,000 psi, has a reduction of area value approximately equal to that indicated by the appropriate point on Patton's average line. The values for the preliminary specimens from material 6, 7, 8, and 9 are not plotted in Fig. 2 since these four steels were not tempered at 212 °F (100 °C). However, the values in the as-quenched condition were above the upper limit of the Patton data, and one might reasonably expect that a tempering treatment at 212 °F (100 °C) would not make these worse.

It is interesting to note that the amount or type of alloying elements studied (other than carbon) appeared to have essentially no effect on ductility as measured by the tensile test.

Brine-Quenched and Refrigerated—A few steels were refrigerated in liquid nitrogen for 15 minutes immediately after brine quenching prior to tempering to see if this treatment had any effect. The results are shown in Table III. A comparison of these data with those in Table II for the same three steels shows that no significant change

Table III
Effect of Refrigeration in Liquid Nitrogen Prior to Tempering On the Tensile Properties

Steel	Heat Treatment	TS	YS (0.1%)	YS (0.2%)	RAL	Elong.	YS (0.1%)	YS (0.2%)	R_c
		psi/1000			%	%	TS	TS	
1D	AQR	Broke at thread							
	RT	230	158	173	53	13	0.69	0.75	
3D	AQR	215	134	158	24	6	0.62	0.74	
	RT	210	148	163	59	15	0.71	0.78	
5D	AQR	183	—	—	2	2	—	—	49
	RT	265	180	194	53	13	0.68	0.73	50

AQR — as-quenched and refrigerated
RT — as-quenched, refrigerated, and tempered

Table IV
Tensile Properties of Low Carbon Steels Quenched in Oil

Steel	Heat Treatment	TS	YS (0.1%)	YS (0.2%)	RAL	Elong.	YS (0.1%)	YS (0.2%)	R_c
		psi/1000			%	%	TS	TS	
1C	AQ	195	131	146	56	14	0.67	0.75	
	T	196	139	153	57	14	0.71	0.78	
3C	AQ	209	145	156	38	10	0.69	0.75	
	T	210	150	163	54	14	0.71	0.78	
4C	AQ	194	133	150	48	12	0.69	0.77	
	T	193	136	152	57	15	0.70	0.79	
V9	AQ	196	—	—	—	—	—	—	43
	T	206	142	158	60	16	0.69	0.77	44
V10	AQ	170	—	—	—	—	—	—	48
	T	235	157	172	55	15	0.67	0.73	49
V11	AQ	221	—	—	15	6	—	—	47
	T	220	158	171	51	14	0.73	0.78	47
V12	AQ	220	—	—	6	3	—	—	49
	T	233	158	176	50	13	0.69	0.76	49
V13	AQ	205	131	150	55	15	0.64	0.73	
	T	202	140	156	59	15	0.69	0.77	
V14	AQ	217	—	—	40	11	—	—	46
	T	213	147	161	56	14	0.69	0.76	45
V15	AQ	220	—	—	9	9	—	—	
	T	226	151	170	52	14	0.67	0.75	
V16	AQ	225	—	—	6	4	—	—	50
	T	240	158	176	50	13	0.66	0.73	49
V17	AQ	199	116	136	52	14	0.58	0.68	42
	T	196	124	134	56	14	0.63	0.68	41
V18	AQ	221	124	147	16	6	0.56	0.67	46
	T	219	142	160	53	14	0.65	0.73	45
V19	AQ	213	110	136	35	9	0.52	0.64	45
	T	209	131	152	58	14	0.63	0.73	44
V20	AQ	222	—	—	5	4	—	—	47
	T	220	148	162	56	16	0.67	0.74	47
V21	AQ	224	—	—	10	3	—	—	47
	T	224	146	164	55	16	0.65	0.73	48
V22	AQ	236	136	160	8	3	0.58	0.68	50
	T	246	146	171	49	13	0.59	0.70	50
V23	AQ	209	—	—	3	2	—	—	49
	T	241	153	161	54	15	0.64	0.67	49
V24	AQ	167	—	—	3	1	—	—	51
	T	257	168	181	51	14	0.65	0.70	51

Tempering temperature was 212 °F (100 °C)

AQ yield strength values are single tests; all other values are averages of two tests.

Tempered yield strength values are averages of three to five tests; all other values are averages of six to ten tests.

in mechanical properties occurred, suggesting that the specimens were essentially 100% martensite at room temperature and contained no appreciable quantity of austenite which might transform to martensite at the lower temperature.

Quenched in Oil—Specimens from 19 steels were austenitized as

before and quenched in Rodman R-2 quenching oil. The results of these tests are shown in Table IV.

The ductility in the as-quenched condition, particularly in steels with more than 0.18% carbon, was again poor and in all steels was improved by tempering at 212 °F (100 °C) for the same times given the brine-quenched specimens.

All of the steels gave reduction of area values after tempering above those shown by Patton. For the same steels, however, higher reduction of area values were obtained with higher yield and tensile strengths after brine quenching. Although the tensile strengths and yield-tensile ratios are lower after oil quenching, suggesting that the quench is inadequate, no significant difference in hardness was obtained even for the lower carbon steels. It seems possible that the 0.252 inch diameter specimens were just about on the critical size for quenching out in oil, since one would expect tensile strength to be a more sensitive indicator because of the greater accuracy with which it can be measured.

The major cause of improved ductility at a given tensile strength resulting from tempering low carbon martensites at 212 °F (100 °C) has not yet been isolated and evaluated. Considerable thought was given to possible effects on ductility of (a) stress relief, (b) microstructural changes—including the formation of the Σ-carbide, (c) hydrogen redistribution, and (d) disordering of carbon atoms in the martensite lattice which occurs during tempering at 212 °F (100 °C). Unfortunately, this thought has so far given no satisfactory explanation of the marked improvement of ductility observed.

Microstructural studies were made but led only to negative results. The appearance of as-quenched and quenched and tempered (24 hours at 212 °F) specimens of Steel 1D which were typical of all steels examined is shown in Figs. 3a and 3b. Three types of area, each with different etching characteristics, were present both before and after this tempering treatment. Even after tempering, there is essentially no difference in the microhardness of these areas; each still had maximum hardness corresponding to the carbon content of the steel (0.20%). Impressions in the three types of differently etching constituents can be seen in Fig. 3b.

The Effect of Specimen Size on Tensile Properties

It was believed that the higher ductilities at equal tensile strengths exhibited by the steels tested in this investigation compared with those obtained by Patton might be due, at least in part, to the fact that the Patton data resulted from tensile tests on specimens of 0.505 inch diameter whereas the present work was carried out on specimens of 0.252 inch diameter. Therefore, specimens of various diameters, up to 0.505 inch, were machined from Steels 3D and 5D; the gage length was standardized at four times the specimen diameter. The specimens were

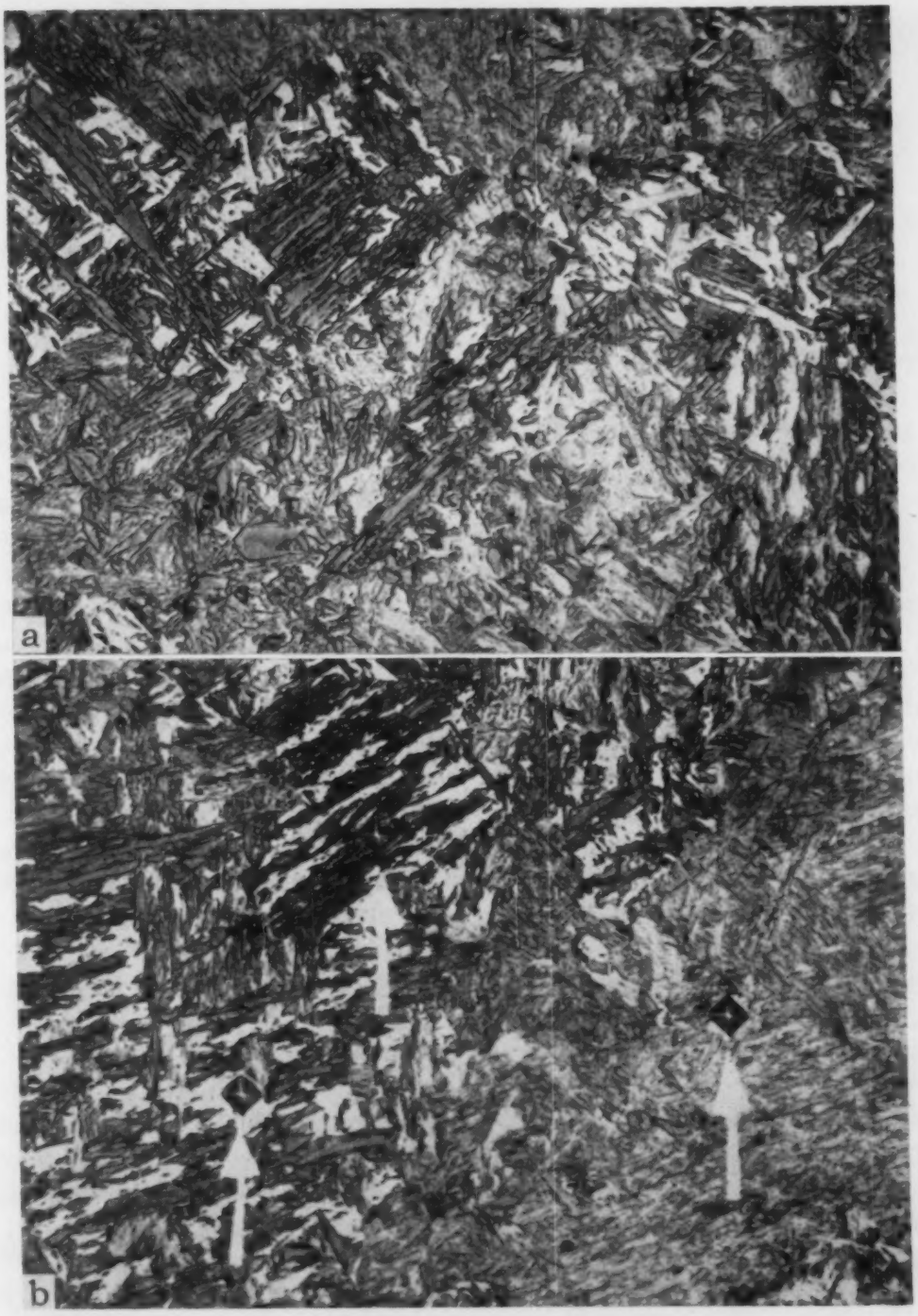


Fig. 3—Photomicrographs Showing the Structures Developed in (a) As-Quenched and (b) Quenched and Tempered Tensile Specimens from Steel 1D. Specimens were quenched in iced brine. Etch 2% Nital. X 500.

	VPN	Converted R_c
White area	533	51.3
Light gray area	515	50.1
Dark gray area	515	50.1

Table V
Effect of Specimen Size on the Tensile Properties

Specimen Diameter (inch)	TS psi/1000	YS (0.2%) psi/1000	RAL %	Elong. %
		Steel 3D		
0.125	201	—	61.1	14.0
0.252	199	155	58.2	15.0
0.357	199	143	58.9	17.0
0.505	197	135	57.1	15.0
		Steel 5D		
0.252	255	194	52.0	13.0
0.505	256	177	51.4	14.0

Values for Steels 3D and 5D are averages of 4 and 3 specimens, respectively.

austenitized as previously described, quenched in iced brine, and tempered at 212 °F (100 °C).

It will be observed that the essential difference between 3D and 5D is the carbon content, 0.15 and 0.28%, respectively. These compositions lie near the ends of the range investigated and should form a fairly adequate check on the dependence of any size effect on carbon content.

Table V shows that the properties of each steel, except for yield strength, for the sizes tested are essentially the same. Yield strength decreases with increasing section size. During the course of this investigation, an interesting observation was made. While a tempering time of four hours was sufficient to give maximum ductility in both steels when 0.252 inch diameter specimens were used and five hours were sufficient for all sizes in Steel 3D (0.15% carbon), a time between 8 and 24 hours was necessary in 0.505 inch diameter specimens of 5D (0.28% carbon). Maximum tensile strength was attained after eight hours in these, but the reduction of area was only 5%. Thus, if the carbon content is high, specimen size also has to be considered in determining the tempering time necessary to reach the maximum of all properties.

This effect of carbon content on the time to reach maximum properties has already been noted in the series of V steels of 0.252 inch diameter. In these steels, it was observed that while all the mechanical properties reached their maximum in less than four hours with less than 0.21% carbon, above this composition it was necessary to use 8 and 12 hour tempering treatments.

Impact Properties of the Steels

Impact strength versus testing temperature curves were obtained for standard V-notch Charpy test bars of all steels in the as-quenched and quenched and tempered conditions. All but three steels were quenched from 1600 °F (870 °C) in iced brine. Steels V22, 23, and 24 were quenched from 1600 °F (870 °C) in Rodman R-2 oil because

Table VI
Summary of Impact Data

Steel		Type	Maximum Impact ft. lbs.	T_a °C	T_5 °C
1C	AQ	1	38	−45	−170
	T	1	36	−35	−155
3C	AQ	1	33	−35	−140
	T	1	30	−30	−135
4C	AQ	2	41	−50	−150
	T	2	42	−48	−170
5C	AQ	1	39	−50	−140
	T	2	44	−30	−150
6C	AQ	1	35	−37	−140
	T	2	38	−52	−160
1D	AQ	1	32	−18	−160
	T	1	30	−53	−120
2D	AQ	1	24	−33	−165
	T	1	25	−61	−165
3D	AQ	1	38	−25	− 80
	T	1	45	−10	− 75
4D	AQ	2	29	− 5	− 75
	T	—	—	—	—
5D	AQ	1	29	− 8	− 50
	T	1	40	−55	−130
V1	AQ	1	46	+ 5	− 70
	T	1	51	−16	− 65
V2	AQ	2	43	−14	−115
	T	1	43	−12	− 60
V3	AQ	1	38	+40	− 65
	T	2	44	−16	−115
V4	AQ	2	31	+50	+ 20
	T	2	30	+50	0
V5	AQ	1	55	− 2	−100
	T	1	55	−10	−130
V6	AQ	2	54	+41	− 60
	T	1	53	−10	− 40
V7	AQ	2	45	+33	− 75
	T	1	51	+34	− 95
V8	AQ	2	38	+52	− 30
	T	2	33	+42	− 60
V9	AQ	2	32	+ 60	− 10
	T	2	62	+ 60	− 60
V10	AQ	2	8	—	+ 45
	T	2	26	+100	− 10
V11	AQ	2	48	− 30	−120
	T	1	49	− 47	−110
V12	AQ	2	42	− 1	−110
	T	1	43	− 30	− 90
V13	AQ	2	57	− 43	−105
	T	1	53	− 75	−125
V14	AQ	2	52	− 43	−100
	T	1	47	− 38	− 70
V15	AQ	2	45	− 27	−120
	T	1	41	− 28	−110
V16	AQ	2	40	+ 23	− 90
	T	1	40	− 25	− 75
V17	AQ	1	57	− 67	−160
	T	1	54	− 73	−170
V18	AQ	1	45	− 65	−160
	T	1	47	− 77	−160
V19	AQ	1	50	− 60	−105
	T	1	52	− 60	−110
V20	AQ	1	43	− 55	−145
	T	1	48	− 55	−110
V21	AQ	1	45	− 35	−145
	T	1	47	− 57	−160
*V22	AQ	1	49	− 90	−196
	T	1	51	− 90	—
*V23	AQ	1	50	−105	−196
	T	1	51	−153	—
*V24	AQ	1	37	− 67	−196
	T	2	49	−142	—

* Oil-quenched.

specimens quenched in iced brine tended to crack at the base of the notch in the finished test piece. The tempering treatment used for all the steels was 24 hours at 212 °F (100 °C).

The majority of the steels developed room temperature impact strengths which were in most cases higher than steels of higher carbon content (0.30 to 0.40% carbon) quenched and tempered to comparable hardnesses (4). Tempering at 212 °F (100 °C) usually raised the impact strength at all testing temperatures and slightly lowered the transition temperature. To avoid the unjustifiable reproduction of every graph of impact strength versus the testing temperature, the following procedure was adopted in presenting the complete data.

Table VI shows pertinent results selected from these impact strength versus testing temperature curves. These curves are essentially of two types, as shown schematically in Fig. 4. By defining the maximum impact strength as that at 212 °F (100 °C), T_a (the transition temperature) as the temperature at which the impact value is the average of those at 212 and −320 °F (100 and −196 °C), and T_5 as the

testing temperature at which the impact value is 5 ft-lb, the data in Table VI may be used to construct sufficiently accurate graphs of the effect of testing temperature on impact strength.

All steels, with three exceptions, gave impact values of 3 to 5 ft-lb at −320 °F (−196 °C). Tempered Steels V22, 23, and 24 gave values

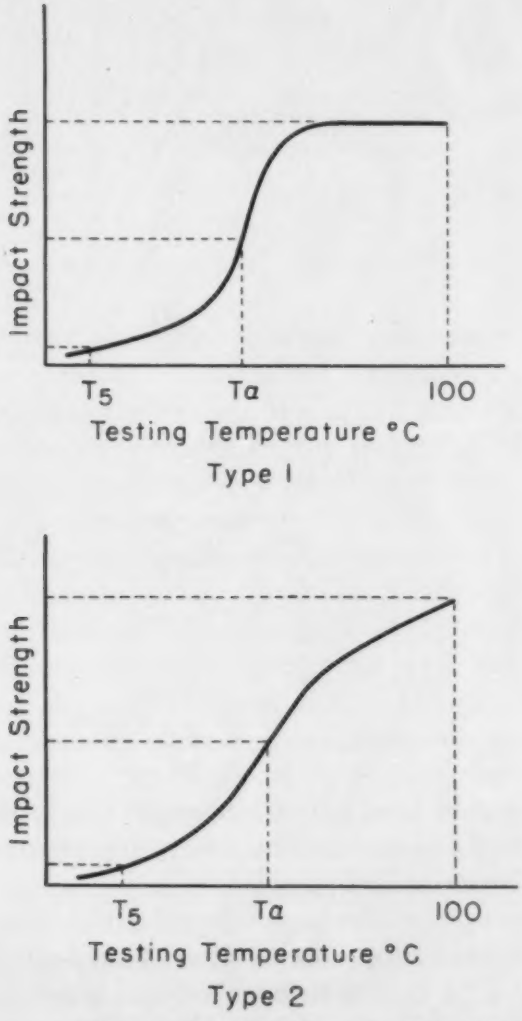


Fig. 4—Schematic Diagrams of the Impact Curves

of 15, 9, and 9 ft-lb., respectively, at this temperature. Thus this information gives one more point on the impact strength—testing temperature graph.

Nine steels showed that tempering at 212 °F (100 °C) changed the shape of the curve from Type 2 to Type 1. However, four steels showed the opposite effect so no definite statement can be made on the effect of this variable. There is no general correlation between T_a and per cent carbon, presumably because of the large number of different compositions involved. However, within a given heat, i.e., with alloy-

Table VII
Tempered Steels Arranged in Order of Increasing Transition Temperature

Base Compositions Per Cent of Element

Steel	Mn	Si	Ni	Cr	Mo	V
V	0.80	0.30	0.85	0.70	0.50	0.10
C	0.79	0.26	2.36	1.07	0.47	0.10
D	0.80	0.30	—	1.00	—	—

Steel V	Steel C	Steel D	Ta °C	C %	Varied Alloy %* V	Varied Alloy %* C	Varied Alloy %* D
23			−153	0.23	5.5 Ni		
24			−142	0.27	5.5 Ni		
22			− 90	0.25	3.0 Ni		
18			− 77	0.21	1.5 Ni		
13			− 75	0.16	2.0 Cr		
17			− 73	0.18	1.5 Ni		
		2	− 61	0.24			Base
19			− 60	0.19	3.0 Ni		
21			− 57	0.23	3.0 Ni		
20			− 55	0.21	3.0 Ni		
		5	− 55	0.28			1.85 Cr
		1	− 53	0.20			Base
	6		− 52	0.14		1.0 Cr + 2.3 Ni	
	4		− 48	0.14		0.0005 B	
11			− 47	0.22	Base		
14			− 38	0.21	2.0 Cr		
	1		− 35	0.16		Base	
	3		− 30	0.18		Base	
	5		− 30	0.11		1.0 Cr + 2.6 Ni	
12			− 30	0.25	Base		
15			− 28	0.23	2.0 Cr		
16			− 25	0.26	2.0 Cr		
1			− 16	0.17	3.0 Cr		
3			− 16	0.23	3.0 Cr		
2			− 12	0.19	3.0 Cr		
		3	− 10	0.15			1.7 Cr
5			− 10	0.18	1.5 Mn		
6			− 10	0.19	1.5 Mn		
7			+ 34	0.22	1.5 Mn		
8			+ 42	0.25	1.5 Mn		
4			+ 50	0.24	3.0 Cr		
9			+ 60	0.15	3.0 Mn		
10			+100	0.22	3.0 Mn		

* Approximate total percentage of the varied alloy after addition was made to the base composition.

ing elements held constant, increasing the carbon content tended to raise the transition temperature.

Arranging the steels in order of increasing T_a shows the general effect of alloying elements other than carbon on T_a, as shown in Table VII. Eleven of the first twelve steels (lowest T_a) contain nickel ranging from 1.5 to 5.5% with the largest lowering of T_a apparently occurring above 3% nickel. In spite of the relatively high carbon content (0.27%), V24, for example, has a T_a of −224 °F (142 °C). The next in order essentially are the chromium steels. However, here the trend appears to be toward higher T_a with higher chromium content. Six of the seven steels with highest T_a contain 1.5 and 3.0% manganese, again the trend being toward higher T_a with increasing manganese content. These effects are for the steels after tempering at 212 °F (100 °C). The order is essentially unchanged in the as-quenched condition, but the transition temperatures are raised slightly.

Thus it appears that nickel is most beneficial in lowering T_a;

chromium is permissible in quantities up to about 2% with all carbon contents up to 0.26% and to 3% if the carbon content does not exceed 0.23%, while steels containing 1.5% manganese or more and 0.22% carbon or more have transition temperatures which are probably too high for many applications. With 3% manganese, even a carbon content as low as 0.15% gives the very high T_a of 140 °F (60 °C). This last material is interesting in that it has the highest impact strength of all the steels examined at a testing temperature of 212 °F (100 °C).

One surprising result for which no explanation can be offered is the high T_a of +14 °F (−10 °C) for Steel 3D (0.15% carbon), especially when it is noted that Steel 5D (0.28% carbon) from the same heat has a T_a of −67 °F (−55 °C). This appears to be the opposite of what might be expected on the basis of carbon content alone. It is believed that the 3D specimens were quenched out since both steels showed essentially maximum hardness on the basis of carbon content.

Effect of Strain Aging on the Tensile Properties

In an endeavor to improve the mechanical properties of the low carbon martensites, in particular the low yield strength and yield-tensile ratio, subsidiary study was made of the effect of strain aging on these properties. Twelve steels varying in carbon content from 0.11 to 0.27% were strained various amounts and aged at low temperatures of 70 to 300 °F (21 to 149 °C). Essentially, the technique consisted of straining quenched or quenched and tempered specimens until a predetermined amount of plastic strain was introduced. This was measured either by local necking or by the extension of the gage length. In specimens which were given small amounts of plastic strain, extension could be measured from the automatically recorded load-extension curve (Fig. 5). When local necking was to be used as a measure of deformation, the specimen diameter was made oversize so that after aging it could be machined to 0.252 inch diameter to remove the necked portion.

Aging in all cases was carried out after the specimens had been removed from the tensile machine. Amounts of deformation varied from an extension of approximately 0.1% to a reduction of area at the neck of 13%. The results of the tests, together with the strain aging treatments, are given in Table VIII.

All the steels showed aging effects, the amount of which depended on the amount of deformation and the aging temperature. Specimens subjected to reductions of area from 5 to 13% showed increases in tensile strength up to 34,000 psi with only a slight decrease of reduction of area. However, the elongation was greatly reduced and the yield-tensile ratio was 1 in all cases. This treatment is obviously useless for structural materials.

The most promising result was obtained on specimens tempered at 212 ° F (100 °C) with extensions of 0.12 to 0.25%. After aging, all

Table VIII
Effect of Strain Aging on Tensile Properties

Tempered Specimens

Steel	Initial TS psi/1000	Initial YS psi/1000 0.1%	Initial YS psi/1000 0.2%	Elong.* %	Aged at °F	Aged at hrs.	Final TS psi/1000	Final YS psi/1000 0.1%	Final YS psi/1000 0.2%	Initial YS (0.1%) TS	Final YS (0.1%) TS
V13	209	144	162	0.25	212	24	212	189	194	0.69	0.89
V15	236	168	185	0.21	212	24	239	—	—	0.71	—
V17	205	139	157	0.17	212	24	204	179	184	0.68	0.88
V18	231	157	177	0.24	212	24	228	203	207	0.68	0.89
V19	221	149	167	0.23	212	24	215	190	197	0.67	0.88
V22	259	166	182	0.18	212	24	253	216	222	0.64	0.85
V23	249	162	185	0.21	212	24	239	205	210	0.65	0.86
V24	266	167	189	0.20	212	24	251	220	224	0.63	0.88
2D	255	181	198	0.12	150	2	255	218	225	0.70	0.86
4D	230	157	174	0.23	150	2	230	215	216	0.69	0.93

All values are averages of two or more tests.
* Introduced during straining before aging.

Steel	As Quenched TS psi/1000	As Quenched RAL %	As Quenched Elong. %	RAL** %	Aging Treatment	New TS psi/1000	New RAL %	New Elong. %
					As-Quenched Specimens			
8	243	47.5	12.5	5	None	248*	41.3	12
				5	24 hrs. at 70 °F	248*	43.1	11.5
				5	1 week at 70 °F	259*	38.9	10
				5	2 hrs. at 150 °F	258	48.9	10
				5	2 hrs. at 300 °F	255	54.6	—
9	197	57.8	15	13	2 hrs. at 150 °F	221	53.3	—
				13	2 hrs. at 300 °F	231	54.2	6

* Individual tests; all other values are averages of two or more tests.
** Introduced during straining before aging.

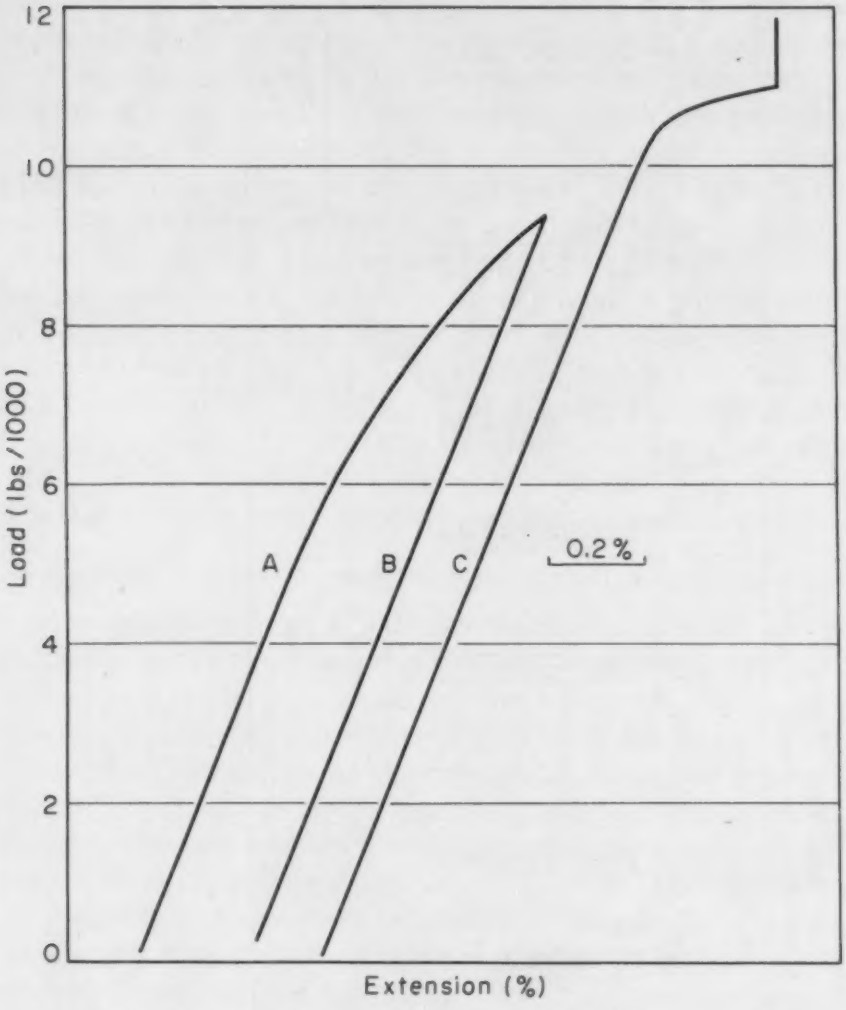


Fig. 5—Load-Extension Curves. A, initial loading; B, unloading; C, after aging at 100 °C (212 °F) for 24 hours.

the tensile properties remained the same except the yield strength. The yield-tensile ratio in all cases examined was raised to approximately 0.90, which would seem to be a satisfactorily high value for many applications.

Effect of Strain Aging on the Impact Properties

A few experiments were carried out to determine the effect of strain aging on impact properties. Impact strength versus testing temperature curves were determined for Heat 9 (0.14% carbon, 5.5% nickel, and 1.51% chromium). Standard impact specimens were austenitized one hour at 1700 °F (927 °C) and quenched in iced brine. Some were tested in the as-quenched condition and others after being tempered two hours at either 150 °F (65 °C) or 300 °F (149 °C). The results of these tests were not included in Tables VI and VII because

of the different tempering treatments used. They show the beneficial effect of nickel on T_a and are as follows:

Treatment	Type	Maximum Impact ft-lb	T_a °C
As-Quenched	1	41	—145
150 °F	1	42	—140
300 °F	1	43	—140

The impact strengths at —320 °F (—196 °C) ranged from 7 to 14 ft-lb.

Blanks ½ inch square from the same steel were pulled in tension in the as-quenched condition until local necking occurred. The specimens were then aged for two hours at 150 or 300 °F (65 or 150 °C) and finish-machined. The notches were placed in the specimens where the reduction of area before this machining was 4%. Impact strength versus testing temperature curves were then determined for these test pieces.

The results of these tests show that strain aging considerably reduced the impact strength by amounts up to 14 ft-lb at all testing temperatures. The transition temperature was also raised slightly by strain aging (15 to 20 °C). The effect of the strain was greater the higher the aging temperature. Essentially maximum R_c hardness was obtained on all specimens; strain aging did not produce any measurable increase in hardness.

An attempt to investigate the effect of strain aging on the higher carbon steels failed because of the limitation of the testing machine. Charpy blanks which were compressed using the maximum load of the tensile machine prior to aging gave test results which were essentially the same as those for quenched and tempered specimens from the same steels.

Summary

1. Low carbon steels containing 0.16 to 0.28% carbon in the as-quenched condition (brine quench) had essentially no ductility as measured by the tensile test. Steels containing 0.15% carbon or less had appreciable ductility in the as-quenched condition.

2. Tempering at 212 °F (100 °C) improved all tensile properties, the ductility to values considerably higher than those reported for 0.30 to 0.50% carbon steels quenched and tempered to comparable tensile strengths. However, the yield strength was not as greatly improved as the tensile strength and, therefore, the yield strength—tensile strength ratio was low (0.70 or so).

3. The amount or type of alloying element added in the range studied had no effect on the tensile properties.

4. Refrigeration in liquid nitrogen prior to tempering appeared to have no effect on the tensile properties.

5. Steels containing 0.18% carbon or more and quenched in oil had essentially no ductility in the as-quenched condition. Steels containing less than 0.18% carbon had appreciable ductility in the as-quenched condition.

6. Tempering at 212 °F (100 °C) after oil quenching improved all tensile properties. However, slightly higher ductilities and yield—tensile ratios at higher tensile strengths were developed by the brine quench.

7. Except for yield strength, the tensile properties of steels of 0.15 to 0.28% carbon tempered at 212 °F (100 °C) were unaffected by specimen diameter up to 0.505 inch. Yield strength decreased with increasing specimen diameter.

8. Most of the steels, as-quenched or tempered at 212 °F (100 °C), developed room temperature impact strengths which were higher than those of 0.30 to 0.50% carbon steels quenched and tempered to comparable hardnesses.

9. Tempering at 212 °F (100 °C) slightly raised the impact strength and lowered the transition temperature.

10. Increasing carbon tended to raise the transition temperature.

11. Nickel was most beneficial in lowering transition temperature, chromium up to 2% also lowered transition temperature somewhat, while manganese in an amount between 0.8 and 1.5% or higher raised transition temperature quite effectively and to that extent damaged impact quality.

12. All of the steels tested showed strain aging effects in both the as-quenched and quenched and tempered conditions; the amount increased with increasing deformation and aging temperature.

13. The few data available suggest that strain aging lowered impact strength and very slightly raised the transition temperature.

Acknowledgments

The authors wish to express their appreciation to the Aeronautical Research Laboratory, Wright Air Development Center, Wright-Patterson Air Force Base, Ohio, for granting permission to publish this work. Thanks are also due to M. A. Redmerski, L. S. Redmerski, and R. E. Cizma of the Metals Research Laboratory, Carnegie Institute of Technology, for assistance in conducting the experimental work and preparing the manuscript.

References

1. J. J. Burns, T. L. Moore, and H. S. Archer, "Quantitative Hardenability," Transactions, American Society for Metals, Vol. 26, 1938, p. 1.
2. J. M. Hodge and M. A. Orehoski, "Relationship Between Hardenability and Percentage of Martensite in Some Alloy Steels," *Transactions*, American Institute of Mining and Metallurgical Engineers, Vol. 167, 1946, p. 627.
3. W. G. Patton, "Mechanical Properties of NE, SAE, and Other Hardened Steels," Metal Progress, Vol. 43, May 1943, p. 726.

4. J. H. Hollomon and L. D. Jaffe, *Ferrous Metallurgical Design*, John Wiley and Sons, Inc., New York, 1947, p. 155.

DISCUSSION

Written Discussion: By Samuel J. Rosenberg, Metallurgist, National Bureau of Standards, Washington, D. C.

The authors' data lend added support to the generally accepted thesis that the use of steel with as low carbon as is possible to develop the strength properties desired is conducive to better toughness.

In reviewing the tensile data presented in this paper, I note the extremely low values (in Table II) for reduction of area and elongation for steel 6C as tempered and for the tensile strength of steel V10 as quenched. Is it possible that these values are missprints? Incidentally, the authors do not specify the gage length of the specimens used for tensile testing.

Normal practice in the preparation of impact specimens is to machine the notch subsequent to heat treatment. This is done to avoid the concentration of stresses at the root of the notch and possibly incipient cracking which must inevitably result if quenching is carried out subsequent to notching. The suspicion exists, therefore, that the results of the impact tests may have been affected by such stresses. Corroboratory evidence is furnished by the fact that steels V22, V23, and V24 tended to crack at the base of the notch when quenched in iced brine. The apparently superior impact properties of these three steels may be, and probably is, due to the fact that they were oil-quenched, with correspondingly lesser stress concentration at the root of the notch. The conclusion is inescapable that the impact data would have been of considerably more value had all steels been quenched alike and had the quenching been carried out prior to notching. The wide difference in the transition temperatures of the duplicate steels V3 and V4 (−16 and +50 °C, respectively), may be due to stresses at the root of the notch.

Although it might be expected that strain aging would reduce the impact strength of steel, I am rather puzzled as to how the author reached this conclusion on the basis of the few data given on page 151, particularly in view of the fact that comparable impact data on this steel as quenched and tempered but not strain aged are not given.

It is extremely difficult to evaluate the effect of the various alloying elements on the transition temperature of the test steels, mainly because of the variations in carbon content. Although it is realized that conclusion 11 of the paper is, of necessity, a general statement, a close study of the data shows so many exceptions to this conclusion (with respect to the effect of nickel and chromium) as to render it questionable. This can best be appreciated by adding the T_α temperatures to Table I and noting the effect of composition on T_α. For instance, steel 3D, with its high nickel and optimum chromium content, has a rather high transition temperature (−10 °C). Strangely enough, steel 5D, of similar chemistry but considerably higher carbon, has a much lower transition temperature (−55 °C), which is exactly the opposite of what might be expected.

Written Discussion: By A. E. Nehrenberg, supervisor, Research Laboratory, Crucible Steel Company of America, Harrison, N. J.

The authors have carried out a great deal of mechanical testing and have

obtained a considerable amount of data on the properties of low carbon martensites tempered at 212 °F for extended periods of time. It should be emphasized that their conclusions apply for this tempering temperature only and that somewhat different conclusions might have been reached in some cases if higher tempering temperatures had been employed. I am wondering if the authors obtained any data for other tempering temperatures during the course of their work.

In our own work we have consistently found that the maximum toughness as measured by a notch impact test is obtained at high strength levels if a tempering temperature of 350 to 450 °F is employed for steels containing normal ranges of silicon. When the silicon content is increased to about 1.5% the tempering temperature for maximum notch toughness is increased to 500 to 600 °F. Also, the ratio of yield to tensile strength, which has been a matter of considerable concern to the authors, is improved in low carbon steels by tempering in these ranges of temperature.

The effect of specimen diameter on yield strength observed by the authors would seem to be of considerable practical significance for their data imply that the yield strength of structural components made from high strength steels would be expected to decrease with increasing thickness or diameter of such parts. We anticipated that the effect observed by the authors might be real when a tempering temperature as low as 212 °F was employed, but we felt that any such effect would perhaps be destroyed if a higher tempering temperature were employed. As a consequence of this reasoning we carried out the following experiment. Tensile specimens both 0.550 and 0.300 inch in diameter were prepared from a commercial alloy steel containing 0.15% carbon, austenitized for 1 hour at 1600 °F and quenched in iced brine. One specimen of each diameter was left in the as-quenched condition and other sets of specimens were tempered for 16 hours at each of the temperatures 212, 350 and 450 °F. The long tempering time was used so that our data would be comparable with those obtained by the authors. Subsequent to heat treatment the tensile specimens were machined to 0.505 and 0.252 inch diameter.

The analysis of the steel used is as follows:

C	Mn	Si	Ni	Cr	V	Mo	Cu
0.15	1.03	0.75	0.99	0.88	0.09	0.21	0.48

The pertinent tensile data obtained are summarized below:

Spec. Dia.	Temper, °F	Tensile Strength psi.	0.1% Yield Strength psi.	Ratio 0.1% Yield To Tensile Strength
0.505	None	202,000	120,000	0.59
	212	198,000	138,000	0.70
	350	197,000	156,000	0.80
	450	195,000	161,000	0.83
0.252	None	202,000	118,000	0.58
	212	200,000	140,000	0.70
	350	194,000	157,000	0.81
	450	193,000	163,000	0.84

All of the specimens were found to have good ductility, the elongation values being about 15% for all specimens with reduction of area varying in the range 50 to 60%.

The data fail to confirm the effect of specimen diameter observed by the authors. Note that the ratio of yield to tensile strength is the same for both the 0.505 and 0.252 inch diameter specimens in the same condition of heat

treatment. Although the above data are the result of a single experiment it appears reasonable to conclude that specimen diameter does not always affect the yield strength of low carbon martensites. Perhaps further work would show that the effect observed by the authors is not attributable to specimen diameter per se, but may be the indirect result of some other factor such as inadequate hardening of the larger specimens, the presence of more retained austenite in the larger specimens because of a somewhat slower cooling rate, etc. I would be interested in knowing whether the authors found a relationship between yield strength and specimen diameter for steels other than those of their Table V and whether there was a consistency in this relationship from steel to steel.

Note also that the data show that the yield to tensile ratio, as mentioned in the first part of this discussion, improves considerably when the tempering temperature is increased from 212 to 350 or 450 °F. It would be enlightening, therefore, if the authors will give us any data they may have for tempering temperatures above 212 °F.

Authors' Reply

The authors wish to thank Messrs. Rosenberg and Nehrenberg for their interest and commentaries on our observations.

Mr. Rosenberg is correct in assuming that the values in Table II for 6C are incorrect. The correct RAL should be 57% and elongation 15%. The values for Steel V10, however, are real; the low tensile strength is due to lack of sufficient ductility. The gage length of all specimens was four times the specimen diameter as stated on page 142.

The question of whether notches should be machined for impact testing in these high strength steels before or after quenching is not so obvious as Mr. Rosenberg suspects. It appears to be to some extent a function of the steel. Experiments on the same steel in both conditions will differ by 4 or 5 ft-lb at any temperature, but the direction of the difference varies from steel to steel. The authors would be interested to hear the experience of other laboratories on this phenomenon. In passing, it may be mentioned that machining problems are simplified if performed before quenching. In summary, then, the conclusion does not seem to be inescapable that "the impact data would have been of considerably more value had all steels been quenched alike (33 of 36 were) and had the quenching been carried out prior to notching."

With reference to the data listed in the table on page 151, it should be pointed out again that these data are for as-quenched and tempered specimens and not for those which had been strain-aged. The data for the strain-aged specimens are not listed in the paper; it was felt that a brief statement of the results was adequate.

Mr. Rosenberg also points out, as was done in the paper, the peculiar behavior of Steels 5D and 3D with respect to T_a. The authors have thought of no further possible explanations for this behavior.

In answer to Mr. Nehrenberg, the bulk of the work was confined to testing steels which were either as-quenched or quenched and tempered at 212 °F. However, a few data were obtained at higher tempering temperatures.

The results of V-notch Charpy impact tests on Steel 8 (Table I) tempered between 70 and 800 °F and broken at temperatures from 70 to −150 °F indicated that maximum toughness was obtained after tempering at 400 °F. This is in agreement with the results of Mr. Nehrenberg. With reference to the

effect of specimen diameter on properties, studies were made only to determine whether or not the increased ductility of the low carbon steels over that of the Patton steels was due to the use of the smaller specimens. As a result, only a few steels were compared. Although the data in the paper show a decrease of yield strength with increased specimen diameter, a few data not reported show the opposite effect. These latter results on as-quenched Steels 8 and 9 are as follows:

Steel	Specimen Diameter	TS psi	YS (0.1%) psi	YS/TS
8	0.252"	243,000	152,000	0.63
	0.505	241,000	177,000	0.73
9	0.252	198,000	122,000	0.62
	0.505	196,000	131,000	0.67

It is evident that much more data at these high strength levels is necessary before a definite conclusion can be made. Mr. Nehrenberg shows the yield-tensile ratio to be the same for both the 0.505 and 0.252 inch diameter specimens in the same condition of heat treatment. The following data, which had been obtained previously but not reported, show the same effect if the 212 °F temper is ignored.

Steel 3D

Specimen Diameter	Temper °F	TS psi	YS (0.2%) psi	YS/TS
0.252 inch	212	199,000	155,000	0.78
	900	172,000	152,000	0.88
	1200	108,000	95,000	0.88
0.505 inch	212	197,000	135,000	0.69
	900	166,000	143,000	0.86
	1200	105,000	93,000	0.89

All values are averages of four tests.

He also demonstrates that the yield-tensile ratio increases with increasing tempering temperature. Data supporting this conclusion had also been obtained by the authors in approximately the same tempering range as that used by Mr. Nehrenberg and are shown below:

0.252-Inch Specimens

Steel	Temper °F	TS psi	YS (0.1%) psi	YS/TS
8	None	244,000	152,000	0.62
	300	227,000	159,000	0.70
	400	214,000	153,000	0.72
	500	211,000	168,000	0.80
	600	208,000	168,000	0.81
9	None	197,000	144,000	0.62
	300	188,000	148,000	0.78
	400	185,000	150,000	0.81
	500	179,000	149,000	0.83
	600	174,000	150,000	0.86

All values are averages of two tests.

THE TENSILE CHARACTERISTICS OF UNALLOYED ZIRCONIUM AT LOW AND MODERATE TEMPERATURES

By J. H. Keeler

Abstract

Increasing strain rate, decreasing test temperature, strain, decreasing recrystallized grain size, strong preferred orientation and small amounts of oxygen-nitrogen impurity (from arc melting) are shown to raise the true-stress level and engineering strengths of unalloyed zirconium. A yield point was observed and found to decrease with increased grain size and decreasing temperature. The tensile behavior of severely cold-reduced zirconium at and above 200 °C (390 °F) shows a maximum load at early strains which is not associated with measurable necking and seems to be related in some manner to recovery, stress-recovery and strain-aging.

Introduction

EARLIER investigations by groups at the Phillips Company, Eindhoven, Netherlands; the Foote Mineral Company; and the Westinghouse Atomic Power Division, producers of crystal-bar zirconium, have done much to make the properties of high purity crystal-bar zirconium familiar to the metallurgist and the engineer. Additional information has been made available from the Massachusetts Institute of Technology and from the Battelle Memorial Institute. The U.S. Bureau of Mines at Albany, Oregon, has made valuable contributions in developing the Chloride process of making ductile zirconium and has frequently reported the properties of their product.

This work is intended to supplement existing knowledge by reporting the effects of various metallurgical and test variables upon the tensile properties and was conducted in order to establish the behavior of unalloyed zirconium (rolled and annealed crystal bar, and arc-melted, rolled, and annealed crystal bar) as a basis for evaluating the quantitative influence of alloying elements. In these tests, a "standard" set of conditions was selected and then each of the variables was altered independently of the others to determine its effect. The interdependence of the variables was not studied in detail, except in one or two instances, since a prohibitive amount of testing would be necessary to establish

A paper presented before the Thirty-sixth Annual Convention of the Society, held in Chicago, November 1 to 5, 1954. The author, J. H. Keeler, is associated with the Research Laboratory, General Electric Co., Schenectady, N. Y. Manuscript received December 29, 1953.

the various relations quantitatively. In the particular combination of material and test conditions constituting the "standard" test (See Fig. 2) crystal-bar zirconium was cold-reduced 97% and then annealed (1 hour at 600°C) to a grain size of approximately 0.005-mm average diameter, and tested at room temperature at a strain rate of 0.09 min^{-1}.

Experimental Procedure

The material used in this investigation was crystal-bar zirconium prepared by the iodide process. The largest impurity was hafnium, which was less than 0.3%. The composition obtained by spectrographic analysis is given in Table I.

Crystal-bar zirconium was cold-rolled from ½-inch to ⅝-inch-diameter bars into sheets 0.020 inch in thickness, about a 97% reduc-

Table I
Composition of Crystal-Bar Zirconium

Element	Weight %
Hf	0.3 maximum
Fe	0.02 to 0.1
Al	0.005 to 0.02
Cr	0.02 to 0.1
Cu	0.001 to 0.005
Ni	0.005 to 0.02
Mg	0.001 to 0.005
Mo	0.01
Na	0.007 *

* Chemical analysis (oxygen and carbon are estimated at 0.02%).

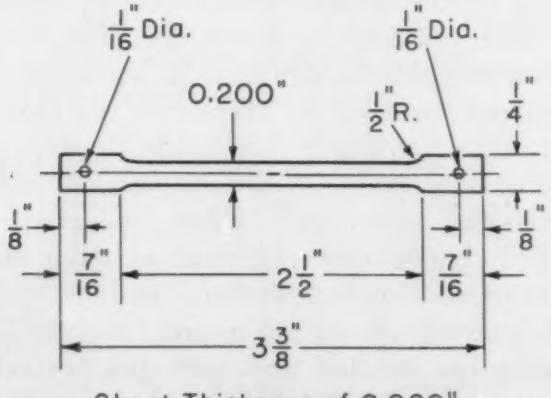


Fig. 1—Drawing and Dimensions of Sheet Tensile Specimen. The holes in the grip sections are for locating pins to facilitate alignment during mounting in grips.

tion in thickness. Tensile specimens of the dimensions shown in Fig. 1 were machined from these cold-reduced sheets.

Arc-melted buttons, weighing 100 grams and made from crystal-bar zirconium, were similarly rolled out, with several exceptions, into 0.020-inch sheet, a reduction of approximately 90%. All but one of the melts mentioned in this report were made in a multiple-hearth furnace

containing nine replaceable water-cooled copper crucibles. This arc-melting furnace uses a wolfram-tipped electrode in an atmosphere of purified argon, and the hearth is rotated after each melting cycle without opening the seal. The charge in each instance was melted down, allowed to solidify, turned over, and remelted. The first of each series of nine melts acted as a getter, taking up the contaminant gases, oxygen and nitrogen, not removed by the vacuum pumps or subsequent gas flush. In this manner, the oxygen and nitrogen impurity in the subsequent melts was greatly reduced.

Annealing was carried out in evacuated tubes of Vycor or quartz containing zirconium foil to take up any remaining oxygen or nitrogen.

Tensile tests were conducted with Instron Engineering Corporation tensile-testing machines, Models TT-B and TT-C. These instruments provide a constant cross-head motion at any of a number of strain rates (jaw speeds) from 0.002 inch per minute to 2 inches per minute. Load is measured by the use of one of several interchangeable load cells which incorporate an SR-4 strain gage. The load-time curve is recorded automatically on a synchronously driven chart. The relation of recorder chart speed to jaw speed is known, and, therefore, the time axis of the chart can be converted to strain. The instrument was calibrated for each series of specimens tested, and the zero load point was checked at desired intervals during the test to insure accurate recording.

Tensile tests were conducted in liquid nitrogen at −195 °C (−319 °F) and in air in the temperature range from 25 to 370 °C (77 to 700 °F). True stress vs true strain and log true stress vs log true plastic strain are plotted for these tests. Yield strength (0.2% offset), tensile strength, reduction in area, and elongation are tabulated. The strain-hardening exponent "m" from the stress-strain relation $\sigma = K\epsilon^m$, which is obtained from the slope of the log true stress vs log true plastic strain plot, is also listed. In those instances where the log-log plot was not a straight line, the slope was taken from that portion of the curve in the vicinity of the strain at maximum load.

Preferred orientation determinations were obtained by the quantitative method of Decker, Asp, and Harker (1)[1], modified by Geisler (2) using an X-ray spectrogoniometer with copper $K\alpha$ radiation as reported previously (3).

Annealed Crystal-bar Zirconium

Crystal-bar zirconium, cold-reduced 97 per cent, was annealed one-half hour at 600 °C (1110 °F) *in vacuo* to provide a recrystallized grain size of approximately 0.005-mm average diameter. Specimens were tested in the temperature range −195 to 370 °C (−351 to 700 °F) in the rolling direction. Typical tensile curves are shown in Figs. 2 and 3. Data are listed in Section A of Table II and plots of

[1] The figures appearing in parentheses pertain to the references appended to this paper.

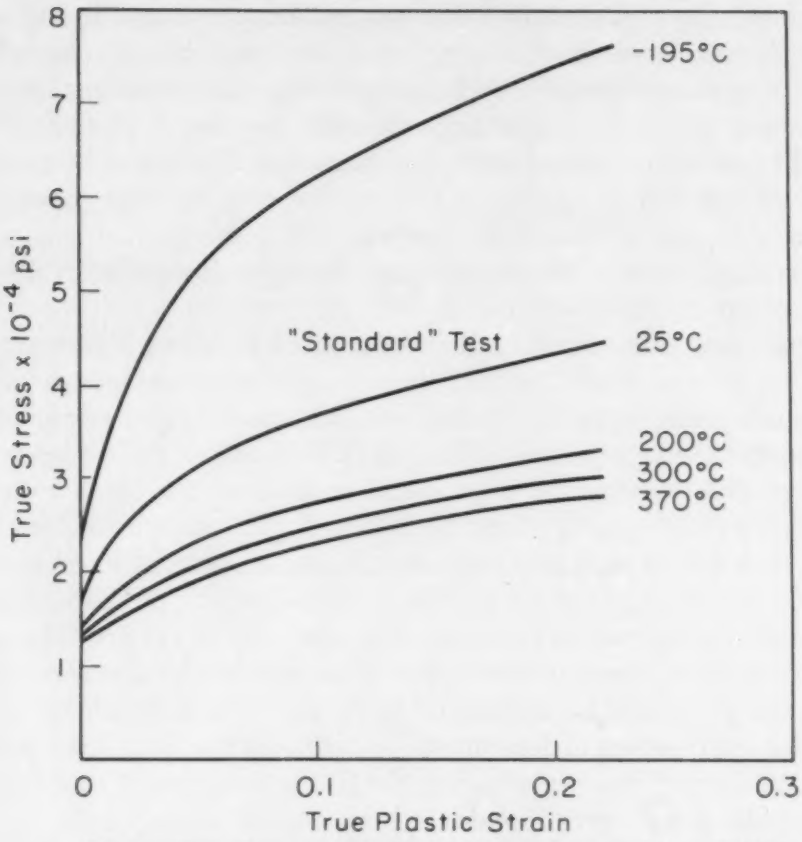


Fig. 2—True Stress vs True Plastic Strain Curves Up to Necking Strain for Annealed Crystal Bar Showing Variation With Testing Temperature. The curve for a "standard" test is indicated.

Table II
Tensile Characteristics of Annealed (600 °C) and of Cold-Rolled Crystal Bar

Test Temp (°C)	Ultimate Strength (psi)	0.2% Offset Yield Strength (psi)	% Elongation	% Reduction in Area	Strain-hardening Exponent
A. ANNEALED					
−195	58,900	20,800	33	56	0.25
25	34,700	17,900	30	56	0.21
200	26,400	13,300	26	75	0.25
300	24,700	12,900	24	86	0.25
370	23,000	12,600	27	86	0.26
B. COLD-ROLLED					
−195	120,000	95,500	7	35	0.06
25	83,600	70,800	4	60	0.08
200	49,000	42,300	12	85	0.045
300	43,400	37,000	14	82	0.04
370	43,900	35,000	16	84	0.04

properties vs temperature are given in Figs. 4 and 5. It was observed that with decreasing temperature the increase in tensile strength was much more pronounced than the increase in 0.2% offset yield strength. The strain-hardening exponent and the elongation changed very little in this temperature range.

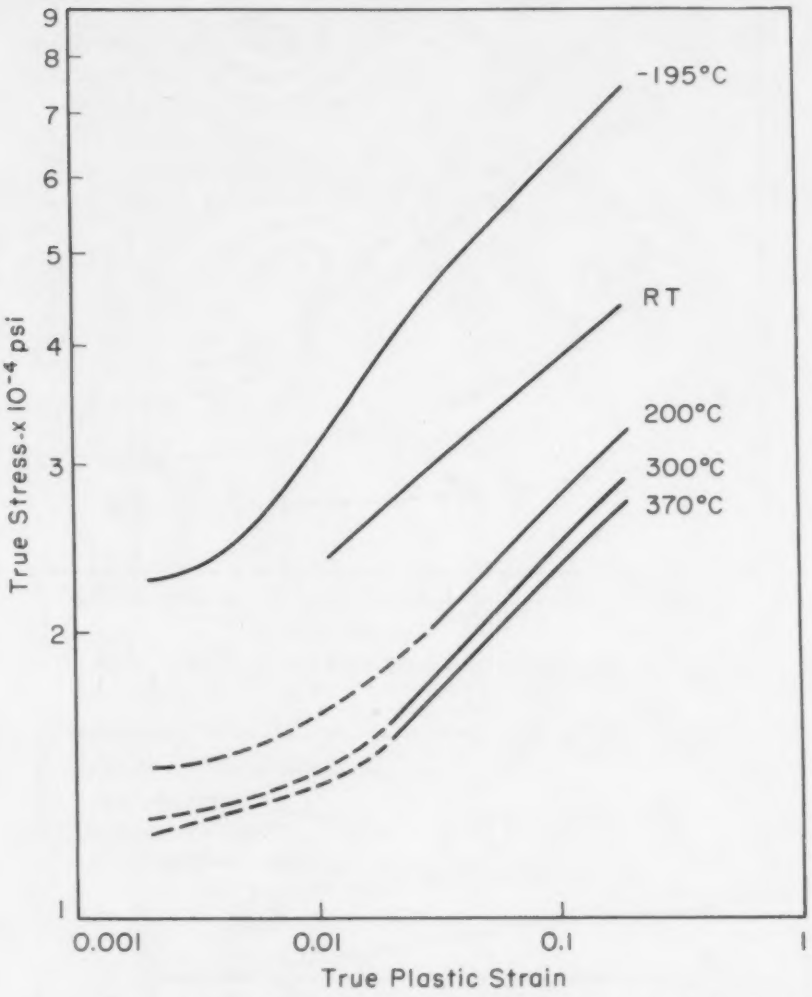


Fig. 3—Logarithmic Plot of True Stress vs True Plastic Strain Curves Up to Necking Strain for Annealed Crystal Bar, Showing Variation With Testing Temperature.

Cold-Rolled Crystal-Bar Zirconium

Specimens of crystal-bar zirconium cold-reduced 97% were tested in the rolling direction. Plots of properties vs temperature for the range from —195 to 370 °C (—351 to 700 °F) are given for the severely deformed zirconium in Figs. 4 and 5. Data are presented in Section B, Table II. It can be seen that, as anticipated, the tensile strength and the yield strength of the cold-rolled material showed a greater increase with decreasing temperature than did these properties of the annealed material.

Tensile tests of 97% cold-rolled crystal-bar zirconium at 200, 300, and 370 °C (390, 570 and 700 °F) disclosed interesting characteristics. It was observed that the maximum load, P_{max}, was obtained very early in the test, at a strain of about 0.02 to 0.05, after which a long gradual falling off of the load occurred. This latter portion of the curve is almost a straight line. Finally, localized necking occurred at a strain

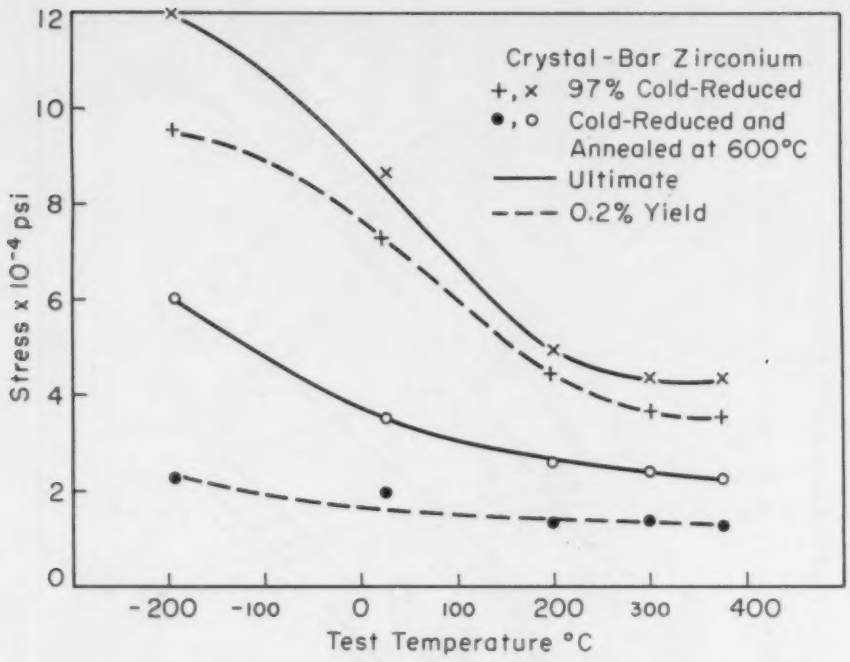


Fig. 4—Ultimate Tensile and 0.2% Offset Yield Stress vs Test Temperature for Cold-rolled and for Annealed Crystal-bar Zirconium.

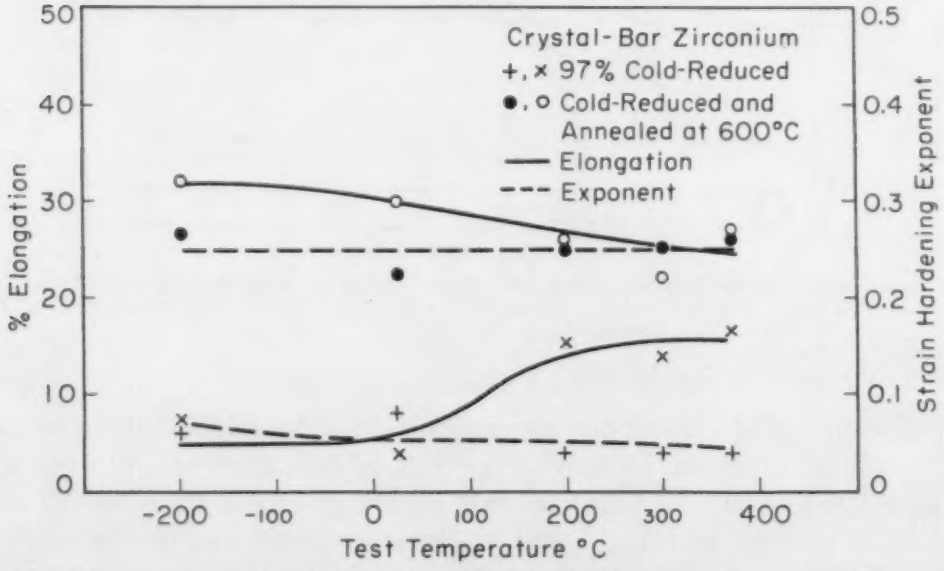


Fig. 5—Per cent Elongation and Strain-hardening Exponent vs Test Temperature for Cold-rolled and for Annealed Crystal-bar Zirconium.

as much as five to ten times as great as the strain at P_{max}, and the specimen fractured. A typical load-elongation curve of this type is shown in Fig. 6. Point A on the curve indicates the point of maximum load. In one experiment of this type, the straining was stopped at the point indicated by B in Fig. 6, about three or four times the strain at P_{max}. The load was removed and the specimen was taken out of the furnace.

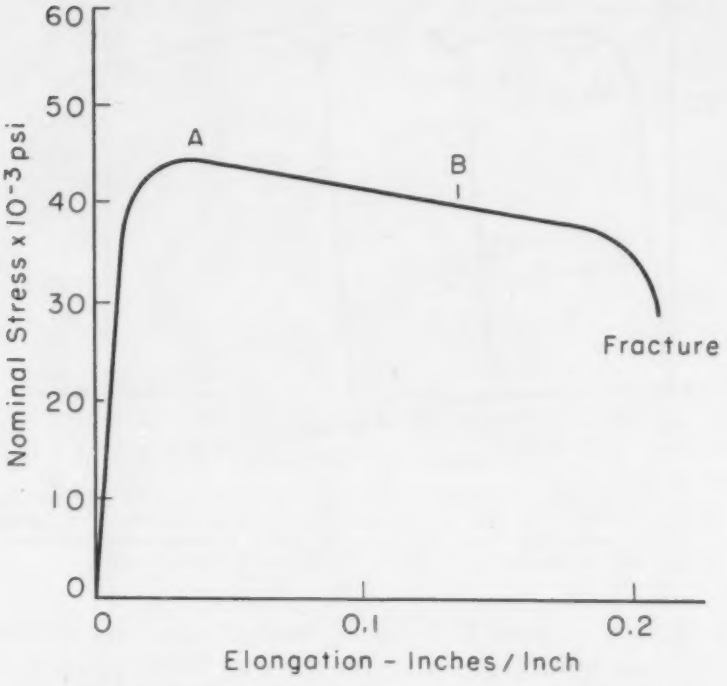


Fig. 6—Typical Stress-strain Curve for Severely Cold-rolled Crystal Bar in the Temperature Range 200-370 °C. Point A indicates maximum load and B indicates strain at which no localized necking is discernible.

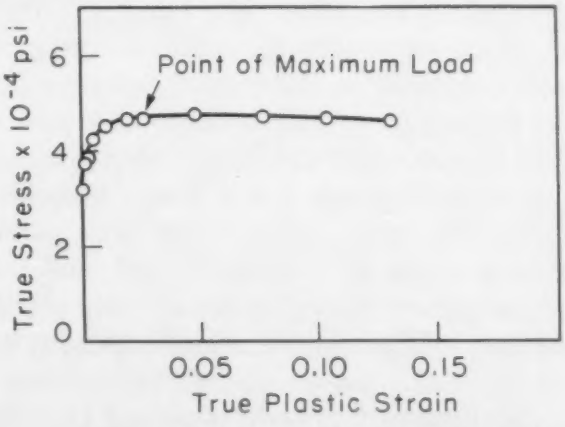


Fig. 7—True Stress-true Strain Curve for Severely Cold-rolled Crystal Bar for the Temperature Range 200-370 °C. The calculations have been carried beyond the maximum load to a point where uniform strain was still found to be occurring.

An examination of the gage area disclosed no localized necking, the straining apparently continuing in a uniform manner.

True stress vs true strain calculations for curves of this type were plotted for points beyond the maximum load, since uniform strain was apparently still taking place. These curves exhibited a flattening beyond the maximum load, with the slope of the curve becoming zero and then slightly negative (Fig. 7).

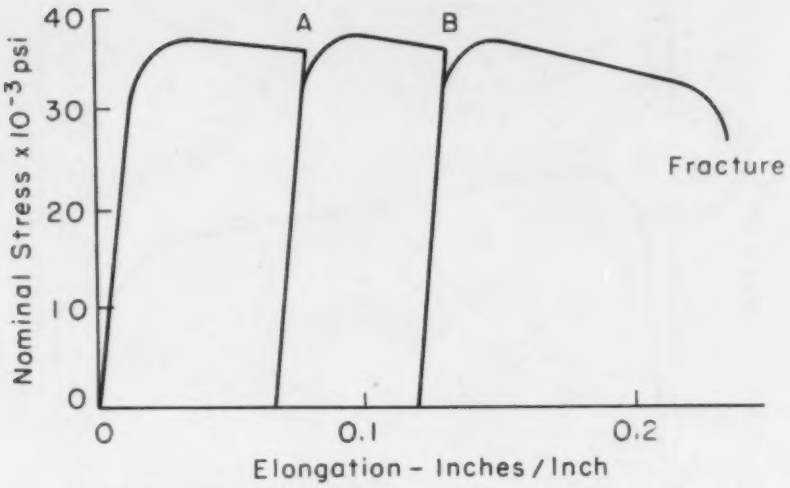


Fig. 8—Stress-strain Curve for Severely Cold-rolled Crystal bar at 300 °C. This test was interrupted twice as indicated by points A and B when the load was removed while the specimen remained at the test temperature for 36 and 12 minutes respectively.

The reduction in area that finally occurred in the necked area of the specimens was very large, in the vicinity of 85%, resulting in a very high value for the apparent true stress at fracture, of the order of 180,000 to 200,000 psi.

The recrystallization temperature for this material is approximately 400 to 500 °C (750 to 930 °F) (in one hour), one hour at 500 °C (930 °F) being necessary to obtain a fine-grained recrystallized structure (as described in the section on annealed crystal bar). Metallographic examination of the necked area and adjoining gage area of fractured tests bars of the cold-reduced crystal bar did not show any evidence of recrystallization. Since it was possible that recovery was occurring during the tensile test, one test was halted at a strain of about three times the strain at maximum load, and the load was removed while the specimen remained in the furnace at 300 °C (570 °F) for about 36 minutes (Point A, Fig. 8). When the test was subsequently continued, the load rose to a value higher than that removed, reached an early maximum load, and continued to display a behavior similar to that during the first part of the test (see Fig. 8). Obviously, more than recovery alone was occurring. The test was again halted (Point B), the specimen was unloaded, and after a period of 12 minutes the test was recommenced. Again, a load greater than that at the stop of the previous part of the test was obtained, and on the basis of a now smaller cross section the stress was higher than previously. These results would suggest that perhaps strain aging was also involved. However, strain aging is usually accompanied by a transient yield point, and no transient yield point was observed in any of the interrupted tests of the material. Some combination of strain aging and recovery may be causing the peculiar results described above. This

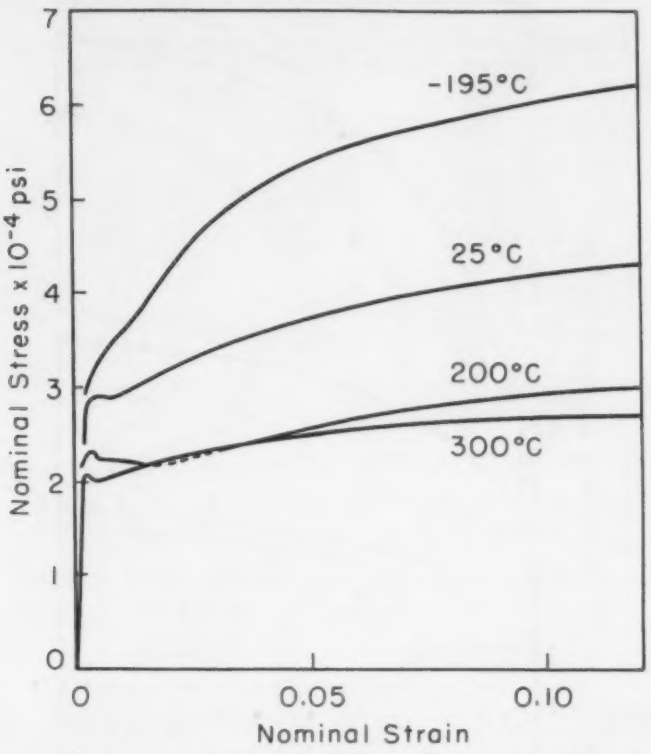


Fig. 9—Stress-strain Curves Showing Yield-point Indications in Cold-rolled and Annealed Crystal Bar (0.003 mm average grain diameter) with Variation in Test Temperature.

behavior may also be related to stress recovery reported for aluminum (4).

A high rate sensitivity was found for the cold-reduced crystal bar at 200 and 300 °C, (390 and 570 °F), as is discussed in another section.

Yield Point

The yield point phenomenon was of interest in this investigation. Cold-rolled crystal-bar zirconium, annealed to a grain size of approximately 0.003-mm average diameter, almost always exhibited a strong yield point indication (see Fig. 9). Occasionally in material with a slightly larger grain size (approximately 0.005-mm average diameter), a sudden change of slope in the stress-strain curve was observed at room temperature, whereas in tests at —195 °C (—351 °F) a yield point was observed. Specimens with a grain size of 0.012-mm average diameter and larger exhibited a smoothly continuous tensile curve.

Fine-grained tests specimens produced from zirconium buttons arc-melted after the first "getter" heat in the multihearth furnace did not exhibit any evidence of a yield point in tests at 200 or 300 °C (390 or 570 °F). In one or two instances, very slight evidence was observed in tests at room temperature. Other fine-grained test specimens made from the "getter" heats in the multihearth furnace showed an upper

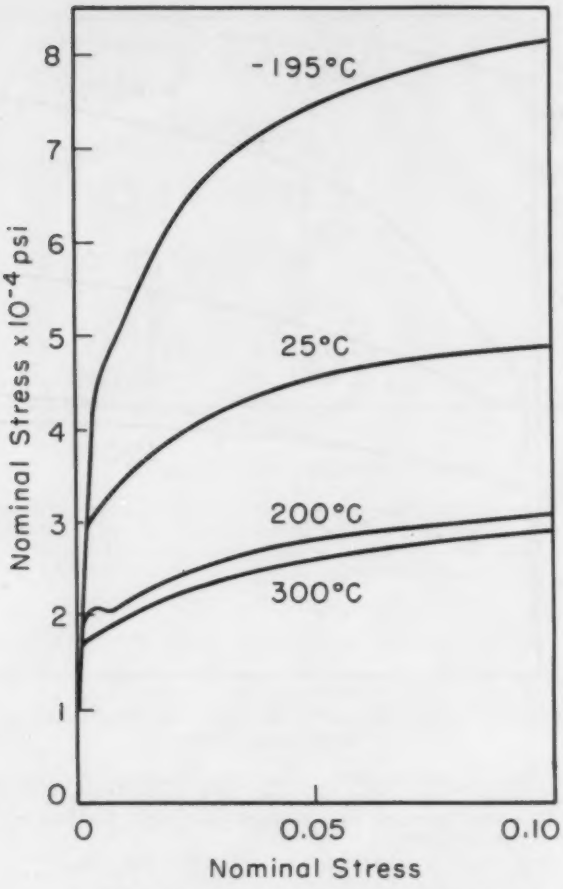


Fig. 10—Stress-strain Curves Showing Yield Point Indications in Cold-rolled and Annealed "Getter melt" with Variation in Temperature.

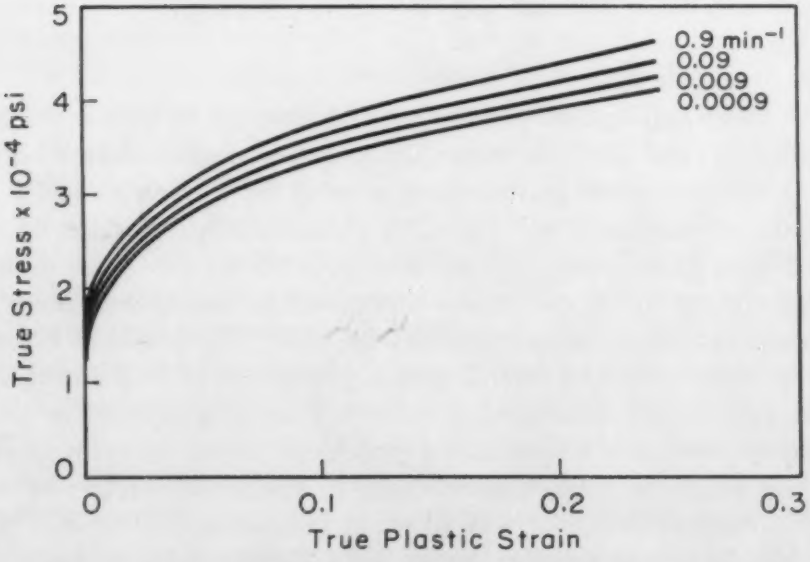


Fig. 11—True Stress vs True Strain Curves up to Necking Strain for Cold-rolled and Annealed Crystal Bar Tested at Room Temperature, Illustrating the Influence of Strain Rate.

Table III
Relation between Yield Strength and Absolute Temperature

Test Temperature (°C)	(°K)	Yield Strength	Strain Rate (min^{-1})	Temp-stress Product (all values × 10^6)
Melt 5061				
−195	78	45,600	0.09	3.56
23	296	29,000	0.09	8.86
200	473	20,600	0.09	9.75
291	564	16,500	0.09	9.30
Melt 540B				
−195	78	56,200	0.09	4.38
23	296	38,600	0.09	11.43
200	473	24,800	0.09	11.73
300	573	18,200	0.09	10.42

and a lower yield point in tests at 200 °C (390 °F) and exhibited a sharp break in the load-extension curve in tests at room temperature and at 300 °C (570 °F) (see Fig. 10). It is of interest that the yield point effect seems to occur in a temperature range with the effect diminishing at higher and lower temperatures. It is also probable that the yield point is associated with presence of gaseous impurities (oxygen and/or nitrogen) picked up by the "getter" heat.

According to Fisher (5), the product of the absolute temperature T and the yield stress, σ, should be almost constant for a given material if the yield point phenomenon depends on a Cottrell-type mechanism. Table III shows that the product of the yield stress and the absolute temperature for the yield stress in two "getter" heats is roughly constant (with standard deviations of 6.3 and 3.7%) in the temperature range from 25 to 300 °C (77 to 570 °F). A variation by a factor of about 3 is encountered at −195 °C (−351 °F). However, this variation might be anticipated, since the yield strength will not be infinite at absolute zero.

Rate Sensitivity

To avoid the difficulty of specimen-to-specimen variation, rate sensitivity tests were conducted on single specimens with tenfold changes in strain rate being made almost instantaneously during the test. The change in stress due to a change in strain rate was determined in experiments over a 1000-fold variation (0.0009 to 0.9 min^{-1}) in strain rate. (See Fig. 11)

The change in stress (in psi) is a measure of the "rate sensitivity". The stress-strain rate relation has been expressed (6) as

$$\sigma = K\epsilon^n \mid \epsilon, T \quad ,$$

where K is a constant, strain and temperature are constant, and n is a constant called the strain-rate exponent. The term "rate sensitivity" has thus been defined (6,7,8) as the ratio of a small change in log stress to the resultant change in log rate for a given strain and temperature:

$$n = \frac{\delta \log \sigma}{\delta \log \epsilon}\bigg|_{\epsilon, T} .$$

This rate sensitivity n can be obtained from a test wherein strain rate is changed quickly from one value to another (9) by the relation

$$n = \frac{\log S_2 / S_1}{\log \dot{\epsilon}_2 / \dot{\epsilon}_1} ,$$

in which S_2 is the stress obtained with strain rate $\dot{\epsilon}_1$, and S_1 the stress obtained with strain rate $\dot{\epsilon}_2$.

It was found that crystal-bar zirconium 97% cold-rolled and annealed at 600 °C (1110 °F) had an increase in stress level of 2.5 to 5% (830 to 1350 psi) with a tenfold increase in strain rate at room

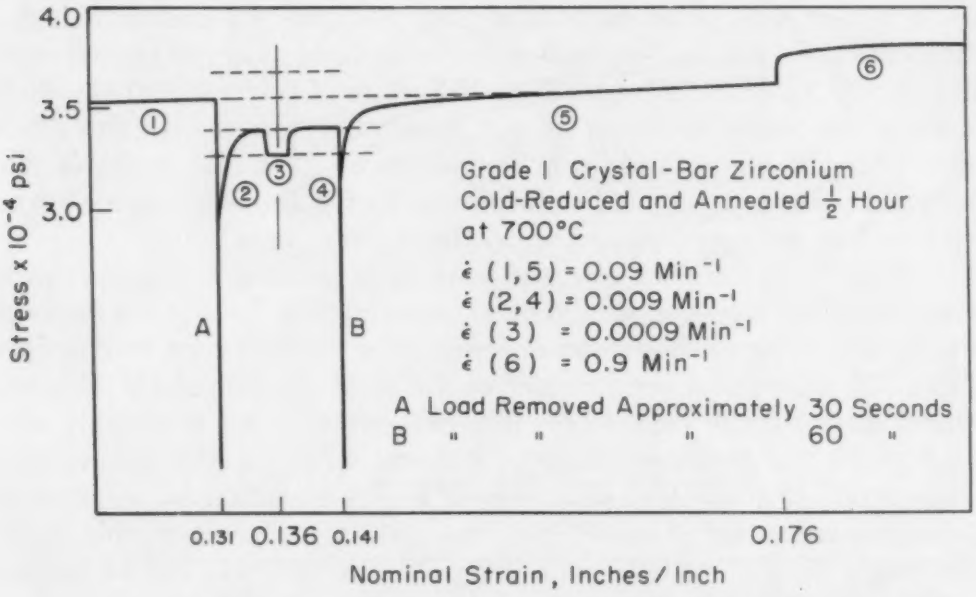


Fig. 12—Portion of Stress-strain Curve Showing Influence of Strain Rate on Stress Level. Extrapolations to a strain of 0.136 are indicated by the broken lines.

temperature. This change corresponds to a rate sensitivity of 0.011 to 0.021. For crystal-bar zirconium cold-rolled and annealed at 700 °C (1290 °F) (Fig. 12), the effect of three tenfold increases (a 1000-fold increase) in strain rate (interpolated to a strain of 0.136 inch) was an increase in stress of 13.6% (4260 psi), or n=0.018.

Several tests were conducted at room temperature on annealed crystal-bar zirconium to see if the amount of strain or the grain size influenced the rate sensitivity. The rate sensitivity values varied between 0.011 and 0.021 and little, if any, effect was attributable to strain or to grain size.

The rate-sensitivity of annealed and of 97% cold-reduced crystal bar was also determined at 200, 300, and 370 °C (390, 570 and 700 °F) and at liquid-nitrogen temperature (—195 °C). The data are listed in Table IV and plotted in Fig. 13. The cold-reduced and the annealed

Table IV
Rate Sensitivity

A. 97% Cold-reduced crystal bar
B. 97% Cold-reduced crystal bar, annealed at 600 °C
C. 97% Cold-reduced crystal bar, annealed at 700 °C
D. 97% Cold-reduced crystal bar, annealed at 800 °C
E. 50% Cold-reduced crystal bar (longitudinal specimen)
F. 50% Cold-reduced crystal bar (transverse specimen)
G. 50% Cold-reduced crystal bar, annealed at 600 °C (long. spec.)
H. 50% Cold-reduced crystal bar, annealed at 600 °C (trans. spec.)

Material	Test Temp (°C)	Rate Sensitivity, n * Range	Average	% Change in Stress Level
A	−195	0.004	0.004	0.8
	25	0.007 to 0.014	0.010	2.4
	200	0.048	0.048	12
	300	0.059 to 0.085	0.070	17
B	−195	0.008 to 0.009	0.0083	1.9
	25	0.011 to 0.021	0.016	2.9
	200	0.015 to 0.019	0.017	4.0
	300	0.013 to 0.014	0.014	3.3
	370	0.011 to 0.015	0.013	3.0
C	25	0.013 to 0.021	0.017	4.0
D	25	0.016 to 0.018	0.017	4.0
E	25	0.008	0.008	1.9
F	25	0.009 to 0.010	0.009	2.1
G	25	0.011 to 0.017	0.014	3.3
H	25	0.010 to 0.016	0.013	3.0

$$* n = \frac{\log (S_2/S_1)}{\log (\dot{\epsilon}_2/\dot{\epsilon}_1)}$$

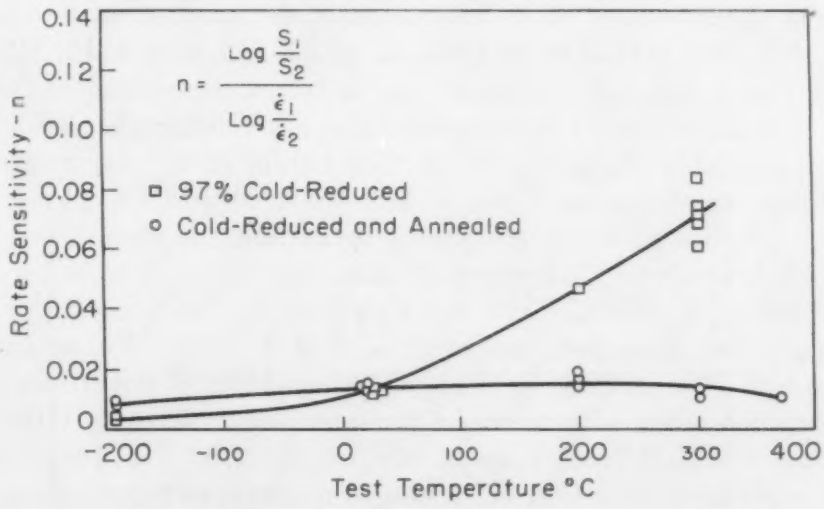


Fig. 13—Rate Sensitivity vs Temperature for Severely Cold-rolled and for Annealed Crystal-bar Zirconium.

crystal bar have nearly the same rate sensitivity values at room temperature. It can be seen that the annealed material showed little, if any, change in rate sensitivity with increased temperature, whereas the severely cold-reduced crystal bar showed considerable increase in rate sensitivity with increased temperature. The rate sensitivity at −195 °C (−351 °F) was about one-half to one-third that at 25 °C for both annealed and for cold-reduced crystal bar.

In another test of 97% cold-reduced crystal bar at 300 °C

Table V
Room-temperature Tensile Properties of 97% Cold-reduced Unrecrystallized Crystal Bar

Annealing Temp (°C)	Ultimate Strength (psi)	0.2% Offset Yield Strength (psi)	% Elongation	% Reduction in Area	Strain-hardening Exponent
—	83,600	70,800	4	60	0.08
300	79,200	60,800	4	53	0.09
400	69,700	56,500	5	55	0.045

* See section concerning influence of texture on tensile properties.

(570 °F), rate sensitivity increased with decreasing average strain rate. With changes in strain rate of 0.09 to 0.9 min^{-1}, 0.009 to 0.09 min^{-1}, and 0.0009 to 0.009 min^{-1}, the rate sensitivity values were 0.059, 0.085, and 0.127, respectively.

Differences in texture, differences in test direction (transverse vs longitudinal) for specimens having a weak texture, and small differences in grain size (0.005—.037-mm average diameter) resulting from annealing at 600, 700 and 800 °C (1110, 1290 and 1470 °F) did not produce a significant change in rate sensitivity, as shown in Table IV.

Annealing Temperature

Test specimens of 97% cold-reduced crystal bar were annealed at 300, 400, 500, 600, 700, and 800 °C (570, 750, 930, 1110, 1290 and 1470 °F) in evacuated Vycor or quartz tubes. Annealing at 300 and at 400 °C (570–750 °F) for one hour did not change the tensile properties appreciably from the properties exhibited by the unannealed crystal bar, as shown in Table V and Figs. 14 and 15. (Pole figure studies also showed these specimens to exhibit the same type of deformation texture (3).) Recrystallization had just begun in the specimens annealed at 400 °C (750 °F), as shown in Fig. 16a.

Specimens annealed one hour at 500 °C (930 °F) or one-half hour at 600, 700, or 800 °C (1110, 1290 or 1470 °F) were recrystallized to grain sizes with average diameters of 0.003 mm, 0.005 mm, 0.012 mm, and 0.037 mm, respectively, as shown in Fig. 16b, c, d, and e. The variations in strain-hardening exponent, per cent elongation, and per cent reduction in area, were not large for these materials. Specimens were also annealed for 48 hours at 500 or 600 °C (930 or 1110 °F). It was found that the grain size was larger (0.007 and 0.084mm. average diameter respectively, Fig. 17a and b) and the hardness and tensile strength were considerably lower than for crystal-bar zirconium annealed only ½ to 1 hour at the corresponding temperatures. See Table VI. The fine-grained recrystallized specimens were significantly stronger than the coarse-grained materials. The ultimate strength increased from 24,000 psi to 43,000 psi with decreasing grain size, and the 0.2% offset yield stress almost tripled in value, increasing from 9400 psi to 26,000 psi with decreasing grain size (see Table VI).

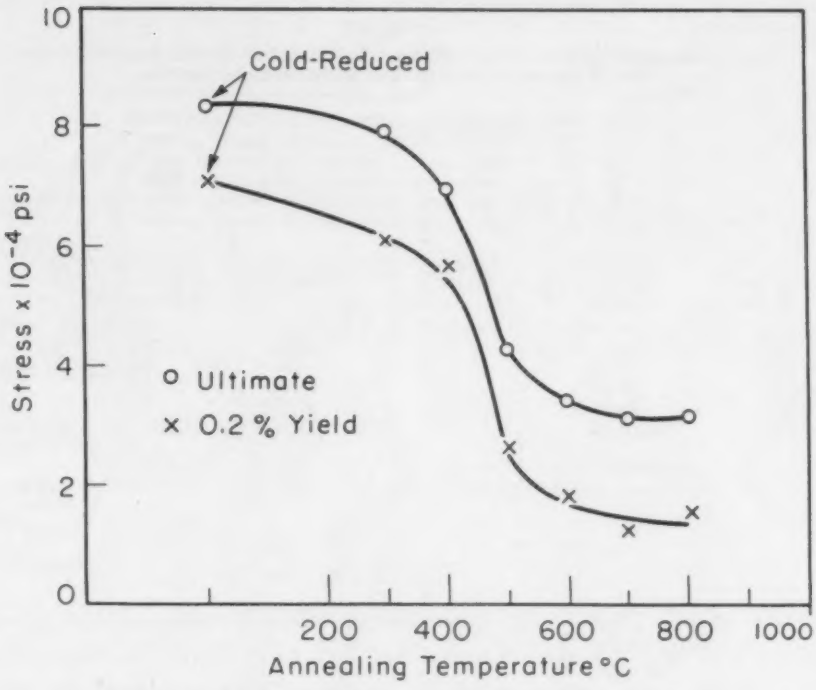


Fig. 14—Ultimate Tensile and 0.2% Offset Yield Stress vs Annealing Temperature for Cold-rolled and for Annealed Crystal Bar Tested at Room Temperature.

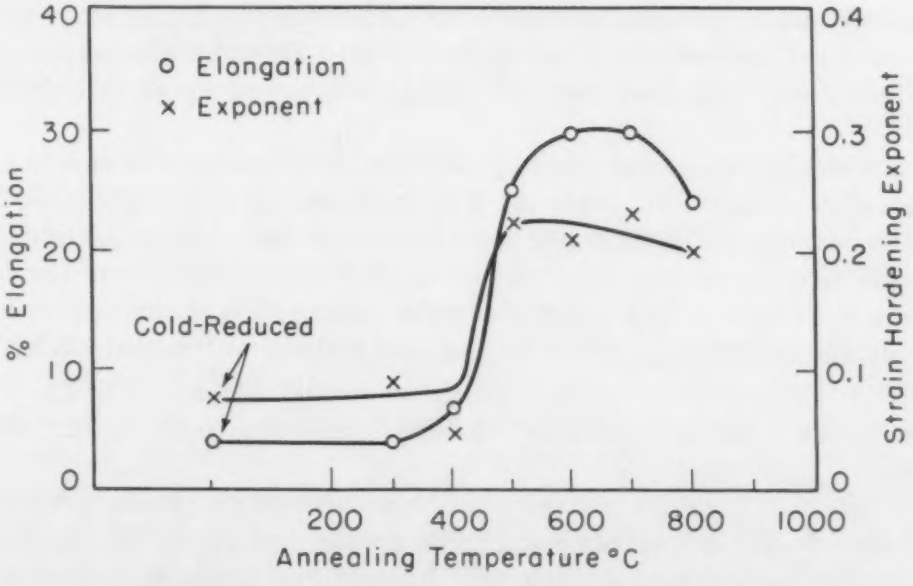


Fig. 15—Per cent Elongation and Strain-hardening Exponent vs Annealing Temperature for Cold-rolled and for Annealed Crystal Bar Tested at Room Temperature.

(It was of interest that the specimens having the finest grain size exhibited an unmistakable yield point, as discussed in another section of this report). Typical true stress vs true strain curves showing the variation of room-temperature properties with prior annealing temperatures are given in Fig. 18.

Table VI
Hardness and Tensile Properties of Crystal-bar Zirconium Annealed for Various Time-temperature Combinations

A 97% Cold-reduced and Annealed 1 hour at 500 °C
B 97% Cold-reduced and Annealed 48 hours at 500 °C
C 97% Cold-reduced and Annealed ½ hour at 600 °C
D 97% Cold-reduced and Annealed ½ hour at 800 °C
E 97% Cold-reduced and Annealed ½ hour at 700 °C
F 97% Cold-reduced and Annealed 48 hours at 600 °C

History	Grain Size (mm avg diam.)	Vickers Hardness Number *	Ultimate Tensile Stress (psi)	0.2% Offset Yield Stress (psi)	% Elongation	% Reduction in Area	Strain-hardening Exponent
A	0.003	121-145	42,900	26,000	25	60	0.22
B	0.007	92-110	35,900	16,900	30	64	0.26
C	0.005	96-109	34,100	18,800	30	55	0.21
D	0.012	92-99	31,200	13,200	30	51	0.23
E	0.037	96-104	31,600	15,100	24	48	0.20
F	0.084	78-80	24,000	9,400	21	45	0.21

* 10-Kg load; hardness impressions taken on plane of rolling.

Texture

Most of the early test specimens were produced by severe cold reduction (97%) of the ductile crystal bar, and any annealing was performed after completion of the rolling. This practice resulted in a strong texture, as was shown previously (3).

However, strong texture in a material is often undesirable, particularly when forming operations are planned. To obtain sheet with a weaker texture, crystal bar was rolled into sheet by alternately cold-reducing by 50% and then annealing *in vacuo* for one-half hour at 600 °C (1110 °F).

Pole figures of specimens cold-rolled and annealed in this manner (3) showed that this material was considerably more isotropic than material prepared by a single cold reduction and then annealing. The double texture produced by the 38- to 40-degree rotations of the basal plane out of the rolling plane about the rolling direction was also present in the material prepared by the cold-reduce and anneal cycle. The $<10\bar{1}0>$ direction of the cold-rolled material and the $<11\bar{2}0>$ direction of the annealed material were approximately in the rolling direction.

The influence of texture on tensile properties can be seen from the data in Table VII, obtained from crystal-bar zirconium specimens prepared by different rolling schedules. (The grain size finally obtained by the two methods was about the same, both being about 0.005 mm in diameter). The 97% cold-reduced zirconium was considerably stronger than the material cold-reduced 50%. The elongation and reduction in area were about the same for the cold-rolled materials. In the transverse specimens, the reduction in area of the 97% cold-reduced material was much lower. The 0.2% offset yield strength and the ultimate tensile strength of annealed material was considerably higher for

Table VII
Comparison of Properties in Cold-Rolled and in Annealed Crystal-bar Zirconium as a Function of Texture

	Cold-rolled		Recrystallized	
	Long.	Trans.	Long.	Trans.
97% Reduction (Strong Texture)				
Crystallographic direction of stress axis	$<10\bar{1}0>$	$<11\bar{2}0>$	$<11\bar{2}0>$	$<10\bar{1}0>$
Strain-hardening exponent	0.07 to 0.08	0.14 to 0.17	0.21 to 0.22	0.10 to 0.11
Tensile strength (psi)	84,500	83,800	35,300	29,600
0.2% offset yield strength (psi)	72,000	71,000	19,300	22,700
% elongation in 2 inches	4	1	30	16
% reduction in area	60	8	55	70
% reduction in width	15 to 20	2 to 3*	30 to 40	45 to 65
% reduction in thickness	45 to 65	5 to 7*	30 to 40	15 to 20
50% Reduction and Anneal Cycle (Weak Texture)				
Crystallographic direction of stress axis	$<10\bar{1}0>$	$<11\bar{2}0>$	$<11\bar{2}0>$	$<10\bar{1}0>$
Strain-hardening exponent	0.04 to 0.05	0.04 to 0.08	0.24 to 0.32	0.15 to 0.23
Tensile strength (psi)	59,400	58,000	28,500	24,300
0.2% offset yield strength (psi)	49,000	50,000	10,700	13,500
% elongation in 2 inches	4 to 6	4	36 to 54	18 to 37
% reduction in area	49 to 60	59 to 73	59 to 68	64 to 73
% reduction in width	33 to 42	50 to 64	44 to 50	55 to 68
% reduction in thickness	24 to 33	13 to 25	24 to 35	18 to 20

* These small changes can be considered approximately equal on the basis of the accuracy of the measurements.

specimens previously cold-reduced 97% than for specimens previously prepared by the 50% cold-reduce and anneal cycle. The reduction in area was about the same for the annealed specimens, and the material with a previous cold-reduction of 50% exhibited slightly greater elongation. Typical true stress vs true strain curves for annealed longitudinal and transverse specimens possessing these textures are shown in Fig. 19.

It was observed that the necking characteristics of the severely cold-reduced and of the recrystallized crystal-bar zirconium differ and that there is considerable evidence of anisotropy. Here correlations may be observed between the strain anisotropy and the previously determined textures. The initial cross section of the sheet tensile specimens was rectangular, being nominally 0.200 by 0.020 inch, a dimensional ratio of 10:1. The percentage reductions in width, thickness and area* were measured for cold-reduced or recrystallized conditions of the metal in the longitudinal and in the transverse orientations. These results are tabulated in Table VIII, which also illustrates the correlation with the texture. Specimens with the $[11\bar{2}0]$ direction parallel to the stress axis in both instances gave about equal percentage reductions in width and thickness, whereas pronounced differences in width and thickness changes were observed for those with $<10\bar{1}0>$ in the stress axis. For those specimens with the $[10\bar{1}0]$ direction parallel to the stress axis, the larger percentage reduction was in the thickness dimension for the cold-rolled longitudinal specimens, and in the width dimension for the annealed transverse specimens. For each crystallographic orientation of the stress axis, the greatest over-all reduction in area

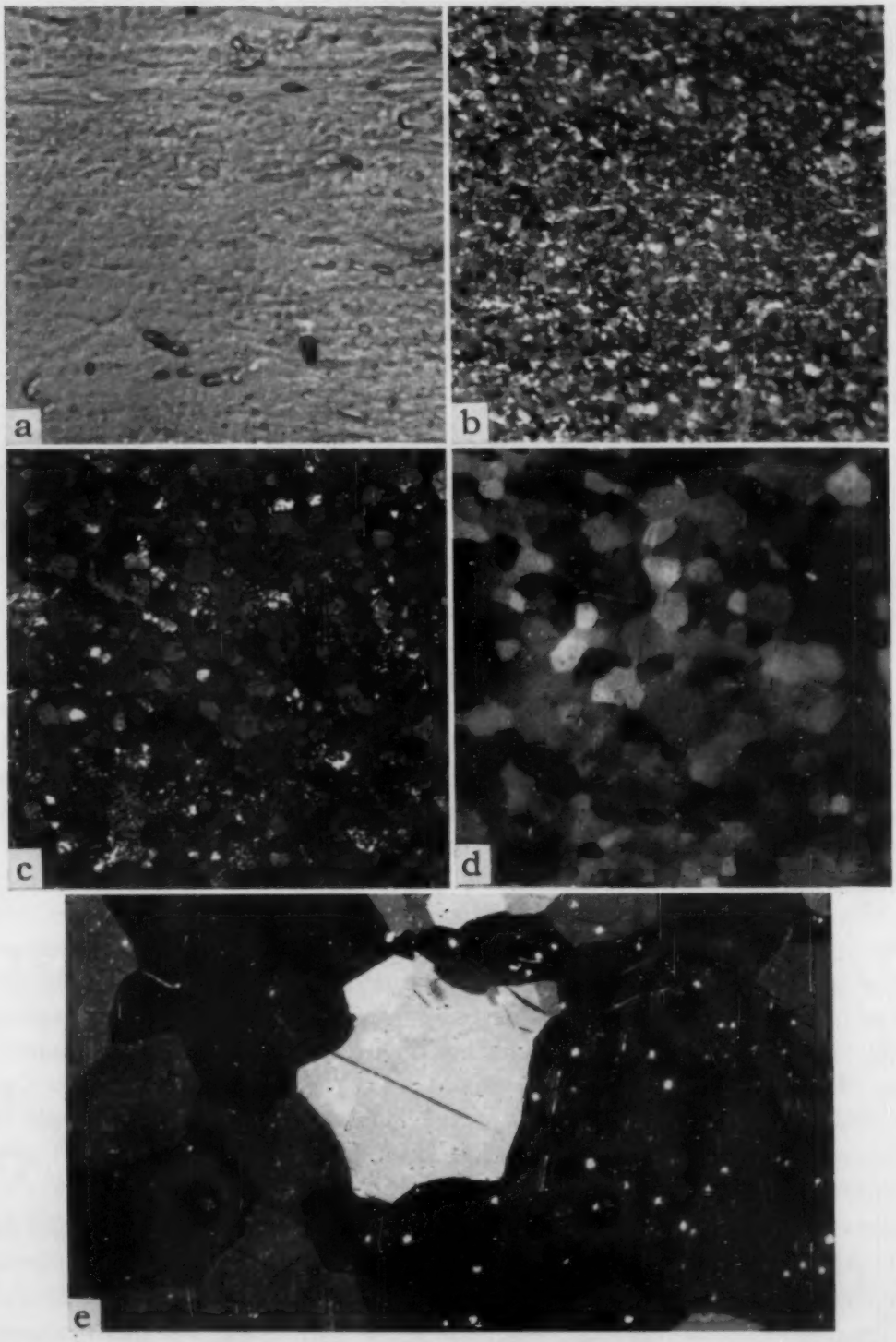


Fig. 16—Crystal-bar Zirconium, 97% Cold-reduced and Annealed as Indicated. Electropolished, longitudinal sections.

a. 1000x, bright field. Recrystallization just started. Annealed 1 hour at 400 °C
b. 250x, Polarized light, annealed 1 hour at 500 °C
c. 250x, Polarized light, annealed ½ hour at 600 °C
d. 250x, Polarized light, annealed ½ hour at 700 °C
e. 250x, Polarized light, annealed ½ hour at 800 °C

The average grain diameters are approximately: (b) 0.003 mm, (c) 0.005 mm, (d) 0.012 mm, and (e) 0.037 mm.

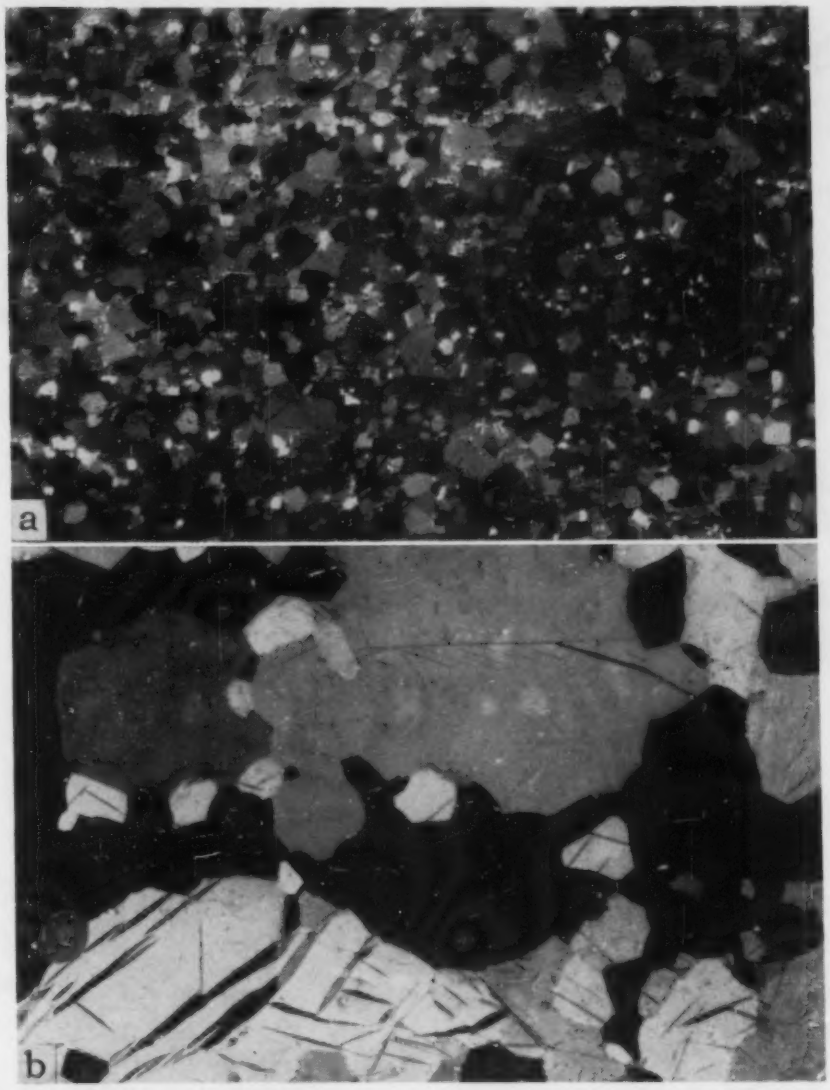


Fig. 17—Crystal-bar Zirconium, 97% Cold-reduced and Annealed 48 Hours at (a) 500 °C, and (b) 600 °C. X 250, Polarized light, electropolished, longitudinal section. The grain diameters are approximately (a) 0.007 mm, and (b) 0.084 mm.

was found for the annealed condition, although the differences are less marked with the $[10\bar{1}0]$ orientation than with the $[11\bar{2}0]$ orientation. Obviously, effects of the specimen geometry are also involved in these changes. These effects should be identified before analysis of the strain during necking is studied in detail.

The necking characteristics of the zirconium with the weaker texture was more readily related to the position (transverse or longitudinal) of the specimen in regard to the rolling direction than to the crystallographic orientation of the stress axis during testing (see Table VIII). The reduction in area for all specimens with the weaker texture was approximately the same. The per cent change in width was seen to be greater in all instances than the per cent change in thickness, and the

Table VIII
Relations between Plastic Strain and Crystallographic Orientation of Test Specimen

Condition	Specimen Direction in Sheet	Crystallographic Direction of Stress Axis	Per Cent Reduction in: Width	Thickness	Area	Elongation	Strain-hardening Coefficient
a. 97% Reduction (Strong Texture)							
Cold-rolled	Long.	$10\bar{1}0$	15 to 20	45 to 65	60	4	0.076 to 0.08
Cold-rolled	Trans.	$11\bar{2}0$	2 to 3*	5 to 7†	8	1	0.14 to 0.17
Annealed	Long.	$11\bar{2}0$	30 to 40	30 to 40	55	30	0.21 to 0.22
Annealed	Trans.	$10\bar{1}0$	45 to 65	15 to 20	70	16	0.10 to 0.11
b. 50% Reduction and Anneal Cycle (Weak Texture)							
Cold-rolled	Long.	$10\bar{1}0$	33 to 42	24 to 33	49 to 60	5	0.04 to 0.05
Cold-rolled	Trans.	$11\bar{2}0$	50 to 64	13 to 25	5? to 73	4	0.04 to 0.08
Annealed	Long.	$11\bar{2}0$	44 to 50	24 to 35	59 to 68	36 to 54	0.24 to 0.32
Annealed	Trans.	$10\bar{1}0$	55 to 68	18 to 20	64 to 73	18 to 37	0.15 to 0.23

* These small changes can be considered approximately equal on the basis of the accuracy of the measurements.
† In the cold-reduced longitudinal specimens, the measurement of the reduction in area at fracture could be handled in several ways, because the fracture surface was not perpendicular to the stress axis. However, it was thought best to measure the area of the fracture surface and then compare it with the original area of the same cross section.

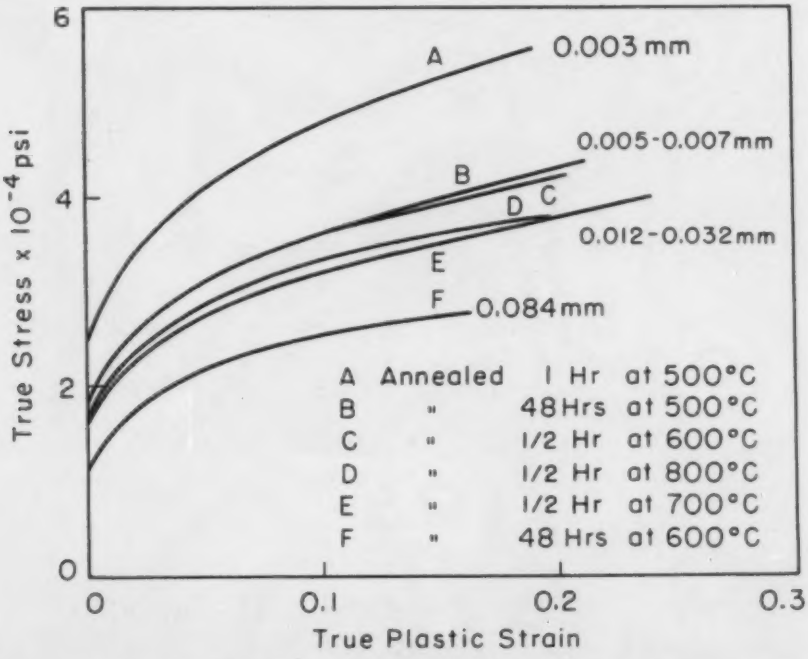


Fig. 18—True Stress vs True Strain Curves Up to Necking Strain for Crystal-bar Zirconium Annealed at Various Temperatures, Showing the Influence of Grain Size.

difference in per cent change was much greater for transverse specimens than for longitudinal specimens.

Other observations that may be made of these same specimens pertain to the elongation behavior, also summarized in Table VIII. Regardless of orientation, the specimens in the annealed condition gave greater elongation than those cold-rolled, as might be expected. However, the cold-rolled longitudinal specimens show a combination of a

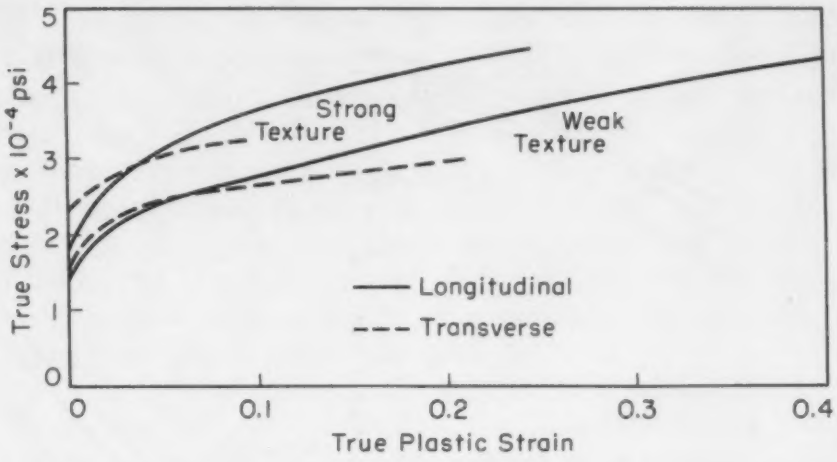


Fig. 19—True Stress vs True Strain Curves for Transverse and Longitudinal Specimens of Recrystallized Zirconium Possessing a Strong Texture (97% reduced material) and Specimens Possessing a Weak Texture (50% Cold Reduction and Anneal Cycle).

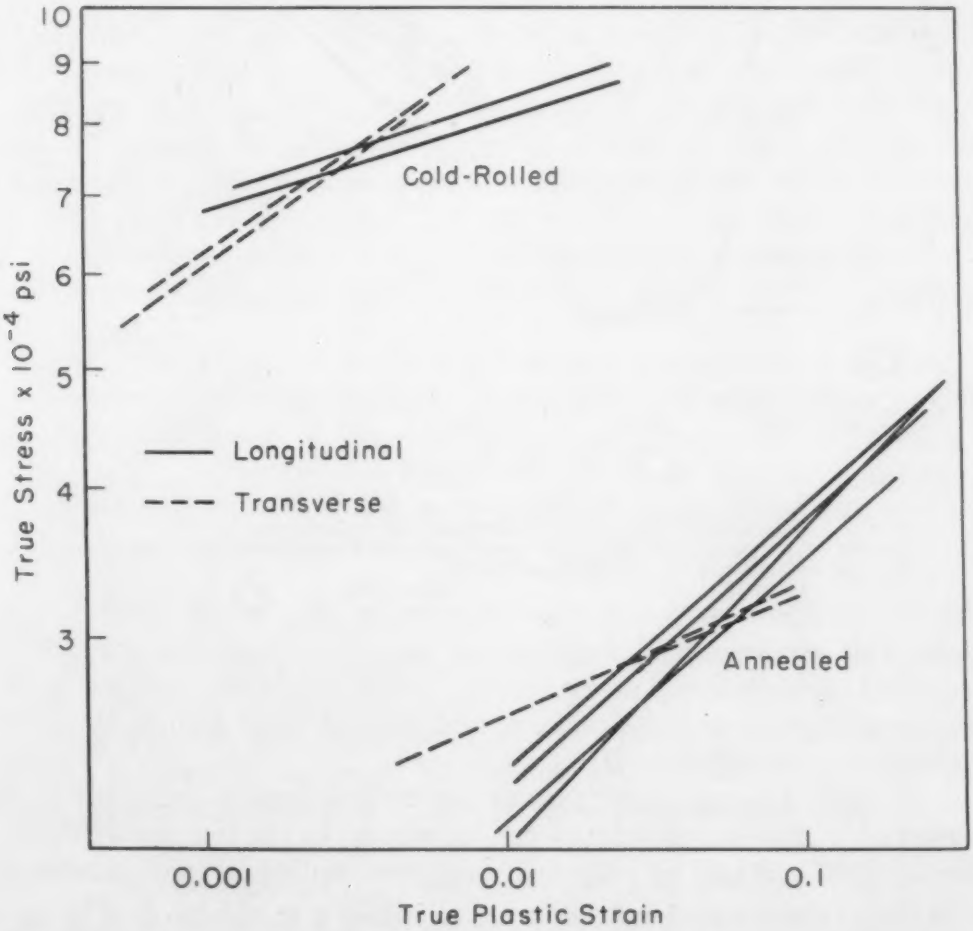


Fig. 20—True Stress-true Plastic Strain Up to Necking Strain Plotted Logarithmically for Cold-reduced and for Annealed Crystal-bar Zirconium. Curves for transverse specimens (broken lines) and for longitudinal specimens (solid lines) are shown.

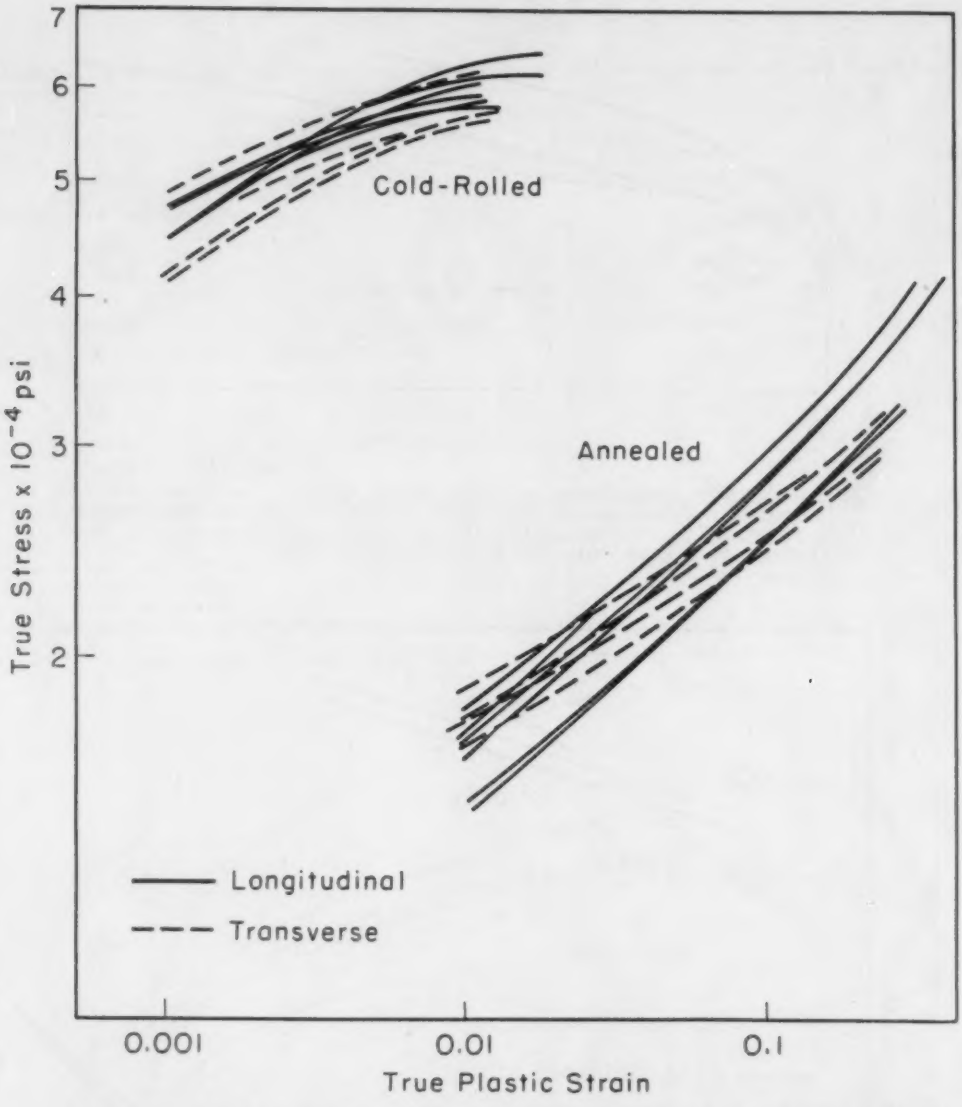


Fig. 21—Logarithmic Plot of True Stress vs True Plastic Strain Up to Necking Strain for Crystal-bar Zirconium Reduced by the 50% Reduction Plus Anneal Cycle. Curves for transverse (broken lines) and longitudinal specimens (solid lines) are shown for cold reduced and for annealed specimens.

high reduction in area with a low elongation, i.e., limited strain hardening. The recrystallized longitudinal specimens, on the other hand, strained considerably during testing, often exhibiting necking in two or three regions before fracture, and thus showed a high elongation and a high reduction in area.

It was also observed that the strain-hardening exponent of the material with a strong texture can be related to the texture of the material. Cold-reduced or annealed specimens pulled in tension with the $<11\bar{2}0>$ direction along the stress axis had a strain-hardening exponent about twice the value of the equivalent material pulled with the $<10\bar{1}0>$ direction along the stress axis. A comparison of these observations is found in Table VIII; see also Fig. 20.

It is apparent that for the zirconium with a weak texture, the strain-hardening exponent was only slightly greater for specimens tested with the $<11\bar{2}0>$ direction in the stress axis, and was increased by strain (see Fig. 21). For this material, the plot of log true stress vs log true strain was not a straight line as shown in Fig. 21. This deviation from the conventional straight-line relation was not due to the presence of a yield point, and the cause of this lack of linearity is not established. The strain-hardening exponent for these instances was obtained from the slope of the log true stress vs log true strain curve at the strain where maximum load occurred.

From the previous observations, it can be seen that the texture of zirconium sheet governs its deformation characteristics to a considerable extent. Control of the drawing properties of zirconium sheet may thus be possible if careful control of the texture of the sheet is maintained.

Arc-Melting

If high purity zirconium could be melted without the introduction of any impurities, there would be no need to study the product of the melting operation, provided the effects of grain orientation during solidification could be removed by subsequent working operations. Zirconium, because of its great affinity for oxygen, nitrogen, carbon, and other elements, picks up impurities readily, and so the melting process must be carefully controlled. For arc-melting in an inert atmosphere in a water-cooled copper crucible, as described in the section on experimental procedure, contamination by oxygen and/or nitrogen must be considered.

In spite of the fact that the multihearth furnace was evacuated to a pressure of less than a micron and then flushed with purified argon, there was significant oxygen and nitrogen remaining in the furnace to be taken up by the first getter melt. Material from "getter" melts had a hardness of about VHN 160 [2], whereas that from subsequent melts in the same series exhibited hardness in the range VHN 120 to 135, as compared with the hardness of unmelted crystal bar of VHN 90 to 105.[3]

In studying the influence of arc-melting (the effect of oxygen and/or nitrogen pickup during arc-melting) on tensile properties, it was not possible to hold constant all the variables maintained in preparing samples of unmelted crystal bar. For instance, the unalloyed melts having a hardness of VHN 160 could not be cold-rolled 97% to the final specimen thickness. Instead, these melts were cold-rolled as far as feasible (about 70%) and then annealed and rolled again. The reduction after annealing amounted to approximately 65%. In these

[2] These hardness values were obtained on specimens arc-melted, severely cold-reduced, and then recrystallized.

[3] The crystal-bar material had been severely cold-rolled and then recrystallized. All hardness indentions were taken in the plane of rolling, and thus to a first approximation in a direction perpendicular to the basal planes.

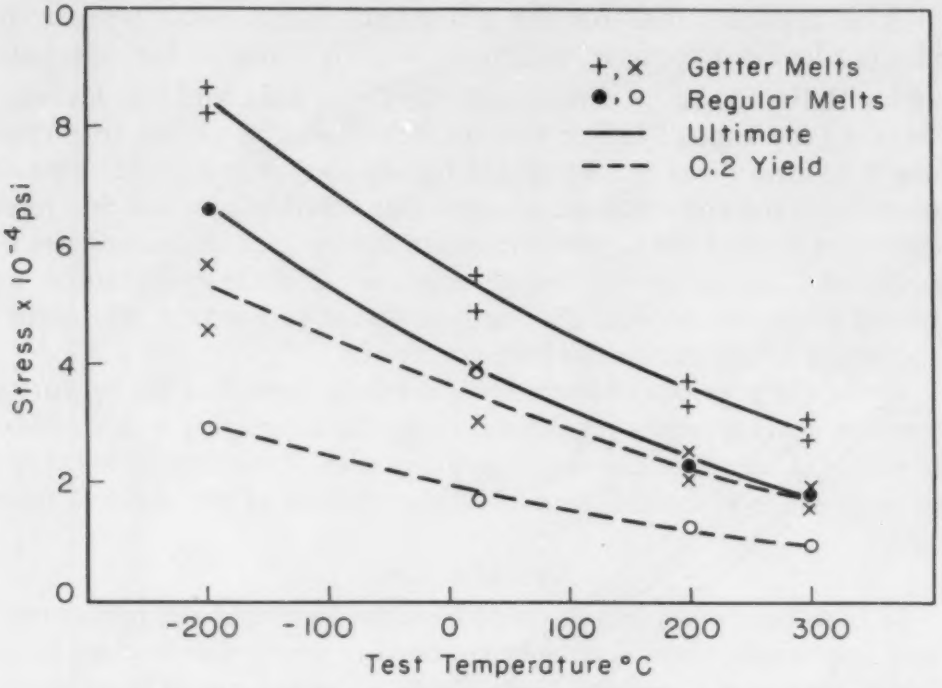


Fig. 22—Ultimate Tensile and 0.2% Offset Yield Stress vs Test Temperature for Arc-melted Zirconium.

cases, the annealing textures may not be exactly like that in the rolled and annealed crystal-bar material; and thus far texture studies of the arc-melted material have not been carried out. However, the grain size, strain rate, and test temperature were made comparable to the conditions maintained in tests on unmelted zirconium.

Tensile tests were conducted in the range from —195 to 300 °C (—351 to 570 °F) on arc-melted zirconium, cold-rolled and then annealed *in vacuo* to a grain size of approximately 0.005-mm average diameter. The melts with a hardness about VHN 150 to 160 had a considerably higher tensile strength and yield stress than the melts with a hardness in the range VHN 120 to 135, as shown in Fig. 22. The differences between the yield strengths of the two materials decreased markedly with increasing test temperature. It would appear that strengthening by the oxygen and nitrogen impurities may be insignificant at temperatures as high as 450 or 500 °C (840 or 930 °F). The per cent elongation and the strain-hardening exponent of the two materials did not differ a great deal, as shown in Fig. 23. The peak in elongation at 200 °C (390 °F) may be due to some strain-aging phenomena. Fig. 24 shows typical true stress vs true strain curves for arc-melted zirconium having these two hardness levels. Average tensile properties for these materials are presented in Table IXa. It was observed that the melts having a hardness in the range VHN 120 to 130 exhibited engineering strengths slightly below that of crystal-bar material in the temperature range 25 to 300 °C (77 to 570 °F) (compare

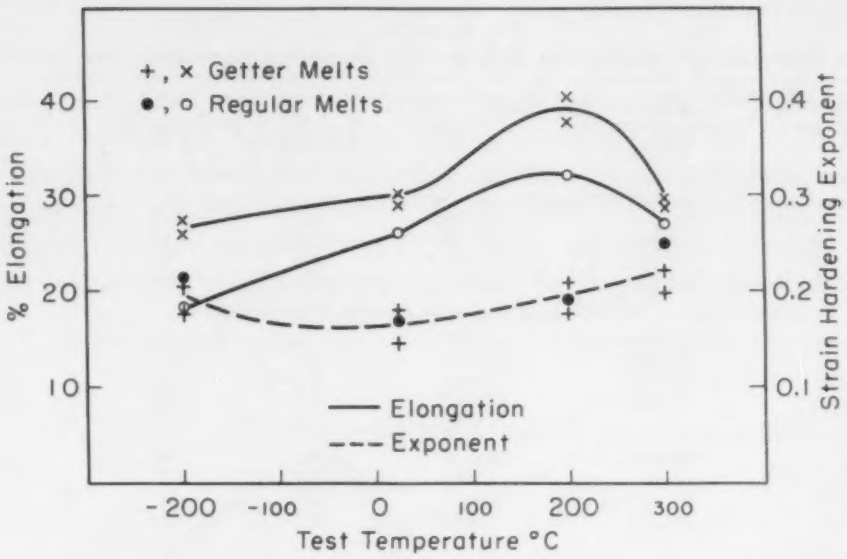


Fig. 23—Per cent Elongation and Strain-hardening Exponent vs Test Temperature for Arc-melted Zirconium.

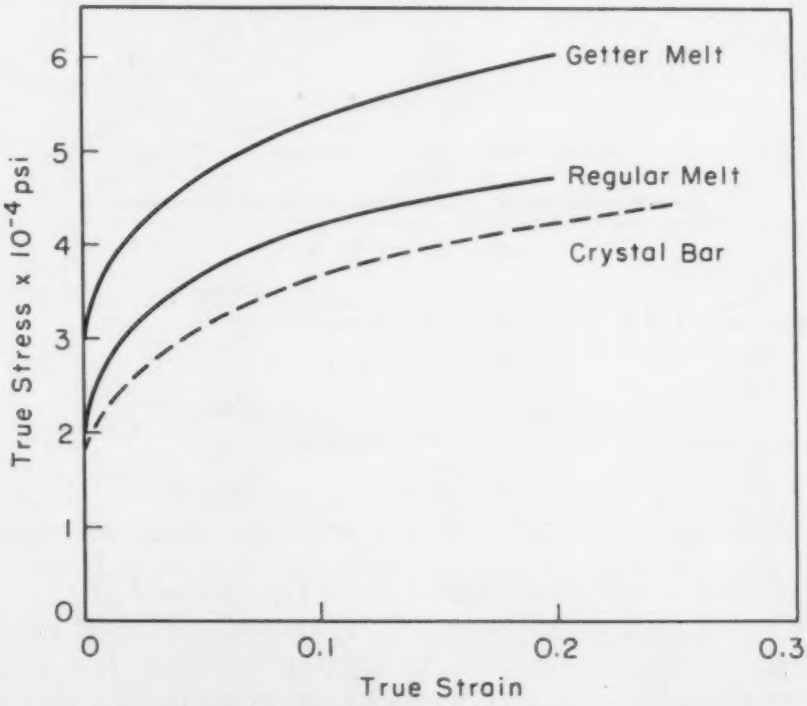


Fig. 24—True Stress vs True Strain Curves for Arc-melted Crystal-bar Zirconium Cold-rolled and Annealed to Obtain an Average Grain Diameter of 0.005 mm. A curve for cold-rolled and annealed crystal-bar is added for comparison.

Tables II and IXa). A difference in texture may account for this observation.

Cold-reduced samples of arc-melted zirconium were also tested at −195 °C, room temperature, and at 300 °C (570 °F). No significant difference in properties was observed between cold-reduced specimens

Table IX
Tensile Properties of Arc-Melted, Crystal-Bar Zirconium, Annealed, and Cold-Rolled

Test Temp (°C)	Ultimate Tensile Strength (psi)	0.2% Offset Yield Strength (psi)	% Elongation	% Reduction in Area	Strain-hardening Exponent
a. Cold-rolled and Annealed					
Arc-melted in Single-hearth Furnace (VHN 150 to 160)					
−195	95,000	56,000	27	43	0.178
25	54,000	40,000	29	61	0.143
200	36,000	25,000	38	73	0.18
300	29,000	18,000	29	81	0.20
First or Getter Melt in Multihearth Furnace (VHN 150 to 160)					
−195	84,000	46,000	26	35	0.21
25	50,000	30,000	30	65	0.175
200	33,000	21,000	40	75	0.21
300	29,000	17,000	29	78	0.23
Regular Melt in Multihearth Furnace (VHN 120 to 130)					
−195	67,000	29,000	18	39	0.21
25	39,000	17,000	26	51	0.17
200	23,000	13,000	32	56	0.19
300	18,000	10,000	27	70	0.25
b. Cold-rolled					
Getter Melts					
−195	125,000	113,000	7	32	0.04
25	99,000	83,000	5	57	0.04
300	71,000	60,000	8	74	0.03
Regular Melts					
−195	130,000	111,000	6	35	0.07
25	97,000	80,000	5	67	0.04

Table X
Rate Sensitivity of Arc-Melted Unalloyed Zirconium

Test Temp (°C)	Rate Sensitivity, n		% Change in Stress Level
	Range	Average	
High Oxygen-nitrogen Melt, 70% Cold-reduced, Annealed at 800 °C			
−195	0.006 to 0.008	0.007	1.6
25	0.019 to 0.024	0.021	5.0
200	0.019 to 0.024	0.022	5.2
300	0.009 to 0.014	0.011	2.5
Low Oxygen-nitrogen Melt, 90% Cold-reduced, Annealed at 760 °C			
25	0.017 to 0.022	0.019	4.6
200	0.029 to 0.034	0.031	7.4
300	0.013 to 0.017	0.014	3.3

from getter melts and from regular melts (see Table IXb).

The rate sensitivity of annealed, arc-melted unalloyed zirconium, either high in oxygen and nitrogen (getter melts) or low in oxygen and nitrogen (melted after a getter melt), generally did not vary a great deal from that of rolled and annealed crystal bar zirconium in the temperature range from −195 to 300 °C (−351 to 570 °F). Comparison of the values obtained for arc-melted zirconium in Table X with those for annealed crystal bar in Table IV shows that only the "low" nitrogen and oxygen arc-melted material at 200 °C (390 °F) varied significantly from the values for the rolled and annealed crystal bar. It is not known why this result averaged from four separate tests should be about twice that of crystal-bar material.

Summary

True stress vs true strain curves and engineering data have been presented, showing the influence, within prescribed limits, of some test variables and metallurgical variables on the tensile properties of unalloyed zirconium. The influence of the test variables, test temperature, and strain rate are summarized in Fig. 25, showing the range of the true stress vs true strain curves obtained by changing these variables

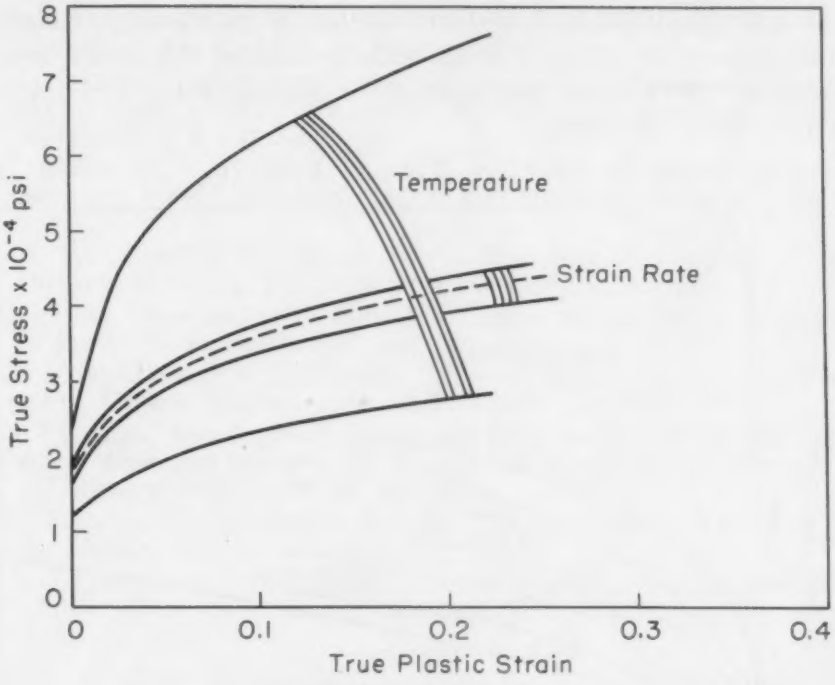


Fig. 25—Summary True Stress vs True Strain Curves Showing Range of Values Resulting from Changes in Test Variables.

within the limits described in this report. The influence of metallurgical variables, texture, oxygen and nitrogen impurity (arc-melting), and recrystallized grain size (as altered by prior annealing) are similarly summarized in Fig. 26.

In addition, the following summarizing statements can be made concerning the properties of unalloyed zirconium, keeping in mind the limits of the variables employed.

The tensile behavior of severely cold-reduced zirconium tested at and above 200 °C (390 °F) shows a maximum load at early strains which is not associated with measurable necking and seems to be related in some manner to recovery, stress-recovery, and strain-aging.

The yield point effect was emphasized by decreasing grain size and was diminished at lower temperatures. Calculations indicate a Cottrell-type mechanism.

The rate sensitivity of recrystallized material was only slightly

affected by changes in temperature, texture, grain size, and relatively small amounts of oxygen and nitrogen impurity. The rate sensitivity of cold-reduced crystal bar increased rapidly at 200 °C (390 °F) and above.

Recrystallization occurred between 450 and 500 °C (840 and 930 °F) in annealing treatments of one hour's duration. Increasing the size of the recrystallized grains appreciably decreased the strength properties, but did not greatly affect ductility and the strain hardening.

The presence of a strong texture was found to increase the stress level at a given strain and also to increase directionality. Relations of the inhomogeneous strain during necking and of the strain-hardening exponent to the relative locations of crystallographic orientation and stress axis were observed.

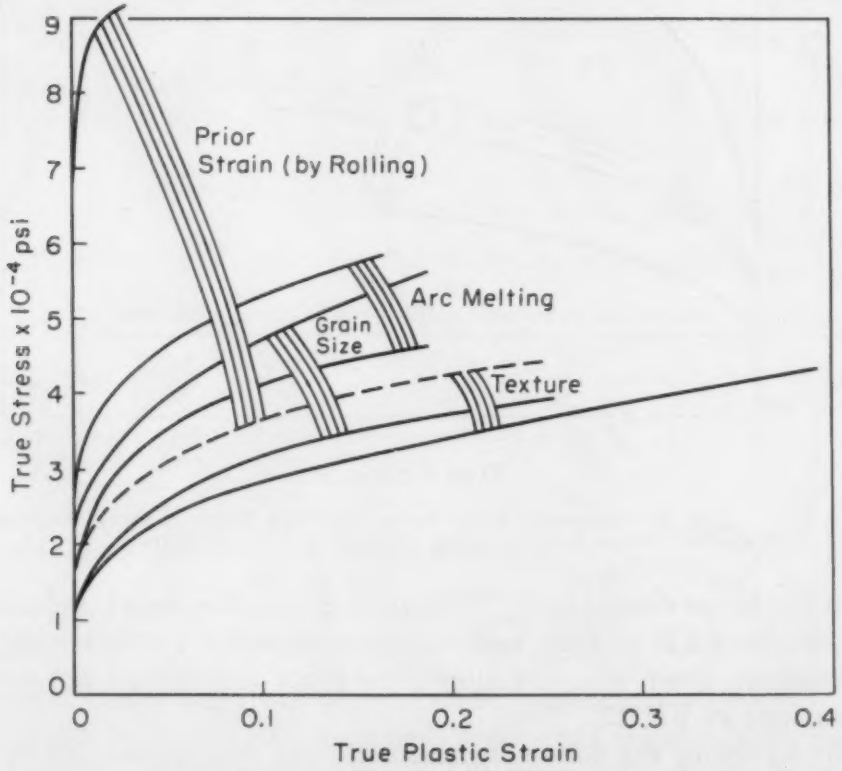


Fig. 26—Summary True Stress vs True Strain Curves Showing Range of Values Resulting from Changes in Metallurgical Variables.

Arc-melting and the accompanying pickup of small amounts of oxygen and nitrogen were found to raise the hardness and strength level without greatly diminishing the values of elongation and reduction in area. The significant strengthening of zirconium by oxygen and nitrogen impurities decreases with increasing temperature, indicating that at elevated temperatures small amounts of oxygen and nitrogen are not effective strengthening elements.

ACKNOWLEDGMENT

The author wishes to acknowledge the many helpful suggestions of W. R. Hibbard, Jr. and J. D. Nisbet; the assistance of L. J. Hartford and other members of the Metallurgy Research Department who aided in the experimental portions of this study. This work was supported by the U. S. Atomic Energy Commission under Contract No. W-31-109-Eng 52.

References

1. B. F. Decker, E. T. Asp and D. Harker, "Preferred Orientation Determinations Using a Geiger Counter X-ray Diffraction Goniometer," *Journal of Applied Physics,* Vol. 19, 1948, p. 388.
2. A. H. Geisler, "Crystal Orientation and Pole Figure Determination," MODERN TECHNIQUES OF PHYSICAL METALLURGY, American Society for Metals, 1953, 1. 131.
3. J. H. Keeler, W. R. Hibbard, Jr. and B. F. Decker, "Textures of Rolled and Annealed Iodide Zirconium," *Journal of Metals,* Vol. 5, No. 7, July 1953, p. 932.
4. W. A. Wood and J. W. Suiter, "Stress-Recovery in Aluminum," *Journal,* Institute of Metals, Vol. 80, Part 9, May 1952, p. 501.
5. J. C. Fisher, "Application of Cottrell's Theory of Yielding to Delayed Yield in Steel," G. E. Research Laboratory Report, to be published.
6. J. H. Hollomon and J. D. Lubahn, "Flow of Metals at Elevated Temperature," *General Electric Review,* February and April 1947.
7. J. D. Lubahn, "Simultaneous Aging and Deformation in Metals," *Transactions,* American Institute of Mining and Metallurgical Engineers, Vol. 105, 1949, p. 702.
8. J. D. Lubahn, "Strain Aging Effects," TRANSACTIONS, American Society for Metals, Vol. 44, 1952, p. 643.
9. H. A. Lequear and J. D. Lubahn, "Some Creep-Tensile Relations in Copper at 350 °C," G. E. Research Laboratory Memo Report M-28, August 15, 1951.

DISCUSSION

Written Discussion: By F. Forscher, senior engineer, Atomic Power Division, Westinghouse Electric Corp., Pittsburgh.

The author has shown that annealing treatment and impurities ("getter" melts) have a pronounced effect on the mechanical properties. He has selected a "standard" set of conditions and set out to investigate a number of variables ("recrystallized" grain size, strong preferred orientation, strain rate, etc.) independently from each other. However from the data available in the literature and at our laboratory the writer believes that the "standard properties" are not at all typical of "unalloyed" zirconium, and therefore are of questionable value as a basis for quantitative evaluation of the influence of alloying elements. A yield point was never observed in our laboratory on unalloyed zirconium and the tensile behavior (as shown by the author's Fig. 6) showed no anomalies although the author's conditions were intentionally duplicated on our material to reproduce the reported effect.

All data reported in this discussion are based on results from arc-melted crystal bar zirconium tensile specimens with an original cross sectional area of 0.05 in^2. Most of the author's material is crystal bar which is formed by vapor deposition; it is not typical of commercial metals and contains a fair amount of

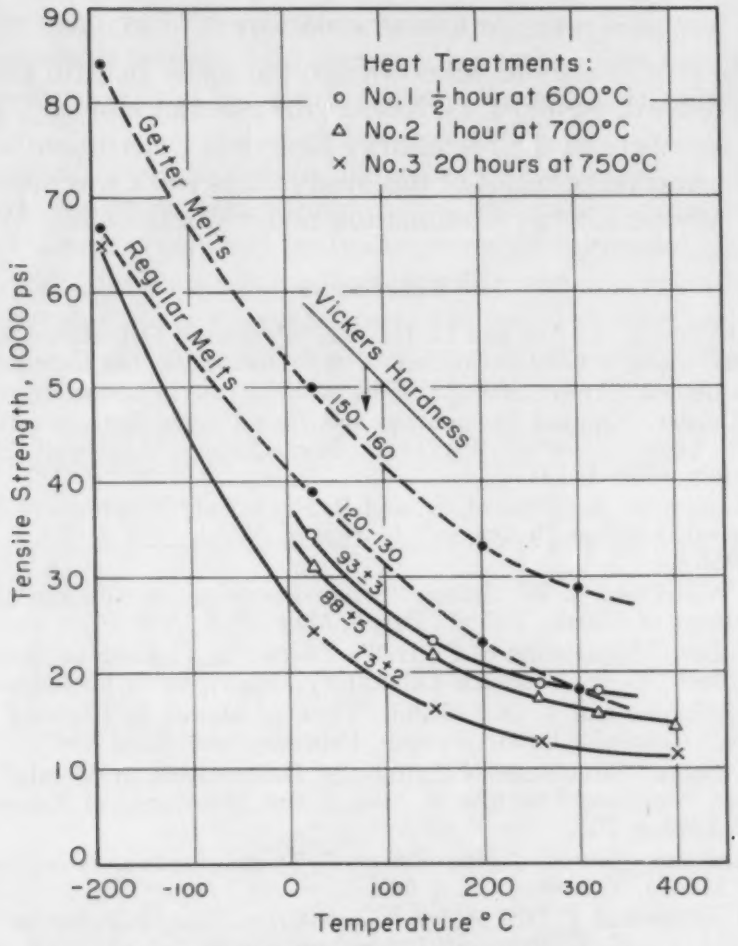


Fig. 27—Arc Melted Crystal Bar Zirconium.

hydrogen impurity. It is believed that the crystal bar material which has been subsequently arc-melted is more representative as an "alloy base" and also more homogeneous than crystal bar zirconium. In spite of possible oxygen and nitrogen pick up it compares favorably in mechanical properties to crystal bar zirconium reported by the author (Fig. 27).

In Fig. 27 is shown the effect of annealing treatments on the tensile strength. Results from Dr. Keeler's equivalent series (of arc-melted crystal-bar zirconium, cold-rolled and annealed, Table IX) are shown by the dashed curves. From the solid curves it is apparent that an annealing treatment of ½ hour at 600 °C (in vacuum) is not sufficient to bring the material into its "base annealed" state. The annealing of crystal bar zirconium has been shown to occur in four successive experimentally distinguishable stages[4] in which the second stage is characterized by a considerable softening and the appearance of a completely equiaxed grain structure. Additional heat treatment however will further anneal the metal until the "base annealed" condition is reached and grain growth is about to occur. The importance of the state of anneal on the mechanical properties has been reported and its effect on creep and hardness was pointed out.[5]

[4] R. K. McGeary and B. Lustman, "Kinetics of Thermal Reorientations in Cold-Rolled Zirconium," *Journal of Metals*, February 1953, p. 284.

[5] M. J. Manjoine and W. L. Mudge, Jr., "Creep Properties of Annealed Unalloyed Zirconium," Presented at the 1954 Annual Meeting of American Society for Testing Materials; to appear in *Transactions*, American Society for Testing Materials, Vol. 54, 1954.

But even when comparing equivalent heat treatments in Fig. 27 it is seen that the dashed curve is above the solid line, which increase is probably due to a higher impurity level. This is also indicated by the author's higher hardness values (VHN 120 to 130 vs. VHN 93 ± 3). For base annealed zirconium a Vickers Hardness Number of 70 to 80 is reasonable, considering an oxygen

Table XI
Comparison of Composition and Room Temperature Properties
(Arc melted crystal bar zirconium)

	Author	WAPD (F544)
weight % Hf	0.3 max	0.04
Fe	0.02 — 0.1	0.05
Al	0.005 — 0.02	0.004
Cr	0.02 — 0.1	0.005
Cu	0.001 — 0.005	0.0005
Ni	0.005 — 0.02	0.005
Mg	0.001 — 0.005	not reported
Mo	0.01	0.001
Si	not reported	0.003
Sn	not reported	0.001
Ti	not reported	0.001
C	estimated 0.02	0.01
N_2	0.007	0.001
O_2	estimated 0.02	0.023
N_2	—	0.0034
0.2% Yield Strength (1000 psi)	17.0	7.7
Tensile Strength (100 psi)	39.0	24.8
Elongation (%)	26	40
Reduction in Area (%)	51	37
Strain hardening exponent	0.17	0.22
VHN	120–130	73 ± 2
Average grain diameter (mm)	0.005	0.05
Annealing treatment (in vacuum)	½ hr–600 °C	20 hr–750 °C

content of 0.02 w/o,[6] although the writer also has found values as low as VHN 55 on some arc-melted crystal bar stock.

A numerical comparison of room temperature properties of arc-melted crystal bar zirconium is tabulated in Table XI. Such differences as are shown cannot solely be due to grain size effects in view of the differences in chemical composition and the state of anneal. It is also interesting to note that heat treatment No. 2 and 3 (Fig. 27) resulted in the same average grain size.

In spite of the pronounced texture of cold-rolled zirconium[7] we have found only minor variation in strength properties between the longitudinal and transverse direction, which is in agreement with the reported values in Table VII. Similarly, we have found only slight differences in ductility properties, e.g. elongation and reduction in area, which is not borne out by Table VII. Our tests were performed on duplicate specimens taken in increments of 10 degrees to the rolling direction. The difference between longitudinal and transverse properties of cold-rolled specimens are within the statistically expected band of values. Similar observations are reported by the Bureau of Mines.[8] Under such condition it seems unreasonable to correlate strong texture with mechanical anisotropy.

The interesting observation on the yield point phenomenon and anomalous necking behavior, although we feel they are not typical of unalloyed zirconium,

[6] R. M. Treco, "Some Properties of High-Purity Zirconium and Dilute Alloys with Oxygen," TRANSACTIONS, American Society for Metals, Vol. 45, 1953, p. 872.
[7] R. K. McGeary and B. Lustman, "Preferred Orientation in Zirconium," *Transactions*, American Institute of Mining and Metallurgical Engineers, Vol. 191, 1951.
[8] R. G. Nelson, H. Kate and R. I. Carpenter, "The Mechanical Properties of Consumable-Arc-Melted Kroll-Process Zirconium," Bureau of Mines, Report No. 5063, June 1954.

warrant further investigation. It is hoped that the author will continue his investigations on arc-melted crystal bar zirconium with low impurity content.

Written Discussion: By R. M. Treco, research section head, Bridgeport Brass Co., Bridgeport, Conn.

Dr. Keeler is to be complimented on this exhaustive study relating to the mechanical and metallurgical properties of pure zirconium. Tables VII and VIII are of particular interest since they show clearly the interdependence of these properties with crystallographic orientation of the lattice structure and the effects of annealing.

In comparing the effects of melting technique on mechanical properties, the author has rightly attributed the increased strength properties of the single-hearth and getter melts to gas absorption. However, in comparing the properties of the so-called regular melt with the original crystal bar it is shown that the strength properties of the melts are somewhat below those of the crystal bar when tested in the range of 25 to 300 °C. A comparison of these room temperature tests with previous work [9] indicates that the original crystal bar of the present investigation had slightly higher strength properties than would be anticipated for the nominal 0.02% oxygen suggested in Table I. The lower strength values of the earlier work are probably due to a high temperature degassing operation, which removes hydrogen. Comparison data are grouped below in Table XII.

Remelting with a good clean vacuum system has an effect similar to degassing so that, if hydrogen were present initially, a general softening could

Table XII
Room Temperature Tensile Properties

Material	Oxygen, wt. %	0.2 Y.S.	U.T.S.	% El.
Regular Melt	0.02 *	17,000	39,000	26
Original Crystal Bar	0.02 *	17,900	34,700	30
Degassed Crystal Bar [4]	0.021–0.026	11,180–14,850	21,750–32,400	16–43

* Estimated

occur, although the data shown in Table IX suggest that there was some oxygen pickup even in the regular melt material.

In respect to the effects of oxygen at elevated temperatures, the tests here confirm previous work [9] showing a strengthening effect with little decrease in ductility. In the earlier work, it was shown that oxygen does enhance the strength of zirconium up to 300 °C, but has little effect at 400 °C. Thus the statement that "small amounts of oxygen and nitrogen are not effective strengthening elements at elevated temperatures" must be considered questionable in the present work in view of the absence of any actual gas analyses and the rather limited range of gas content.

Finally, it would be highly desirable to include typical values of Young's modulus of elasticity, both for the record and to show the agreement of the

[9] R. M. Treco, "Some Properties of High Purity Zirconium and Dilute Alloys with Oxygen," TRANSACTIONS, American Society for Metals, Vol. 45, 1953, p. 872.

author's method of strain measurement with conventional extensometer techniques.

Written Discussion: By Arthur J. Opinsky, Sylvania Electric Products, Inc., Bayside, N. Y.

The author has given evidence that necking need not begin at maximum load; this is contrary to the general presumptions concerning necking and hence requires a different outlook on the problem of the beginning of necking. The tensile autographic curve is the complete record of the strain of the specimen, including the necking deformation, and thus should permit an analysis which would determine the point of the beginning of necking. If L is the load, a the instantaneous area, and σ the true stress,

$$L = a\sigma. \qquad \text{Equation 1}$$

Taking logarithms and differentiating with respect to $d\ln\delta$ (δ is the true or logarithmic strain)

$$\frac{d\ln L}{d\ln\delta} = \frac{d\ln\sigma}{d\ln\delta} + \frac{d\ln a}{d\ln\delta}. \qquad \text{Equation 2}$$

But $\delta = \int_{eo}^{e} \frac{dl}{e}$ and $v = al$ (where l is the length).

$$\text{Thus } \delta = \int_{v_o}^{v} \frac{dv}{v} - \int_{a_o}^{a} \frac{da}{a},$$

$$\text{or } \delta = \ln\frac{v}{v_o} + \ln\frac{a_o}{a}; \qquad \text{Equation 3}$$

$$\text{therefore } d\delta = d\ln V - d\ln a,$$

$$\text{or } \frac{d\ln a}{d\delta} = \frac{d\ln V}{d\delta} - 1.$$

$$\text{Therefore } \frac{d\ln a}{d\ln\delta} = \frac{d\delta}{d\ln\delta}\cdot\delta = \frac{d\ln V}{d\ln\delta} - \delta. \qquad \text{Equation 4}$$

Substituting Equation 4 into Equation 2,

$$\frac{d\ln L}{d\ln\delta} = \frac{d\ln\sigma}{d\ln\delta} - \delta + \frac{d\ln V}{d\ln\delta}. \qquad \text{Equation 5}$$

If constancy of volume be assumed,

$$\frac{d\ln L}{d\ln\delta} = \frac{d\ln\sigma}{d\ln\delta} - \delta. \qquad \text{Equation 6}$$

At maximum load, $\frac{d\ln L}{d\ln\sigma} = 0$; $\frac{d\ln\sigma}{d\ln\delta} = \delta$: the slope of the log true stress-log true strain curve at maximum load is equal to the true strain at maximum load regardless of the functional relation between σ and δ.

If $\frac{d\ln\sigma}{d\ln\delta}$ is a constant ($\sigma = K\delta^n$) or if $\frac{d\ln\sigma}{d\ln\delta}$ is a linear function of δ Equation 6 predicts that $\frac{d\ln L}{d\ln\delta}$ will be a linear function of δ. If, however, $\frac{d\ln L}{d\ln\delta}$ is calculated by the relation

$$\frac{d\ln L}{d\ln\delta} = \frac{dL}{d\epsilon}\cdot\frac{d\epsilon}{d\delta}\cdot\frac{\delta}{L}, \qquad \text{Equation 7}$$

where ϵ is the elongation, the true value of $\frac{d\ln L}{d\ln\sigma}$ will be quite close to that

calculated by Equation 7 only in the region of uniform deformation. When a neck forms, the value calculated from Equation 7 plotted against apparent δ (calculated from ϵ) begins to deviate downward from a straight line.

Since the author apparently has some data as to where the neck did form in the "early P_{max}" curves, it would be interesting to see if the results predicted by the above mathematical analysis are in agreement with his observations.

This analysis was developed under contract AF 33(616)2352, and the Air Force is thanked for permission to discuss it at this time.

Authors' Reply

Dr. Forscher's discussion is interesting, but several of the comments result from a misunderstanding of the purpose of this study. The selection of "standard properties" was only to serve as a starting place for examination of metallurgical and test variables on the flow characteristics. This selection, although arbitrary, was made with the realization that knowing the characteristics imposed by a range of metallurgical variables would be most useful for subsequent comparison with alloys.

It is not intended that this study should be considered as representing results on commercial material since, as Dr. Forscher must realize, arc-melted sponge-process zirconium would then be a preferable choice to arc-melted crystal bar.

Unfortunately, the influence of impurity content has received more attention in the discussion than is warranted. Certainly the two compositions cited in the discussion are somewhat different. However, the crystal-bar zirconium used in the investigation reported in the paper was obtained through the Atomic Energy Commission and was received from Westinghouse in Pittsburgh. We had no control of its purity.

The so-called "base-annealed" zirconium properties given in the discussion are not inconsistent with the data in the paper. The grain size of the "base-annealed" material was 0.05 mm average diameter, ten times larger than the 0.005 of the arc-melted material described in the paper. Obviously, the yield strength and tensile strength are much lower for the large-grained material. Approximately the same differences in grain size for the crystal-bar material can be seen in Table VI of the paper to give about the same difference in properties.

Crystal Bar [x]				Arc-Melted Crystal Bar [xx]			
Grain Size	Yield Str., psi	Tensile Str., psi	VHN	Grain Size	Yield Str., psi	Tensile Str., psi	VHN
0.005	18,000	34,100	96–109	0.005	17,000	39,000	120–130
0.084	9,400	24,100	78– 80	0.050	7,700	24,800	73

The "base-annealed" zirconium, which according to Dr. Forscher is reached when "grain growth is about to occur," has a grain size ten times greater than the arc-melted zirconium reported in the paper. To obtain this large grain size prior to grain growth suggests that there was only a small amount of cold deformation before the annealing. This in turn indicates a small amount of preferred orientation. Here again would be a reason for the lower strength values.

Needless to say, I do not agree with Dr. Forscher that the annealing of crystal-bar zirconium has been shown to occur in four successively experimen-

---

[x] Table VI in Paper
[xx] Table by Dr. Forscher

tally distinguishable stages. The discussion by Geisler, Keeler and Hibbard of his Ref. 1 in which the data of McGeary and Lustman are replotted indicates our view on this subject.

The ductility differences in the cold-reduced material were not in agreement with Dr. Forscher's results. Obviously, the elongation differences are not significant, but, on the other hand, the reduction in area values, particularly when related with the specific dimensional changes, were striking. Specimen geometry has something to do with this as pointed out in the text of the paper, and without knowing more of Dr. Forscher's specimens I cannot compare his results with those of the sheet specimens used in the present investigation.

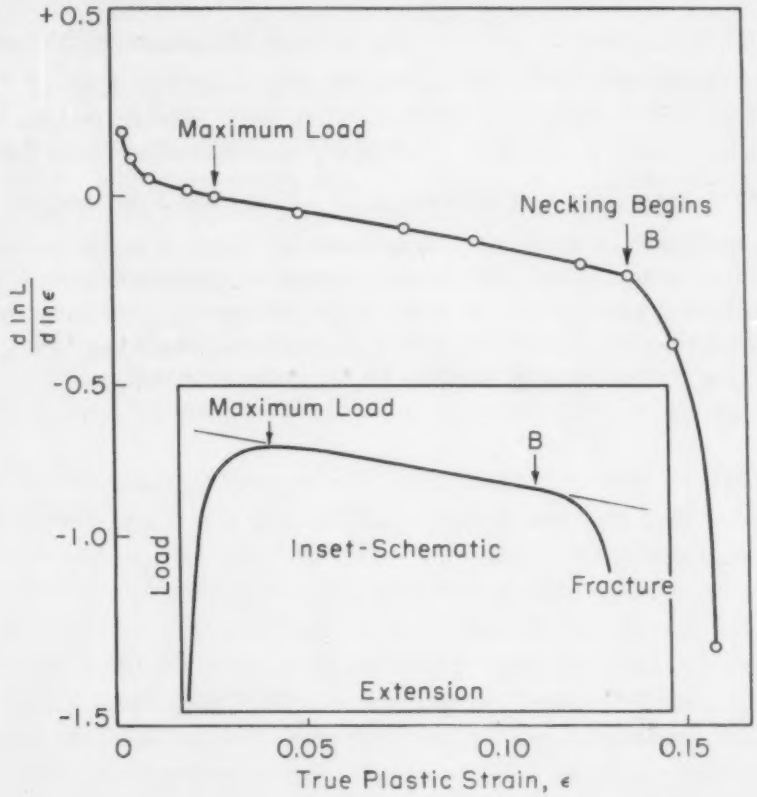


Fig. 28—97% Cold-Reduced Zirconium Tested at 300 °C.

Mr. Treco's and Dr. Forscher's comments on the possible contribution of hydrogen are well taken. That the strength of this regular melt was slightly below that of the original crystal bar may be due to hydrogen as Mr. Treco suggests. However, I had considered this as perhaps resulting from less preferred orientation in the arc-melted material since experimental work performed after the paper was submitted has indicated a less strong preferred orientation in arc-melted zirconium containing oxygen and nitrogen impurities.

The degassed crystal bar in Table XII of Mr. Treco's discussion has lower yield stress values which he attributes to prior degassing. This lower yield stress may also be due to less preferred orientation since the samples were cold reduced only 20% prior to annealing or to the larger grain size which in his reference is stated to be relatively coarse.

Unfortunately, at the time of the investigation reported in the paper, facilities

were not available for accurate oxygen analyses. I would like to have made direct comparison with the quantitative results of Mr. Treco's earlier investigation.

Values for Young's modulus cannot be obtained using the Instron Testing Machine, since the strain measurement also includes any strain and take-up in the pull rods and linking members. As a result, a straight line is drawn through the elastic portion of the recorded load-extension curve, the slope of this line is ignored, and only the plastic strain portion of the remainder of the curve is considered. All plastic strain is measured from the corresponding stress level of this straight line which is drawn through the elastic portion of the curve and is extrapolated to stress levels higher than the initiation of plastic flow.

Dr. Opinsky's analysis was of interest, and his suggested plot of $\frac{d \ln L}{d \ln \epsilon}$ versus true plastic strain, ϵ, was tried with data from two tests of 97% cold-reduced zirconium tested at 300 °C. Both plots were similar, and, as shown in Fig. 28 which includes a schematic inset of the load-extension curve for this test, deviation from a straight line relation of $\frac{d \ln L}{d \ln \epsilon}$ versus ϵ did not occur at the maximum load point, but occurred near point B. Point B is the point where a straight line drawn through the linear decreasing load portion of the load-extension curve begins to break away from the actual load-extension curve. It is estimated that true localized necking began near this point. Thus, it is apparent that the test results agree with Dr. Opinsky's analysis.

THE EFFECT OF COLD WORK AND RECRYSTALLIZATION ON THE FORMATION OF THE SIGMA PHASE IN HIGHLY STABLE AUSTENITIC STAINLESS STEELS

By A. J. Lena and W. E. Curry

Abstract

A study of the effect of cold work on sigma formation in Type 310 and chromium-manganese stainless steels has shown that recrystallization is essential for pronounced acceleration of sigma formation in highly stable austenitic stainless steels. A recrystallization transformation is described in which sigma and unstrained austenite of an equilibrium composition are produced by the recrystallization of highly strained austenite of a nonequilibrium composition. If the amount of cold work is less than that required for recrystallization at a given temperature, then the accelerating effect of cold work is very small or nonexistent. Actually, small degrees of cold work may retard sigma formation by restraining or preventing the formation of Widmanstätten type precipitates which form in annealed steels at certain aging temperatures.

THE accelerating effect of cold work on the rate of formation of sigma has been recognized for some time and numerous investigators have made use of this effect in establishing the compositional limits of sigma formation in various alloy systems. Because of the difficulties encountered in measuring the amounts of sigma, much of the early work on the effect of cold working was qualitative in nature and only recently have quantitative rate curves been obtained (1,2).[1] The amount of data available, however, is sparse and there has been no systematic investigation of the effects of cold work on any single alloy over a large range of deformation. Guarnieri (1) and co-workers have derived rate curves for a Type 314 stainless steel with 25 and 50% deformation and have shown an accelerating effect for both cases in the temperature range of 1200 to 1800 °F (650 to 980 °C). Morley and Kirkby (3) have shown that 5% deformation has no effect on the rate of formation of sigma in Type 310 and state that large amounts of deformation are necessary before sigma formation is enhanced. On the

[1] The figures appearing in parentheses pertain to the references appended to this paper.

A paper presented before the Thirty-sixth Annual Convention of the Society, held in Chicago, November 1 to 5, 1954. Of the authors, A. J. Lena is associate director of research and W. E. Curry is chief metallographer, Allegheny Ludlum Steel Corporation Research Laboratory, Brackenridge, Pa. Manuscript received April 16, 1954.

Table I
Composition of Steels

Type	Heat	C	Mn	Si	Cr	Ni	N_2
310	44122	0.033	1.81	0.44	25.26	20.91	—
310	98077	0.06	1.54	0.48	24.90	19.87	—
CM	23433	0.095	16.83	0.54	15.12	1.03	0.21

basis of their results with a 36% cold drawn Type 310 steel aged at 1300 °F (705 °C), Dulis and Smith (2) suggest that the effect of cold work is to form additional nuclei for subsequent sigma growth. This suggestion, however, is at variance with the work of Morley and Kirkby unless one assumes that a certain minimum amount of cold work is necessary before any increased nucleation effect is observed.

The research reported in this paper was conducted in order to promote a better understanding of the effect of cold work on sigma formation and is the first part of an overall project which is intended to include all types of stainless steels. The results described in this paper pertain to highly stable austenitic stainless steels which do not transform to ferrite during cold working; hence, the accelerating effect which ferrite formation is known to exert on sigma formation was not a consideration in this work.

Experimental Procedure

Two heats of commercial Type 310 and one heat of a commercial grade of an austenitic chromium-manganese steel were employed in this investigation. The composition of each of these alloys (Table I) was such that no ferrite was present in the annealed condition and the austenite stability was sufficiently great to prevent any ferrite formation during subsequent cold rolling.

Sections of 0.064 inch thick mill annealed sheets from each of these heats were cold rolled various amounts as listed in Table II. No change in permeability as a result of cold working was observed in any of the heats. Samples 1 x 2 inches were cut from the annealed and the cold-rolled sheets and were aged at the temperatures shown in Table II for times ranging from 1 to 500 hours. Hardness and bend tests were made on each sample after which they were sectioned and prepared for metallographic examination. Various etchants were used to differentiate the carbides from sigma. Best results were achieved in the Type 310 steels

Table II
Cold-Rolled Conditions and Aging Temperatures

Type	Heat	Cold-Rolled Conditions —%	Aging Temperature —°F
310	44122	0,25,50,75,90	1475
310	98077	0,5,10,20,40	1250, 1475, 1600
CM	23433	0,10,25,50,75,90	1200, 1400

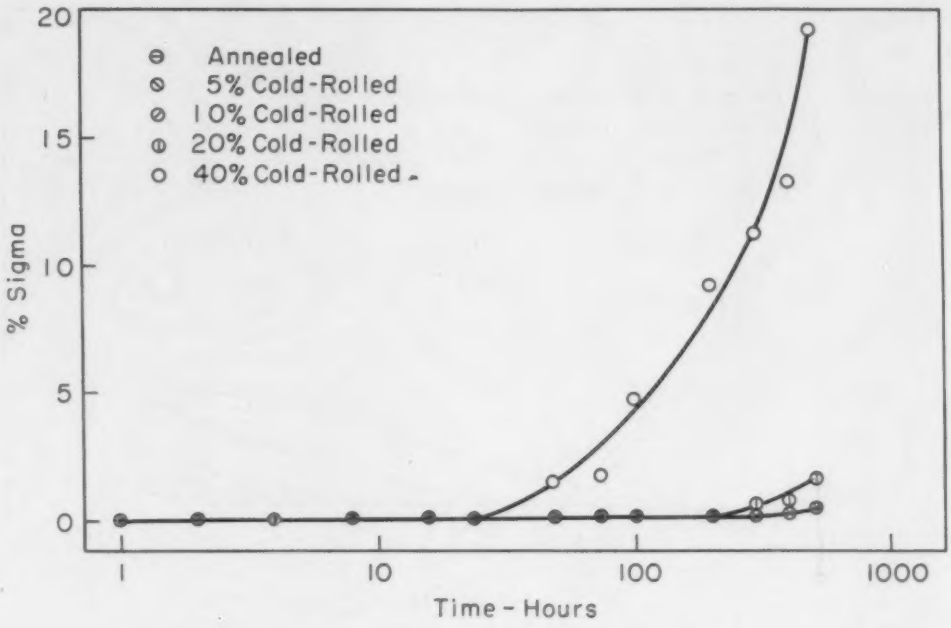


Fig. 1a—Effect of Cold Work on the Rate of Formation of Sigma in Type 310 (Heat 98077) Aged at 1250 °F.

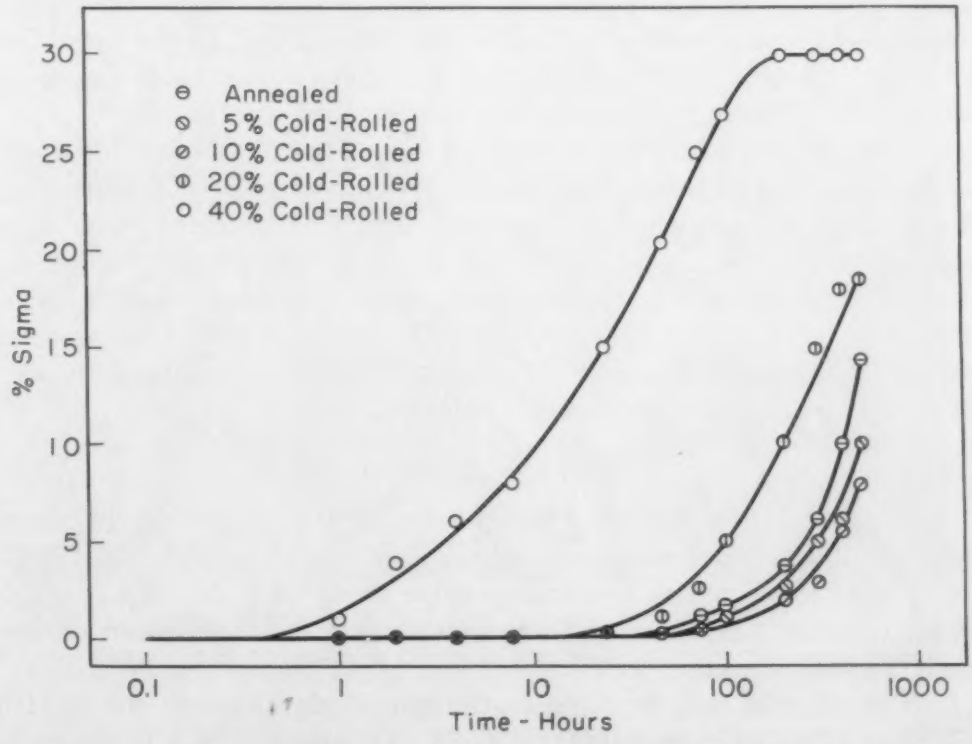


Fig. 1b—Effect of Cold Work on the Rate of Formation of Sigma in Type 310 (Heat 98077), Aged at 1475 °F.

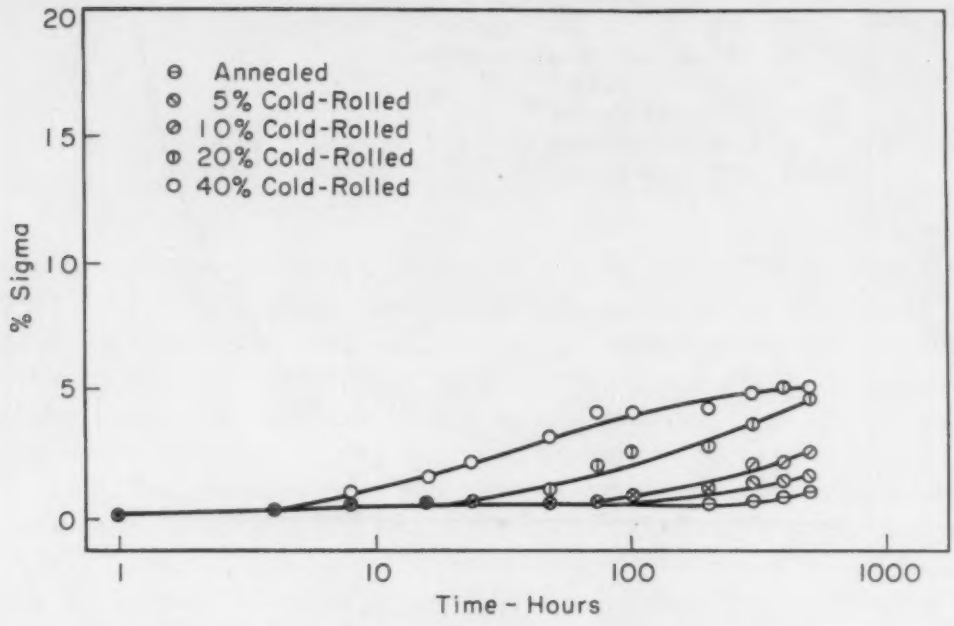


Fig. 1c—Effect of Cold Work on the Rate of Formation of Sigma in Type 310 (Heat 98077), Aged at 1600 °F.

with the electrolytic hydroxide solutions suggested by Gilman (4) who found that strong hydroxide solutions used electrolytically color the sigma phase more rapidly than the carbides if the solutions are concentrated and have the opposite effect if they are diluted. In the case of the CM steel, electrolytic 10% chromic acid attacks the carbides vigorously while leaving the sigma unattacked but outlined and in relief.

The amount of sigma in samples from Heat 98077 was estimated by comparison with standard charts provided by G. J. Guarnieri of the Cornell Aeronautical Laboratory, Inc. The percentage of sigma was determined by averaging the estimated amount of sigma in at least fifty fields of view at a magnification of X500. The start of sigma formation in samples aged at 1250 and 1475 °F (675 and 800 °C) was determined by X-ray diffraction of extracted residues obtained by electrolysis in a 10% sodium chloride solution.

Experimental Results

Because of the difficulty in determining the percentage of sigma, the quantitative work was confined primarily to Heat 98077. All of the steels were subjected to a metallographic study and photomicrographs of the other two heats are used to substantiate the conclusions derived from the work on Heat 98077.

The effect of cold working on the rate of sigma formation in Heat 98077 at 1250, 1475 and 1600 °F (675, 800 and 870 °C) is shown by the rate curves of Fig. 1. Examination of these curves discloses that a

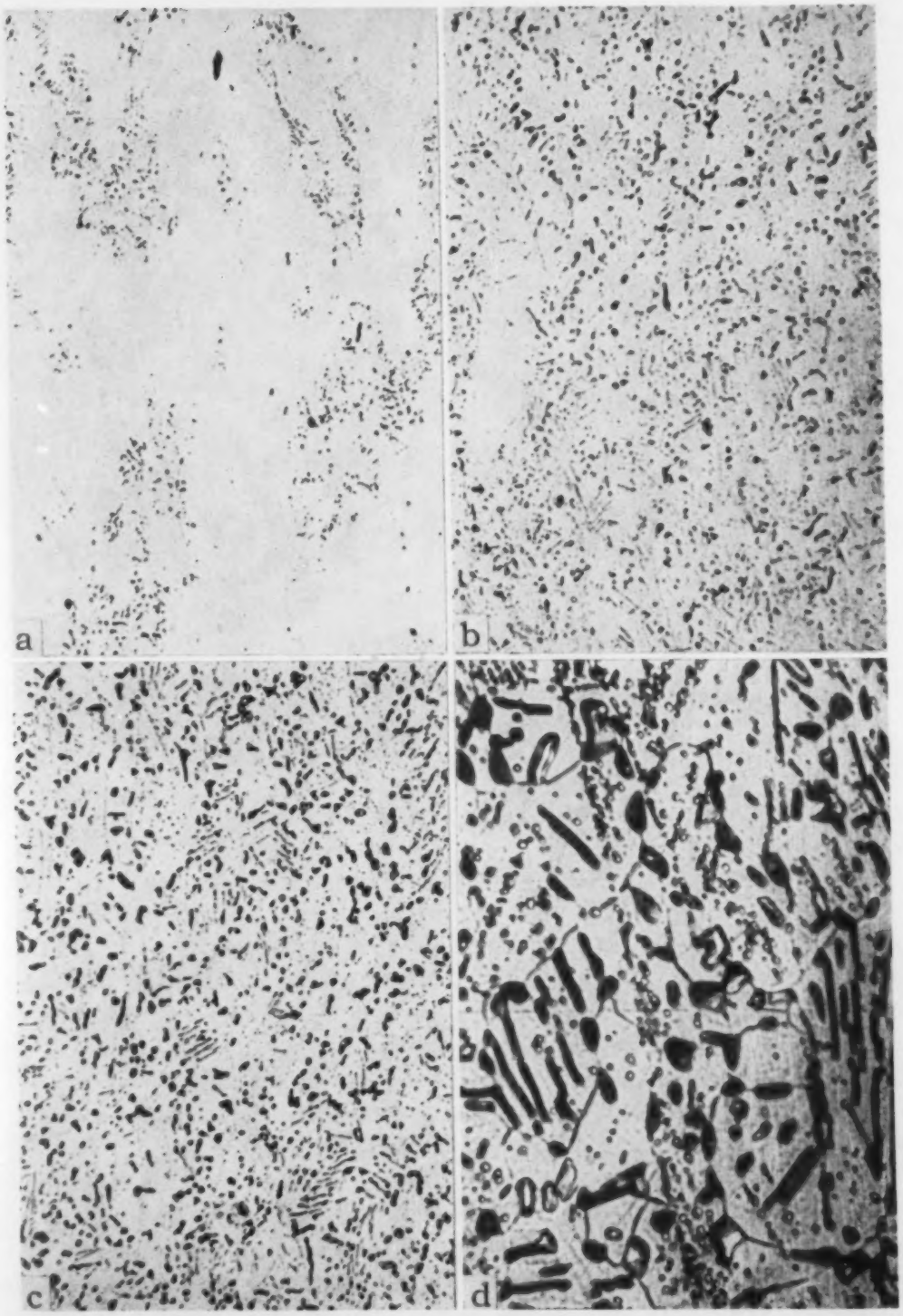


Fig. 2—Photomicrographs Showing Extent of Sigma Formation in 40% Cold-Rolled Type 310 (Heat 98077) Aged at 1475 °F. (a) 2 Hours. (b) 48 hours. (c) 500 hours. Etchant—electrolytically in saturated sodium hydroxide. X 250. (d) 500 hours. Etchant —electrolytically in 10% oxalic acid. X 1000.

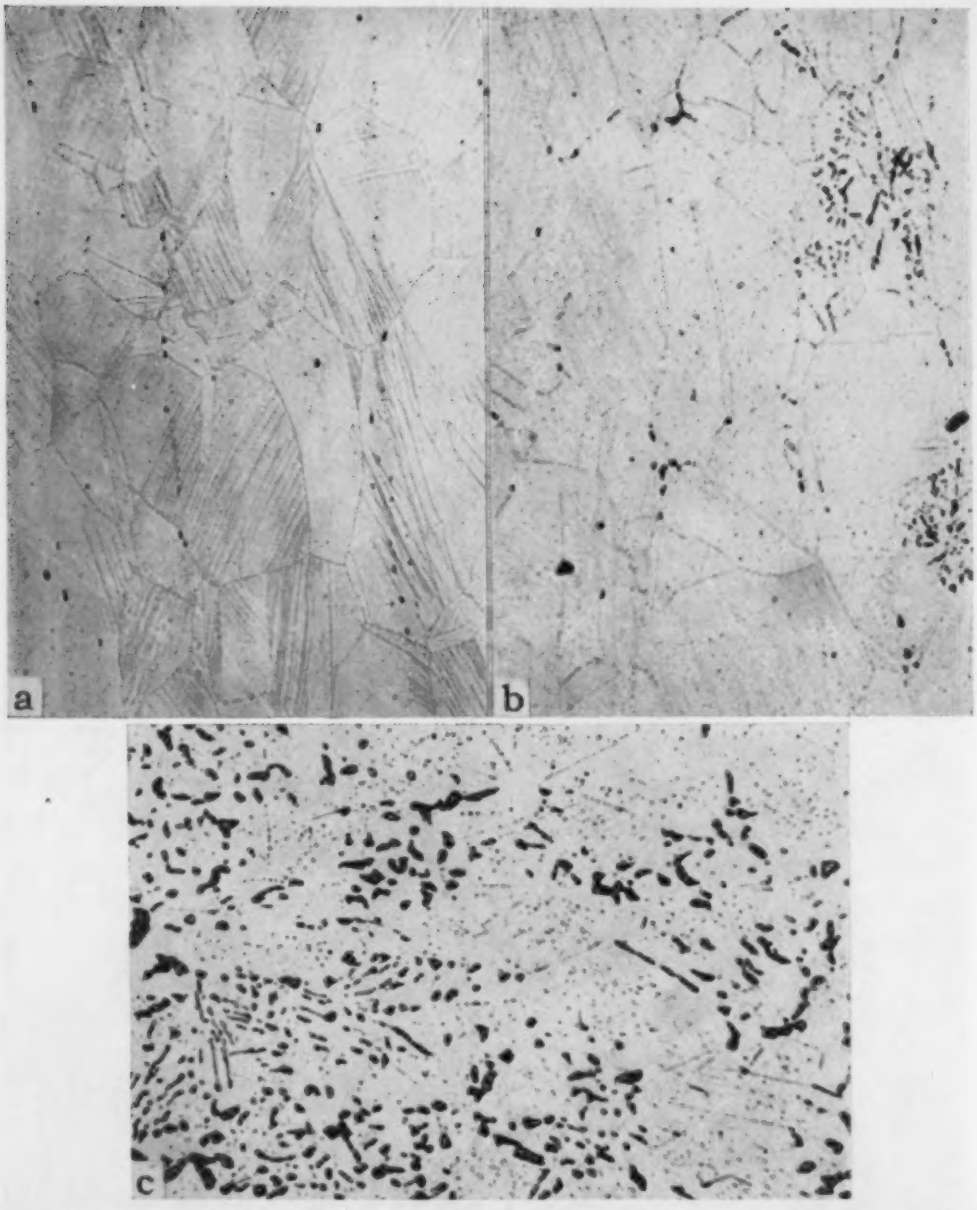


Fig. 3—Photomicrographs Showing Extent of Sigma Formation in 20% Cold-Rolled Type 310 (Heat 98077) Aged at 1475 °F. (a) 2 hours. (b) 48 hours. (c) 500 hours. Etchant—electrolytically in saturated sodium hydroxide. X 250.

certain minimum amount of cold work is necessary for pronounced acceleration of sigma formation in this type of steel. This is particularly true at 1250 and 1475 °F (675 and 800 °C) where cold rolling to the extent of 20 and 40% promotes sigma formation whereas 5 and 10% has either no effect or as is the case at 1475 °F (800 °C), actually retards the formation of sigma. The equilibrium amount of sigma is attained in the 40% cold worked samples within 200 hours at 1475 °F (800 °C) but is not reached in any of the other samples aged at 1250 or 1475 °F (675 or 800 °C) within 500 hours.

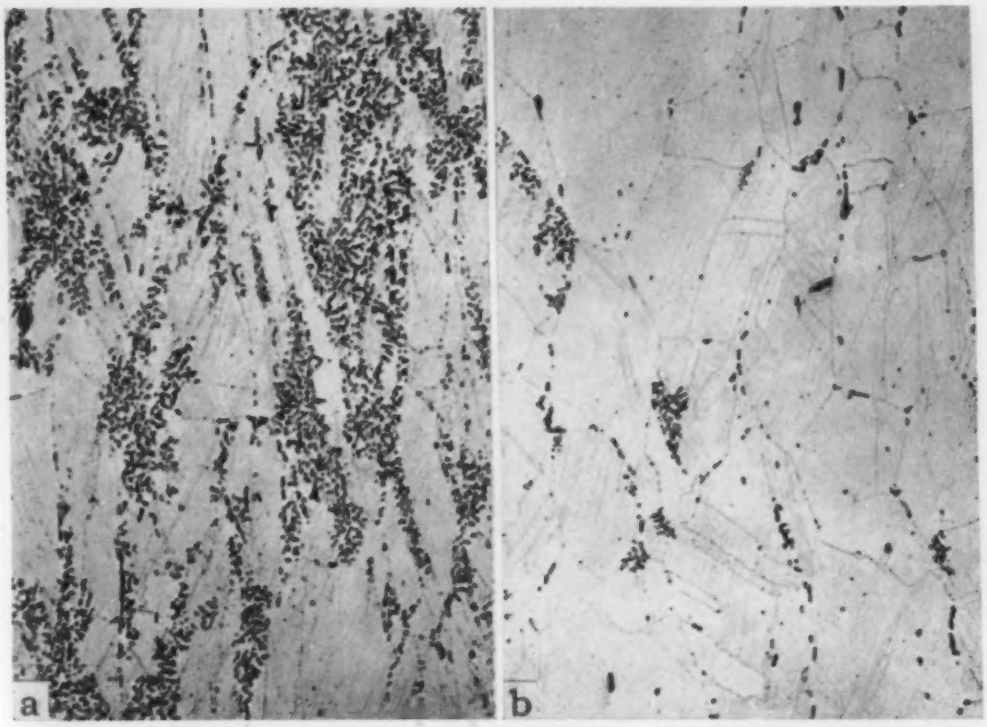


Fig. 4—Photomicrographs Showing the Formation of Sigma in Type 310 (Heat 98077) which had been Aged for 300 Hours at 1250 °F. (a) 40% Cold-Rolled. (b) 20% Cold-Rolled. Etchant—electrolytically in saturated sodium hydroxide. X 250.

A study of the metallography of this steel has provided an insight into the nature of the effect of cold work on sigma formation. Figs. 2 and 3 show that sigma begins to form in a concentrated form in sporadic areas in the 20 and 40% cold-rolled steel during aging at 1475 °F (800 °C). (The sodium hydroxide etchant attacks the sigma vigorously with only slight attack on the carbides (4); hence, the sigma particles etch black as shown in the photomicrographs. However, it is necessary not to confuse sigma with the dark etching inclusions such as those in Fig. 3a where no sigma is present). The concentrated formation of sigma in isolated areas is even better shown in samples aged at 1250 °F (675 °C) (Fig. 4) for at this temperature the rate of coalescence is less and the particles retain their original shape and distribution for much longer periods of time. These isolated regions are areas where recrystallization has occurred. The relationship between recrystallization and accelerated sigma formation is discussed in more detail later in this paper.

Although cold working 20 and 40% promotes the formation of sigma at 1600 °F (870 °C), the effect on structure is somewhat different from that which occurs at lower temperatures in that no areas of high sigma concentration are observed. This can be attributed to the relatively small amount of stable sigma at this temperature which per-



Fig. 5—Photomicrograph Showing Formation of Sigma in 20% Cold-Rolled Type 310 (Heat 98077) Aged for 72 hours at 1600 °F. Etchant—electrolytically in 10% oxalic acid. X 500.

mits large quantities of recrystallized austenite to form in association with only small amounts of sigma. That accelerated sigma formation at this temperature is also related to recrystallization is shown in Figs. 5 and 6. In the case of Fig. 5, one grain can be seen where two plates of sigma have formed in conjunction with an advancing recrystallized grain [2] interface while a second recrystallized grain is almost completely surrounded by sigma. Fig. 6 shows the sequence of events in 40% cold-rolled samples aged at 1600 °F (870 °C) and it can be seen that recrystallization is extensive (Fig. 6b) before sigma formation is observed in the recrystallized grain boundaries (Fig. 6c). In order to show the grain boundaries in these samples it was necessary to etch electrolytically in 10% oxalic acid which attacks both sigma and carbides. The use of the sodium hydroxide etchant as well as X-ray analysis of extracted residues confirmed the absence of sigma in the sample of Fig. 6b. After longer aging times, essentially all of the sigma can be found in a coalesced form at the grain boundaries of the completely recrystallized steel (Fig. 6d).

In contrast to the behavior of the 20 and 40% cold-rolled material, the 5 and 10% samples did not recrystallize within 500 hours at any of the temperatures investigated and there was no pronounced effect on increasing the rate of sigma formation. At 1475 °F (800 °C) it was observed that small degrees of cold work restrained or prevented the formation of a Widmanstätten type precipitate which formed in the annealed steel at this temperature (Fig. 7). This effect, which accounts

[2] The recrystallized grains can be recognized by their lack of carbide precipitation along slip planes.

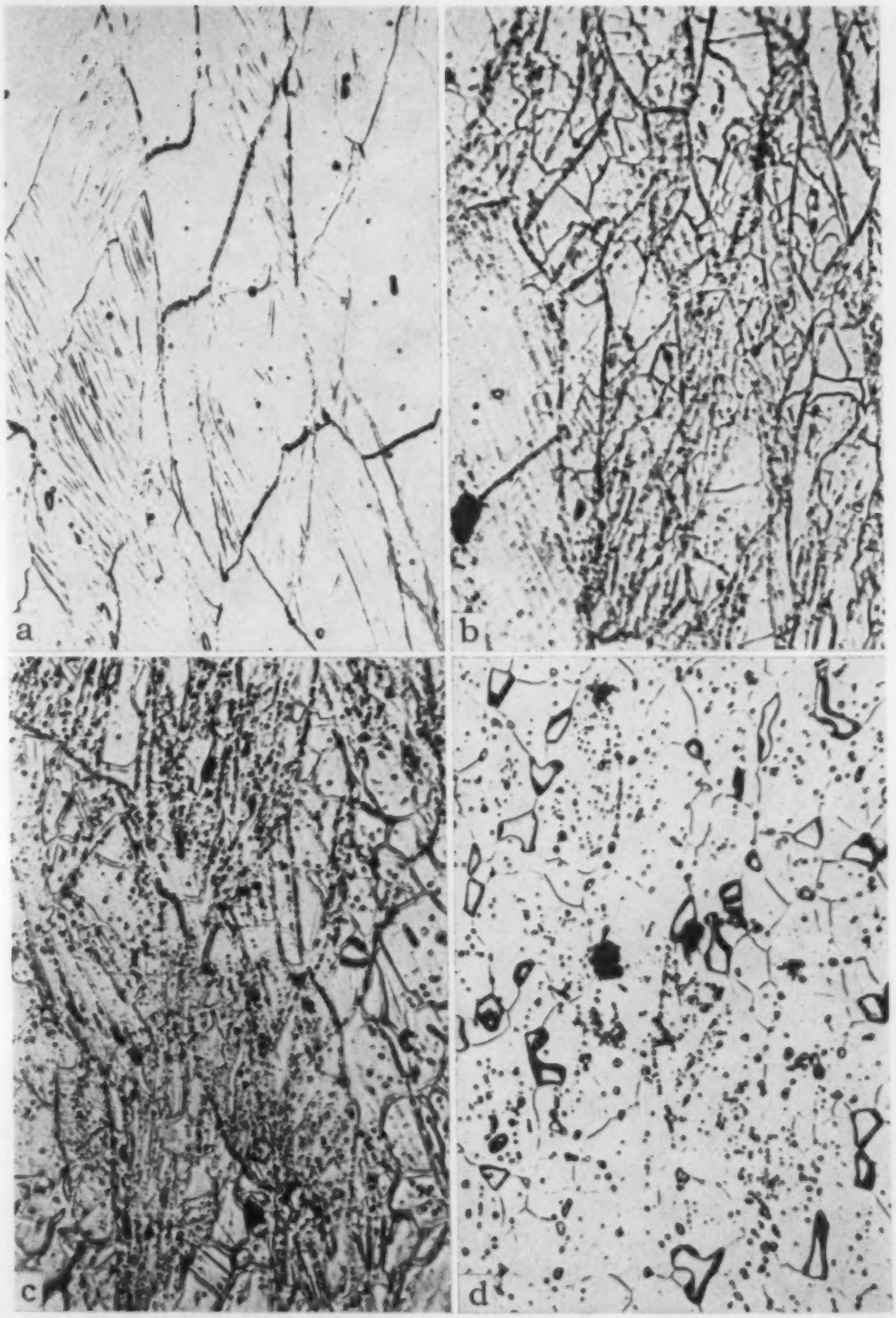


Fig. 6—Photomicrographs Showing Sequence of Recrystallization and Sigma Formation in 40% Cold-Rolled Type 310 (Heat 98077) Aged at 1600 °F. (a) As cold-rolled. (b) 1 hour. (c) 4 hours. (d) 400 hours. Etchant—electrolytically in 10% oxalic acid. X 500.

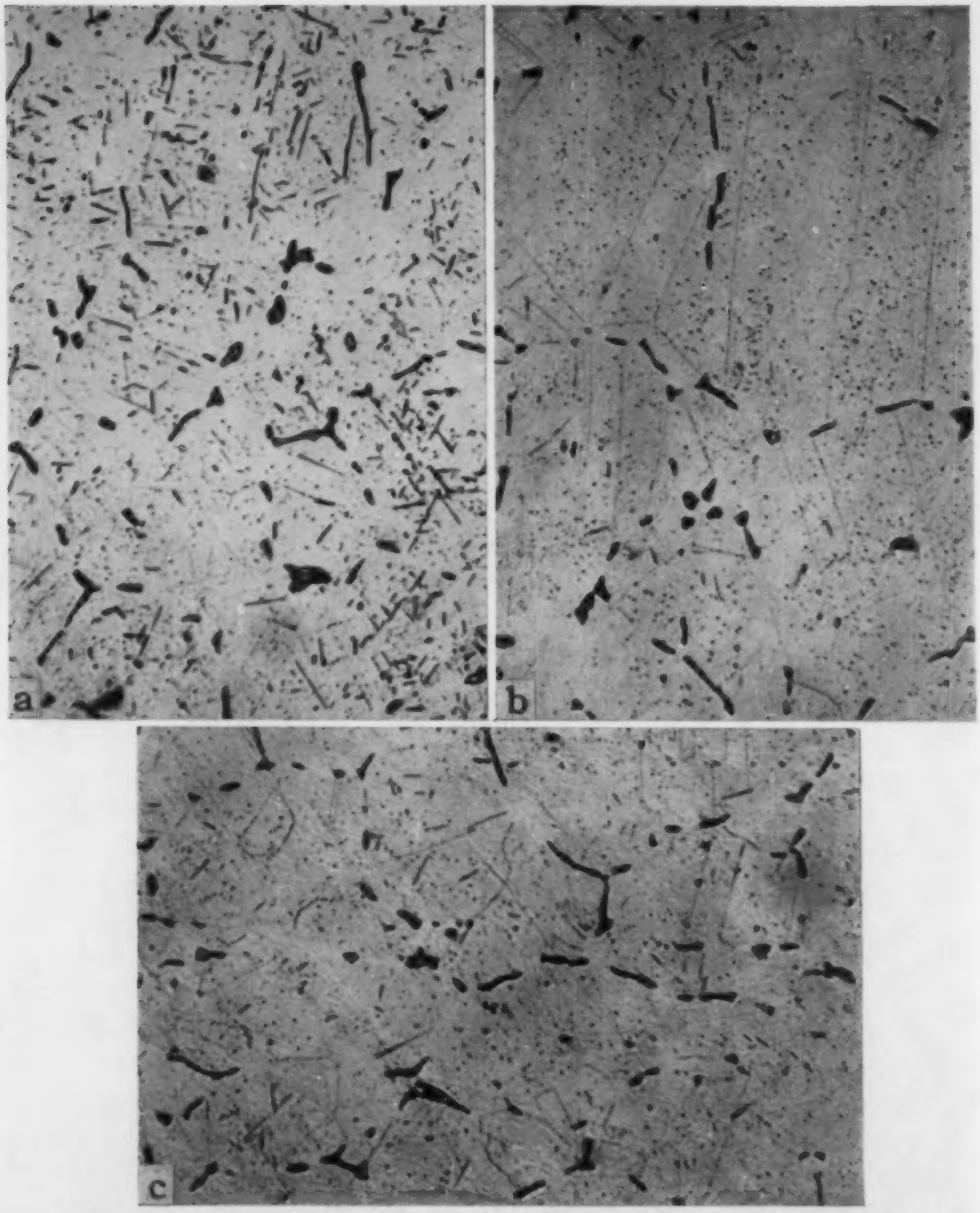


Fig. 7—Photomicrographs Showing Extent of Sigma Formation in Type 310 (Heat 98077) After 500 Hours at 1475 °F. (a) Annealed. (b) 5% cold-rolled. (c) 10% cold-rolled. Etchant—electrolytically in saturated sodium hydroxide. X 250.

for the more rapid rate of sigma formation in annealed steels than in those which were cold-rolled 5 or 10%, was observed only at 1475 °F (800 °C) because it was the only temperature at which the Widmanstätten type precipitate was found. A slightly increased rate of sigma formation was observed in the 5 and 10% samples aged at 1600 °F (870 °C) where sigma formed exclusively at the grain boundaries but the effect was minor in comparison to that which occurred in recrystallized samples.

Discussion of Results

The Effect of Cold Work and Recrystallization

Suitable etching of those samples which contain localized regions of high sigma concentration reveals that these are regions where recrystallization has occurred. An example of this is the photomicrograph of Fig. 8b which shows that all of the sigma is contained within newly recrystallized grains whose advancing boundaries are very irregular. The photomicrographs of Fig. 8 are of samples from the low carbon heat of

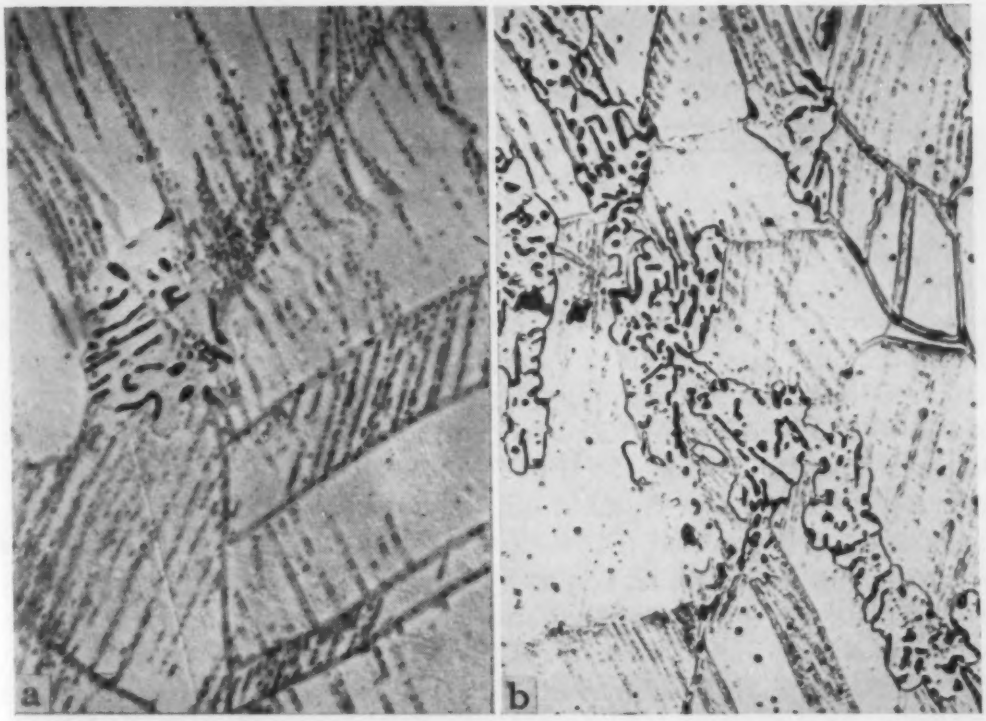


Fig. 8—Photomicrographs Showing Extent of Sigma Formation and Association With Recrystallization in Type 310 (Heat 44122) which had been 25% Cold-Rolled and Aged at 1475 °F. (a) 8 hours. (b) 24 hours. Etchant—(a) Electrolytically in 10% Chromic Acid: X 1000 (b) Electrolytically in 10% oxalic acid. X 500.

Type 310 (Heat 44122) which displayed the same characteristics with respect to cold work and sigma formation as the higher carbon heat. The morphology of the sigma and the recrystallized matrix in the early stages of formation (that is, before appreciable coalescence of the sigma destroys the original morphology) is often similar to that of pearlite formation in that alternate plates of sigma and recrystallized matrix are observed (Fig. 8a). Accordingly, the accelerated formation of sigma in this manner can be attributed to a recrystallization transformation which can be described by the following reaction:

$$\text{Strained Austenite of Composition } C_1 \rightarrow \text{Sigma} + \text{Unstrained Austenite of Composition } C_2$$

This reaction is one in which the nuclei of the recrystallized matrix and

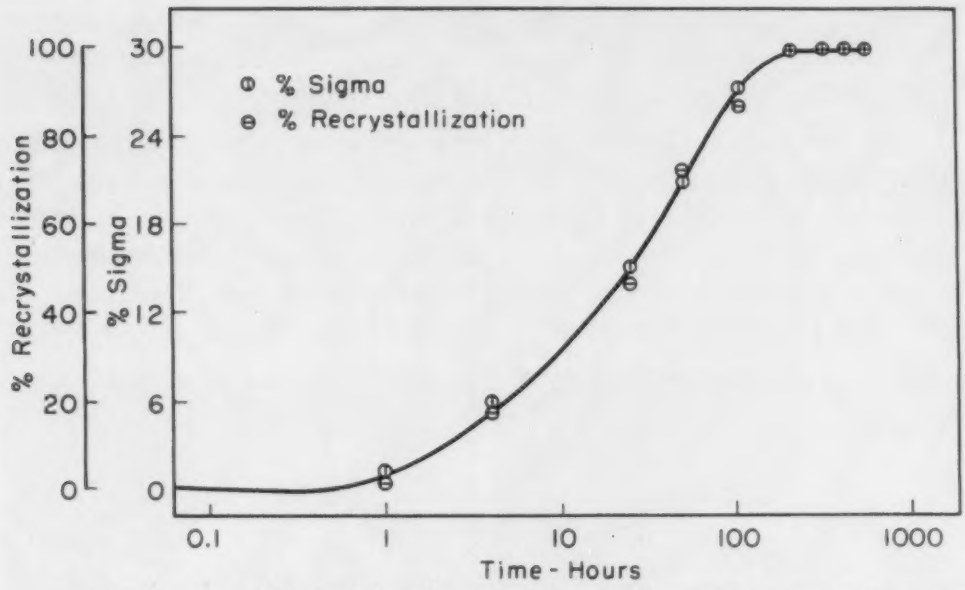


Fig. 9—Rate of Sigma Formation and Rate of Recrystallization in Type 310 (Heat 98077) which had been 40% Cold-Rolled and Aged at 1475 °F.

sigma are of the equilibrium composition for a particular aging temperature. Support for this is given by the fact that a single curve can describe the rate of formation of sigma and the rate of recrystallization of the 40% cold-rolled material from Heat 98077 which had undergone complete transformation at 1475 °F (800 °C) (Fig. 9). Since the accelerated formation of sigma in this manner requires recrystallization, it becomes apparent that if the amount of cold work is not sufficiently great to cause recrystallization at a given aging temperature, then cold work can have no effect on increasing the rate of sigma formation which is the case for 5 and 10% cold-rolled steels aged at 1250 and 1475 °F (675 and 800 °C). It can perhaps be said that cold working itself does not have a pronounced effect on accelerating sigma formation but recrystallization does.

The retarding effect of small degrees of cold work in samples aged at 1475 °F (800 °C) can be attributed to the fact that the Widmanstätten precipitate forms more readily in annealed materials than in those which have been cold-worked. Apparently the lattice distortion introduced by cold working restrains or prevents the precipitate from forming with the proper orientation relationship with respect to the matrix. The effect increases with increasing amounts of cold work (the 10% cold-rolled samples contained less of this type of precipitate than the 5% cold-rolled samples) and it was observed only at 1475 °F (800 °C). Actually, the 10% material contained more grain boundary sigma than the annealed steel but this was more than offset by the amount of Widmanstätten precipitate in the annealed steel. In view of this effect on grain boundary sigma in the samples annealed at 1475 °F (800 °C) and the previously mentioned results at 1600 °F (870 °C), it appears that

cold working may increase the tendency toward grain boundary sigma formation but the accelerating effect is small in comparison to that which is due to recrystallization.

The effect of cold work and recrystallization on pronounced sigma acceleration at 1600 °F (870 °C) is identical to that at lower temperatures but the morphology of sigma formation is somewhat different. Instead of pearlitic-like-sigma within the boundaries of recrystallized grains, the sigma is located at the grain boundaries of the recrystallized austenite. This condition occurs as a result of the partitioning of alloying elements during recrystallization in which case the unrecrystallized austenite approaches the composition of sigma as recrystallization progresses. If sigma has not formed by the time that two recrystallizing grains approach impingement, the grain boundary area must be of a suitable composition for sigma formation. This mechanism is indicated by the microstructures of Figs. 5 and 6. At the start of sigma formation (Fig. 6c) the recrystallized grain boundaries have appreciable width indicating a difference in composition which is not apparent after longer aging times when sigma formation is complete (Fig. 6d). Fig. 5 shows a recrystallizing grain interface which is almost completely surrounded by sigma.

The morphological formation of grain boundary sigma in this manner may apply to a lesser degree to 40% cold-worked material aged at 1475 °F (800 °C) for, in addition to the pearlitic sigma, some grain boundary sigma is observed after long aging times (Fig. 3d). This may be partially due to coalescence but the presence of some small particles suggests that they were initially formed at the grain boundaries. The results at 1600 °F (870 °C), however, indicate that the formation of grain boundary sigma in the manner prescribed above may be most pronounced when conditions of deformation and aging temperature are such as to produce rapid rates of recrystallization with a resultant fine grain size. Accordingly, one should expect to find large amounts of grain boundary sigma in heavily cold worked steels aged at temperatures lower than 1600 °F (870 °C). This was confirmed by the microstructure of 75 and 90% cold-rolled samples from Heat 44122 which had been aged at 1475 °F (800 °C), an example of which is shown in Fig. 10. The grain size after recrystallization was calculated to be ASTM 20 and 22 in the 75 and 90% cold-rolled samples respectively.

There is one major difference in comparing the formation of grain boundary sigma at 1600 °F (870 °C) with that at 1475 °F (800 °C); the difference in equilibrium amounts of sigma at these temperatures. Because of the small amount of stable sigma at 1600 °F (870 °C) (approximately 5% as compared to 30% at 1475 °F), the composition of the equilibrium austenite is closer to that of sigma than it is at lower temperatures and the amount of partitioning of alloying elements between the unrecrystallized and recrystallized austenite must be cor-

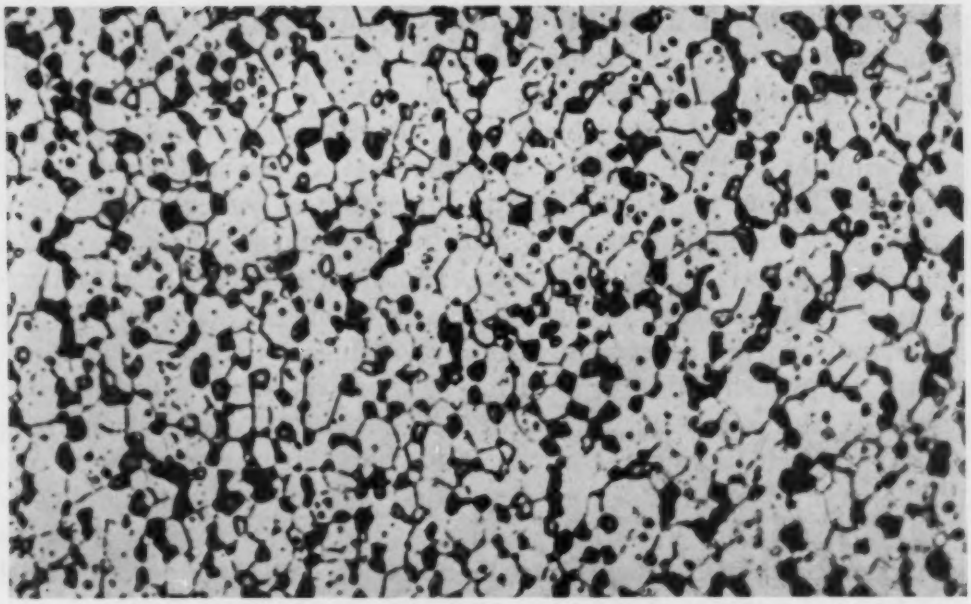


Fig. 10—Photomicrograph Showing Sigma at Grain Boundaries of a Sample from Heat 44122 which had been Cold-Rolled 90% and Aged at 1475 °F for 100 Hours. Etchant—electrolytically in 10% oxalic acid. X 1000.

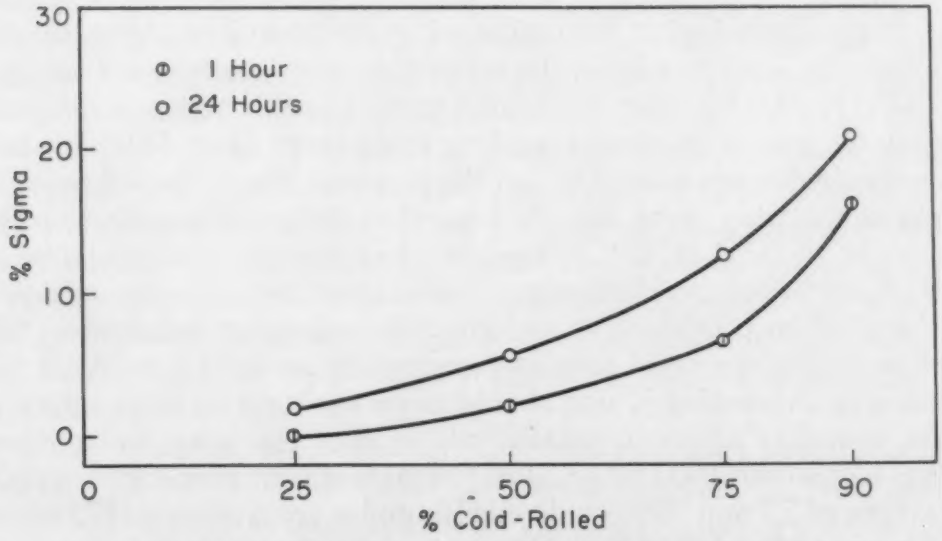


Fig. 11—Effect of Cold Work on the Rate of Sigma Formation in Type 310 (Heat 44122) after 1 Hour and 24 Hours at 1475 °F.

respondingly less. Under these conditions recrystallization can progress further before sigma formation occurs and the final recrystallized grain size can be larger at high temperatures and still have the sigma located at the grain boundaries. In the case of the 40% cold-rolled material aged at 1600 °F (870 °C), the recrystallized grain size was ASTM-8. It is because of this condition that it takes longer for the start of sigma formation in the 40% cold-rolled steel at 1600 °F (870 °C) than at 1475 °F (800 °C) in spite of the fact that recrystallization begins in

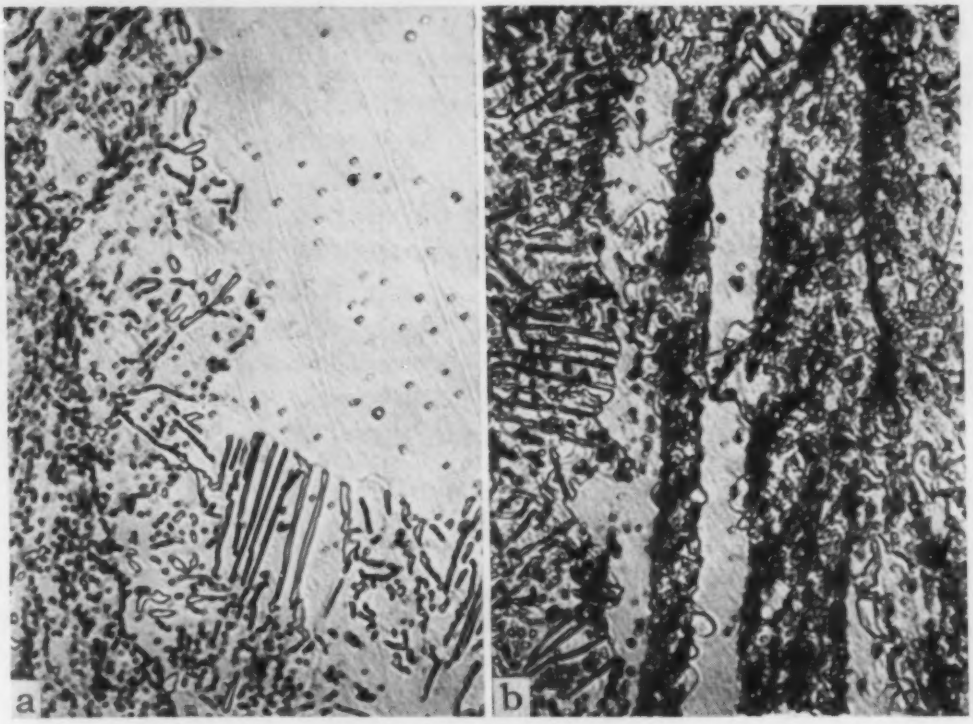


Fig. 12—Photomicrographs Showing Formation of Sigma in Recrystallized Regions of Chromium—Manganese Steel which had been Cold-Rolled 50% and Aged for 200 Hours at 1200 °F. Etchant—(a) Electrolytically in 10% chromic acid. X 1000 (b) Electrolytically in 10% chromic 10% oxalic acid. X 1000.

shorter times at the higher temperature. If it were not for this difference in equilibrium amounts of sigma, one should expect the rate of sigma formation to increase with increasing rates of recrystallization. This is true for samples aged at a single temperature where the equilibrium amount of sigma is a constant which is shown in Fig. 11 where the percentage of sigma obtained by aging Heat 44122 for 1 and 24 hours at 1475 °F (800 °C) is plotted as a function of the degree of deformation in the range of 25 to 90%. Within this range the accelerated formation of sigma was associated with recrystallization.

Effect of Cold Work on Sigma Formation in Austenitic Chromium-Manganese Steel

In order to determine if the same effects of cold work and recrystallization observed in the Type 310 steels applied to other highly stable austenitic steels, a study was made of the chromium-manganese steel listed in Table I. Microscopic examination of cold worked specimens after aging showed that a similar effect existed in this steel in that recrystallization was required for pronounced sigma acceleration in cold-worked samples. The pearlitic-like-sigma which formed in the recrystallized areas of a 50% cold-rolled sample that had been aged for 100 hours at 1200 °F (650 °C) is shown in Fig. 12. (The 10% chromic acid etch attacks carbides vigorously but does not attack sigma in this

Table III
Effect of Sigma Formation on Hardness and Bend Angle of Type 310 (Heat 98077)

Aging Time (Hours)	Hardness*				Bend Angle (degrees)**			
	Annealed	10% CW	20% CW	40% CW	Annealed	10% CW	20% CW	40% CW
				Aged at 1475 °F				
0	78	96	Rc22	Rc34	180	180	180	90
1	78	89	93	95	180	180	180	180
8	79	85	91	85	180	180	180	180
100	79	85	90	86	180	180	180	180
500	86	87	86	86	180	180	180	180
				Aged at 1250 °F				
1	78	93	98	32	180	180	180	80
8	79	92	97	27	180	180	180	80
100	82	93	98	27	180	180	180	85
300	82	96	98	27	180	180	180	100
500	82	95	97	25	180	180	180	115
				Aged at 1600 °F				
1	79	89	93	81	180	180	180	180
8	78	88	91	80	180	180	180	180
100	80	87	85	77	180	180	180	180
500	80	86	85	80	180	180	180	180

* Rb unless otherwise noted
** Bent over pin whose diameter was twice the thickness

steel). Because of the large amount of carbide in this steel, no quantitative work was attempted.

Carbide Precipitation and Resolution

The precipitation of chromium carbide ($Cr_{23}C_6$) preceeds the formation of sigma in both Type 310 and the chromium-manganese steel regardless of initial condition and aging temperature. In the case of Type 310, the alteration in composition of the austenite as a result of sigma formation apparently increases the solubility of carbon because much of the chromium carbide is taken back into solution during the recrystallization transformation. Microscopic evidence of this can be seen in Fig. 8a which shows essentially no chromium carbide in the recrystallized region where the sigma exists but appreciable amounts of carbide in the surrounding regions. This observation was confirmed by the X-ray diffraction patterns of extracted residues where the line intensities for chromium carbide after 500 hours at 1475 °F (800 °C) were much weaker than after 1 hour at 1475 °F (800 °C). In the case of the low carbon heat (44122), the lines were extremely faint after long time aging which would indicate that the solubility of carbon in the recrystallized austenite may even be greater than the initial carbon content of the steel provided the solubility of carbon in sigma is very low as has been reported (5).

Effect of Sigma Formation on Hardness and Bend Angle

Some of the hardness and bend data which illustrate the changes observed in Type 310 (Heat 98077) as a result of aging at 1250, 1475

and 1600 °F (675, 800 and 870 °C) are given in Table III. These data show that the formation of sigma, even in amounts as large as 30%, has very little effect on the hardness and bend ductility of Type 310 steel treated in the manner described in this paper. Aging at 1475 °F (800 °C) results in a slight hardening of annealed samples while softening is observed in all of the cold-worked conditions. After long time aging, all of the samples regardless of initial condition have essentially the same hardness and bend 180° without breaking in spite of large differences in amounts of sigma. At 1250 °F (675 °C) the transformation produces a continual increase in bend angle in the 40% cold-worked material but due to a slower rate of softening and recrystallization, a full 180° bend is not attained within 500 hours.

Summary

The increased rate of sigma formation in cold-worked austenitic stainless steels which do not form ferrite during cold working can be attributed to a recrystallization transformation according to the following equation:

$$\text{Strained Austenite of Composition } C_1 \rightarrow \text{Sigma} + \text{Unstrained Austenite of Composition } C_2$$

If the conditions of deformation and aging temperature are such that recrystallization does not occur, then the accelerating effect of cold work is at most very small. Actually, small amounts of cold work may retard sigma formation by restraining or preventing the formation of oriented Widmanstätten precipitates which occur in annealed steels at certain aging temperatures.

The recrystallization transformation results in at least two morphological forms of sigma. One of these is similar to pearlite with alternate plates of sigma and recrystallized austenite while the other has the sigma predominantly at the recrystallized grain boundaries. This latter form is favored by rapid recrystallization rates with a resultant fine grain size such as is obtained with moderately cold-worked samples aged at high temperatures or heavily cold-worked samples aged at moderate temperatures.

As a result of this work, it can be concluded that the effect of cold work is not to simply produce more nuclei of sigma which grow after recrystallization as postulated by Dulis and Smith (2) but rather that recrystallization itself accelerates the formation of sigma.

Acknowledgments

The authors should like to express their gratitude to the staff of the Allegheny Ludlum Research Laboratory at Brackenridge, Pennsylvania, for their assistance in making this work possible and to the Allegheny Ludlum Steel Corporation for permission to publish these results.

References

1. G. J. Guarnieri, J. Miller and F. J. Vawter, "The Effect of Sigma Phase on The Short-Time High Temperature Properties of 25 Chromium-20 Nickel Stainless Steel," TRANSACTIONS, American Society for Metals, Vol. 42, 1950, p. 981.
2. E. J. Dulis and G. V. Smith, "Effect of Cold Work on Sigma Formation," METAL PROGRESS, September 1952, p. 86.
3. J. I. Morley and H. W. Kirkby, "Sigma-Phase Embrittlement in 25 Cr-20 Ni Heat-Resisting Steels," *Journal,* Iron and Steel Institute, Vol. 72, 1952, p. 129.
4. J. J. Gilman, "Electrolytic Etching—The Sigma Phase Steels," TRANSACTIONS, American Society for Metals, Vol. 44, 1952, p. 566.
5. F. J. Shortsleeve and M. E. Nicholson, "Transformations in Ferritic Chromium Steels Between 1100 and 1500 °F (595 and 815 °C). TRANSACTIONS, American Society for Metals, Vol. 43, 1951, p. 142.

THE LAVES AND Chi PHASES IN A MODIFIED 12 Cr STAINLESS ALLOY

By F. L. VerSnyder and H. J. Beattie, Jr.

Abstract

The phases Ti(C,N), Chi, and a Laves phase (AB_2) have been identified in a series of 12 Cr-4Mo heats with varying additions of titanium as the precipitation promoting element. The composition of the Laves phase was determined approximately as $(Ti_{21}Mo_9)(Fe_{50}Cr_5Si_5)$. Increasing the titanium content in these heats appeared to promote the formation of the Chi phase.

Introduction

MANY a design engineer and metallurgist has no doubt dreamed of the desirability of a practical precipitation or age hardenable ferritic stainless steel (12 Cr variety). However, very little information is available in the literature concerning attempts to devise such an alloy, although the idea has certainly been advanced in a general form (1-2).[1] An evaluation of just such a series of alloys is being conducted in our laboratory.

One aspect of such a study is the need for information concerning the phases present and their relationships. Recently considerable information concerning the Fe-Cr-Mo and Fe-Cr-W equilibrium structures has become available (2-6) which has been most helpful in the present study. This paper presents information concerning the phases encountered in a 12Cr-4Mo ferritic stainless alloy with varying amounts of titanium as the precipitation promoting addition.

Experimental Procedure

The heats or alloys studied were air induction melted, with the customary procedure used in melting titanium containing melts. The resulting castings were 25-pound ingots. The titanium was added to the melt just prior to pouring as a ferro-titanium addition. The chromium was added as a low nitrogen ferro-chromium alloy.

The ingots were subsequently preheated at 1650 °F (900 °C) for 5 hours and equalized at 2050 °F (1120 °C) for 3 hours prior to forging. Swaging was performed at 1975 to 2050 °F (1080 to 1120 °C) to

[1] The figures appearing in parentheses pertain to the references appended to this paper.

A paper presented before the Thirty-sixth Annual Convention of the Society, held in Chicago, November 1 to 5, 1954. The authors, F. L. VerSnyder and H. J. Beattie, Jr., are associated with the Thomson Laboratory, General Electric Co., West Lynn, Mass. Manuscript received May 14, 1954.

Table I
Chemical Composition in Weight Per Cent

Heat No.	C	Mn	Si	P	S	Cr	Ni	Mo	Ti	Al
SM185	0.05	0.43	0.34	0.017	0.034	11.40	0.12	4.06	0.11	0.71
SM186	0.08	0.63	0.81	0.006	0.028	11.70	0.11	4.06	0.74	0.07
SM187	0.04	0.65	0.47	0.005	0.028	11.35	0.12	3.92	2.53	0.62
SM188	0.07	1.75	0.42	0.006	0.026	11.80	0.08	4.12	3.14	0.21
SM189	0.05	1.65	0.40	0.005	0.018	12.00	4.17	4.06	2.87	0.58

¾ inch square size. The stock was annealed after forging at 1700 °F (925 °C) for 1 hour and air-cooled.

The specimens studied in this investigation were all oil-quenched after 1 hour at 1700 °F (925 °C).

The method of study of the phases present was essentially the complementary use of X-ray diffraction and metallography. Samples were first studied microscopically to determine the number of microconstituents present, and to estimate the number and possibly the identity of the phases present in the microstructure. The samples were then electrolytically digested to separate the microconstituents from the matrix as an insoluble residue. Electrolytic digestion of heat SM187 was performed in a 10% HCl electrolyte while heat SM188 was digested using a 5% HCl electrolyte. Drying of the collected residue resulted in a powder suitable for subsequent X-ray diffraction analysis using the Debye-Scherrer powder method. Both a photographic camera and a Geiger counter spectrometer (G.E. XRD-3) were used in obtaining the diffraction patterns.

Differentiation of the phases in the microstructure, in correlation with X-ray diffraction results, was accomplished by the use of metallographic techniques.

The preceding X-ray and metallographic techniques are described in detail elsewhere (7).

Standard quantitative chemical analysis was determined on each heat studied in this investigation. Results of the analyses are listed in Table I.

The Laves phase (AB_2), identified in this work, was essentially the only phase recovered in the electrolytic residue of heat SM187. As a consequence it was decided to obtain a quantitative chemical analysis of this residue.

Results

Examination, in the unetched condition, of metallographic specimens taken from forged bars revealed the presence of titanium carbonitrides in all of the heats. Since this constituent is considered as mechanically included in the alloys during their melting and casting, it is not believed to play a significant role in the phase relationships of the alloys (7) and will henceforth be ignored in the discussion presented in this paper.

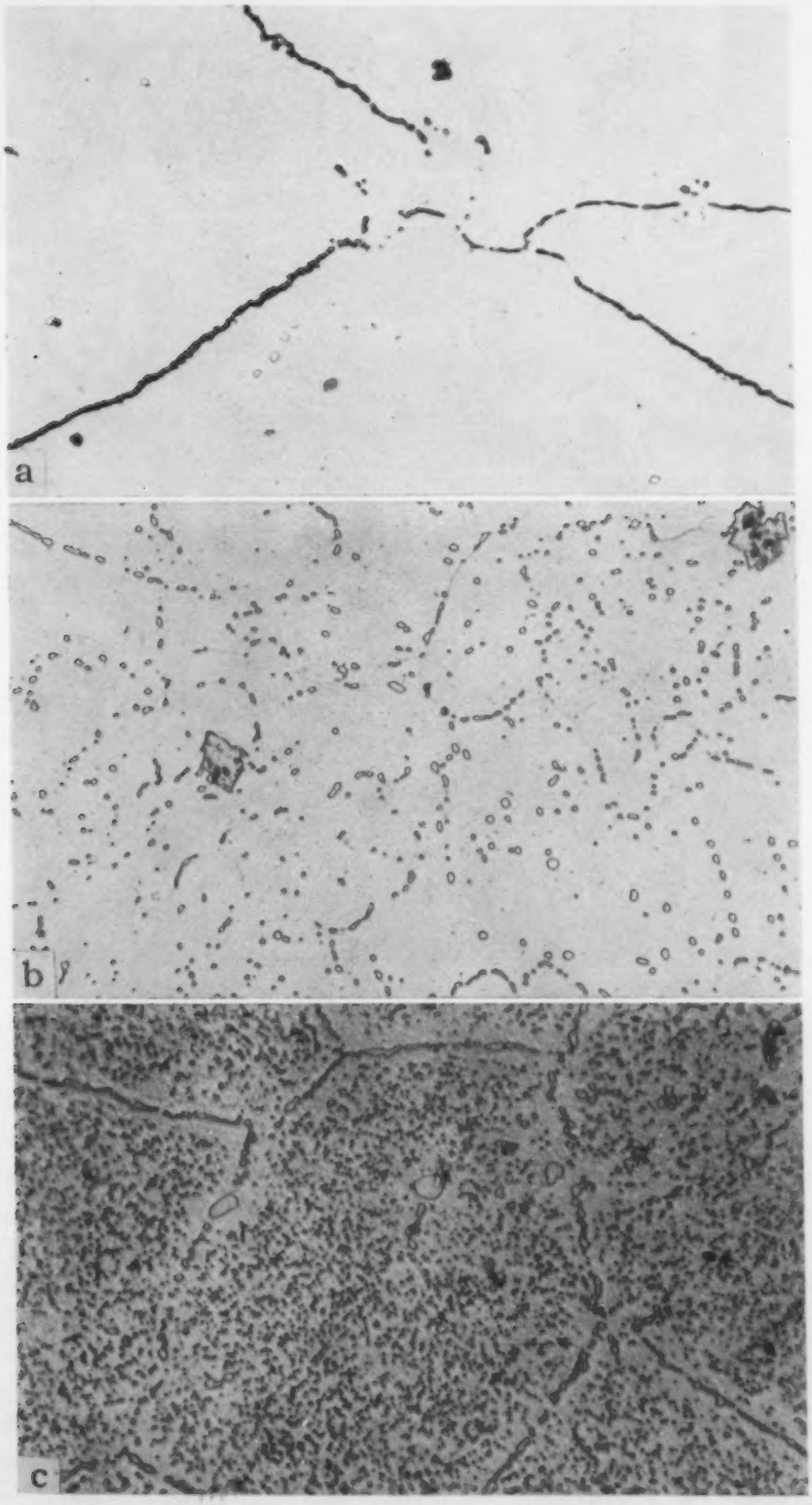


Fig. 1—Specimens Solution Treated at 1700 °F for 1 Hour and Oil-Quenched. Electrolytically etched in 10% chromic acid, 4.5 volts, platinum the cathode. X 500. a—0.11% titanium, heat SM185; b—0.74% titanium, heat SM186; c—2.53% titanium, heat SM187.

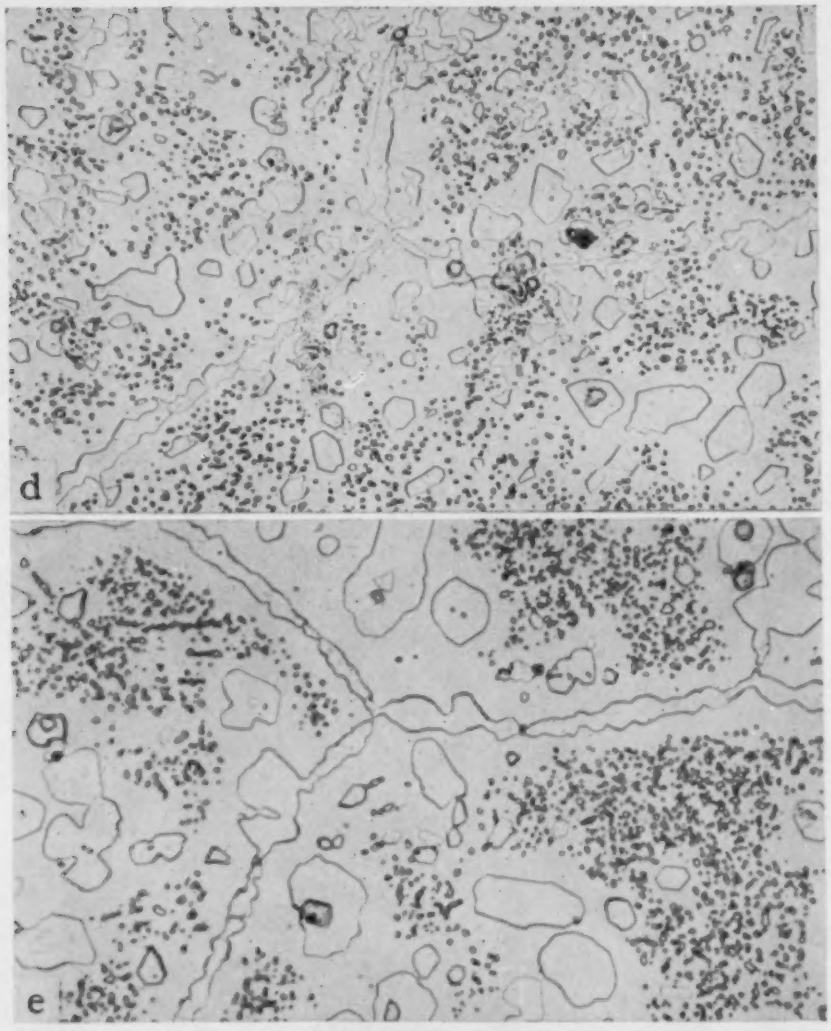


Fig. 1 (Con't)—Specimens Solution Treated at 1700 °F for 1 Hour and Oil-Quenched. Electrolytically etched in 10% chromic acid, 4.5 volts, platinum the cathode. X 500. d—2.87% titanium, heat SM189. e—3.14% titanium, heat SM188.

A forged specimen from each heat was examined microscopically after being oil-quenched from 1700 °F (925 °C). It is observed that one may arrange the microstructures in an orderly succession according to increasing titanium content (Fig. 1a-e). One notes only a small amount of minor phase and grain boundary precipitation in the heat with the lowest titanium content (Fig. 1a). The heat containing 0.74% titanium has an increased amount of minor phase distributed throughout the structure (Fig. 1b). The appearance of a profuse fine spheroidal phase both at the grain boundaries and throughout the structure is evident in the 2.53% titanium heat (Fig. 1c). Up to this point one might consider that the increasing titanium content is bringing about an increase in a single secondary phase. However, a further increase of titanium content to 2.87% results in the appearance of a second minor

Table II
Electrolytic Extract of SM187

d	photographic I*	Geiger-counter I/I_1	Laves phase AB_2 Hex; C6/mmc $a_o = 4.768$Å $c_o = 7.79$Å; $c_o/a_o = 1.63$ (hkl)
2.390Å	ms	50%	(110)
2.198	s	82	(103)
2.070	w	14	(200)
2.034	s+	100	(112)
1.998	s	94	(201)
1.943	mw	20	(004)
1.826	mw	12	(202)
1.760	mw−	6	(104)
1.377	w	4	(300)
1.338	ms+	18	(213)
1.298	ms	18	(006) (302)
1.242	ms	19	(205)
1.215	mw	4	(214)
1.191	ms	14	(220)
1.098	mw	4	(206)
1.047	m	7	(313)
1.020	mw	—	(401)
1.010	mw	—	(224)
0.898	w	—	(118) (410)
0.887	mw	—	?
0.877	m	—	(208)
0.858	mw	—	(405)
0.8226	w	—	(218)
0.8065	vw	—	(406)
0.795	w	—	(330)
0.780	w	—	(0,0,10)
0.7795	m	—	(420)
0.777	s	—	(421)

* s — strong
ms — moderately strong
m — medium
mw — moderately weak
w — weak
vw — very weak

phase (Fig. 1d). An increase in the amount and particle size of this latter appearing phase is noted as the titanium content is increased to 3.14% (Fig. 1e), with a corresponding decrease in the initial minor phase.

As to the identity of the two significant minor phases:

The Laves Phase—The X-ray diffraction data on the electrolytic extract from alloy SM187, the microstructure and thermal treatment of which is indicated in Fig. 1c, are shown in Table II. A photographic pattern using nickel-filtered copper radiation was taken first to reveal the maximum number of lines. The relative intensities in the second column and the interplanar spacings less than 1.04Å in the first column are taken from this pattern.

Next, the powder was mixed with a thin binder and pressed into a shallow recessed trough in a Textilite block for use with the General Electric XRD-3 Spectrogoniometer. From the latter instrument, again using nickel-filtered copper radiation, a recording was made, and the

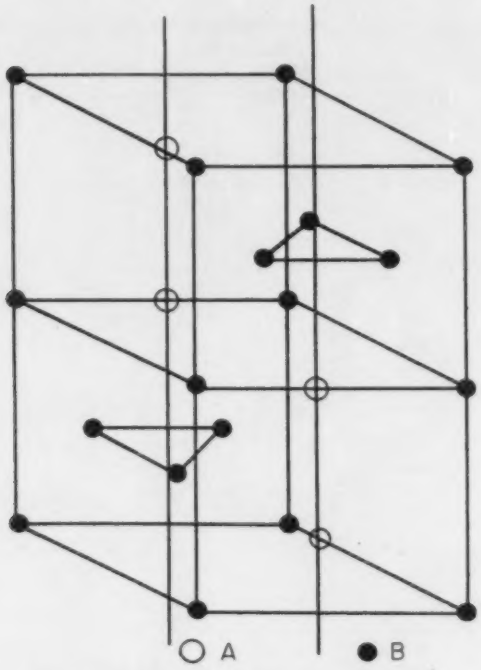


Fig. 2—The Laves Phase AB_2.

interplanar spacings greater than 1.04Å were determined from this. A 3 degree beam slit and 0.1 degree detector slit were used for the recording.

The detector slit then was changed to 0.3 degree, and, setting the goniometer on each of the 16 peaks observed in the recording, the intensities were determined by noting the time intervals required to count 65,536 pulses from the Geiger counter. The background intensity, which was constant over the entire range of angles, was subtracted from these intensities, and the net relative intensities are given as a fraction of the strongest intensity in the third column of Table II. Since the diffraction peaks were less than 0.3 degree in width, these values should represent the integrated intensities. They ranged from 12 to 282 counts per second above background (406 cps.).

In the last column are listed the indices for the hexagonal lattice whose parameters are given at the top of the column. Note that all lines (with one large angle exception from the photographic pattern) can be indexed to this lattice, which is characteristic of a Laves phase similar to one found previously in modified M252-type alloys (7).

Since the patterns indicate that this is essentially the only phase present in the electrolytic extract, it was considered that a quantitative chemical analysis of the extract would provide important information. This yielded the following quantitative analysis for the electrolytic extract:

Element	Fe	Ti	Mo	Cr	Si	Ni	Al
% Weight	54.25	19.00	16.60	5.06	3.11	0.06	0.07
Laves phase/alloy	0.675	7.5	4.24	0.45	5.0	0.5	0.113

The last row is the ratio of per cent weight in extract to per cent weight in alloy, and indicates the tendency for each element to concentrate in the Laves phase. Thus titanium, molybdenum, and silicon strongly tend to concentrate in the phase; iron, chromium, and nickel remain at about the same composition with respect to each other; and, surprisingly, aluminum prefers to remain in the matrix.

The Laves structures represent a close packing of spheres of two sizes, there being about a 20% difference in diameters. This geometrical close packing requires that the smaller atoms be twice as numerous as the larger atoms; this gives a chemical formula of AB_2, where B represents the smaller atom.

Since the chemical analysis of the electrolytic extract shows the presence of more than two elements, the components must be divided into two groups according to atomic size. Below are given the two groups of elements, their Goldschmidt atomic radii, and their atomic per cent based on the above chemical analysis:

A-atoms			B-atoms		
element	atomic radius	atomic %	element	atomic radius	atomic %
Ti	1.49Å	22.63%	Fe	1.26Å	55.45%
Mo	1.36	9.87	Si	1.18	6.32
Al	1.43	0.15	Cr	1.25	5.55
			Ni	1.24	0.06
total atomic %		32.65%A			67.38%B

From their total atomic per cent values it is seen that the composition of the extract corresponds to AB_2 within the uncertainty of the analysis.

Further confirmation has been obtained by considering the integrated intensities of the X-ray diffraction peaks.

This Laves phase is isomorphous with $MgZn_2$ reported by Friauf (8) and also with WFe_2 reported by Arnfelt and Westgren (9). There are 4 A-atoms and 8 B-atoms per unit cell positioned as follows, according to the Wyckoff nomenclature:

2B in 2a: 0, 0, 0; 0, 0, ½

6B in 6h: x, 2x, ¼; 2$\bar{x}$, $\bar{x}$, ¼; x, $\bar{x}$, ¼;
x, 2x, 3/4; 2x, x, 3/4; x, x, 3/4

4A in 4f: 1/3, 2/3, $\bar{z}$; 2/3, 1/3, z;
2/3, 1/3, ½-z; 1/3, 2/3, ½ + z.

This gives the structure depicted in Fig. 2. Friauf gives x=0.170; z=0.062 for $MgZn_2$, while Arnfelt and Westgren give x=⅛; z=0.067 for WFe_2. With the axial ratio c/a very close to the ideal value $\sqrt{8/3}$= 1.633 setting x=⅛ places all B atoms equally distant from each other. The axial ratio of the electrolytic extract is within experimental error of this value. For this reason, and because the electrolytic extract is more similar to WFe_2 than it is to $MgZn_2$, the Arnfelt-Westgren parameters are used.

The intensities of the first 16 lines of Table II were computed according to the formula for powder patterns

$$I_{(hkl)} \sim \frac{1 + \cos^2 2\theta}{\sin^2 \theta \cos \theta} \; p_{(hkl)} \, F^2_{(hkl)},$$

where θ is the Bragg angle, $p_{(hkl)}$ is the multiplicity of the planes (hkl), and $F_{(hkl)}$ is the structure factor for the planes (hkl) determined by the X-ray atomic scattering factors and the atomic positions summed over the unit cell. Following the chemical analysis, it was assumed that the B-atoms consisted of iron, chromium and silicon in the ratio of 10:1:1, and the A-atoms were titanium and molybdenum in the ratio 21:9. The atoms were assumed to occupy their respective A- or B-group positions at random.

Under the experimental conditions, *viz.*, reflection from a thick block of powder with the incident and reflection angles maintained equal, the absorption factor is constant over the entire angular range and therefore need not be considered for relative intensities. However, the temperature correction factor to these calculated intensities is a function of the interplanar spacing and must be applied to the calculated intensities. This factor is

$$\exp\left(\frac{-2B \sin^2 \theta}{\lambda 2}\right),$$

where B is related to the mean square atomic displacement due to thermal motion. By assuming the value $B = 2 \times 10^{-16}$ cm.^{2}, good agreement with the observed intensities is brought about.

Having chosen the temperature parameter B, the relative intensities were calculated for all indices whose spacings are greater than 1.04Å, except those forbidden by the extinction rules, *viz,*

(hhl) ; l odd, and (3h 0 l) ; odd.

These intensities were calculated for the extremities of the A-atom composition ($Ti\,Fe_2$ and $Mo\,Fe_2$) as well as for the complex composition assumed from the chemical analysis ($Ti_{21}Mo_9$) ($Fe_{50}Cr_5Si_5$). These three sets of calculated intensities as well as the observed intensities (including that for the (100) planes taken later) are given in Table III. The reliability indices,

$$R = \frac{\Sigma |I_{obs.} - I_{calc.}|}{\Sigma I_{obs.}}$$

are given at the bottom of each calculated-intensities column; the lowest value for the assumed complex composition shows that it is the best choice of the three.

The satisfactory agreement of observed and calculated intensities shows that the Arnfelt-Westgren positional parameters for WFe_2 is a good choice for the electrolytic extract, for the relative intensities are much more sensitive to atomic position than they are to composition. With the positional parameters and unit cell dimensions determined, the internuclear distances of nearest neighbors to the three positional types (the 2-fold B-atoms, the 6-fold B-atoms, and the 4-fold A-atoms)

Table III
Comparison of Observed Intensities of Laves Phase With Those Calculated for Various Compositions

(hkl)	$I_{calc.}$ $Ti\ Fe_2$	$I_{calc.}$ $Mo\ Fe_2$	$I_{calc.}$ Complex	$I_{obs.}$
(100)	21.8%	0.6%	4.7%	5%
(002)	8.8	0.4	2.5	—
(101)	5.2	3.6	0.3	—
(102)	0.1	7.0	1.7	—
(110)	25.8	56.7	38.5	50
(103)	68.9	101.0	83.7	82
(200)	10.0	14.6	11.8	14
(112)	100.0	100.0	100.0	100
(201)	98.5	73.2	87.5	94
(004)	41.8	9.6	15.7	20
(202)	25.3	5.9	15.3	12
(104)	14.7	8.4	11.7	6
(203)	2.1	0.3	1.5	—
(210)	1.5	0.1	0.3	—
(211)	0.5	0.5	0.06	—
(114)	0.1	0.2	0.2	—
(105)	0.3	4.1	1.4	—
(212)	0.02	1.2	0.3	—
(204)	0.4	0.1	0.2	—
(300)	2.7	6.4	4.1	4
(213)	17.1	24.5	20.8	18
(006)(302)	17.3	17.8	17.6	18
(205)	18.4	18.3	18.3	19
(106)	1.7	2.4	2.1	—
(214)	5.9	3.4	4.7	4
(220)	16.3	14.9	15.0	14
(310)	0.4	0.03	0.08	—
(116)	0.3	0.3	0.00	—
(222)	0.7	0.06	0.13	—
(311)	0.1	0.07	0.00	—
(304)	0.03	0.07	0.04	—
(215)	0.2	2.4	0.8	—
(312)	0.00	0.4	0.08	—
(206)	7.3	5.8	6.8	4
(107)	0.9	0.7	0.8	—
(313)	6.0	9.1	7.3	7
reliability index	0.301	0.232	0.118	

are readily calculated. These are tabulated in Table IV. This information is condensed in the following list of distances between neighboring pairs of atoms:

atomic pair types:	A-A	A-B	B-B
	2.85Å	2.78Å	2.38Å
	2.95	2.80	
		2.83	

These internuclear distances may be checked with the Goldschmidt atomic radii of the elements already given in this paper.

The Chi Phase—Table V is a composite of X-ray diffraction data from two photographic patterns, one taken with nickel-filtered copper radiation and the other with vanadium-filtered chromium radiation. The specimen is the electrolytic extract of alloy SM188, the microstructure and thermal treatment of which is indicated in Fig. 1e.

Table IV

Internuclear Distances for Laves Phase

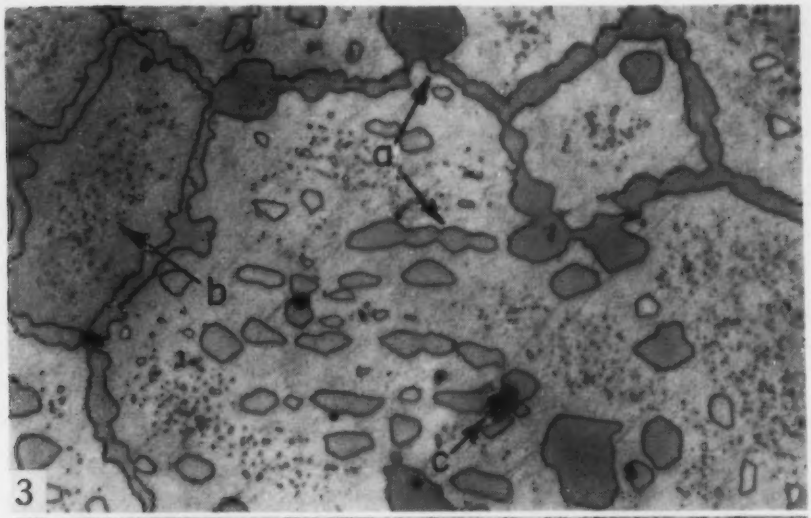
Atom	Neighboring Atoms	Internuclear Distances Å
B|in|2a	6B|in|6h	2.38
	6A|in|4f	2.80
B in 6h	2B in 2a	2.38
	4B in 6h	2.38
	4A in 4f	2.78
	2A in 4f	2.83
A in 4f	3B in 2a	2.80
	3B in 6h	2.83
	6B in 6h	2.78
	1A in 4f	2.85
	3A in 4f	2.95

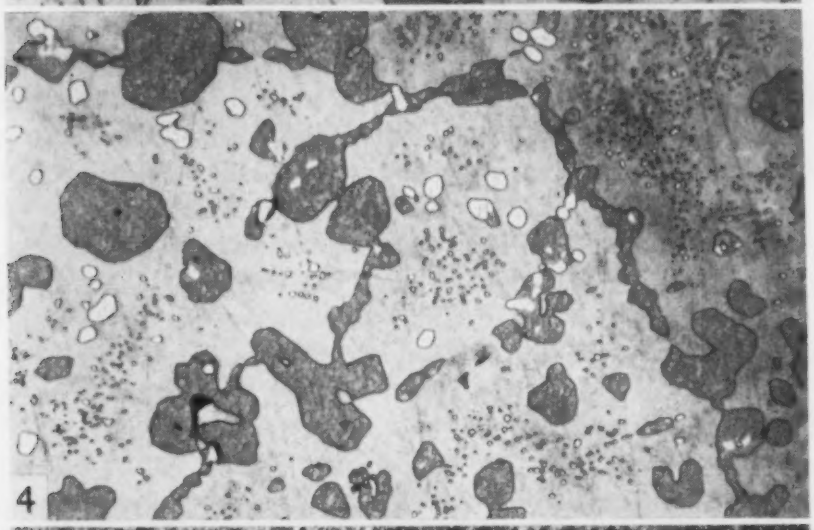
Table V

Electrolytic Extract of SM188

Powder Camera CuKα and CrKα		Chi-phase cub.; I 43m a4 = 8.885Å		Laves phase hex.; C6/mmc aO = 4.768Å cO = 7.79Å c/a = 1.63	TiC cub.; Fm3m aO = 4.32+Å
d	I*	Σh^2	(hkl)	(hkl)	(hkl)
2.546A	w	12	(222)		
2.495	mw				(111)
2.385	m+	14	(321)	(110)	
2.224	w	16	(400)		
2.198	ms			(103)	
2.167	w				(200)
2.096	vs	18	(330)(411)		
2.060	w			(200)	
2.037	ms			(112)	
2.000	ms			(201)	
1.941	mw			(004)	
1.894	ms	22	(332)		
1.814	m	24	(422)		
1.743	m	26	(510)(431)		
1.530	w				(220)
1.479	w	36	(442)(600)		
1.374	w			(300)	
1.336	m+	44	(622)	(213)	
1.298	m			(006)(302)	
1.280	mw	48	(444)		
1.256	m	50	(550)(543)(710)		
1.240	m			(205)	
1.208	s	54	(721)(552)(633)		
1.190	mw			(220)	
1.185	w	56	(642)		
1.126	w	62	(732)(651)		
1.093	w	66	(811)(741)(554)	(206)	
1.046	m	72	(660)(822)	(313)	
0.831	w	114	(855)(871)		
0.817	m	118	(10,3,3)(961)		
0.810	mw	120	(10,4,2)		
0.804	m	122	(11,1,0)(954)		
0.791	ms	126	(10,5,1)(11,2,1)(963)		

*vs — very strong
s — strong
ms — moderately strong
m — medium
mw — moderately weak
w — weak





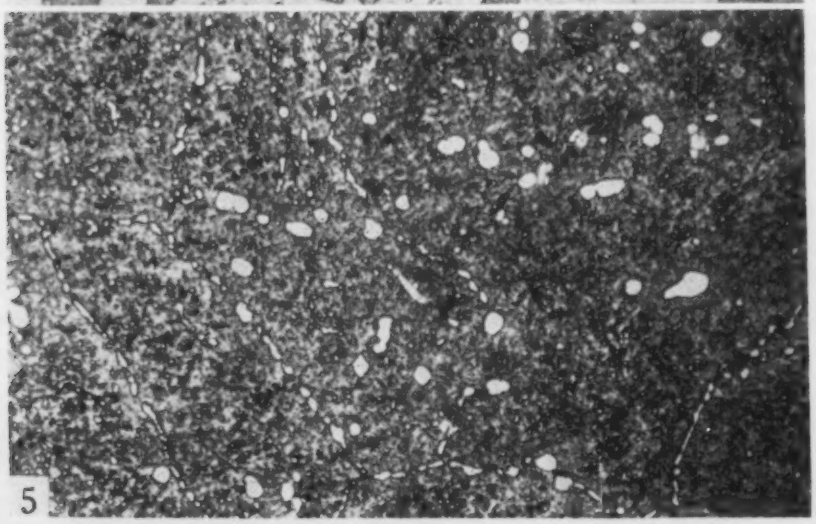


Fig. 3—Specimen Solution Treated at 1700 °F for 1 Hour and Oil-Quenched. Electrolytically etched in 10N NaOH, 1.5 volts, 90 seconds, platinum the cathode. Heat SM188. Microconstituent (a) Chi phase, (b) Laves phase, and (c) Ti(C,N) particles. X 500.

Fig. 4—Specimen Solution Treated at 1700 °F for 1 Hour and Oil-Quenched. Electrolytically etched in saturated $Ba(OH)_2$, 4.5 volts, 20 seconds, platinum the cathode. Heat SM188. X 500.

Fig. 5—Specimen Solution Treated at 1700 °F for 1 Hour and Oil-Quenched. Electrolytically etched in saturated $Ba(OH)_2$, 4.5 volts, 20 seconds, platinum the cathode. Heat SM187. X 500.

The third and fourth columns list the indices for the Chi phase and the Laves phase respectively. Three of the lines belong to titanium carbide, TiC (indexed in last column). From the relative intensities (second column) it is noted that the Chi phase is much more abundant than the Laves phase.

Chi phase was first reported by K. W. Andrews (11) as being present in Cr-Ni-Mo steels. Andrews did not give the molybdenum content, but the stated presence of the carbide $M_{23}C_6$ suggests that it was 5% or less by weight. (More than 5% Mo usually causes the M_6C carbide to appear instead.) Chi phase has also been reported by others (12), (3), with support for Andrews' tentative conclusion that Chi phase is isomorphous with alpha-Mn.

Recently, J. S. Kasper analyzed powdered specimens from an homogenous Chi-phase alloy by X-ray and neutron diffraction (13). He found Chi phase to be completely isomorphous with alpha-Mn, with the positional parameters within ± 0.005 of those found by Bradley and Thewlis for alpha-Mn (14). The composition of the homogenous alloy corresponded to the formula ($Fe_{36}Cr_{12}Mo_{10}$), in consistence with the 58 atoms per unit cell. The phase was found to be ordered with the 10Mo atoms occupying the 2a and 8c positions, these positions having the greatest space available in the structure to accommodate the larger Mo atoms. The lattice parameter for this alloy was 8.920Å.

The lattice parameter of the Chi phase found in Andrews' steel was 8.878Å (reported as 8.860kX.), while that found here in alloy SM188 is 8.885Å, which, like that of Andrews, is appreciably smaller than that found by Kasper. Note that the molybdenum content of Kasper's alloy is greater than that of the other two.

As to differentiation of the phases in the microstructure and correlation with X-ray diffraction results:

Preliminary identification of the Chi phase by metallographic means was performed using the selective etching technique adapted from Gilman (10) by McMullin, Reiter, and Ebeling (3). A forged specimen of heat SM188 was oil-quenched from 1700 °F (925 °C) and etched according to the procedure outlined (3). The Chi phase in this specimen was, using the 10% chromic etchant (Fig. 1e), at least partially recognizable due to its somewhat angular form and the marked difference in its particle size from that of the Laves phase (comparatively small spheroids). When the 10N NaOH etchant was applied the Chi phase passed through the light tan color stage and eventually achieved the blue-gray tint as expected (Fig. 3). The three minor constituents present in this series of alloys have been labeled in this photomicrograph. However, the length of etching time necessary for this to occur was at variance with the etching time reported by McMullin, Reiter, and Ebeling although identical conditions were used. This can most likely be explained by the fact that most stain etchants are extremely sensitive to slight variations in technique and are not precisely

reproducible when applied to similar yet different alloys whose thermal treatments are not the same. In addition, there was a lack of sensitivity of differentiation between the Chi and Laves phase which was disturbing. This was particularly true when attempting to determine if there might be minute amounts of Chi phase in heat SM187 (Fig. 1c) which had not been recovered in the electrolytic extract but which might be observed in the microstructure. In Fig. 1c one notes some comparatively large rather spheroidal particles within the grains as well as a rather heavy grain boundary precipitation, either of which might be Chi phase. It was not possible to discern the exact nature of these particles using the NaOH selective etchant.

The problem was resolved by experimenting with various selective etchants, eventually successfully using the barium hydroxide etchant described by Gilman (10).

Since the Chi phase had been reasonably well ascertained in heat SM188 (Fig. 3) this specimen was re-etched using the $Ba(OH)_2$ etchant. It was found that the Chi phase stained mottled-purple, the matrix stained tan, and the Laves phase remained unstained, i.e., white (Fig. 4). When this same etching procedure was applied to the specimen of heat SM187 (Fig. 1c) the matrix stained darkish-tan, but all of the secondary phase remained unetched (Fig. 5). Naturally in both specimens which were etched using this procedure, the "dot-size" particles appear dark. This is true of only those particles whose size causes them to appear as dots. Particles with a resolvable interior remained unetched. This problem of "dot-size" particles is quite common and does not seriously interfere with the interpretations presented here.

It would seem, then, that excellent correlation is obtained between the microscopic observations and X-ray diffraction results. There is but one secondary phase (Laves) in heat SM187 and two well-distinguished phases in heat SM188 (Chi and Laves).

Discussion

The first item to bring to the reader's attention is that the heat treatment of the specimens studied did not bring about equilibrium conditions, nor was this intended. Rather, it was thought to study the results of a more or less practical heat treatment in an attempt to ascertain the phases present after a rather low solution anneal. Nevertheless, the results obtained should be of general interest.

A consideration of the equilibrium diagrams of the Fe-Cr-Ti (1) and the Fe-Cr-Mo systems would seem to indicate that the Laves phase described by Witte and Wallbaum (15) should be one of the secondary phases observed in this series of heats. That such a phase was identified in these heats is not surprising. However, in view of the complexity of these analyses, it was thought significant that a quantitative chemical determination revealed the Laves phase as being essentially Fe_2Ti, with small amounts of chromium and silicon replacing iron as the B atoms

and molybdenum substituting for almost one-third of the titanium as A atoms. This last observation is somewhat surprising in view of the fact that one would expect aluminum to substitute for titanium, but in this case the aluminum seems to prefer to stay in solid solution. Since aluminum and molybdenum atoms are similar in size, the definite preference of the Laves phase for molybdenum indicates that forces other than geometric packing are involved. Such a force is indicated by the apparent characterization of each of the three Laves structures (all of which have the same local packing principle but differ in stacking arrangements of the hexagonal layers) by ranges of valence-electron densities among the elements magnesium, aluminum, cobalt, nickel, copper, zinc and silver (16). In dealing with transition metals, however, there is considerable difficulty in deciding on the number of "valence electrons." There is a regular succession of the Laves structures in the series with titanium as the A atoms and the B atoms ranging from chromium and nickel as follows (17):

	$TiCr_2$	$TiMn_2$	$TiFe_2$	$TiCo_2$	$TiNi_2$
Structure type:	$MgCu_2$	$MgZn_2$	$MgZn_2$	$MgNi_2$	No Laves phase

The Laves phase observed in this work has an over-all electron structure[2] between that of $TiMn_2$ and $TiFe_2$; and, since the observed structure is of the $MgZn_2$ type, it would seem to fit into the above series.

As titanium is added to this series of heats, the appearance of first the Laves phase followed by the three phase structure containing Laves plus Chi was observed. Titanium, therefore, is apparently established as a Chi phase promoter. Without a chemical analysis of this phase, however, it cannot be established whether titanium is to be found in Chi phase. The observed lattice parameter is smaller than that found elsewhere (3), (13) for Chi phase in the Fe-Cr-Mo system; and since titanium atoms are larger than molybdenum atoms, it seems unlikely that titanium could be present in the Chi phase to any large extent. Titanium may, for instance, occupy the 2-fold (a) positions (which are the most roomy ones), with molybdenum occupying the 8-fold (c) positions, but not to saturation. Alternatively, the titanium may not be in Chi phase at all; but its presence in the matrix may give the molybdenum an increased effective concentration, moving the system toward the alpha/alpha-plus-chi phase boundary for 12% chromium in the Fe-Cr-Mo system (3). Again, perhaps the Chi phase is present as a strictly nonequilibrium product; however, this seems unlikely.

Conclusion

The results of applying the techniques involved in identification of the phases present in these modified 12Cr Stainless heats have led to the following conclusions:

(a) An hexagonal Laves phase (AB_2) has been identified in the

[2] Taking the average number of electrons per atom outside of closed shells.

various heats by both metallographic and X-ray diffraction techniques.

(b) The Chi phase has been identified in the heats of higher titanium content by both X-ray diffraction and metallographic techniques.

(c) The presence of the Laves phase (AB_2) in heat SM187, having the approximate composition (Ti_{21} Mo_9) (Fe_{50} Cr_5 Si_5), has been established.

(d) It would appear that increasing the titanium content in these heats promoted the formation of the Chi phase.

ACKNOWLEDGMENTS

The authors are indebted to R. Sakamoto for providing the materials for this investigation, as well as for helpful discussion; to A. P. Scanzillo, who supervised the analytical chemical methods and S. J. Gootman for the quantitative determinations of the residue containing the Laves phase; to N. E. Brown and others for metallographic work; also, to other members of the Thomson Laboratory who gave willingly and helpfully of their time and experience.

References

1. G. F. Comstock, S. F. Urban, and M. Cohen, *Titanium in Steel,* Pitman Metallurgy Series, Pitman Publishing Corporation, Copyright 1949.
2. H. J. Goldschmidt, "Symposium on High-Temperature Steels for Gas Turbines," *Journal,* Iron and Steel Institute, 1951, p. 249.
3. J. G. McMullin, S. F. Reiter, and D. G. Ebeling, "Equilibrium Structures in Fe-Cr-Mo Alloys," TRANSACTIONS, American Society for Metals, Vol. 46, 1954, p. 799.
4. J. W. Putman, R. D. Potter, and N. J. Grant, "The Ternary System Cr-Mo-Fe," TRANSACTIONS, American Society for Metals, Vol. 43, 1951, p. 824.
5. S. R. Baen and P. Duwez, "Constitution of Fe-Cr-Mo Alloys at 1200°F," TRANSACTIONS, American Institute of Mining and Metallurgical Engineers, Vol. 191, 1951, p. 331.
6. S. Rideout, W. D. Manly, E. L. Kamen, B. S. Lement, and P. A. Beck, "Intermediate Phases in Ternary Alloy Systems of Transition Elements," *Transactions,* American Institute of Mining and Metallurgical Engineers, Vol. 191, 1951, p. 872.
7. H. J. Beattie, Jr., and F. L. VerSnyder, "Microconstituents in High Temperature Alloys," TRANSACTIONS, American Society for Metals, Vol. 45, 1953, p. 397.
8. J. B. Friauf, "The Crystal Structure of Magnesium Di-Zincide," *Physical Review,* Vol. 29, 1927, p. 34.
9. H. Arnfelt and A. Westgren, JERNKONTORETS ANNALER, Vol. 118, 1935, pp. 185–196.
10. J. J. Gilman, "Electrolytic Etching—The Sigma Phase Steels," TRANSACTIONS, American Society for Metals, Vol. 44, 1952, p. 566.
11. K. W. Andrews, *Nature,* Vol. 164, 1949, p. 1015.
12. P. K. Koh, "Occurrence of Chi Phase in Molybdenum-Bearing Stainless Steels," *Transactions,* American Institute of Mining and Metallurgical Engineers, Vol. 197, 1953, p. 339.
13. J. S. Kasper, "The Ordering of Atoms in the Chi Phase of the Fe-Cr-Mo System," ACTA METALLURGICA, Vol. 2, 1954, p. 456.

14. A. J. Bradley and J. Thewlis, "The Crystal Structure of α-Manganese," *Proceedings,* Royal Society, Series A, Vol. 115, 1927, p. 456.
15. H. Witte and H. J. Wallbaum, *Zeitschrift für Metallkunde,* Vol. 30, 1938, p. 221.
16. G. V. Raynor, "Progress in the Theory of Alloys," *Progress in Metal Physics,* 1950, Interscience Publishers, Inc.
17. W. Arbiter, "New High Temperature Intermetallic Materials," WADC Technical Report 53-190, May 1953.

DISCUSSION

Written Discussion: By K. W. Andrews, The United Steel Companies Limited, Research and Development Department, Rotherham, England.

It is gratifying that since the existence of chi phase was first reported, several investigators, including the present authors, have provided further evidence of its nature, constitution and mode of occurrence. This paper would have been of interest to me on that account alone but becomes of double interest because we too have encountered a hexagonal Laves type phase under similar conditions.

Our earlier experience with steels containing chi phase was gained with compositions including nickel as well as chromium and molybdenum,[3] but we were then unable to reach any definite conclusions about its composition or whether it was a stable phase. The work of McMullin and colleagues [4] established that it was a stable constitutent. Although it exists in a definite composition and temperature range in the system Fe-Cr-Mo, it is also clear that chi phase can vary considerably in composition in some of the steels in which it has been observed. More recently we have been interested in chromium base steels containing molybdenum and titanium, including compositions of both higher and lower chromium than those of the authors. The higher chromium steels show that chi phase, the carbides M_6C, $M_{23}C_6$ and possibly other constituents may appear (the work is still in hand). We do not find chi phase in the lower (8% chromium) range but here the constituent based on Fe_2Ti is important.

This Laves phase is probably of similar composition to that of the authors. Its lattice parameters are a = 4.770 Å and c = 7.780 Å. It is intended to publish further details later. In the meantime, it is of interest to refer to the first sentence in the introduction to the paper—concerning the desirability of producing a practical precipitation hardenable ferritic stainless steel. In our experience the presence of the strong ferrite formers molybdenum and titanium means that the chromium content can be considerably lower than 12, e.g. 7 or 8, and still maintain the ferritic condition. It is of interest that although some of the titanium is combined as TiC this phase does not have a very marked effect on the properties of the steel and does not generally undergo appreciable solution or re-precipitation. On the other hand, the Laves phase does dissolve or precipitate readily, but it does not act as a precipitation hardening constitutent. In fact, although it is the main precipitating phase between 1050 and 750 °C, it weakens the alloy by removing titanium from solid solution. Hence the role of titanium

[3] K. W. Andrews and P. E. Brooks, "Chi Phase in Alloy Steels; Its Relationship to Sigma Phase," *Metal Treatment and Drop Forging,* Vol. 18, July 1951, p. 301.
[4] J. W. McMullin, S. F. Reiter and D. G. Ebeling, "Equilibrium Structures in Fe-Cr-Mo Alloys," TRANSACTIONS, American Society for Metals, Vol. 46, 1954, p. 799.

in a steel of this kind is in a solid solution hardening capacity, and precipitation of the intermetallic phase should be avoided.

Appreciable precipitation hardening is obtained at 750 °C or below by precipitation of the carbide $(Cr, Mo, Fe)_{23} C_6$. Considerable amounts of this carbide can precipitate, in spite of the presence of titanium, which although still regarded in many quarters as a "carbide stabilizer" is quite clearly only partially effective in this capacity. This fact has been noted in connection with many other types of titanium bearing steel. Titanium itself is, however, beneficial in other ways and the chromium base carbide can itself be a valuable constituent. We hope to publish fuller details of this work in due course.

Written Discussion: By Kehsin Kuo, research metallurgist, Royal Institute of Technology, Stockholm.

The authors are to be complimented on their excellent correlation of the chemical, microscopic, and X-ray examinations of the minor phases existing in a modified 12 chromium stainless alloy.

The authors' finding of the existence of the Laves phase AB_2 with a composition very close to $(Ti_{21}Mo_9)(Fe_{80}Cr_5Si_5)$ is most interesting. Though the authors have mentioned the composition limits for this compound as $TiFe_2$ and $MoFe_2$ and have also used these formulae for the intensity calculations, they have not taken into consideration the existence of the binary phase $MoFe_2$.

According to earlier works on the constitution of the Fe-Mo binary system,[5] the existence of $MoFe_2$ has not been confirmed. Recently Zaletaeva, Lashko, Nesterova and Inganova [6] reported that they have found this compound together with carbides in a steel with a nominal composition of 0.1% carbon, 16% chromium, 25% nickel, and 6% molybdenum after annealing for 100 hours at 700 °C or 6 hours at 850 °C. The reported lattice constants are: $a = 4.73$ Å and $c = 7.72$ Å, comparable to those of WFe_2 found by Arnfelt and Westgren,[7] $a = 4.727$ Å and $c = 7.704$ Å. Zaletaeva et al. mentioned nothing about the chemical composition of this Laves phase, and since their steel contains besides molybdenum also chromium and nickel, we cannot be certain that their Laves phase is a binary compound of molybdenum and iron, especially when quite a large number of ternary Laves phases of transition metals are known to exist.[8]

A Laves phase has also been found by this writer to exist together with the M_6C carbide in a molybdenum-nickel steel with 0.17% carbon, 0.38% silicon, 0.40% manganese, 0.006% phosphorus, 0.013% sulphur, 10.1% molybdenum, and 2.27% nickel after annealing at 800 °C for 25 hours and the lattice constants are: $a = 4.738$ Å, $c = 7.740$ Å. The nickel content of the extracted mixture of carbide and Laves phase was only about 1–2%; in other words, nickel is not an essential element for the formation of these phases. This may perhaps be considered as an indirect evidence of the existence of $MoFe_2$ in the molybdenum-iron binary system and may also serve to explain why in the authors' alloy SM187 it is molybdenum but not aluminum that substitutes for titanium in $TiFe_2$. Have the authors also found this compound in the low-titanium alloys (SM185 and SM186)?

---

[5] M. Hansen, "Der Aufbau der Zweistofflegierungen," Julius Springer, 1936.

[6] R. P. Zaletaeva, H. F. Lashko, M. D. Nesterova, and S. A. Inganova, "A New Intermatallic Compound in The Binary System Fe-Mo," *Doklady Akademii Nauk SSSR*, 1951, Vol. 81, p. 415–416.

[7] H. Arnfelt and A. Westgren, *JERNKONTORETS ANNALER*, Vol. 118, 1935. p. 185–196.

[8] K. Kuo, "Ternary Laves And Sigma-Phases of Transition Metals," ACTA METALLURGICA, Vol. 1, 1953, p. 720–724.

Besides the Chi phase in the Fe-Cr-Mo ternary system, an analogous phase has also been found by the present writer in the iron-chromium-tungsten ternary system with a composition very close to 40% iron, 20% chromium, and 40% tungsten.

Written Discussion: By A. G. Allten and P. Lillys, Crucible Steel Co. of America Research Laboratory, Harrison, N. J.

We were considerably interested in this paper and, particularly, in the work reported on the Chi phase. We have studied an experimental steel analyzing 0.04% carbon, 1.0% manganese, 4.0% nickel, 16.0% chromium, 3.0% molybdenum. Chi phase was found in this steel after treatments of 16 hours at temperatures between 1400 and 1700 °F from the as-forged condition.

The amount of Chi phase present after a 16 hour treatment at 1400 °F, was sufficient to permit complete identification of the phase from an X-ray diffraction pattern obtained from a microsection of the steel. However, an electrolytic extraction of the Chi phase was also made. The extracted Chi phase had a lattice parameter of 8.887Å. The line intensities of the diffraction pattern compared well with the intensities reported by Ver Snyder and Beattie for the Chi phase extracted from their steel, SM188.

The steel studied by us is similar in composition to the authors' steel, SM189, except that our steel contained no titanium or aluminum. The chemical composition of SM189 suggests that this steel was completely ferritic at 1700 °F. Our steel, on the other hand, contained both austenite and ferrite in the 1400 to 1700 °F temperature range.

Also, we found only traces of Chi phase after a 1700 °F, 16 hour treatment, whereas the authors show a considerable amount in their Fig. 1d for the titanium-bearing SM189 steel as treated 1700 °F, 1 hour. This observation may be interpreted as favorable evidence for the authors' conclusion that titanium supports the formation of Chi phase.

The amount of Chi phase present in our steel in the range 1400 to 1700 °F was greatest at 1400 °F and decreased markedly as the temperature was raised to 1700 °F. Also there was somewhat more Chi phase present after 16 hours at 1600 °F than after only one hour.

The Chi phase formed initially in the boundaries between the austenite and ferrite. Lineal analysis of samples heated for 1 and 16 hours at 1600 °F indicated that the amount of austenite in the steel increased slightly with an increase in time. Thus, the steel became less ferritic as the amount of Chi phase increased. We attribute this increase in amount of austenite to removal of some of the chromium and molybdenum from solution in the ferrite by formation of the Chi phase.

We found that extreme brittleness was associated with the presence of large amount of Chi phase in our steel and we would be interested to know if the authors found this brittleness in the steels which they studied.

Authors' Reply

The authors are grateful to the discussers for their valuable contributions.

Dr. Kuo's information about Laves phases close to the $MoFe_2$ composition is enlightening. We did not mean to imply that such a phase exists when we calculated its theoretical X-ray intensities for comparison with those of other compositions.

Dr. Kuo's data from nickel-molybdenum steels appear to give strong evi-

dence for the existence of $MoFe_2$. The discovery of a Laves phase in 16-25-6 by Zaletaeva et al, however, is surprising. We have observed a minor phase other than the carbides in this alloy during aging and interpret it as a double nitride of chromium and molybdenum (Reference 7).

In reference to the chi phase of the approximate composition—40% iron, 20% chromium, and 40% tungsten, we presume these are weight percentages of a homogenous chi phase. This leads to the unit cell atomic formula $Fe_{31.5}$ Cr_{17} $W_{9.5}$, as compared with the molybdenum ternary chi phase formula Fe_{36} Cr_{12} Mo_{10} (Reference 13). It might be interesting to see whether the X-ray intensities of the iron-chromium-tungsten chi phase indicate that the essentially ten tungsten atoms are ordered at the 2a and 8c positions, where Dr. J. S. Kasper finds the ten molybdenum atoms.

The Laves phase was identified in Heats SM-185 and 186 by metallographic means only and was not correlated with X-ray diffraction.

We are pleased that Dr. Andrews's work on similar steels agrees generally with the work reported in this paper.

Apparently, Dr. Andrews's steels were higher in carbon content than ours. We are particularly interested in Dr. Andrews's indication that $M_{23}C_6$ is a more stable carbide in these ferritic alloys than TiC. We have had similar indications concerning M_6C in higher molybdenum austenitic alloys.

The view that titanium is a "carbide stabilizer" can lead to quite erroneous impressions—particularly if one relies on titanium to carbon ratios for an indication of expected room or high temperature physical properties. Actually, in the "superalloy" class of materials considering titanium as a carbide stabilizer is quite unjustified, for the reactions occurring in these alloys cannot be compared to those of a titanium stabilized 18-8 stainless.

The more complicated lattice structures appear to be very stable. The simpler intermediate structures like TiC precipitate more rapidly, but their formation is only temporary until the complicated, sluggishly formed structures like $M_{23}C_6$ and M_6C replace them. The steel tempering reaction martensite $\longrightarrow$ epsilon carbide $\longrightarrow$ Fe_3C is another example of this, as it proceeds from the simplest, least stable to the most complicated, most stable lattice structure.

Thinking along these lines, a structure as complicated as chi phase should be very stable. Since writing this paper we have obtained further evidence of its stability in these stainless alloys. As stated in the paper, all heats had been annealed for one hour at 1700 °F (925 °C), and heat SM-187 gave a profuse precipitation of Laves phase only. Reannealing this heat for 200 hours at the same temperature caused the precipitation of the chi phase. The X-ray diffraction pattern of its electrolytic extract is very similar to that of SM-188 shown in Table V. The lattice parameters of the Laves phase remained unchanged, while the lattice parameter of chi was 8.90Å.

We are grateful to Messrs. Allten and Lillys for reporting the similarity in lattice parameter and X-ray intensities between their chi phase and ours. As their steel contained no titanium or aluminum but was otherwise similar to ours, this further suggests the lack of participation in this phase by titanium even when it is present in the alloy.

Allten and Lillys give our annealing temperature as the upper limit for the appearance of chi phase in their steel. Apparently the addition of titanium extends this limit in our steels.

As to the mechanical properties of these alloys, those having lower titanium

concentrations are brittle and have poor high temperature strength properties. Perhaps the latter is due to the removal of titanium from solid solution by the precipitation of the Laves phase, as suggested by Dr. Andrews. Those heats having enough titanium to precipitate the chi phase had good high temperature properties and were ductile at elevated temperatures but were quite brittle at room temperature.

AUSTENITIC CHROMIUM-MANGANESE-NICKEL STEELS CONTAINING NITROGEN

By Russell Franks, W. O. Binder and James Thompson

Abstract

A comprehensive study has been made of the structure of chromium-manganese-nickel steels containing nitrogen in view of the interest in developing high manganese stainless steels to conserve nickel. The principal object of this investigation was to determine the composition ranges which provide stable austenite, optimum mechanical properties, and corrosion resistance. Stable austenitic structures are desired because the presence of critical amounts of delta ferrite at grain boundaries during hot working is known to promote hot working difficulties due to cracking. The investigation deals principally with steels of high nitrogen content thus taking advantage of the improved hot workability imparted to the steels by nitrogen because of its stabilizing influence on austenite.

To establish the austenitic regions, the structural constitution of steels containing 0.10% carbon was studied in the range of 12 to 18% chromium, 1 to 22% manganese, and 0 to 14% nickel to evaluate the influence of chromium, manganese, and nickel on austenite formation. The formation of austenitic structures in the cast condition requires greater amounts of nickel and nitrogen than in the hot-worked condition.

It was found that steels containing 16 to 17.5% chromium, 3.5 to 4.5% nickel, 7 to 9% manganese, 0.06 to 0.12% carbon, and 0.12 to 0.18% nitrogen have excellent austenitic stability, and the mechanical properties and work hardening characteristics of these steels are comparable to those of the austenitic 18% chromium—8% nickel steels. Large ingots of these steels should exhibit good hot working properties if their initial hot working temperature is kept at a maximum of 1225 °C (2235 °F).

THE first semicommercial experiments made on the chromium-manganese-nickel steels were started in December of 1930(1).[1] Many of the early steels investigated contained up to slightly over 1%

[1] The figures appearing in parentheses pertain to the references appended to this paper.

A paper presented before the Thirty-sixth Annual Convention of the Society, held in Chicago, November 1 to 5, 1954. Of the authors, Russell Franks is manager, Technical Service and Development Department, Electro Metallurgical Co., Pittsburgh, W. O. Binder is group manager, Technical Service and Development Laboratory, and James Thompson is associated with the Technical Service and Development Laboratory, Electro Metallurgical Co., Niagara Falls, N. Y. Manuscript received April 16, 1954.

copper in addition to chromium contents between about 12 and 25%, with manganese contents between 5 and 20%, and nickel contents up to about 10%. This work showed that while copper (2,3) had a stabilizing influence on the austenitic structure, it was necessary to add more than 5% nickel, with chromium contents in the vicinity of 17 to 18% and an excess of 6% manganese to obtain an austenitic structure. These steels also contained up to 0.20% carbon, and it was observed that, as the carbon approached this value, less difficulty was encountered in securing the austenitic structure.

The austenitic structure obtained in these steels was not so stable as that of the well known 18% chromium—8% nickel steel, especially at the hot-rolling temperatures. Further, it was observed that the chromium-manganese-nickel steels had a tendency to tear during the initial hot working into bars, rods, and strip. The investigation of these steels was continued, and it was subsequently found that nitrogen (4,5), also, was effective in stabilizing the austenite, which resulted in improved hot workability. The nitrogen was found to be far more influential than copper in promoting austenite formation, and while the investigation strongly indicated commercial possibilities for austenitic stainless steels of this type, full information was not obtained on the structural constitution of the steels as influenced by changes in the contents of the major and minor elements.

The present study of the chromium-manganese-nickel steels containing nitrogen has been prompted by an effort to conserve nickel, and at the same time, to aid in expanding the utilization of stainless steels. The chief object has been to investigate the structure and mechanical properties of a number of steels containing different percentages of chromium, manganese, nickel, and carbon, with and without nitrogen, to take advantage of the improved hot-workability imparted to the steels by nitrogen because of its stabilizing influence on the austenitic constituent. The data in this paper represent results of a recent investigation of the chromium-manganese-nickel steels conducted by the Technical Service and Development Laboratory of the Electro Metallurgical Company.

Steels Investigated

The work was conducted on a series of steels containing 12 to 18% chromium, 1 to 20% manganese, 0 to 14% nickel, and 0.06 to 0.12% carbon with nitrogen contents between about 0.03 and 0.18%. The majority of the heats were melted in a high frequency induction furnace using charges weighing about seventeen pounds. The basic raw materials consisted of Armco iron, low carbon ferrochromium, high nitrogen ferrochromium, or high nitrogen manganese bearing alloys, low carbon ferromanganese metal, electrolytic nickel, and silicon metal.

The steels were cast into 2-inch square ingots, which were hot-

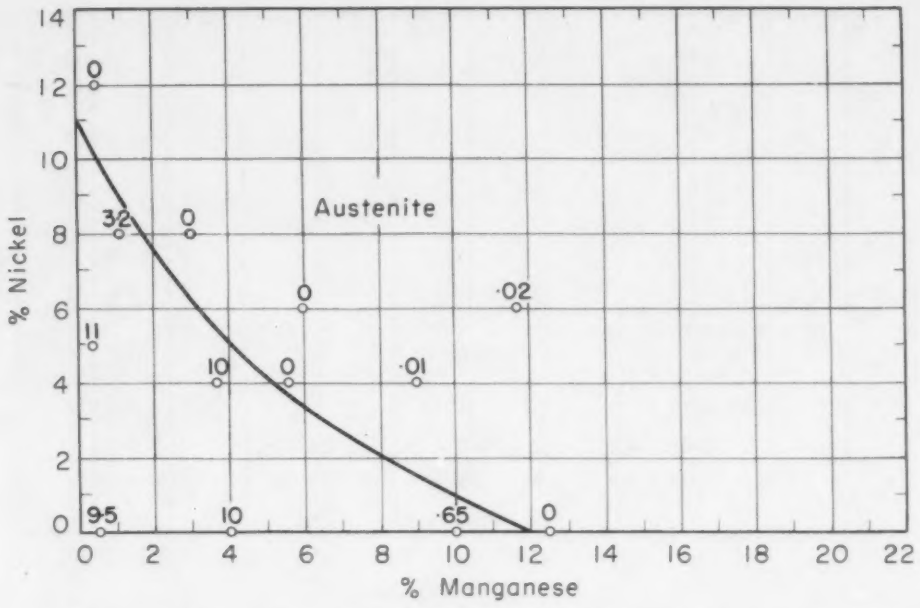


Fig. 1—Phases Present in 12% Chromium Steels Containing 0.10 to 0.12% Carbon and 0.08 to 0.09% Nitrogen After Heating 15 Minutes at 1075 °C and Air Cooling.

worked at an initial temperature of 1150 to 1175 °C (2100 to 2145 °F) into ¼ and 1/16-inch thick strips. After hot working, these were solution-treated fifteen minutes at 1075 °C (1965 °F) and air-cooled prior to testing. Some of the steels were cold-reduced 20% in thickness by cold rolling for austenite stability tests. In these cases, the steels were hot-rolled to 0.075-inch thick strip, heat treated at 1075 °C (1965 °F), air-cooled, and subsequently cold-rolled to 0.06-inch thick strip after descaling.

Phases in Wrought Steels After Heating at 1075 °C and Air Cooling

All the steels were examined by means of a magnetic test for the presence of the delta ferrite constituent, after the heat treatment at 1075 °C (1965 °F). On a number of occasions, the magnetic test was checked by metallographic examination. The relative magnetism was measured by using a magnetic balance that determined the force in grams necessary to separate a ¼-inch thick sample 1-inch square from the pull of a small electromagnet. The steels that exhibited no readily detectable quantity of the delta ferrite constituent at X500 magnification were separated from the magnet by a weight of 0.1 gram or less. With increasing quantities of ferrite in the structure, the force required to separate the sample increased proportionately.

The information obtained from these tests was used to construct the diagrams illustrated in Figs. 1 through 8. The numerals on the diagrams represent the grams force necessary to separate the steel from

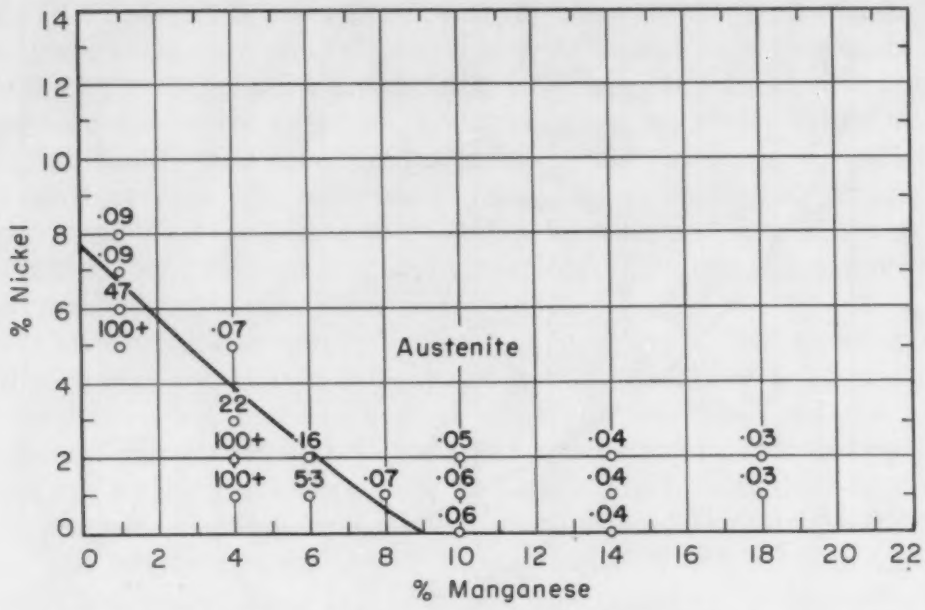


Fig. 2—Phases Present in 14.3% Chromium Steels Containing 0.10 to 0.12% Carbon and 0.12 to 0.15% Nitrogen After Heating 15 Minutes at 1075 °C and Air Cooling.

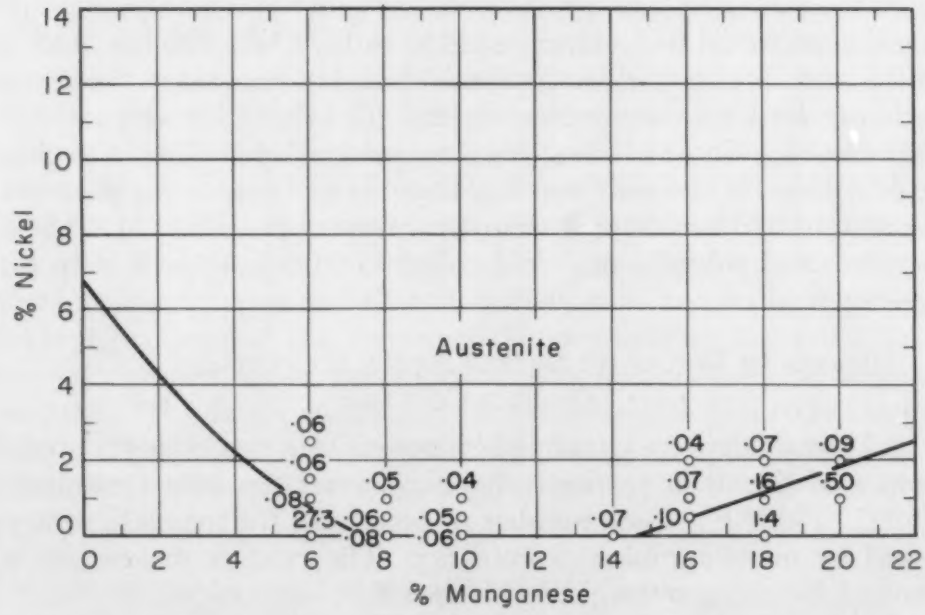


Fig. 3—Phases Present in 15.3% Chromium Steels Containing 0.10 to 0.12% Carbon and 0.12 to 0.15% Nitrogen After Heating 15 Minutes at 1075 °C and Air Cooling.

the magnet. The diagrams are, to a large extent, self-explanatory, but it is worthwhile to discuss them briefly.

The influence of chromium at levels of 12,14,15,16, and 17% on the extent of the austenitic region at 1075 °C (1965 °F) is illustrated in Figs. 1 through 5, inclusive. These steels contained about 0.10% carbon and from 0.08 to 0.15% nitrogen with the different percentages

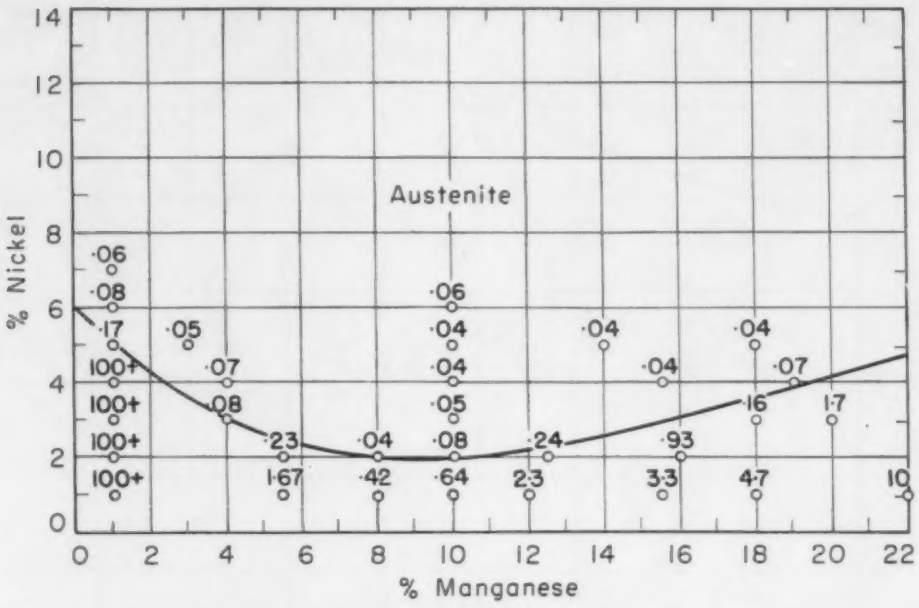


Fig. 4—Phases Present in 16.3% Chromium Steels Containing 0.10 to 0.12% Carbon and 0.12 to 0.15% Nitrogen After Heating 15 Minutes at 1075 °C and Air Cooling.

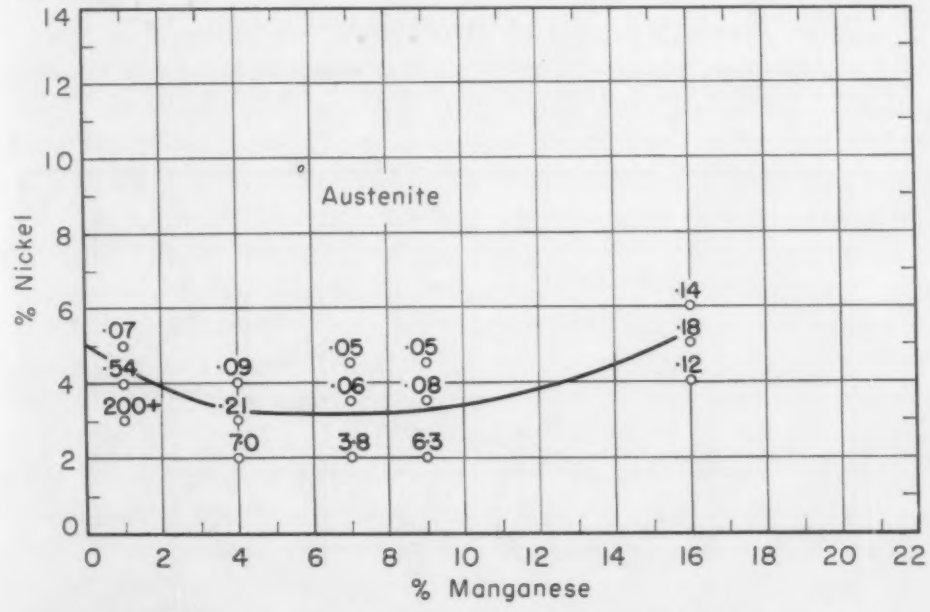


Fig. 5—Phases Present in 17.3% Chromium Steels Containing 0.10 to 0.12% Carbon and 0.12 to 0.15% Nitrogen After Heating 15 Minutes at 1075 °C and Air Cooling.

of manganese and nickel designated on the diagrams. It is observed that, when chromium exceeds about 15%, it is no longer possible, with manganese alone, to make the steels fully austenitic by rapid cooling from 1075 °C (1965 °F). Also, there is a tendency for the delta ferrite constituent to increase with increasing manganese content. On the other hand, it will be shown later that increasing the manganese content increases the relative stability of the austenite in the steel. The figures

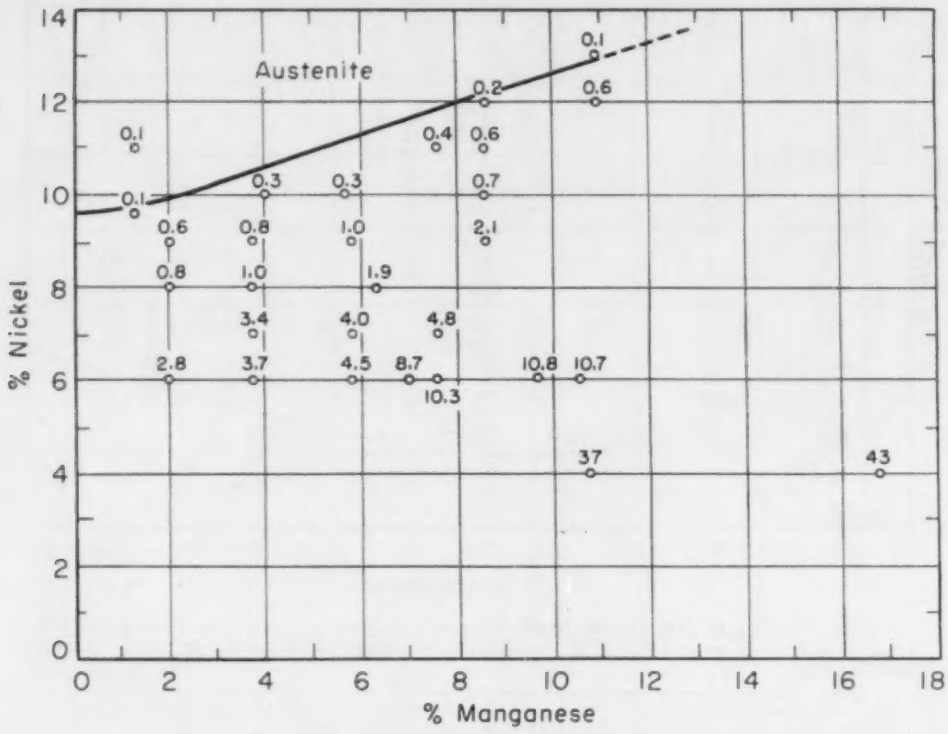


Fig. 6—Phases Present in 18.5% Chromium Steels Containing 0.05 to 0.08% Carbon and 0.03 to 0.05% Nitrogen After Heating 15 Minutes at 1075 °C and Air Cooling.

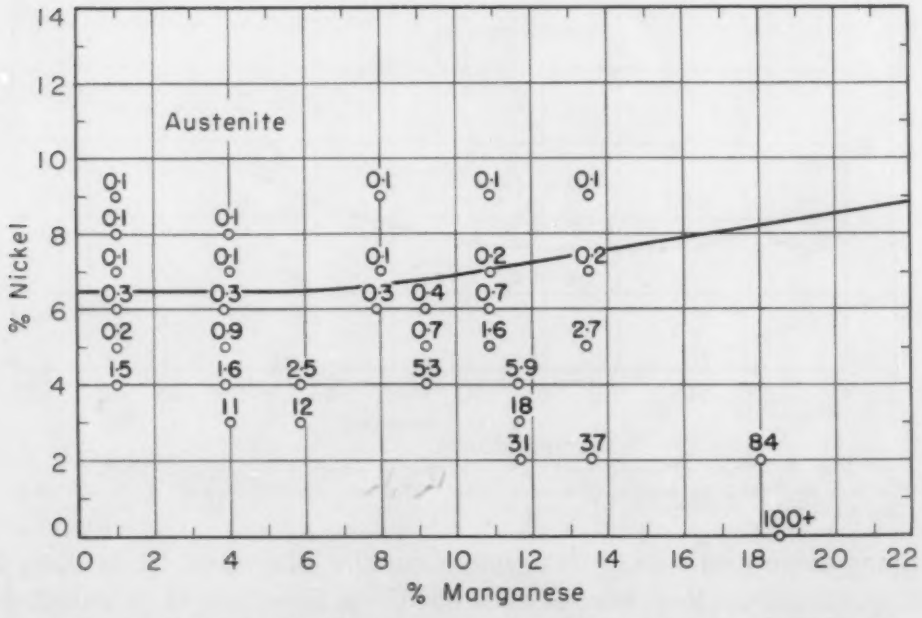


Fig. 7—Phases Present in 18.5% Chromium Steels Containing 0.05 to 0.08% Carbon and 0.12 to 0.15% Nitrogen After Heating 15 Minutes at 1075 °C and Air Cooling.

further show that a fully austenitic steel cannot be secured at the 1% nickel level without decreasing the chromium content below 16% or increasing the nitrogen beyond 0.15%.

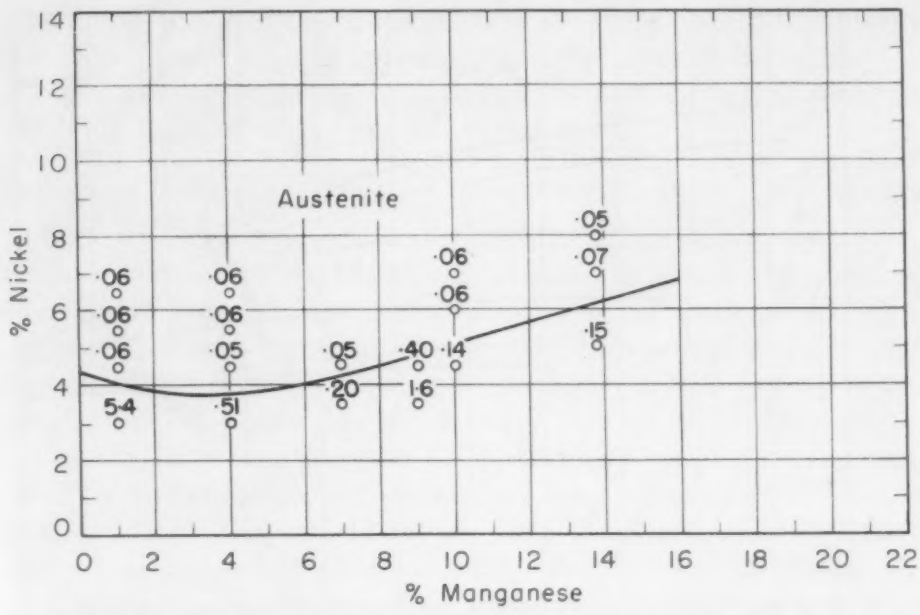


Fig. 8—Phases Present in 18.5% Chromium Steels Containing 0.10 to 0.12% Carbon and 0.12 to 0.15% Nitrogen After Heating 15 Minutes at 1075 °C and Air Cooling.

Fig. 6 presents the significant structural features of the 18% chromium steels containing 0.05 to 0.08% carbon and about 0.03% nitrogen. It is shown here that increasing manganese at a constant nickel content increases the relative quantity of the delta ferrite in the steel. The increased size of the delta ferrite-austenite field was not anticipated in view of the austenite forming tendency of manganese when added to iron and iron-chromium alloys. Thus, it appears that at this chromium level manganese functions primarily as a stabilizer of the austenite formed through the influence of carbon, nitrogen, and nickel.

Fig. 7 shows the structure of steels of similar compositions to which 0.12 to 0.15% nitrogen has been added. The outstanding difference between Figs. 6 and 7 is in the size of the delta ferrite-austenite region. This region is greatly contracted by the increase in nitrogen, and, depending upon manganese content, the boundary up to 14% manganese for an austenitic structure lies between 6.5 and 7.5% nickel.

The foregoing data reveal the effectiveness of nitrogen as an austenite-former and indicate the significant savings in nickel to be gained by incorporating nitrogen in steels of this kind.

In the next series, the carbon content was increased to 0.10% with about 18% chromium and 0.12 to 0.15% nitrogen. The data on these steels are illustrated in Fig. 8, which show that carbon also markedly contracts the delta ferrite-austenite region. It is clear that in the presence of 0.10% carbon only 4 to 5% nickel is required to produce a fully austenitic structure. A greater reduction in nickel would require a lowering of the chromium or an increase of the nitrogen content.

Fig. 9 is a summary chart showing the structures of the chromium-

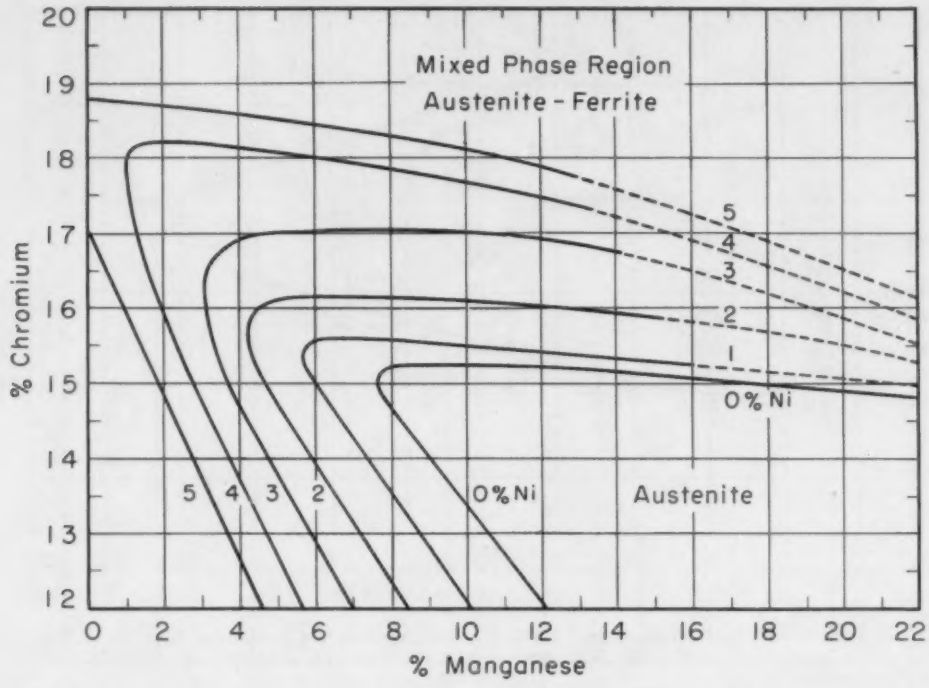


Fig. 9—Structure of 12 to 18% Chromium—0 to 22% Manganese—0 to 10% Nickel Steels Containing 0.10 to 0.12% Carbon and 0.08 to 0.15% Nitrogen After Heating 15 Minutes at 1075 °C and Air Cooling.

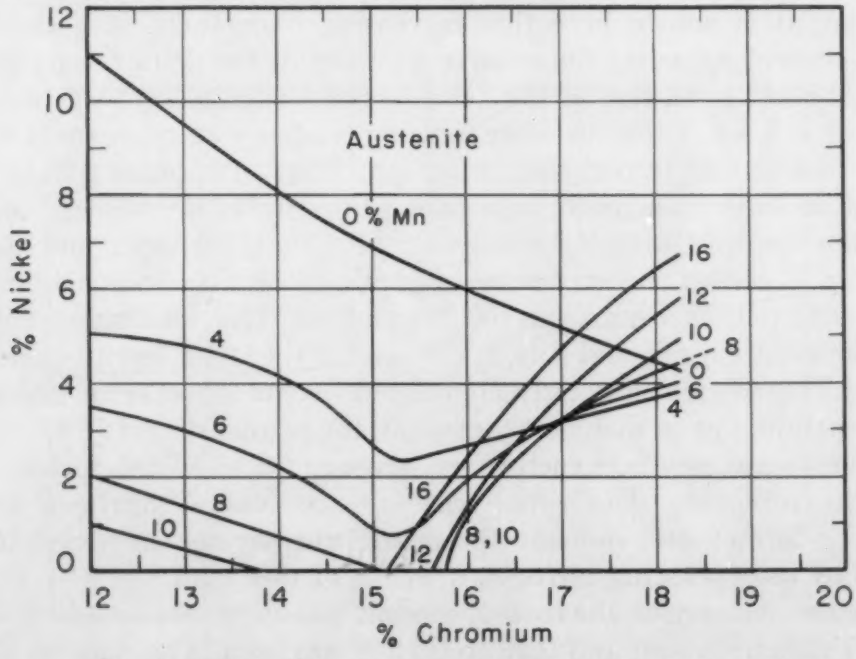


Fig. 10—Effect of Manganese or Size of Austenitic Region in Steels Containing 0.10 to 0.12% Carbon and 0.08 to 0.15% Nitrogen After Heating 15 Minutes at 1075 °C and Air Cooling.

manganese-nickel steels air-cooled from 1075 °C (1965 °F) that contain from 12 to 18% chromium, 0 to 22% manganese, 0 to 5% nickel, about 0.10% carbon, and 0.12 to 0.15% nitrogen. It is clear from this diagram that the austenitic region is greatly expanded by the addition

of nickel and that increasing manganese above 6% at chromium levels above 15% causes a slight contraction in the austenitic region.

Fig. 10 gives further information, showing the effect of manganese in reducing the size of the austenitic region.

Phases in Chill-Cast Ingot Samples at Various Temperatures

This series of tests was conducted to secure data on delta-ferrite formation in cast sections of the steels heated to temperatures normally used in hot rolling stainless steels. Information of this type is of practical importance in view of the detrimental influence of delta-ferrite on hot workability. It is known that large ingots with a mixed structure generally exhibit poorer hot workability than those of fully austenitic steels or the fully ferritic steels. The samples for the tests represented 3/8-inch thick transverse sections of the 2-inch square ingots. They were heated at 1175, 1225, and 1300 °C (2145, 2235 and 2370 °F), respectively, for 2 hours followed by water quenching. The samples were heated in an argon atmosphere to retard decarburization and to avoid nitrogen pickup. They were selected from steels containing 16 to 18% chromium, 1.5 to 4.5% nickel, 7 to 9% manganese, 0.06 to 0.10% carbon, and 0.15 to 0.18% nitrogen.

Table I and Fig. 11 summarize the results of the magnetic tests, while Fig. 12 describes the structural features of the cast specimens after the heat treatments at 1175 and 1225 °C (2145 and 2235 °F). It is evident from these data that the nickel and chromium contents of the steels and the rolling temperatures must be controlled to ensure a fully austenitic structure in the hot rolling temperature range. For instance, a steel containing 17% chromium requires about 4.75% nickel when heated to 1225 °C (2235 °F), but only 4% nickel when heated to 1175 °C (2145 °F), to maintain a fully austenitic structure. Initial temperatures of 1150 to 1200 °C (2100 to 2190 °F), therefore, appear to be the optimum range for hot rolling steels containing 16 to 17.5% chromium, 6 to 9% manganese, and 3.5 to 4.5% nickel.

Mechanical Properties

Information on the mechanical properties of the steels was obtained from tensile tests conducted on 0.06-inch thick standard ASTM sheet specimens of 0.5-inch wide reduced section. In preliminary tests, it was established that 18% chromium steels containing 2 to 6% nickel in the solution-treated condition were extremely susceptible to work hardening unless manganese was present to stabilize the austenite. The amount of manganese required to decrease work-hardening was not linear, as shown in Fig. 13. These tests placed the manganese content of steels containing 4% nickel at between 7 and 9% for satisfactory work hardening characteristics.

In view of the great effect of composition on work hardening, the

Table I
Results of Magnetic Pull Tests

Heat No.	Nominal Composition, % Cr	Ni	Mn	C*	N*	As-Cast	Cast Condition, g. 2 Hr. at 1175 °C W.Q.	2 Hr. at 1225 °C W.Q.	2 Hr. at 1300 °C W.Q.	Wrought Condition, g. 15 Min. 1075 °C A.C.	15 Min. 1125 °C A.C.	15 Min. 1175 °C A.C.
R898	16	3.5	7	0.083	0.15	1.9	0.08	0.08	4.1	0.05	—	—
R892	16	3.5	7	0.066	0.19	1.3	0.09	0.07	16.4	0.05	—	—
R886	16	3.5	9	0.096	0.15	2.1	0.07	0.07	4.7	0.05	—	—
R880	16	3.5	9	0.063	0.17	2.2	0.07	0.09	5.7	0.05	—	—
R899	16	4.5	6.53*	0.098	0.14	0.5	0.07	0.06	0.4	0.05	—	—
R893	16	4.5	7	0.061	0.18	0.4	0.09	0.05	1.0	0.05	—	—
R887	16	4.5	9	0.098	0.15	0.5	0.08	0.06	0.23	0.05	—	—
R881	16	4.5	9	0.060	0.17	0.7	0.06	0.13	0.5	0.05	—	—
R838	16.25	1.5	9	0.11	0.14	16	7.5	18	100+	0.20	0.24	0.75
R858	16.40*	2.47*	6.63*	0.094	0.14	7.4	0.33	0.90	31	0.07	0.09	0.07
R859	16.25	2.5	8	0.099	0.14	7.9	0.65	2.2	33	0.06	0.11	0.07
R839	16.25	2.5	8.9*	0.11	0.14	6.5	0.20	0.9	49	0.05	0.04	0.05
R860	16.25	2.5	12	0.11	0.11	6.7	0.90	1.3	42	0.07	0.08	0.08
R861	16.25	2.5	14.77*	0.11	0.13	8.7	1.5	3.9	27	0.17	0.18	0.17
R840	16.25	3.5	9	0.11	0.14	3.2	0.04	0.13	24	0.03	0.04	0.05
R841	16.25	4.5	9	0.10	0.14	1.5	0.04	0.04	7	0.04	0.04	0.05
R842	16.75	1.5	9	0.13	0.14	30	24	60	100+	3.0	4.7	7.5
R843	16.75	2.5	9	0.09	0.15	16	2.6	10	81	0.25	0.30	0.60
R844	16.75	3.5	9.34*	0.12	0.14	7.0	0.15	1.0	25	0.05	0.05	0.05
R845	16.75	4.5	9	0.11	0.14	3.0	0.05	0.10	10	0.04	0.03	0.04
R900	17	3.5	7	0.096	0.16	8.7	0.50	0.9	32	0.06	—	—
R894	17	3.5	7	0.069	0.16	9.4	0.30	2.2	58	0.07	—	—
R888	17	3.5	9.46*	0.11	0.15	9.4	0.36	0.86	19	0.08	—	—
R882	17	3.5	9	0.059	0.18	9.9	0.44	0.60	36	0.06	—	—
R901	17	4.5	6.49*	0.10	0.16	4.2	0.06	0.20	19	0.05	—	—
R895	17	4.5	7	0.063	0.18	4.2	0.10	0.20	9	0.05	—	—
R889	17	4.5	9	0.10	0.15	3.3	0.08	0.10	3	0.05	—	—
R883	17	4.5	9	0.066	0.19	4.1	0.08	0.06	1.6	0.06	—	—
R846	17.5	1.5	9	0.10	0.14	52	63	85	100+	12	17	21
R847	17.5	2.5	9	0.13	0.14	29	15	25	100+	1.8	2.1	5.8
R848	17.5	3.5	9	0.11	0.13	14	2.5	6.0	84	0.18	0.14	0.26
R849	17.5	4.5	9	0.09	0.14	8.0	0.11	0.4	27	0.05	0.04	0.05
R902	18	3.5	7	0.098	0.16	12	1.3	2.5	58	0.20	—	—
R896	18	3.5	6.87*	0.064	0.18	24	9.1	18	100+	1.0	—	—
R890	18	3.5	9	0.098	0.16	21	10	12	54	1.6	—	—
R884	18	3.5	9	0.064	0.19	25	11	14	89	1.8	—	—
R903	18	4.5	6.93*	0.099	0.16	5	0.10	0.2	7	0.05	—	—
R897	18	4.5	7	0.066	0.15	15	1.8	1.9	28	0.25	—	—
R891	18	4.5	9	0.091	0.15	13	2.8	2.6	27	0.40	—	—
R885	18	4.5	9	0.066	0.15	18	6.2	5.5	45	0.50	—	—
R850	17	7	1	0.10	0.027	9.0	0.06	0.07	0.30	0.10	0.14	0.10
R862	16.25	0.75	17.93*	0.11	0.14	19.5	21	42	78	2.3	2.9	5.8

*Actual analysis

mechanical properties of 9% manganese steels in the solution-treated condition were studied in detail at various chromium and nickel levels, maintaining carbon at about 0.10% and nitrogen at 0.15%. These data are summarized in part (a) of Table II and in Fig. 14, and show that work hardening, as measured by tensile strength, decreases rapidly with increasing chromium, particularly in the range of 1.5 and 2.5% nickel, but above this level of nickel, chromium is less influential.

To further examine the stabilization of austenite with manganese, tests were conducted on a series of 16.25% chromium steels containing

Table II
Mechanical Properties of 0.060-Inch Thick Sheet
Heated 15 Minutes at 1075 °C. and Air-Cooled

Heat No.	Nominal Composition, % Cr	Ni	Mn	C*	N*	Yield Strength, Psi (0.2% Offset)	Tensile Strength Psi	% Elong.	R.B Hard.	Izod Imp. Ft.-lb.** R.T.	Izod Imp. Ft.-lb.** −183 °C	Erich. mm.***
						—(a)—						
R838	16.25	1.5	9	0.11	0.14	48,000	154,600	64	88	120	15–24	15.3
R839	16.25	2.5	8.90*	0.11	0.14	45,300	119,800	63	87	120	30–34	14.7
R840	16.25	3.5	9	0.11	0.14	45,600	107,500	60	86	120	62–73	13.2
R841	16.25	4.5	9	0.10	0.14	44,200	103,200	55	85	120	84–85	12.7
R842	16.75	1.5	9	0.13	0.14	48,400	133,000	58	90	120	22–30	14.6
R843	16.75	2.5	9	0.09	0.15	47,700	114,400	60	89	120	30–36	13.9
R844	16.75	3.5	9.34*	0.12	0.14	44,400	105,000	60	86	120	68–72	12.9
R845	16.75	4.5	9	0.11	0.14	44,000	102,200	59	84	120	89–120	13.0
R846	17.5	1.5	9	0.10	0.14	52,300	119,900	55	94	120	15–22	13.6
R847	17.5	2.5	9	0.13	0.14	48,100	111,200	59	89	120	29–59	13.5
R848	17.5	3.5	9	0.11	0.13	44,400	103,000	57	85	120	62–62	13.2
R849	17.5	4.5	9	0.09	0.14	43,200	100,800	60	82	120	85–117	12.7
						—(b)—						
R858	16.40*	2.47*	6.63*	0.094	0.14	45,000	136,500	41	92	120	12–12	14.9
R859	16.25	2.5	8	0.099	0.14	45,600	135,200	77	87	120	23–34	14.5
R839	16.25	2.5	8.90*	0.11	0.14	45,300	119,800	63	87	120	30–34	14.7
R860	16.25	2.5	12	0.11	0.11	41,800	101,000	66	82	120	51–54	13.1
R861	16.25	2.5	14.77*	0.11	0.13	43,100	102,700	66	83	120	64–75	13.1
						—(c)—						
R898	16	3.5	7	0.083	0.15	46,500	115,700	62	86	120	32–35	15.1
R892	16	3.5	7	0.066	0.19	47,200	115,700	64	87	120	28–32	15.2
R886	16	3.5	9	0.096	0.15	46,300	108,300	61	84	120	54–70	13.9
R880	16	3.5	9	0.063	0.17	46,100	113,200	69	83	120	82–116	14.0
R899	16	4.5	6.53*	0.098	0.14	45,400	103,600	60	84	120	56–58	13.8
R893	16	4.5	7	0.061	0.18	46,500	104,000	60	85	120	42–61	13.9
R887	16	4.5	9	0.098	0.15	44,200	104,300	59	83	120	81–82	13.5
R881	16	4.5	9	0.060	0.17	47,000	105,200	60	82	120	95–115	13.7
R900	17	3.5	7	0.096	0.16	46,000	110,200	62	86	120	38–41	14.2
R894	17	3.5	7	0.069	0.16	47,100	108,800	62	85	120	62–108	14.4
R888	17	3.5	9	0.11	0.15	48,500	108,900	58	86	120	56–58	13.6
R882	17	3.5	9	0.059	0.18	48,500	108,300	60	86	120	54–82	13.7
R901	17	4.5	6.49*	0.10	0.16	45,900	103,300	61	84	120	69–71	13.9
R895	17	4.5	7	0.063	0.18	46,600	103,200	56	83	120	72–77	14.5
R889	17	4.5	9	0.10	0.15	45,000	104,000	60	84	120	92–94	13.9
R883	17	4.5	9	0.066	0.19	47,500	104,800	61	84	120	120–120	13.1
R902	18	3.5	7	0.098	0.16	45,200	102,600	59	83	120	42–68	13.8
R896	18	3.5	7	0.064	0.18	49,700	108,300	56	87	120	61–79	14.0
R890	18	3.5	9	0.098	0.16	48,900	108,900	59	87	120	40–46	13.7
R884	18	3.5	9	0.064	0.19	50,000	106,700	49	87	120	91–102	13.2
R903	18	4.5	6.93*	0.099	0.16	48,900	108,900	58	86	120	74–75	14.0
R897	18	4.5	7	0.066	0.15	47,700	103,200	56	84	120	74–79	13.4
R891	18	4.5	9	0.091	0.15	46,000	103,400	57	83	120	42–68	13.5
R885	18	4.5	9	0.066	0.15	49,800	105,900	56	86	120	119–120	13.0
						—(d)—						
R850	17	7	1	0.10	0.027	29,200	129,200	55	76	87	38–44	15.6
R862	16.25	0.75	17.93*	0.11	0.14	44,600	104,000	62	86	120	48–52	12.6

* Actual analysis
** Specimens prepared from ⅝-Inch diameter hot-rolled bar
*** 0.038-Inch thick sheet

2.5% nickel, 0.10% carbon, and 0.15% nitrogen, in which the manganese content was varied from 6 to 14%. The results are summarized in part (b) of Table II and in Fig. 15. With an increase in manganese, there is a sharp decrease in tensile strength, but the improvement in ductility is also very noteworthy. For example, increasing the manganese content from 6 to 8% almost doubles the elongation of the steel. Beyond 8%, however, manganese has a greater effect on tensile strength than on ductility.

The mechanical properties of the 7 and 9% manganese, 3.5 and

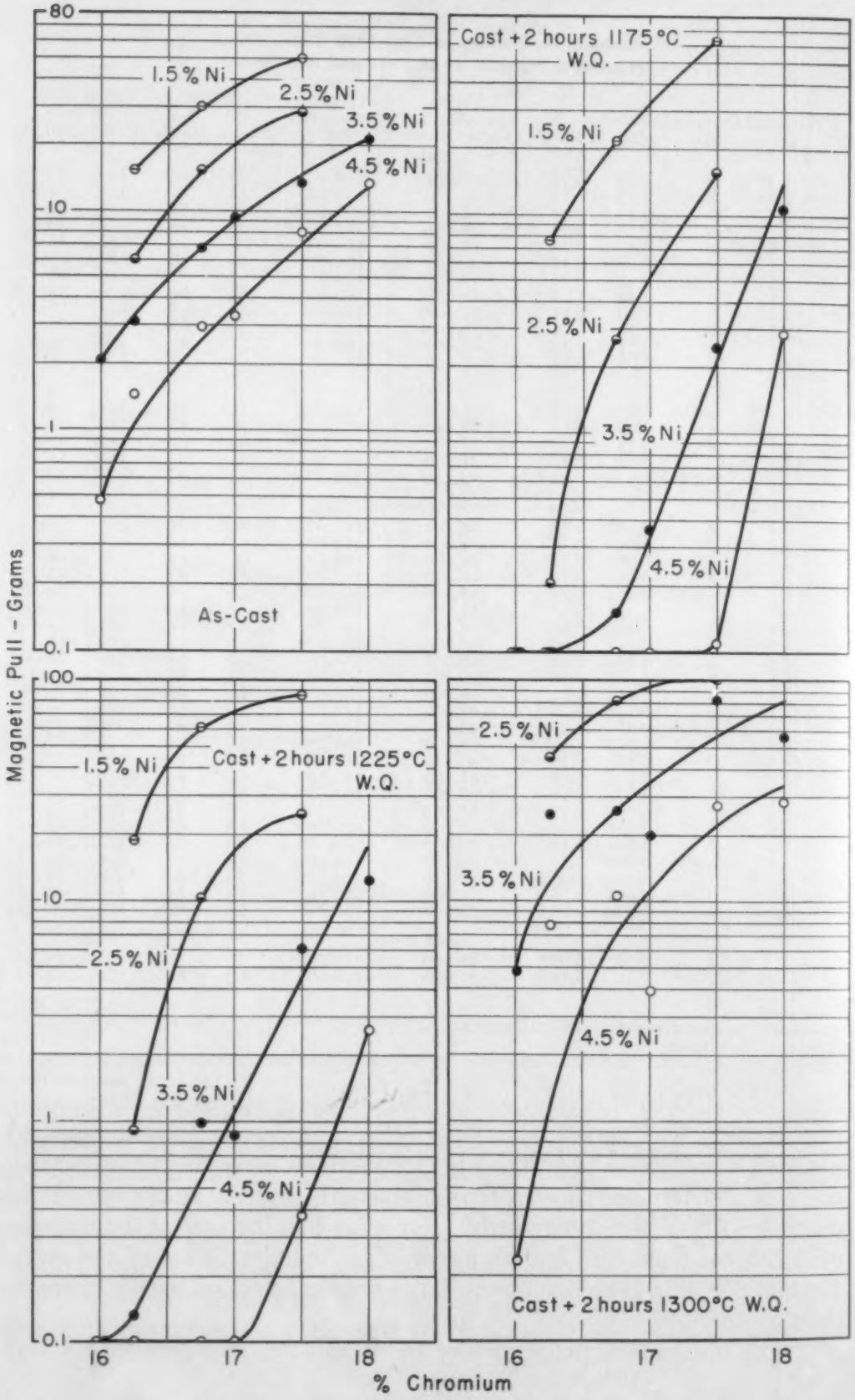


Fig. 11—Relative Magnetism of Cast Specimens Machined From 2-Inch Square Ingots. Steels contained 9% manganese, 0.10% carbon and 0.15% nitrogen.

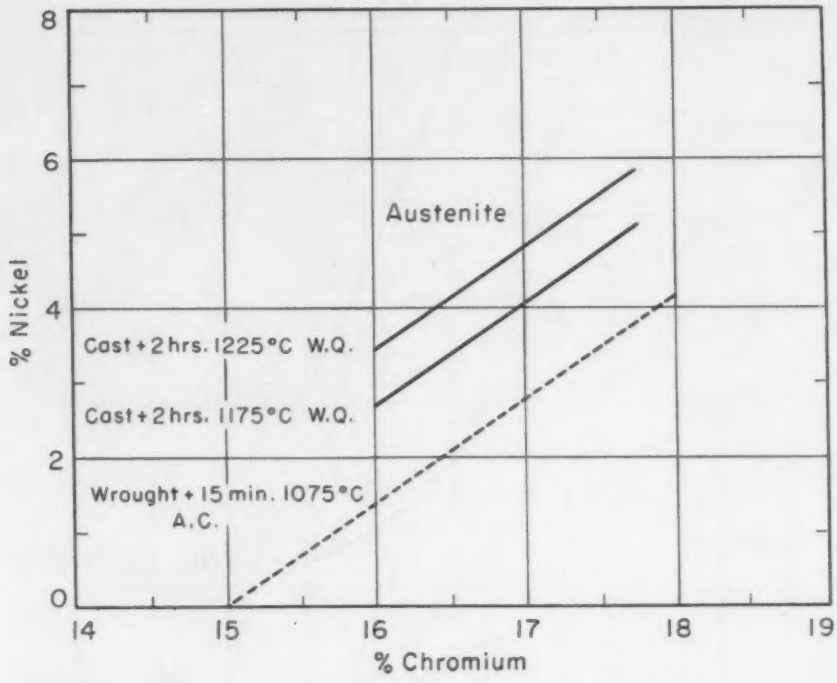


Fig. 12—Structure of Cast 16 to 18% Chromium—1.5 to 4.5% Nickel —9% Manganese Steels Containing 0.10% Carbon and 0.15% Nitrogen.

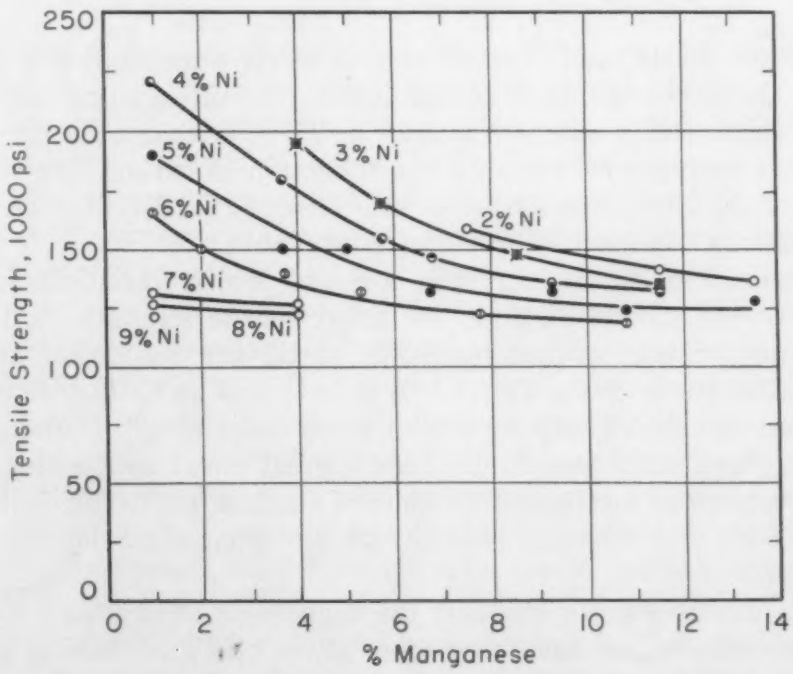


Fig. 13—Effect of Manganese on Work Hardening of 18.5% Chromium Steels Containing 2 to 9% Nickel, 0.05 to 0.08% Carbon, and 0.12 to 0.15% Nitrogen. Specimens Reduced 20% by Cold Rolling.

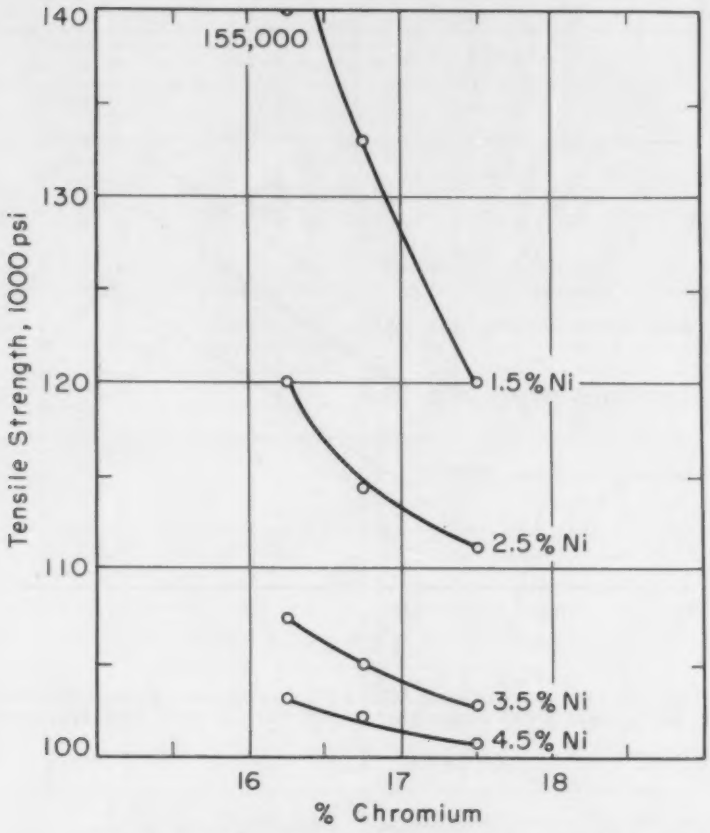


Fig. 14—Effect of Chromium and Nickel on the Tensile Strength of Austenitic Steels Containing 9% Manganese, 0.10% Carbon, and 0.15% Nitrogen After Heating 15 Minutes at 1075 °C and Air Cooling.

4.5% nickel, 16, 17, and 18% chromium steels were studied in greater detail at the 0.06 and 0.10% carbon levels. The nitrogen content of the 0.10% carbon steels was held at 0.15%. To compensate for the loss of austenite-forming power due to the reduction of carbon, the nitrogen content of the 0.06% carbon steels was raised to 0.18%. The results of these tests are summarized in part (c) of Table II.

The chief point of interest in part (c) is that variations in chromium between 16 and 18% do not affect tensile strength or ductility significantly. Steels containing 3.5% nickel are somewhat stronger than similar steels containing 4.5% nickel; and steels containing 7% manganese are slightly stronger than steels containing 9% manganese; however, these variations do not have a great effect on the elongation. The differences in mechanical properties attributable to the differences in the carbon and nitrogen contents of the steels are relatively insignificant.

It is worthwhile to mention the high yield strength of the high nitrogen steels before discussing some of the other mechanical properties listed in Table II. This is a characteristic of these steels, and undoubtedly will be advantageous when utilizing them for structural

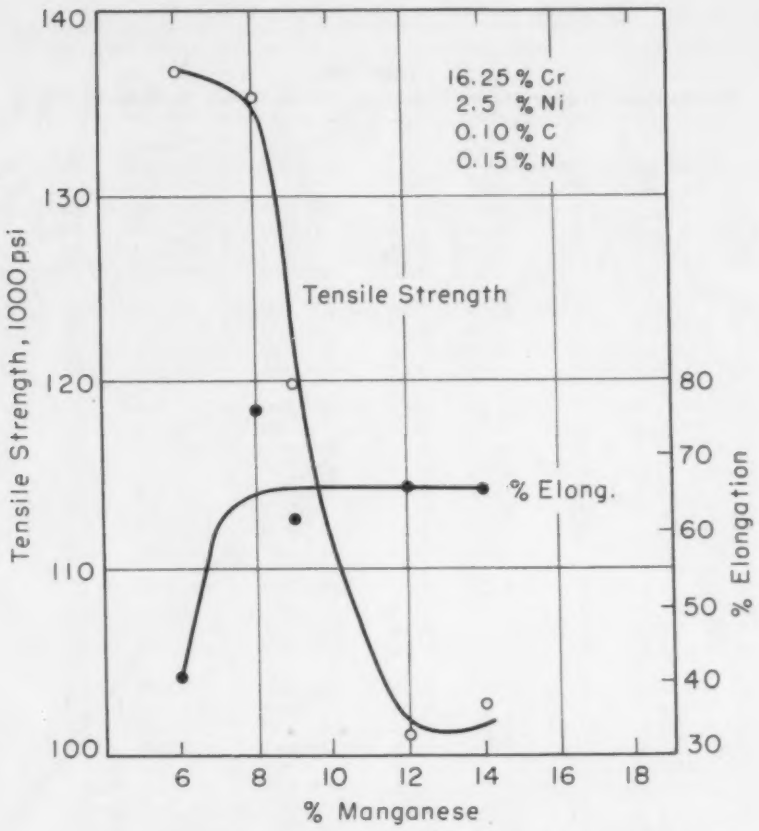


Fig. 15—Effect of Manganese on Tensile Strength and Elongation of 16.25% Chromium Steel Containing 2.5% Nickel, 0.10% Carbon, and 0.15% Nitrogen After Heating 15 Minutes at 1075 °C and Air Cooling.

purposes in the solution-treated condition. Nitrogen also increases the hardness of the steels in the solution-treated condition.

The Erichsen values of the steels after heat treatment at 1075 °C (1965 °F) are recorded in Table II. The highest values are exhibited by the steels most susceptible to work hardening, and they decrease slightly with increasing chromium, nickel, or manganese, but carbon and nitrogen exert relatively little influence. The Erichsen values are all good, although somewhat lower than those for the 17% chromium—7% nickel steel. This is in agreement with the observed influence of work hardening since the 17-7 steel is a high work hardening steel.

The foregoing data were obtained from samples air-cooled from 1075 °C (1965 °F). The effects of cold working on strength and ductility were also examined in view of the interest in this type of steel (6,7). These samples were cold-rolled 20% to a final thickness of 0.06 inch, and the results of the tensile tests made on them are given in Table III.

Those steels which exhibited high strength in the solution-treated condition increased greatly in strength when cold-worked, as a result of austenite decomposition. It is again apparent that to avoid excessive

Table III
Mechanical Properties of 0.06-Inch Thick Sheet Cold-Rolled 20%

Heat No.	Nominal Composition, % Cr	Ni	Mn	C*	N*	Yield Strength Psi	Tensile Strength Psi	% Elong.	R.e Hard.	Mag. Pull, g.
R898	16	3.5	7	0.083	0.15	107,000	164,300	32	34	6.4
R892	16	3.5	7	0.066	0.19	91,000	163,700	28	33	7.9
R886	16	3.5	9	0.096	0.15	111,700	147,500	28	32	2.1
R880	16	3.5	9	0.063	0.17	107,300	148,000	28	31	2.1
R899	16	4.5	6.53*	0.098	0.14	107,700	145,200	30	32	2.1
R893	16	4.5	7	0.061	0.18	101,400	146,300	30	33	1.9
R887	16	4.5	9	0.098	0.15	107,200	139,000	27	30	0.52
R881	16	4.5	9	0.060	0.17	104,000	136,500	27	29	0.35
R838	16.25	1.5	9	0.11	0.14	107,200	199,500	30	42	28
R858	16.40*	2.47	6.63*	0.094	0.14	106,000	198,500	30	40	31
R859	16.25	2.5	8	0.099	0.14	104,000	174,000	27	37	9.3
R839	16.25	2.5	8.90*	0.11	0.14	104,700	172,000	29	38	9.1
R860	16.25	2.5	12	0.11	0.11	105,200	140,200	25	32	0.50
R861	16.25	2.5	14.77*	0.11	0.13	98,500	131,000	29	29	0.08
R840	16.25	3.5	9	0.11	0.14	116,800	165,200	24	37	5.9
R841	16.25	4.5	9	0.10	0.14	117,100	154,000	23	34	1.1
R842	16.75	1.5	9	0.13	0.14	110,700	184,000	27	39	16
R843	16.75	2.5	9	0.09	0.15	115,000	171,000	26	37	6.9
R844	16.75	3.5	9.34*	0.12	0.14	111,000	148,000	28	34	1.7
R845	16.75	4.5	9	0.11	0.14	106,300	138,200	28	31	0.30
R900	17	3.5	7	0.096	0.16	104,800	158,500	31	34	4.8
R894	17	3.5	7	0.069	0.16	110,300	153,200	31	33	3.7
R888	17	3.5	9	0.11	0.15	106,800	142,200	29	31	1.2
R882	17	3.5	9	0.059	0.18	99,700	138,000	29	31	0.84
R901	17	4.5	6.49*	0.10	0.16	108,300	144,100	35	31	1.1
R895	17	4.5	7	0.063	0.18	106,000	141,800	30	30	1.3
R889	17	4.5	9	0.10	0.15	106,200	136,200	29	29	0.17
R883	17	4.5	9	0.066	0.19	107,700	132,200	30	30	0.20
R846	17.5	1.5	9	0.10	0.14	121,000	178,800	25	39	19
R847	17.5	2.5	9	0.13	0.14	107,100	155,200	31	34	3.7
R848	17.5	3.5	9	0.11	0.13	105,800	140,600	30	32	1.1
R849	17.5	4.5	9	0.09	0.14	102,500	130,400	31	29	0.14
R902	18	3.5	7	0.098	0.16	103,500	153,500	33	31	2.9
R896	18	3.5	7	0.064	0.18	104,200	155,200	28	33	4.7
R890	18	3.5	9	0.098	0.16	113,400	145,600	25	31	1.2
R884	18	3.5	9	0.064	0.19	111,600	141,000	27	31	1.0
R903	18	4.5	6.93*	0.099	0.16	107,000	140,200	31	32	0.50
R897	18	4.5	7	0.066	0.15	109,000	138,200	30	31	0.50
R891	18	4.5	9	0.091	0.15	105,700	136,500	28	29	0.23
R885	18	4.5	9	0.066	0.15	109,500	131,500	24	28	0.17
R850	17	7	1	0.10	0.027	107,200	182,400	27	36	50
R862	16.25	0.75	17.93*	0.11	0.14	108,700	143,300	22	33	1.1

* Actual analysis

work-hardening, the composition of the steel must be balanced with respect to chromium, manganese, and nickel.

From the standpoint of uniformity after cold rolling, the 16 to 18% chromium steels containing 7 to 9% manganese and 3.5 to 4.5% nickel show promise. Some significant differences in strength exist among the steels falling within this range, but they are not excessive, especially when the nickel, manganese, and chromium are on the high side of the range.

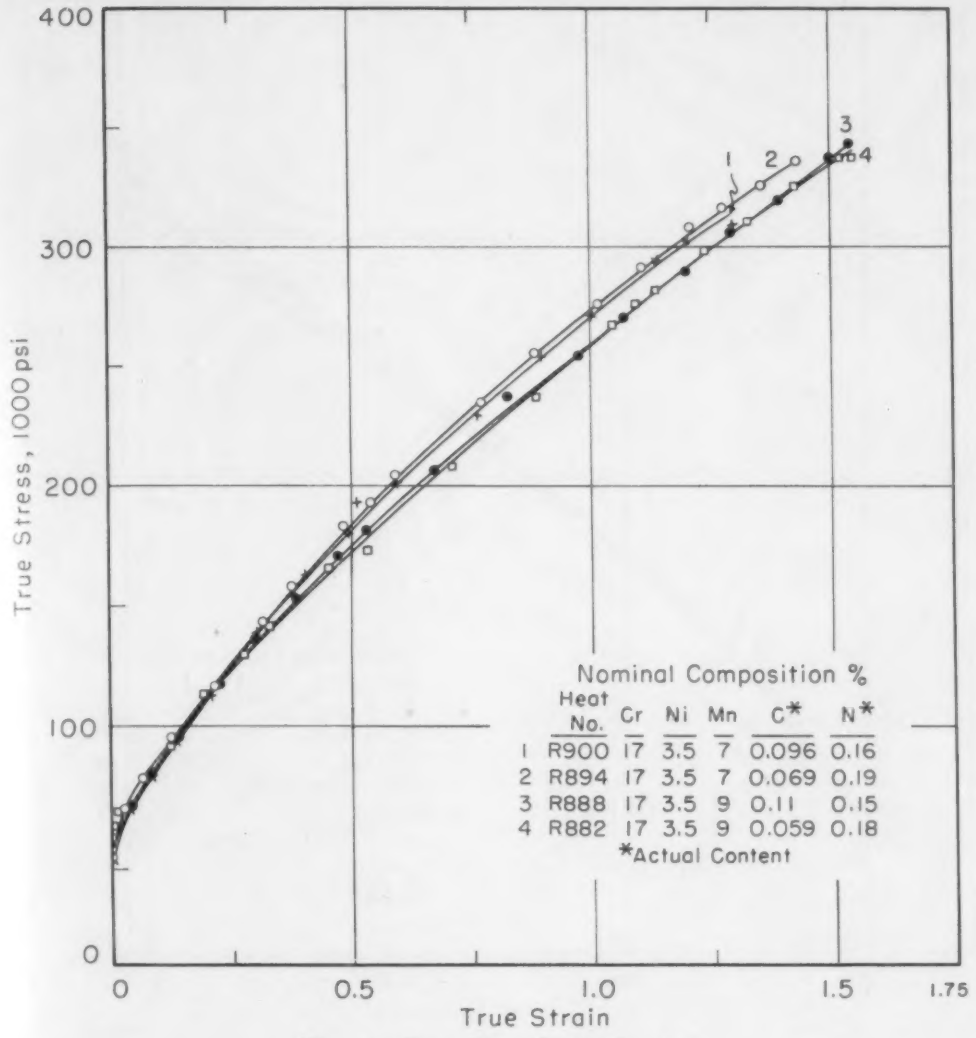


Fig. 16—True Stress-Strain Curves.

True Stress-Strain Tests

Information on total work hardening of a selected group of the steels was obtained because of the importance of this property in the application of the steels. The true stress-strain tension test was selected instead of the ordinary stress-strain test to show total work hardening, because it has the advantage of revealing the influence of composition and strain on both work hardening and rate of work hardening. True stress is the load divided by the minimum area prevailing at the instant of loading, and true strain is defined as

$$\log_e \frac{(Ao)}{(A)}$$

where Ao is the original cross sectional area and A the area at the instant of loading. Total work hardening is defined as the combined effects of ordinary strain hardening and the work hardening due to transformation of austenite to ferrite.

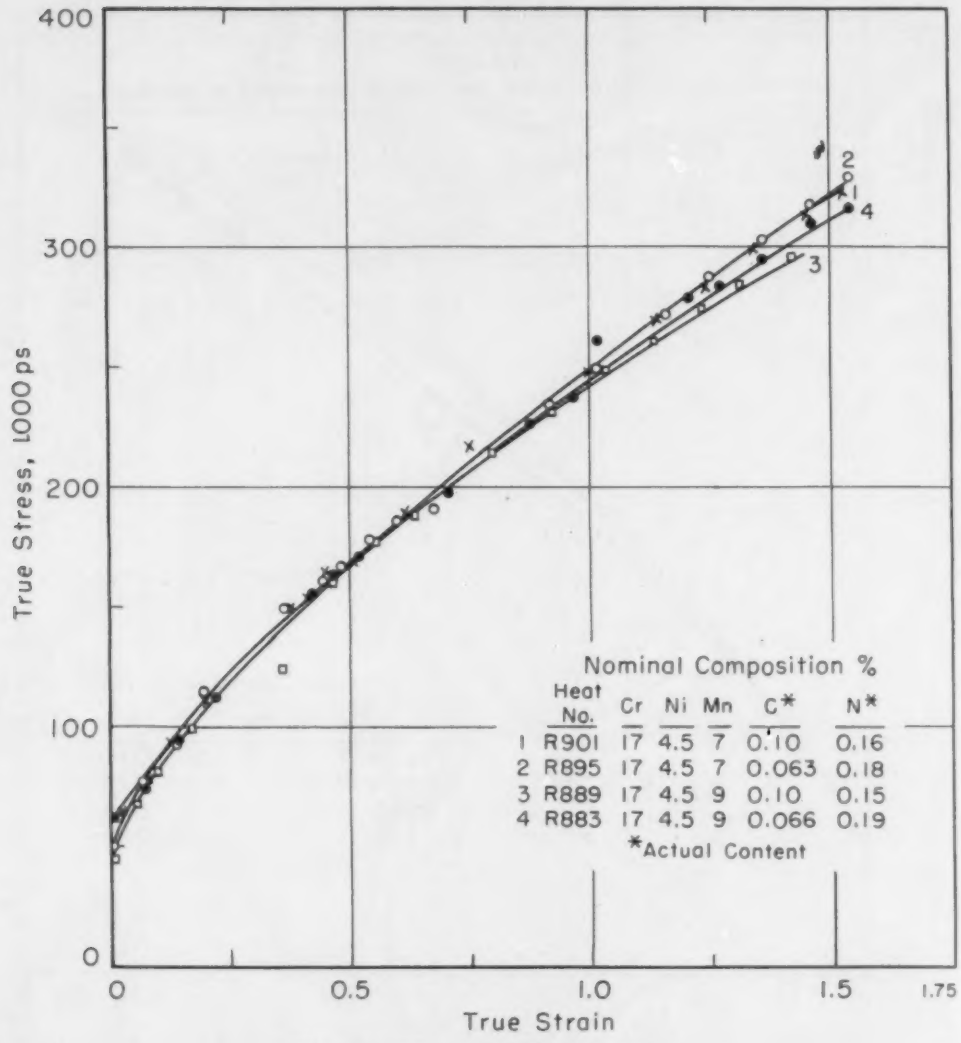


Fig. 17—True Stress-Strain Curves.

Figs. 16 through 19 show the true stress-strain curves obtained at room temperature from specimens of 17% chromium steel containing 3.5 to 4.5% nickel, and 7 to 9% manganese, heat treated fifteen minutes at 1075 °C (1965 °F) and air-cooled. Similar tests were conducted on the 17% chromium—7% nickel and 18% chromium—9% nickel steels and on the 16% chromium—16% manganese—1% nickel steel, and these data are also included in the figures. The 17-7 steel is designed for applications requiring a combination of high strength and good formability, and its composition is balanced so that it retains good ductility at high strength levels. The 18-9 steel is generally more desirable for deep drawing operations because it work hardens more slowly. Experience has shown that the 15.5% chromium—16% manganese—1% nickel steel has good forming qualities.

From Figs. 16 and 17, it is evident that the 0.06 and 0.10% carbon steels show similar total work hardening characteristics. Increasing

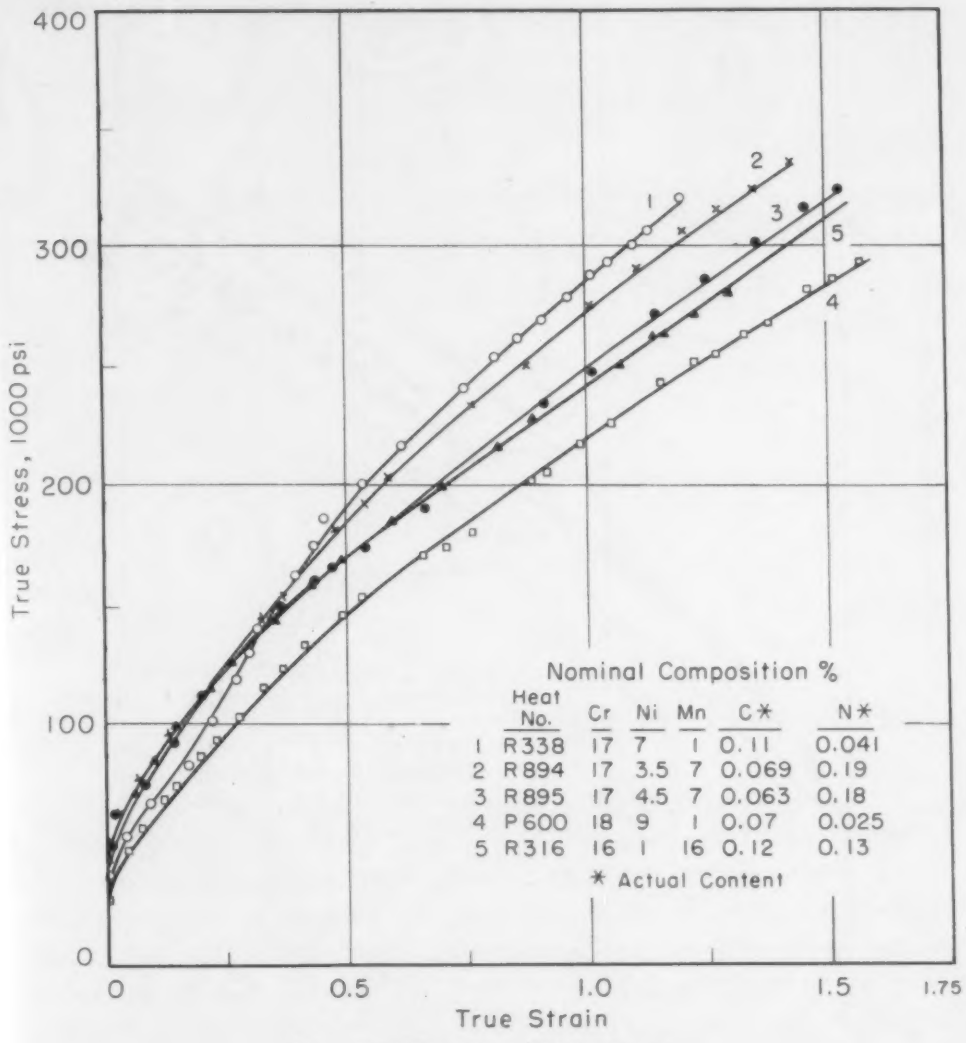


Fig. 18—True Stress-Strain Curves.

manganese from 7 to 9% decreases work hardening slightly, particularly in the steels containing 3.5% nickel. When the steels are compared with the commercial steels (Figs. 18 and 19), it is observed that the true stress-strain curves fall between those of the 17% chromium—7% nickel and 18% chromium—9% nickel steels, and slightly above that of the 16% chromium—16% manganese—1% nickel steel. Based on this comparison, it may be stated that 17% chromium steels containing 7 to 9% manganese and 3.5 to 4.5% nickel are well suited for severe cold forming operations, and should display forming characteristics similar to those of the 18% chromium—9% nickel and 16% chromium—16% manganese—1% nickel steels.

Influence of Composition on Impact Properties

Nickel, carbon, and nitrogen are austenite formers and chromium, silicon, and, to a certain extent, manganese are ferrite formers. These

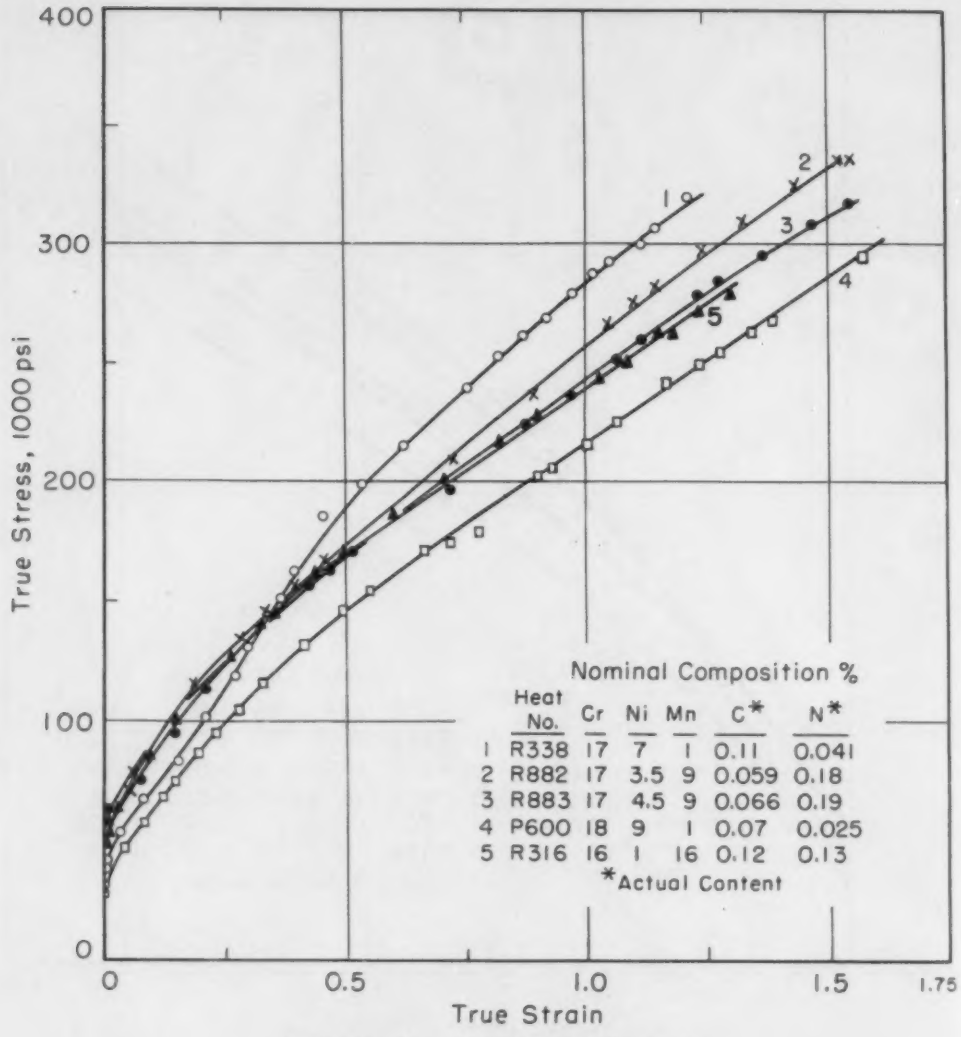


Fig. 19—True Stress-Strain Curves.

latter elements lower the temperature of spontaneous martensite formation on cooling the austenitic stainless steels from elevated temperatures. They also decrease the tendency of the austenite to transform to martensitic ferrite during plastic deformation of the steel. Changes in composition can, therefore, have a significant influence on the notch-sensitivity of the austenitic chromium-manganese-nickel stainless steels.

Izod impact tests were made, and Table II summarizes the results obtained at room temperature and at —183 °C (—300 °F) on steels varying in austenite stability. The specimens were machined from ⅝-inch diameter hot-rolled bars solution-treated fifteen minutes at 1075 °C (1965 °F) and air-cooled.

All the steels exhibited high toughness at room temperature despite the wide range of compositions tested. The values exceeded 120 ft-lb. reflecting the high strength of the austenitic chromium-manganese-nickel steels containing nitrogen.

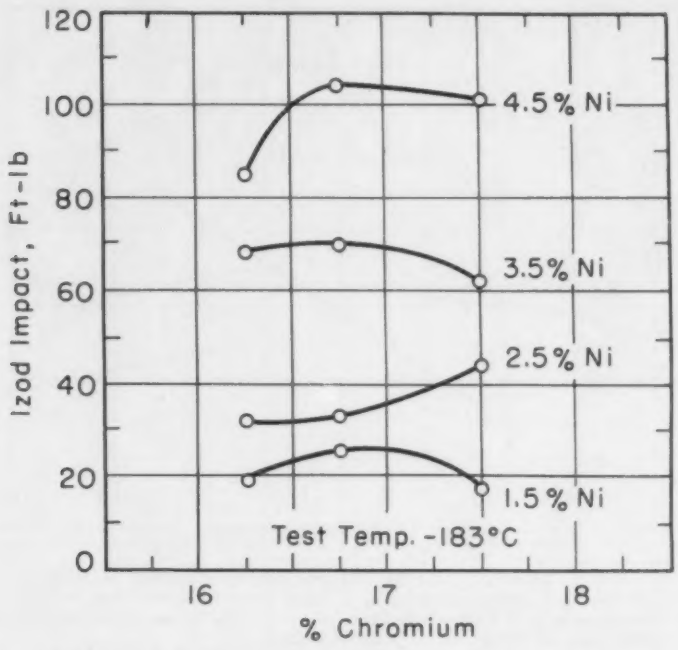


Fig. 20—Effect of Nickel and Chromium on Izod Impact Toughness of Steels Containing 9% Manganese, 0.10% Carbon, and 0.15% Nitrogen at—183 °C After Heating 15 Minutes at 1075 °C and Air Cooling.

The effect of composition on the notch sensitivity of the steels was more noticeable at —183 °C (—300 °F) than at room temperature. This was expected for two reasons: (a) low temperatures favor the transformation of austenite to martensitic ferrite by plastic deformation, and (b) low temperatures promote the spontaneous transformation of austenite to ferrite. The greatest loss of toughness was exhibited by the high work hardening steels containing austenite of the lowest stability. This is revealed in Fig. 20 which shows that the toughness decreases to between 10 and 20 ft-lb when the nickel content of the steel is lowered to 1.5%. Chromium is not very critical in the range of 16 to 18% although there appears to be some advantage in keeping the chromium in the neighborhood of 17%.

Fig. 21 reveals the improvement in toughness in a 16.5% chromium—2.5% nickel steel gained from manganese. The improvement in toughness is undoubtedly due to the increase in the stability of the austenite since it will be recalled that manganese lowered the work hardening and greatly improved the room temperature tensile ductility of this steel.

Fig. 22 shows the beneficial effect of lowering carbon and increasing nitrogen on toughness at —183 °C (—300 °F). The lower toughness of the 0.10% carbon steels is believed to be due to a small amount of carbide precipitation occurring at the grain boundaries during cooling. The effect of carbide precipitation is to raise the M_s temperature of the metal at the grain boundaries.

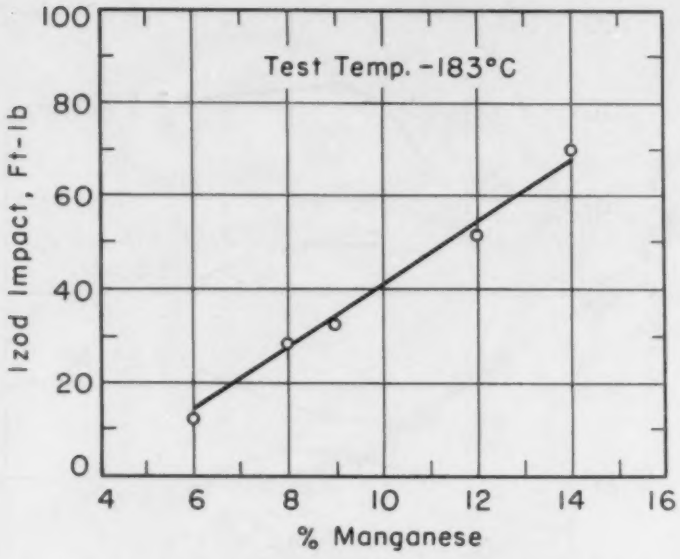


Fig. 21—Effect of Manganese on Izod Impact Toughness of 16.5% Chromium—2.5% Nickel Steels Containing 0.10% Carbon and 0.15% Nitrogen at—183 °C After Heating 15 Minutes at 1075 °C and Air Cooling.

The foregoing data show that steels falling within the ranges of 16 to 18% chromium, 3.5 to 4.5% nickel, and 7 to 9% manganese possess good toughness at low temperatures and should be suitable for applications requiring this characteristic.

Influence of Temperature on Impact Properties

The effect of exposure at temperatures between 538 and 815 °C (1000 and 1500 °F) on impact toughness at room temperature was in-

Table IV
Izod Impact Values at Room Temperature After Exposure to Elevated Temperatures

Heat No.	Time, Hours	Temperature, °C 538	593	650	704	760	815
S1	0	120	120	120	120	120	120
	4	120	120	111	106	112	115
	8	120	120	110	113	117	112
	16	120	120	116	105	110	108
	32	120	118	105	113	109	99
	64	120	102	91	112	91	82
	128	120	94	109	100	70	69
	256	120	99	82	90	72	76
S2	0	120	120	120	120	120	120
	4	120	120	120	120	120	117
	8	120	120	117	119	118	112
	16	119	117	118	119	116	109
	32	120	120	120	116	112	105
	64	120	118	120	113	107	98
	128	119	120	116	100	82	79
	256	119	119	113	91	81	82

Heat No.	Composition, % Cr	Ni	Mn	Si	C	N
S1	17.60	3.93	7.58	0.40	0.051	0.16
S2	17.50	4.00	9.46	0.40	0.070	0.16

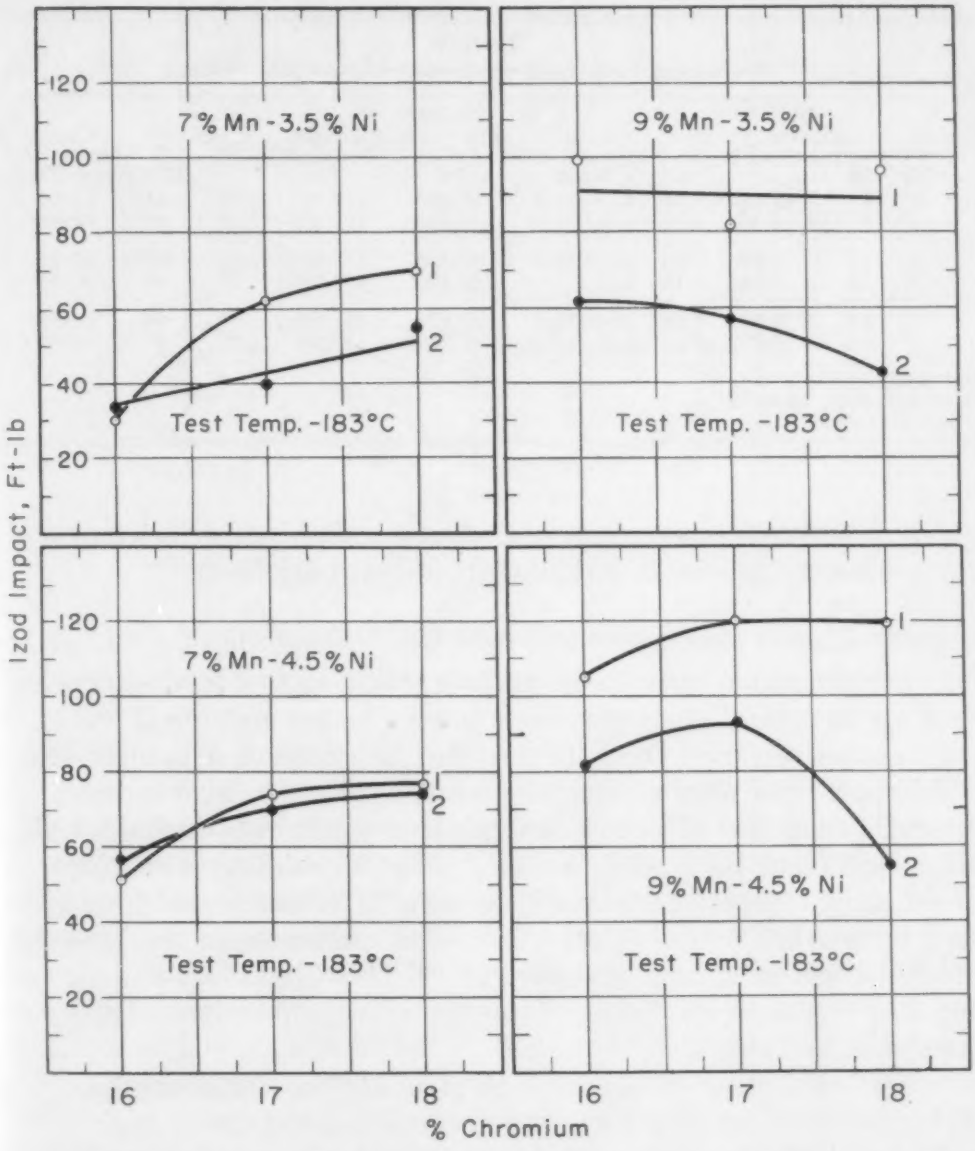


Fig. 22—Effect of Carbon and Nitrogen on Izod Impact Toughness at—183 °C After Heating 15 Minutes at 1075 °C and Air Cooling.
Curve 1 0.08 Per Cent C—0.18% N Curve 2 0.10 Per Cent C—0.15% N

vestigated since it is important to know what changes in mechanical properties occur when the steels are held at elevated temperature for extended periods. These tests were made on steels containing 17.5% chromium, 4% nickel, 7.5 and 9.5% manganese, 0.06% carbon, and 0.15% nitrogen, hot-rolled to 5/8-inch diameter bars. Prior to exposure, the steels were solution-treated one hour at 1065 °C (1950 °F) and air-cooled.

Table IV shows the changes in impact strength at room temperature after aging for time periods up to 256 hours. The maximum effect of aging occurs at 760 and 815 °C (1400 and 1500 °F), but the impact values do not decrease significantly within the total time period investi-

Table V
Mechanical Properties of ½-Inch Thick Plate Welds

Heat No.	Nominal Composition, % Cr	Ni	Mn	C*	N*	Condition of Metal	Yield Str. 0.2% Offset Psi	Tensile Strength Psi	% Elong. in 1½"	% R.A.	Charpy Keyhole Impact Value, Ft.-lb. Room Temp.	—183 °C
R922	17	3.5	7	0.05	0.14	As-welded	67,200	112,700	45	43	52–59	14–18
R922	17	3.5	7	0.05	0.14	S.H.T.(1)	54,500	109,000	55	54	58–59	26–43
R923	17	3.5	9	0.05	0.13	As-welded	66,300	105,400	47	60	53–56	17–18
R923	17	3.5	9	0.05	0.13	S.H.T.(1)	53,600	100,000	57	65	54–55	40–43
R924	17	4.5	7	0.053	0.15	As-welded	63,600	101,800	48	64	53–55	35–40
R924	17	4.5	7	0.053	0.15	S.H.T.(1)	47,200	95,400	60	66	65–66	43–51

* Actual analysis
(1) Heated ½-hour at 1075 °C. and air-cooled

gated. The 9.5% manganese steel shows a slight superiority over the 7.5% manganese steel in retaining its impact toughness.

Welding Characteristics

Consideration must be given to welding in the development of a steel for structural purposes. Since joining by arc welding is one of the most extensively used procedures in the fabrication of structures, tensile and impact tests were conducted on inert gas arc-welded samples of a selected group of the steels. The welds were made in ½-inch thick plate, air-cooled from 1075 °C (1965 °F) prior to welding, with electrodes of the same composition as the base metal. The tensile and Charpy impact tests were made on all-weld-metal specimens in the as-welded condition and after heat treatment at 1075 °C (1965 °F) and air cooling. The results of the tests and the nominal compositions of the steels are shown in Table V.

The weld metal possessed high yield and tensile strength coupled with good ductility in the as-welded condition, indicating high quality weld metal relatively free of fissuring. Solution treating at 1075 °C (1965 °F) lowered the yield strength about 20% and raised the elongation about the same amount.

At room temperature, the Charpy impact values ranged between 52 and 59 ft-lb in the as-welded condition and between 58 and 66 ft-lb in the solution-treated condition. At —183 °C (—300 °F), the impact values of the welds containing 3.5% nickel fell to between 14 and 18 ft-lb in the as-welded condition. Increasing the nickel content to 4.5% raised the impact value at —183 °C (—300 °F) to between 35 and 40 ft-lb in the as-welded condition. The toughness of the 3.5% nickel steel welds was considerably improved at —183 °C (—300 °F) by solution treating at 1075 °C (1965 °F), particularly when the manganese content was increased to 9%.

It is apparent from these tests that steels containing 17% chro-

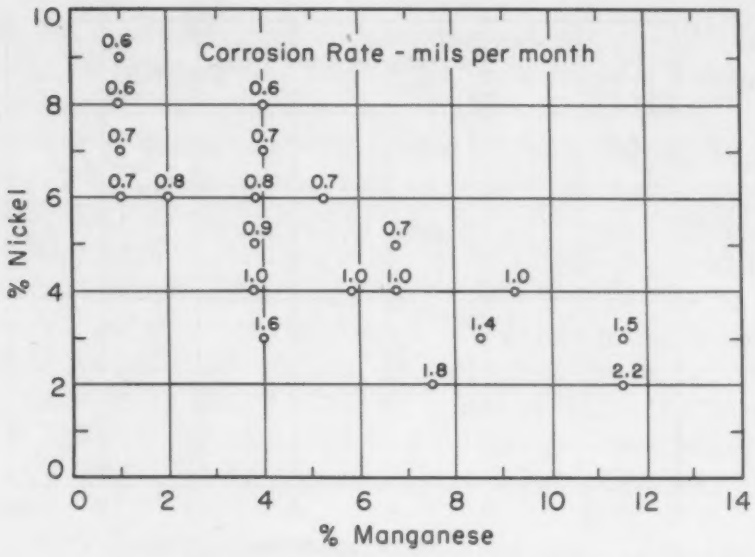


Fig. 23—Boiling 65% Nitric Acid Corrosion Tests. 18% Chromium, 0.05 to 0.08% Carbon, and 0.12 to 0.15% Nitrogen.

mium, 3.5 to 4.5% nickel, and 6 to 9% manganese possess adequate weldability for all types of practical applications.

Corrosion Resistance

The general corrosion resistance of the chromium-manganese-nickel steels was investigated. It is recognized that actual service tests are the most satisfactory means of determining the suitability of a steel for a given environment, but at least laboratory data serve to indicate the relative resistance of a steel in different types of environments.

The steels were tested in boiling 65% nitric acid for five periods of 48 hours each and in air-free 10% sulphuric acid at 70 °C (158 °F) for 2 periods of 16 hours each. The former acid represents strongly oxidizing acid conditions toward which the stainless steels containing 16% or more chromium are usually extremely resistant. The second solution represents a nonoxidizing acid environment. Nickel is the chief element in the stainless steels imparting resistance to nonoxidizing acids. Usually, the stainless steels are not suited for such environments except where the concentration or temperature is low, as they destroy the passivity of the steel. Tests in dilute sulphuric acid are helpful, however, in showing the influence of composition on the resistance of the steel to reducing acid conditions.

In Fig. 23, the average corrosion rate in boiling 65% nitric acid, expressed as mils per month, is shown for several of the 18% chromium steels. Other factors being the same, resistance to nitric acid decreases with lowering the nickel and remains essentially unchanged over the range of 2 to 14% manganese at any given concentration of nickel. Despite some slight loss of resistance to nitric acid as the nickel content

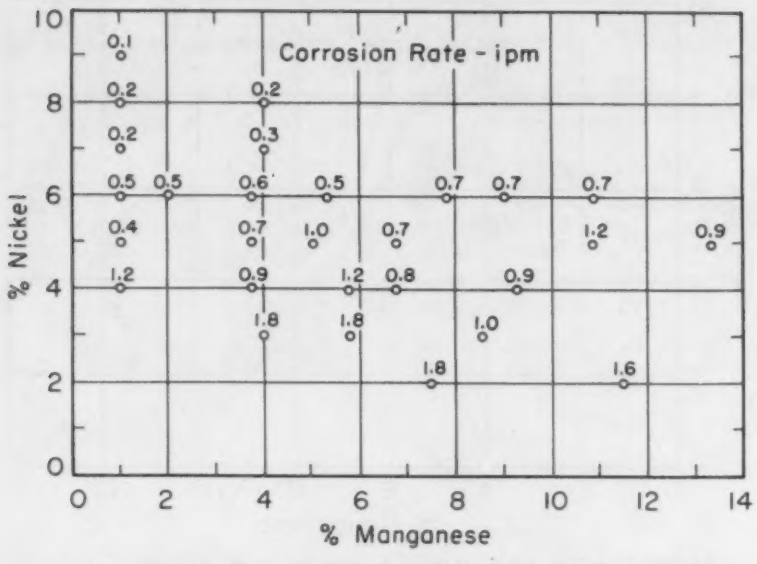


Fig. 24—Air-Free 10% Sulphuric Acid at 70 °C Corrosion Tests. 18% Chromium, 0.05 to 0.08% carbon, and 0.12 to 0.15% nitrogen.

Table VI
Corrosion Test Results

Heat No.	Nominal Composition, % Cr	Ni	Mn	C*	N*	Boiling 65% HNO_3, In. Pen. per Month Solution Heated 20 Min. Heat treated at 1075 °C A.C.	At 650 °C Air-Cooled	Heated 2 Hr. At 550 °C A.C.	Non-aerated 10% H_2SO_4 at 70 °C, In. Pen./Mo. Solution Heat treated at 1075 °C
R898	16	3.5	7	0.083	0.15	0.00230	0.020	0.00218	1.5
R892	16	3.5	7	0.066	0.19	0.00229	0.00246	0.00226	1.6
R886	16	3.5	9	0.096	0.15	0.00208	0.013	0.00218	1.5
R880	16	3.5	9	0.063	0.17	0.00230	0.00375	0.00216	1.5
R899	16	4.5	6.53*	0.098	0.14	0.00169	0.0139	0.00177	1.2
R893	16	4.5	7	0.061	0.18	0.00180	0.00186	0.00181	1.2
R887	16	4.5	9	0.098	0.15	0.00172	0.030	0.00177	1.3
R881	16	4.5	9	0.060	0.17	0.00169	0.00212	0.00172	1.3
R900	17	3.5	7	0.096	0.16	0.00178	0.0395	0.00188	1.5
R894	17	3.5	7	0.069	0.16	0.00165	0.00169	0.00157	1.5
R888	17	3.5	9.46*	0.11	0.15	0.00166	0.041	0.00178	1.3
R882	17	3.5	9	0.059	0.18	0.00164	0.00270	0.00159	1.6
R901	17	4.5	6.49*	0.10	0.16	0.00130	0.0147	0.00137	1.1
R895	17	4.5	7	0.063	0.18	0.00136	0.00170	0.00140	1.1
R889	17	4.5	9	0.10	0.15	0.00135	0.032	0.00128	1.2
R883	17	4.5	9	0.066	0.19	0.00144	0.00740	0.00143	1.2
R902	18	3.5	7	0.098	0.16	0.00158	0.015	0.00167	1.5
R896	18	3.5	6.87*	0.064	0.18	0.00136	0.00149	0.00135	1.6
R890	18	3.5	9	0.098	0.16	0.00136	0.063	0.00172	1.5
R884	18	3.5	9	0.064	0.19	0.00141	0.00435	0.00159	1.5
R903	18	4.5	6.93*	0.099	0.16	0.00126	0.024	0.00125	1.1
R897	18	4.5	7	0.066	0.15	0.00107	0.00124	0.00111	1.0
R891	18	4.5	9	0.091	0.15	0.00116	0.074	0.00118	1.0
R885	18	4.5	9	0.066	0.15	0.00097	0.00236	0.00103	1.0
R850	17	7	1	0.10	0.027	0.00084	0.0028	0.00100	0.2
R862	16	1	17.93*	0.11	0.14	0.00500	0.055	0.010	2.8

* Actual analysis

is lowered, the steels modified with manganese and nitrogen are probably suitable for resisting this acid over a wide range of concentrations and temperatures.

The effect of dilute sulphuric acid at 70 °C (158 °F) is summarized in Fig. 24. The corrosion rate increased approximately tenfold when nickel was lowered from 9 to 2%, and although it did not offset this loss, manganese in the range of 1 to 14% was not detrimental to corrosion resistance in this acid.

Table VI summarizes the results of similar tests on steels containing 16,17, and 18% chromium. This phase of the investigation was limited to steels containing 3.5 and 4.5% nickel, 7 and 9% manganese, 0.06 and 0.10% carbon, and 0.15 and 0.18% nitrogen, heated fifteen minutes at 1075 °C (1965 °F) and air-cooled after hot rolling to ¼-inch plate.

These data show that the 16% chromium steels are somewhat less resistant to boiling 65% nitric acid than similar steels containing 17 or 18% chromium, but in the range of 16 to 18%, lowering chromium has relatively no effect on the resistance of the steels to reducing acid conditions.

It is clearly seen in all these tests that manganese has little or no effect on the corrosion resistance of the steels in oxidizing or reducing acids. Lowering chromium to 16% reduces the resistance of the steel to nitric acid somewhat but not to dilute sulphuric acid.

Intergranular Corrosion Tests

The strong austenitizing power of carbon and nitrogen in austenitic chromium-manganese-nickel steels has been discussed. The use of carbon for this purpose involves disadvantages since chromium carbide precipitation can destroy the excellent corrosion resistance of these steels. The presence of carbide precipitation is undesirable in steels to be used at low temperatures because of the detrimental effect chromium carbide precipitation may have on impact toughness. Also, the corrosion resisting properties of the austenitic chromium-manganese-nickel steels cannot be properly judged without including data on the influence of carbide precipitation.

Steels containing 0.06 and 0.10% carbon were selected for this study. The nitrogen content of the 0.06% carbon steel was placed at 0.18% and that of the 0.10% carbon steels at 0.15%. The aging treatments employed were twenty minutes at 650 °C (1200 °F) and two hours at 550 °C (1020 °F). The results of the third period of 48 hours in boiling 65% nitric are recorded in Table VI which shows that the precipitation of carbides resulted in an increase in corrosion rate at 650 °C (1200 °F) but not at 550 °C (1020 °F). It further shows that the lowering of carbon to 0.06% produced a marked improvement in resistance to intergranular corrosion.

The relatively insignificant effect of 0.15 to 0.18% nitrogen in the steels, as compared with that of carbon, is in agreement with previous experience which has shown that the precipitation of chromium nitrides is not so detrimental to corrosion resistance as the precipitation of chromium carbides.

Although carbon and nitrogen are effective austenite formers and stabilizers, it is evident that low carbon steels utilizing nitrogen are preferred to those containing higher carbon for stainless steel applications involving corrosive atmospheres and solutions.

Summary

The structural constitution of high nitrogen (0.15%), chromium-manganese-nickel steels containing about 0.10% carbon has been determined at chromium levels of 12,14,15,16,17, and 18% with 0 to 22% manganese, and 0 to 14% nickel to determine the influence of chromium, manganese, and nickel on austenite formation.

The austenitic region is greatly restricted by increasing the chromium content and expanded by raising the nickel content. Manganese in excess of 8% tends to enlarge the delta ferrite-austenite region at chromium levels in excess of 15%. The latter is the maximum chromium content in which a fully austenitic structure can be produced with manganese alone.

An increase in austenite stability takes place with an increase in manganese in steels containing 15% or more chromium. But contrary to expectations the austenite forming capacity of manganese is weak, as it acts primarily as an austenite stabilizer rather than as an austenite former in the relatively low carbon steels of this type.

Both nitrogen and carbon generally expand the austenitic region in steels falling within the above composition range, and they are more potent in this respect than nickel. Of the two, carbon is somewhat the stronger.

The formation of a fully austenitic structure in the cast condition in steels of the above composition range requires greater amounts of nickel and nitrogen than in the hot-worked condition. The homogenizing action of hot working is probably responsible for the difference. Since the presence of too much delta ferrite may cause hot working difficulties, the composition of the steel must be adjusted to ensure a substantially austenitic structure in the cast condition.

Steels within this category are those containing 16 to 17.5% chromium, 3.5 to 4.5% nickel, 7 to 9% manganese, 0.06 to 0.10% carbon, and 0.12 to 0.18% nitrogen, and ingots of the steels should exhibit good hot working characteristics if their initial temperature is kept at a maximum of 1225 °C (2235 °F).

The latter steels have good mechanical properties in the hot-worked, solution-treated condition. A solution treating temperature of

about 1075 °C (1965 °F) has been found suitable for imparting high ductility and toughness, and in this condition, the mechanical properties of the steels are comparable to those of the austenitic chromium-nickel steels. The work hardening properties of the chromium-manganese-nickel steels containing nitrogen are intermediate between those of the 17% chromium—7% nickel and the 18% chromium—9% nickel steels.

The steels have good welding characteristics, and welds made in them have high toughness both at room and subzero temperatures. The stabilizing influence of manganese on the austenitic constituent is particularly helpful in retarding notch sensitivity at the low temperatures.

The general corrosion resistance of the steels in oxidizing solutions and atmospheres is comparable to that of the 17% chromium—7% nickel steel. As would be expected, chromium-manganese-nickel steels containing up to 0.08% carbon are more resistant to intergranular attack than similar steels of higher carbon content.

References

1. Private Communication from the Metals Research Laboratories, Electro Metallurgical Company, Niagara Falls, N.Y.
2. E. E. Thum, THE BOOK OF STAINLESS STEELS, American Society for Metals, 1935.
3. F. F. Himushin, "Chromium-Manganese-Nickel Rustless Steels of Austenitic and Austenitic-Ferritic Types," *Transactions,* All-Union Research Institute Aviation Materials, No. 32, Part 1, 1935.
4. Frederick M. Becket and Russell Franks, U. S. Patent 2,225,440.
5. A. B. Kinzel and Russell Franks, "Alloys of Iron and Chromium," Vol. II, *High-Chromium, Alloys of Iron Monograph,* The Engineering Foundation, 1940.
6. Russell Franks and W. O. Binder, "Cold-Rolled Stainless Steels in Aircraft," *Mechanical Engineering,* Vol. 64, 1942, p. 589.
7. Russell Franks and W. O. Binder, "Tension and Compression Stress-Strain Characteristics of Cold-Rolled Austenitic Chromium-Nickel and Chromium-Manganese-Nickel Stainless Steels," *Journal, of Aeronautical Sciences,* September, 1942.

DISCUSSION

Written Discussion: By J. M. Bates, Carbide and Carbon Chemicals Co., South Charleston, W. Va.

I feel sure that the users of the stainless steels owe a great deal to the authors of this paper for presenting in such clear and concise form a large amount of significant data on the properties of the chromium-nickel-manganese stainless steels containing nitrogen. If these steels are commercially accepted and properly used in applications where the corrosive resistance is sufficiently great, it seems that significant quantities of strategic nickel may be conserved.

Several questions have been raised concerning this paper because of our interest in fabricating problems as well as the proper use of the stainless steels in the chemical industry. Since nitrogen is such a strong austenite former, has any work been done in further increasing the nitrogen content and decreasing the

nickel and/or manganese content of these steels to such a point that straight chromium austenitic steels may be produced? Would the authors anticipate that the properties of such steels would be attractive? Since the chromium-nickel-manganese stainless steels containing nitrogen are as susceptible to carbide precipitation as the regular grades of 18-8 stainless steels, has any work been done to determine the effect of columbium or titanium additions in preventing this precipitation? Would the addition of these alloying constituents appreciably affect the composition and mechanical properties of such steels? Would the lowering of the carbon content to 0.03% maximum to minimize carbide precipitation require a major readjustment in the chemical composition of the alloys?

A limited number of corrosion tests have been made by our laboratory in order to compare the corrosion resistant properties of these steels with that of the regular grades of 18-8 types 304 and 316 stainless steels. Samples have been exposed both in laboratory equipment and in plant equipment under actual operating conditions at random locations where it was thought that the stainless steels might be used successfully. These tests have indicated that in severely corrosive media the corrosion resistance of the chromium-nickel-manganese steels containing nitrogen is not as great as is that of the regular grades of stainless steels. Under mildly to slightly corrosive conditions, however, the corrosion resistance of these steels compares favorably with that of the regular grades. As would be expected, the overall corrosion resistant properties of these alloys approached more closely those of the type 304 stainless steel than those of the usually more corrosion resistant type 316 alloy. From the very limited data obtained so far it appears that these steels may have an important field of application in mild to slightly corrosive media but the greater corrosion resistance of the regular grades will still be required in highly corrosive environments. Tests are being continued in order that more data concerning the potential uses for this relatively new family of stainless steels may be obtained.

Written Discussion: By Samuel J. Rosenberg, Metallurgist, National Bureau of Standards, Washington, D. C.

It is fair to presume that many of the graphs given in this excellent paper will find their way into other articles and reviews concerned with stainless steels. Because of the predilection of some writers to reproduce such graphs without careful consideration of the conditions under which the originals were obtained, errors of fact frequently creep into the technical literature. In an effort to minimize such possibilities, it behooves the original researchers to present their data in such a manner that misinterpretation is impossible.

The authors' Fig. 10 is of particular interest, fixing, as it does, the austenite region of the various alloys as a function of chromium, nickel, and manganese. This austenite region, however, also is influenced by the carbon and nitrogen. By checking against some of the other figures, I believe that this graph applies to the alloys of 0.10 to 0.12% carbon and 0.08 to 0.15% nitrogen. This information should be incorporated in the legend and the austenite field should be labelled. The manganese, carbon and nitrogen levels also should be specified in Fig. 11. Apparently, these values are 9%, 0.10 to 0.12%, and 0.13 to 0.19%, respectively.

Other figures that need attention are Fig. 13 (is the stress the tensile strength?) and Fig. 14, which apparently applies to the steels as heated 15 minutes at 1075 °C and air-cooled.

The authors specify that the Izod impact tests summarized in Table II were

made on specimens machined from ½-inch diameter bars—an obvious impossibility for standard size specimens. I hope that the authors were in error in respect to the size of the original bars so that the impact specimens were not subsize. This hope is strengthened by the fact that the impact tests reported in Table IV were made on specimens machined from ⅝-inch diameter bars. Incidentally, why did the authors change to Charpy keyhole specimens for the data given in Table V and thus make it impossible to make any comparisons with their other impact data?

The authors state that they believe that the lower toughness of the 0.10% carbon steels was due to carbide precipitation at the grain boundaries. It is apparent that some metallographic examination should have been made to establish the validity of this belief.

The data presented in Table VI are of considerable interest and reemphasize the deleterious effect of carbon on intergranular corrosion. It should be noted, however, that the sensitizing treatments used were relatively mild, such as might be encountered during fabrication. For evaluation of performance at elevated temperatures, more severe sensitizing treatments should be used, such as several days exposure at 550 °C. It is possible that after such a treatment all of the steels would have exhibited a high degree of susceptibility to intergranular corrosion, particularly if subjected to the boiling copper sulphate-sulphuric acid test. This possibility leads to the conjecture as to whether these steels could be stabilized by the addition of titanium or columbium. In view of the high nitrogen contents, I imagine that considerably larger amounts of stabilizing elements would be required than would appear necessary from the carbon contents alone. This, in turn, might introduce problems in fabrication of the steels. The authors, having made such a notable contribution to the metallurgy of these new stainless steels, should be encouraged to study the possibilities of stabilizing additions.

Written Discussion: By D. J. Carney, chief development metallurgist, United States Steel Corp., South Works, Chicago.

The United States Steel Corporation has been conducting studies of many variations of austenitic chromium-manganese-nickel steels for the past six years. These studies have been greatly intensified in the past three years. The prime reason for initiating these studies was, of course, to conserve nickel. This is still an excellent objective since it appears that manganese and nitrogen will be more plentiful than nickel in the future, particularly in view of the fact that, for many expanding applications, nickel is almost essential, while for many other applications such as architectural trim, pots, pans and silverware, nickel may not be necessary. It has been demonstrated even at the present time that in periods of emergency the supply of nickel is not adequate to meet the demand. Thus, it is an obligation of the steel producing and steel consuming industries to test and evaluate substitute stainless steels in those periods when nickel is more readily available so that we may be prepared for emergency restrictions, and for the years ahead when the world supply of nickel may not be adequate.

In the recent work of the United States Steel Corporation, we have studied considerably wider variations in chemical composition than the steels reported by the present authors. We hope to publish results of our studies in the near future. However, our studies of steel compositions very similar to those reported by Franks, Binder and Thompson, confirm their observations. For example, we have observed the powerful influence of carbon and nitrogen on ex-

panding the austenite field at high temperatures and the slight tendency of manganese to narrow rather than to expand the austenite field at high temperatures. Manganese has been found, as the authors stated, to be an austenite stabilizer and not an austenite former in these steels. We have also confirmed certain portions of the phase diagrams given in Fig. 9 of the present paper. Further, the authors recommended, on the basis of their laboratory study, a steel containing 0.06 to 0.10% carbon, 7.0 to 9.0% manganese, 3.5 to 4.5% nickel, 16.5 to 17.5% chromium and 0.12 to 0.18% nitrogen. Steels of this type have been produced on a commercial basis by the United States Steel Corporation and have been very successfully processed to sheet product. Other types of chromium-manganese-nickel-nitrogen steels have also recently been successfully produced in commercial quantities. We have found that, while there are certain problems in producing these new types of steels, these problems are not insurmountable.

While our work and that of the Electro-Metallurgical Company was initially directed at developing substitute steels for AISI Types 301 and 302, our present data and the data given in the above paper suggest that these new chromium-manganese-nickel-nitrogen steels may be more than just substitutes, but actually may be better steels for certain applications. It is almost essential that the stainless steel consuming industry conduct as careful an evaluation of these new steels as has been conducted by certain of the steel producing companies. If cooperative effort is attained, it is not without the realm of possibility that a new series of useful austenitic stainless steels may be developed.

We would like to ask the present authors if they have any information concerning the elevated temperature strength and oxidation resistance of the steels they recommend. We have observed that these steels with high nitrogen have markedly superior high temperature tensile and creep rupture properties to those of 301,302 and 304, at least up to 1200 °F. Further, such nitrogen additions in the order of 0.15 to 0.20% appear to enhance the room temperature ductility and the yield strength as much as 10 to 15,000 psi in the annealed condition.

Authors' Reply

The authors wish to thank the discussers for their interesting and constructive comments. It is very gratifying to know that the results of the studies made by the United States Steel Corporation are in good agreement with those presented in the paper. Such confirmation strengthens the value of the investigation. That the commercial problems connected with the production of these steels have not been serious is also of extreme interest.

We agree with Dr. D. J. Carney that the properties of the austenitic chromium-manganese-nickel steels are sufficiently different from the austenitic chromium-nickel steels that they deserve special consideration to avoid needless difficulties in their adoption. It is believed that these steels will find wide use in structural parts operating at room temperature and at elevated temperatures, since they possess interesting creep-rupture properties at elevated temperatures and high yield strength coupled with good ductility at room temperature.

Data on the elevated temperature properties of the steels falling within the recommended ranges are given in Figs. 25 and 26. The tests were conducted on ¼-inch diameter tensile specimens machined from ½-inch diameter hot-rolled bar stock solution heat treated 1 hour at 1960 °F. and air-cooled. Prior to stressing, the specimens were heated ½ hour at the test temperature.

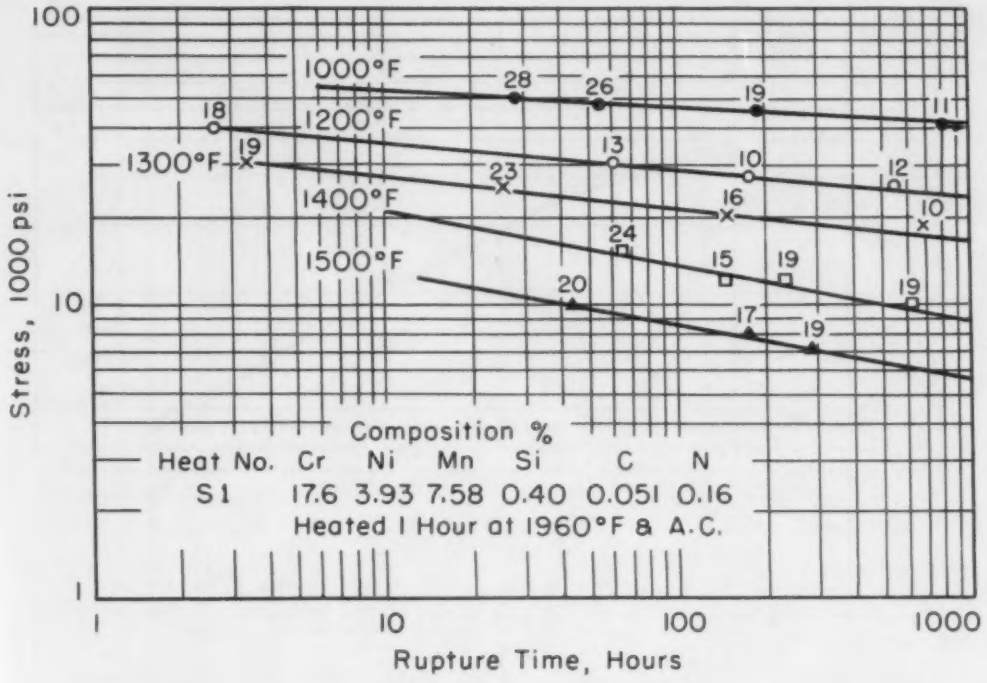


Fig. 25

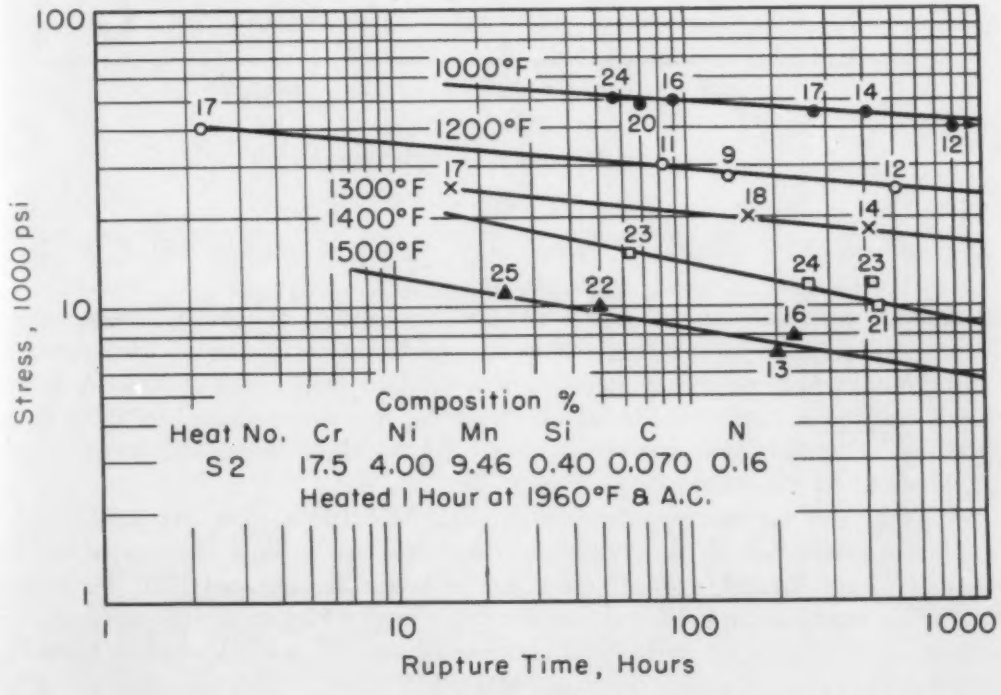


Fig. 26

As shown in Figs. 27 and 28, the stress-rupture strength of the steels is comparable to that of Type 347 steel in the range 1200 to 1500 °F and is higher than that of Type 304 steel. The marked influence of nitrogen on elevated temperature is apparent from these data. No evidence of serious loss of ductility at fracture was observed after prolonged exposure to stress (see Figs. 25 and 26),

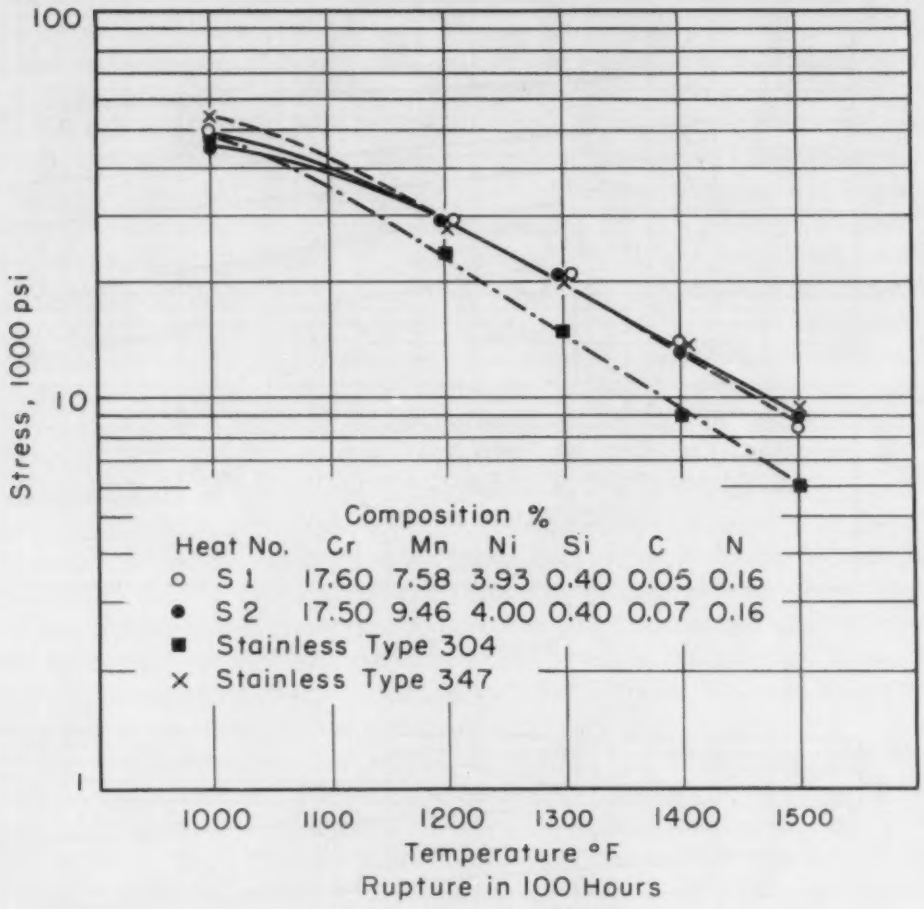


Fig. 27

and subsequent metallographic examination did not reveal any major change in microstructure forewarning embrittlement.

Since good surface stability is required for service at elevated temperature, some consideration also was given to the oxidation resistance of the austenitic chromium-manganese-nickel steels. The oxidation tests were conducted in air for a continuous period of 144 hours. Descaling was accomplished by light sand-blasting. The oxidation specimens were cylindrical in shape and were 1 inch in diameter by 1¼ inches long.

Table VII summarizes the results of the oxidation tests. At 1350 °F, the oxidation resistance of the chromium-manganese-nickel steels is comparable to that of Types 301,304, and 347 steels but is lower at 1550 and 1750 °F. Metallographic examination indicated that the steels have a high order of intergranular oxidation resistance up to 1500 °F. Increasing the manganese content from 7.5 to 9.5% improves oxidation resistance at 1750 °F.

In reply to Mr. Bates' comments, the formation of a fully austenitic chromium-manganese steel without the use of nickel is feasible and has been demonstrated in the Laboratories. Such steels require somewhat higher manganese and nitrogen than those described in the paper. It is anticipated that such steels will be useful for structural parts operating at normal and elevated temperature strength; however, further work will be required before the full possibilities of these steels are known.

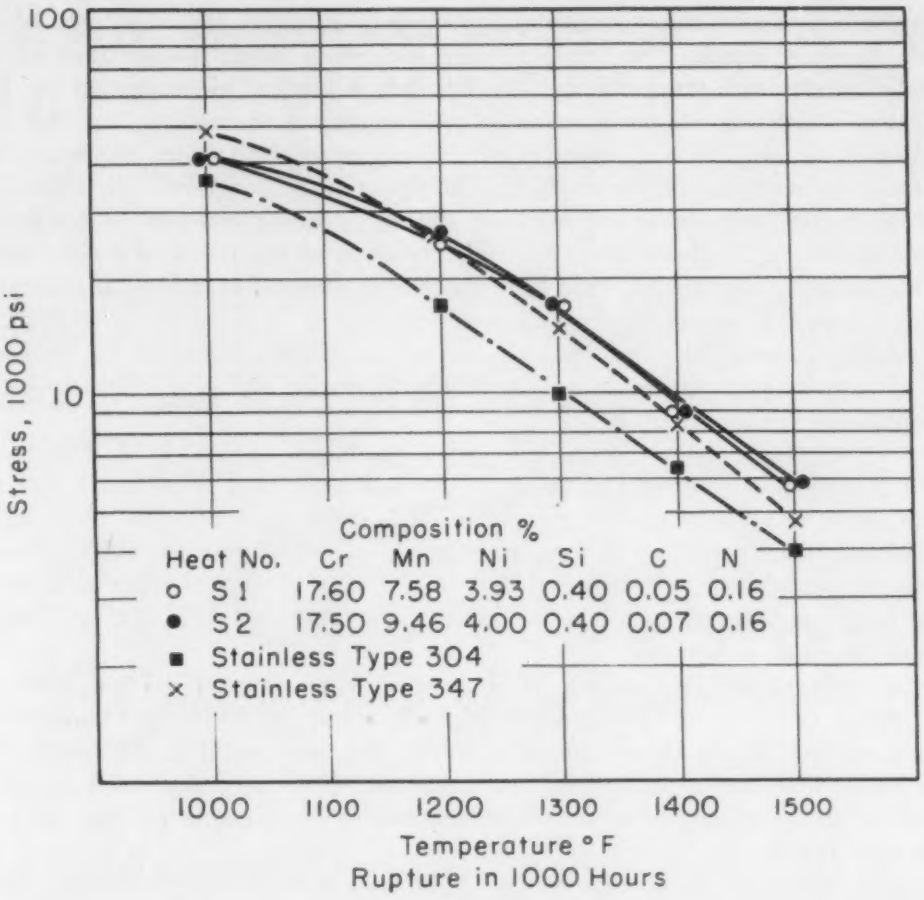


Fig. 28

Table VII
Results of Oxidation Tests at 1350 to 1750 °F*

Sample No.	Composition, % Cr	Ni	Mn	Cb	Si	C	N	1350 °F % Loss In Weight	1350 °F Loss in Grams Per Square Inch In 144 Hours	1550 °F % Loss In Weight	1550 °F Loss In Grams Per Square Inch In 144 Hours	1750 °F % Loss In Weight	1750 °F Loss In Grams Per Square Inch In 144 Hours
S1	17.6	3.93	7.58	—	0.40	0.05	0.16	0.13	0.03	1.8	0.43	5.6	1.2
S2	17.5	4.0	9.46	—	0.40	0.07	0.16	0.10	0.02	1.4	0.30	3.6	0.8
Type 301	17.3	7.09	1.06	—	0.40	0.11	0.03	0.06	0.015	0.4	0.09	1.7	0.4
Type 304	18.3	10.0	1.5	—	0.40	0.06	0.04	0.07	0.016	0.2	0.04	1.4	0.3
Type 347	17.9	10.7	1.5	0.72	0.40	0.05	0.04	0.07	0.016	0.1	0.02	0.2	0.04

* 144 Hour Test Period

The conjecture raised by both Messrs. Bates and Rosenberg, whether these steels could be stabilized by the addition of titanium or columbium so as to improve their resistance to intergranular corrosion, has received some consideration. The tests made at the Electro Metallurgical Company Laboratories show

that the addition of these elements significantly improves the resistance of the steels to such attack. The steels require somewhat larger proportions of the stabilizing elements than indicated by the carbon content alone due to the fact that the stabilizing elements combine with nitrogen as well as carbon. The formation of carbides and nitrides of columbium and titanium, however, unbalances the structure of the steels, and they contain delta ferrite. The formation of delta ferrite may cause hot working difficulties under commercial conditions and constitute a disadvantage. The transformation of the delta ferrite to sigma during subsequent heat treatment also may be detrimental to corrosion resistance and toughness. To avoid the formation of delta ferrite, it is necessary to increase the nickel content. The lowering of carbon to 0.03% maximum to minimize carbide precipitation also causes delta ferrite formation unless a readjustment of chemical composition is made.

The results of the corrosion tests being conducted by Mr. J. M. Bates will be of considerable interest and value to the consumer, and it is hoped that the results will be published when completed. It is quite apparent that these steels can be improperly applied if they are considered substitutes for the austenitic chromium-nickel steels. It is hoped that in the development of these new steels their inherent properties will be recognized and that they will not necessarily be considered as substitutes.

In reply to Mr. Rosenberg, it is customary to express the toughness of weld metal in terms of Charpy keyhole notch values, and we were simply following custom. While direct comparison with the base metal is impossible, the data show that the toughness of the austenitic 17% chromium—3.5 to 4.5% nickel—6 to 9% manganese steels weld metal is comparable to that of 18-8 steel weld metal.

In regard to the toughness of the 0.10% carbon steels at low temperatures, no attempt was made metallographically to establish the validity of our postulation that the low toughness was due to carbide precipitation at the grain boundaries since previous experience had shown that the high carbon steels in the form of relatively heavy sections are prone to show susceptibility to intergranular corrosion when air-cooled from the solution heat treating temperature range and that rapid cooling of the steels eliminates the susceptibility and improves their low temperature toughness.

The data presented in Table VI of the paper were intended to show the probable intergranular corrosion susceptibility that might be encountered during fabrication. They should not be interpreted to show that the low carbon steels would be resistant to such attack after longer periods of exposure at elevated temperature. The time of exposure to elevated temperatures of the low carbon steels is subject to the same limitations as those for unstabilized 18-8 steels of similar carbon content.

THE EFFECT OF DEFORMATION ON THE MARTENSITIC TRANSFORMATION IN AUSTENITIC STAINLESS STEELS

By H. C. Fiedler, B. L. Averbach and Morris Cohen

Abstract

The martensitic transformation in austenitic stainless steels on cooling and on deformation was investigated in 18–8 alloys containing 0.006 to 0.127% carbon. The M_s temperature is found to decrease markedly with increasing carbon content, and the isothermal formation of martensite is observed on holding at subzero temperatures. The amount of martensite produced by plastic tensile strain increases as the temperature of deformation is lowered. Small amounts of plastic strain in the austenite have a stimulating effect on the subsequent transformation during cooling; the maximum stimulation is attained after elongations of 2–4%. Mechanical stabilization of the austenite, or even complete suppression of the martensitic transformation during subsequent cooling, is achieved by larger plastic strains.

Introduction

STAINLESS steels of the 18% chromium, 8% nickel type are normally austenitic at room temperature. A portion of the austenite can, however, be transformed to martensite by plastic deformation under suitable conditions of temperature and strain. Numerous investigators have been concerned with the mechanical properties of these steels and with an evaluation of such variables as the temperature of deformation (1–4),[1] the composition of the alloy (5–9), the composition and temperature of deformation (10,11), and the rate of deformation (12). There is general agreement that unusually high strength properties are produced at subatmospheric temperatures and that these properties are associated with the presence of a magnetic phase, referred to either as ferrite or martensite.

Krivobok and Talbot (13) and Ziegler and Brace (14) have

[1] The figures appearing in parentheses pertain to the references appended to this paper.

This paper is taken from a thesis submitted by H. C. Fiedler in 1953 in partial fulfillment of the requirements for the degree of Sc.D. in Metallurgy at the Massachusetts Institute of Technology.

A paper presented before the Thirty-sixth Annual Convention of the Society, held in Chicago, November 1 to 5, 1954. Of the authors, H. C. Fiedler is associated with the Research Laboratory, General Electric Co., Schenectady, N. Y. and B. L. Averbach and Morris Cohen are associated with the Department of Metallurgy, Massachusetts Institute of Technology, Cambridge, Mass. Manuscript received April 9, 1954.

demonstrated that austenitic stainless steels mechanically worked at liquid nitrogen temperature exhibit greater strengthening and hardening compared to steels worked at room temperature. The latter investigators also fixed the composition limits within the iron-chromium-nickel ternary system which displayed the most pronounced effects. Starr, Reporter and Dorn (15) determined the relative amount of martensite by magnetic measurements as a function of plastic strain over a range of temperatures. While their data indicated that the M_d (the temperature above which martensite is not formed by plastic deformation) lies below room temperature, severe reduction in thickness by rolling at room temperature did produce martensite, from which it was concluded that a "plastic critical point" does not exist.

Little has been reported on the martensitic transformation in 18–8 stainless steels which transform during cooling, inasmuch as the commercial materials remain austenitic down to at least liquid nitrogen temperature in the absence of strain. Uhlig (16) demonstrated the influence of nitrogen on the transformation in high purity carbon-free alloys. Eichelman and Hull (17) have evaluated the effect of chromium, nickel, manganese, silicon and carbon plus nitrogen on the M_s. Smith, Wycke and Gorr (18) utilized the martensitic transformation in hardening steel containing both titanium and aluminum. The kinetics of the isothermal formation of martensite in a 14% chromium, 9% nickel alloy have been reported by Kulin and Speich (19).

The work reported here was undertaken with the object of acquiring some understanding of: (a) the characteristics of the martensitic transformation in high purity alloys of the 18–8 type which transform spontaneously on cooling, and (b) the effect of plastic deformation on the transformation in these alloys both during the deformation and during subsequent cooling to subatmospheric temperatures.

Materials and Procedure

The alloys used in this investigation are listed in Table I, and except for the commercial alloy, will be designated by their carbon contents. The first four are high purity alloys prepared by the Vacuum Metals Corporation, using vacuum melting and casting methods. The last alloy is 304 ELC (extra low carbon grade); however, the nickel content is somewhat lower than is typical for this material.

Table I
Composition of Alloys

C	N	Cr	Ni	Mn	Si	Mo	O
0.127	0.0004	19.76	8.06	0.003	—	—	0.028
0.058	0.0002	18.50	8.48	—	—	—	0.056
0.016	0.0001	18.60	8.42	—	—	—	0.045
0.006	0.0011	18.09	8.33	—	—	—	0.031
0.04*	0.020	18.5	9.1	0.56	0.59	0.20	—

* Type 304 ELC

After being reduced to 0.04—0.06 inch diameter rods by swaging, samples were sealed in evacuated Vycor tubes and austenitized for 20 minutes at 1090 °C (1995 °F). The tubes were quenched into oil and broken beneath the surface. The heat treatment produced an ASTM No. 3 grain size in the high purity alloys and No. 5 in the 304 ELC steel. It was found unnecessary to stress relieve the samples to obtain reproducible results. Usually a surface layer of 0.001—0.003 inch was removed by electropolishing.

Changes in electrical resistance were found to give a satisfactory measure of the inception and the amount of the transformation, with the formation of martensite producing an increase in resistance. The M_s was determined by a deviation in the linear relationship between resistance and temperature on cooling. A Kelvin double bridge was used to measure resistance values to four significant figures on specimens which were two inches long.

The relationship between the amount of martensite and the percent increase in resistance as compared to the austenitic state was determined from room temperature down to −195 °C (−317 °F) as follows: (a) Lattice parameter measurements were made of the austenite and martensite, and from these values the specific volumes of the two phases at room temperature were calculated. The lattice parameters were 3.588 and 2.870 x 10^{-8} cm for the austenite and martensite, respectively, and the specific volumes were 0.1256[2] and 0.1286 cm^3 per gram. (b) The change in resistance at room temperature of samples 0.25 inch diameter was compared to the change in density as the amount of martensite was increased by cooling below M_s. (c) The percent increase in resistance at various temperatures below room temperature was compared to the increase at room temperature for the same change in amount of martensite.

A linear relationship was found between the percent increase in resistance at 20 °C and the percent martensite as determined by density measurements; the formation of 2.1% martensite increased the resistance 1%. From a consideration of the accuracy of the lattice parameter and specific volume measurements, this relationship is believed accurate to ±0.1% martensite. The percent increase in resistance per percent martensite as measured at temperatures from 20 to −195 °C (68 to −317 °F) is shown in Fig. 1. The sensitivity of the bridge and galvanometer was such that a relative change of 0.1% in the amount of martensite could readily be detected. All resistance measurements were made in agitated liquid baths. Alcohol cooled by powdered dry ice was used down to −75 °C (−103 °F), and a mixture of 75% petroleum ether and 25% methyl cyclohexane from −75 °C to −150 °C (−103 to −238 °F).

[2] The specific volume of the austenite was also measured directly and this value (0.1257) checked with that calculated from the lattice parameters.

Wire samples 0.04 inch in diameter were conveniently elongated up to 45% by a lever device. The load was measured with a spring scale, and the strain was obtained from the change in length between gage marks scratched in drops of solder two inches apart.

Electropolishing and electroetching were performed in a solution of 25 gram of chromium oxide, 133 milliliters of glacial acetic acid and

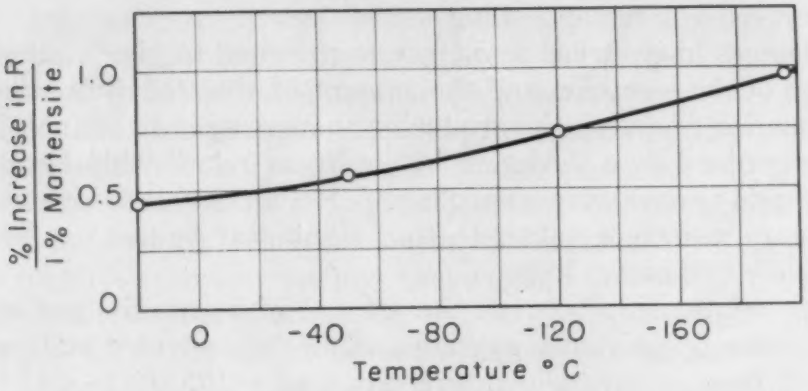


Fig. 1—The % Increase in Resistance Per Per Cent of Martensite Formed Between 20 and — 195 °C.

7 milliliters of water (23). A current density between 1.5 and 1.9 amperes per square inch for polishing and between 0.3 and 0.4 amperes per square inch for etching gave good results.

Results and Discussion

The Transformation in Undeformed Austenite

Table II compares the M_s as determined by resistance measurements and as calculated from the equation of Eichelman and Hull (17) relating M_s and composition. The range of values shown for the measured M_s temperature of each alloy is believed to result from slight differences in composition. However, samples from the same length of forged bar usually had M_s temperatures within a few degrees of one another. The M_s values of the 0.058% carbon and 0.016% carbon alloys, which are nearly matched in chromium and nickel, indicate the

Table II
Comparison of Measured and Calculated Values of M_s

Alloy	Measured M_s, °C	Calculated † M_s, °C
0.127C	<−195	−227
0.058C	−45 to −60	−81
0.016C	0 to −20	−9
0.006C	+3 to +10*	+33
304ELC	<−195	−170

† From the equation of Eichelman and Hull [17]
* These M_s values are uncertain because the as quenched 0.006 C alloy was slightly ferromagnetic at room temperature prior to the subatmospheric cooling.

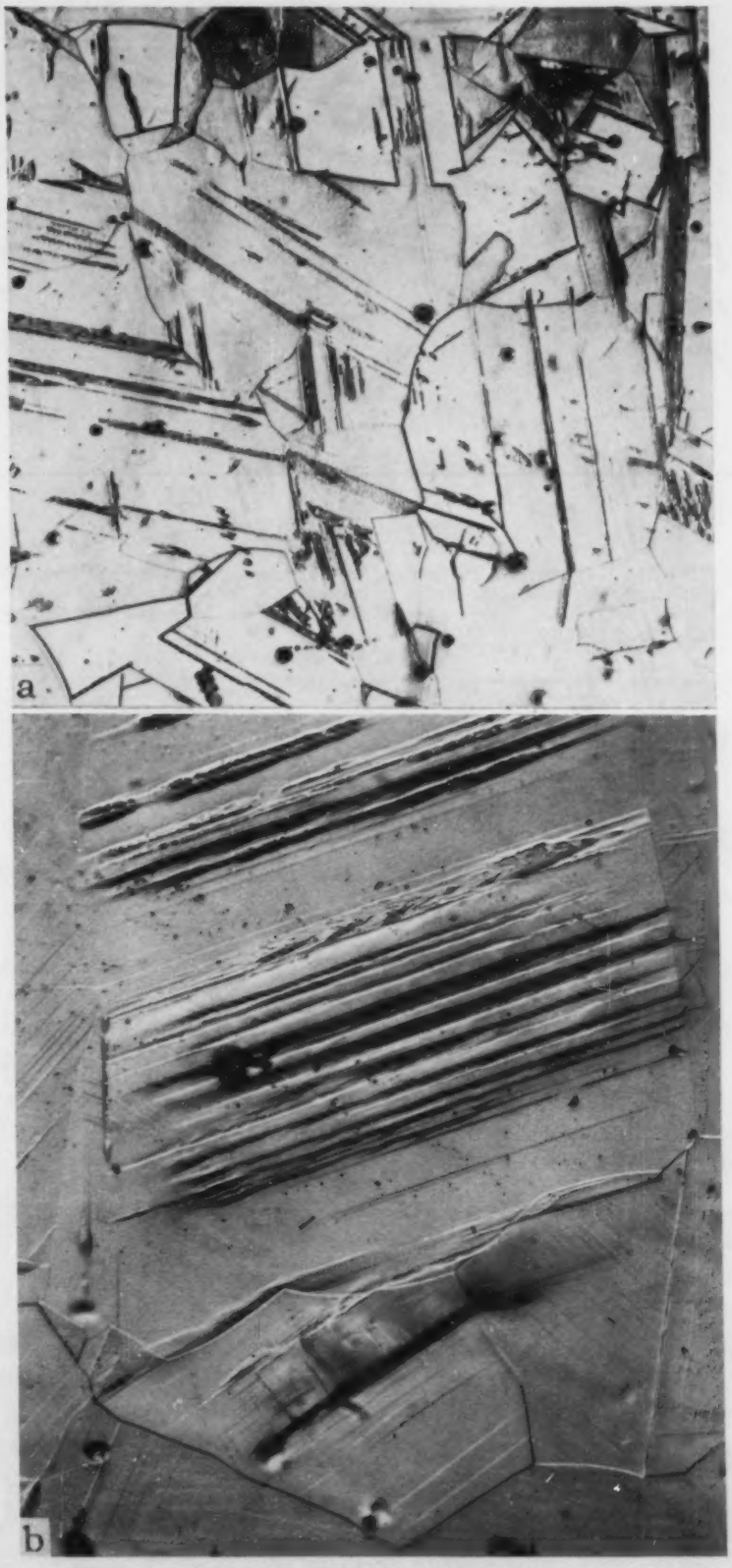


Fig. 2—Upper: Martensite in 0.058% Carbon Formed by Cooling to —195 °C for 15 Seconds. X 150 Lower: Surface markings on electropolished and electroetched sample of 0.058% carbon after cooling to —195 °C. Oblique illumination. X 500

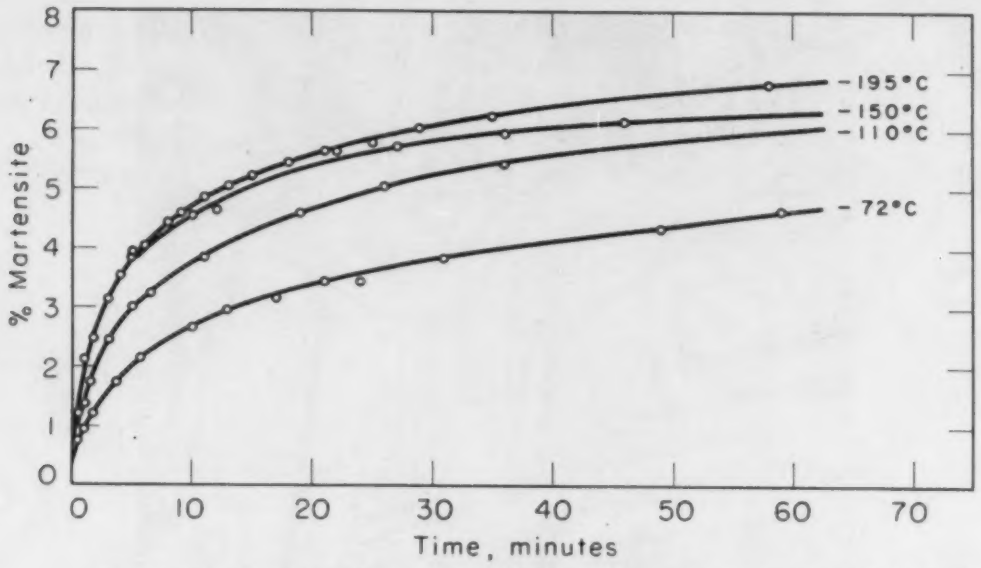


Fig. 3—The Isothermal Formation of Martensite in the 0.006% Carbon Steel at the Temperatures Indicated. Each specimen was first quenched to —195 °C for 20 seconds. At "zero" time there was between 27 and 34% martensite present as a result of the first quench.

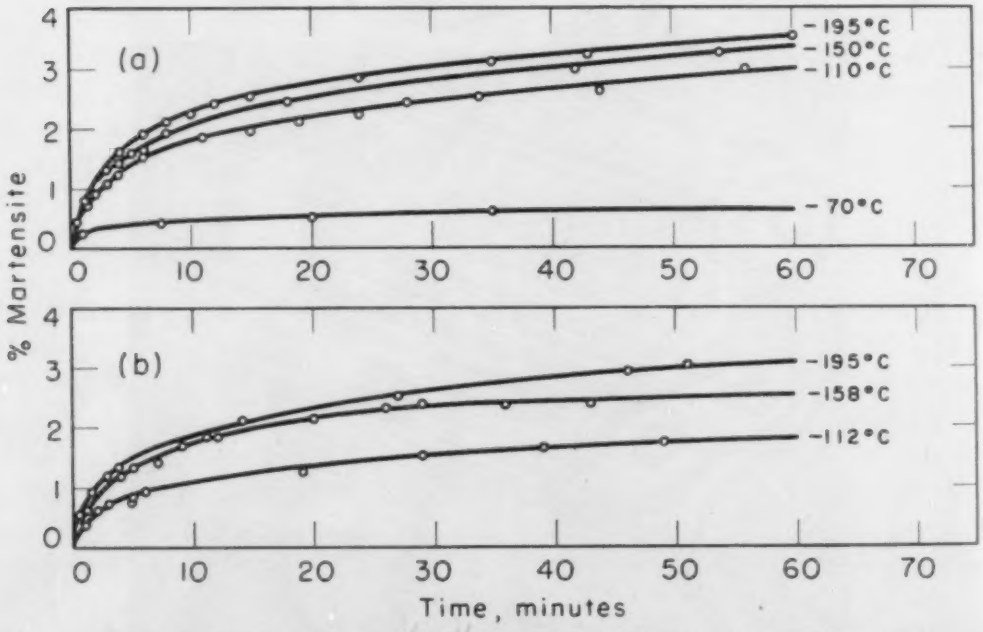


Fig. 4—The Isothermal Formation of Martensite in (a) 0.016% Carbon and (b) 0.058% Carbon at the Temperatures Indicated. Each specimen was first quenched to —195 °C for 20 seconds. At "zero" time there was between 12 and 14% martensite present in the 0.016% carbon alloy and between 3 and 4% in the 0.058% carbon alloy as a result of the first quench.

strong influence of carbon content on the transformation. The M_s is lowered approximately 10 °C for each 0.01% carbon.

The nature of the martensitic product in these alloys is shown in Fig. 2 for the 0.058 C alloy after cooling to —195 °C (—317 °F). The lath-shaped plates usually extend entirely across the grains, being ter-

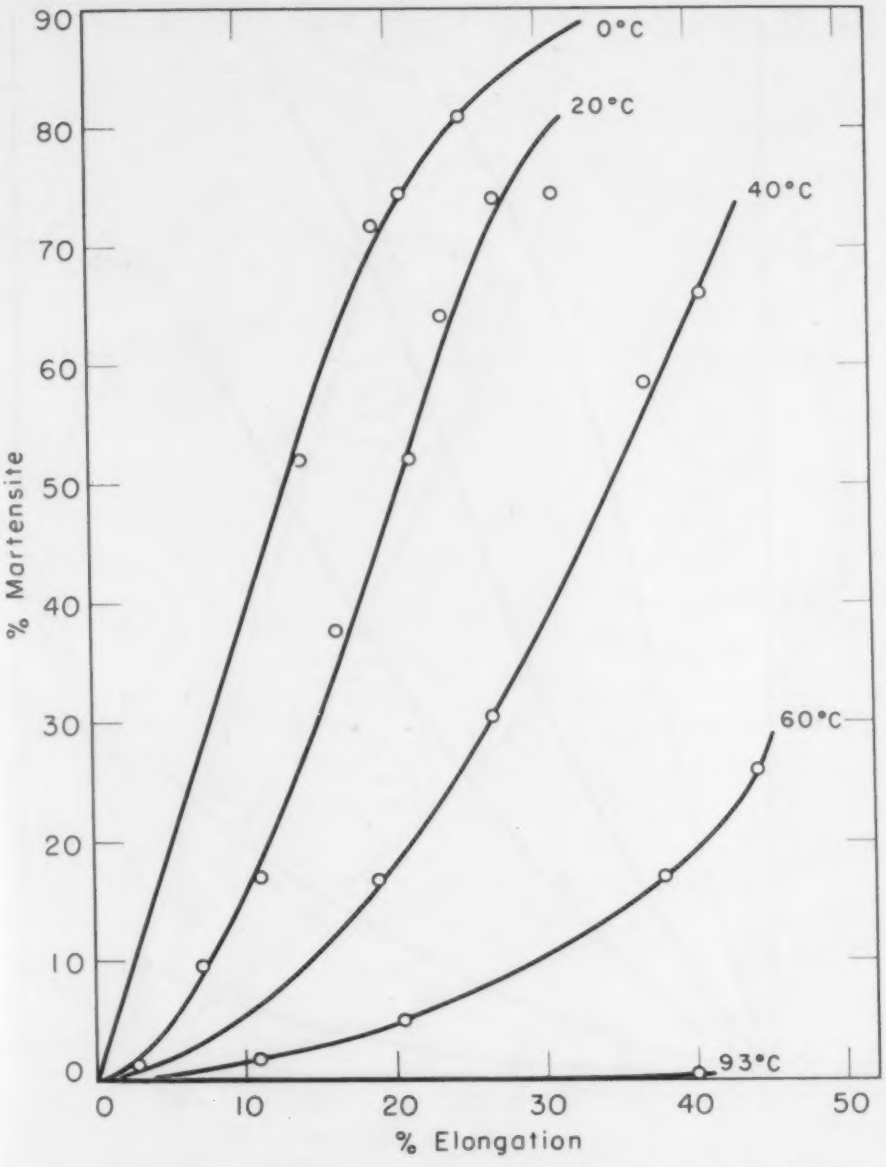


Fig. 5—The Amount of Martensite Produced in 0.016% Carbon by Plastic Deformation at the Temperatures Indicated.

minated by twins or grain boundaries. Although the narrow plates are predominant, chevron-shaped plates are sometimes seen at twin boundaries. The surface upheavals produced by the transformations are clearly illustrated in Fig. 2b. The hardness of the plates, as measured with a Tukon Tester equipped with a Knoop indentor and loaded with 100 gram, was 310 as compared to 210 for the austenite.

The isothermal transformation in the 0.006, 0.016 and 0.058% carbon alloys was measured during a period of one hour and are shown in Figs. 3 and 4. All the samples were first prequenched to −195 °C (−317 °F) for 20 seconds and then upquenched to the holding temperatures. As a result of the prequench, at "zero" time there was

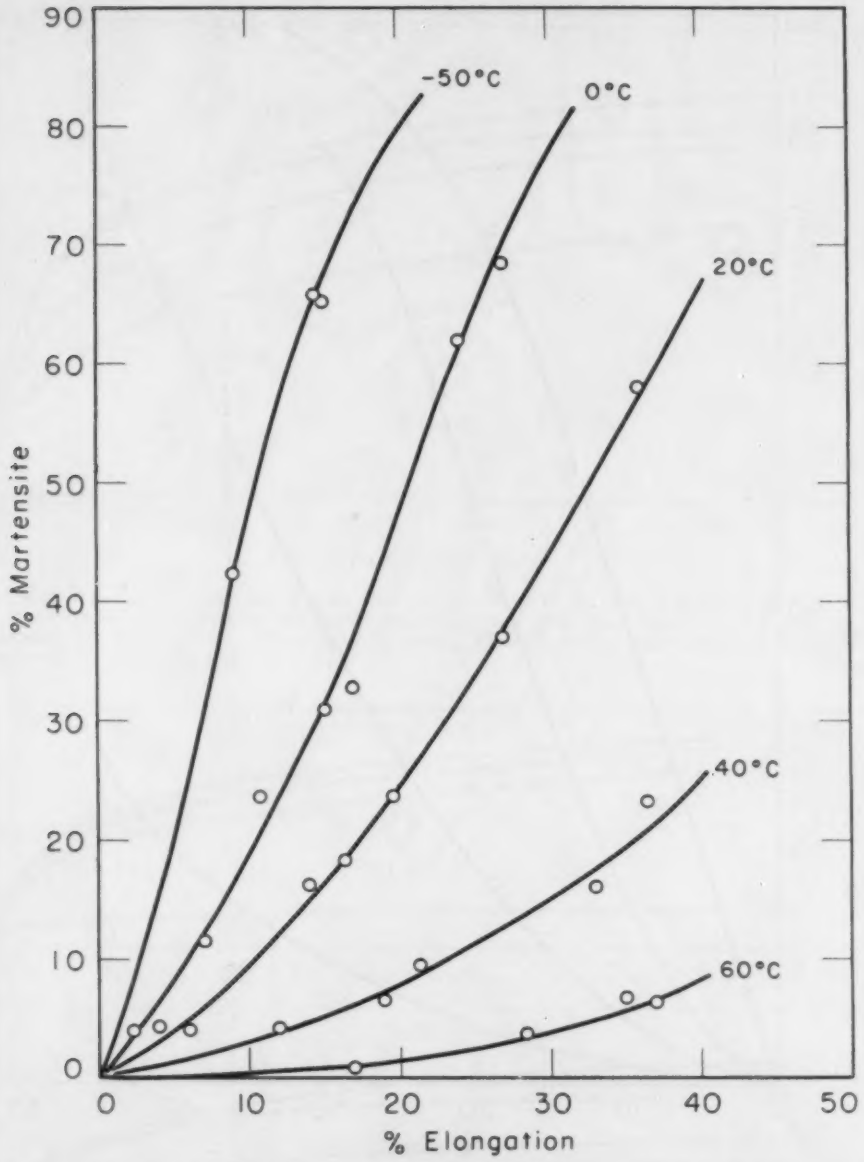


Fig. 6—The Amount of Martensite Produced in 0.058% Carbon by Plastic Deformation at the Temperatures Indicated.

between 3 and 4% martensite present in the 0.058% carbon alloy, between 12 and 14% in the 0.016% carbon alloy, and between 27 and 34% (exclusive of what may already have been present prior to the prequench) in the 0.006% carbon alloy. The amount of martensite formed during the prequench is small as compared to that in other iron-base alloys with similar M_s temperatures. The maximum initial transformation rate occurs at —195 °C (—317 °F) (the lowest temperature studied) for each of the three alloys. It is possible that the initial transformation rate would eventually decrease at some lower temperature.

The initial transformation rates are of the order 10^{-2}% marten-

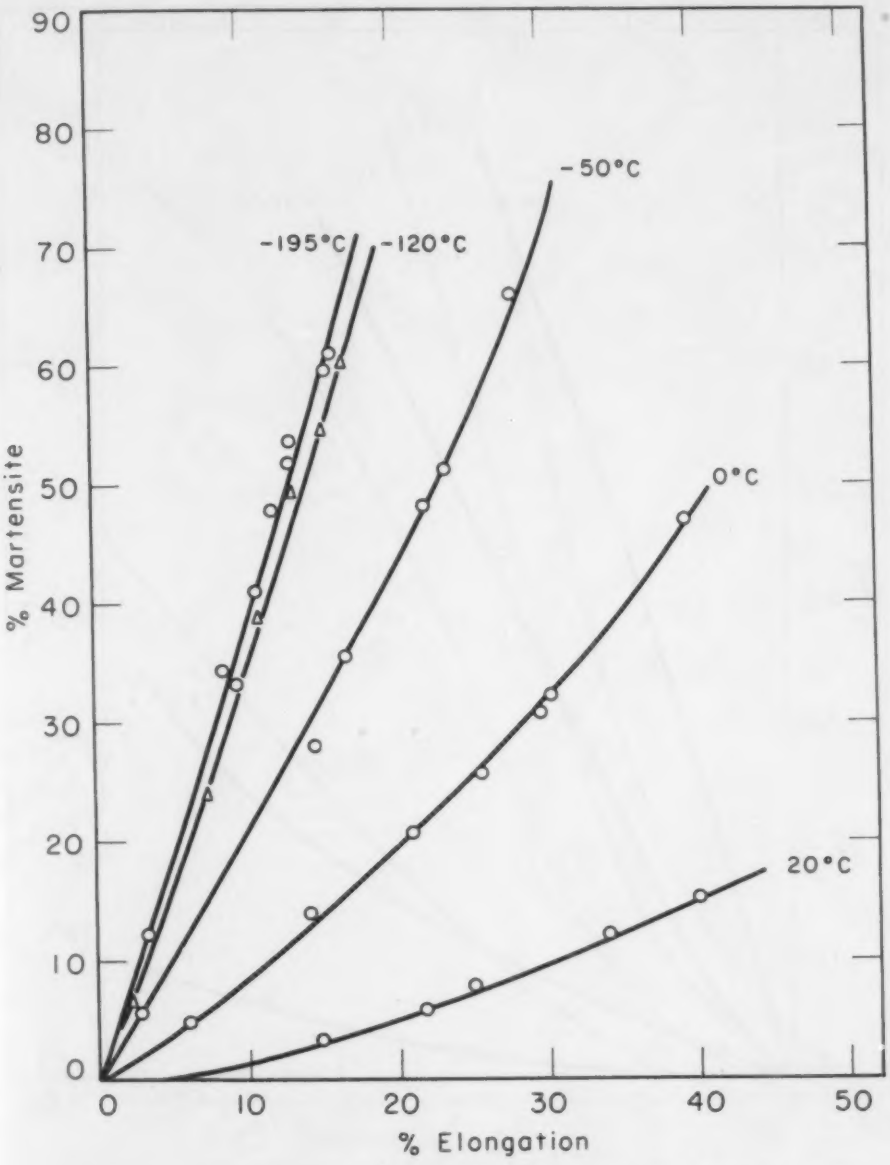


Fig. 7—The Amount of Martensite Produced in 0.127% Carbon by Plastic Deformation at the Temperatures Indicated.

site/second in the 0.058 and 0.016% carbon alloys, and 10^{-1}% martensite/second in the 0.006% carbon alloy. Zanardi (20) found a maximum initial rate of the order 10^{-1} at —120 °C (—184 °F) in a high chromium steel, and Machlin (21) found a maximum initial transformation rate of the order 10^{-3} at —120 °C (—184 °F) in an iron-nickel alloy. In all these instances, athermal martensite was present prior to the isothermal transformation.

The Transformation During Deformation

The amount of martensite produced during deformation as a func-

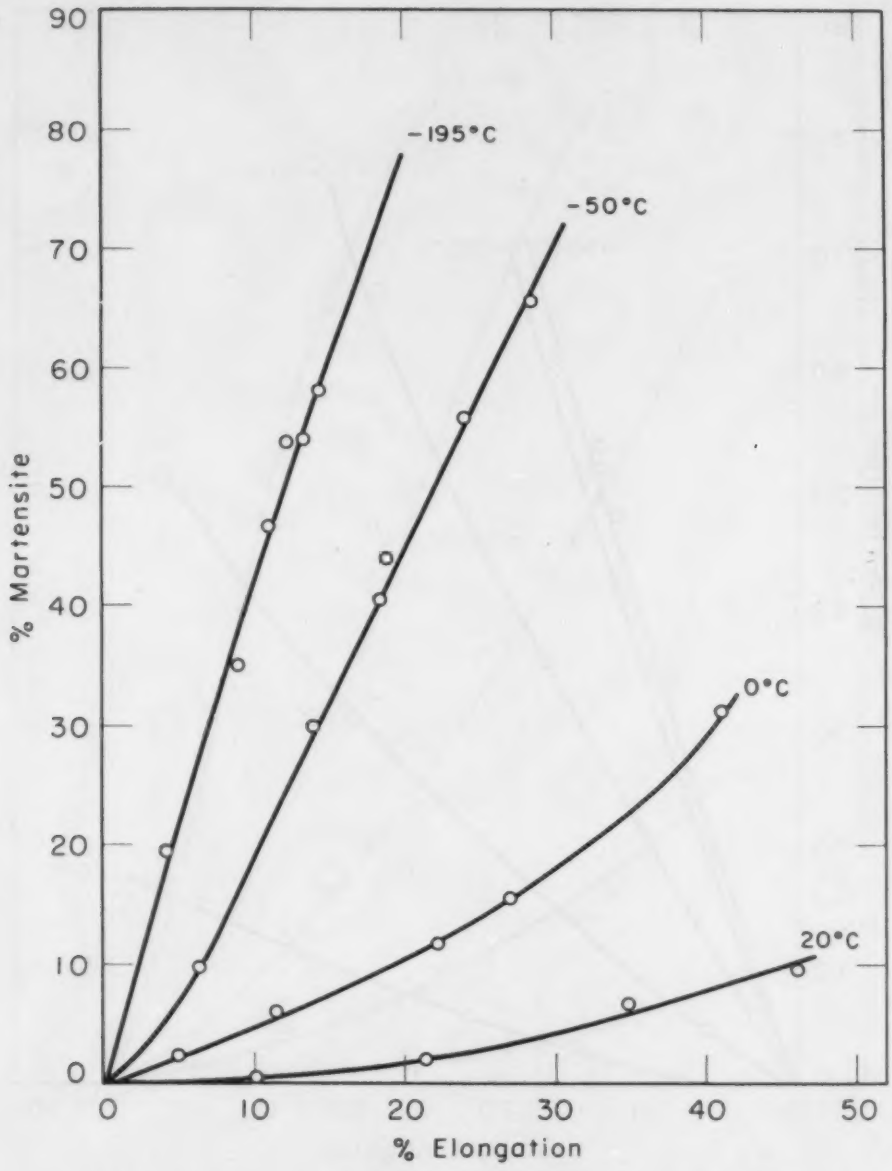


Fig. 8—The Amount of Martensite Produced in 304 Extra Low Carbon Grade by Plastic Deformation at the Temperatures Indicated.

tion of elongation for a range of deformation temperatures is presented in Figs. 5,6,7,8. The quantity of martensite increases as the strain is increased and as the temperature of straining is lowered. The relative strain sensitivity among the alloys is consistent with their M_s temperatures and with the extent of martensitic transformation during cooling to —195 °C (—317 °F). The 0.127% carbon alloy and the 304 ELC steel are nearly identical in their sensitivity to strain in forming martensite.

Fig. 9 was derived from Fig. 5 to illustrate the percent martensite in the 0.058% carbon alloy as a function of temperature of deformation

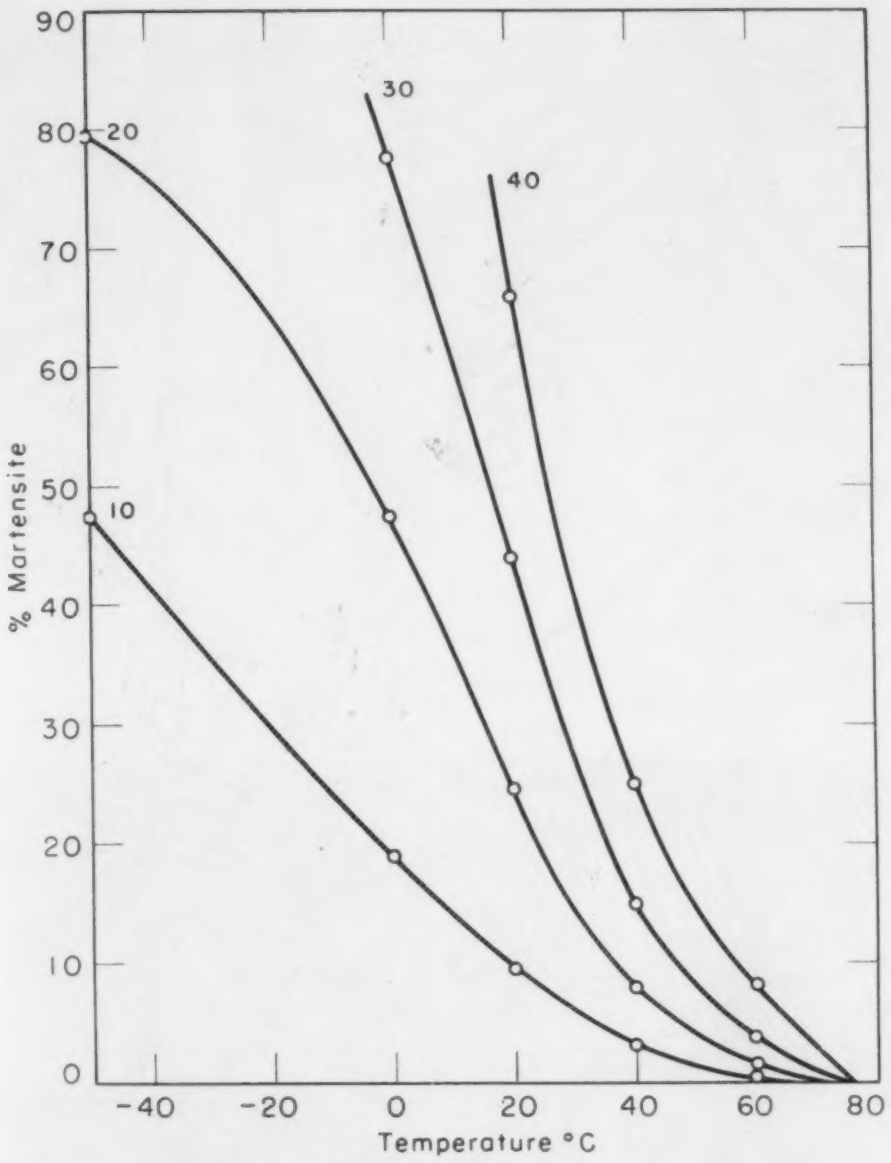


Fig. 9—The Amount of Martensite Produced During Deformation of 0.058% Carbon as a Function of Temperature for 10, 20, 30 and 40% Elongation.

for 10,20,30 and 40% elongation. Similar curves were obtained for the other alloys but are not shown here. The curves extrapolate to zero percent martensite in the vicinity of 80,75,25 and 30 °C for the 0.016, 0.058, 0.127% carbon and 304 ELC alloys, respectively. These temperatures appear to be considerably less sensitive to composition than are the M_s temperatures.

M_d is defined as the temperature above which the martensitic transformation cannot be induced by deformation. The concept of an M_d arises from Scheil's (22) view that the martensitic transformation and slip are competing mechanisms of yielding under stress, each having

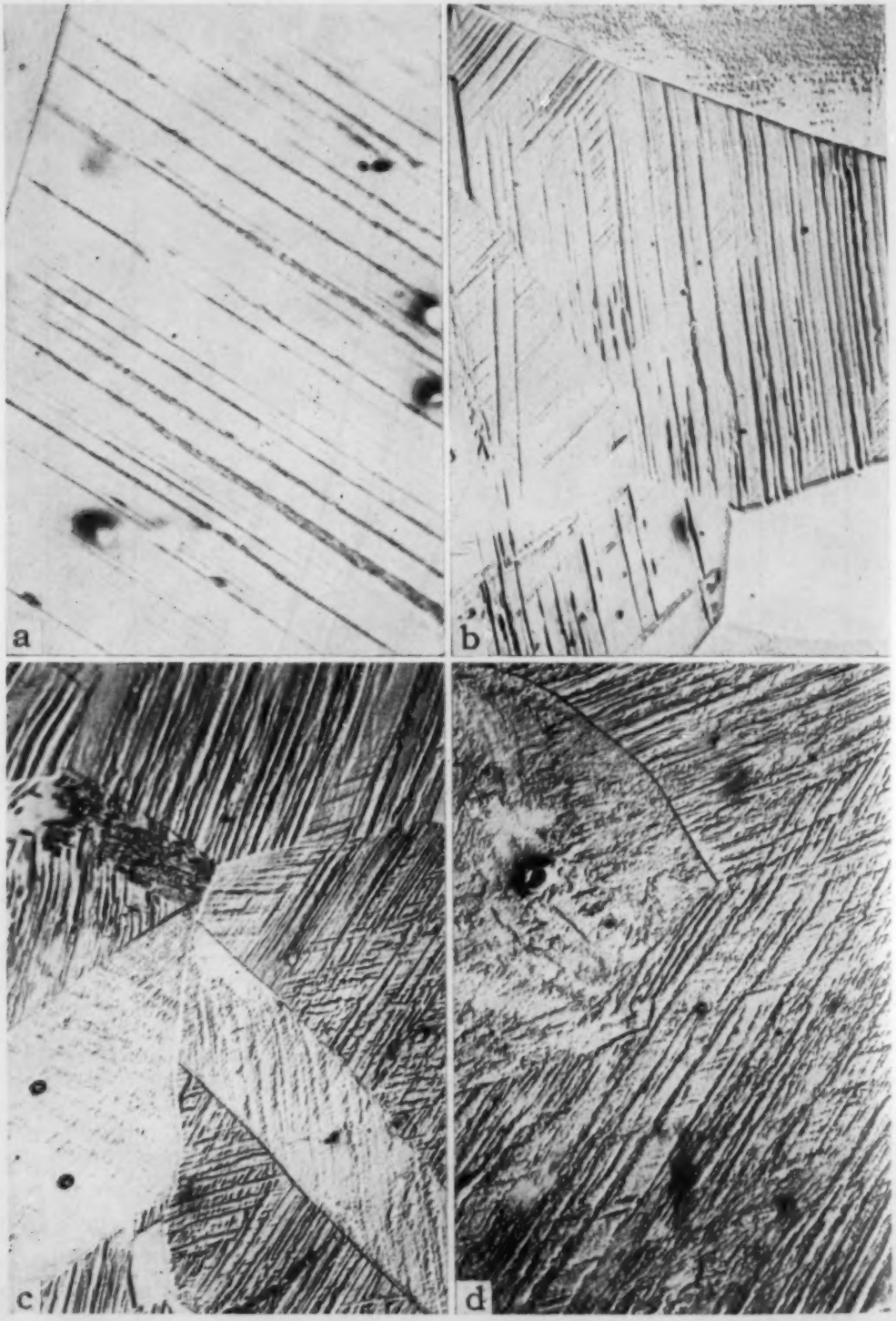


Fig. 10—Martensite in 0.058% Carbon Produced by Deformation at 20 °C. Oblique illumination. X 500 (A) Elongated 6%; 4% martensite. (B) Elongated 10%; 8% martensite. (C) Elongated 25%; 26% martensite. (D) Elongated 35%; 56% martensite.

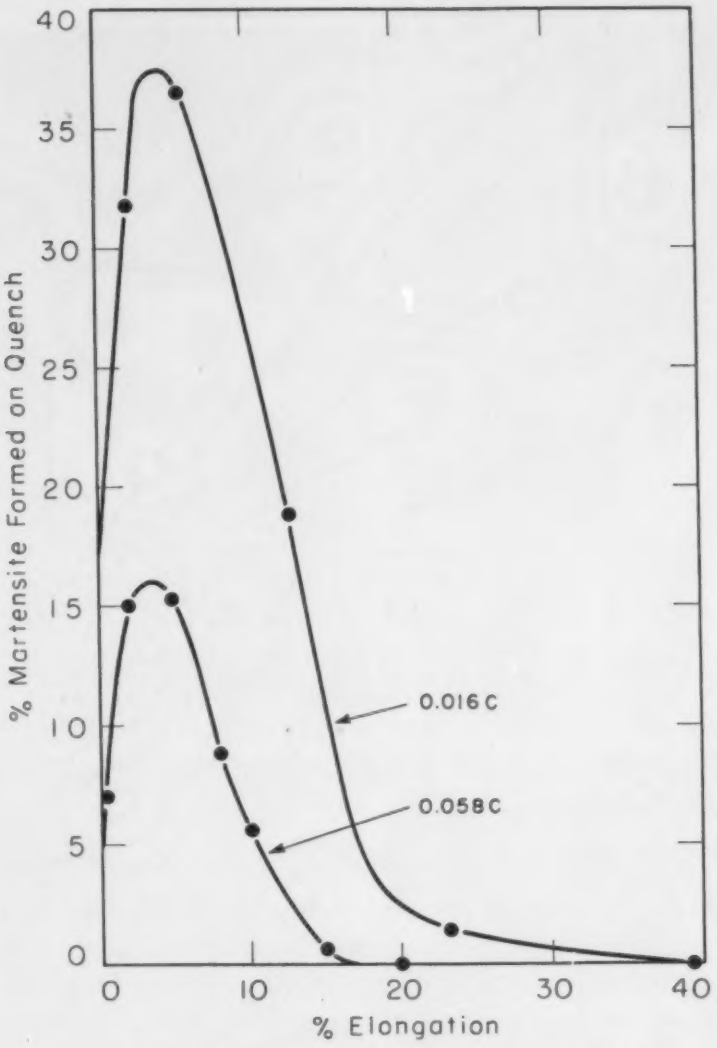


Fig. 11—The Amount of Martensite Formed by First Elongating at 93 °C and then Cooling to —195 °C for 15 Seconds. No martensite was formed during the elongation.

a characteristic dependence upon temperature. The maximum deformation of 40% elongation employed in this investigation was insufficient to ascertain the M_d temperatures. For example, although the elongation experiments indicated that no martensite is produced in the 0.127% carbon alloy by strains up to 40% elongation at temperatures above 25 °C, cutting a wire sample at 100 °C caused the cut edges to be magnetic. Thus, the extrapolated temperature cited above should not be construed as M_d temperatures in the general sense.

Photomicrographs of the 0.058% carbon alloy elongated between 6 and 35% at 20 °C are shown in Fig. 10. The number but not the width of the plates increases with deformation. Observation under the microscope indicated that up to and including 25% elongation some whole grains or twins within a grain exhibit no evidence of transforma-

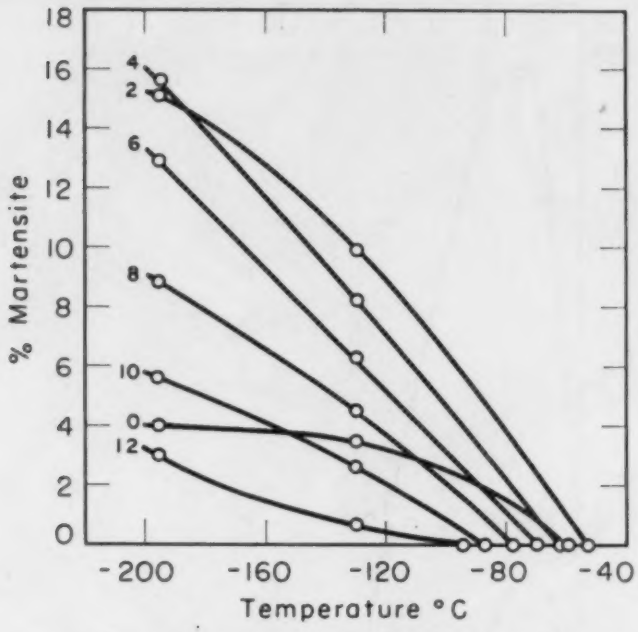


Fig. 12—The Effect of Plastic Deformation at 93 °C on the Formation of Martensite for the 0.058% Carbon Steel. The % elongations are shown at the left of the curves.

tion. Apparently such orientations were highly unfavorable for slip or transformation or both.

Effect of Plastic Strain on Subsequent Transformation

It is found that small plastic strains favor whereas larger strains hinder the subsequent transformation on cooling. Within limits, these effects of plastic strain become more potent as the temperature of straining is increased and are greatest for temperatures at which no martensite forms during the deformation.

The influence of plastic deformation at 93 °C on the amount of martensite formed during cooling to liquid nitrogen temperature is shown in Fig. 11, while the effect of plastic deformation on the range curve of the 0.058% carbon alloy is given in Fig. 12. M_s in the 0.058% carbon alloy is raised about 8 °C by 2% elongation and then decreases almost linearly with strain up to 11% elongation. The amount of martensite formed on quenching below M_s is a maximum after 2–4% elongation. The transformation on cooling is completely suppressed after 16% or more elongation. The 0.016% carbon alloy strained at 93 °C also exhibits maximum stimulation on cooling after 2–4% elongation. However, approximately 40% elongation is necessary to cause complete inhibition of the cooling transformation.

The photomicrographs in Fig. 13 a,b,c,d depict the change in the martensite which appears on cooling. With increasing deformation, the plates appear to broaden as the result of many parallel plates forming close together, and the plates are more likely to terminate short of a

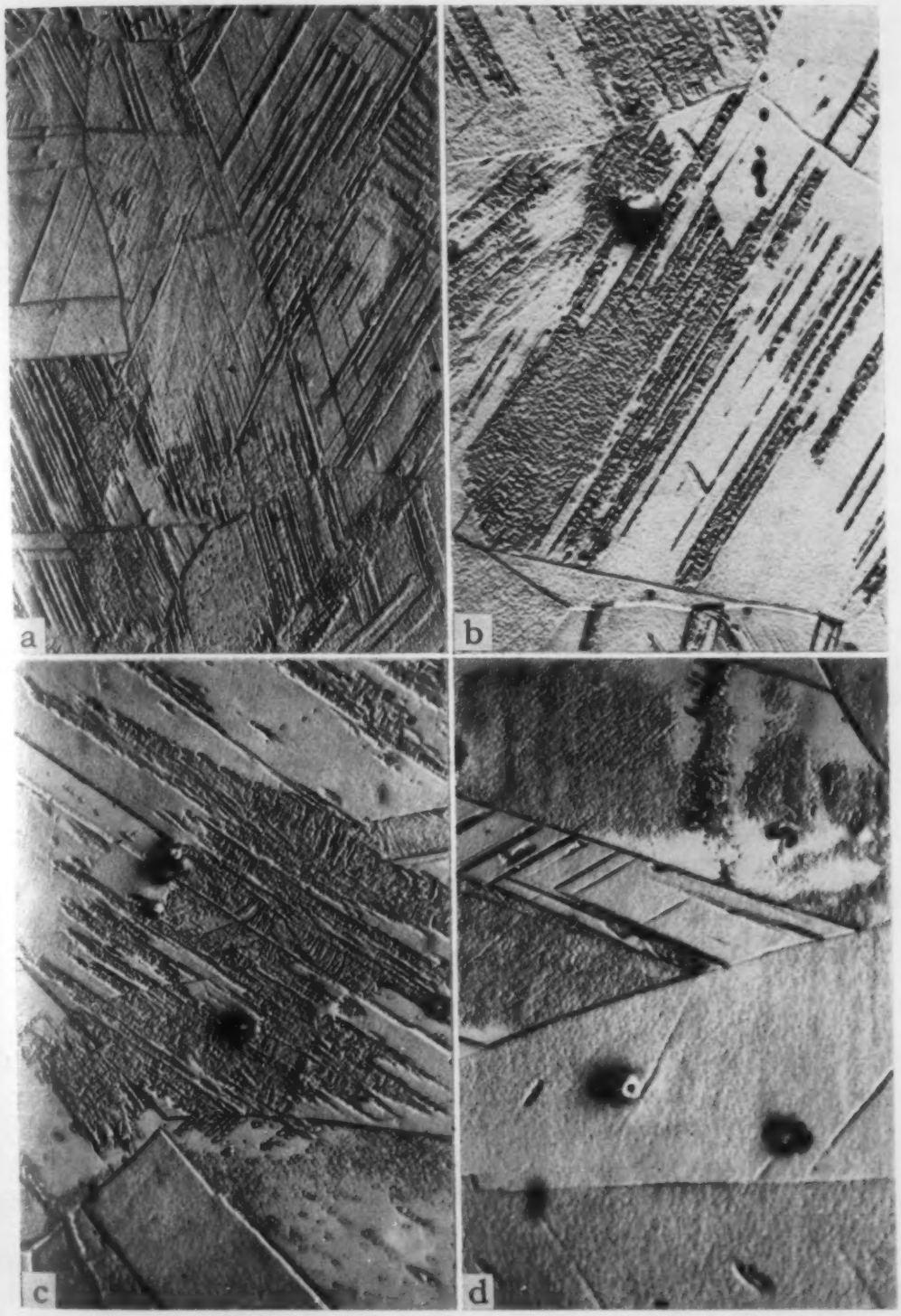


Fig. 13—Martensite in 0.058% Carbon Formed by Cooling to —195 °C. for 15 Seconds After Deforming at 93 °C. Oblique illumination. X 500. (A) 2.8% elongation; 19.0% martensite. (B) 4.7% elongation; 19.7% martensite. (C) 10.0% elongation; 6.0% martensite. (D) 16.0% elongation; no martensite.

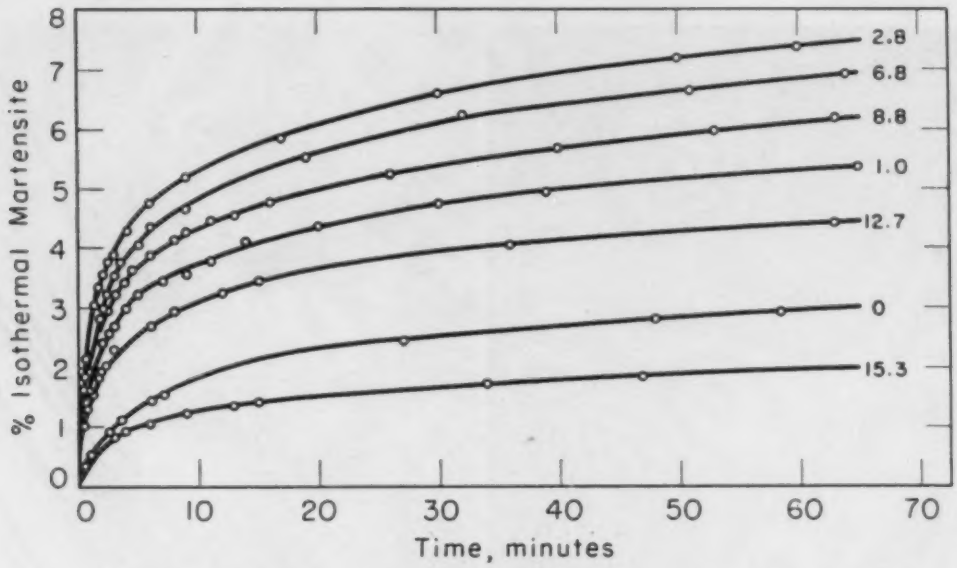


Fig. 14—The Effect of Plastic Deformation at 93 °C on the Isothermal Transformation in 0.058% Carbon Steel at —195 °C. The % elongations are shown at the right of the curves. The amounts of martensite present at "zero" time are shown in Fig. 11.

grain or twin boundary. Although Fig. 13d shows some roughening of the surface, there was no change in resistance after cooling to —195 °C, and thus no martensite formation.

The isothermal transformation is similarly affected. Samples of the 0.058% carbon alloy were elongated between 0 and 15% at 93 °C and cooled to —195 °C. As can be seen in Fig. 14, small amounts of deformation favor and larger amounts hinder the isothermal transformation, with the stimulation reaching a peak at 2–4% elongation. Samples elongated 2.5–3.0%, prequenched to —195 °C (—317 °F), and held at temperatures between —195 and —70° C (—317 and —94 °F) have a maximum transformation rate at —195 °C (—317 °F), as do the undeformed samples.

The stimulating effect of plastic strain may be attributed to: (a) the formation of strain embryos during the deformation from which the martensite is nucleated, and (b) the introduction of residual stresses which promote the transformation by raising the free energy of the embryos. The potency of residual stresses may be demonstrated by straining samples in elastic tension. Stressing at 10,000 psi raises the M_s by 4 °C, and 15,000 psi raises the M_s by 10 °C.

These "acceleration" phenomena are also characteristic of nucleation and growth reactions which occur more rapidly in cold worked than in annealed materials. However, the opposite effects due to greater amounts of plastic deformation would not normally be expected with nucleation and growth reactions. On the other hand, "mechanical stabilization" as a result of plastic deformation is well known in the case of martensitic transformations.

The usual explanation given for mechanical stabilization originated with Scheil (22) who presented metallographic evidence that slip or deformation bands act as barriers in limiting the size of the plates that can form. However, it was observed in the present work that martensitic plates in deformed specimens frequently stop short of any detectable obstruction. This suggests that mechanical stabilization may be related to the distortion or to the substructure existing in the cold-worked austenite. Possibly the propagating mechanism which depends upon precise cooperative displacements tends to become clogged in a severely distorted lattice.

It was thought that the role of the fine distorted structure, as compared to gross slip or deformation bands, in hindering transformation on cooling could be pointed up by annealing experiments below the recrystallization temperature. Such a heat treatment would not be expected to disturb the configuration of the slip and deformation bands, but the local distortions and the substructure might be altered. It was found that the transformation was restored in the 0.058% carbon alloy elongated 16 to 19% by heat treating for one hour at 650 °C (1200 °F) or higher (the recrystallization temperature being approximately 925 °C). However, carbide precipitation occurred in the same temperature range, and it was thus impossible to determine unambiguously whether the restoration was due solely to structural changes in the austenite or to changes in the chemistry of the austenite. The transformation was also restored in deformed samples of the 0.016% carbon alloy, but carbide precipitation also occurred in the same temperature range.

Summary and Conclusions

The martensitic transformation has been investigated in four high purity alloys of the 18–8 type and one commercial alloy, 304 ELC. The carbon contents of the high purity alloys ranged from 0.127 down to 0.006% carbon. The following conclusions can be drawn:

(a). The M_s is highly sensitive to the carbon content; each 0.01% carbon lowers M_s approximately 10 °C. The M_s of 0.127% carbon and 304 ELC is below −195 °C (−317 °F).

(b). The amount of martensite which forms isothermally is greater and the initial transformation rate is higher, the lower the carbon content. The isothermal transformation rate is, however, in each case most rapid at −195 °C (−317 °F), the lowest temperature studied.

(c). The amount of martensite produced by plastic tensile strain is increased as the temperature of deformation is lowered and as the amount of deformation is increased.

(d). Small amounts of plastic strain have a stimulating effect on subsequent transformation during cooling. Maximum stimulation is achieved by elongations of 2–4%.

(e). Mechanical stabilization, or complete suppression of the transformation during cooling, can be achieved by large elongations. Increasing amounts of deformation are required to achieve mechanical stabilization as the carbon content is decreased. It is suggested that this inhibiting effect of plastic strain is due to the distorted or subgrain structure of the deformed austenite which may interfere with the propagation of the martensite.

ACKNOWLEDGMENTS

The authors wish to acknowledge the financial support of the M.I.T. Instrumentation Laboratory and the Air Force in this research program. Important laboratory assistance was rendered by Harold Ludwig.

References

1. E. W. Colbeck, W. E. MacGillivray and W. R. D. Manning, "Austenitic Stainless Steels at Low Temperatures," *Transactions,* Institution of Chemical Engineers, Vol. 11, 1933, p. 89.
2. S. S. Rosenberg, "Effect of Temperature on the Properties of Aircraft Metals," *Journal of Research,* National Bureau of Standards, Vol. 25, 1940, p. 673.
3. R. A. Lincoln and W. H. Mather, "Effect of Temperature of Cold Rolling, Temperature of Testing and Rate of Pulling on Tensile Properties of Austenitic Stainless with Low Nickel Content," Regional Technical Meetings of American Iron and Steel Institute (1948) 57–74.
4. W. D. Binder, "Effect of Cold Work at Low Temperature on Austenitic 18-8," METALS PROGRESS, Vol. 58, 1950, p. 201.
5. F. K. Bloom, G. N. Goller and P. G. Mabus, "The Cold Work Hardening Properties of Stainless Steel in Compression," TRANSACTIONS, American Society for Metals, Vol. 39, 1947, p. 843.
6. N. B. Pilling, "Some Effects of the Nickel Content in Austenitic Iron-Chromium-Nickel Alloys," *Proceedings,* American Society for Testing Materials, Vol. 30, Part 2, 1930, p. 278.
7. L. B. Pfeil and D. G. Jones, "A Contribution to the Study of the Properties of Austenitic Steels," *Journal,* Iron Steel Institute, Vol. 127, No. 1, 1933, p. 337.
8. C. B. Post and W. S. Eberly, "Stability of Austenite in Stainless Steels," TRANSACTIONS, American Society for Metals, Vol. 39, 1947, p. 868.
9. V. N. Krivobok and R. A. Lincoln, "Austenitic Stainless Alloys," TRANSACTIONS, American Society for Metals, Vol. 25, 1937, p. 637.
10. K. Mathieu, "Influence of Alloy Content and Conditions of Cold Working Upon Gamma-Alpha Transformation of Austenitic Steels," *Archiv Eisenhuttenwesen,* Vol. 16, No. 6, 1942, p. 215.
11. D. J. McAdam, G. W. Geil and F. J. Cromwell, "Influence of Low Temperatures on the Mechanical Properties of 18-8 Cr-Ni Steel," NBS *Journal of Research,* Vol. 40, 1948, p. 375.
12. S. Storchheim, "How Draw Speed Affects Stainless Wire," *American Machinist,* Vol. 96, 1952, p. 124.
13. V. N. Krivobok and A. M. Talbot, "Effect of Temperature on the Mechanical Properties, Characteristics and Processing of Austenitic Stainless Steels," *Proceedings,* American Society for Testing Materials, Vol. 50, 1950, p. 895.
14. N. A. Ziegler and P. H. Brace, "Hardening of Austenitic Stainless Steels by Mechanical Working at Sub-zero Temperatures," American Society for Testing Materials, Preprint, 1952.

15. C. D. Starr, N. Reporter and J. E. Dorn, "Investigations on the Mechanism of the Strain Induced Martensitic Reaction in 18-8 Stainless Steel," Fifteenth Technical Report, Series 22, Issue 15, N7-onr-295, Task Order II, NR-013-048.
16. H. H. Uhlig, "The Role of Nitrogen in 18-8 Stainless Steel," TRANSACTIONS, American Society for Metals, Vol. 30, 1942, p. 947.
17. G. H. Eichelman, Jr. and F. C. Hull, "Effect of Composition on the Temperature of Spontaneous Transformation of Austenite to Martensite in 18-8 Type Stainless Steel," TRANSACTIONS, American Society for Metals, Vol. 45, 1953, p. 77.
18. R. Smith, E. H. Wycke and W. W. Gorr, "Precipitation Hardening Stainless Steel," *Transactions,* American Institute of Mining and Metallurgical Engineers, Vol. 167, 1946, p. 313.
19. S. A. Kulin and G. R. Speich, "Isothermal Martensite Formation in an Iron-Chromium-Nickel Alloy," *Transactions,* American Institute of Mining and Metallurgical Engineers, Vol. 194, 1952, p. 661.
20. T. J. Zanardi, "The Martensitic Transformation in High Chromium Steels," SM Thesis, M.I.T. 1952.
21. E. S. Machlin and Morris Cohen, "The Isothermal Mode of the Martensitic Transformation," *Transactions,* American Institute of Mining and Metallurgical Engineers, Vol. 194, 1952, p. 489.
22. E. Scheil, "Uber die Umwandlung des Austenits in Martensit in Eisen-Nickellegierungen unter Belastung," *Zeitschrift für anorganische und allgemeine Chemie,* Vol. 207, 1932, p. 21.
23. C. E. Morris, "Electropolishing of Steel in Chrome-Acetic Acid Electrolyte," METAL PROGRESS, Vol. 56, 1949, p. 696.

DISCUSSION

Written Discussion: By B. J. Connolly, research manager, Engineering Research Department, Billingham Division, Imperial Chemical Industries Limited, Billingham, England.

The authors have demonstrated the powerful effect of carbon in causing a rapid change in the stability of austenite and this is confirmed in some work that we have done recently at Billingham.

As part of a program to determine the subzero temperature mechanical properties of various metals, we have tested a number of chromium-nickel austenitic steels and the results obtained with three of these confirm the powerful stabilizing effect of carbon. Analyses of the steels were:

Type	C	Si	Mn	Cr	Ni	Mo	Cu	N
18/8	0.10	0.21	0.80	17.9	8.6	0.16	0.22	0.03
ELC 18/8	0.021	0.40	0.47	17.1	8.0	0.05	0.08	0.01
ELC 18/10	0.022	0.48	0.49	17.4	10.2	0.05	0.06	0.01

Soaking these steels for 4 hours at —195 °C (without any straining) produced some transformation of the austenite to martensite as judged by magnetic testing at room temperature after warming up from —195 °C; and the relative stabilities of the three austenites can be judged from the following figures:

Type	% Ferromagnetism Before Soaking at —195 °C (due to initial ferrite)	% Ferromagnetism After Soaking at —195 °C (due to initial ferrite and transformed austenite (martensite)
18/8	Nil	1%
ELC 18/8	22%	45%
ELC 18/10	Nil	25%

When the analyses of the three steels are compared, the effect of carbon on

austenite stability becomes evident, although it should be noted that the most stable austenite (18/8) also contains the higher nitrogen content which, of course, makes the austenite more stable. However, the ELC 18/10, even with its extra 2% nickel, is much less stable than the higher carbon steel.

No precise figures are available for the amount of ferromagnetism induced by deformation at −195 °C but the heavily necked ends of the broken −195 °C tensile testpiece in the stable 18/8 were strongly magnetic at room temperature, and exhibited much martensite when examined microscopically. Other parts of the specimen not heavily deformed at the low temperature were nonmagnetic.

The extreme stability of the more highly alloyed austenites was demonstrated in some further tensile tests which we did on 25/20 and 25/27 chromium-nickel steels. Neither of these steels showed any martensite at all, even at the fractured ends of the −195 °C testpiece which had necked considerably.

It would be very interesting indeed if the authors could provide some information on the amount of ferromagnetic phase present in their alloys initially. The 0.006 and 0.016% carbon alloys should contain an appreciable amount of ferrite in the initial fully softened condition, and it would be interesting to know what their microstructures were like.

Written Discussion: By C. H. Shih, Department of Metallurgy, Massachusetts Institute of Technology, Cambridge, Mass.

Experimental results which have been obtained recently on studies of martensite formation in high manganese steels are quite similar to the data reported here on stainless steels. There has also been a report[3] that the M_s temperature may be raised on the application of elastic tensile stress and additional evidence on this point has been obtained with manganese steels. Duplicate wire samples of one of these steels (0.78% carbon, 6.16% manganese) were plastically elongated various amounts in the same apparatus used by the authors. In one case the sample was unloaded and immediately quenched to the normal M_s temperature (−65 °C), while in the other case the sample was quenched to the same temperature with the load being maintained. Fig. 15 shows that more martensite was formed in the specimen quenched in the loaded condition than in the unloaded condition. In the loaded condition, both elastic and plastic stresses were affecting the martensitic transformation, whereas in the unloaded condition only the plastic strain and residual elastic stresses were active. It is also evident that the discrepancy between the loaded and unloaded samples increased as the plastic extension was increased. These samples were loaded at a series of temperatures from room temperature down to −50 °C and Fig. 15 also shows that the lower the temperature the greater was the effect of the elastic component of the strain. The reversal in the unloaded curves signified the onset of mechanical stabilization.

Observations were also made on the formation of martensite in specimens of another manganese steel (0.6% carbon, 7.94% manganese) which had been deformed in compression at 50 °C above its M_s temperature (−50 °C). Fig. 16 shows that the martensite plates were nucleated at slip bands and propagated to a limited extent from these sites. It thus appears that the propogation may be inhibited in these cases by another slip band or by some other defect arising from cold work in the austenite. Hence mechanical stabilization such as that reported

[3] S. A. Kulin, M. Cohen and B. L. Averbach, "Effect of Applied Stress on the Martensitic Transformation," *Transactions*, American Institute of Mining and Metallurgical Engineers, Vol. 194, 1952, p. 661.

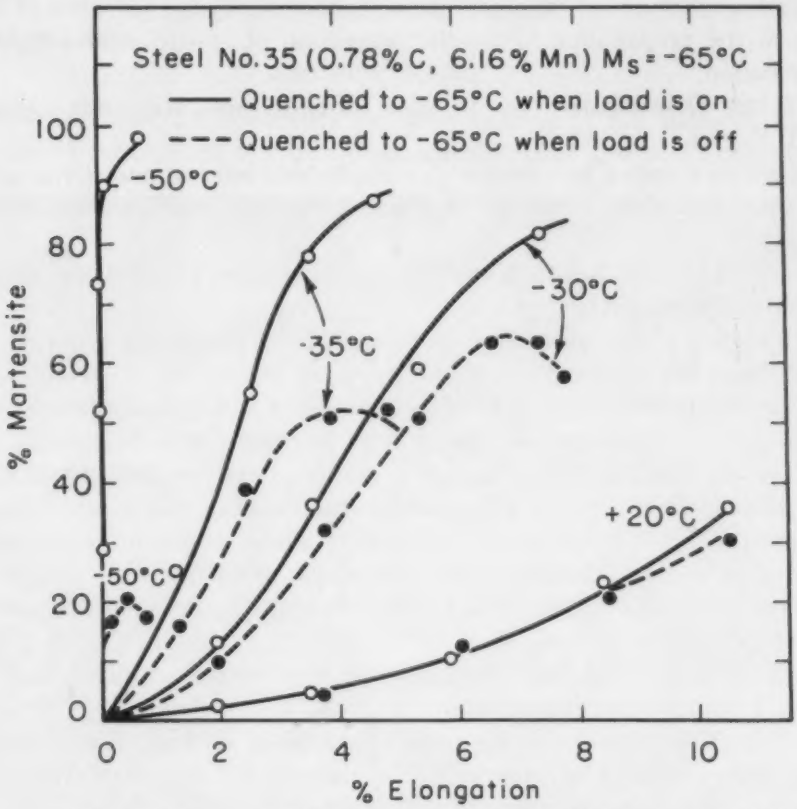


Fig. 15—Amount of Martensite Formed by Cooling to —65 °C After Elongation at Temperatures Indicated.

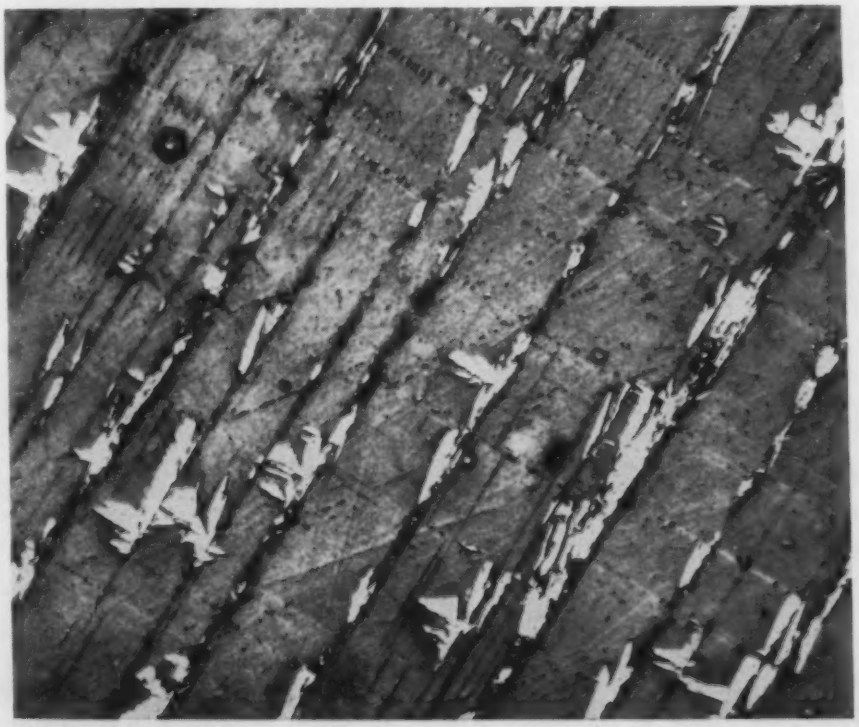


Fig. 16—Steel 33 (0.60% Carbon, 7.94% Manganese). Ms: —50 °C. Martensite formed on compression to 50% at 0 °C. Etched with Vilella's reagent. X 500.

by the authors in stainless steels might be influenced by the presence of slip band barriers to the propagation or by the relaxation of elastic strains through slip band formation.

Written Discussion: By B. Cina, Brown-Firth Research Laboratories, Sheffield, England.

The authors' paper was read with considerable interest and it was gratifying to note the many observations in it which confirmed those recently obtained by the writer.[4]

There are several points, however, on which some clarification or comment by the authors is sought.

With regard to the isothermal formation of martensite, no explanation is offered for the prequenching of all the alloys to —195 °C for 20 seconds. As Cech and Hollomon [5] have shown that the initial rate of isothermal martensite formation in an iron-nickel-manganese alloy first increases, and eventually decreases with decreasing holding temperature, the authors have not demonstrated that by their prequench they have not affected the initial rate of martensite formation at the several holding temperatures. The lower carbon alloys in particular would be expected to be most affected by this prequench as the authors' results actually show. Thus, with the 0.006% carbon alloy, between 27 and 34% martensite were formed on cooling to and holding for 20 seconds at —195 °C (the prequench treatment) whereas less than 7% martensite was formed on subsequent holding for about 1 hour at this temperature. For the low carbon alloys at least, the rates of isothermal martensite formation illustrated in Figs. 3 and 4 therefore represent those obtained toward the end of the possible extent of transformation at the particular holding temperatures.

It would be interesting to know whether the rates of isothermal formation of martensite were determined for the several temperatures investigated without the prequench to —195 °C and whether any such results were obtained at temperatures higher than —70 °C, the lowest reported, at least for the low carbon alloys. Could the authors also give the constitution of their low carbon alloys at R.T. prior to any subzero treatment. The authors have shown that the M_d point is one which it is most difficult to determine and can be placed at higher and higher temperatures if one troubles to deform the alloy by greater and greater amounts. The writer suggests that the M_s point may also be less simple to determine accurately than has previously been supposed. Thus the authors have clearly shown the stimulating effect of only about 2 to 4% deformation at 93 °C on the formation of martensite on cooling to —195 °C, the effect being most marked on the alloy of lower carbon content. Therefore stresses set up on cooling, for example by quenching, would also be expected to affect the M_s point determined. Recent work [4] has shown what a marked effect quenching stresses can have on the extent of martensite formation, the magnitude of the stresses being determined both by cooling rate and the mass of the sample. Thus a small sample of an alloy of the following composition

C	Cr	Ni	N
0.0097	18.01	8.14	0.009

[4] B. Cina, "Effect of Cold Work on the Gamma ⟶ Alpha Transformation in Some Fe-Ni-Cr Alloys," *Journal*, Iron and Steel Institute, Vol. 177, 1954, p. 406.

[5] R. E. Cech and J. H. Hollomon, "Rate of Formation of Isothermal Martensite in Fe-Ni-Mn Alloy," *Journal of Metals*, Vol. 5, May 1953; *Transactions*, American Institute of Mining and Metallurgical Engineers, Vol. 197, 1953, p. 685.

was found to contain 7% α on furnace cooling from 850 °C to R.T. but 43.3% α on water quenching.

Authors' Reply

We wish to thank the discussers for their interest in this paper. Dr. Shih's comments nicely supplement our own data, and Dr. Cina and Mr. Connolly raise

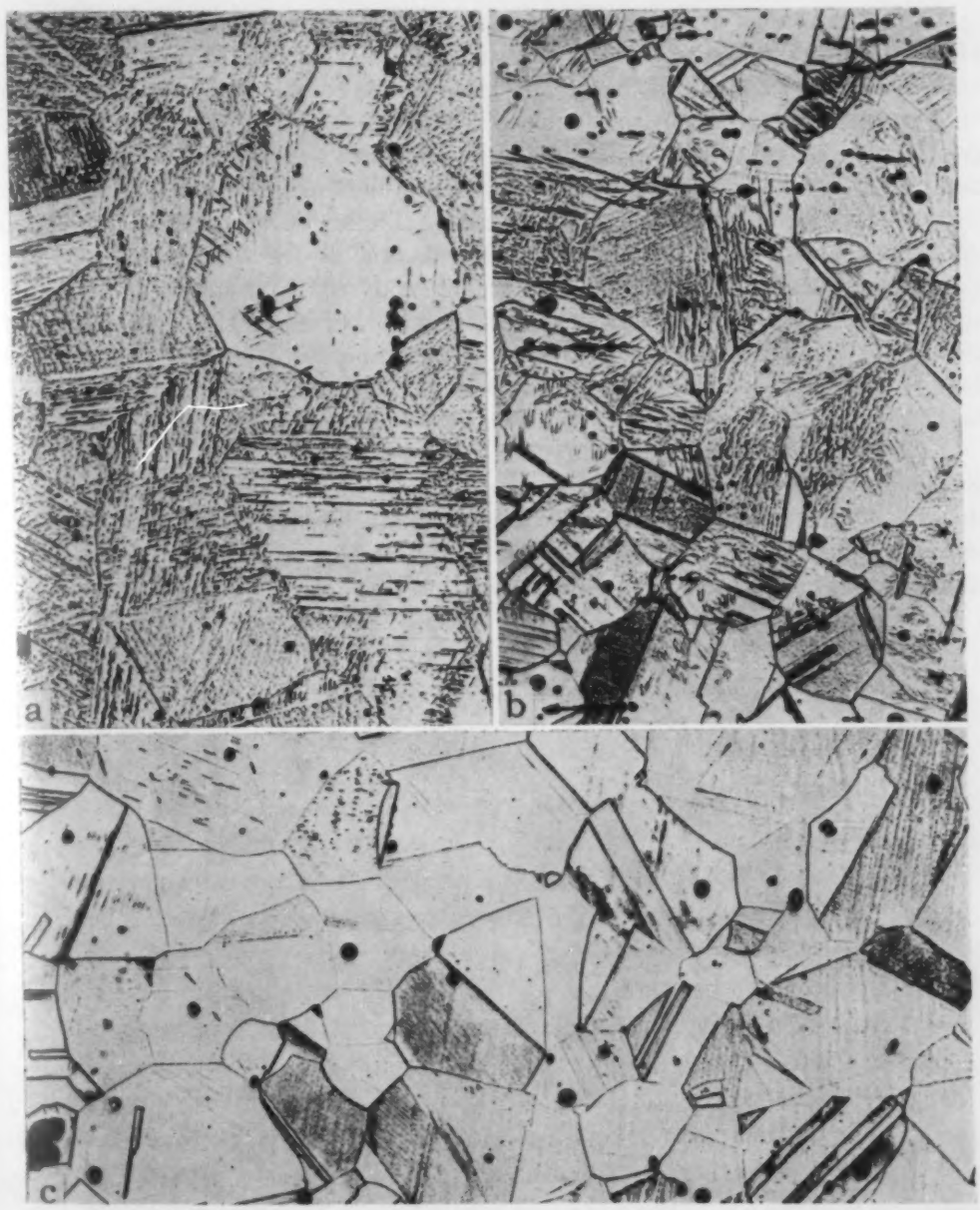


Fig. 17—Microstructure After Oil Quenching from 1090 °C (20 Minutes). (a) 0.006% carbon; (b) 0.016% carbon; (c) 0.058% carbon. Electropolished and electroetched as described in text of paper. X 150.

a pertinent question concerning the structure of the alloys in the quenched condition. The microstructures of the 0.006, 0.016 and 0.058% carbon alloys after austenitizing and quenching to room temperature are shown in Fig. 17. The 0.006% carbon alloy was invariably ferromagnetic at room temperature, and occasionally this was also the case for samples of the 0.016% carbon alloy. The

precipitated phase observed in the two lower carbon alloys is apparently ferrite. However, the marked difference in morphology between these structures and those formed in the 0.058% carbon alloy on cooling to subatmospheric temperatures suggests that the major portion of the ferrite in the low carbon alloys on quenching to room temperature is the result of another type of transformation at an elevated temperature.

Dr. Cina raises an interesting question regarding the isothermal formation of martensite. The object of the prequench to —195 °C was to provide approximately the same amount of martensite in all of the samples at "zero" isothermal holding time, regardless of the temperature at which the isothermal transformation was measured. This was deemed advisable since the martensitic transformation is known to be autocatalytic, and we wanted to measure the effects of temperature alone without the complicating factor of a variable amount of initial martensite. The isothermal transformation in the 0.058% carbon alloy was also determined without the prequench and the maximum transformation again occurred at —195 °C, the lowest testing temperature. However, the initial amount of austenite varied with the holding temperature because the athermal component of the transformation was not suppressed. No measurements were made at holding temperatures above —70 °C.

The authors agree in general with Dr. Cina's remarks on the influence of quenching stresses on the M_s temperature. These effects were investigated; but stress relief heat treatments made no discernible difference in the M_s, and it was concluded that residual quenching stresses were not a problem in the small diameter specimens used for this investigation.

FURTHER STUDY OF MICROSTRUCTURAL CHANGES ON TEMPERING IRON-CARBON ALLOYS

By B. S. Lement, B. L. Averbach, and Morris Cohen

Abstract

This investigation represents the continuation of a previous study of the microstructural changes that occur in high purity iron-carbon alloys during tempering. Such changes were followed by means of both the electron and light microscopes in the tempering range of 700 °F (370 °C) to Ac_1. It was found that coarsening and extension of grain boundary cementite films take place concurrently with solution of cementite particles within the acicular grains inherited from the tempered martensite. These phenomena are accompanied by coalescence and spheroidization, which occur more readily the lower the carbon content of the alloy. On the basis of interfacial energy considerations, an expression was derived for the minimum stable size of spheroidized cementite particles that eventually form at ferritic grain boundaries. Such factors as small carbide size, coherency strain, and a departure in carbon content of cementite from the formula Fe_3C are considered responsible for the enhanced solubility of carbon in ferrite that is reported to occur in plain carbon steels during tempering.

Introduction

THIS paper is a continuation of an investigation of the tempering of high purity iron-carbon alloys. A previous paper (1)[1] dealt with tempering in the range of room temperature to 700 °F (370 °C). whereas the present study covers the range of 700 °F (370 °C) to Ac_1. It was shown that the first stage of tempering in iron-carbon alloys containing above about 0.25% carbon consists of the formation of an ϵ-carbide network at subboundaries in martensite and is completed at 350–400 °F (175–205 °C) in a tempering time of about 1 hour. This is followed by the initial part of the third stage[2] of tempering, which starts at a tempering temperature of about 400 °F (205 °C) and involves precipitation of cementite concurrently with solution of the

[1] The figures appearing in parentheses pertain to the references appended to this paper.

[2] The second stage of tempering, transformation of retained austensite to bainite, was not investigated in reference (1).

A paper presented before the Thirty-sixth Annual Convention of the Society, held in Chicago, November 1 to 5, 1954. Of the authors, B. S. Lement is on the research staff (Division of Industrial Cooperation), B. L. Averbach is associate professor, and Morris Cohen is professor of physical metallurgy, Massachusetts Institute of Technology, Cambridge, Mass. Manuscript received April 5, 1954.

ϵ-carbide. Complete solution of ϵ-carbide occurs at a tempering temperature of about 600 °F (315 °C) or lower. Cementite forms initially as elongated films at martensitic boundaries, and as both platelets and globules within the martensite. The boundary films coarsen and the amount of cementite formed within the martensitic plates increases as tempering is continued up to 700 °F (370 °C).

In the present investigation, the microstructural changes in four high purity iron-carbon alloys on tempering above 700 °F (370 °C) were investigated by means of both electron and light microscopy. Supplementary measurements of hardness were also made. The most pertinent features of this study were the observations on the carbide morphology, on ferritic grain growth, on rates of softening, and on the completion of the third stage of tempering.

Experimental Details

Metallographic Techniques—Specimens were etched in a modified picral solution consisting of 4% picric acid and 0.01% hydrochloric acid in ethyl alcohol to reveal carbide morphology, and in a combination of 2% ammonium persulphate in water and 3% nital recommended by Fisher (2) to delineate ferritic boundaries for grain size determinations.

Electron Microscopy—The details of electron microscopy which involved use of negative parlodion replicas and rotary shadowing with chromium are given elsewhere (1).

Hardness Tests—Rockwell A hardness tests were carried out on the tempered specimens and the hardness values obtained were converted to Rockwell C units. The precision of these measurements is estimated to be about ± 0.3 Rockwell C unit.

Experimental Results

Chemical Composition and Grain Size—The chemical composition, austenitizing treatments, and resulting austenitic grain sizes of the four high purity iron-carbon alloys are listed in Table I.

Table I
Carbon Content, Hardening Treatment, and Grain Size of Iron-Carbon Alloys

Nominal Carbon Content, %	Actual Carbon Content,* %	Austenitizing Temp.**	ASTM Austenitic Grain Size No.
1.4	1.43	2200 °F	<1
0.8	0.78	1500 °F	>8
		2200 °F	<1
0.4	0.39	1550 °F	6–7
		2200 °F	1–3
0.15	0.14	1650 °F	3–4
		2200 °F	1–2

* Mn, S, P <0.001 %
Si, O <0.01 %
N <0.0002%
** Quenched into 10% brine at 40 °F.

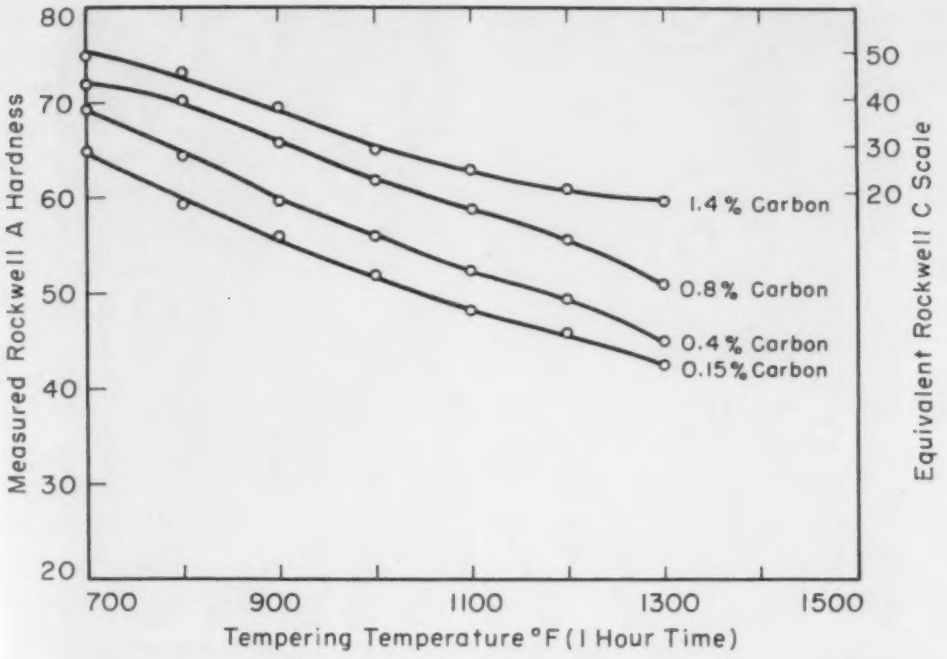
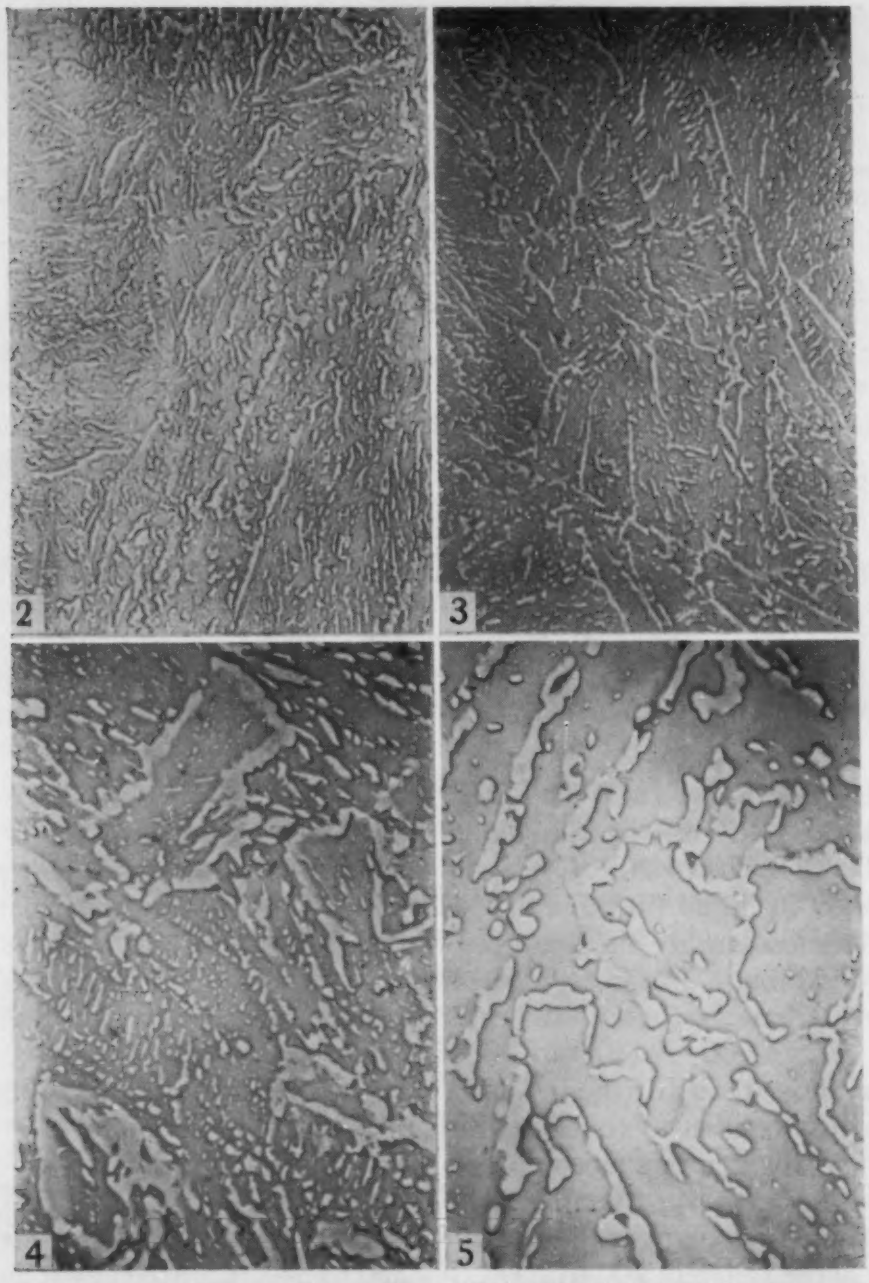


Fig. 1—Hardness Versus Tempering Temperature for Four Iron-Carbon Alloys.

Hardness Results—The effect of tempering temperature on the hardness of the four iron-carbon alloys tempered in the range of 700 to 1300 °F (370 to 705 °C) is shown in Fig. 1. All specimens were subcooled in liquid nitrogen at −320 °F (−196 °C) after hardening in order to minimize the amount of retained austenite. The curves in Fig. 1 exhibit a progressive decrease in hardness with increase in tempering temperature; however, the rate of softening in the range of about 700 to 900 °F (370 to 480 °C) is lower for the 1.4 and 0.8% carbon alloys than for the 0.4 and 0.15% carbon alloys. This observation will be shown to correlate with the difference in microstructural change of high carbon as compared to low carbon alloys.

Microstructural Changes on Tempering at 700 to 1000 °F—The microstructural changes that occur on tempering the four iron-carbon alloys in the range of 700 to 1000 °F (370 to 540 °C) are shown by the series of electron micrographs in Figs. 2 to 17.

1.4% Carbon Alloy—The structure of the 1.4% carbon alloy tempered at 700 °F (370 °C) (Fig. 2) is characterized by elongated cementite films and numerous smaller cementite particles in a matrix that may be either body-centered tetragonal martensite or body-centered cubic ferrite, or both. For the sake of convenience, the matrix will be referred to as ferrite even though it is believed that there is an appreciable amount of carbon in solid solution even after a 700 °F (370 °C) temper. The grains of ferrite comprising the matrix inherit an acicular shape from the plate-like structure of the tempered martensite.



Figs. 2–5—Electron Micrographs at X 5000 of 1.4% Carbon Alloy Quenched From 2200 °F and Tempered 1 Hour at Temperatures Indicated. Negative Parlodion replica rotary shadowed with chromium. Fig. 2—Tempered at 700 °F. Cementite present both as particles within grains and as elongated films at grain boundaries of matrix. Fig. 3—Tempered at 800 °F. Partial solution of cementite particles within grains along with extension of grain boundary cementite films has occurred. Fig. 4—Tempered at 900 °F. Pronounced coarsening of grain boundary cementite films has occurred concurrently with solution, coalescence and spheroidization of cementite particles within grains. Fig. 5—Tempered at 1000 °F. Virtually all of the cementite is present as films at grain boundaries. A few globular particles remain within grains.

As pointed out previously (1), the elongated cementite films are at ferritic boundaries whereas the smaller particles are mainly in the form of platelets within the ferrite. Tempering at 800 and 900 °F (425 and 480 °C) (Figs. 3 and 4) results in marked coarsening and exten-

sion of the grain boundary films along with increasing solution and spheroidization of the particles within the grains. Although the total volume of the particles within the grains of ferrite decreases, the average particle size[3] increases due to coalescence. This phenomenon involves growth of the larger size particles at the expense of the smaller ones which selectively dissolve. The overall result of this process is for most of the cementite to collect in the form of grain boundary films, as is virtually the case after a 1000 °F (540 °C) temper (Fig. 5). These cementite films are discontinuous and vary in thickness. Some indications of initial spheroidization of the grain boundary films can also be seen in Fig. 5.

0.8 and 0.4% Carbon Alloys—The structures of the 0.8 and 0.4% carbon alloys after a 700 °F (370 °C) temper have been shown (1) to consist of cementite films at ferritic grain boundaries and a mixture of platelets and globules within the grains. Marked coarsening and extension of the grain boundary cementite films at the expensé of cementite solution within the grains occur in these lower carbon alloys. This feature is evident in Figs. 6,7, and 8 for the 0.8% carbon alloy and in Figs. 10,11, and 12 for the 0.4% carbon alloy. However, this process occurs more rapidly than in the 1.4% carbon alloy and is virtually completed at 900 °F (480 °C) in the 0.8% carbon alloy (Fig. 8) and at 800 °F (425 °C) in the 0.4% carbon alloy (Fig. 11). Due to the occurrence of marked spheroidization accompanied by coalescence, the grain boundary cementite films in these lower carbon alloys are considerably less continuous than in the 1.4% carbon alloy. Further coalescence of the grain boundary cementite occurs after a 1000 °F (540 °C) temper, which is illustrated in Figs. 9 and 13 for the 0.8 and 0.4% carbon alloys respectively.

0.15% Carbon Alloy—As shown in Fig. 14, tempering of the 0.15% carbon alloy at 700 °F (370 °C) results in the formation of elongated cementite films at grain boundaries and numerous fine cementite particles within the grains. It had been previously shown (1) that these fine particles are mainly in the form of globules after a 600 °F (315 °C) temper. Tempering at 800 °F (425 °C) (Fig. 15) causes the displacement of most of the cementite particles within the grains to the grain boundaries. Partial spheroidization and coalescence of the cementite at grain boundaries also occurs. Further coalescence of the grain boundary cementite particles results from 900 and 1000 °F (480 and 540 °C) tempers (Figs. 16 and 17).

Light Micrographs—Light micrographs at × 2000 of the four iron-carbon alloys tempered 1 hour at 1000 °F (540 °C) and 24 hours at 1300 °F (705 °C) are shown in Figs. 18 to 25. The micrographs of specimens tempered at 1000 °F (540 °C) (Figs. 18,19,20, and 21)

[3] This refers to the average size of the globules resulting from spheroidization of the cementite platelets within the grains.

Table II
Ferritic Grain Size of Tempered Iron-Carbon Alloys

% Carbon Alloy	Austenitizing Temperature	Tempering Treatment	Average Linear Intercept, Cm.	Interfacial Area Per Unit Volume, $Cm.^{-1}$	Equivalent A.S.T.M. Grain Size No.
1.4	2200 °F	900 °F-1hr.	2.7×10^{-4}	7.4×10^{3}	13.5
		1000 °F-1hr.	3.0×10^{-4}	6.7×10^{3}	13.5
		1100 °F-1hr.	3.9×10^{-4}	5.1×10^{3}	12.5
		1200 °F-1hr.	4.7×10^{-4}	4.3×10^{3}	12
		1300 °F-1hr.	5.6×10^{-4}	3.6×10^{3}	11.5
		1300 °F-24hrs.	5.5×10^{-4}	3.6×10^{3}	11.5
0.8	1500 °F	900 °F-1hr.	2.2×10^{-4}	9.1×10^{3}	14
		1000 °F-1hr.	3.0×10^{-4}	6.7×10^{3}	13.5
		1100 °F-1hr.	3.4×10^{-4}	5.9×10^{3}	13
		1200 °F-1hr.	3.5×10^{-4}	5.7×10^{3}	13
		1300 °F-1hr.	3.5×10^{-4}	5.7×10^{3}	13
		1300 °F-24hrs.	7.0×10^{-4}	2.9×10^{3}	11
0.4	1550 °F	900 °F-1hr.	3.5×10^{-4}	5.7×10^{3}	13
		1000 °F-1hr.	3.6×10^{-4}	5.5×10^{3}	12.5
		1100 °F-1hr.	4.2×10^{-4}	4.7×10^{3}	12
		1200 °F-1hr.	3.7×10^{-4}	5.4×10^{3}	12.5
		1300 °F-1hr.	3.9×10^{-4}	5.1×10^{3}	12.5
		1300 °F-24hrs.	7.0×10^{-4}	2.9×10^{3}	11
0.15	2200 °F	900 °F-1hr.	6.5×10^{-4}	3.1×10^{3}	11
		1000 °F-1hr.	7.0×10^{-4}	2.9×10^{3}	11
		1100 °F-1hr.	4.6×10^{-4}	4.4×10^{3}	12
		1200 °F-1hr.	7.1×10^{-4}	2.8×10^{3}	11
		1300 °F-1hr.	3.9×10^{-4}	3.9×10^{3}	11.5
		1300 °F-24hrs.	5.7×10^{-4}	3.5×10^{3}	11.5

reveal that cementite films are present at prior austenitic as well as prior martensitic boundaries of the matrix. Tempering above 1000 °F (540 °C) produces further spheroidization and coalescence of the grain boundary cementite in all steels. However, as shown in Figs. 22,23,24 and 25, remnants of cementite films are present at prior austenitic grain boundaries even after a temper of 24 hours at 1300 °F (705 °C) which is just below the Ac_1 point (1333 °F) (722 °C).

Ferritic Grain Size—Determination of the ferritic grain size of the matrix was accomplished by counting the number of intercepts with ferritic grain boundaries in a lineal traverse of known distance over the polished and etched surface of tempered specimens under the light microscope. Measured values for the four iron-carbon alloys tempered in the range of 900 to 1300 °F (480 to 705 °C) are reported in Table II. From these data, it is possible to calculate the ferritic interfacial area per unit volume using the relation of Smith (3):

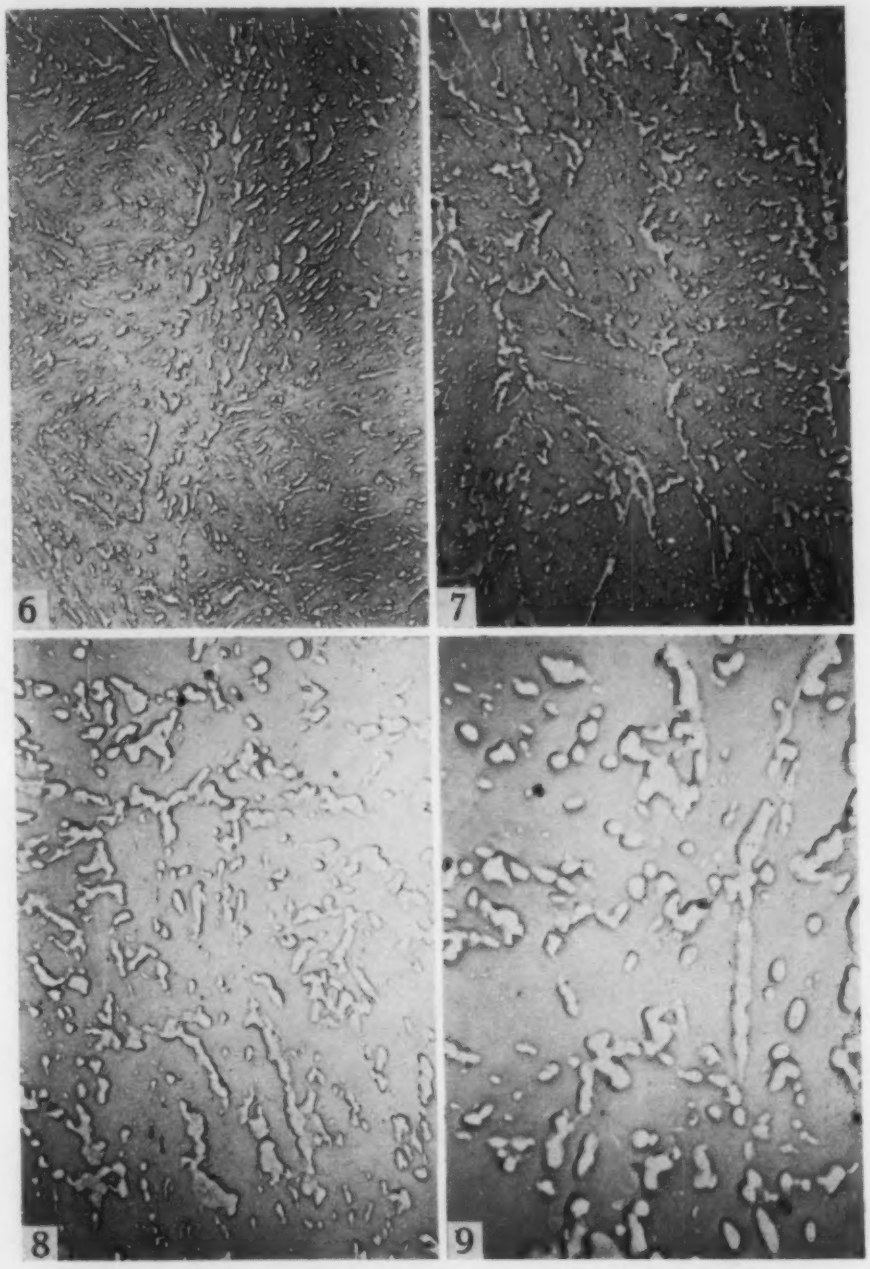
$$S_v = 2 - \frac{\bar{N}}{L} \qquad \text{Equation 1}$$

where S_v = Interfacial area per unit volume.

$\bar{N}$ = Average number of grain boundary intercepts in a lineal traverse of distance L.

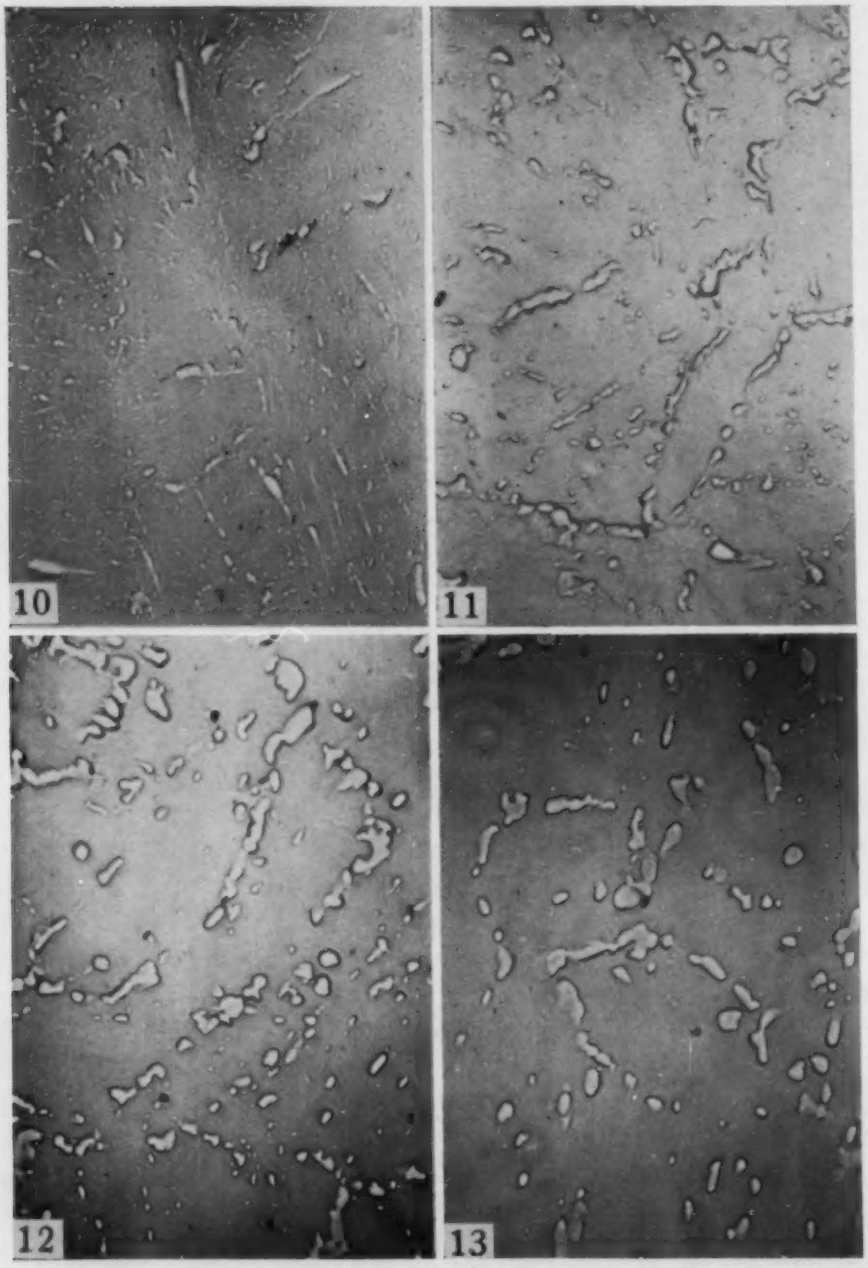
$\frac{L}{\bar{N}}$ = Average linear intercept.

The resulting values of interfacial area per unit volume and equivalent



Figs. 6—9—Electron Micrographs at X 5000 of 0.8% Carbon Alloy Quenched From 1500 °F and Tempered 1 Hour at Temperatures Indicated. Negative parlodion replica rotary shadowed with chromium. Fig. 6—Tempered at 700 °F. Cementite present both as particles within grains and as elongated films at grain boundaries of matrix. Fig. 7—Tempered at 800 °F. Coarsening of grain boundary cementite films has occurred concurrently with partial solution and coalescence of cementite particles within grains. Fig. 8—Tempered at 900 °F. Most of the Cementite is present as films at grain boundaries. Fig. 9—Tempered at 1000 °F. Spheroidization of grain boundary cementite films has occurred to an appreciable extent.

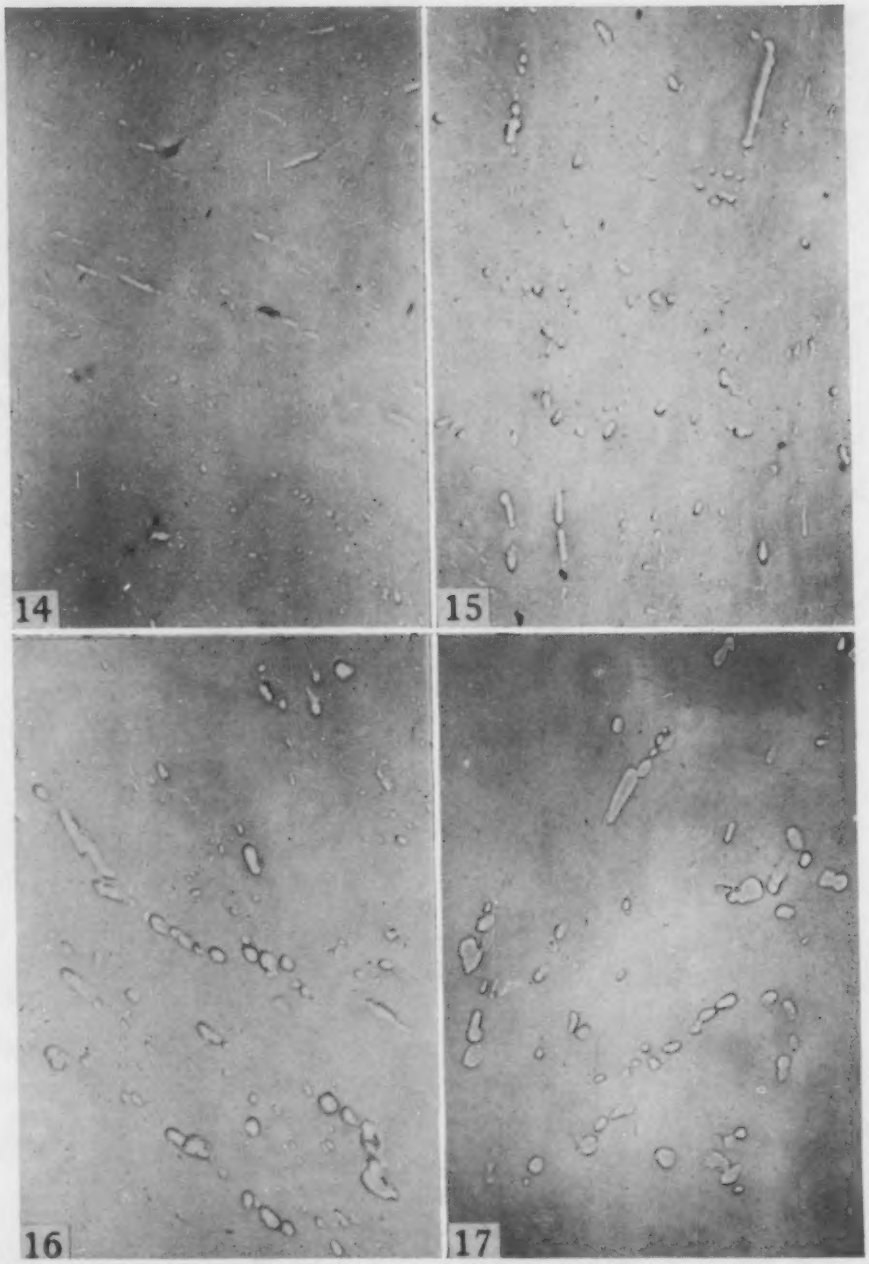
ASTM grain size numbers are also given in Table II. The ASTM grain size numbers were determined by the method of Rutherford (4,5) who computed interfacial areas per unit volume on the assumption that the grains are essentially equiaxed and have the shape of Kelvin's cubo-



Figs. 10–13—Electron Micrographs at X 5000 of 0.4% Carbon Alloy Quenched from 1550 °F and Tempered 1 Hour at Temperatures Indicated. Negative parlodion replica rotary shadowed with chromium. Fig. 10—Tempered at 700 °F. Cementite present both as particles within grains and as elongated films at grain boundaries of matrix. Fig. 11—Tempered at 800 °F. Virtually all of the cementite is present as partially spheroidized grain boundary films. Fig. 12—Tempered at 900 °F. Extent of spheroidization of grain boundary cementite films has increased and coalescence has occurred. Fig. 13—Tempered at 1000 °F. Further spheroidization and coalescence has occurred.

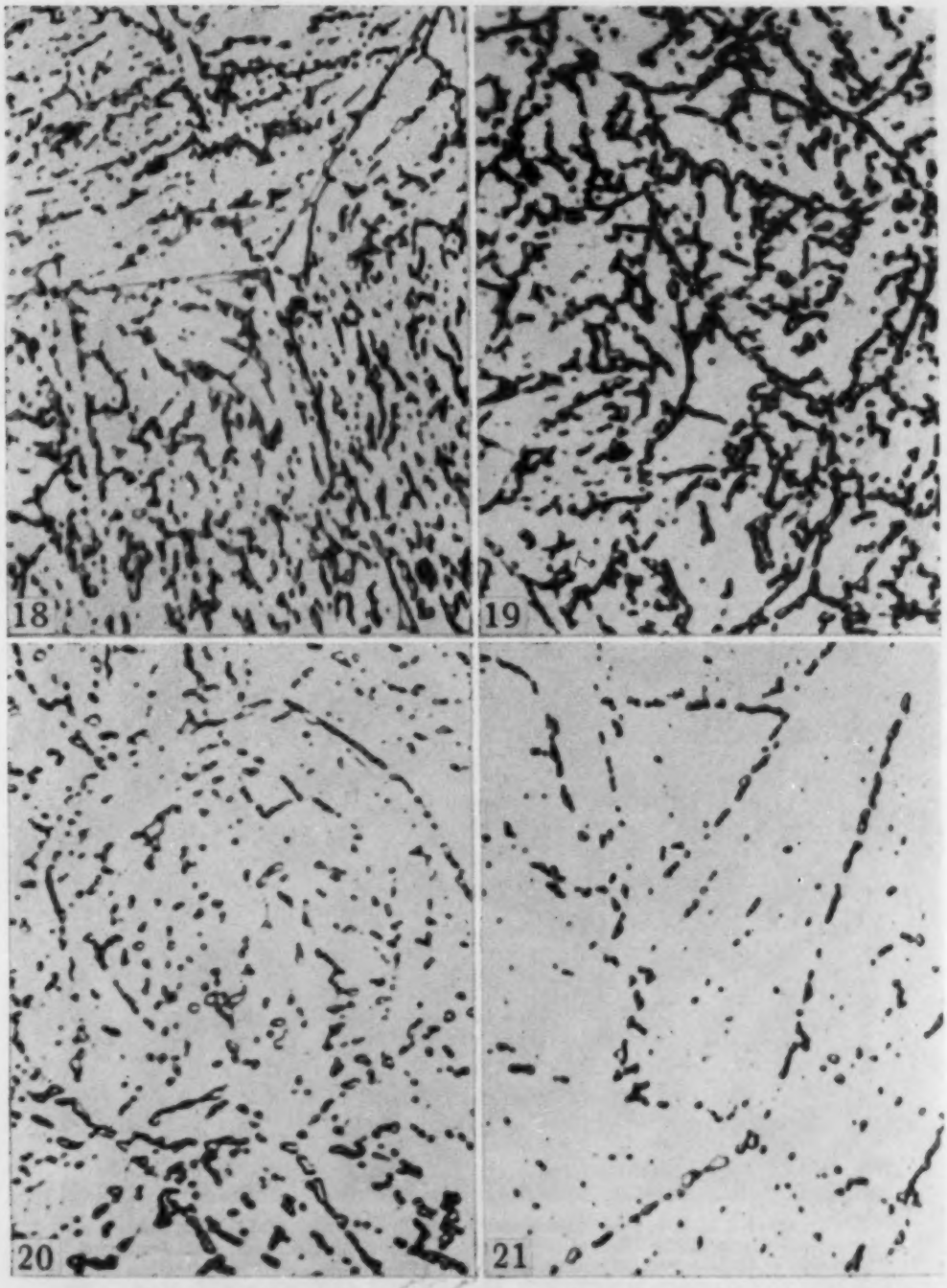
octohedra. Since the ferritic grains are derived from martensitic plates which are acicular rather than equiaxed, the ASTM grain size numbers reported in Table II are only approximate. However, they serve for comparison of grain size in familiar terms.

As shown in Table II, the ferritic grain size of the 1.4, 0.8, and



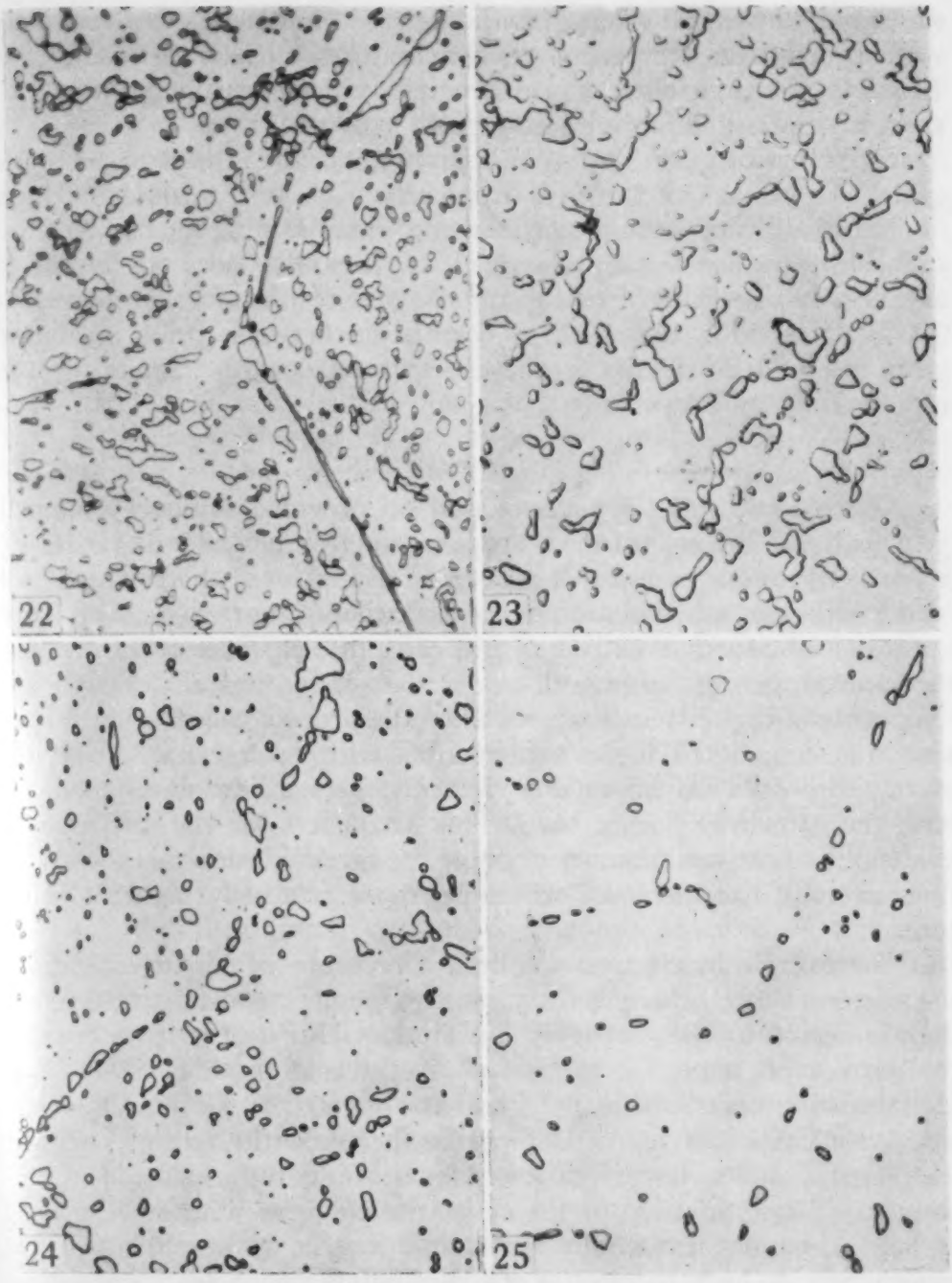
Figs. 14–17—Electron Micrographs at X 5000 of 0.15% Carbon Alloy Quenched From 2200 °F and Tempered 1 Hour at Temperatures Indicated. Negative parlodion replica rotary shadowed with chromium. Fig. 14—Tempered at 700 °F. Cementite present both as spheroidal particles within grains and elongated films at grain boundaries of matrix. Fig. 15—Tempered at 800 °F. Cementite present mainly at grain boundaries. Partial spheroidization of grain boundary films and coalescence of globules have occurred. Fig. 16—Tempered at 900 °F. Further coalescence of cementite globules at grain boundaries has occurred. Fig. 17—Tempered at 1000 °F. Still further coalescence of cementite globules at grain boundaries has occurred.

0.4% carbon alloys after a 900 °F (480 °C) temper are approximately equivalent, ASTM No. 13–14; whereas the ferritic grain size of the 0.15% carbon alloy after a 900 °F (480 °C) temper is appreciably larger, ASTM No. 11. Tempering for 1 hour at temperatures in the



Figs. 18–21—Light Micrographs at X 2000 of 1.4, 0.8, 0.4 and 0.15% Carbon Alloys Tempered at 1000 °F Showing Presence of Cementite Films at Prior Austenitic Grain Boundaries. Etched with 4% picral containing 0.01% hydrochloric acid. Fig. 18—1.4% Carbon Alloy. Quenched from 2200 °F and tempered one hour at 1000 °F. Fig. 19—0.8% Carbon Alloy. Quenched from 1500 °F and tempered one hour at 1000 °F. Fig. 20—0.4% Carbon Alloy. Quenched from 1550 °F and tempered one hour at 1000 °F. Fig. 21—0.15% Carbon Alloy. Quenched from 2200 °F and tempered one hour at 1000 °F.

range of 900 to 1300 °F (480 to 705 °C) produces only a slight increase in grain size as evidenced by a change of 1–2 ASTM units for the 1.4, 0.8, and 0.4% carbon alloys, and practically no change for the 0.15% carbon alloy. Increasing the tempering time at 1300 °F (705 °C)



Figs. 22–25—Light Micrographs at X 500 of 1.4, 0.8, 0.4, and 0.15% Carbon Alloys Tempered 24 Hours at 1300 °F Showing Persistence of Elongated Cementite Films at Prior Austenitic Grain Boundaries. Etched with 4% picral containing 0.01% hydrochloric acid. Fig. 22—1.4% Carbon Alloy. Quenched from 2200 °F and tempered 24 hours at 1300 °F. Fig. 23—0.8% Carbon Alloy. Quenched from 1500 °F and tempered 24 hours at 1300 °F. Fig. 24—0.4% Carbon Alloy. Quenched from 1550 °F and tempered 24 hours at 1300 °F. Fig. 25—0.15% Carbon Alloy. Quenched from 2200 °F and tempered 24 hours at 1300 °F.

from 1 to 24 hours causes an increase in the grain size of the 0.8 and 0.4% carbon alloys corresponding to 1.5–2 ASTM units, but virtually no alteration in grain size of the 1.4 and 0.15% carbon alloys. These

findings indicate that grain growth of the ferritic matrix is a relatively slow process on tempering at temperatures up to about 1300 °F (705 °C). Presumably, the presence of carbide at ferritic grain boundaries is responsible for inhibiting grain growth.

The ferritic grain size is considerably finer than the prior austentic grain size in each of the four iron-carbon alloys. As indicated by a limited number of experiments, raising the austenitizing temperature to increase the austenitic grain size in a given alloy does not appear to appreciably affect the ferritic grain size that results after tempering to 900 °F (480 °C). This lack of correlation between prior austenitic grain size and the ferritic grain size that develops by tempering was reported also by Baeyertz (6).

Discussion of Results

Microstructural Changes—Based on previous evidence obtained principally with the light microscope, tempering has been regarded as a relatively simple process. It was generally believed that virtually all of the carbon in solid solution in the as-hardened martensite eventually appears in the form of extremely fine cementite particles at some intermediate tempering temperature, and that spheroidization occurs on tempering at higher temperature. Thus the process called spheroidization was considered to be synonomous with coalescence, involving merely the solution of smaller cementite spheroids simultaneously with the growth of larger ones. This accounted for the microscopic evidence that the total number of cementite spheroids decreases whereas their average size increases on tempering at relatively high temperatures.

As revealed by electron and light microscope in this investigation, the microstructural changes that occur on tempering are more complex than indicated by the foregoing description. During the early part of the third stage, cementite forms both as extremely small platelets and globules within martensitic plates and as elongated thin films at martensitic boundaries. On further tempering the cementite particles within the plates dissolve concurrently with coarsening and extension of the boundary films. Solution of the cementite particles within the grains of what becomes essentially a ferritic matrix is accompanied by spheroidization and coalescence of the remaining particles. Coarsening of the films at the ferritic boundaries is also attended by spheroidization and coalescence; however, the latter processes occur more slowly the higher the carbon content of the alloy. Thus a situation can be attained in hypereutectoidal alloys in which virtually all of the cementite is in the form of a discontinuous network at ferritic boundaries. In lower carbon alloys, all of the cementite also forms eventually at ferritic boundaries; however, due to the occurrence of more rapid spheroidization, this grain boundary carbide takes the form of globular particles

as well as films. With further tempering, spheroidization of cementite films continues concurrently with coalescence of the globular particles that result. All of these carbide particles remain at grain boundaries, but their number decreases as their average size increases. Some remnants of elongated films at prior austenitic boundaries persist even at tempering temperatures close to Ac_1.

The eventual location of cementite at grain boundaries can be understood on the basis of interfacial energy considerations. Although most of the cementite is initially precipitated within the grains, the sum total of ferrite-cementite and ferrite-ferrite interfacial energy can be decreased by displacement of these particles to ferritic grain boundaries. In this fashion, lower energy ferrite-cementite interfaces are substituted for higher energy ferrite-ferrite interfaces. While this displacement process is going on, an additional decrease in interfacial energy can result from spheroidization and coalescence of the remaining cementite particles within the grains. The geometrical shape of the cementite at grain boundaries depends on the relative rates of nucleation, growth, spheroidization, and coalescence at such locations. The fact that cementite films at martensitic boundaries are observed even before the precipitation of cementite particles within the martensitic plates in the 1.4% carbon alloy indicates that a relatively high rate of grain boundary nucleation is involved. Although coarsening of these films occurs simultaneously with precipitation of cementite particles within the grain, the rate of coarsening markedly increases during the displacement of the cementite particles to grain boundaries. This thickening of the cementite films at the expense of the numerous particles within the grains is probably a consequence of the attendant reduction in interfacial area between the cementite and ferrite. However, grain boundary films may still be considered unstable since a further decrease in total interfacial energy results if spheroidization and coalescence take place. As will be shown later, the grain boundary cementite globules that eventually form must be above a certain size in order for the total interfacial energy to be lower than for the condition corresponding to uniform and completely continuous grain boundary cementite films.

As the cementite globules at grain boundaries continue to coalesce during further tempering, many of the particles tend to remain at grain corners where three or more ferrite grains meet because these locations offer the greatest replacement of ferrite-ferrite interfacial area for a given size of cementite particle. Prior austenitic grain boundaries also appear to be favored sites, presumably because of higher ferrite-ferrite interfacial energy due to greater differences in grain orientation on the average than exist between ferrite grains derived from neighboring martensitic plates within a prior austenitic grain. The state of minimum interfacial energy should result from the removal of all the ferrite-

ferrite boundaries by grain growth and coalescence of all of the cementite into a single particle. This condition has never actually been attained.

Growth of the ferritic grains on tempering, in the range of 900 to 1300 °F (480 to 705 °C) was found to be a relatively minor process in the high purity iron-carbon alloys studied. Even less growth would be expected if alloying elements were present, as in commercial steels. The ferritic grains tend to maintain the acicular form inherited from the initial martensitic plates over a wide range of tempering temperatures due to the fact that the grain boundary carbide particles are quite potent in controlling grain growth. However, some readjustments in grain shape occur even below 900 °F (480 °C), apparently because the grain boundary intersections strive to attain equilibrium angles. Long tempering times at temperatures close to Ac_1 are evidently required for the grains to coarsen appreciably and to become essentially equiaxed.

Relation of Microstructure to Hardness Changes—It was found that the hardness of iron-carbon alloys progressively decreases as a result of tempering above 700 °F (370 °C). In the range of 700 and 1000 °F (370 to 540 °C), the factors considered responsible for softening are as follows: a) decrease in carbon content of the matrix; b) solution, spheroidization, and coalescence of the cementite particles within prior martensitic plates; and c) spheroidization and coalescence of cementite at the boundaries of prior martensitic plates. These softening factors are opposed by a hardening effect due to formation and extension of cementite films at the prior martensitic boundaries. However, even in the 1.4% carbon alloy where the cementite films are found to be most pronounced, no overall hardening is observed. This signifies that the formation of cementite films is not a dominant factor although it acts to retard the rate of softening.

The rate of softening was found to be higher for the 0.15 and 0.4% carbon alloys than for the 0.8 and 1.4% carbon alloys on tempering in the range of about 700 to 900 °F (370 to 480 °C). This would be expected on the basis that thinner grain boundary cementite films which form in the lower carbon alloys are less resistant to spheroidization and coalescence. Furthermore displacement of the small cementite particles from within the grains to grain boundaries of the matrix occurs more readily in the lower carbon alloys. As will be discussed later, this may permit greater depletion of the carbon content of the matrix and may consequently result in softening. Above 900 °F (480 °C), the observed softening in all the alloys is probably due mainly to increased spheroidization and coalescence of the grain boundary cementite particles, although ferritic grain growth may also be a factor on tempering at temperatures close to Ac_1.

Minimum Size of Stable Cementite Particles at Ferritic Grain Boundaries—According to Smith (*7*), a stable form of cementite at

ferritic grain boundaries should have a lenticular shape with a dihedral angle that is dependent on the ratio of the interfacial energy between cementite and ferrite to that between two ferrite grains, $\frac{\gamma_{a\text{-}c}}{\gamma_{a\text{-}a}}$. The average dihedral angle in an SAE 1020 steel spheroidized at 1275 °F (690 °C) was found to be 115°, which corresponds to $\frac{\gamma_{a\text{-}c}}{\gamma_{a\text{-}a}} = 0.93$. As shown in Appendix A, the ratio of thickness to diameter of such a lenticular cementite particle should be 0.54 assuming its two surfaces are spherical.

In order to determine the stable dimensions of lenticular particles at ferritic grain boundaries, a comparison was made of the total interfacial energy for this case and that corresponding to all of the cementite in the form of a uniform and completely continuous grain boundary film. It is demonstrated in Appendix A, that lenticular particles are favored if their size is above the minimum value given by the following:[4]

$$\bar{d}_{min.} = 4.4\ t \qquad \text{Equation 2}$$

where $\bar{d}$ = One half the sum of the diameter and thickness of a lenticular particle.

t = Thickness of a uniform and completely continuous cementite film at ferrite grain boundaries.

Based on the carbon content and interfacial grain boundary area, the following expression gives the value of t:

$$t = \frac{0.15_p}{S_v} \qquad \text{Equation 3}$$

where p = Weight % carbon in alloy.

S_v = Interfacial ferritic area per unit volume.

Combining Equation 2 and Equation 3:

$$\bar{d}_{min.} = \frac{6.6_p}{S_v} \qquad \text{Equation 4}$$

Thus both the thickness of a grain boundary cementite network and the minimum size of stable grain boundary lenticular cementite should increase with carbon content and ferritic grain size. In Table III these calculated quantities are compared with actual measurements on specimens tempered to deposit virtually all of the cementite at ferritic grain boundaries. The thickness of a cementite network and the minimum stable size of lenticular cementite particles were calculated from Equations 3 and 4 respectively using values of S_v obtained from Table II. The measured average thickness of the grain boundary cementite films is 10 to 20 times larger than the calculated thickness

[4] An analysis similar to that in Appendix A shows that if the stable form of cementite at grain boundaries were a sphere, the minimum stable diameter would equal 4.8 t.

Table III
Size of Cementite Films and Globules in Iron-Carbon Alloys

Comparison of Calculated and Measured Film Sizes.

% Carbon Alloy	Tempering Temperature	Interfacial Area per Unit Volume, Cm.$^{-1}$	Calculated Thickness of Grain Boundary Cementite Network, Cm.	Measured Average Thickness of Grain Boundary, Cementite Films, Cm.
1.4	1000 °F	6700	3.2×10^{-6}	33×10^{-6}
0.8	900 °F	9100	1.3×10^{-6}	27×10^{-6}
0.4	800 °F	5700*	1.1×10^{-6}	21×10^{-6}
0.15	800 °F	3100*	0.7×10^{-6}	11×10^{-6}

Comparison of Calculated and Measured Globular Particle Sizes.

% Carbon Alloy	Tempering Temperature	Interfacial Area per Unit Volume, Cm.$^{-1}$	Calculated Minimum Size of Stable Grain Boundary Cementite Lenticular Particles, Cm.	Measured Average Diameter of Grain Boundary Cementite Globules, Cm.
1.4	1100 °F	5100	14×10^{-6}	30×10^{-6}
0.8	1000 °F	6700	5.7×10^{-6}	25×10^{-6}
0.4	900 °F	5700	4.8×10^{-6}	20×10^{-6}
0.15	900 °F	3100	3.1×10^{-6}	20×10^{-6}

* Assumes that ferritic grain size is the same for 800 °F as that measured for a 900 °F temper.

of a cementite network, which is in line with the observation that the films are neither uniform nor continuous. On the other hand, the measured average diameter of the grain boundary particles in each of the four alloys is only 2 to 7 times larger than the calculated minimum size of stable grain boundary lenticular cementite. This is considered quite good agreement because the actual cementite films undergoing spheroidization were thicker on the average than would have been the case starting with a continuous and uniform network. Thus as shown in Table III, the size of the actual cementite globules that resulted from spheroidization are more in line with the measured average thickness of the observed grain boundary films.

Effect of Particle Size on Solubility of Cementite in Ferrite—According to Konobeevski (8) and Cottrell and Leak (9) the Thomson-Freundlich relation which is based on vapor pressure considerations can be utilized to determine the solubility of carbon in ferrite as a function of the size of the cementite particles present. In this relation, it is assumed that the strain energy between cementite and ferrite is zero.

$$\ln \frac{C_s}{C_\infty} = \frac{2 M \gamma_{\alpha-c}}{R T \rho s} \qquad \text{Equation 5}$$

where C_s = Carbon concentration of supersaturated ferrite in metastable equilibrium with cementite particles of size s.

C_∞ = Carbon concentration of ferrite in equilibrium with cementite particles of infinite radius.

s = Size parameter of cementite particles in cm.

$\gamma_{\alpha-c}$ = Interfacial energy per unit area between cementite and ferrite.

M = Molecular weight of cementite (180 grams).
ρ = Density of cementite (7.7 grams/cm^3).
R = Gas constant (8.3×10^7 ergs/mol/K °).
T = Absolute temperature.

On the assumptions that $\frac{\gamma_{\alpha\text{-}c}}{\gamma_{\alpha\text{-}\alpha}} = 0.93$ as determined by Smith (7) and $\gamma_{\alpha\text{-}\alpha} = 765$ ergs/cm. as determined by Van Vlack (10) are relatively independent of tempering temperature in the range studied, a value of $\gamma_{\alpha\text{-}c} = 710$ ergs/cm.[2] can be used in Equation 5. Making the indicated substitutions:

$$\ln \frac{C_s}{C_\infty} = \frac{0.00040}{T\,s} \qquad \text{Equation 6}$$

The variation of C_∞ with temperature has been found by Wert (11) to be

$$\ln C_\infty = 0.936 - \frac{4850}{T} \qquad \text{Equation 7}$$

Combining Equations 6 and 7:

$$\ln C_s = 0.936 + \frac{0.00040 - 4850s}{T\,s} \qquad \text{Equation 8}$$

Based on Equation 8, the carbon concentration of ferrite due to small carbide size is plotted in Fig. 26 as a function of the particle size parameter for a series of temperatures ranging from 500 to 1000 °K (440 to 1340 °F). The particle size parameter depends on the shape of the cementite particles. By derivations similar to that of Equation 5, the s-equivalents for five possible cases can be shown to be as follows:

Case	*Shape*	*Size Parameter*
1	Sphere of radius r	$s = r$
2	Long cylindrical rod of radius r neglecting area of flat ends	$s = 2r$
3	Thin circular plate of radius r and uniform thickness assuming flat faces are coherent with matrix, and the corresponding interfacial energy is zero	$s = 2r$
4	Thin circular plate of uniform thickness t neglecting area of cylindrical surface	$s = t$
5	Thin lenticular plate of maximum thickness t	$s = \frac{t}{2}$

According to observations made with the electron microscope, the cementite particles in iron-carbon alloys tempered below about 800–900 °F (425–480 °C) are in the form of platelets and globules within the grains of the matrix. The thickness of these platelets and the radius of the globules were found to vary from the limit of resolution, about 10^{-6} cm. to as high as 10^{-5} cm. Assuming the lower extreme, thin lenticular platelets 10^{-6} cm. in thickness with a size parameter of

5×10^{-7} cm., the enhanced solubility at 900 °F (480 °C) is only about 0.02% according to Fig. 26.

Crangle (12) has reported that measurements of the intensity of magnetization made on a 1.7% carbon steel tempered at 570 °F (300 °C) can be explained if (a) the precipitated phase is cementite containing 6.7% carbon and the matrix contains 0.20% carbon in solution; or if (b) the precipitated carbide contains 7.7% carbon and the matrix is essentially pure ferrite. He rejects the first possibility on

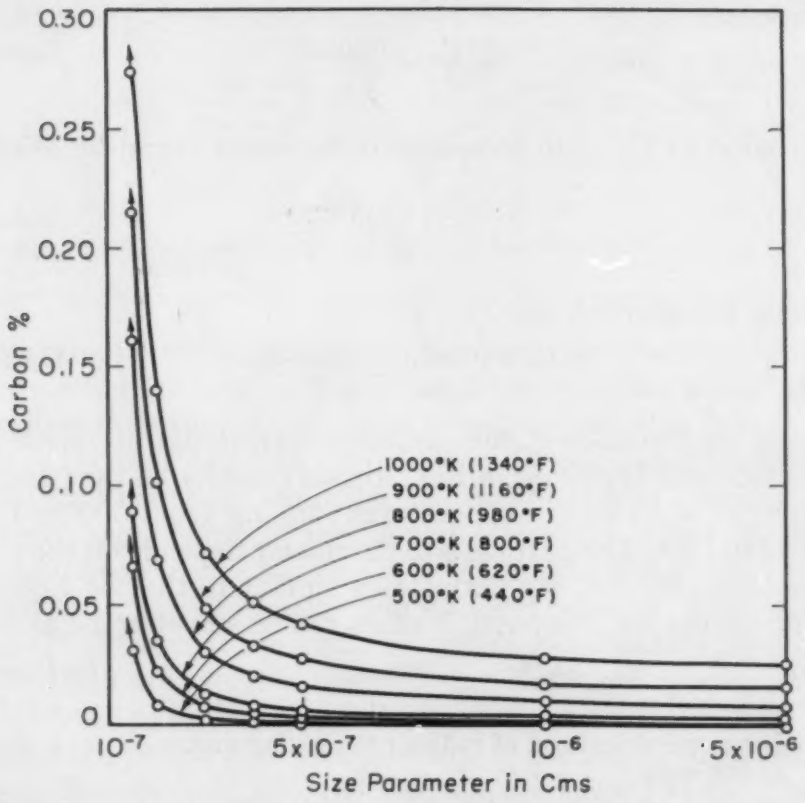


Fig. 26—Solubility of Carbon in Ferrite as a Function of Cementite Particle Size.

the ground that Kurdjumov (13) found the matrix to contain less than 0.05% carbon after a 570 °F (300 °C) temper, and therefore accepts the second possibility as being more likely. On this basis, Crangle postulates that the Hägg carbide rather than cementite forms during the early part of the third stage. However, as previously discussed (1), the results of X-ray and electron diffraction studies indicate that cementite forms right at the beginning of the third stage; whereas no such direct evidence was found for the occurrence of the Hägg carbide. Furthermore, a recent investigation by Bokshtein (14) has indicated that the carbon content of the matrix of 0.4 and 0.7% carbon steels is about 0.15% after a 570 °F (300 °C) temper, and con-

ceivably the matrix of Crangle's 1.7% carbon steel could be even higher in carbon content.

In order to have a 0.20% carbon in the matrix at a temperature of 570 °F (300 °C), the effective particle size parameter would have to equal 10^{-7} cm. according to Equation 5. Although such a small value is below the resolution of the electron microscope, it is unlikely that a sufficient number of particles of this size could be present to affect the solubility to the required extent. On the other hand, if the effective size parameter were 5×10^{-7} cm. as considered previously, Equation 5 indicates that γ_{a-c} would have to be about 3000 ergs/cm^2 in order to achieve a carbon solubility of 0.20%. This value of γ_{a-c} is at least 4 times greater than the probable value of 710 ergs/cm.[2] Thus it would appear that the magnitude of the increased solubility cannot be explained on the basis of interfacial energy alone. However, inasmuch as the matrix may still be martensitic rather than ferritic after a 570 °F (300 °C) temper, it is possible that the value of the interfacial energy between matrix and cementite may actually be higher than 710 ergs/cm.[2]

As suggested by Wilson (15), the existence of strain due to coherency between cementite particles and the ferritic matrix could also result in increased solubility. Although strain energy was disregarded in deriving Equation 5, it may have a larger effect than interfacial energy. Wilson (16) has recently demonstrated that plastic deformation due to a hardness indentation significantly retards the carbide precipitation associated with the tempering of martensite up to at least 840 °F (450 °C). In a previous investigation (17), he found that subjecting a high carbon steel to either elastic or plastic deformation resulted in a small increase in the Curie point of cementite. For a tensile stress of 120,000 psi. which was in the elastic range, an increase of about 15 °F was reported; whereas after 80% reduction in compression, an increase which estimated to be about 40 °F was obtained. Balluffi (18) showed that the Curie point of cementite in a 1% plain carbon steel decreased on tempering up to at least 1100 °F (595 °C) by an amount which is estimated to be about 70 °F. A check of the 0.8% carbon alloy used in the present investigation revealed that the Curie point of cementite decreased about 30 °F on tempering in the range of 800 to 1200 °F (425 to 650 °C).[5] In view of all this evidence, it is conceivable that coherency strains associated with the precipitation of cementite particles within the grains of the matrix may be at least partially responsible for both the enhanced carbon solubility of the matrix and the higher Curie point of cementite which are observed in tempered steel.

The fact that a decrease in the Curie point of cementite occurs

[5] The Curie point of cementite was not detected after tempering 1 hour at 600 °F (315 °C) or below.

somewhat beyond the tempering temperature corresponding to virtually complete displacement of this carbide to ferritic boundaries suggests that some other effect is occurring in the cementite phase than merely loss of coherency. This raises the possibility that the initial cementite to form may differ somewhat in carbon content than the value of 6.7% that corresponds to Fe_3C. Although Popova (19) has reported that the carbon content of cementite remains constant at a value of 6.7% on tempering above about 400 °F (205 °C), the estimated uncertainty of this value amounts to about ± 0.3% carbon and may mask small changes in carbon content that occur as a result of tempering. An initial divergence in the carbon content of cementite is reasonable on the grounds that this phase forms at a much lower temperature during tempering than in the case of annealing for which the formula Fe_3C has been better established.

From the available evidence it is not possible to decide whether an increase or decrease in the carbon content of cementite actually occurs during tempering. However, any change in the carbide composition would be expected to influence the carbon content of the matrix because of the condition of metastability that is eventually established on tempering. Based on an analysis of Balluffi's (18) results, Owen (20) concluded that the main portion of the third stage reaction in plain carbon steels is controlled by the diffusion of carbon in the matrix, but that a marked retardation in the rate of the reaction occurs during the end of this stage. Although Owen's results on silicon steels indicated that transfer of silicon atoms from the cementite phase to the matrix was responsible for retardation of the third stage, no explanation was offered for the retardation effect in the absence of a significant amount of silicon. The retardation effect in plain carbon steels might be explained on the basis that with continued tempering the cementite phase tends to approach the Fe_3C composition. Diffusion of either carbon or iron atoms within the cementite lattice would be required to effect the change in composition. Either process is likely to be slower than diffusion of carbon in ferrite and therefore would be expected to control the reaction rate during the end of the third stage.

Conclusions

1. On tempering iron-carbon alloys above about 700 °F (370 °C), coarsening and extension of cementite films at grain boundaries of the ferritic matrix occur at the expense of cementite particles which dissolve within the acicular grains inherited from the martensite. Cementite films form at both prior martensitic and prior austenitic grain boundaries, but appear to be more persistent at the latter locations on tempering at higher temperatures.

2. The process of displacement of cementite to grain boundaries is accompanied by spheroidization and coalescence of cementite both

within the grains and at grain boundaries. All of these processes occur more readily the lower the carbon content of the alloy. Although formation of cementite films may be a hardening factor during the tempering, it is apparently overbalanced by such softening effects as spheroidization, coalescence, and depletion of the carbon content of the matrix.

3. On the basis of interfacial energy considerations, spheroidized cementite particles at ferritic boundaries must be above a certain minimum size in order to be favored over cementite films. The calculated minimum size increases with both the carbon content of the alloy and the ferritic grain size.

4. Ferritic grain growth in the tempering range of 900 to 1300 °F (480 to 705 °C) is relatively small due to the inhibiting effect of grain boundary cementite.

5. The enhanced solubility of carbon in the matrix reported to exist in plain carbon steels during tempering is attributed to the presence of small, coherent particles of cementite which may differ in composition from the formula Fe_3C.

Appendix A

Minimum Size of Stable Cementite Lenticular Particles at Ferritic Boundaries

Let $\gamma_{a\text{-}a}$ = Interfacial energy per unit area between two ferritic grains.
$\gamma_{a\text{-}c}$ = Interfacial energy per unit area between ferrite and cementite.
S_v = Ferritic grain boundary interfacial area per unit volume.
t = Thickness of uniform and completely continuous cementite films at ferritic grain boundaries.
n = Number of lenticular cementite particles at ferritic grain boundaries per unit volume.
V, A, h, d, r, θ = Volume, surface area, thickness, diameter, radius of curvature of spherical surfaces, and dihedral angle respectively of each lenticular cementite particle.
E_1 = Total interfacial energy per unit volume with uniform cementite film completely covering ferritic grain boundary surface.
E_2 = Total interfacial energy per unit volume with n lenticular cementite particles at ferritic grain boundaries.

From the geometry of a lenticular particle:

$$1) \qquad \sin\frac{\theta}{2}=\frac{d}{2r} \text{ and } h=d\left[\frac{1}{\sin\frac{\theta}{2}}-\sqrt{\left(\frac{1}{\sin\frac{\theta}{2}}\right)^2-1}\right]$$

For $\theta = 115°$ as determined in reference No. 7:

$$2) \qquad r=0.60\,d, \quad \text{and } h=0.54\,d$$

The surface area and volume of a lenticular particle are given by:

$$3) \qquad A=2\pi rh \quad \text{and } V=2/3\pi\left(\frac{h}{2}\right)^2 \quad \left[3r=\frac{h}{2}\right]$$

Substituting for r and h from (2):

$$4) \qquad A=0.65\pi d^2 \quad \text{and } V=0.074\pi d^3$$

For cementite film completely covering ferritic grain boundary surface:

5) $$E_1 = 2\,S_v\ \gamma_{\alpha-c}$$

For n lenticular particles at ferritic grain boundaries:

6) $$E_2 = \left(S_v - n\pi\frac{d^2}{4}\right)\gamma_{\alpha-\alpha} + n\,0.65\pi d^2\,\gamma_{\alpha-c}$$

To obtain n in terms of t:

7) $$n = \frac{S_v\,t}{0.074\pi d^3}$$

8) $$E_2 = S_v\gamma_{\alpha-\alpha} - \frac{3.3\,S_v\,t\,\gamma_{\alpha-\alpha}}{d} + \frac{8.8\,S_v\,t\,\gamma_{\alpha-c}}{d}$$

Equating (8) and (5) to obtain minimum d:

9) $$d_{min} = \left[\frac{8.8\,\gamma_{\alpha-c} - 3.3\,\gamma_{\alpha-\alpha}}{2\,\gamma_{\alpha-c} - \gamma_{\alpha-\alpha}}\right] t$$

Since $\frac{\gamma_{\alpha-c}}{\gamma_{\alpha-\alpha}} = 0.93$ from reference No. 12:

10) $$d_{min} = 5.7\ t \quad \text{and} \quad h_{min} = 3.1\ t$$

The mean linear size of a cementite lenticular particle $\bar{d}$, may be taken as

11) $$\bar{d}_{min} = \frac{d_{min} + h_{min}}{2} = 4.4\ t^*$$

*Equation 2 of text.

Acknowledgments

The authors wish to express their appreciation to Miss Miriam Yoffa who prepared the specimens for electron microscopy; to Leonard Sudenfield who carried out the heat treatment and hardness tests; to Walter Fitzgerald and to Lauren P. Neal who were responsible for the maintenance of the electron microscope. The authors are also indebted to the Instrumentation Laboratory of M.I.T. for financial support of this investigation.

References

1. B. S. Lement, B. L. Averbach, and M. Cohen, "Microstructural Changes on Tempering Iron-Carbon Alloys," TRANSACTIONS, American Society for Metals, Vol. 46, 1954, p. 851.
2. R. M. Fisher and J. F. Boyce, Discussion to Reference 6, *Transactions*, American Institute of Mining and Metallurgical Engineers, Vol. 191, 1951, p. 1064.
3. C. S. Smith and L. Guttman, "Measurement of Internal Boundaries in Three-Dimensional Structures by Random Sections," *Journal of Metals*, Vol. 5, Jan. 1953, p. 343.
4. J. B. Rutherford, R. H. Aborn, and E. C. Bain, "Relation of Grain Area on a Plane Section and the Grain Size of a Metal," *Metals and Alloys*, Vol. 8, 1937, p. 345.
5. METALS HANDBOOK, American Society for Metals, 1948, p. 405.
6. M. Baeyertz, W. F. Craig, and E. S. Bumps, "Effect of Ferrite Grain Structure upon Impact Properties of 0.80 Pct. Carbon Spheroidite," *Transactions*, American Institute of Mining and Metallurgical Engineers, Vol. 188, 1950, p. 1465.
7. C. S. Smith, "Grains, Phases, and Interfaces—An Interpretation of Microstructure," *Transactions*, American Institute of Mining and Metallurgical Engineers, Vol. 175, 1948, p. 15.

8. S. T. Konobeevski, "A Thermodynamical Theory of Restoration Phenomena in the Aging of Copper Aluminum Alloys," *Journal,* Institute of Metals, Vol. 69, 1943, p. 397.
9. A. H. Cottrell and G. M. Leak, "Effect of Quench Aging on Strain Aging in Iron," *Journal,* Iron and Steel Institute, Vol. 122, Nov. 1952, p. 301.
10. L. H. Van Vlack, "Intergranular Energy of Iron and Some Iron Alloys," *Transactions,* American Institute of Mining and Metallurgical Engineers, Vol. 191, March 1951, p. 251.
11. C. A. Wert, "Solid Solubility of Cementite in Alpha Iron," *Transactions,* American Institute of Mining and Metallurgical Engineers, Vol. 188, Oct. 1950, p. 1243.
12. J. Crangle and W. Sucksmith, "Magnetic Analysis of Iron-Carbon Alloys,—The Tempering of Martensite and Retained Austensite," *Journal,* Iron and Steel Institute, Vol. 168, June 1951, p. 144.
13. G. V. Kurdjumov and L. Lyssak, "The Application of Single Crystals to the Study of Tempered Martensite," *Journal,* Iron and Steel Institute, Vol. 156, 1947, p. 29.
14. S. Z. Bokshtein, "Influence of Alloy Elements on Decomposition of Martensite," *Reports of the Academy of Sciences* USSR., Vol. 73, 1950, p. 491.
15. D. V. Wilson, Discussion to Reference 12, *Journal* Iron and Steel Institute, Vol. 170, March 1952, p. 248.
16. D. V. Wilson, "Effect of Plastic Deformation on Carbide Precipitation in Steels," *Journal,* Iron and Steel Institute, Vol. 176, Jan. 1954, p. 28.
17. D. V. Wilson, "Relation of Changes in the Cementite Curie Temperature to Textural Strains in Steel," *Nature,* Vol. 167, 1951, p. 899.
18. R. W. Balluffi, M. Cohen, and B. L. Averbach, "The Tempering of Chromium Steels," TRANSACTIONS, American Society for Metals, Vol. 43, 1951, p. 497.
19. N. M. Popova, "Determination of the Chemical Composition of Iron Carbide in Steel," *Zavodskaya Laboratoriya,* Vol. 15, 1949, p. 264.
20. W. S. Owen, "The Effect of Silicon on the Kinetics of Tempering," TRANSACTIONS, American Society for Metals, Vol. 46, 1954, p. 812.

DISCUSSION

Written Discussion: By Stuart T. Ross, project engineer, Chrysler Corp., Detroit.

The authors are to be congratulated for noteworthy additions to the knowledge of phenomena concerned with tempering of steel. As in a previous paper [6] they have divided microstructural changes associated with tempering into three stages as functions of temperature. The time of tempering has been held constant at one hour.

Since tempering operations are usually performed at constant temperature, it seems logical to consider microstructural changes as being not only temperature-dependent but also time-dependent. The work of Engel,[7] for example, indicates that Rc hardness of martensite tempered at a given temperature is a function of the time the work is held at that temperature. Therefore, as an addition to the above paper, work done in our laboratories concerning the time-dependence of tempering operations is presented for consideration.

Recently, an investigation by our laboratory on a commercial SAE 1090

[6] B. S. Lement, B. L. Averbach and M. Cohen, "Microstructural Changes on Tempering Iron-Carbon Alloys" TRANSACTIONS, American Society for Metals, Vol. 46, 1954, p. 851.
[7] E. H. Engel, "The Softening Rate of a Steel When Tempered from Different Initial Structures," TRANSACTIONS, American Society for Metals, Vol. 29, 1937, p. 1.

steel indicated dependence of its microstructure on the time of tempering. Disks of this steel 0.10 inch thick and 1.0 inch in diameter were austenitized at 1500 °F for 16 hours and water-quenched. They were then tempered at 800 °F in molten

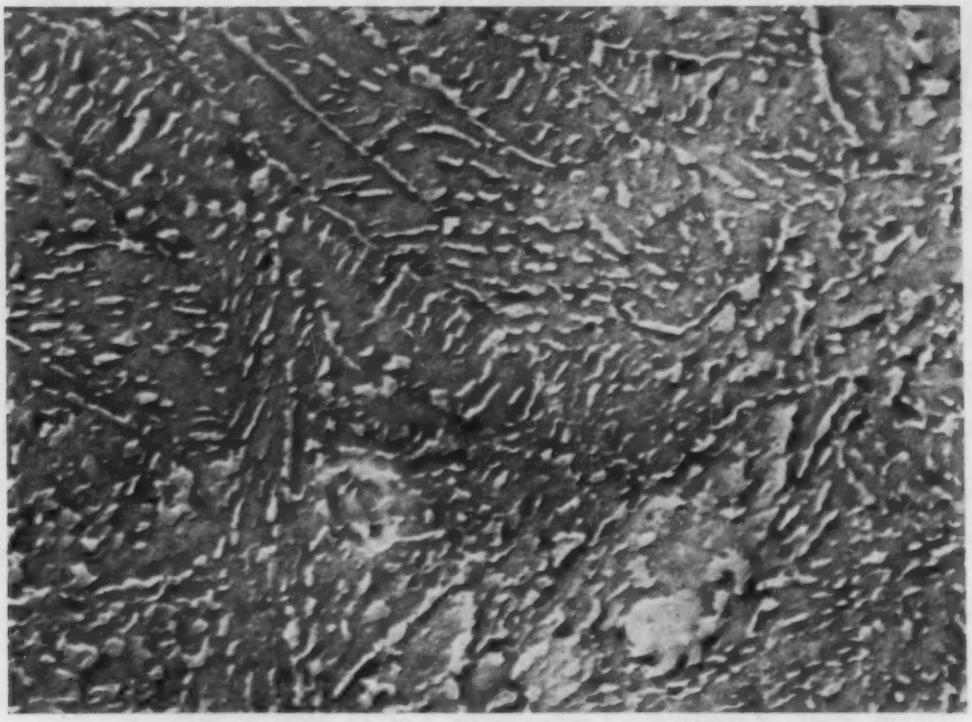


Fig. 27—SAE 1090 Steel Quenched from 1500 °F and Tempered 1 minute at 800 °F. Formvar replica, chromium shadowed at 45 degrees. Original magnification × 15,000, reduced 1/3. A lacy, film-like constituent is present in the habit of martensite subgrain structure. Elongated cementite films are seen at matrix boundaries.

salt for times varying from 1 to 60 minutes. Table IV indicates the Rc hardness obtained at various tempering times.

Electron micrographs of these tempered specimens were taken at × 15,000. Replication was accomplished by casting Formvar onto surfaces etched with 4% picral containing 0.1% zephiran chloride. The replicas were dry-stripped and shadowed with chromium at an angle of approximately 45 degrees.

Table IV
Hardness of SAE 1090 Steel Specimens Tempered Various Times at 800 °F

Tempering Time (at 800 °F)	Hardness (R_c)
As Quenched	66.0
1 Minute	50.0
15 Minutes	47.0
30 Minutes	45.5
60 Minutes	45.0

Fig. 27 indicates that a lacy, film-like constituent remains after tempering for 1 minute at 800 °F. It is in the habit of the martensite subgrain structure reported both by the above and work done at the Chrysler Corporation. Elongated cementite films are also present at matrix boundaries.

Fig. 28 shows that evidences of martensite subgrain structure remain even

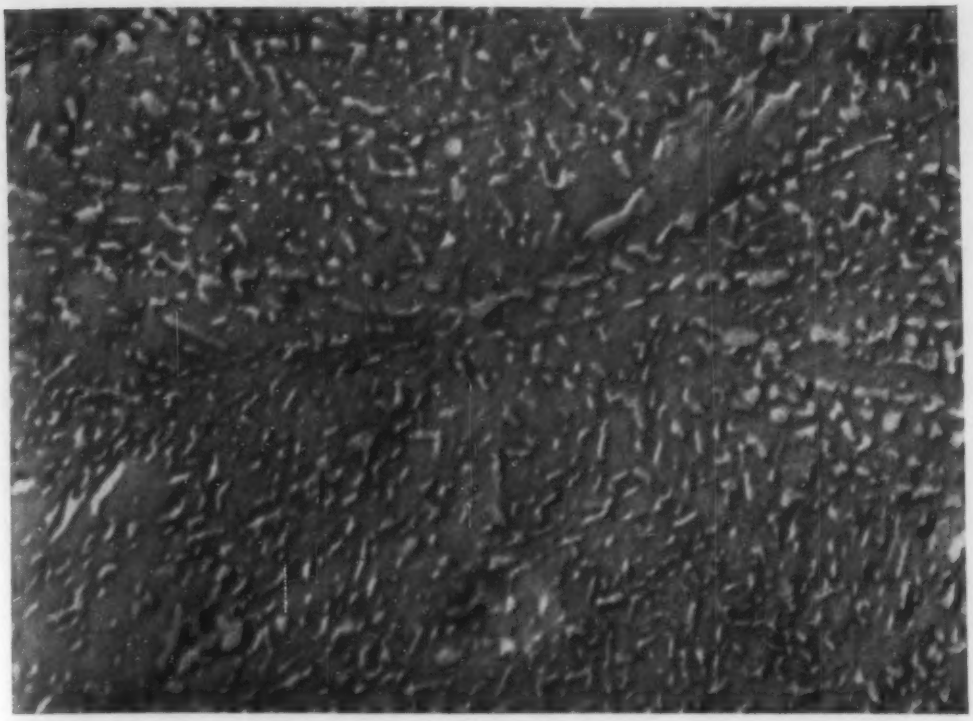


Fig. 28—SAE 1090 Steel Quenched from 1500 °F and Tempered 15 Minutes at 800 °F. Formvar replica, chromium shadowed at 45 degrees. Original magnification × 15,000, reduced 1/3. Evidence of martensite subgrain structure remain. Most of the carbides appear to be cementite.

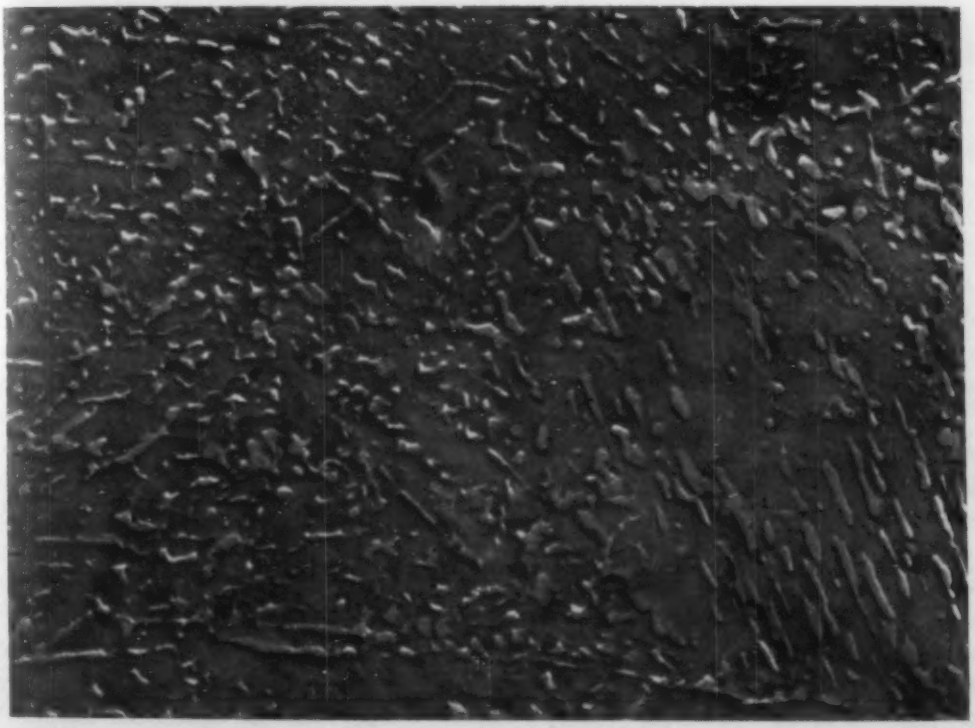


Fig. 29—SAE 1090 Steel Quenched from 1500 °F and Tempered 30 Minutes at 800 °F. Formvar replica, chromium shadowed at 45 degrees. Original magnification × 15,000, reduced 1/3. More elongated cementite particles have formed along prior grain boundaries. The fine, lacy constituent has virtually disappeared.

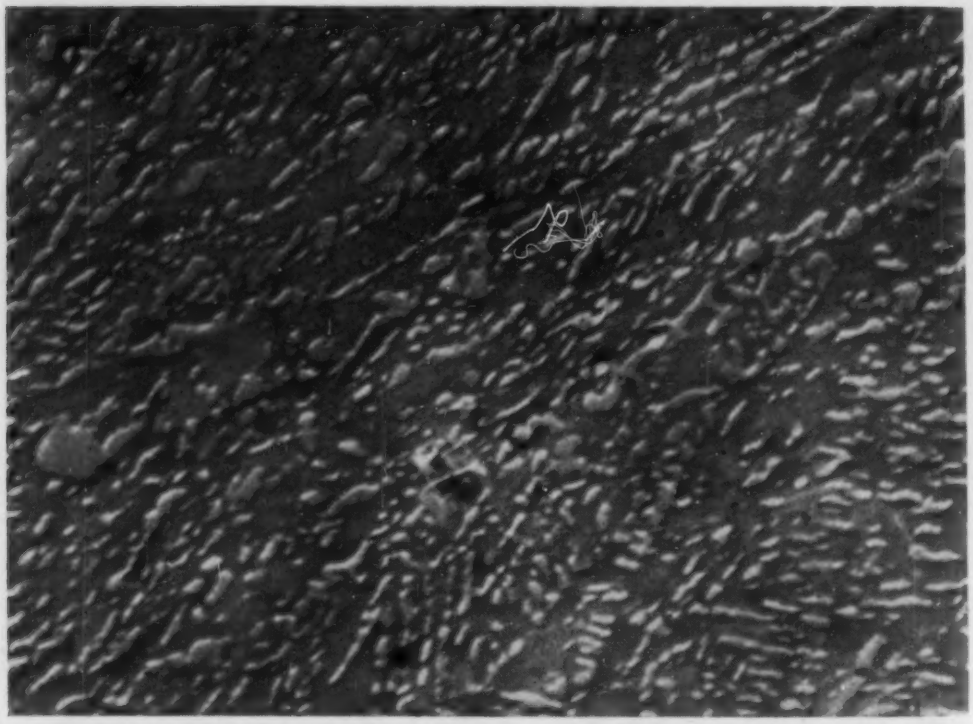


Fig. 30—SAE 1090 Steel Quenched from 1500 °F and Tempered 60 Minutes at 800 °F. Formvar replica, chromium shadowed at 45 degrees. Original magnification × 15,000, reduced 1/3. Cementite particles have begun to agglomerate and broaden. Fewer elongated particles are present and no remnants of the martensite subgrain structure can be seen.

after tempering for 15 minutes at 800 °F. However, most of the carbides appear to be cementite.

In Fig. 29, it can be seen that more of the elongated cementite particles have formed along prior grain boundaries. This has been accomplished at the expense of the fine, lacy constituent which has virtually disappeared after tempering for 30 minutes at 800 °F.

The last micrograph, Fig. 30, indicates that after 60 minutes of tempering at 800 °F, cementite particles have begun to agglomerate and broaden. Fewer elongated particles are present and no remnants of the martensite subgrain structure can be seen.

Thus, it is suggested that when the time factor is considered, temperature limits dividing tempering into several stages are either extremely wide or non-existent. The authors' previous paper indicates that the structure precipitated in martensite subgrains is found after tempering at 250 to 350 °F for an hour or more. This discussion indicates that such a structure can persist up to 15 minutes at a tempering temperature of 800 °F. It is reasonable to predict that this structure can form and remain on the order of 30 to 60 seconds even at tempering temperatures of 1000 °F or higher. Therefore, transitory formation of epsilon carbide and decomposition of austenite could well take place as intermediate stages no matter what the tempering temperature. Relative duration of these phenomena must, of course, depend upon the temperature at which the tempering operation is performed.

Written Discussion: By Cyril Stanley Smith, director, Institute for the Study of Metals, The University of Chicago, Chicago.

The authors make a most important point in remarking that under some conditions discrete lenticulate particles can be replaced with a plate-like form at a saving of surface free energy. However, one should be careful to avoid the impression that the dihedral angle is size dependent or that at some particular dimension the dihedral angle changes from a positive value to zero. Under surface tension forces with particles more than a few atoms in diameter there will be no change in shape with size. The change in geometry occurs only because boundaries of a different type are involved in equilibrium. The "cementite film" appears only when the ferrite boundary disappears from the system. Actually, the authors' effect is in essence the same as the redistribution that occurs when two lenticulate particles meet and merge under surface-tension forces into contiguous crystals with a new grain boundary between them but with a decrease

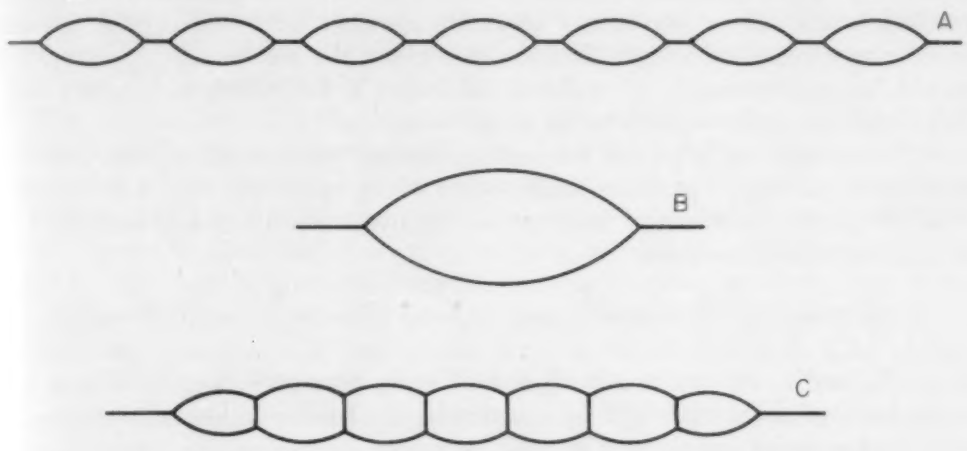


FIG. 31

of total surface area and energy. This saving of surface energy will occur regardless of scale and regardless of number of particles whenever two or more particles touch provided only that $\gamma < 2\gamma_{a_c}$. In the case under consideration this saving of energy can occur only if there is multiple nucleation and only if and when the particles have grown or moved until they come into contact. It is unreasonable to depend upon the miracle which would produce a full-grown single crystal plate or film over the whole α-α boundary. The "cementite film" of the authors is actually many crystals of cementite in contact with each other and completely blotting out the original ferrite grain boundary. The cementite must contain an approximately hexagonal network of its own grain boundaries, the energy of which cannot be ignored. Moreover, its interface with ferrite cannot be flat but must be covered with a series of nearly spherical "hills" meeting in an approximately hexagonal valley network at the correct dihedral angle

$$\theta = 2 \cos^{-1} \frac{\gamma_{cc}}{2\gamma_{a_c}}.$$

If two ferrite-cementite interfaces meet with a ferrite grain boundary, the dihedral angle will be the proper one, and the spreading of the "plate" over the grain boundary will be hindered by surface energy forces not helped, except for a moment following contact with a pre-existing adjacent particle.

Fig. 31 illustrates this point. A shows a series of discrete particles on the boundary. B represents the effect of merging them if the effect of orientation

difference is ignored and they are replaced with a single crystal. C shows the polycrystalline plate that would result in practice by merging many separate crystals. To a first approximation it is the plate of the authors, but the details necessary for surface energy equilibrium are important. Configuration B, of course, represents the ultimate equilibrium configuration for a given amount of precipitate at the grain boundary and eventually configuration C will transform into this by slow diffusion.

The above discussion, like that of the authors', is based on elementary surface energy equilibrium, using an essentially fluid model, and neglecting orientation effects. On the whole, I believe that the plate-like precipitate at the grain boundaries that the authors observe and which is not infrequently seen in other systems is more a kinetic than an equilibrium phenomenon. A real film or plate of a single orientation could, however, result from growth from a single nucleus which had a low-energy coherent interface with one crystal, growing rapidly as a result of a high diffusion rate along the incoherent boundary. This would be approximately of uniform thickness if the coherent interface could form approximately parallel to the grain boundary.

The authors' relation for the surface energy involved in a grain boundary containing lenticulate particles might be of wider value if it was not associated with the particular energies involved in the iron-carbon system. Rewritten for the general case it becomes

$$E_s = \gamma_{\alpha\text{-}\alpha} - n_s\pi r^2 \left(1-\cos^2\frac{\theta}{2}\right)\gamma_{\alpha\text{-}\alpha} + 4\pi n_s r^2 \left(1-\cos\frac{\theta}{2}\right)\gamma_{\alpha\text{-}\epsilon} \qquad \text{Equation 12}$$

where E_s and n_s related to a unit area of grain boundary (i.e. E_2/S_v and n/S_v in the authors' nomenclature). By substituting the basic relation between dihedral angle and energies and simplifying, this becomes

$$E_s = \gamma_{\alpha\text{-}\alpha} + n\pi r^2 \left(4\gamma_{\alpha\text{-}\epsilon} - 3\gamma_{\alpha\text{-}\alpha} + \frac{\gamma^3_{\alpha\text{-}\alpha}}{4\gamma^2_{\alpha\text{-}\epsilon}}\right) \qquad \text{Equation 13}$$

The assistance of Messrs. Lement and Cohen in eliminating errors in a preliminary form of this discussion is gratefully acknowledged.

Authors' Reply

As Mr. Ross points out, there is a time as well as temperature dependence associated with the reactions that occur during the tempering of steel. His study of the solution of ϵ-carbide at 800 °F is interesting since it indicates that this carbide is more persistent than one might expect on the basis of our previous paper (1). However, one should not overlook the possible role of residual alloying elements in commercial 1090 steel. In the presence of extraneous elements and particularly if microsegregation occurs, solution of ϵ-carbide may be delayed somewhat. Therefore a direct comparison with the kinetics of the high purity iron-carbon alloys used in the present investigation should be regarded with caution.

In the previous paper, it was shown (1) that ϵ-carbide in a 0.8% carbon alloy virtually disappears after 1 hour at 550 °F, which corresponds to a hardness of Rockwell C-52. In the 1090 steel of Ross, ϵ-carbide virtually disappears after 30 minutes at 800 °F, with a corresponding hardness of Rockwell C-45. If both sets of data are assumed to reflect the role of carbon and not alloy content, it may be concluded that an increase in tempering temperature has the effect of speeding up cementite formation (as well as the subsequent changes in

morphology and distribution) relative to the solution of ϵ-carbide. In addition to explaining the lower hardness after obtaining complete solution of ϵ-carbide at 800 °F, this viewpoint indicates that a given hardness achieved by different time temperature tempering combinations does not necessarily represent a definite microstructure.

Dr. Smith points out that it is possible to form a polycrystalline or multi-lenticular plate of cementite by merging of pre-existing lenticulates of cementite at grain boundaries. He further states that a multi-lenticular plate could transform to a single crystal lenticulate by slow diffusion, which may be interpreted as grain growth within the carbide or removal of cementite-cementite boundaries. However, the films of cementite that form at ferritic grain boundaries are observed to "spheroidize" eventually or break up into globular particles which are much smaller than one would expect on the basis of a change from a multi-lenticulate to a single lenticulate. Therefore, it seems unlikely that the process postulated by Dr. Smith actually occurs during the tempering of iron-carbon alloys even if it is energetically possible.

The authors agree with Dr. Smith on the exceeding low probability of forming a single crystal cementite film over the whole α-α boundary even though it is energetically possible. For the purpose of simplicity, a comparison was made of the total interfacial energy corresponding to a uniform and continuous film of cementite with that of an equal volume of lenticulates in order to show that their size is of importance. However, it can likewise be shown that if the film is discontinuous or plates form, a lower total interfacial energy also results as compared to a system of lenticulates below a certain minimum size. In fact, it is possible for a system of grain boundary cylindrical plates (discs) to be more stable than a continuous grain boundary. For the case of a comparison with a system of cylindrical plates of cementite, the minimum diameter of stable lenticulates can be shown to be given by:

$$d_{min} = \frac{4.9\ h}{0.86 + \frac{h}{R}} \qquad \text{Equation 14}$$

where h is the thickness and R is the radius of the plates. If $\frac{h}{R}$ is very small, $d_{min} = 5.7\ h$ which is the same result obtained in Appendix A for the case of a continuous film of thickness t. However, more stable plates result if $\frac{h}{R}$ is increased. It can be shown that for the most stable system of grain boundary cylindrical plates,

$$\frac{h}{R} = \frac{2\gamma_{\alpha-c} - \gamma_{\alpha-\alpha}}{\gamma_{\alpha-c}} = 0.93 \qquad \text{Equation 15}$$

Substituting this ratio of $\frac{h}{R}$ in Equation 14:

$$d_{min} = 2.7\ h \qquad \text{Equation 16}$$

where h now equals $\left[\frac{V(0.93)^2}{n\pi}\right]^{1/3}$ or depends on the volume of cementite (V) and number of plates (n) per unit volume of alloy.

As suggested by Dr. Smith, the formation of grain boundary plates might occur by the growth of nucleus possessing a coherent interface with one grain and an incoherent interface with the adjoining grain of the matrix. However, in view of the fact that diffusion of carbon atoms is probably faster along α-α boundaries than within α-grains, it does not appear necessary to make assumptions regarding the state of coherency of the cementite interfaces. If carbon atoms were supplied edgewise at a sufficiently rapid rate, a cementite nucleus could spread along the α-α interface and thereby result in a film or plate. Thickening would presumably result from bulk diffusion as well as grain boundary diffusion of carbon atoms.

Equations 12 or 13 given by Dr. Smith for the case of lenticular particles at grain boundaries can be made even more general by taking into account the total volume of precipitate (V) per unit volume of alloy:

$$E_s = \gamma_{\alpha-\alpha}\left[1 + \frac{n^{1/3}\,(1.5\pi^{1/2}V)^{2/3}}{S_v}\right]\left[\frac{4(1-\cos\frac{\theta}{2})\frac{\gamma_{\alpha-c}}{\gamma_{\alpha-\alpha}} - (1-\cos^2\frac{\theta}{2})}{(2 - 3\cos\frac{\theta}{2} + \cos^3\frac{\theta}{2})^{2/3}}\right]$$

Equation 17

For a given dihedral angle θ, E_s increases with $n^{1/3}$ and is a minimum if $n = 1$ (one particle). To find the value of $\frac{\theta}{2}$ which makes E a minimum for a given value of n, $\frac{dE_s}{d(\frac{\theta}{2})}$ is set equal to zero.

This gives the dihedral angle relation:

$$\cos\frac{\theta}{2} = \frac{\gamma_{\alpha-\alpha}}{2\,\gamma_{\alpha-c}}$$

Equation 18

Thus it is possible to derive the dihedral angle relation on the basis of energy considerations as well as on the basis of an equilibrium of interfacial tensions as Dr. Smith has done.

EFFECTS OF COLD WORK ON CEMENTITE IN STEEL

By D. V. Wilson

Abstract

The influence of cold work on cementite in steel has been explored, using the methods of magnetic analysis and X-ray diffraction.

When a carbon steel is plastically deformed the cementite Curie point changes. The extent of this change is strongly dependent on the microstructure of the steel and the amount of deformation applied. On heating a cold-worked steel in the temperature range 200 to 500 °C (390 to 930 °F), progressive recovery of the Curie point occurs.

The observed magnetic intensity/temperature relationships demonstrate the existence of structural conditions of the carbide intermediate between that of undeformed cementite and the state produced by severe cold working. It has been shown that the displacements of the cementite Curie point are mechanically reversible and there is some evidence that this Curie point may be directly influenced by elastic distortion of the cementite. These observations are consistent with the possibility that elastic textural strains present in the cementite particles may provide a sufficient explanation of the Curie point displacements.

Cold working also causes a small increase in the intensity of magnetisation which persists up to temperatures approaching 500 °C (930 °F). The characteristics of this change are considered in relation to the possibility of decomposition of cementite in cold-worked steels.

X-ray examination has confirmed that the textural stress system, set up between the ferrite and cementite as a result of cold working, may impose intense elastic strains on the cementite particles. These textural stresses may have an important influence on mechanical properties.

Introduction

THE changes in the saturation intensity of magnetization and in the cementite Curie point of a steel which occur as a result of plastic deformation (1) [1] are of particular interest because these two prop-

[1] The figures appearing in parentheses pertain to the references appended to this paper.

A paper presented before the Thirty-sixth Annual Convention of the Society, held in Chicago, November 1 to 5, 1954. The author, D. V. Wilson, is lecturer, Department of Industrial Metallurgy, The University of Birmingham, Edgbaston, Birmingham, England. Manuscript received August 3, 1953.

erties are generally regarded as being dependent only on chemical composition and crystal structure.

The saturation intensity/temperature relationships shown by cold-worked carbon steels bear resemblance to those shown by similar steels which have been quench-hardened and subsequently tempered at a temperature in excess of about 280 °C (535 °F). In the case of the heat treated steels, the occurrence of a modified carbide Curie point has been ascribed to the initial precipitation of carbides having crystal structures different from that of cementite (2). That the first precipitate occurring during the low temperature tempering of martensite is the hexagonal ϵ-iron carbide has been established by the structural investigations of Heidenreich, Sturkey and Woods (3) and of Jack (4). More recently it has been suggested that another intermediate carbide, resembling iron percarbide, may occur during the third stage of tempering carbon martensites (5), (6).

The possibility that similar modifications in the carbide structure may underlie the magnetic behaviour of cold-worked steels has been considered. Andrew, Lee and Wilson (7), in an X-ray crystallographic examination of cold-worked high carbon steels, found no evidence of a new carbide phase but they observed that the residual textural stress system, set up between the cementite and the ferrite as a result of cold working, may impose intense strains on the cementite particles. As a result of this observation a second possible cause of the displacement of the cementite Curie temperature was suggested, namely, that the changes in interatomic distances in the carbide structure, due to the textural stresses, might in themselves sufficiently modify the exchange interaction factor to give rise to a significant change in Curie temperature.

However, a new carbide phase would probably occur in the form of small, highly strained particles, therefore the absence of X-ray diffraction evidence of a new carbide cannot be regarded as conclusive evidence that a structural transformation does not occur during cold working.

In the present investigation, thermomagnetic analysis, supplemented by some X-ray observations, has been used in an examination of the effects of cold work on cementite in steel.

Experimental Methods

The Thermomagnetic Balance

The general principles involved in the method of thermo-magnetic analysis, using the Sucksmith magnetic balance, have been outlined in (8) and in subsequent papers describing experimental investigations in which this method has been used (9,10,6).

The magnet constructed for the present research was similar in principle to that developed by Sucksmith but a considerably larger

specimen, suitable for cold working by compression, was used: this was in the form of a disk of 0.2 inch diameter and 0.1 inch thick.

The arrangement of the specimen assembly and the furnace between the pole-pieces of the electromagnet is illustrated in Fig. 1. The specimen was set up with a diameter in the field direction, therefore no angular setting of the specimen in the horizontal plane was required Despite the relatively large magnetic moment of the specimen and the variations in the field gradient over distances of the order of the dimensions of the specimen, tests demonstrated that no serious inaccuracies resulted from the use of the larger specimen provided a 'null' method of force measurement was employed.

The magnet coils were water-cooled at their inner surfaces and a coil current of 15 amps could be used giving a field strength of 17,500 oersteds between the ferrocobalt pole faces.

The specimen "1," contained in a platinum thimble "4," was placed symmetrically in the pole gap in the region of minimum variation in field gradient with vertical displacement. The field gradient, provided by the shaping of the pole faces, was so arranged that the magnetic force pulled the specimen upward against the lower end of the silicia tube "2," which was ground flat. The force on the specimen was communicated to the copper-beryllium ring balance "3" by the silica tube, lateral movement being restrained by spiral springs "5." The elastic distortion of the ring balance was measured by means of an optical lever. Light from a projection lamp passed through lens "7," was reflected by the mirrors "6" and was then brought to focus in the plane of a graticule, which was observed through a microscope. This arrangement permitted the observation of a specimen movement of 10^{-5} cms.

A steel specimen, weighing ⅓ gram, experienced a force equivalent to about 60 grams weight at room temperatures: This was counterbalanced to the nearest gram by weights placed on the platform "8," the residual force being taken up by distortion of the ring balance. The vertical setting of the silica tube "2," hence that of the specimen, was checked to 2×10^{-4} cms. by means of a second optical system employing a fine cross-wire mounted directly on the silica tube at "11": and a lens "10" which focused an enlarged image of this cross-wire onto the microscope graticule.

During an experiment the specimen was heated by means of a small, externally water-cooled, furnace mounted vertically between the pole faces: the Nichrome tape heating element was wound non-inductively. The specimen's temperature was measured by means of a platinum, platinum/rhodium thermocouple which passed down the inside of the specimen-supporting tube, the hot junction "9" being in direct contact with the specimen. At elevated temperatures a stream of purified nitrogen was passed through the furnace tube to protect the specimen from oxidation.

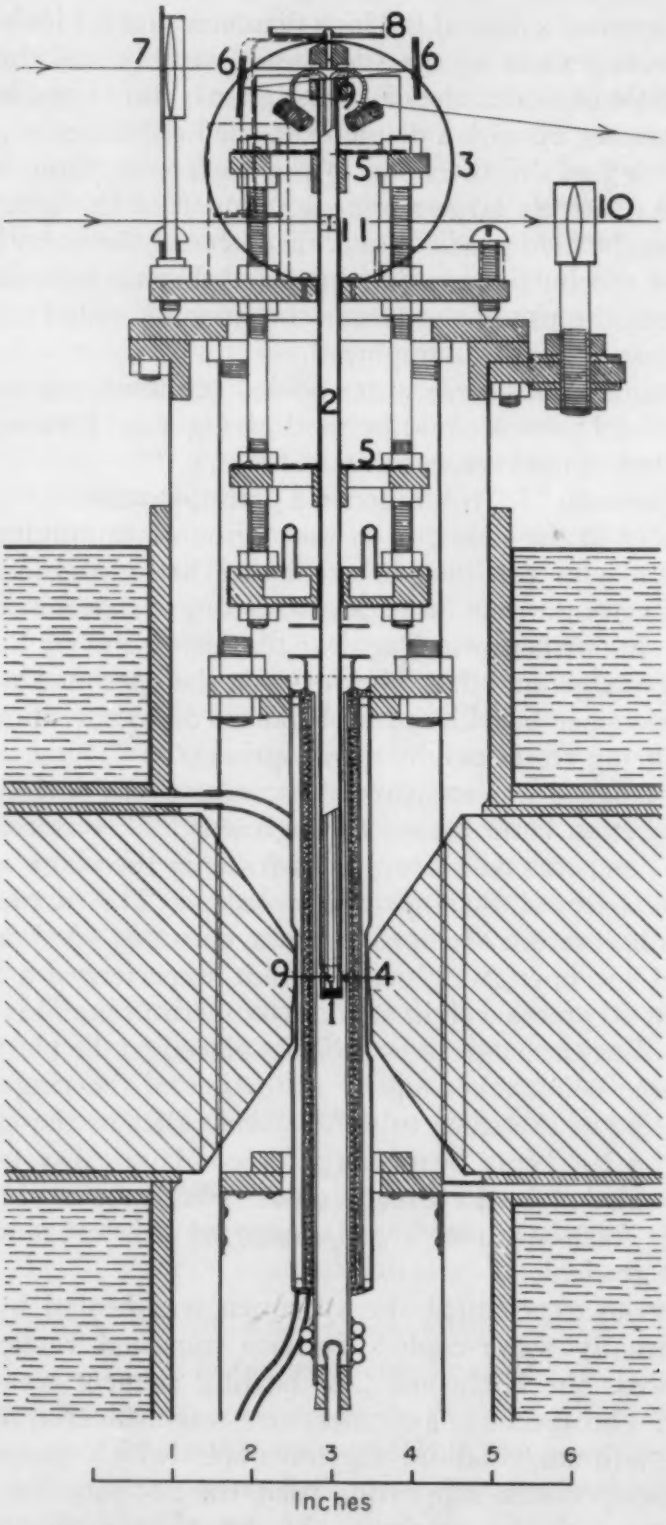


Fig. 1—Thermomagnetic Balance. Diagram of specimen assembly and furnace.

Tests using specimens having known mass ratios and intensity ratios demonstrated that errors due to magnetic image effects were negligible in the range of variation of magnetic moment met with in the research. An applied field in excess of about 5000 oersteds was sufficient to overcome the self-demagnetizing field of a soft iron specimen, but with magnetically hard materials a considerably higher applied field was required to achieve a close approach to saturation. The achievement of approximate saturation intensity was tested by observing the variation of the force ratios with applied fields in the range 8000 to 17,000 oersteds.

With a single specimen a magnetic intensity change of 0.15% could be detected with certainty in the normal working range. Reproducibility of results obtained with different specimens was normally within ± 0.4%. Reduced accuracy in the latter case was largely due to the influence of small errors in specimen setting.

Preparation of the Specimens

The majority of the experiments made in this research have employed one of the following steels, which were originally in the form of hot-rolled rods.

	0.50% C	0.70% C	1.26% C	15% Cr
C%	0.50	0.70	1.26	1.00
Mn%	0.30	0.66	0.31	0.69
Si%	0.09	0.15	0.27	0.55
S%	0.007	0.010	0.012	0.029
P%	0.03	0.015	0.023	0.020
Cr%	—	—	—	14.9
Ni%	—	—	0.05	—

After machining, heat treatments were carried out using a vertical tube electric furnace. The specimens were heated in evacuated silica tubes which were arranged to fracture as they entered the quenching bath. This gave uniformly quenched specimens free from surface oxidation and decarburization.

With few exceptions, cold working was carried out by slow compression using a hydraulic testing machine.

Experimental Results

Preliminary Observations

The first magnetic experiments were made in order to explore the general characteristics of the changes in the saturation intensity/temperature relationships of plain carbon steels which occur as a result of cold working.

Tests, made with 1.26% carbon steel specimens of fine carbide particle size and having heavy reductions, demonstrated that the intensity/temperature relationships shown by the cold-worked steel

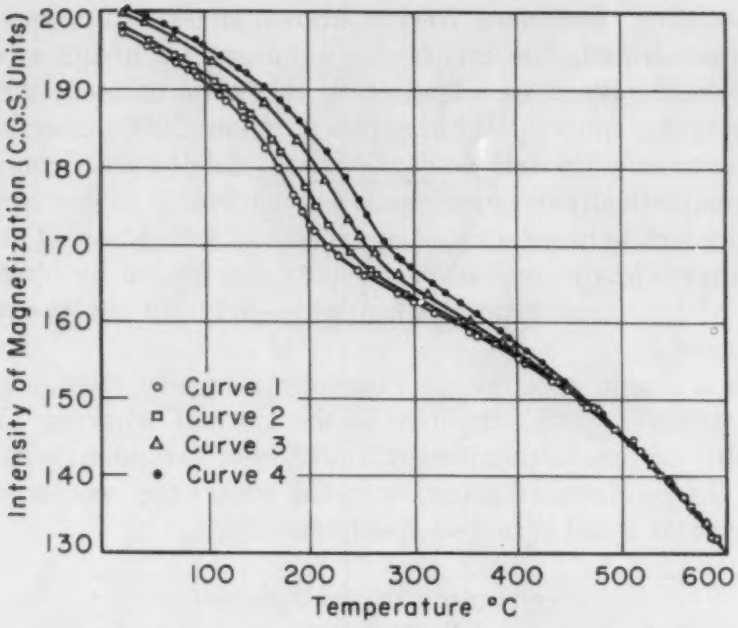


Fig. 2—Influence of Initial Microstructure on the Change in the Magnetic Intensity/Temperature Relationship of a 1.26% Carbon Steel Due to Cold Working. Curve 1—Fully softened condition (annealed 680 °C). Curve 2—Spheroidized microstructure, 89% reduction. Curve 3—Fine pearlitic microstructure, 87% reduction. Curve 4—Fine sorbitic microstructure, 87% reduction. Curves 2, 3 and 4 were obtained on heating. Curve 1 represents a reversible relationship.

were essentially independent of the relationship between the direction of magnetization if an applied field in excess of about 15,000 oersteds was used. Subsequently, with one exception, all experiments were made using an applied field of 16,000 oersteds. The rate of heating and cooling was approximately 2 °C per minute.

It was found that the initial condition of the steel exerted a marked influence on the extent of the change which resulted from a given degree of deformation. Fig. 2 illustrates the results obtained with the 1.26% carbon steel after cold working to similar extents in three different conditions. These were:

a) Annealed at 680 °C (1255 °F) for 8 hours, (spheroidized microstructure).

b) Isothermally transferred at about 600 °C (1110 °F) (fine pearlitic structure).

c) Water-quenched from 950 °C (1740 °F) and tempered at 480 °C (895 °F) (fine sorbitic structure).

After these heat treatments each specimen received approximately 88% reduction by compression. In their undeformed conditions the spheroidized and pearlitic materials gave intensity/temperature relationships similar to that of the "fully softened" material (annealed at 680 °C after cold working), but the relationship of the hardened and tempered material in the undeformed condition showed some differences from that in the softened condition (this is shown in Fig. 5.)

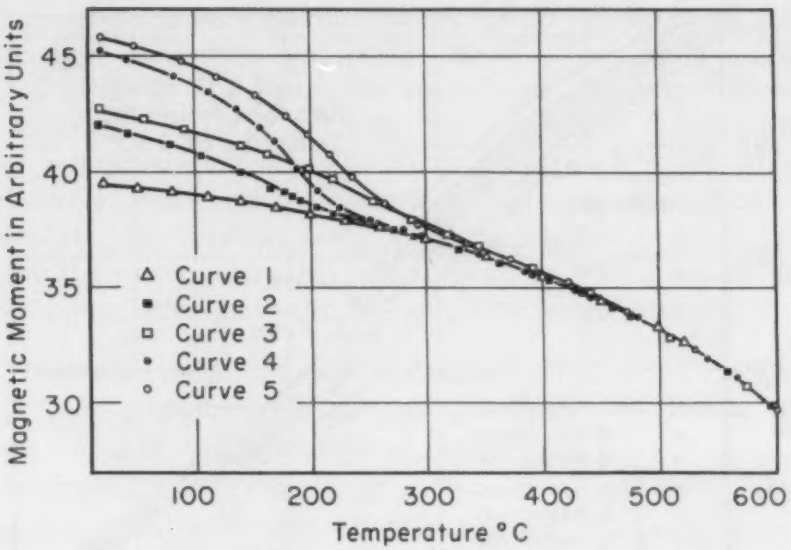


Fig. 3—Comparison of the Effects of Cold Work on Steels of Differing Carbon Content. (The scales are adjusted to represent samples having equal quantities of ferrite). Curve 1—Carbon free iron. Curve 2—0.70% carbon steel; fine pearlitic structure; undeformed. Curve 3—0.70% carbon steel; fine pearlitic structure; 84% reduction. Curve 4—1.26% carbon steel; fine pearlitic structure; undeformed. Curve 5—1.26% carbon steel; fine pearlitic structure; 85% reduction.

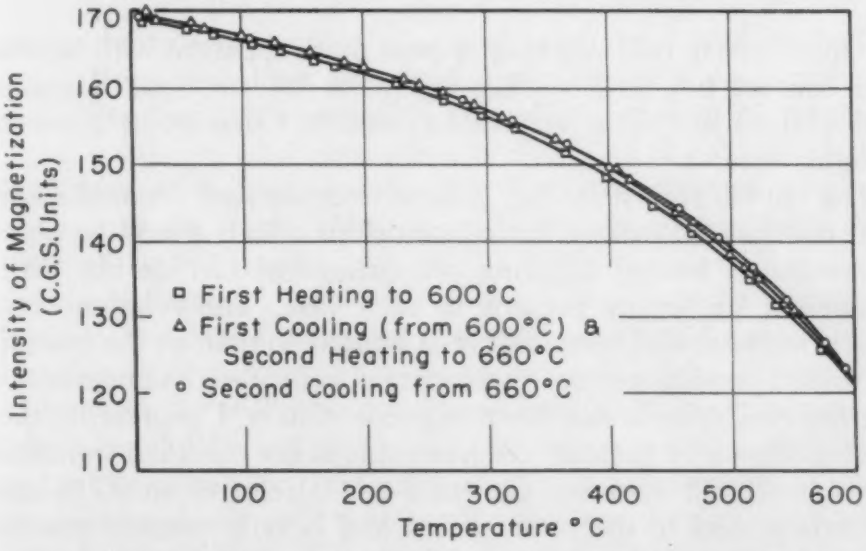


Fig. 4—Influence of Cold Working on Intensity/Temperature Relationship of 15% Chromium, 1% Carbon Steel. The specimen was quenched from 1000 °C, tempered at 600 °C and then received 63.5% reduction.

In addition to the 1.26% carbon steel, a carbon-free iron, an 0.50% carbon steel and an 0.70% carbon steel were examined; the steels being treated to give fine pearlitic microstructures. Carbon-free iron showed no detectable change in the intensity/temperature relationship after reductions of up to 93% by compression. With steels of differing carbon contents, but otherwise comparable microstructures,

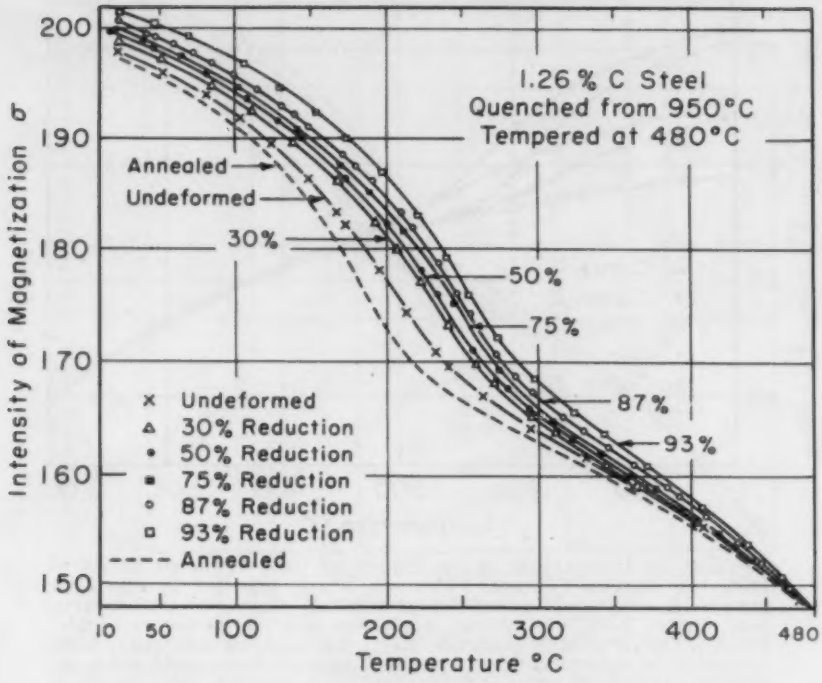


Fig. 5—Influence of Differing Degrees of Deformation on Cementite Curie Point Change. Relationships observed on heating.

the changes due to cold working became more apparent with increasing carbon content, but, with similar degrees of deformation, the temperature displacements of the apparent cementite Curie point appeared to be roughly similar.

The curves shown in Fig. 3 have been derived from the experimental results to illustrate the relationships which would be obtained with specimens having differing proportions of carbide but with the same weight of ferrite present in each case. The relation between magnetic moment and temperature is plotted so that, in the case of the undeformed conditions, the three curves coincide at temperatures at which the cementite is not ferromagnetic. Curve 1 represents the relationship shown by carbon-free iron; this is not modified significantly as a result of cold working. Curves 2 and 3 refer to an 0.7% carbon plain carbon steel in the undeformed and heavily worked conditions respectively: Curves 4 and 5 to a 1.26% carbon steel, again in the undeformed and heavily worked conditions respectively. With the cold-worked conditions the relationships (3 and 5) do not become effectively coincident with that shown by carbon-free iron until a temperature in the neighborhood of 500 °C (930 °F) is reached.

Fig. 4 shows the influence of cold working on the intensity/temperature relationship of the 15% chromium 1% carbon steel. This was oil-quenced from 1000 °C (1830 °F) and tempered at 600 °C (1110 °F) before working. This gave an initial hardness (410 V.P.N.)

and microstructure very similar to that of the 1.26 carbon steel, after the latter had been quenched from 950 °C (1740 °F) and tempered at 480 °C (895 °F) however, the carbide in the chromium steel was in the trigonal $(Fe,Cr)_7C_3$ form. The change in the intensity/temperature relationship of this chromium steel, as a result of working, was relatively small and the direction of the change opposite to that of a similar plain carbon steel. (The characteristics of the change shown by the chromium steel resemble those which would arise as a result of a small change in the ferrite Curie temperature).

The Progressive Changes in the Magnetic Intensity/Temperature Relationship Due to Cold Working and During Subsequent Reheating.

More detailed examinations were next made, using steel having a composition and structure which permitted relatively large changes in the intensity/temperature relationship as a result of cold working. The specimens used were of the 1.26% carbon plain carbon steel, water-quenched from 950 °C (1740 °F) and subsequently tempered at 480 °C (895 °F) for 1 hour. This treatment gave a fine sorbitic microstructure and an initial hardness of 410 ± 6 V.P.N. After cold working the specimens were aged for several days before testing.

Fig. 5 shows the effect of several different degrees of cold work on the intensity/temperature relationship of the 1.26% carbon steel in the condition described. In this diagram, the individual curves have been combined on the assumption that all the specimens returned to the same condition after annealing at 700 °C (1290 °F). If the intensity values were calculated directly from the specimen weights and positions, then the results obtained in the 'annealed' conditions showed a scatter of approximately ½% of the intensity value. It is probable that these differences were due principally to errors in specimen setting. On this assumption, the standard provided by the 'annealed' relationship of each specimen was preferred as a basis of comparison.

Although the different specimens used in this experiment were machined from adjacent portions of the same bar and were all heat treated in the same batch, the magnitude of the increments in intensity value considered are such that small variations in the initial samples may also be significant.

For these reasons quantitative comparisons of the different curves given in Fig. 5 cannot be made with the same degree of confidence as in the case of the 'recovery' experiment which will be described next.

It is considered that the following conclusions can be drawn from the results of this experiment:

a) The room temperature saturation intensity increased progressively with degree of deformation up to the highest reduction examined.

b) There was a progressive increase and 'smoothing out' of the apparent cementite Curie point with increasing cold work; but for similar increments in cold work, the rate of change of this Curie temperature appeared to decrease with increasing cold work.

c) After heating to temperatures above about 480 °C (895 °F), there was little difference in the observed intensity values, irrespective of the initial condition of the steel but, above the apparent cementite Curie temperature, in the temperature range from 300 to about 480 °C (570–895 °F) the observed intensity of magnetization was dependent on the amount of previous deformation. In this temperature range there was a suggestion that the increments in intensity value may become greater in the later stages of deformation.

The next experiment was designed to investigate the characteristics of the recovery of the intensity/temperature relationship during reheating of a heavily worked steel. A specimen of the 1.26% carbon steel, quenched from 950 °C (1740 °F), tempered at 480 °C (895 °F) and having 87% reduction by compression, was used. The specimen was aged at room temperature for one week before testing. The experiment consisted of following the changes in the intensity/temperature relationship of the material during heating to, and cooling from, successively higher temperatures in the range 90 to 700 °C (195 to 1290 °F). The results are summarized in Fig. 6. Details of the heating and cooling operations are given with this diagram and the small vertical arrows on the graph also indicate the temperature steps. The rates of heating and cooling were approximately 2 °C per minute.

Since this experiment was made using a single specimen and the setting position was unchanged throughout the experiment, high comparative accuracy could be achieved. In the particular conditions an 0.1% change in the intensity value could be recognized.

The results indicated that the intensity/temperature relationship was reversible up to 172 °C (340 °F) but, above about 200 °C (390 °F), there was evidence of the start of the recovery process. Recovery became marked after heating to temperatures above about 250 °C (480 °F) but only after heating to temperatures of the order of 500 °C (930 °F) was it largely completed.

Evidence of the Mechanical Reversibility of the Cementite Curie Point Displacement

The textural stress system, set up between cementite and ferrite as a result of plastic deformation, is orientated with respect to the direction of working. If the displacement of the cementite Curie temperature in a cold-worked steel were associated with the presence of textural elastic strains in the cementite particles, then one might sup-

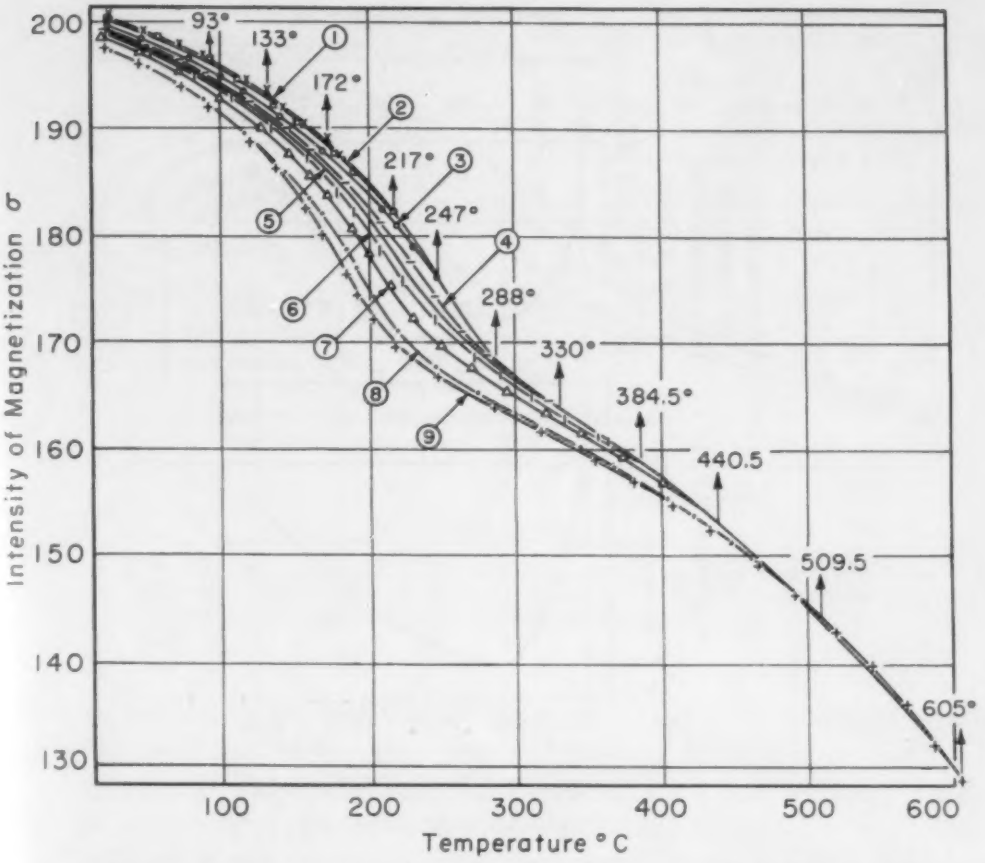


Fig. 6—Recovery of the Cementite Curie Point Change During Reheating After Cold Work. 1.26% carbon steel, quenched from 950 °C, tempered at 480 °C, 87% reduction. Progressively heated to and cooled from the following temperatures: Curve 1—First heating to 93 °C; first cooling from 93 °C; second heating to 133 °C; second cooling from 133 °C; third heating to 172 °C; third cooling from 172 °C; fourth heating to 217 °C. Curve 2—Fourth cooling from 217 °C; fifth heating to 247 °C. Curve 3—Fifth cooling from 247 °C; sixth heating to 288 °C. Curve 4—Sixth cooling from 288 °C; seventh heating to 330 °C. Curve 5—Seventh cooling from 330 °C; eighth heating to 384.5 °C; Curve 6—Eighth cooling from 384.5 °C; ninth heating to 440.5 °C. Curve 7—Ninth cooling from 440.5 °C; tenth heating to 509.5 °C. Curve 8—Tenth cooling from 509.5 °C; eleventh heating to 605 °C. Curve 9—Eleventh cooling from 605 °C, twelfth cooling from 700 °C.

pose that a significant reduction in the magnitude of the change could be effected by deforming the metal in the opposite direction to that in which the original deformation was applied. On the other hand, certain structural transformations and planar fragmentation effects would not be expected to show mechanical reversibility.

In initial experiments, samples of an 0.7% carbon steel wire of fine pearlitic microstructure, which had been severely cold drawn, were 'reverse strained' by compression along the wire axis, (using a composite specimen to reduce buckling). Axial compression can give only approximately the reverse of the deformation in wire drawing; moreover some buckling and barreling of the specimens occurred when severe 'reversed straining' was applied. Despite these limitations the result suggested that some degree of recovery of the cementite Curie point may be achieved by 'reversed straining.'

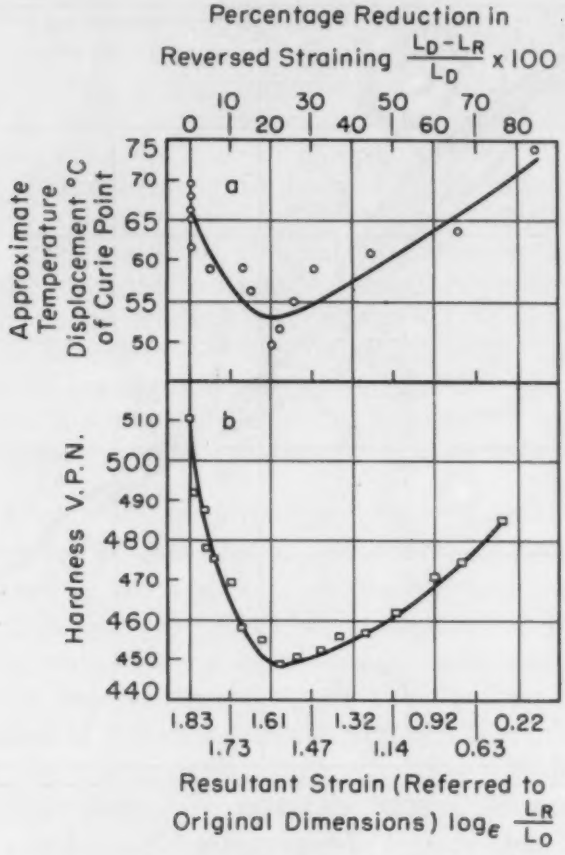


Fig. 7—0.7% Carbon Steel; Fine Pearlitic Structure; Initially Cold Drawn to 84% Reduction. Figure shows influence of subsequent "reversed straining" on: 7a—The temperature displacement of the cementite Curie point; 7b—The indentation hardness. L_O = length before drawing; L_R = length after drawing; L_D = length after reversed straining.

Using specimens cut from adjacent portions of the same wire, which had previously received 84% reduction by cold drawing, the effects of a number of different degrees of reversed straining were examined.

Fig. 7a shows the observed trend in the relationship between the estimated cementite Curie point displacement (i.e. the difference between the carbide Curie temperature of the cold-worked material and that of the same material in the undeformed condition) and the degree of 'reversed straining.' It is interesting to compare the general form of this relationship with the variations in indentation hardness which occurred during 'reversed straining' of the same material. Each point in Fig. 7b represents the mean of six hardness determinations made on a suitably prepared cross section of the wire. The wire was fully aged at room temperature after drawing, but the hardness determinations were made within 24 hours of the 'reversed straining' operations. The maxi-

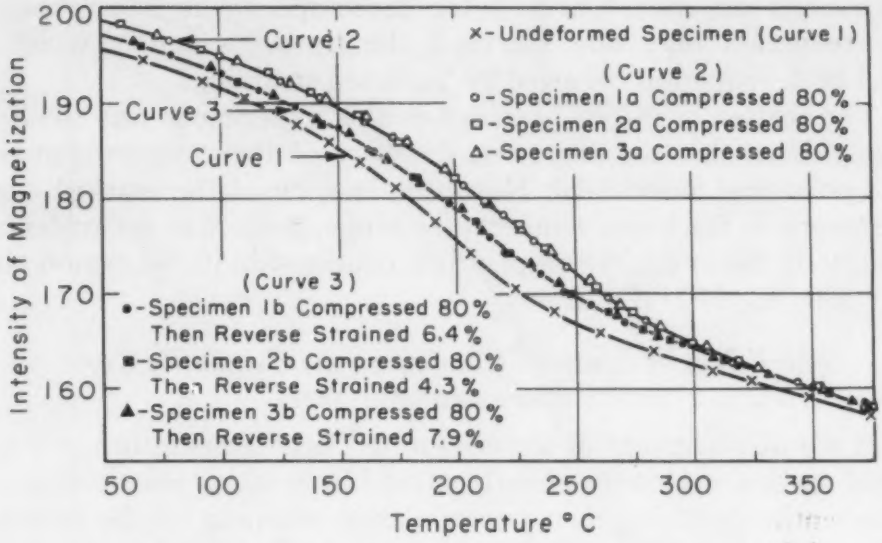


Fig. 8—Influence of "Reversed Straining" on Cementite Curie Point Change. 1.26% carbon steel; fine pearlitic structure. (Reversed strains are represented as a proportion of the original deformation.

mum reduction in hardness occurred with a degree of reversed straining which was small compared with the original deformation. Although the scatter was large, the results concerned with the recovery of the carbide Curie point appeared to follow a similar trend.

Following this observation an improved experimental technique was devised which proved suitable for the testing of higher carbon steels, thus allowing more precise estimates of the position of the carbide Curie point inflexion. This employed disk specimens which were, in effect, first expanded radially, by compression and then reduced radially by pushing through well lubricated, low angle carbide dies. When more than one die was used for 'reversed straining' the disks were turned over between each stage to reduce the effective shear deformation near the edges.

The results of an experiment which employed this method are summarized in Fig. 8. All samples used in this experiment were cut from a single large compression cylinder of the 1.26% carbon steel. This was heated at 810 °C (1490 °F), and then quenched in a salt bath. Transformation occurred at about 600 °C (1110 °F), giving a fine pearlitic microstructure. The specimen was compressed to 80% reduction in height by stages, keeping the deformation as homogeneous as possible, and it was then cut into six equal sectors. From each sector one test specimen was made, all the test specimens being cut at similar distances from the center of the original large compression piece. The six test specimens were selected alternatively, the first being tested without 'reversed straining,' the adjacent one with 'reversed straining,' and so on. Curve 1 in Fig. 8 represents results obtained with the

undeformed material, Curve 2 the three specimens which received 80% reduction only and Curve 3 the three specimens which received 80% reduction followed by 'reversed straining.'

The scatter of results obtained in this experiment was small and it was evident that the degree of recovery of the apparent cementite Curie point was substantial. However, in spite of the marked degree of recovery in the lower temperature range, there was no evidence of recovery of the intensity/temperature relationship in the region above about 300 °C (570 °F).

The Effect of Elastic Straining on the Cementite Curie Temperature of a Steel

If the displacement of the cementite Curie temperature in a cold-worked carbon steel were directly caused by textural elastic strains in the cementite particles, then purely elastic straining of the steel as a whole might be expected to cause small, immediately reversible, changes in this Curie temperature. In the present case it seemed impossible to devise a satisfactory method of applying and removing a known large stress to a small specimen in the thermomagnetic balance, therefore it was necessary to use a solenoid to provide the magnetic field. This had the disadvantage that the maximum attainable field strength was insufficient to saturate the specimen.

The Solenoid Apparatus—The solenoid used in these experiments was similar to that used by Andrew, Lee and Fang in their investigation of the effects of cold work on steel (1). In principle the electrical circuits associated with the solenoid, including the method of calibrating the ballistic galvanometer throw, were also the same as those described by these investigators.

The specimen, of circular cross section, had a central portion 12cms. long with a uniform cross section of about 0.1 square centimeter. On this was placed a search coil of fine nichrome wire, insulated from the specimen by a layer of asbestos paper. On top of the search coil a platinum, platinum-rhodium thermocouple was fixed with the hot junction in line with the center of the search coil. The load was communicated to the specimen through two austenitic steel tubes.

Essentially the experiment was concerned with an estimation of the differences in intensity values in the stressed and the unstressed conditions respectively. An indication of the influence of stress-induced differences in permeabilities was gained by exploring the variation of the observed intensity differences in the range of available field strengths (100 to 1200 oersteds). It was found that these observed intensity differences became less sensitive to the magnitude of the applied field with increasing temperature until, above 200 °C (390 °F), the intensity difference approached closely to a constant value with the field strengths above 1000 oersteds. Hence, although ob-

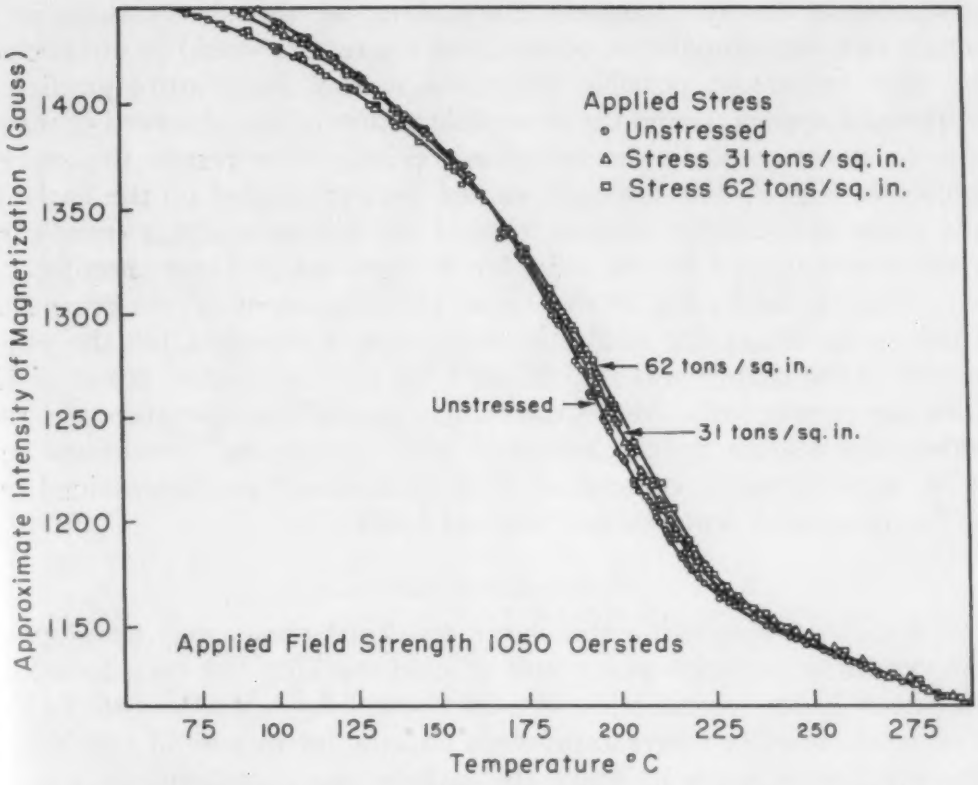


Fig. 9—Influence of Elastic Straining on Magnetic Intensity/Temperature Relationship of 1.26% Carbon Steel.

servations made below about 170 °C (340 °F) were of little value for present purposes, the relative intensity values obtained in the neighborhood of the cementite Curie point were not strongly field-dependent if an applied field in excess of 1000 oersteds were used.

Details of the Experiment—The 1.26% carbon steel specimen used in this investigation was heated to 950 °C (1740 °F) in a protective atmosphere and then quenched in a lead bath at 540 °C (1005 °F) to give a fine pearlitic microstructure. Before the final machining operations the specimen was drawn through a carbide die, giving about 5% reduction of area. Such a specimen would sustain a stress of about 65 tons per square inch up to a temperature of 350 °C (660 °F), without significant creep for periods sufficient to make the magnetic experiments. Before making the principal experiment, the specimen was heated to 350 °C (660 °F) and then prestressed up to 63 tons per square inch.

In the principal experiment the temperature was raised, slowly and continuously, from room temperature to 350 °C (660 °F) in a period of about 10 hours. Using an applied field of 1050 oersteds, readings were taken alternatively, firstly in the unstressed condition, then with a stress of 31 tons per square inch, then a stress of 62 tons per square inch, then again in the unstressed condition and so on, as the

temperature slowly increased. By making all the observations in a single run, the comparative accuracy of the results would be unaffected by such factors as possible variations in the temperature gradients within the apparatus and the reversible nature of the observed changes due to stress could be demonstrated directly. The results are represented in Fig. 9. The intensity values were calculated on the basis of the room temperature cross section of the specimen and a small correction was applied for the influence of stress on this cross section.

The results in Fig. 9 show that a displacement of the cementite Curie temperature due to elastic straining was observed, but the magnitude of the change was only about 6 °C with an applied stress of 62 tons per square inch. Above the cementite Curie temperature the relationships shown in the "stressed" and "unstressed" conditions became approximately coincident. This coincidence was maintained up to the maximum temperature reached (380 °C).

X-ray Examination

Evidence suggesting that large textural strains may develop in the cementite particles as a result of cold working has been found in an earlier X-ray examination of a cold-worked spheroidized steel (*7*). The work described here represents an attempt to extend the X-ray investigation to steels in which the carbide was distributed on a finer scale.

The specimens were worked by compression and were gently ground down to about 2/3rds of their original height using wet emery paper. The prepared surfaces were not etched before examination. The X-ray photographs were taken in a 10 cm. glancing-angle camera using monochromatized Cobalt Kα radiation. Reference lines, provided by a 'calibrating substance' painted on the specimen surface, were used in measuring the films. The 1.26% carbon steel used in the first experiments possessed a fine pearlitic microstructure, produced by heating the steel at 810 °C (1490 °F) and then transforming at about 600 °C (1110 °F).

Examples of microphotometer records obtained from the films are reproduced in Fig. 10. The two calibration lines which may be observed in the films are marked Al 111 and Al 311 respectively. (Aluminum was used because its other diffraction lines are approximately coincident with ferrite lines and, therefore, do not further obscure the carbide diffraction pattern). The three ferrite lines have been marked Fe 110, Fe 200 and Fe 211 respectively. The remainder of the indices refer to carbide lines.

The angle of incidence of the X-ray beam on the specimen surface was in all cases about 40° ; therefore, the reflecting planes corresponding to the carbide lines observed between the Fe 110 and Fe 211 lines were within 12° of being parallel to the prepared surface of the specimen.

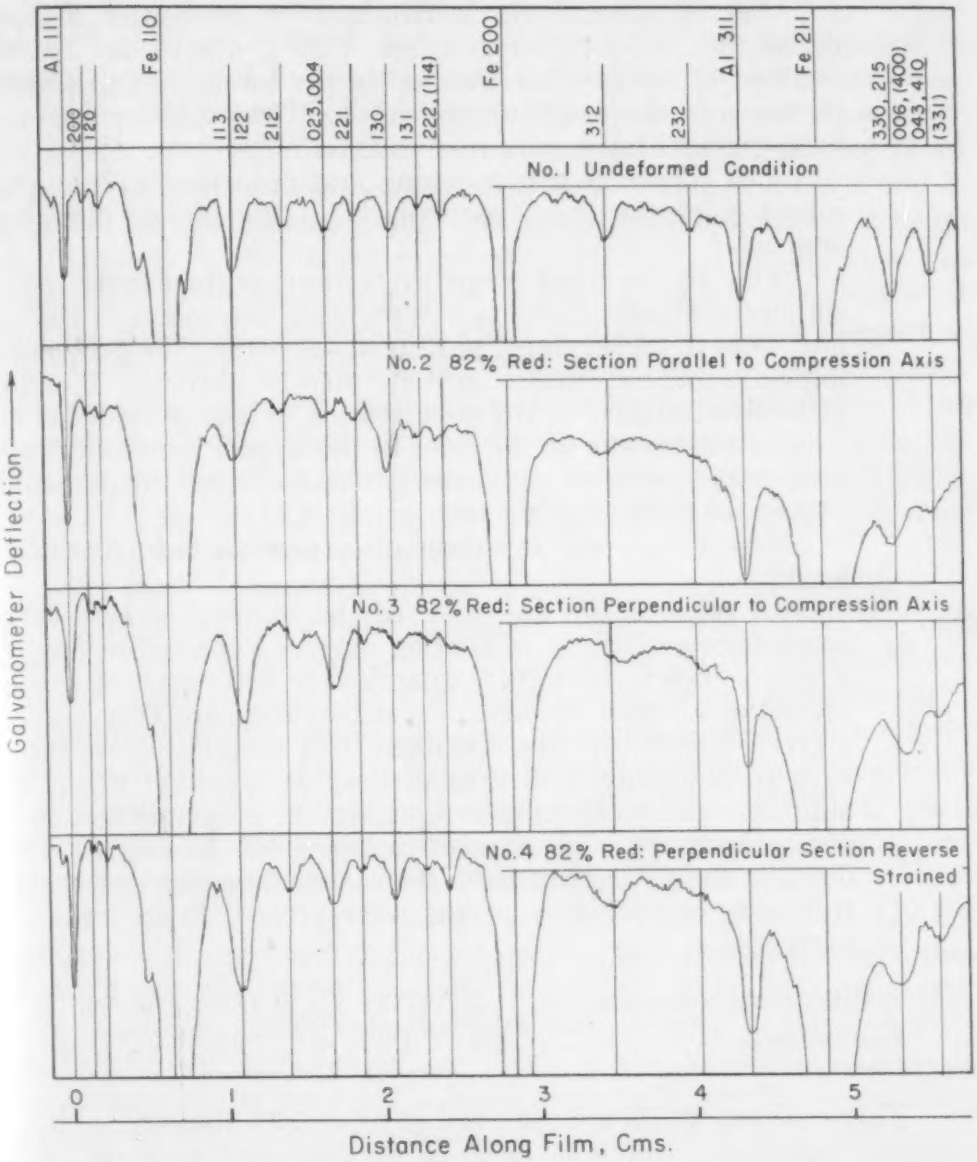


Fig. 10—1.26% Carbon Steel. Fine pearlitic structure. Photometer records.

Record No. 1 represents the diffraction pattern given by the pearlitic steel in the undeformed condition. Record No. 3 shows the influence of severe compression (about 80% reduction) on the diffraction pattern given by a section taken perpendicular to the compression axis of the specimen. Record No. 2 refers to a specimen similar to that giving record No. 3, but in this case the section examined was taken parallel to the compression axis.

The changes in the cementite diffraction pattern, which resulted from cold working, were qualitatively similar to those observed in the case of the spheroidized steel (*7*). They may be summarized as follows:—

(a) A nonuniform distribution of intensities develops round the Debye-Scherrer rings. This is due to the development of a preferred orientation of the cementite; probably a direction in the neighborhood of the [001] direction tends to be aligned with the compression axis.

(b) There is a broadening and reduction in maximum intensity of the lines, particularly at the higher diffraction angles.

(c) In the films given by sections perpendicular to the compression axis, there is a systematic movement of the carbide lines to higher angle positions, suggesting the presence of high compressive strains in the cementite particles. The films of sections parallel to the compression axis give evidence of a smaller movement of the lines in the opposite direction, suggesting the presence of tensile strains in directions perpendicular to the compression axis.

(d) No X-ray evidence of a new carbide phase was found.

In spite of the fine scale of the textural stress system, some degree of stress relaxation may be expected to occur at a free surface. However, quantitative estimates of the observed directional strains suggest that they are very high. In a given direction in the specimen their magnitude appears to vary considerably with crystallographic direction in the carbide. For example, considering a section perpendicular to the compression axis of a pearlitic specimen having 82% reduction, the displacements of the carbide lines suggest that the following compressive strains were present in the cementite particles:—

Crystallographic direction ...	[113] [122]	[212]	[023] [004]	[221]	[130]	[312]
Apparent strain % ..... (contraction)	0.6	1.0	0.5	0.6	0.7	1.0

These values, which are the average of results obtained with four separate exposures, can give only an approximate estimate of the distribution of strain. The individual results for the stronger carbide lines were within 12% of the quoted values but those for the weakest line examined covered a range of about ± 35%. Moreover, results calculated for the composite lines are subject to errors arising from changes in the relative intensities of the two components. The magnitudes of the observed line movements corresponding to tensile strains in directions perpendicular to the compression axis were of the order of one half of those corresponding to compressive strains in the direction of compression.

A small movement of the ferrite 211 line, in the opposite direction to the movement shown by the carbide lines, was detected in the film measurements corresponding to worked specimens. This observation is consistent with the results obtained by Brookes (11) and with sub-

sequent conclusions about the nature of the textural stress system in cold-worked steels. A considerable increase in the background level in the neighborhood of the higher order ferrite lines was also noted.

In Fig. 10, record No. 4 represents the pattern given by a specimen which, with regard to heat treatment and the initial degree of compression, was similar to those used in obtaining records 2 and 3, but in this case the specimen was 'reverse-strained' by pushing through low angle dies in the manner previously described. The specimen was similar to those which gave curve No. 3 in Fig. 8, the degree of 'reversed straining' representing about 7% of the original deformation. The surface examined was perpendicular to the compression axis. This degree of 'reversed straining' was evidently sufficient to restore the cementite line positions approximately to those shown by an undeformed specimen. On the other hand, judging from the high order reflections, the line broadening was not greatly reduced by 'reversed straining' of the worked specimen.

Cold-worked specimens of the same steel were also examined in the sorbitic condition (water-quenched from 950 °C (1740 °F) and tempered at 480 °C). Sections of specimens having 0, 30, 50, 75 and 95% reductions in height were examined on surfaces perpendicular to the compression axis. With this fine microstructure the lines of the cementite diffraction pattern became so weak and diffuse as a result of cold working that, beyond 50% reduction, the only 'line,' other than the lowest order lines, which could be measured on the microphotometer, was that due to the 113, 122 spacings.

Insofar as the observed movements of the composite 113, 122 line can be taken as representing the changes in these crystal spacings, they suggested that the strain reached about 0.9% after 30% reduction, about 1.2% after 50% reduction and very roughly 1.3% after 75% reduction in height, (Compressive strain in the direction of the compression axis of the specimen). Apart from the difficulty of estimating the positions of the peak intensities of the extremely broad lines given by the more heavily worked specimens, further inaccuracy is introduced by the changes in the relative intensities of the two components of the composite line due to the development of preferred orientation. The latter change appears to be such as to lead to an underestimation of the strain present.

The results suggest that the textural strains may have developed rapidly in the early stages of deformation and that, in similar conditions of working, the strains which developed in the fine sorbitic steel were significantly greater than those in the softer pearlitic material. Considering the results as a whole, it appears likely that mean directional strains as high as 1.5% may occur in the carbide particles in a severely deformed steel of fine microstructure.

Up to the present only the average strains, derived from the ob-

served displacements of the Debye-Scherrer lines, have been considered. So far as may be judged from the extent of line broadening, the range of strain also increases as deformation increases. This effect was particularly noticeable in the case of the specimens having a fine sorbitic microstructure.

Interpretation and Discussion of Results

The Displacement of the Cementite Curie Point

The first group of magnetic experiments have shown that, as a result of cold working a plain carbon steel, the carbide Curie point inflexion is apparently displaced and extended and also that there is an increase in the saturation intensity of magnetization. Such changes do not occur in the absence of cementite, and the extent to which they may develop in carbon steels is greatly influenced by the initial microstructure. The results of more detailed examinations have shown that the apparent carbide Curie temperature of a given plain carbon steel increases smoothly and gradually as the degree of cold work increases and also, during reheating after cold working, that this Curie temperature recovers in the same way.

In terms of the suggestion that a new carbide structure may be formed as a result of pastic deformation, these observations could be explained by supposing that cold-worked steels contain a mixture of cementite and new carbide, the proportion of the new carbide increasing with the amount of cold work applied.

In general the intensity/temperature relationships of a material containing different ferromagnetic phases will show separate inflexions corresponding to the different Curie points of the phases present, but, if two Curie points are sufficiently close together, the inflexion corresponding to the lower Curie point may be masked. In the present case, however, the apparent carbide Curie points observed with the heavily deformed conditions indicate that the Curie point of the proposed new carbide would be high enough to allow recognition of two separate inflexions in the intensity/temperature relationships. This can be demonstrated by considering the variations in the gradients of 'synthetic' intensity/temperature relationships, derived by combining results obtained with the annealed and the heavily deformed conditions respectively. In Fig. 11 the gradients of such a 'synthetic' relationship, representing a condition intermediate between the severely deformed and the annealed states, are compared with those of a corresponding intermediate relationship which was observed experimentally. The latter refers to a specimen which was tempered at 384 °C (715 °F) after severe cold working.

Because none of the experimental curves give evidence of a tendency to resolve into two component carbide Curie point inflexions, a simple explanation of the results cannot be made in terms of the oc-

currence of varying proportions of two discrete carbide structures. It is necessary to assume the existence of structural conditions of the carbide intermediate between that of undeformed cementite and the state produced by severe cold working. The observed changes are, in fact, consistent with the suggestion that it is the extent of the change in the cementite, rather than the proportion of cementite affected, which varies with the degree of deformation (or with the degree of recovery).

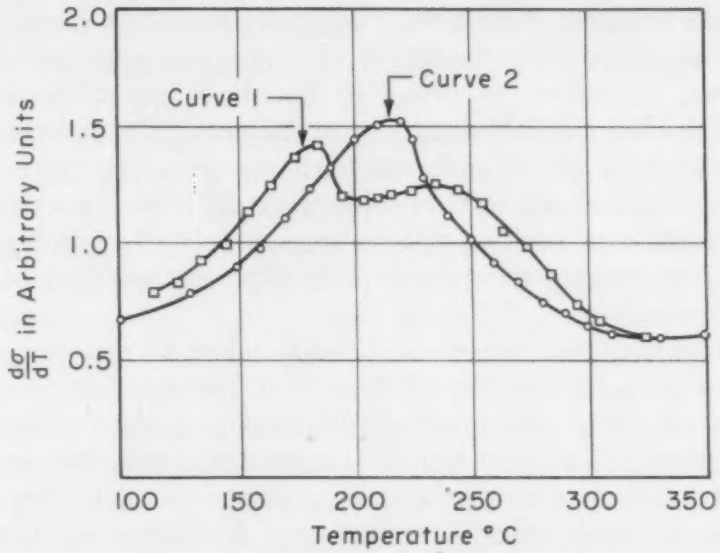


Fig. 11—Gradients of Magnetic Intensity/Temperature Relationships (1.26% Carbon Steel; Sorbitic Structure). Curve 1—Calculated "intermediate" relationship, using results obtained with the heavily deformed (87% reduction) and with the fully softened conditions. Curve 2—Corresponding "intermediate" relationship observed experimentally. Specimen reduced 87% and then tempered at 384 °C.

It is a limitation of the magnetic method that a cold-worked steel must be heated in the range 200 to 300 °C (390 to 570 °F) before the carbide Curie point inflexion may be observed. However, it may be noted that these experiments have given no evidence that the change in the carbide Curie temperature is promoted by reheating the steel. The changes observed during low temperature reheating of a cold-worked steel were in the direction of recovery.

It has been demonstrated that, in a cold-worked steel, a substantial degree of recovery of the displaced cementite Curie point toward its normal value may be effected by applying a second plastic deformation, which is directionally opposite to the first (Fig. 8). This recovery may be achieved by a 'reversed strain' which is small relative to the magnitude of the original strain and X-ray observations have shown that the degree of 'reversed strain' which effects the maximum degree of recovery of the carbide Curie point is probably similar to that required to eliminate the directional component of the residual textural stress system between cementite and ferrite (Fig. 10).

On reheating a cold-worked steel, the temperature range in which

the textural strains are relaxed (judging from X-ray evidence, Ref. 7) is similar to that in which the carbide Curie temperature has been observed to recover towards its normal value (Fig. 6).

It seems probable, therefore, that the changes causing the displacement of the cementite Curie point are in some way associated with the presence of the intense residual stresses set up between cementite and ferrite as a result of cold working. Although Curie temperatures are generally insensitive to the effects of mechanical strains of ordinary magnitudes, ferromagnetic theory suggests that this characteristic is not independent of lattice distortion. The simplest explanation of these observations, therefore, is provided by the suggestion that elastic changes in the interatomic distances in the cementite structure, due to textural stresses, might be sufficient in themselves to cause the observed Curie point displacements. However, with different materials the expected magnitude of such an effect varies widely (12) and, at present, it is difficult to make a theoretical prediction of the effect of stress in the case of cementite.

The final magnetic experiment consisted of an examination of the influence of uniaxial elastic straining on the intensity/temperature relationship of a high carbon steel. Although magnetic saturation was not achieved in this experiment, it is considered that the applied field strength was sufficient to permit useful comparisons in the neighborhood of the cementite Curie temperature. Evidence was found of a small, immediately reversible, displacement of the cementite Curie point, produced by elastic straining of the specimen. The magnitude of the observed displacement (an increase of about 6 °C with an applied stress of 60 tons per square inch) was small compared with those obtained after severe plastic deformation, even when the observations were made at similar field strengths. This suggested that, if textural strains are directly responsible for the displacement of the cementite Curie point in cold-worked steels, these strains must be large compared with those induced by an applied stress of 60 tons per square inch.

X-ray examination of severely deformed high carbon steels has confirmed that the textural strains, which develop in the cementite particles as a result of cold working, can be very large. These strains are orientated with respect to the direction of working; also, in a given direction in the specimen, they vary in magnitude with crystallographic direction in the cementite. There is evidence that the magnitudes of the strains which may be attained by severe cold working increase as the carbide particle size decreases: probably the mean directional strains in small carbide particles may reach values as high as 1.5%.

The extent of line broadening in the cementite diffraction patterns suggests that the textural strains probably became increasingly irregular with increasing deformation, particularly in the case of steels having

a small carbide particle size. So far as the Curie point change is concerned, it is reasonable to suppose that it is not merely the influence of the mean directional strains, but the combined effects of the full range of strains present, which must be considered.

The Changes in Intensity of Magnetization

Although the development of large textural strains in the cementite particles during cold working may underly the observed displacements of the cementite Curie point, the presence of these strains is unlikely to provide a sufficient explanation of the observed changes in the intensity values.

A cold-worked steel of fine microstructure may show a displacement of the cementite Curie point inflexion to temperatures approaching 300 °C (570 °F), but the intensity of magnetization may remain greater than that of the annealed material up to temperatures in the neighborhood of 500 °C (930 °F). The reversible intensity/temperature relationships of a cold-worked steel (Fig. 6) indicate that the material responsible for the additional ferromagnetism in the temperature range 300 to 500 °C (570 to 930 °F) must have a Curie point considerably in excess of 500 °C (930 °F). The existence of an iron carbide having such a high Curie point is unlikely (6) and it is probable that the effect is due to the presence of additional free ferrite.

Further investigation of the factors influencing the intensity values is required but the following conclusions are suggested by present results:

a) The extent of the increase in intensity above 300 °C (570 °F) is not generally consistent with the extent of the carbide Curie point displacement (Fig. 5), and the relative magnitudes of these two effects appear to vary with the state of internal stress in the steel (Fig. 8).

b) Steels of widely different carbon contents but otherwise comparable microstructures, which have been cold-worked to give approximately similar displacements of their apparent cementite Curie points, may show an increase in the intensity value above 300 °C (570 °F) which is clearly not proportionate to the amount of cementite present (Fig. 3).

These observations do not suggest that the displacement of the cementite Curie point and the increase in the intensity values above 300 °C (570 °F) in a cold-worked steel have one direct cause, such as a change in composition of the carbide.

Cottrell (13) has shown that carbon atoms will tend to diffuse to the highly strained regions associated with dislocations in the ferrite lattice. If insufficient carbon is available in solid solution, it is probable that a limited amount of cementite decomposition can occur as a result of this behavior. In the present case, however, the transfer of carbon, from cementite to ferrite, required to provide an explanation of the

magnetic intensity increases is quite large (up to about 0.1% by weight of carbon in the case of a heavily deformed steel of fine microstructure). Possible metallographic evidence of carbide solution in cold-worked steels is now being examined in this connection.

Since an unequivocal interpretation of the magnetic changes cannot yet be made, the immediate value of the investigation is in illustrating some of the important influences which textural stresses may have on the properties of cold-worked steel.

Other Evidence of Textural Stresses in Cold-worked Steels

It is believed that the residual stresses, which develop in the cementite particles of a cold-worked steel, are compensated by opposing stresses in the surrounding ferrite. On the basis of this assumption a rough check of the present estimates of cementite strain may be derived from the work of previous investigators.

Andrew, Lee and Brookes (11) measured the directional strains in the ferrite of cold drawn steel wires. In the case of pearlitic 0.6% carbon steel having 60% reduction, they observed compressive strains in the range 0.1% to 0.2% for the Fe 211 and the Fe 220 spacings in a direction close to that of the wire axis. This steel contained about 9% cementite by volume, therefore, assuming that the measured strains represent the mean directional strain in the ferrite, that these strains are compensated entirely by opposing strains in the cementite and that the elastic modulus of cementite is similar to that of ferrite, the mean strain in the cementite would be in the range 1 to 2% (tensile strain in the direction of drawing).

Andrew, Lee and Chang (14) have computed the total change in length, due to relaxation of the textural strains, on reheating a cold drawn steel wire. With a pearlitic 0.58% carbon steel wire which had been cold drawn 60%, the effective increase in length due to heating to 600 °C (1110 °F) was 0.2%. Again assuming that the directional strains in the ferrite were compensated entirely by strains in the cementite, and also, in this case, that the recovery of the ferrite was entirely elastic, this implies an average directional strain in the cementite of the order of 2%.

The order of magnitude of the strains in the cementite derived in these two different ways is in reasonable agreement with the direct X-ray measurements made in this research. The second estimation, which is based on the bulk properties of the material, may appear to be evidence that the direct X-ray measurements have underestimated the strains present in the interior of the steel. Probably, however, the assumption that the directional strains in the ferrite are compensated entirely by opposing strains in the cementite is incorrect.

Stress concentration occurs at the cementite particles during working because they restrict plastic flow locally. The mechanism of the

development of the textural stress pattern may be considered in terms of the dislocation model of plastic flow in a duplex alloy which was suggested by Orowan (15). In this model, as deformation proceeds, dislocation loops are considered to form round the hard particles of the second phase. The elastic strains which develop in the matrix at interfaces with the hard particles will be of about the same magnitude as those in the particles themselves but, in general, the elastic strains will decrease rapidly with distance from the particles. On removal of the external load which has caused deformation, these inhomogeneous elastic strains set up during plastic flow will give rise to a residual stress system. The stresses affecting the bulk of the matrix will then be reversed and the relatively large stresses associated with the particles will be reduced in magnitude, giving an internally-balanced system of stresses. However, in small regions of the matrix close to the particles, the stresses will remain similar to those in the particles themselves. In this picture, therefore, the stresses in the matrix are partly self-compensated and a calculation based on the simple assumptions made previously (14) may to some extent overestimate the stresses affecting the particles.

In the case of a piece of cold-worked steel, on reheating, yielding may first occur in the highly stressed ferrite adjacent to the cementite particles. If this occurs, not only the cementite, but also the bulk of the ferrite, which is stressed in the opposite sense, may recover elastically; this would explain the macroscopic changes in shape which are observed to accompany stress relief.

It is considered that evidence of the influence which textural stresses may have on mechanical properties is provided by certain 'work-softening' effects. Polakowski (16) has pointed out that when a cold-worked metal is subjected to reversed deformation there is at first a reduction in internal strain energy and a decrease in indentation hardness. Wilson (17) has drawn attention to the important influence of microstructure on the extent of this effect. With single phase materials the degree of softening is small but with a medium or high carbon steel it may be considerable, (e.g., Fig. 7b of this paper). Probably these relatively large 'work softening' effects are associated with a reversal of interphase stresses which are large compared with the reversible residual stresses which can develop in single phase materials.

Acknowledgment

The author's thanks are due to Professor J. H. Andrew for helpful advice and discussions.

References

1. J. H. Andrew, H. Lee, B. Fang, "The Effect of Cold-Work on Steel. Section 1," *Journal,* Iron and Steel Institute, Vol. 165, 1950, p. 158.

2. D. P. Antia, S. G. Fletcher, M. Cohen, "Structural Changes During the Tempering of High-Carbon Steels," TRANSACTIONS, American Society for Metals, Vol. 32, 1944, p. 290.
3. R. D. Heidenreich, L. Sturkey, H. L. Woods, "Investigation of Secondary Phases in Alloys by Electron Diffraction and the Electron Microscope," *Journal of Applied Physics,* Vol. 17, 1946, p. 127.
4. K. H. Jack, "X-ray Structural Investigation of the Iron-Carbon and Iron-Nitrogen Systems and of Related Interstitial Alloys," *Acta Crystallographica,* Vol. 3, 1950, p. 392.
5. L. J. E. Hofer and E. M. Cohn, "Some Reactions in the Iron-Carbon System: Application to the Tempering of Martensite," *Nature,* Vol. 167, 1951, p. 977.
6. J. Crangle, W. Sucksmith, "Magnetic Analysis of Iron-Carbon Alloys," *Journal,* Iron and Steel Institute, Vol. 168, 1951, p. 141.
7. J. H. Andrew, H. Lee, D. V. Wilson, "The Effect of Cold-Work on Steel. Section 5," *Journal,* Iron and Steel Institute, Vol. 165, 1950, p. 376.
8. W. Sucksmith, "The Measurement of Magnetic Saturation Intensites at Different Temperatures," *Proceedings,* Royal Society, London, Series A. Vol. 170, 1939, p. 551.
9 and 10. A. T. Pickles, W. Sucksmith and K. Hoselitz, W. Sucksmith, "A Magnetic Study of Two-Phase Iron-Nickel Alloys," *Proceedings,* Royal Society, London, Series A. Vol. 175, 1940, p. 331 and Vol. 181, 1943, p. 303.
11. J. H. Andrew, H. Lee, P. E. Brookes, "The Effect of Cold-Work on Steel. Section 3," *Journal,* Iron and Steel Institute, Vol. 165, 1950, p. 370.
12. R. M. Bozorth, *Ferromagnetism,* Van Nostrand Co., 1951, p. 723.
13. A. H. Cottrell, "Effect of Solute Atoms on the Behavior of Dislocations," Report of Conference on Strength of Solids, Physical Society, London, 1948, p. 30.
14. J. H. Andrew, H. Lee, P. L. Chang, "The Effect of Cold-Work on Steel, Section 1," *Journal,* Iron and Steel Institute. Vol. 165, 1950, p. 150.
15. E. Orowan, Discussion, *Symposium on Internal Stresses in Metals and Alloys,* Institute of Metals. London, 1948, p. 451.
16. N. H. Polakowski, "Softening of Metals During Cold-Working," *Journal,* Iron and Steel Institute, Vol. 169, 1951, p. 337.
17. D. V. Wilson, Discussion of (16), *Journal,* Iron and Steel Institute, Vol. 172, 1952, p. 29.

DISCUSSION

Written Discussion: By H. P. Tardif, physical metallurgist, Canadian Armament Research and Development Establishment, Quebec, Canada.

The author is to be congratulated for this excellent piece of work. The experimental results obtained and the large number of theories presented to explain them are most interesting, but indicate the need for further investigation of this extremely complex subject.

Concerning the method of determination of the Curie temperature, it appears from the paper that the latter is taken as the temperature at the point of inflection on the intensity of magnetization-temperature curve. This method of determining Curie temperature, although rapid, may, however, not be very reliable for the following reason. It is possible that the shape of the intensity-temperature curves if determined independently for both cementite and ferrite would change under the effect of elastic and plastic stresses without any change

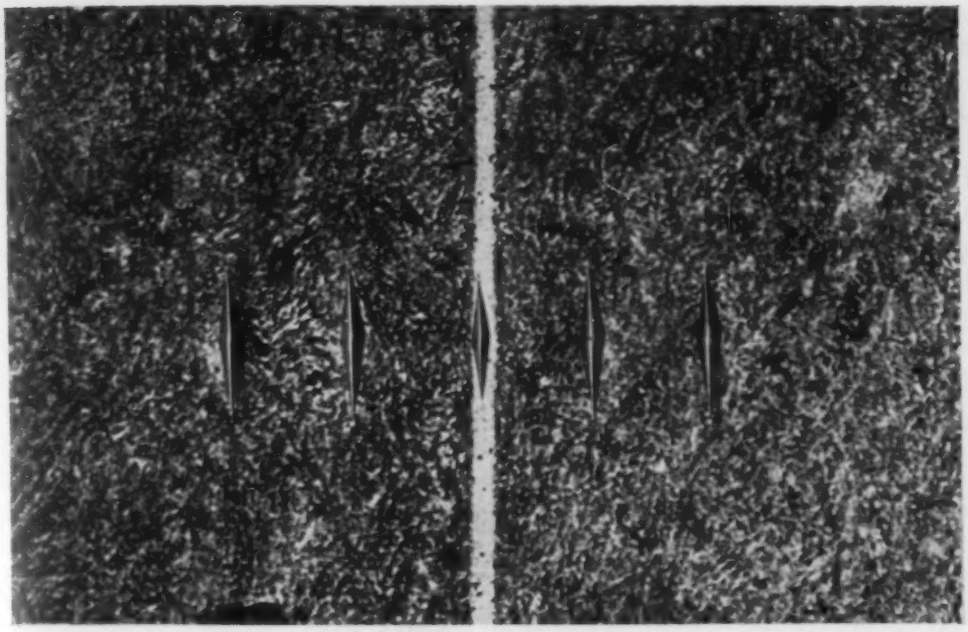


Fig. 12—White Layer of Martensite and Austenite Produced During High Speed Deformation. Nital etch. X 630.

in their respective Curie temperatures. The fact that the cementite and ferrite curves merge at high temperature cannot be taken as a proof that the ferrite contribution to the magnetization is independent of cold work at low temperature. The ferrite curve might be affected by the phenomenon of stress-relief and recovery below —210 °C and possibly by the beginning of recrystallization. Consequently the sum of these two curves cannot in my estimation give any accurate information on the cementite. In other words, I am wondering if the increase in intensity between 0 and 200 °C and up to 500 °C in certain cases would not be due to intensity changes taking place in the ferrite only. In this respect the intensity/temperature curves could be determined for carbon-free iron deformed by different amounts and the increase in intensities in the same temperature ranges compare with those obtained, for example, in a 0.7% carbon steel deformed by the same amounts.

On the subject of diffusion the problem of strain aging arises. The results shown in Figs. 5 and 7 were obtained after full aging at room temperature. It is possible that the hardness changes shown in Fig. 7b would have been different if the tests had been carried out after straining without the aging treatment at room temperature. It is appreciated that strain aging will take place eventually as the temperature is raised but it would be important to know if, at low temperatures, the intensity of magnetization is affected by strain aging. For example a plot of intensity of magnetization versus amount of cold work with the intensity measured at room temperature before and after aging could be most informative. If the intensity of magnetization is affected by strain aging then in accordance with the dislocation theory of strain aging one could get an idea of the effect of the state of the carbon atoms in steel (i.e. in solution or segregated at dislocations) on the intensity of magnetization. If there are any changes in intensity of magnetization with time during strain aging, these could be measured at different low temperatures (e.g. 0–60 °C) and the activation energy of the process compared with that for carbon diffusion in alpha-iron. There is no doubt that

drastic changes may take place in the carbides during straining. In fact it has been shown before that when adiabatic conditions are obtained, for example with very high speed deformation, austenite is produced by the solution of carbides along certain shear planes,[2] with subsequent transformation to martensite during rapid cooling. This has been observed in our laboratories in a piece of armour plate perforated by the Munroe Effect.[3] A photomicrograph is shown in Fig. 12. At lower rates of deformation no such drastic changes take place in the carbide but Dr. Wilson's future attempt to find metallographic evidence of carbide solution in cold-worked steels will certainly prove worthwhile and I think he has already obtained some results along these lines.

There is one other point, that of the effect of iron nitrides that may be present in the steel on the intensity curves. Because of the very small amount of nitrides in steel, it is expected that their effect would be minor. However, Fe_4N has a Curie temperature of 488 °C and other forms of the nitride possibility produced during the cold working may also have fairly high Curie points, and might possibly have a greater effect on the intensity of magnetization. Could this be one explanation for the fact that the intensity in cold-worked steels remains greater than that of annealed material from about 300 to 500 °C?

Authors' Reply

I wish to thank Dr. Tardif for his interest in this paper. Although there can be no doubt of the value of the thermomagnetic method I agree that further investigation and care in interpretation of results is required at present.

Saturation intensity/temperature relationships observed on heating give information about transformations which are accompanied by a change in the intensity of magnetization but, as Dr. Tardif points out, it is possible that the occurrence of such a transformation could invalidate estimations of the Curie point temperatures. However, it must be remembered that, under conditions of equilibrium or quasi-equilibrium, estimations of the Curie points are not subject to limitations of this type.[4] In the present investigation, for example, the reversible intensity/temperature relationships represented in Fig. 6 provide unequivocal evidence of the displacement of the carbide Curie point.

Turning to a consideration of the changes which may affect the contribution of the ferrite to the observed intensities of magnetization, the following observations are relevant to Dr. Tardif's specific questions:—

1. Carbon-free iron showed no detectable change in its intensity/temperature relationship as a result of severe cold working.

2. A cold-worked 15% chromium, 1% carbon steel, in which the textural stress pattern in the ferrite would be qualitatively similar to that in a cold-worked plain carbon steel, showed a relatively very small change in its intensity/temperature relationship.

These results lend support to the idea that the principal changes in the intensity/temperature relationship of a cold-worked carbon steel are due to changes in the cementite itself and/or to interactions between cementite and ferrite.

No experiments on strain aging at room temperature were made, but it is not expected that magnetic saturation intensity will be sensitive to the segrega-

[2] J. H. Andrew, H. Lee, et al, "The Effect of Cold Work on Steel," Journal, Iron and Steel Institute, Vol. 165, 1950, p. 374.

[3] C. E. Munroe, "Modern Explosives," Scribners Magazine, Vol. 3, 1888, p. 563.

[4] J. Crangle, W. Sucksmith, "Magnetic Analysis of Iron-Carbon Alloys," *Journal*, Iron and Steel Institute, Vol. 168, 1951, p. 141.

tion of solid-solution carbon to lattice defects. On the other hand, transfer of carbon atoms from cementite to lattice defects in the ferrite is expected to give rise to an increase in the intensity of magnetization. Perhaps it is in this direction that saturation intensity measurements are most likely to make a contribution to present knowledge of strain aging.

Considering now the suggestion that a nitride might be responsible for the increase in intensity values observed in the temperature range 300 to 500 °C with a cold-worked steel; it may be noted that the magnitude of this increase is almost certainly sufficient in itself to rule out an explanation in terms of the formation of Fe_4N. The possibilities are considerably narrowed by a more detailed analysis of results; the salient points are:—

(a) The reaction occurring on heating a cold-worked carbon steel in the temperature range 300 to 500 °C causes a reduction in intensity values. (Therefore, in this temperature range, the reaction product has lower intensity values than the material from which it is formed.)

(b) Within the prescribed limits of sensitivity, the only ferromagnetic materials present after heating a cold-worked steel to a temperature in excess of about 500 °C are ferrite and cementite.

(c) The reversible intensity/temperature relationships (Fig. 6) show that the material responsible for the additional ferromagnetism in the temperature range 300 to 500 °C has a Curie temperature considerably in excess of 500 °C. (Therefore, this material is unlikely to be a carbide or nitride or carbo-nitride which is ferromagnetic above 300 °C and which transforms to cementite on heating.)

A more detailed analysis of very similar features observed in the intensity/temperature relationships of tempered-martensitic steels has been made by Crangle and Sucksmith.[4] These investigators concluded that, in the case of heat treated steels, the additional ferromagnetism observed in the temperature range 300 to 500 °C was very probably due to the presence of additional free ferrite. To this extent the analysis and the conclusion are the same in the present case of cold-worked steels.

Dr. Tardif has given an interesting example of carbide solution due to the formation of austenite, and thence martensite, during the plastic deformation of steel at a very high strain rate. In the present investigation, only if sufficient martensite were formed to involve a large proportion of the cementite present could this transformation give rise to the type of change observed in the neighborhood of the cementite Curie temperature. In this event the decomposition of the untempered martensite at about 100 °C should be detected magnetically. Moreover, the possibility of the formation of any appreciable proportion of high carbon martensite during plastic deformation, at ordinary rates of straining and with effective surface lubrication, is ruled out by the results of earlier investigators. (For example, the electrical resistivity results of Andrew, Lee, Chang and Guenot.[5])

Although the decomposition of even a small proportion of austenite, on heating a carbon steel at about 200 °C, would affect the intensity/temperature relationship appreciably in the neighborhood of the cementite Curie point, the reversible relationships illustrated in Fig. 6 sufficiently demonstrate that austenite

---

[5] J. H. Andrew, H. Lee, P. L. Chang, R. Guenot, "The Effect of Cold-Work on Steel. Section 2," *Journal*, Iron and Steel Institute, Vol. 165, 1950, p. 166.

formation has also made no significant contribution to the changes discussed in the present paper. However, because magnetic analysis is sensitive in detecting the austenite:ferrite transformation, it may be useful to outline conclusions on this point more precisely.

Using the 15% chromium, 1% carbon steel, whereby complications due to a ferromagnetic carbide were avoided, it was estimated that quantities of austenite in excess of about 0.2% could be detected magnetically. With specimens of fine microstructure, slowly compressed, generally in the range 60 to 70% reduction, it was found:—

1. A small quantity of austenite (probably less than 1%) was detected with reasonable certainty in specimens which cracked very severely during compression.

2. No certain indication of austenite was found in similar specimens slowly deformed without fracture. Experiments made with very thin specimens suggested that a trace of austenite may be formed at surfaces subject to high friction even during slow compression, but with specimens of ordinary dimensions (0.2 inch diameter by 0.1 inch thick) the austenite present was insufficient to give a detectable change in intensity values.

As Dr. Tardif points out, strain aging has a marked influence on the characteristics of observed "work softening" effects, but in itself strain aging does not provide an explanation of the strongly directional behavior of a cold-worked steel in this respect. It is this latter characteristic which may provide a clue to the nature and influence of the fine-scale internal stresses.

ISOTHERMAL TRANSFORMATION OF AUSTENITE UNDER EXTERNALLY APPLIED TENSILE STRESS

By Subrata Bhattacharyya and George L. Kehl

Abstract

The effect of externally applied tensile stress and consequent plastic deformation on the isothermal transformation of austenite to bainite in AISI 1085, 4340, and 1045 steels at 535 and 700 °F (280 and 370 °C), 650 and 845 °F (345 and 450 °C), and 700 °F (370 °C), respectively, has been investigated. The applied stress was varied, in general, between no stress and a stress of 60,000 psi, and, in a few cases, stress up to 100,000 psi was applied.

It has been observed that applied stress has a marked effect on both the beginning and the ending times of transformation; they are shortened by factors ranging from 2 to 100,000, depending on the steel and temperature of transformation. For certain times of isothermal transformation, the amount of austenite transformed increases greatly at a certain stress range, and this stress is observed to be well correlated with the yield stress of unstable austenite. It is also possible to correlate, in a similar manner, the increase in the amount of austenite transformed with plastic strain and applied strain energy.

It has been observed further that the effect of stress on the transformation of austenite persists even when the applied stress has been removed. The applied stress is most effective in accelerating transformation when it is applied to austenite after an elapsed time equivalent to the beginning time of transformation under no stress.

Applied stress exceeding the yield stress of austenite is observed to produce a marked orientation effect on the resulting bainite needles. Under high stress, twinning is observed to occur in the austenite.

WHEN austenite is isothermally transformed at a temperature level between the pearlite knee of the C-curve and the M_s temperature, it transforms to an aggregate of acicular ferrite and carbide particles, known as bainite. Since the experiments of Daven-

This paper is based upon part of the dissertation submitted by Subrata Bhattacharyya in partial fulfillment of the requirements for the D. Eng. Sc. degree, Columbia University, New York, N. Y.

A paper presented before the Thirty-sixth Annual Convention of the Society, held in Chicago, November 1 to 5, 1954. The authors, Subrata Bhattacharyya and George L. Kehl are associated with the Division of Metallurgy, School of Mines, Columbia University, New York. Manuscript received April 12, 1954.

port and Bain (1),[1] extensive work has been carried out to determine the structure and mechanism of its formation. The structure of bainite has been accurately determined and the difference between the structures of the high temperature and the low temperature types has been clearly established. On the other hand, the exact mechanism of bainite formation still remains controversial.

Several authors (1–8) suggest that bainite is formed from austenite by a martensite-type mechanism through an intermediate stage of martensite, or in general, supersaturated ferrite. Thermodynamic calculations have been made in support of this suggestion, indicating strong possibilities of this type of transformation mechanism.

On the other hand, investigations by others (9–12) indicated that the austenite-bainite transformation is a nucleation and growth process. Gradual thickening and lengthening of bainite needles with time were shown to occur and thus lend support to this type of transformation mechanism.

As early as 1924, Thompson and Millington (13) expressed the view that the formation of martensite is the result of mechanical stress sufficient to exceed the elastic limit of the parent austenite. They proposed that under the stress to which the crystals of austenite are subjected during quenching, the easy glide movement shear on the {111} plane of the austenite is initiated. Normally, this produces twinned material in a close-packed cubic metal. In the present case, however, austenite being an unstable cubic phase at the temperature of transformation, the easy glide movement causes the atoms to reorient themselves into a stable crystallographic form to become alpha iron, with the carbon in supersaturated solid solution. The presence of a stress factor was also suggested by Bain (14) in commenting on work by Mathews (15) who observed that in a considerable variety of steels, oil hardening retained more austenite than water hardening. Bain suggested that water hardening induces a large stress factor, and these stresses are responsible for the larger amount of transformation in water-hardened steel.

Several investigators have studied the effect of stress on the transformation of austenite (16–35).

Cottrell (24) conducted a series of experiments on unstable austenite and concluded that plastic strain causes a breakdown to ferritic structures. He also observed that at temperatures where austenite transforms readily, complete transformation may be induced by straining, but at temperatures where the reaction is sluggish, partial transformation may be obtained. In conclusion, he remarked that the generation of transformed material is linearly proportional to the plastic strain at 645 °F (340 °C).

Guarnieri and Kanter (26) conducted a series of experiments us-

[1] The figures appearing in parentheses pertain to the references appended to this paper.

ing standard 0.505 inch tensile test specimens of 5% Cr + ½% Mo steel mounted in a modified creep testing machine. Their data indicated that stresses capable of plastically deforming the austenite at the transformation temperature of 800 to 1200 °F (425 to 650 °C) definitely accelerated both the nucleation and the growth processes of the reaction. This effect was observed at temperatures below the knee of the C-curve. At temperatures above the knee, they noticed little effect of stress in accelerating transformation. They observed that in the latter case the temperatures were sufficiently high so as to render the more rapid diffusion rates relatively insensitive to the strain factor.

Using 0.16 inch diameter eutectoid carbon steel specimens, under both tensile and compressive stresses, Jepson and Thompson (30) observed that the imposition of stress during transformation increases the rate of austenite decomposition. They also observed that transformation under stress to low temperature bainite is marked by certain distributional effects, transformation taking place preferably within slip or twin bands present in the parent austenite. To explain these observations, they suggested that the formation of low temperature bainite was due to combined action of shear and nucleation. The transformation was initiated by shear and continued by nucleation. The importance of the two effects varied with temperature, nucleation being of greater importance at higher temperatures and shear of greater importance at lower temperature. As regards transformation in the pearlite range and high temperature bainite, they suggested that deformation produced nuclei of alpha iron in greater abundance than under no deformation.

It is of interest to note that Savage (27), investigating the geometrical aspects of the mechanism of gamma to alpha transformation in iron, concluded that if the {110} planes of a face-centered cubic lattice of iron were sheared at 19° 28′, a structure that was nearly body-centered cubic would be obtained. Through this shearing process the original {110} planes of gamma iron were transformed into {211} planes of alpha iron. This mechanism, he observed, involved no distortion of {110} planes of the face-centered lattice, but consisted of a pure translation in the direction of the closest atomic packing. Such movements of rows of atoms are very characteristic of slip processes during plastic deformation. He also demonstrated that during the shearing of parallel sets of these {110} planes, all intermediate stages between the shear angles of 0° and 19° 28′ had a structure that was nearly body-centered tetragonal.

No systematic investigations have been carried out to determine the effect of varying amounts of plastic deformation on the rate of transformation of austenite and the distribution and orientation of the resulting phases. So far, no conclusive experiments have been carried out to establish a quantitative relationship between applied stress producing acceleration in austenite transformation and some mechanical

property of the unstable austenite at the transformation temperature level. In the work to be described experiments were conducted in the bainite transformation range with three commercial steels. The experimental results indicate the effect of applied stress to be similar for the three steels and thus data for only one of the steels (0.89%C), isothermally transformed at 535 °F (280 °C) is presented in detail in the paper. Wherever it was believed desireable, however, data of the other steels were included for comparative purposes.

Experimental Procedure

The chemical composition of the three steels is given in Table I.

The steels were obtained in the form of round bars, 1-⅛ inch in diameter, and initially heat treated to form a spheroidite structure.

Table I
Check Analysis of Steels Investigated

Steel AISI	Percent C	Mn	P	S	Si	Ni	Cr	Mo
1085	0.89	0.29	0.013	0.013	0.19	—	0.08	—
4340	0.42	0.78	0.018	0.027	0.24	1.79	0.80	0.33
1045	0.44	0.86	0.027	0.035	0.20	0.02	0.04	—

They were then machined to ⅜ inch diameter, subsequently wire drawn, and centerless ground to a finished diameter of 0.05 ± .0002 inch. The specimen wire was then cut into 5-½ inch lengths. To provide a means for attaching the specimen to the grips of the apparatus, spherically shaped beads were formed on each end of the specimen by melting the ends within a graphite mold. The specimens were copper plated to prevent decarburization during subsequent austenitizing, and finally normalized in an argon atmosphere to ensure a uniform initial structure.

A line diagram of the apparatus is shown in Fig. 1. It consists of an automatically operated transport system that moves the wire specimen from a vertically mounted austenitizing furnace to an isothermal transformation salt bath, and thence to an air quenching fixture to interrupt the transformation; an air-operated piston to release the lever arm and dead weights at an appropriate time; and a timing system that could be preset to allow the specimen to remain for a given time in the austenitizing furnace, the transformation bath, and the air-quenching manifold, and to apply the stress to the specimen at any time during the cycle of specimen movement.

A split-type vertical electric tube furnace was used to austenitize the specimens. A constant flow of argon was maintained within the furnace as an added precaution in avoiding decarburization of the specimen. The control of the furnace temperature was within ±5 °F (3 °C) of the desired austenitizing temperature.

The isothermal salt bath was continuously agitated by means of

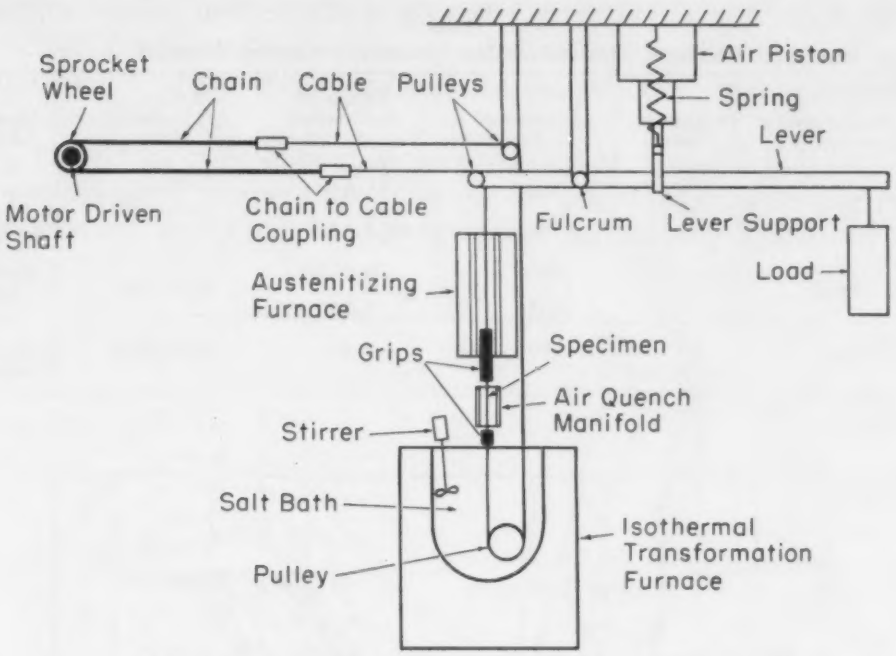


Fig. 1—Schematic Diagram of the Transformation Apparatus.

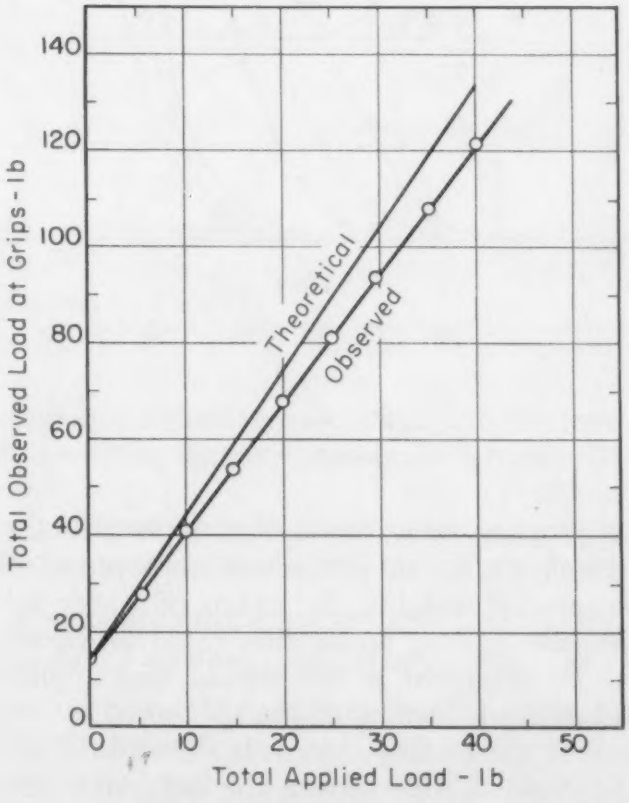


Fig. 2—Calibration Curve of the Dead Weight Loading System.

Table II
Range of Transformation Times and Applied Stresses

Steel AISI	Austenitizing Temperature, °F	Treatment Time, min	Isothermal Transformation Temperature, °F	Range of Isothermal Transformation Time, sec	Range of Applied Stress, psi	Austenitic Grain Size, A.S.T.M.
1085	1620	7	535	15–1800	0–60,000	Large number of 5, some 6, few 4
			700	5–150		
4340	1550	7	650	10–1200	0–60,000	Predominantly 10, some 9
			845	5–100,000		
1045	1560	7	700	0.5–80	0–60,000	Predominantly 8, some 7

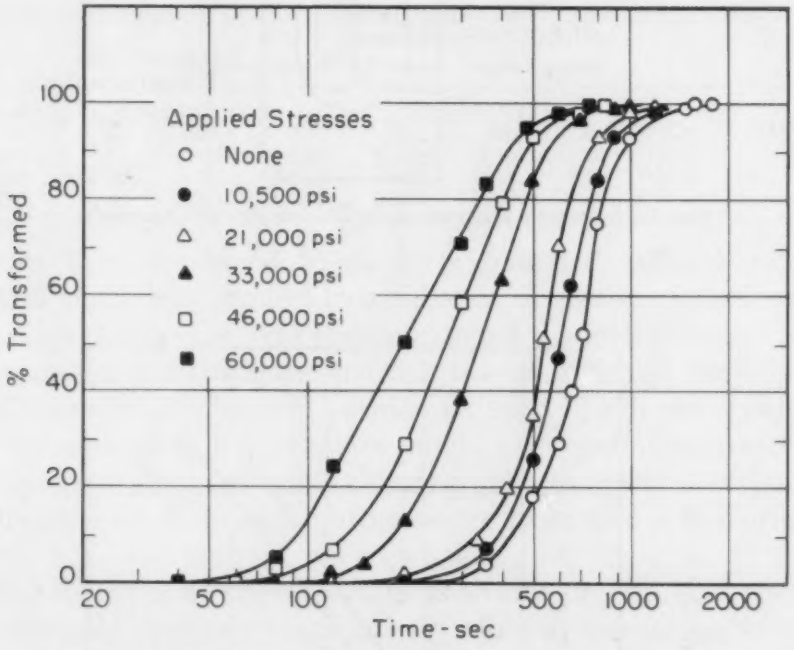


Fig. 3—AISI 1085 Steel Isothermally Transformed at 535 °F.

an electric stirrer. The variation in salt bath temperature was within ±1 °F (0.5 °C) in the temperature range of investigation, 535 to 845 °F (280 to 450 °C).

At an appropriate time, stress was applied to the specimen by means of dead weights. An air-piston was employed to release the lever arm and its suspended weights. By means of a leak valve in the air-piston line, the rate of load application could be varied, and for the experiments to be described, a low rate of load application was employed to avoid dynamic loading of the specimen.

Calibration of the loading system is shown in Fig. 2. A theoretically calculated curve is also shown, the difference between the two curves at any applied load being attributable to reproducible friction

and other losses in the cable-transport system.The origin of the curves at 14.5 lb. (ordinate) corresponds to the load applied at the grips owing to the weight of the lever arm and the weight counterpoise located at the end of the lever.

The actual cycle of operations consisted of austenitizing the specimen at a desired temperature for a pre-set length of time, isothermally transforming at the salt-bath temperature for varying lengths of time

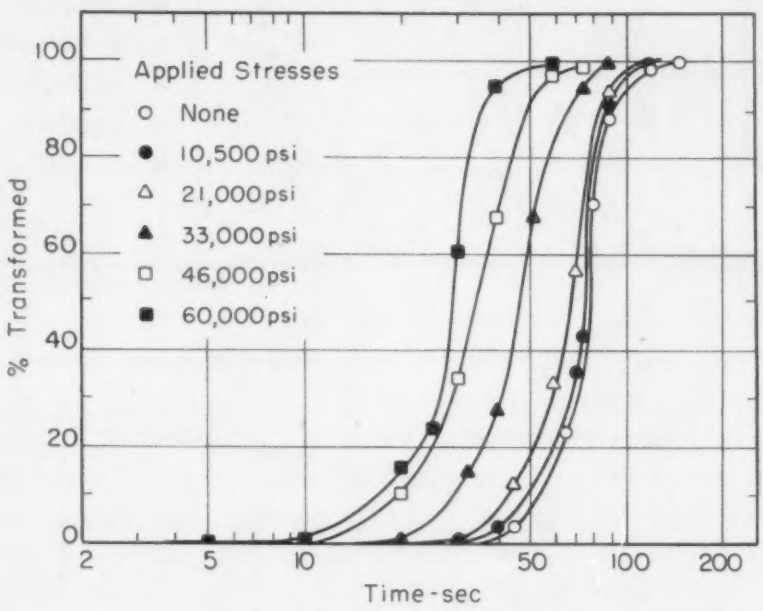


Fig. 4—AISI 1085 Steel Isothermally Transformed at 700 °F.

under different applied stresses, and finally quenching the untransformed austenite to martensite in an air blast. The range of these variable factors is given in Table II.

The transport of the specimen from the austenitizing furnace to the salt bath, and from the salt bath to the air-quench manifold, took about 1 second and ½ second, respectively. Two seconds were allowed in the salt bath for the specimen to attain the temperature of the transformation bath.

Percentage of transformation was determined metallographically using both chart-comparison and lineal analysis methods.

Experimental Results and Discussion

Effect of Stress on the Beginning and Ending Times of Transformation

The amount of bainite formed isothermally under different average stress conditions (ranging from 0 to 60,000 psi) is plotted vs. log-time, and is shown in Figs. 3 and 4, 5 and 6, and 7 for 1085, 4340, and 1045 steels, respectively. It is evident from these data that under increasing

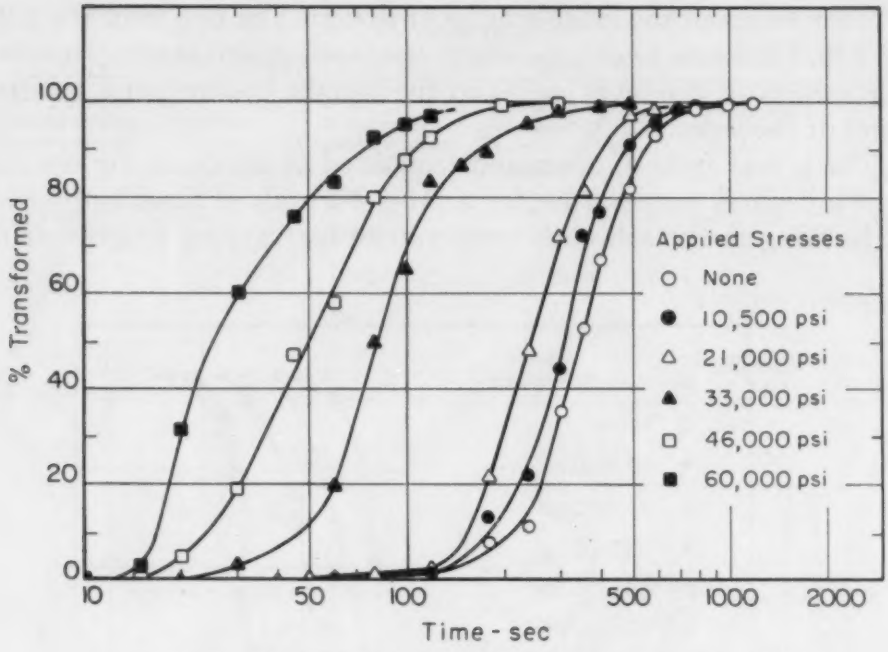


Fig. 5—AISI 4340 Steel Isothermally Transformed at 650 °F.

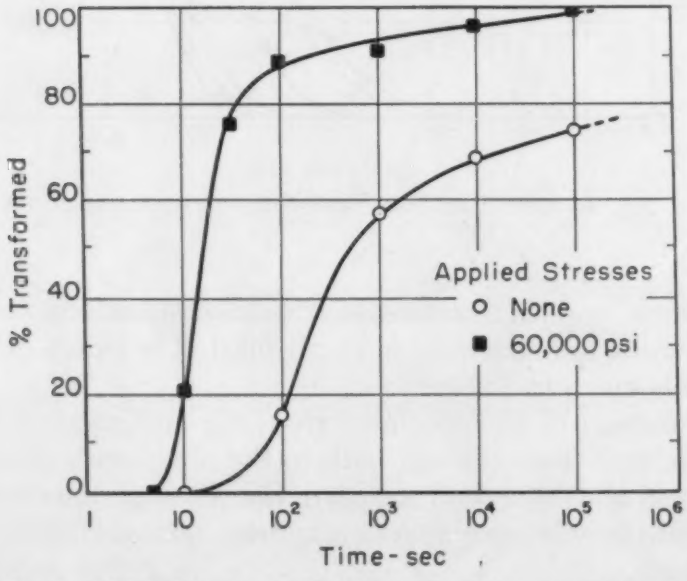


Fig. 6—AISI 4340 Steel Isothermally Transformed at 845 °F.

amounts of stress the beginning and ending times[2] of transformation are shortened and the rates of transformation are increased as evident by the slopes of the curves. It is to be noted that the effect of applied stress in shortening the beginning and ending times of transformation is not so pronounced in the applied stress range of 0 to 21,000 psi as

[2] The criteria of the beginning and ending of transformation are 1% and 99% bainite formation, respectively.

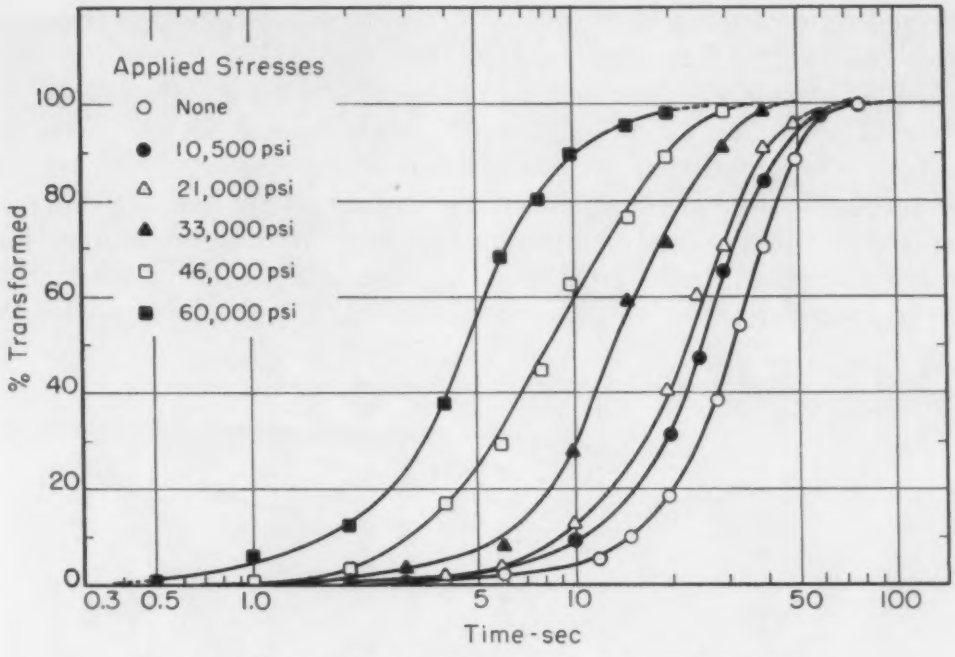


Fig. 7—AISI 1045 Steel Isothermally Transformed at 700 °F.

compared to that in the range of 33,000 psi to 60,000 psi. It may be further observed in Table III that the beginning time of transformation is shortened by a stress of 60,000 psi to a greater extent than is the ending time, with one exception. In the case of 4340 steel transformed at 845 °F (450 °C), the data indicate that a stress of 60,000 psi shortens the ending time of transformation by a factor of 10,000 to 100,000.

Relation Between Applied Stress and Percent Transformation; Determination of a Critical Stress Range

From Figs. 3,4,5 and 7, there can be obtained a relationship between the applied stress and percentage of bainite formed for any

Table III
Effect of a Stress of 60,000 psi on the Beginning and Ending Time of Bainite Formation

Steel AISI	Isothermal Transformation Temperature, °F	Ratio of Time to Form 1% Bainite Without Stress to Time to Form 1% Bainite With 60,000 psi Stress	Ratio of Time to Form 99% Bainite Without Stress to Time to Form 99% Bainite With 60,000 psi Stress
1085	535	6	2.5
	700	4	2.5
4340	650	7	5
	845	4	10,000–100,000*
1045	700	8	3

* Owing to uncertainties in extrapolation of the no stress curve (Fig. 6) to the time for completion of transformation, these data are shown as a range of time factors.

selected time of transformation at the given transformation temperature. The derived data thus obtained from Fig. 3 is plotted in Fig. 8.

All of the stress data shown in plotted form are in terms of "true" stress. These data, as well as "true" strain measurements to be described, were calculated on the basis of final cross sectional area of the specimen, and in consequence, the values so derived are not true stresses by conventional definition. The final cross sectional area was used, rather than the original area, because after an initial elongation of the specimen when the load was applied, the specimen no longer

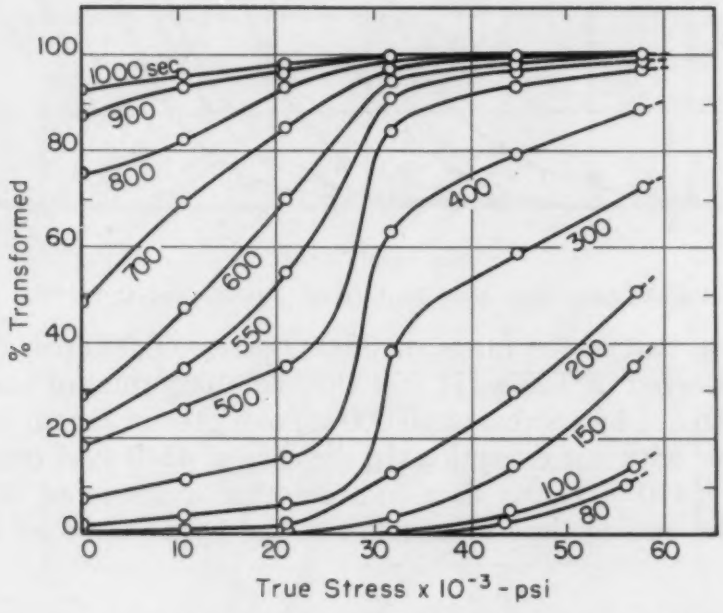


Fig. 8—Variation in the Amount of Bainite as a Function of True Stress in AISI 1085 Steel Isothermally Transformed at 535 °F.

elongated to any significant extent. The error involved in the true stress calculations is estimated to be about $\pm 5\%$, and comprise mainly variation in the diameter of the specimens, and volume changes accompanying the formation of bainite during transformation and formation of martensite during subsequent quenching of the untransformed austenite.

The data shown in Fig. 8 indicates that the amount of bainite formed isothermally increases rapidly over a certain stress range, henceforth to be called the critical stress range. The increase in the amount of bainite formation in the critical stress range, however, is most significant only for certain periods of isothermal transformation times. For a selected time of transformation, a series of photomicrographs is shown in Fig. 9 for 1085 steel. These photomicrographs indicate clearly the effect of a stress just exceeding the critical stress range

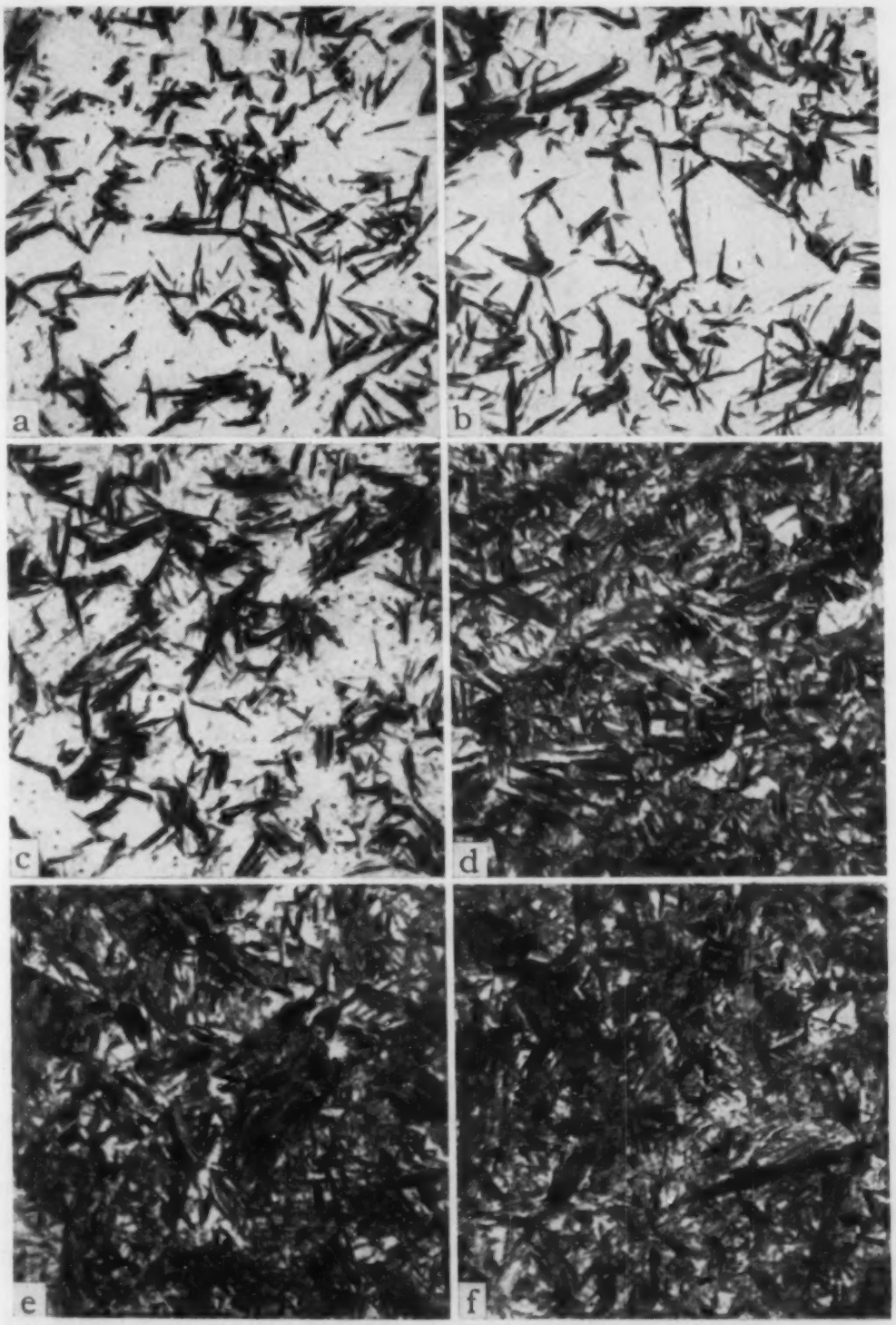


Fig. 9—Photomicrographs of Bainite Illustrating the Effect of Stress on the Amount of Bainite Isothermally Formed in 500 seconds at 535 °F in AISI 1085 Steel. (a) No Stress, (b) 10,500 psi, (c) 21,000 psi, (d) 33,000 psi, (e) 46,000 psi, (f) 60,000 psi X 500. Etchant—Saturated Picral.

Table IV
Determined Critical Stress Range Within Which Bainite Formation May Be Significantly Accelerated

Steel AISI	Isothermal Transformation Temperature, °F	Critical Stress Range psi
1085	535	25,000–28,000
	700	25,000–28,000
4340	650	23,000–26,000
1045	700	26,000–29,000

in promoting the formation of large amounts of bainite. The critical stress ranges determined for the steels used in this investigation are shown in Table IV.

As will be shown later, the large increase in the amount of transformation occurring within the critical stress range is related to deformation of the austenite. In order to determine the significant relationship between true strain and amount of austenite transformed for different isothermal transformation times, it is necessary to consider the fact that deformation of the austenite varies with transformation time and attendant increasing amounts of transformation product. The approach is best made through first determining the relationship between true strain and time of transformation.

True Strain vs. Time; the Creep Behavior

True strain is defined as a $\log_e \left(\frac{do}{d}\right)^2$, where *do* is the original diameter and *d* the instantaneous diameter of the specimen, with the assumption of volume constancy. As described heretofore, however, the final diameter was used in true strain calculations rather than the instantaneous diameter.

After an experimental run, the copper plating of the specimen is carefully dissolved in nitric acid. After dissolution of the plating, the diameter is measured by micrometric methods at ten or more different places close to the central parts of the 5-½ inch long specimen and the average diameter determined. The variation of ±0.0002 inch in diameter of the specimen, and the estimated volume strains and those associated with recovery of elastic strains, produce an estimated error of ±0.010 inch per inch in the final true strain measurements.

The variation of true strain with transformation time under different average applied stresses is illustrated in Fig. 10 for 1085 steel. These curves are similar to conventional creep curves, except that those in Fig. 10 represent a situation where decomposition of one phase into others is continuously occurring during extension. The new constituent, bainite, being harder than the decomposing phase austenite,

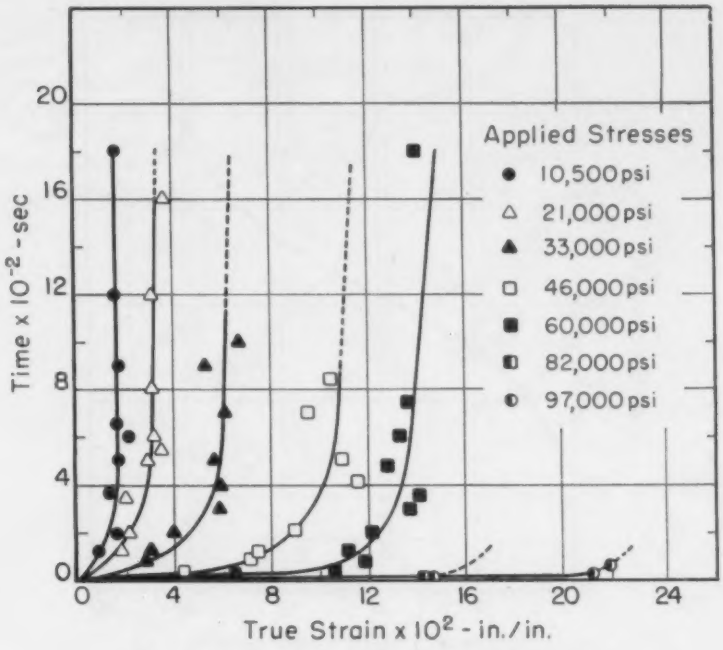


Fig. 10—Variation of True Strain Under Different Average Stress With Transformation Time in AISI 1085 Steel Isothermally Transformed at 535 °F.

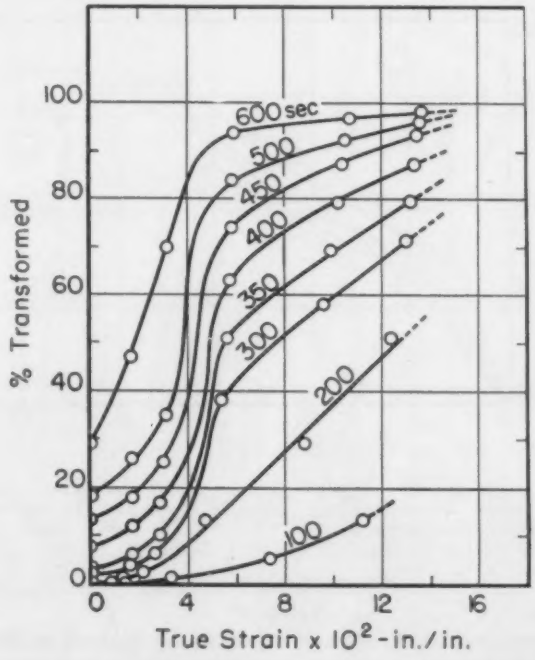


Fig. 11—Variation in the Amount of Bainite Formed With Strain in AISI 1085 Steel Isothermally Transformed at 535 °F.

thus modifies the creep behavior of the unstable austenite. At all of the temperature levels studied, the applied stresses for the time of transformation involved was chosen so as not to cause any necking down of the specimen.

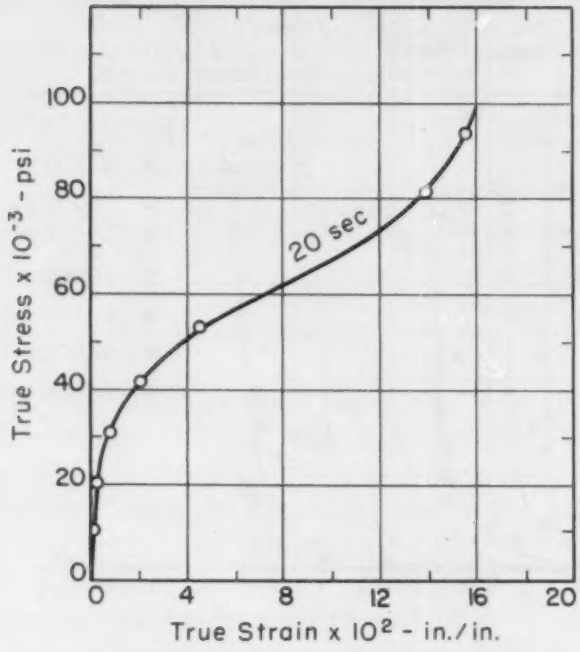


Fig. 12—Stress—Strain Relationship of Unstable Austenite Prior to Isothermal Transformation at 535 °F in AISI 1085 Steel.

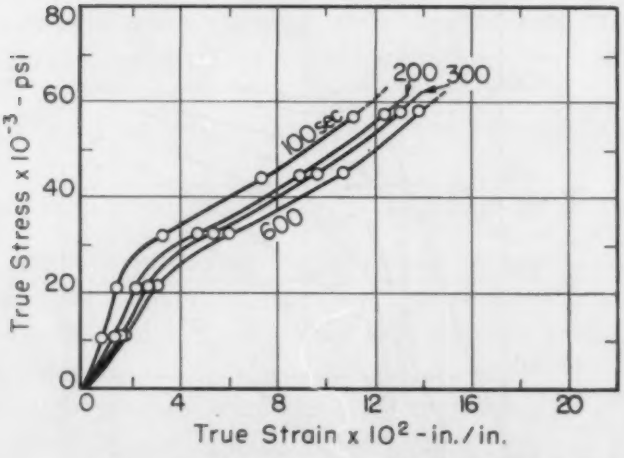


Fig. 13—Stress—Strain Relationship of Unstable Austenite Prior to and Including Isothermal Transformation at 535 °F in AISI 1085 Steel for Different Isothermal Holding Times.

Table V
Relationship between Critical Stress and Yield Stress Ranges of Unstable Austenite

Steel AISI	Isothermal Transformation Temperature, °F	Critical Stress Range psi	Yield Stress Range of Unstable Austenite psi
1085	535	25,000–28,000	25,000–29,000
	700	25,000–28,000	25,000–27,000
4340	650	23,000–26,000	22,000–26,000
1045	700	26,000–29,000	24,000–28,000

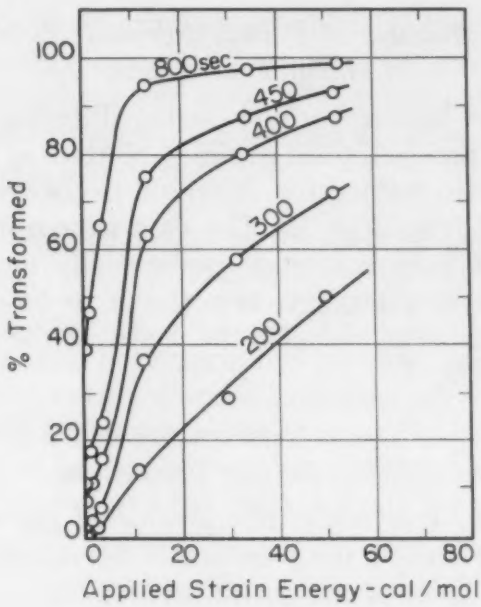


Fig. 14—Variation in the Amount of Bainite Formed With Applied Strain Energy in AISI 1085 Steel Isothermally Transformed at 535 °F.

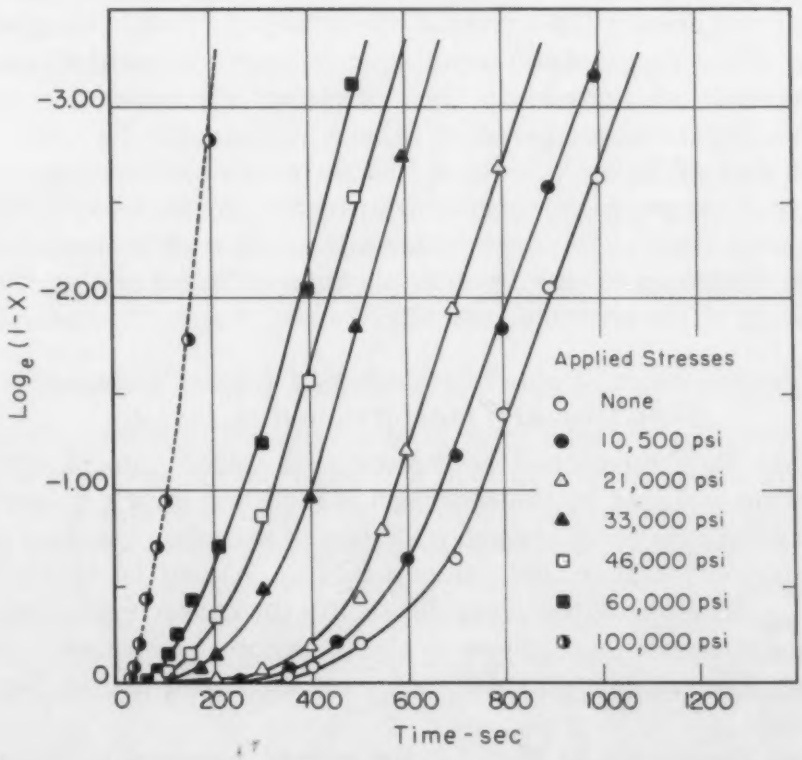


Fig. 15—Relationship Between the Amount of Untransformed Austenite and Transformation Time at 535 °F in AISI 1085 Steel for Different Applied Stresses.

True Strain vs. Amount of Bainite Formed; Determination of a Critical True Strain

The amount of bainite formed during different constant periods of transformation time vs. true strain is plotted in Fig. 11 for 1085 steel. The true strain values for different isothermal transformation times were derived from Fig. 10. The data shown in Fig. 11 indicate that the amount of bainite formed isothermally increases to a great extent in a certain strain range, henceforth to be called the critical strain range. In almost all respects the shape of the curves in Fig. 11 is similar to that in Fig. 8.

True Stress—True Strain Relationship of Unstable Austenite Prior to Bainite Formation

If a true stress—true strain relationship of the unstable austenite could be established without the presence of any decomposition product, then the true significance of the critical stress range could be evaluated. As derived from Fig. 10, Fig. 12 illustrates the true stress—true strain relationship of unstable austenite in 1085 steel. The isothermal transformation time of 20 seconds, for which the curve is drawn, is sufficiently short that even under the highest stress no transformation of austenite to bainite occurs.

It is clearly indicated in Fig. 12 that the stress-strain relationship deviates from linearity in a certain stress range, which is designated as the yield stress range of the unstable austenite. The yield stress range of the unstable austenite in the three steels at their respective transformation temperatures are given in Table V.

The data of Table V indicate that the critical stress range and the yield stress range of the unstable austenite are identical within the experimental error. The large increment in transformation, shown in Fig. 8, is therefore arising from application of stress within the yield stress range of the unstable austenite.

True Stress—True Strain Relationship of Unstable Austenite with Simultaneous Transformation to Bainite

It has been mentioned heretofore that under applied stress the deformation suffered by the specimen is modified owing to increasing amounts of bainite being formed with time. For certain constant periods of transformation time, data shown in Fig. 13 can be derived from that of Fig. 10. Fig. 13, therefore, illustrates the characteristic deformation of the austenite as modified by the presence of increasing amounts of bainite. The similarity in shape of these curves to that in Fig. 12 is to be noted.

From the curves of Fig. 13, the energy required to deform the specimens with any given stress and for any definite period of trans-

formation time can be determined graphically. From such determinations, the strain energy in units of psi may be readily converted into more familiar units of cal per mole. The relationship between strain energy and the amount of bainite formed at different transformation times for 1085 steel is shown in Fig. 14.

The Effect of Applied Stress on the Rate of Decomposition of Austenite

From the data in Figs. 3,4,5,6, and 7, the true rate of austenite decomposition can not be determined readily since the amount of austenite remaining untransformed continuously decreases as transformation proceeds. Inasmuch as the true rate of austenite decomposition must be related to a unit volume of untransformed austenite, it becomes necessary to determine the true rate by plotting $\log_e (1-x)$ vs. transformation time under different average stresses, where x is the fractional amount of austenite transformed isothermally in a given time. Such a determination is illustrated in Fig. 15 for 1085 steel. The slopes of the curves represent the rate of decomposition of residual austenite per unit volume of untransformed austenite, and may be expressed,

$$\frac{d}{dt}\left\{\log_e (1-x)\right\} = \frac{d}{d(1-x)}\left\{\log_e (1-x)\right\} \cdot \frac{d}{dx}(1-x) \cdot \frac{dx}{dt} = -\frac{1}{1-x} \cdot \frac{dx}{dt}$$

where $\frac{dx}{dt}$ is the rate of decomposition and $(1-x)$ is the fractional amount of austenite remaining after a transformation time t.

It can be observed in Fig. 15 that the rate of decomposition per unit volume of untransformed austenite increases with increase in transformation time up to some limiting value and then becomes constant. The onset of this constant decomposition rate is shown to occur at shorter times of transformation the higher the applied stress, and the constant rate increases with increasing stress. These data are summarized in Tables VI and VII.

The Character of Bainite Formed Under Applied Stress

As illustrated in Fig. 16 for 1085 steel, which is representative of all the steels investigated, there is a definite preference in orientation of low-temperature bainite with increasing amounts of applied stress. As related to prior deformation of the austenite, the orientation effect becomes more pronounced at stress greater than the yield stress of the austenite. Although not illustrated, a more random orientation of the high temperature bainite occurred in 1085 steel at comparable stress applications, and a completely random orientation in 4340 steel. There is indication in Fig. 16, and particularly in Fig. 16c, that the fineness of the bainite needles increase with increase in applied stress, although this was not observed in the case of high temperature bainite.

Table VI
Variation in the Amount of Decomposed Austenite After Which a Constant Rate of Decomposition of Residual Austenite Is Obtained Under Different Applied Stresses

Steel AISI	Isothermal Transformation Temperature, °F	Amount of Austenite Decomposed After Which a Constant Rate of Decomposition of Residual Austenite Is Obtained Under Different Applied Stresses							
		No Stress	10,500 psi	21,000 psi	33,000 psi	46,000 psi	60,000 psi	80,000 psi	100,000 psi
1085	535	55	55	55	55	50	35	—	20
	700	53	53	53	53	46	41	—	31
4340	650	50	50	50	35	30	5	3	—
1045	700	65	65	65	45	35	30	—	—

Note: Average critical stresses for 1085, 4340, and 1045 steels are 26,500, 24,500, and 27,500 psi, respectively.

Figs. 16c and 17 illustrate the twinning that occurs in the austenite at stresses greater than about 45,000 psi. It is of interest to note in Fig. 17 no transformation has occurred in the twin band, although the parent grain surrounding it has undergone considerable transformation.

At comparatively high values of applied stress, where significant differences exist in the degree to which the variously-oriented austenite grains have been strained, preferential transformation occurs. As illustrated in Fig. 18, some of the austenite grains have suffered complete transformation whereas others have only partially transformed and some not at all.

Transformation Under Applied Stress for Only a Portion of the Total Transformation Time

The curve in Fig. 19 illustrates the reaction curve of austenite transformation in 1085 steel under an applied stress of 60,000 psi. The lettered plotted points correspond to the respective transformation schedule described in Table VIII. From the proximity of the plotted

Table VII
Variation of the Constant Rate of Decomposition of Residual Austenite with Applied Stress

Steel AISI	Isothermal Transformation Temperature, °F	Ratio of The Constant Rate of Decomposition of Residual Austenite Under Applied Stress to The Constant Rate of Decomposition of Residual Austenite Under No Applied Stress						
		10,500 psi	21,000 psi	33,000 psi	46,000 psi	60,000 psi	80,000 psi	100,000 psi
1085	535	1.0	1.1	1.3	1.3	1.4	—	3.0
	700	1.0	1.0	1.0	1.3	2.0	—	3.0
4340	650	1.1	1.4	2.2	3.3	4.6	10.0	—
1045	700	1.0	1.0	1.1	1.4	2.7	—	—

Note: Average critical stresses for 1085, 4340, and 1045 steels are 26,500, 24,500, and 27,500 psi, respectively.

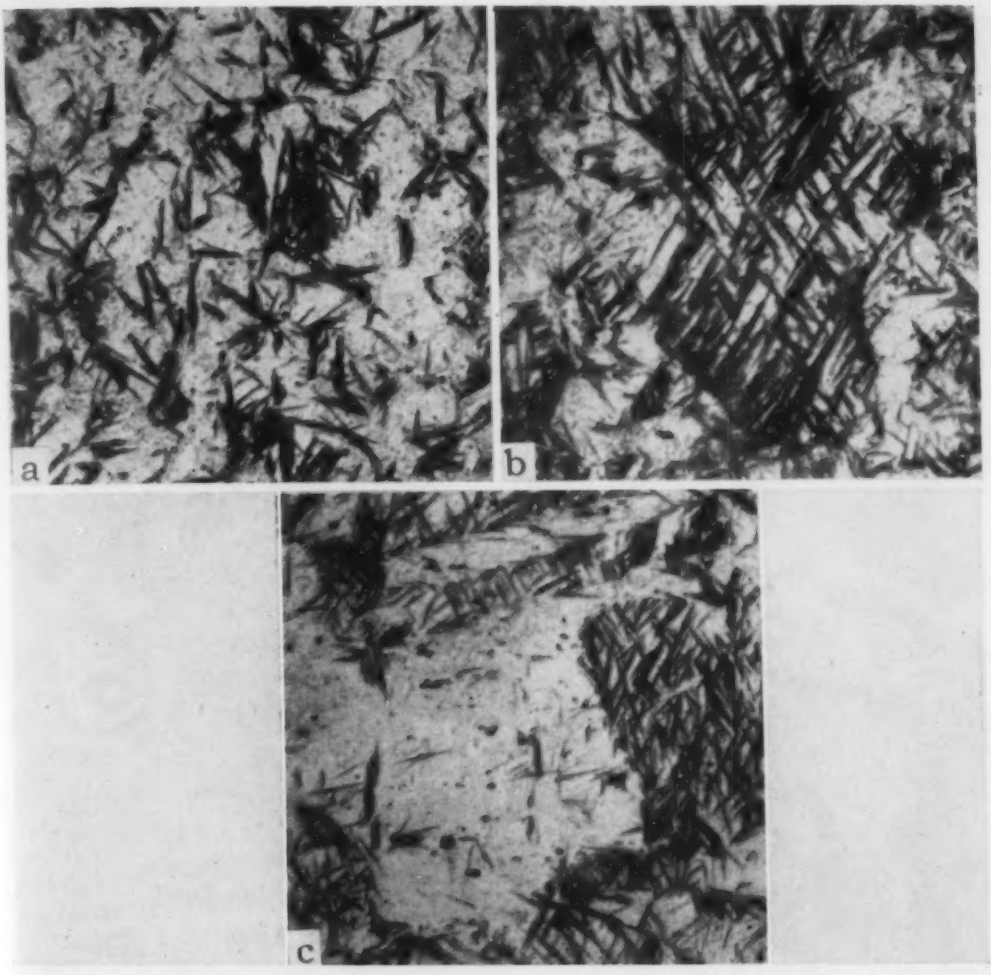


Fig. 16—Illustrating the Preferential Orientation of the Bainite Needles as a Function of Stress in AISI 1085 Steel Isothermally Transformed at 535 °F. X 500.
(a) 21,000 psi; 450 sec., (b) 33,000 psi; 300 sec., (c) 60,000 psi; 120 seconds. Etched in Saturated Picral

data with respect to the reaction curve, it is evident that the amount of austenite transformed in a given time under a stress of 60,000 psi continuously applied is equivalent to that transformed when the stress is removed and the austenite is allowed to transform further under no stress for the same total time. Fig. 19, along with other data not given, indicates that the total time of transformation is the significant con-

Table VIII
The Amount of Bainite Formed at 535 °F (1085 Steel) as Influenced by Stress Application for Different Times Prior to Transformation Under No Stress

Transformation Schedule		Amount of Bainite Initially Formed Under 60,000 psi	Total Transformation	Letter Symbols In Fig. 19
Time Under 60,000 psi sec	Subsequent Time Under No Stress sec	%	%	
20	60	0	<1	N
120	60	24	39	M
300	60	71	86	L
480	60	95	98	K



Fig. 17—Illustrating Twinning in a Prior Austenite Grain in AISI 1085 Steel Transformed at 535 °F Under a Stress of 60,000 psi. X 1500. Etched in Saturated Picral.

Table IX

The Amount of Bainite Formed at 535 °F (1085 Steel) as Influenced by Different Isothermal Holding Times Under No Stress Prior to Application of Stress for Various Times

	Transformation Schedule		Amount of Bainite Initially Formed Under No Stress	Total Transformation	Letter Symbols in Figs. 20 and 21	True Strain $\times 10^2$
	Time Under No Stress sec	Subsequent Time Under 60,000 psi sec	%	%		in/in
Fig. 20	720	180	52	91	A	1.7
	600	180	29	79	B	2.8
	480	180	16	60	—	3.2
Fig. 21	360	180	4	45	I	9.8
	240	180	1	44	H	10.9
	210	180	<1	47	G	11.0
	180	180	0	42	F	11.0
	150	180	0	41	E	11.1
	120	180	0	40	D	11.2
	30	180	0	39	C	11.9

sideration, and regardless of the times of transformation under stress and with the stress subsequently removed, the plotted points would conform to the reaction curve. This will occur, however, only when the stress is allowed to remain for a time sufficient to deform the austenite.

Conversely to the transformation schedule described, data in Table IX (pertaining to Fig. 20) and Fig. 20 show the amount of austenite transformed under a schedule of partial transformation un-

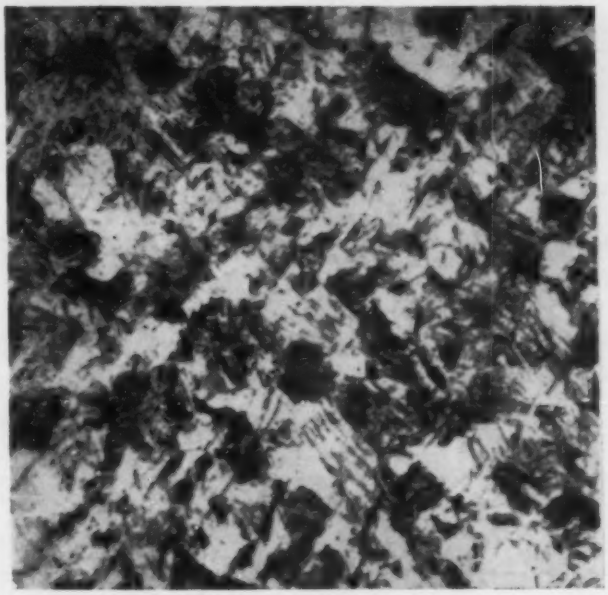


Fig. 18—Illustrating the Preferred Transformation of Some Prior Austenitic Grains with Respect to Others. AISI 4340 Steel Isothermally Transformed at 650 °F for 30 sec. Under stress of 60,000 psi. X 500. Etched in Saturated Picral.

der no stress to form varying amounts of bainite (about 30 to 50%), and then a stress of 60,000 psi subsequently applied and transformation allowed to proceed for a given time. The data indicate that an applied stress of 60,000 psi has little effect in accelerating austenite decomposition if the stress is applied to an aggregate structure of austenite and bainite containing bainite in excess of about 30%. This circumstance is probably related to the increased strength of the aggregate and the consequential lower influence of stress on the austenitic phase (see Fig. 22).

Fig. 21 and the data in Table IX pertaining to this figure are the results of a transformation schedule similar to that shown in Fig. 20. An exception is that no transformation (or practically none) of the austenite had occurred prior to the application of 60,000 psi stress. It is significant to note that the influence of stress in accelerating the formation of bainite is most pronounced when applied at the end of the no-stress incubation period. This is specifically illustrated by

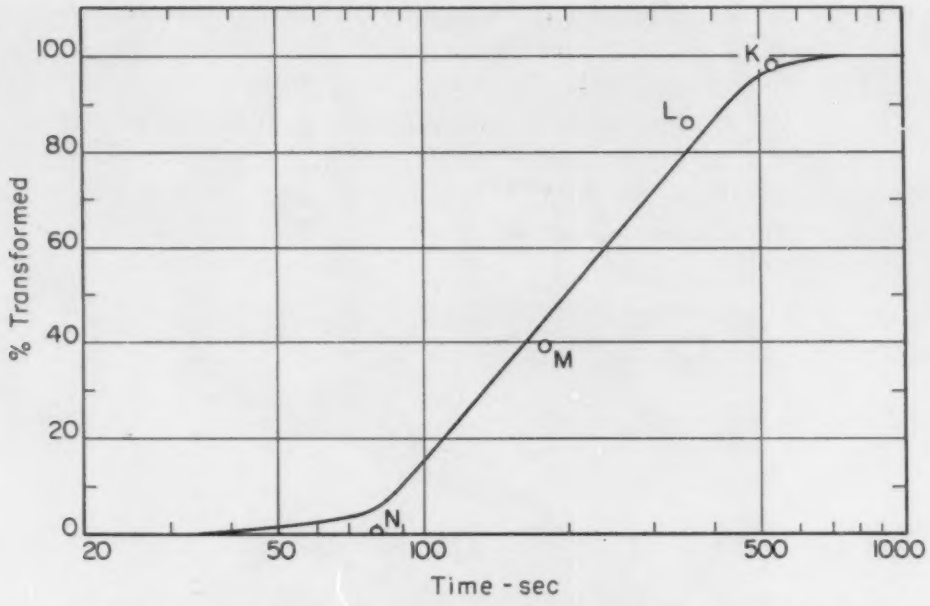


Fig. 19—The Austenite Decomposition Curve for AISI 1085 Steel Isothermally Transformed at 535 °F Under 60,000 psi. Lettered Data Pertaining to Transformation Schedule Described in Table VIII.

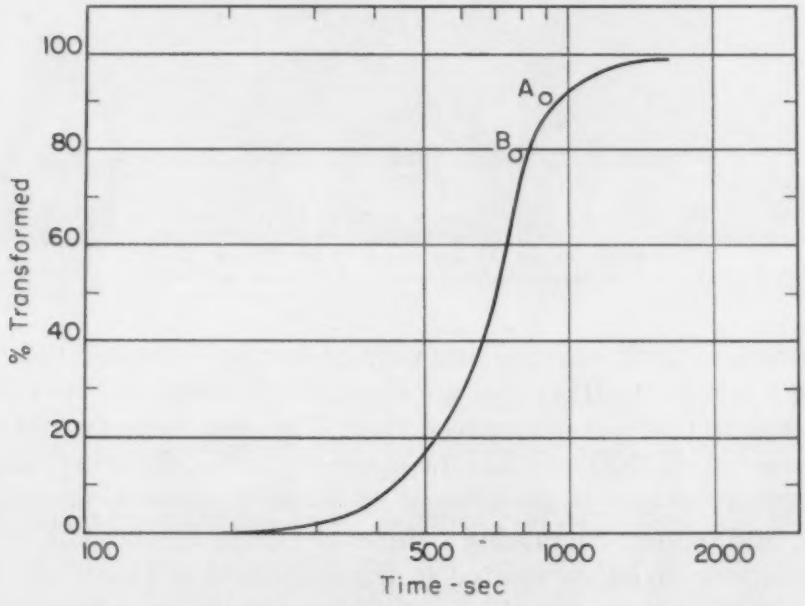


Fig. 20—The Austenite Decomposition Curve for AISI 1085 Steel Isothermally Transformed at 535 °F Under No Stress. Lettered Data Pertaining to Transformation Schedule Described in Table IX.

point *G*, and arises from two simultaneously operative effects; the progressive increase in the total amount of bainite formed with time and the strengthening of the aggregate structure owing to increasing amounts of bainite initially formed under no stress.

The data shown in Fig. 22 were derived through a transformation schedule similar to that employed to secure the data of Fig. 21. The

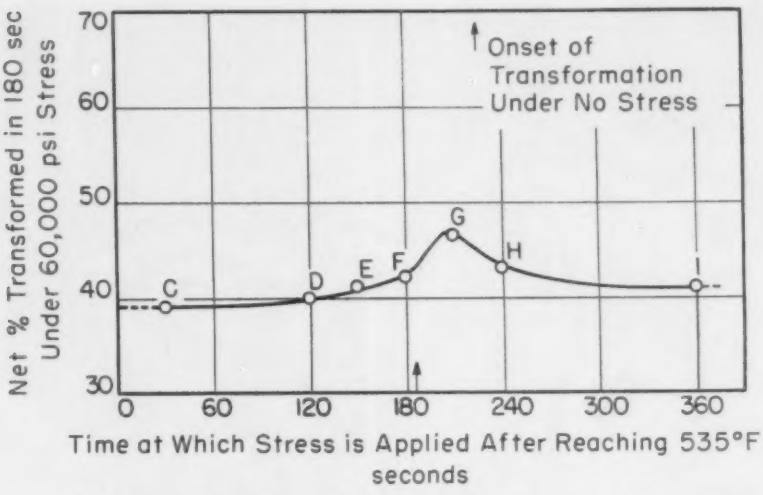


Fig. 21—Influence of the Time of Stress Application on the Net Amount of Austenite Transformed in 180 Seconds. Under 60,000 psi. AISI 1085 Steel Isothermally Transformed at 535 °F.

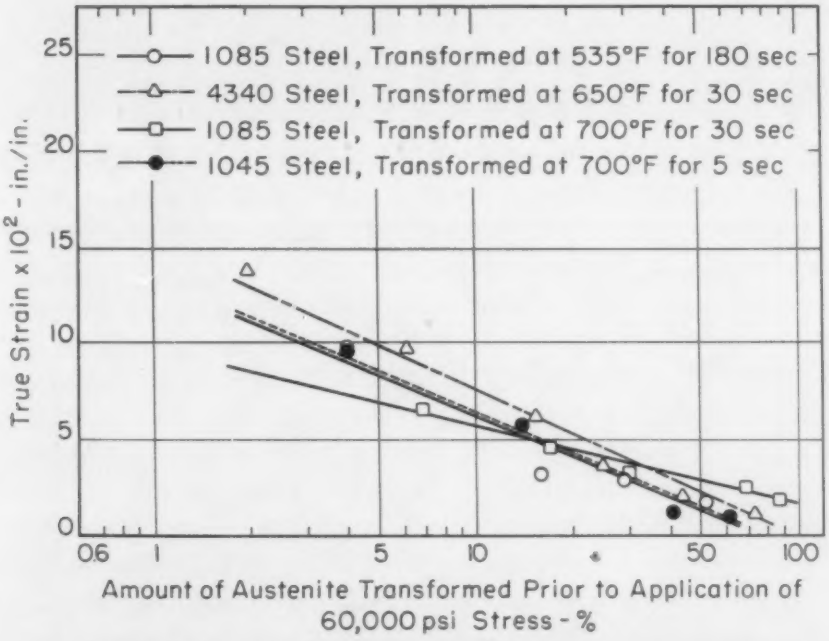


Fig. 22—Variation of True Strain With Amount of Austenite Transformed at the Time a Stress of 60,000 psi is Applied.

curves reflect the mechanical strength of the austenite-bainite aggregate at the transformation temperature, and it is evident that the relationship is logarithmic with respect to the amount of bainite present in the structure prior to application of stress. This relationship is undoubtedly associated with the extent of the mean free path in the continuous austenitic phase.

Electron Microscope and Diffraction Observations

To determine whether or not the formation of bainite under stress

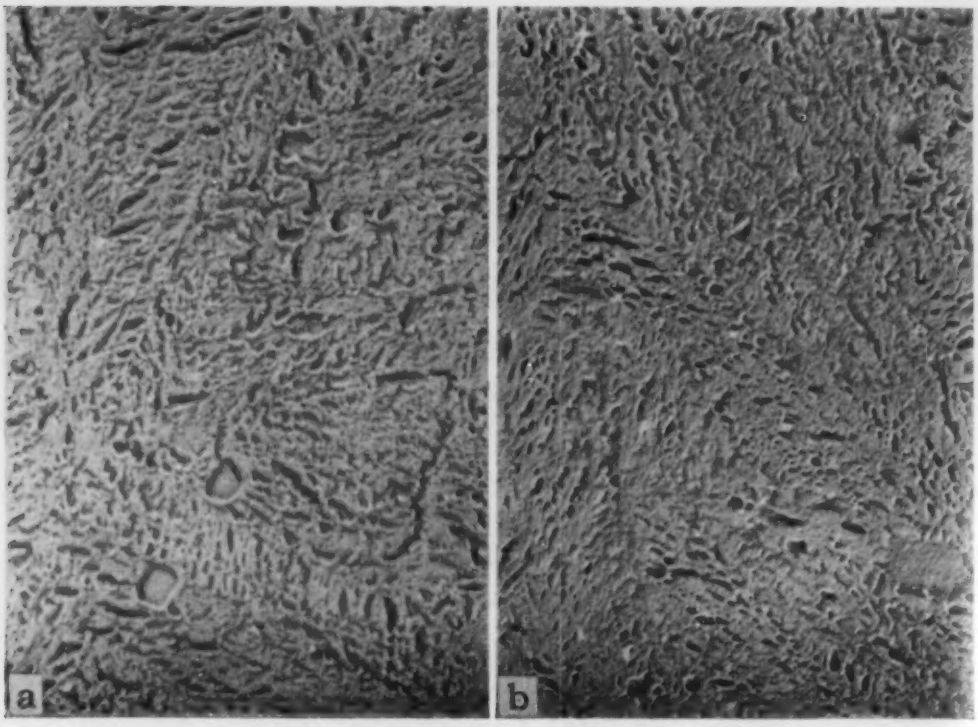


Fig. 23—Electron photomicrographs of Bainite Formed at 535 °F in AISI 1085 Steel. X 12,000. a. Without Stress b. 60,000 psi

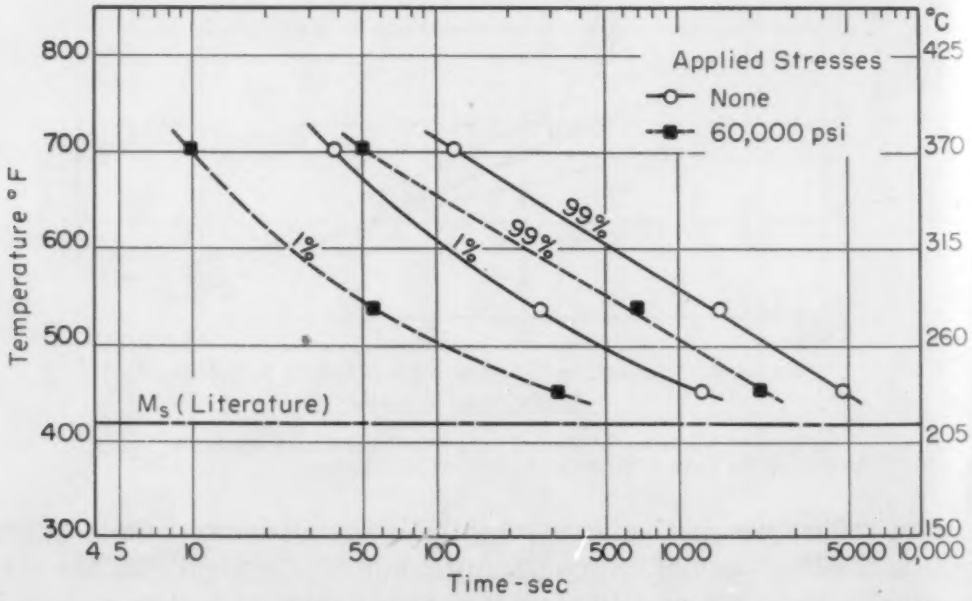


Fig. 24—Illustrating the Displacement of the Beginning and Ending Times of Bainite Formation in AISI 1085 Steel Due to Stress of 60,000 psi.

resulted in any significant change in the character of the carbide phase in bainite, not detected by optical microscopy, selected observations were made by means of the electron microscope. As illustrated in Fig. 23, which is typical of the structures examined, there appears to be

no significant difference between that formed under no stress and a stress of 60,000 psi.

Using the extraction replica technique, (36) electron diffraction patterns were secured of the carbide particles in bainite of 1085 steel, formed at 535 °F (280 °C), under no stress and 60,000 psi.[3]

It is known that in eutectoid carbon steel the hexagonal epsilon carbide structure exists in bainite formed under no stress at a temperature of 500 °F (260 °C), but not in bainite formed at 550 °F (290 °C). Therefore, the purpose of the electron diffraction observations was to determine if the presence of hexagonal epsilon carbide existed in bainite at the transformation temperature of 535 °F (280 °C) and if applied stress in any way altered the character of the carbide structure. The diffraction patterns indicated that in both cases only the conventional carbide phase was present.

Conclusions

An applied stress exceeding the yield stress of unstable austenite accelerates the isothermal transformation of austenite to bainite in AISI 1085, 4340, and 1045 steels.

Both the beginning and ending times of the austenite to bainite transformation are shortened by applied stress. This is illustrated in Fig. 24 for a stress of 60,000 psi, in terms of the attendant shift in the lower part of the C-curve for 1085 steel.

A pronounced increment in the amount of transformation to bainite occurs within the critical stress range. This critical range is observed to be identical with the yield stress range of unstable austenite.

Relationships of true strain and strain energy with the amount of bainite formed isothermally are observed to be similar to the relationship between true stress and the amount of bainite formed.

Owing to slip and twinning along preferred planes and in preferred directions in the austenite lattice, the formation of bainite is preferred with respect to distribution and orientation.

Under large stress applications, compartmentalization in deformed austenite grains, due to competing slip systems, reduces the coarseness of the bainite needles.

The mechanical strength of the austenite-bainite aggregate at the transformation temperature is observed to be a logarithmic function of the amount of bainite present in the aggregate.

Electron microscopical observations indicate close similarity in the size, shape and distribution of the cementite particles in bainite formed with and without applied stress. The structure of the cementite particles in bainite in AISI 1085 steel formed at 535 °F (280 °C), as revealed by electron diffraction patterns, is observed to be unaffected by applied stress.

[3] The electron diffraction patterns were secured through the courtesy of R. M. Fisher, Research Laboratory, U. S. Steel Corp. Kearny, New Jersey.

ACKNOWLEDGMENTS

Conduction of this research was made possible through support of the Office of Naval Research under Contract No. Nonr–266(18). An appropriation was provided by Columbia University, through the Eugene Higgins Trust Fund, to design and construct the experimental apparatus.

The assistance of Paul Rothstein with the experimental work, and the contribution of selected steels by Raymond A. Grange of the Research Laboratory, U. S. Steel Corp., Kearny, N. J., are gratefully acknowledged.

References

1. E. S. Davenport and E. C. Bain, "The Transformation of Austenite at Constant Subcritical Temperatures," *Transactions,* American Institute of Mining and Metallurgical Engineers, Vol. 90, 1930, p. 117.
2. J. R. Villela, G. E. Guellich, and E. C. Bain, "On Naming The Aggregate Constituents in Steel," TRANSACTIONS, American Society for Metals, Vol. 24, 1936, p. 225.
3. F. Wever and H. Lange, "Zur Umwandlungskinetik des Austenits," *Mitteilungen aus dem Kaiser-Wilhelm Institut für Eisenforschung,* Dusseldorf, Vol. 14, 1932, p. 71.
4. A. Portevin and P. Chevnard, "The Transformations on the Cooling of Steel," *Comptes Rendus,* Vol. 204, 1937, p. 772.
5. E. P. Klier and T. Lyman, "The Bainite Reaction in Hypoeutectoid Steels," *Transactions,* American Institute of Mining and Metallurgical Engineers, Vol. 158, 1944, p. 394.
6. H. J. Wiester, "The Intermediate Phase Structures in Steel and Their Origin," *Archiv für das Eisenhuttenwesen,* Vol. 18, 1944, p. 97.
7. C. Zener, "Kinetics of the Decomposition of Austenite," *Transactions,* American Institute of Mining and Metallurgical Engineers, Vol. 167, 1946, p. 550.
8. J. C. Fisher, THERMODYNAMICS IN PHYSICAL METALLURGY, 1950, p. 201. American Society for Metals, Cleveland.
9. G. V. Smith and R. F. Mehl, "Lattice Relationships in Decomposition of Austenite to Pearlite, Bainite, and Martensite," *Transactions,* American Institute of Mining and Metallurgical Engineers, Vol. 150, 1942, p. 211.
10. A. Hultgren, "Isothermal Transformation of Austenite," TRANSACTIONS, American Society for Metals, Vol. 39, 1947, p. 915.
11. A. Hultgren, "Isothermal Transformation of Austenite," *Jernkontorets Annaler,* Vol. 135, No. 8, 1951, p. 403.
12. T. Ko and S. A. Cottrell, "The Formation of Bainite," *Journal,* Iron and Steel Institute, Vol. 172, 1952, p. 307.
13. F. C. Thompson and W. E. W. Millington, "The Plastic Deformation of Alpha and Gamma Iron," *Journal,* Iron and Steel Institute, Vol. 109, 1924, p. 67.
14. E. C. Bain, "The Persistence of Austenite at Elevated Temperatures," TRANSACTIONS, American Society for Steel Treating, Vol. 8, 1925, p. 14.
15. J. A. Mathews, "Retained Austenite—A Contribution to the Metallurgy of Magnetism," TRANSACTIONS, American Society for Steel Treating, Vol. 8, 1925, p. 565.

16. K. Honda and K. Iwase, "On the Transformation of Retained Austenite into Martensite by Stress," *Science Reports,* Tohoku Imperial University, First Series, Vol. 16, 1927, p. 1.

17. J. H. Hall, "Studies of Hadfield's Manganese Steel with the High-power Microscope," *Transactions,* American Institute of Mining and Metallurgical Engineers, Vol. 84, 1929, p. 382.

18. R. H. Aborn and E. C. Bain, "Nature of the Nickel-Chromium Rustless Steels," TRANSACTIONS, American Society for Steel Treating, Vol. 18, 1930, p. 837.

19. E. Scheil, "Über die Umwandlung des Austenits in Martensit in Eisen-Nickellegierungen unter Belastung," *Zeitschrift für anorganische und allgemeine Chemie,* Vol. 207, 1932, p. 21.

20. Z. Nishiyama, "Transformation Gamma-Alpha of Stainless Invar," *Science Reports,* Tohoku Imperial University, First Series, Vol. 25, 1936, p. 94.

21. von G. Wassermann, "Untersuchungen an einer Eisen-Nickel Legierung über die Verformbarkeit während der Gamma-Alpha Umwandlung," *Archiv für das Eisenhüttenwesen,* Vol. 10, 1937, p. 321.

22. K. Mathieu, "Effect of Alloy-element Content and Testing Conditions on Gamma to Alpha Transformation in Cold-Deformation of Austenitic Steels," *Archiv für das Eisenhuttenwesen,* Vol. 16, 1942, p. 215.

23. F. Lazlo, "Tesellated Stresses, Part II," *Journal,* Iron and Steel Institute, Vol. 148, 1943, p. 137.

24. A. H. Cottrell, "Tensile Properties of Unstable Austenite and Its Low Temperature Decomposition Products," *Journal,* Iron and Steel Institute, Vol. 151, No. 1, 1945, p. 93p.

25. C. B. Post and W. S. Eberly, "Stability of Austenite in Stainless Steels," TRANSACTIONS, American Society for Metals, Vol. 39, 1947, p. 868.

26. G. J. Guarnieri and J. J. Kanter, "Some Characteristics of the Metastable Austenite of 4 to 6% Chromium + ½% Molybdenum Cast Steel," TRANSACTIONS, American Society for Metals, Vol. 40, 1948, p. 1147.

27. J. Savage, "Mechanism of Gamma-Alpha Transformation in Iron," *Iron and Coal Trades Review,* Vol. 157, July 16, 1948, p. 137.

28. P. A. Dixon, Jr., "The Effect of Stress on the Transformation Rate of Austenite," M. S. Thesis, Columbia University, 1949 (Unpublished).

29. B. L. Averbach, S. A. Kulin, and M. Cohen, "The Effect of Plastic Deformation on Solid Reactions," Part II, TRANSACTIONS, American Society for Metals, Vol. 41A, 1949, p. 290.

30. M. D. Jepson and F. C. Thompson, "The Acceleration of the Rate of Isothermal Transformation of Austenite," *Journal,* Iron and Steel Institute, Vol. 162, 1949, p. 49.

31. A. W. McReynolds, "Effects of Stress and Deformation on the Martensite Transformation," *Journal of Applied Physics,* Vol. 20, 1949, p. 896.

32. R. Schnitzel and S. Bhattacharyya, "The Effect of Externally Applied Tensile Stress on the Isothermal Transformation Rate of Austenite," M. S. Thesis, Columbia University, 1950, (Unpublished).

33. G. V. Kurdymov, G. P. Maksimova, and T. V. Tagunova, "Transformation of Deformed Austenite into Martensite," *Doklady Akademii Nauk,* S.S.S.R., Vol. 71, No. 2, 1950, p. 307.

34. O. P. Maksimova and A. I. Nikonorova, "Influence of Deformation Upon Kinetics of Martensite Transformation," *Doklady Akademii Nauk,* S.S.S.R., Vol. 81, No. 2, 1951, p. 183.

35. S. A. Kulin, M. Cohen, and B. L. Averbach, "Effect of Applied Stress on the Martensite Transformation," *Transactions,* American Institute of Mining and Metallurgical Engineers, Vol. 194, 1952, p. 661.

36. R. M. Fisher, "Electron Microstructure of Steel by 'Extraction Replica' Technique," Symposium on Techniques for Electron Metallography, ASTM Special Technical Publication No. 155, January 1954, p. 49.

DISCUSSION

Written Discussion: By F. Wever, Max-Planck-Institut für Eisenforschung, Dusseldorf, Germany.

It gives us pleasure that the authors have now systematically investigated the influence of mechanical stress and plastic deformation on isothermal intermediate transformation, as until now, stress and deformation influences have only been studied on martensite transformation. I should like, however, to indicate a difficulty which arises from the given experimental results on precipitation and transformation processes, when one tries to conclude the most interesting factors, namely, rate of nucleation and rate of growth. I would expect and as it is suggested in the given data and in Fig. 9, that stress and deformation mainly influence the rate of nucleation. The question remains uncertain as far as effect of stress on the rate of growth. It should not be very difficult to answer the latter question with the metallographic methods employed and I should like to ask the authors if they have already done the work.

The authors are giving as a fact the very pronounced increment in bainite formation in a critical stress range which is identical with the yield stress. According to Fig. 8 of their paper in AISI 1085 steel, this sharp increment occurs between 300 and 500 sec holding time. With smaller stresses in the elastic range an influence on the transformation rate can be seen after longer holding time after which a range of remarkably higher increment is not to be seen. Maybe in the same sense as the authors', one might explain this on the basis of plastic deformation, lattice distortions such as vacancies, and internal stresses, which are working favorably for nucleation and shortening of the incubation period. Being specially sensitive to small variations in stress and holding time, the influence will be in that range where deformation is just becoming measurable, i.e., in the yield stress range.

An orientation effect has been observed chiefly in the regions of plastic deformation. The less pronounced effect in the elastic region may be due to the fact that the specimen is polycrystalline and there are quenching stresses present which, compared to the externally applied stress, are not large. In the same field the results obtained in the Max-Planck-Institut für Eisenforschung, Dusseldorf, will be of interest.[1] When austenitic single crystals of Fe-Ni-C alloy of 26% Ni and 0.23% C are held under a normal stress of about 75% of the shear stress of the austenite and they are transformed to martensite, all of the martensite needles show the same orientation, provided the temperature is not lowered more than about 15 °C below the martensite temperature and slow cooling follows under a temperature gradient. Only at lower temperatures will other orientations occur. From this it can be concluded that in an originally stress-free crystal with sharp Laue-pattern spots an elastic stress is sufficient to influence nucleation in such a way that from all the possible orientations one is chosen, when the temperature is not too low. As it clearly seems, at lower temperatures the other contributions to enthalpy are becoming predominant in comparison to the energy of externally applied stress.

It would be interesting to do this type of investigation on the austenite-bainite transformation.

---

[1] H. G. Müller, Diploma in Engineering, University of Köln. A. Kochendörfer and H. G. Müller, Arch. Eisenhuttenw., in press.

Authors' Reply

In our transformation studies of austenite to bainite we did not investigate separately the effect of stress and deformation on the rate of nucleation and the rate of growth of bainite. We have ample evidence, however, as typically illustrated in Fig. 16 of our paper, that the bainite needles formed under stress are shorter in length and thinner in width compared to those formed under no stress. Thus, it is suggested that the overall growth rate has decreased under stress. Since, under stress, both total transformation and rate of transformation have increased, it can be concluded that the rate of nucleation must have increased to a large extent.

We agree with Dr. Wever's suggestion that the large increment in transformation observed over long transformation times under stresses less than the yield stress might arise from lattice distortions owing to vacancies and internal stresses. Under applied stresses less than the yield stress, plastic deformations up to 0.01 to 0.02 inch per inch in true strain were attained. Consequently, at such degrees of extension considerable deformation could be expected to take place and we would be inclined to consider this deformation to be the major cause for the observed increase in transformation.

It is to be expected that upon quenching to the transformation bath temperature quenching stresses will develop in the specimen. It is also to be expected that at comparatively high temperatures these stresses would be relaxed within a relatively shorter period of time. If one considers that quenching stresses are present, then it may be expected that in certain local regions of the specimen stresses favorable to the applied tensile stress would exist and in these regions one should be able to observe an orientation of the bainite needles formed under an applied stress less than the yield stress. Such local orientation effects, however, were not observed.

The work of Dr. Wever and his associates carried out at the Max-Planck-Institute für Eisenforschung, Dusseldorf, on iron-nickel-carbon alloy is of great interest to us. It would be of great help in resolving the mechanism of bainite formation if such a study could be carried out isothermally with stress-free single crystals of austenite of steels of commercial compositions.

The authors thank Dr. Wever for his stimulating discussion of this paper.

THE ELASTIC LIMIT AND YIELD BEHAVIOR OF HARDENED STEELS

By Hugh Muir, B. L. Averbach, and Morris Cohen

Abstract

A method of high strain sensitivity is described for investigating the elastic limit and the initial yielding of heat treated steels. The elastic limit measured by this technique is shown to be equivalent to the stress above which there is increasing permanent deformation on repeated tensile loading to a given stress level. Discontinuous yielding is observed for steels tempered at the higher temperatures, but in each case, considerable plastic deformation precedes the yield point.

The elastic limit and other tensile data are presented for hardened steels containing 0.20, 0.41 and 0.82% carbon as a function of the tempering temperature. The elastic limits are remarkably low in the as-hardened steels, being approximately 20,000 to 30,000 psi but increase to values of 100,000 to 130,000 psi on tempering in the range of 500 to 700 °F (260 to 370 °C), and then decrease to 13,000–60,000 psi on tempering at 1300 °F (705 °C). Except when brittle fracture occurs, the yield, tensile, and fracture strengths generally decrease with decreasing hardness as the tempering temperature is raised.

Introduction

ONE of the most fundamental engineering design criteria is the stress below which the deformation is purely elastic. In practice, however, it is much easier to determine the 0.2% yield strength and the tensile strength. Moreover, the elastic limit has been suspect as a definite property because of the feeling that this stress value would become lower and lower with the improvement in strain measuring devices. Recent experiments (1)[1] have shown that the initial plastic deformation can be detected with high sensitivity by observing the onset of a permanent change in the length of the test specimen on unloading

[1] The figures appearing in parentheses pertain to the references appended to this paper.

This research was sponsored by the Office of Naval Research and represents a portion of the thesis submitted by Hugh Muir in partial fulfillment of the requirements for the Sc.D. degree at the Massachusetts Institute of Technology.

A paper presented before the Thirty-sixth Annual Convention of the Society, held in Chicago, November 1 to 5, 1954. Of the authors, Hugh Muir is senior lecturer in metallurgy at the University of Otago, Dunedin, New Zealand; B. L. Averbach is associate professor, and Morris Cohen, professor of physical metallurgy, Massachusetts Institute of Technology, Cambridge, Mass. Manuscript received April 14, 1954.

from successively higher stresses. In the present work, electrical resistance strain gages have been used to detect the first permanent deformation on unloading (2) and it is shown that it is possible to define an elastic limit which is a significant property of the material. It is demonstrated that the elastic limit is equivalent to the stress above which progressive permanent deformation occurs on repeated tensile loading. Furthermore, even in steels which display sharp yield points

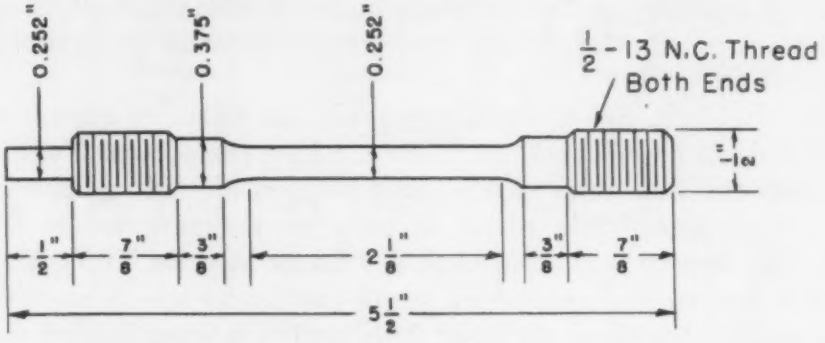


Fig. 1—Sketch of Typical Specimen for Elastic Limit Determination.

there is appreciable plastic deformation prior to the upper yield stress.

The elastic limit and other tensile properties are studied as a function of tempering temperature for three plain carbon steels. The yield, tensile, and fracture strengths usually fall off with decreasing hardness unless brittle fracture takes place, but the elastic limits exhibit maximum values on tempering in the range 400 to 800 °F (205 to 425 °C); at lower tempering temperatures the elastic limits are quite low even though the hardness is high. There is apparently no unique relationship between the hardness and elastic limit.

Experimental Procedure

The mechanical properties were determined on the 0.252 inch diameter test bars illustrated in Fig. 1. The short cylindrical portion at the end of each specimen was cut off after heat treatment for microexamination and hardness determinations. Three steels, containing

Table I
Chemical Analyses of Steels

Steel	Type	Weight Per cent C	Mn	Si	P	S
A	AISI 1020	0.20	0.89	0.17	0.015	0.064
B	AISI 1040	0.41	0.72	0.15	0.012	0.045
C	AISI 1080	0.82	0.84	0.12	0.012	0.050

Steel	Heat Treatment Data Austenitizing Temperature (°F)	Quenching Medium
A	1675	10% brine
B	1550	oil (fast quenching)
C	1550	oil (fast quenching)

0.20, 0.41 and 0.82% carbon as given in Table I, were investigated. The specimens were machined from 5/8 inch hot-rolled rods and austenitized in a lead bath at the temperatures listed in Table I. The austenitic grain size was always between ASTM 5 and 7. The hardened test bars were tempered at temperatures up to 1300 °F (705 °C); two sets of specimens were used for most temperatures, with one set being water-quenched and the other being air-cooled from the tempering treatment. After heat treatment, the specimens were cleaned by gentle wire brushing and were lightly polished with emery cloth. Microexamination indicated freedom from decarburization and gross segregation.

Two Baldwin SR-4 strain gages with an effective gage length of about 7/8 inch (Type A-1, A-3, or AD-1) were attached with Duco cement on opposite sides of the gage portion of each specimen. The gages were connected in series in order to compensate for bending effects. The cement was allowed to dry for at least 24 hours, and electrical tape was wound around the gages and lead wires to provide protection against handling damage. The test bars were loaded through two alloy steel chains to ensure axiality of stress; during the loading and unloading cycles, the specimens were immersed in a steel beaker of silicon oil maintained at 68 °F. A duplicate unstressed specimen with strain gages was kept in the oil bath in order to provide temperature compensation for the active strain gages.

The following procedure was adopted to establish the elastic limit. A small predetermined load was applied, then removed, and the specimen supported so that there was no applied force on it. The residual strain at zero load was obtained by balancing the strain indicator before and after the load application. This cycle was repeated with successively higher loads, and the permanent set (if any) or unloading was measured in each case. If the residual strain was zero, it was assumed that the corresponding stress was below the elastic limit. If a net tensile strain was observed, it was assumed that yielding had occurred. A typical curve is shown at the left in Fig. 2; the elastic limit could be detected within a strain sensitivity of about 2×10^{-6}.

Occasionally negative (compressive) residual strains appeared after loading below the elastic limit and then unloading, as shown in the center curve of Fig. 2. These initial negative strains were quite small, usually below 20×10^{-6}, but they reflected a real behavior of the specimen rather than of the strain gages since measurements of total length of several such specimens demonstrated that the test bar was actually shorter than its original length. In such cases, the elastic limit was defined as the stress above which the residual strain continued to increase toward the positive direction.

The above elastic limit criterion for each type of residual strain behavior was justified by the following observations. Specimens were

loaded repeatedly to a stress level below the selected elastic limit, and in each instance the residual strain remained zero or at the same negative value. However, when the stress level for repeated loading was raised above the elastic limit, an additional increment of residual strain was observed after each cycle. These successive increments of strain were larger, the higher the applied stress above the elastic limit. For example, the right hand curve in Fig. 2 (specimen B) was obtained with a sample which was a duplicate of that used for the central curve (specimen A).

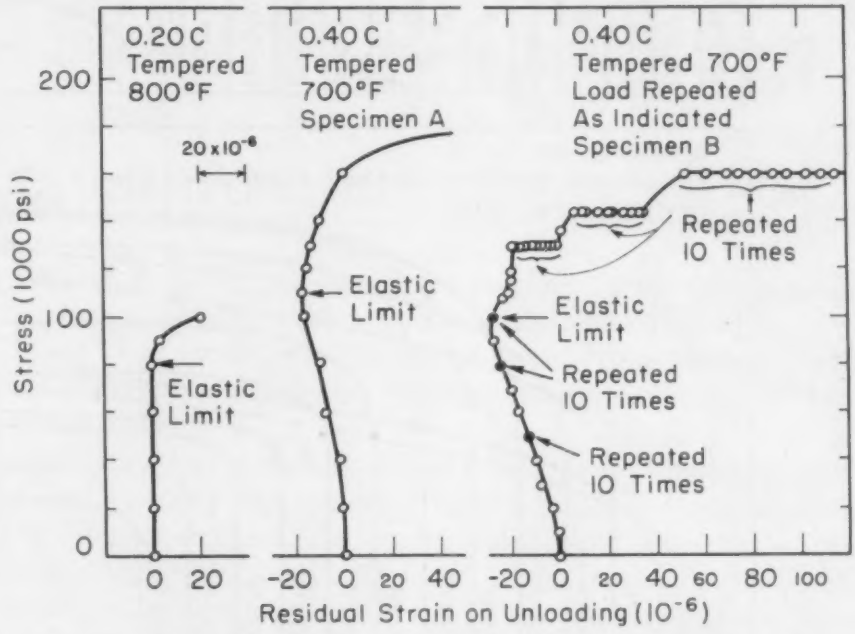


Fig. 2—Initial Early Portions of Typical Stress-Residual Strain Curves.

In the case of specimen B, however, the load was repeated ten times at 50,000, 80,000 and 100,000 psi with no change in residual strain. The elastic limit for this specimen was 100,000 psi (compared to 110,000 psi for specimen A). At higher stress levels, repeated applications of the load caused a progressively increasing tensile strain. Ten repetitions of a stress at 130,000 psi produced a 20×10^{-6} increase in strain; ten repetitions at 140,000 psi produced a 30×10^{-6} increase in strain; ten repetitions at 160,000 psi produced a 60×10^{-6} increase in strain. Similar findings were observed with a number of specimens of each steel, and this general behavior was considered to justify the adopted criterion of the elastic limit; namely, the stress above which the residual strain starts to increase toward the positive direction, whether an initial negative set occurs or not. The elastic limit defined in this way seems to have real physical significance in the problem at hand. Similar procedures involving cyclic loading were used by Bauschinger (3) and Bairstow (4) to define "true elastic limits."

The basic cause of the initial negative strains has not been ascer-

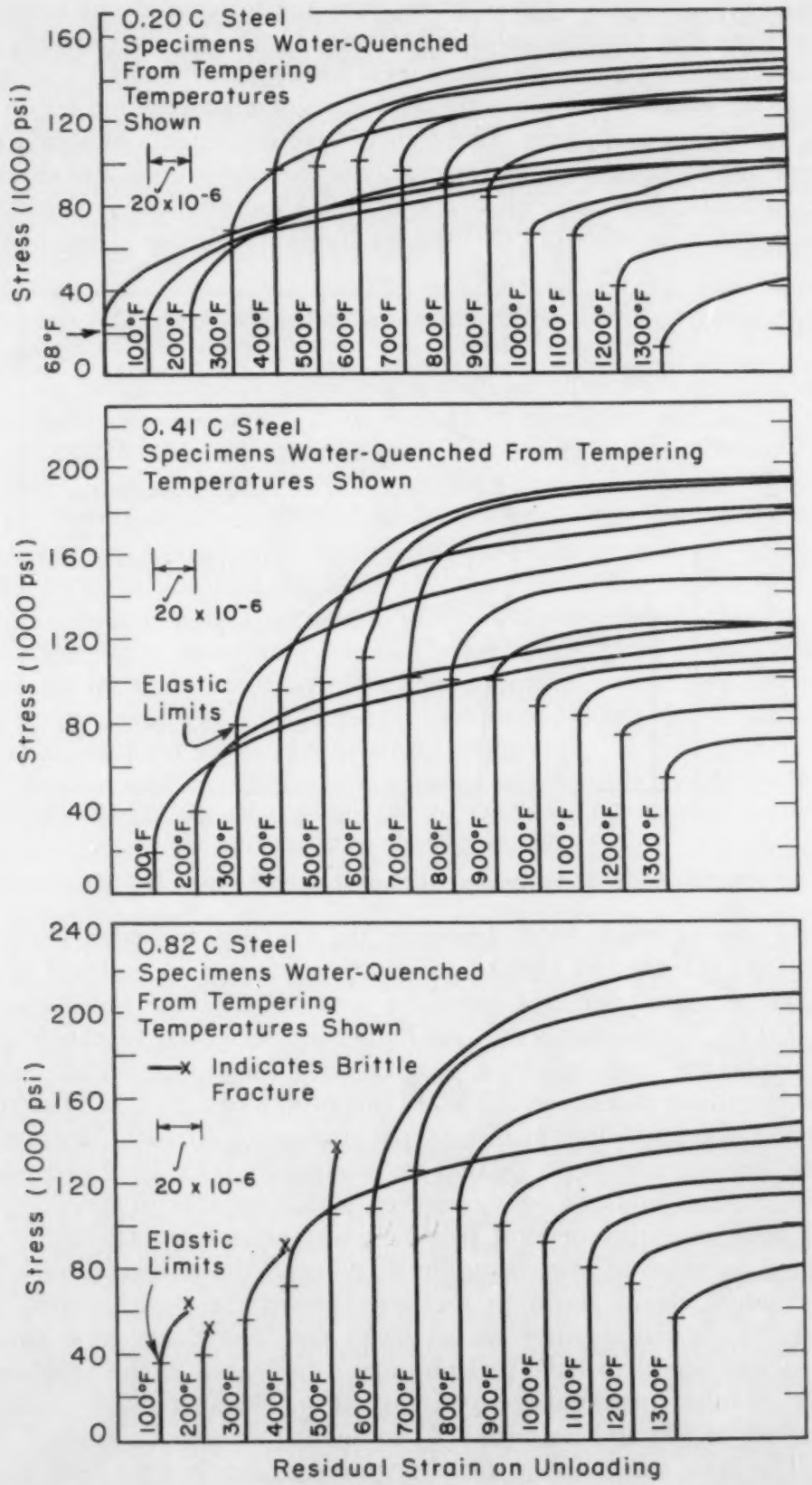


Fig. 3—Typical Stress-Residual Strain Curves.

Table II
Mechanical Test Results—0.20% Carbon Steel

Tempering Temp. °F	No. of Samples	* Elastic Limit 10^3 psi	** Yield Strength 10^3 psi	** Tensile Strength 10^3 psi	** Fracture Stress 10^3 psi	** Reduct. of Area Percent	** Elong. (2 inch) Percent	** Hardness Rockwell A
68	3	24	163	214	284	26	5	71
100	3	24	163	214	285	26	5	71
200	3	28	164	212	272	31	6	71
300	3	65	178	216	273	32	6	71
400	3	96	181	208	294	42	7	72
500	5	98	173	195	281	47	7	70
600	3	104	167	178	248	42	6	70
700	5	97	154	168	247	41	7	68
800	5	88	129	137	250	68	11	64
900	5	80	112	118	229	70	14	62
1000	7	65	100	108	218	71	15	59
1100	7	64	89	92	209	73	17	56
1200	7	46	78	86	208	77	21	54
1300	7	13	62	77	194	76	26	52

* Average value for samples water-quenched from tempering temperature.
** Average value for samples water-quenched and air-cooled from tempering temperature.

tained, but it is possible that they are associated with the presence of internal stresses. Although the negative strains were found from time to time in all three steels over the entire range of tempering temperatures, the phenomenon was not sufficiently reproducible to permit definite conclusions.

In each run, the cyclic loading was increased progressively until discontinuous yielding took place or until a residual strain of 2000 x 10^{-6} (0.2%) was reached. At small strains, anelastic effects on unloading were negligible, but during and after discontinuous yielding, rapid strain relaxation was observed. The total relaxation strains rarely exceeded 50 x 10^{-6} after straining to 2000 x 10^{-6}, confirming previous observations (1). When discontinuous yielding occurred, it was always preceded by a measurable amount of yielding (from 50 to

Table III
Mechanical Test Results—0.41% Carbon Steel

Tempering Temp. °F	No. of Samples	* Elastic Limit 10^3 psi	** Yield Strength 10^3 psi	** Tensile Strength 10^3 psi	** Fracture Stress 10^3 psi	** Reduct. of Area Percent	** Elong. (2 inch) Percent	** Hardness Rockwell A
68	2	20	—	—	—	—	—	77
100	3	20	191	243	(254)	2.5	1	78
200	3	40	204	(246)	(250)	1.6	1	77
300	3	80	217	—	—	0.2	1	77
400	3	96	226	(266)	(270)	1.4	2	76
500	5	101	218	248	298	31	6	75
600	3	112	208	226	300	38	7	73
700	5	106	186	202	284	44	7.5	71
800	5	102	154	—	—	—	—	68
900	5	102	130	144	242	55	11	66
1000	6	90	114	128	224	58	14.4	64
1100	7	84	99	116	213	62	15.6	62
1200	7	75	85	100	205	67	20	58
1300	7	56	71	84	189	70	25	55

* Average value for samples water-quenched from tempering temperature.
** Average value for samples water-quenched and air-cooled from tempering temperature.
Data in parentheses are doubtful because of brittle fracture.

Table IV
Mechanical Test Results—0.82% Carbon Steel

Tempering Temp. °F	No. of Samples	* Elastic Limit 10^3 psi	** Yield Strength 10^3 psi	** Tensile Strength 10^3 psi	** Fracture Stress 10^3 psi	** Reduct. of Area Percent	** Elong. (2 inch) Percent	** Hardness Rockwell A
68	1	30	—	—	—	—	—	83
100	3	38	—				—	82
200	4	40	—				—	82
300	4	55	—	BRITTLE			—	83
400	3	73	—	FRACTURE			—	81
500	5	103	—				—	80
600	4	108	260	—	—	—	3	77
700	5	128	230	253	322	35	7	76
800	6	108	192	215	303	42	9	72
900	6	100	160	188	265	43	11	70
1000	5	92	137	161	238	44	12	68
1100	6	82	115	135	208	49	16	65
1200	8	72	100	118	186	56	19	62
1300	7	58	85	101	177	55	22	59

* Average value for samples water-quenched from tempering temperature.
** Average value for samples water-quenched and air-cooled from tempering temperature.

500 x 10^{-6}) at lower stress levels. The magnitude of these pre-yield strains varied regularly with tempering temperature.

After the elastic limit determinations were completed, the strain gages were removed and the usual engineering tensile data were obtained.

Experimental Results

Typical stress vs. residual strain curves are shown in Fig. 3 for the three steels. It is evident that the elastic limits and initial yield behavior undergo considerable variation with tempering temperature. The mechanical test data are summarized in Tables II, III, and IV.

The elastic limits are plotted in Figs. 4, 5, and 6 as a function of the tempering temperature. It is seen that the elastic limits of the untempered steels are quite low, irrespective of the carbon content, and are all in the range of 20,000–30,000 psi. On tempering at 600 to 700 °F (315 to 370 °C), a maximum of 104,000 psi is reached for the 0.20C steel, 112,000 psi for the 0.41C steel, and 128,000 psi for the 0.82C steel. However, the elastic limits tend to remain relatively high over the broad tempering range of 400 to 800 °F (205 to 425 °C). These values then decrease appreciably with further tempering. For example, after tempering at 1300 °F (705 °C), the elastic limits are 13,000, 56,000 and 58,000 psi respectively for the three steels. It is worth emphasizing that the low tempering temperatures (below 400 °F) characteristic of high hardness and strength levels do not lead to high elastic limits.

The hardness, strength, and ductility parameters are also given in Figs. 4–6. Unlike the elastic limits, the hardness and strength properties generally decrease as the tempering temperature is raised, although the yield strength does reflect some initial increase at the lower

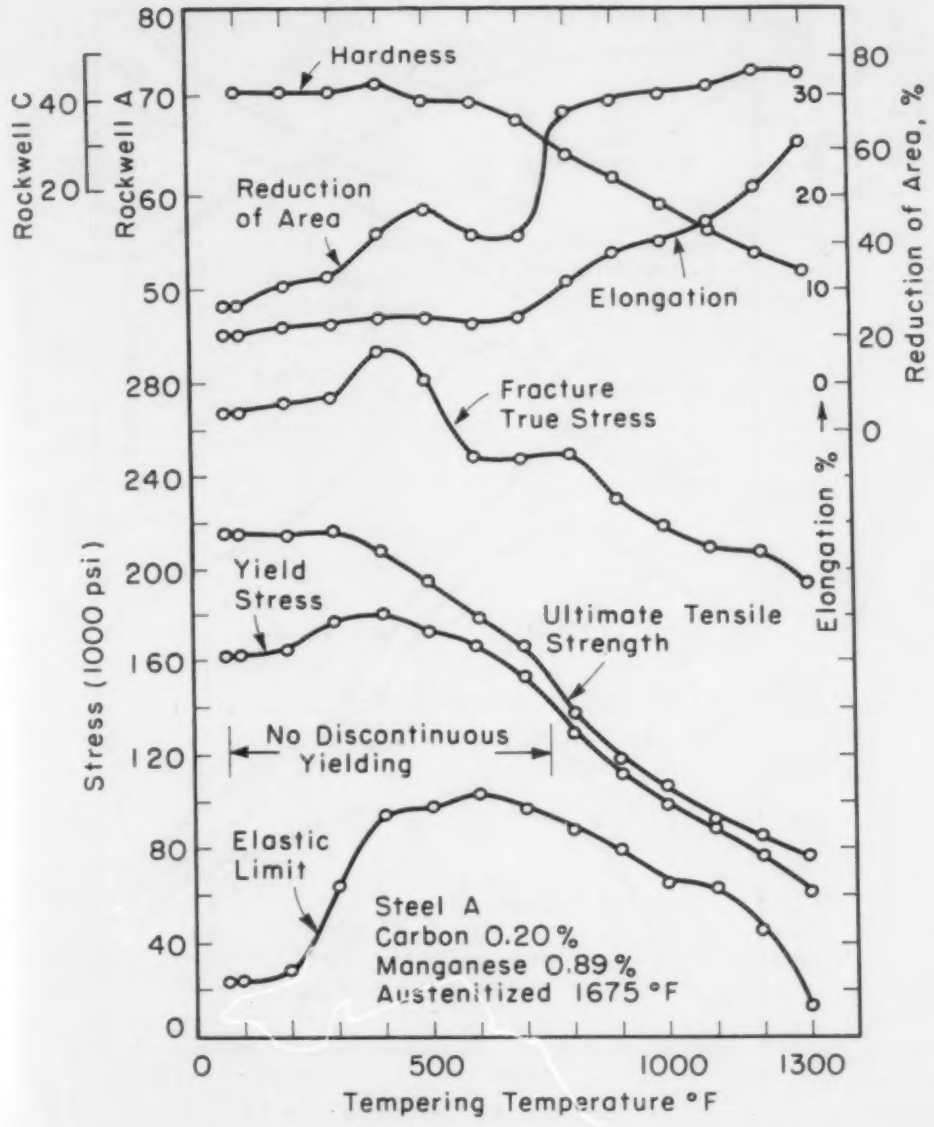


Fig. 4—Average Mechanical Test Results for 0.20% Carbon Steel.

tempering temperatures. The two higher carbon steels exhibit brittle fractures at the low tempering temperatures, and hence, the tensile data byond the elastic limit are both doubtful and incomplete in these regions.

The strength properties increase with the carbon content when compared at the same tempering treatment, as in Fig. 7. On this basis, the elastic limit is less affected by the carbon content than are the other strength parameters.

The mechanical properties of the three steels are replotted as a function of the hardness in Fig. 8 and 9. The yield and tensile strengths correlate directly with the hardness, notwithstanding the differences in carbon content. Two different criteria have been used for the yield

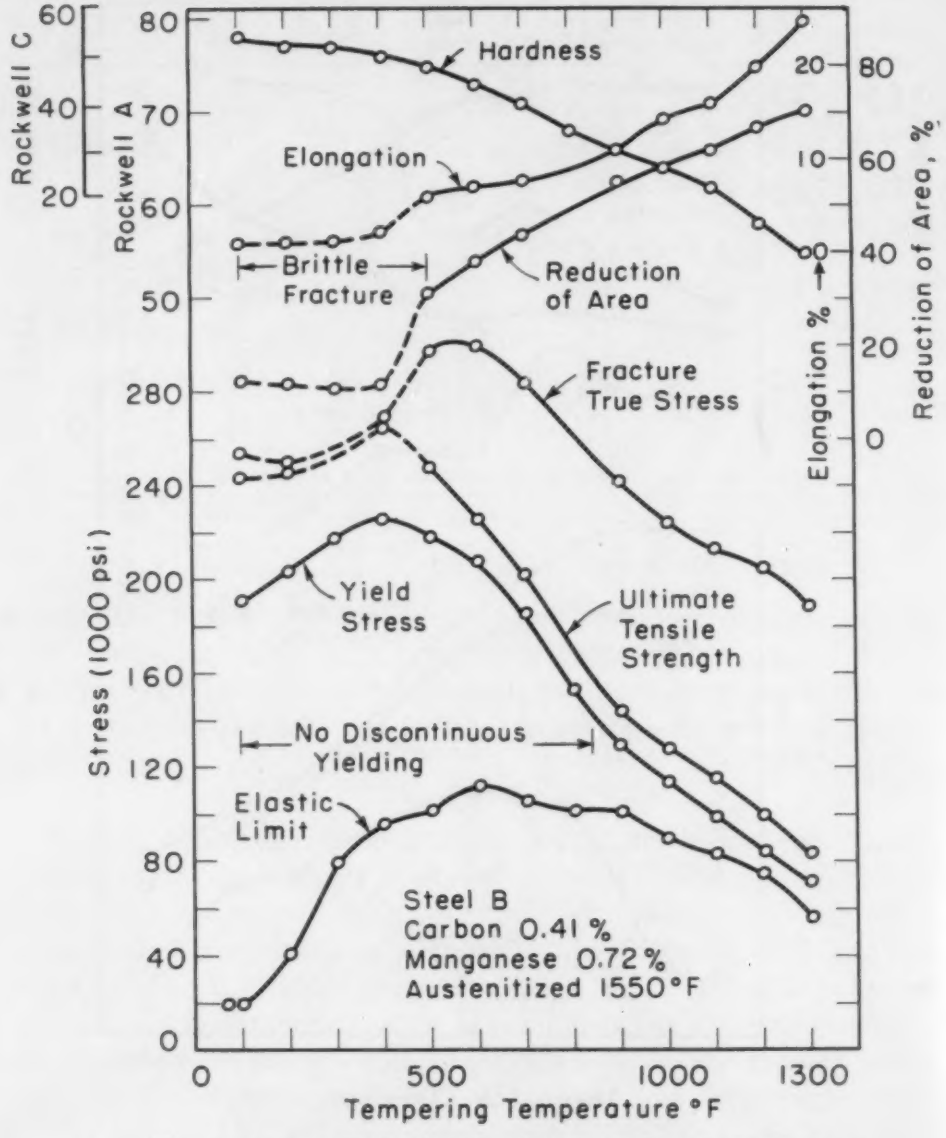


Fig. 5—Average Mechanical Test Results for 0.41% Carbon Steel.

strength curves. Specimens tempered at the higher temperatures undergo discontinuous yielding, and in such cases the upper yield point has been recorded.[2] At the lower tempering temperatures, discontinuous yielding does not take place, and the 0.2% yield stress was chosen. The fact that the yield strength curves in Figs. 4,5,6 and 8 have no sharp irregularities over the whole range of tempering temperatures or hardness values implies that both methods of indicating the yield strength are comparable in these steels.

Fig. 8 shows that the maximum elastic limit achieved on tempering not only increases somewhat with the carbon content, but occurs at higher hardness (and therefore strength) levels with increasing

[2] When discontinuous yielding occurred, little difference is found between the upper and lower yield points by the load-unload method.

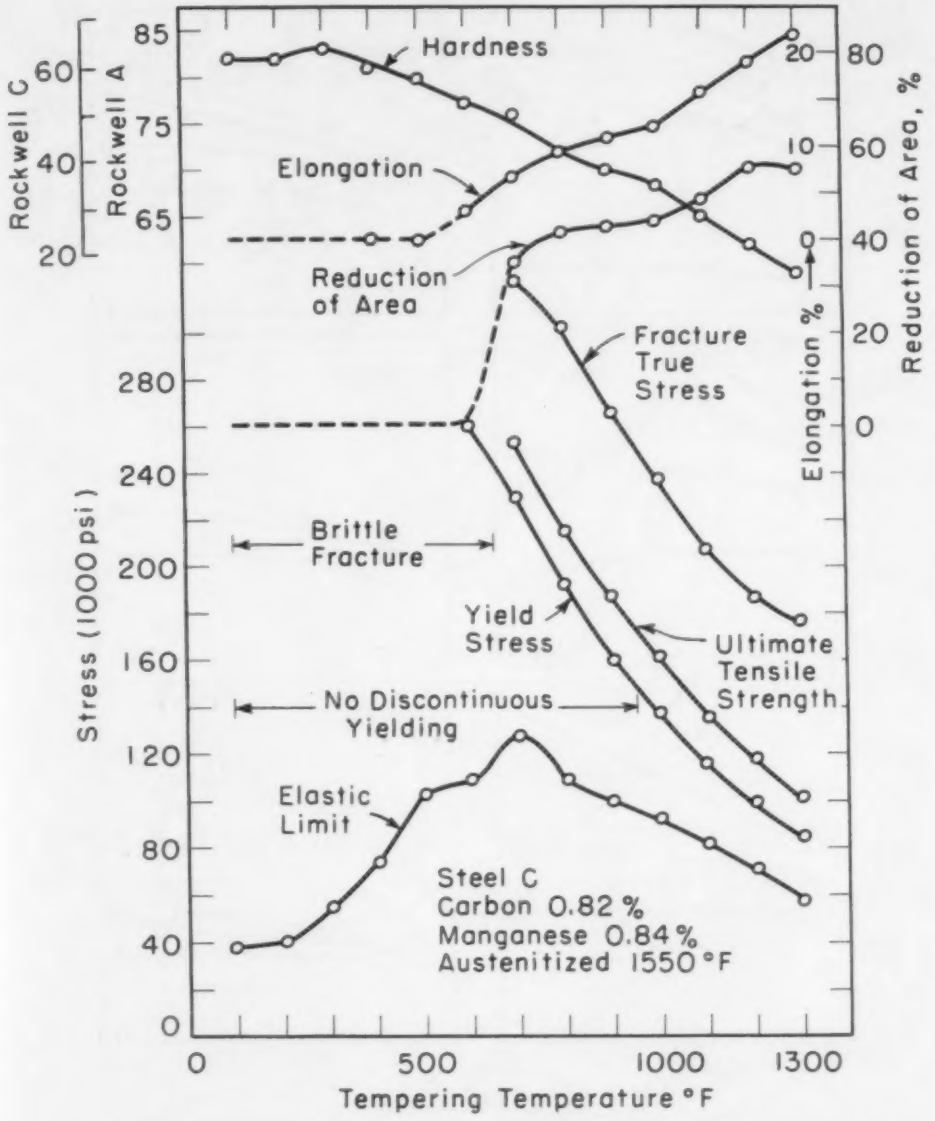


Fig. 6—Average Mechanical Test Results for 0.82% Carbon Steel.

carbon content. Below about Rockwell C-40 the elastic limits are slightly higher, for a given hardness, the lower the carbon content. However, when comparisons are made at the higher hardness levels, the elastic limits are decidedly inferior in the lower carbon steels because of the lower tempering temperatures that are required to retain the given hardness.

The fracture stress and reduction of area properties in Fig. 9 exhibit considerable scatter. In the higher hardness range, the incidence of brittle fracture undoubtedly contributes to the scatter. The reduction of area curves cross each other at about Rockwell C-40. Below this hardness, the greatest ductility at a given hardness level is obtained with the steel of lowest carbon content. Above Rockwell C-40, the greatest ductility is manifest in the highest carbon steel. This situation

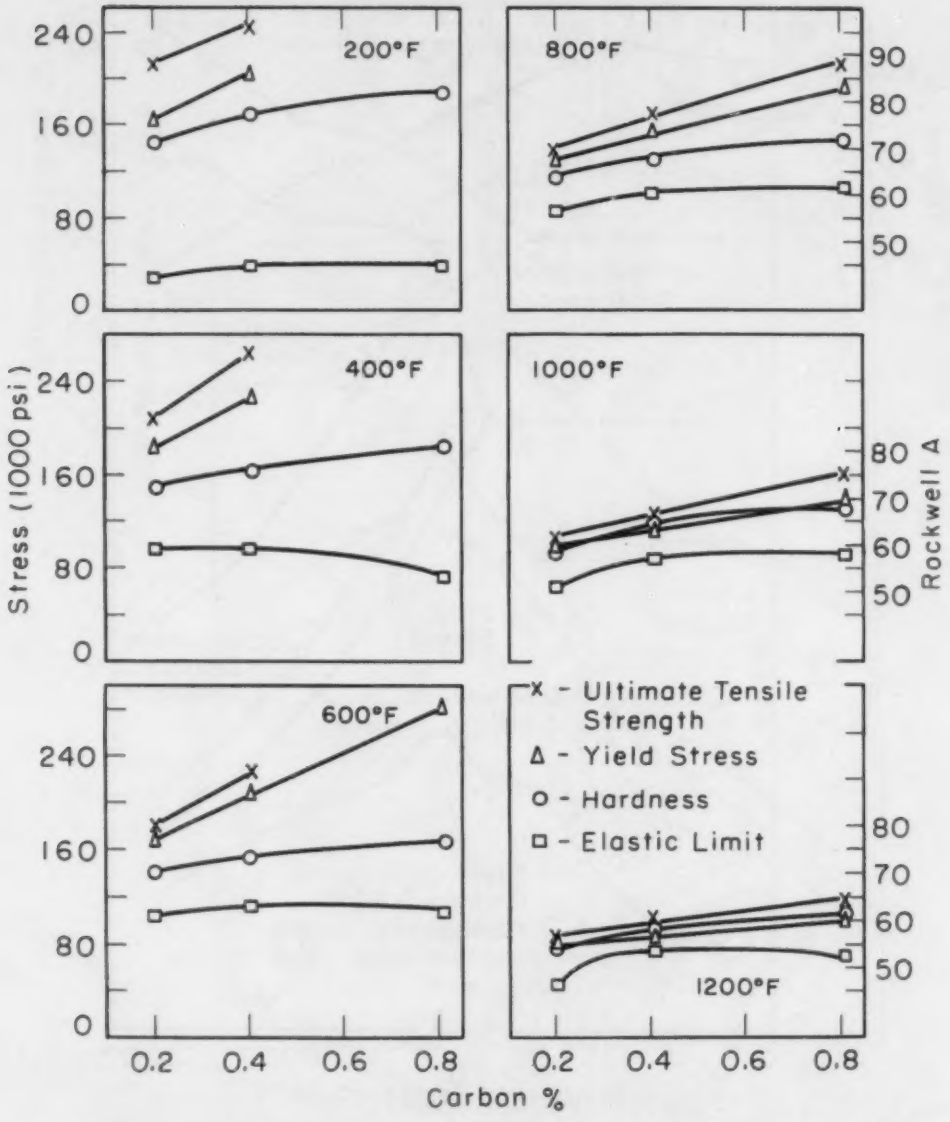


Fig. 7—Variation in Strength Parameters with Carbon Content After Various Tempering Treatments.

results from the fact that in order to maintain a hardness in excess of Rockwell C-40 with the 0.20% carbon steel, tempering above 500 °F (260 °C) cannot be used; whereas with the 0.82% carbon steel, such hardness value can be secured at higher temperatures, with a consequent improvement in ductility. The fracture stress relationships in Fig. 9 are probably related to the ductility behavior but the trends are not so obvious because of the uncertainty in the stress measurements due to the premature fractures that occur in the high hardness range.

Effect of Rate of Cooling from the Tempering Temperature

A comparison of specimens water-quenched from the tempering temperature with those air-cooled showed that the rate of cooling from

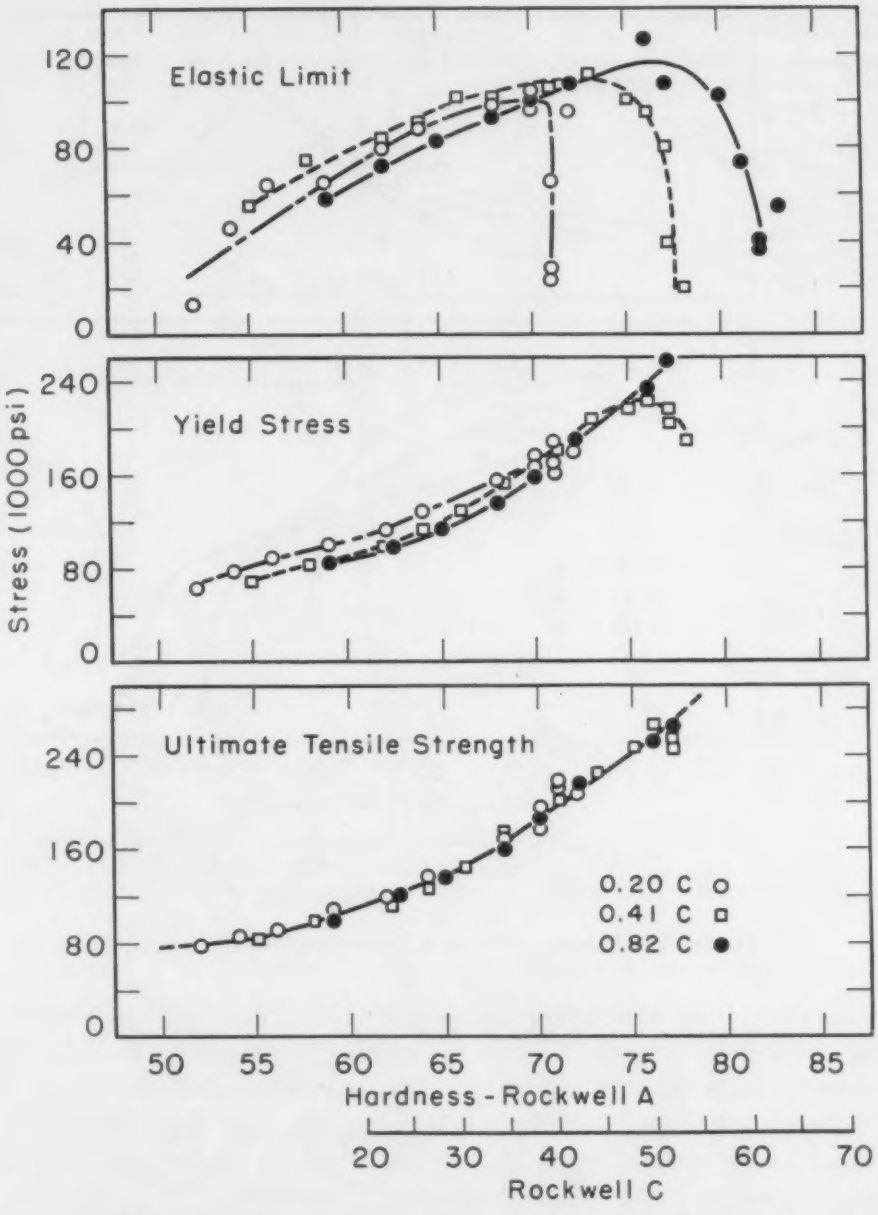


Fig. 8—The Relation Between Hardness and the Mechanical Properties.

the tempering has no significant effect on the conventional tensile properties. However, the elastic limits tend to be somewhat higher in the air-cooled condition (Tables V, VI and VII), the difference becoming most pronounced in the 0.20% carbon steel at the higher tempering temperatures. These tables also reveal that the amount of pre-yield plastic strain associated with the discontinuous yielding is appreciably larger in specimens water-quenched from the tempering temperature than in those that are air-cooled.

The ratio of elastic limit to yield strength is plotted in Fig. 10 as a function of the tempering temperature. Again the influence of cool-

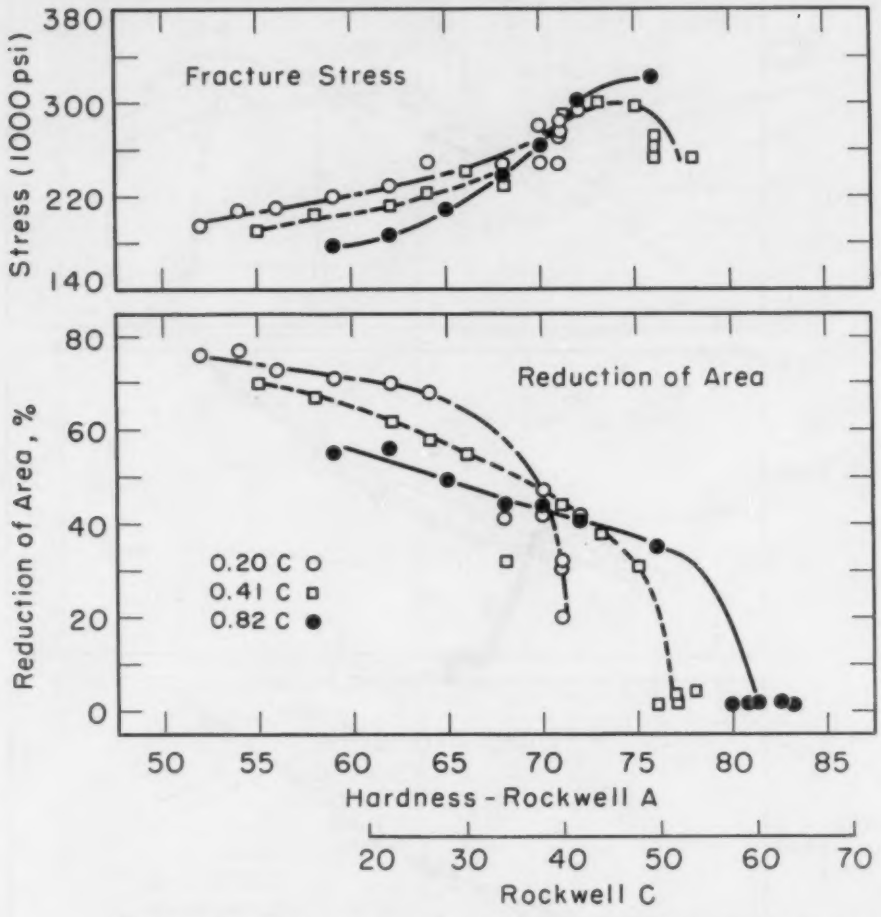


Fig. 9—The Relation Between Hardness and the Mechanical Properties.

ing rate from the tempering temperature is most conspicuous in the 0.20% carbon steel at the higher tempering temperatures. It is also interesting to note that at low tempering temperatures, the elastic limit may be only one-tenth of the yield strength, but the ratio generally improves as the tempering temperature is raised and reaches 0.7 to 0.9 in the vicinity of 1100°F (595 °C).

Elastic Limit after Isothermal Annealing

Elastic limits were measured for a few isothermally annealed specimens. Four tensile specimens of each steel were austenitized for 1 hour and quenched rapidly into a lead bath at 1100°F (595 °C). After holding at this temperature long enough for complete transformation (15 minutes), two samples of each steel were air-cooled and the other two water-quenched. Elastic limit and yield data are shown in Table VIII.

The elastic limits observed after isothermal annealing at 1100°F (595 °C) are considerably lower than for specimens tempered at the same temperature. In the 0.82% carbon steel, this is true even though

Table V
Effect of Cooling Rate on Elastic Limit and Yield Strength—0.20% Carbon Steel

Tempering Temp. °F	Cooling after Tempering	Elastic Limit 10^3 psi	Yield Strength 10^3 psi	Pre-Yield Strain 10^{-6}	Ratio E.L./Yield	Nature of Yield Phenomenon
68	WQ*	24	158	(2000)	0.15	Smooth-continuous
100	WQ	24	158	(2000)	0.15	Smooth-continuous
200	WQ	28	164	(2000)	0.17	Smooth-continuous
300	WQ	65	178	(2000)	0.37	Smooth-continuous
400	WQ	96	181	(2000)	0.53	Smooth-continuous
500	AC*	103	176	(2000)	0.59	Smooth-continuous
500	WQ	98	170	(2000)	0.58	Smooth-continuous
600	WQ	104	166	(2000)	0.62	Smooth-continuous
700	AC	97	152	(2000)	0.64	Smooth-continuous
700	WQ	97	156	(2000)	0.62	Smooth-continuous
800	AC	88	123	100	0.72	Slight drop of load
800	WQ	88	134	300	0.65	Slight drop
900	AC	94	114	120	0.82	Large drop
900	WQ	80	110	110	0.72	Large drop
1000	AC	82	100	160	0.82	Small drop
1000	WQ	65	100	500	0.65	Smooth
1100	AC	73	89	90	0.83	Large drop
1100	WQ	64	91	200	0.71	Large drop
1200	AC	68	76	5	0.90	Large drop
1200	WQ	46	81	400	0.57	Small drop
1300	AC	38	60	160	0.62	Large drop
1300	WQ	13	64	(2000)	0.20	Small drop

* WQ = water-quenched
* AC = air-cooled
Values in parentheses indicate that the 0.2% yield is listed.

the annealed and tempered specimens have the same hardness. The effect of water quenching vs. air cooling after the isothermal anneal is similar to that after tempering; the elastic limit is lower and the pre-yield strain is larger in the water-quenched specimens than in the air-cooled ones.

Discussion of Results

It is clear from this work that high elastic limits are not necessarily obtained at high strength and hardness levels. Such consideration might be of some importance in spring and bearing applications, wherein permanent set has been observed after repeated loading at stresses well below the engineering yield strength. Furthermore, the relatively low ratio of elastic limit to yield strength in slightly tempered steels may become a significant limitation in the development of very high strength steels.

In fact, it has been reported by Aitchison (5) that the proportional limit in fully hardened steels is much lower than would be expected on the basis of hardness and strength; he also reported that the proportional limit could be improved by tempering at 600 °F (315 °C). Similar data were obtained by Rees (6) Brown (7) and Edwards

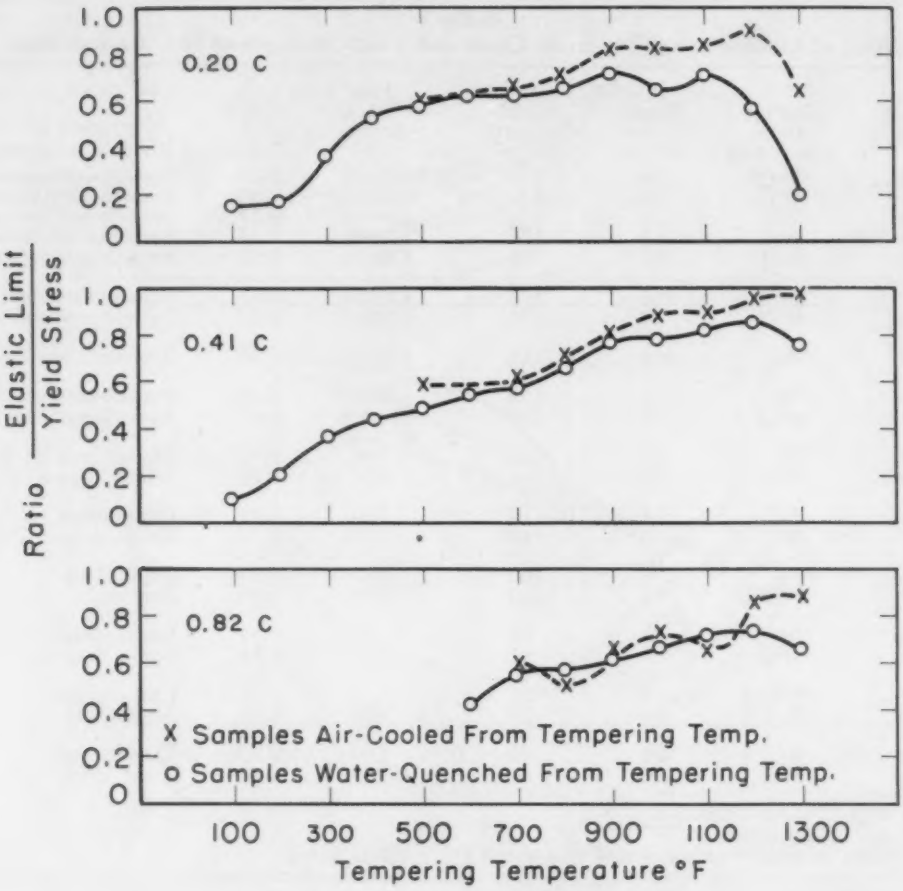


Fig. 10—Effect of Cooling Rate from Tempering Temperature.

(8,9) who showed that highly cold drawn steel wires have low proportional limits which can be raised by subcritical annealing. The curves of the proportional limit vs. annealing temperature are quite similar to those for the elastic limit vs. tempering temperature observed here. The main difference is that the proportional limit variations in the cold-worked steels are matched by corresponding changes in hardness and strength, whereas this is not the case for the elastic limit in tempered steels. Clearly, the elastic limit behavior must be kept in mind if the useful strength of steel is to be realized.

It is conceivable that these elastic limit and initial yield phenomena may be related to fatigue behavior, inasmuch as repeated loading above the elastic limit results in progressive residual strain. Such a correlation would be in line with the suggestion of early investigators (3,4,10).

A possible explanation for the low elastic limits in as-hardened steels lies in the presence of quenching and transformation stresses. Both micro- and macrostresses having tensile components in the direction of tensile loading should promote localized yielding and thereby cause an effective lowering of the elastic limit. Thus, the improvement

Table VI
Effect of Cooling Rate on Elastic Limit and Yield Strength—0.41% Carbon Steel

Tempering Temp. °F	Cooling after Tempering	Elastic Limit 10^3 psi	Yield Strength 10^3 psi	Pre-Yield Strain 10^{-6}	Ratio E.L./Yield	Nature of Yield Phenomenon
100	WQ*	20	191	(2000)	0.10	Smooth-continuous
200	WQ	40	204	(2000)	0.20	Smooth-continuous
300	WQ	80	217	(2000)	0.37	Smooth-continuous
400	WQ	96	226	(2000)	0.42	Smooth-continuous
500	AC*	120	208	(2000)	0.58	Smooth-continuous
500	WQ	101	212	(2000)	0.48	Smooth-continuous
600	WQ	112	208	(2000)	0.54	Smooth-continuous
700	AC	112	186	(2000)	0.60	Smooth-continuous
700	WQ	106	187	(2000)	0.57	Smooth-continuous
800	AC	108	152	(2000)	0.71	Smooth-continuous
800	WQ	102	155	—	0.66	Smooth-continuous
900	AC	102	128	160	0.80	Very slight drop of load
900	WQ	102	132	160	0.78	Very slight drop
1000	AC	95	112	36	0.89	Very slight drop
1000	WQ	90	115	200	0.78	Very slight drop
1100	AC	86	97	16	0.89	Small drop
1100	WQ	84	102	90	0.82	Small drop
1200	AC	80	84	5	0.95	Sudden drop
1200	WQ	75	87	96	0.86	Slight drop
1300	AC	67	68	2	0.98	Large drop
1300	WQ	56	74	130	0.76	Slight drop

* WQ = water-quenched
* AC = air-cooled
Values in parentheses indicate that the 0.2% yield is listed.

in elastic limit on tempering may be associated with the partial relief of stress (11). The existence of retained austenite in the hardened steel and its removal on tempering may also play a role, but this cannot be the only factor because the effects are quite pronounced even in the 0.20% carbon steel. In addition, the lowering of the elastic limit by water quenching, rather than air cooling from the tempering or isothermal annealing temperature is consistent with the internal stress hypothesis.

Thus, it appears that tempering at 500 to 700 °F (260 to 370 °C) to achieve the maximum elastic limit in each steel represents an optimum combination of stress relief and retention of strength. More complete stress relief at higher tempering temperatures is evidently offset by decreasing resistance to slip due to the coalescence of the carbides. Accordingly, one might expect that the further stress relief above 700 °F (370 °C) would result in higher ratio of elastic limit to yield strength. The ratios of elastic limit to yield strength in Tables V, VI and VII demonstrate that this is actually the case.

The principal influence of the carbon content on the elastic limit at a given hardness level lies mainly in the effect of carbon on the tempering temperature required to achieve the given hardness. For

Table VII
Effect of Cooling Rate on Elastic Limit and Yield Strength—0.82% Carbon Steel

Tempering Temp. °F	Cooling after Tempering	Elastic Limit 10^3 psi	Yield Strength 10^3 psi	Pre-Yield Strain 10^{-6}	Ratio E.L./Yield	Nature of Yield Phenomenon
100	WQ*	38	Premature Fracture			
200	WQ	40	Premature Fracture			
300	WQ	55	Premature Fracture			
400	WQ	73	Premature Fracture			
500	AC*	—	Premature Fracture			
500	WQ	103	Premature Fracture			
600	WQ	108	260	(2000)	0.42	Smooth-continuous
700	AC	136	228	(2000)	0.60	Smooth-continuous
700	WQ	128	231	(2000)	0.55	Smooth-continuous
800	AC	97	196	(2000)	0.50	Smooth-continuous
800	WQ	108	189	(2000)	0.57	Smooth-continuous
900	AC	101	159	(2000)	0.64	Smooth-continuous
900	WQ	100	161	(2000)	0.61	Smooth-continuous
1000	AC	98	136	320	0.72	Very slight drop of load
1000	WQ	92	137	(2000)	0.67	Smooth
1100	AC	91	114	140	0.65	Small drop
1100	WQ	82	116	315	0.71	Small drop
1200	AC	84	98	36	0.86	Marked drop
1200	WQ	72	98	220	0.73	Marked drop
1300	AC	73	83	8	0.88	Marked drop
1300	WQ	58	88	415	0.66	Marked drop

* WQ = water-quenched
* AC = air-cooled
Values in parentheses indicate that the 0.2% yield is listed.

Table VIII
Comparison of Annealed and Tempered Specimens Air-Cooled and Water-Quenched from 1100 °F

	Cooling Rate	0.20% Carbon Steel 1100 °F Anneal	0.20% Carbon Steel 1100 °F Temper	0.41% Carbon Steel 1100 °F Anneal	0.41% Carbon Steel 1100 °F Temper	0.82% Carbon Steel 1100 °F Anneal	0.82% Carbon Steel 1100 °F Temper
Hardness Rockwell A		48	56	56	62	65	65
Elastic Limit (10^3 psi)	WQ*	30	64	48	84	48	82
	AC*	36	73	54	86	76	91
Yield Strength (10^3 psi)	WQ	53	91	64	102	96	116
	AC	51	89	62	97	95	114
Pre-Yield Strain 10^{-6}	WQ	155	200	140	90	2000	315
	AC	18	90	4	16	36	140
Ratio Elastic Limit / Yield Strength	WQ	0.56	0.71	0.75	0.82	0.50	0.71
	AC	0.70	0.83	0.87	0.89	0.80	0.65
Nature of Yield Phenomenon	WQ	Small drop	Large drop	Small drop	Small drop	Smooth	Small drop
	AC	Large drop	Large drop	Large drop	Small drop	Small drop	Small drop

* WQ = water-quenched
* AC = air-cooled

example, with hardness values above Rockwell C-40 the elastic limit decreases with decreasing carbon content because the tempering temperatures must be reduced below the optimum range to maintain the required hardness.

Where discontinuous yielding is observed, measurable plastic flow occurs prior to the yield point. This is in confirmation of previous work (1,2), and is consistent with the data of Clark et al (12,13) and Winlock and Leiter (14) who have found pre-yield strains even at high loading rates. In the present experiments, the pre-yield strains are markedly increased, and the yield behavior tends to switch from the discontinuous to the continuous type, if the specimens are water-quenched instead of air-cooled from the tempering or isothermal annealing temperature. The fact that these differences became more pronounced in the lower carbon steel at temperatures above 900 °F (480 °C), suggests that a precipitating reaction may be operative in the slowly cooled specimens, causing a reduced pre-yield strain and a propensity toward discontinuous yielding. This cooling rate effect is reminiscent of temper embrittlement and it is possible that further work along these lines with alloy steels may disclose a relationship between the initial yield point behavior and notch sensitivity.

The conventional tensile properties vary in a fairly regular way with tempering temperature, although the 0.20% carbon steel does exhibit some evidence of 500 °F (260 °C) embrittlement in the reduction of area curve (Fig. 4). The latter observation is somewhat unusual since the 500 °F-embrittlement is generally detected only by notched-bar testing or by the reduction of area at subzero testing temperatures (15). In any event, it is worth noting that the 500 °F-embrittlement and the maximum elastic limit occur in the same tempering range. The 500 °F-embrittlement has been identified with the formation of cementite films at the martensitic boundaries at the onset of the third stage of tempering (16). If the improvement in elastic limit on tempering is attributable to stress relief, as tentatively suggested here, it is conceivable that the phenomena may be separated in tempering experiments with other steels, thus permitting the attainment of high elastic limits without the occurrence of simultaneous embrittlement. Such an investigation is underway.

Conclusions

The following conclusions have been reached concerning the elastic limit and the mechanical properties of hardened and tempered steels containing 0.20, 0.41 and 0.82% carbon.

1. The elastic limit can be determined to within a strain sensitivity of about 2×10^{-6} by the use of electrical resistance strain gages and a progressive load-unload technique. Initial yielding phenomena can also be studied conveniently by this method.

2. The elastic limit is affected by tempering in a manner quite different from the conventional tensile properties. Values 20,000–30,000 psi are obtained for the as-hardened steels, and these rise to 100,000–130,000 psi on tempering at 500 to 700 °F (260 to 370 °C). With increasing tempering temperature, the elastic limits decrease to 13,000–60,000 psi after tempering at 1300 °F (705 °C). The practical implications of these findings are discussed.

3. The indications are that internal stresses due to hardening or quenching from high tempering temperatures have a detrimental effect on the elastic limit. On the other hand, rapid cooling from high tempering temperatures enhances the pre-yield strain and tends to avoid discontinuous yielding.

4. When the mechanical properties are considered as function of hardness, the following interrelations are observed:

a) The yield and ultimate tensile strengths increase with hardness and are essentially independent of carbon content.
b) Ductility decreases with increasing carbon content at hardness levels below Rockwell C-40, but at higher hardness levels the reverse is true.
c) The maximum attainable elastic limit for a given hardness above Rockwell C-40 increases with carbon content, the maximum elastic limit corresponding to a tempering temperature in the range 500 to 700 °F (260 to 370 °C).

Acknowledgments

The authors wish to express their thanks for the able assistance of Sergei Lorris, who was responsible for most of the specimen preparation and heat treatment, and much of the mechanical testing; and to Robert Huston and George Black who were responsible for machining the large number of specimens required. The investigation was conducted under sponsorship of the Office of Naval Research.

References

1. C. S. Roberts, R. C. Carruthers and B. L. Averbach, "The Initiation of Plastic Strain in Plain Carbon Steels," TRANSACTIONS, American Society for Metals, Vol. 44, 1952, p. 1150.
2. B. L. Averbach and H. Muir, Discussion to Vreeland, Wood and Clark's paper (reference 13), TRANSACTIONS, American Society for Metals, Vol. 45, 1953, p. 632.
3. J. Bauschinger, "Changes of the Elastic Limit and Modulus of Elasticity in Various Metals" (in German), *Zivilingenieur,* Vol. 27, 1881, p. 289.
4. L. Bairstow, "The Elastic Limits of Iron and Steel Under Cyclical Variations of Stress," *Transactions,* Royal Society, (London) Section A, Vol. 210, 1911, p. 35.
5. L. Aitchison, "Some Fundamental Defects of Hardened Steels," TRANSACTIONS, American Society for Steel Treating, Vol. 5, 1924, p. 491.
6. S. H. Rees, "Some Properties of Cold-drawn and of Heat-treated Steel Wire," *Journal,* Iron and Steel Institute, (London), Vol. 118, No. 2, 1928, p. 195.

7. R. S. Brown, "Plastic Strain and Hysteresis in Drawn Steel Wire," *Journal,* Iron and Steel Institute, (London) Vol. 162, 1949, p. 189.
8. C. A. Edwards, H. N. Jones and B. J. Walters, "A Study of Strain-Age Hardening in Mild Steel," *Journal,* Iron and Steel Institute, Vol. 139, 1939, p. 341.
9. C. A. Edwards, *The Structure and Properties of Mild Steel,* London: Garnet Miller, 1st edition, 1952, p. 118–169.
10. A. Wöhler, *Zeits. fürBauwesen,* Nos. 8, 10, 13, 16, 1858. Abstracted in *Engineering* (London), Vol. 11, 1871.
11. H. J. Snyder, "The Effect of Quenching and Tempering on Residual Stresses in Manganese Oil Hardening Tool Steel," TRANSACTIONS, American Society for Metals, Vol. 45, 1953, p. 605.
12. D. S. Clark and D. S. Wood, "Time Delay for the Initiation of Plastic Deformation at Rapidly Applied Constant Stress," *Proceedings,* American Society for Testing Materials, Vol. 49, 1949, p. 717.
13. T. Vreeland, Jr., D. S. Wood and D. S. Clark, "A Study of the Mechanism of the Delayed Yield Phenomenon," TRANSACTIONS, American Society for Metals, Vol. 45, 1953, p. 620.
14. J. W. Winlock and R. W. E. Leiter, "Some Factors Affecting the Plastic Properties of Sheet and Strip Steel and Their Relation to Deep Drawing Properties," TRANSACTIONS, American Society for Metals, Vol. 25, 1937, p. 163.
15. E. J. Ripling, "Tensile Properties of Heat Treated Low Alloy Steel at Subzero Temperatures," TRANSACTIONS, American Society for Metals, Vol. 42, 1950, p. 439.
16. B. S. Lement, B. L. Averbach, and Morris Cohen, "Microstructural Changes on Tempering Iron-Carbon Alloys," TRANSACTIONS, American Society for Metals, Vol. 46, 1954, p. 851.

DISCUSSION

Written Discussion: By Edward Dugger, senior project engineer, Design Criteria Section, Wright Air Development Center, Wright-Patterson Air Force Base, Ohio.

The investigation by the authors into the determination of the actual elastic limit of steel is of particular interest because of unpublished work by the writer which gave results very similar to those obtained by the authors.

The purpose of the writer's investigation was to determine the relationship between the tensile properties and the magnetic or electrical properties of metals. To accomplish this, a high frequency instrument known as the Cyclograph[3] was used. This instrument has a test coil which is placed around the tensile specimen. Hysteresis losses occurring in the field of the test coil due to the application of load to the test specimen decreases the output of the oscillator and this decrease can be measured.

The general type of curve that occurs in such a test is that as the tensile load increases, the core hysteresis losses also increase until a maximum core loss is obtained. After this, as the load continues to increase, the core losses decrease. This, as is readily seen, creates a peak core loss.

SAE 4340 steel, heat treated to five nominal strength levels ranging from 110,000 psi to 210,000 psi was used. The core loss peaks occurred at stresses ranging from approximately 17 to 60% of the proportional limit of the material. In addition, considering the strength range of the material, the stresses at these peaks did not show much variation, ranging from 21,000 to 31,000 psi.

[3] P. E. Cavanagh, "Stress Comparisons by Correlation with High Frequency Magnetic and Eddy Current Losses," TRANSACTIONS, American Society for Metals, Vol. 36, 1946, p. 137.

Another peculiarity of this type test was that after loading beyond that load which created the peak but below the proportional limit a second loading decreased the peak core loss at least 35% and, more significantly, the stress at which the peak occurred increased. This indicates that the first loading effectively changed the physical and mechanical properties of the material. The loading apparently causes small irreversible changes in internal microstresses which, as a result, change the magnetic properties and creates a specimen which has basically different properties at least up to the original stress applied. This change is reflected in the Cyclograph readings.

The same sort of phenomena as shown by the SR-4 gage and Cyclograph was also shown by Cornelius [4] using a coil around a specimen but with change in frequency with applied stress as the measuring parameter. In this case, a reversal in frequency also occurred at a load appreciably below the observable proportional limit. He also indicates a marked proportional limit by this method.

In conjunction with the use of the Cyclograph an isolated test was made using SAE 1020 steel having an ultimate tensile strength of 97,000 psi. This involved a comparison of the elastic limit as determined by Tuckerman optical strain gages and the location of the Cyclograph peak. The elastic limit as determined by the Tuckerman gages using the same procedure, incidentally, as employed by the authors was 51,000 psi whereas the Cyclograph peak occurred at 33,800 psi. While this was only a single test it tends to substantiate the statements by the authors and Cornelius that the elastic limit value would become less with the improvement in strain measuring methods.

The question will probably arise, however, as to whether this very definite change that occurs prior to the proportional limit can actually be called the elastic limit as now universally defined and there may possibly be some basis for argument. Each of the measuring instruments which have located this phenomena are sensitive to electrical or magnetic changes and this undoubtedly is a factor in these results. On the other hand, these methods also have definite advantages in studying action of metals under stress.

Written Discussion: By W. R. Johnson and J. H. Maker, Wallace Barnes Company, Division of Associated Spring Corp., Bristol, Conn.

It is gratifying to see this interest in the field of high strength and hardness properties of steel. The authors have performed a valuable service in helping to re-evaluate and disseminate information which has been empirically developed in the spring industry over many years of production. Their finding that higher carbon levels are important in raising stress carrying capacity through the effect on tempering temperature is one of the ruling facts of the spring industry. This is in contrast to the relatively new studies of high strength levels in alloy structural steels, whose proponents recommend carbon levels as low as possible to promote ductility. Neglecting such special applications as elevated temperature service, the spring industry has not had available any alloy steels which add sufficiently to the effect of the high carbon (0.70 to 1.00%) to warrant their use in most applications, unless an unusually heavy section demands the use of a medium carbon alloy steel for hardenability. However, some use is made of medium carbon alloy steels for combinations of high elastic limit and ductility since the alloy additions permit the use of higher tempering temperatures. We are looking forward to the authors'

[4] J. R. Cornelius, "The Rapid Determination of the Elastic Limit in Steels," *Machinery* (London), Vol. 69, November 7, 1946, p. 590.

further work toward high elastic limits, and hope their investigation will include alloy steels with higher carbon levels.

The authors' comment "that high elastic limits are not necessarily observed at high strength and hardness levels" has been often observed. This is an important study, for the yield strength of the material, and not the hardness or tensile strength determines the engineering serviceability. The material used for highly stressed springs, such as clock springs (1.00% carbon) has an elastic limit so low after hardening, despite a 100% martensitic structure, that strip stock will take a coil set from the reeling drum if the tempering temperature is too low. Such material will produce springs of low torque due to their setting in service, despite the fact that the hardness and tensile strength may be the same as for satisfactory stock.

It might be of interest to note that this 1% carbon steel, is spheroidized before hardening and austenized so that a considerable amount of undissolved carbides remain. This undissolved carbide seems to act as favorably in the elastic limit as if it were dissolved. The extreme case of high elastic limit is in the case of watch springs which contain up to 1.15% carbon. The tensile strengths of this material are often above 350,000 psi with proportional limits of over 200,000 psi. (We have not measured the elastic limit with the authors' precision.) In considering the effect of high carbon, it should be borne in mind that these outstanding properties are not obtained in heavy sections.

The authors' tentative explanation of internal stresses causing the low elastic limits is in complete agreement with our thinking. We find that tempering temperatures up to 500 °F for clock spring steel increase its resistance to set. From 500 to 600 °F there is a sharp drop in elastic limit accompanied by an increase in toughness. At 650 °F and above, our data agree with that reported by the authors. We have also found experimentally that if this hardened and tempered spring steel is cold-worked slightly, the elastic limit is severely depressed though the hardness and tensile are almost unaffected. A temper after the cold work, to relieve the internal stress, restores the elastic limit without affecting the tensile strength, a procedure long used in the industry.

From time to time there have been accounts of the tempering of high carbon steels for long periods of time at relatively low temperatures to give combinations of high hardness and ductility. We would like to know the tempering times used in the authors' work, and hear their opinion on low tempers for long time cycles to reduce the internal stress. We hope that this work will be the forerunner of other studies pertinent to the field of high elastic limit load bearing structures.

Written Discussion: By N. H. Polakowski, LaSalle Steel Co., Chicago.

This paper deals with two distinctly different problems:

Firstly, the authors describe experiments which, in their opinion, prove that the so called "elastic limit" is a real and physically significant property of heat treated carbon steels. Secondly, they show that quench-hardened but untempered steels exhibit perceptible permanent deformations at quite low stresses, and they attempt to explain this effect.

Insofar as the first question is concerned, I believe that the term "truly elastic behavior" in the sense used in the paper implies exactly equal specimen dimensions before and after an application of any external stress below the alleged elastic limit. The curves in Fig. 2 would suggest that this condition

was not generally realized although I agree that the negative strains shown are confounding. But whatever the reason for this irregularity may be, the implication is that the authors have actually developed artificial elasticity in tension by the classical method of repeated loading.

In order to convey conviction, the values of the alleged elastic limits should have been double checked by applying compressive loads to the specimens previously tested in tension. Only an absence of a Bauschinger effect could be accepted as a conclusive proof of their claim.

Turning to the problem of semiplastic behavior of fully hardened steel at low stresses it may be recalled that the basic facts about this phenomenon were known for a very long time. However, it would be an overstatement to say that its fundamental cause had been positively identified.

The present authors endorse the old explanation attributing this peculiar behavior of untempered austenite to locked-up thermal and transformation stresses. On this assumption we would expect the residual stresses to exhibit a spectacular drop upon heating the specimen to between 200 and 400 °F because the raise of the elastic limit is most pronounced in this range (cf. Fig. 3 and Tables I–III). Bühler's experiments[5] indicate, however, that the residual stresses are virtually unaffected by heating to 300 °F and very little by tempering at about 550 °F. Incidentally, Boegehold's views[6] seem to be similar to those held by Bühler in this matter.

An alternative, but highly unorthodox and therefore not widely known explanation of the initial plasticity of frech Fe-martensite was advanced several years ago be Kishkin[7]. Kishkin suggested that untempered or even lightly tempered martensite is quite soft initially but it strain hardens rapidly when being plastically deformed. He has attributed this high rate of strain hardening to the formation of a highly dispersed cementite from the elementary carbon contained in the martensite. To prove his point, Kishkin deformed by stretching a number of quench-hardened and lightly tempered steels and investigated by means of chemical extraction the form of carbon at various stages of deformation. The resulting curves showed a gradual increase of Fe_3C content with increasing extension, the rate of carbide production being extremely high in the initial stages of the test. According to the same source, unstrained martensite was supposed to contain elementary carbon only but no cementite.

On this hypothesis, the gradual improvement of the elastic properties on tempering is also due to a precipitation of cementite caused by heating and, as is well known, the tempering process is known to be associated with iron carbide formation. In other words, Kishkin believes that tempering increases and not decreases the initial hardness of martensite, a possibility which seems logical if the main argument is regarded as acceptable or at least feasible.

The aforesaid concept is somewhat bizarre and it contains several oversimplifications and loopholes. However, there are certain experimental facts in existence which lend it a measure of support and which were never explained on their own right. It would lead too far to enumerate and discuss these here but I would be interested to hear any comments that the authors may care to make from the fundamental angle.

---

[5] H. Buchholtz and H. Buhler, "Determination of Residual Stresses in Steel Cylinders from Stress-Time Curves," *Archiv für das Eisenhuttenwesen*, Vol. 6, 1932, p. 253.

[6] A. L. Boegehold, "Some Effects of Quenching and Tempering on Residual Stresses in Steel," METAL PROGRESS, Vol. 57, No. 2, Feb. 1950, p. 183.

[7] S. T. Kishkin, "Nature of the Steel Strengthening Process and of the High Hardness of Martensite," *Bulletin*, Academy of Sciences of the USSR, Division of Technical Sciences, No. 12, Dec. 1946, p. 1799.

Written Discussion: By George A. Roberts, vice president—technology, and Arthur H. Grobe, research metallurgist, Vanadium-Alloys Steel Co., Latrobe, Pa.

The very low stress level at which permanent plastic deformation can take place in hardened steels is again clearly shown by the precise technique for determining the elastic limit developed by the authors. The results, particularly those shown in the top portion of Fig. 8 where the elastic limit is shown as a function of hardness, are closely similar to the trends obtained in our Laboratory by the bend test on hardened alloy tool steels. It is felt that publication of our results as a discussion to this paper will be of interest.

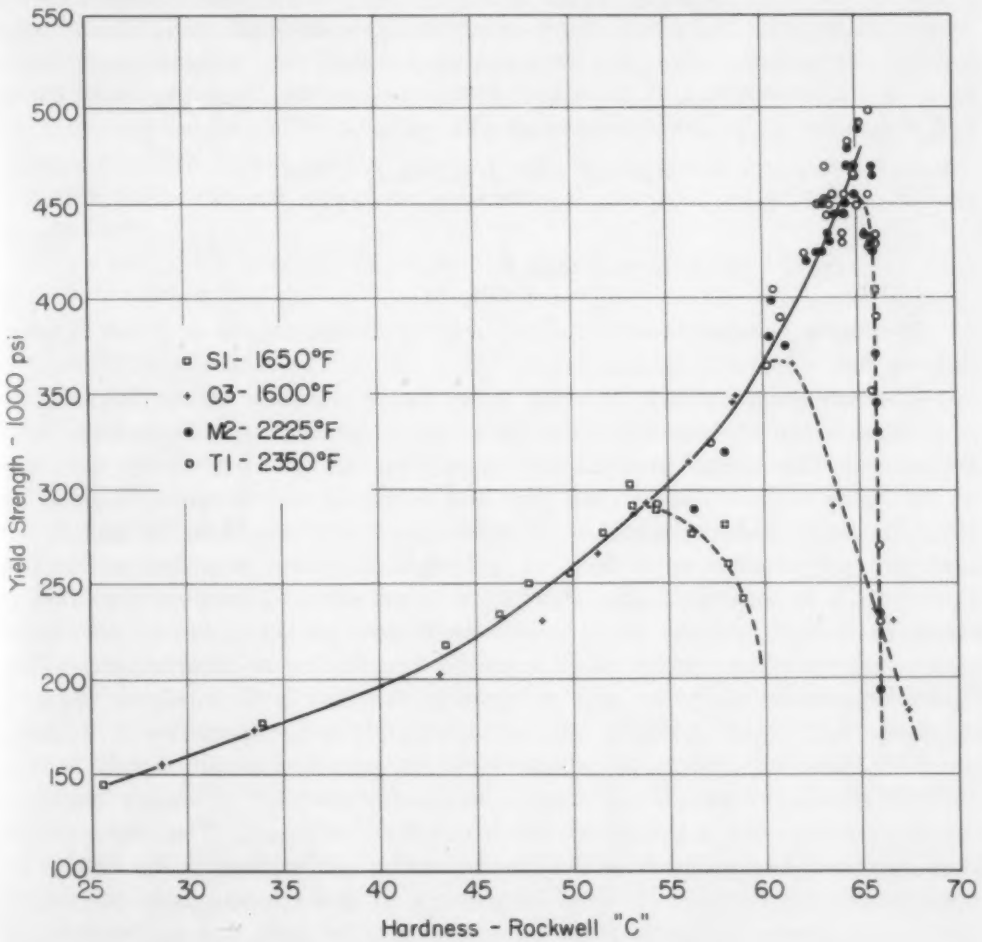


Fig. 11—Yield Strength of Four Steels After Stress Relief Treatments.

The bend test for hardened steels, previously described[8] uses a specimen 0.140 inch thick by 0.500 inch wide and approximately 2 inches long. By carefully measuring the load and deflection, and noting the point at which the load-deflection curve deviates from a straight line, we have determined a property which, while described as "yield strength" in our reports, is truly more closely akin to a proportional limit at a low sensitivity of measurement. Conducting tests on four different steels as shown below, it was apparent that the as-hardened steels have a very low "yield strength" or "proportional limit."

[8] Arthur H. Grobe and George A. Roberts, "The Bend Test for Hardened High Speed Steel," TRANSACTIONS, American Society for Metals, Vol. 40, 1948, p. 435.

This property increases quite rapidly as tempering relieves internal stresses and removes retained austenite. Finally, at a certain hardness the strength property goes through a maximum and starts to decrease as the tempering temperature is further raised.

Beyond this maximum the elastic property was exactly the same regardless of composition. It is striking that this was found to be true even in steels of such widely diverging compositions as the four under investigation, namely, two common high speed steels of the tungsten and tungsten-molybdenum type respectively, a high carbon low alloy tungsten die steel, and a medium carbon low alloy tungsten chisel steel.

The values of strength shown in Fig. 11 of this discussion cannot directly be compared with the elastic limit determinations made in the authors' paper, but it is important to note the very similar trend of the "yield strength" measured by the bend test, and the elastic limit measured by the progressive loading and unloading technique employed by the authors.

Nominal Analysis of Steels Tested

	C	W	Cr	V	Mo
T 1	0.7	18	4	1	
M 2	0.8	6	4	2	5
O 3	1.2	2	0.7	0.2	0.3
S 1	0.5	2	2	0.2	

Written Discussion: By B. B. Hundy, British Iron & Steel Research Association, Sheffield, England.

The authors of this interesting paper draw attention to the fact that the proportional limit of worked steel rises on tempering at temperatures below the critical. This is well known and I have observed this effect in my own work on the aging of hard drawn rope wire and on rolled and drawn mild steel. The effect in worked steels, however, is definitely due to strain aging and is both time and temperature dependent, i.e. a long aging time at a low temperature (say 20 °C) is equivalent to a short time at an elevated temperature. This increase in the proportional limit is now recognized as being due to diffusion of carbon and/or nitrogen atoms through the iron lattice to dislocations, locking these dislocations in place and postponing yielding until a higher stress is reached. Is it possible that a similar effect might be operative in quenched steels? Quenching from the austenitizing temperature would result in steel with the carbon atoms not anchored in the positions of minimum energy at the dislocations, but scattered in the martensitic structure. Tempering of this steel may lead to migration of the carbon atoms to the dislocations and to any substructural boundaries that may be present. If this hypothesis is correct, the rise in the elastic limit due to tempering should be time and temperature dependent and the activation energy for the process should be that for the diffusion of carbon in iron. Even if this hypothesis should prove to be correct, I agree with the authors in attributing most of the effect to a relief of the stresses in the quenched steels.

Our work at B.I.S.R.A. also suggests that the suppression of the yield point by quenching from high temperatures is mainly due to residual stresses caused by the quenching. Our work[9] has shown the residual stresses can mask the yield point in mild steel; if high residual stresses are present in the steel,

[9] B. B. Hundy, "Elimination of Stretcher Strains in Mild Steel Pressings." *Journal*, Iron and Steel Institute, Vol. 178, 1954, p. 127.

yielding cannot occur instantaneously through the thickness, but takes place in one or two grains at a time and gradually spreads as the applied stress is raised. Some tests on water-quenched aluminum-killed mild steel sheet showed that aging for 2 weeks at 70 °C did not restore the yield point and so I think that the suppression of the yield point is more probably due to the quenching stresses than to a precipitation reaction as suggested by the authors.

Authors' Reply

The bend test data presented by Drs. Roberts and Grobe confirm the concept that the optimum yield properties are not developed at the highest hardness in hardened steels. Furthermore, their results indicate that the maximum yield strength depends primarily on the tempering characteristics of the steel, and through this, on the carbon and alloy contents. The higher that a steel can be tempered and still retain high hardness, the higher is the maximum attainable yield strength. It is recognized that the yield strength may not be as sensitive to these factors as the elastic limit, but the bend test data presented in the discussion suggest that these general ideas are valid for a wide variety of tool steels.

It is difficult for us to evaluate the significance of Mr. Dugger's cyclographic determinations during the tension test. The core hysteresis losses may be influenced by a large number of variables and these effects appear to be incompletely understood. At the moment, we are not in a position to correlate these measurements with our elastic limit value. If further work demonstrates that the elastic limits have important physical and engineering significance, it would be most desirable to have a quick procedure that could replace the tedious load-unload measurements.

We appreciate having the comments of Messrs. Johnson and Maker relative to present practice in the spring industry. It is pleasing to know that our data are pertinent to spring applications and are consistent with many practical observations. The only exception seems to be the sharp drop in elastic limit noted by Messrs. Johnson and Maker at 500 to 600 °F. It would be worth tracking down this discrepancy. Additional information is now being obtained on the influence of alloying elements. The possible advantage of very long tempering times is also being investigated, as suggested by the discussers.

Mr. Polakowski has raised several points with respect to the elastic limit measurement itself. We chose to define the elastic limit in terms of a repetitive stress criterion in order to avoid the difficulty that some bars apparently shortened on the first application of stress. However, even when such shortening occurred, it was shown that subsequent applications of stress to the same level did not produce any additional change in length, if this stress was below the elastic limit. Such a stress can then be considered to be truly elastic if an exception is made of the first stress application. We agree that compression data are required and experiments in this direction are under way.

We did not intend our tentative explanation for the low elastic limit of untempered steel to be more than a starting point for future experiments on the nature of this phenomenon. The stresses involved are probably quite localized and consist of a superposition of macro and microstresses. These stress peaks could undergo appreciable relief even at 500 to 600 °F, but it is difficult to measure them because of their localized nature. It is also likely that the im-

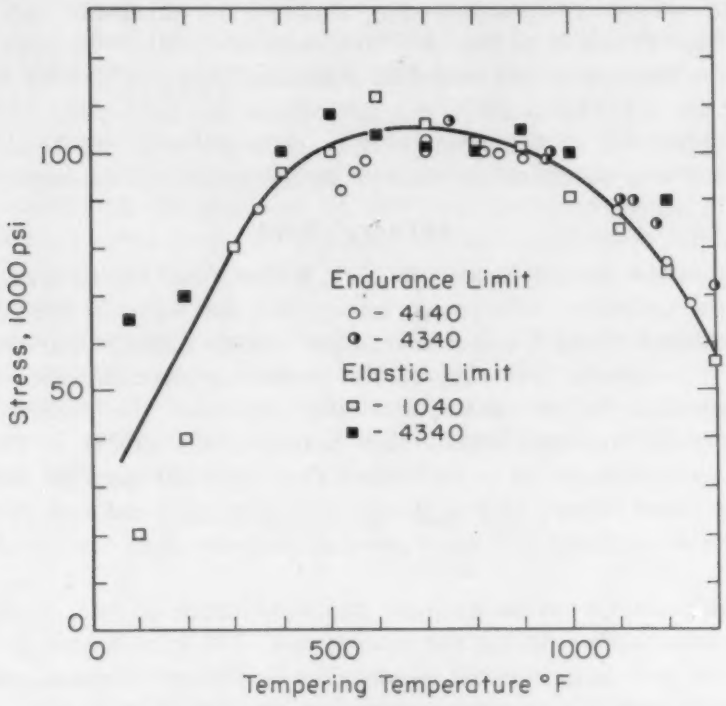


Fig. 12—Effect of Tempering Temperature on Endurance and Elastic Limits of 0.4% Carbon Steels.

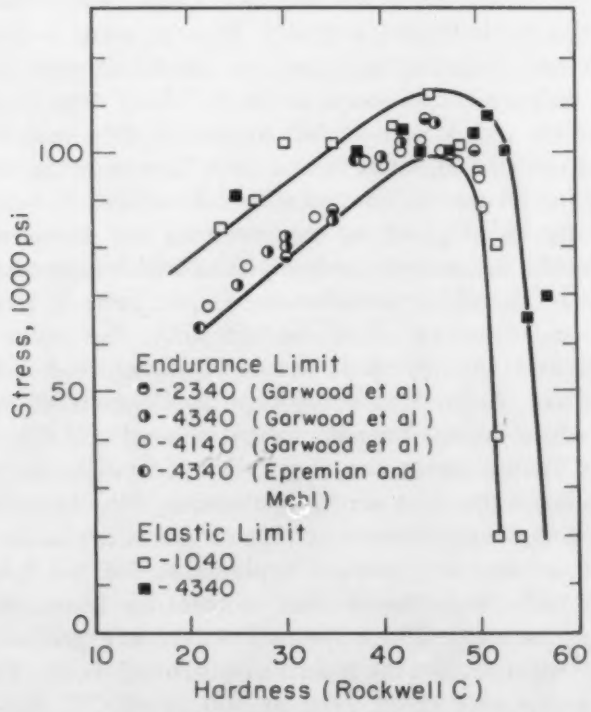


Fig. 13—Variation of Endurance and Elastic Limits of 0.4% Carbon Steels with Hardness.

perfections in martensite introduced as a result of the transformation may influence the elastic limit.

We cannot subscribe to the viewpoint of S. T. Kishkin, as cited by Mr. Polakowski, that precipitation of cementite at 400 °F might account for the increase in elastic limit. It is well known that ϵ-carbide precipitates in large quantities at subgrain boundaries on tempering in the range 200 to 300 °F; yet the elastic limit remains low after such tempering treatments. If the mere precipitation process were responsible for an increase in elastic limit, the finely dispersed ϵ-carbide would be at least as effective as the cementite which comes out in more massive form later. On the other hand, the residual stress hypothesis is further supported by the fact that after the elastic limit of hardened steel is raised by suitable tempering, it can be lowered again by plastic deformation.

Mr. Hundy has suggested that the increase in elastic limit on tempering may be due to the precipitation of carbon atoms at dislocations. This mechanism seems unlikely although it may contribute somewhat to the phenomenon. The diffusion rate of carbon in martensite is at least as great as in ferrite and it would seem that the increase in elastic limit should occur at much lower temperatures, as in ferrite. In addition, a yield point phenomenon would also be expected and this is not seen until much higher tempering temperatures when the ferritic constituent is well developed. The diffusion of carbon may be still involved in the raising of the elastic limit on tempering but this may act as a rate limiting process for the precipitation of carbides at subboundaries in the martensite. It is conceived that the high localized stresses induced in the freshly quenched martensite by the transformation itself may reduce the elastic limit of the fresh martensite and also act as an additional driving force for the precipitation of carbides at preferred sites. The relief of the localized stresses may thus be partially dependent on the rate of carbon diffusion although we have no evidence that this is the case.

It is also interesting to note that the fatigue endurance limit behaves very much like the elastic limit as a function of hardness. Figs. 12 and 13 summarize some of the available data on the variation of the endurance limit with tempering temperature and hardness in a series of 0.40% carbon steels. The endurance limits were obtained from rotating beam experiments.[10, 11] The elastic limits for 1050 (listed in this paper) and 4340 steels (from work now under way in collaboration with Dr. C. Shih) are also plotted on the same graph. It is evident that the elastic and the endurance limits follow the same trends and it appears that the elastic limit may be directly equivalent to the endurance limit under these restricted conditions. This apparent correlation also suggests that the onset of fatigue damage may coincide with the onset of plastic flow.

[10] M. F. Garwood, H. H. Zurburg, M. A. Erickson, "Correlation of Laboratory Tests and Service Performance," *Interpretation of Tests and Correlation with Service*, 1951, American Society for Metals.

[11] E. Epremain and R. F. Mehl, "The Statistical Behavior of Fatigue Properties and the Influence of Metallurgical Factors," *Symposium on Fatigue with Emphasis on Statistical Approach*, II, 1952, p. 25, American Society for Testing Materials.

EFFECT OF COMPOSITION ON TRANSVERSE PROPERTIES OF SLACK-QUENCHED STEEL

By John Vajda and Paul E. Busby

Abstract

The effect of composition on the transverse mechanical properties of structures formed on continuous cooling was studied. Ten different compositions were selected to show the effects of boron, rare earth oxides, silicon, nickel, and carbon on hardenability in heavy sections, and on the mechanical properties of tempered slack-quenched structures. The effectiveness of ferroboron and Grainal No. 79 in increasing hardenability was compared. Mechanical properties obtained on two steels of similar composition from different heats were found to be in good agreement. The applicability of the end-quench method to heavy sections is discussed, and some data on the effect of mass on the mechanical properties are presented.

Introduction

THE information presented in this paper is supplementary to that contained in an earlier publication (1)[1] which gives a detailed account of an end-quench method for developing reproducible slack-quenched structures in heavy forgings and contains mechanical property data obtained on seven different compositions treated by this method. Recently more data have been obtained in this manner on ten additional steels to show the effects of boron, rare earth oxides, silicon, nickel, and carbon on transverse properties. The end-quench method is discussed in relation to its applicability to heavy sections, and some data on the effect of mass on the properties are presented.

Results already published showed that (a) the technique for developing reproducible slack-quenched structures was satisfactory, (b) steels rated in order of hardenability by the Jominy test did not always maintain that order when quenched in heavy sections, (c) rare earth metals had little effect on the hardenability and on the mechanical properties of slack-quenched structures, and (d) transition tempera-

[1] Figures appearing in parentheses pertain to the references appended to this paper.

This study forms a part of a larger program sponsored by the Aeronautical Research Laboratory, Department of the Air Force, Wright Air Development Center, Wright-Patterson Air Force Base, Ohio, under Contract AF 33(038)-10218.

A paper presented before the Thirty-sixth Annual Convention of the Society, held in Chicago, November 1 to 5, 1954. The authors, John Vajda and Paul E. Busby, are associated with the Metals Research Laboratory, Carnegie Institute of Technology, Pittsburgh. Manuscript received April 15, 1954.

tures in the impact test were progressively raised by the presence of increasing amounts of slack-quenched structures. The primary purpose of this paper is to present new material to indicate more clearly the extent to which the above findings are generally valid and to extend that information, especially with regard to the effect of composition on the transverse properties of slack-quenched steels.

Recently a paper was published (2) covering the subject "Effect of Composition on Transverse Mechanical Properties of Steel"; in this instance, the steels were in general fully-quenched before being tempered. By comparing the material included in that paper with material in the present one, a more comprehensive picture of the overall effect of composition on the transverse mechanical properties of steel, whether fully or slack-quenched, may be obtained.

Experimental Work

The experimental procedure consisted of making tensile and impact traverses on tempered end-quenched slabs which had been removed from a larger slotted 7 inch round by 7 inch long section of the subject steel. A complete description of the section, together with details of the experimental procedure, is given in an earlier publication (1).

The compositions of the ten additional steels studied are given in Table I; all were fine-grained, basic electric steels, and were aluminum-killed. Additions were made to the steels in the mold during pouring. Seven inch rounds were rolled from ingots which were 25 inches square for all steels, except 4A, for which the ingots were 20½ inches round.

Data

Following austenitizing and end-quenching, hardness traverses were made on a slab removed from each of the steels. These data are presented with standard Jominy data on the same steels in Fig. 1.

Tensile and impact traverses were made on tempered slabs from each steel in a manner described in the previous paper (1). Results of these property traverses were corrected to a constant tensile strength in order to facilitate comparison among these steels. The corrected data were plotted as functions of distance from the quenched end and are given in Figs. 2,3,4,5 and 6.

Discussion of Results

Hardenability—The standard Jominy hardenability curves for all steels are given in Fig. 1 with those obtained on end-quenched 7-inch rounds. Curves for Steels 1A and 5A, as well as those for 3J and 5J which were presented in the previous paper, have been included with Steels 4A and 4J, respectively, in order to show the available hardenability information on these heats in one reference.

Table I
Chemical Composition

Steel	C	Mn	P	S	Si	Ni	Cr	Mo	V	B	Rare Earths
						% of Element					
1A*	0.33	0.78	0.013	0.018	0.31	0.80	0.68	0.50	0.10	—	
4A	0.51	0.77	0.013	0.017	0.31	0.79	0.66	0.50	0.10	—	
5A*	0.33	0.76	0.013	0.018	0.31	0.79	0.66	0.50	0.10	0.001	
3E	0.40	0.86	0.015	0.019	0.31	0.54	0.46	0.23		—	
4E	0.38	0.88			0.30	1.58	0.48	0.23		—	
5E	0.40	0.88			0.32	0.54	0.48	0.23		0.0014	
1H*	0.20	0.67	0.010	0.008	0.30	2.07	0.91	0.39		—	
2H*	0.21	0.68	0.010	0.009	0.30	2.05	0.91	0.39		0.0005	
3H*	0.23	0.67	0.010	0.008	0.28	2.06	0.91	0.38		—	Lan-cer-amp (4#/ton)
3J*	0.39	0.88	0.018	0.022	0.27	0.51	0.51	0.24		—	
4J	0.40	0.88	0.018	0.022	1.26	0.50	0.53	0.24		—	
5J*	0.41	0.91	0.021	0.009	0.28	0.51	0.53	0.24		0.0015	Lan-cer-amp (2.5#/ton)
1K	0.32	0.82	0.010	0.010	0.35	0.48	0.52	0.17		—	
2K	0.32	0.81	0.010	0.011	0.36	0.47	0.52	0.16		0.0003	
3K	0.33	0.83	0.010	0.011	0.35	0.48	0.52	0.17		0.0006	T-compound (3#/ton)
4K	0.34	0.81	0.010	0.010	1.37	0.46	0.52	0.17		—	Lan-cer-amp (2.5#/ton)
5K	0.33	0.81	0.010	0.011	1.36	0.47	0.51	0.16		0.0004	Lan-cer-amp (2.5#/ton)

Boron added as ferroboron (with excess aluminum) to Steels 2K, 3K, 5K and as Grainal #79 to 5A, 5E, 2H and 5J.
Rare earth added as T-compound or Lan-cer-amp as indicated. T-compound is a mixture of rare earth oxides and Lan-cer-amp is a mixture of rare earth metals.
The underlined figures represent modifications to the base compositions.

* Studied previously (1)

The compositions of the K steels (Fig. 1A) were designed to show the effects of added (a) ferroboron—2K, (b) ferroboron plus rare earth oxides (T-compound)—3K, (c) ferrosilicon plus rare earth metals (Lan-cer-amp)—4K, and (d) ferrosilicon plus ferroboron plus rare earth metals (Lan-cer-amp)—5K on the base AISI 8630 composition—1K.

Added boron to Steel 2K in the form of ferroboron produced a moderate increase in hardenability in both 1-inch and 7-inch rounds. This increase is less pronounced than that observed in the A steels (1A vs. 5A—Fig. 1B) which have the same carbon content but a slightly higher alloy content. Steel 3K, containing ferroboron as well as rare earth oxides, has a slightly higher hardenability than both 1K and 2K. The hardenability increase is believed to be associated with the boron addition only, the difference between the two boron steels perhaps being due to the differences in the amount of boron present (see Table I); T-compound normally does not contribute to the hardenability despite the fact that it contains boron in the form of calcium boride. Silicon added to Steel 4K appears to increase hardenability more effectively

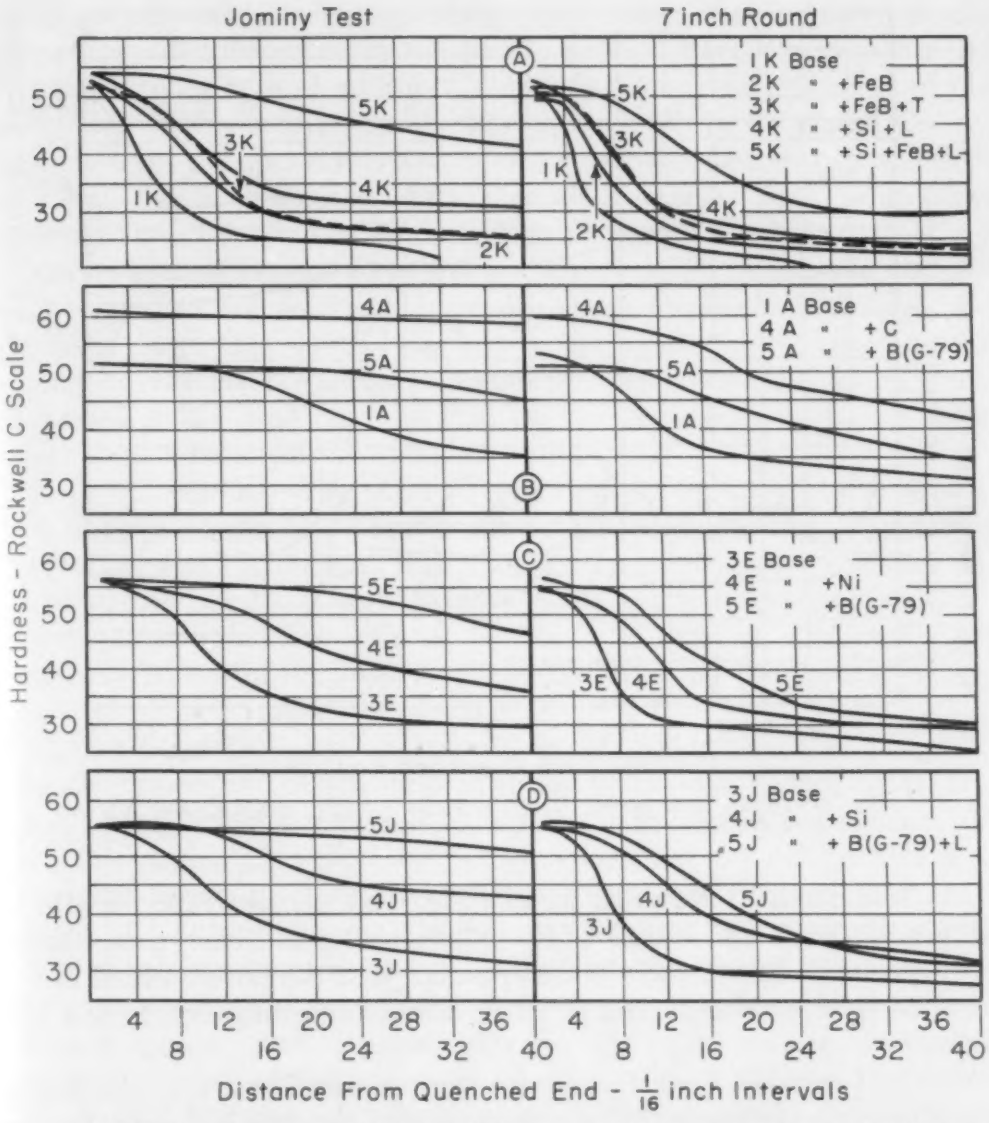


Fig. 1—Comparison of Hardenability Curves Obtained on Standard Jominy Specimens and End-Quenched 7-Inch Rounds.

than the ferroboron addition (2K) in both the 1-inch and 7-inch rounds. Addition of silicon plus ferroboron (5K) brings about a marked increase in the hardenability in both sizes of round; the observation that the effect of the combined additions appears to be multiplicative suggests that the silicon addition improved the effectiveness of the ferroboron.

In the second panel (Fig. 1B), the curves show the effect of added carbon (4A–0.51% carbon) as compared with that of added boron (5A—Grainal No. 79) on the base composition (1A–0.33% carbon). In terms of hardenability and especially on the basis of data from the 7-inch round, the boron addition appears to be almost as effective as the added 0.18% carbon.

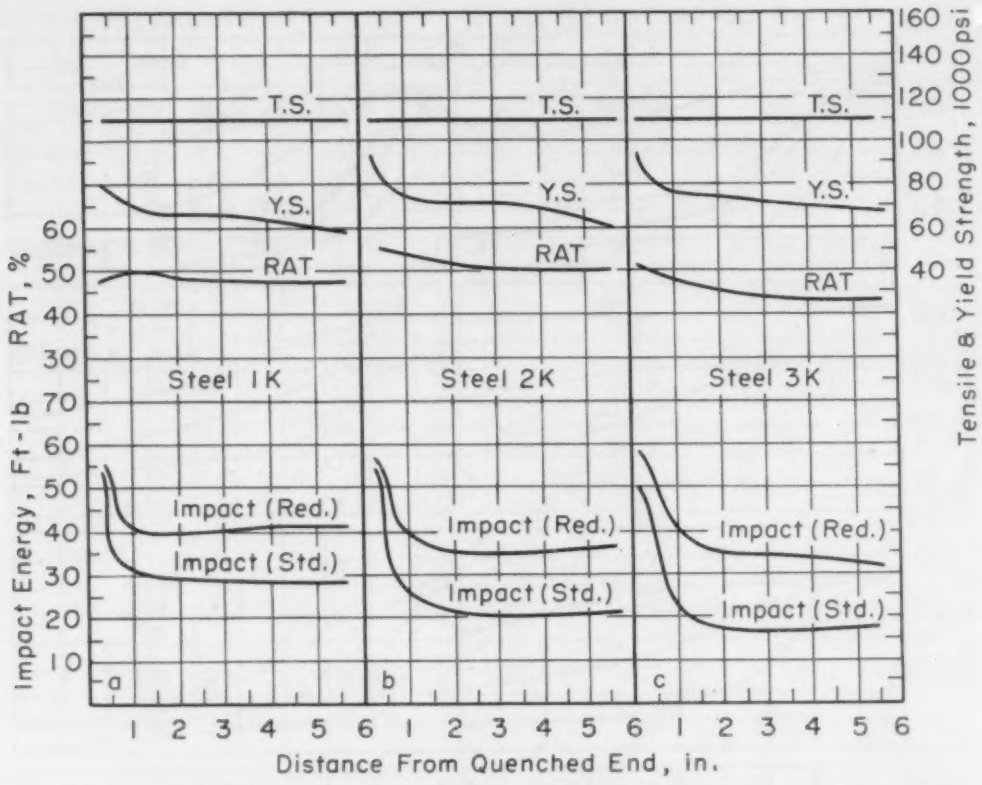


Fig. 2—Tensile and Impact Data on Steels (a) 1K, (b) 2K, and (c) 3K. Corrected to a Constant Tensile Strength of 110,000 Psi.

The curves in the third panel (Fig. 1C) demonstrate the effects of nickel (4E) and boron (5E) additions on the base composition (3E), an AISI 8640. It is quite apparent that the boron added in the form of Grainal No. 79 is a more effective hardening agent than 1% nickel.

The J steels in Fig. 1D have the same nominal base composition as the E steels and thus permit a comparison of the various properties on a heat basis. The hardenability curves of the base compositions, 3E and 3J, as well as those of the boron-treated steels, 5E and 5J, are in very good agreement. Comparison of the data for Steels 4E and 4J indicate, as expected, that the improvement in hardenability resulting from the addition of 1% Si (4J) is slightly greater than that produced by the addition of the same percentage of nickel (4E).

Despite basic differences in chemical composition among the four heats represented in Fig. 1, the data suggest that effective additions of boron can be made more frequently with Grainal No. 79 than with ferroboron. The hardenability of each of those steels to which Grainal No. 79 was added (5A, 5E, 5J) is markedly higher than their respective base compositions, but only a minor improvement is noted in Steel 2K as a result of the ferroboron addition. Although it may be observed from Table I that the amount of boron present (as analyzed) in the

ferroboron-treated steel is less than that of the Grainal-treated steels, the observed differences in the hardenability effect are probably attributable to the type of addition. This difference in effectiveness of the two types of boron addition agents used in the present study is responsible for the apparently anomalous result that boron is more effective than 1% Si in an AISI 8640 steel (compare 4J and 5J) and less effective than 1% Si in an AISI 8630 steel (compare 2K and 4K).

Tensile and Impact Properties—In discussing the tensile and impact properties, reference will be made to the curves in Figs. 2,3,4,5, and 6 plotted from data which have been corrected to the indicated tensile strengths. The level of tensile strength selected for each group of steels discussed below was close to that of the slack-quenched portion in order to avoid excessive correction of the data.

(a) Steel 1K—This steel (Fig. 2a) represents the base composition of the K series. The tensile strength level chosen for purposes of correction was 110,000 psi. The choice of this level was necessary because of the low basic hardenability of this series of steels. In subsequent paragraphs, the effects of the additions on properties are generally based on the relative property values of this base steel and those of the steel under discussion.

(b) Steel 2K—The addition of ferroboron to this steel (Fig. 2b) slightly improved the tensile properties, transverse reduction of area (RAT), and yield strength. Values for the impact tests closest to the quenched end of this steel are the same as those for comparable tests from the base composition. In view of the improvement in yield strength (from 81,500 to 91,200 psi), which may be due to the higher hardenability in this steel and should probably be accompanied by an increase in impact strength, one might conclude that the absence of improvement in these impact values demonstrates that the boron addition was detrimental to impact strength even in specimens taken from the quenched end. Impact values in the slack-quenched regions have been decreased about 8 ft-lb for the standard specimens and about 5 ft-lb for the subsize specimens. These results substantiate the conclusions previously drawn in connection with Steels 5A and 5J (1) that boron lowers the impact properties when a steel is slack-quenched. Although a composition variable does exist between this steel and 5A, comparison of results on these two steels does give interesting results. Steel 5A (base plus Grainal No. 79) showed a simultaneous drop in impact to a level of approximately 3 ft-lb for both standard and subsize specimens at the onset of slack quenching. Although the tensile strength of 2K is 110,000 psi as compared with 140,000 psi for 5A, it appears from the pattern of the impact curves for these two steels that boron in 2K had a less detrimental effect on this property than Grainal No. 79 in 5A. A possible explanation of this difference in behavior may be the presence of strong carbide-formers in Steel 5A; the base composition of this steel

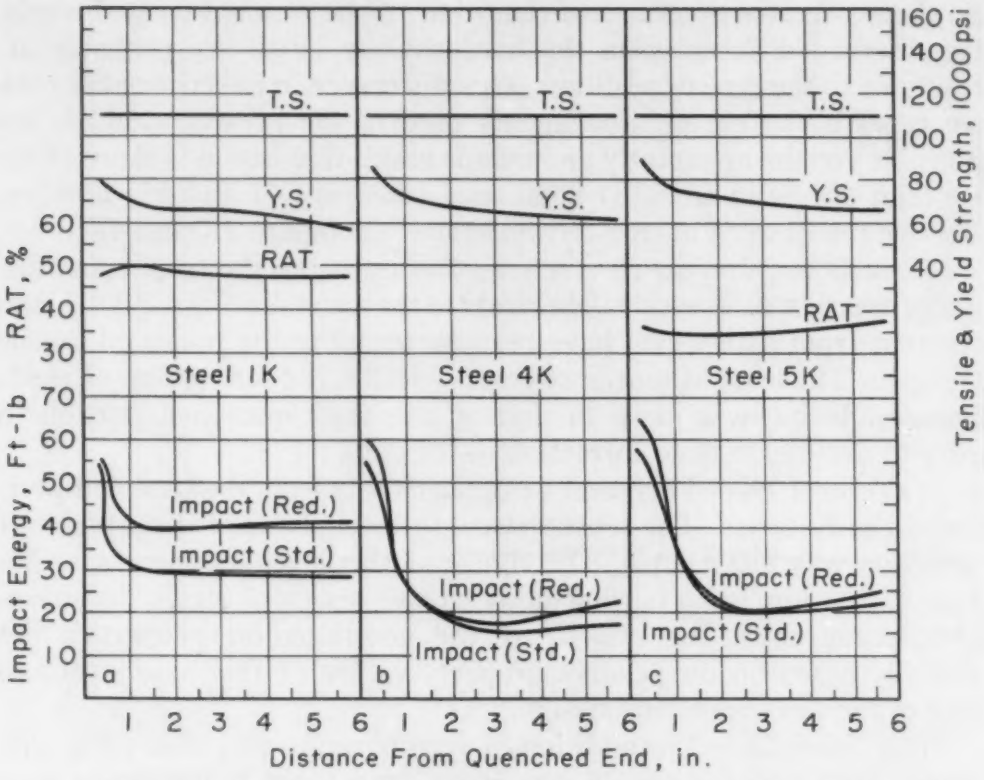


Fig. 3—Tensile and Impact Data on Steels (a) 1K, (b) 4K, and (c) 5K. Corrected to a Constant Tensile Strength of 110,000 Psi.

contained vanadium, and boron was added in the form of titanium-rich Grainal No. 79. Steel 2K was produced by adding ferroboron to a vanadium-free base.

(c) Steel 3K—The combined additions of boron and rare earth oxides in the form of ferroboron and T-compound, respectively, appear to have raised the yield strength slightly over the entire length of the quenched section (Fig. 2c). This result, which is concomitant with increased hardenability as shown by the R_c hardness versus distance curves for the 7-inch round given in Fig. 1A, is believed to be associated with the hardenability effect of the boron addition. Both RAT and impact appear to have been decreased to some extent over practically the entire range of structures. A comparison of the data for Steels 2K and 3K, which are practically identical except for the T-compound in 3K, suggests that this addition tends to lower both RAT and impact strength.

(d) Steel 4K—Added silicon plus Lan-cer-amp slightly raised the yield strength of this steel (Fig. 3b) near the quenched end. The RAT values are rather erratic and therefore are not included in Fig. 2b. However, the uncorrected data for this steel indicate that the RAT values are generally lower than those obtained on the base composition, 1K. Impact strength of the specimens closest to the quenched end is improved, but, in slack-quenched structures, this property is decreased

to a level approximating that observed for standard specimens in Steels 2K and 3K. Apparently, the addition of 1% Si to the base composition has about the same detrimental effect as boron on impact strength of standard specimens. It is of interest that impact values obtained on both the standard and subsize specimens are practically identical over the full range of structures.

(e) Steel 5K—Added boron plus silicon plus Lan-cer-amp (Fig. 3c) increased the yield strength by virtue of increased hardenability, but the RAT level is still lower than that for the base composition. Impact strength of standard specimens up to 1 inch from the quenched end also reflects the improvement in hardenability. Beyond this point, however, these values, like those for 4K, drop as much as 10 ft-lb below comparable values for the base. Added boron in Steel 5K appears to have improved both yield strength and impact values (Figs. 3b and 3c). The similarity of impact results obtained on standard and subsize specimens of Steel 4K is also observed in 5K.

Because of the higher hardenability of Steels 4K and 5K, correction for tensile strength was necessary even for the property values obtained on the slack-quenched structures. For this material, the differences between the actual tensile strength and the level to which the values were corrected amounted to about 10,000 psi for Steel 4K and about 25,000 psi for 5K. The magnitude of error in impact strength resulting from applying the correction factor developed for fully-quenched structures to the slack-quenched material is difficult to estimate. On the basis of the relationship between tensile and impact strength in the slack-quenched regions of Steels 4K and 5K, it would appear that the estimated impact values for the slack-quenched materials should be somewhat lower than those shown in Fig. 2. However, a further lowering of these values based on a more valid tensile strength—impact strength relation would not materially affect the conclusions presented in this article.

(f) Steel 3E—This AISI 8640 steel (Fig. 4a) represents the base composition of the E series of three steels. Test results on this steel were corrected to a level of 120,000 psi. In subsequent paragraphs, the separate effects of added nickel (4E) and boron (5E) on the mechanical properties will be discussed.

(g) Steel 4E—Added nickel to this steel (Fig. 4b) appears to have had little effect on the tensile properties as compared with the base composition, 3E. Impact properties appear to have been improved at all positions in the section. This effect may be due primarily to the influence of nickel in lowering the transition temperature of slack-quenched products.

(h) Steel 5E—The boron addition had little effect on the tensile properties, but the improvement in hardenability is reflected to some extent by the impact property (Fig. 4c). Independent of the harden-

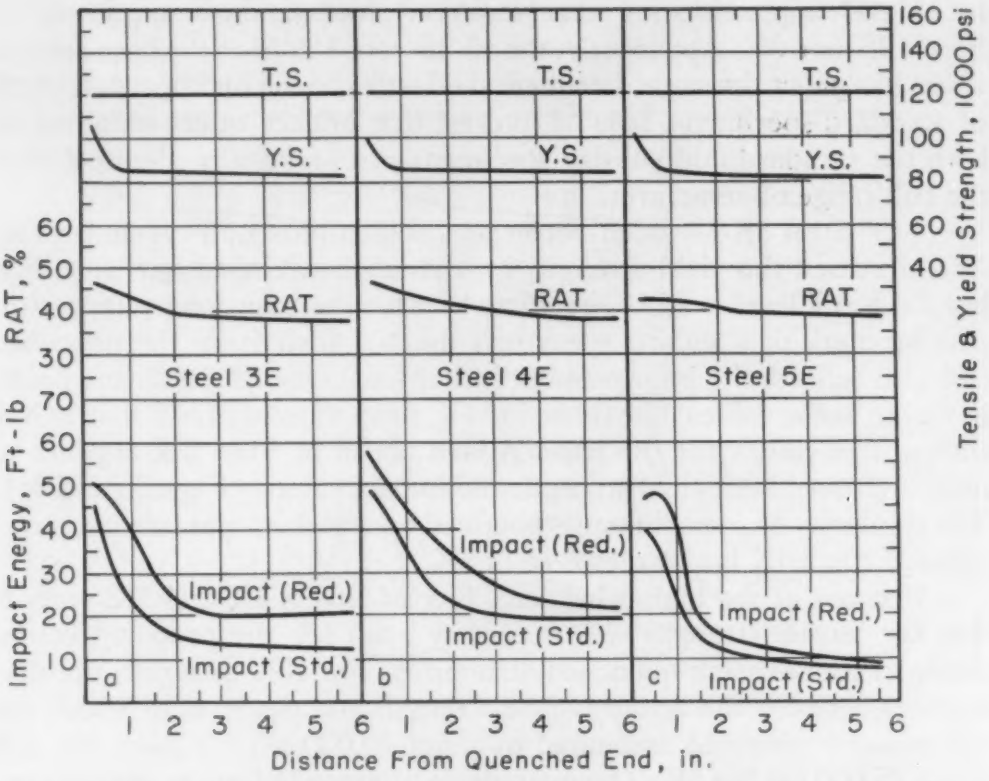


Fig. 4—Tensile and Impact Data on Steels (a) 3E, (b) 4E, and (c) 5E. Corrected to a Constant Tensile Strength of 120,000 Psi.

ability effect, however, the general level of impact values has been decreased. This steel is practically identical to Steel 5J (1) in composition, except for the Lan-cer-amp added to the latter steel (see Fig. 5c). The hardenability traverses almost coincide; however, Lan-cer-amp in 5J may have been beneficial to RAT, especially near the quenched end. Standard impact values are higher for the Lan-cer-amp treated steel only at positions up to approximately ½ inch from the quenched end. Over this same distance, subsize test results are slightly lower than those in 5E but higher throughout the remainder of the section.

(i) Steel 4J—The data obtained on this composition are to be compared with those obtained on the previously-studied Steels 3J and 5J for the purpose of showing the effect of added silicon. In order to facilitate comparison among these steels, data on Steel 4J (Fig. 5b) are shown, together with those obtained on 3J (base—Fig. 5a) and 5J (base plus boron plus Lan-cer-amp—Fig. 5c). The RAT level is increased slightly over the entire range of structures as compared to the base composition. However, the yield strength, especially in the slack-quenched region, is decreased appreciably. Impact values (standard specimens) up to 1 inch from the quenched end have been slightly improved as a result of the increase in hardenability. It is observed that the impact values obtained on the subsize specimens tend to approach the values obtained on the standard specimens. This tendency was

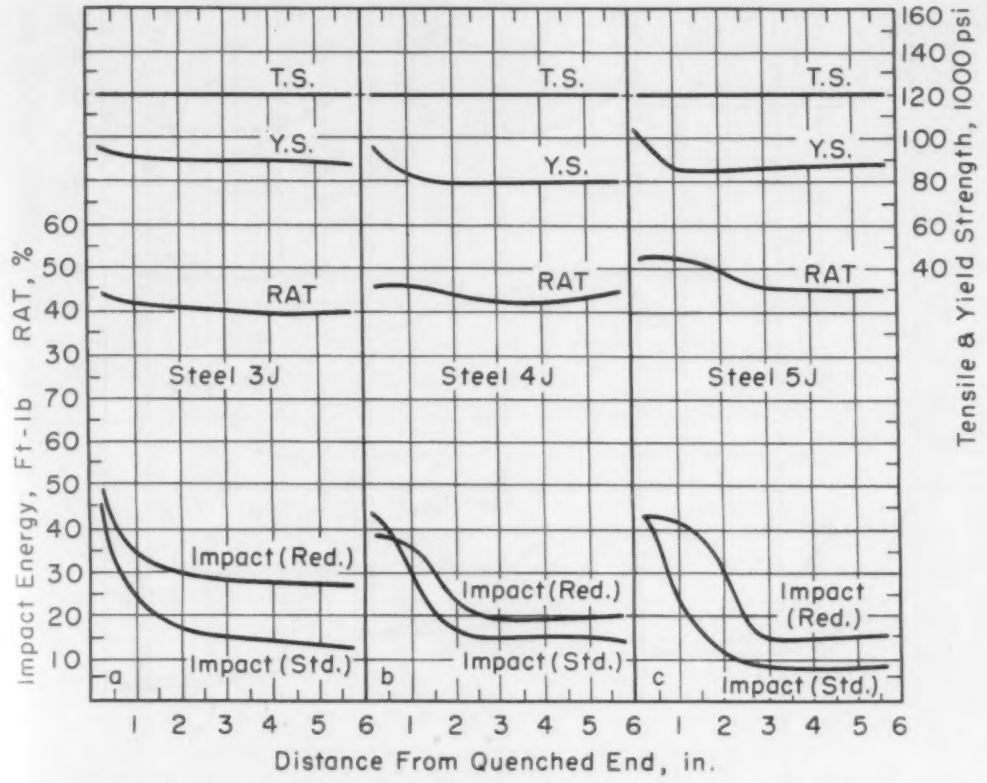


Fig. 5—Tensile and Impact Data on Steels (a) 3J, (b) 4J, and (c) 5J. Corrected to a Constant Tensile Strength of 120,000 Psi.

more pronounced in the results obtained on Steels 4K and 5K which were also treated with silicon. It appears, therefore, that the absence of the expected size effect may in some manner be related to the presence of silicon.

Attention is called to Steel 3E (Fig. 4a) whose composition is practically identical to that of Steel 3J (Fig. 5a). Although the hardenability curves obtained on the 7-inch round and the RAT curves for these two steels are identical within the limits of experimental error, the yield strength of the 3E steel, tempered at 980 °F (525 °C) is somewhat lower than that of 3J, tempered at 1035 °F (555 °C) in the slack-quenched region. The standard impact curves for both steels are practically identical.

(j) Steel 4A—Steel 4A is one of a group of steels (A steels) included in the earlier publication, and its composition was designed to show the effect of added carbon (0.51% C) to the base composition (1A—0.33% C). Comparing the data on 4A (Fig. 6b) with that of 1A (Fig. 6a), it is noted that added carbon in 4A has decreased the general level of both RAT and yield strength to some extent. The yield-tensile strength ratios for tests on 4A are consistently lower than those at corresponding positions in 1A throughout the section. This behavior is not understood. Impact values, except those near the quenched end, appear to have been improved.

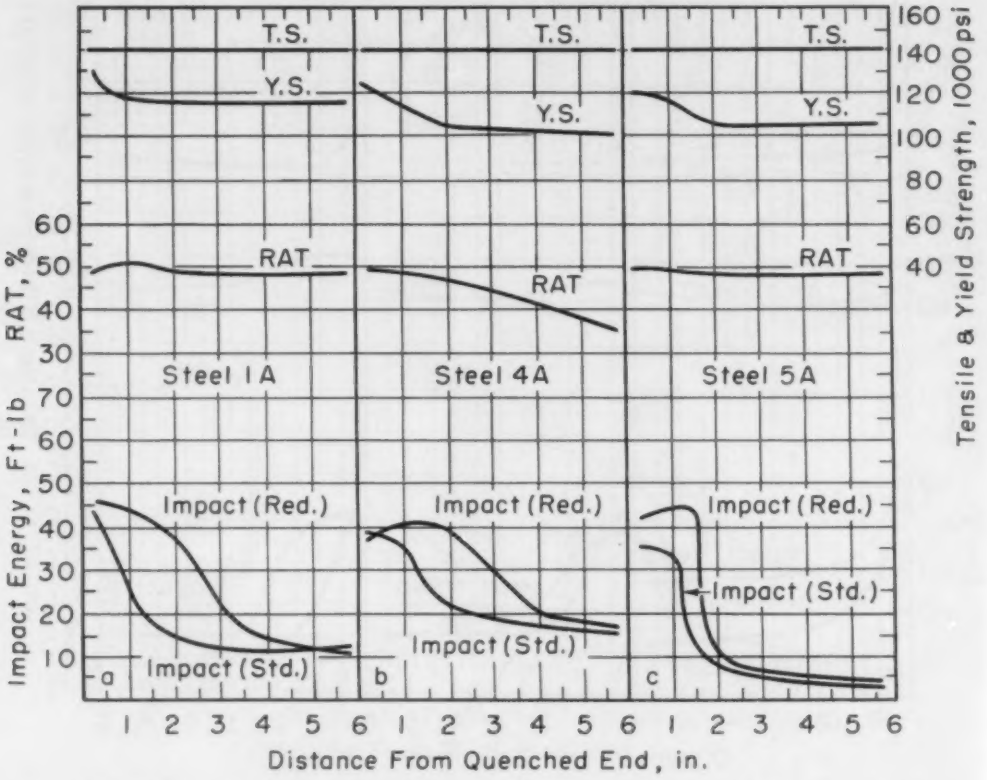


Fig. 6—Tensile and Impact Data on Steels (a) 1A, (b) 4A, and (c) 5A. Corrected to a Constant Tensile Strength of 140,000 Psi.

Effect of Mass on Properties

The application of results obtained on end-quenched 7-inch rounds to heavy sections may be questioned on the basis that differences in mass may lead to differences in mechanical properties. Although the cooling rates in the 7-inch section may approach those at equivalent positions from the quenched surface in heavy sections, transformation and cooling stresses which may be high in heavy sections are greatly reduced in the slotted 7-inch round. Many believe that these stresses significantly affect the formation of various decomposition products of austenite in large sections and, because of this, influence the mechanical properties of large sections in such a manner that they cannot be predicted from results obtained on small sections.

A simple experiment was designed in order to obtain some information regarding this effect. The method consisted of obtaining properties of a 7- by 7-inch cylindrical section, which was austenitized and quenched as a solid, and comparing these data with those obtained on a slotted 7-inch by 7-inch round of the same steel. Thus cooling rates were held fairly constant, but the size of the cross section was varied from ½ inch by 3 inches to 7 inches diameter.

Two steels, 1H and 4A, were chosen for this study. Steel 1H(1),

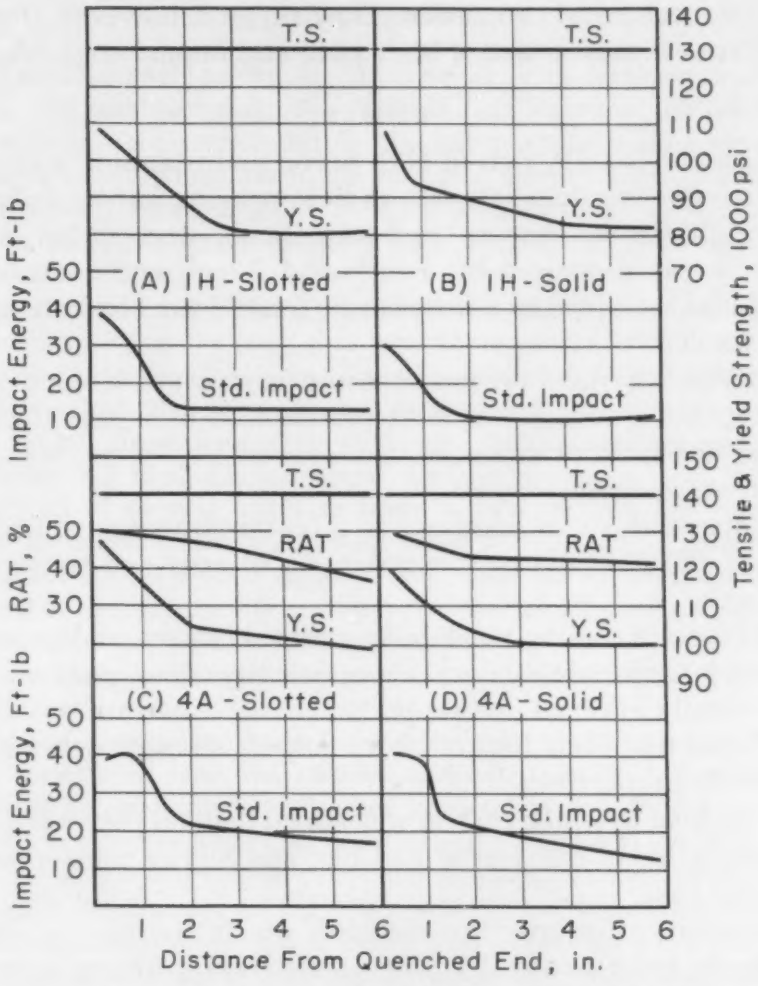


Fig. 7—Tensile and Impact Data on Steels (A) 1H—Sectioned Bar, (B) 1H—Solid Bar, (C) 4A—Sectioned Bar, and (D) 4A—Solid Bar. Corrected to the Indicated Tensile Strength Levels.

a modified AISI 4320, was selected because of its low carbon content, so that the low as-quenched hardness permitted the removal of slabs from an untempered end-quenched section for obtaining hardness determinations. The hardness curve on this section agreed well with that obtained on the slotted section. Steel 4A, a modified AISI 8650, was selected because its carbon content was the highest of the available steels. It was believed that the effect of mass might be more pronounced in this relatively high carbon, high hardenability steel than in a lower carbon, lower hardenability steel, in which less martensite would be formed on quenching. This steel was austenitized and end-quenched in the form of a solid 7- by 7-inch round, tempered, and then sectioned. The various test results on these solid sections are compared with those obtained on slabs taken from slotted rounds. The results, corrected for tensile strength, are given in Fig. 7.

The results given in Fig. 7 are not conclusive in showing the effect

of mass on mechanical properties. They suggest, however, that, if anything, increased mass lowered both yield and impact strength.

Summary

1. Grainal No. 79, rich in both boron and titanium, was observed to be more effective than ferroboron in improving hardenability.

2. Additions of boron, carbon, silicon, and nickel improved hardenability as measured by 1-inch and 7-inch end-quenched bars; rare earth oxides added to a ferroboron-treated steel had no significant effect on hardenability.

3. Boron lowered the transverse impact strength of slack-quenched structures; this lowering was least pronounced in a steel treated with ferroboron and most pronounced in a Grainal No. 79 treated steel containing strong carbide-formers.

4. Rare earth oxide additions to a boron-treated steel had a small detrimental effect on transverse reduction of area and transverse impact strength.

5. At certain cooling rates, silicon raised impact quality as a result of increased hardenability, but at sufficiently slow rates of cooling silicon generally lowered this property.

6. Nickel additions improved the impact strength without affecting the tensile properties.

7. The steel to which carbon was added had, on the average, lower yield strength, lower transverse ductility, and higher transverse toughness than the base.

8. Mechanical properties obtained on tempered end-quenched 7-inch rounds from two AISI 8640 steels from different heats are in good agreement.

9. Experimental evidence on the effect of mass on the mechanical properties was inconclusive. However, the results suggest that, if anything, increased mass lowered transverse impact quality and perhaps yield strength.

Acknowledgment

The authors are grateful to the Air Force for sponsoring this research and for permission to publish results. They also wish to thank M. A. Redmerski, E. L. Fraticelli, and Dr. Cyril Wells, of the Metals Research Laboratory, Carnegie Institute of Technology, for help received in carrying out this research.

References

1. John Vajda and Paul E. Busby, "Transverse Mechanical Properties of Slack-Quenched and Tempered Wrought Steel," Transactions, American Society for Metals, Vol. 46, 1954, p. 1331.
2. C. Wells, J. V. Russell, and S. W. Poole, "Effect of Composition on Transverse Mechanical Properties of Steel," Transactions, American Society for Metals, Vol. 46, 1954, p. 129.

DISCUSSION

Written Discussion: By A. O. Schaefer, vice president in charge of engineering and manufacturing, The Midvale Co., Nicetown, Philadelphia.

The authors were commended by me last year for adding carefully obtained data in a field which has in the past been surrounded by much mystery, which is gradually being dispelled by work such as this. The present report, stated to be part of a larger program, adds measurably to our supply of information.

I remember that last year I questioned the technique of slotting the bar before quenching it, on the basis that we had no proof that this did not alter the rates of cooling in the piece, the stresses imposed on various elements during cooling and, therefore, the end products of transformation. As proof that we need not concern ourselves with these factors, evidence was presented based on traverse hardness on several surfaces indicating that cooling was identical in all of them. I admit to being unsatisfied with this reasoning. In this paper the authors have added tests taken from a solid 7 inch round and from a slotted 7 inch round, quenched and tempered in the same way. It is freely admitted that the results are inconclusive. At this time I will admit that the results tend to support the authors' conclusions.

The results in general are in agreement with those reported in Ref. 2 in the appended references.

In general, the authors have avoided the very obvious danger of drawing too many conclusions from the evidence at hand. Data of this sort represents steel made by a certain practice, handled in a certain way, forged or rolled and heat treated in a certain way. This paper does not attempt to evaluate the effects of chemistry on the longitudinal properties of slack-quenched steel. We cannot conclude that the changes in chemistry which have been made have similar effects on longitudinal properties or even if their effects are more or less marked in transverse tests than in longitudinal tests. Nor have the authors overgeneralized the effects of the various alloying elements. Their results apply only in the ranges they have reported, and they have wisely refrained from going farther.

In only one respect, in my opinion, have they drawn conclusions unwarranted by the data. I do not think the evidence at hand permits the bald statement, ". . . Grainal No. 79 . . . was observed to be more effective than ferroboron in improving hardenability." This is obviously true in the heats of steel reported here. The trouble is that no information is given on how these heats were melted and deoxidized. Would it be true if aluminum and titanium additions, made prior to the addition of ferroboron, protected it as the titanium in Grainal 79 protects the boron in it?

The answer to this question may be in the affirmative. However, the evidence presented in this paper is not sufficient to support the broad conclusion.

There is another point on which more evidence would be extremely helpful. The harmful effects of phosphorus on RAT and transverse impact properties have been previously noted. In this report, the phosphorus content of the A, J, and E series averages 50% higher than that in the A series. In only a few instances are conclusions drawn between the different series. Perhaps in another portion of the report of which this paper is a part, the authors may have included some work on the effects of phosphorus.

It is hoped that, in the final printing of this paper, the chemical compositions will be included of those steels which were in the previous paper [2] and which are again used for comparison in the present paper.

The need for information in this field is obvious. The authors are to be congratulated for adding needed data, carefully taken. It is our hope that they will continue.

Authors' Reply

The authors appreciate the discussion and comments by Mr. Schaefer. Stimulating discussions such as these improve the quality of the paper and also suggest new ideas for future studies. In fact, a part of the work in the present paper is a direct result of Mr. Schaefer's discussion of the previous paper.

In reference to the comment concerning the effectiveness of Grainal No. 79 and ferroboron as hardenability agents, we wish to emphasize that the statement in the paper is in the form of an observation based on our few data. However, we should not be greatly surprised if the statement were found to be generally true in the sense that the chances of improving the hardenability of a given heat are greater with a Grainal No. 79 addition than with a ferroboron addition. In our opinion, an examination of all the boron heats made to date would probably show that the frequency of failure to improve hardenability as much as expected with a boron addition is higher when the addition agent is ferroboron rather than Grainal No. 79. This, of course, does not mean that the full boron effect cannot be realized with ferroboron under the proper conditions of deoxidation and steel making, for we know that the desired effect can thus be produced.

In direct answer to the question posed, we believe that the increase of hardenability due to boron would be about the same whether a given heat were treated with aluminum, titanium, and finally ferroboron or whether the same heat were deoxidized with aluminum and subsequently treated with Grainal No. 79. It should be pointed out, however, that the simultaneous additions of ferroboron and aluminum to the steels in the present investigation after they had already been fully killed with aluminum did not give the maximum boron hardenability effect. Higher nitrogen in these basic electric steels as compared to basic open hearth steels probably accounts for this behavior.

With regard to the influence of phosphorus on transverse ductility, no attempt was made to evaluate the effects of phosphorus among different heats because RAT quality is a so-called "heat characteristic"; i.e., similar compositions from different heats may exhibit wide differences in RAT quality. It is this basic premise that led to the procedure of adding an individual element to various ingots of one heat in order to determine the effect of that element on RAT quality. Unfortunately, in the present study, no single heat is available in which phosphorus was intentionally varied.

While we concede that phosphorus is detrimental to mechanical properties, we believe that the "among heat" variables, excluding phosphorus, are such that any apparent effect of phosphorus on mechanical properties would not be statistically significant.

---

[2] John Vajda and Paul E. Busby, "Transverse Mechanical Properties of Slack-Quenched and Tempered Wrought Steel," TRANSACTIONS, American Society for Metals, Vol. 46, 1954, p. 1331.

THE STATISTICAL FATIGUE PROPERTIES OF LAMELLAR AND SPHEROIDAL EUTECTOID STEEL

By G. E. Dieter, R. F. Mehl, and G. T. Horne

Abstract

Statistical methods were utilized to investigate the effect of carbide morphology on the fatigue properties and their statistical variability for a plain carbon eutectoid steel heat treated to coarse pearlite and to spheroidite of the same tensile strength. The fatigue tests were supplemented by metallographic observations and measurements of the position of failure in the fatigue specimens. The pearlitic structure showed a lower fatigue limit and smaller scatter in both the fatigue life and the fatigue limit than the spheroidized structure. The lower fatigue limit is attributed to the higher stress concentrating effects of the carbide lamellae in pearlite. Evidence is presented which supports the belief that the fatigue cracks are not initiated by the carbide particles but by nonmetallic inclusions.

WITHIN recent years a considerable amount of interest has been shown in the statistical analysis of fatigue data and in the sources of this variability inherent in the fatigue test. Several investigators (1–3) [1] have shown that even the utmost care in the preparation of specimens and in the conduct of the fatigue test cannot minimize the scatter in fatigue life and the uncertainty in the fatigue limit beyond a point where statistical techniques are needed for a proper interpretation of the results. An important consequence of the statistical approach has been the realization that it is not possible to predict the fatigue life of an individual specimen with even a fair degree of accuracy. It is now recognized that for a correct representation of the S-N curve we must include the probability of failure as an additional parameter.

Survey of the Literature

Muller-Stock (4) conducted the first recorded statistical fatigue tests by testing 200 steel fatigue specimens at a single stress. He found

[1] The figures appearing in parentheses pertain to the references appended to this paper.

This paper is part of a thesis presented by G. E. Dieter to the graduate Committee of the Carnegie Institute of Technology in partial fulfillment of the requirements for the degree of Doctor of Science.

A paper presented before the Thirty-sixth Annual Convention of the Society, held in Chicago, November 1 to 5, 1954. Of the authors, G. E. Dieter is Lieutenant, Ordnance Corps, U. S. Army, R. F. Mehl is Dean of Graduate Studies and Director, Metals Research Laboratory and G. T. Horne is member of staff, Metals Research Laboratory, Carnegie Institute of Technology, Pittsburgh. Manuscript received April 12, 1954.

that the frequency distribution of the number of cycles to failure, N, was skewed to the right, but that the frequency distribution with respect to logN followed the Gaussian or normal distribution. This logarithmic normal distribution of fatigue life at constant stress has been utilized by more recent investigators (2,3) in this field. The use of a logarithmic normal distribution has been criticized on the basis that the extreme tails of the distribution do not agree with physical facts. It has been argued that if the logarithmic normal distribution is theoretically correct then there is a finite, although very small, probability of failure occurring at extremely low or high numbers of cycles relative to the mean life at any stress within the finite life region of the S-N curve. To obviate this difficulty Weibull (5,6) proposed an exponential distribution function and Freudenthal and Gumbel (7) advocated the use of the extreme value distribution. While both of these distribution functions provide finite limits to the distribution of the number of cycles to failure at a constant stress there is little practical advantage to their use in place of the logarithmic normal distribution. All three distributions are practically identical over their central range of values. In fact Weibull has estimated that it would require the testing of about 10,000 specimens at one stress in order to distinguish between them to a high degree of significance. Thus, for engineering purposes the logarithmic normal distribution is adequate. It possesses the marked advantage that the standard statistical methods for the interpretation of tests of small numbers of specimens developed for the normal distribution can be used with logN as the variable.

A different type of statistical analysis is required when the fatigue limit is considered. Up until recently the fatigue limit was generally considered to be a sharp threshold value, below which all specimens would presumably have infinite lives. In 1949 Ransom and Mehl (1) first reported on the statistical variability of the fatigue limit. The $\pm 2\sigma$ limits on the mean fatigue limit, the stress range which would include the fatigue limits of about 95.4% of the specimens, were found to extend from 40,500 to 52,000 psi for a heat treated alloy forging steel. This work utilized a statistical method known as "staircase testing" (8) in determining the fatigue limit statistics. This method consists of testing a series of specimens, each succeeding one of which is run at a slightly higher or lower stress depending on whether the preceding specimen ran out (lasted 10^7 cycles) or failed.

Epremian and Mehl (3) made a statistical study of the fatigue limit of several steels using the classical approach of determining the mortality curve of per cent failure vs. stress level by means of a technique known as "probit analysis." The experimental procedure consisted of testing groups of specimens at different stress levels bracketing the expected fatigue limit. The number of specimens failing and not failing (runouts) were determined at each stress. With this in-

formation it was possible to determine the mean fatigue limit, $\bar{S}$, and its $\pm 2\sigma$ limits.

The same investigators (3) made an extensive study of the effect of metallurgical variables on the scatter in fatigue life and in the fatigue limit. Normalized SAE 1050 steel, Armco iron, and SAE 4340 heat treated to quenched and tempered (168,000 psi tensile strength) and quenched and spheroidized (104,000 psi tensile strength) structure were tested. It was concluded that the chief metallurgical variable which influenced the scatter both in fatigue life and fatigue limit was the inclusion content of the steel; the greater the inclusion rating of the steel the greater the variability. Their work indicated that the scatter of the fatigue limit was more sensitive to metallurgical variables than was the scatter in the fatigue life.

This work indicated that the influence of inclusions on the scatter of fatigue properties masks the effect of differences in metallurgical structure. Moreover, their tests on SAE 4340 steel provided no directly comparable information on the influence of metallurgical structure on fatigue scatter since the two structures were at markedly different tensile strength levels. Hence, it was felt that the effect of the morphology of the cementite phase on the fatigue properties should be definitely established, this time with both structures at the same strength level and with two structures of well defined carbide distributions. Gensamer and co-workers (10) have shown that the tensile properties depend primarily upon the mean free ferrite path irrespective of the shape of the carbide particles. Since in fatigue the ductility of the metal has less opportunity to exert its influence in dissipating stress concentrations than under static loads, it might be expected that lamellar pearlite would fracture more easily and would have lower fatigue properties than a spheroidal structure with equivalent mean free ferrite path.

A plain carbon eutectoid steel was selected for this investigation because with such a steel it is possible to obtain well defined extremes in carbide morphology without the interference of a proeutectoid constituent.

The use of the same steel for both structures removes the important influence of inclusion content from the list of factors contributing to the scatter in fatigue properties. Little information is available on the fatigue properties of eutectoid steels because of their commercial unimportance. Gensamer et al. (10) made a limited number of fatigue tests on an eutectoid steel reacted isothermally at several temperatures in the pearlite and bainite regions of the T-T-T curve. The results showed that the fatigue limit increased linearly with decreasing reaction temperature, with a discontinuity in the region of 900 °F (480 °C) where mixtures of both pearlite and bainite were obtained. However, recent work by Grant (11) with fatigue tests on flake and nodular cast

UNIVERSITY OF MICHIGAN LIBRARIES

Table I
Mechanical Properties of Eutectoid Steel

Structure	Ultimate Strength psi	Yield Strength psi	Elongation %	Reduction in Area %	Rockwell Hardness
Spheroidite	92,680	71,130*	28.9	57.7	92
Pearlite	98,180	35,500**	17.8	25.8	89

Prior Austenitic Grain Size: ASTM No. 6
SAE Inclusion Rating: $4^{vd} - 1.8^{200vd} - C$

* lower yield point: ** 0.1% offset

iron has shown the effect of the morphology of a brittle constituent on the fatigue properties. Tests on the two structures at comparable tensile strengths showed that the nodular iron had the higher endurance limit. In the notched or grooved condition there was no advantage for the nodular iron. Grant made no study of the statistics of fatigue.

Materials and Testing

A plain carbon eutectoid steel containing 0.78% carbon, 0.22% silicon, 0.27% manganese, 0.016% sulphur, and 0.011% phosphorus was used throughout this investigation. A coarse pearlitic structure was obtained by austenitizing specimen blanks at 1550 °F (845 °C) for one hour and then reacting them isothermally in a salt pot at 1300 °F (705 °C) for 20 hours. They were then air cooled to room temperature. To produce the spheroidized structure, specimen blanks were austenitized at 1550 °F (845 °C) for one hour and quenched in oil to produce a martensite-fine pearlite structure amenable to spheroidizing. The blanks were then spheroidized in a high temperature salt pot at 1265 °F (685 °C) for 15 hours. The mechanical properties resulting from these heat treatments are given in Table I. An approximate equivalence in the mean free ferrite paths of the two structures of nearly the same tensile strength is to be expected in accordance with the work of Gensamer (10).

Unnotched R. R. Moore rotating beam fatigue specimens of conventional design (12) were machined from the heat treated specimen blanks. The specimens had a minimum diameter of 0.300 inches and a longitudinal radius of 5 inches. Standard machining and polishing techniques were used to produce highly polished specimens in which the fine scratches ran parallel with the longitudinal direction. The polished specimens were stress relieved for one hour in a vacuum furnace at 1100 °F (593 °C). No change in mechanical properties resulted from this treatment and there was no evidence of oxidation or decarburization. The minimum diameter of each specimen was measured optically on a comparator to 0.0001 inch. All specimens were examined at 100 diameters before testing for circumferential scratches and other surface defects.

The fatigue specimens were tested on four R. R. Moore rotating

beam machines at speeds between 8000 to 10,000 rpm. The weights were accurately calibrated and the effective dead weight determined for each machine. The applied stress was calculated from elastic theory considering the fatigue specimen and bearing housing assembly to be a simply supported beam. The average percentage error in stress was about $\pm 0.7\%$. The machines were equipped with a set-screw device which actuated a relay to stop the test when a small change in the deflection of the specimen occurred. Thus, the specimens were not run to complete failure but to the point where a crack formed, varying in size from one not visible without a microscope to one about one quarter of the way through the diameter. Tests showed that there was no significant difference between this criterion of failure and complete fracture. With this criterion of failure it was hoped to obtain better microscopic correlation between the location of failure and the metallurgical structure.

Approximately 20 specimens were tested at each stress level for each structure. In the finite life region of the S-N curve the mean of the distribution of logN, $\overline{\log N}$, its standard deviation, σ, the standard error of the mean, $\sigma_{\overline{\log N}}$, and the relative standard deviation, V, were calculated at each stress from the 20 observations of fatigue life. Each of these statistics will be discussed briefly in the next section. It was assumed in all instances that the distribution of fatigue life at constant stress was adequately represented by the logarithmic normal distribution. In the endurance range 20 specimens were tested at each stress level and the mean fatigue limit, $\bar{S}$, and its standard deviation were determined from the percentage of failures at each stress using the probit method. This will be described in more detail in the next section. The criterion for a nonfailure was taken as 2.5×10^7 cycles, although several specimens were run until 5×10^7 cycles to see if there was any tendency for delayed failure.

Statistical Methods

This section presumes that the reader has a knowledge of elementary statistics so that discussion will be required of only those methods which are peculiar to the analysis of fatigue data. Reference (13) and (14) are recommended for a concise review of the concepts of statistics, while the recent book by Hald (15) includes an excellent discussion of the logarithmic normal distribution.

As was mentioned earlier, it has been found by experiment that the distribution of number of cycles to failure at a constant stress may be adequately represented by the logarithmic normal distribution, i.e., the familiar normal or Gaussian distribution where N is replaced by logN. Making this substitution in the conventional equations for calculating the mean and standard deviation of a normal distribution we get expressions for the mean of log N, $\overline{\log N}$, and its standard deviation, σ.

$$\overline{\log N} = \frac{\sum_{i=1}^{i=n} \log N_i}{n}$$

$$\sigma = \left[\frac{\sum_{i=1}^{i=n} \left(\log N_i - \overline{\log N} \right)^2}{n-1} \right]^{\frac{1}{2}}$$

The mean of a sample provides an unbiased estimate of the mean of the universe from which the sample was drawn. Thus, confidence limits can be placed on the observed value of the mean by calculating the standard error of the mean, $\sigma_{\overline{\log N}}$.

$$\sigma_{\overline{\log N}} = \frac{\sigma}{\sqrt{n}}$$

If the distribution is normal the true mean of the universe will lie within the interval $\overline{\log N} \pm 1.96\, \sigma_{\overline{\log N}}$ with a confidence of 95%. The relative standard deviation, V, is sometimes useful for expressing the degree of dispersion on a relative basis.

$$V = \frac{\sigma}{\overline{\log N}}$$

Although $\overline{\log N}$ is the mean of the distribution of logN it does not follow that the antilogarithm of $\overline{\log N}$ is the mean of the distribution of N. This results from the fact that while the distribution is normal with respect to logN it is skewed to the right for N. The antilog of $\overline{\log N}$, $\overline{N}$, is actually the median [2] of the distribution of N, assuming a continuous distribution. The mean of N, $\hat{N}$, is given by the following equation.

$$\log \hat{N} = \overline{\log N} + 1.1513\, \sigma^2$$

It will be noted that the median is less than the mean and that the greater the standard deviation the greater will be this difference. The difference between the mean and the median of N is small for moderate values of σ and is usually negligible when the scale of the S-N diagram is considered. However, for values of σ greater than about 0.3 this difference can be detected on the S-N plot. The custom has arisen in presenting statistical fatigue data to report $\overline{\log N}$ and the antilog of this value, $\overline{N}$. It is this value, $\overline{N}$, which is usually plotted to a log scale on the S-N diagram.

The standard statistical tables prepared for use with the normal frequency distribution can be used with the logarithmic normal distribution provided that all calculations are performed in terms of log N. The

[2] It is realized that the notation for $\hat{N}$ is in disagreement with standard statistical notation where the bar indicates the mean value. However, the notation given has become standard in papers on the statistics of fatigue.

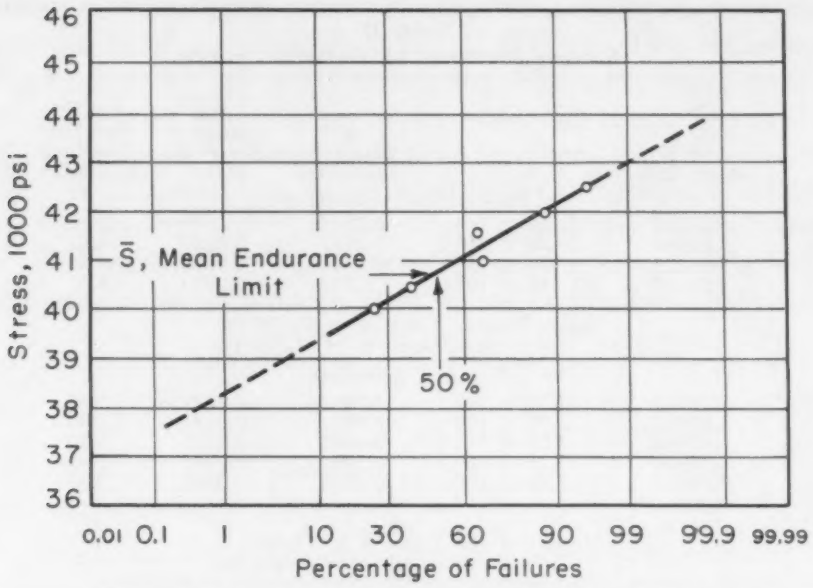


Fig. 1—Percentage of Failures, in Probability Coordinates, Plotted Against Stress. (Epremian and Mehl (3)).

common tests of significance such as the F test for the difference in variability between two sets of data and the t test for the difference between two means can be employed without difficulty provided this precaution is observed.

The determination of the fatigue limit is a typical example of a type of experiment known in statistics as a "sensitivity experiment." Thus, when a specimen is tested at a stress within the endurance range the only information which we obtain is whether the specimen fails or runs out. If it fails we are unable to determine what the maximum stress would have been at which the specimen would have run out. Conversely, if the specimen runs out, we cannot find the lowest stress at which it would fail, since we often have reason to believe that cycles of understress alter the properties of the specimen. Thus, in the endurance range, fatigue is a "go-no go" proposition and all that we can do is estimate the behavior of a universe of specimens (the population) with a suitable sample.

Probit analysis is a statistical technique suitable for the analysis of this problem. The procedure is to test at least 20 specimens at each of at least 3 stress levels, noting the percentage of the specimens which fail at each stress. It has been found that the percentage of failures is approximately normally distributed with respect to stress. If the percentage of failures is plotted against stress on normal probability paper a straight line will be obtained, as is shown in Fig. 1. If the data fall on a good straight line and only moderately precise results are required this plot may be used to obtain the value of the mean fatigue limit and its standard deviation. The mean fatigue limit, $\bar{S}$, is the stress at 50%

Table II
Fatigue Statistics for Eutectoid Steel

Stress psi	$\overline{\text{Log N}}$ Mean Life	$\bar{N}$	σ Standard Deviation	$\sigma_{\overline{\log N}}$ Standard Error of Mean	%V Relative Standard Deviation	Per Cent Failure
		Spheroidized Structure				
47,500	5.33315	2.153×10^5	0.1644	0.0367	3.09	100
45,000	5.81040	6.462×10^5	0.2797	0.0253	4.82	95
43,000	5.92829	8.478×10^5	0.2743	0.0665	4.63	85
41,500	6.24127	1.743×10^6	0.2713	0.0904	4.35	45
40,000						21
		Mean Fatigue Limit $\bar{S}$ = 41,550 psi				
		σ Fatigue Limit σ = 1,750 psi				
		Pearlitic Structure				
42,000	5.18280	1.53×10^5	0.0696	0.0174	1.35	100
38,800	5.57452	3.75×10^5	0.0823	0.0184	1.48	100
36,000	6.07108	1.21×10^6	0.0920	0.0217	1.51	90
35,000	6.29904	1.99×10^6	0.1644	0.0387	2.61	90
34,000	6.51126	3.24×10^6	0.3420	0.0987	5.25	50
33,500						10
32,500						5
		Mean Fatigue Limit $\bar{S}$ = 34,000 psi				
		σ Fatigue Limit σ = 960 psi				

failure and the standard deviation is the stress range between $\bar{S}$ and the stress for which the percentage failure is 84%.

However, if a straight line cannot be fitted through the points without indecision or if greater accuracy is desired, the percentage failures should be converted to probits and the methods of probit analysis employed. The probit, abbreviation of probability unit, is a statistical transformation which eliminates negative values from the standardized normal cumulative distribution function. The ordinary form of this function has a mean of zero, while the transformation to probits results in a mean of 5. The detailed procedure is too lengthy for inclusion here. A straightforward description of the calculation has been given by Finney (9).

Experimental Results

Fatigue Statistics

The finite life and fatigue limit statistics for both the spheroidized and pearlitic structures are given in Table II. Unfortunately, the range of stress which could be studied was limited by severe heating of the specimens at stresses above 47,500 psi. The generation of heat within the specimen was pronounced even when the fatigue machines were operated at the slow speed of 4500 rpm and is evidence of elastic hysteresis within the material. It should be noted that the stress at which this heating became pronounced, 50,000 psi, was well below the static yield point of the spheroidized structure. At stress levels above 35,000 psi the pearlite specimens were above their static yield strength. However, tests[3] on a fatigue machine especially instrumented so as

[3] These tests were performed through the courtesy of Prof. E. D'Appolonia of the Civil Engineering Dept., Carnegie Institute of Technology.

to record very minute deflections showed that the specimens behaved essentially elastically at stresses up to 46,000 psi. The initial application of a load above the yield strength produced a small amount of plastic strain. After a few cycles of load reversal the deflection became elastic and remained so until just before fracture.

The F test for a significant difference in the variability of two sets of data (16) was applied to the standard deviations for each structure at a series of stresses. It was found that the scatter in fatigue life increased significantly with decrease in stress. It should be noted that for

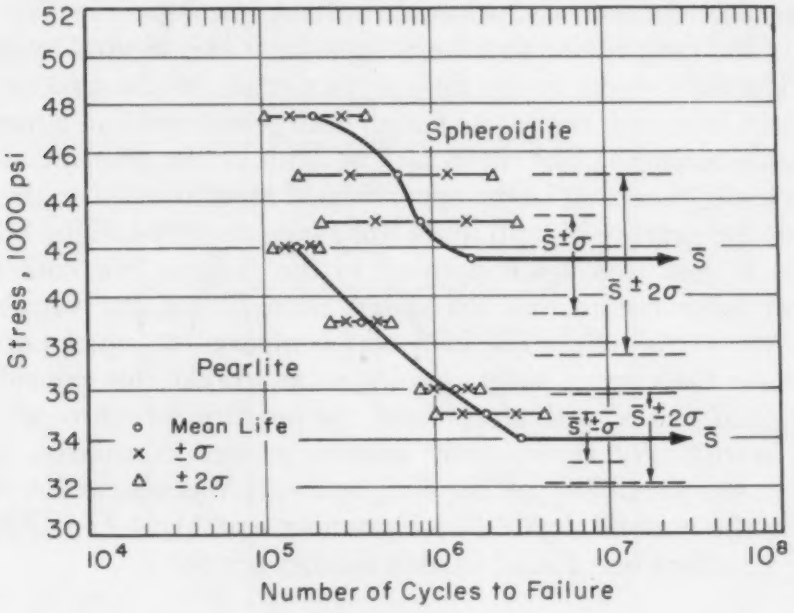


Fig. 2—Statistical S-N Curves for Pearlite and Spheroidite.

the spheroidized structure only the stress of 47,500 psi was outside of the statistical range of the fatigue limit. Thus, at lower stresses the statistics of finite life are based only on the number of specimens out of the 20 tested at that stress which failed. These statistics are therefore not as reliable as for stresses where all of the specimens tested failed. This procedure of calculating the fatigue life statistics at the stresses near the $+2\sigma$ limit of the mean fatigue limit where the statistics of the finite life curve and the fatigue limit overlap may be criticized on the grounds that it is an arbitrary division to consider part of a sample of 20 specimens in a distribution of fatigue life at constant stress while at the same time considering the same sample in the distribution of per cent failure with stress of the fatigue limit statistics. However, the authors know of no statistical measure of dispersion which could include values of infinite life.

The procedure which was adopted seems to take into consideration the physical facts. The specimens which run out at these stresses usually

endure at least ten times the number of cycles undergone by those specimens which failed at the same stress. This gap in life is so great that it seems justifiable to consider the runouts as coming from a different population. This treatment of the data certainly does make sense from the design standpoint. The first question that a designer would ask is, at a given stress, will the part break or run out? For his answer he has only to look at the fatigue limit statistics to find the probability of a runout. If the probability of a runout is small, his next question is, at what number of cycles will it break? The answer to this question is found from the finite life statistics.

The S-N curves for the two structures are shown in Fig. 2. The scatter in the fatigue life and the fatigue limit is indicated by the $\pm 2\sigma$ limits. The differences in the fatigue properties of the two structures are evident from this curve. Although both structures had almost identical tensile strengths, the mean fatigue limit of the pearlitic structure is much lower than that of the spheroidized structure. Also, the scatter is less for the pearlite in both finite life range and the fatigue limit.

The F test was again applied to the fatigue life data to give statistical assurance to this last observation. When the variability in fatigue life of the two structures was compared at equal percentage stress above their mean fatigue limits, so as to take into consideration the change of scatter with stress level, the pearlitic structure was found to have statistically significantly smaller scatter. Similarly, the difference in the variability of the fatigue limits was checked with the t test using the method devised by Epremian and Mehl (3). Again the pearlitic structure was found to have smaller scatter.

Crack Location

A study of the position of the fatigue crack with respect to the point of minimum diameter in the R. R. Moore fatigue specimen was made for both structures. The fact that failure frequently occurs at positions removed from the point of minimum diameter or maximum applied stress is an indication of the local variations in the strength of the material. If the differences in fatigue statistics observed for these two materials are results of differences in strength arising from their carbide morphology, then it might be expected that the two structures would show different behavior with respect to the location of the fatigue crack.

Each specimen was divided into zones 3/64 inches in width, starting at the point of minimum diameter. Section number A extended 3/64 inches on each side of the central position, section number B extended from 3/64 to 6/64 inches from the central position on each side of the minimum diameter, etc. The number of fatigue cracks occurring within each section was determined and a distribution of location of failure plotted for each structure for all specimens which failed, re-

gardless of stress level. The number of specimens tested at each stress was not sufficient to determine differences in position of failure as a function of stress level. As can be seen from Fig. 3, there was no apparent difference in the distribution of the location of failure for the two structures.

Metallographic Observations

An attempt was made to relate the path of crack propagation to the morphology of the carbide phase in the two structures. The unetched surfaces of spheroidized specimens tested at high stresses usually showed a network of fine particles which are believed to be fine carbides which were brought into relief by plastic deformation of the ferrite

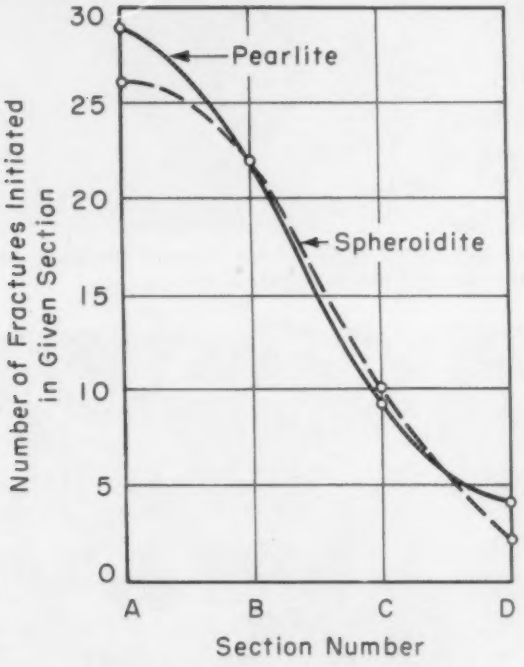


Fig. 3—Distribution of Location of Failure in Pearlite and Spheroidite Fatigue Specimens.

matrix. These particles were not present on the surface of the specimen before testing nor were they very prominent in specimens tested at low stresses within the endurance range. Fig. 4 shows such a network, together with a fine crack apparently starting at an inclusion. On many other instances the fatigue crack was found in close proximity to a large inclusion, although the frequency of this observation was not as high as has been reported recently by Ransom (17) for transverse fatigue specimens. However, there is little doubt that inclusions are a major point of initiation of fatigue cracks in longitudinal fatigue specimens.

It was not always possible to resolve clearly the fatigue crack in relation to the microstructure on the surface of the fatigue specimens.

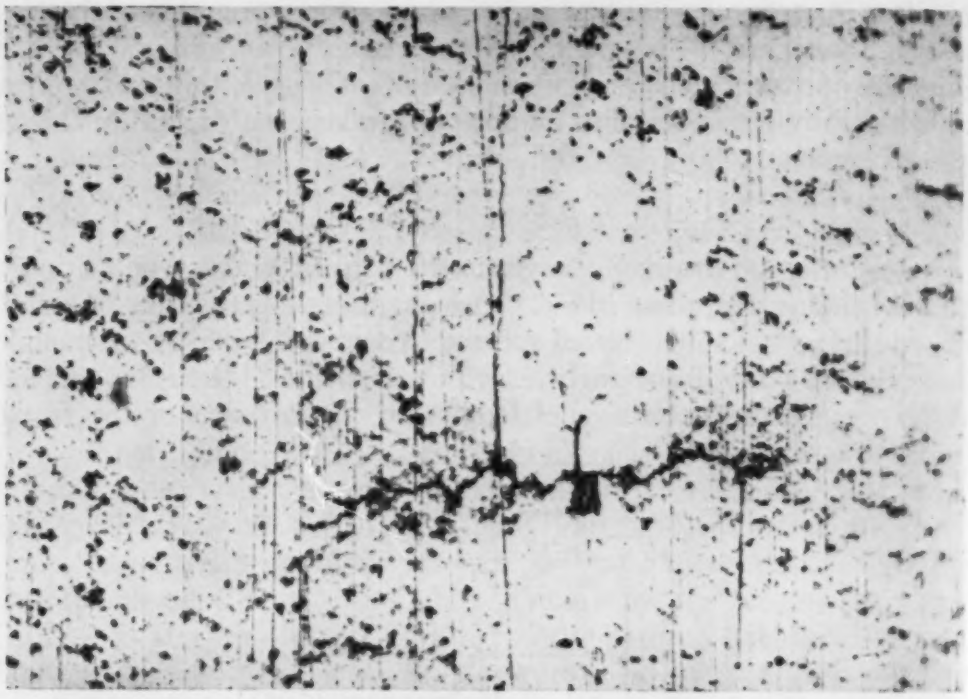


Fig. 4—Unetched Surface of Spheroidized Fatigue Specimen Showing Carbides and an Inclusion in Relation to the Fatigue Crack, X 400.

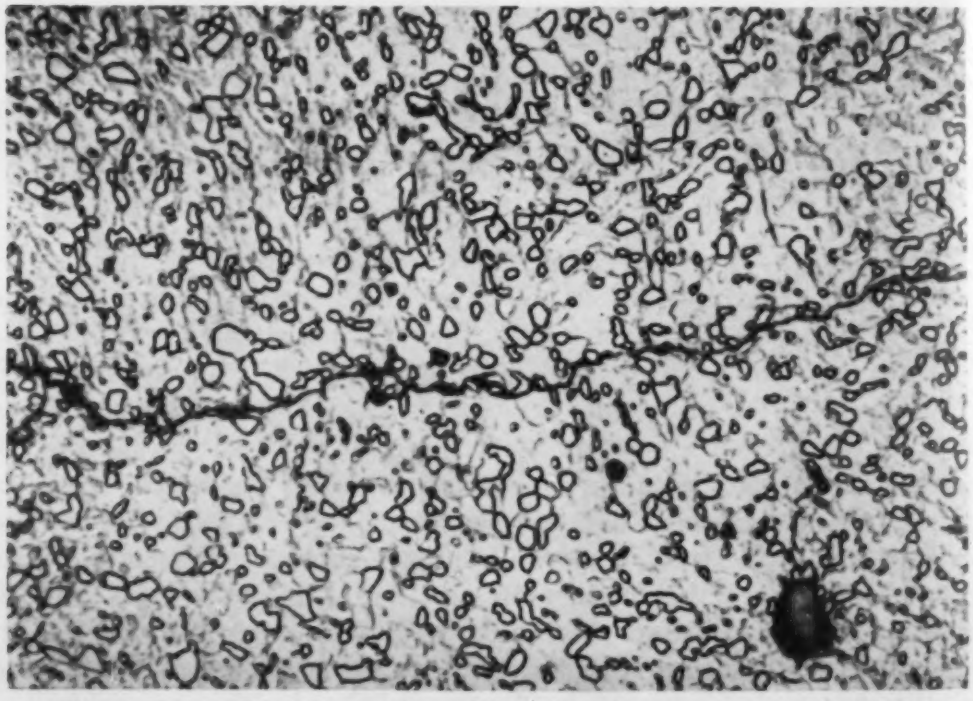


Fig. 5—Fatigue Crack Propagation in Spheroidized Structure. X 1500 Nital Etch.

Therefore it was necessary to section and mount the specimens in the neighborhood of a fine crack. Thus, Figs. 5 and 6 show the appearance of a fatigue crack at a few thousandths of an inch below the surface of

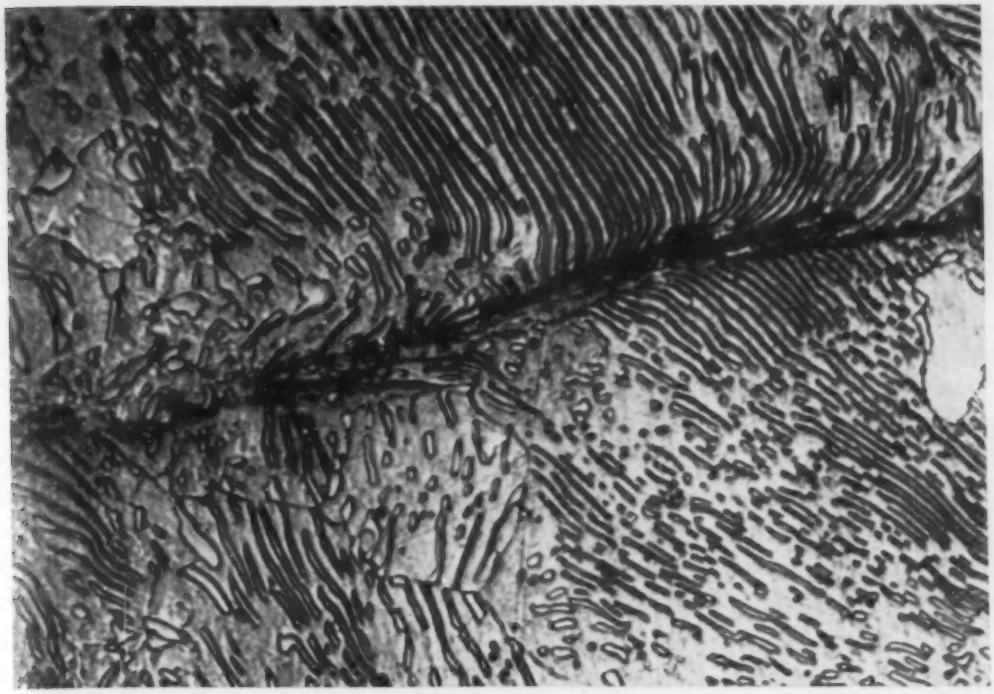


Fig. 6—Fatigue Crack Propagation in Pearlitic Structure. X 1500 Nital Etch.

the fatigue specimen. Fig. 5 shows that the crack propagates in spheroidite entirely in the ferrite matrix with no apparent distortion of the carbides. Although in many places the crack appears to travel in a stepwise manner from carbide to carbide, there are instances where the crack seemingly deliberately by-passes a carbide particle. In pearlite, as the crack propagates through the ferrite matrix there seems to be no preferential relationship between the crack and the carbide lamellae. Cracks were often observed to propagate directly through a pearlite colony causing marked distortion and bending of the lamellae, Fig. 6. Cracks were also observed to pass either perpendicularly through a carbide, around the tip of the carbides, or parallel to the lamellae, depending on the location of the carbide with relation to the advancing crack. The fatigue cracks did not follow the boundaries of the pearlite colonies. Therefore, the direction of the fatigue crack is probably determined by the applied stress field and by the planes of easiest slip in the ferrite. The function of the carbide phase appears to be chiefly that of modifying the stress distribution existing on a micro-scale in the ferrite matrix.

Discussion

It has been shown that the fatigue properties of an eutectoid steel are affected by the morphology of the carbide phase. Both the fatigue strength at a constant number of cycles and the mean fatigue limit are lower for a pearlitic structure than for a spheroidized structure of the same tensile strength. Thus, although the mean free ferrite path ap-

UNIVERSITY OF MICHIGAN LIBRARIES

pears to be the chief factor determining the static tensile properties of steel, it does not determine the fatigue properties. In fatigue, the shape as well as the distribution of the carbide particles is of importance.

However, it has also been shown that the distributions of location of failure were not very different for the two structures and showed a large number of specimens failing away from the point of minimum diameter. This would indicate, at least for this steel, that the carbide second phase is not the primary cause of crack initiation. If the carbide lamellae in pearlite were a source of crack initiation it would be reasonable to assume that there would be some optimum orientation of the lamellae with respect to the applied stress which would most easily initiate failure. However, since all possible orientations of carbide lamellae are to be expected in a 3/64 inch wide annular ring of surface at the minimum diameter of the fatigue specimen, it would be expected that the frequency of fracture at this region of maximum applied stress would be much higher than that actually observed, if the carbide lamellae served as sources of crack initiation. Similarly, we would expect a much higher percentage of failures occurring at the point of minimum diameter in the spheroidized fatigue specimens if the carbides were chiefly influential in causing fracture. In this case, however, the orientation requirement would be less critical.

Therefore, it is believed in this instance, as indeed may in general be true for steel, that the initiation of fatigue fracture is primarily caused by inclusions. Although the inclusion rating of this steel is only relatively high, the number of effective inclusions in a given surface area is certainly much lower than the number of properly oriented carbide particles. The inclusion rating given in Table I indicates that 200 inclusions ½ inch or greater in length at × 100 were found on an area of ½ inch square. Such an arrangement of imperfections would explain the large observed variation of location of fracture. As mentioned in the previous section, there was considerable metallographic evidence to substantiate this conclusion. The metallographic study further indicated that there were no unusual effects associated with the presence of the carbide particles.

It is believed that the primary influence of the carbide phase is in modifying the stress distribution existing in the ferrite matrix through stress concentrating effects. The thin lamellar carbides in pearlite act as more severe stress concentrators than the spheroidal carbides of spheroidite. Thus, the stress distribution existing in the ferrite is not that calculated from simple strength of materials but is vastly altered by the carbide particles. In pearlite the localized stresses are higher than in spheroidite. The stress axis of the S-N diagram indicated only the applied macrostress and tells nothing about the localized stresses existing in the ferrite. The lower fatigue limit of the pearlitic structure is a manifestation of the stress concentrations produced by this form of

Table III
Comparison for Actual Stresses for Pearlite and Spheroidite

Pearlite			Spheroidite		
Nominal Stress psi	Actual Stress psi		Nominal Stress psi	=	Actual Stress psi
42,000	51,200				
38,800	47,500		47,500		
36,000	44,000		45,000		
35,000	42,600		43,000		
34,000	41,500		41,500		

carbide morphology. For a given critical stress to initiate fracture in the ferrite the necessary applied stress is appreciably lower for pearlite than that required by spheroidite with its lower stress concentrating effect.

The quite plausible assumption can be made that at the two fatigue limits (in terms of applied stress), the actual stress required to initiate a crack in the ferrite is the same for both pearlite and spheroidite. (The assumption of equivalent active stress is implicit in the terminology for notches of 'fatigue strength reduction factor'; the assumption of the active crack initiation being in the ferrite is also not new,—Zener (18) has shown possible mechanisms for this and the overall similarity of behavior, especially in position of failure, found in this investigation points to ferrite as being the weaker link). On the assumption, the ratio of the fatigue limit of spheroidite to that of pearlite should be a measure of the stress concentrating effect of the carbide lamellae in pearlite. This ratio is approximately 1.22. If the nominal stress levels at which the pearlite specimens were tested are multiplied by this factor to obtain the "actual stress" it is seen (Table III) that the "actual stresses" for both structures are almost equal.

The observed similarity in the distributions of position of failure for the two structures lends support to, and is explained by this stress concentrating effect. As can be seen from Table III, the pearlite and spheroidite fatigue specimens were tested at equivalent "actual stress." Therefore, similar distributions of position of failure would be expected from fatigue specimens containing the same distributions of inclusions acted upon by the same stresses.

If these arguments be valid, two additional observations need clarification. When the values of $\overline{\log N}$ for the two structures are compared at equal 'actual' stress using the t test (19), it is found that $\overline{\log N}$ for pearlite is significantly greater at each stress. The authors believe that this greater length of life at equivalent stress for the pearlite is a manifestation of a slower rate of crack propagation in the pearlite where the crack is not wholly confined to the ferrite but must, perforce, cross the cementite lamellae. This also is consistent with the ferrite being the weaker link.

The other observation, of significantly lower scatter in the fatigue

limit and in the finite life statistics of the pearlite, is of unknown significance. There appear to be several possibilities, none of which seems to be other than an *ad hoc* assumption.

Conclusions

1. The fatigue properties of an eutectoid steel are affected by the morphology of the carbide phase. Both the fatigue strength at a constant number of cycles and the mean fatigue limit are lower for a pearlitic structure when compared with a spheroidized structure of the same tensile strength. Thus, the mean free ferrite path is not the determining factor in fatigue properties although it appears to be so in the case of static tensile properties.

2. The scatter in fatigue life increases with decrease in stress. It has been shown by statistical tests of significance that the scatter in both fatigue life and fatigue limit is smaller for the pearlitic structure when compared with the spheroidized structure under equivalent stress conditions.

3. The scatter in position of failure is about the same for both structures.

4. It is proposed that the chief influence of the morphology of the carbide phase is in modifying the localized stress distributions existing in the ferrite. Such an effect can explain the lower fatigue properties exhibited by the pearlite and the similar distribution of position of failure in the two structures.

5. Further support for the belief that inclusions are the primary outward cause of the statistical scatter in the fatigue properties of steel has been presented.

Acknowledgment

The authors take pleasure in acknowledging the invaluable assistance of J. P. Bucci and W. T. Reynolds in conducting the fatigue tests. This work received the financial support of the National Advisory Committee for Aeronautics.

References

1. J. T. Ransom and R. F. Mehl, "The Statistical Nature of the Endurance Limit," *Transactions,* American Institute of Mining and Metallurgical Engineers, Vol. 185, 1949, p. 364.
2. A. S. Freudenthal, "Planning and Interpretation of Fatigue Tests," Symposium on Statistical Aspects of Fatigue, ASTM Special Technical Publication No. 121, 1951, p. 3.
3. E. Epremian and R. F. Mehl, "The Statistical Behavior of Fatigue Properties and the Influence of Metallurgical Factors," ASTM Special Technical Publication No. 137, 1952.
4. H. Muller-Stock, "Der Einfluss dauernd und unterbrochen Wirkender schwingender Uberbeanspruchung auf die Entwicklung des Sauerbruchs," *Mitteilung,* Kohle and Eisenforshung, Vol. 8, 1938.
5. W. Weibull, "A Statistical Distribution Function of Wide Applicability," *Journal of Applied Mechanics,* Vol. 18, Sept. 1951, p. 293.

6. W. Weibull, "Statistical Design of Fatigue Experiments," *Journal of Applied Mechanics,* Vol. 19, March 1952, p. 109.
7. A. M. Freudenthal and E. J. Gumbel, "On the Statistical Interpretation of Fatigue Tests," *Proceedings,* Royal Society (London), series A, Vol. 216, 1953, p. 309.
8. J. T. Ransom and R. F. Mehl, "The Statistical Nature of the Fatigue Properties of SAE 4340 Steel Forgings," ASTM Special Technical Publication No. 137, 1952.
9. D. J. Finney, "Probit Analysis," 2nd Edition, Cambridge University Press, London, 1952.
10. M. Gensamer, E. Pearsall, W. S. Pellini, and J. R. Low, "The Tensile Properties of Pearlite, Bainite, and Spheroidite," TRANSACTIONS, American Society for Metals, Vol. 30, 1942, p. 983.
11. J. W. Grant, "Notched and Unnotched Fatigue Tests on Flake and Nodular Cast Irons," British Cast Iron Research Association Research Report Number 251.
12. "Manual on Fatigue Testing," ASTM Special Technical Publication No. 91, 1949, p. 30.
13. W. J. Dixon and F. J. Massey, "Introduction to Statistical Analysis," 1951, McGraw-Hill, New York.
14. E. G. Olds and C. Wells, "Statistical Methods for Evaluating the Quality of Certain Wrought Steel Products," TRANSACTIONS, American Society for Metals, Vol. 42, 1950, p. 845.
15. A. Hald, *Statistical Theory with Engineering Applications,* 1952, John Wiley & Sons, New York.
16. W. J. Dixon and F. J. Massey, Op. cit., p. 88.
17. J. T. Ransom, "The Effect of Inclusions on the Fatigue Strength of SAE 4340 Steels," TRANSACTIONS, American Society for Metals, Vol. 46, 1954.
18. C. Zener, "The Micro-Mechanism of Fracture," FRACTURING OF METALS, American Society for Metals, Cleveland, 1948.
19. W. J. Dixon and F. J. Massey, Op. cit., p. 105.

UNIVERSITY OF MICHIGAN LIBRARIES

EFFECT OF STATIC STRESS ON THE DAMPING OF SOME ENGINEERING ALLOYS

By A. W. Cochardt

Abstract

Wires of alloy type AISI 403 and Refractaloy 26,[1] with weights suspended on them, were twisted, and the decay of the free torsion vibration was measured. The static stress was varied between 910 and 51,000 psi, the vibrational torsion stress between 0 and 40,000 psi, and the temperature between 70 and 1300 °F (21 and 705 °C). It was found that the damping of alloy type 403 is considerably affected by a superimposed static stress; for example, at a temperature of 750 °F (400 °C) its damping decreases with static stress by a factor of 5 at lower vibrational stresses. A different effect is observed in Refractaloy 26 whose damping always increases with static stress. The data are found to be in agreement with our present concept of the mechanism of damping, from which it follows that at lower vibrational stresses the damping generally decreases with stress in ferromagnetic materials while the opposite effect occurs in nonferromagnetic alloys. At larger vibrational stresses the damping behavior is governed by strain hardening and recovery.

Introduction

UNCONTROLLED stresses that build up during vibration at or near resonance are the major cause of service failures in modern turbines and other high speed engines (1,2)[2]. These failures can be prevented if machine members with high damping capacities are used because, due to the damping, the induced stresses are then kept low (3,4).

A major portion of the total damping of a machine member often arises from the material damping. As a consequence, it is often necessary to know the magnitude of the material damping for calculating ultimate vibrational stresses. In the past, damping capacities of a great number of alloys have been measured (5,6,7,8). However, it seems the effect of a static stress on the material damping has not been considered before. The results of previous tests are therefore of little value for design engineers who want to know the actual damping of machine

[1] Registered Trade Mark.
[2] The figures appearing in parentheses pertain to the references appended to this paper.

A paper presented before the Thirty-sixth Annual Convention of the Society, held in Chicago, November 1 to 5, 1954. The author, A. W. Cochardt, is associated with the Research Laboratories, Westinghouse Electric Corp., East Pittsburgh, Pa. Manuscript received May 5, 1954.

members that are subjected to large centrifugal stresses, such as turbine or compressor blades, unless it is shown how the internal damping is affected by a larger superimposed static stress.

The present paper deals with this problem. To determine the influence of centrifugal stresses on the damping of alloys, damping tests were made using wires on which various weights were suspended. The results of these tests are reported on two typical alloys: AISI 403,

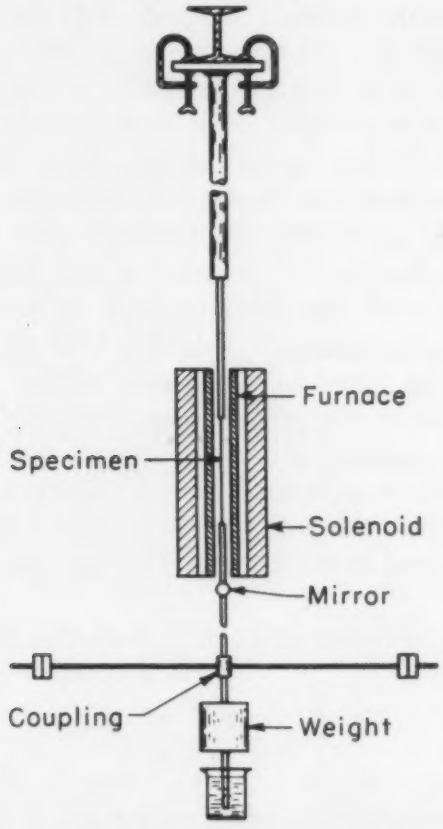


Fig. 1—Apparatus for Measuring the Effect of Static Stress on Damping.

which is a ferromagnetic stainless steel and is extensively used as blade material for steam turbines, and Refractaloy 26, which is a nonferromagnetic high temperature alloy. It is believed from theoretical considerations that other alloys, when under the influence of a static stress, will behave at lower vibrational stresses like one or the other of these two alloys depending upon whether they are ferromagnetic or not. At higher vibrational stresses the damping behavior is more complex and depends mainly upon strain hardening and recovery.

Experimental Arrangement

Fig. 1 shows the apparatus which was used for measuring the effect of static stress on damping. A test wire is silver-soldered at both

ends into brass rods of ⅜ inch diameter. Two set screws clamp the upper brass rod firmly in a steel bar of 1 inch diameter and 4 feet long. The steel bar itself is welded to a ¾ by 6 by 6 inch steel plate which, in turn, is clamped to an I-beam with four C-clamps. Whereas the top part is rigidly mounted, the bottom part of this arrangement is free to rotate. The lower brass rod is connected, through a coupling, to another brass rod on which a heavy lead weight is suspended and whose bottom end is immersed in a silicone fluid of proper viscosity. An inertia arm with variable weights on its ends is soldered to the coupling. The wire is inside a furnace and the furnace inside a solenoid.

The test wire is twisted, and the decay of the torsion vibration is measured optically on a circular scale onto which a light beam is reflected from the mirror. Lateral vibrations damp down quickly due to the immersion of the brass rod in the silicone fluid. The static stress is varied by suspending different weights from the brass rod, and the vibrational stress is changed by increasing the amount of twist. The weight of the inertia arm, the coupling, and the two lower brass rods is 2.83 pounds. By connecting the solenoid to a direct current source, the test wire can be subjected to a magnetic field of about 500 oersted. In this manner the two types of damping, damping due to plastic flow and due to magneto-mechanical hysteresis, can be differentiated.[3] The frequency of the torsion vibration is 0.3 cycles/second. If different lead weights are suspended from the wire, the small weights on the inertial arm are changed in such a way that the frequency remains essentially constant.

The damping is expressed in terms of the damping capacity δ given by the relation

$$\sigma = \frac{2}{n} \frac{a_1 - a_n}{a_1 + a_n}$$

where n is the number of cycles between the two amplitudes a_1 and a_n. To increase the accuracy of the measurements, n is varied between 1 and 10 depending upon whether the damping is high or low. δ differs from the logarithmic decrement by not more than 1% for most measurements. The results of the damping tests are reported in graphs where δ is plotted against the shear strain γ at the surface. γ was calculated from the diameter of the wire d and its length l, from the distance D between mirror and scale, and from the deflection a measured on the circular scale by making use of the relation

$$\gamma = \frac{da}{4lD}$$

[3] However, the results of measurements taken in a magnetic field are not reported in this paper. The data in Figs. 3 to 8 simply represent the total damping. The magneto-mechanical effect has been explained in considerable detail elsewhere (9–11). Magneto-mechanical damping arises from the irreversible motion of ferromagnetic domains, and it was shown that this type of damping is the major cause of damping in certain cases (4, 9).

Since it was uncertain whether an appreciable portion of the measured damping was due to the silver-soldered ends, an alternative clamping device was used. Both ends of the test wire were bent 90 degrees and were mechanically clamped using grips of Discaloy [4] which are

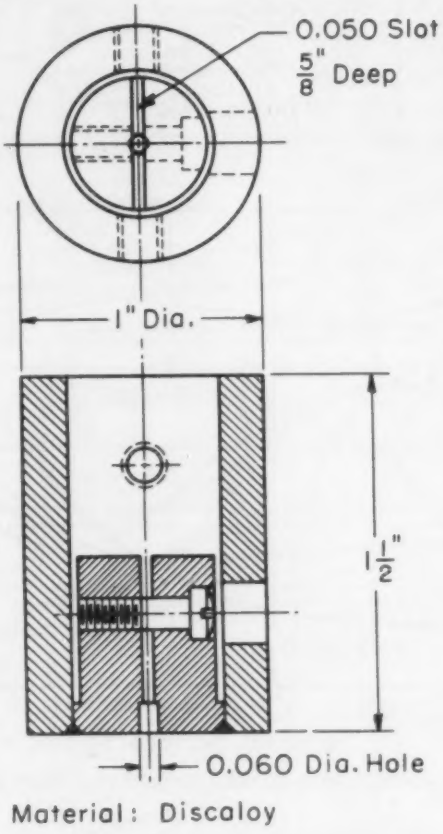


Fig. 2—Clamping Device for Test Wires.

drawn in Fig. 2. The results of tests using this grip device differed by not more than the experimental error from those results that were obtained with the prior device (Fig. 1). This finding and the fact that damping values as low as 0.001 were measured seem to indicate that end effects were negligibly small.

Preparation of the Test Wires

The composition and the dimensions of the test wires are listed in Table I. The alloys were melted in air, forged, and swaged. They

Table I
Composition and Dimensions of the Test Wires

Specimen No.	Diameter Inches	Length Inches	Fe %	Ni	Co	Cr	Mo	C	Mn	Si	Ti	Al
1,3,4,5,	0.064	8	85	0.6	—	12.3	0.5	0.1	0.5	0.34	—	—
2,6	0.064	8	16	38	20	18	3.2	0.03	0.8	1	2.6	0.2

[4] Registered Trade Mark.

UNIVERSITY OF MICHIGAN LIBRARIES

Table II
Heat Treatment of Test Wires

Specimen No.	Alloy	Solution Treatment Temp. °F	Solution Treatment Time Hrs.	Cooling From Solution Treatment Temperature	Aging Temp. °F	Aging Time Hrs.	Cooling From Aging Temp.	Cold-Work, Reduction of Area
1	AISI 403	1850	1	Oil-Quenched	1100	½	Air-Cooled	—
2	Refractaloy 26	1950	1	Oil-Quenched	1500	7	Air-Cooled	—
3	AISI 403	1850	1	300 °F/hr.	—	—	———	—
4	AISI 403	1850	1	Oil-Quenched	—	—	———	—
5	AISI 403	1850	1	Air-Cooled	—	—	———	70
6	Refractaloy 26	1950	1	Oil-Quenched	—	—	———	—

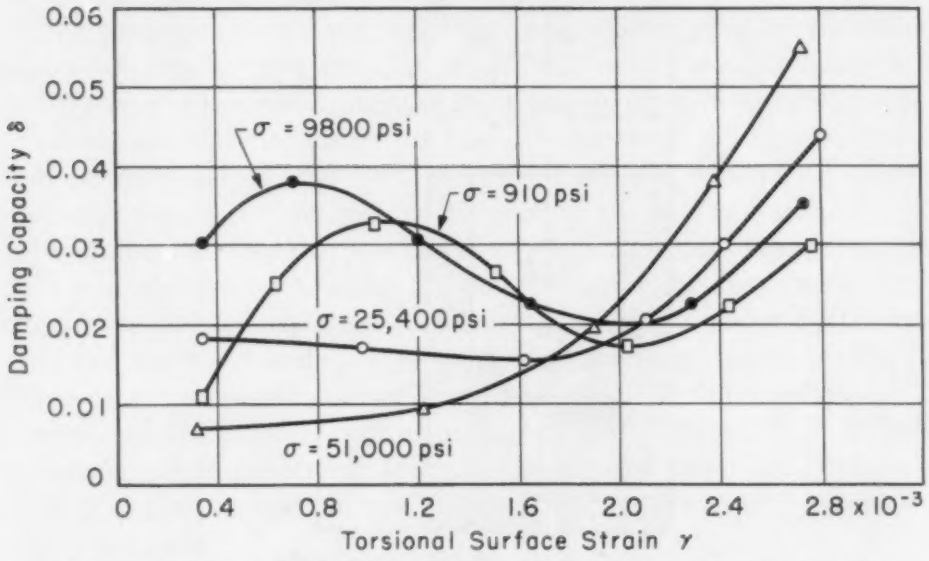


Fig. 3—Effect of Static Stress on the Damping of a Wire of Alloy Type AISI 403 (Specimen 1).

were then heat treated in a hydrogen atmosphere as described in Table II. To eliminate as much as possible the effect of stress history on damping, a wire that was severely deformed during a test was re-annealed or replaced by another after the test.

Results of the Measurements

Measurements were made on all the wires at room temperature (Figs. 3,5,7, and 8) and on wires 1 and 2 at temperatures up to 1300 °F (705 °C) (Figs. 4 and 6). Fig. 3 shows that the damping of wire 1 is considerably affected by a superimposed static stress σ. For example, at a shear strain of 0.7×10^{-3}, which corresponds to a shear stress of about 8,500 psi, δ first increases and then decreases with σ; in all, it may decrease by a factor of more than 5. Essentially the opposite effect is observed at larger shear strains since in that case δ is found to increase with σ. For example, at 2.8×10^{-3} shear strain or about 34,000 psi shear stress, the damping capacity increases almost twofold when the heaviest weight is hung onto the wire resulting in a

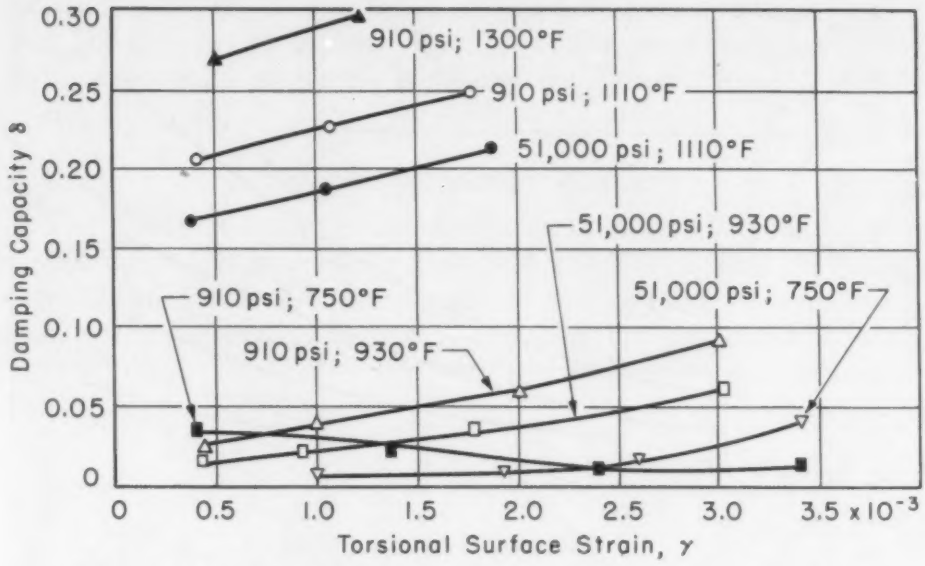


Fig. 4—Effect of Static Stress and Temperature on the Damping of a Wire of AISI 403 (Specimen 1).

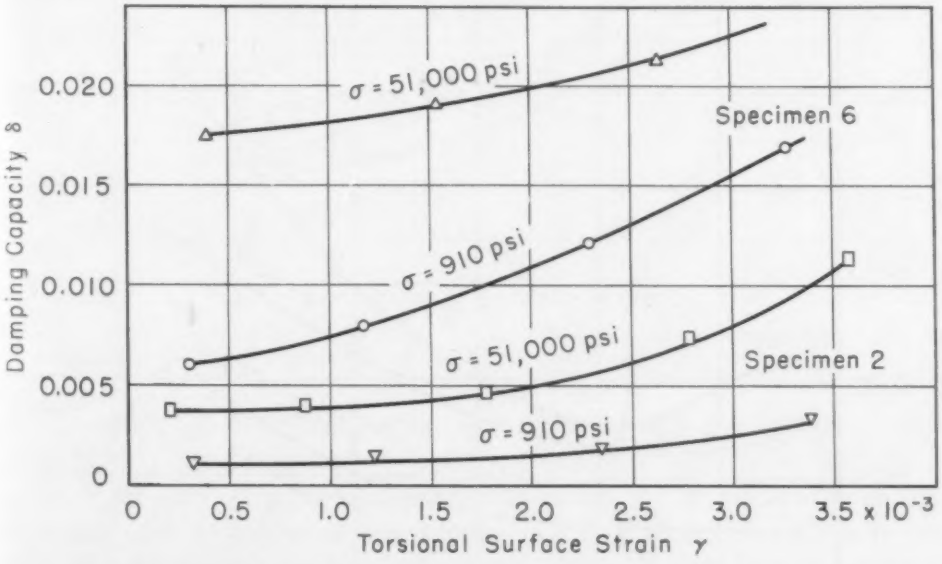


Fig. 5—Effect of Static Stress on the Damping of an Aged and an Unaged Wire of Refractaloy 26 (Specimen 2 and 6).

static stress of 51,000 psi. The effect of temperature is described in Fig. 4 for the same wire. The damping curves taken at 750 °F (400 °C) are basically the same as those taken at room temperature. But they change considerably at still higher temperatures. Not only does the damping rapidly increase, but also the direction of the effect of static stress reverses as is seen from the curves taken at 930 and 1110 °F (500 and 600 °C). Wire 1 finally broke when subjected to a static stress of 9,800 psi at 1300 °F (705 °C).

Contrary to wire 1, wire 2 exhibits a simple relationship between static stress, shear strain, and temperature. Its damping increases with

UNIVERSITY OF MICHIGAN LIBRARIES

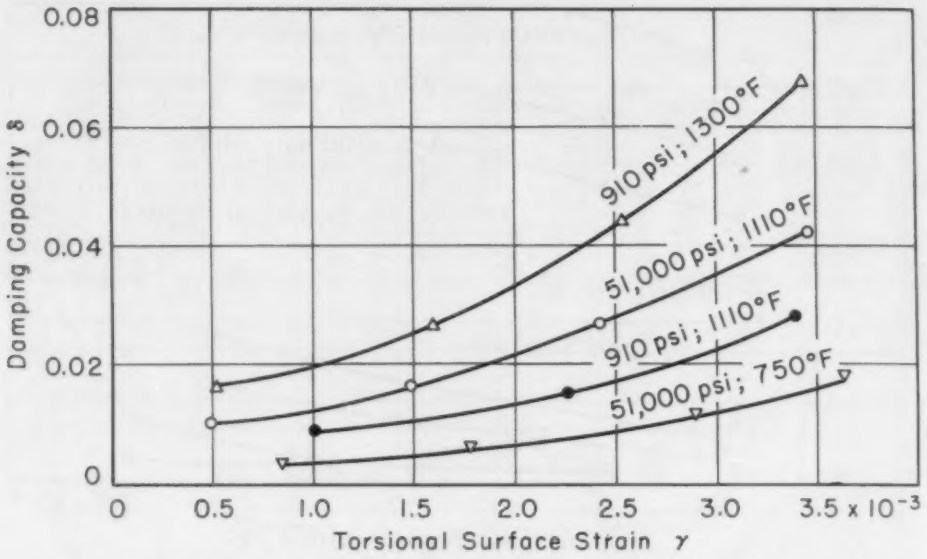


Fig. 6—Effect of Static Stress and Temperature on the Damping of a Wire of Refactaloy 26 (Specimen 2).

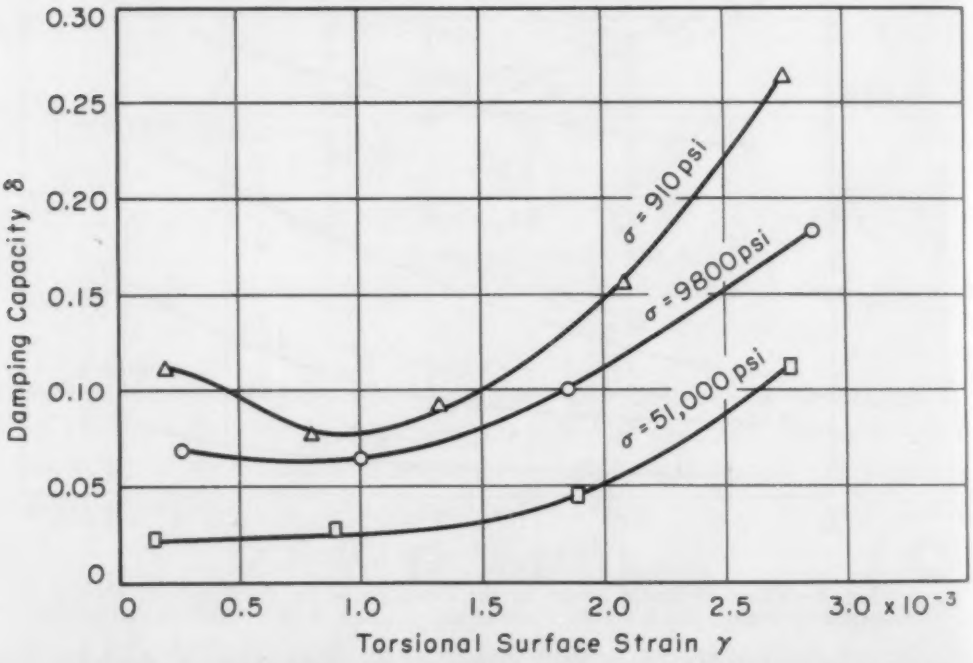


Fig. 7—Effect of Static Stress on the Damping of a Slowly Cooled Wire of Alloy AISI 403 (Specimen 3).

these three quantities in a continuous fashion throughout the entire range of applied stress and temperature (Figs. 5 and 6). It is further noted that its damping is considerably smaller than that of wire 1. For example, at small stress the damping capacity of wire 2 is 0.001 compared to values between 0.01 and 0.03 for wire 1.

The results obtained on the other wires are less important, in a practical sense, since alloys under such conditions (Table II) are hardly encountered in practice. These tests were made to show how

the effect of static stress itself is affected by heat treatment and cold work. The data are plotted in Figs. 5,7, and 8 and show once more that a static stress may cause the damping to increase (Figs. 5 and 7) or decrease (Fig. 6).

Discussion of the Results

The effect of static stress may appear to be abstruse because of the peculiar shape of some of the experimental curves. Nevertheless, the results of the measurements are in full agreement with our concept of strain hardening, recovery, and magneto-mechanical hysteresis.

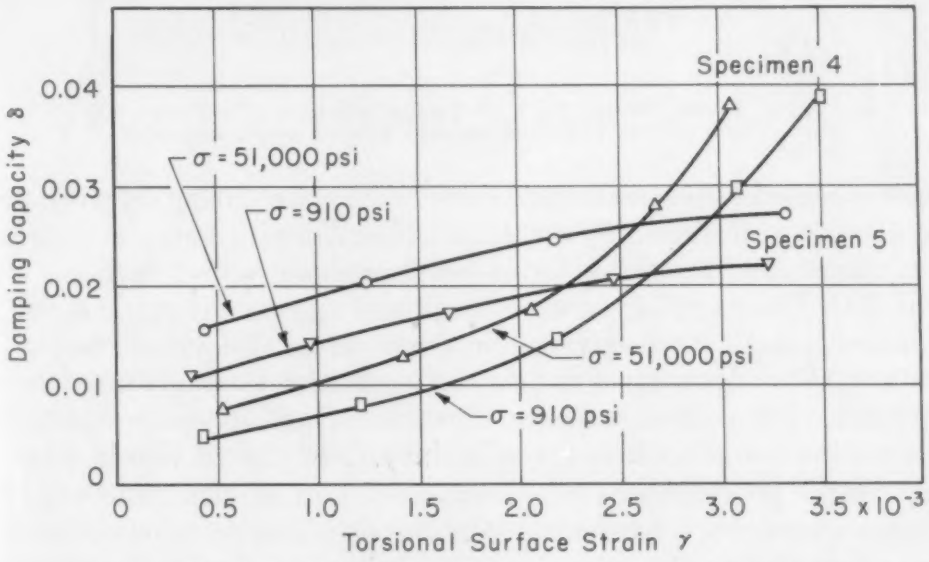


Fig. 8—Effect of Static Stress on the Damping of an Oil-Quenched and a Cold-Worked Wire of Alloy AISI 403 (Specimen 4 and 5).

Damping in ferromagnetic materials, and in the range of stress applied here, has two basic causes: magneto-mechanical hysteresis and plastic flow (9). Magneto-mechanical damping is generally the predominant part at lower stresses whereas it is usually small compared to the plastic flow damping at higher stresses (10). Whether the one or the other type of damping is more desirable in practice, depends largely upon the stress system of a particular member (4).

The effect of a static stress on the magneto-mechanical damping has been demonstrated elsewhere (11) and is well understood. According to this phenomenon, the damping decreases gradually with static stress and finally disappears. Fig. 9 shows a drastic example of this effect for a Fe-40% Co wire for which δ decreases by a factor of 33 at a vibrational shear stress of 2500 psi, when a weight is hung onto the wire causing a static stress of 10,000 psi. The influence of static stress on the plastic flow damping is more complex. It is observed that the damping first increases with static stress, but then it may de-

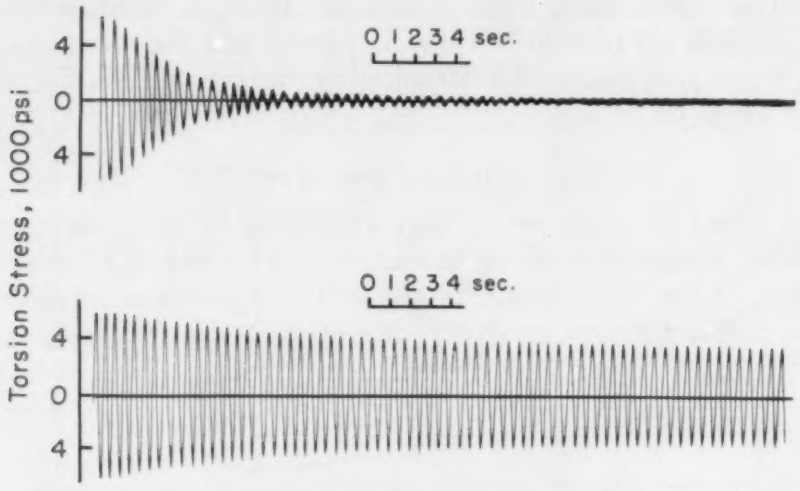


Fig. 9—The Decay of a Free Torsion Vibration of a Fe-40% Co Wire. Above: with no weight; below: with a heavy weight suspended on the wire.

crease if considerable strain hardening takes place during the vibration. Fig. 10 shows schematically the shape of the damping curve as expected from these considerations for a ferromagnetic alloy, such as type AISI 403. The damping capacity is plotted against the static stress in an arbitrary scale for a given vibrational stress, frequency, and temperature. The damping first decreases due to magneto-mechanical hysteresis, then increases due to flow, and then decreases again due to extensive work hardening (solid line). The dashed line in Fig. 10 indicates the possibility of a continuous rise of the damping capacity in cases where work hardening is not appreciable or where recovery takes place during the vibration. The behavior of nonferromagnetic materials is somewhat different due to the absence of magneto-mechanical hysteresis. For those substances the curve is the same except that before point a there is simply a rise rather than a fall in Fig. 10.

From this schematic graph the results of the measurements are understandable. That the damping decreases with σ by a factor of 5 at $\gamma = 0.7 \times 10^{-3}$ in Fig. 3 is the result of magneto-mechanical hysteresis as is also evidenced from measurements taken with a magnetic field. The increase of damping with σ at larger shear strains in Fig. 3 is due to plastic flow. At higher temperatures (Fig. 4) the direction of the effect of static stress is found again reversed, and this is due to strain hardening in accordance with Fig. 10. All other curves can be interpreted in the same manner. The simple shape of the curves taken on Refractaloy 26 is explained by the fact that the material is not ferromagnetic and that it does not appreciably strain harden under the applied stresses.

A vibrational torsion stress and a static tension stress were applied to the test specimens in the present work. The question may

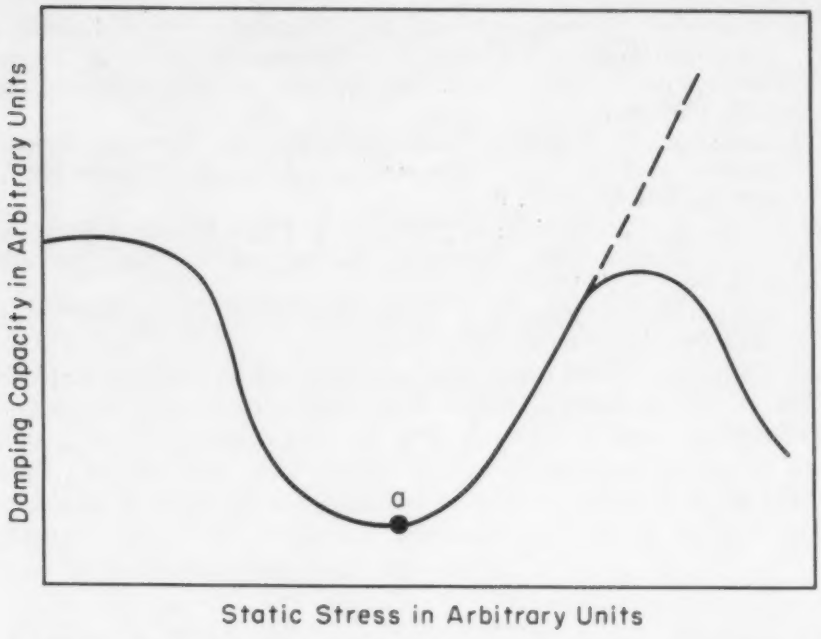


Fig. 10—Schematic Plot of Damping Capacity Versus Static Stress.

therefore arise how the results of the tests would have been if the stress conditions were different. It should be mentioned that the Mises criterion, which states that a torsion stress is 1.73 times more effective than a tensile stress, was found to be applicable when damping curves measured in bending and torsion were correlated (9). Thus it is believed that the present data can be utilized for the more common stress systems.

ACKNOWLEDGMENT

The author wants to thank A. G. Hartwick for his assistance in taking the measurements. Thanks are also due to D. F. Miller and other members of the Mechanics Department, Westinghouse Research Laboratories, for stimulating discussions.

References

1. L. Perlmutter, "Service Failures of Turbine Buckets," Air Force Technical Report No. 5716, July, 1948.
2. R. P. Kroon, "Turbine-Blade Vibration Due to Partial Admission," *Transactions,* American Society of Mechanical Engineers, Vol. 62, 1940, p. A-161.
3. B. J. Lazan, "Effect of Damping Constants and Stress Distribution on the Resonance Response of Members," *Transactions,* American Society of Mechanical Engineers, Vol. 75, 1953, p. A-201.
4. A. W. Cochardt, "A Method for Determining the Internal Damping of Machine Members," (presented at the Annual Meeting of the American Society of Mechanical Engineers, December, 1953).
5. O. Föppl, E. Becker, and G. V. Heydekampf, *Die Dauerprüfung der Werkstoffe hinsichtlich ihrer Schwingungsfestigkeit und Dämpfungsfähigkeit,* J. Springer-Verlag, Berlin, 1929.

6. O. Föppl, "The Practical Importance of Damping Capacity of Metals, Especially Steels," *Journal,* Iron and Steel Institute, Vol. 134, 1936, p. 393.
7. J. M. Robertson and A. J. Yorgiadis, "Internal Friction in Engineering Alloys," *Transactions,* American Society of Mechanical Engineers, Vol. 68, 1946, p. A-173.
8. B. J. Lazan and L. J. Demer, "Damping, Fatigue and Dynamic Stress-Strain Properties of Mild Steel," *Proceedings,* American Society for Testing Materials, Vol. 51, 1951, p. 611.
9. A. W. Cochardt, "The Origin of Damping in High-Strength Ferromagnetic Alloys," *Transactions,* American Society of Mechanical Engineers, Vol. 75, 1953, p. A-196.
10. A. W. Cochardt, "A Method of Measuring Magnetostriction," *Journal of Applied Physics,* Vol. 25, 1954, p. 91.
11. A. W. Cochardt, "Some New Magneto-Mechanical Torsion Experiments," *Journal of Applied Physics,* Vol. 25, 1954.

APPLICATION OF COTTRELL'S THEORY OF YIELDING TO DELAYED YIELD IN STEEL

By John C. Fisher

Abstract

According to Cottrell, dislocations in iron are pinned by adsorbed carbon, nitrogen, and other solute atoms. Yielding occurs when dislocations are freed from their adsorbed solute atoms with the aid of thermal energy fluctuations. Based upon this model, the temperature and stress dependence of the delay time for the yielding of steel is calculated and is compared with experiment. The temperature dependence of the yield stress also is calculated, and found to be of the form (stress) x (temperature) = constant, in good agreement with experiment over a wide temperature range.

WHEN a dislocation is present in a solid solution alloy, the composition of the alloy near the dislocation will be altered. In the neighborhood of an edge dislocation, for example, atoms of those components of an alloy that tend to increase the lattice parameter will be concentrated in the region of dilatation and atoms of those components that tend to decrease the lattice parameter will be concentrated in the region of compression.

Solute atoms segregate at a dislocation because the strain energy of the crystal is decreased thereby. If the dislocation were to move, leaving the segregated solute atoms behind, its energy would have to increase. For this reason the dislocation is bound to its original position, and glide is inhibited.

Cottrell (1)[1] has pointed out that yield points and strain aging are caused by preferential segregation of this type. If all the dislocations in a metal are pinned by solute atoms, the applied stress must rise to a relatively high value in order to start the glide process. This stress is the (upper) yield stress.

Cottrell further suggests that a dislocation will not pull away from its excess solute atoms all at once, but rather that a small loop of dislocation will pull away, as sketched in Fig. 1, dragging the rest of the dislocation after it. The original small loop is formed by a nucleation process that requires a thermal energy fluctuation (2).

This report analyzes the Cottrell yield point mechanism in a

[1] The figures appearing in parentheses pertain to the references appended to this paper.

The author, John C. Fisher, is associated with the Metallurgy Research Department, General Electric Co., Schenectady, N. Y. Manuscript received June 22, 1953.

UNIVERSITY OF MICHIGAN LIBRARIES

rather simple way, and gives a quantitative description of the delayed-yield phenomenon as observed in steels by Clark and Wood (3–5).

Energy to Form a Critical Size Loop

In Fig. 1, the position of a dislocation anchored by solute atoms is denoted by ABCDE. A loop BC'D is moved away from its original position leaving the solute atoms behind. In forming the loop BC'D the energy of the crystal is increased because the dislocation segment BC'D is longer than BCD; moreover, its energy per unit length is greater because of the absence of preferential segregation. If the

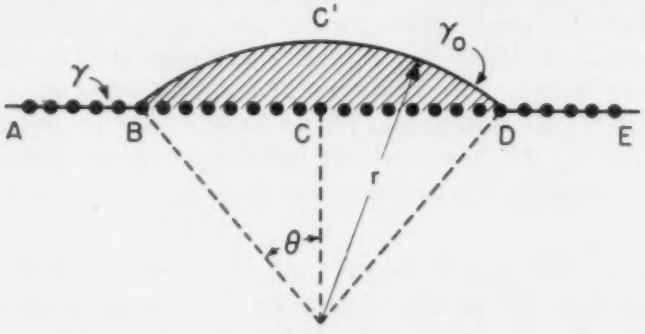


Fig. 1—Nucleation of the Dislocation Loop BC'D. ABCDE gives the original position of a dislocation anchored by solute atoms. Slip has occurred over the shaded area.

crystal is under stress, there is an energy decrease caused by the motion of the dislocation, because a small amount of local slip occurs.

Quantitatively, the work of formation of a loop that is a circular arc is

$$W = (2r\,\theta)\,\gamma_o - (2r \sin\theta)\,\gamma - b\tau\,(\theta r^2 - r^2 \sin\theta \cos\theta),$$

where r is the radius of the loop and θ is its half-angle. γ_o and γ are the energies per unit length of dislocation when free from absorbed solute atoms and in the presence of them, respectively, and $b\tau$ is the product of the slip vector length and the resolved shear stress on the slip plane, giving the work done per unit area swept out by the loop. The first term is the energy of the loop BC'D, the second is the negative of the energy of the original segment BCD, and the third is the product of $b\tau$ and the area BC'DCB swept out by the loop.

If we envision the growth of the Arc BC'D as occurring by the lengthening of the chord BD, the radius of the arc is free at all times to assume the value corresponding to minimum energy. This value is constant for a given stress, and is

$$r = \gamma_o/b\tau. \qquad \text{Equation 1}$$

Substituting this value of r in the Equation for W,

$$W = (\gamma_o/b\tau)\,[2\theta\gamma_o - 2\gamma \sin\theta - \gamma_o\,(\theta - \sin\theta \cos\theta)]. \qquad \text{Equation 2}$$

The critical value of W for dislocation loop nucleation is that for which $\partial W/\partial \theta = 0$, or for which

$$\cos \theta = \gamma/\gamma_o. \qquad \text{Equation 3}$$

Substituting this value of θ in the equation for W, the work of formation of the critical size loop is seen to be

$$W^* = (\gamma_o^2/b\tau)\, f\,(\gamma/\gamma_o) \qquad \text{Equation 4}$$

where the function $f(\gamma/\gamma_o)$ is defined by the relationship

$$\begin{aligned} f(x) &= \arccos x - x\,(1-x^2)^{1/2}, \\ &\approx (2/3)\,[2\,(1-x)\,]^{3/2} \quad (\text{for } x \approx 1). \end{aligned} \qquad \text{Equation 5}$$

This expression for W* is simpler than the one derived by Cottrell and Bilby (2), who based their analysis on a more detailed model of solute-atom segregation.

Rate of Thermal Nucleation of Loops

The work W* is the minimum work associated with the nucleation of a loop that can grow with ever-decreasing energy. In order for yielding to occur, the energy W* must be supplied by a spontaneous thermal fluctuation. The number of such loops that form in one second is proportional to exp $(-W^*/kT)$. The proportionality factor is the product of a frequency factor ν and the number of possible sites for loop formation n_s,

$$\dot{n} = n_s \nu \exp\,[-\gamma_o^2 f(\gamma/\gamma_o)/b\tau kT]. \qquad \text{Equation 6}$$

Since $\dot{n}$ is the mean number of loops that are generated in a second, its reciprocal is the mean time between the generation of successive loops. Setting $1/\dot{n} = \Delta t$,

$$\Delta t = (n_s \nu)^{-1} \exp\,[\gamma_o^2\, f\,(\gamma/\gamma_o)/b\tau kT] \qquad \text{Equation 7}$$

and

$$\log \Delta t = -\log n_s \nu + \gamma_o^2 f(\gamma/\gamma_o) \log e/b\tau kT. \qquad \text{Equation 8}$$

Interpretation of Delayed Yield in Polycrystalline Iron

Clark and Wood have observed a phenomenon of delayed yield in annealed mild steel. They apply a constant stress to a tensile specimen and report that when the applied stress exceeds the static upper yield stress, the specimen behaves (nearly) elastically for a certain period of time, after which pronounced yielding begins rather abruptly. If the beginning of pronounced yielding is assumed to be the nucleation of the first dislocation loop from a number of solute-anchored dislocations, the delay time for yielding is given by Δt in Equation 7 or 8.

A more realistic interpretation would identify the delay time with the time required to generate a large number of dislocation loops, for Clark and Wood give good evidence that a nonelastic strain of as much as $30(10)^{-6}$ precedes the pronounced yielding in steel. If the

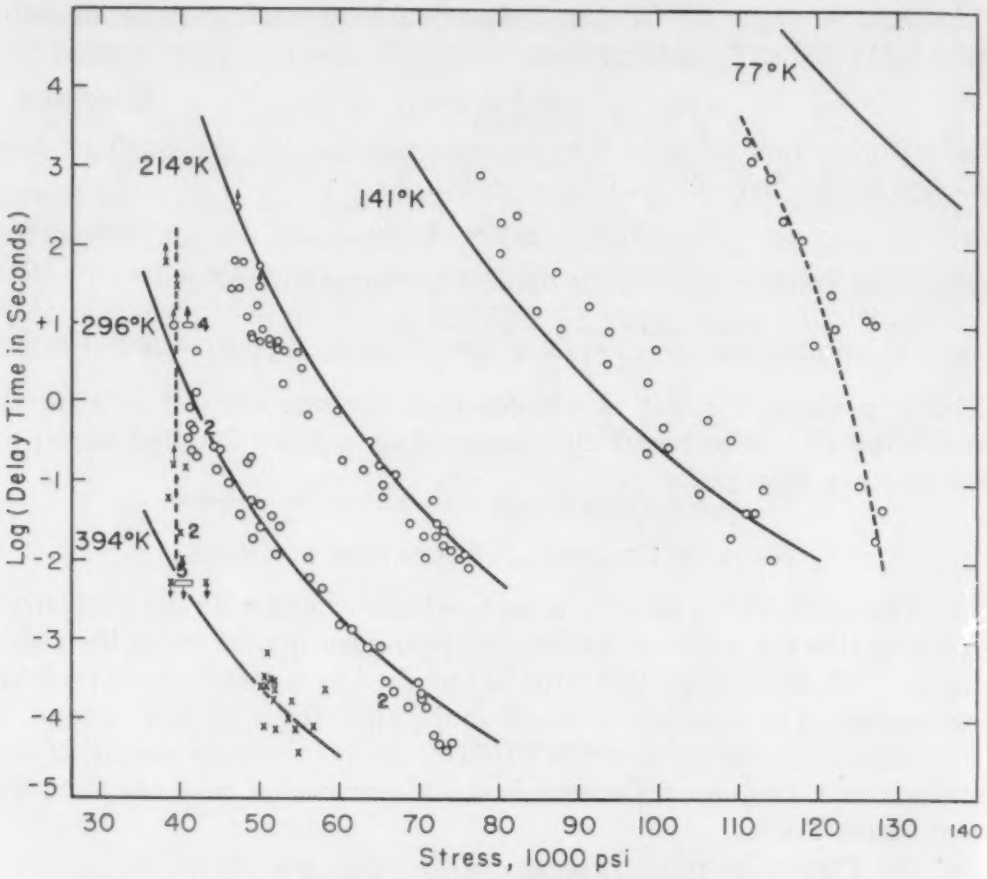


Fig. 2—Delay Time for Yielding of Annealed 0.17% Carbon Steel, as a Function of Stress and Temperature. Experimental points from Clark and Wood (3–5). Solid curves calculated from the relationship $\log t = -A + B\,G^2/\tau T$ (equation 9), using constants in Table I.

number of loops generated during the delay time is denoted by n_1, the delay time itself is $n_1\Delta t$, and

$$\left.\begin{aligned}\log(\text{delay time}) &= -\log(n_s\nu/n_1) + \gamma_o^2 f(\gamma/\gamma_o)\log e/b\tau kT \\ &= -\log(n_s\nu/n_1) + [\gamma_o^2 f(\gamma/\gamma_o)\log e/G^2bk]\,G^2/\tau T \\ &= -A + B\,G^2/\tau T,\end{aligned}\right\}\ \text{Equation 9}$$

$$\left.\begin{aligned}\text{where}\quad A &= \log(n_s\nu/n_1) \\ B &= \gamma_o^2 f\,(\gamma/\gamma_o)\log e/G^2bk.\end{aligned}\right\}\ \text{Equation 10}$$

The quantity $G^2/\tau T$, where G is the rigidity modulus, has been written as a separate factor in Equation 9, for it probably determines the entire temperature and stress dependence of the delay time. The dislocation energies γ_o and γ both are proportional to the rigidity modulus G, and the ratios γ/γ_o and γ_o^2/G^2 that appear in the coefficient of $G^2/\tau T$ should therefore be independent of temperature.[2]

The data of Clark and Wood are plotted in Figs. 2–6 together

[2] Strictly speaking, only γ_o is known to be proportional to G. The assumption that γ also is proportional to G is plausible.

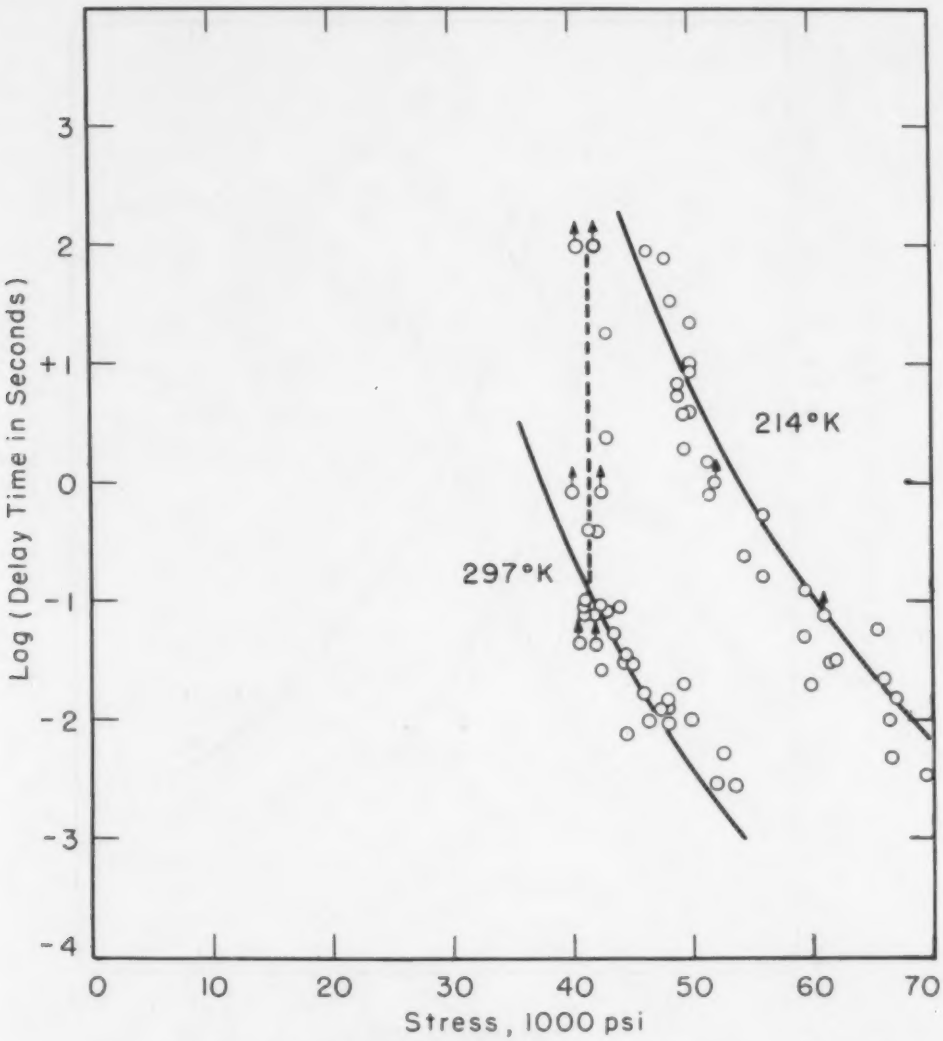


Fig. 3—Delay Time for Yielding of Annealed 0.12% Carbon Steel. Experimental points from Clark and Wood (3-5). Solid curves calculated from equation 9.

with the curves calculated from Equation 9. The effective shear stress was taken to be half the tensile stress. The shear modulus G was calculated from the relationship $10^{-6}\ G = 13.30 - 0.0030\ T$, in units of pounds per square inch (based upon Köster's measurements (6) of the elastic modulus E, and the assumption that Poisson's ratio is independent of temperature). Values of A and B in Equations 9 and 10 were chosen to give the best fit, and are summarized in Table I. Except for stresses below about 40,000 psi for the steels in Figs. 2 and 3, and for tests at liquid nitrogen temperature, the agreement is good.

Discussion of Delay-Time

Figs. 2–6 show that the delay time for the yielding of mild steel under constant stress depends upon the single parameter $G^2/\tau T$ and not upon stress or temperature independently, throughout a wide range

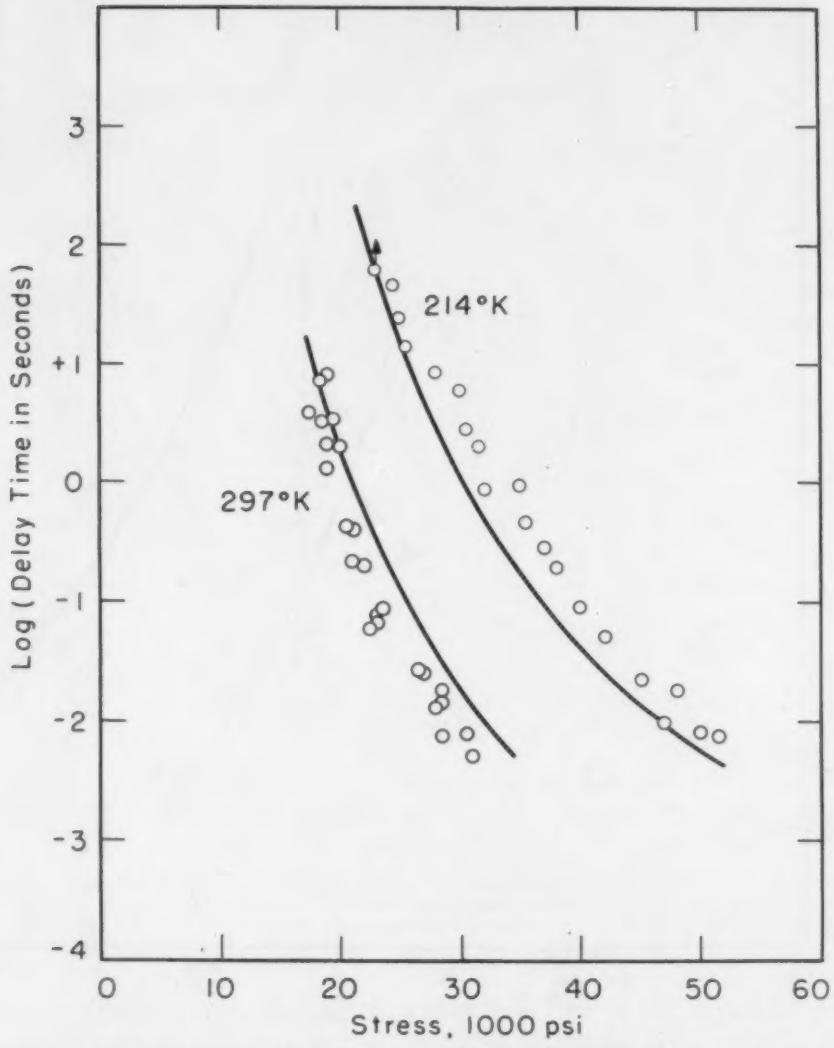


Fig. 4—Delay Time for Yielding of Wet Hydrogen-Treated (previously 0.12% Carbon) Steel. Experimental points from Clark and Wood (3-5). Solid curves calculated from equation 9. Note that dislocation pinning occurs even when most carbon and nitrogen has been removed. It is possible that substitutional alloying elements are responsible.

of stresses and temperatures. The mathematical form of the relationship is given by Equation 9.

The relationship breaks down at very low temperatures, where the yield stress approaches a constant value. The break-down is not unexpected. The loop-nucleation model analyzed in this report should fail at very low temperatures or very short delay times, for which the stress predicted by Equation 9 approaches the limiting value needed to rip a dislocation off its solute atmosphere without thermal fluctuations. A calculation of the limiting stress, and of the delay-time at stresses approaching it, would require an improved estimate of the energy of a dislocation as a function of position. The model in which the energy leaps discontinuously from γ to γ_0 is too crude, because it is the quantity $\partial\gamma_x/\partial x$, derived from a position-dependent dislocation energy γ_x, that

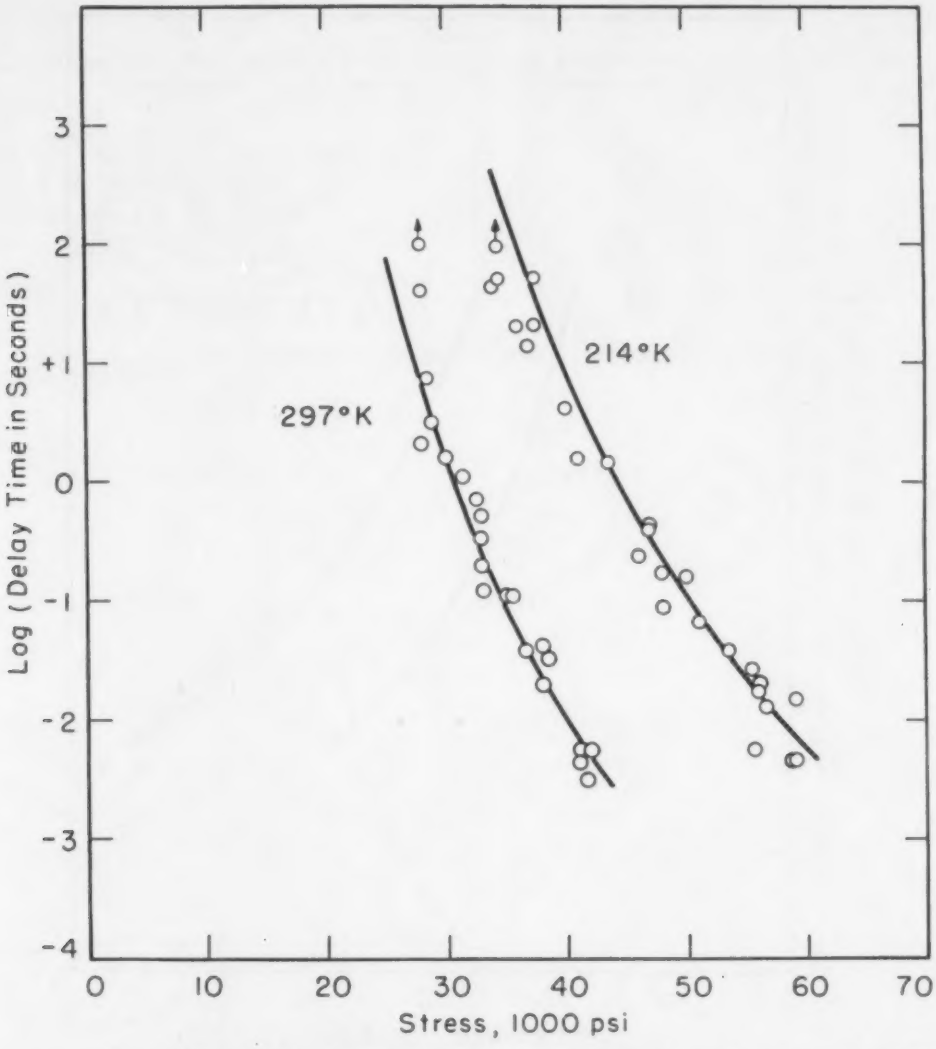


Fig. 5—Delay Time for Yielding of Wet Hydrogen-Treated and Recarburized (previously 0.12% Carbon) Steel. Experimental points from Clark and Wood (3-5). Solid curves calculated from equation 9.

determines the limiting stress for freeing a dislocation without loop nucleation.

The relationship in Equation 9 can break down at low stresses (high temperatures), as well, there sometimes being a stress below which yielding does not occur at all. Carbon and nitrogen diffuse rapidly in iron at these temperatures, in times comparable with the expected delay times. It may be that strain aging of the pre-yield creep, caused by diffusion of these elements, can be responsible for the absence of yielding.

Ratios of γ to γ_o can be estimated from the values of $B = \gamma_o^2 f(\gamma/\gamma_o) \log e/G^2 bk$, given in Table I. Dislocation theory gives $\gamma_o \approx Gb^2/2$ whence

$$B = b^3 f(\gamma/\gamma_o) \log e/4k. \qquad \text{Equation 11}$$

Setting $b = 2.48(10)^{-8}$ cm for iron, and equating the right-hand

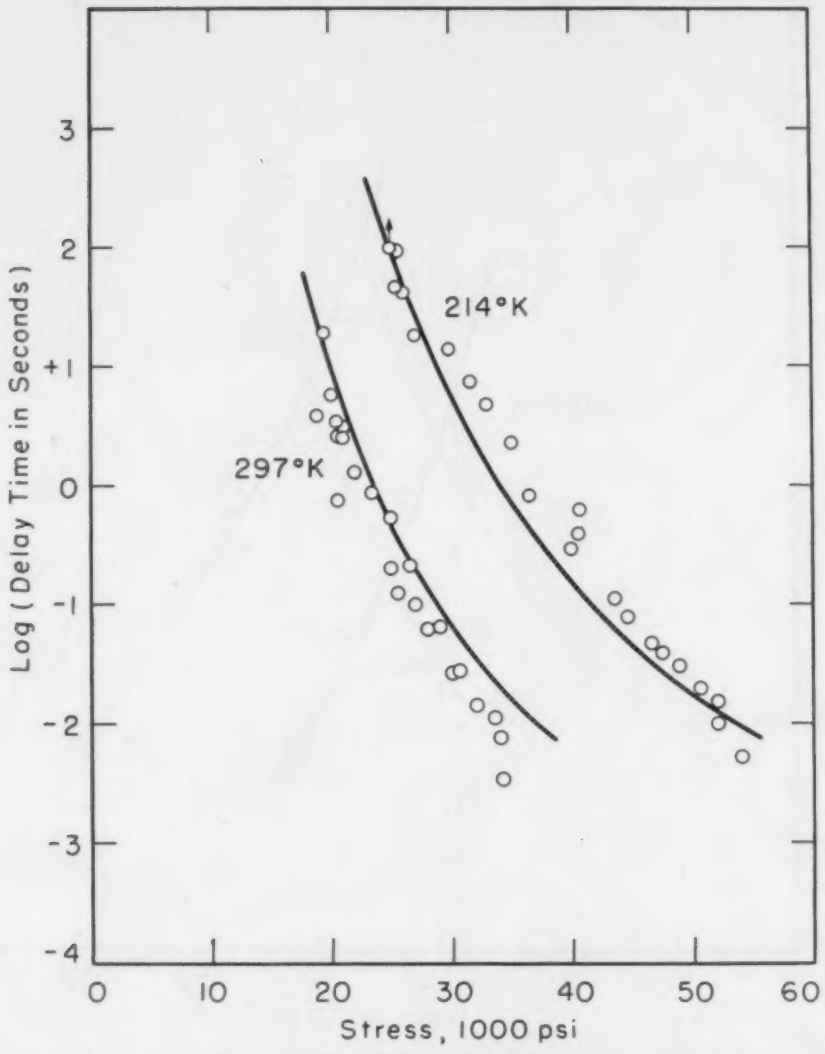


Fig. 6—Delay Time for Yielding of Wet Hydrogen-Treated and Renitrided (previously 0.12% Carbon) Steel. Experimental points from Clark and Wood (3-5). Solid curves calculated from equation 9.

member of Equation 11 to the values of B in Table I, the corresponding values of γ/γ_0 were calculated and are included in the Table.

Yield Stress as a Function of Temperature

The yield stress in iron and in other body-centered cubic metals is known to increase as the testing temperature is decreased. Consider yielding tests similar to those carried out by Clark and Wood. If the yield stress σ is defined as the stress to produce yielding after a standard delay time, the relationship between yield stress and temperature is simply

$$\sigma T/G^2 = \text{constant.} \qquad \text{Equation 12}$$

The validity of Equation 12 for the data of Clark and associates is

Table I
Values of the Quantities A and B in the Delay-Time Relationship $\log t = -A + BG^2/\tau T$ (Equations 9 and 10), and of the Dislocation-Energy Ratio γ/γ_0

Material	A	10^7 B	$1-\gamma/\gamma_0$
1. Annealed 0.17% C steel	8.9	3.55	.00373
2. Annealed 0.12% C steel	9.8	3.55	.00373
3. Steel 2, wet H_2 treated	5.7	1.15	.00176
4. Steel 3, recarburized	8.6	2.55	.00298
5. Steel 3, renitrided	5.5	1.25	.00187

A log(sec)
B inch^2 °K/pound

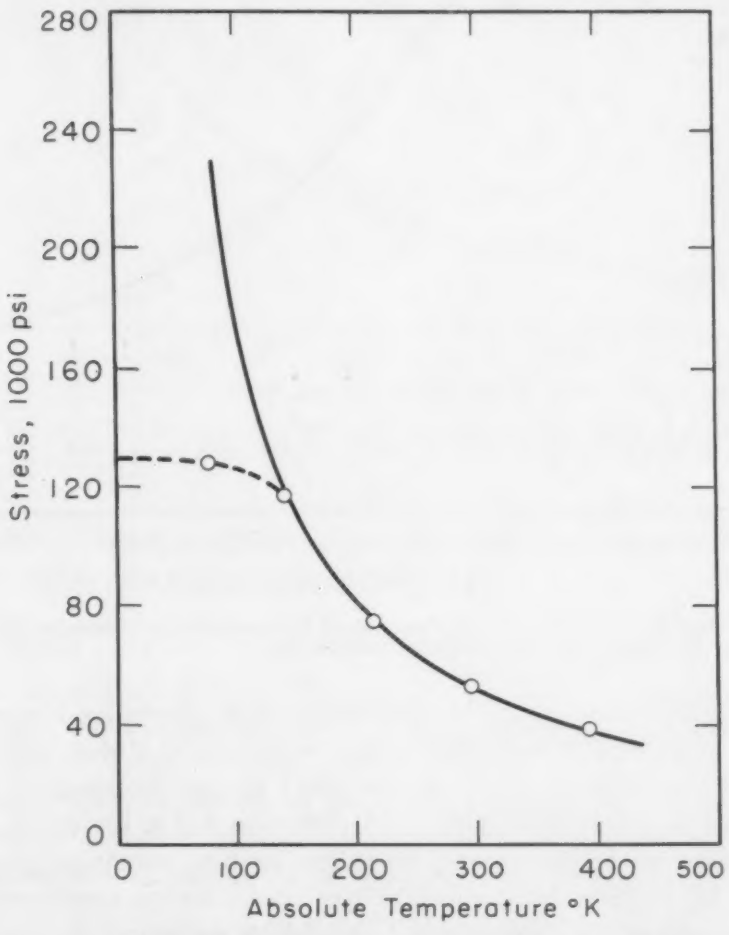


Fig. 7—Stress Corresponding to a Delay Time of 0.01 Second, as a Function of Temperature, for an Annealed 0.17% Carbon Steel. Experimental points from Clark and Wood (3-5). Solid curve from equation 12.

shown in Fig. 7 for a delay time of 0.01 second. The value of the constant was chosen to give the best fit. Only at temperatures below about 140 °K does the relationship cease to hold, and then presumably because dislocation-loop nucleation no longer is required for yielding, as discussed above.

Most yield stress determinations are carried out with steadily increasing stresses, usually increasing at a rate that is reproduced from

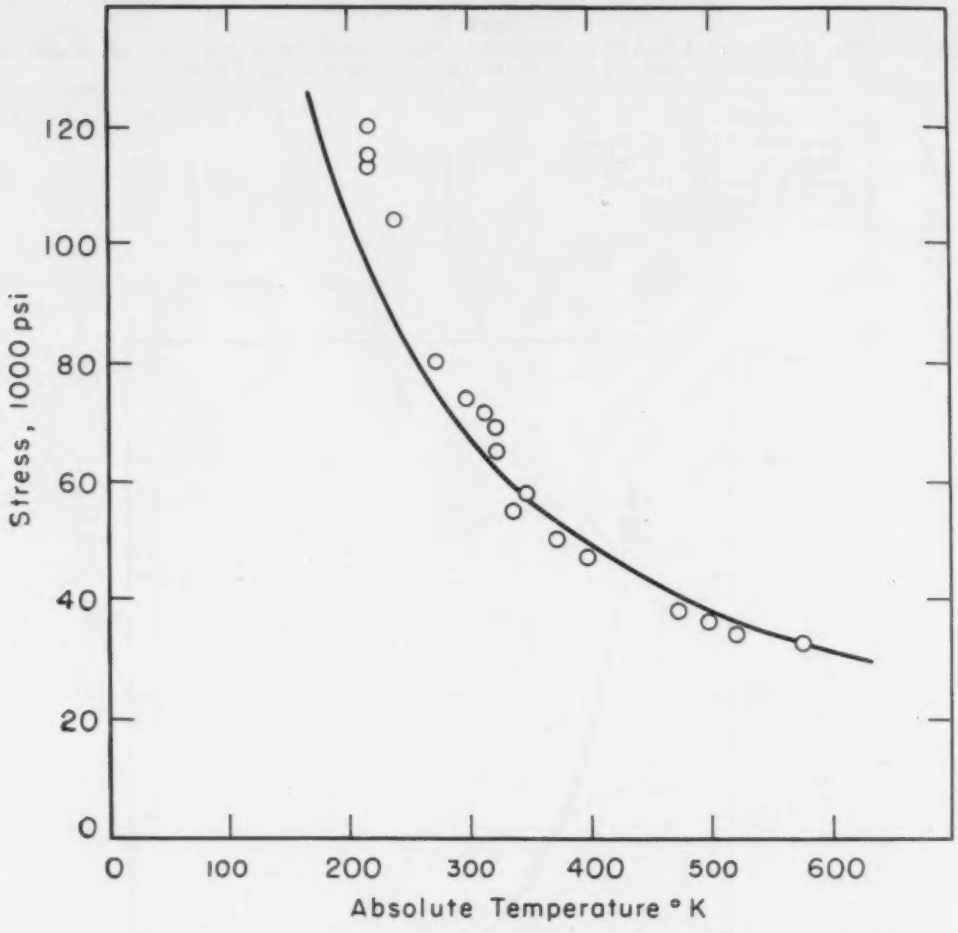


Fig. 8—Yield Stress as a Function of Temperature for Annealed Molybdenum, after Carreker (7). Curve from equation 12.

test to test. The rate of nucleation of loops n, given by Equation 6, is essentially zero at stresses slightly below the yield stress, and increases sharply in the neighborhood of the yield stress. Because of the rapid variation of $\dot{n}$ with stress, the yield criterion for a series of tests at a standard rate of stressing can be taken as $\dot{n} = \text{constant}$, from which Equation 12 follows immediately. For yield stress measurements, as for delay-time tests, Equation 12 should be expected to apply over a fairly broad temperature range. Figs. 8 and 9 show plots of yield stress versus temperature for molybdenum (7) and iron (8), together with the best calculated curves of the form $\sigma T/G^2 = \text{constant}$.

Cottrell and Bilby (2), assuming a dislocation energy γ_x that depends upon dislocation displacement, have derived an alternative expression for the temperature dependence of the yield stress. Although their expression is more complex than the simple one $\sigma T/G^2 = \text{constant}$, the two are equally valid throughout the range of temperature covered by the data of McAdam and Mebs (8), as shown in Fig. 9

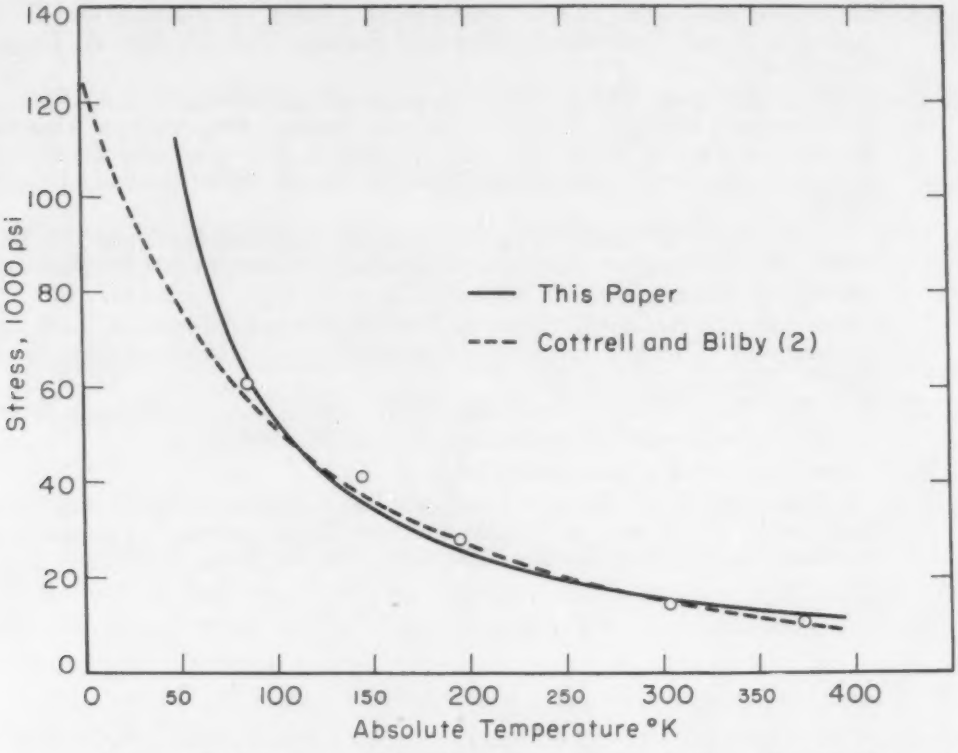


Fig. 9—Yield Stress as a Function of Temperature for Iron, after McAdam and Mebs (8). Solid curve from equation 12, dashed curve from analysis of Cottrell and Bilby (2).

where they are compared. Except perhaps at the lowest temperatures, the simpler analysis appears to be adequate.

Conclusion

The delay-time for yielding under constant stress is a function of the single parameter $G^2/\tau T$ (where G is the shear modulus, τ the shear stress, T the absolute temperature) for a wide range of stresses and temperatures, as can be derived from a simple analysis of Cottrell's mechanism of yielding. Within the same stress and temperature ranges, the yield stress in tension σ is given by the relationship $\sigma T/G^2 =$ constant.

Acknowledgment

I wish to thank Prof. D. S. Clark and Prof. D. S. Wood of the California Institute of Technology for their stimulating correspondence on the subject of delay-times; and G. W. Ardley, R. P. Carreker, J. J. Gilman, and E. W. Hart of the General Electric Research Laboratory for their advice and criticism.

References

1. A. H. Cottrell, *Report on the Strength of Solids,* Physical Society, London, 1948, p. 30.

2. A. H. Cottrell and B. A. Bilby, "Dislocation Theory of Yielding and Strain Aging of Iron," *Proceedings,* Physical Society, Vol. 62, Sec. A, January 1949, p. 49.
3. D. S. Clark and D. S. Wood, "The Time Delay for the Initiation of Plastic Deformation at Rapidly Applied Constant Stress," *Proceedings,* American Society for Testing Materials, Vol. 49, 1949, p. 717. See also the first six technical reports to the Office of Naval Research, under contract N6-onr-24418.
4. D. S. Wood and D. S. Clark, "The Influence of Temperature Upon the Time Delay for Yielding in Annealed Mild Steel," TRANSACTIONS, American Society for Metals, Vol. 43, 1951, p. 571.
5. D. S. Wood and D. S. Clark, "Delayed Yield in Annealed Steels of Very Low Carbon and Nitrogen Content," TRANSACTIONS, American Society for Metals, Vol. 44, 1952, p. 726.
6. W. Köster, "Die Temperaturabhangigkeit des Elastizitatsmoduls reiner Metalle," *Zeitschrift fur Metallkunde,* Vol. 39, 1948, p. 1.
7. R. P. Carreker, private communication.
8. D. J. McAdam and R. W. Mebs, "The Technical Cohesive Strength and Other Mechanical Properties of Metals at Low Temperatures," *Transactions,* American Society for Testing Materials, Vol. 43, 1943, p. 661.

CONDITIONS FOR DENDRITIC GROWTH IN ALLOYS

By W. Morris, W. A. Tiller, J. W. Rutter and W. C. Winegard

Abstract

The beginning of dendritic growth in alloy systems is shown to depend not only upon the concentration of the solute, but upon the rate of solidification (R) and the temperature gradient (G) existing in the liquid ahead of the solid-liquid interface. It is shown that for a given composition there exists a critical ratio of R/G which must be exceeded for dendritic growth to occur.

Introduction

WHEN a melt of impure metal or alloy is allowed to solidify, a redistribution of solute occurs which produces several segregational effects that can be directly related to the conditions of solidification.

The work of Pfann (1)[1] for the case of complete mixing in the melt and of Tiller et al (2) for the case of no mixing in the melt, allows calculation of the end-to-end variation of concentration which occurs in a sample produced by the progressive solidification from one end of a melt of constant cross section. This segregation results from the fact that the equilibrium concentration of solute in the solid at the interface between solid and liquid is different from the equilibrium concentration of solute in the liquid adjacent to it; the ratio of the former to the latter is called the distribution coefficient "k." Because of this difference in concentration, for a distribution coefficient less than unity, solute is rejected into the liquid at the interface during solidification. Therefore, for the condition of no convection, the solute concentration in the liquid at the interface will rise as growth proceeds. A steady-state distribution of solute in the liquid is reached (2) and is given by

$$C = C_o \left(\frac{1-k}{k}\right) e^{-\frac{R}{D}x} + C_o \qquad \text{Equation 1}$$

where C_o = initial solute concentration in the homogeneous melt
R = rate of solidification
D = diffusion coefficient of solute in the liquid
k = distribution coefficient
x = distance measured from the interface into the liquid

[1] The figures appearing in parentheses pertain to the references appended to this paper.

A paper presented before the Thirty-sixth Annual Convention of the Society, held in Chicago, November 1 to 5, 1954. The authors, W. Morris, W. A. Tiller, J. W. Rutter and W. C. Winegard, are associated with the Department of Metallurgical Engineering, University of Toronto, Toronto, Canada. Manuscript received April 24, 1954.

UNIVERSITY OF MICHIGAN LIBRARIES

Wagner (3) shows that for the rates of growth used in this research the effect of natural convection for mixing is negligible and the above solute profile exists at the solid-liquid interface.

As a result of this impurity distribution in the liquid, the equilibrium liquidus temperature of the melt will vary with distance from the interface. In accord with the equilibrium diagram, a liquidus temperature, T_E, can therefore be assigned to the liquid at each point ahead of the interface. This distribution of liquidus temperature is given by

$$T_E = T_o + m C_o \left(1 + \frac{(1-k)}{k} e^{-\frac{R}{D}x}\right) \qquad \text{Equation 2}$$

where T_o = melting point of the pure metal
and m = slope of the liquidus line.

If the temperature at a given point, as maintained by the temperature gradient existing in the liquid, is lower than the value of T_E at that point, then that portion of the liquid is said to be constitutionally supercooled (4). If this condition exists, a smooth interface is unstable and will change shape in order to eliminate the supercooling. This change of interface shape manifests itself in the formation of a substructure of prismatic form, studied by Rutter and Chalmers (4). This substructure, termed "corrugations," consists of parallel elements of rod-like form having a hexagonal cross section which is of the order of 0.1 mm. in diameter. Its formation is accompanied by a segregation of solute to the boundaries of the elements of the structure. It has been postulated by Weinberg and Chalmers (5) that dendritic growth begins as an extension of the corrugated structure.

Dendritic freezing in pure metals has been investigated extensively by Weinberg and Chalmers (5). They have shown that for the formation of dendrites it is necessary to have absolute supercooling, caused by the imposition of a negative temperature gradient in the liquid ahead of the advancing interface. The case of dendritic freezing in alloys has been considered by Winegard and Chalmers (6), who have shown that the formation of dendrites depends upon the existence of an extensive zone of either absolute or constitutional supercooling in the liquid adjacent to the advancing interface. They have postulated that the necessary condition for the occurrence of dendritic freezing is that $ds(x)/dx$ must be positive near the interface. $s(x)$ represents the supercooling as a function of distance, x, measured from the interface into the liquid.

It is the purpose of the present investigation to determine whether dendrites form under conditions of constitutional supercooling as a natural transition from an unstable "corrugation" structure and, if this is true, to determine the conditions of solidification under which the transition from one structure to the other takes place. Since the length of the constitutionally supercooled zone depends upon R, C_o, k and the temperature gradient G, these will be the important para-

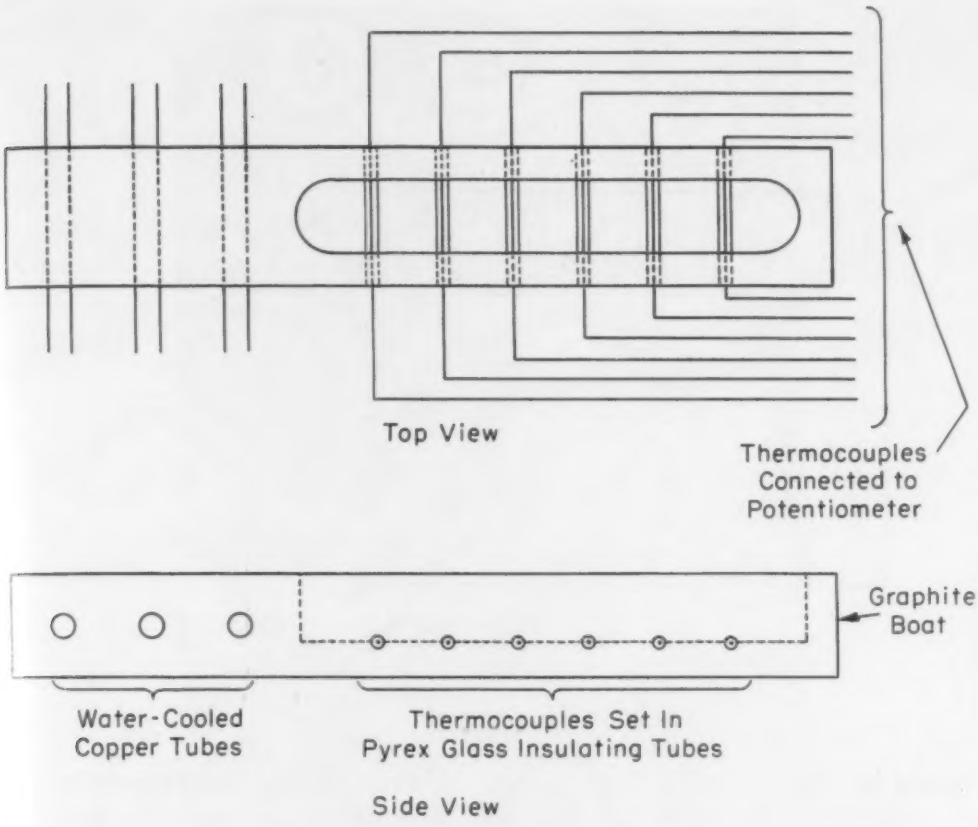


Fig. 1—Diagram of Apparatus.

meters governing the onset of dendritic growth as the extension of the corrugation structure.

The onset of dendritic growth will be defined as that point at which branching of the structure formed becomes observable.

Experimental Procedure

Crystals containing from 0.5 to 3% tin in lead were grown by the Chalmers technique (7) using various rates of growth and different temperature gradients. The distribution coefficient is approximately 0.5 for the alloys investigated.

The temperature gradient was controlled by passing water through copper tubes located at the cold end of the graphite boat. The apparatus used is shown schematically in Fig. 1. The temperatures along the boat were measured by iron-constantan thermocouples placed in fine pyrex tubes located at regular intervals in the melt. The thermocouples were connected to a Leeds and Northrup speedomax recorder by a rotating switch mechanism which connected each in turn to the instrument for five second intervals. In this way, time temperature cooling curves were obtained for all thermocouple positions as

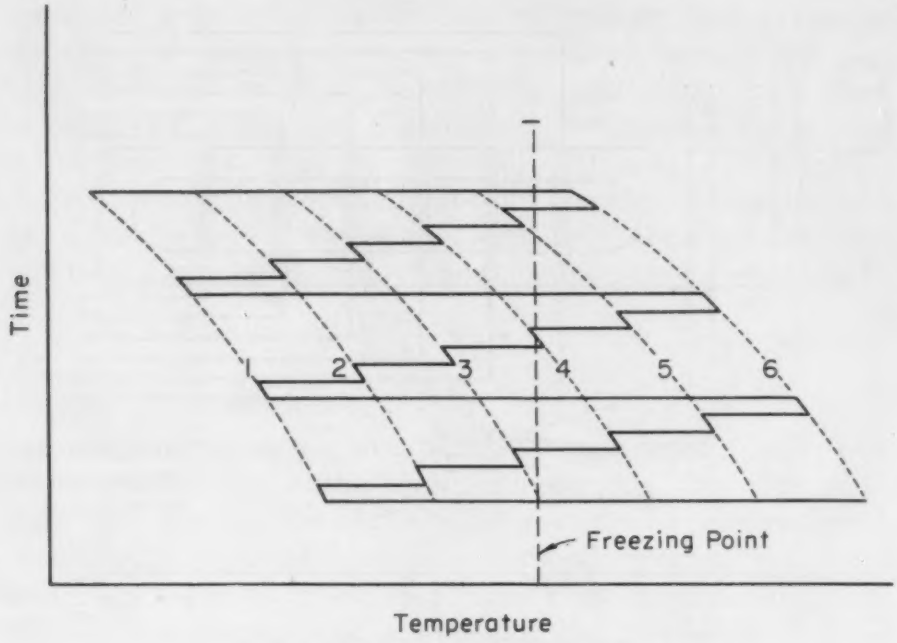


Fig. 2—Portion of Potentiometer Record.

shown in Fig. 2. From these curves, it is possible to determine the rate of advance of the solid-liquid interface and the temperature gradient existing in the liquid for any position of the interface.

Since the top of the specimen was not in contact with the graphite the surface was skimmed periodically to prevent the formation of a heavy oxide layer. Thus, specimens had a clean surface which readily showed whether the crystal was corrugated or dendritic. The surface of the specimen was examined under a stereoscopic microscope to determine the point at which the corrugations began to show side branching—i.e., the beginning of dendritic growth.

Experimental Observations and Results

The transition from corrugations to dendrites was observed on the surface of the crystal, as shown in Fig. 3. Side branches form in the corrugation boundary region. When the supercooled zone becomes large enough, well developed dendrites form; these are shown in Fig. 4. The point of breakdown of corrugations depends to some extent on the crystallography of the specimen. In the present investigation, the only corrugations and dendrites considered were those running parallel to the direction of growth; since the dendritic direction in lead is the [100] direction (6), this means that in every case considered the direction of growth was the [100] direction. Only corrugations in the center of the specimen were considered to avoid any edge effect due to the graphite boat.

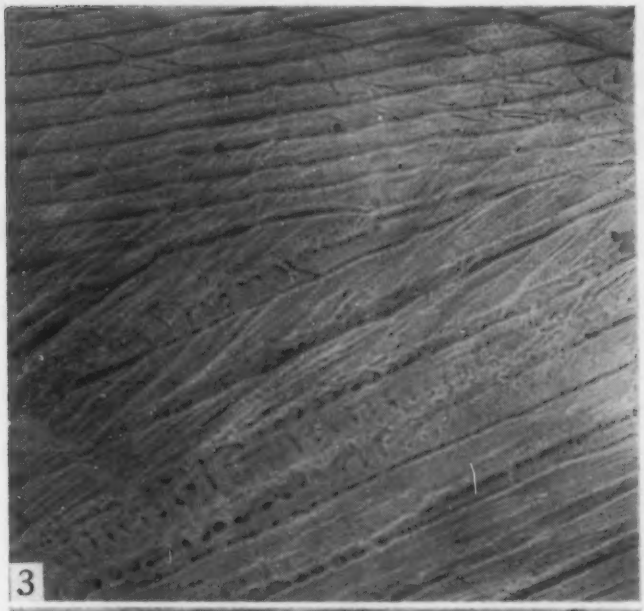




Fig. 3—Photograph of Transition from Corrugations to Dendrites—X 90.

Fig. 4—Photograph of dendrite Formation—X 90.

Since the breakdown from corrugations to dendrites in alloys depends upon the existence of a layer of high solute concentration ahead of an advancing solid-liquid interface, it is readily seen that the rate of solidification and the temperature gradient will each have an effect on the size of the constitutionally supercooled zone. In the alloys investigated, it was found that the transition occurred at a definite R/G ratio for each composition. The results are shown in Table I. A curve of R/G versus per cent tin in Fig. 5 shows the critical values of R/G for which the transition occurs. Thus, it may be seen that for

Table I
Results

% Sn (C_o)	R (cm/min)	G (°C/cm.)	R/G	Avg. R/G (cm²/°C min.)
0.50	4.4	10.1	0.43	
	4.1	8.3	0.49	0.45
	2.6	6.0	0.43	
0.75	2.4	10.0	0.24	
	3.05	12.5	0.24	0.24
	3.56	15.2	0.23	
1.0	3.8	20.0	0.19	
	4.2	22.0	0.19	0.18
	2.6	16.0	0.16	
	2.5	14.0	0.18	
2.0	3.1	19.3	0.16	0.16
	1.3	8.1	0.16	
3.0	2.85	18.5	0.15	0.15
	3.2	22.0	0.15	

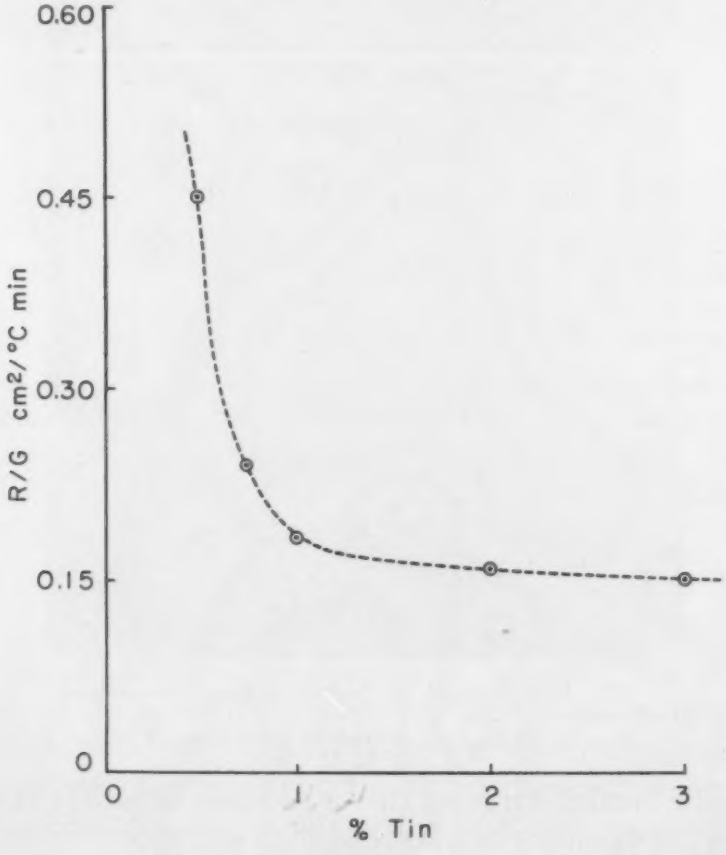


Fig. 5—Graph of R/G versus Tin Concentration.

a given composition there exists a value of R/G below which no dendrites will form; for example, if an alloy of 1% tin is solidified such that at no time does R/G exceed 0.18, then no dendrites will form.

During the growth of one of these crystals, the interface was investigated by decanting the liquid prior to the formation of dendrites.

It was observed that the appearance of the hexagonal cells had changed; the base of the cell retained the original appearance but the tip had developed a pyramidal shape. This appears to be the first stage in the transition to dendrites and is probably the explanation for the structures observed by Rosi (8) in the alloys which he investigated.

Discussion

If it is assumed that the solid-liquid interface remains plane during solidification, then it is possible to calculate the extent of the constitutionally supercooled zone which would exist in the liquid. The amount of constitutional supercooling, S, as a function of distance measured from the interface into the liquid is given by

$$S = T_E - T \qquad \text{Equation 3}$$

where T_E is the equilibrium liquidus temperature given by Equation 2, and T is the actual temperature. The gradient of the supercooling, considered by Winegard and Chalmers (6) to be an important factor controlling the formation of dendrites, may be calculated from Equation 3 as

$$\frac{ds}{dx} = -m C_o \frac{(1-k)}{k} \frac{R}{D} e^{-\frac{R}{D}x} - G \qquad \text{Equation 4}$$

However, it may be shown that a zone of constitutional supercooling is unstable, and will not persist. If, due to a local fluctuation of temperature or composition, one part of the interface advances slightly ahead of the neighboring areas, it will enter a region of greater supercooling. It will, therefore, grow more rapidly than the neighboring interface, and a projection will be formed. As shown by Rutter and Chalmers (4), an array of projections formed in this manner constitutes the "cellular" interface which accompanies the formation of the "corrugation" structure. Since the cellular interface is the stable form, the redistribution of solute and temperature which occurs when the structure is present must result in the elimination of the constitutional supercooling. As the conditions of solidification change, the shape of the cellular interface changes to correspond to the extent of the constitutional supercooling which must be eliminated. As shown by the present investigation, there is a limit to the extent of constitutional supercooling which can be relieved by an interface of cellular form. If the amount of constitutional supercooling exceeds that which can be accommodated by a cellular interface, then dendrites develop. It seems reasonable that the formation of such a branched structure will begin from an existing projection, as shown in Fig. 4, and will lead to more effective elimination of the supercooling.

It is clear that the formation of dendrites in alloys depends upon the extent of the constitutionally supercooled zone which would exist

adjacent to a smooth solid-liquid interface. As previously discussed, the extent of this zone depends upon the coefficient of diffusion of the solute in the melt, D, the distribution coefficient, k, the slope of the liquidus, m, the rate of solidification, R, and the temperature gradient, G, existing in the melt. For a given alloy, D, k, and $\dot{m}$ are constant. Therefore, the variables which will control the onset of dendrite formation are R and G. Dendrite formation will be favored by a rapid rate of solidification and a low temperature gradient. The results of the present investigation indicate that the factor controlling the onset of dendritic growth is, in fact, the ratio R/G.

ACKNOWLEDGMENTS

The authors are indebted to the National Research Council (Canada), Defence Research Board (Canada) Grant 183, and the University of Toronto for financial support.

References

1. W. G. Pfann, "Principles of Zone Melting," *Journal of Metals,* Vol. 4, 1952, p. 747.
2. W. A. Tiller, K. A. Jackson, J. W. Rutter and B. Chalmers, "The Redistribution of Solute Atoms During the Solidification of Metals," ACTA METALLURGICA, Vol. 1, 1953, p. 428.
3. Carl Wagner, "Theoretical Analysis of Diffusion of Solutes During the Solidification of Alloys," *Journal of Metals,* February, 1954, p. 154.
4. J. W. Rutter and B. Chalmers, "A Prismatic Substructure Formed During the Solidification of Metals"—*Canadian Journal of Physics,* Vol. 31, 1953, p. 15.
5. F. Weinberg and B. Chalmers, "Further Observations on Dendritic Growth" *Canadian Journal of Physics,* Vol. 30, 1952, p. 488.
6. W. C. Winegard and B. Chalmers, "Supercooling and Dendritic Freezing in Alloys," TRANSACTIONS, American Society for Metals, Vol. 46, 1954, p. 1214.
7. B. Chalmers, "Preparation of Single Crystals and Bicrystals," *Canadian Journal of Physics,* Vol. 31, 1953, p. 132.
8. F. D. Rosi, "Surface Structures on Single Crystals Produced from Melt"—*Journal of Metals,* Vol. 5, 1953, p. 1661.

DISCUSSION

Written Discussion: By F. Weinberg, Physical Metallurgy Division, Mines Branch, Department of Mines and Technical Surveys, Ottawa, Ontario.

In obtaining the experimental results reported in the paper, the authors related temperature gradients and rates of growth, as measured by thermocouples immersed in the metal, to structural changes observed on the top surface of the specimen. This assumes that the temperature distribution on the liquid-air surface is identical to that in the body of the material which may not be justified, particularly since the authors state the liquid surface was skimmed during growth. In examining the dendritic growth of pure lead the writer observed that flat "fern type" dendrites occasionally grew along the top surface

of the liquid well ahead of the interface, (Fig. 12)[2] suggesting that the top surface of the liquid was cooler than the body of liquid. Also, temperature measurements in pure lead similar to those made by the authors, indicated that there was a marked progressively increasing difference between the position of the interface, as measured by the thermocouples, and that of the top surface of the specimen, as the rate of growth increased. (Fig. 5).[3] Did the authors decant any of their specimens after dendritic growth became apparent on the top surface, and observe branching of structures projecting from the general interface?

It is also not clear to the writer, from Fig. 3 of the authors' paper, how rapidly and universal the transition from nondendritic to dendritic growth takes place. Also, in the same figure, it is not clear why the direction of the structure on the lower half of the photograph is rotated with respect to that of the upper half, since both structures would be expected to grow parallel to the direction of growth for the crystal orientations the authors used.

One further point. Do the authors attribute the dendritic growth they observed entirely to constitutional supercooling of the liquid? Did they observe any thermal supercooling in their temperature measurements?

Written Discussion: By R. J. Dunworth, associate metallurgist, Argonne National Laboratory, Chicago.

The authors are to be congratulated on another fine paper in their series on phenomena associated with the solidification of metals. The concept of a high concentration of solute at the freezing interface explains quite well the formation of hexagonal projections, dendrites and lack of segregation. The equation developed to calculate the concentration gradient, however, apparently does not describe the actual data obtained. According to Rutter and Chalmers,[4] the hexagonal projections can extend 0.1 cm. into the liquid. If dendrites are an additional growth of these hexagonal projections then it may be expected that the dendrites will extend 0.3 or 0.4 cm. into the liquid. If, in the equation,

$$C = C_o\left(\frac{1-k}{k}\right)e^{-Rx/D} + C_o$$

$D = 10^{-5}$ cm²/sec., $R = 10^{-2}$ cm/sec. (6 mm/min) and $x = 0.1$ cm. then the exponential is $e^{-100} \sim 2(10^{-9})$. If $x = 0.01$ cm, the exponential is $e^{-10} \sim 5(10^{-5})$. The excess solute concentration at these values of x is practically nothing and it is difficult to imagine a growth being produced by such a slight amount. The length of the projection extends, in fact, about 100 times as far as there can be any concentration effect.

Secondly, the effect of the initial concentration on the structure resulting from solidification is not considered in the equation. It is quite well established, both by the authors and others, that an increase in initial solute concentration produces a definite change in the solidified structure. Whether C_o equals 0.1, 1.0 or 10%, the excess concentration is still negligible when multiplied by a factor like 10^{-5}.

It is suggested, then, that the equation be modified somewhat so as to fit the

---

[2] F. Weinberg and Bruce Chalmers, "Dendritic Growth in Lead," *Canadian Journal of Physics*, Vol. 29, 1951, p. 382.

[3] F. Weinberg and Bruce Chalmers, "Further Observations on Dendritic Growth of Metals," *Canadian Journal of Physics*, Vol. 30, 1952, p. 488.

[4] J. W. Rutter and B. Chalmers, "A Prismatic Substructure Formed During Solidification of Metals," *Canadian Journal of Physics*, Vol. 31, January 1953, p. 15.

observed data more closely. The exponential factor in the equation would be

$$e^{-\frac{100D}{R}\, x\sqrt{C_o}}$$

The initial concentration factor, C_o, is diminished because the effect of a linear factor is too drastic.

Authors' Reply

The authors would like to thank Dr. Dunworth for his discussion. It should be noted that to calculate the amount of constitutional supercooling, it is necessary to consider both the equilibrium liquidus temperature distribution ahead of the interface and the actual temperature distribution in the liquid as imposed by the growth conditions. Calculations of this sort are shown in Fig. 11 of a paper by Tiller, Jackson, Rutter and Chalmers.[5] The zone of supercooling may be quite long, depending upon the value of the temperature gradient in the liquid. Consider, for example, a 3% tin in lead alloy solidifying at 2.85 cm./min. Calculations show that the region of high tin concentration is confined to about 10^{-3} cm. ahead of the interface. Consequently, the equilibrium liquidus temperature rises from 311 °C (corresponding to 6% tin) at the interface to 319 °C (corresponding to 3% tin) in this distance. However, with a temperature gradient of 18.5 °C/cm. in the liquid, the actual temperature of the liquid does not reach 319 °C. for a distance of about 4 mm.

The figure that Dr. Dunworth quotes concerning the extent to which hexagonal cells project into the liquid is at least one order of magnitude too large. Rutter and Chalmers[6] found the length of the projections to be approximately 0.001 to 0.01 cm.

Concerning the discussion by Dr. Weinberg, it is important to note that the method of growth used in Dr. Weinberg's experiments was quite different than in the present experiments. The study of dendritic growth in pure materials necessitates rapid cooling of the liquid ahead of the interface so that it can become thermally supercooled. In Dr. Weinberg's experiments, to accomplish this the liquid-air surface would have to be at a lower temperature than the main body of liquid. Because of this increased supercooling, "fern type" dendrites would be observed growing on the top surface of the liquid. In our experiments, however, the liquid was in all cases at a temperature higher than the interface temperature. There was never any thermal supercooling; in fact, considerable care was taken to make certain that growth always occurred under a positive temperature gradient in the liquid in order that it could be definitely stated that the formation of the dendritic structure was caused by constitutional supercooling and not thermal or absolute supercooling.

Specimens used in this investigation were not single crystals; the structures in Fig. 3 merely exhibit the orientation of their respective grains. As shown by Rutter and Chalmers,[6] the direction of formation of the corrugations depends on the orientation of the growing crystal.

In the apparatus used, it was difficult to decant the specimens, so that the authors were not able to decant after dendritic growth became apparent on the top surface. The only decanted specimens were those mentioned in the paper.

---

[5] W. A. Tiller, K. A. Jackson, J. W. Rutter and B. Chalmers, "The Redistribution of Solute Atoms During the Solidification of Metals," ACTA METALLURGICA, Vol. 1, 1953, p. 428.

[6] J. W. Rutter and B. Chalmers, "A Prismatic Substructure Formed in the Solidification of Metals," *Canadian Journal of Physics*, Vol. 31, 1953, p. 15.

STRESS-CORROSION MECHANISM IN A MAGNESIUM-BASE ALLOY

By D. K. Priest, F. H. Beck and M. G. Fontana

Abstract

The mechanism of stress-corrosion in the magnesium base alloy (J1) containing 6% aluminum, 1% zinc and 0.2% manganese has been studied in a 3% NaCl—3% K_2CrO_4 solution at room temperature. All specimens were taken from 1/2-inch diameter extruded rod. The effects on stress-corrosion of heat treatment, grain size, lattice orientation, cathodic protection, and the pH value of the testing solutions were evaluated. Observations of crack propagation were made by means of a microscope located above the solution container. Motion picture microscopy of the cracking was accomplished and this proved to be an effective tool. A half-hour film on stress-corrosion was prepared.

Specimens of small grain size, furnace-cooled from solution temperature, cracked intergranularly in stress-corrosion tests. Water quenching of specimens of small grain size resulted in transgranular stress-corrosion. In specimens with grain sizes larger than ASTM No. 7, transgranular stress-corrosion occurred regardless of heat treatment.

In contrast to stress-corrosion data previously reported for hard rolled AM-C 57 S-H, an alloy having the same nominal composition as J1, the pH value of the salt-chromate testing solution had no effect on whether cracking was transgranular or intergranular in the annealed specimens used in this investigation. Heat treatment was the criterion for the type of failure which occurred.

Transgranular stress-corrosion was found to take place along the (0001) plane of the HCP lattice of this alloy. This was determined by stereographic analyses of twin and crack traces on the surface of very large grained specimens.

Cathodic protection by means of an external current prevented the initiation of both transgranular and intergranular stress-corrosion. It also stopped stress-corrosion which was in progress.

Based on a thesis submitted in partial fulfillment of the requirements for the degree, Doctor of Philosophy, from the Ohio State University, Columbus, Ohio.

A paper presented before the Thirty-sixth Annual Convention of the Society, held in Chicago, November 1 to 5, 1954. Of the authors, D. K. Priest is associated with the Pfaudler Co., Rochester, N. Y., F. H. Beck is assistant research professor, Engineering Experiment Station, and M. G. Fontana is professor and chairman, Department of Metallurgy, The Ohio State University, Columbus, Ohio. Manuscript received March 26, 1954.

The mechanism of transgranular stress-corrosion is believed to be essentially electrochemical in nature because of the action of cathodic protection. Heidenreich, Gerould and McNulty have shown that a segregation of cathodic FeAl exists in the solution-quenched condition of this alloy. The presence of this compound increases susceptibility to stress-corrosion. This segregation appears to occur on only one plane. It has been shown in the present work that transgranular stress-corrosion takes place predominantly along the basal plane. It is reasonable to state, then, that preferential attack occurs along the basal plane because of the presence of FeAl. The function of stress is believed to be that of exposing film-free metal by plastic deformation brought about by the stress concentration at the base of the crack.

Introduction

STRESS-corrosion is a corrosive attack which, in its usual form, produces cracking in metals. The mechanisms which operate in this type of corrosion are not well understood, particularly if the cracking proceeds transgranularly.

The purpose of this investigation was to study the stress-corrosion behavior of an extruded magnesium alloy with a view to developing a mechanism of stress-corrosion. This magnesium-base alloy of nominal composition 6% aluminum, 1% zinc and 0.2% manganese, was chosen as the material to be tested because of its susceptibility to stress-corrosion under relatively convenient testing conditions. Particular attention was directed to the mechanism of transgranular stress-corrosion.

Survey of Literature

The Nature of Stress-Corrosion—Stress-corrosion is defined as the acceleration of the rate of corrosion by stress (1).[1] In this type of attack, stress and corrosion, acting together, produce failure much more quickly than corrosion acting alone and at stresses which would not produce failure at all in the absence of corrosion (2). It has been shown that only tensile stresses promote stress-corrosion (3).

The stress-corrosion attack usually takes the form of a rapid penetration or cracking along grain boundaries although many systems exhibit transgranular stress-corrosion cracking. Intergranular stress-corrosion usually occurs under conditions favorable to metal dissolution at grain boundaries but the exact causes of transgranular failure are not well understood (3,4). Stress-corrosion has been observed in almost all metals or their alloys but each metal or alloy often requires a certain characteristic corrosion environment (3). This type of corrosion is usually confined to systems which are intermediate between

[1] The figures appearing in parentheses pertain to the references appended to this paper.

an active and a passive state where severe local attack may develop.

Stress-Corrosion of Magnesium Alloys—Few contributions have been made toward an understanding of the stress-corrosion of magnesium alloys. One of these is the work by Mears, Brown and Dix (3) in which both intergranular and transgranular cracking in the J1 alloy was reported. They observed that in hard rolled material, AM-C 57 S-H, intergranular stress-corrosion occurred in acidic salt-chromate solution and that transgranular stress-corrosion took place in basic salt-chromate solution. Intergranular stress-corrosion in magnesium alloys has not been extensively discussed elsewhere.

Heidenreich, Gerould and McNulty (5) have pointed out that magnesium-base alloys become more susceptible to transgranular stress-corrosion as the aluminum content of the alloy is increased. They also report that the amount of a so-called "fine structure" is similarly dependent on the aluminum content. The conclusion was reached that the "fine structure," which is observable only by the electron microscope, was caused by the presence of some iron-aluminum compound, probably FeAl. Such a structure was present in material either water-quenched or furnace-cooled from 400 °C (825 °F). The solution potential differences between iron-aluminum compounds and the magnesium-aluminum solid solution have been found to be relatively large (6). For this reason, the authors above conclude that the presence of the "fine structure" increases the susceptibility to transgranular stress-corrosion.

Logan (7) has indicated that film breakage by plastic deformation may play an important role in stress-corrosion. A potential difference of 0.24 volts between filmed and film-free areas was measured on a magnesium alloy, with the film-free area being anodic. The importance of films in stress-corrosion has also been discussed by Edeleanu and Evans (8).

Apparatus and Experimental Procedure

Preparation of Specimens—The material used in this investigation was a magnesium-base alloy, J1, supplied by the Dow Chemical Co. Its composition was aluminum 6.54%, manganese 0.30%, zinc 1.28%, silicon 0.01% and iron 0.0015%. This alloy, of nominal composition 6% aluminum, 1% zinc and 0.2% manganese, has the ASTM designation AZ61a. It is designated as J1 by the Dow Chemical Company and as AM—C 57 S by the American Magnesium Corporation. The designations —C and 1 stand for controlled high purity metal low in iron, nickel and chlorine.

Specimens 3/16 x 3/16 x 4-1/2 inches were machined from 1/2 inch diameter extruded rod which had received previous heat treatment. The surfaces of the specimens were finished on 500 grit metallographic paper, washed in water and dried in air prior to testing.

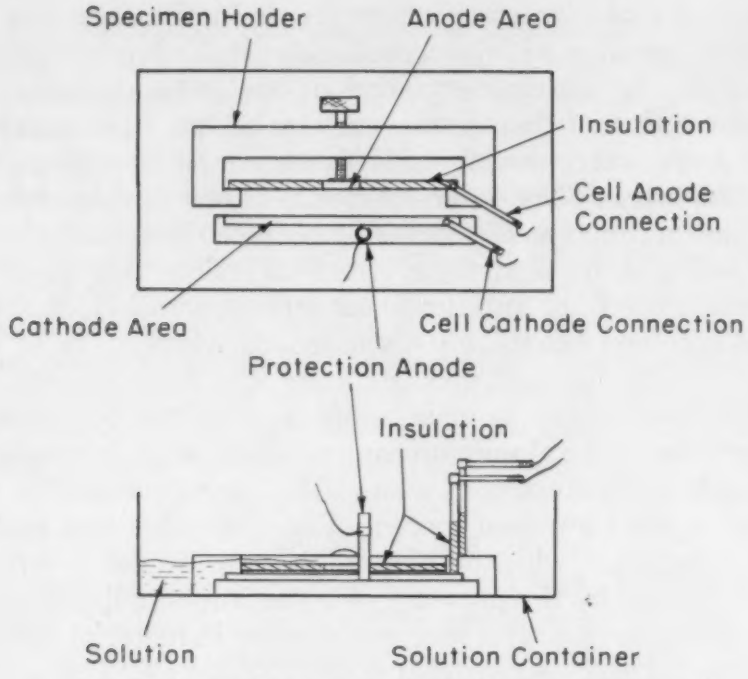


Fig. 1—Stress-Corrosion Specimen, Specimen Holder and Solution Container. Electrical connections and insulation required for current measurements are shown.

Heat treatments consisted of heating the alloy at 345 °C (650 °F) for 24 hours followed by furnace cooling or quenching in water from that temperature. Very large grain sizes were obtained by a strain-anneal treatment consisting of a 6% decrease in rod length followed by heating at 480 °C (900 °F). All material heated to this temperature was enclosed in sealed Pyrex glass capsules in order to prevent excessive oxidation.

Preparation of metallographic samples was as follows. The samples were abraded on 500 grit metallographic paper, washed and further polished on a medium speed wheel by a suspension of 600 grit carborundum in a soap and water solution. Final polishing was on a slow speed wheel using Shamva (MgO). A picric acid etch composed of 100 milliliter ethanol, 10 milliliter distilled water, 5 milliliter glacial acetic acid and 5 grams of picric acid was used.

Experimental Apparatus.—The prepared specimens were placed in a specimen holder of Synthane, an electrical insulating material. This holder and the manner in which the specimens were stressed is shown in Fig. 1. The specimen is insulated from the thumbscrew by a small sheet of Teflon. The distance between the end supports of the specimen holder is 4 inches. The stress in the outer fibers of the specimen is proportional to the amount of deflection imposed at the midpoint of the specimen. The nominal value of stress is given by the equation

$$S = \frac{12\,YEC}{L^2}$$

where S is the stress (psi), Y is the deflection (inches), E is Young's modulus, C is half the specimen width (inches) and L is the specimen length (inches). The value of stress given by this equation is only approximately correct because of the onset of plastic deformation at the stress levels employed. Accurate stress values cannot be calculated but the values obtained using the equation above give some idea of the orders of magnitude involved. A deflection of 0.120 inches was used (55,000 psi nominal stress). The strain-deflection data shown in Fig. 2

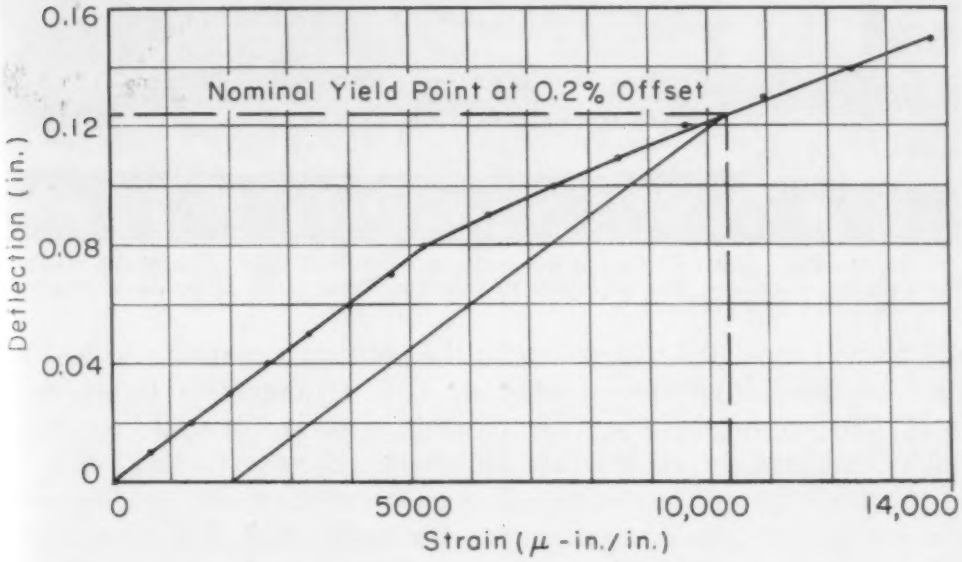


Fig. 2—The Curve Shows Extent of Plastic Deformation and Position of Yield Point in Terms of Specimen Deflection and Strain Measured on Tension Surface Specimen.

show that the specimens were stressed above the yield point (32,000 psi at 0.2% offset). These data were obtained by direct measurement of strain using A-7 gages (¼ inch gage length) mounted on the tension surface of the specimens.

The specimen and its holder were placed in a solution container which was placed on the stage of a microscope. The position of the specimen was adjusted with respect to the microscope objective by a traveling stage. This arrangement is shown in Fig. 3. Visual observations or motion picture data were taken through the microscope. The motion picture equipment used for filming the stress-corrosion process is also shown in this figure.

Corrosion currents were measured between anodes (stress-corrosion specimens) and cathodes (unstressed specimens) of the J1 alloy. The electrodes were placed parallel to each other with approximately ¼ inch separation at the anode (the point of maximum stress). The wire leads to the electrodes were insulated and an insulating coating was applied to both ends of the stress-corrosion specimen leaving

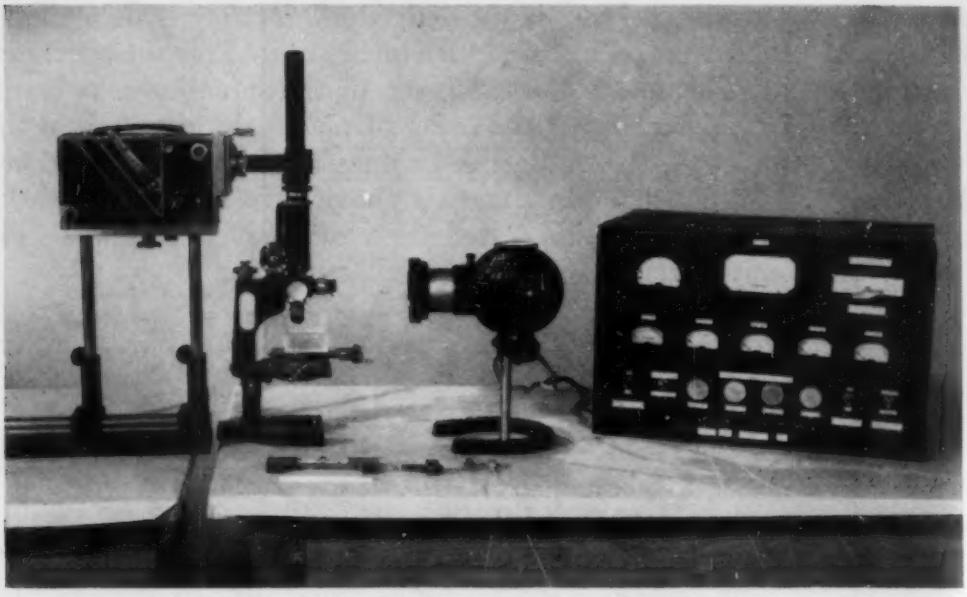


Fig. 3—Equipment for Study of Stress-Corrosion, Left to right—Cine Kodak Special, beam splitter, microscope with adjustable stage and metering panel. Stress-corrosion specimen and holder in foreground.

only a small area (0.4 inches long at the point of maximum stress) exposed to the salt-chromate solution. This arrangement is shown in Fig. 1. Current measurements were made by means of a microammeter which completed the external circuit between the two electrodes.

Cathodic protection was applied to stress-corrosion specimens by means of an external current source. Cathodic protection current data and changes in corrosion current caused by cathodic protection were taken with apparatus arranged as in Fig. 4. Cathodic protection current and corrosion current were measured on M1 and M2 respectively when both switches were closed. The electrical connections to the specimen are shown in Fig. 1. A protection anode of carbon rod was used.

The test procedure is as follows: At the start of the test a large cathodic protection current is applied with both switches SW1 and SW2 closed. This makes the protective anode anodic to both the anode and the cathode of the corrosion cell. As the cathodic protection current is gradually decreased to a sufficiently low value, the corrosion currents of the cell become operative and allow stress-corrosion to proceed with the flow of positive corrosion current. The corrosion current increases as the cracking proceeds. When the corrosion current reaches a certain predetermined value, which is an arbitrary standard for all specimens, a large cathodic protection current is applied and the stress-corrosion process is stopped. The cathodic protection is again decreased to the value at which stress-corrosion resumes. This procedure then gives the values of cathodic protection current which will

a. Allow stress-corrosion to start.
b. Allow stress-corrosion to re-start after a crack has been formed.

The corrosion current is then allowed to reach its maximum at which time the cathodic protection current is adjusted to a fixed value which reduced the corrosion current to zero. Corrosion current readings are then made with and without the application of the fixed amount of protective current by moving switch SW1.

Testing Solution—Stress-corrosion testing was carried out in a salt-chromate solution (pH = 9.0) of 40 grams of NaCl-40 grams of K_2CrO_4 per liter of water with the exception of the tests in salt-

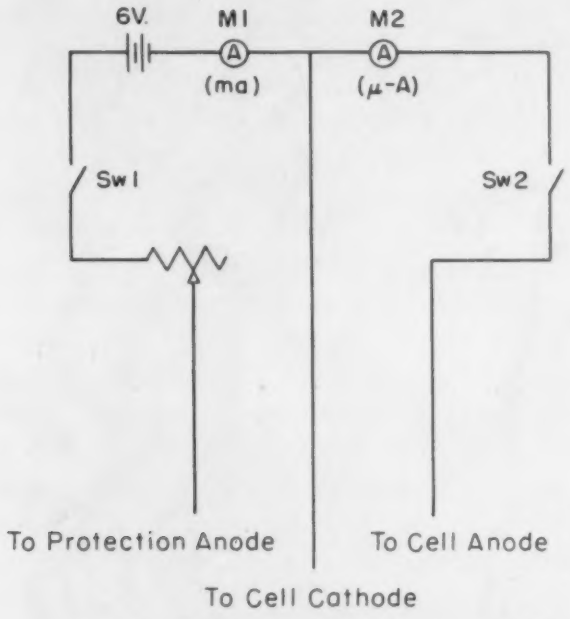


Fig. 4—Basic Metering Diagram used for Measuring Corrosion Current and Cathodic Protection Current.

chromate solutions of high and low pH values. The latter solutions were composed of 35 grams of NaCl-20 grams of K_2CrO_4 per liter of water (pH = 8.7) and 35 grams of NaCl-20 grams of $K_2Cr_2O_7$ per liter of water (pH = 3.5). All tests were performed at room temperature.

Results and Discussion

Heat Treatment—Stress-corrosion specimens which had been furnace-cooled from 345 °C (650 °F) exhibited intergranular stress-corrosion cracks when tested in the salt-chromate solution. Specimens which had been water-quenched from this temperature cracked transgranularly. These results were obtained from 40 specimens, 20 specimens furnace-cooled and 20 specimens water-quenched.

A difference in microstructure exists in the two types of specimens. Fig. 5 is a photomicrograph which shows an intergranular stress-corrosion crack and the microstructure of a furnace-cooled specimen. The grain boundary precipitate is $Mg_{17}Al_{12}$, the compound which

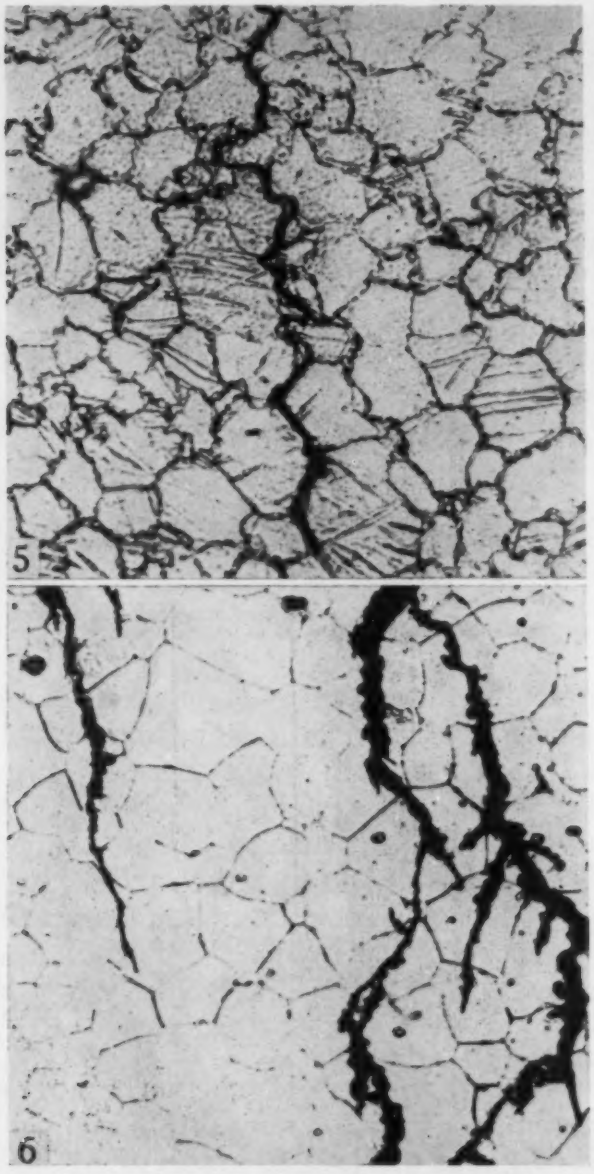


Fig. 5—Intergranular Stress-Corrosion Crack with Microstructure Characteristic of Furnace Cooling from 345 °C (650 °F). Picricacetic etch. X 600

Fig. 6—Transgranular Stress-Corrosion Crack with Microstructure Characteristic of Solution Quenching from 345 °C (650 °F). Picricacetic etch. X 600

normally appears in the J1 alloy with this heat treatment. Fig. 6 is a photomicrograph of the solid solution microstructure of a water-quenched specimen in which precipitate is absent. This photomicrograph also shows the transgranular cracking typical of water-quenched specimens.

The occurrence of intergranular stress-corrosion or transgranular stress-corrosion has been shown to depend upon heat treatment. In order to understand this effect of heat treatment on the type of failure, it is necessary to examine closely the microstructure associated with

each kind of specimen. Heidenreich, Gerould and McNulty (5) have shown by the use of the electron microscope that an intragranular segregation of FeAl exists in the J1 alloy. They suggest that temperatures of solution heat treatment of the J1 alloy are temperatures favorable to precipitation of this compound. The FeAl segregation is shown to exist even if the J1 alloy is furnace-cooled instead of being quenched in water from solution heat treating temperatures (9). This compound, then, is present in all of the J1 specimens tested in this investigation.

The grain boundary precipitate $Mg_{17}Al_{12}$ is produced in only those specimens furnace-cooled from solution temperatures. The specimens solution treated at from 345 to 480 °C (650 to 900 °F) and quenched in water have only the FeAl precipitation in their microstructures but those furnace-cooled from the solution treating temperatures mentioned above possess both the FeAl precipitation and the intergranular $Mg_{17}Al_{12}$ precipitation.

The results which have been obtained indicate that a different mechanism exists for transgranular stress-corrosion than for intergranular stress-corrosion in the salt-chromate solution. $Mg_{17}Al_{12}$ has been shown to be sufficiently cathodic to the magnesium-aluminum solid solution to cause corrosive attack in the regions immediately adjacent to it (6,9). The presence of $Mg_{17}Al_{12}$ in the furnace-cooled specimen accounts for the intergranular stress-corrosion observed. The compound FeAl also is cathodic to the solid solution and its presence accounts for the transgranular stress-corrosion of specimens quenched in water from solution treating temperatures. A mechanism of transgranular stress-corrosion will be discussed in detail in another section. FeAl is more cathodic to the solid solution than $Mg_{17}Al_{12}$ (6,9) but because much more intergranular $Mg_{17}Al_{12}$ than intragranular FeAl is present in furnace-cooled specimens, intergranular stress-corrosion occurs. This explanation of intergranular and transgranular stress-corrosion in terms of heat treatment and resulting microstructure holds true only for small-grained specimens prepared by solution treating at 345 °C (650 °F).

Specimens with very large grains resulting from the strain-anneal treatment always exhibited transgranular stress-corrosion whether furnace-cooled or water-quenched. This indicates that some limiting grain size is necessary in order for intergranular stress-corrosion to occur even when $Mg_{17}Al_{12}$ is present in the microstructure. The maximum grain size for intergranular corrosion was found to be approximately ASTM grain size No. 7, the grain size being controlled by the temperature of solution heat treatment. All specimens having grain sizes larger than this failed transgranularly regardless of heat treatment. Stress-corrosion cracks tend to propagate in as straight a line as possible in the direction normal to the tensile stress present. Thus,

Table I
Effects of pH and Heat Treatment on Manner of Stress-Corrosion

Heat Treatment	pH of Testing Media	Manner of Cracking
650 °F — water-quenched	3.5	transgranular
650 °F — water-quenched	8.7	transgranular
650 °F — furnace-cooled	3.5	intergranular
650 °F — furnace-cooled	8.7	intergranular

for wholly intergranular stress-corrosion to occur many grain boundaries must be present to allow crack propagation to take place in the prescribed direction. If grain size is large, the fewer number of grain boundaries tends to cause the crack to detour around large grains and an irregular crack forms. When both transgranular and intergranular stress-corrosion is possible, as in the furnace-cooled J1 alloy, an increase in grain size causes a transition from intergranular to transgranular cracking, because it becomes easier for the crack to propagate across grains than around them in spite of the local cell action possible at the grain boundaries.

It should be pointed out that heat treatment of the J1 alloy determines whether transgranular or intergranular stress-corrosion occurs only when testing is done in the salt-chromate solution. In other corrosive media this criterion for failure may not be operative because different potential relationships may exist between the phases present or because different electrode reactions are possible. For example, the J1 alloy fails by transgranular stress-corrosion in distilled water regardless of heat treatment. This has been also reported by Perryman (10).

It has been indicated that the pH value of the salt-chromate testing solution is the factor which determines if the path of stress-corrosion will be transgranular or intergranular in AM-C 57 H, a hard rolled alloy having the same nominal composition as J1 (3). In the present investigation, the results of stress-corrosion tests on specimens furnace-cooled or water-quenched from 345 °C (650 °F) and tested in salt-chromate solutions of pH value 3.5 and 8.7 indicate that heat treatment is the factor which controls the type of failure and the pH value has no effect. Typical results of these tests are recorded in Table I.

Direction of Transgranular Cracking—Early in this investigation it was noticed that transgranular cracks did not always propagate in the direction normal to the applied stress as is usually the case in stress-corrosion. Instead, the direction of these cracks appeared to be dependent upon grain orientation. This behavior suggested that the cracking was proceeding predominantly along a certain crystallographic plane. Fig. 7 is a series of frames from the motion picture of stress-corrosion showing the progress of a crack across a single grain. The

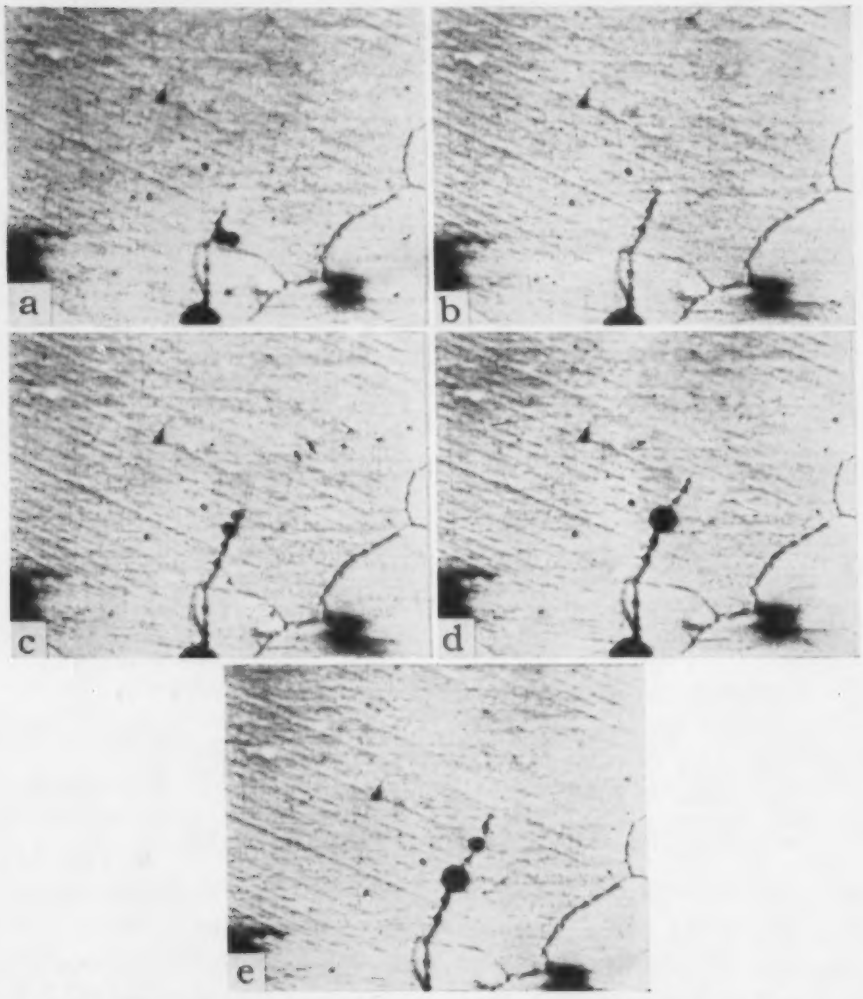
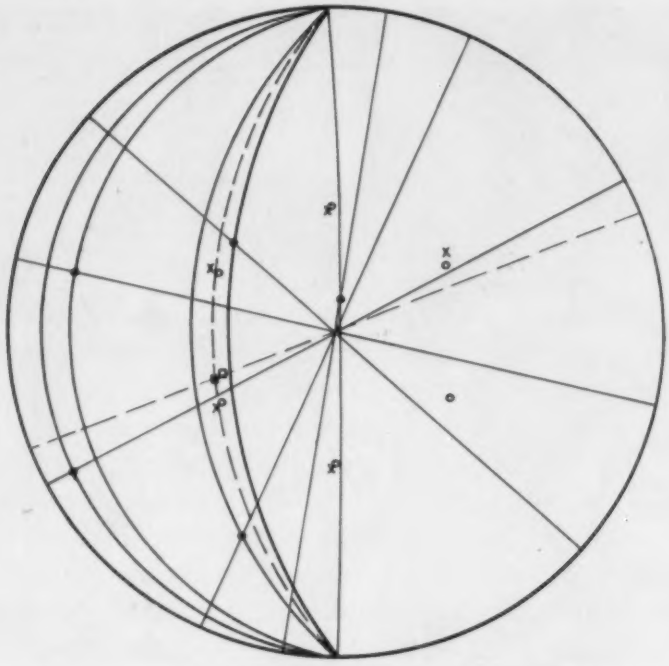


Fig. 7—Frames from Motion Picture of Stress-Corrosion. Frames are 1 second apart. Picricacetic etch. X 20

frames are at 1 second intervals. The crack changes direction at the grain boundary.

The plane along which transgranular cracking took place was determined to be the (0001) plane of the HCP lattice of this alloy. The determination of the crack plane was carried out by stereographically plotting the poles of observed twin planes and finding by trial the amount of rotation needed to place these poles in their correct positions on the standard (0001) projection. This value of rotation was found to be the same as that necessary to rotate the pole of the crack plane to the position of the pole of the (0001) plane as it appears on the standard (0001) projection. This shows the crack plane to be the basal plane. Fig. 8 is a stereographic projection of one of several specimens analyzed in this manner.

Cathodic Protection—Current measurements were made on both water-quenched and furnace-cooled specimens to determine the effect



Orientation of Hexagonal Crystal Determined from Traces on Two Surfaces

Normals to Twin Traces are Full Lines
Normals to Crack Traces are Dashed Lines

• {10T2} Poles in Orientation Explaining Traces

∘ Standard Projection of {10T2} Poles

x {10T2} Poles After Rotation of 40° Right with 21° Counterclockwise Inclination of Wulff Net

▪ Experimentally Determined Pole of Crack Plane

□ (0001) Pole Predicted by Orientation

Fig 8—Stereographic Projection of Poles of Twinning Planes and a Stress-Corrosion Crack Plane in a Single Grain.

of cathodic protection on corrosion currents and on control of stress-corrosion. Table II shows some data developed for a water-quenched specimen. The data obtained in all of the tests on either water-quenched or furnace-cooled specimens do not differ significantly from those in this table. Tests of this type indicate that only a small amount of cathodic protection current, in order of 0.06 ma, is required to prevent the initiation of stress-corrosion. The amount of cathodic protection current needed to prevent the restarting of a stress-corrosion crack was found to be in the range 0.06 to 0.1 ma. Much higher cathodic protection currents were required to stop stress-corrosion which was in progress. The data in Table II indicate that when a maximum in the corrosion current was reached, a protective current of 0.33 ma was required to reduce the corrosion current to zero. Protective current in excess of this value was required to overcome local cell action on the

Table II
Effect of Cathodic Protection on Corrosion Currents in Stress-Corrosion

Time (min.)	Corrosion Current (CC), μ — A	Cathodic Protection Current (CPC), ma*	Remarks**
0	−23	4 (1.58 ma/sq. in.)	no S-C
10	−15	4	no S-C
15	−5	0.4	no S-C
20	−3	0.2	no S-C
25	+2	0.1	S-C after 24 min.
27	+12	0	S-C occurring
28	−22	4	no S-C
30	−18	4	no S-C
35	−5	0.4	no S-C
35.5	−3	0.2	no S-C
39.5	+1	0.2	S-C started
40	+3	0.2	S-C occurring
41	+18	0	no applied CPC
44	+25.5	0	maximum CC
44.25	0	0.33	adjusted to zero CC
46	+22	0	no applied CPC
46.25	−3	0.33	CPC applied
48	+14	0	no applied CPC
48.25	−8	0.33	CPC applied

* Cathode area = 2.53 sq. in.
** S-C, stress corrosion
CPC, cathodic protection current
CC, corrosion current

stress-corrosion specimen and stop the stress-corrosion cracking completely. In general the amount of cathodic protection current needed to stop the attack was proportional to the corrosion current being generated at the time of application of protection.

Transgranular Stress-Corrosion Mechanism—A reasonable mechanism for transgranular stress-corrosion in the J1 alloy can be proposed by combining the results of this investigation with information cited in the literature. An electrochemical contribution has been shown to be an important part of transgranular attack but there exists no obvious source of the potential difference necessary to explain such attack. However, as has been mentioned previously, Heidenreich, Gerould and McNulty (5) have shown by the use of the electron microscope, that a segregation of FeAl exists in the J1 alloy. This compound has been shown to be approximately one volt cathodic to the magnesium-aluminum solid solution in salt-chromate solution. Furthermore, the "fine-structure" caused by the presence of FeAl appears in electron photomicrographs to be composed of platelets or of parallel lines, apparently depending upon the orientation of the observer with respect to the lattice structure. This strongly suggests that the FeAl segregation is predominantly confined to one crystallographic plane. When the fact that transgranular stress-corrosion cracking usually occurs along the basal plane is coupled with the information concerning the appearance of the FeAl segregation, a reasonable explanation of transgranular stress-corrosion is realized if the assumption is made that the FeAl segregates at the basal plane. In addition, Beck (11) has

written that ordinary corrosion of magnesium alloy castings is related to the crystallographic orientation of the grains. The attack takes place primarily on the basal planes.

Other sources of potential difference add their effects to the one already mentioned. Motion picture microscopy (a motion picture concerning stress-corrosion was produced as a part of this investigation) has shown that much plastic deformation continuously takes place at the tip of an advancing transgranular crack. Such deformation would prevent any film formation and allow a potential difference to be maintained between the filmed and film-free areas. The function of stress in stress-corrosion, while probably somewhat subordinate to that of electrochemical action, is to produce film-free (anodic) areas by plastic deformation at the crack tip. This importance of stress in preventing film formation has been discussed by Logan (7).

Summary and Conclusions

1. Transgranular stress-corrosion of the J1 alloy in salt-chromate solutions occurs predominantly along the (0001) plane of the HCP lattice.

2. Furnace cooling from 345 °C (650 °F) of fine grained J1 alloy produces intergranular stress-corrosion in salt-chromate solutions. This heat treatment permits the formation of $Mg_{17}Al_{12}$ at grain boundaries, thereby rendering the material subject to intergranular attack. Fine grained material which is water-quenched from 345 °C (650 °F) exhibits transgranular stress-corrosion cracks. This material does not have the $Mg_{17}Al_{12}$ precipitate.

3. Transgranular stress-corrosion always takes place in salt-chromate solutions whether the alloy is furnace-cooled or water-quenched from 345 °C (650 °F) when the grain size of the material is larger than ASTM grain size No. 7.

4. The pH value of the salt-chromate testing solution has no effect on whether stress-corrosion is transgranular or intergranular in annealed specimens. Heat treatment determines the type of failure.

5. Cathodic protection by impressed current of J1 alloy stress-corrosion specimens prevents the initiation of stress-corrosion and stops stress-corrosion which is in progress when protection is applied.

6. Local plastic deformation is shown by motion picture microscopy to be present near the tip of advancing transgranular cracks.

7. A mechanism for transgranular stress-corrosion in salt-chromate solutions of the J1 alloy is proposed.

Acknowledgment

The work reported here was carried out as part of a contract (N6ori-17 Task Order II) between The Ohio State University Research Foundation and the Office of Naval Research, Department of

the Navy. The assistance of Dr. R. S. Busk and Mr. H. A. Robinson of the Dow Chemical Company and Messrs. E. R. Dix and R. H. Brown of the Aluminum Company of America is greatly appreciated. The authors also wish to express their appreciation to the Department of Photography, the Ohio State University for assistance in the motion picture microscopy.

References

1. M. G. Fontana, "Stress-Corrosion and Corrective Measures," METAL PROGRESS, Vol. 53, 1948, p. 838–40.
2. U. R. Evans, "Stress-Corrosion—Its Relationship to Other Types of Corrosion," *Corrosion,* Vol. 7, 1951, p. 238–44.
3. R. B. Mears, R. H. Brown and E. H. Dix, Jr., "A Generalized Theory of the Stress-Corrosion of Alloys," *Symposium on Stress-Corrosion Cracking of Metals,* ASTM-AIME, 1944, p. 323–39.
4. J. J. Harwood, "The Influence of Stress on Corrosion," *Corrosion,* Vol. 6 1950, p. 249–59, 290–307.
5. R. D. Heidenreich, G. H. Gerould and R. E. McNulty, "Electron Metallographic Methods and Some Results for Magnesium Alloys," *Transactions,* American Institute of Mining and Metallurgical Engineers, Vol. 166, 1946, p. 15–36.
6. J. D. Hanawalt, C. E. Nelson and J. A. Peloubet, "Corrosion Studies of Magnesium and Its Alloys," *Transactions,* American Institute of Mining and Metallurgical Engineers, Vol. 147, 1942, p. 273–99.
7. H. L. Logan, "Film-Rupture Mechanism of Stress-Corrosion," *Journal of Research, National, Bureau of Standards,* Vol. 48, 1952, p. 99–105.
8. C. Edeleanu and U. R. Evans, "The Causes of the Localized Character of Corrosion on Aluminum," *Transactions, Faraday Society,* Vol. 47, 1951, p. 1121–35.
9. Research Laboratory, Dow Chemical Company, Private Communication.
10. E. C. W. Perryman, "Stress-Corrosion of Magnesium Alloys," *Journal,* Institute of Metals, Vol. 78, 1951, p. 621–42.
11. A. Beck, *The Technology of Magnesium and Its Alloys,* London: F. A. Hughes and Co., Ltd., 1940, p. 275, 295.

DISCUSSION

Written Discussion: By F. L. LaQue, vice president and manager, Development and Research Division, The International Nickel Co., Inc., New York.

This discussion of this interesting paper is based not only on the paper itself, but on certain impressions gained from seeing the motion picture made during the course of the investigations.

The mechanisms of attack as proposed in the paper appear to be quite plausible. It is especially interesting that, in this case, we appear to have a satisfactory mechanism to account for transgranular cracking which generally has been difficult to explain in other systems, e.g., austenitic stainless steels in chloride environments.

The motion picture shows that when cracking is occurring there is a copious evolution of hydrogen at, or near, the head of the advancing crack. This is what would be expected if the cathode of the corrosion reaction were to exist along the crack and, therefore, is in line with the proposed explanation of the cracking mechanism. In view of the amount of hydrogen liberated, it seems likely, also,

that the products of corrosion result in a sharp decrease in the pH of the solution in the immediate vicinity of the corrosion. From this it follows that the suppression of the cracking by the application of current may well include the neutralization of acid corrosion products by the alkali generated in the cathodic reactions. Since there was evolution of hydrogen in both the intergranular and transgranular cracks, presumably associated with an electrolyte of low pH within these advancing cracks, there is support here for the authors' observation that the pH of the surrounding electrolyte is not a crucial factor in the location of the cracks.

It was noted, also, that the experimental setup included an external cathode of unstressed metal of the same composition. Possibly this was the cathode that was involved in the initiation of cracking, while the one that promoted the propagation of cracking was one or other of the intermetallic compounds mentioned.

These views are supported by the fact that while hydrogen evolution occurred during cracking, there was no evidence of this in the motion picture when current of the same order of magnitude was supplied from the external anode. This means either that the cathodic reaction was different or that it occurred at some other place when cathodic protection was applied.

It would be interesting to have the authors comments on what might have happened if there had been no external specimen connected to the one under stress.

Written Discussion: By R. B. Mears, director, Applied Research Laboratory, United States Steel Corp., Pittsburgh.

The authors have made a very important advance in the study of the mechanism of stress-corrosion. They have verified the effect of electrochemical factors and given a reasonable explanation for the transition from an intragranular path of fracture to a transgranular path depending on the type of thermal treatment used. Older mechanisms suggested for other alloys have generally made use of a triple area hypothesis. For example, in the case of aluminum-copper alloys it has been suggested that precipitation of the aluminum-copper constituent at the grain boundaries results in an adjacent area of the grain, immediately next to the boundary, that is depleted in copper and hence is anodic to the main body of the grain (as well as to the aluminum-copper constituent). It has been postulated that since the exposed area of the aluminum-copper constituent is so small it could not greatly accelerate attack of adjacent grain areas itself, since it would polarize too readily. It is necessary to assume that a much larger cathodic area is available, namely the grain centers, to account for the high current densities required adjacent to the grain boundaries. Are the authors certain that the grain centers are not serving as effective cathodes to depleted zones adjacent to grain boundaries or slip planes in the case of the magnesium-base alloy studied?

Written Discussion: By R. S. Busk, The Dow Chemical Co., Midland, Mich.

The authors of this paper are to be congratulated on their careful and informative work. As they state, the literature on the stress-corrosion mechanism of magnesium alloys is meagre and therefore their contribution is doubly welcome.

During the past decade, many workers at The Dow Chemical Company have studied the stress corrosion of magnesium. I would like to offer a small part of this work as a discussion to this paper.

I believe the essentially electrochemical nature of stress corrosion must be accepted now by all workers in the field. The authors have very nicely demonstrated that a protective current will control the onset or course of stress corrosion. In like manner we have also been able to control stress corrosion by impressing a sufficiently large voltage on the system. We have also shown that

substitution of dry benzene for an electrolyte stops stress corrosion which is in progress.

Thus current flow is an essential ingredient in stress corrosion. The cathodes responsible for the voltage which drives this essential current must be sufficiently cathodic to magnesium to release hydrogen. This requirement may be satisfied by a number of different impurities but the most likely candidate normally present in magnesium alloys is Fe. The "fine structure" discussed in reference (6) and referred to by the authors has been positively identified as FeAl since the publication by Heidenreich, McNulty and Gerould. The presence of this compound can be controlled by alloying or by heat treatment. By these means we have been able to vary stress-corrosion sensitivity in a way to show that FeAl can be responsible for stress-corrosion failure. However, as suggested by the authors, FeAl is not the only possible cathode capable of causing stress-corrosion cracking. Even sublimed magnesium with a purity of 99.99+% will stress corrode in 3% NaCl.

It seems clear that the role of stress must be that of providing, by plastic flow and film rupture, the freshly exposed, highly anodic surfaces needed to accelerate local galvanic action and thereby giving the rapid failures so characteristic of stress corrosion. Chemical or mechanical damage to the film on magnesium surfaces has been shown, both at Dow and elsewhere, to shift the potential toward decidedly more anodic values, the ultimate, theoretical value being about 2.4 volts anodic to calomel as compared to the 1.6 $\pm$ 0.1 volts ordinarily measured on filmed surfaces. Thus the freshly exposed surface becomes markedly more anodic, not only to previously cathodic impurities but to the undamaged, film-bearing magnesium surface itself. The attendant increase in local corrosion cell voltage combined with the highly localized film damage at the crack apex would then result in very high anode current densities and correspondingly high rates of penetration at the anodic sites. Evidence of some such process is seen in the almost explosive expulsion of hydrogen from the deepening crack and the tendency for the potential of stressed samples to attain more anodic values during the cracking process.

We suggest that the path of stress-corrosion cracks is at least as dependent upon the deformation mechanism as upon the location of cathodes. It is the plastic flow of the metal which exposes fresh, unfilmed magnesium upon which current from nearby cathodes can concentrate. When this exposure is quite small, as at a slip-line jog, the current density will be very large and rapid penetration along the slip line is reasonable. Slip in polycrystalline magnesium strained at room temperature has been observed both on the (0001) plane and on nonbasal planes. It seems likely that both basal and nonbasal slip will occur in J-1 alloy. Thus it would be expected that transgranular stress-corrosion cracks would be primarily parallel to the basal plane with an occasional branching in some other direction. This is what is observed, both at the Dow Chemical Laboratories and in many of the authors' pictures. The branching is particularly characteristic of stress corrosion. In addition to intracrystalline slip, polycrystalline magnesium deforms by viscous flow at the grain boundaries. This latter type of deformation is encouraged by decrease in grain size, increase in time at stress, and increase in temperature. Thus the large-grained sample of the authors may always fail transgranularly because almost all deformation is within the grains. Furnace cooling of J-1 alloy does several things: It precipitates $Mg_{17}Al_{12}$ at the grain boundaries thus forming a locus of cathodes at grain boundaries; it precipitates discontinuously and therefore forms a number of new grain boundaries; it tends to dissolve FeAl and thus

removes much of this compound as a separate phase. Intergranular cracking can then be due to a combination of localization of cathodes at the grain boundaries and the encouragement of a greater amount of grain boundary deformation.

We have observed that FS-1a (Mg+3%Al+1%Zn+0.2%Mn) fails by transgranular cracking in 3% NaCl and by intercrystalline cracking in air. The time to failure is much longer in air and therefore grain boundary deformation is encouraged.

Written Discussion: By M. Metzger, research assistant professor of physical metallurgy, University of Illinois, Urbana, Ill.

Of the observations made in the course of this valuable work, those of principal interest to the writer are the ones which suggest that the influence of the mechanical factors in the transgranular failure of this alloy is greater than has been generally recognized. For one thing, the instantaneous rate of advance of the crack is at times so rapid that the propagation of the crack during these periods must be attributed almost entirely to stress, as has been pointed out by Harwood.[2] Thus, the authors' observation that the crack tends to follow the basal plane would direct attention to the significance of the basal plane as regards deformation and fracture as well as to its significance with regard to the potential corrosion paths, i.e., the alignment of the FeAl platelets discussed by the authors. It may also be noted that the wave of plastic deformation ahead of an advancing transgranular crack will not only affect electrochemical action through rupturing of the surface film, as indicated by the authors, but will also alter the condition of the material ahead of the crack tip and may therefore affect the ability of the crack to be propagated through this material by the applied stress or the ability of another crack to be formed in this region.

Additional evidence of the importance of deformation has been noted in a brief survey made by F. Meller and the writer of the path of failure in single crystals of this alloy exposed to dilute hydrofluoric acid under relatively low stresses (below 5000 psi). The path of failure was in every case related to the deformation pattern; however, the crystal plane involved was not in general the basal plane. It is important to note that our specimens were not comparable with those used by the authors since our crystals were larger so that there was less constraint on their plastic deformation. Perhaps the extent of the deformation of the grains in the specimen was a significant factor in the tendency noted by the authors for failure to be transgranular regardless of heat treatment when the grain size was made sufficiently large.

As to the role of corrosion, mention may be made of the recent proposal of Harwood[2] that the role of corrosion is to provide the initial crack and also to reactivate the crack whenever its propagation by the applied stress has been halted by a structural barrier. This proposal appears applicable under the conditions of the authors' experiments where, with the high stress level employed, it would not be unreasonable to assume that a sharp crack could be propagated between barriers by stress alone.

Written Discussion: By E. C. W. Perryman, Metallurgy Branch, Atomic Energy of Canada Limited, Chalk River, Ont., Canada.

The authors are to be congratulated on presenting some extremely interesting results. Although it seems very attractive to correlate the stress corrosion susceptibility with the presence of the FeAl compound, I think that much more work

[2] J. J. Harwood, *Symposium on Stress Corrosion Phenomena*, Boston, 1954. To be published by the Electrochemical Society.

needs to be done before this can be accepted. Although it is possible to obtain localized corrosion at the interface of a cathodic compound it seems rather unlikely that this could cause stress corrosion cracking. On the other hand such a localized corrosion may serve the purpose of forming a point where a stress concentration can build up and thus lead to stress corrosion cracking by film formation and break down. If the FeAl is acting in this respect localized corrosion in the absence of stress should be observed such as I observed in distilled water. Could the authors say whether they observed localized corrosion in the absence of stress and if so was it transcrystalline for water-quenched and intercrystalline for furnace-cooled material and did the type of localized corrosion change with the grain size as did the authors' stress corrosion results. The authors in their discussion suggest that the effect of stress is somewhat subordinate to that of electrochemical action. This does not seem to be true for the stress corrosion of magnesium base alloys in distilled water, for the localized corrosion in the absence of stress does not penetrate very far, at the most one or two grains. From this it is apparent that stress plays a very important part.

Authors' Reply

Dr. LaQue's question can be answered by stating that stress-corrosion occurred in the same fashion whether an external cathode was connected or not. That is, the initiation and propagation of the cracks appeared to be controlled primarily by local cell effects. Therefore, although corrosion current was measured by means of an external electrode, this did not represent all of the corrosion current and probably did not represent the more important corrosion current—that produced by local cell action.

The reason for the absence of hydrogen evolution during cathodic protection was that the current density was not sufficiently great to allow such evolution. From direct observation of the stress-corrosion process however, we have seen that the very high current density results in conditions favorable for hydrogen evolution.

In answer to Dr. Mears' question, we believe that cathodic grain centers may account for part of the total corrosion current but because of the slight difference in activity between the magnesium-aluminum solid solution and pure magnesium, depletion should not cause too much local cell effect. A mechanism which may be operative here is one proposed by Evans in which localized attack is explained in terms of local pH changes and film formation. With high local current density, hydrogen ions will accumulate and cause increased local attack and so stifle any tendency for film formation. Since the presence of a cathodic precipitate has been shown to influence the type of cracking it must be assumed that these cathodic precipitates play a decisive role in the cathodic reaction. This line of thought is borne out by the observation of local hydrogen evolution near the tip of the stress-corrosion crack.

The authors are grateful for the illuminating discussion by Dr. Busk. The complexity of the problem is indicated and the need for a better definition of the role of stress in the determination of cracking path is evident.

Those remarks concerning the high current density likely at crack tips are especially appropriate for explaining the authors' belief that corrosive attack plays the primary and continuous part in stress-corrosion. The function of stress, then is to contribute to the electrochemical reaction by causing tearing of film at the crack tip.

The authors' interpretation of the results obtained in this investigation have led them to state that electrochemical reactions play a primary and continuous role in the stress-corrosion of the J-1 alloy under the conditions described. This interpretation of results, of course, indicates that stress does not cause purely mechanical failure as Mr. Metzger and Mr. Harwood have postulated. It is the authors' belief that the role of stress is a secondary one in that it contributes to the electrochemical reaction by tearing films. It seems reasonable that plastic deformation caused by stress concentrations could take place along certain preferred crystallographic planes for large-grained material and at grain boundaries for small grain material but the precipitation of cathodic phases in locations which completely explain the type of cracking makes a very strong case for a primary role for electrolytic reaction.

As suggested in the discussion it does seem likely that the extent of the deformation of the grains in the specimen is a significant factor in the transgranular cracking of specimens larger than ASTM grain size 7 but the authors cannot comment on this since the investigation did not cover this particular aspect.

Mr. Metzger's comments and suggestions should prove of interest to future workers in the field of stress-corrosion.

With regard to the discussion contributed by E. C. W. Perryman, the linking of the presence of the FeAl compound with a propensity for transgranular stress-corrosion has been borne out by investigations at the Dow Chemical Company[3, 4] as well as in the work under discussion. This interdependence now seems fairly well established. It is possible, even likely, that film breakdown caused by plastic deformation at the crack tip contributes significantly to the total electrochemical reaction. It is the authors' opinion that the FeAl precipitate also contributes significantly since the crack direction apparently is determined by its location.

Stress was assigned a subordinate role because it only contributes to the overall electrochemical mechanism by causing film breakage and consequent local cell action between large filmed areas and extremely small film-free areas at the crack tip. In order for stress to be assigned a primary role it would be necessary to show that strictly mechanical failure occurs as the major mechanism of stress-corrosion. The authors do not believe this to be true. This distinction of mechanism is arbitrary and statements concerning the relative importance of stress or electrochemical reaction should be examined with reference to this distinction.

Observations of localized corrosion in the absence of stress were not made in this investigation but it is interesting to note the corrosion of magnesium castings has been reported by Beck[5] as occurring on the basal plane.

---

[3] R. D. Heidenreich, G. H. Gerould and R. E. McNulty, "Electron Metallographic Methods and Some Results for Magnesium Alloys," *Transactions,* American Institute of Mining and Metallurgical Engineers, Vol. 166, 1946, p. 15.

[4] Research Laboratory, Dow Chemical Company, Private Communication.

[5] A. Beck, *The Technology of Magnesium and Its Alloys,* London, F. A. Hughes and Co., Ltd., 1940, p. 275, 295.

THERMODYNAMICS OF BINARY INTERSTITIAL SOLID SOLUTIONS

By Rudolph Speiser, and J. W. Spretnak

Abstract

The thermodynamics of binary interstitial solid solutions is treated theoretically, taking into account strain energy and compound formation. It is shown that the interstitial solid solubility of the metalloids is less in body-centered cubic metals than in the close-packed metals, principally because of the greater strain energy in the former crystalline structures than the latter. As a consequence, the body-centered cubic crystalline phases are relatively less stable than the close-packed crystalline phases in binary alloys such as iron-carbon, iron-nitrogen, titanium-carbon, titanium-nitrogen, and titanium-oxygen. The directions of the solvus lines are explained by this concept.

Introduction

THE thermodynamics of binary substitutional solid solutions has been treated theoretically by a large number of investigators, whereas the thermodynamics of interstitial solid solutions has received relatively little attention (1).[1] Darken and Smith (2) have made a statistical mechanical treatment of the solid solubility of carbon in iron-carbon alloys and have calculated the activity of carbon in solid solution taking into account nearest neighbor interstitial interaction. Zener (3) has considered the thermodynamics of interstitial solid solutions in medium-alloy steels. However, the effect of strain energy and compound formation has not been explicitly considered in the thermodynamic formulation of interstitial solid solutions.

Treatment of Interstitial Solid Solutions

Equilibrium diagrams of the interstitial alloys usually exhibit the existence of one or more stable compounds in addition to a rather restricted solubility of the solute in the solvent. Compound formation between the first row nonmetallic elements and the transition metals is to be expected because of the complementary electronic structure of

[1]The figures appearing in parentheses pertain to the references appended to this paper.

This research is sponsored by the Aeronautical Research Laboratory, Wright Air Development Center, under Contract No. AF18(600)-94.

A paper presented before the Thirty-sixth Annual Convention of the Society, held in Chicago, November 1 to 5, 1954. The authors, Rudolph Speiser and J. W. Spretnak, are associate professors, Department of Metallurgy, The Ohio State University, Columbus, Ohio. Manuscript received April 6, 1954.

these elements and because of the large differences in the electronegativity in some instances. It seems best to formulate the free energy functions of the solid solution and of the compound using the conventional thermodynamic standard states for the pure components (but always with reference to one gram-atom of pure component, so that in the case of a diatomic gas like oxygen one would take one-half of the usual value for one gram-mole of oxygen gas in its standard state). Then one approximate free energy function can be devised for the interstitial solid solution and another function for the compound with which it is in equilibrium. (A single free energy function effectively describing the state of the system over the whole composition range is not feasible, since the crystal structure and the bond type are in general not the same for the solid solution and the compound. It is possible for example to consider a hypothetical or supersaturated interstitial solid solution of the same composition as the compound, but differing in structure. Of course, solutions showing some degree of supersaturation may actually be observed, and represent metastable systems.) The process of alloy formation can be represented by expressions of the type

$$\begin{aligned} &C\ (\text{graphite}) = C\ (g) \\ &C\ (g) + M\ (s) = M\ (\text{C in solid solution}) \\ &aM(s) + bC(g) = M_aC_b(s) \end{aligned} \qquad \text{Equation 1}$$

for a solute which is solid in its standard state, and

$$\begin{aligned} &O_2(g) = 2O(g) \\ &O\ (g) + M(s) = M(\text{O in solid solution}) \\ &aM(s) + \tfrac{1}{2}\, bO_2(g) = M_aO_b(s) \end{aligned} \qquad \text{Equation 2}$$

for a solute which is gaseous in its standard state.

The energetics of the formation of an interstitial solid solution can be represented diagrammatically by the energy level diagrams in Fig. 1. That is, in the case of the interstitial solid solution of elements such as boron or carbon, it may be considered that the solute is first sublimed to an ideal monatomic vapor (with the atoms in a definite electronic state) which requires the absorption of energy equivalent to the heat of sublimation; the atoms of the vapor are then dissolved in the interstices of the metallic crystal. However, in this second step it is useful conceptually to distinguish between the interaction energy, ΔH_{int}, of the solute atom with the metal atoms due to forces of an essentially chemical or electrical nature (bonding, polarization, etc.), and the elastic strain energy, ΔH_{strain}, stored in the crystal as a result of the deformation of the lattice by the solute atoms, since the latter can be treated, at least approximately, by the methods of elastic theory. *The algebraic sum of these terms is the overall heat of solution.* In the case of solutes such as O_2 or N_2, the heat of dissociation is the proper quantity to be used rather than the heat of sublimation. The enthalpy of the system consisting of 1 g-atom of metallic crystal (N atoms,

where N is Avogadro's number), and n_2 g-atoms of solute ($N_2 = Nn_2$ atoms), may then be written as

$$H^{sol} = H_1^\circ + n_2 H_2^\circ + n_2 (\Delta H_D^\circ + \Delta H_{int.}^\circ + \Delta H_{strain}^\circ) \qquad \text{Equation 3}$$

where H_1° and H_2° are the molal enthalpies of the pure metal and pure solute in their standard states, the ΔH°'s are molal values and ΔH_D° is the heat of sublimation or dissociation. It is assumed that the solution is sufficiently dilute so that the heats of solution at infinite dilution can be used; i.e., the contributions of the solute atoms are additive. Other-

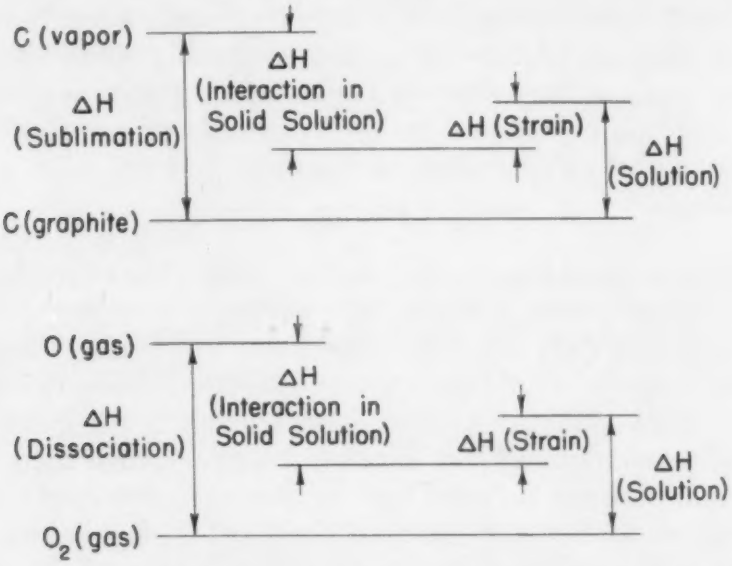


Fig. 1—Models for the Energetics of Formation of Interstitial Solid Solutions.

wise it would be necessary to introduce partial molal heat contents, which are ordinarily not known for solutions in metals, and in any case probably do not differ significantly from the values at infinite dilution, for the small solubilities considered.

In order to obtain the free energy, the entropy of the solid solution is also required. The treatment of the entropy is based on the assumption, consistent with the third law of thermodynamics, that at the absolute zero of temperature the entropy of the solid solution would be simply the *configurational entropy* associated with the disordered arrangement of the solute atoms in the lattice, which we write as S^{conf}. At temperatures above 0 °K the crystal will possess vibrational entropy associated with the vibrational modes of the crystal, and possibly additional entropy associated with degenerate or excited electronic states. If, as will usually be true, the pure solvent crystal obeys the third law, and has zero entropy at 0 °K, then its standard entropy (per mole), S_1°, at a given temperature, representing the vibrational (and elec-

tronic) entropy of the pure crystal, may be taken as a first approximation to be the entropy possessed by the solid solution over and above the configurational entropy. In this approximation, then, the entropy of the solid solution (containing one mole of solvent) would be $S_1^\circ + S^{conf}$. In a higher approximation one should include: (a) a correction for the effect of the solute atoms on the vibrational (and possibly electronic) entropy of the crystal; (b) the direct contribution, if any, of the solute atoms to the entropy. The addition of solute atoms increases the number of vibrational modes of the crystal, and at the same time alters the masses and force constants (the latter effect is related to the strains produced by the solute atoms), so that the effect (a) may be of some significance. Under (b) would be included entropy associated with degenerate or excited electronic states of the solute atoms (or ions) *as they exist in the solution.* The sum of corrections (a) and (b) will be denoted by S_2^* (per mole of solute atoms). The total entropy of the dilute solid solution will then be

$$S^{sol} = S_1^\circ + n_2 S_2^* + S^{conf} \qquad \text{Equation 4}$$

If the solute is crystalline in its standard state (for example, carbon), then the standard state entropy, S_2°, probably provides a reasonable approximation to S_2^*, since S_2° represents vibrational (and possibly electronic) entropy of the pure solute crystal. However, if the solute is gaseous in its standard state, and particularly if the gas is diatomic and the solute monatomic (for example, oxygen), then there should be little relation between S_2° and S_2^*. In this case one might take as an approximation to S_2^* the standard entropy of the dissociated monatomic gas, which can be written $S_2^\circ + \Delta S_D^\circ$, where ΔS_D° is the standard entropy of dissociation. The translational entropy of the monatomic gas would then serve as a rough correction to the vibrational entropy of the crystal (half the equipartition value for the added degrees of vibrational freedom). Whether the electronic entropy, if any, of the monatomic gas should be carried over into the crystal depends on the strength of interaction of the solute atoms with the lattice atoms. The formation of chemical bonds would, in general, completely alter the nature of the electronic levels, and even without bond formation the crystalline electric field could split degenerate levels and shift their energies appreciably.

The configurational entropy of the solid solution will now be calculated by a method which is approximate, but is certainly preferable to the use of the usual ideal entropy of mixing for two components.[2] The number of interstitial holes per metal atom will be noted by θ ($\theta = 1$ for the, Octahedral, O_h, holes in a face-centered cubic or close-packed hexagonal lattice, and $\theta = 3$ for the tetragonal, D_{4h}, holes,

[2] See Darken and Smith (2) for a statistical mechanical treatment of the entropy of mixing in γ — Fe.

and 6 for the ($\frac{1}{2}\frac{1}{4}0$), S_{4v}, holes, in a body-centered cubic lattice). If N is the number of solvent atoms, then the number of interstitial holes is θ N. It is assumed that a solute atom occupying a hole excludes the occupation of z′ neighboring interstitial holes by other solute atoms (because of the distortion of the sites adjacent to an occupied site). According to this model, the maximum number of solute atoms which the crystal can accommodate will be $N_2(\max) = (\theta N/z)$. Where $z = z' + 1$ in actual cases it is expected that the solution will become saturated with respect to compound formation long before this "maximum" concentration is reached. However, the exclusion of neighboring sites by occupancy of a given hole does affect the configurational entropy, and therefore, the solubility. Thus, the number of configurations, or thermodynamic probability, is

$$W = \frac{\theta N(\theta N - z)(\theta N - 2z) \ldots . (\theta N - \{Nz - 1\}z)}{N_2!}$$

$$= \frac{z^{N_2}\left(\frac{\theta N}{z}\right)!}{N_2!\left(\frac{\theta N}{z} - N_2\right)!} \qquad \text{Equation 5}$$

where N is the number of solvent atoms assumed equal to Avogadro's number, and N_2 is the number of solute atoms. If z is set equal to unity, then the equation for the number of configurations, W, is similar to one previously derived by Zener (3). The configurational entropy of the system of N metal atoms and N_2 solute atoms is then

$$S^{\text{Conf.}} = k \ln W$$

$$= R\left\{\frac{N_2}{N}\ln z + \frac{\theta}{z}\ln\frac{\theta}{z} - \frac{N_2}{N}\ln\frac{N_2}{N} - \left(\frac{\theta}{z} - \frac{N_2}{N}\right)\ln\left(\frac{\theta}{z} - \frac{N_2}{N}\right)\right\}$$

$$= -R\left\{x'_2 \ln\frac{x'_2}{z} + \left(\frac{\theta}{z} - x'_2\right)\ln\left(\frac{\theta}{z} - x'_2\right) - \frac{\theta}{z}\ln\frac{\theta}{z}\right\} \qquad \text{Equation 6}$$

where k is Boltzmann's constant, R the molal constant ($= Nk$), and $x_2' = \frac{N_2}{N}$ is the ratio of solute atoms to metal atoms in the alloy (not the mole fraction, which will be designated by x_2). It will be noted that the right-hand side of Equation 6 becomes meaningless if x_2' exceeds θ/z, which corresponds to the "maximum" concentration previously referred to.

From Equation 6

$$S^{\text{Conf}} = 0, \text{ at } x'_2 = 0$$

and

$$S^{\text{Conf}} = R\left\{\frac{\theta}{z}\ln z\right\}, \text{ at } x'_2 = \frac{\theta}{z} \qquad \text{Equation 7}$$

The maximum configurational entropy is obtained at $x'_2 = \theta/(1+z)$, and is

$$S^{\text{Conf}}_{\max} = R\left\{\frac{\theta}{z}\ln(1+z)\right. \qquad \text{Equation 8}$$

Differentiation of Equation 6 shows that the derivative of the configu-

rational entropy with respect to x_2' is $+\infty$ at $x_2' = 0$, and $-\infty$ at $x_2' = \theta/z$. The infinite slope of the configurational entropy curve at $x_2' = 0$ is in accord with the thermodynamic requirement that the partial molal free energy, or chemical potential, approach $-\infty$ at zero concentration. However, little physical significance can be attached to the detailed form of the entropy curve in the neighborhood of $x_2 = \theta/z$, in view of the crudeness of our model. For $z = 1$, the occupation of sites adjacent to an occupied site is not restricted in any way, and Equation 6 reduces to

$$S^{Conf} = -R\{x'_2 \ln x'_2 + (\theta - x'_2)\ln(\theta - x'_2) - \theta \ln \theta\} \qquad \text{Equation 9}$$

This is equivalent to the ideal entropy of mixing of N_2 occupied holes and $(\theta N - N_2)$ vacant holes, which is

$$\begin{aligned} S^{Conf}_{ideal} &= -k\left\{N_2 \ln \frac{N_2}{\theta N} + (\theta N - N_2)\ln\left(\frac{\theta N - N_2}{\theta N}\right)\right\} \\ &= -R\left\{x'_2 \ln \frac{x'_2}{\theta} + (\theta - x'_2)\ln\left(\frac{\theta - x'_2}{\theta}\right)\right\} \\ &= -R\{x'_2 \ln x'_2 + (\theta - x'_2)\ln(\theta - x'_2) - \theta \ln \theta\} \end{aligned} \qquad \text{Equation 10}$$

For $\theta = 1$, as it is in the face-centered cubic lattice,

$$S^{Conf}_{ideal} = -R\{x'_2 \ln x'_2 + (1 - x'_2)\ln(1 - x'_2)\} \qquad \text{Equation 11}$$

The entropy function of Equation 6 is asymmetrical with respect to $x_2' = \frac{1}{2}$ for all values of $z > 1$, whereas the function described by Equation 11 is symmetrical. The magnitude of z will depend principally upon the ratio of the solute atom diameter to the diameter of the interstitial hole (and to a small degree upon the repulsive force between solute atoms): the larger the size ratio, the larger the value of z and consequently the greater the asymmetry of the entropy function. In Fig. 2, the entropy is plotted as a function of x_2' for several values of z and $\theta = 1$. The curve for $z = 1$ extends to $x_2' = \frac{1}{2}$, the other curves to $x_2' = \theta/z$.

The free energy of the interstitial solid solution is defined as

$$F^{sol} = H^{sol} - TS^{sol} \qquad \text{Equation 12}$$

Combining Equations 3, 4, 6 and 12 yields

$$\begin{aligned} F^{sol} &= H_1^\circ + n_2 H_2^\circ + n_2(\Delta H_D^\circ + \Delta H^\circ_{int} + \Delta H^\circ_{strain}) \\ &+ RT\left\{x'_2 \ln\left(\frac{x'_2}{z}\right) + \left(\frac{\theta}{z} - x'_2\right)\ln\left(\frac{\theta}{z} - x'_2\right) - \frac{\theta}{z}\ln\frac{\theta}{z}\right\} \\ &- TS_1^\circ - n_2 TS_2^* \end{aligned} \qquad \text{Equation 13}$$

In order to apply a well-known graphical method (4) for the study of solubilities and other phase equilibria, it is convenient to deal with the free energy of the system per mole of total components. We therefore divide both sides of Equation 13 by $n = n_1 + n_2 = 1 + n_2$, noting that $1/n$ is the mole fraction, x_1, of the solvent, and n_2/n is the mole frac-

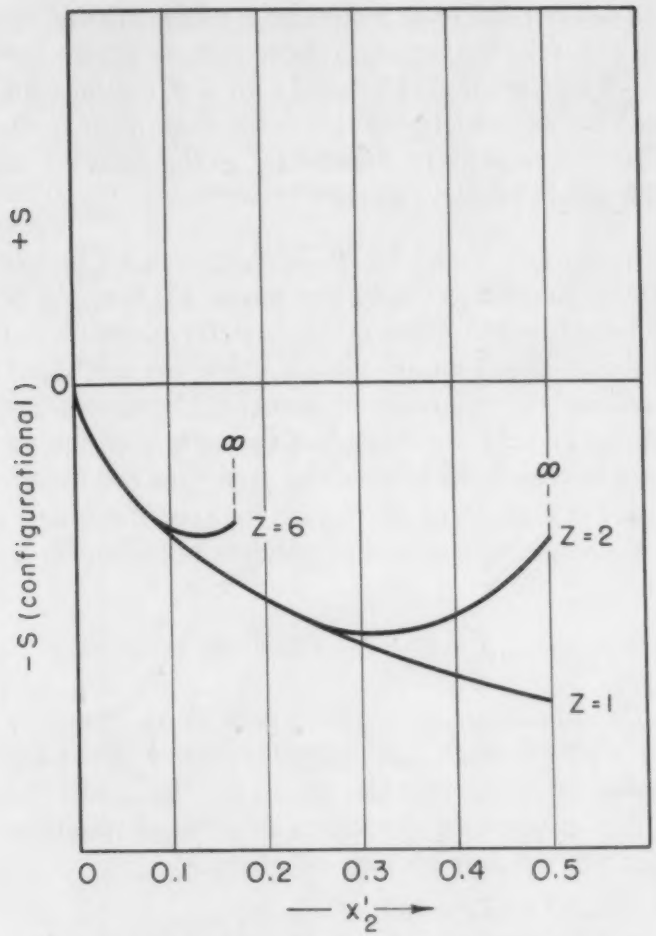


Fig. 2—Configurational Entropy as a Function of the Parameter z Representing the Exclusion of Nearest Neighbor Interstitial Holes to Solute Atoms.

tion, x_2, of the solute. The factor $1/n$ multiplying the configurational entropy term is conveniently expressed as $1/(1+x_2')$. Then

$$F^{sol}/_n = x_1F_1^\circ + x_2F_2^* + x_2(\Delta H_D^\circ + \Delta H^\circ_{int} + \Delta H^\circ_{strain}) + \frac{RT}{1+x'_2}\left\{x'_2 \ln \frac{x'_2}{z} + \left(\frac{\theta}{z} - x'_2\right)\ln\left(\frac{\theta}{z} - x'_2\right) - \frac{\theta}{z}\ln\frac{\theta}{z}\right\} \qquad \text{Equation 14}$$

where $F_1^\circ = H_1^\circ - TS^\circ$ is the standard free energy of the pure solvent crystal, and $F_2^* = H_2^{\circ *} - TS_2^*$ is a hybrid free energy for the solute having no simple interpretation. For the method referred to, $F^{sol}/_n$ is best regarded * as a function of the concentration variable x_2,

* It should be noted that the third term in Equation 14 (the heat of solution) is a linear function of the composition rather than the usual quadratic function used for regular solutions. That is, the coefficient of this term is x_2, rather than $x_1x_2 = x_2 - x_2^2$. This is justified for the dilute solutions with which we are concerned. For more concentrated solutions an x_2^2 term should be added, but there exists as yet no data for the determination of the coefficient of this term. The form x_1x_2 assumes that the coefficient of x_2^2 is the negative of the coefficient of x_2, and would seem to have little justification for *interstitial* solid solutions. For *substitutional* solid solutions, with miscibility over the entire range $0 \leq x_2 \leq 1$ the form x_1x_2 is convenient since it vanishes at $x_2 = 0$ and at $x_2 = 1$, where the enthalpy reduces to the standard state enthalpies H_1° and H_2°, respectively. However, for an interstitial solid solution, $x_2 = 1$ corresponds, in general, to a completely hypothetical lattice of solute atoms, with an enthalpy having no relation to the standard state enthalpy H_2°, and there is therefore no basis for the form x_1x_2.

although it is convenient to express the configurational entropy term in terms of x_2'. The relation between these two variables is $x_2' = x_2/x_1 = x_2/(1-x_2)$. The factor $1/(1+x_2')$ in the configurational entropy term increases the asymmetry of this term somewhat further.

It will be convenient to denote by β the heat of solution terms other than the strain energy, so that

$$\beta = \Delta H_D^\circ + \Delta H^\circ_{int} \qquad \text{Equation 15}$$

ΔH_D° is usually known, so that the value of β could be obtained if ΔH°_{int} could be estimated. Conversely, a determination of β (for example from solubility data) would yield a value for ΔH°_{int}. The strain energy can be estimated by a method described by Lawson (5), Prescott (6), and Frenkel (7). If one considers the solid solution as a continuous elastic medium in which the interstitial positions are holes of radius R_o, then ΔH°_{strain} (per mole of solute atoms) is the work necessary to force N (N = Avogadro's number) spheres of radius R_1 into N of these holes. Then

$$\Delta H^\circ_{strain} = \tfrac{2}{3}\frac{\Delta V^2}{V_0} GN = 8\pi R_0 (R_1 - R_0)^2 GN \qquad \text{Equation 16}$$

where G is the modulus of rigidity and it is assumed that $\Delta V = 4\pi R_o^2 \Delta R$ and $V_o = \tfrac{4}{3}\pi R_o^3$. This work is stored in the lattice as strain energy. It should be noted that the strain energy is always positive and therefore causes a positive deviation from ideal solution laws. Substituting Equations 15 and 16 into 14 gives

$$F^{sol}_{/n} = x_1 F_1^\circ + x_2 F_2^* + x_2(\beta + \Delta H^\circ_{strain}) + \frac{RT}{1+x_2'}\left\{x_2' \ln \frac{x_2'}{z} + \left(\frac{\theta}{z} - x_2'\right)\ln\left(\frac{\theta}{z} - x_2'\right) - \frac{\theta}{z}\ln\frac{\theta}{z}\right\} \qquad \text{Equation 17}$$

In the treatment of solubility it is convenient to deal with the free energy of formation of a mole of solution from the components (elements) in their standard states (at the same temperature), or

$$\Delta F_f^{sol} = \frac{F^{sol}}{n} - x_1 F_1^\circ - x_2 F_2^\circ \qquad \text{Equation 18}$$

Equations 17 and 18, together with the relation $F_2^* - F_2^\circ = -T(S_2^* - S_2^\circ)$, yield

$$\Delta F_f^{sol} = x_2(\beta + \Delta H_{strain}) - x_2 T(S_2^* - S_2^\circ) + \frac{RT}{1+x_2'}\left\{x_2' \ln \frac{x_2'}{z} + \left(\frac{\theta}{z} - x_2'\right)\ln\left(\frac{\theta}{z} - x_2'\right) - \frac{\theta}{z}\ln\frac{\theta}{z}\right\} \qquad \text{Equation 19}$$

The nature of the entropy term $S_2^* - S^{2\circ}$ has been discussed in some detail previously. This term is likely to be considerably less important in determining solubility than the others, but it can be estimated if necessary.

An illustrative plot of ΔF_f^{sol} versus x_2 is shown in Fig. 3, where

the heat and configurational entropy terms, and their sum are shown separately. As is well known, (4) a tangent to the $\Delta\overline{F}_f^{sol}$ versus x_2 curve has intercepts at $x_2=0$ and $x_2=1$ of $F_1^{sol}-F_1^\circ$ and $\overline{F}_2^{sol}-F_2^\circ$, respectively, where the partial molal free energies, $\overline{F}_1^{sol}$ and $\overline{F}_2^{sol}$, refer to the composition, or value of x_2, at the *point of tangency*.

Now suppose that the solution is in equilibrium with a solid compound formed from the same components. The free energy of for-

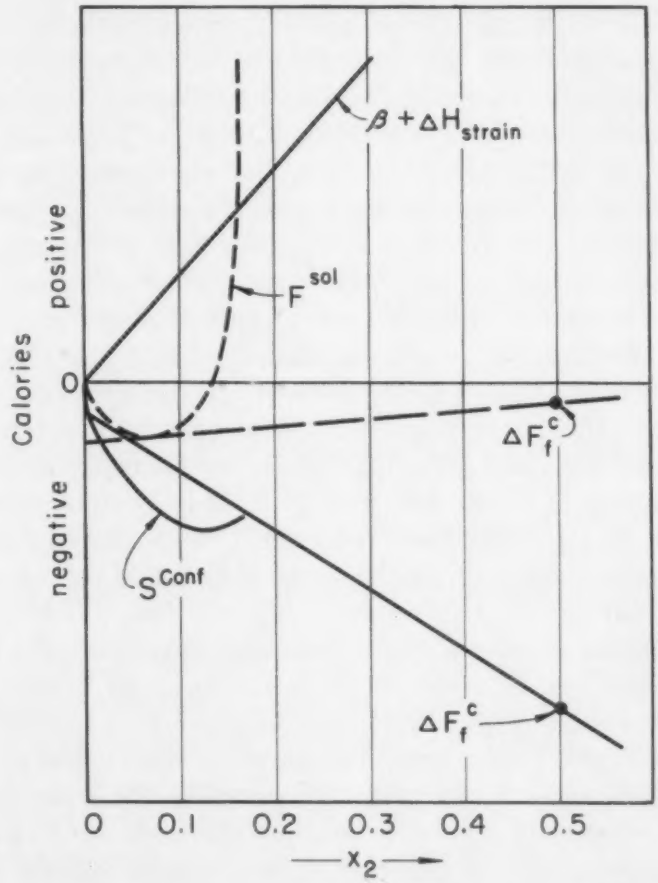


Fig. 3—Free Energy and Separate Contributions to the Free Energy Plotted as a Function of Solute Composition.

Note Different Point of Tangency of the Dashed Line Depiciting the Case of a Less Stable Compound.

mation (per mole) of the compound, ΔF_f^c, which can usually be determined by thermodynamic measurements, may be thought of as a point on the ΔF_f versus x_2 plot at the value of x_2 corresponding to the stoichiometric composition of the compound. More accurately, however, the compound can deviate from the stoichiometric composition to a lesser or greater extent, and ΔF_f^c should therefore be represented by a curve having, in most cases, an extremely sharp minimum at the

stoichiometric composition.* A tangent to this curve will have intercepts $\overline{F}_1^c - F_1^\circ$ and $\overline{F}_2^c - F_2^\circ$, where $\overline{F}_1^c$ and $\overline{F}_2^c$ are the partial molal free energies in the compound. This conclusion is thermodynamically exact, regardless of whether the form of the curve is known. The compositions at which the solution and compound are in equilibrium, and therefore the solubility of the *solute* (not the compound) in the solid solution *in the presence of the solid compound,* is obtained by drawing a common tangent to the ΔF_f curves for the solution and compound. For, since this tangent is common to both curves, its intercept at $x_2 = 0$ is equal to $\overline{F}_1^{sol} - F_1^\circ$ at x_2^{sat}, and also to $\overline{F}_1^c - F_1^\circ$ at x_2^c (essentially). Therefore $\overline{F}_1^{sol}(\text{at } x_2^{sat}) = \overline{F}_1^c(\text{at } x_2^c)$. Here x_2^{sat} represents the composition of the saturated solution, and x_2^c the stoichiometric composition of the compound. Similarly, from the intercept at $x_2 = 1$, $\overline{F}_2^{sol}(\text{at } x_2^{sat}) = \overline{F}_2^c(\text{at } x_2^c)$. But these are just the thermodynamic conditions of equilibrium for the two phase system.

As a result of the extreme sharpness of the minimum in the ΔF_f^c curve, one may assume for practical purposes that the point of tangency on this curve coincides with the point representing the stoichiometric compound (abscissa, x_2^c; ordinate, ΔF_f^c). The determination of the solubility (4) then reduces to the problem of constructing a line which passes through the latter point and is tangent to the free energy of formation curve for the solution, as given, for example, by Equation 19. This construction is illustrated in Fig. 3. It is evident from this construction that the greater the free energy of formation of the compound, the steeper the slope of the tangent line, and therefore the lower will be the solubility of the solute in the solvent. Thus the existence of a compound in an equilibrium diagram usually implies a low solid solubility. If the deformation in the lattice is large, the strain energy is large, and z is also large. The effect of these two factors is to move the minimum of the free energy function for interstitial solid solution toward the composition, $x_2 = 0$, thus moving the point of tangency toward still lower solid solubility limits. Although the strain energy is a linear function of the composition at low concentrations, it must rise very rapidly as $x_2' \longrightarrow \theta/z$ or $z_2 \longrightarrow \dfrac{\theta}{\theta + z}$; this is in conformity with the model used for calculating the configurational entropy.

An approximate analytical expression for the interstitial solid solubility limit is readily obtained from the construction just described, and illustrated in Fig. 3. The intercepts of the tangent line are $\overline{F}_1^{sol} - F_1^\circ$, at $x_2 = 0$ and $\overline{F}_2^{sol} - F_2^\circ$, at $x_2 = 1$. The geometry of

---

* It is likely that the half-width of this curve varies inversely as ΔF_f^c, so that it might be represented qualitatively by an error function of the form

$$\Delta F_f^c \exp\left[-\left(x_2 - x_2^c\right)^2 (\Delta F_f^c/RT)^2\right]$$

where x_2^c is the stoichiometric composition. As ΔF_f^c increases without limit this becomes a "delta" function.

similar triangles yields the proportion

$$\frac{(\overline{F}_2^{sol}-F_2^\circ)-(\overline{F}_1^{sol}-F_1^\circ)}{1}=\frac{\Delta F_f^e-(\overline{F}_1^{sol}-F_1^\circ)}{x_2^e} \qquad \text{Equation 20}$$

If the assumption is made that $\overline{F}_1^{sol} \approx F_1^\circ$, which is a good assumption for dilute solutions,

$$\overline{F}_2^{sol} \approx F_2^\circ + \frac{\Delta F_f^e}{x_2^e} \qquad \text{Equation 21}$$

F_2^{sol} may be obtained by differentiating Equation 17. However, it is first necessary to multiply Equation 17 by $n(=n_1+n_2)$ to obtain F^{sol}, the total free energy, and also to express x_2 and x_2' explicitly in terms of n_1 and n_2. One then obtains

$$\overline{F}_2^{sol}=\left(\frac{\partial F^{sol}}{\partial n_2}\right)_{n_1}=F_2^*+\beta+\Delta H^\circ_{strain} + RT\left\{\ln\frac{x_2'}{z}-\ln\left(\frac{\theta}{z}-x_2'\right)\right\} \qquad \text{Equation 22}$$

Equations 21 and 22, and the relation $F_2^* - F_2^\circ = -T(S_2^* - S_2^\circ)$, now yield

$$\beta+\Delta H^\circ_{strain}-T(S_2^*-S_2^\circ)+RT\left\{\ln\frac{x_2'}{z}-\ln\left(\frac{\theta}{z}-x_2'\right)\right\}=\frac{\Delta F_f^e}{x_2^e} \qquad \text{Equation 23}$$

Dividing both sides of Equation 23 by RT and solving for x_2'

$$x_2'=\frac{\theta\exp\left\{\frac{1}{RT}\left(\frac{\Delta F_f^e}{x_2^e}-\beta-\Delta H^\circ_{strain}\right)\right\}\exp\left(\frac{S_2^*-S_2^\circ}{R}\right)}{1+z\exp\left\{\frac{1}{RT}\left(\frac{\Delta F_f^e}{x_2^e}-\beta-\Delta H^\circ_{strain}\right)\right\}\exp\left(\frac{S_2^*-S_2^\circ}{R}\right)} \qquad \text{Equation 24}$$

But remembering that $x_2' = \frac{x_2}{1-x_2}$, one obtains

$$x_2=\frac{\theta\exp(-K/RT)\exp\left(\frac{S_2^*-S_2^\circ}{R}\right)}{1+(\theta+z)\exp(-K/RT)\exp\left(\frac{S_2^*-S_2^\circ}{R}\right)} \qquad \text{Equation 25}$$

where $K=(\beta+\Delta H^\circ_{strain}-\frac{\Delta\overline{F}_f^e}{x_2^e})$. K is usually a rather large positive number, in interstitial alloys, so that

$$x_2 \approx \theta\exp(-K/RT)\exp\left(\frac{S_2^*-S_2^\circ}{R}\right) \qquad \text{Equation 26}$$

If the first approximation to x_2, given by Equation (26), is denoted

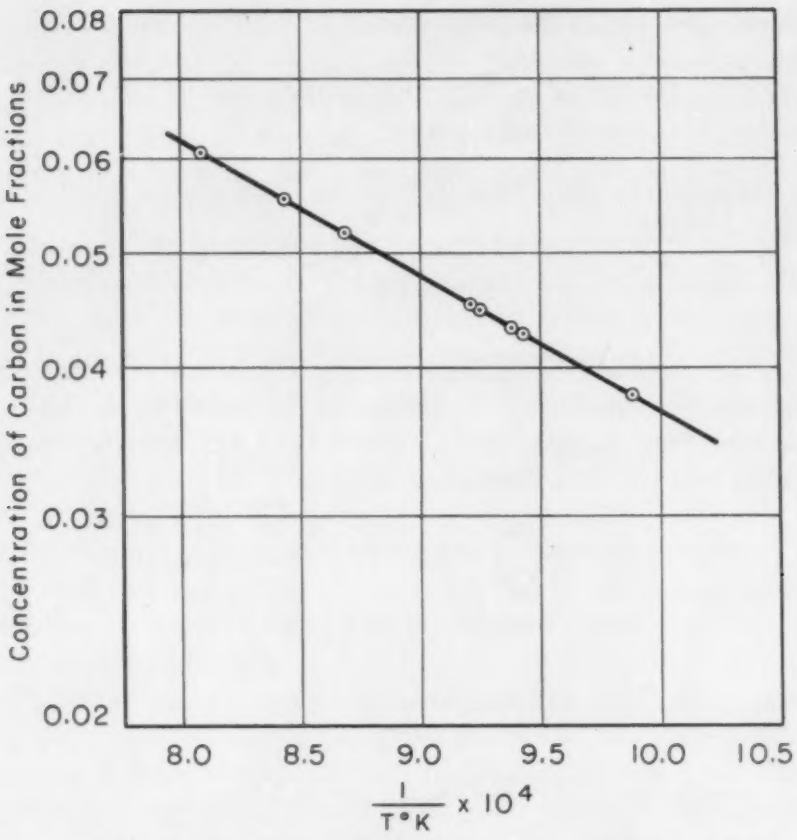


Fig. 4—Solubility of Cementite in Gamma Iron Plotted as a Function of the Reciprocal of the Absolute Temperature.
Data from R. F. Mehl and C. Wells: Constitution of High Purity Iron-Carbon Alloys, Trans. AIME (1937), *125*, 429.

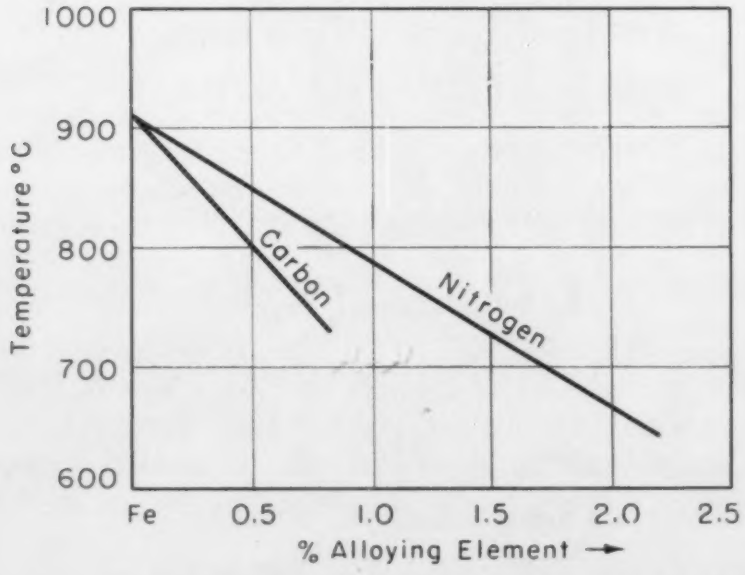


Fig. 5—Effect of Carbon and Nitrogen on the Gamma-Alpha Transformation Temperature in Iron.
Data from Metals Handbook (1948), American Society of Metals, Cleveland, Ohio.

by $x_2^{(1)}$, Equation (25) may be written

$$x_2 = \frac{x_2^{(1)}}{1+\left(1+\frac{z}{\theta}\right)x_2^{(1)}} \approx x_2^{(1)}\left[1-\left(1+\frac{z}{\theta}\right)x^{(1)}{}_2\right]$$

$$= x^{(1)}{}_2 - \left(1+\frac{z}{\theta}\right)\left[x^{(1)}{}_2\right]^2$$

which shows the effect of z. Equation 27

Equation 26 is similar to the expression derived by Zener (3). ΔF_f^c is usually negative, although in the case of metastable interstitial compounds such as Fe_3C it is positive. β can be either positive or negative, and $\Delta H°_{strain}$ is always positive and has an order of magnitude of about 1 to 20 kcal. In most interstitial solid solutions, K/RT is a large enough positive number so that the solubility limit as given by Equations 25 or 26 is low. Furthermore, a plot of the ln x_2 vs. 1/T should yield a straight line if K/RT is large and positive (assuming that K does not change very rapidly with the temperature). This kind of functional dependence of the solubility upon the temperature is observed for many binary systems. For example, data (8) for the composition of austenite in equilibrium with cementite (Fig. 4) yield an excellent straight line as predicted and yield a K of -5.2 kcals and a value of $\theta \exp\left(\frac{S_2^* - S_2^\circ}{R}\right)$ of ≈ 0.2. In this case, θ is equal to unity so that $\exp\left(\frac{S_2^* - S_2^\circ}{R}\right) \approx 0.2$ and $(S_2^* - S_2^\circ) \approx 2.4$ cal/deg mole.

This treatment can be easily extended to the case of equilibrium between two crystalline phases at a given temperature, such as the equilibrium between the alpha and gamma phases in an Fe-C alloy. Utilization of Equation 25 or more approximately Equation 26, and omission of the entropy terms, lead to the expression

$$K = \frac{x_2^{I}}{x_2^{II}} \approx \frac{\theta^{I}}{\theta^{II}} \exp\left(\frac{-K^{I}+K^{II}}{RT}\right) \qquad \text{Equation 28}$$

Where superscripts I and II refer to the phases I and II in equilibrium, and K is the equilibrium constant for the reaction I $\rightleftarrows$ II.

If it is assumed that phases I and II differ only in crystal structure and that the chemical interactions between the solute and solvent are identical in the two phases, Equation 28 reduces to the approximate result

$$\frac{x_2^{I}}{x_2^{II}} \approx \frac{\theta^{I}}{\theta^{II}} \exp\left(\frac{-\Delta H^{I}_{strain} + \Delta H^{II}_{strain}}{RT}\right) \qquad \text{Equation 29}$$

That is, the ratio of the solubility of the solute element in the two phases at equilibrium at a given *temperature* is principally a function of the difference in the interstitial strain energy in the two crystalline phases.

Table I
Comparison of Solubility in Several Lattice Types

Solute	Solvent	Crystal structure	Solid solubility limit (weight per cent)
N	γ - Fe	f.c.c.	2.35 at 590 °C
N	α - Fe	b.c.c.	0.10 at 590 °C[a]
C	γ - Fe	f.c.c.	0.80 at 732 °C[b]
C	α - Fe	b.c.c.	0.02 at 732 °C[c]
C	α - Ti	h.c.p.	0.45 at 920 °C[d]
C	β - Ti	b.c.c.	0.07 at 920 °C[d]

[a] V. G. Paranjpe, M. Cohen, M. B. Bever and C. F. Floe, "The Iron-Nitrogen System," *Transactions*, American Institute of Mining and Metallurgical Engineers, Vol. 188, 1950, p. 261.
[b] C. J. Smithells, Metals Reference Book, Interscience Pub. Inc., N. Y. 1949.
[c] J. K. Stanley, "The Diffusion and Solubility of Carbon in Alpha-Iron," *Transactions*, American Institute of Mining and Metallurgical Engineers, Vol. 185, 1949, p. 752.
[d] R. I. Jaffee, H. R. Ogden and D. J. Maykuth, "Alloys of Titanium with Carbon, Oxygen and Nitrogen," *Transactions*, American Institute of Mining and Metallurgical Engineers, Vol. 188, 1950, p. 1261.

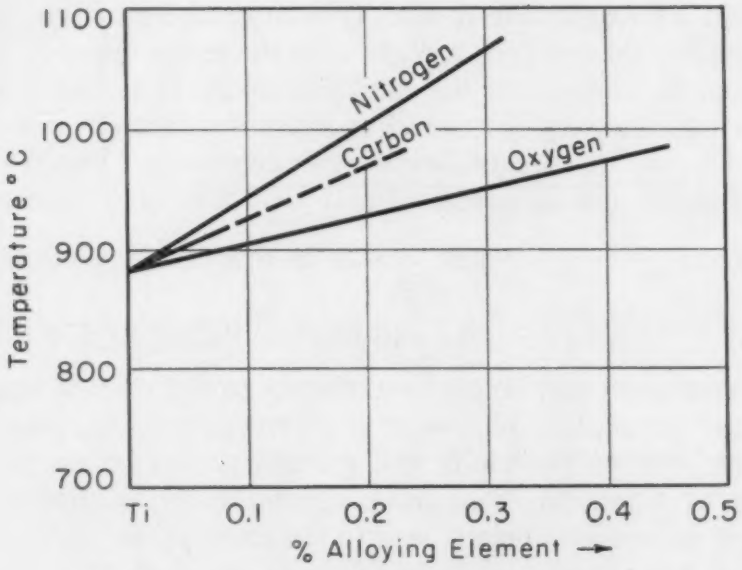


Fig. 6—Effect of Carbon, Oxygen and Nitrogen on the Beta to Alpha Transformation in Titanium.
Data from R. I. Jaffee, H. R. Ogden and D. J. Maykuth: Alloys of Titanium with Carbon, Oxygen and Nitrogen, Trans. AIME (1950), *188*, 1261.

It is evident that if $\Delta H^{I}_{strain} > \Delta H^{II}_{strain}$, then $\frac{x_2^{I}}{x_2^{II}} > \frac{\theta^{I}}{\theta^{II}}$ and the solvus line will have a negative slope, whereas if $\Delta H^{I}_{strain} < \Delta H^{II}_{strain}$, then $\frac{x_2^{I}}{x_2^{II}} < \frac{\theta^{I}}{\theta^{II}}$ and the solvus line will have a positive slope.

The former case is illustrated by Fe-C and Fe-N alloys (see Fig. 5). In these cases phase I is α-Fe and phase II is γ-Fe. The interstitial strain energy in (b.c.c.) α-Fe is considerably greater than the strain energy in interstitial (f.c.c.) γ-Fe*. The relative solubilities of C

* See bottom page 507.

and N in α-Fe and γ-Fe are given in Table I, and it can be seen that this expectation is borne out by experiment.

The latter case is illustrated in the case of Ti-C alloy (see Table I). The solubility of C in α-Ti (h.c.p.) and β-Ti (b.c.c.) can again be predicted from the relative strain energies in these two structures. The directions of the solvus lines for Ti-C, Ti-N and Ti-O alloys are depicted in Fig. 6. The strain energies could be estimated with the aid of Equation 16 if the modulus of rigidity at a given temperature were known.

The authors wish to acknowledge the invaluable aid of Dr. W. J. Taylor in writing this paper.

References

1. C. Wagner, *Thermodynamics of Alloys,* 1951, Addison-Wesley Press, Cambridge, Mass.; R. W. Gurney, *Introduction to Statistical Mechanics,* McGraw-Hill Book Co., Inc., New York.
2. R. P. Smith, "Equilibrium of Iron-Carbon Alloys with Mixtures of CO-CO_2 and CH_4-H_2," Journal, American Chemical Society, Vol. 68, 1946, p. 1163.
3. C. Zener, "Equilibrium Relations in Medium-Alloy Steels," *Transactions,* American Institute of Mining and Metallurgical Engineers, Vol. 167, 1946, p. 513.
4. L. S. Darken, "Application of Thermodynamics to Heterogeneous Equilibria," *Thermodynamics in Physical Metallurgy,* 1950, American Society for Metals, Cleveland; L. S. Darken and R. W. Gurry, *Physical Chemistry of Metals,* 1953, McGraw Hill Book Co., New York.
5. A. W. Lawson, "On Simple Binary Solutions," *Journal of Chemical Physics,* Vol. 15, 1947, p. 831.
6. J. Prescott, *Applied Elasticity,* Chapter XII, 1946, Dover Publishing Co., New York.
7. J. Frenkel, *Kinetic Theory of Liquids,* 1946, p. 11, Clarenden Press, Oxford, England.
8. C. Wells and R. F. Mehl, "Rate of Diffusion of Carbon in Austenite in Plain Carbon, in Nickel and Manganese Steels," *Transactions,* American Institute of Mining and Metallurgical Engineers, Vol. 145, 1941, p. 279.

---

* In b.c.c. structures, the largest interstitial hole is a flattened octahedron. In one direction, the hole is very small: $(1-\sqrt{3}/2)a$ (a is the lattice parameter) or a hole diameter/atom diameter $= (1-\frac{\sqrt{2}}{3})\frac{2}{\sqrt{3}} = 0.154$.

In f.c.c. structures, the largest interstitial holes are regular octahedrons. The hole diameter/atom diameter is $\frac{2}{\sqrt{2}}(1-\sqrt{\frac{2}{2}}) = 0.414$.

The largest interstitial hole in h.c.p. structures likewise has a hole diameter/atom diameter $= 0.414$. Therefore, it is evident that the strain energy will be considerably greater in b.c.c. than in close-packed structures.

INFLUENCE OF SUBSTRUCTURE ON THE SHAPE OF THE CREEP CURVE

By Thomas H. Hazlett and Rosa D. Hansen

Abstract

Pure nickel and solid solution nickel alloys were strained-controlled amounts in tension at room temperature, given a recovery anneal and then crept at 700 °C (1290 °F). The amount of initial strain was considered to be an index of the amount of substructure present in the specimen when the creep test was started. Resultant creep curves were correlated to show the effect of the amount of substructure. The shape of the curves varied drastically with different amounts of substructure. Varying the alloy content has also been shown to affect the influence of substructure on the shape of the creep curve.

Introduction

A LARGE amount of research effort has been expended during the past few years in investigating the mode of formation and the nature of substructure in metals. Ever since the early work of Wood (1) [1] and of Cahn (2) the interest in this subject has been steadily increasing. Essentially all of the results published to date have been qualitative in nature, and they have usually been obtained with single crystals or with very coarse-grained polycrystalline material.

Quantitative data have been recently presented (3), however, which seemed to show the effect of induced substructures on the tensile properties of both polycrystalline high purity nickel and a solid solution nickel-titanium alloy. This investigation demonstrated that a controlled amount of substructure could be produced in these materials by room temperature straining followed by a high temperature recovery anneal. Tensile properties of pure nickel treated in this manner are shown in Fig. 1 and of the alloy in Fig. 2. An almost linear increase of flow stress was obtained with increasing prestrain.

Quantitative measurements of the amount of substructure present in the prestrained and recovered specimen revealed that the substructure was also increased by increasing the prestrain as shown in

[1] The figures appearing in parentheses pertain to the references appended to this paper.

A paper presented before the Thirty-sixth Annual Convention of the Society, held in Chicago, November 1 to 5, 1954. The authors, Thomas H. Hazlett and Rosa D. Hansen, are research engineers, Minerals Research Laboratory, Department of Engineering, University of California, Berkeley, Cal. Manuscript received April 5, 1954.

Fig. 3. From these data it may be concluded that the tensile strength of a given material is greatly dependent upon the substructure state, i.e. the larger the amount of substructure, the greater the strength. This conclusion is supported by the curves of Fig. 4 which show that the flow stress increases as the amount of stable substructure increases.

The investigation reported in the present paper was undertaken

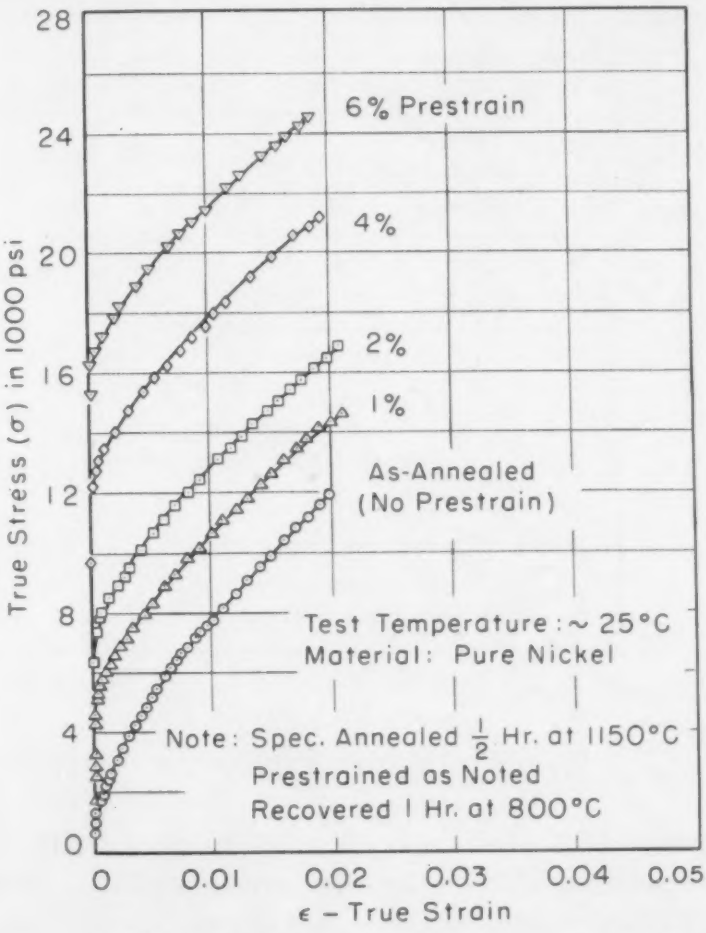


Fig. 1—Effect of Prestrain and Recovery Treatment on Strength of Pure Nickel.

to determine the effect of the substructure state on the creep properties of pure nickel and some solid solution nickel alloys.

Test Procedure and Results

Tandem gage length specimens of the type previously described (4) were used for this program. All room temperature tensile strains were measured with extensometers which clamped directly onto the three inch long reduced section of the specimens. Creep tests were made at 700 °C (1290 °F) and 5750 psi constant applied stress using the creep strain measuring techniques and test equipment also described in the previous paper.

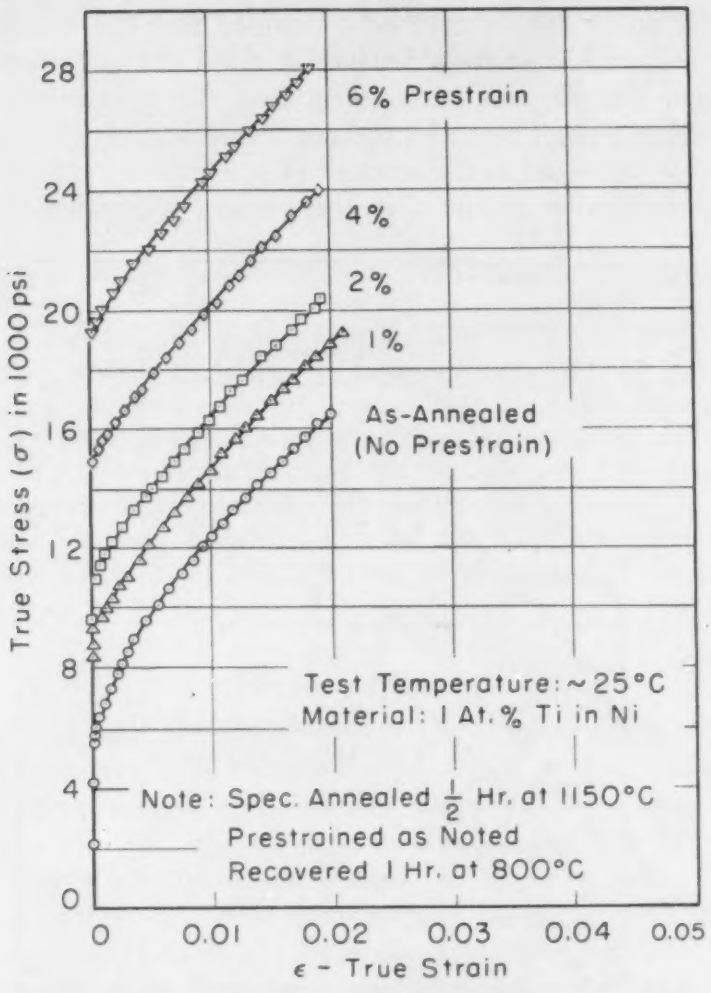


Fig. 2—Effect of Prestrain and Recovery Treatment on Strength of Nickel-Titanium Alloy.

Nickel of 99.95% purity was used for the most detailed study, but several solid solution alloys were also investigated to a lesser degree. These are listed in Table I.

The test specimens were fully annealed in air at 1150 °C (2100 °F) for one-half hour after machining. These were then tensile strained various amounts at room temperature (hereafter this initial straining will be referred to as "prestrain") and recovered for one hour at 800 °C (1470 °C). Some of these specimens were then tensile tested at room temperature and others subjected to creep tests.

Table I

Alloy Series	Alloy Addition in Atomic Per/Cent
Ni-Ti	½% Ti
Ni-Fe	5% Fe
Ni-Co	2½% Co
	20% Co

Results

Tensile properties resulting from this treatment have already been shown in Fig. 1 for pure nickel. Similar results were obtained from tests on the alloys. It may be noted in Fig. 5 that the tensile properties of these alloys also increase regularly as the amount of prestrain increases. The very slight difference between the indicated yield strength of the pure nickel and that of the 2.5% cobalt alloy is in ac-

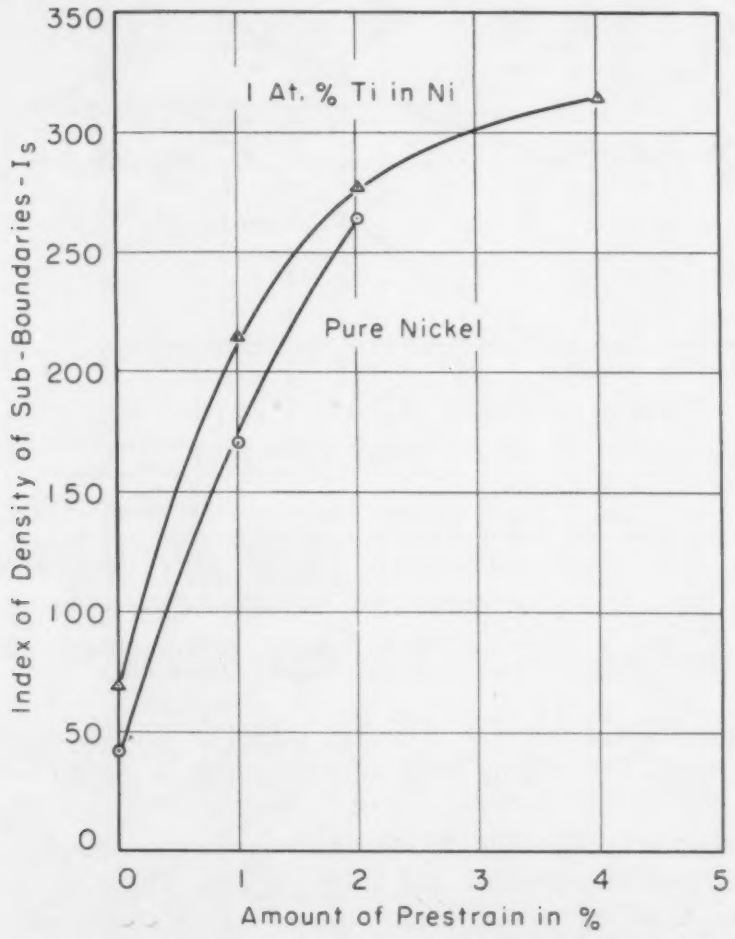


Fig. 3—Change in Density of Subboundaries Produced by Indicated Amount of Prestrain Followed by an 800 °C Anneal.

cordance with the results from previous studies (5) which showed that the addition of even substantial amounts of cobalt had very little effect on the tensile properties of nickel.

Creep curves obtained from prestrained and recovered specimens of pure nickel are shown in Fig. 6 where it may be seen that the shape of the creep curve is drastically affected by the amount of prestrain. The form changes from a normal curve which exhibits a continuously decreasing creep rate to one which has a continuously accelerating rate.

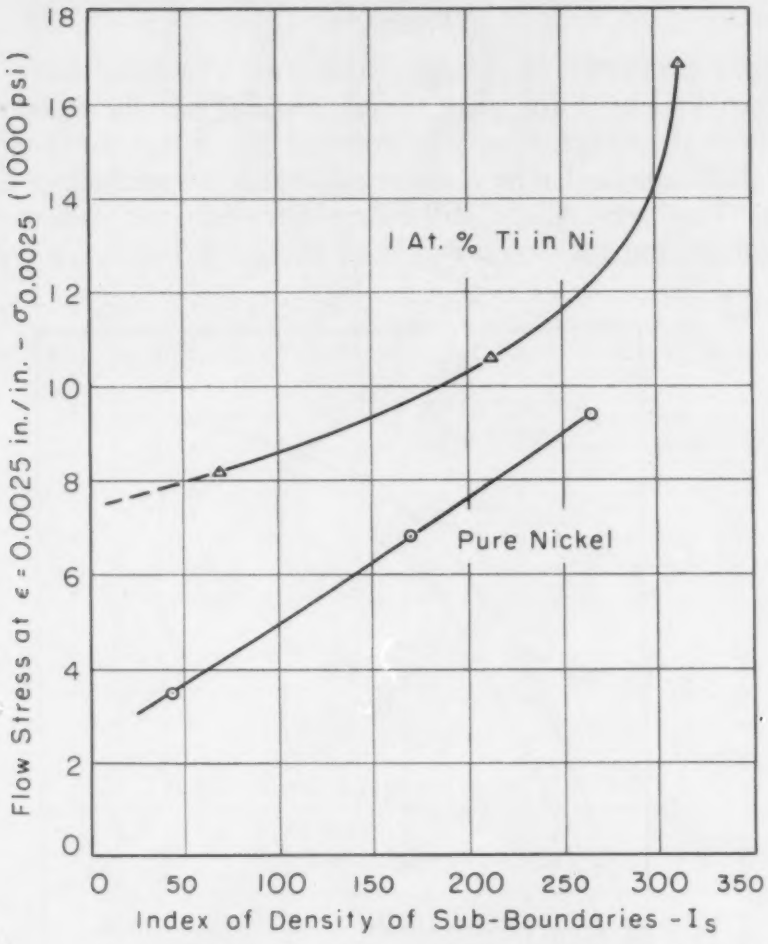


Fig. 4—Relationship between Density of Subboundaries and Flow Stress for Pure Nickel and a Nickel-Titanium Alloy.

This change in behavior for different states of the material is also illustrated by the behavior of solid solution alloys as shown in Figs. 7,8 and 9.

The creep curves in Fig. 10 show that the shape is dependent upon both the amount of prestrain and alloy content. These data were obtained from tests on two different nickel-cobalt alloys and on pure nickel, all of which had been prestrained 4% and recovered before creep testing.

Discussion of Results

There has been a renewal of speculation during the past two years as to the true shape of the creep curve obtained under conditions of constant stress. Lubahn (6) pointed out that the region of constant or "secondary" creep rate was probably fictitious for creep specimens tested under conditions of constant stress; the creep rate changes continuously. Carrecker's data on platinum (7) and Lubahn's results (8) on mild steel substantiated this hypothesis.

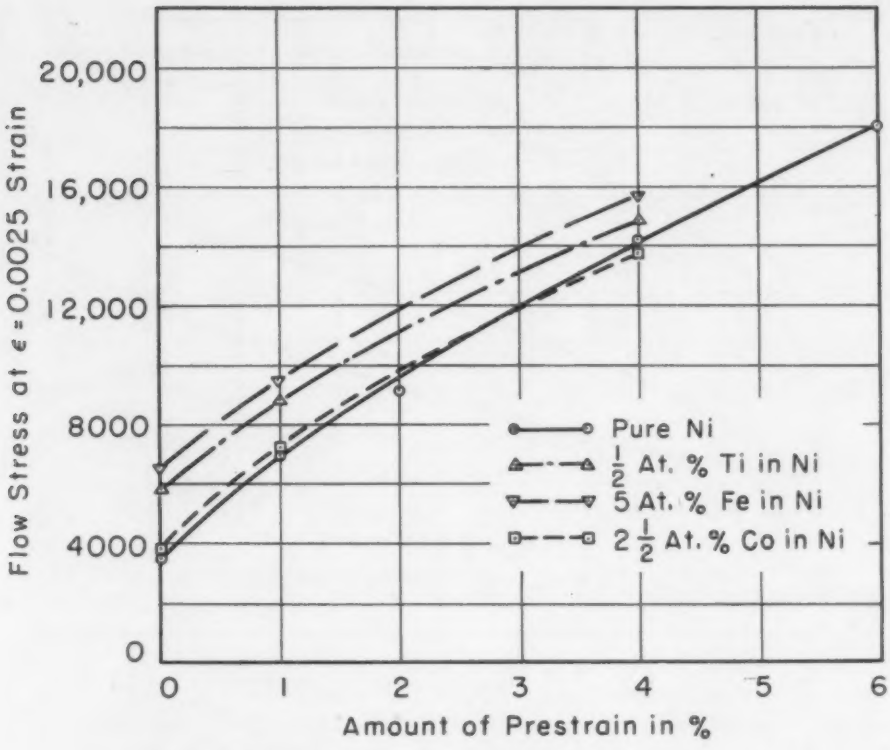


Fig. 5—Change of Flow Stress Produced by Indicated Amounts of Prestrain Followed by an 800 °C Anneal.

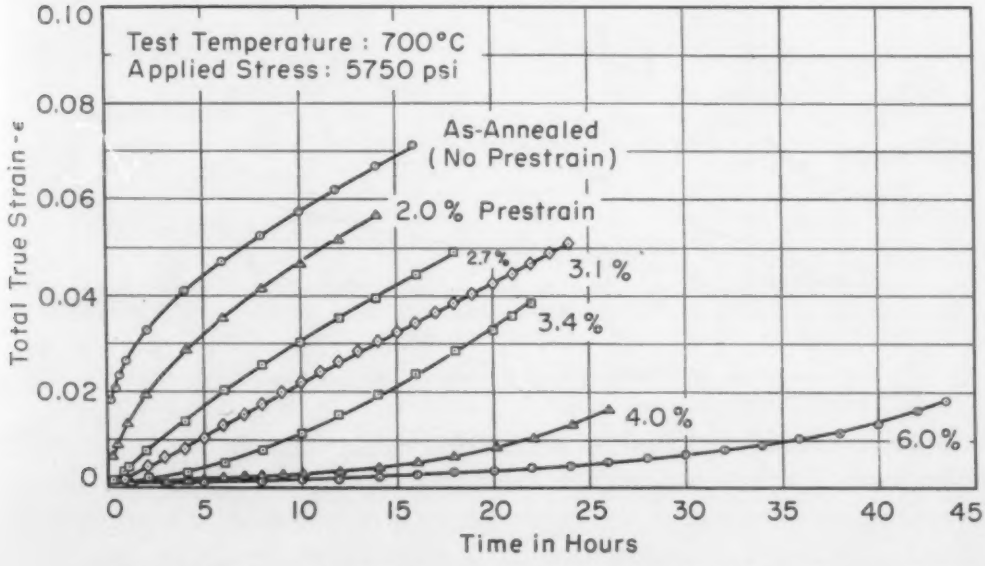


Fig. 6—Effect of Prestrain and Recovery Treatment on Creep Curves of Pure Nickel.

They proposed that the initial portion of the creep curve could be adequately described by a power equation of the form $E = At^b$ in which E = total strain and t = time, while A and b are constants. Subsequently, Hazlett and Parker (4) and Bhattacharyya, Congreve and Thompson (9) independently proposed that this equation should be

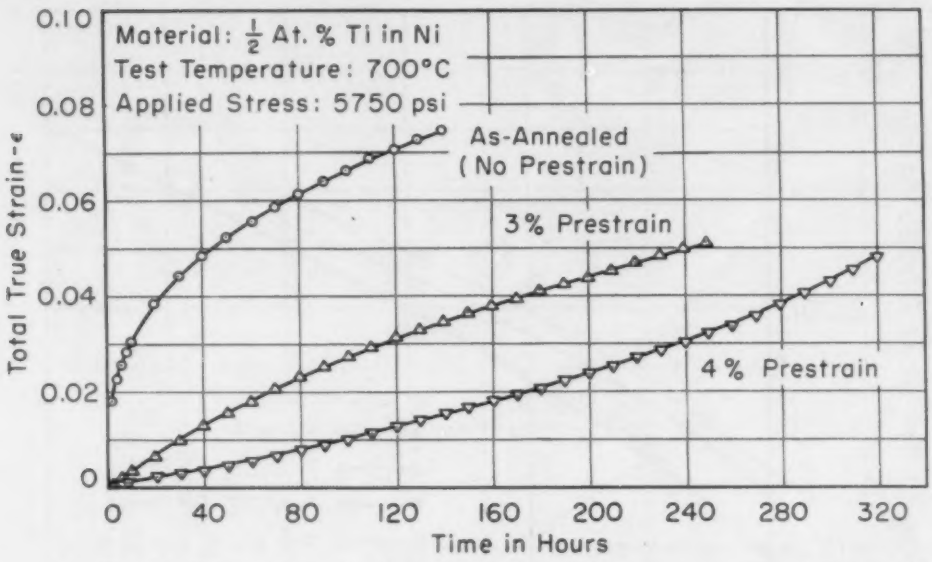


Fig. 7—Effect of Prestrain and Recovery Treatment on Creep Curves of Nickel-Titanium Alloy.

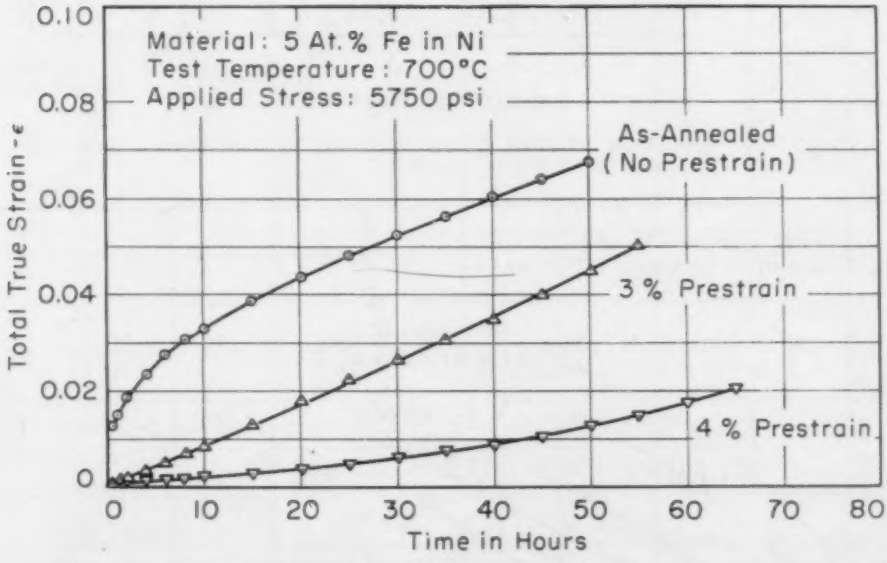


Fig. 8—Effect of Prestrain and Recovery Treatment on Creep Curves of Nickel-Iron Alloys.

modified to consider the initial strain that occurs due to the application of the load. Their equation has the form $E-E_o = At^b$ where E_o = instantaneous strain and the other terms are the same as previously defined. Although this equation still appears to be valid for fully annealed, metallurgically stable materials, the test results reported in the present paper may clarify some apparently contradictory results obtained by other investigators. Grant (4), in discussing the paper by Hazlett and Parker, presented creep data on high temperature alloys which departed quite drastically from the behavior predicted by the proposed equation. In another discussion of the same paper, Roberts argued that a true constant creep rate region does exist, particularly

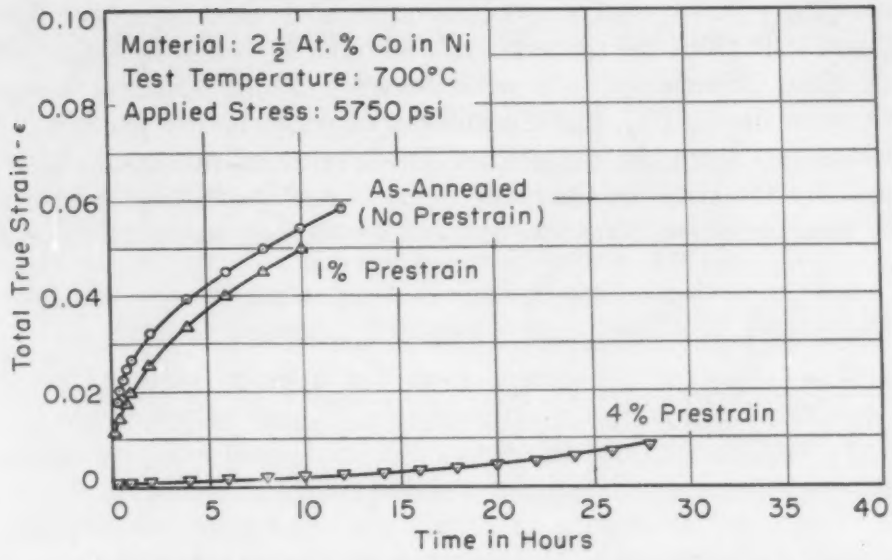


Fig. 9—Effect of Prestrain and Recovery Treatment on Creep Curves of Nickel-Cobalt Alloy.

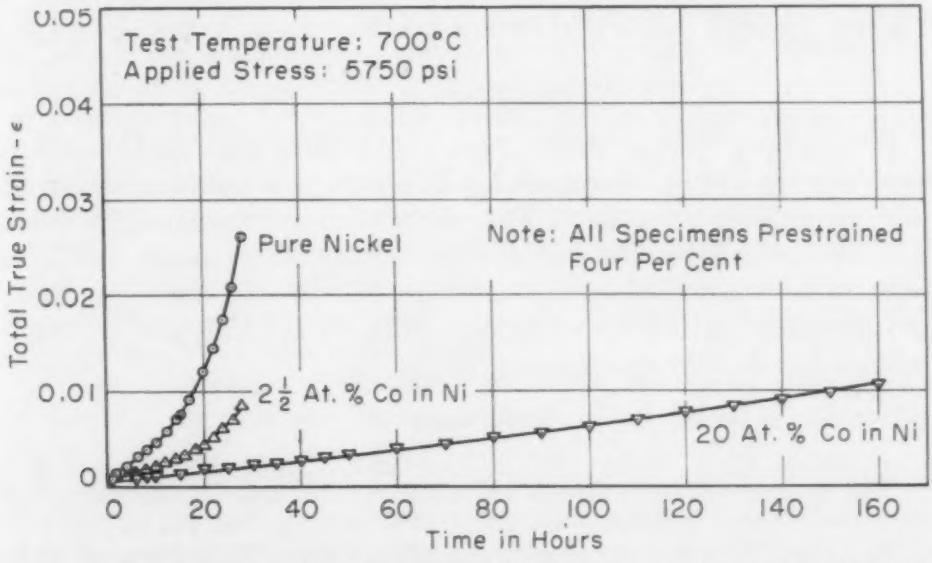


Fig. 10—Effect of Alloy Content on Creep Curves of Prestrained Nickel-Cobalt Alloys.

under conditions of high temperature and/or low stress. The data presented in Figs. 6 to 10 might appear to substantiate these views, but the varying shapes in this case may be specifically attributed to the different substructure states existing in the specimens at the start of the creep test. Since these substructures persist even at relatively high temperatures, it seems probable that in the cases cited by both Grant and Roberts, the apparent straight line portion of the creep curve was due to the existence of an uncontrolled and unknown amount of substructure present in the original material.

Although only the pure nickel data, Fig. 6, is sufficiently complete

to define the precise prestrain required to make the creep curve linear, it appears that all of the materials tested have such constant rate creep curves when prestrained to a value between 3 and 3.5%. It has previously been shown (3), that the amount of substructure present in the various alloys is not the same for a fixed value of prestrain. Thus, it appears that the shape of the creep curve is not specifically determined by the amount of substructure present at the beginning of the creep test.

Summary and Conclusions

The data reported herein may be summarized as follows:

1. The shape of the creep curve for a given material may be changed drastically from continuously decreasing to continuously increasing creep rate by first subjecting the specimens to a prestrain and recovery treatment which induces a stable substructure in the material.

2. The creep resistance of pure nickel and solid solution nickel alloys is vastly increased by the prestrain and recovery treatment prior to creep testing.

3. The amount of substructure present at the beginning of a creep test is not the only factor that determines the shape of the creep curve.

Acknowledgments

The authors wish to thank the U. S. Atomic Energy Commission for sponsoring the work on which this paper is based and for permission to publish these data. They also wish to express their sincere appreciation to Earl R. Parker for his helpful suggestions; to George Kilbourne for interested co-operation in performing the tests; and to Paul Langston for his conscientious work in refining and producing the metals for the test specimens.

References

1. W. A. Wood, G. R. Wilms, W. A. Rachinger, "Three Basic Stages in the Mechanisms of Deformation of Metals at Different Temperatures and Strain Rates," *Journal,* Institute of Metals, 1951, Vol. 79, p. 159.
2. R. W. Cahn, "Slip and Polygonization in Al," *Journal,* Institute of Metals, 1951, Vol. 79, p. 129.
3. E. R. Parker and T. H. Hazlett, "Principles of Solution Hardening," Transactions, American Society for Metals, Vol. 46A, 1954.
4. T. H. Hazlett and E. R. Parker, "Nature of the Creep Curve," *Transactions,* American Institute of Mining and Metallurgical Engineers, Vol. 197, p. 318.
5. V. F. Zackay and T. H. Hazlett, "Some Plastic Properties of Nickel Alloys," *Acta Metallurgica,* Vol. 1, Nov. 1953.
6. J. D. Lubahn, "Creep of Metals," Cold Working of Metals, American Society for Metals.
7. R. P. Carreker, Jr., "Plastic Flow of Platinum Wires," *Journal of Applied Physics,* Vol. 21, No. 12, p. 1289.
8. J. C. Fisher and J. H. Hollomon, "Wanted: Experimental Support for Theories of Plastic Flow," A Symposium on the Plastic Deformation of Crystalline Solids, Mellon Institute, Pittsburgh, May, 1950.

9. S. Bhattacharyya, W. K. A. Congreve and F. C. Thompson, "Creep Time Relationship Under Constant Tensile Stress," *Journal,* Institute of Metals, October, 1952.

DISCUSSION

Written Discussion: By Allen T. Robinson, U. S. Naval Ordnance Test Station, Inyokern, China Lake, Cal.

The authors are to be commended on an extremely worthy and timely paper demonstrating the influence of previous straining and annealing on the creep strain-time curve. Furthermore, it shows that it is highly desirable to have a uniform initial substructure when investigating creep properties of different metals and alloys.

This brings up a few questions which I feel are shared by others working in this field—how can solid solution alloys of various solute percentages be brought to equal subboundary densities without adding an additional variable? Also, of what significance is the instantaneous strain during application of the creep load to the already existing substructure?

The figure showing the change in the density of subboundaries with varying amounts of prestrain reveals that relatively large differences in the density of subboundaries are formed by prestrains of very low magnitude. Inasmuch as the yield strengths of annealed and the leaner alloys have been sufficiently lowered at the test temperature, it is not uncommon to induce some plastic straining during application of the higher creep loads. Such deformation in the presence of a high temperature might be sufficient to further modify any predetermined substructure.

If the instantaneous creep strain is of consequence in adding to the density of subboundaries, would it not be possible for various investigators using different methods of creep loading to find the resulting shape of their strain-time curves to be somewhat in variance?

I would appreciate any comments or remarks on these questions from those in attendance as well as those of the authors.

Written Discussion: By W. R. Hibbard, Jr. and R. W. Guard, Metallurgy Research Department, General Electric Co., Research Laboratory, Schenectady, N. Y.

The effects of substructure on mechanical properties is an important, although difficult, problem to study. We are now doing work in this field and would like to make several comments on this paper.

(1) Did the authors determine the substructure distribution after testing to establish that it was stable and unchanged?

(2) How should the fact that the prestrain differs quite widely from grain to grain affect the results?

We have also examined the equation of Parker and Hazlett and would like to point out here that the data of Carreker (Ref. 7) are in agreement with it since the initial strain on loading could not be measured and $E = E - E_o$ for his data. In some tests on high-purity aluminum we have found that the exponential curve is adequate only at small strains ($\epsilon < 0.15$). At large strains it gives values of strains which are too low.

Written Discussion: By William D. Jenkins, National Bureau of Standards, Washington, D. C.

The authors' analysis of the data presented in this paper is indeed interest-

ing; however, there are several questions and comments the writer would like to submit on the results.

Is the alloy (1 atomic % of titanium in nickel), described in Figs. 2, 3, and 4, the same alloy used to obtain the data in Figs. 5 and 6?

As the nickel and the nickel-titanium alloy were strained in unidirectional tension and then annealed above the recrystallization ranges, it is to be expected that the subsequent flow properties in tension, at room temperature, of the materials were affected by such factors as recrystallization accompanied by various amounts of grain growth; preferred orientation of the grains induced by the initial straining; incomplete removal of stresses due to the use of a recovery temperature below that of the original annealing temperature; and redistribution of dislocations or flow units.

The results of research on nickel, copper and nickel-copper alloys at the National Bureau of Standards tend to confirm the above line of reasoning. The position of the flow curves for specimens tested in tension at room temperature varied not only with the amount of prestrain but also with the recovery temperature, strain rate, and temperature at which the prestrain was obtained. The creep data confirm the observation that the equation ($E-E_o = At^b$) has only limited usage over limited ranges in strain, temperature and strain rate. Furthermore, the shape of the strain-time curves during the various stages of creep of specimens tested in tension is affected by the time at stress as well as by the stress and temperature. It would be interesting in this respect to see whether sigmoidal strain-time or sinusoidal creep rate-time curves of the type obtained on nickel in the National Bureau of Standards laboratories would be observed by the authors if the tests were carried out for appreciably longer times. The shape of the initial portion of the curves on high-purity nickel appear to have a direct relation to the amount and temperature of prestraining.

It would also be of interest to know whether the creep-stress value of 5750 psi (Figs. 6–10) was based on the original cross-sectional area of the specimen before the prestraining treatment as the interpretation of the recovery process can be more accurately evaluated with this information.

Authors' Reply

The authors wish to thank the discussers for their thoughtful comments and shall endeavor to answer some of the questions that have been raised. First, regarding the enquiries of Hibbard and Guard, subsequent work, which is still unpublished, has shown that the magnitude and nature of the substructure are changed by the creep test. In answer to the question concerning the differing prestrain in individual grains, we should like to make clear that this fact is recognized. The substructure also differs widely from grain to grain. That is the reason statistical methods were used for this investigation.

As to the questions raised by Mr. Robinson, it is really not known whether the increase in the substructure by alloy addition and by prestrain is equivalent. However, studies reported in another paper by Ancker and Parker indicate that this may be the case, at least for pure nickel and nickel-titanium alloys. The recent work mentioned above indicates that the instantaneous strain probably has a pronounced effect upon the substructure although no study has been made of this on specimens subjected to creep test conditions for time intervals less than about one half hour.

More recent studies indicate that a new and very stable substructure is

formed under creep test conditions during the initial part of the creep test. It is, therefore, highly improbable that the instantaneous strain contributes to the substructure reported in this paper. For this reason the authors doubt that the method of loading will have much effect upon the shape of the creep curves.

We wish to thank Hibbard and Guard for indicating the existence of additional data which substantiates the equation of the creep curve proposed by Parker and Hazlett. We should like to reiterate, however, as was pointed out in the paper, that this equation is only valid for fully annealed, metallurgically stable metals and alloys.

In reply to the questions and comments of Jenkins regarding the alloys of Fig. 5 and 6, it should be pointed out that 1 atomic per cent nickel-titanium data are not used in Fig. 5. The only nickel-titanium alloy in this series is 0.5%. On the other hand, Fig. 6 consists of creep curves of pure nickel only. All the curves in Fig. 2 and the upper curves for Fig. 3 and 4 are for 1 atomic per cent titanium in nickel.

We should like to reiterate that the "annealing" temperature after the tensile straining is not above the recrystallization range for the materials and strains used in this study. These specimens were, for all practical purposes, completely recovered but not recrystallized.

The authors are interested to learn of the work of the National Bureau of Standards on nickel, copper, and nickel-copper alloys which showed that the room temperatures tensile stress-strain curves varied with strain rate. No strain rate effect was detected for the alloys described in this paper when the rate was varied by a factor of 50 to 1. It is, of course, recognized that the stress-strain curves will vary significantly with both temperature and time of recovery in the lower temperature range, but there was little difference in the curves obtained from these alloys recovered at 800 or 900 °C if the time at temperature was at least one hour.

The creep ~~strain~~ stress value of 5750 psi was based upon the cross sectional area at the beginning of the creep test and this stress remained essentially unchanged during the test.

THE ALUMINUM-VANADIUM ALLOY SYSTEM

By O. N. Carlson, D. J. Kenney and H. A. Wilhelm

Abstract

The aluminum-vanadium system has been investigated by thermal, microscopic and X-ray methods. Four intermediate phases, $Al_{11}V$, Al_6V, Al_3V and Al_8V_5, have been identified from microstructures and from X-ray data. All four phases are peritectic in nature. $Al_{11}V$ undergoes a peritectic transformation at 685 °C (1265 °F), Al_6V at 735 °C (1355 °F), Al_3V at 1360 °C (2480 °F) and Al_8V_5 at 1670 °C (3038 °F). There is very limited solid solubility of vanadium in aluminum, but the solid solubility of aluminum in vanadium is quite extensive.

AN INVESTIGATION of the aluminum-vanadium system was undertaken to determine the phase relationships existing and to propose a phase diagram. The high melting point, ease of fabrication and ductility of vanadium coupled with its relatively low capture cross section for certain energy range neutrons make vanadium and its alloys of interest in the development of materials for nuclear reactors.

At the time the present investigation was initiated, the literature dealing with aluminum-vanadium alloys gave an incomplete and confusing picture of the system. Czako (1) [1] reported two single intermetallic phases: one occurring near 37.9 weight % vanadium, and another, near 79.3%. Czako suggested the formulae Al_3V and AlV_2, respectively. Brauer (2) determined the structure of Al_3V which he found to have tetragonal symmetry and to be isomorphous with Al_3Ti. Roth (3) made a thorough study of the solid solubility of vanadium in aluminum; his data have been incorporated in the construction of the phase diagram in this report. Mondolfo (4) did not indicate the extent of his experimental work on these alloys but, in commenting on the compounds of the system, added other possibilities. He showed a photomicrograph of a commercial alloy containing 2.4% vanadium, 0.42% silicon and 0.56% iron. In this picture he assumes five phases, namely: Al_3V, Al_4V, Al_7V, (Al-Fe-Si) and aluminum solid solution. There are numerous other studies involving aluminum-vanadium alloys reported in the literature but these show little effort directed toward determining the alloy phase diagram.

[1] The figures appearing in parentheses pertain to the references appended to this paper.

A paper presented before the Thirty-sixth Annual Convention of the Society, held in Chicago, November 1 to 5, 1954. The authors, O. N. Carlson, D. J. Kenney and H. A. Wilhelm, are associated with the Institute for Atomic Research and Department of Chemistry, Iowa State College, Ames, Iowa. Manuscript received March 3, 1954.

Experimental Procedure

Materials

Massive aluminum having a reported purity of 99.9% was obtained from the A. D. McKay Company and this metal was used in the preparation of all samples whose properties are reported in this paper.

No commercial source of vanadium having the ductility and purity desired was available to the authors at the outset of the investigation. Thus, the vanadium was prepared in this laboratory by the reduction of vanadium pentoxide with calcium, employing the method reported by Long (5). The vanadium pentoxide was C. P. grade obtained from the Vanadium Corporation of America and the calcium used was high purity material which had been redistilled at the Ames Laboratory. Complete quantitative analysis of the vanadium metal thus produced was not obtained but the metal was ductile and could be cold-rolled readily. The vanadium was prepared in sheet form for use in alloy formation.

Alloy Preparation

Alloys were prepared by arc-melting vanadium sheet, together with the aluminum, under argon in conventional arc-melting equipment employing a tungsten electrode and water-cooled copper crucible. Because of the relatively low boiling point of aluminum, great care had to be taken in preparing the alloys to assure a macroscopically uniform sample. By limiting the alloys to 10 gram specimens and by remelting four or five times, inverting the samples between melts, homogeneous alloys could be prepared in most cases. In the region of 0 to 30% vanadium, where segregation proved unusually troublesome, it was found necessary to give the arc-melted samples an additional treatment to obtain homogeneity. The alloys were cold-pressed to about 50% of their original thickness, sectioned into small pieces and again given repeated arc-meltings.

By carefully weighing the charge materials and the resulting alloy, it was found that in many instances the weight change upon arc melting was small. Chemical analyses were performed on most of the alloys although in some cases, where the weight losses were negligible, nominal compositions have been used. In preparing vanadium-rich alloys, loss of aluminum by volatilization was encountered and the final composition shifted as much as 1 to 2% from that intended. In the composition range of 40 to 60% vanadium, a rare but reproducible phenomenon which occurred in connection with the arc-melting made the nominal composition of these alloys uncertain. These alloys would shatter or sometimes even explode with considerable violence during the cooling following solidification.

Heat Treatment of Alloys

Samples prepared by the above procedures were generally quite uniform, but the microstructures showed that most of the alloys were in a nonequilibrium condition. The rapid cooling that followed the arc-melting in many of the alloys suppressed peritectic reactions and resulted in complex microstructures. Often as many as four or five phases were readily detected in a single alloy. To homogenize these specimens the parent alloy was first cold-worked, if possible, and annealed under a vacuum of approximately 0.001 micron. The time and temperature selected for the homogenization treatment depended upon the composition and melting range of the alloys. These treatments varied from 500 hours at 625 °C (1155 °F) for some aluminum-rich alloys to 10 hours at 1100 °C (2010 °F) for those containing principally vanadium.

A large number of quenching experiments were conducted to obtain data on the phase boundaries of the system. These were carried out by annealing alloy specimens at the temperature of interest, admitting helium into the system at that temperature and quenching the samples in water. Microscopic examinations of the structures of the quenched alloys were made to determine the proper time for equilibrium at the annealing temperatures.

Alloy Examination

On the basis of microscopic, X-ray and thermal data obtained on the heat treated alloys, a phase diagram for the aluminum-vanadium alloy system was proposed.

Grinding and polishing operations were carried out in the conventional manner. Several different etching procedures were tested, but immersion of the sample in an acid mixture containing 1000 parts H_2O, 25 parts HCl, 10 parts HNO_3 and 5 parts 48% HF was found to be satisfactory for many of the alloys. A KOH solution was satisfactory for etching the aluminum-rich alloys and either electrolytic or cathodic etching for vanadium-rich alloys. In the electrolytic etching, a 3N HNO_3 solution containing 1 weight per cent KF was used at a current density of about 0.1 amp per square cm.

In the metallographic studies extensive use was made of visual examination of the samples under polarized light. Two of the four intermediate phases in this system proved to be anisotropic, since they exhibited extinctions on being rotated in polarized light. This property proved useful in differentiating the phases in many of the alloys.

X-ray diffraction data were used in identification of the phases, measurement of their lattice constants, and the determination of their crystal structures. A 114.6 millimeter diameter Debye-Scherrer powder camera was employed in the phase identification work. For

precision measurements of lattice constants either the Norelco X-ray diffractometer was used with polycrystalline solid specimens or a back-reflection, self-focusing precision camera was used with powder specimens. When single crystals could be obtained, a Weissenberg or a precession camera was employed to study the crystal structures.

Since the system covered such a wide range of melting temperatures, several different techniques had to be employed to obtain the thermal data. Due to the reactivity of the metals, it was necessary to obtain the thermal data with the samples in vacuum or in an inert atmosphere. The use of a Kanthal wire resistance furnace, a quartz vacuum tube and a chromel/alumel differential thermocouple arrangement provided accurate data in the range up to 1100 °C (2010 °F). In the range of 1100 to 1500 °C (2010 to 2730 °F), cooling curve data were obtained by means of a platinum/platinum-10% rhodium thermocouple and a graphite resistor furnace. Also, in this temperature range and above, solidus points were determined by measurements with an optical pyrometer on samples that were heated either by internal resistance or by induction.

With the optical pyrometer method and heating by internal resistance (6), a hole of small diameter is drilled into a rod or bar of the alloy specimen. The sample is clamped between two electrodes and is heated by passing a high current through it. During the heating the temperature within the hole is continuously observed until melting is evident.

Because of the apparent volatility of both vanadium and aluminum above 1700 °C (3090 °F) when heated in a vacuum, data on the high vanadium alloys were obtained employing an atmosphere of helium. Some of the alloys in the middle region of the system were too brittle to permit drilling, so partial melting was observed on irregularly shaped pieces placed in a graphite crucible which was heated in an induction furnace.

Experimental Results

The results of the investigation are summarized in the proposed phase diagram shown in Fig. 1. Designation of the phases has been made in accordance with the system of nomenclature first proposed by Dix and Keith and later modified by Fink and Willey (7). For purposes of discussion this section of the paper has been divided into two parts. These parts have been arbitrarily designated as aluminum-rich alloys for compositions from 0 to 38 weight per cent vanadium and as vanadium-rich alloys for those containing 38 to 100% vanadium.

The Aluminum-Rich Alloys

The aluminum-rich portion of the diagram contains three peritectic compounds. Heating and cooling curves have confirmed a transition at 660 °C (1220 °F) and have established peritectic horizontals

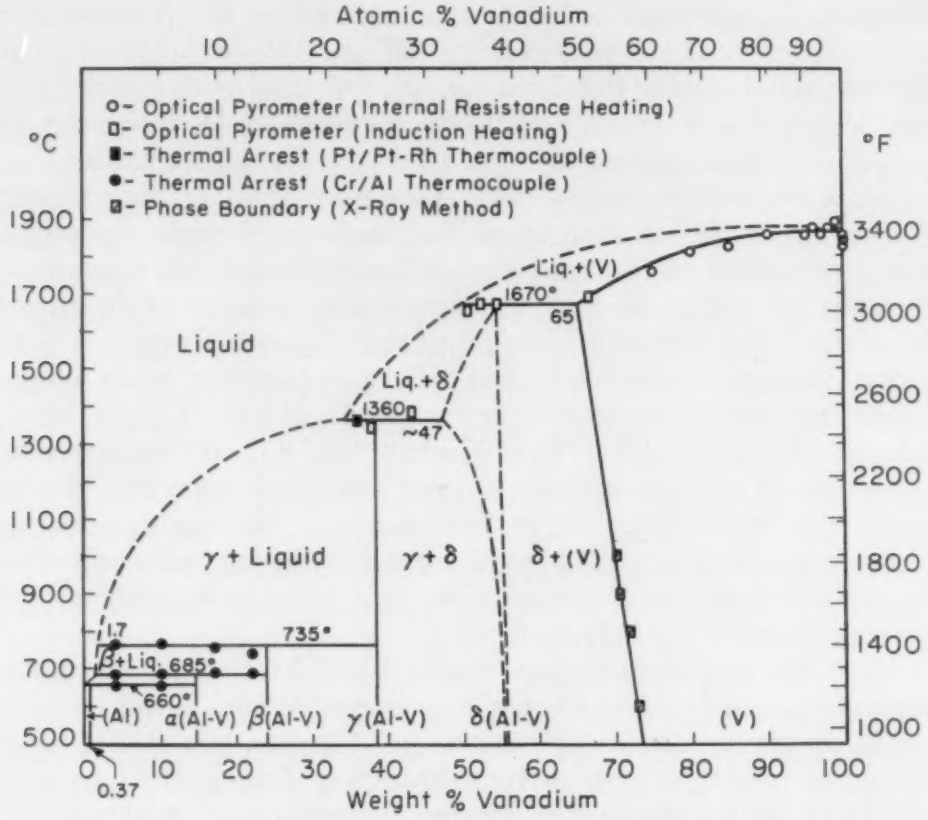


Fig. 1—Aluminum-Vanadium Phase Diagram and Plot of Thermal Data.

at 685 °C (1265 °F), 735 °C (1355 °F) and 1360 °C (2480 °F) corresponding to decomposition temperatures of the intermediate phases of α(Al-V), β(Al-V), and γ(Al-V), respectively.

The solid solubility of vanadium in aluminum was determined by Roth (3) who employed electrical resistivity and lattice constant measurements. His value of 0.37% vanadium at 630 °C (1166 °F) and lower temperatures has been accepted in the construction of the phase diagram.

A distinct break in the heating and cooling curves as recorded by a differential thermocouple was observed at 660 °C ± 2 (1220 °F) for the 5 and 10% alloys. Since the melting point of pure aluminum is within this range the method of analysis was not sufficiently accurate to determine whether this transformation is eutectic or peritectic in nature. Therefore the phase relationships near pure aluminum at its melting point may not be properly represented in the diagram. The photomicrographs of Figs. 2, 3 and 4 are of annealed alloys containing 0.4, 1.6 and 10.1% vanadium, respectively. They show increasing amounts of a primary phase identified as α(Al-V). Since this phase is peritectic in nature and does not exist above 685 °C (1265 °F) it is seldom found in an alloy as cast. It is difficult to distinguish this phase from the aluminum solid solution, (Al), since the two phases have

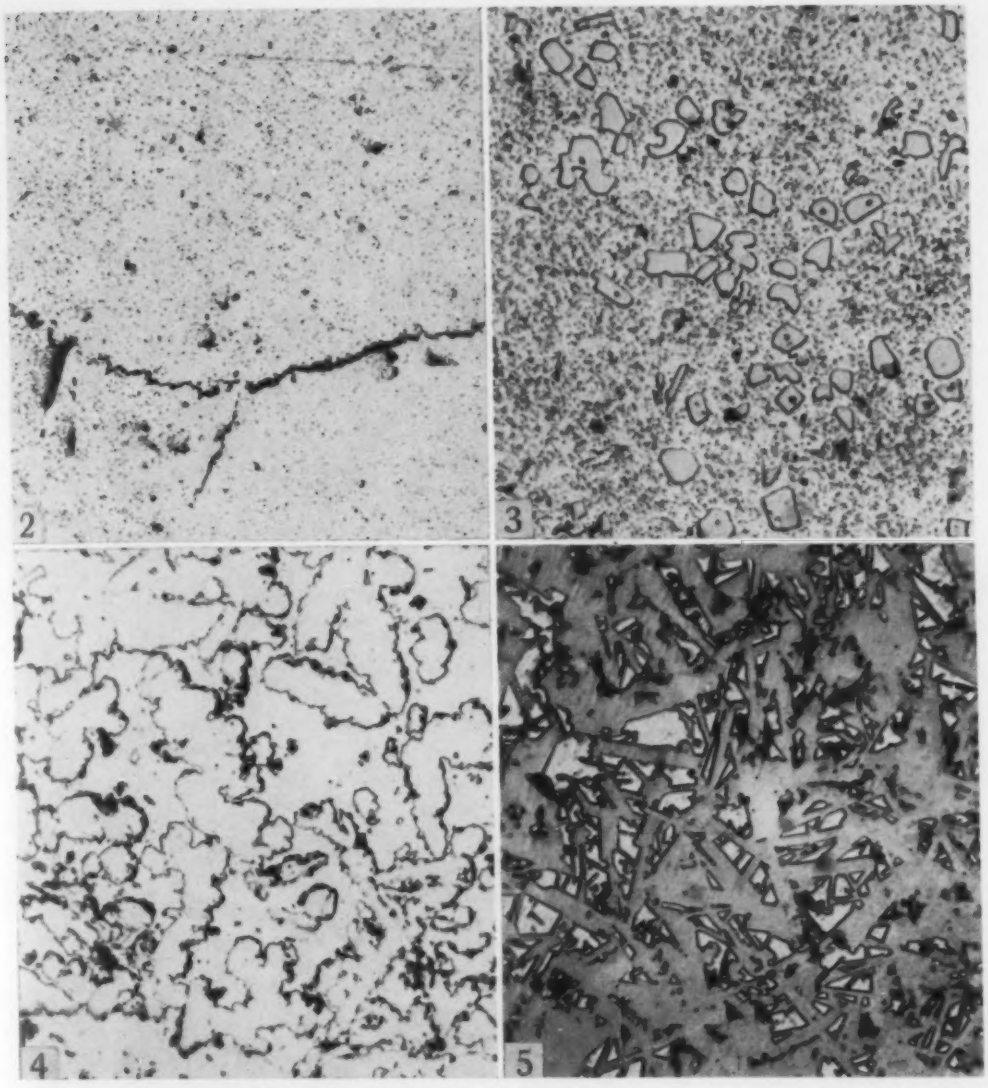


Fig. 2—0.4% V Alloy. Annealed for 500 hours and quenched from 625 °C. Aluminum solid solution phase (Al). Etchant: Conc. KOH. X 250.

Fig. 3—1.6% V Alloy. Annealed and quenched from 625 °C. (Al) plus small crystals of α. Etchant: KOH. X 250.

Fig. 4—10.1% V Alloy. Annealed and quenched from 625 °C. α (smooth) plus (Al). Etchant: 5 cc. HF, 10 cc. HNO_3, 25 cc. HCl in 1000 cc. H_2O. X 250.

Fig. 5—17% V Alloy. Annealed and quenched from 625 °C. Sharp crystals of β in α matrix. Etchant: HF-HNO_3-HCl. X 250.

similar etching characteristics. Then, too, both are optically inactive under polarized light. The exact composition of α(Al-V) could not conveniently be established microscopically. On the basis of microscopic data alone α(Al-V) probably lies somewhere between 12 and 15% vanadium since a 17% alloy (Fig. 5) contains a considerable amount of a new anisotropic phase identified as β(Al-V).

The peritectic nature of the α(Al-V) phase as shown in Fig. 1 was determined by the cooling curve data indicated on the diagram and by microstructures of quenched alloys. This phase, present in the annealed

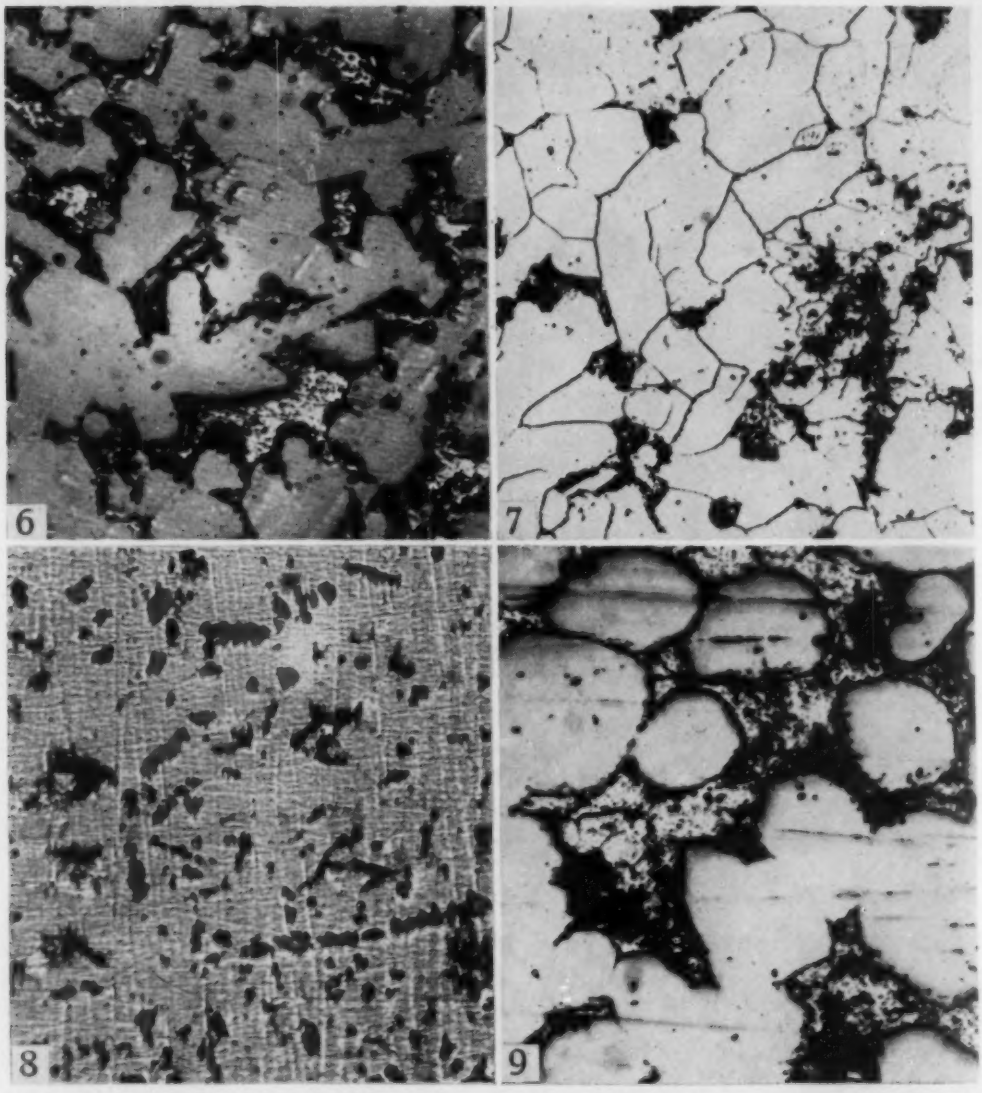


Fig. 6—17.7% V Alloy. Quenched from 710 °C. β plus quenched liquid (rough). Etchant: HF-HNO_3-HCl. X 250.

Fig. 7—23.8% V Alloy. Annealed for 325 hours and quenched from 710 °C. One phase β alloy; dark areas are voids. Etchant: HF-HNO_3-HCl. X 250.

Fig. 8—25.3% V Alloy. Annealed at 625 °C. Small amounts of γ (dark) in matrix of β. Etchant: HF-HNO_3-HC1. X 250.

Fig. 9—23.8% V Alloy. Quenched from 750 °C. γ plus quenched liquid (rough areas). Etchant: HF-HNO_3-HCl. X 250.

17% alloy, is entirely absent from the alloy when quenched from 710 °C (1310 °F) as can be seen in Fig. 6. Annealing at this temperature transformed the α(Al-V) into β(Al-V) plus liquid. The β(Al-V) phase can readily be distinguished from α(Al-V) by etching characteristics and by examination under polarized light.

A small crystal of α(Al-V) was isolated from a slowly cooled, high aluminum casting. This crystal was indexed from a rotation pattern as face-centered cubic with $a_o = 14.5$ Å. The following condi-

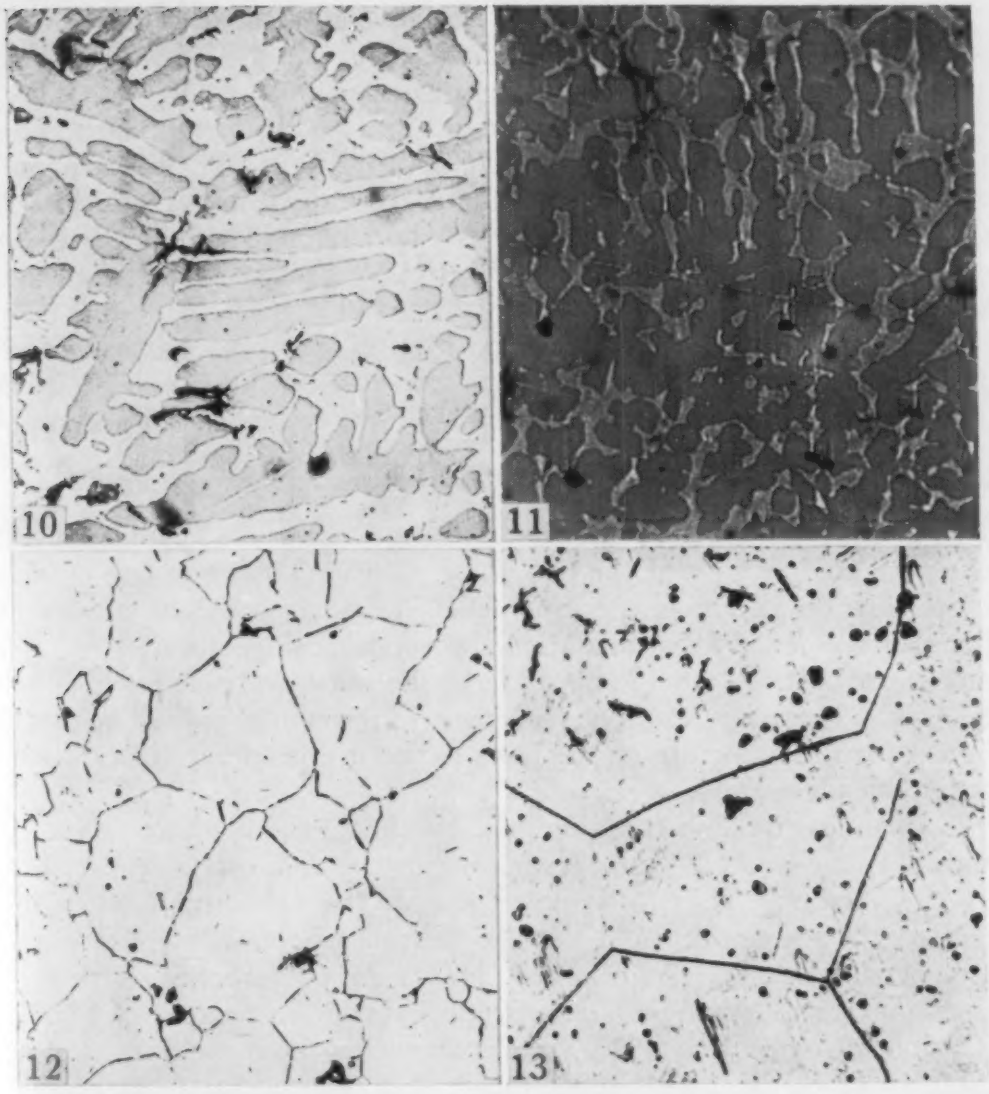


Fig. 10—32.7% V Alloy. Annealed and quenched from 625 °C. γ (dark) plus β Etchant: HF-HNO_3-HCl. X 250.

Fig. 11—36.3% V Alloy. Annealed and quenched from 625 °C. γ (dark) plus small amount of β. Etchant: HF-HNO_3-HCl. X 250.

Fig. 12—38.9% V Alloy. Annealed for 200 hours and quenched from 800 °C. One phase, γ. Etchant: HF-HNO_3-HCl. X 250.

Fig. 13—Vanadium Metal, as Arc-Melted. Contains some inclusions. Cathodic etch. X 120.

tions for nonextinction were noted in the rotation pattern: for the hk0 reflections, only the $h + k = 4n$ reflections are present and for the hhl, only the $h + 1 = 2n$ are present. On the basis of these observations and data from oscillation photographs, the crystal was shown to belong to the space group O^7_h — Fd3m. A powder pattern taken on a 12% vanadium alloy was indexed on this same basis and a_o was determined more accurately as 14.586 Å. On the basis of symmetry considerations, density and atomic size factors, α(Al-V) corresponds most simply to $Al_{11}V$ with 192 atoms per unit cell.

A one phase region is observed in the microstructures of annealed alloys at approximately 24% vanadium (Fig. 7 and 8). The peritectic nature of this phase which has been identified as β(Al-V) was determined from the thermal data plotted in Fig. 1 and from microstructures of alloys quenched from above 735 °C (1355 °F). Fig. 9 is a photomicrograph of the 23.8% vanadium alloy quenched from 750 °C (1390 °F) which is above the peritectic horizontal. The microstructure gives evidence that on annealing the β(Al-V) phase decomposed into solid γ(Al-V) plus liquid.

The structure and exact composition of β(Al-V) have not been fully determined. From single crystal X-ray data this phase has been shown to be hexagonal with $a_o = 7.718$ Å and $c_o = 17.15$ Å and probably to belong to the space group $D^4_{6h} - \frac{C6mc}{m}$.

From these cell dimensions, the measured density (3.07 g/cc) and chemical composition of the one phase alloy (23.8% V), one obtains by calculation 55.5 atoms per unit cell. On the basis of these considerations, Al_6V (23.94% vanadium theoretical composition) with 56 atoms per unit cell would appear to be the most probable formula for β(Al-V). However, a unique packing arrangement could not be determined for this structure on the basis of steric considerations or qualitative intensities.

In annealed alloys containing 32.7 and 36.3% vanadium (Figs. 10 and 11), the γ(Al-V) phase appears in the microstructure with a β(Al-V) matrix. It is to be noted that as the vanadium content increases, the amount of γ(Al-V) also increases, approaching one phase at the composition 39% (Fig. 12). This phase corresponds to the previously reported Al_3V with a theoretical vanadium content of 38.6%. It has been found that γ(Al-V) has an incongruent melting point at 1360 °C (2480 °F). This temperature was determined from cooling curve and optical pyrometer data (Fig. 1). The crystal structure of Al_3V has previously been reported by Brauer (2) as face-centered tetragonal with $a_o = 5.334$ Å and $c_o = 8.305$ Å. The lattice constants of γ(Al-V) were also determined by the authors in an attempt to determine whether there exists any solid solubility in the compound. Precision X-ray patterns were taken on alloys of compositions lying on either side of Al_3V which had been quenched from 625 °C (1155 °F). No change in lattice constants with quenching temperature was observed for a particular composition. Any solid solubility is therefore essentially independent of temperature. The lattice constants for alloys on the aluminum-rich side of γ(Al-V) were $a_o = 5.343$ Å and $c_o = 8.324$ Å, while those for alloys on the vanadium-rich side of the compound were $a_o = 5.346$ Å and $c_o = 8.313$ Å. This small but reproducible variation in the c_o lattice constant indicates that γ(Al-V) is a region of very limited solid solubility. The extent of solid solution

would be so slight, however, that it has been neglected in the construction of the phase diagram.

Vanadium-Rich Alloys

The experimental results for the part of the system between Al_3V and pure vanadium will be presented by approaching this compound from the pure vanadium side. In this manner the data on pure vanadium will be followed by data on alloys with decreasing vanadium contents. There is a rather wide solid solubility region (V) associated with pure vanadium. Only one other intermediate phase δ(Al-V) has been identified between Al_3V and (V). δ(Al-V) has a solid solubility range and also has an incongruent melting point at 1670 °C (3038 °F).

The vanadium prepared for use in this investigation was found to have a melting point of 1845 °C ± 10 (3355 °F) as determined by the method referred to in Fig. 1. Fig. 13 is a photomicrograph of the vanadium as-arc-melted and shows some inclusions. The lattice constant (a_o for the body-centered cubic structure) has a value of 3.031 Å for the annealed metal as determined by precision X-ray methods.

The solid solubility limit for the one phase region (V) at 600 °C (1110 °F) has been shown by metallographic observations to be in the vicinity of 70% vanadium. Alloys containing 86.1 and 78.7% vanadium which have been quenched from 600 °C (1110 °F) are entirely one phase (Figs. 14 and 15), whereas a 66% alloy similarly treated contains a large amount of a second phase (Fig. 16). The solid solubility of aluminum in (V) has also been shown by quenching experiments to be dependent upon temperature. The microstructure of the 66% alloy, quenched from 1100 °C (2010 °F), shows that a considerable amount of the precipitated phase in the 600 °C (1110 °F) quench has gone back into the solid solution (V) at the higher temperature (compare Fig. 16 and 17).

The exact location of the solvus for the (V) region was not determined from microscopic evidence since this would have required many more alloys and treatments. The application of X-ray diffraction studies to this problem, however, proved feasible and this boundary was determined with some degree of precision. X-ray patterns of six alloy compositions in the solid solution region, (V), showed only body-centered cubic reflections related to vanadium. The lattice constant increases linearly with increasing atomic percentage of aluminum (decreasing vanadium) as is shown graphically in Fig. 18. The above mentioned 66% vanadium alloy containing the saturated (V) phase was also quenched from 800, 900, and 1000 °C (1470, 1650 and 1830 °F) and the lattice constant measured for each quenched specimen. These measured values when applied to the extended lattice constant-composition relationship indicate the solubility limits at the

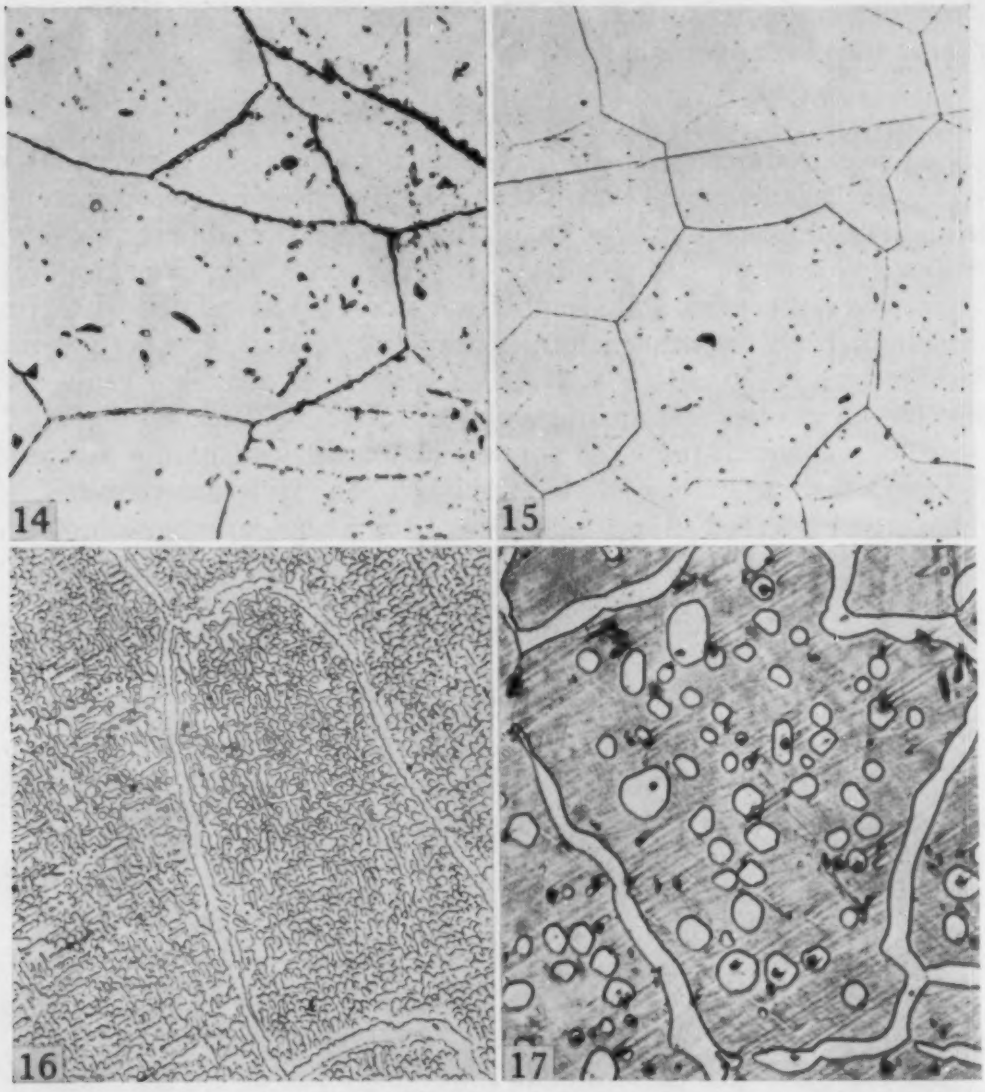


Fig. 14—86.1% V Alloy. Annealed at 800 °C for 100 hours, slow-cooled to 600 °C and quenched. One phase, (V). Etchant: Electrolytic etch in HNO_3-KF solution. X 250.

Fig. 15—78.7% V Alloy. Annealed at 800 °C and quenched from 600 °C. One phase (V). Electrolytic etch. X 250.

Fig. 16—66% V Alloy. Annealed at 800 °C and quenched from 600 °C. Heavy precipitation of δ from (V). Etchant: HF-HNO_3-HCl. X 250.

Fig. 17—66% V Alloy. Annealed for 10 hours and quenched from 1100 °C. δ within grains and at grain boundaries of (V). Etchant: HF-HNO_3-HCl. X 250.

various quenching temperatures (Fig. 18). These data on solubility limits have been employed in constructing the (V) solvus curve in the phase diagram on Fig. 1.

The solidus over the region (V) was constructed from the thermal data plotted in Fig. 1. There seems to be a slight tendency toward formation of a maximum in the solidus at 98–99% vanadium; however, the curve is constructed as horizontal as it approaches the melting point. This discrepancy may possibly be caused by impurity effects or scatter due to inaccuracies in the measurements. There is a possibility

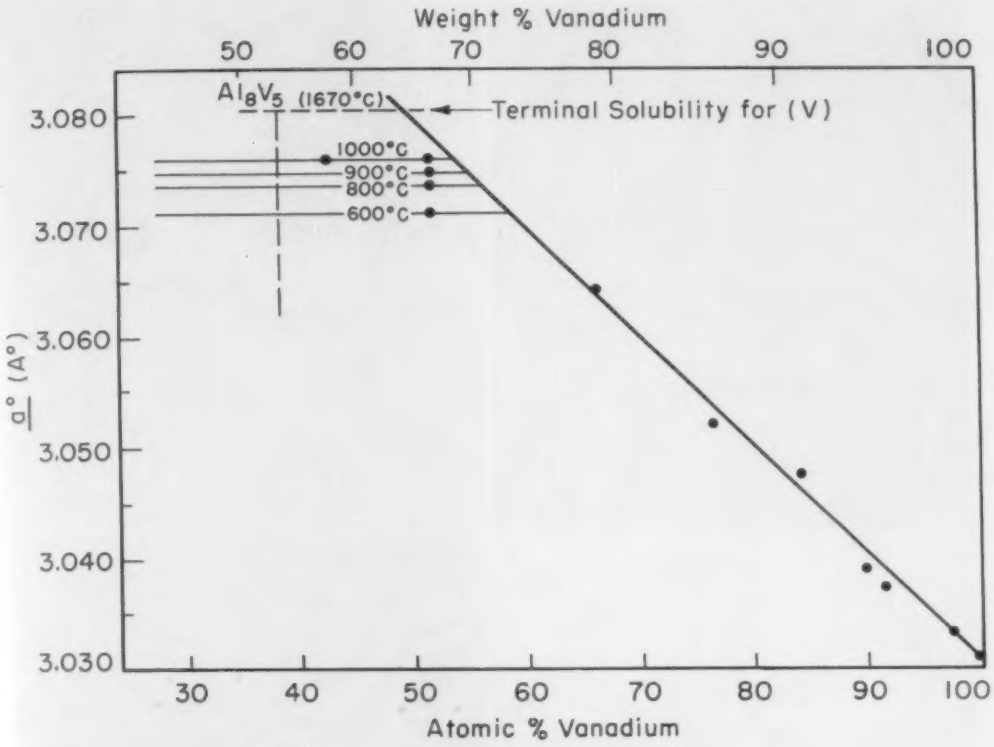


Fig. 18—Lattice Constant-Composition Relationship for (V).

that the addition of aluminum first acts as a getter to remove minor impurities that affect the melting point of vanadium.

The maximum solid solubility in the (V) phase has been estimated to be 65% vanadium at the δ(Al-V) peritectic, 1670 °C (3040 °F). A linear projection of the solvus determined by X-ray diffraction studies, the independently established (V) solidus and the 1670 °C peritectic horizontal all converge toward a composition near 65%. Furthermore, microstructures of alloys in the region of this composition show an abrupt change in the grain size between 66 and 64%, as can be seen upon comparing the size of the grains in Figs. 16 and 19. This difference in grain size has been interpreted as indicating that the small grains of Fig. 19 are due to the formation of a peritectic, δ(Al-V) rim about the (V) crystals during solidification, inhibiting their subsequent growth, while the alloy of Fig. 16 had no such inhibiting factor. This observation of difference in behavior of these two alloys lends support to selection of the 65% vanadium value.

As more aluminum is added to vanadium the amount of primary (V) decreases as can be seen by comparing Figs. 20,21 and 22, approaching a new one phase region at a composition near 56% vanadium. This new intermediate phase, δ(Al-V), was found to have a γ-brass type of structure belonging to the space group T^3_d — $I\bar{4}3m$. Since no single crystals of this phase could be isolated, X-ray data have been obtained from powder patterns only.

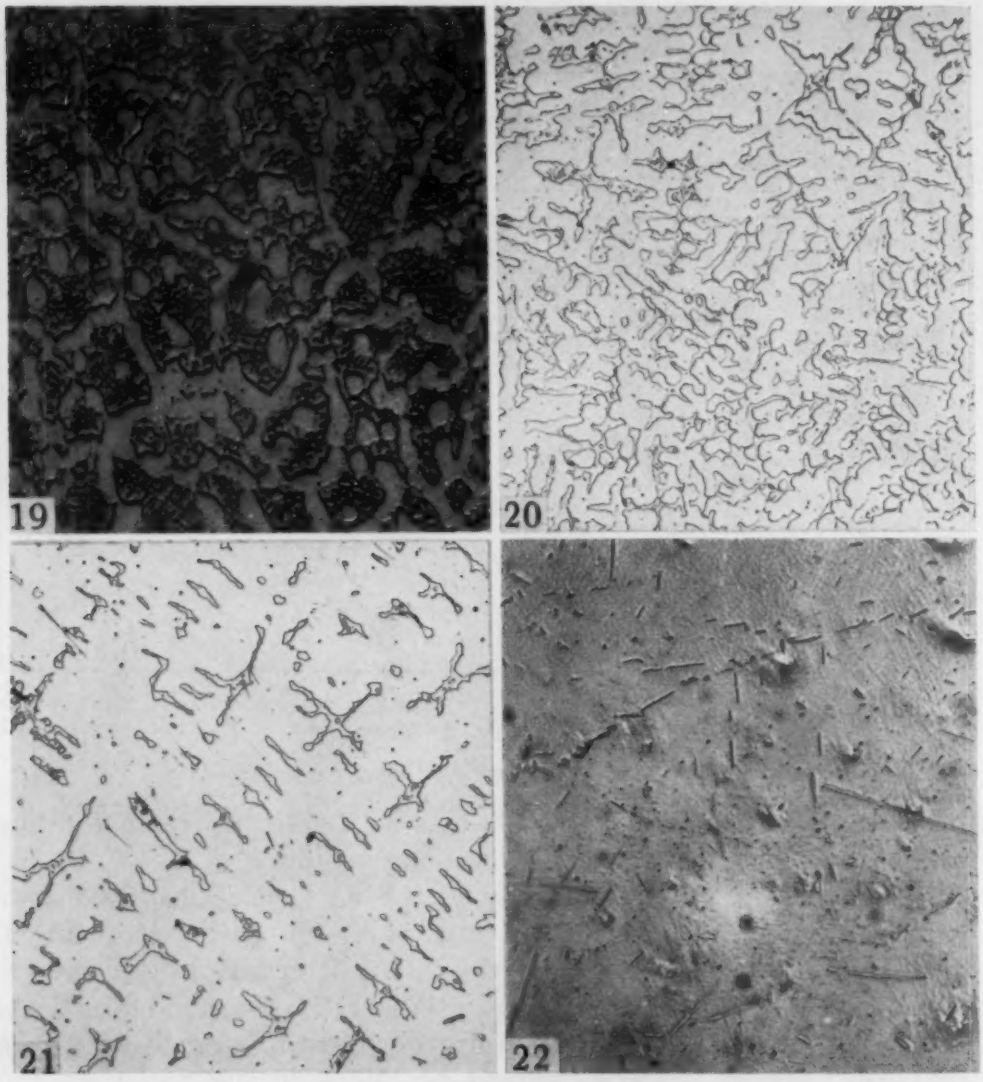


Fig. 19—64% V Alloy. Annealed at 800 °C and furnace-cooled. Contour lighting. δ in relief from (V) matrix. Etchant: HF-HNO_3-HCl. X 250.

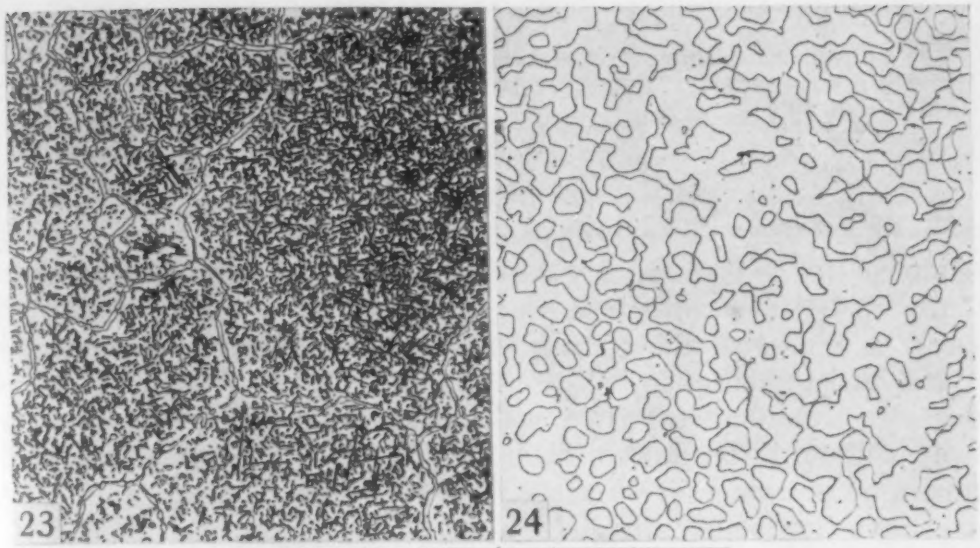
Fig. 20—60% V Alloy. Annealed at 800 °C and furnace-cooled. Dendrites of (V) in δ matrix. Etchant: HF-HNO_3-HCl. X 250.

Fig. 21—58% V Alloy. Annealed at 800 °C and quenched from 600 °C. Dendrites of (V) in δ. Etchant: HF-HNO_3-HCl. X 250.

Fig. 22—56% V Alloy. Annealed at 800 °C for 200 hours and quenched. Fine needles of (V) in δ. Etchant: HF-HNO_3-HCl. X 250.

δ(Al-V) has a body-centered cubic structure with $a_o = 9.207$ Å. On the basis of this information and density measurements, an assignment of 52 atoms per unit cell has been made.

Intensity calculations have been made in an effort to establish a unique formula by comparison with the observed intensities of the powder photograph. In this manner the formula Al_8V_5 (54.25% vanadium theoretical composition) was assigned in preference to other γ-brass types such as Al_7V_6 and Al_9V_4. Of the two possible structures of Al_8V_5, the one isomorphous with Zn_8Ag_5 shows best agreement be-



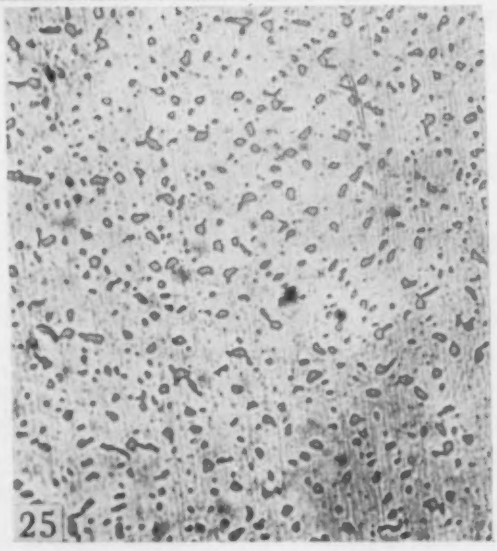


Fig. 23—52% V Alloy. Annealed and quenched from 600 °C. γ at the grain boundaries and within the grains of δ. Etchant: HF-HNO_3-HCl. X 250.

Fig. 24—45% V Alloy. Annealed and quenched from 1100 °C. δ in γ matrix. Etchant: HF-HNO_3-HCl. X 250.

Fig. 25—42.7% V, Alloy. Annealed for 100 hours and quenched from 900 °C. Small crystals of δ in γ matrix. Etchant: HF-HNO_3-HCl. X 250.

tween observed and calculated X-ray intensities. The structure of δ(Al-V) has a super-lattice relation to the saturated (V) phase since a_o is exactly three times as great as a_o for (V) and the strong lines of δ(Al-V) are the body-centered lines of (V); i.e., the 110 reflection of (V) is the 330 line of δ(Al-V).

The δ(Al-V) phase actually extends over a solid solubility region which is very narrow below 600 °C (1110 °F), but appears to broaden considerably at higher temperatures. The data of Table I show the variations of the a_o values for δ(Al-V) with temperature in the two regions on either side of the δ(Al-V) solid solution. These data can

Table I
Effect of Quenching Temperature on Lattice Constant of δ (Al-V)

Quenching temperature	a_0 for δ(Al-V) In γ + δ region	In δ + (V) region
600 °C	9.205 Å	9.208 Å
900	—	9.223
1000	9.241	9.233
1100	9.248	9.240

be interpreted to give roughly the range of the solid solubilities associated with δ(Al-V) at each of the quenching temperatures. It must be borne in mind that the addition of an aluminum atom expands the crystal lattice; hence, an increase in lattice constant represents an increase in aluminum content for the phase. The measurements were made with a 12-centimeter diameter, back-reflection type precision camera on powdered specimens. From these data there appears to be essentially no solid solubility in the δ(Al-V) phase at 600 °C (1110 °F) and only a slight solid solubility at 1000 °C (1830 °F). Furthermore, on the basis of these data, it appears that the saturated solid solution on either side of the one phase region increases in aluminum content with temperature. These measurements indicate that these two-phase boundaries have the same sign of slope.

On the basis of metallographic investigation, there is a pronounced increase in solid solubility of aluminum in δ(Al-V) in the range of the Al_3V peritectic temperature. Fig. 23 represents a 52% vanadium alloy which contains a precipitate of the established Al_3V phase in a δ(Al-V) matrix. This microstructure is typical of that of an alloy which has, on cooling, emerged from a one-phase solid solution region. A boundary showing decreasing solubility with decreasing temperature is therefore assumed to extend to the peritectic temperature at less than 52% vanadium. A 45% vanadium alloy (see Fig. 24) gives evidence of having undergone some peritectic transformation on cooling. On the basis of these and other observations a value of 47% vanadium was selected as representing the limit of the solid solubility of aluminum in δ(Al-V) at the 1360 °C (2480 °F) peritectic.

As the vanadium content is further decreased, the relative amount of δ(Al-V) diminishes and γ(Al-V) increases (Fig. 25), approaching the one phase region discussed earlier in this paper and shown to be Al_3V.

Discussion of Results

In the phase diagram as proposed in Fig. 1, the location of a phase boundary which is represented by a dashed line is to be regarded with a degree of uncertainty, whereas considerable confidence in the position of the boundary is expressed by a solid line.

X-ray diffraction studies sufficient to assign empirical formulae have been made on all intermediate phases reported in this paper. The X-ray and metallographic data agree quite well in all of these cases.

The β(Al-V) phase is the only one about which there is some uncertainty as to the exact formula. Its chemical composition apparently is very close to Al_6V, but an actual structure determination would eliminate any uncertainty.

Subsequent to the completion of the present investigation, Rostoker and Yamamoto (8) reported the existence of a simple cubic phase with $a_o = 14.47$ to which they assigned the formula $Al_{5-6}V$. This reported cubic symmetry indicates that their $Al_{5-6}V$ could not be the hexagonal Al_6V phase reported here. Comparison of their data for the $Al_{5-6}V$ with the results obtained on the $Al_{11}V$ of this investigation indicates strongly that these are one and the same phase. Lattice constants, indices of reflections and relative intensities of corresponding lines obtained in both investigations agree quite well. Inspection of their data employed in assigning simple cubic symmetry to the $Al_{5-6}V$ shows a remarkable parallelism with data which the authors interpreted as face-centered cubic for $Al_{11}V$ (9). The difference in reported compositions is difficult to explain although the presence of so many peritectic compounds in this region may be responsible for the dissimilar findings.

The boundaries for the solid solution region δ(Al-V) have been represented in the diagram as dashed lines. This has been done in spite of the fact that the formula Al_8V_5 is reasonably well established from X-ray data. The uncertainty exists in whether the composition Al_8V_5 (54.25% vanadium) actually lies outside the one-phase δ(Al-V) region at the lower temperatures. Interpretation of metallographic data places this narrow single phase region close to 56% at 600 °C (1110 °F); the composition Al_8V_5 then falls outside the one-phase region at this temperature. However, the true chemical compositions of alloys in this region were somewhat doubtful.

Although the discussion of thermal analysis has been treated somewhat superficially in this paper, it should be emphasized that, particularly in the aluminum-rich alloys, great care had to be exercised to obtain reliable results. For example, the 685 °C (1265 °F) and the 660 °C (1220 °F) thermal arrests occur so close together that the lower break often masks the other in heating and cooling curves. This masking is due to the sluggish nature of the 685 °C (1265 °F) transformation and its relatively low heat effect. Complete equilibrium is difficult to obtain during cooling; without proper precautions this can result in the appearance of a 660 °C (1220 °F) thermal arrest in alloys of compositions greater than 15% vanadium.

Summary

An investigation of the aluminum-vanadium system covering the complete composition range was conducted and the following salient features were established:

1. The solid solubility limit of vanadium in aluminum is 0.37% V at 660 °C (1220 °F) and lower temperatures.

2. An intermediate phase, α(Al-V), exists at approximately 14% V and has been indentified as $Al_{11}V$ (14.6% V). It undergoes a peritectic transformation at 685 °C (1265 °F).

3. Another peritectic phase β(Al-V) exists at approximately 24% V, undergoing a peritectic reaction at 735 °C (1355 °F). This phase has been assigned the formula Al_6V (23.9% V).

4. γ(Al-V), established as Al_3V prior to this investigation, was found to undergo a peritectic transformation at 1360 °C (2480 °F).

5. A fourth intermediate phase δ(Al-V) occurring at approximately 56% V has been shown to correspond to the formula Al_8V_5, (54.2% V). This compound undergoes a peritectic transformation at 1670 °C (3040 °F).

6. There is a region of extensive solid solubility of aluminum in vanadium, (V), extending to 70% V.

ACKNOWLEDGMENT

The authors appreciate the help of many of their associates at the Ames Laboratory. Thanks are particularly due to Mr. Harold Smith for his assistance in the X-ray studies on the crystal structures, to the analytical group of the Ames Laboratory under the direction of Dr. C. V. Banks for the chemical analyses, and to B. A. Loomis for his assistance in performing the many experiments and metallographic studies.

References

1. M. N. Czako, "Sur les Alliages d'Aluminium avec le Vanadium," *Comptes rendus,* Vol. 156, 1913, p. 140.

2. G. Brauer, "Konstitution der Aluminum-Vanadin Verbindung, VAl_3," *Zeitschrift Elecktrochem,* Vol. 49, 1943, p. 208.

3. A. Roth, "Ein Beitrag sur Kenntnis des Systems Aluminum-Vanadium," *Zeitschrift Metallkunde,* Vol. 32, 1940, p. 356.

4. L. F. Mondolfo, *Metallography of Aluminum Alloys,* John Wiley and Sons, Inc., New York, N. Y., 1943, p. 48 and 207.

5. J. R. Long and H. A. Wilhelm, "Preparation of Vanadium Metal," Ames Laboratory Report, ISC-244, 1951.

6. H. A. Wilhelm and P. Chiotti, "Thorium-Carbon System," TRANSACTIONS, American Society for Metals, Vol. 42, 1950, p. 1295.

7. W. L. Fink, F. Keller, W. E. Sicha, J. A. Nock, Jr. and E. H. Dix, Jr., PHYSICAL METALLURGY OF ALUMINUM ALLOYS, American Society for Metals, Cleveland, Ohio, 1949, p. 4.

8. W. Rostoker and A. Yamamoto, "A Survey of Vanadium Binary Systems," TRANSACTIONS, American Society for Metals, Vol. 46, 1954, p. 1136.

9. D. J. Kenney, H. A. Wilhelm and O. N. Carlson, "Aluminum-Vanadium System," Ames Laboratory Report, ISC-353, 1953.

DISCUSSION

Written Discussion: By W. Rostoker, supervisor, Physical Metallurgy Research, Armour Research Foundation, Chicago.

The authors appear to have conducted a very thorough study of the system. The writer does not think that his own limited work on this system can really invalidate any of the critical points in the diagram presently submitted. However, certain points of information, corroboration and disagreement might well be recorded:

1. The reference to our work might better be changed to its source[2] so that it may be more available to interested persons.
2. There is excellent agreement between our estimate of the maximum solid solubility of aluminum in vanadium (65.4 to 70% vanadium) and the authors' (65% vanadium).
3. There is excellent agreement between our measurement of the temperature by which VAl_3 is formed peritectically (1370 °C) and the authors' (1360 °C).
4. An alloy containing 21% vanadium in the as-cast state contained two phases micrographically which by X-ray diffraction were identified as aluminum and the cubic phase designated by the authors as VAl_{11}. This is incompatible with their diagram and with any reasoning on lines of nonequilibrium solidification.
5. An alloy containing 45% vanadium annealed for one week at 900 °C yielded a two-phase microstructure identified by X-ray diffraction as VAl_3 plus vanadium solid solution. This too is clearly incompatible with the authors' diagram.
6. The authors would perform a service to the readers and render their work more authoritative if they were to list the compositions of alloys prepared and the equilibrating heat treatments applied.

Written Discussion: By H. A. Saller, F. A. Rough and A. A. Bauer, Battelle Memorial Institute, Columbus, Ohio.

The authors are to be congratulated on having done an excellent piece of work on a complex and difficult system.

It is interesting that evidence of a transformation in vanadium was not reported by the authors, since Seybolt and Sumsion[3] have reported that a polymorphic transformation occurs in vanadium at 1550 °C. This point might be resolved by high temperature X-ray studies, such as have been made on other metals at the Institute of Atomic Research. If a polymorphic transformation does occur in vanadium, then additional proof might be obtained by a study of the corresponding two-phase region in the vanadium-aluminum solid solution region.

In any investigation of a polymorphic change which has not been confirmed, an important variable is the purity of the metals which are used.

The authors have reported that cracking and even explosive bursting have been encountered during cooling after arc melting of 40 to 60 w/o vanadium. This phenomenon has been observed a number of times at Battelle, particularly in alloys in which a transformation occurs. This bursting has been attributed to

[2] W. Rostoker and A. Yamamoto, "A Survey of Vanadium Binary Systems," TRANSACTIONS, American Society for Metals, Vol. 46, 1954, p. 1136.

[3] A. U. Seybolt and H. T. Sumsion, "Vanadium-Oxygen Solid Solutions", *Transactions*, American Institute of Mining and Metallurgical Engineers, Vol. 197, 1953, p. 292.

partial suppression of the transformation and a consequent build-up of both thermal and transformational stresses. We would like to inquire whether any evidence of a polymorphic transformation in one or the other of the intermetallic compounds involved in the 40 to 60 w/o vanadium alloys has been observed.

Again, we wish to congratulate the authors and to urge them to continue their fine work in this field.

Written Discussion: By F. R. Morral, head, X-Ray Section, Kaiser Aluminum & Chemical Corp., Spokane, Wash.

The results of some exploratory work done on this system some four years ago may be of interest in relation to this paper.

A 2.7% vanadium-aluminum hardener was melted and heated to 982 °C (1800 °F), held at temperature, fluxed, and allowed to cool at approximately 33.4 °C per hour to 593 °C (1100 °F)—(Treatment I). Another sample of the same aluminum-vanadium hardener was remelted and slowly cooled from 732 °C (1350 °F) to 649 °C (1200 °F) at 14 °C per hour, (Treatment II). A third sample of this hardener was remelted to 954 °C (1750 °F) and centrifuged which caused separation of the solid phase toward the far end and rapid cooling (Treatment III). The intermetallic compounds were separated from the alloys by leaching with hydrochloric acid or by electrolytic extraction. The crystals separated, as well as the alloys, were submitted to microscopic examination, chemical and X-ray diffraction analysis.

The Debye-Scherrer pattern obtained from crystals by Treatment I corresponded to a face-centered cubic cell with $a_o = 14.465$Å. This compares with 14.586Å reported in the paper for α (Al–V) or $Al_{11}V$. Some of the lines obtained in this pattern could not be properly indexed for this parameter value, however, they could be indexed on a face-centered cubic lattice if $a_o = 21.76$Å were used. The crystals analyzed 14.8% vanadium which corresponds with the theoretical value of $Al_{11}V$ namely 14.66%V.

Crystals from Treatment II appeared both as hexagonal plates, and long prismatic needles. Their Debye-Scherrer patterns were identical and corresponded to the β(Al–V) or Al_6V phase. These crystals analyzed 22.6% where the theoretical value for Al_6V is 23.9%.

The crystals separated by centrifugation (III) gave the typical powder pattern of Al_3V.

In conclusion, using an aluminum alloy of 2.7% vanadium composition and by treatment at approximately the regions indicated in the phase diagrams of the authors, we had separated the phases indicated. This would be further confirmation of the authors' interesting study.

Written Discussion: By Rodney P. Elliott, associate metallurgist, Armour Research Foundation, Chicago, and Lucio F. Mondolfo, professor, Department of Metallurgical Engineering, Illinois Institute of Technology, Chicago.

In conjunction with experiments on grain refining of aluminum alloys by peritectic nucleation, it was necessary to determine accurately the aluminum end of the aluminum-vanadium equilibrium diagram. Inasmuch as the liquidus and peritectic compositions were of extreme importance, more precise techniques were employed than those described by the authors. In this way, data were obtained that supplement and confirm the authors' findings.

High purity aluminum (99.9+%) was supplied by Alcoa and calcium-

reduced vanadium (99.7%) was obtained from the Armour Research Foundation. A master alloy was prepared by induction melting techniques.

An alloy containing approximately 10% vanadium was prepared from the master alloy. This alloy was held at a constant temperature twenty-four hours, at which time a sample of the liquid in equilibrium with the solid was taken for chemical analysis. The temperature was then lowered. At the end of the following 24 hours a second sample of the liquid was taken, etc. The liquidus shown in

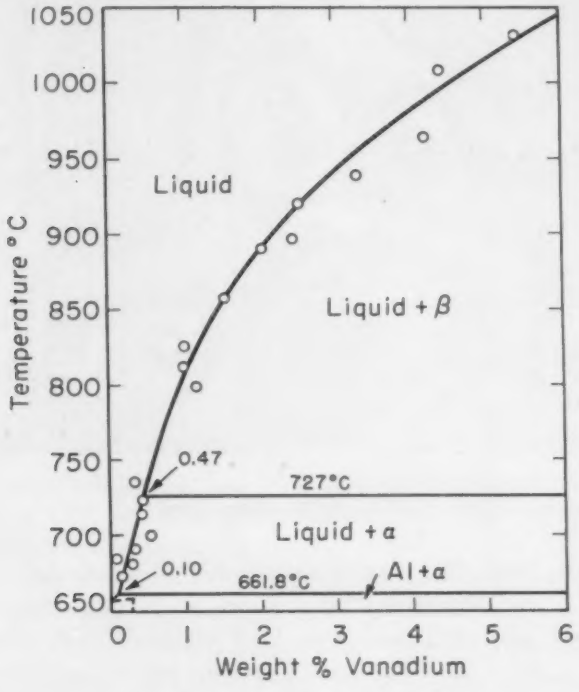


Fig. 26—The Aluminum—Rich End of the Aluminum—Vanadium Equilibrium Diagram.

Fig. 26 was drawn by rectifying the results of the analyses on a scale of the reciprocal absolute temperature versus the logarithm of the composition.

By metallographic examination, the temperature of the peritectic reaction $L + \beta(Al\text{–}V) \rightarrow \alpha(Al\text{–}V)$ was established as 727 ± 2 °C. As in the liquidus determination, a 6% vanadium alloy was held isothermally for twenty-four hours. The molten alloy was then stirred, chill-cast and examined to establish which phase was present. Shape and etching characteristics of the compound were criteria for identification. $\beta(Al\text{–}V)$ was in equilibrium with the liquid above 727 °C, and $\alpha(Al\text{–}V)$ below. When examined under polarized light, $\beta(Al\text{–}V)$ is active, exhibiting six extinctions per 360 degree revolution of the metallograph stage; $\alpha(Al\text{–}V)$ is inactive under polarized light. X-ray examination of the powder patterns of $\beta(Al\text{–}V)$ showed that it may be indexed as described by the authors; X-ray powder patterns of $\alpha(Al\text{–}V)$ showed this structure to be very complex.

The temperature of the peritectic reaction $L + \gamma(Al\text{–}V) \rightarrow \beta(Al\text{–}V)$ was found to be above 850 °C, which was the maximum temperature investigated to determine this reaction.

It was our experience during these investigations that reliable data for the

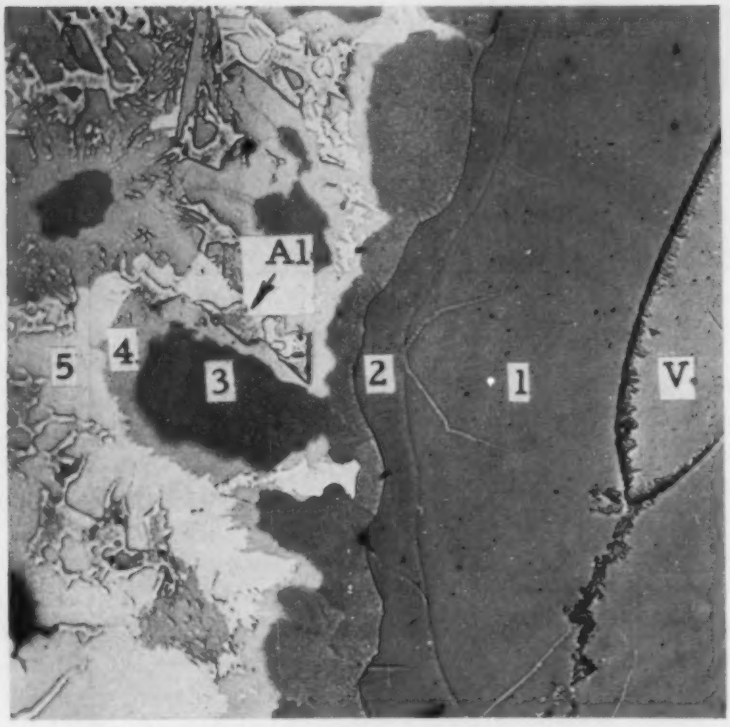


Fig. 27—As-Cast Structure of a Nonhomogeneous Alloy Showing Phases of the Aluminum-Vanadium System.

peritectic reactions involving two intermetallic compounds could not be obtained by thermal analyses. For this reason, it is possible that the authors' determination of the peritectic reactions L + β(Al–V) → α(Al–V) at 685 °C and L + γ(Al–V) → β(Al–V) at 735 °C are erroneous because of supercooling.

The freezing reaction was definitely established as peritectic by a series of thermal analyses. By using a Speedomax recorder which could be read to ± 0.01 millivolt and a chromel-alumel thermocouple, the freezing temperature of a sample of high purity aluminum was measured. The temperature of the freezing reaction of a 6% vanadium alloy was then measured and with the same thermocouple the freezing point of pure aluminum was then once again measured. In this manner, it was established that the temperature of the freezing reaction in this system was 1.6 ± 0.2 °C greater than the melting point of pure aluminum. Thus, the freezing reaction is a peritectic reaction, L + α(Al–V) → Al and occurs at 661.8 ± 0.2 °C.

During the initial preparation of the master alloy, a specimen showing all the phases from vanadium to aluminum was examined. A photo of this structure is shown in Fig. 27. Five intermediate phases are visible in addition to vanadium and aluminum. Since the phase labeled "3" is the one active under polarized light (β) it is probable that the aluminum end of the diagram may be more complicated than shown by the authors.

Written Discussion: By Bruce W. Gonser, Battelle Memorial Institute: Although probably having little appreciable effect on the diagram as presented by these authors, I would like to point out that 99.99+ aluminum is readily available for commercial as well as experimental use. The calcium-reduced vanadium is the purest now available commercially, but, by the iodide

method, a substantially purer metal can be obtained. This 99.9 metal may have a Vickers hardness of only 64 after cold rolling and annealing.

The difficulty mentioned from volatility of aluminum in making the alloys is surprising, since we do not have trouble from this source in making titanium alloys containing aluminum.

Authors' Reply

The authors wish to thank the discussers of this paper for their interesting comments and criticisms. Mr. Rostoker is concerned about the presence of the phase designated as $Al_{11}V$ in an as-cast 21% vanadium alloy which he has investigated. The authors are unable to explain this discrepancy either. As for the identification of VAl_3 plus vanadium solid solution in a 45% vanadium alloy the fact that δ(Al–V) appears to have a super-lattice relation to (V) could explain this apparent discrepancy since the strong diffraction lines of δ(Al–V) coincide with those of saturated (V).

The comments and data of Mr. Morral on the aluminum-rich compounds are gratifying to receive. They appear to substantiate the authors' findings for both $Al_{11}V$ and Al_6V.

Messrs. Saller, Rough and Bauer inquire about a possible phase transformation in vanadium. High temperature X-ray studies performed by Chiotti in this laboratory have produced no evidence for a phase transformation in vanadium at temperatures up to about 1675 °C. This is based upon a rather preliminary investigation however. Their comments on a possible polymorphic transformation in one of the intermediate phases are interesting. No real effort was made to investigate this point, however.

The data on the aluminum-rich end of the system presented by Messrs. Elliott and Mondolfo are appreciated. The aluminum-rich liquidus data and work on the aluminum peritectic horizontal at 661.8 degrees add further clarification to that region of the diagram. Their photomicrograph of a diffusion study in which evidence for a fifth intermediate phase in the system is presented is of particular interest.

Recently additional work has been done by Smith[1] of this laboratory on the structure of the compounds in this system which has produced evidence for another compound. In one attempt to prepare single crystals of α(Al–V) at 670 °C, crystals were obtained whose X-ray diffraction patterns were entirely different from those of any of the phases previously identified. Chemical analyses of these crystals showed them to contain 20.9% vanadium. Thus, another peritectic compound corresponding to approximately Al_7V appears to be quite probable. If another compound does exist in the system the authors feel its peritectic horizontal will be very close to that of α(Al–V).

The higher peritectic temperature of both α(Al–V) and β(Al–V) reported by Elliott and Mondolfo are a little disturbing. The possibility of super-cooling during thermal analysis does not seem likely since the breaks were also observed on heating curves of samples which had been annealed at 625 °C before heating. Also quenches made from 710 and 750 °C place the peritectic horizontals for α(Al–V and β(Al–V) below these respective temperatures as is shown in this paper. In addition to the 17% vanadium specimen, (Figs. 5 and 6) a 6.3% vanadium and the 10.1% vanadium were also annealed and quenched from 710 °C

[1] J. F. Smith, private communication, October 1954.

and gave similar evidence of having undergone peritectic decomposition at or below that temperature. Similarly in addition to the 23.8% vanadium alloy (Figs. 7 and 9) the 6.3, 10.1, 17.7 and a 27.2% vanadium alloys quenched from 750 °C all gave evidence of having undergone peritectic decomposition of β(Al–V) at that temperature.

Mr. Gonser points out that both aluminum and vanadium of higher purity than those used in this study are available. About 50 grams of 99.99% aluminum was obtained from the Aluminum Company of America which was used in determining some of the critical points in the aluminum-rich end of the diagram. The melting point of aluminum and some of the points on (Al) and α(Al–V) peritectic horizontals were determined on this material. Iodide vanadium is not commercially available and we do not have equipment for iodide processing in our laboratory. We have received samples of other metals which were prepared by the iodide method from Battelle for which we have been most appreciative but did not wish to trouble them for vanadium.

Actually no real difficulty was encountered from volatilization of aluminum in preparing the alloys. The vanadium-rich alloys analyzed from 1 to 2% lower in aluminum than the intended composition. This the authors attributed to a slight loss of aluminum vapor in the arc.

PARTIAL PHASE DIAGRAM OF THE IRON-CERIUM SYSTEM

By James O. Jepson and Pol Duwez

Abstract

The phase diagram up to 5 weight per cent cerium and the structure of the intermediate phases of the iron-cerium system have been studied. It is established that the solubility of cerium in both alpha and gamma iron is less than 0.5 weight per cent. The alpha to gamma transformation temperature is very slightly raised by the addition of cerium and it is probable that the diagram is of the peritectoid type. The iron-rich intermediate phase corresponds to the composition $CeFe_5$ and decomposes at 1060 °C (1940 °F). The second intermediate phase is $CeFe_2$, which has a face-centered cubic structure of the C15 ($MgCu_2$) type, $a = 7.302$ Å.

As a result of a literature survey, it was found that the iron-cerium system had not been studied since 1917 (1)[1], when Vogel published a tentative phase diagram. A portion of this diagram is reproduced in Fig. 1. A new investigation of this system was motivated by two reasons: first, a better knowledge of the iron-cerium system would eventually be useful in understanding the more complex problem of the effect of rare earth additions to steel; second, the diagram presented by Vogel was thought to be inaccurate. In particular, the high solubility of cerium in alpha and gamma iron (12 and 15% respectively) found by Vogel appeared to be very improbable, considering the fact that the atomic diameter of cerium is about 45% greater than that of iron.

Experimental Procedure

The iron used in this investigation was obtained in the form of a vacuum-cast ingot from the National Research Corporation, Cambridge, Mass. A typical analysis supplied by the manufacturer is: 0.001% nitrogen; 0.02% oxygen; 0.005% hydrogen; 0.005% carbon; 0.01% silicon; and traces of other metals. The cerium, obtained from the Institute for Atomic Research of the Iowa State College, has the

[1] The figures appearing in parentheses pertain to the references appended to this paper.

A paper presented before the Thirty-sixth Annual Convention of the Society, held in Chicago, November 1 to 5, 1954. Of the authors, James O. Jepson is research engineer, Jet Propulsion Laboratory and Pol Duwez is professor of mechanical engineering, California Institute of Technology, Pasadena, Calif. Manuscript received April 15, 1954.

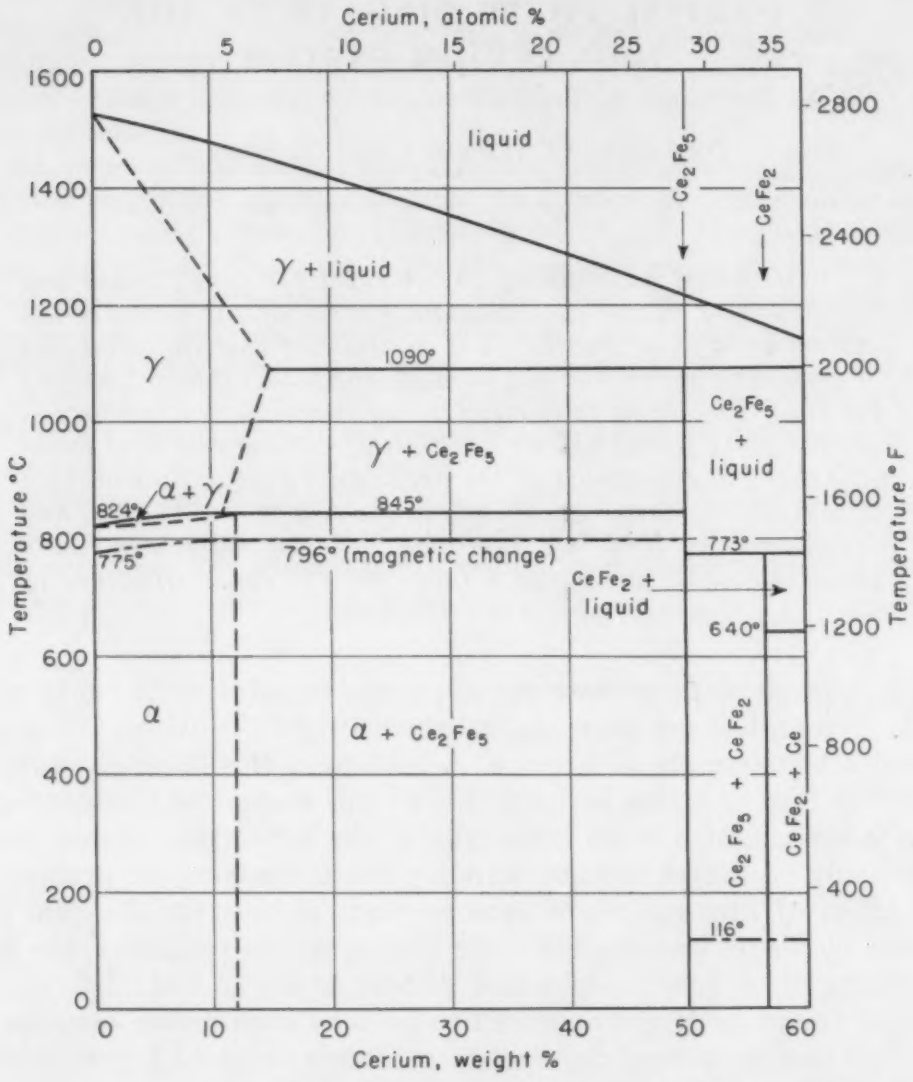


Fig. 1—Portion of the Iron-Cerium Phase Diagram as Published by Vogel (1).

following spectrographic analysis: 0.03% calcium; 0.01% iron; 0.02% magnesium; 0.02% praseodymium; 0.03% silicon; 0.05% tantalum; no trace of lanthanum, neodymium, or thorium.

All the alloys used in this investigation were melted in an arc under helium atmosphere. In order to minimize the oxidation of cerium previous to melting, the specimen was processed in the arc melting unit immediately after weighing.[2] The specimens weighed approximately 10 grams, except for the high percentage cerium alloys, which weighed as low as 0.5 gram. Various melting procedures were tried in an effort to overcome serious weight losses. The method finally used was to have the cerium completely surrounded by iron, either by insertion of the solid cerium in a cavity drilled in a piece of iron and covered with an

[2] A 0.7-gram sample of cerium showed no measurable (0.1 mg) weight gain on exposure to air for 2 hours.

iron cap or by wrapping iron foil around the cerium, so that the arc did not come in contact with the cerium. In spite of these precautions, some of the cerium was lost and the actual composition of the specimens was based on a chemical analysis of cerium after melting (see Appendix for method of analysis).

The arc melted buttons containing up to 5% cerium[3] were ductile enough to be cold-rolled into small rectangular bars. The specimens were then sealed in evacuated fused silica tubes and homogenized by holding at 1095 °C (2000 °F) for 2 hours and slow-cooled at a rate of 55 °C per hour to below the allotropic transformation temperature (800 °C) and furnace cooled from that point to room temperature. All the subsequent heat treatments, carried out in evacuated fused silica tubes, were isothermal, followed by a quench in which the tubes were broken under water.

Thermal analysis to detect the allotropic transformation temperature was carried out in vacuum using small specimens heated by a molybdenum coil furnace. The heating and cooling rates used were 1.0 to 2.5 °C per second and 0.6 to 1.6 °C per second, respectively; the average of the temperatures found on heating and cooling was used.

The temperature of incipient melting of some alloys in the range 0.5 to 5% cerium was obtained by microscopic observation. A specimen in the form of a bar about ⅛ inch in cross section and 1 inch in length was placed in a tube furnace where an approximately linear temperature distribution existed. The temperature at both ends of the bar was measured by thermocouples which were inserted into small holes drilled into the specimen. Because of the relatively high conductivity of the alloy, it was assumed that the temperature distribution along the specimen was linear and thus the temperature could be obtained at each point. The specimen was then examined under the microscope along its length, and the point (thus the temperature) at which the transformation occurred could be determined. For all microscopic observations the specimens were polished by conventional methods, finishing with Hyprez diamond compound 1-W-47 and etching with a 2% nital solution.

The structures of the intermediate phases were investigated by X-ray diffraction, using a 14.32-centimeter powder camera and cobalt $K\alpha$ radiation. The film was mounted asymmetrically in the camera (Straumanis method) and the readings were corrected for film shrinkage. To obtain sharp diffraction patterns, especially for the high angle reflections, 200 mesh powder, obtained by crushing or filing, was annealed in vacuum for 2 hours at 540 °C (1005 °F). Intensity measurements were made using the same annealed powder and a recording X-ray spectrometer.

[3] All compositions are given in weight percentages.

Phase Boundary Determinations

The phase boundaries established as a result of the present study up to 5% cerium are presented in Fig. 2. The alloy containing 0.19% cerium was a one-phase iron solid solution. In the next alloy, containing 0.48% cerium, a very small amount of a second phase was found after quenching from 1095, 1040, 980, 925, 870, and 815 °C (2000, 1905, 1795, 1700, 1600 and 1500 °F). The solubility of cerium in both alpha and gamma iron is therefore close to 0.4% cerium. Two phases were found in alloys containing 0.66, 1.57, 2.40, 3.40, and 4.62% cerium. An X-ray powder pattern of a two-phase 1.57% cerium alloy, as compared to a pure iron pattern, showed no change in the lattice parameter to an accuracy of 0.001 Å. To detect the effect of the solid solution of cerium on the lattice parameter a more precise back-reflection technique is necessary.

The effect of cerium on the allotropic transformation of iron was studied by thermal analysis. The thermal analysis apparatus was calibrated using pure iron, whose transformation temperature averaged 910 °C (1670 °F). The transformation temperature was 914 °C (1680 °F) for the alloy containing 0.19% cerium. For the alloys containing more than 0.48% cerium the transformation temperature was practically the same, namely 920 °C (1690 °F), as indicated on the graph of Fig. 2. The fact that the addition of cerium raises the allotropic transformation of iron leads to the conclusion that the equilibrium diagram is of the peritectoid type. The approximate phase boundaries shown in Fig. 2 have been traced on the basis of this conclusion.

The temperature of incipient melting of alloys in the range 0.5 to 5% cerium was first approximately located by heat treating five specimens within this range of composition at 1095 and 1040 °C (2000 and 1905 °F). Microscopic observation indicated that incipient melting took place in all the specimens heated to 1095 °C (2000 °F). Two specimens containing 3.40 and 4.62% cerium were then heated to 1065 °C (1950 °F) and indication of incipient melting was found. Consequently, the incipient melting temperature was somewhere in the range from 1040 to 1065 °C (1905 to 1950 °F). The final measurement was made on two specimens containing 1.25 and 1.46% cerium using the "temperature gradient" method described under "Experimental Procedure." By this method the incipient melting temperature was found to be 1060 ± 5 °C.

In the diagram published by Vogel (1), based entirely on thermal analysis, two intermediate phases were assigned compositions corresponding to the formulae Ce_2Fe_5 (49.9% cerium) and $CeFe_2$ (55.6% cerium). In the present study, alloys were prepared in the range of 26.3 to 51.7% cerium and after being homogenized for 120 hours at 760 °C (1400 °F) were investigated by X-ray diffraction methods.

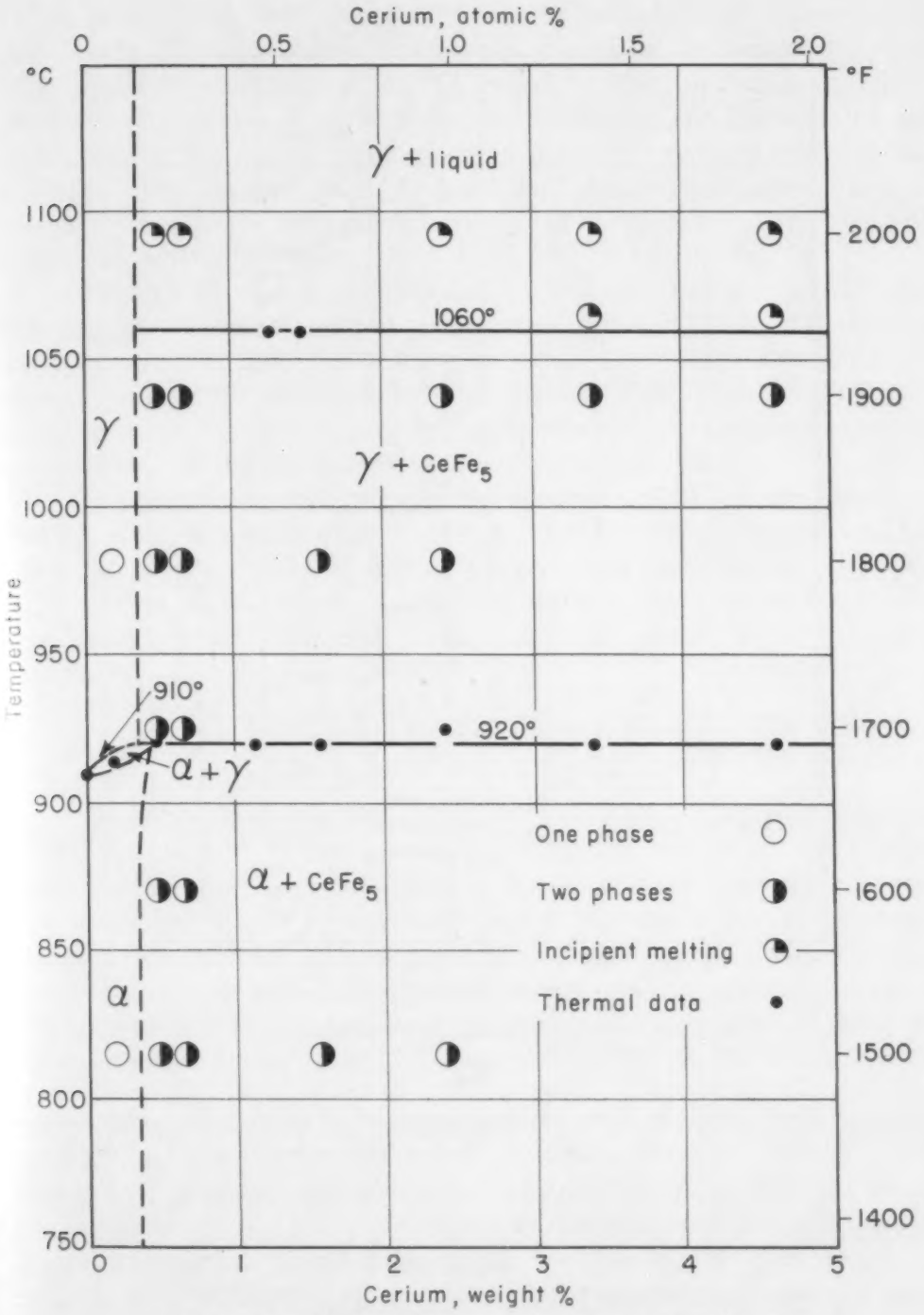


Fig. 2—Partial Phase Diagram of the Iron-Cerium System.

Two compounds were identified by their characteristic X-ray powder patterns and corresponded to the stoichiometric formulae $CeFe_5$ and $CeFe_2$.

The proof of the existence of $CeFe_5$ resulted from the examination of X-ray powder patterns near the stoichiometric composition $CeFe_5$ (33.5% cerium). In an alloy containing 32.3% cerium, the

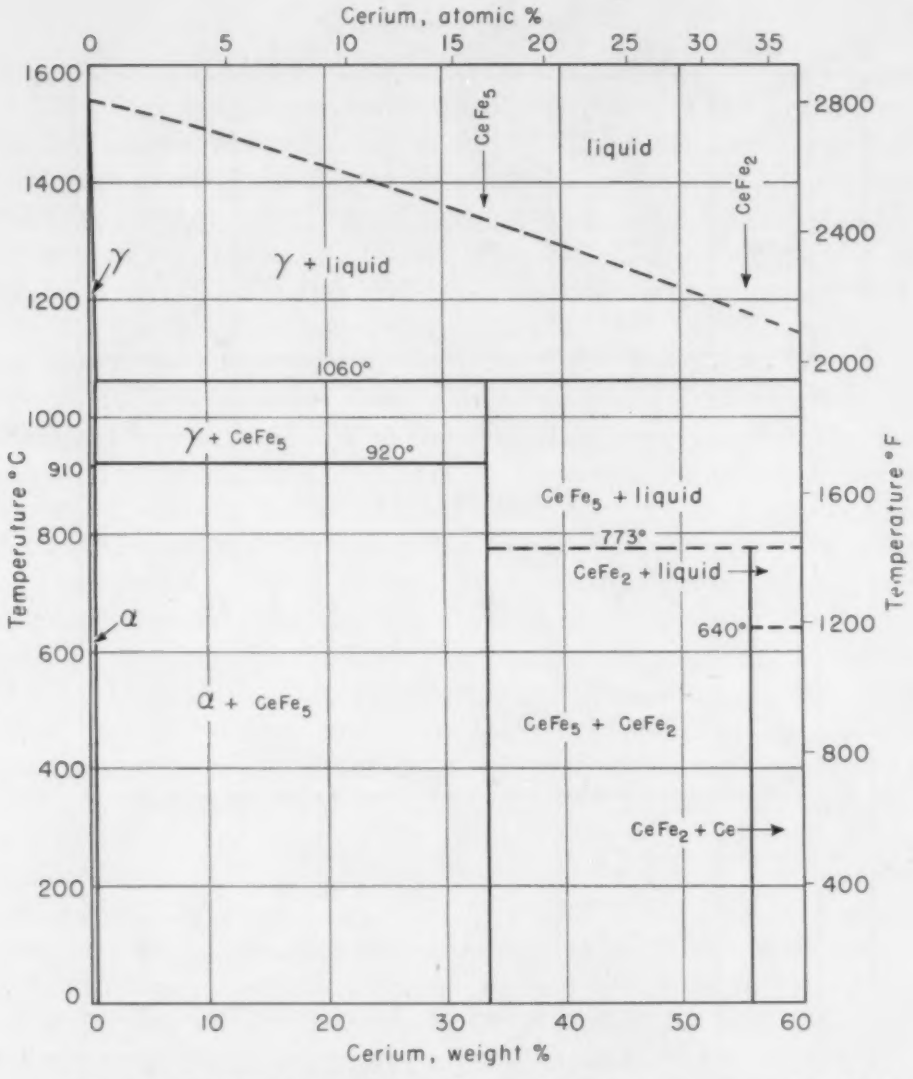


Fig. 3—A Modification of the Iron-Cerium Phase Diagram Proposed by Vogel (1) as a Result of the Present Study.

strongest line of alpha iron was present, and in an alloy containing 36.8% cerium, several reflections from the compound $CeFe_2$ were found. In addition, other alloys of compositions between $CeFe_5$ and $CeFe_2$ contained these two phases only.

In view of the results of the present study, a modification of Vogel's phase diagram is proposed; it is presented in Fig. 3. The main differences between the two diagrams are: 1) the solubility of cerium in iron is 0.4% instead of about 12%; and 2) the iron-rich phase corresponds to $CeFe_5$ rather than Ce_2Fe_5.

The Structure of the Intermediate Phases

A. The $CeFe_5$ Phase—The study of the $CeFe_5$ phase was made on an alloy containing 32.3% cerium. This composition is very close

to the ideal $CeFe_5$ stoichiometric formula (which is 33.5% cerium). The X-ray diffraction powder pattern contained 40 reflections, and only one very weak line at 2.02 Å could be identified as a reflection from the iron phase. No evidence was found for the presence of the $CeFe_2$ phase. An attempt was made to index the pattern with the aid of Hull-Davey charts. Only 32 lines out of the 39 could be indexed on the basis of a simple hexagonal lattice with an axial ratio of 0.844 and a unit cell with dimensions $a = 4.900$Å and $c = 4.136$ Å.

Although this tentative unit cell is probably not the correct one, it might be somewhat related to the true unit cell. This statement is based on the fact that two other intermetallic compounds which could logically be isomorphous with $CeFe_5$, namely $CeCo_5$ and $CeNi_5$, have been reported to have hexagonal symmetry with lattice parameters very close to those found in this investigation. According to Nowotny (2), the parameters of the $CeNi_5$ phase are $a = 4.874$ Å, $c = 4.004$ Å, and $c/a = 0.822$; according to Heumann (3), the parameters of the $CeCo_5$ phase are $a = 4.955$ Å, $c = 4.055$ Å, and $c/a = 0.818$. The crystal structure of these two phases is claimed to be that of the $CaZn_5$ type, space group C6/mmm (D^1_{6h}) with six atoms in the following positions:

1. A in (a) : 000
2. B_I in (c) : 1/3, 2/3, 0; 2/3, 1/3, 0
3. B_{II} in (g) : ½0½; 0½½; ½½½.

The suggestion that the crystal structure of $CeFe_5$ would also be of the $CaZn_5$ type is not substantiated by the results of the present investigation. As shown in Table I, the agreement between observed and computed $\sin^2 \theta$ is relatively good (especially for large Bragg angles), but obvious discrepancies exist between the intensities computed on the basis of a $CaZn_5$ type structure and the observed ones. In addition, as previously stated, 7 reflections out of a total of 39 could not be indexed on the basis of the assumed unit cell. As a consequence of these results, it appears that the crystal structure of $CeFe_5$ is not of the $CaZn_5$ type, but has a unit cell which is probably somewhat related to that of $CaZn_5$.

A logical consequence of the foregoing discussion is that $CeFe_5$ would not be isomorphous with $CeNi_5$ and $CeCo_5$. The crystal structure determinations of $CeNi_5$ by Nowotny (2) and of $CeCo_5$ by Heumann (3), however, were not sufficiently accurate to prove without doubt that these two compounds are of the $CaZn_5$ type. So little experimental data were presented by Heumann that the reliability of his conclusion concerning $CeCo_5$ cannot be estimated. The study of $CeNi_5$ by Nowotny was based on an X-ray diffraction powder pattern in which only 16 lines, all corresponding to Bragg angles less than 60 degrees, were indexed. The resolution of the camera (whose diameter is not given in the text) must have been small, since two lines computed to be sepa-

Table I
Diffraction Data for $CeFe_5$

hkl	d (Å)	$\sin^2\theta$ observed	$\sin^2\theta$ computed*	Relative Intensity visual	Intensity computed*
100	—	—	0.0444	—	15
001	—	—	0.0468	—	75
101	2.95	0.0922	0.0912	vw	584
—	2.85	0.0984	—	vvw	—
—	2.69	0.1103	—	vvw	—
110	2.44	0.1341	0.1333	vw	330
200	2.12	0.1786	0.1777	m	343
111	2.10	0.1813	0.1801	s	1000
002	2.06	0.1883	0.1870	w	289
201	1.88	0.2256	0.2245	vw	52
102	1.84	0.2356	0.2315	vvw	6
210	—	—	0.3110	—	4
112	1.58	0.3218	0.3203	vw	162
211	1.492	0.3595	0.3578	m	139
202	1.478	0.3662	0.3648	m	217
300	—	—	0.3999	—	56
003	—	—	0.4208	—	3
301	1.337	0.4477	0.4466	m	231
103	1.310	0.4658	0.4653	vw	48
—	1.289	0.4819	—	vvw	—
212	1.266	0.4993	0.4981	w	5
220	1.225	0.5335	0.5332	m	181
—	1.214	0.5425	—	w	—
113	1.201	0.5550	0.5541	m	189
310	—	—	0.5776	—	2
221	1.174	0.5799	0.5799	vvw	15
302	1.166	0.5889	0.5869	vvw	75
203	1.153	0.6019	0.5986	vvw	11
311	1.131	0.6250	0.6244	m	77
400	1.061	0.7110	0.7109	m	63
222	1.054	0.7198	0.7202	m	342
213	1.046	0.7316	0.7319	m	82
004	1.033	0.7494	0.7482	vw	61
401	—	—	0.7577	—	12
312	—	—	0.7646	—	5
104	1.002	0.7967	0.7926	vvw	2
303	0.9876	0.8203	0.8207	s	217
320	0.9737	0.8438	0.8442	vw	3
—	0.9683	0.8533	—	w	—
114	0.9526	0.8817	0.8815	vw	111
321	0.9478	0.8906	0.8909	s	123
402	0.9444	0.8970	0.8979	m	193
204	0.9297	0.9255	0.9259	w	232
410	0.9256	0.9337	0.9331	vw	152
223	—	—	0.9540	—	38
411	0.9040	0.9791	0.9798	s	133
—	0.9028	0.9816	—	w	—
—	0.9009	0.9857	—	m	—
313	—	—	0.9984	—	108

s = strong; m = medium; w = weak; vw = very weak; vvw = very, very weak

* Assuming the $CaZn_5$ type structure.

rated by 25 minutes of arc were not resolved. The intensities were estimated visually and although the agreement with computed intensities might be considered satisfactory, the number of reflections used for the analysis was too small to provide the necessary data for a reliable structure determination.

From the foregoing discussion, it appears that additional work is required in order to definitely establish that $CeNi_5$ and $CeCo_5$ have the $CaZn_5$ type structure. Since it is shown in this report that $CeFe_5$ is not of the $CaZn_5$ type, the possibility that the three compounds are isomorphous cannot yet be discarded.

Table II
Diffraction Data for $CeFe_2$

hkl	d (Å)	$\sin^2\theta$ observed	$\sin^2\theta$ computed	Relative Intensity visual	Relative Intensity computed
111	—	—	0.0450	—	128
220	2.57	0.1215	0.1200	w	654
311	2.19	0.1665	0.1651	m	1000
222	2.10	0.1813	0.1801	vw	150
400	—	—	0.2401	—	5
331	—	—	0.2851	—	35
422	1.488	0.3615	0.3601	w	235
511 – 333	1.403	0.4063	0.4051	w	319
440	1.289	0.4819	0.4802	w	248
531	—	—	0.5253	—	31
620	1.154	0.6005	0.6002	vw	133
533	1.114	0.6452	0.6452	vw	156
622	1.100	0.6618	0.6602	vvw	76
444	—	—	0.7202	—	3
711 – 551	1.022	0.7656	0.7653	vvw	30
642	0.9758	0.8402	0.8403	m	349
553 – 731	0.9507	0.8853	0.8853	s	714
800	0.9127	0.9604	0.9603	w	278

Quadratic form for cobalt $K\alpha_1$ ($\lambda = 1.78890$ Å):
$\sin^2\theta = 0.015005\ (h^2+k^2+l^2)$
Lattice parameter $a = 7.302$ Å
s = strong; m = medium; w = weak; vw = very weak; vvw = very, very weak

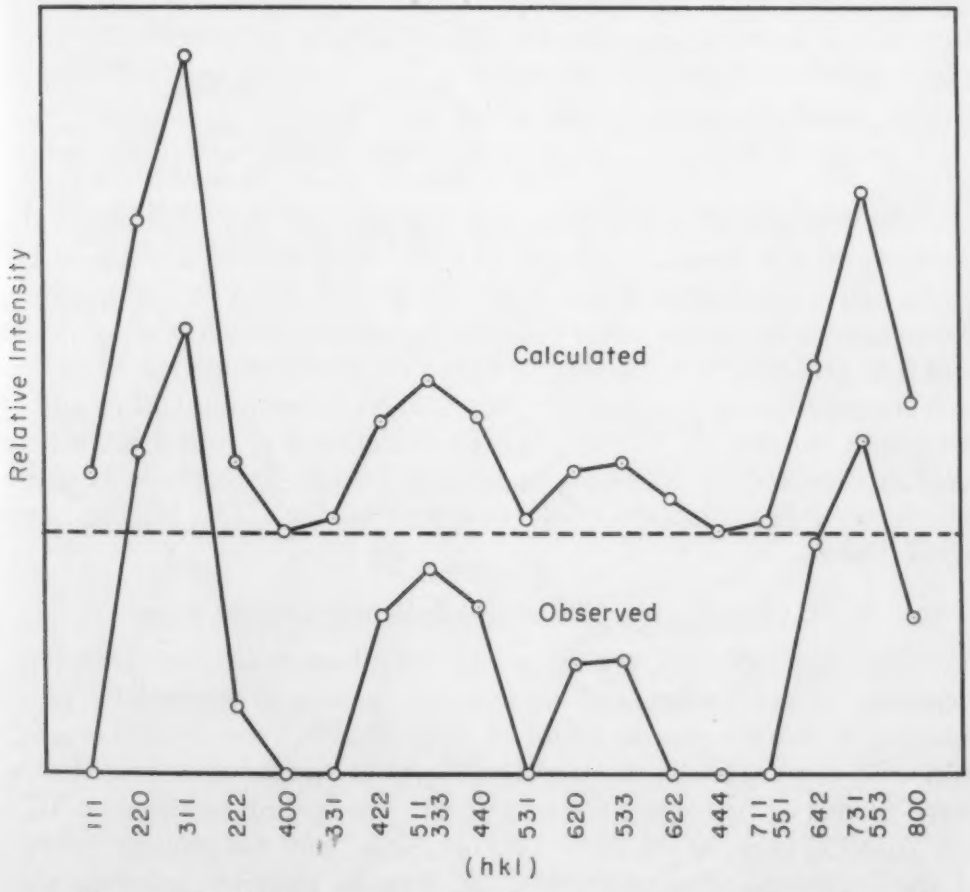


Fig. 4—A Graphical Comparison of Calculated and Observed Relative Intensities for $CeFe_2$ ($MgCu_2$ type).

B. The $CeFe_2$ Phase—The only information found in the literature on the crystal structure of $CeFe_2$ is one sentence inserted at the end of a paper by Fülling, Moeller, and Vogel saying that just before this paper was printed, Moeller found that the structure of $CeFe_2$ was of the $MgCu_2$ type (4). The present investigation confirms this statement. A specimen containing 51.7% cerium (the stoichiometric composition would correspond to 55.6% cerium) was studied; its diffraction pattern containing 13 reflections was readily indexed on the basis of a face-centered cubic cell with $a = 7.302$ Å. The results (Cf. Table II) show a reasonable agreement between observed and calculated $\sin^2 \theta$. The intensities of the diffraction maxima were computed on the basis of an $MgCu_2$ structure and were measured by means of a recording X-ray spectrometer. The correlation between computed and measured intensities is shown graphically in Fig. 4 and is close enough to be reasonably certain that the structure of $CeFe_2$ is of the $MgCu_2$ type.

The interatomic distances in $CeFe_2$, based on a unit cell with $a = 7.302$ Å, are: cerium to cerium, 3.16Å; iron to iron, 2.58 Å; and cerium to iron, 3.03 Å. A comparison of these distances with the atomic diameters of iron and cerium in their elemental state indicates that in the $CeFe_2$ structure the cerium atoms have been compressed 13% and the iron atoms have been expanded 2%. Changes in atomic size of the same order of magnitude also exist in the two compounds $CeNi_2$ and $CeCo_2$, which are isomorphous with $CeFe_2$ (5).

Conclusions

As a result of the present investigation, it was established that, contrary to the results of Vogel (1), the solubility of cerium in both alpha and gamma iron is less than 0.5%. The alpha to gamma transformation temperature is very slightly raised by the addition of cerium and it is probable that the diagram is of the peritectoid type. The iron-rich intermediate phase corresponds to the composition $CeFe_5$ and decomposes at 1060 °C (1940 °F). No evidence was found for a phase Ce_2Fe_5 reported by Vogel. The second intermediate phase is $CeFe_2$, which has a face-centered cubic structure of the C15 ($MgCu_2$) type, $a = 7.302$ Å.

Appendix

Determination of Cerium in Iron-Cerium Alloy

The method used, presupposing the absence of such interfering elements as chromium and manganese, consisted essentially of the solution of the samples in 50 ml of 20% H_2SO_4; the oxidation of the iron with 2 ml HNO_3; dilution to 200 ml of the solution boiled to remove oxides of nitrogen; the addition to the boiling solution of 10 ml 3% $AgNO_3$ plus 10 ml 25% $(NH_4)_2S_2O_8$, and subsequent titration of the cooled solution with 0.02 N. ferrous sulphate solution using several drops of ortho-phenanthroline indicator.

Only very small samples were available, and consequently analyses were not duplicated except in the case of high cerium content alloys. The precision of the method is ± 0.001 milliequivalents of cerium, or in terms of a 1 gram sample (about the average sample available), ±0.01% cerium. If desired, the titrated sample could be reheated to boiling, 10 ml of 25% $(NH_4)_2S_2O_4$ added to reoxidize the cerium, and the cooled solution again titrated.

ACKNOWLEDGMENT

This work was done at the Jet Propulsion Laboratory, California Institute of Technology, under contract number DA-04-495-ORD-18 with the Army Ordnance Corps, Washington, D.C. The authors wish to thank this agency for permission to publish the results of this investigation. The authors wish also to express their appreciation to Mr. Stephen Vango, who performed the chemical analyses.

References

1. R. Vogel, "Über Cer-Eisenlegierungen," *Zeitschrift für Anorganische und Allgemeine Chemie,* Vol. 99, 1917, p. 25.
2. H. Nowotny, "Die Kristallstrukturen von Ni_5Ce, Ni_5La, Ni_5Ca, Cu_5La, Cu_5Ca, Zn_5La, Zn_5Ca, Ni_2Ce, MgCe, MgLa, und MgSr," *Zeitschrift für Metallkunde,* Vol. 34, 1942, p. 247.
3. T. Heumann, "Beitrag zur Kenntnis der A_5B Phasen," *Nachr. Wiss. Göttingen,* Vol. 1, 1948, p. 21.
4. W. Fülling, K. Moeller and R. Vogel, "Röntgenographische Untersuchungen in den Systemen Cer-Kobalt un Cer-Nickel," *Zeitschrift für Metallkunde,* Vol. 34, 1942, p. 253.
5. R. Berry and G. Raynor, "The Crystal Chemistry of the Laves Phases," ACTA CRYSTALLOGRAPHICA, Vol. 6, 1953, p. 178.

THE TITANIUM-COBALT SYSTEM

By F. L. Orrell, Jr. and M. G. Fontana

Abstract

The phase diagram for part of the titanium-cobalt system has been determined, with particular emphasis on the titanium-rich portion. The principal techniques employed were metallography of cast and heat treated samples, detection of incipient melting, and X-ray diffraction analysis. Alloys containing from 1 — 55% by weight of cobalt were prepared by arc melting in a copper crucible furnace provided with a protective atmosphere of helium and a tungsten-tipped electrode.

Literature Review

AMONG the literature pertaining to titanium-rich phase equilibria in the titanium-cobalt system is a paper by Craighead, Simmons and Eastwood (1)[1] in which the authors suggest a solubility of 1.5% cobalt in alpha titanium and indicate that additions of cobalt lower the temperature of the titanium allotropic transformation. McQuillan (2) also reported on this effect at temperatures above 725 °C (1335 °F) and to cobalt contents of approximately 6% by weight.

The only extensive treatment of the titanium-cobalt system is given by Wallbaum (3) who stated:

a. There is a eutectic reaction between Ti and Ti_2Co occurring at 1590 °C (2895 °F).

b. The eutectic composition lies at 25% cobalt.

c. The compound Ti_2Co melts congruently at 1600 °C (2910 °F) and has a face-centered cubic crystal structure with 96 atoms per unit cell.

d. The compound TiCo is formed by peritectic reaction at 1450 °C (2640 °F) and has a body-centered cubic structure of the CsCl type.

Duwez and Taylor (4) have reported crystal structures for Ti_2Co and TiCo substantially in agreement with those given by Laves and Wallbaum (5), except that they did not find evidence of ordering

[1] The figures appearing in parentheses pertain to the references appended to this paper.

This paper is based on a dissertation submitted to The Ohio State University in partial fulfillment of the requirements for the degree of Doctor of Philosophy.

A paper presented before the Thirty-sixth Annual Convention of the Society, held in Chicago, November 1 to 5, 1954. Of the authors, F. L. Orrell, Jr. was formerly Titanium Alloy Manufacturing Division, National Lead Company Research Fellow at The Ohio State University, now with Dow Chemical Company, Midland, Michigan, and M. G. Fontana is head of the Department of Metallurgy, The Ohio State University, Columbus, Ohio. Manuscript received April 7, 1954.

(CsCl structure) for the TiCo phase as indicated by Laves and Wallbaum. Karlsson (6) has discussed a Co_3Ti_3O phase which he suggests (7) as being identical to the Ti_2Co phase of Laves and Wallbaum. Rostoker (8) has also examined the Ti_2X problem with results generally in agreement with those of Karlsson.

Experimental Procedure

Materials—All alloys studied in the course of this investigation were prepared from iodide crystal bar analyzing 99.9+% titanium. The crystal bar was manufactured by the New Jersey Zinc Company and was made available to this program by J. B. Johnson of the Air Material Command, Wright-Patterson Air Force Base. The cobalt used for the preparation of the alloys was generously supplied by Mr. J. Kurtz of the Kulite Tungsten Company and analyzed approximately 99.5% cobalt.

Preparation of Alloys—Alloys were prepared by arc melting weighed charges in a tungsten-tipped electrode arc furnace of the type described by McPherson and Fontana (9). A copper insert similar to that described by the Armour group (10) was used with the addition of a tungsten igniter button. Melting was performed in a protective atmosphere of Bureau of Mines Grade A helium. Three, five and ten-gram melts were made. The buttons were melted at least four times and from various directions (bottom, edge, etc.) to insure thorough mixing. The 10-gram buttons were cut into two pieces and melted from the cut faces as a further precaution against incomplete melting.

Heat Treatments—To protect the alloys samples from gaseous contamination during heat treatment they were sealed in Vycor capsules. In most cases the samples were separated from the capsule wall by a piece of titanium sheet. Prior to sealing, the capsules were carefully evacuated and filled with argon at a pressure sufficient to yield one atmosphere at the heat treating temperature.

The initial heat treatment for all alloys was a homogenization treatment. This consisted of heating alloys of 1 — 9% cobalt at 1025 °C (1875 °F) and the remainder at 930 °C (1705 °F) for 72 hours. Alloys of 1 — 6% cobalt were cold compressed to various degrees prior to the heat treatments. Following the homogenization treatment samples were equilibrated by heating for various combinations of time and temperature ranging from 4 hours at 1000 °C (1830 °F) to 564 hours at 675 °C (1245 °F). At the end of the equilibration period the samples were quenched by crushing the capsules under water.

The furnace apparatus provided specimen temperatures within ±10 °C of the temperatures reported.

Melting Range Determinations—Solidus data and liquid reaction isotherm temperatures were obtained by heating small samples of homogenized alloys at a series of temperatures above the homogeni-

zation temperature. When visual examination of the heat treated sample did not conclusively indicate that melting had occurred, the samples were examined metallographically for incipient melting.

Calibration of the furnace against the gold-point showed the specimen temperature for these treatments to be within ±3 °C of the temperature reported.

X-Ray Diffraction Techniques—X-ray diffraction patterns were obtained for many of the alloys for phase identification. The patterns were taken with a 114-millimeter diameter Debye-Scherrer powder camera, using filtered characteristic cobalt and molybdenum radiation. Specimens were prepared by filing or by crushing and screening through a 325-mesh screen. Exposure times of 8 to 16 hours were required.

Results and Discussion

The Phase Diagram—Alloys containing 1, 2, ... 9, 10 (in increments of 1%), and 10, 12, . . . 36, 38 (in increments of 2%) and 42, 46, 50, 52, 54, 55 weight % cobalt were prepared. These alloys were examined micrographically in the as-cast conditions (which revealed many of the important features of the system) and the heat treated condition. Melting determinations and X-ray diffraction analyses were also used for portions of the study. The results of these studies are the basis for the phase diagram presented in Fig. 1. Since, as is shown in Table I below, the analyzed composition agreed closely with the intended composition for nearly all of the alloys studied, data are plotted on the basis of nominal composition.

Metallographic Studies—Microscopic examination of alloys in the as-cast condition revealed several important characteristics of the diagram. Solidification of the melt by means of a eutectic reaction was

Table I
Chemical Analysis of Alloys

Nominal % Co	Composition (weight per cent) Ti	Co	Cu	W
1	98.91	1.09	none	none
2	98.03	1.97	—	—
3	96.66	3.34	—	—
4	95.89	4.11	—	—
5	95.01	4.99	none	none
6	93.93	6.07	—	—
7	92.99	7.01	—	—
8	91.96	8.04	—	—
9	90.25	9.75	—	—
10	89.76	10.25	—	—
12	87.80	12.20	—	—
14	86.18	13.82	—	—
16	83.70	16.30	—	—
18	82.15	17.85	—	—
24	76.71	23.29	none	none
28	71.77	28.23	none	none
32	67.75	32.25	none	none
38	63.68	36.32	none	none
55	45.17	54.83	—	—

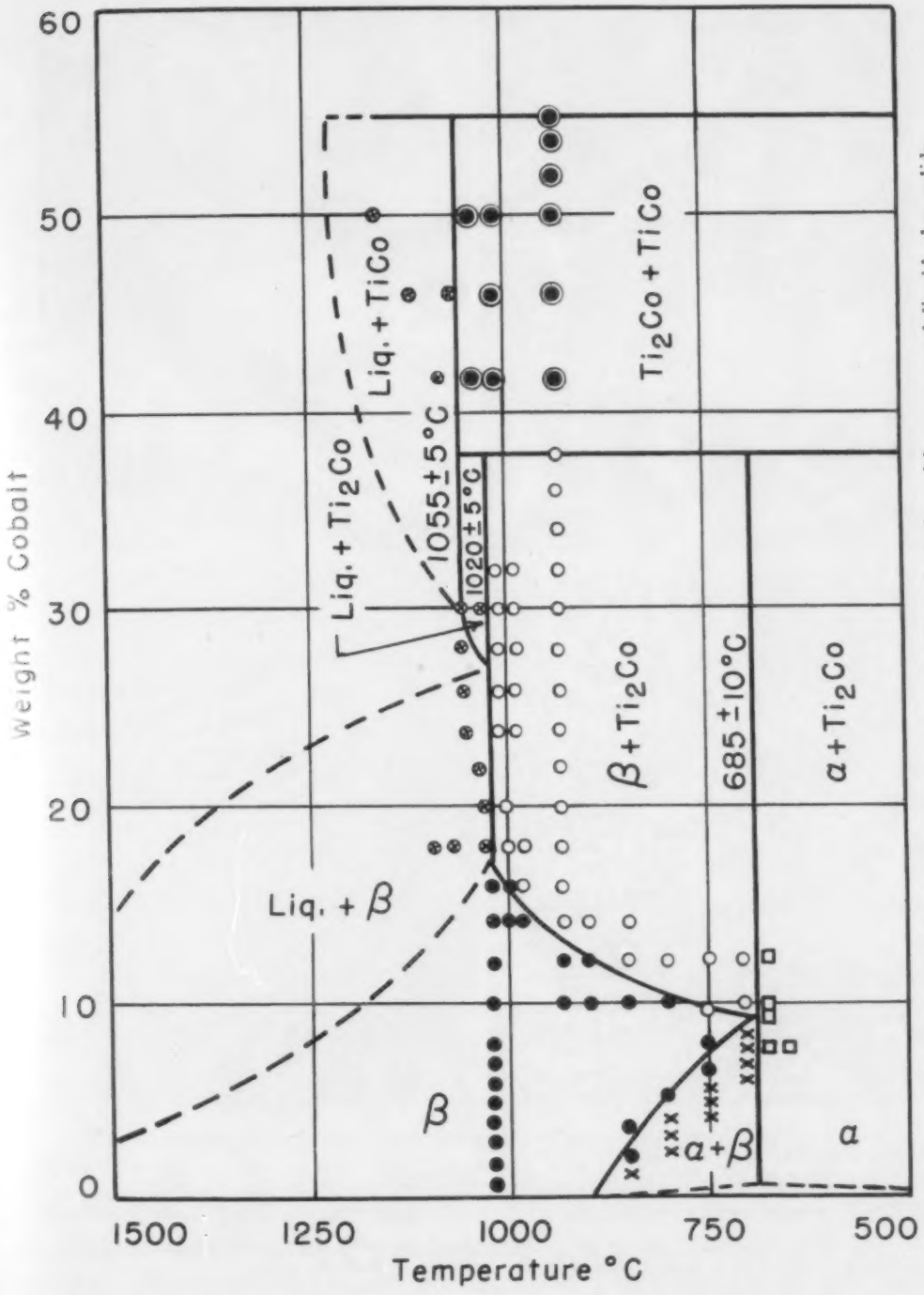


Fig. 1—Titanium-Cobalt Phase Diagram. Plotted circles with cross equal liquid plus solids.

clearly indicated in alloys above 16% cobalt. Fig. 2 shows a typical microstructure of primary dendrites surrounded by the eutectic matrix in a 22% cobalt alloy. Subsequent X-ray diffraction analysis of the homogenized alloy showed the phases to be beta (dark etching) and Ti_2Co (light). As the cobalt content increased beyond 16% the amount of primary dendrite decreased until at 28% the alloy was nearly 100%

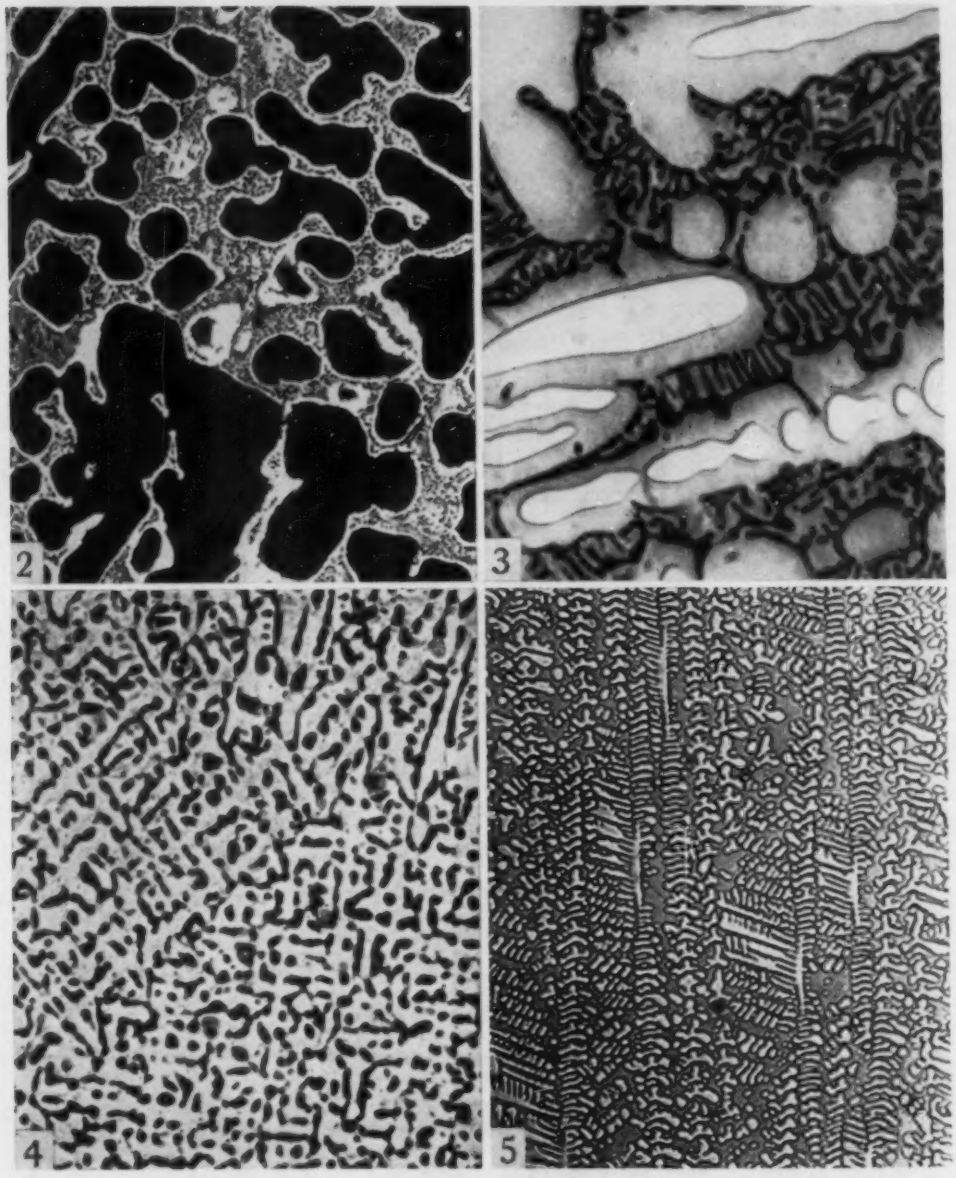


Fig. 2—22% Cobalt Alloy, As-Cast. Primary beta plus eutectic mixture of beta + Ti_2Co. Etchant: HF-H_2O_2 X 600

Fig. 3—38% Cobalt Alloy, As-Cast. Primary TiCo (white) plus peritectic rims of Ti_2Co in eutectic matrix of beta (black) + Ti_2Co (grey). Etchant: HF-H_2O_2 X 1200

Fig. 4—32% Cobalt Alloy, Water-Quenched After Annealing 72 Hours at 930 °C (1705 °F). Ti_2Co in a beta matrix (dark). Etchant: HF-H_2O_2 X 70.

Fig. 5—46% Cobalt Alloy, Water-Quenched After Annealing 72 Hours at 930 °C (1705 °F). TiCo in a Ti_2Co matrix. Etchant: HF-H_2O_2. X 70.

eutectic. For compositions above 28% cobalt the primary phase became Ti_2Co the amount of which increased as the cobalt content increased to 32%. On the basis of the as-cast microstructures and melting data for alloys in the 24–32% cobalt range the eutectic composition was estimated to lie at 27% cobalt.

Above 32% cobalt the nonequilibrium microstructures of the as-cast alloys indicated the peritectic reaction: liquid + TiCo $\leftrightharpoons$ Ti_2Co. This is shown in Fig. 3 by the primary dendrites of TiCo (white) which are surrounded by the peritectic reaction rim of Ti_2Co (grey) and the eutectic matrix of Ti_2Co + beta (black). As the composition of the alloys increased beyond 38% cobalt the amount of the non-equilibrium eutectic mixture of Ti_2Co + beta decreased but persisted up to 46% cobalt.

Microscopic examination of the homogenized alloys served mainly to indicate whether they were in the required homogeneous condition before proceeding with subsequent treatments. A typical microstructure of the beta + Ti_2Co alloys is shown in Fig. 4 for a 32% cobalt alloy. Here the primary phase is a light etching dendritic phase of Ti_2Co surrounded by a matrix of beta (dark etching). Fig. 5 of a homogenized 46% cobalt alloy shows primary dendrites of TiCo in a matrix of Ti_2Co. It is noteworthy that the dark etching constituent of the as-cast alloy (beta) has disappeared during homogenization.

The low-cobalt alloys indicated that 6 to 8% cobalt was required to suppress completely the beta $\rightarrow$ alpha transformation and retain the beta under ordinary quenching conditions. Alloys below 6% showed the typical acicular transformed-beta structure after quenching from the homogenization temperature.

Beta Decomposition—Alloys containing 1 to 18% cobalt were homogenized at 1025 °C (1875 °F), equilibrated at various temperatures from 650 to 1000 °C (1200 to 1830 °F), quenched, and examined micrographically. The microscopic examination revealed readily the isothermal decomposition or transformation of beta into alpha or into Ti_2Co as the composition of the alloy fell below or exceeded the beta solubility limits. The Widmanstatten arrangement of the precipitated Ti_2Co in the retained-beta matrix as shown in Fig. 6 is representative of the microstructures obtained in this portion of the study. From the results obtained thereby it was possible to plot on the phase diagram the $\beta/(\alpha+\beta)$ solvus and the $\beta/(\beta + Ti_2Co)$ solvus.

Alloys containing 8 to 12% cobalt were equilibrated at 650 and 675 °C (1200 to 1245 °F) for times ranging from 200 to 564 hours. Fig. 7 shows a typical microstructure in which the presence of the alpha phase (matrix) and Ti_2Co (spheroids) were confirmed by diffraction analysis. From these results the $\beta \rightleftharpoons \alpha + Ti_2Co$ isotherm was set at 685 ± 10 °C (1265 °F). A eutectoid composition of about 9% cobalt is indicated.

Intermediate Phases—Homogenized and quenched alloys in the composition range 20–55% cobalt were studied by X-ray diffraction methods to identify the equilibrium phases. In the samples taken from alloys in the 20–38% range (two-phase) a body-centered cubic phase (beta) was readily recognized which consistently showed a parameter

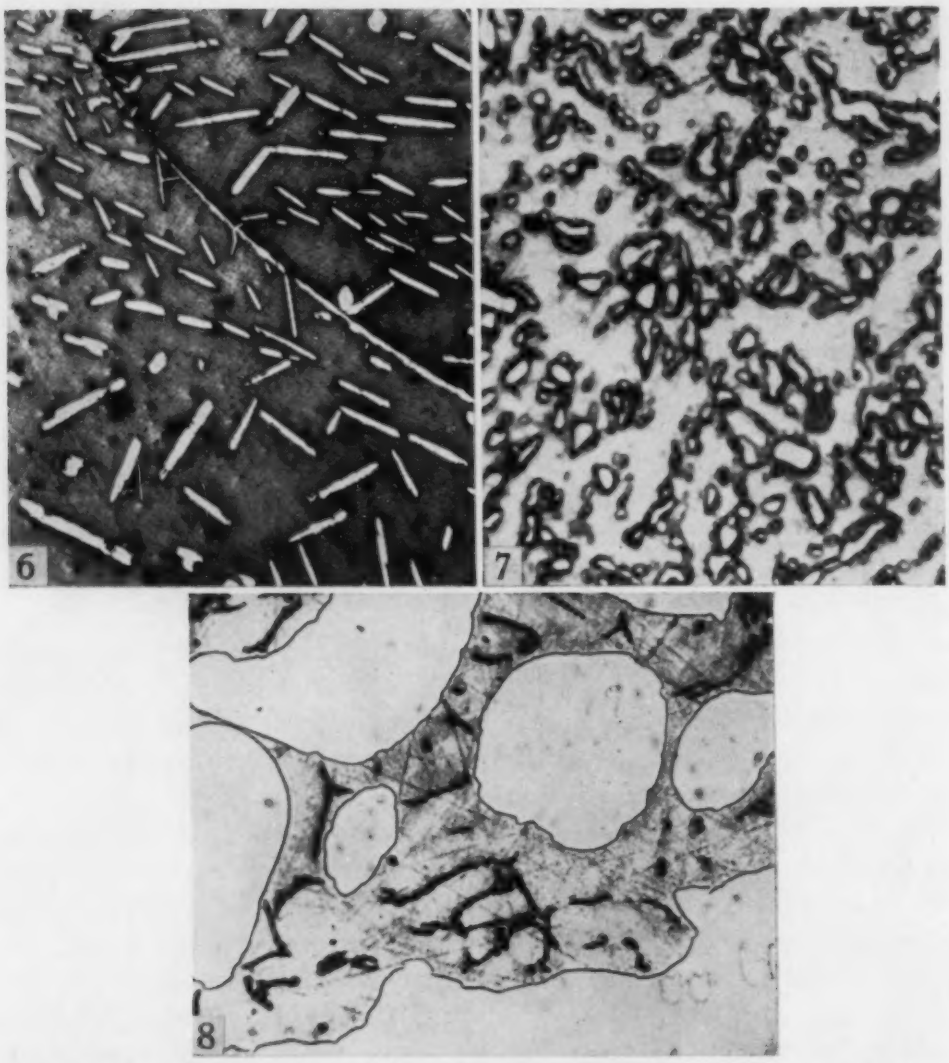


Fig. 6—12% Cobalt Alloy, Homogenized 72 Hours at 930 °C (1705 °F), Water-Quenched, Equilibrated 360 Hours at 700 °C (1290 °F), Water-Quenched. Ti_2Co in a matrix of retained-beta. Etchant: $HF-H_2O_2$. X 65.

Fig. 7—8% Cobalt Alloy, Homogenized 72 Hours at 1025 °C (1875 °F), Water-Quenched, Equilibrated 510 Hours at 650 °C (1200 °F), Water-Quenched. Ti_2Co in a matrix of alpha-Ti. Etchant: aqueous HF. X 1200

Fig. 8—46% Cobalt-Alloy, Homogenized 72 Hours at 930 °C (1705 °F), Heated to 1060 °C (1940 °F). TiCo grains (white) surrounded by nonequilibrium beta (black) and Ti_2Co from grain boundary melting. Etchant: $HF-H_2O_2$. X 375.

of 3.21Å. Since these samples were quenched from 903 °C (1705 °F), this value represents the effect of about 13% cobalt on the room temperature parameter of unalloyed beta-titanium (3.282Å) (11). Alloys in the 42–55% cobalt range also showed a body-centered cubic phase with a cell edge of 2.99Å. No evidence of ordering was noted. These results are in agreement with those reported by Duwez and Taylor (4) for TiCo.

Diffraction patterns for the second phase in all of the foregoing samples were readily indexed on the basis of a face-centered cubic

Table II
Comparison of Interplanar Spacings and Relative Intensities for Ti_2Co

hkl	This Investigation d(Å)	This Investigation I/I_o	Duwez & Taylor(4) d(kx)	Duwez & Taylor(4) I/I_o
111	6.407	4	6.53	w
220	—	—	3.97	vw
222	3.226	3	3.26	w
331	2.579	4	2.59	w
422	2.295	6	2.31	m
333	2.167	10	2.17	s
440	1.988	6	2.00	m
531	1.903	3	1.91	vw
442	1.877	4	1.88	w
622	—	—	1.72	w
444	1.629	1	1.63	w
711	1.580	2	1.59	w
642	1.507	1	1.51	w
731	1.468	4	1.472	w
800	1.412	1	1.413	vw
733	1.380	1	1.382	w
822	1.330	8	1.334	m
751	1.304	4	1.305	w
911	1.241	2	1.242	vw
842	1.231	2	1.234	w
933	1.136	6	1.136	m
862	1.109	3	1.109	vw
951	1.092	2	1.095	vw
666	1.087	2	1.087	vw
775	—	—	1.019	vw
884	0.9416	6	0.9423	m
777	0.9318	6	0.9330	m
10.64	0.9164	6	0.9172	m

Table III
Vacuum Fusion Analysis of Heat Treated Alloys

Nominal Composition	Thermal History	Gas Content-Weight Per Cent H_2	O_2	N_2
30% Co	72 hours at 930 °C	0.013	0.050	0.031
32% Co	72 hours at 930 °C	0.007	0.020	0.057
32% Co	72 hours at 930 °C plus 8 hours at 975 °C	0.011	0.041	0.077
38% Co	96 hours at 930 °C	0.003	0.073	0.067

Table IV
Melting Range Determinations

Alloy Wt. % Cobalt	Incipient Melting Observed, °C.	No Melting, °C.
18	1025	1018
20	1025	—
22	1032	—
24	1043	1014
26	1043	1014
28	1027	1014
30	1043	1014
32	—	1014
42	1080	1050
46	1060	1025
50	1150	1050

structure with a lattice parameter of 11.30Å. Extinctions, relative intensities, and "d" spacings (Table II) were in close agreement with those reported for Ti_2Ni (4), an isomorph of Ti_2Co. Gas contents of certain of the samples studied are shown in Table III.

Rostoker (8) has suggested a structure, "predominately cubic, $MgCu_2$ type," for the Ti_2Co phase. However, cobalt has an atomic

diameter about 14% less than that of titanium (12) and the usual condition for the Laves AB_2 phases is D_A/D_B ratio varying between 1.2 and 1.3 (13).

Both Rostoker (8) and Karlsson (6,7) have studied the structures of Ti_2X and Ti_4X_2O phases. Both report essentially the same structure (Fe_3W_3C type) for Ti_4Co_2O as that shown in this investigation for Ti_2Co. While Karlsson has stated that this same structure persists when cobalt atoms are substituted for titanium to the limit of Ti_3Co_3O, neither has discussed the effects of various oxygen contents

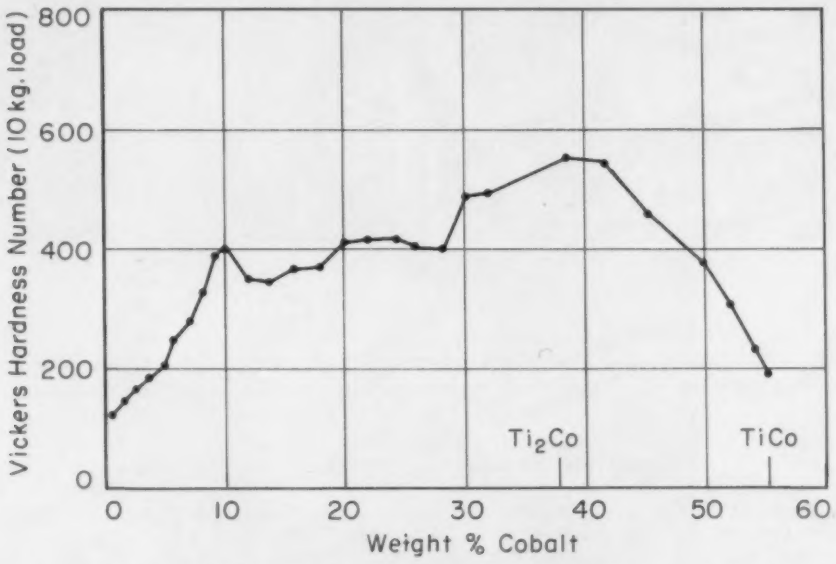


Fig. 9—Hardness Versus Composition for Binary Ti-Co Alloys. Water-quenched following homogenization.

on the structure of the Ti_4Co_2O phase. The results of this investigation show that the reported Fe_3W_3C type structure for the stoichiometric phase Ti_4Co_2O persists in the oxygenated Ti_2Co phase to low levels of gas content and suggest that cobalt may be similar in behavior to copper and nickel (8), for which both the Ti_2X and Ti_4X_2O phases have the Fe_3W_3C structure.

Melting Range Determinations—The method employed for determining melting ranges accurately established the temperature for the eutectic reaction $\beta + Ti_2Co \rightleftharpoons$ liquid at 1020 °C (1870 °F) and for the peritectic reaction liquid + TiCo $\rightleftharpoons$ Ti_2Co at 1055 °C (1930 °F). Fig. 8 shows incipient melting in a 46% cobalt alloy. Results of determinations are shown in Table IV.

Hardness of Titanium-Cobalt Alloys—The hardness of the alloys as quenched from the homogenizing temperature was measured on a Vickers Hardness Tester using a 10-Kg load and a 2/3" objective. The hardness as a function of composition for the alloys studied is shown in Fig. 9. Peaks at 10% and 38% and a pronounced minimum at 55% cobalt will be noted.

Summary

Additions of cobalt to titanium stabilize the beta phase and lower the transformation temperature until a eutectoid decomposition occurs between 9 and 10% cobalt and at 685 °C (1265 °F). Beta with 17% cobalt and Ti_2Co form a eutectic at 27% cobalt and 1020 °C (1870 °F). Ti_2Co is formed by peritectic reaction between TiCo and the melt at 1055 °C (1930 °F).

Acknowledgments

The authors express their gratitude to Dr. S. F. Urban, Titanium Alloy Manufacturing Division, National Lead Company, for his many contributions to the prosecution of this investigation and to R. V. Hilkert of the same company for the vacuum fusion analyses shown in Table III. The authors also thank J. B. Johnson of the Air Material Command, Wright-Patterson Air Force Base for supplying the iodide-titanium used in this investigation.

References

1. C. M. Craighead, O. W. Simmons and L. W. Eastwood, "Titanium Binary Alloys," *Transactions,* American Institute of Mining and Metallurgical Engineers, Vol. 188, 1950, p. 485–513.
2. A. D. McQuillan, "The Effect of the Elements of the First Long Period on the Alpha-Beta Transformations in Titanium," *Journal,* Institute of Metals, Vol. 80, March, 1952, p. 363–368.
3. H. J. Wallbaum, "The Systems of the Iron Group Metals with Titanium, Zirconium, Niobium, and Tantalum," *Archiv fur das Eisenhuttenwesen,* Vol. 14, 1941, p. 521–526.
4. P. Duwez and J. L. Taylor, "The Structure of Intermediate Phases in Alloys of Titanium with Iron, Cobalt, and Nickel," *Transactions,* American Institute of Mining and Metallurgical Engineers, Vol. 188, 1950, p. 1173–1176.
5. F. Laves and H. J. Wallbaum, "The Crystal Chemistry of Titanium Alloys," *Die Naturwissenschaften,* Vol. 27, 1939, p. 674–675.
6. N. Karlsson, "Metallic Oxides with the Structure of High-Speed Steel Carbide," *Nature,* Vol. 168, September 29, 1951, p. 558.
7. N. Karlsson, "An X-Ray Study of the Phases in the Copper Titanium System," *Journal,* Institute of Metals, Vol. 79, 1951, p. 391.
8. W. Rostoker, "Observations on the Occurrence of Ti_2X Phases," *Transactions,* American Institute of Mining and Metallurgical Engineers, Vol. 194, 1952, p. 209–210.
9. D. J. McPherson and M. G. Fontana, "Preparation and Properties of Titanium-Chromium Binary Alloys," TRANSACTIONS, American Society for Metals, Vol. 43, 1951, p. 1098–1125.
10. M. Hansen, H. D. Kessler and D. J. McPherson, "The Titanium-Silicon System," TRANSACTIONS, American Society for Metals, Vol. 44, 1952, p. 518–538.
11. B. W. Levinger, "Lattice Parameter of Beta Titanium at Room Temperature," *Transactions,* American Institute of Mining and Metallurgical Engineers, Vol. 197, 1953, p. 195.

12. W. Hume-Rothery, "The Structure of Metals and Alloys." 1950, p. 52–54. The Institute of Metals, London.

13. G. V. Raynor, "Progress In The Theory of Alloys." "Progress in Metal Physics," Vol. 1, 1949, p. 34. Interscience Publishers, Inc., New York.

DISCUSSION

Written Discussion: By W. Rostoker, supervisor, Physical Metallurgy Research, Armour Research Foundation, Chicago.

The publication of this paper fills one of the few remaining gaps in our knowledge of binary phase equilibria in titanium-base systems. The authors make reference to a technical note of a few years ago in which I reported that a Ti_2Co phase isomorphous with Ti_2Cu and Ti_2Ni was not found. Since the authors have identified such a phase metallographically and by X-ray diffraction analysis, there appears to be a contradiction. After reading the preprint, we melted a 10 gram ingot of normal composition Ti_2Co and examined it in both the as-cast and as-annealed (950 °C—24 hours) states, using metallography and powder pattern analysis. Our results are in complete agreement with the authors', that a single phase does exist at the approximate atomic proportions Ti_2Co, and that this phase is apparently isomorphous with Ti_2Cu and Ti_2Ni. The cube unit cell dimensions were calculated to be 11.28 kX. It must be inferred that the alloy examined and reported upon in my earlier technical note was not of the analysis intended.

Since for practical purposes, the phase equilibria in the region 0 to 20% cobalt is most important, the authors would perform a valuable service by replotting their data on a magnified scale. The diagram as shown does not permit easy or accurate reconstruction.

Can the authors make any estimate of the rates of eutectoid reaction? This is a point of some interest to alloy development.

Authors' Reply

The authors are grateful to Dr. Rostoker for his discussion and are pleased to have his more recent results corroborating our report of the existence of the Ti_2Co phase. His comment on the size of the figure showing the diagram is well made and steps are being taken to increase the scale of the reproduction. Since, in general, only a single heat treatment time was used at each temperature in the course of this study, the authors can make only the qualitative observation that the eutectoid reaction is "sluggish."

THE SYSTEM TITANIUM-ALUMINUM-MANGANESE

By R. F. Domagala and W. Rostoker

Abstract

Phase equilibria in the titanium-aluminum-manganese system have been investigated in the composition range defined by titanium and the two binary intermediate phases TiAl and $TiMn_2$ and in the temperature range 700 to 1200 °C (1290 to 2190 °F). Six isothermal sections, six vertical sections, projections of the beta space and of the surface of visible melting are presented.

Introduction

AS PART of a program under the sponsorship of the Watertown Arsenal, on the development of titanium-base ternary phase diagrams of technical importance, the titanium-rich corner of the system titanium-aluminum-manganese has been studied in detail. The scope of the investigation included the composition range roughly defined by the titanium corner and the first binary intermediate phases encountered at elevated temperature in titanium-aluminum and titanium-manganese systems. Phase equilibria were established in the solid state between 700 and 1200 °C (1290 to 2190 °F). A surface of incipient melting was constructed from measurements on a large number of alloys.

The binary system titanium-aluminum has been established (1)[1]. The alpha modification of titanium is stabilized to increasingly higher temperatures by progressive aluminum additions terminating in a peritectoid reaction ($\beta + L \longrightarrow \gamma$). The first intermediate phase (γ) has the atomic proportions TiAl, stoichiometrically 36% aluminum,[2] and possesses a substantial homogeneity range.

In the binary system titanium-manganese (2) the beta phase is stabilized to lower temperatures with increasing manganese content. The maximum solubility of manganese in alpha titanium is less than 0.5%. At about 550 °C (1020 °F), beta solid solution (20% manganese) decomposes eutectoidally into alpha and an intermediate phase

Sponsored by the Ordnance Corps, U. S. Army, Watertown Arsenal, Watertown, Mass., under Contract No. DA-11-022-ORD-272.

[1] The figures appearing in parentheses pertain to the references appended to this paper.
[2] All compositions refer to weight percentages.

A paper presented before the Thirty-sixth Annual Convention of the Society, held in Chicago, November 1 to 5, 1954. Of the authors, R. F. Domagala is associate metallurgist and W. Rostoker is supervisor, Physical Metallurgy Research, Metals Research Department, Armour Research Foundation of Illinois Institute of Technology, Chicago. Manuscript received January 27, 1954.

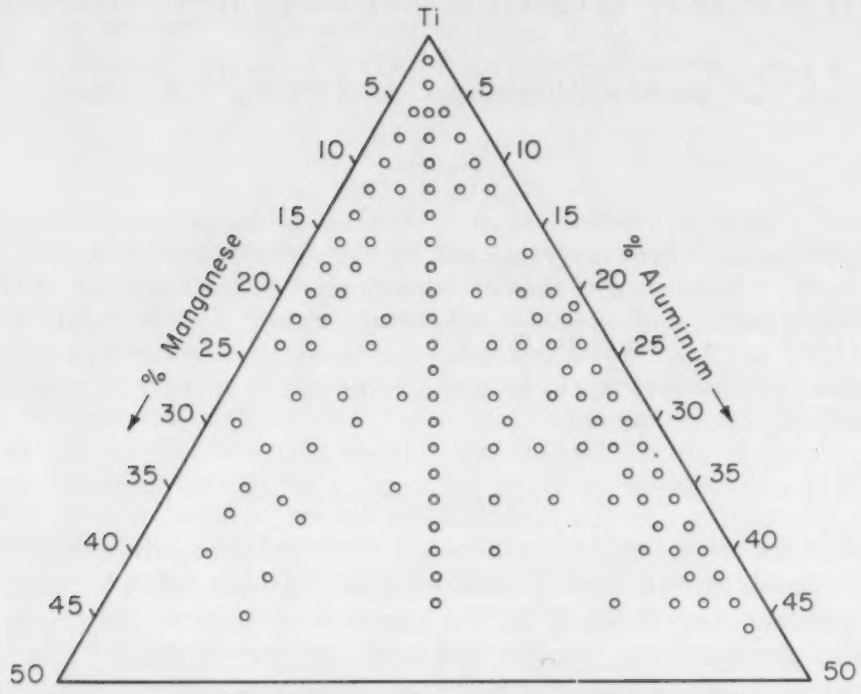


Fig. 1—Compositions of Alloys Prepared, System Titanium-Manganese-Aluminum.

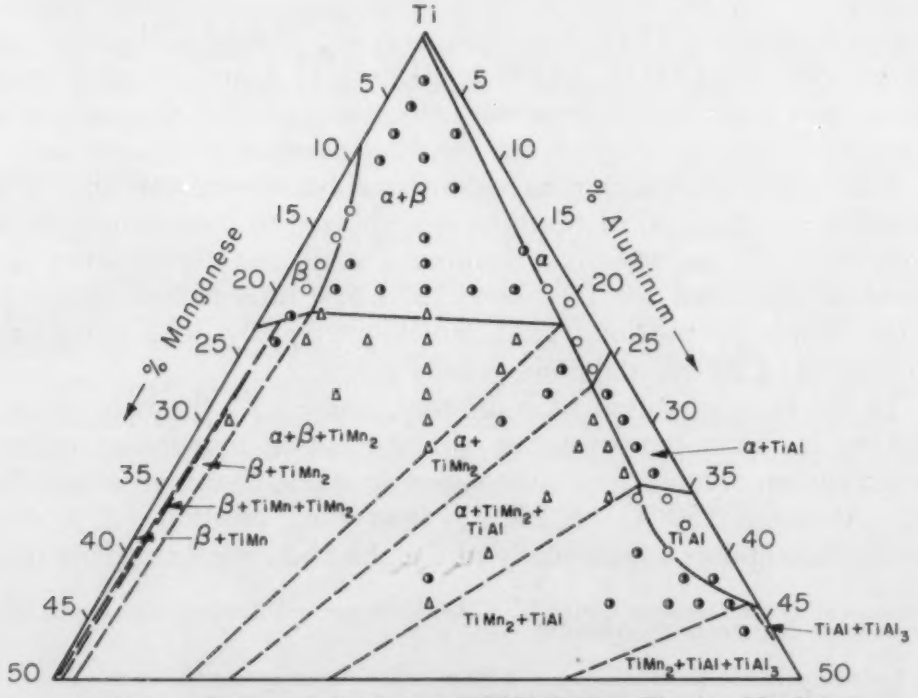


Fig. 2—Isothermal Section at 750 °C, System Titanium-Manganese-Aluminum. Open circle—one phase; half circle—two phases; triangle—three phases.

having the tentative formula TiMn. Two intermediate phases TiMn (53% manganese) and $TiMn_2$ (65% manganese) are known to enter into equilibrium with the primary solid solutions of titanium. Evidence

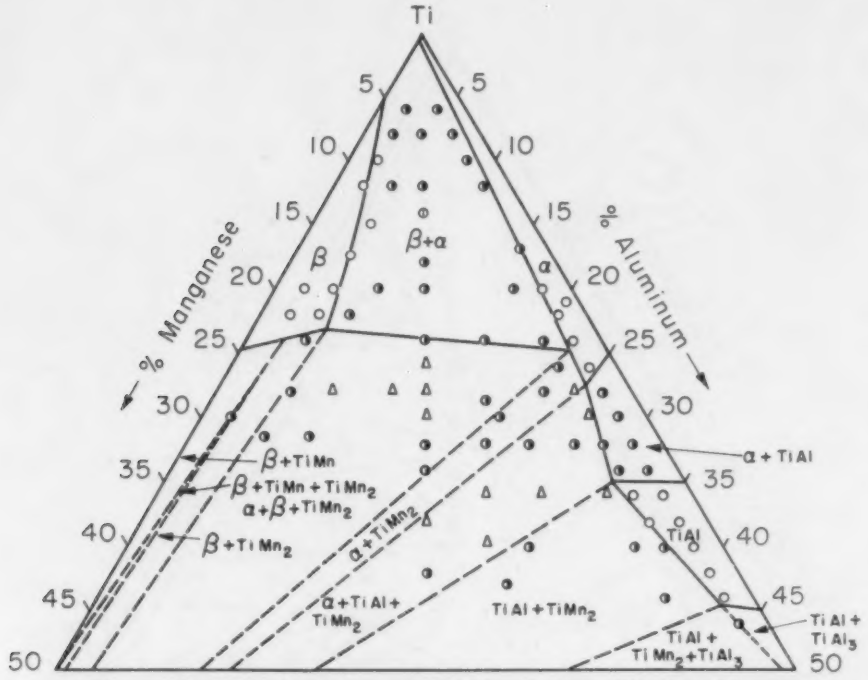


Fig. 3—Isothermal Section at 800 °C, System Titanium-Manganese-Aluminum. Open circle—one phase; half open circle—two phases; triangle—three phases.

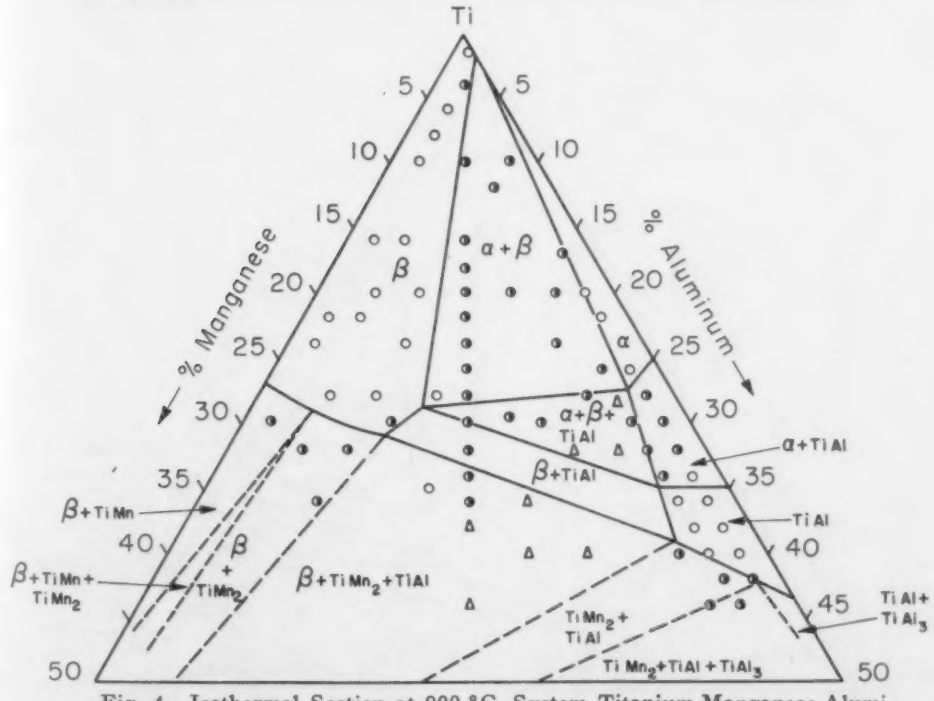


Fig. 4—Isothermal Section at 900 °C, System Titanium-Manganese-Aluminum. Open circle—one phase; half open circle—two phases; triangle—three phases.

has been presented (3) to show that the reported peritectic origin of TiMn is incorrect, and that this phase actually forms by a peritectoid reaction: $\beta + TiMn_2 \rightleftharpoons TiMn$ at some temperature between 900 and 1000 °C (1650 and 1830 °F).

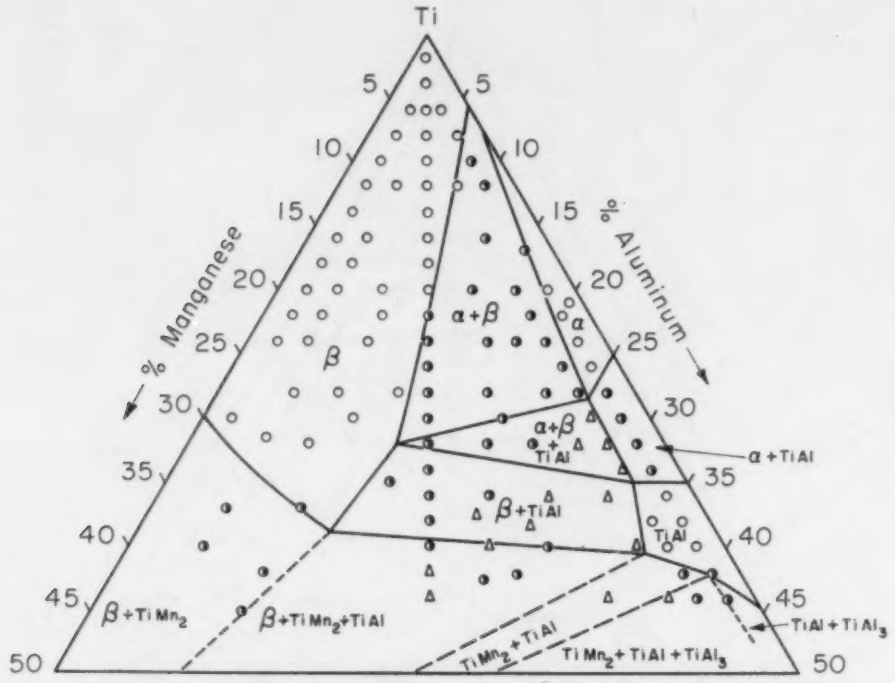


Fig. 5—Isothermal Section at 1000 °C, System Titanium-Manganese-Aluminum. Open circle—one phase; half open circle—two phases; triangle—three phases.

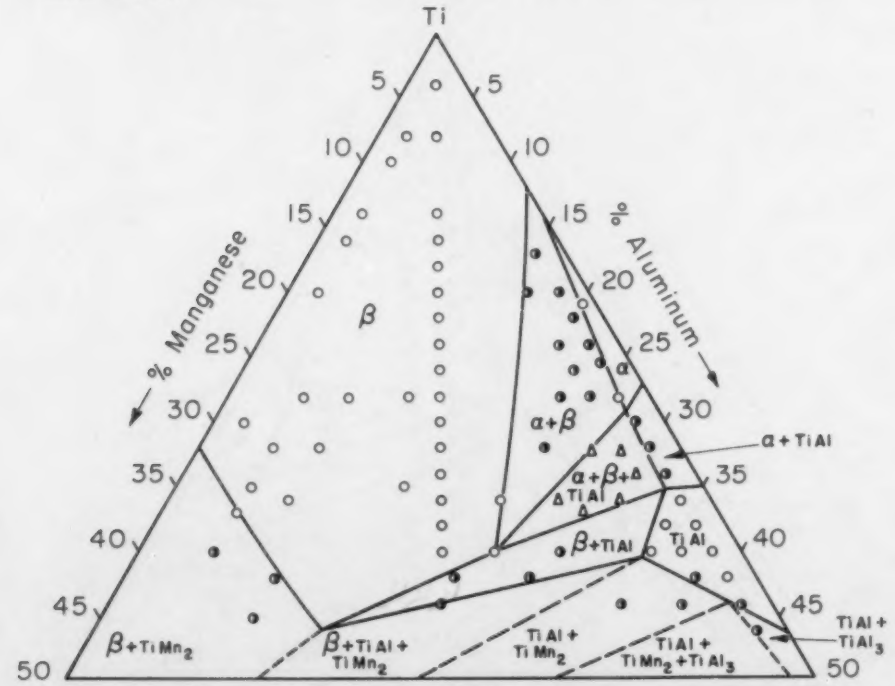


Fig. 6—Isothermal Section at 1100 °C, System Titanium-Manganese-Aluminum. Open circle—one phase; half open circle—two phases; triangle—three phases.

The ternary equilibrium at the titanium-rich corner may be expected to involve the interaction between the peritectoid, $\beta + TiMn_2 \rightleftharpoons TiMn$ (900–1000 °C) and the eutectoid, $\beta \rightleftharpoons \alpha + TiMn$ (550 °C) of the Ti-Mn system.

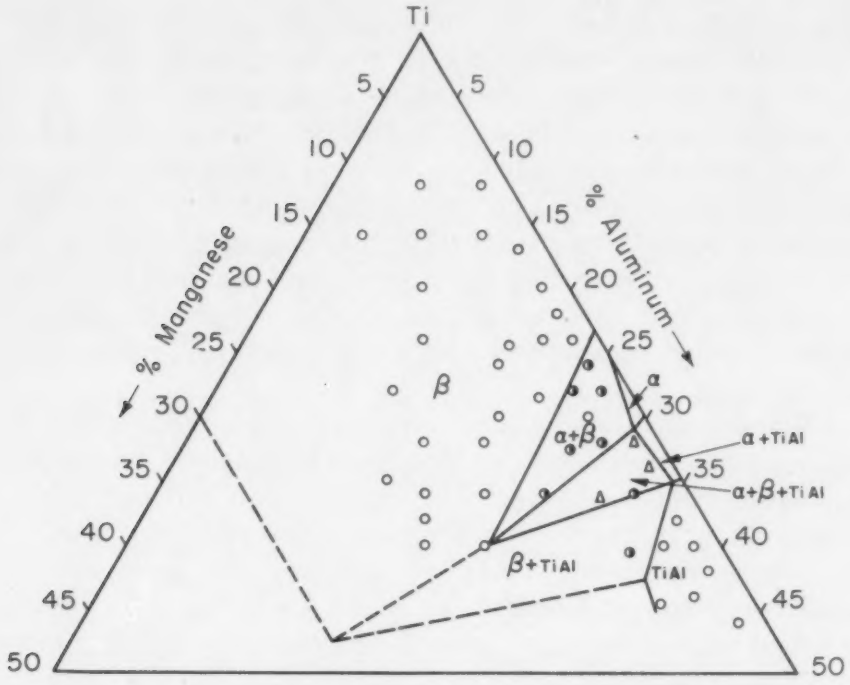


Fig. 7—Isothermal Section at 1200 °C, System Titanium-Manganese-Aluminum. Open circle—one phase; half open circle—two phases; triangle—three phases.

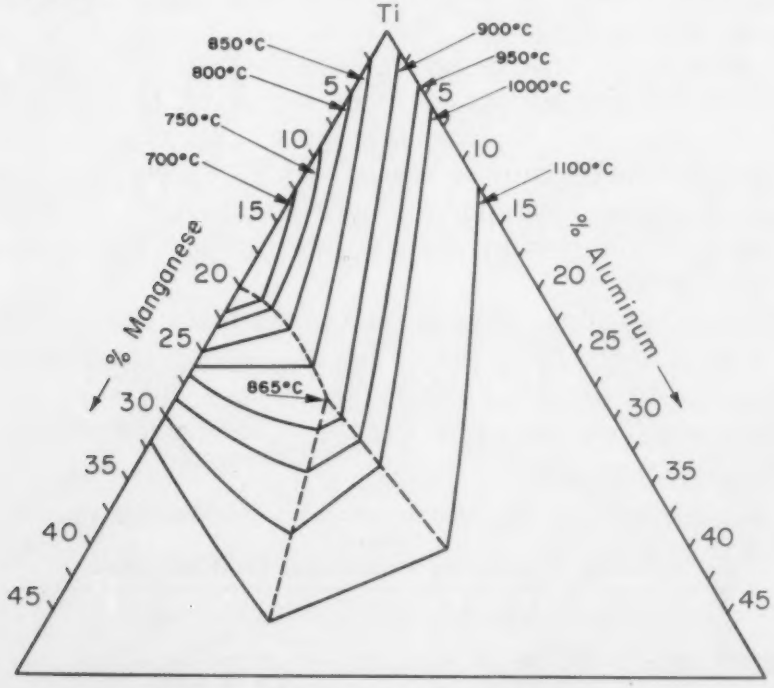


Fig. 8—Contour Projection of the Beta Space, System Titanium-Manganese-Aluminum.

Preparation and Treatment of Alloys

More than 100 alloy compositions were prepared for the study of this system. By preliminary arc melting experiments, two important

points were established. First, metallic volatilization was observed to be confined almost exclusively to the manganese. By comparison, titanium and aluminum volatilize to a negligible extent. Because of this, weight losses could be used to correct nominal to actual analyses. Chemical analyses conducted on selected alloys agreed closely with weight loss corrections. The compositions of alloys shown in Fig. 1 are believed to be correct to ± 1% manganese. Second, a systematic correlation exists between weight losses and nominal manganese content. By means of this correlation, it was possible to prepare alloys close to intended compositions by the addition of precalculated extra manganese.

Fifteen-gram alloy buttons were prepared by arc melting in a nonconsumable electrode furnace using inert atmosphere protection, and a water-cooled copper crucible. The construction and operation of this type of melting unit have been adequately described elsewhere (4). To ensure complete solution of all alloy additions, the ingots were remelted alternately on top and bottom as many as five times. This was accomplished without removal from the furnace by a suitable mechanism for flipping over the ingots.

Iodide titanium (99.97% titanium) was used as the alloy base. Aluminum of 99.99+% purity and a specially refined electrolytic manganese were used as alloy additions.

Specimens heat treated below 1100 °C (2010 °F) were enclosed in Vycor bulbs. For temperatures in excess of 1100 °C (2010 °F), quartz bulbs were used. Reduced pressures of argon prevented collapse of the bulbs at temperatures above 950 °C (1740 °F). Bulbs were simply evacuated for treatment at lower temperatures. Heat treatments were conducted in resistance element tube furnaces with a temperature control of ± 3 °C.

All as-melted alloys were given a preliminary homogenization anneal at 1000 °C (1830 °F) for 24 hours. Homogenized buttons were broken or cut to provide sufficient specimens for subsequent equilibrium anneals. Time schedules for the equilibrium anneals are given in Table I. No annealing times were carried beyond 30 days. To pre-

Table I
Schedule of Annealing Treatments, Ti-Al-Mn Alloys

Temperature—°C	Time—Hours
1300	2
1200	4
1100	7, 24*
1000	24
950	75
900	100
850	150
800	200
750	300
700	400

*Two sets of alloys annealed.

serve the equilibrium structure characteristic of the annealing temperature, bulbs were quenched into water and broken at the moment of quench.

Examination of Alloys

The isothermally annealed alloys were prepared for examination by metallographic polishing and etching. An etchant containing 10% HF, 60% HNO_3, and 30% glycerine was found suitable for the whole range of alloys. In specimens quenched from elevated temperatures the individual phases were sufficiently coarse to identify; this was not always possible at lower temperatures because of the fineness of the dispersions. It was therefore necessary to establish isothermal sections at least in part on the basis of the number of phases and the known forms of the binary systems, in conjunction with elementary requirements of the Phase Rule. Repeated construction of critical vertical sections served to establish phase boundaries with more exactness than the data for individual isothermal sections would permit. In particular the shape of the beta space supplied the key to the four-phase invariant reaction encountered between 700 and 1200 °C (1290 and 2190 °F).

It is generally very difficult to measure the liquidus and solidus temperatures of refractory metal systems by thermal arrest methods. An approximation of the solidus temperature is achieved by the use of incipient melting techniques. In principle, sharp corners of small specimens are observed to round or collapse on heating to a temperature above the solidus at which sufficient liquid has formed to destroy the ability of the specimen to retain its external shape. When this observation is made with an optical pyrometer, the temperature at which incipient melting occurs can be measured concurrently. Specimens are suspended on a tungsten wire in a high temperature vacuum induction furnace. The design and operation of this unit have been described elsewhere (4).

The incipient melting measurement apparatus was calibrated against a selection of pure metals with sufficiently diverse melting points that the correction curve covered the range encountered in the alloys under study. Thus, all corrections were based on interpolations. During testing, it was observed that alloys in the high manganese, low aluminum regions evolved volatilized manganese. For this reason, it is probable that such measurements are in error on the high side.

Phase Equilibria

Isothermal sections were constructed at 50-degree intervals between 700 and 1000 °C (1290 and 2190 °F), inclusive, and at 100-degree intervals between 1000 and 1200 °C (1830 and 2190 °F), inclusive. Six of these sections corresponding to the 750, 800, 900, 1000, 1100 and 1200 °C (1380, 1470, 1650, 1830, 2010 and 2190 °F) levels are shown in Figs. 2 to 7, documented with the observed data

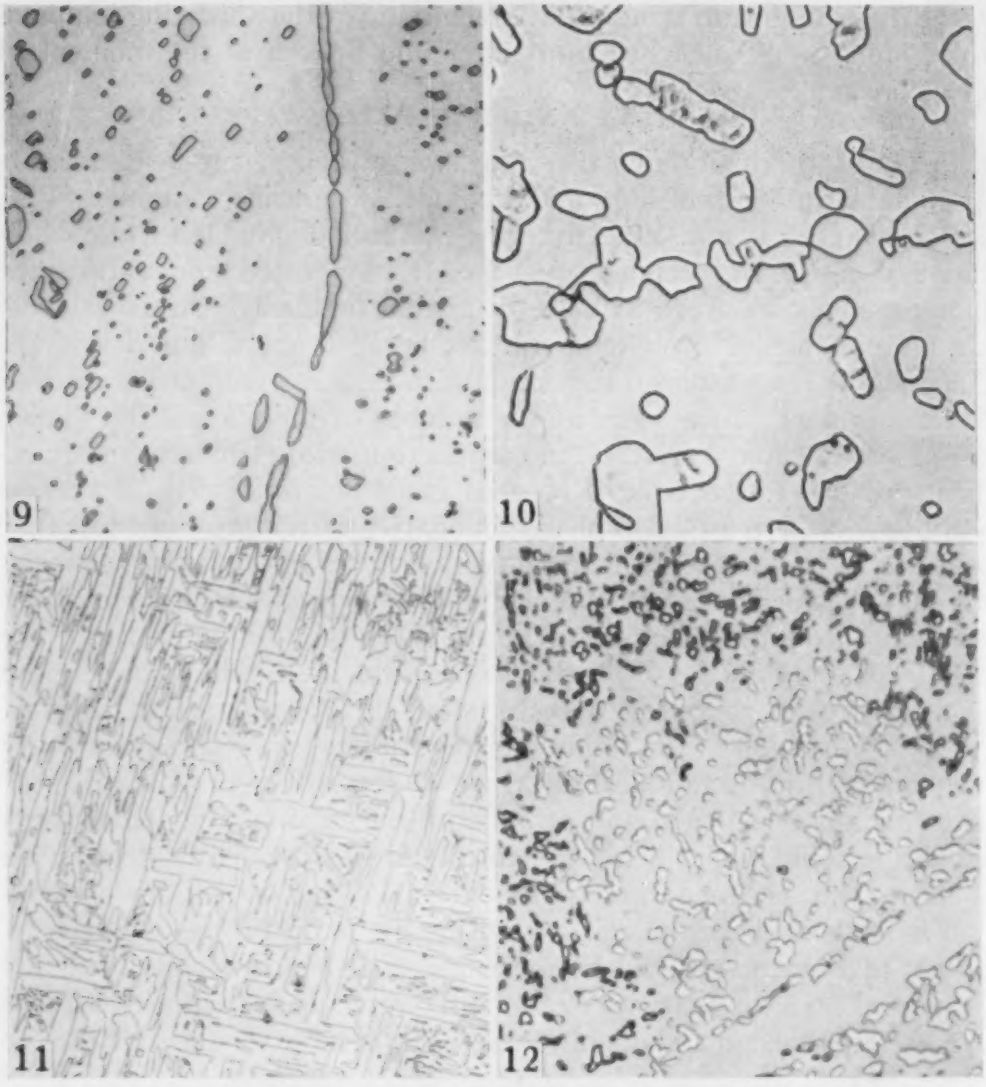


Fig. 9—Alloy with 14% Manganese, 14% Aluminum Annealed at 100 °C for 24 Hours Showing a Two-Phase Structure ($\alpha + \beta$). X 150.

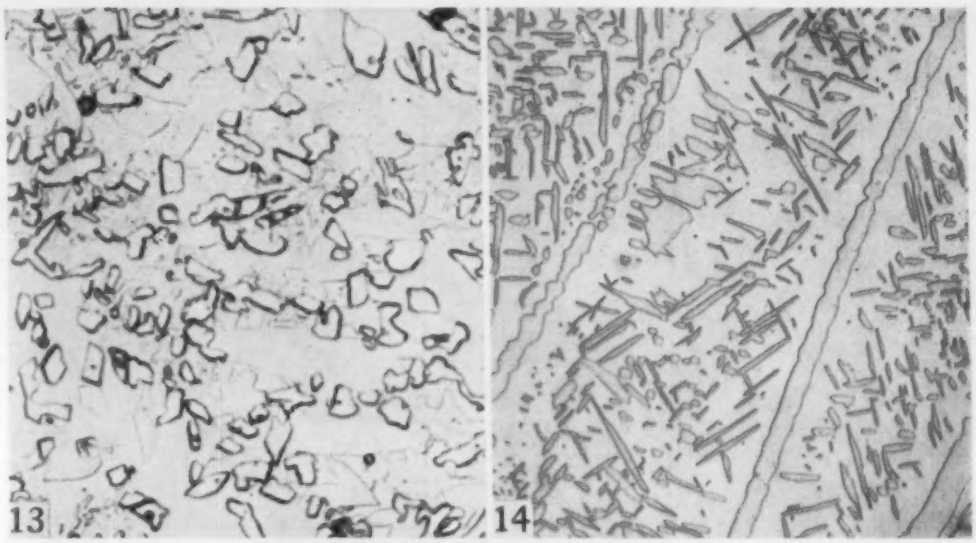
Fig. 10—Alloy with 22% Manganese, 22% Aluminum Annealed at 100 °C for 24 Hours Showing a Three-Phase Structure (β + $TiMn_2$ + TiAl). X 750.

Fig. 11—Alloy with 12% Manganese, 12% Aluminum Annealed at 800 °C for 200 Hours Showing Two-Phase Structure ($\alpha + \beta$). X 250.

Fig. 12—Alloy with 13% Manganese, 13% Aluminum Annealed at 800 °C for 200 Hours Showing Three-Phase Structure ($\alpha + \beta$ + $TiMn_2$). X 1000.

points. For the complete set of nine isothermal sections, the reader is referred to reference (5).

At elevated temperatures, the phase fields α, β, ($\alpha + \beta$), ($\alpha + \beta$ + TiAl), (β + TiAl), and (β + TiAl + $TiMn_2$) were clearly established. This set the pattern for subsequent transformations. The shape of the beta space as shown in Fig. 8 showed that the (β + TiAl) field narrowed with progressively lower temperatures. By the construction of critical vertical sections, the (β + TiAl) field was judged



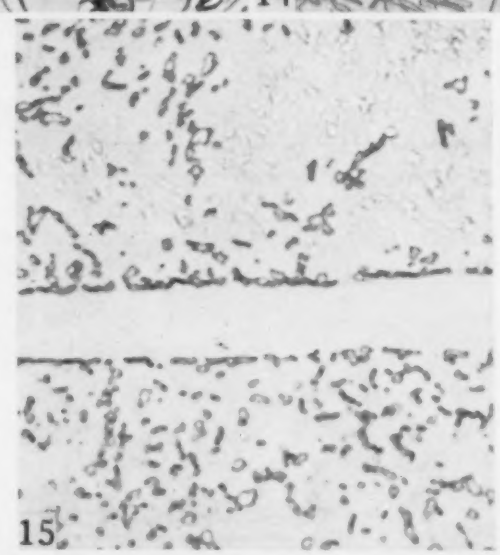


Fig. 13—Alloy with 19% Manganese, 19% Aluminum Annealed at 800 °C for 200 Hours Showing Three-Phase Structure (α + TiAl + $TiMn_2$). X 750.

Fig. 14—Alloy with 14% Manganese, 14% Aluminum Annealed at 900 °C for 100 Hours Showing Two-Phase Structure ($\alpha + \beta$). X 150.

Fig. 15—Alloy with 14% Manganese, 14% Aluminum Annealed at 800 °C for 200 Hours Showing Three-Phase Structure ($\alpha + \beta$ + $TiMn_2$). X 1000.

to disappear at 865 °C (1590 °F). This trend necessitates the occurrence of a four-phase reaction at that temperature of the type:

$$\beta + \text{TiAl} \rightleftharpoons \text{TiMn}_2 + \alpha$$

The TiMn phase is excluded from this reaction by an intervening (β + $TiMn_2$) field which necessarily persists even below the temperature of the binary peritectoid reaction: $\beta + \text{TiMn}_2 \rightleftharpoons \text{TiMn}$.

The (β + $TiMn_2$) field may be expected to enter into a second four-phase reaction of the type: $\beta + \text{TiMn}_2 \rightleftharpoons \alpha + \text{TiMn}$ before the disappearance of the beta space. No indications of this reaction were

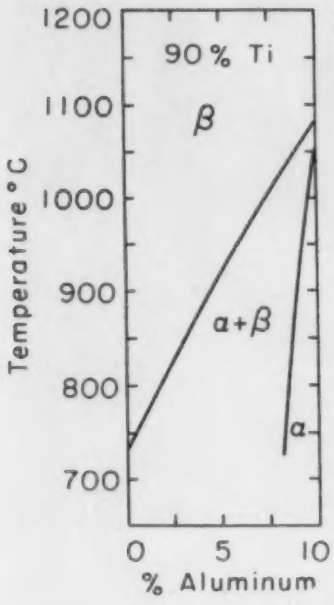


Fig. 16—Vertical Section at 90% Titanium, System Titanium-Manganese-Aluminum.

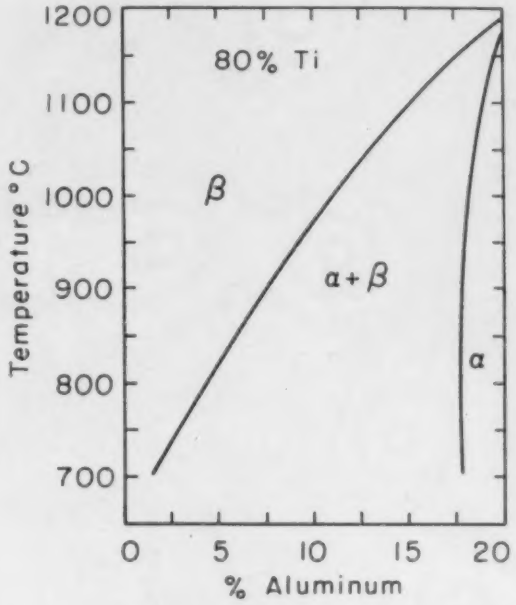


Fig. 17—Vertical Section at 80% Titanium, System Titanium-Manganese-Aluminum.

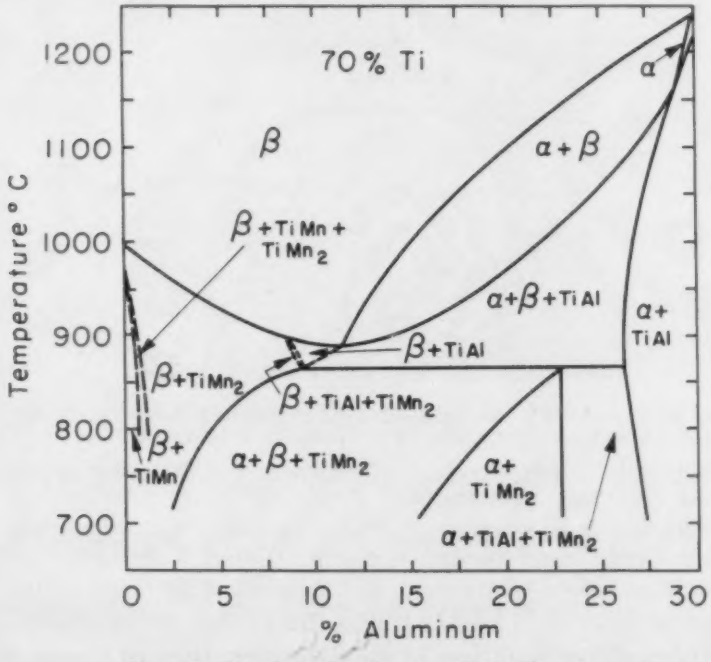


Fig. 18—Vertical Section at 70% Titanium, System Titanium-Manganese-Aluminum.

found at temperature levels as low as 700 °C (1290 °F) and it must therefore be inferred that it occurs between 550 and 700 °C (1020 and 1290 °F). The (α + TiMn) field so formed would then swing toward the titanium corner with falling temperature to appear finally as the eutectoid transformation in the binary system titanium-manganese.

A selection of photomicrographs is presented to illustrate the

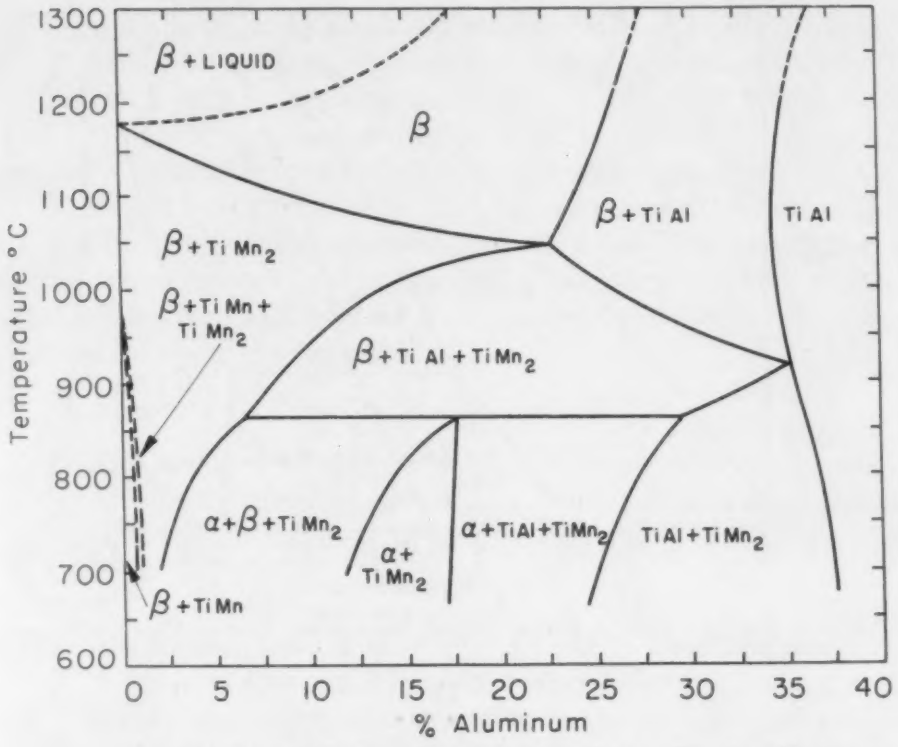


Fig. 19—Vertical Section at 60% Titanium, System Titanium-Manganese-Aluminum.

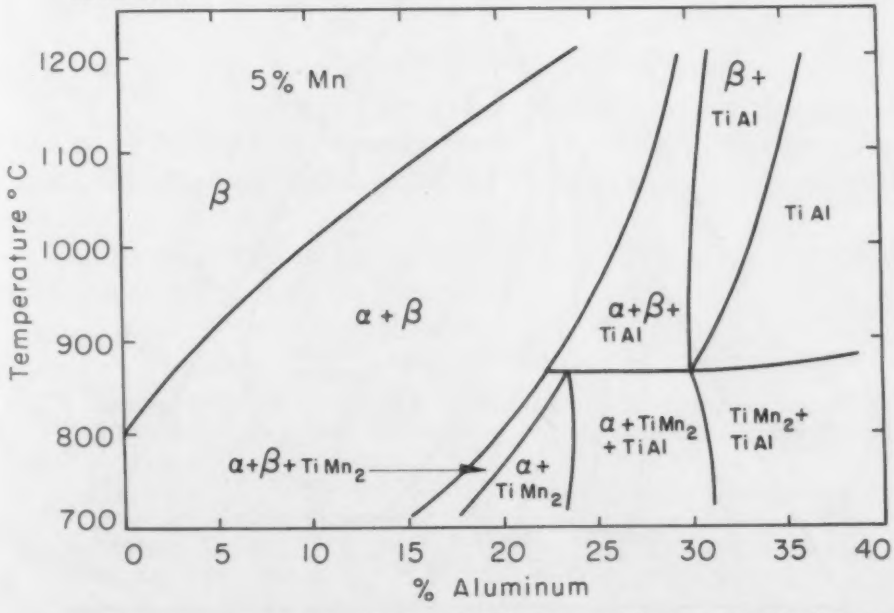


Fig. 20—Vertical Section at 5% Manganese, System Titanium-Manganese-Aluminum.

variations in structures encountered in the composition range of the four-phase reaction: $\beta + \mathrm{TiAl} \rightleftharpoons \alpha + \mathrm{TiMn_2}$. Two structures at 1000 °C (1830 °F) along a line of Al:Mn = 1:1 are given in Figs. 9 and 10 to show the change from $(\alpha + \beta)$ to $(\beta + \mathrm{TiMn_2} + \mathrm{TiAl})$. At 800 °C (1470 °F), i.e., below the temperature of the four-phase reac-

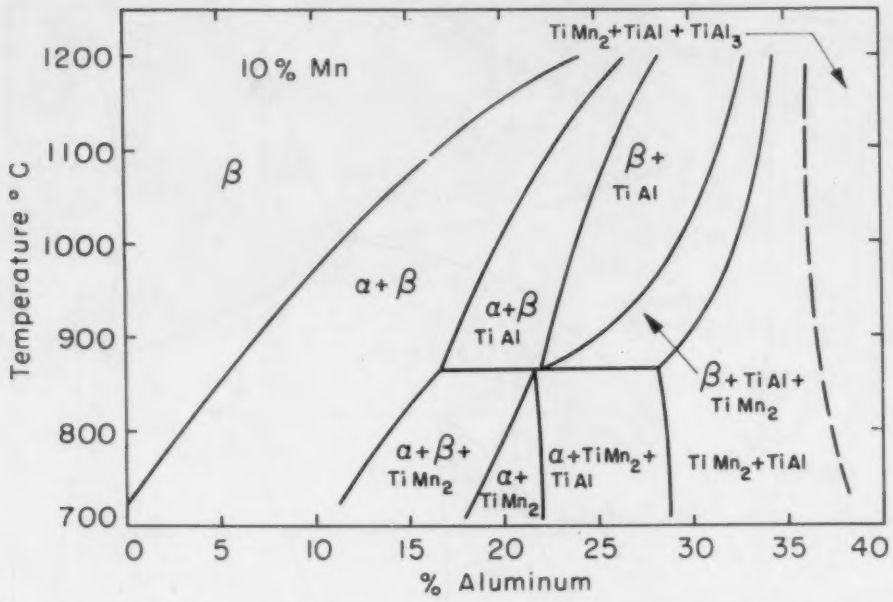


Fig. 21—Vertical Section at 10% Manganese, System Titanium-Manganese-Aluminum.

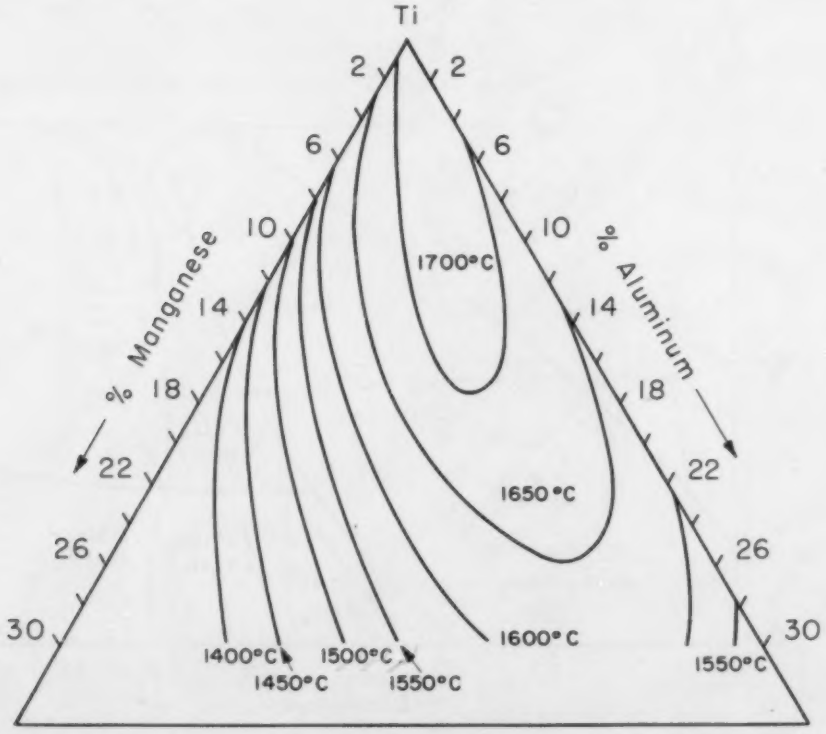


Fig. 22—Contour Projection of the Surface of Visible Melting, System Titanium-Manganese-Aluminum.

tion, the three photomicrograph sequence in Figs. 11,12 and 13 along the same direction shows a progression of structures from ($a + \beta$) to ($a + \beta + TiMn_2$) to ($a + TiAl + TiMn_2$). No microstructure was available in the narrow intervening ($a + TiMn_2$) field. Figs. 14 and 15 show the change in structure of an alloy containing 14% aluminum

and 14% manganese as observed above 900 °C (1650 °F) and below 800 °C (1470 °F) the four-phase reaction temperature.

Selected vertical sections at 90, 80, 70 and 60% titanium, and at 5 and 10% manganese are shown on Figs. 16, 17, 18, 19, 20 and 21, respectively, as constructed from the nine isothermal sections.

The surface of visible melting is represented as a contour plot in Fig. 22. The surface was constructed from an assembly of visible melting temperatures of 28 alloys by a graphical method which is essentially the same as that used by Anderson and Jette (6) in the construction of a parametric surface.

Summary

1. The ternary equilibria of the titanium-aluminum-manganese system has been investigated in the composition range defined by Ti-TiAl-$TiMn_2$ and in the temperature range between 700 and 1200 °C (1290 and 2190 °F).

2. A four-phase invariant reaction to the type: $\beta + TiAl \rightleftharpoons \alpha + TiMn_2$ was found to occur at 865 °C (1590 °F).

3. A second four-phase invariant reaction of the type: $\beta + TiMn_2 \rightleftharpoons \alpha + TiMn$ was logically inferred to occur between 550 and 700 °C (1020 and 1290 °F).

4. A surface of visible melting temperatures has been constructed.

Acknowledgments

The authors wish to express their appreciation of the sponsorship of this work by the Ordnance Corps, U.S. Army, Watertown Arsenal, Watertown, Massachusetts, and for their permission to publish this paper.

The metallographic preparation and photography were done under the supervision of C. A. Johnson.

References

1. E. S. Bumps, H. D. Kessler and M. Hansen, "Titanium-Aluminum System," *Transactions*, American Institute of Mining and Metallurgical Engineers, Vol. 194, 1952, p. 609.
2. D. J. Maykuth, H. R. Ogden, R. I. Jaffee, "Titanium-Manganese System," *Journal of Metals*, February, 1953 Supplement, p. 225.
3. W. Rostoker, R. P. Elliott, D. J. McPherson, Discussion contributed to reference (2), *Journal of Metals*, November, 1953, Section 2, p. 1566.
4. M. Hansen, H. D. Kessler, D. J. McPherson, "The Titanium-Silicon System," Transactions, American Society for Metals, Vol. 44, 1952, p. 518.
5. W. Rostoker, D. J. McPherson, M. Hansen, Final Technical Report to Watertown Arsenal on Contract No. DA-11-922-ORD-272, 1953.
6. A. G. H. Anderson, E. R. Jette, "X-ray Methods for Ternary Systems," Transactions, American Society for Metals, Vol. 24, 1936, p. 519.

CONSTITUTION OF ORDERING ALLOYS OF THE SYSTEM COPPER-GOLD

By F. N. Rhines, W. E. Bond and R. A. Rummel

Abstract

The constitution of the ordering alloys of the copper-gold system has been re-surveyed from 19.5 to 70 atomic percentage gold. No evidence is found for a third low temperature phase at 41 atomic percentage gold; there is, instead, a eutectoid equilibrium between the CuAu and Cu_3Au solid solutions at 36 atomic percentage gold and 284 °C (545 °F). Near 70 atomic percentage gold there is a reversal in the electrical resistance change upon ordering, possibly related to the appearance of ordered $CuAu_3$, as postulated by Ogawa and Watanabe. Observations upon the rates of transformation indicate that ordering and disordering proceed as nucleation and growth processes.

THE copper-gold alloy system is the prototype of a group of systems which are isomorphous at high temperature and which undergo ordering transformations at lower temperature. It is generally accepted that two types of ordered structures are formed, one ideally having equal numbers of atoms of the two metals and being referred to as the CuAu type, the other ideally having three copper atoms for every gold atom and being called the Cu_3Au type. The former is characteristically of tetragonal crystal symmetry, the latter face centered cubic; both transform into an isomorphous face-centered cubic disordered solid solution at higher temperature. There is general agreement also that ordering is not confined to the alloys of ideally stoichiometric composition, but occurs in the copper-gold system in the range from about 18 atomic percentage gold to approximately 70 atomic percentage, or higher.

There have been a number of constitutional investigations of the copper-gold system, of which the most commonly accepted is that of Haughton and Payne (1),[1] Fig. 1. These authors presented a phase diagram drawn in accordance with the Phase Rule. The two ordered phases were represented as undergoing congruent transformation at

[1]The figures appearing in parentheses pertain to the references appended to this paper.

A paper presented before the Thirty-sixth Annual Convention of the Society, held in Chicago, November 1 to 5, 1954. Of the authors, F. N. Rhines is Aluminum Company of America professor of light metals, Carnegie Institute of Technology, Pittsburgh, W. E. Bond is research assistant and R. A. Rummel is laboratory assistant, Metals Research Laboratory, Carnegie Institute of Technology, Pittsburgh. Manuscript received April 26, 1954.

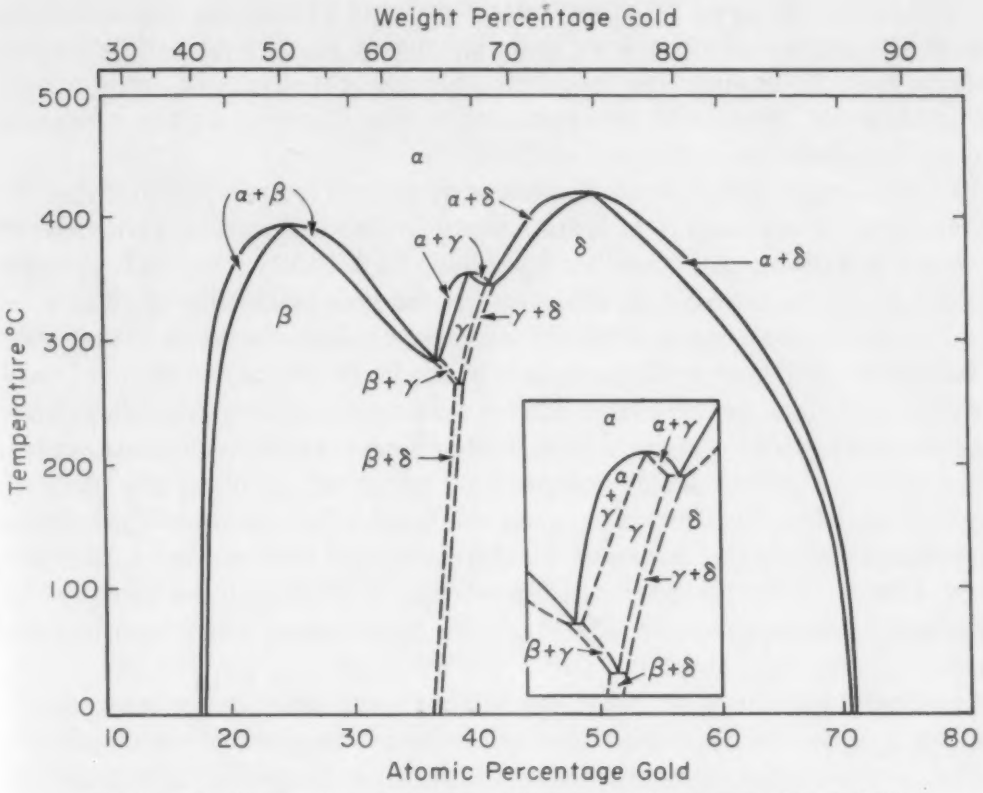


Fig. 1—Haughton and Payne's Phase Diagram of the System Copper-Gold.

temperature maxima at their respective stoichiometric compositions, existing at lower temperatures as two ordered solid solution series together spanning the composition range of ordering. The conjugate single phase regions were separated, according to rule, by two-phase regions which were estimated to be very narrow. A unique feature of the Haughton and Payne diagram is the representation of a third, possibly ordered, phase near 41 atomic percentage gold, and thought to exist over a very limited temperature range. These conclusions were based largely upon carefully conducted thermal studies. More recent electron diffraction studies by Ogawa and Watanabe (2), indicate the possible occurrence of yet another ordered phase, $CuAu_3$, with an ordering temperature of 243 °C (470 °F).

Subsequently, the Haughton and Payne diagram was thrown into doubt as a consequence of the promulgation of a concept of ordering transformation which was incompatible with the existence of Phase Rule type equilibria. This concept contemplated a homogeneous transformation from the disordered to the ordered state, and vice versa, so that no two-phase regions of order plus disorder should exist. Since the evidence of the co-existence of order and disorder at equilibrium was all either indirect, or considered inconclusive, it was thought that the ordered state should not be represented as a unique phase on the phase diagram.

The existence of an intermediate ordered phase was doubted, also, upon the basis that no simple and reasonable pattern of ordered atom arrangement, having the required atomic ratio, could be devised. Furthermore, there was no crystallographic evidence of the existence of such a phase, only thermal evidence.

The initial portion of the present research dealt with the question of the co-existence, at equilibrium, of the ordered and disordered phases and the results have been published (3). Direct crystallographic evidence of the co-existence of the ordered and disordered phases, at equilibrium, was presented. It was concluded therefrom that the Haughton and Payne diagram is correct in its representation of two-phase equilibria and that the order-disorder transformation is subject to the restrictions of the Phase Rule. These studies were, however, limited to a rather narrow composition range adjacent to the stoichiometric alloy Cu_3Au. In this range it was found that equilibrium is established very slowly at constant temperature and that much of the confusion relative to the nature of the transformation may be assigned to the failure of many of the investigators to achieve equilibrium in their experiments.

There remains a broad range of intermediate alloys whose constitution is imperfectly established and whose transformation characteristics remain almost unstudied. Within this range lies the disputed "intermediate ordering phase." Further knowledge of these alloys is desirable, both to extend the understanding of the ordering characteristics of nonstoichiometric alloys, and, because of a growing technical interest in the heat treatment of analogous alloys, some of which involve useful magnetic properties, in particular the system cobalt-platinum (4).

Accordingly, the present studies consisted in a re-examination of the constitution of twenty-four ordering alloys covering the range 19.5 to 70 atomic percentage gold, using a technique that was selected for the opportunity that it offered to establish true equilibrium. This consisted in measuring the electrical resistance at a sequence of constant temperatures after sufficient time at each temperature had elapsed to ensure the attainment of equilibrium and proving equilibrium by repeating the process, approaching the equilibrium from the opposite direction. This method is arduous, inasmuch as very long times at constant temperature are required, but it seemed that the questions at issue could scarcely be answered as certainly by less laborious means. The alloy series studied did not include the composition of $CuAu_3$ (75 atomic percentage gold) because information concerning ordering at this composition appeared too late.

In the process of establishing equilibrium, certain features of the dynamics of the ordering transformations were revealed. From these observations it is apparent that the ordering process proceeds by the

nucleation and growth of the precipitating phase, as in all other types of phase transformations. Some details of the analyses leading to this conclusion are presented in this paper.

Materials

High purity copper-gold and cobalt-platinum alloys were used in this research; compositions are given in Table I. Charges totalling 10 grams of the purest available grades of electrolytic gold and oxygen-free electrolytic copper were sealed in aqua-dag lined silica glass capsules. At the time of sealing, the capsules were evacuated and partially filled with an atmosphere of purified argon. The assembly was then held in a gas-oxygen flame until the metals were melted, shaken to effect stirring and alternately re-melted and shaken several times to ensure complete mixing. Frozen in the capsule, the resulting ingots were approximately one inch long by 3/16 inch in diameter. These were annealed 30 hours at 500 °C (930 °F), in argon, to minimize dendritic segregation, and were then cold forged, with intermediate flame annealing, to produce strips that could be further reduced with wire dies. After each heating the surface was removed by filing, to eliminate any oxidized copper and to point the rod for passage through the next die. The final draws, to a finished diameter of 0.017 inch, were made with tungsten carbide dies, in order to ensure roundness and smooth surface. The resulting wires, after a final anneal, became the subject materials of the research.

Experimental Equipment

Inasmuch as the objective of the research was to establish equi-

Table I
Copper-Gold Alloys

Nominal Composition	Analyses			
Atomic % Au	Atomic % Au	Weight % Au	Weight % Cu	Total Wt. %
19.5	19.569	43.00	56.96	99.96
22	22.066	46.73	53.24	99.97
25	25.004	50.81	49.16	99.97
28	28.038	54.69	45.28	99.97
32	32.011	59.33	40.65	99.98
35	34.977	62.49	37.45	99.94
36	36.096	63.64	36.32	99.96
37	37.027	64.56	35.40	99.96
38	38.013	65.51	34.44	99.95
39	39.098	66.52	33.40	99.92
40	39.969	67.35	32.61	99.96
41	40.941	68.24	31.73	99.97
42	42.076	69.23	30.72	99.95
43	43.057	70.08	29.88	99.96
45	44.983	71.70	28.27	99.97
47	46.942	73.27	26.70	99.97
49	49.012	74.85	25.11	99.96
50	49.986	75.58	24.39	99.97
51	51.056	76.38	23.59	99.97
54	53.948	78.40	21.58	99.98
59	59.028	81.69	18.28	99.97
64	64.002	84.63	15.35	99.98
66	66.018	85.74	14.23	99.97
70	69.971	87.81	12.15	99.96

librium at relatively low temperatures, where a long time at constant temperature would be required, the chief characteristics required of the equipment were: (a) to maintain uniform temperature over the specimen length and constant over long time intervals and (b) to prevent the contamination of the electrical resistance sample by any materials coming in contact with it. The latter requirement was met satisfactorily by maintaining about the wire a stagnant atmosphere of purified argon and by permitting the specimen wire otherwise to come into contact only with tungsten leads and pure alumina insulating beads, all of which

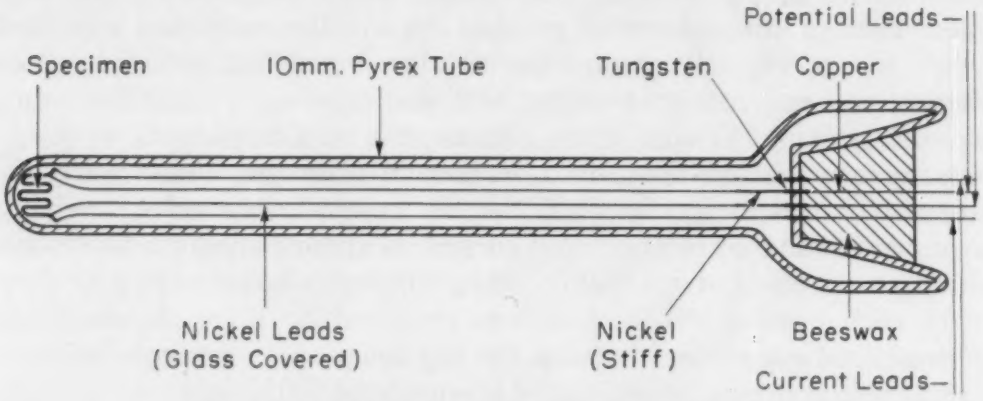


Fig. 2—Schematic Drawing of the Specimen Assembly.

materials are of negligible solubility in the alloys concerned, at least at the temperatures of the experiments.

A schematic drawing of the specimen assembly is given in Fig. 2. The sample, which was a wire 0.017 inch in diameter and 20 centimeters between potential contact points, was bent into a grid about one inch long, so as to minimize the problem of maintaining a uniform temperature throughout its length. Two current and two potential leads of nickel, with short tungsten wire links, were spot welded to the ends of the specimen and extended about one foot to the cold end of the assembly, where they were spot welded to tungsten glass-seal wires leading to the exterior. The long nickel wires were used in order to avoid heat losses by conduction along the lead wires. Pyrex glass tubing was used for enclosing the assemblies. There is no evidence that the samples deteriorated chemically, during more than 2 years at the temperatures of the experiments.

Uniformity of temperature throughout the specimen was maintained without difficulty and constancy of temperature, within $\pm$ ½ °C, was achieved for considerable intervals. But occasional temperature changes of one to three degrees, resulting from causes beyond control, imposed a limitation upon the length of the effective stabilizing periods.

The resistivity of each sample was measured with a Leeds and Northrup Type K potentiometer. In so doing a very small current was used, in order to avoid altering the temperature of the specimen.

Prior to taking readings, the current was allowed to flow until all potential drift had ceased. Then the resistivity was measured with the current flowing alternately in opposite directions, and the average of such readings was taken, in order to compensate for stray potentials that might result from temperature differences at various points in the external circuit.

Experimental Procedure

The general plan of the experimental procedure was to measure the electrical resistance, *at equilibrium,* at a series of temperatures covering the range within which the solid state transformations occur, locating the temperatures of these transformations by the occurrence of inflections in the resulting resistance temperature curves. To do this, the sample was held at constant temperature until all resistance change had ceased; then the temperature was lowered, (or raised) by a few degrees and the process repeated, continuing thus until the entire range of interest had been scanned.

By scanning with progressively falling temperature and then with progressively rising temperature, the coincidence of the temperature of the inflections, or lack of coincidence, served to prove, or disprove, the attainment of true equilibrium.

When it was possible to maintain the temperature constant until effective equilibrium had been attained, this state was signaled by constancy in the resistance readings over an extended period. No less than three days of constant resistance was considered adequate, and, where transformation temperatures were being approached closely, this time was extended to a matter of weeks, because it was found that a long induction period usually precedes the beginning of transformation, where the increments of temperature change are small.

When it was not possible to maintain the temperature constant until equilibrium had been attained, as was the case wherever much more than a month was needed, another procedure was employed. This consisted in utilizing the accidental temperature deviations to indicate how closely equilibrium had been approached. For example, if just prior to an upward temperature deviation the resistance had been falling gradually and continued to decline, despite a temperature rise of a degree or two, then the equilibrium value had not yet been approached at the prior temperature. But if the resistance rises more with a slight temperature increase, than can be accounted for by the thermal coefficient alone, then it is apparent that equilibrium had very nearly been attained. These criteria are most useful where phase changes accompanied by large resistivity changes are occurring within a narrow temperature range; fortunately, this condition prevailed over most of the composition range under study, but there were some areas in which it could not be applied.

As a supplement to the resistivity studies, changes in the crystal structure of the alloys were followed by X-ray diffraction means, using a Debye-Scherrer rotating wire camera. Short pieces of the wires were sealed with argon in small glass capsules and were brought to equilibrium in the same furnaces with the corresponding resistance samples. The resulting photograms were used to identify the phases present, but no attempt was made to determine the relative quantities of the phases, or to measure their lattice spacings. By this means, an estimate of the span of existence of the one and two-phase fields, at subcritical temperatures was obtained.

Results of Equilibrium Studies on Copper-Gold Alloys

A maximum of two sharp inflections was found in each of the resistance temperature graphs developed in this study; only in some

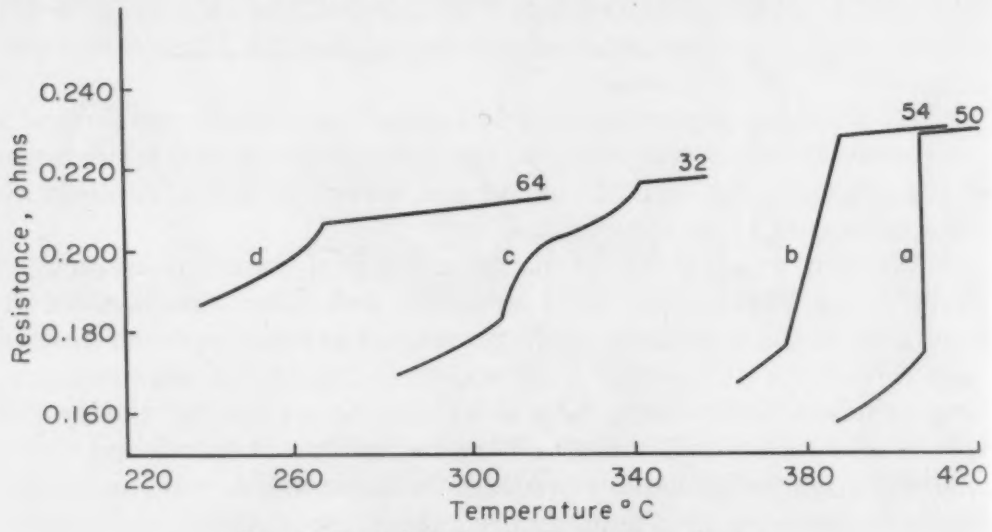


Fig. 3—Typical Resistivity-Temperature Curves.

of those alloys which commenced transformation from the disordered to the ordered state at relatively low temperature was a second inflection at yet lower temperature lacking. The four curves reproduced in Fig. 3 illustrate the range of shapes assumed. Curve "a" represents an isothermal, or nearly isothermal, phase change; curves of this type were encountered only at and adjacent to 25 and 50 atomic percentage gold.

Nonisothermal total transformation from a high to a low temperature solid state is indicated by curves of the types "b" and "c" in Fig. 3. The first of these corresponds to the condition in which the conjugate solid state boundaries are substantially straight over the temperature range concerned. Such curves were encountered in alloys upon both sides of compositions at which the type "a" curves were found.

The other variation upon nonisothermal transformation, represented by curve "c," can be accounted for upon the basis of substantial

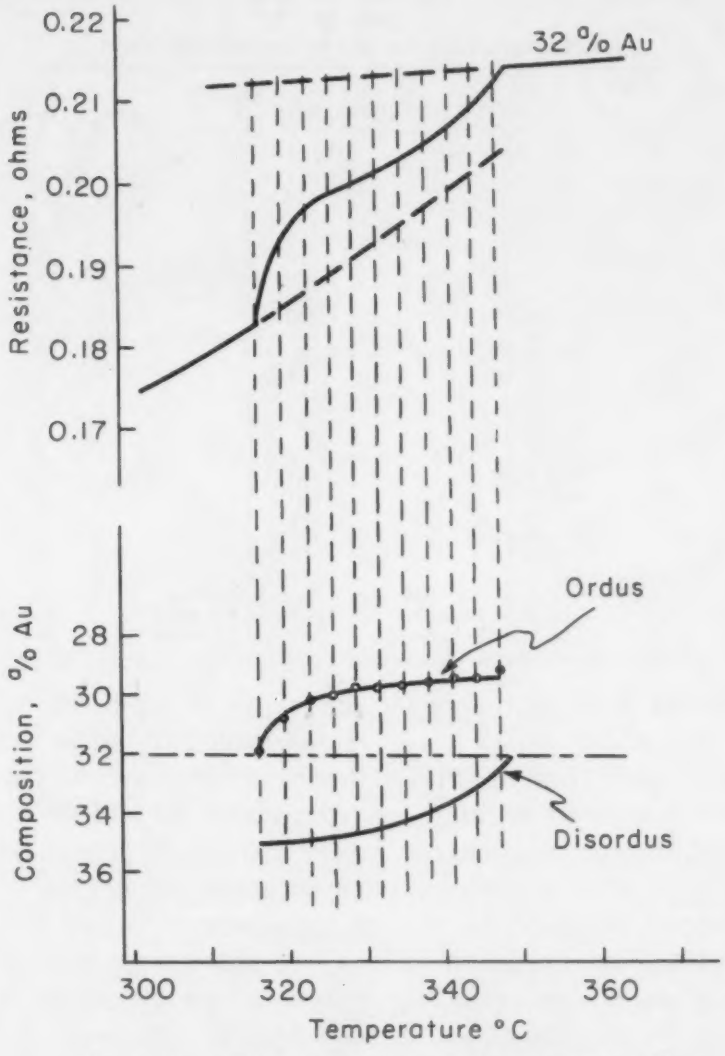


Fig. 4—Derivation of Disordus and Ordus Curves from a Resistivity-Temperature Plot.

curvature of one or both of the conjugate solubility limits, within the temperature range of transformation, and in a manner such that the composition range of two-phase coexistence decreases with declining temperature. The argument is presented in Fig. 4. Here it is assumed that the resistance, at a specific temperature within the transformation range, may be computed as a volume average of the extrapolated resistances of the high and low temperature states. Considering one of the dashed isothermal (vertical) lines in Fig. 4, the lengths between the resistance curve and the extrapolated resistance of the high and low temperature phases respectively are inversely proportional to the lengths between the gross composition of the alloy (horizontal dash-dot line) and the ordus and disordus curves respectively. The absolute length of the tie-line between ordus and disordus remains unbroken, but if the further assumption is made that the disordus line (upper

Table II
Equilibrium Data for the System Copper-Gold

SAMPLE NO. (Atomic %) (gold content)	TEMPERATURE °C		Type of curve (See Fig. 3)
	First Inflection	Second Inflection	
19.5	287 ± 3	281 ± 3	b
22	367 ± 1	352 ± 2	b
25	390 ± 1	390 ± 1	a
28	385 ± 2	378 ± 2	b
32	344 ± 1	312 ± 2	c
35	302 ± 3	None identified	d
36	285 ± 1	None identified	d
37	298 ± 2	290 ± 3	c
38	321 ± 3	None identified	d
39	317 ± 3	295 ± 3	b
40	359 ± 2	339 ± 1	c
41	365 ± 1	352 ± 3	c
42	374 ± 2	366 ± 2	c
43	386 ± 2	371 ± 2	c
45	403 ± 3	397 ± 2	b
47	409 ± 1	405 ± 1	a
49	411 ± 1	410 ± 1	a
50	411 ± 1	411 ± 1	a
51	409 ± 1	407 ± 1	a
54	392 ± 1	379 ± 2	b
59	344 ± 2	339 ± 2	b
64	268 ± 2	None identified	d
66	240 ± 2 (Inverse)	227 ± 2 (Inverse)	b–Inverse
70	231 ± 2 (Inverse)	212 ± 2 (Inverse)	b–Inverse

transformation limit in the phase diagram) is a smooth curve, it is seen that the ordus line (lower transformation limit) must curve toward higher gold content at lower temperature. Cases of this kind are found in the composition range between about 30 and 45 atomic percentage gold, except for a narrow range around 36 atomic percentage.

The fourth kind of resistance-temperature curve, type "d," Fig. 3, may correspond either to incomplete transformation (no lower inflection) or to an alloy that is stable in a two-phase state at low temperature. From 66 atomic percentage gold upward the curves are the inverse of type "b"; the inflections are in the opposite directions. This means that the low temperature (ordered) phase has higher resistivity than the high temperature (disordered) phase at the same temperature. A type "d" curve, was found at 64 atomic percentage gold. Also at 35 and 36 atomic percentage gold rather similar curves, probably representing failure to attain equilibrium below the upper inflection, were obtained.

A summary of the equilibrium data, obtained from all of the copper-gold alloys, is given in Table II. An estimate of the range of error in the determination of the temperature of each inflection is derived from the uncertainty in locating the inflection upon the resistance-temperature curve. Since all other experimental errors are believed to have been of much smaller magnitude, it is assumed that these may be ignored. The last column of Table II indicates the type of the resistance-temperature curve. From these data have been plotted the ordus and disordus curves of the phase diagram of Fig. 5. The temperatures of first inflection correspond to points upon the disordus curve, those of

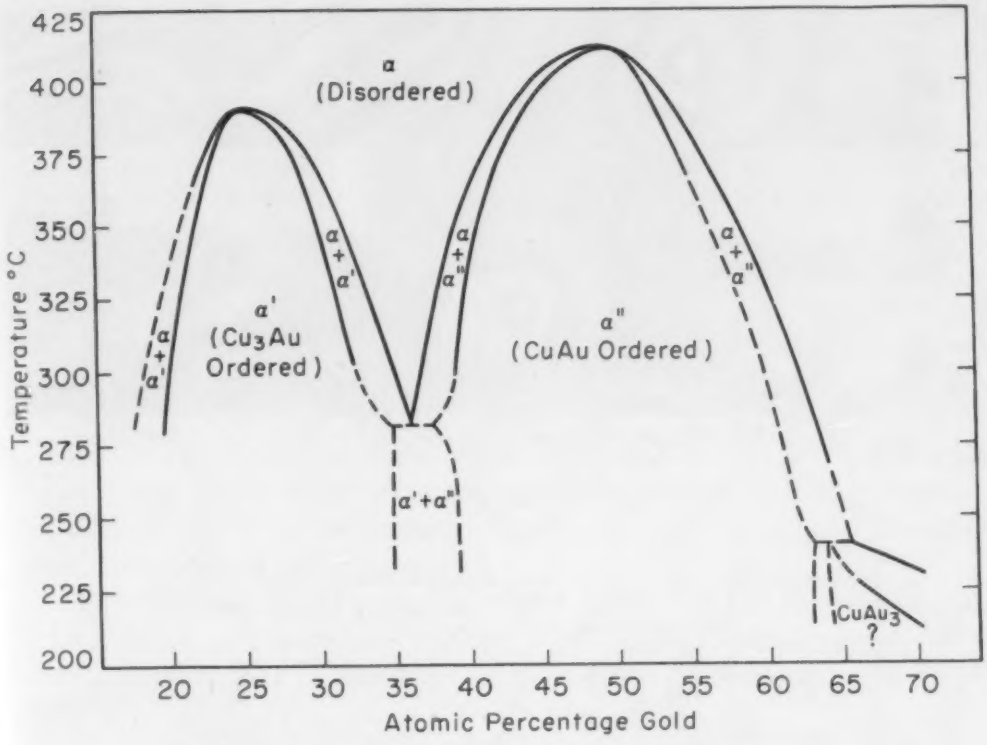


Fig. 5—Partial Phase Diagram of the System Copper-Gold.

second inflection to points upon the ordus. The shape of the ordus, relative to the disordus, is further checked by the type of the resistance-temperature curve, according to the principle illustrated in Fig. 4.

The resistance data fail to define completely the equilibrium relationships in the neighborhood of 36 atomic percentage gold and X-ray diffraction studies were used in an effort to clarify these relationships. In Fig. 6 are presented reproductions of three Debye-Scherrer patterns representing the crystal structures of alloys containing 25, 37 and 49 atomic percentage gold, which, after disordering at 500 °C (930 °F), were held at 270 °C (520 °F) for 14 days and quenched in water. Shaded areas in these photograms are portions covered with nickel foil, to filter out β radiation. The first of these patterns may be identified as typical of Cu_3Au, the third as typical of CuAu and the second displays both patterns superimposed. Thus, the co-existence of the two ordered phases, Cu_3Au and CuAu, below the minimum in the disordus on the phase diagram of Fig. 5 is indicated. In order to obtain an estimate of the span of this two-phase field, all alloys between 28 and 45 atomic percentage gold were similarly examined. The dashed boundaries shown on the phase diagram are rather crude estimates of the immiscibility limits, made by this procedure; at 270 °C (520 °F) the two-phase field appears to extend from slightly above 35 to just short of 41 atomic percentage gold.

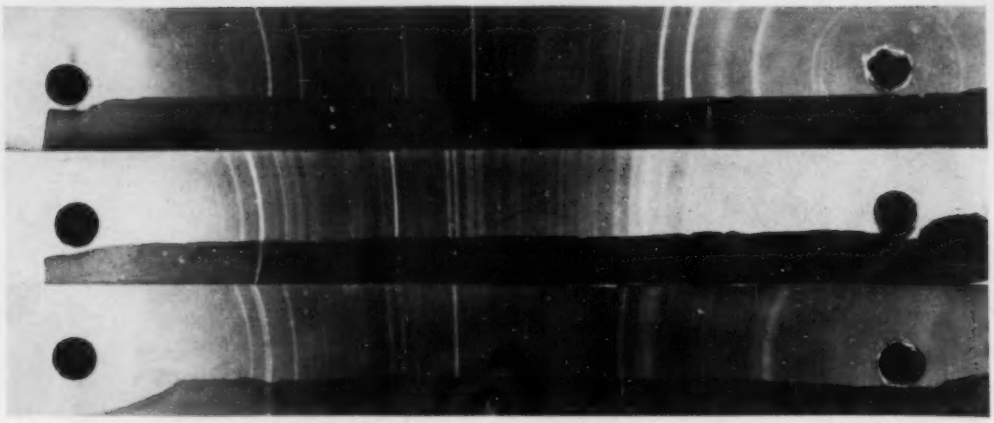


Fig. 6—Some Typical Debye-Scherrer Patterns of Alloys 25, 37 and 49 Stabilized at 270 °C.

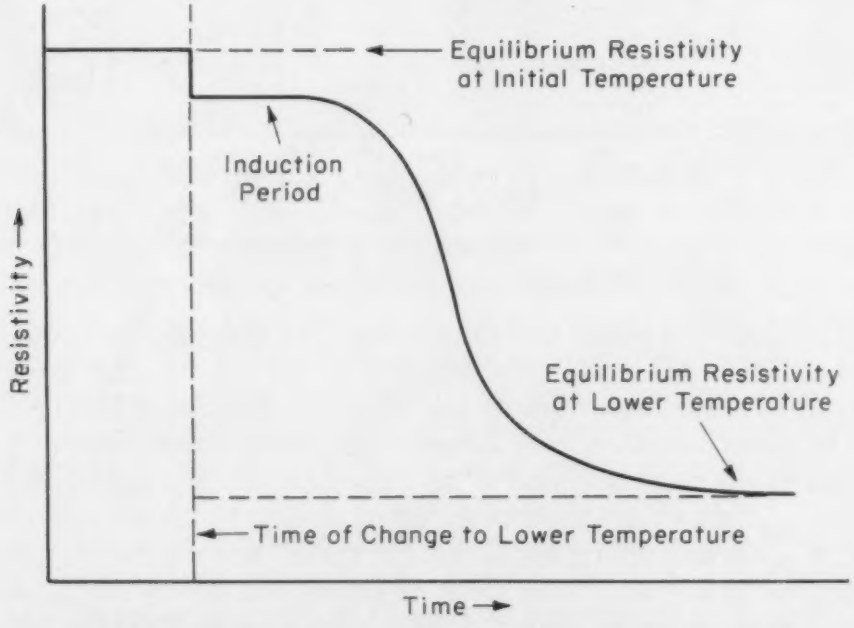


Fig. 7—Schematic Representation of a Typical Time-Resistivity Plot, Temperature Constant.

Constitutionally there are just two possible forms that the phase diagram might assume in the neighborhood of the minimum in the disordus. This point might correspond to a minimum transformation temperature where ordus meets disordus in an isomorphous series between Cu_3Au and CuAu (which is difficult to conceive!), or the minimum might correspond to a eutectoid reaction. That two-phase equilibrium occurs at 270 °C (520 °F) in this composition range is strong evidence that eutectoid equilibrium does, in fact, exist. It is surprising, however, that the resistivity-temperature curves failed to register isothermal transformation in this composition range. Two possible explanations present themselves; either the eutectoid reaction is so slug-

gish that equilibrium was not attained in this range, or the length of the eutectoid reaction tie-line is negligible. It is difficult to decide which of these, if either, is the correct explanation; possibly both contribute to the observed results.

Something new and unexpected is found at 66 and 70 atomic percentage gold. Here the disordus curve assumes a sharply different shape and the presence of an ordus curve is again evident. This has never before been reported. It is at least possible that these configurations are to be associated with the appearance of the newly discovered ordered phase $CuAu_3$. Since the data are insufficiently detailed to reveal the constitutional relationships at this inflection in the disordus, it is postulated that a peritectoid equilibrium exists, perhaps among the phases CuAu, $CuAu_3$, and the disordered phase, Fig. 5. The type "d" curve displayed by alloy 64 is compatible with this proposal, although the occurrence of an isothermal arrest near 230 °C (445 °F) would have strengthened the argument.

Another noteworthy characteristic of alloy 66 is the almost complete absence of resistance change in the temperature range 240 to 270 °C (465 to 520 °F) and very little change all the way up to 350 °C (660 °F).

Rates of Approach to Equilibrium in the Copper-Gold Alloys

In following the resistance change in each sample during the periods of establishment of equilibrium, measurements of time-resistance relationships were obtained, which are capable of giving information of value in understanding the mechanism and dynamics of the crystallographic changes that were taking place. These data are so voluminous, however, that it is impractical to do more here than display the several modes of approach to equilibrium that were found and to enumerate some of the conclusions that emerged from a detailed examination of the data.

When observed in detail, by taking frequent readings, all time-resistance sequences displayed the essential features of the schematic curve shown in Fig. 7. Immediately upon lowering the temperature, from a level at which equilibrium had been established, to a new constant temperature, a few degrees lower, the resistivity decreased by a small amount corresponding to the thermal coefficient of resistivity of the material. Then followed an induction period during which no change in resistance was detected. Presently the resistance began to decrease again at an accelerating pace, with a maximum rate of decrease shortly being attained. The rate of decrease then declined gradually to near zero, as the new equilibrium state was approached. In the various alloys and in various temperature ranges this typical curve was modified by the exaggeration or suppression of its several parts.

Steep time-resistance curves, such as that of Fig. 8, having al-

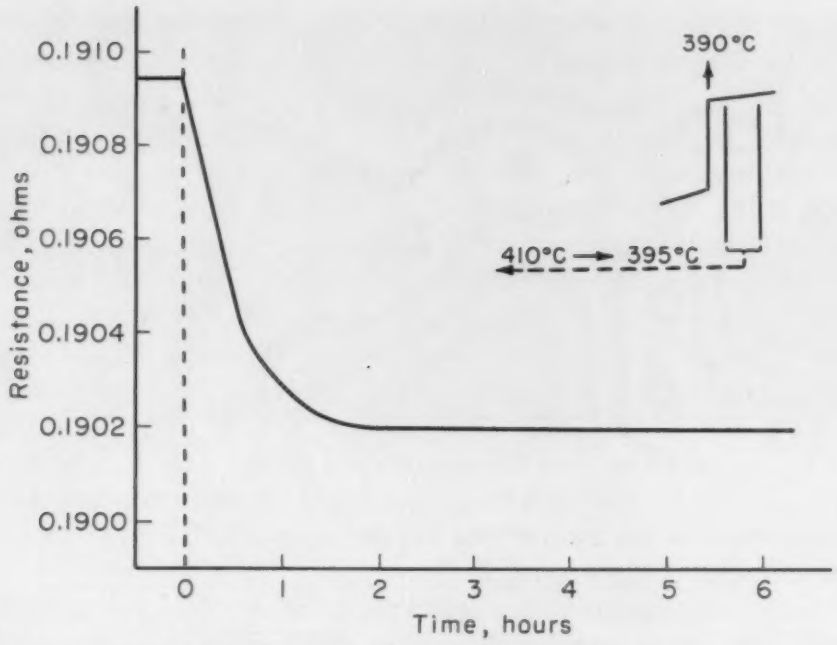


Fig. 8—Time-Resistivity Plot for Alloy 25, Progressing from Equilibrium at 410 °C to Equilibrium at 395 °C.

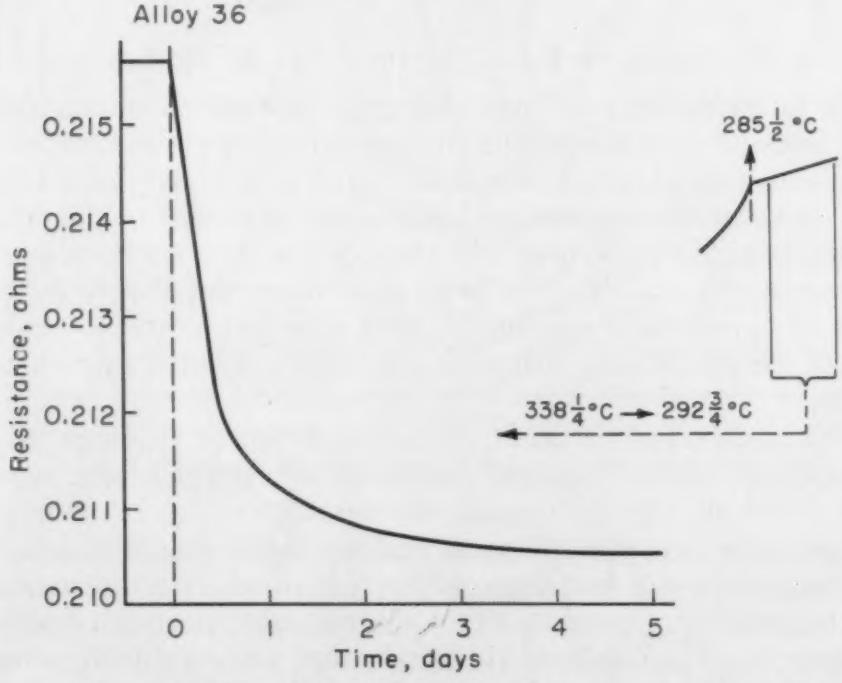


Fig. 9—Time-Resistivity Plot for Alloy 36, Progressing from Equilibrium at 338.25 °C to Equilibrium at 292.75 °C.

most no induction period, were found to be typical of the approach to equilibrium within one-phase fields, where no phase transformation was taking place and also of those cases in which so large a difference was imposed between the new and initial temperature that the transformation was from one single-phased state all the way to another

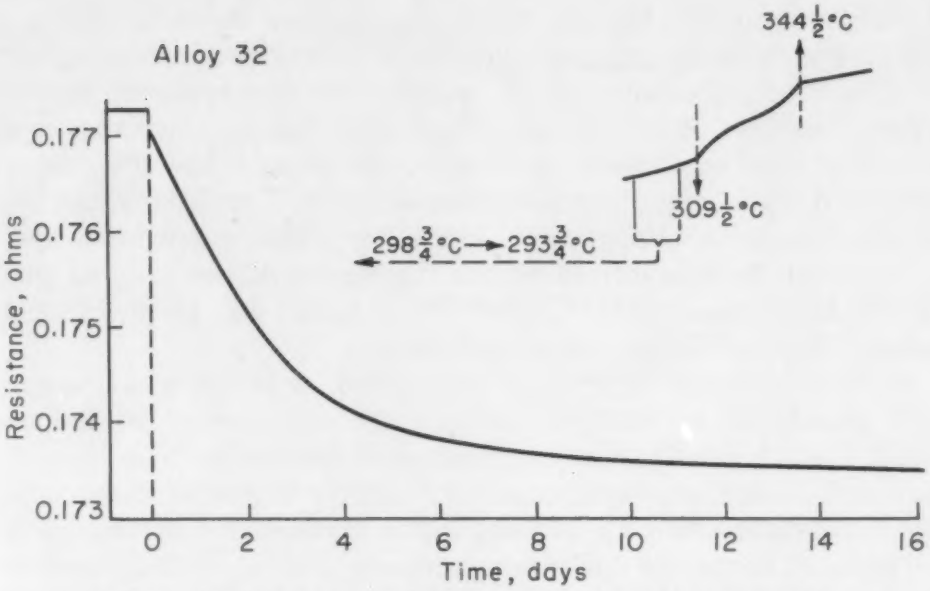


Fig. 10—Time-Resistivity Plot for Alloy 32, Progressing from Equilibrium at 298.75 °C to Equilibrium at 293.75 °C.

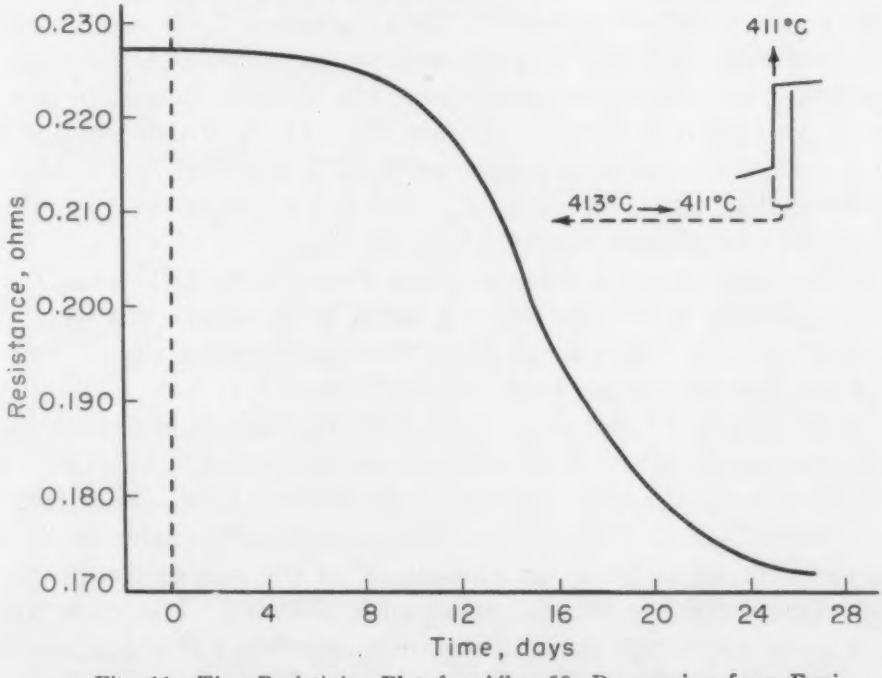


Fig. 11—Time-Resistivity Plot for Alloy 59, Progressing from Equilibrium at 413 °C to Equilibrium at 411 °C.

single-phased state. The insert sketch, included in this and subsequent time-resistance plots, indicates the portion of the equilibrium resistance-temperature curve within which the equilibrium state is being changed.

With temperature change wholly within the region of the disordered phase (high temperature), equilibrium was usually attained within a matter of minutes. The crystallographic change involved is merely one of adjustment of the degree of short range order and is

expected to be rapid, because diffusion over very short distance is the only time consuming process involved. The very pronounced effect of the slowing of diffusion at lower temperatures was apparent, however, in the alloys near 36 atomic percentage gold, Fig. 9, which remain disordered at relatively low temperatures; the time for the attainment of disordered equilibrium increases to a matter of 2 or 3 days just above the transformation temperature. The latter effect was evident also in the approach to equilibrium within the region of the ordered phase, Fig. 10. Below about 200 °C (390 °F) progress was so slow that it is doubtful that equilibrium was ever attained.

Where a change of phase was involved, as in the transformation from disordered to ordered CuAu, there was always an induction period, Fig. 11, but its duration generally decreased with an increasing magnitude of temperature change, i.e., with the degree of undercooling. This is characteristic of a process which involves the nucleation of a new phase. The rate of nucleation increases, at first, with the extent of undercooling. Since this kind of transformation is essentially diffusionless, the growth rate is high and the transformation proceeds very rapidly once nuclei are present. Rather unexpectedly it was found that the induction period was much longer when, instead of lowering, the temperature was raised, so as to cause the alloy to change in one step from an ordered to a disordered state, Fig. 12. A possible explanation of this difference is that a larger nucleus is required to establish the disordered than the ordered state, requiring a longer time for the appearance of disordered clusters of suitable size.

A large increase in the total time required to attain equilibrium was immediately noticeable when a small temperature change, calling for transformation from a one-phase to a two-phase state, or from one two-phase state to another, was imposed, Fig. 13.

In the former of these two cases, both the induction period and the subsequent period of resistance change are magnified. This is also to be expected, because the composition of the nucleus must differ from the gross composition of the alloy and the growth of particles of the new phase can proceed only so fast as material of the proper composition is delivered by diffusion from considerable distance. The case for the change from one two-phase equilibrium to another, a few degrees above or below, differs only in that there is no nucleation requirement, and accordingly no induction period, since particles of both phases are already present. Here it is noteworthy, however, that the approach to equilibrium (the growth of particles of the waxing phase) is the more rapid the larger the temperature change, Fig. 14, presumably because of the larger composition potential and the correspondingly larger diffusion velocity thus imposed.

It is interesting to observe also, that for a given temperature change, the rate of transformation from a one-phase state to a two-

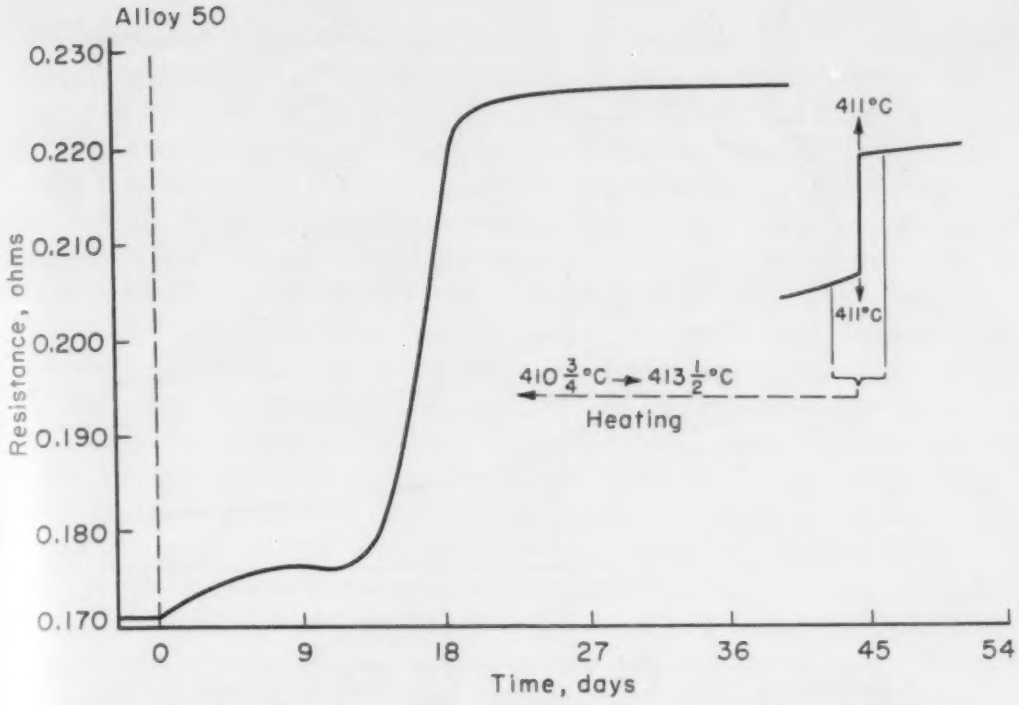


Fig. 12—Time-Resistivity Plot for Alloy 50, Progressing from Equilibrium at 410.75 °C to Equilibrium at 413.50 °C.

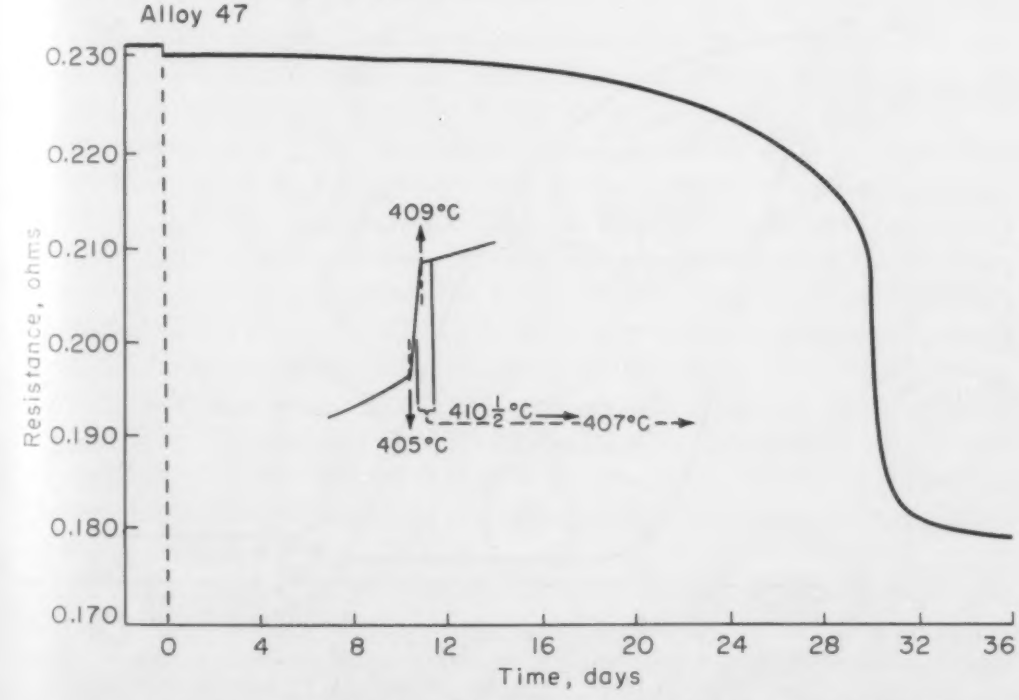


Fig. 13—Time-Resistivity Plot for Alloy 47, Progressing from Single-Phase Equilibrium at 410.5 °C to Two-Phase Equilibrium at 407 °C.

phase state is smaller near the stoichiometric compositions, Fig. 15. Perhaps this is because the ordus and disordus boundaries are nearly horizontal in this region, making the tie-lines longer and calling for a

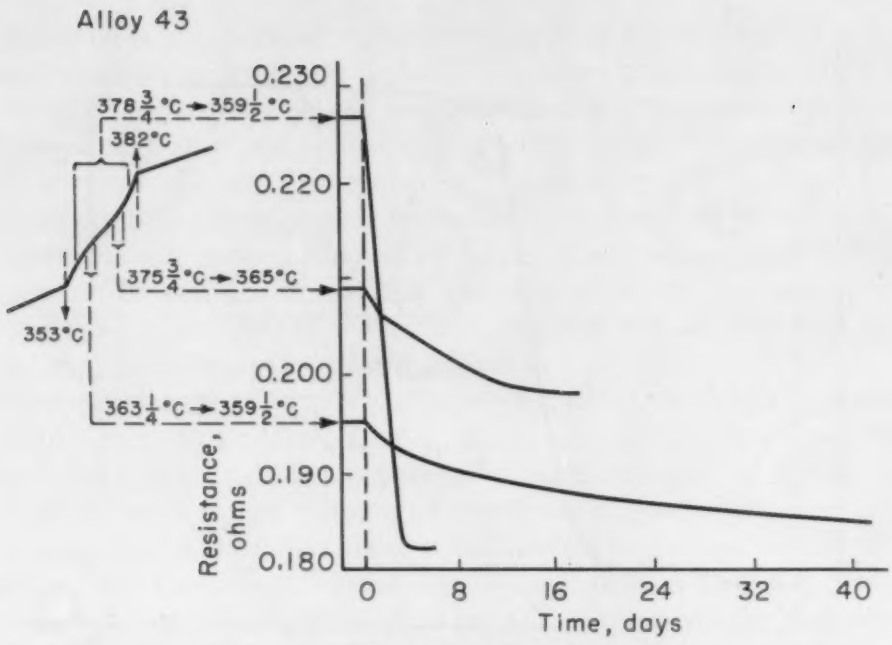


Fig. 14—Time-Resistivity Plots for Alloy 43, Progressing from Equilibria Respectively, at 378.75, 375.75 and 363.25 °C to Equilibria at 359.5, 365 and 359.5 °C.

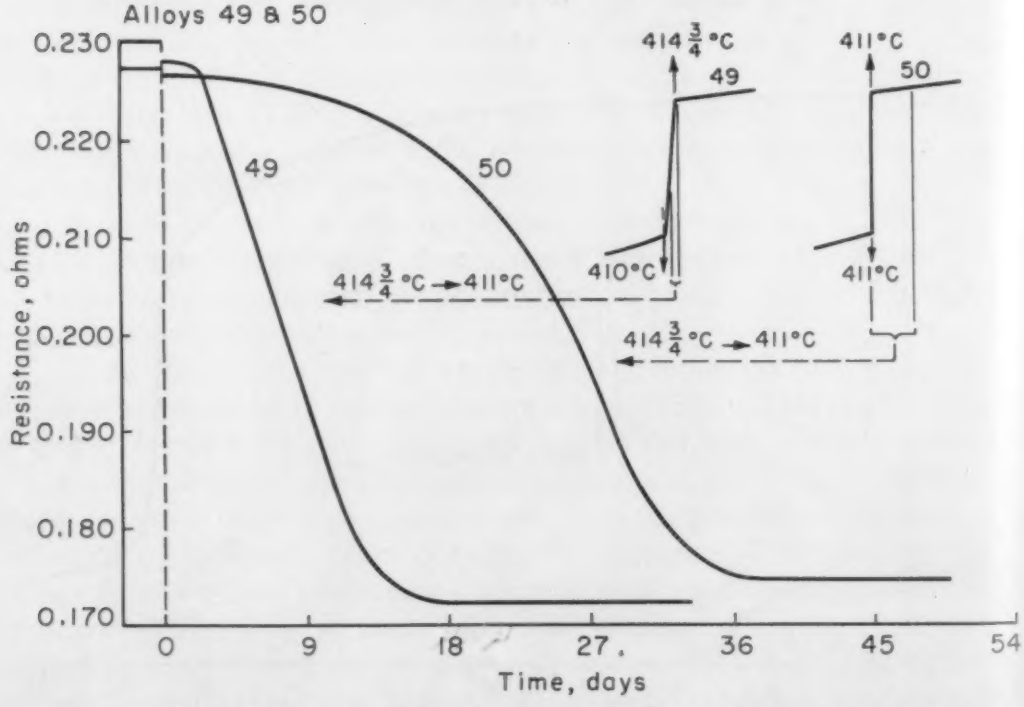


Fig. 15—Time-Resistivity Plots for Alloys 49 and 50, Progressing from Equilibrium at 414.75 °C to Equilibrium at 411 °C.

larger chemical segregation between the two phases that are required to coexist, i.e., more diffusion.

The greater reluctance to transform in the direction of disordering is also very marked in one-phase to two-phase transformations.

An impressive example of this was encountered in the 32 atomic percentage gold alloy, which, after ordering at a subcritical temperature, was superheated 10 °C above the ordus line and held three months without the development of any of the disordered phase. Upon subsequent heating to 20 °C above the ordus, the disordering transformation began and then continued, even when the temperature was dropped back to a few degrees above the ordus. This is clearly an example of an extremely slow nucleation rate for the disordered phase.

The influence of departure from stoichiometric composition upon the rates of approach to equilibrium is made somewhat ambiguous by the fact that the temperatures of two-phase coexistence decrease simultaneously. Thus, the slower transformation rates, near the minimum in the disordus and at the extremes of the composition range studied, may be due solely to the slower diffusion rates at low temperatures. So great is the difference in rate, however, especially in the middle region, near 36 atomic percentage gold, that it seems probable that the lower degree of perfection of the nonstoichiometric ordered state contributes to the slackening of the rate of phase change, by decreasing the energy difference between the ordered and disordered states.

Discussion

The observations that have been described make it clear that the copper-gold phase diagram of Haughton and Payne is correct in its general form, except for the inclusion of a fourth solid phase near 41 atomic percentage gold. Neither the present equilibrium studies, nor X-ray diffraction studies, provide any basis for postulating the existence of this phase. The diagram presented in Fig. 5 is believed to be more precise than the Haughton and Payne diagram, especially in the location of the ordus boundaries, the positions of which were only crudely estimated in the earlier work. Good agreement exists between the short span of disordus recently determined by Newkirk (5), using X-ray diffraction measurements and the corresponding section of the boundary in Fig. 5. Less perfect agreement exists with Newkirk's corresponding section of ordus curve, which lies in a composition range several percent higher in gold content than that section of the curve established by the present studies.

That a eutectoid reaction exists near 36 atomic percentage gold and 284 °C (545 °F), seems almost inevitable. A degree of uncertainty must be recognized, however, in the failure of the equilibrium measurements to report an isothermal resistivity change at this temperature. An adequate reason for this behavior is to be found in the extreme sluggishness of reaction in this composition range, but the fact remains that the existence of the eutectoid can be argued only from the observation that three two-phase regions meet at this location. It is perhaps worthy of note that the CuAu + Cu_3Au region that exists below the eutectoid

has a span of nearly 5 atomic percentage gold. Preston (6), in 1931, was unable to detect the co-existence of these two phases and concluded that the two-phase region must be very narrow indeed.

Of particular interest is the observation that the low temperature phase near 70 atomic percentage gold exhibits higher resistivity than the high temperature phase, at the same temperature. This has not been predicted, and no explanation can be offered here. So little is presently known of the characteristics of $CuAu_3$ that it remains difficult to associate the observations presently in hand.

The rate studies leave little room for doubt that the ordering and disordering reactions proceed as conventional nucleation and growth processes. The nucleation rate, estimated from the inverse of the induction period, increases with undercooling and superheating, as it should. It also increases as the composition difference between the precipitating and parent phases decreases and ceases to be significant where no new phase is appearing. The growth rate is obviously responsive to the requirements of diffusion, being very high, as should be expected, where no composition change is requisite to growth and low where the precipitating phase differs in composition from the parent phase.

Although others have proposed that the ordering reaction occurs as a nucleation and growth process, this clear demonstration is important, because it shows that the homogeneous transformation concept, upon which the modern order-disorder transformation theory has been constructed, is untenable. Some comfort is to be derived, however, from the fact that a nucleation and growth process, framed within the limitations of phase equilibria, leads qualitatively, at least, to the same predictions with respect to the forms of electrical resistivity and specific heat curves, as does the modern theory.

Conclusions

1. By means of measurements made at equilibrium, the ordus and disordus boundaries of the system copper-gold have been re-located and the existence of such conjugate boundaries has been proved; a new phase diagram is presented.

2. A eutectoid transformation (disorder to ordered CuAu and ordered Cu_3Au occurs at about 36 atomic percentage gold and 284 °C (545 °F).

3. The existence of a field of coexistence of the ordered phases Cu_3Au and CuAu, between about 35 and 40 atomic percentage gold, has been demonstrated.

4. There is no evidence of an intermediate phase at 41 atomic percentage gold, such as had been postulated by Haughton and Payne.

5. Evidence exists of the occurrence of another phase near 70 atomic percentage gold; this phase seems to have higher electrical resistivity than the conjugate disordered phase at like temperature.

6. A copper-gold alloy, containing 66 atomic percentage gold, exhibits a nearly zero temperature coefficient of electrical resistivity between 240 and 270 °C (465 and 520 °F) and a very small coefficient at higher temperature.

7. Ordering in the copper-gold system proceeds in a manner typical of phase changes that occur by nucleation and growth processes.

ACKNOWLEDGMENT

The authors wish to express indebtedness to Wright Air Development Center under USAF Contract AF 33 (616)–39, which supported the research upon which this paper is based.

References

1. J. L. Haughton and R. J. W. Payne, "Transformations in the Copper-Gold Alloys," *Journal,* Institute of Metals, Vol. 46, 1931, p. 457.
2. S. Ogawa and D. Watanabe, "Electron Diffraction Study on the Ordered Alloy Au_3Cu," *Journal of Applied Physics,* Vol. 22, December 1951, p. 1502.
3. F. N. Rhines and J. B. Newkirk, "The Order-Disorder Transformation Viewed as a Classical Phase Change," TRANSACTIONS, American Society for Metals, Vol. 194, 1952, p. 1029.
4. J. B. Newkirk, A. H. Geisler, D. L. Martin and R. Smoluchowski, "Ordering Reaction in Cobalt-Platinum Alloys," *Transactions,* American Institute of Mining and Metallurgical Engineers, Vol. 188, 1950, p. 1249.
5. J. B. Newkirk, "Order-Disorder Transformation in Cu-Au Alloys Near the Composition CuAu," *Journal of Metals,* Vol. 5, 1953, p. 823.
6. G. D. Preston, "The X-ray Examination of Gold-Copper Alloys," *Journal,* Institute of Metals, Vol. 46, 1931, p. 477.

DISCUSSION

Written Discussion: By J. B. Newkirk, General Electric Research Laboratory, Schenectady, N. Y.

This paper, representing several years of very careful experimental work, illustrates the importance and the difficulty of approaching equilibrium conditions when studying structure transformations in copper-gold alloys. In the past a regrettably large amount of effort has been wasted because experimental observations, made under transient conditions, were interpreted as representing equilibrium.

There are a few somewhat disconnected points on which I shall comment.

1. The authors' interpretation (Fig. 4) of their type "c" resistivity curves could lend added support to the ordus and disordus construction which they have proposed in Fig. 5. It would be interesting to see similar analyses of the other experimentally determined temperature versus resistance curves and the results correlated on a single temperature versus composition diagram. The quality of the fit of the curves from one specimen to the next, or of the slopes where the curves overlap, would comprise a test of the interpretation of this type of datum.

2. I have found that initially disordered copper-gold wire specimens do not

give sharp Debye-Scherrer lines after they have been annealed below 300 °C for periods as long as 187 days. This is true even when the wires were initially in the "as-drawn" condition. I was therefore surprised to learn that the authors' specimens, initially softened and disordered by annealing at 500 °C, gave patterns representing structural equilibrium after having been subsequently treated for only fourteen days at 270 °C. Nevertheless, if these Debye-Scherrer patterns are sharp enough to permit an estimate of the line positions, one could deduce approximate composition limits for the two-phase region at 270 °C. The validity of the proposed eutectoid reaction could be greatly strengthened by this information.

3. I should like to know if the authors have found any X-ray evidence for the existence of a $CuAu_3$ superlattice. In an attempt to produce this structure I have annealed two wires of $CuAu_3$ for two months at 200 °C in a static atmosphere of low pressure argon. One of the wires was initially in the "as-drawn" condition and the other had been thermally disordered by quenching from 500 °C. After two months at 200 °C, the wires were furnace cooled and then photographed in a 10 cm diameter Debye-Scherrer camera using Cu radiation. The diffraction lines given by the initially "as-drawn" wire were diffuse and the doublets were unresolved, indicating that the crystal distortion attending the drawing operation was not relieved by the long anneal at 200 °C. All diffraction lines given by the other specimen were sharply resolved and corresponded to reflections expected from a disordered face-centered cubic metal of composition copper + 75.8 atomic per cent gold. No visible superlattice lines were given by either wire although heavy exposures were made.

4. It is well known that another crystal structure, usually described as orthorhombic, is found in alloys near CuAu which have been equilibrated between the ordus and about 395 °C. I would ask the authors if they ever found any electrical resistance or other effect which might be used to define the boundary between this orthorhombic phase and the tetragonal phase which is stable at lower temperatures.

5. I should like to know if the authors have included any microscopic studies in this research.

Authors' Reply

1. The type "C" resistivity curve is characteristic of alloys whose transformation temperatures are relatively low. We lack sufficient equilibrium data in the temperature-composition range concerned to apply this analysis (vicinity of the eutectoid). Times to reach equilibrium at these temperatures are of the order of months or years.

2. A heat treatment of 14 days at 270 °C, of course, will not give equilibrium structures. We maintain only that the transformation is sufficiently complete to gain an estimate of the limits of the proposed two-phased field at this temperature.

3. Replying to Mr. Newkirk's item 3, the answer is "no." Its occurrence was discovered too late in the research program.

4. Accelerated nonequilibrium temperature-resistivity runs, which were made for all of the alloys to determine the approximate temperatures of transformation, did not show any indication of the phase in question. True equilibrium runs would most probably verify the existence of this phase provided that there is a sufficient difference between the resistivities of the two phases in equilibrium.

THE EFFECTS OF TWISTING ON TUNGSTEN WIRES AT HIGH TEMPERATURES

By Takeo Fukutomi

Abstract

Behaviors of two kinds of tungsten wires under the influence of twisting were compared at high temperatures. Sample wires were first twisted and then released after a definite time of heating. The ratios of the angle of free rotation after releasing to the angle of given torsion were measured at various temperatures. There was little difference between the values of this ratio of nonsag wires and wires which show a large sag by hairpin tests, until a definite high temperature, T_g and T_o, respectively, was reached. But, a sudden change occurred in the wires, especially in nonsag wires, at those temperatures. The ratio for nonsag wires decreased to a large extent at T_g, whereas the ratio for sag wires decreased only a little, at T_o.

Besides these experimental results, a short discussion was given on the correlation between the grain structure of tungsten wire and its resistivity to torsional deformation.

Introduction

AMONG the many physical properties of tungsten filaments, their degree of resistivity to deformation at high temperatures is one of the most important for such technical purposes as the manufacture of incandescent lamps and thermionic valves. Many makers of incandescent lamps have been annoyed by the sagging of tungsten filaments which causes many inconvenient results. According to Smithells' theory, the sag of a coil is caused by alternate deformation of the filament under gravity and relief of strain by recrystallization, both processes being concurrent (1).[1] The addition of thoria, which restricts the grain growth in tungsten wires, was successful to reduce the sag (2). The so-called nonsag wires, now exclusively employed for coiled filaments, are produced by the addition to pure tungsten of mixtures of volatile alkali compounds and nonvolatile oxides, such as SiO_2, or Al_2O_3. These additions promote oriented growth and produce overlapping, extremely large crystals of tungsten in the wires.

When a coil is suspended horizontally, it is bent downward and is elongated by the action of gravity. Elongation of a coil produces tor-

[1] The figures appearing in parentheses pertain to references appended to this paper.

The author, Takeo Fukutomi, is assistant professor Gifu University, Gifu, Japan. Manuscript received April 8, 1953.

sion in any section of wire perpendicular to the axis of the wire. The observation of the effect of twisting on straight wires, therefore, provides a method to investigate the effect of gravity on coils which are suspended horizontally. This is the basic idea of the following experiment in which the behaviors of twisted tungsten wires were examined at high temperatures by the author. Two kinds of wires, one of which is a nonsag wire and the other is a wire which sags to a great extent, were used as samples and their behaviors were compared.

Apparatus

A glass tube, as shown in Fig. 1, is supported vertically and a tungsten sample wire F is suspended along the axis of the tube. The length of the glass tube is about 60 cm and its internal diameter is

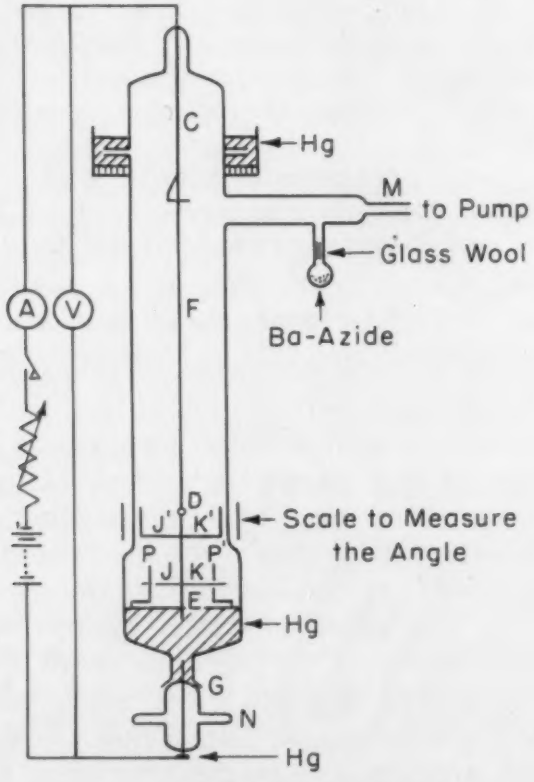


Fig. 1—Apparatus of Experiment.

about 3.3 cm. The upper end of sample F, which is 18 cm long, is attached to a thick nickel wire C by pressing the sample filament in the bended tip of C, and the lower end is attached to another thick nickel wire E at the point D by the same way. E has two needles which are perpendicular to E. The one K is made of molybdenum and used to twist F, and the other K′ is used to measure the angle of torsion. The lower end of E dips into a mercury pool at the bottom of the glass

tube and can rotate freely around its axis. N is the handle which can be rotated around its axis by the aid of a ground glass joint G. Two iron needles, P and P′, are connected with N and give the sample F a desired torsion by the aid of K. N is operated by hand. The total weight of K, K′, and E is 0.5 gram and there was no apparent elongation of sample wires caused by this weight throughout the whole period of this high temperature experiment.

The air in the apparatus was pumped out by an oil diffusion pump without traps at first until a high vacuum of ca. 10^{-5} mm-Hg was reached. Then barium azide was burnt by the aid of a gas burner and the whole apparatus was evacuated again until the pressure fell to 10^{-3} mm-Hg. Finally, the apparatus was sealed off at M, and the experiment was begun.

Experimental Procedure

There are four possible procedures of twisting and heating.

1. The heating current is allowed to pass through the sample filament and then the sample is twisted. After t minutes of heating, the sample is made free and then the heating current is cut off.
2. The heating current is passed at first and then the wire is twisted. After t minutes of heating, the current is cut off and the sample is released.
3. The sample is twisted and then heated. After t minutes of heating, the sample is released and then the current is cut off.
4. The sample is twisted and then heated. After t minutes of heating, the current is cut off and then the sample is released.

Actual filaments of incandescent lamps are always lighted and cut off in the field of gravity. And so, actual cases are best represented by method No. 4. This process was adopted for the experiment.

The sample was first treated by preparatory heating which will be described subsequently. Then, by the aid of N, P, and P′, F was twisted by the desired angle α. It was kept at a certain temperature T° for a convenient period of t minutes by an electric current passing through it. And then, the heating current was cut off and P and P′ were detached from K. K′, being made free, rotated in the direction opposite to α by an angle γ and ceased to rotate. The residual angle, β, which is equal to α minus γ, was dependent upon the temperature of heating, the kind of sample wire, its heat treatment, and the magnitude of given torsion, α, the length of the sample being kept constant. The ratio, β/α, however, was independent of α if α was smaller or not too much larger than 90 degrees, and the ratio did not change as the torsion test was repeated as far as the preparatory heating was applied to the sample before each measurement.

The temperature of the filament F was determined from the table of Smithells (4) by calculating the value of specific resistivity from the values of heating current and voltage applied to that sample.

Samples Used and Preparatory Heating

In the experiment group No. 1, NT–2 wires produced by a Japanese factory were used. These wires are nonsag wires. (mg = 12.0, length = 18 cm, diameter = 0.063 mm.)

In the experiment group No. 2, NS–2–29 wires produced by another Japanese factory were used. These wires showed a large sag by hairpin tests. (mg = 8.0, length = 18 cm, diameter = 0.051 mm.)

Attached graphite was not removed before the experiment. Removal of graphite by boiling the wire with caustic soda and wiping it afterwards, did not show any serious effect on the results.

When the sample filament was heated and kept at a definite temperature, it began to rotate in either direction except when the filament had been treated with preparatory heating at the same temperature or above. But, after sufficient time of heating, (15 minutes of heating was necessary, in general) the wire ceased to rotate. When a measurement was made without this preparatory heating, the ratio β/α changed as the torsion test was repeated and gave quite random values. So, every sample was treated with this preparatory heating just before each measurement was made.

To heat the wire, the use of alternating current is preferable because in most actual cases incandescent lamps are heated by alternating current. But, when a sample was heated by alternating current, it began to vibrate and the measurement became impossible. This vibration was probably caused either by the periodical change of length of the wire due to alternating heating and cooling, or by the mutual action of alternating current and terrestrial magnetism. The latter explanation is more probable as the vibration always occurred on a plane perpendicular to a meridian of the earth. The use of direct current, therefore, was necessary to heat the samples.

Results

Freely suspended and treated with preparatory heating at the temperature of the following measurement or above that, the sample filament was twisted about $\alpha = 40 \sim 90°$ and heated and kept at T for three minutes. (A series of tests which was held at 1880 °F (1025 °C) indicated three minutes was the most convenient period of heating to compare the values of β/α.) Typical examples of β/α vs. temperature curves are shown in Fig. 2. The numbers show the order of experiment.

NT–2 wires—Before the wire is heated to a certain temperature T_g, the value of β/α always lies on curve a. The order of choice of heating temperature had nothing to do with the ratios of β/α. But, when the

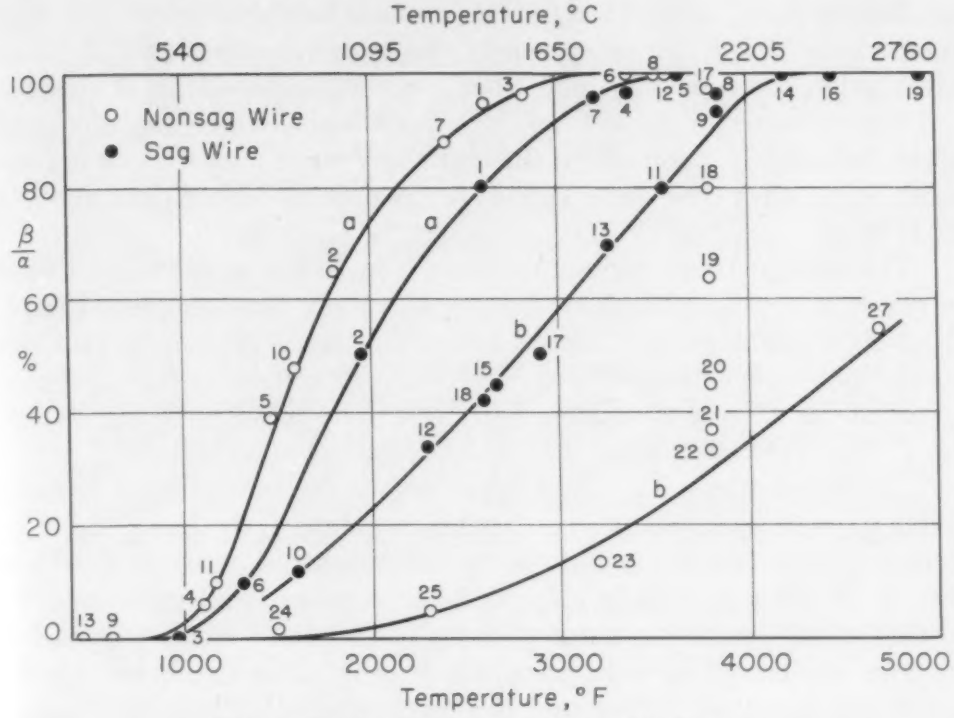


Fig. 2—Heating Temperature Versus β/a Curves.

sample was heated to T_g, β/a decreased suddenly. When the measurement was repeated, the values of β/a became less and less. After several measurements it stopped decreasing and stayed at a constant value. After this change β/a began to lie on curve b. The order of choice of temperature had nothing to do with the β/a value in this case, again. The change from curve a to curve b was irreversible. The values of T_g ranged between 3770 °F (2075 °C) and 3950 °F (2175 °C) for the five samples used.

NS–2–29 wires—Before the sample was heated to a certain high temperature T_o, the values of β/a increased with temperature and curve a was quite similar to that of NT–2. When it was heated to T_o, which was always in the vicinity of 3860 °F (2130 °C), β/a slightly decreased. The degree of decrease was very small compared with that of NT–2 wire. After this change β/a values lay on curve b, which was almost linear between 1340 and 4040 °F (730 and 2230 °C). The values changed from 0% to 100% within this temperature range and the value remained at 100% at higher temperatures. In other words, if the sample were twisted and heated for three minutes, the heating temperature being above 4040 °F (2230 °C), the sample would not rotate at all after it was released.

Discussion

As seen in Fig. 2, in the case of nonsag wires, the value of β/a, which lay originally on curve a, decreased and lay on curve b after it

was heated at T_g. This fact indicates immediately that nonsag wires become very "hard," in other words, the resistivity to torsional plastic deformation becomes very high when a nonsag wire is kept at a certain high temperature for some time. NS–2–29 wires, which sag to a great extent, behaved in a somewhat different way since they did not become "hard" even after they were kept at temperatures higher than 4040 °F (2230 °C).

The change from curve a to curve b in Fig. 2 is considered to be the result of crystal growth, and curve b for sag wire suggests that, in NS–2–29, crystal growth occurs to only a small extent. In fact, the average size of crystal grains in NS–2–29 remained as small as the diameter of the sample wire after a life test. The curve b for sag wire in Fig. 2, therefore, corresponds to polycrystalline structure.

The temperature T_g can be explained as the temperature of rapid crystal growth which was investigated previously by Robinson (5). He reported the crystal growth becomes very rapid between 2960 and 3500 °F (1630 and 1930 °C) for nonsag wires of 0.076 mm diameter and that the temperature range goes up for wires of smaller diameter.

The similarity between curves a in Fig. 2 is explained by the assumption that they correspond to polycrystalline structures, the size of grains being very small.

ACKNOWLEDGMENT

The author wishes to offer his cordial thanks to Dr. N. Sasaki of Kyoto University for his profitable guidance and to Dr. R. Tajime for his valuable suggestions. This work owes much to Matsushita Electric Co. in Kyoto for many conveniences given, and also to the Ministry of Education of Japan for the grant for the scientific research.

References

1. C. J. Smithells, *Tungsten,* 2nd edition, 1936, p. 84. Chapman & Hall Ltd., London.
2. C. J. Smithells, "High Temperature Phenomena of Tungsten Filaments," *Transactions,* Faraday Society, Vol. 17, 1921, p. 485.
3. J. Wulff, POWDER METALLURGY, 1942, p. 420, American Society for Metals, Cleveland, Ohio.
4. C. J. Smithells, *Tungsten,* 2nd edition, 1936, p. 130. Chapman & Hall Ltd., London.
5. C. S. Robinson, "Rate of Crystal Growth in Drawn Tungsten Wire as a Function of Temperature," *Journal of Applied Physics,* Vol. 13, 1942, p. 647.

TRANSFORMATION STUDIES IN IRON-CARBON-TITANIUM-VANADIUM ALLOYS AND THE DISTRIBUTION OF CARBON BETWEEN THESE ELEMENTS

By Moss V. Davis and W. P. Fishel

Abstract

The Ac_3 and Ac_1 transformations in a number of iron-carbon-titanium-vanadium alloys were determined and were compared to alloys of similar compositions containing no carbon. The partition of carbon between iron, vanadium and carbon was determined in fully annealed alloys. The vanadium and titanium uncombined with carbon gave transformation temperatures which fit the binary iron-vanadium diagram and the ternary iron-vanadium-titanium diagram.

Introduction

THE purpose of this paper is to compare the carbide forming tendencies of titanium and vanadium, and to show the effects of each of these elements, upon the transformations when combined with carbon and when uncombined or in solid solution in iron.

The Distribution of Carbon

The alloys listed in Table I were prepared from Armco Iron, ferro-vanadium, sponge titanium and graphite. They were fully annealed so as to approach equilibrium. All alloys were analyzed for total titanium, vanadium and carbon; for the titanium and vanadium combined with carbon; for the uncombined titanium and vanadium; and for the carbon combined with titanium and vanadium. The determination of carbides of titanium and vanadium depends upon their insolubility in dilute H_2SO_4. This separation for VC is not exactly complete, i.e. VC dissolves slightly. This may be responsible for the almost constant value of 0.15% of combined vanadium in column 6.

These alloys fall into three classes: Class 1. Those (6–12) having an excess of carbon over that required to unite with all the vanadium and titanium. These alloys contained Fe_3C as pearlite, and only a small amount of uncombined vanadium. Class 2. Those (1 and 2) in which all of the carbon is combined with all of the titanium and with part of the vanadium. The excess vanadium is in solid solution. Class 3. Those

---

The authors, Moss V. Davis and W. P. Fishel, are associated with the Department of Chemistry, Vanderbilt University, Nashville, Tenn. Manuscript received April 19, 1954.

Table I
Chemical Analyses of Iron-Titanium-Vanadium-Carbon Alloys

Alloy No.	V	Total Ti	C	Vanadium			Titanium			Combined C as
				Combined	Uncombined	Total	Combined	Uncombined	Total	VC TiC
1	3.99	1.42	1.13	3.79	0.17	3.96	1.43	0.00	1.43	1.09
2	2.52	1.09	0.56	1.39	1.05	2.44	1.11	0.00	1.11	0.56
4	0.68	0.91	0.18	0.04	0.59	0.63	0.81	0.09	0.90	0.18
5	1.36	1.39	0.27	0.06	1.27	1.33	1.30	0.12	1.42	0.27
19	2.19	1.27	0.22	0.06	2.11	2.17	0.94	0.36	1.30	0.22
6	1.69	1.25	0.72	1.48	0.15	1.63	1.25	0.00	1.25	0.58
7	1.49	0.54	0.78	1.32	0.17	1.49	0.53	0.00	0.53	0.41
10	0.59	0.78	0.96	0.41	0.18	0.59	0.80	0.00	0.80	0.28
11	0.53	1.26	0.57	0.36	0.13	0.49	1.25	0.00	1.25	0.35
12	0.97	1.13	0.59	0.80	0.16	0.96	1.12	0.00	1.12	0.40

(4,5 and 19) in which all the carbon is combined with part of the titanium and the remaining titanium and almost all of the vanadium all uncombined.

The data of Table I indicate that in the annealed state carbon reacts with titanium in preference to vanadium; that very little vanadium carbide is formed unless the carbon content exceeds that required to unite with the titanium present; and that pearlite appears only with an excess of carbon over that required to unite with both titanium and vanadium. The order for the affinities of carbon is: titanium, vanadium and iron. These conclusions are also supported by the transformation studies.

Transformation Studies

Additional alloy of each class were made and analyzed as described above. Their Ac_3 and Ac_1 transformation temperatures were determined dilatometrically using the procedure described by Lucas and Fishel (1).[1] Class I alloys are listed in Table II. These alloys contain an excess of carbon and therefore show, on heating, transformations similar to plain carbon steels, since titanium and vanadium carbides are practically insoluble at temperatures below 1050 °C

Table II
Chemical Analyses and Dilatation Results of Class I Alloys

Alloy No.	Total V	Total Ti	Total C	Pearlitic C*	Transformation °C		
					Ac_1 Begins	Ac_3 Ends	Difference
21	2.19	0.49	0.59	0.09	753	923	170
6	1.69	1.25	0.71	0.13	755	904	149
12	0.97	1.13	0.59	0.19	745	877	132
22	1.15	0.34	0.54	0.25	745	852	107
7	1.49	0.54	0.78	0.41	745	805	60
10	0.59	0.78	0.95	0.67	745	752	7

* Obtained by subtracting the carbon combined with titanium and vanadium (C in residue) from the total carbon.

[1] The figures appearing in parentheses pertain to the references appended to this paper.

(1920 °F). Therefore, the controlling factor should be the amount of carbon in excess of that required to unite with titanium and vanadium.

Class I. Alloys Containing Pearlite

In Fig. 1 the amount of excess carbon, pearlitic carbon, has been plotted against the temperatures of transformation. The open points are the end of the Ac_3 transformation, and the open points with the

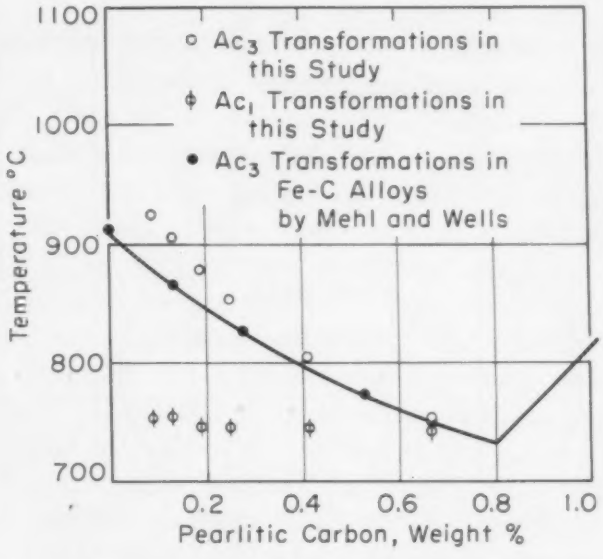


Fig. 1—Ac_1 and Ac_3 Transformations in Iron-Titanium-Vanadium-Carbon Alloys Having Pearlitic Carbon.

vertical line through them indicate the beginning of Ac_1. Ac_1 was found to be the same for all alloys except those of low carbon, alloys 6 and 21.

For comparison, Fig. 1 shows the Ac_3 curves for pure iron-carbon alloys as determined by Mehl and Wells (2), using dilatation methods and a heating rate of 2 °C per minute. Class 1 alloys containing titanium and vanadium as carbides and the excess carbon as pearlite show the usual transformations of plain carbon steels. This is evidence that the titanium and vanadium carbides are separated above the critical range, as a microscopic study indicates, and that they are not in solid solution since they have little effect upon the transformations.

Class 2. Alloys Having Vanadium Alloyed With Ferrite

Alloys of this class have all of the carbon combined with all of the titanium and part of the vanadium as titanium and vanadium carbides. The vanadium not combined with carbon will be alloyed with ferrite. A comparison of the transformation temperatures of alloys used in this study with the transformation temperatures of alloys of the iron-

Table III
Chemical Analyses and Dilatation Results of Class 2 Alloys

Alloy No.	Total V	Total Ti	Total C	Un-Comb. V	Transformation—°C Ac3 Begins	Ac3 Ends	Difference	Contraction During Ac3 x 10^3 Inches
26	1.41	0.19	0.23	0.30	892	984	92	5.0
13	1.13	1.08	0.34	0.49	926	1004	78	4.0
24	1.06	0.44	0.14	0.74	951	1018	67	2.4
25	1.23	0.26	0.12	0.80	945	1022	77	4.5
2	2.42	1.09	0.56	1.04	974	1060	86	2.0
18	1.33	1.79	0.43	1.32	1052	1083	31	—

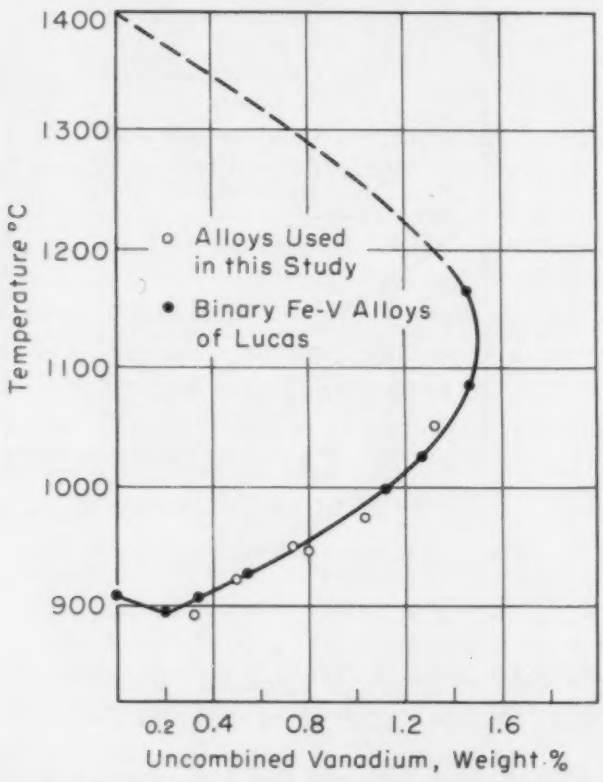


Fig. 2—Ac_3 Transformations in the Iron-Titanium-Vanadium-Carbon System Having Uncombined Vanadium.

vanadium binary system has been made. Since the carbides of titanium and vanadium are practically insoluble in iron in the range of temperatures employed, the uncombined vanadium, as determined by analysis, is the actual amount of vanadium alloyed with ferrite. The amounts of uncombined vanadium, vanadium alloyed with ferrite, in these alloys should, therefore, be equivalent to equal amounts of vanadium in iron-vanadium binary alloys, and the transformation temperatures of equivalent alloys should agree closely. The transformation temperatures of a series of six alloys in this class has been determined. The results are given in Table III.

In Fig. 2, the uncombined vanadium, vanadium alloyed with

Table IV
Chemical Analyses and Dilatation Results Per Cent by Weight Class 3 Alloys

Alloy No.	Total V	Total Ti	Total C	Uncmb. V	Uncmb. Ti	Transformation—°C Ac3 Begins	Ac3 Ends	Difference	Contraction During Ac3 x 10^3 In.
33	0.70	0.78	0.14	0.70	0.20	971	1037	66	5.7
35	1.14	0.39	0.08	1.14	0.07	1007	1077	70	4.6
29	1.03	1.01	0.16	1.02	0.37	1040	1114	74	2.2
20	1.39	2.07	0.20	1.37	1.29	No transformation			
30	0.64	0.94	0.04	0.64	0.77	No transformation			

ferrite, has been plotted against the temperature of transformation. The curve shown on the plot is the beginning of the Ac_3 transformation for equivalent alloys in the iron-vanadium binary system determined by Lucas (1) using the same rate of heating as employed in this study. The open points indicate the beginning of the Ac_3 transformation for alloys used in this study. The end of the Ac_3 transformation was not plotted since it varies with the rate of heating.

The transformation temperatures of alloys used in this study, plotted in Fig. 2, compare favorably with transformation temperatures of equivalent alloys in the iron-vanadium binary system. This may be cited as further proof that all of the titanium and part of the vanadium are combined with all of the carbon in the range of temperatures employed. It may also be considered as further proof that titanium and vanadium carbides are practically insoluble in iron in this range of temperatures. These alloys although carbon is present have no Ac_1 transformation.

Class 3. Alloys Having Titanium and Vanadium Alloyed With Ferrite

Alloys of this class have all of the carbon combined with part of the titanium, leaving some titanium and practically all of the vanadium alloyed with the ferrite. A comparison was made between the transformation temperatures of alloys used in this study and the transformation temperatures of alloys of the iron-titanium-vanadium ternary system. Since titanium carbide is known to be practically insoluble below 1100 °C (2010 °F), the uncombined titanium and vanadium, as determined by analysis, should represent the amounts of these elements dissolved in ferrite.

The amount of uncombined titanium, titanium alloyed with ferrite, and the amount of uncombined vanadium, vanadium alloyed with ferrite, in these alloys should be equivalent to equal amounts of titanium and vanadium in iron-titanium-vanadium ternary alloys, and the transformation temperatures should agree closely.

The transformation temperatures of a series of five alloys in this class have been determined. The results are shown in Table IV. This class also has no Ac_1 transformation.

The transformation temperatures of alloys in this class show good agreement with the ternary diagram of Lucas (1) if the amounts of titanium and vanadium alloyed with the ferrite, uncombined titanium and uncombined vanadium, are compared with the ternary diagram.

Consider Alloy 29 as a typical alloy of this class. The analysis indicated 1.03% vanadium, 1.01% titanium and 0.16% carbon. An alloy of this composition without carbon would be outside the gamma loop. Alloy 29 has 1.03% vanadium, and 0.37% titanium alloyed with the ferrite, with the remaining titanium combined with carbon as titanium carbide. This alloy shows an Ac_3 transformation beginning at 1040 °C (1905 °F). This tends to substantiate the prior assumption that the carbides have very little effect on the temperature of transformation, and the amount of alloying element tied up as a carbide may not be considered as a factor in the transformation of these alloys.

Summary

A series of alloys in the iron-titanium-vanadium-carbon system has been prepared. Alloys of this system have been classified as indicated in the previous section on partition studies and their alpha to gamma allotropic transformation temperatures have been determined by dilatometric methods.

It may be concluded that titanium and vanadium carbides exert very little influence on the transformation temperatures. Only the titanium and vanadium actually alloyed with ferrite are the controlling factors for the alpha to gamma transformation.

References

1. W. R. Lucas, "Gamma Loop Studies in the Iron-Vanadium and the Iron-Vanadium-Titanium Systems," Transactions, American Society for Metals, Vol. 46, p. 277–291.
2. R. F. Mehl and C. Wells, "Constitution of High Purity Iron-Carbon Alloys," Tech. Pub. No. 798, 1937, American Institute of Mining and Metallurgical Engineers.

ELEVATED TEMPERATURE PROPERTIES OF DUCTILE CAST IRONS

By Charles R. Wilks, Norman A. Matthews and R. Wayne Kraft, Jr.

Abstract

Creep and stress rupture properties are presented for three types of ductile cast iron over the temperature range of 800 to 1200 °F (425 to 650 °C); the familiar standard ferritic and pearlitic grades (60-45-15 and 80-60-03 respectively) and a high alloy austenitic type. Tensile properties at room and elevated temperatures are included along with growth tests. The superior growth and scaling characteristics of the standard ductile irons in comparison with grey irons, together with enhanced creep properties comparable to low carbon steel over the applicable temperature range, suggest wide utility for the ductile irons for elevated temperature service. Markedly higher hot strength at 1000 °F (540 °C) and above can be obtained with the high alloy austenitic grade.

Introduction

CAST irons with spheroidal graphite, variously termed ductile, nodular or spherulitic graphite irons, have become recognized standard materials during the past four years. Considerable research and development and field testing have provided the essential background leading to substantial and increasing commercial production for a wide range of applications. The ductile cast irons combine many of the processing or foundry handling qualities of grey cast irons with product or mechanical property characteristics approaching those of the annealed or normalized plain carbon cast steels.

Data have been published demonstrating the superior growth and oxidation resistance of ductile irons compared to flake irons (Gagnebin, Millis and Pilling (1)[1] and White, Rice and Elsea (2) and suggesting attractive characteristics for elevated temperature service.

However, published data on elevated temperature mechanical properties are limited. Saunders and Sinnott (3) reported the tensile and impact properties of one ductile iron heat over the temperature range of 800 to 1200 °F (425 to 650 °C) and obtained stress-rupture

[1]The figures appearing in parentheses pertain to the references appended to this paper.

A paper presented before the Thirty-sixth Annual Convention of the Society, held in Chicago, November 1 to 5, 1954. Of the authors, Charles R. Wilks is metallurgist, Norman A. Matthews is assistant chief metallurgist, and R. Wayne Kraft, Jr. is metallurgist, American Brake Shoe Co., Metallurgical Department, Mahwah, N. J. Manuscript received April 14, 1954.

properties at 1200 °F (650 °C). Long term creep data have, however, not been generally available.

The purpose of this paper, therefore, is to make available general base line data on the creep and stress rupture properties of ductile irons of three types and to indicate the level of properties which may be expected. Tensile properties at both room and elevated temperatures and growth test data are also included.

Compositions

The properties of ductile irons are controlled primarily by matrix structure in a manner similar to steels. The graphite present as spheroids instead of flakes minimizes the potential effects of graphite volume and distribution on mechanical properties. Within the last five years research and development on ductile irons has accurately defined the effects of individual elements, heat treatments and section size on metallographic structures and resultant room temperature mechanical properties. However, two standard types have emerged which account for the majority of current production and are termed ferritic and pearlitic from their predominating matrix structures. Austenitic types have become commercially important and have been utilized for many special and critical type applications. Although other modifications have been tested, the scope of this presentation has been limited to the two standard types and a special austenitic grade in the interest of clarity and brevity. The nominal compositions of the three types which were studied are shown in Table I whereas analyses of individual heats appear with the detailed data in Table II.

Table I
Ductile Cast Irons

	Nominal Compositions*							
Type	T.C.%	Mn%	P%	S%	Si%	Ni%	Mg%	Heat Treatment
Ferritic	3.7	0.4	Low	Low	2.6	1.0	0.07	Annealed
Pearlitic	3.7	0.4	Low	Low	2.6	1.0	0.07	Normalized
Austenitic	3.0	2.0	Low	Low	2.5	22.0	0.08	None

*Chemical compositions of individual heats are shown in Table II.

Experimental Procedure

Melting

All of the heats which were extensively studied were made by basic induction practice. Pig iron, mild steel punchings and ferro-alloys constituted the charge except in the case of two austenitic iron heats EK-A and EL-A, where 50% shop returns were utilized. Heat sizes ranged from 100 to 1000 pounds. The furnaces were tapped at approximately 2700 °F (1480 °C) and treated with a proprietory nickel-magnesium alloy with the subsequent addition of 1% silicon as 85

Table II-A
Summary of Creep and Stress Rupture Data of Ferritic Ductile Iron

Heat No.	Chemical Analysis TC%	Mn%	P%	S%	Si%	Ni%	Mg%	Heat Treatment
EA-F	3.64	0.46	0.032	0.014	2.66	0.66	0.076	1650 °F-4-FC
CD-F	3.60	(0.3)(c)	(0.03)(c)	0.008	2.56	1.26	0.06	1650 °F-4-FC to 1300-4-FC
CE-F	3.95	(0.3)(c)	(0.03)(c)	0.009	2.56	1.22	0.08	1650 °F-4-FC to 1300-4-FC
CF-F	4.15	(0.3)(c)	(0.03)(c)	0.005	2.63	1.18	0.07	1650 °F-4-FC to 1300-4-FC
CG-F	3.57	(0.3)(c)	(0.03)(c)	0.008	2.63	1.22	0.06	1650 °F-4-FC to 1300-4-FC
CH-F	3.85	(0.3)(c)	(0.03)(c)	0.008	2.79	1.14	0.07	1650 °F-4-FC to 1300-4-FC
CJ-F	3.90	(0.3)(c)	(0.03)(c)	0.009	2.70	1.14	0.09	1650 °F-4-FC to 1300-4-FC

	Creep & Stress Rupture Data					Residual Room Temperature Properties		
Heat No.	Temp. °F	Stress psi	Life Hours (a)	Min. Rate %/Hr.	Elong. % (b)	Yield Str. psi	Tensile Str. psi	Elong. %
EA-F	800	40,000	4.1	3.7	22.0			
CD-F	800	40,000	3.4	2.9	15.0			
CE-F	800	40,000	6.3	2.15	23.0			
CF-F	800	40,000	7.5	1.8	21.0			
CG-F	800	40,000	7.9	1.9	22.0			
CH-F	800	40,000	9.1	1.65	24.0			
CJ-F	800	40,000	10.4	1.5	23.0			
EA-F	800	30,000	127.8	0.078	18.0			
EA-F	800	18,000	(1411)	0.0009	(1.45)	51,800	67,500	18.7
EA-F	1000	15,000	4.5	2.2	13.0			
EA-F	1000	10,000	98.0	0.093	17.0			
EA-F	1000	4,000	(1697)	0.0001	(0.32)	48,600	64,200	20.0
EA-F	1200	8,000	0.64	18.0	24.0			
EA-F	1200	5,000	10.1	1.14	28.0			
EA-F	1200	3,000	170.0	0.074	31.0			
EA-F	1200	1,000	(1200)	0.001	(1.3)	43,500	58,250	23.0
EA-F	1200	0	(see Fig. 14)—growth test			50,600	62,600	16.9

(a) Times in parentheses indicate duration of creep tests not run to fracture.
(b) Elongation in parentheses indicate total plastic deformation in creep tests when discontinued.
(c) Analyses in parentheses are nominal analyses.

grade ferrosilicon on reladling in accordance with the practices defined by International Nickel Company patents.

Test bars were also obtained from six heats of ferritic ductile iron which were produced in a basic (magnesite) lined cupola. One ton taps were treated similarly to the induction heats. Ductile iron returns constituted 25 to 40% of the cupola charge.

Heat Identification Code

For simplicity and clarity, the following heat identification code has been adopted: The prefix letter identifies the melting procedure, "E" for induction and "C" for cupola; the second letter is an arbitrary heat identification; and the suffix letter describes the type of material, "F" for ferritic, "P" for pearlitic, and "A" for austenitic. Thus, EB-A is heat B which was induction melted austenitic ductile iron.

Heat Treatment

Ferritic grade: The ferritizing heat treatment normally given to ductile iron is 1650 or 1700 °F (900 or 925 °C) for four hours (to dissolve any massive carbides that may be present in the as-cast con-

Table II-B
Summary of Creep and Stress Rupture Data of Pearlitic Ductile Iron

Heat No.	Chemical Analysis TC%	Mn%	P%	S%	Si%	Ni%	Mg%	Heat Treatment
EA-P	3.64	0.46	0.032	0.014	2.66	0.66	0.076	1650 °F–4–A.C.

Creep & Stress Rupture Data					Residual Room Temperature Properties		
Temp. °F	Stress psi	Life Hours	Min. Rate %/Hr.	Elong. %	Yield Strength psi	Tensile Strength psi	Elong. %
		(a)		(b)			
* 800	70,000	5.2	1.2	11.0			
* 800	50,000	201.3	0.031	16.0			
800	50,000	162.3	0.042	16.0			
800	25,000	(1917)	0.0005	(1.34)	82,000	111,800	2.6
* 1000	35,000	1.3	5.9	20.0			
* 1000	25,000	12.6	0.70	17.0			
* 1000	18,000	67.2	0.13	18.0			
* 1000	10,000	701	0.0098	24.0			
1000	4,000	(1819)	0.00092	(3.3)	51,100	67,100	17.4
1000	0	(See Fig. 13) — growth test			53,800	68,800	14.3
1200	8,000	6.8	1.85	34.0			
1200	5,000	36.5	0.32	38.0			
1200	3,000	375.5	0.052	29.0			
1200	1,000	(1290)	0.0013	(4.0)	45,200	58,800	22.0
* 1200	0	(See Fig. 14) — growth test			45,400	58,200	19.5

(a) Times in parentheses indicate duration of creep tests not run to fracture.
(b) Elongation in parentheses indicate total plastic deformation in creep tests when discontinued.
* These bars originally heat treated 1650 °F–4–F.C. and then reaustenitized at 1650 °F and normalized as shown above.

dition) followed by a slow cool (100 °F per hour max.) to prevent reprecipitation of pearlite. This practice was followed except for six test bars which were heat treated in a smaller laboratory furnace. As the normal cooling rate of this furnace was fast enough to cause some pearlite to form (250 °F per hour), the cooling cycle was interrupted at 1300 °F (705 °C) to graphitize this pearlite and to provide time for the graphite to migrate to the original carbon spherulites, thus producing an essentially ferritic matrix.

A typical ferritic structure is shown in Fig. 1.

Pearlitic grade: This grade was heat treated at 1650 °F (900 °C) to dissolve any carbides as above, and then air-cooled to yield a fine pearlite. The microstructure typical of this grade is shown in Fig. 2.

Austenitic grade: The austenitic grade is normally used in the as-cast condition and contains some massive carbide, as shown in Fig. 3.

Test Bars and Specimen Preparation

One inch Y block castings, Fig. 4, suitable for duplicate tensile or creep bars, were used exclusively. Immediately after pouring, an insulating compound was added to the riser to assure soundness throughout the test coupon. A few of the test bars poured in the production foundry (cupola heats) had only one test coupon beneath the riser section. This modified Y block and the one illustrated have essen-

Table II-C
Summary of Creep and Stress Rupture Data of Austenitic Ductile Iron

Heat No.	Chemical Analysis TC%	Mn%	P%	S%	Si%	Ni%	Mg%	Heat Treatment
EB-A	2.84	2.13	0.030	0.011	2.67	23.2	0.064	None
EC-A	2.96	2.13	0.020	0.013	2.65	23.1	0.100	None
EK-A	2.86	1.93	0.026	0.013	2.49	22.0	0.127	None
EL-A	2.92	1.82	0.032	0.010	2.47	21.6	0.114	None
EM-A	3.04	1.94	0.025	0.015	2.50	22.2	0.134	None
EN-A	3.05	1.85	0.014	0.015	2.44	22.2	0.138	None

Heat No.	Creep & Stress Rupture Data Temp. °F	Stress psi	Life Hours	Min. Rate %/Hr.	Elong. %	Residual Room Temperature Properties Yield Strength psi	Tensile Strength psi	Elong. %
			(a)		(b)			
EB-A	800	45,000	26.3	0.14	16.0			
EB-A	800	40,000	134.4	0.037	15.0			
EB-A	800	35,000	(500)	0.0054	(9)	45,570	64,800	22.6
EB-A	800	25,000	(1508)	0.00058	(2.0)	36,400	57,200	29.0
EB-A	1000	30,000	22.9	0.45	17.0			
EC-A	1000	30,000	17.7	0.37	13.0			
EK-A	1000	30,000	12.5	0.76	14.0			
EL-A	1000	30,000	12.9	0.65	14.0			
EM-A	1000	30,000	20.6	0.25	12.0			
EN-A	1000	30,000	26.0	0.23	14.0			
EB-A	1000	25,000	161.0	0.05	16.0			
EB-A	1000	20,000	(821)	0.0044	(7.0)	39,000	55,900	12.6
EB-A	1000	14,000	(1464)	0.0002	(1.2)	40,200	59,600	26.5
EB-A	1000	0	(1003)	Growth nil		37,200	60,600	26.5
EC-A	1200	20,000	1.4	5.2	12.0			
EC-A	1200	18,000	3.3	not obt.	14.0			
EC-A	1200	15,000	16.3	0.43	14.0			
EC-A	1200	9,000	910	0.0024	7.0			
EC-A	1200	6,000	(1172)	0.00014	(.57)	36,600	54,200	20.0
EC-A	1400	9,000	3.0	1.7	11.0			
EC-A	1400	6,000	66.9	0.054	12.0			
EC-A	1400	3,000	1315	0.0013	6.5			

(a) Times in parentheses indicate duration of creep tests not run to fracture.
(b) Elongation in parentheses indicate total plastic deformation in creep tests when discontinued.

tially the same cooling rate, which is equivalent to that of an infinite plate 0.9 inch thick (4).

For the room temperature tensile tests, shouldered 0.505 inch diameter by 2.0 inch gage length specimens were prepared from the coupons cut from the Y blocks. Threaded specimens ¾ inch diameter by 5 inch long with a 0.357 inch diameter by 2.0 inch gage length (1/10 square inch) were machined for all of the elevated temperature tensile and creep work. The smaller gage diameter was required to permit reaching the requisite stress levels at the lower temperatures with the loading capacity of the creep testing units. The system was followed for consistency for all elevated temperature work.

Testing

Testing followed in general the applicable ASTM procedure. Elevated temperature creep and stress-strain rupture tests require

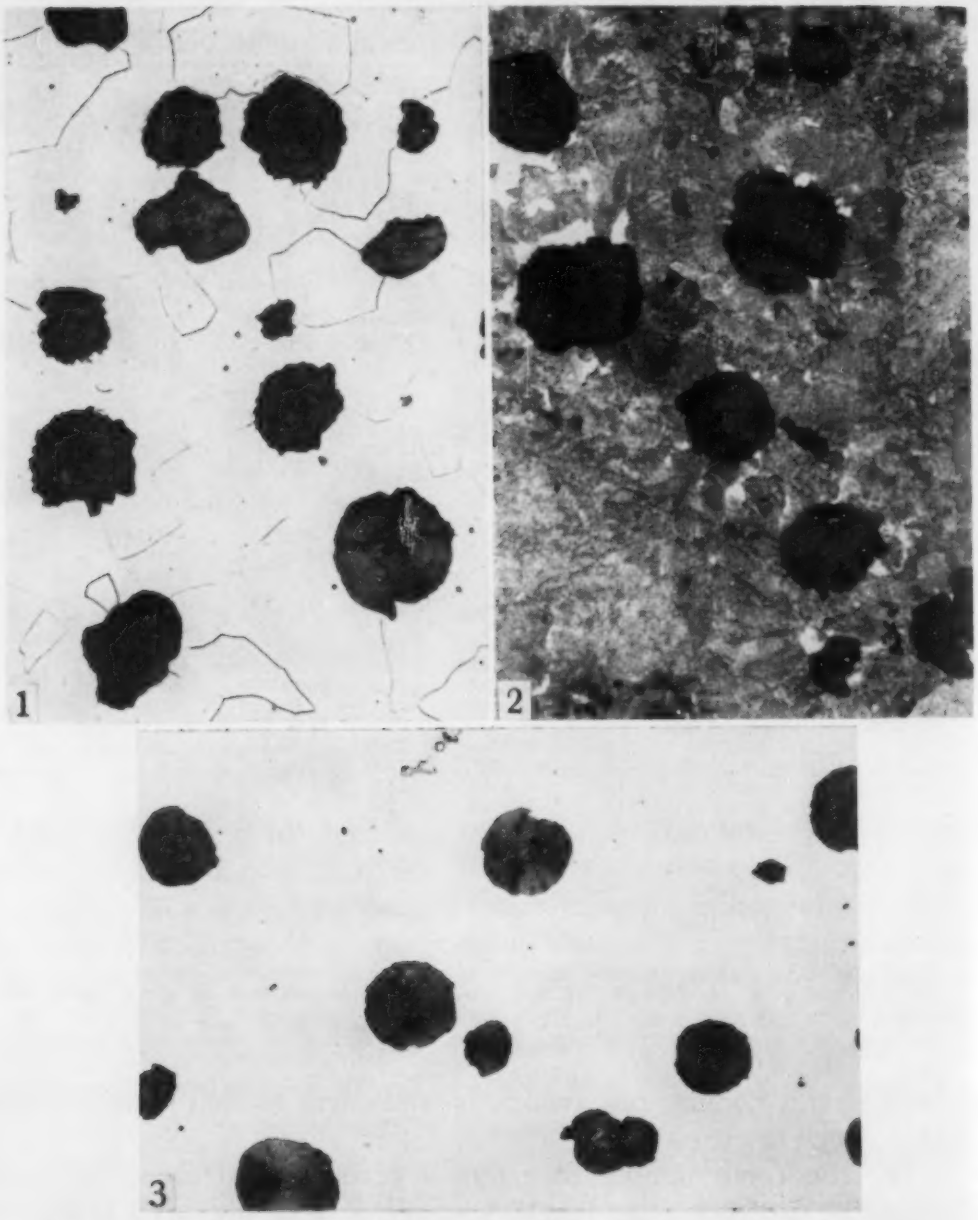


Fig. 1—Ferritic Ductile Iron, Heat EA-F, As Heat Treated (1650 °F for Four Hours and Furnace-Cooled). Etchant—3% nital. X 250.

Fig. 2—Pearlitic Ductile Iron, Heat EA-P, As Normalized From 1650 °F. Etchant—3% nital. X 250.

Fig. 3—Austenitic Ductile Iron, Heat EC-A, As-Cast. Etchant—3% nital. X 250.

careful and critical control to obtain consistent and reproducible data. These testing procedures further conformed to previously described techniques (5) as standardized at the American Brake Shoe Company's Metallurgical Laboratory for the study of iron-chromium-nickel heat resistant alloys. Where tests were discontinued before fracture, residual room temperature tensile properties were subsequently ob-

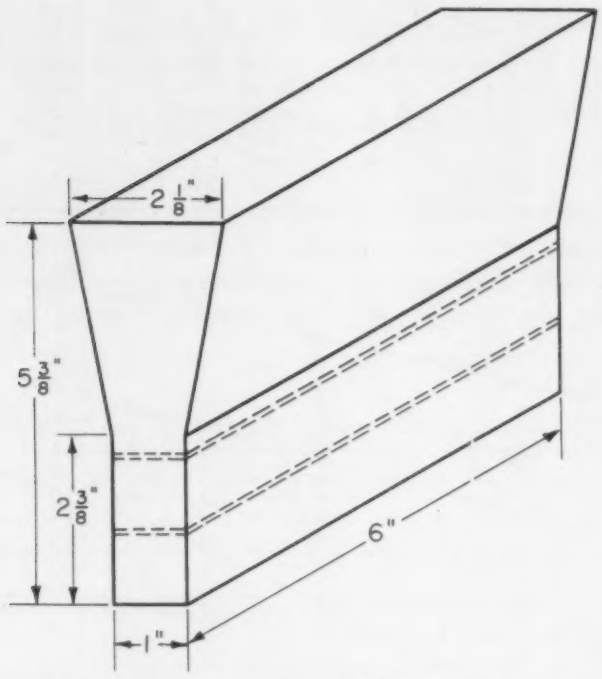


Fig. 4—One Inch "Y" Block Casting.

tained. Growth was measured in the creep testing units with the test bar under zero load.

Tensile tests were pulled at a strain rate of 0.1 inch per minute. The yield strengths were determined by the "dial arrest" method. For the elevated temperature tests, three thermocouples were spot welded at 1-inch intervals along the gage length. The bars were held at the testing temperature for a period of 15 minutes minimum, and temperatures over the gage length were held within ±10 °F of the nominal test temperature.

Microspecimens of the "as-tested" materials were cut from the Y blocks adjacent to the tensile bars. Those taken after elevated tem-

Table III
Summary of Creep and Rupture Properties of Ductile Irons

Type	Temp. °F	Limiting Creep Stress (for 0.0001% per Hr. Min. Rate) psi	Limiting Rupture Stress (psi) for Fracture in 10 Hours	100 Hours	1000 Hours
Ferritic	800	14,000	37,000	31,000	25,000
	1,000	4,000	13,000	10,000	7,500
	1,200	550	5,000	3,300	2,200
Pearlitic	800	19,000	65,000	52,000	42,000
	1,000	1,750	26,000	17,000	9,100
	1,200	480	7,100	4,100	2,400
Austenitic	800	18,500	50,000	41,000	35,000
	1,000	13,000	33,000	26,000	21,000
	1,200	5,700	15,500	12,000	9,000
	1,400	2,000	7,800	5,700	3,300

Heat	Code	TC%	Mn%	P%	S%	Si%	Ni%	Mg%	Heat Treat.
EA-F	o	3.64	0.46	0.032	0.014	2.66	0.66	0.08	1650°F-4-FC
CD-F	• 1	3.60	(0.3)	(0.03)	0.008	2.56	1.26	0.06	1650°F-4-FC to 1300°F-4-FC
CE-F	• 2	3.95	"	"	0.009	2.56	1.22	0.08	
CF-F	• 3	4.15	"	"	0.005	2.63	1.18	0.07	
CG-F	• 4	3.57	"	"	0.008	2.63	1.22	0.06	
CH-F	• 5	3.85	"	"	0.008	2.79	1.14	0.07	
CJ-F	• 6	3.90	"	"	0.009	2.70	1.14	0.09	

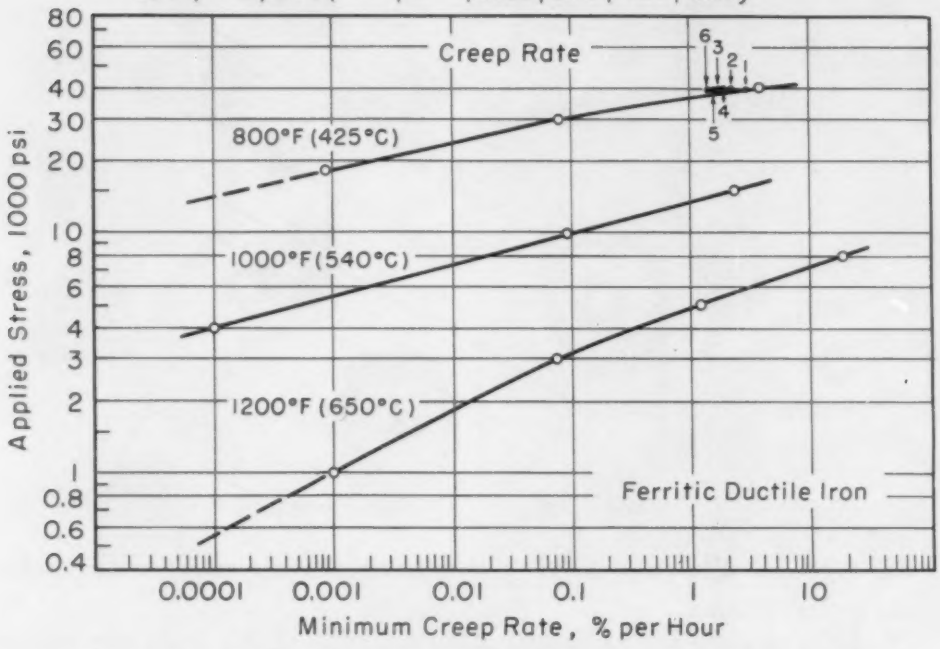


Fig. 5—Log Applied Stress Versus Log Minimum Creep Rate for Ferritic Ductile Iron.

Heat	TC%	Mn%	P%	S%	Si%	Ni%	Mg%	Heat Treat.
EA-P	3.64	0.46	0.032	0.014	2.66	0.66	0.08	1650°F-4-AC

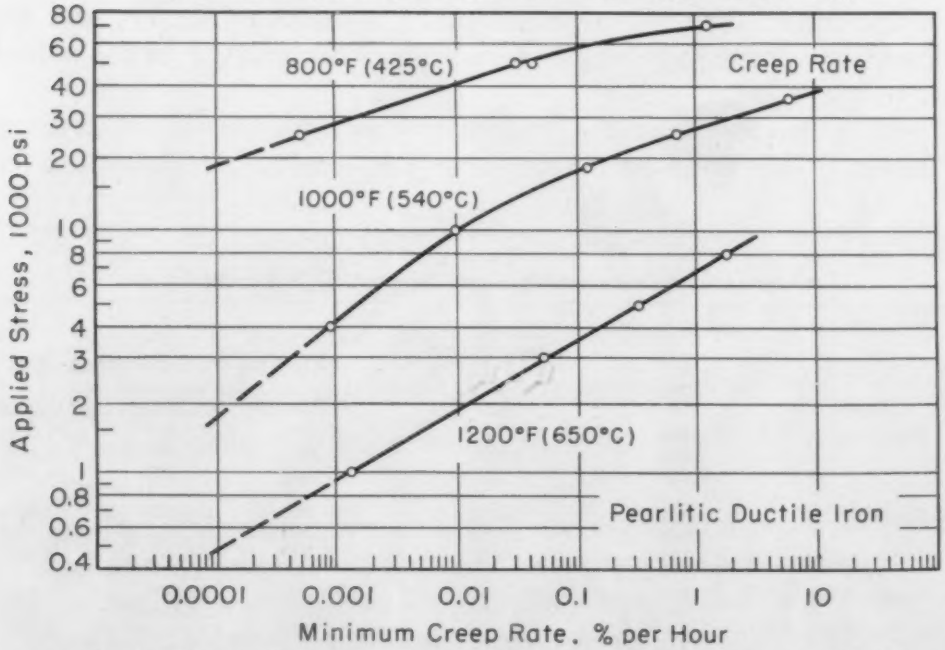


Fig. 6—Log Applied Stress Versus Log Minimum Creep Rate for Pearlitic Ductile Iron.

perature tests were cut longitudinally from the gage length of the specimens. All were etched with 3% nital.

Elevated Temperature Properties

Creep and Stress-Rupture Properties

Preliminary testing of earlier heats of all three grades had shown that creep was, for all practical considerations, of negligible importance at 600 °F (315 °C), paralleling the behavior of steels. Extended creep testing on these materials was therefore confined to the tem-

Heat	Code	TC%	Mn%	P%	S%	Si%	Ni%	Mg%	Heat Treat.
EB-A	o	2.84	2.13	0.030	0.011	2.67	23.2	0.064	As-Cast
EC-A	Δ	2.96	2.13	0.020	0.013	2.65	23.1	0.10	" "
EK-A	• 1	2.86	1.93	0.026	0.013	2.49	22.0	0.127	" "
EL-A	• 2	2.92	1.82	0.032	0.010	2.47	21.6	0.114	" "
EM-A	• 3	3.04	1.94	0.025	0.015	2.50	22.2	0.134	" "
EN-A	• 4	3.05	1.85	0.014	0.015	2.44	22.2	0.138	" "

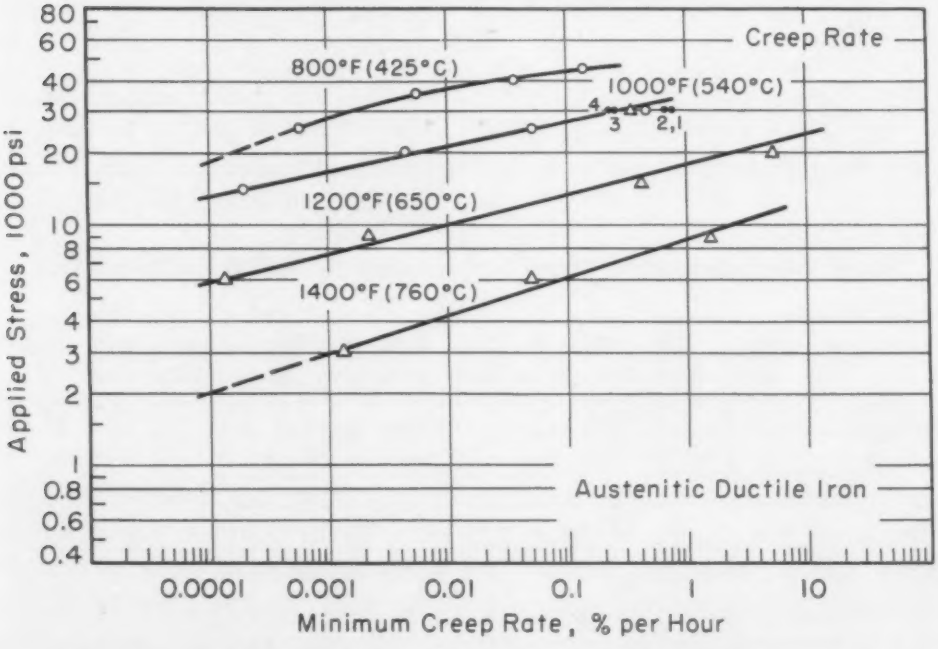


Fig. 7—Log Applied Stress Versus Log Minimum Creep Rate for Austenitic Ductile Iron.

perature range of 800–1200 °F (425–650 °C). In addition, a few tests were made on the austenitic grade at 1400 °F (760 °C).

Detailed results of the stress-strain rupture and standard creep tests are summarized in Table II. The creep rate data are plotted for each grade in Figs. 5–7, and Figs. 8–10 illustrate the effect of temperature and stress on fracture time. Values of limiting creep stress (0.0001% per hour minimum rate) and limiting rupture stress (for 10, 100, and 1000 hour life) are summarized in Table III. Graphic com-

Heat	Code	TC%	Mn%	P%	S%	Si%	Ni%	Mg%	Heat Treat.
EA-F	○	3.64	0.46	0.032	0.014	2.66	0.66	0.08	1650°F-4-FC
CD-F	• 1	3.60	(0.3)	(0.03)	0.008	2.56	1.26	0.06	1650°F-4-FC to 1300°F-4-FC
CE-F	• 2	3.95	"	"	0.009	2.56	1.22	0.08	
CF-F	• 3	4.15	"	"	0.005	2.63	1.18	0.07	
CG-F	• 4	3.57	"	"	0.008	2.63	1.22	0.06	
CH-F	• 5	3.85	"	"	0.008	2.79	1.14	0.07	
CJ-F	• 6	3.90	"	"	0.009	2.70	1.14	0.09	

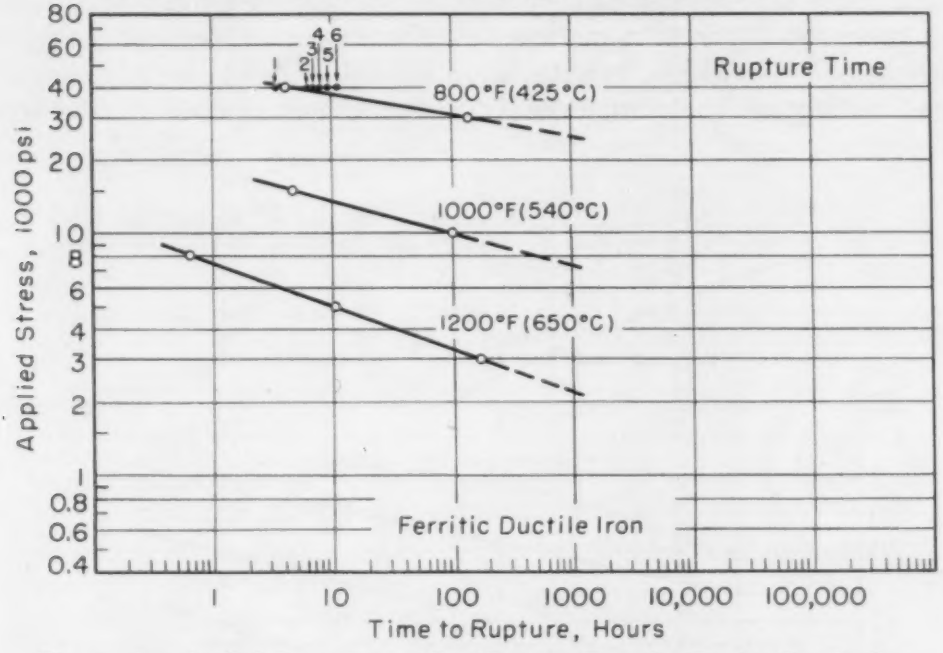


Fig. 8—Log Applied Stress Versus Log Rupture Time for Ferritic Ductile Iron.

Heat	TC%	Mn%	P%	S%	Si%	Ni%	Mg%	Heat Treat.
EA-P	3.64	0.46	0.032	0.014	2.66	0.66	0.08	1650°F-4-AC

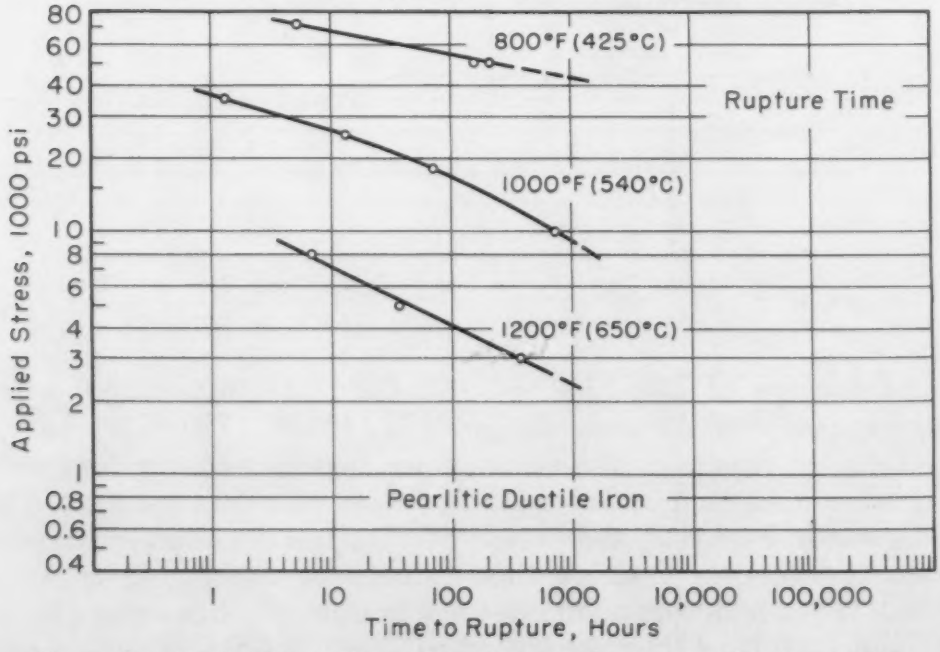


Fig. 9—Log Applied Stress Versus Log Rupture Time for Pearlitic Ductile Iron.

Heat	Code	TC%	Mn%	P%	S%	Si%	Ni%	Mg%	Heat Treat.
EB-A	○	2.84	2.13	0.030	0.011	2.67	23.2	0.064	As-Cast
EC-A	△	2.96	2.13	0.020	0.013	2.65	23.1	0.10	" "
EK-A	•1	2.86	1.93	0.026	0.013	2.49	22.0	0.127	" "
EL-A	•2	2.92	1.82	0.032	0.010	2.47	21.6	0.114	" "
EM-A	•3	3.04	1.94	0.025	0.015	2.50	22.2	0.134	" "
EN-A	•4	3.05	1.85	0.014	0.015	2.44	22.2	0.138	" "

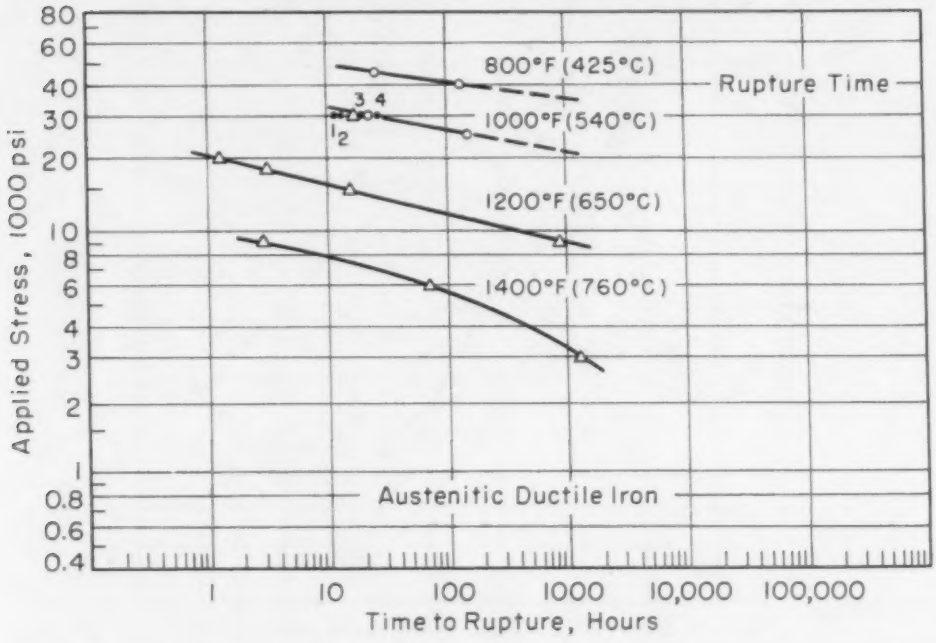


Fig. 10—Log Applied Stress Versus Log Rupture Time for Austenitic Ductile Iron.

parisons are shown in Figs. 11 and 12 respectively, with comparative data for low carbon steels (6,7).

At 800 °F (425 °C) creep becomes prominent, with limiting creep stress values that range from approximately 20 to 40% of the ultimate tensile strength at this temperature. Marked differences in short-term rupture strength are evident, with the pearlitic iron being superior to both the ferritic or austenitic grades. Under long-term creep conditions, at lower stresses, these differences are moderated although the pearlitic iron retains a margin of superiority based on expected life. On the basis of limiting creep stress values, the pearlitic and austenitic grades are essentially equivalent (19,000 psi and 18,500 psi respectively). The ferritic grade is definitely weaker with a limiting creep stress value of 14,000 psi.

Above 800 °F (425 °C), the creep strength of both the ferritic and pearlitic grades falls rapidly as temperature is increased. While industrial experience is as yet inadequate, utility of these grades appears limited to a maximum temperature of 1000 to 1100 °F (540 to 595 °C) for long-term load carrying applications when scaling resistance as well as strength is considered. This does not preclude their potential usefulness at higher temperatures where other special con-

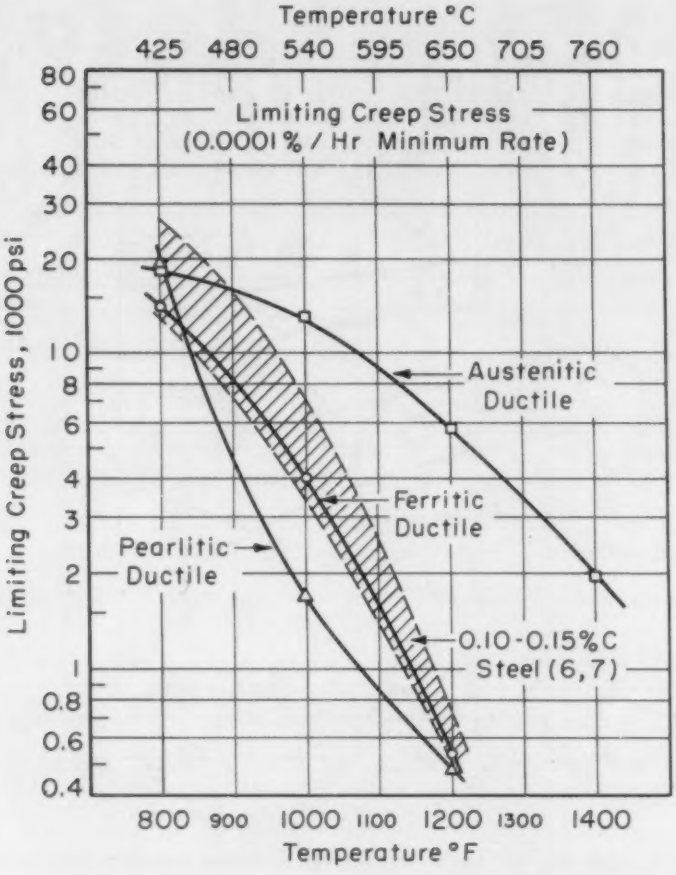


Fig. 11—Limiting Creep Stress Versus Temperature for Ductile Irons and Low Carbon Steel.

siderations apply, for shorter term applications, or for essentially functional shapes.

The comparisons with carbon steel, with similar temperature limitations based on strength and scaling resistance, are of interest. From Fig. 11 it is evident that ferritic ductile iron and low carbon steel have similar creep properties over the temperature range of 800–1200 °F (425–650 °C). It is plausible to suppose that the weakening effect of the spheroidal graphite in the ductile iron is compensated for by the higher alloy content (particularly silicon) of the ferrite in the ductile iron. The low carbon steel is, however, superior to the ferritic iron on the basis of rupture strength as shown in Fig. 12.

The austenitic iron has markedly superior strength at and above 1000 °F (540 °C) in comparison with the ferritic and pearlitic types. This reflects the greater resistance to creep which characterizes the face-centered cubic structures at higher temperatures. The higher strength, coupled with the greater resistance to scaling conferred by the high nickel content, suggests that for long-term load carrying applications this alloyed grade might have utility as high as 1200 °F (650 °C), possibly 1300 °F (705 °C). The practical limit can be set

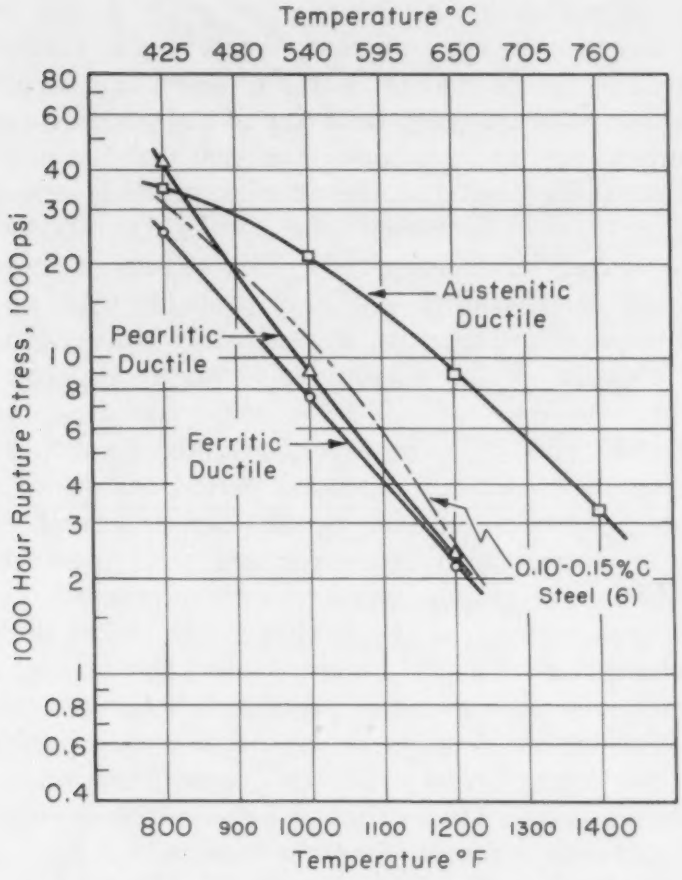


Fig. 12—1000 Hour Rupture Stress Versus Temperature for Ductile Irons and Low Carbon Steel.

only through industrial experience and the limiting factor will be generally oxidation resistance.

A limited number of short-term rupture tests were made on test bars poured from current production heats of ferritic and austenitic iron to determine at least partially the range of properties that might be encountered and to ascertain whether the base line data were reasonably typical. The ferritic heats (CD-F to CJ-F, Table II) were tested at 800 °F under a stress of 40,000 psi. These data have been included in the ferritic ductile iron plots of creep characteristics (Fig. 5), and time to rupture (Fig. 8). The tests on the austenitic irons (EK-A to EN-A, Table II) were at 1000 °F—30,000 psi and the data are included in Fig. 7 and 10.

Both the ferritic and austenitic irons from recent production show good reproducibility. Comparisons suggest that the base line data are reasonably representative.

Structural Stability and Growth

The pearlitic grade progressively graphitizes at the higher temperatures and thus is structurally unstable. The net effect is the

"ferritizing" or conversion of the pearlitic grade to the ferritic type, if time and temperature are sufficient. While this is further discussed and illustrated in the section on metallography, this structural instability is manifested in the creep behavior of the pearlitic grade. Where the time-temperature test conditions are such that the pearlite matrix remains substantially unaltered, the pearlitic grade is stronger than its ferritic counter-part. These conditions prevail at 800 °F (425 °C) even for the longer term creep tests. The effects of more extended times have not been studied, but it is probable that, up to 800 °F (425 °C), the pearlitic structure is reasonably stable; graphitization, if it does actually occur, undoubtedly would proceed extremely slowly.

At 1000 °F (540 °C), however, graphitization proceeds at a finite rate, but over such an extended period that the shorter-term stress-rupture properties are those of the pearlitic structure essentially unaltered. The longer-term stress-rupture tests, however, provide additional time for the graphitization process to proceed. The resultant properties approach those of the ferritic grade rather than reflecting the higher strength that would be anticipated by extrapolation of the short-time properties, a reasonable procedure if no structural changes were to have occurred. With more extended testing periods, such as characterize the lower stress creep test, graphitization can proceed essentially to completion. Under these conditions the originally pearlitic grade exhibits lower strength than the iron which had been in the ferritic condition from the start of testing. The additional impairment, beyond that expected from ferritizing per se, appears associated with modifications of the grain size and of the graphite spheroids which are further discussed in the section on metallography.

The progressive ferritization of the pearlitic grade is further evidenced by the residual room temperature properties obtained on those creep tests at 1000 °F and 1200 °F (540 and 650 °C) which were discontinued before fracture.

Except for the primary growth of the pearlitic iron as the result of the volume changes produced by graphitization, no significant growth was expected in these irons at these moderately elevated temperatures, particularly under constant temperature creep test conditions. Precision growth tests, Figs. 13 and 14, at 1000 and 1200 °F (540 and 650 °C) confirm this. The tests on the pearlitic iron serve to delineate the progress of graphitization and the marked effect of increasing temperature is readily apparent. Graphitization proceeds quite slowly at 1000 °F (540 °C) and appears to be essentially complete in about 1500 hours. At 1200 °F (650 °C), however, a major portion occurs in the first forty hours and graphitization appears essentially complete in less than 200 hours. The ferritic grade was checked at 1200 °F (650 °C) and showed, as expected, negligible growth.

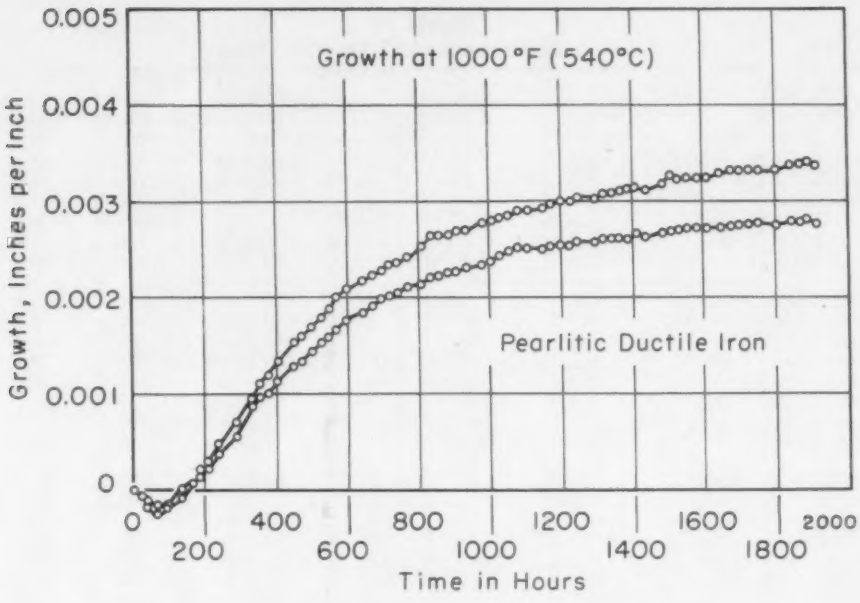


Fig. 13—Growth of Pearlitic Ductile Iron at 1000 °F.

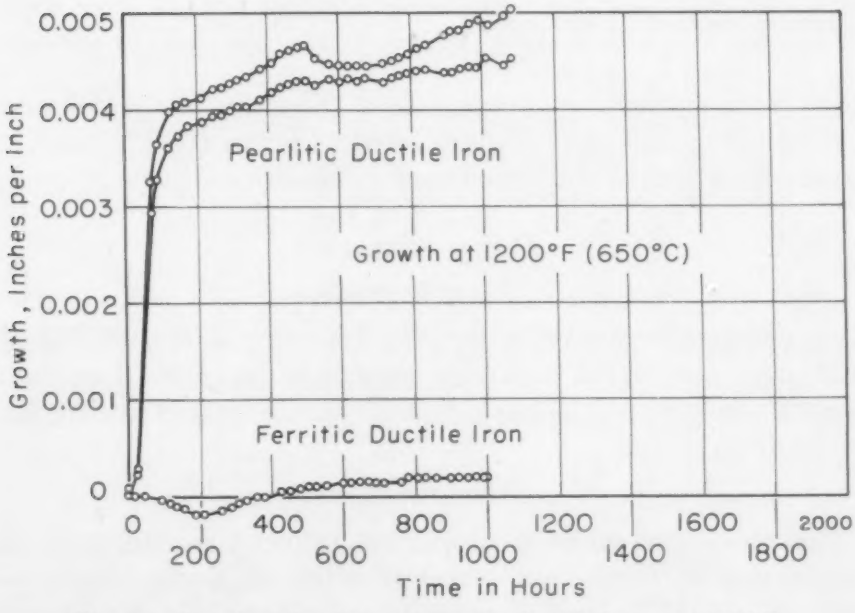


Fig. 14—Growth of Pearlitic and Ferritic Ductile Irons at 1200 °F.

Hot Tensile Properties

Table IV summarizes the hot tensile test data which are plotted in Fig. 15. Ductility as well as strength of the ferritic and pearlitic grades first decreases with increasing temperature, up to about 1100 °F (595 °C) and 800 °F (425 °C) respectively. Above these temperatures elongation rises sharply as the strength further decreases.

Austenitic ductile iron shows more moderate loss of strength and

Table IV
Tensile Properties of Ductile Irons

Type and Heat Treatment	Heat	Temperature of Test	Tensile Strength psi	Yield Strength psi	Elong. %	Brinell Hardness
Ferritic–1650 °F–4–FC	EA-F	70 °F – 21 °C	65,500	47,900	24.0	156
Ferritic–1650 °F–4–FC	EA-F	70 °F – 21 °C	65,000	48,100	24.0	
Ferritic–1650 °F–4–FC	EA-F	800 °F – 425 °C	45,400	36,200	12.5	
Ferritic–1650 °F–4–FC	EA-F	1000 °F – 540 °C	26,800	25,200	9.8	
Ferritic–1650 °F–4–FC	EA-F	1200 °F – 650 °C	10,800	10,400	11.3	
Ferritic–1650 °F–4–FC	EA-F	1400 °F – 700 °C	5,000	4,950	56.0	
Pearlitic–1650 °F–4–AC	EA-P	70 °F – 21 °C	127,500	118,000	5.0	269
Pearlitic–1650 °F–4–AC	EA-P	70 °F – 21 °C	125,500	98,500	4.0	
Pearlitic–1650 °F–4–AC *	EA-P	70 °F – 21 °C	147,200	109,200	6.0	277
Pearlitic–1650 °F–4–AC *	EA-P	800 °F – 425 °C	89,000	64,200	2.8	
Pearlitic–1650 °F–4–AC *	EA-P	900 °F – 480 °C	67,000	60,400	6.4	
Pearlitic–1650 °F–4–AC *	EA-P	1000 °F – 540 °C	49,000	46,200	13.1	
Pearlitic–1650 °F–4–AC	EA-P	1200 °F – 650 °C	25,500	25,200	15.7	
Pearlitic–1650 °F–4–AC	EA-P	1400 °F – 760 °C	7,800	7,200	24.0	
Austenitic – As Cast	EB-A	70 °F – 21 °C	64,000	27,000(a)	36.0	126
Austenitic – As Cast	EB-A	70 °F – 21 °C	65,500	28,200(a)	41.5	
Austenitic – As Cast	EC-A	70 °F – 21 °C	63,600	34,100	36.5	126
Austenitic – As Cast	EC-A	70 °F – 21 °C	60,300	34,200	26.0	
Austenitic – As Cast	EB-A	800 °F – 425 °C	52,400	26,200	22.8	
Austenitic – As Cast	EB-A	1000 °F – 540 °C	42,000	23,100	19.3	
Austenitic – As Cast	EC-A	1200 °F – 650 °C	28,000	24,200	9.8	
Austenitic – As Cast	EC-A	1400 °F – 760 °C	17,200	16,600	13.3	

* These specimens first ferritized and then reheat treated and normalized from 1650 °F(900 °C).
(a) Yield strength at 0.2% offset determined by SR4 resistance wire strain gages. All other values were determined by dial arrest method.

ductility with increasing temperatures than the unalloyed materials. The yield strength is only slightly affected up to 1000 °F and, at temperatures higher than this, decreases gradually.

Metallography

Ferritic grade

No changes in the basic ferritic structure shown in Fig. 1 were evident after any of the high temperature tests, other than the deformation of the graphite spheroids and ferrite grains which occurred under load.

Pearlitic grade

The creep and rupture properties reflect the effects of pearlite decomposition to ferrite and graphite after relatively long exposures at 1000 °F (540 °C) and shorter exposures at higher temperatures. Figs. 16 and 17 illustrate the salient features of the accompanying microstructural changes.

The intermediate structure between the normalized pearlite of Fig. 2 and a completely graphitized iron is a spheroidized and partly graphitized pearlite (Fig. 16). The product after long exposures at subcritical temperatures, essentially completely graphitized, is shown in Fig. 17. The finer but markedly less uniform ferrite grain size and the more highly irregular deposition of the secondary graphite on the original graphite spheroids, contrasted with the normal ferritic struc-

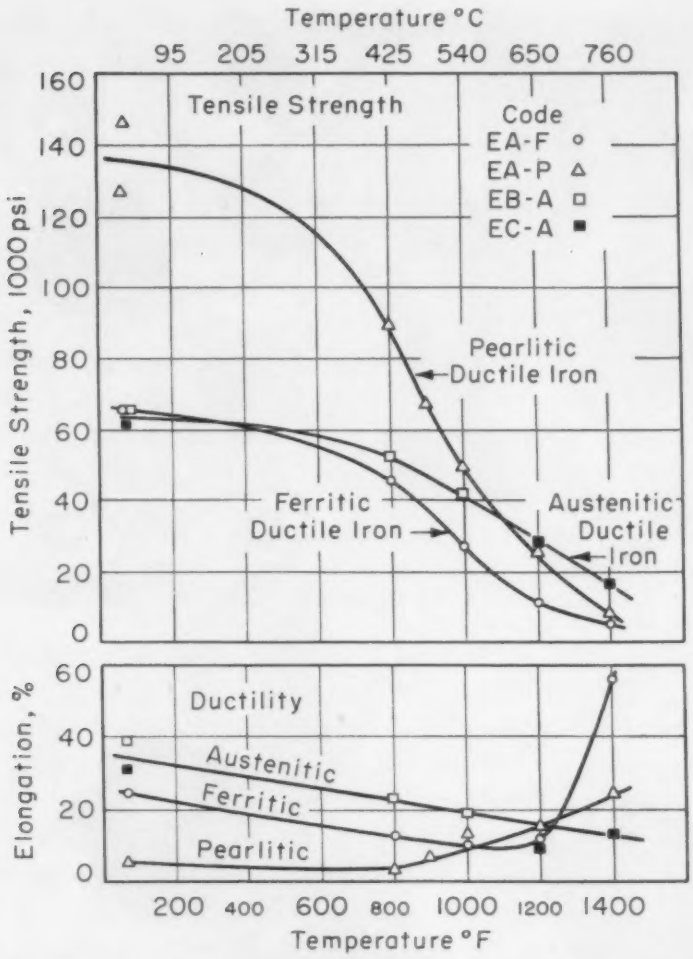
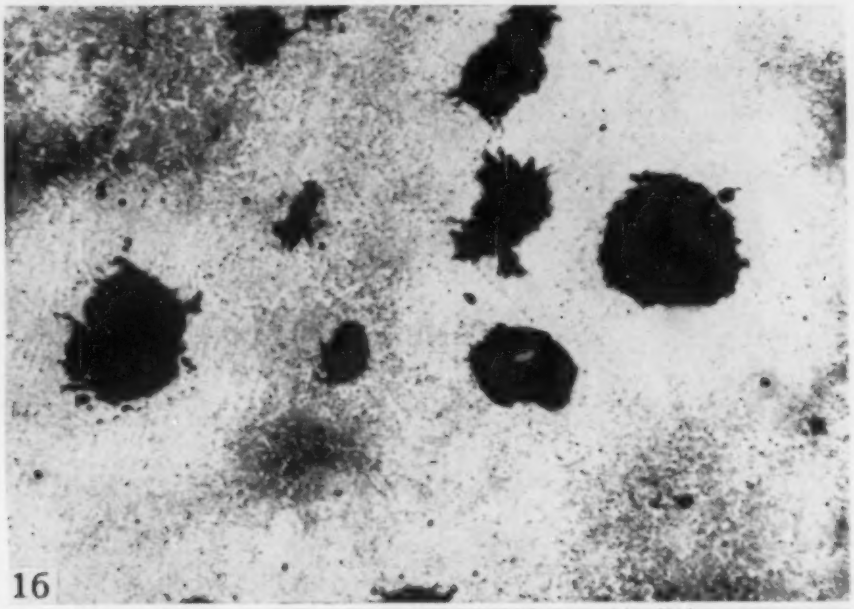


Fig. 15—Effect of Temperature Upon Tensile Properties of Ductile Irons.

Table V
Microstructure Evaluation and Combined Carbon Content of Pearlitic Iron Specimens

Temperature °F	Temperature °C	Hours Exposure at Temperature	Combined Carbon Content	Microstructure Matrix Evaluation *	Reference Figure Number
70	21	As normalized mat'l.	0.69/0.88	Fine lamellar pearlite	2
800	425	5.2	0.82	No change from normalized condition	
800	425	1917	0.68	No change from normalized condition	
1000	540	1.3	0.79		
1000	540	12.6	0.84		
1000	540	67.2	0.87	No significant change from normalized condition	
1000	540	701	0.18	25% spheroidized pearlite — 75% ferrite	16
1000	540	1819	0.04		
1000	540	1917		1% spheroidized pearlite — 99% ferrite	17
1200	650	6.8	0.48	50% spheroidized pearlite — 50% ferrite	
1200	650	36.5	0.26	10% spheroidized pearlite — 90% ferrite	
1200	650	375.5	0.01	1% spheroidized pearlite — 99% ferrite	
1200	650	1079	0.16		
1200	650	1290		Negligible spheroidized pearlite — 100% ferrite	

* Pearlite-ferrite ratios are estimated.



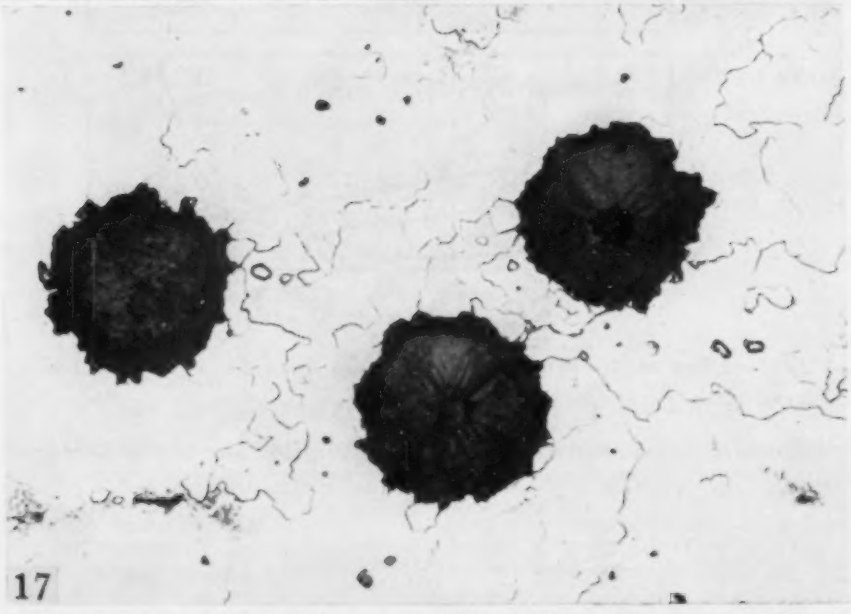


Fig. 16—Pearlitic Ductile Iron After 701 Hours Exposure at 1000 °F Under a Load of 10,000 psi. Heat EA-P. Etchant—3% nital. X 250.

Fig. 17—Completely Graphitized Pearlitic Ductile Iron After 1917 Hours Exposure at 1000 °F in a No Load Growth Test. Heat EA-P. Etchant—3% nital. X 250.

ture of Fig. 1, were found to be typical. Both of these conditions likely contribute to the impaired creep strength of the ferritized pearlitic iron in comparison with the stable ferritic grade.

Table V summarizes an evaluation of the microstructural changes and combined carbon contents. From this tabulation and from the growth test data it appears that (a) at 800 °F (425 °C) pearlitic ductile iron is essentially stable, (b) at 1000 °F (540 °C) the pearlite sphe-

roidizes during the first few hundred hours, the iron subsequently graphitizes and eventually will be somewhat weaker than the basic ferritic iron, and (c) at 1200 °F (650 °C) the pearlite spheroidizes and graphitizes rapidly, within less than 100–200 hours.

Austenitic grade

No change was observed in the microstructure of austenitic iron after testing at 800 °F (425 °C) or at 1000 °F (540 °C) for times up to about 1000 hours. After 1464 hours at 1000 °F (540 °C), approximately 1000 hours at 1200 °F (650 °C) and 67 hours at 1400 °F (760 °C) an extremely fine precipitate was noted in the austenite adjacent to the original carbides. Undoubtedly carbide, it could be resolved only with difficulty at X2000 using an oil immersion lens.

Summary and Conclusions

1. The short term tensile and rupture properties of pearlitic ductile iron are superior to those of the ferritic grade. Correspondingly superior creep properties, reflecting long-term behavior, hold only to about 800 °F (425 °C). At higher temperatures, the potential long-term superiority cannot be realized as the pearlitic iron, structurally unstable, progressively graphitizes and reverts to a ferritic iron which has lower creep strength than the standard ferritic grade. Creep strength of the stable ferritic iron is comparable to that of low carbon steel from 800 to 1200 °F (425 to 650 °C).

2. The austenitic iron is markedly stronger at and above 1000 °F (540 °C) than the ferritic and pearlitic grades, which lose strength rapidly above 800 °F (425 °C).

3. Utility of the standard ferritic and pearlitic grades appears limited to a maximum temperature of 1000 to 1100 °F (540 to 595 °C) for long-term load carrying applications when both scaling resistance as well as strength is considered. The high nickel austenitic iron should have similar utility to 1200 or 1300 °F (650 to 705 °C).

Acknowledgment

The authors wish to acknowledge with appreciation the co-operation of many associates, particularly John A. Ward for execution of high temperature testing, Bruce E. Sockman for analytical work, and John W. Gleassey for preparation of microspecimens and the photomicrographs. The authors are indebted to the American Brake Shoe Co. in general and R. H. Schaefer, Vice President and Director of Research, in particular, for permission to publish this material.

References

1. Albert P. Gagnebin, Keith D. Millis and Norman B. Pilling, "Ductile Cast Iron—A New Engineering Material," *Iron Age*, Vol. 163. No. 7, February 17, 1949, p. 76–84.

2. W. H. White, L. P. Rice and A. R. Elsea, "Influence of Silicon Content on Mechanical and High Temperature Properties of Nodular Cast Iron." *Transactions,* American Foundrymens Society, Vol. 59, 1951, p. 337–347.
3. M. S. Saunders and M. J. Sinnott, "Some Properties of a Nodular Iron at Elevated Temperatures," TRANSACTIONS, American Society for Metals, Vol. XLV, 1953, p. 362–376.
4. R. W. Kraft and R. A. Flinn, "Inter-relation of Mechanical Properties, Casting Size, and Microstructure of Ductile Cast Iron," TRANSACTIONS, American Society for Metals, Vol. XLIV, 1952, p. 282–309.
5. J. A. Fellows, Earnshaw Cook and H. S. Avery, "Precision in Creep Testing," *Transactions,* American Institute of Mining and Metallurgical Engineers, Vol. 150, 1942, p. 358–372.
6. "Steels for Elevated Temperature Service," Carnegie Illinois Steel Corporation, Pittsburgh, Penna., 1949.
7. Frances H. Clark, "Metals at High Temperatures," 1950, Chapter 3. Reinhold Publishing Company, 330 West 42nd St., New York 18, N. Y.

DISCUSSION

Written Discussion: By W. Lee Williams, metallurgist, U. S. Naval Engineering Experiment Station, Annapolis, Md.

Very little has been published on the elevated temperature properties of ductile cast irons. So we think it would be worthwhile to augment the data in this excellent paper by contributing a summary of data from our own experiments.

Our tests were limited to a single iron with a practically complete ferritic structure. The composition was:

TC	3.47%	Ni	0.55%
Si	2.49%	Cu	0.30%
Mn	0.42%	Mg	0.048%

Room and elevated temperature tension data follow.

Temperature °F	Tensile Str. psi	0.2% Yield psi	Elong. %	Red. of Area %
Room	63000	45000	24	23
700	55800	35400	10	9
800	47200	32600	7	6
900	40000	28000	12	10

A summary of our creep and rupture test findings follows.

Temperature °F	Stress, psi, for rupture in		Stress, psi, for min. creep rate of	
	100 hrs.	1000 hrs.	0.0001%/hr.	0.00001%/hr.
700	45000	41000	27000	19000
800	30000	23000	13000	8200
900	18500	13500	6800	3900 (?)

Comparison of our 800 °F data with those in the author's Table III shows excellent agreement. Our material showed no microscopic evidence of growth or structural change during exposure up to 2000 hours at 900 °F.

Written Discussion: By A. P. Gagnebin, Development and Research Division, The International Nickel Co., Inc., New York.

We should like to congratulate the authors on their excellent work in measuring the elevated temperature properties of ductile iron and on the clear presentation of their results.

The International Nickel Company, Inc. laboratory in Bayonne has been doing work along the same lines and will subsequently publish a paper giving their results in detail. Broadly speaking the Inco laboratory results confirm the values given by the authors for ductile iron in the pearlitic condition and also confirm that pearlitic irons are stable at temperatures up to 800 °F. Some of the test bars have been under load at this temperature for 7000 hours with no evident deterioration.

In connection with ferritic ductile irons, the Bayonne results indicate that variation within the normal compositional ranges of such elements as manganese, copper and phosphorus has an important bearing on creep strength. These results tentatively indicate that it will be necessary to specify composition in the ferritic ductile irons in order to assure a given level of creep strength. By deliberately alloying with nickel and molybdenum, it has been possible to develop creep strengths of 25,000 psi at 800 °F for a rate of 1% in 10,000 hours in ferritic ductile iron.

Authors' Reply

The authors wish to thank Mr. Williams and Mr. Gagnebin for their discussion of this paper.

Mr. Williams' tabulation of properties which they obtained on a ferritic ductile cast iron is a welcome addition, and it is gratifying that the results are in excellent agreement with those which we have reported.

Mr. Gagnebin's comments on the pearlitic grade indicate substantial agreement on the properties of this material, and provide confirmation on the stability of this grade up to 800 °F.

Our testing of ferritic ductile cast irons was limited to a single base-line analysis, and thus we have no data to evaluate the effects of compositional variations. The effects on hot strength of variations within normal compositional ranges of such elements as manganese, copper, and phosphorous, as reported by Mr. Gagnebin, are certainly of interest. We look forward to the detailed data which are to be subsequently published.

EFFECT OF COLD WORK ON THE HIGH TEMPERATURE CREEP PROPERTIES OF DILUTE ALUMINUM ALLOYS

By Robert E. Frenkel, Oleg D. Sherby and John E. Dorn

Abstract

The creep rate of annealed and cold-worked aluminum alloys at elevated temperatures can be represented by the equation $\dot{\epsilon} = Se^{-\Delta H_c/RT}e^{B\sigma}$ *where* ΔH_c *= activation energy for creep,* R *= gas constant,* T *= absolute temperature,* σ *= applied stress,* B *= stress parameter and* S *= structure parameter. The activation energy for creep is unaffected by cold work and S is only slightly increased by the previous cold deformation. The principal effect of cold work on the creep resistance of aluminum appears to arise from a decrease in B by this factor. The results are discussed in terms of a new recovery model for creep.*

Introduction

A NUMBER of routine investigations (1–6)[1] have been made in order to determine the effect of prior cold work on the creep properties of metals. Since the basic laws for high temperature creep were not then known, the results of such investigations were not readily interpretable. Recent progress in formulating the laws for high temperature creep (7–12) has now provided a better basis for evaluating the effect of cold work on the creep properties of metals. It is the purpose of this investigation to study the effect of prior cold work on each of the significant parameters that determine the high temperature creep behavior of metals.

Materials

Sheets of the high purity aluminum alloys listed in Table I were used in this investigation. These alloys were homogenized, cold-rolled from 0.100 to 0.070 inch in thickness and then recrystallized to about the same grain size. Their chemical composition, recrystallization treatment and grain size are recorded in Table I. Creep specimens were machined with their tensile axes in the rolling direction.

[1] The figures appearing in parentheses pertain to the references appended to this paper.

A paper presented before the Thirty-sixth Annual Convention of the Society, held in Chicago, November 1 to 5, 1954. Of the authors, Robert E. Frenkel and Oleg D. Sherby are research engineers, Institute of Engineering Research, and John E. Dorn is professor of physical metallurgy, University of California, Berkeley. Manuscript received August 28, 1953.

Effect of Cold Work on the Activation Energy for Creep

Extensive investigations on the creep of annealed metals (7–9,11) have shown that the creep strain, ϵ, for a constant stress σ_c is related to the time, t, and the test temperature, T, in accordance with the functional relationship

$$\epsilon = f(\theta) \qquad \sigma_c = \text{const.} \qquad \text{Equation 1}$$

where $$\theta = te^{-\Delta H_c/RT} \qquad \text{Equation 2}$$

ΔH_c = activation energy for creep

and R = gas constant.

In general, Equation 1 has been found to be valid for annealed materials (11) over the high temperature range of creep (above about 0.45 of the absolute melting temperature up to the melting temperature) where the rates of crystal recovery are rapid. The activation energy for creep of initially annealed metals was found to be constant, independent of temperature, duration of test, creep strain, stress, grain size and the various subgrain structures developed during creep (7,8,11). Furthermore, ΔH_c was found to be insensitive to minor alloying additions (7,11) and to small amounts of dispersed intermediate phases (9). Therefore the activation energies for creep of relatively pure metals approached those for the elements, and were shown to exhibit a normal periodic variation with atomic number (11). Wherever appropriate data were available (11) the activation energy for creep, ΔH_c, agreed well with the activation energy for self-diffusion, ΔH_D, suggesting that the rate controlling mechanism for the high temperature creep process is that of self diffusion.

Although the activation energy for creep was found to be insensitive to the series of subgrain structures that were developed during creep of a previously annealed alloy, ΔH_c might nevertheless be affected by more severe structural changes such as those induced by prior cold work. In order to examine this possibility, each of the alloys listed in Table I was creep tested in three different initial states. As shown in Table II, state A refers simply to the as-annealed condition, and the resulting creep curves for this initial condition are shown by the solid

Table I
Composition, Recrystallization Treatment and Grain Size of Aluminum Solid Solution Alloys Investigated †

Alloying Element	Atomic Percent	Chemical Composition Weight percent of impurities Si	Fe	Cu	Mg	Mn	Recrystallization Treatment (after 30% cold rolling)	Mean Grain Diameter (mm)
Pure Al	(99.987)	0.003	0.003	0.006	0.001	—	860 °F 30 mins.	0.25
Mg	1.617	0.003	0.004	0.006	—	—	800 °F 10 mins.	0.26
Cu	0.101	0.003	0.003	—	0.0006	0.001	800 °F 43 mins.	0.29

† The authors wish to acknowledge their appreciation to the Aluminum Company of America Research Laboratories for the preparation of these alloys and the determination of their chemical composition.

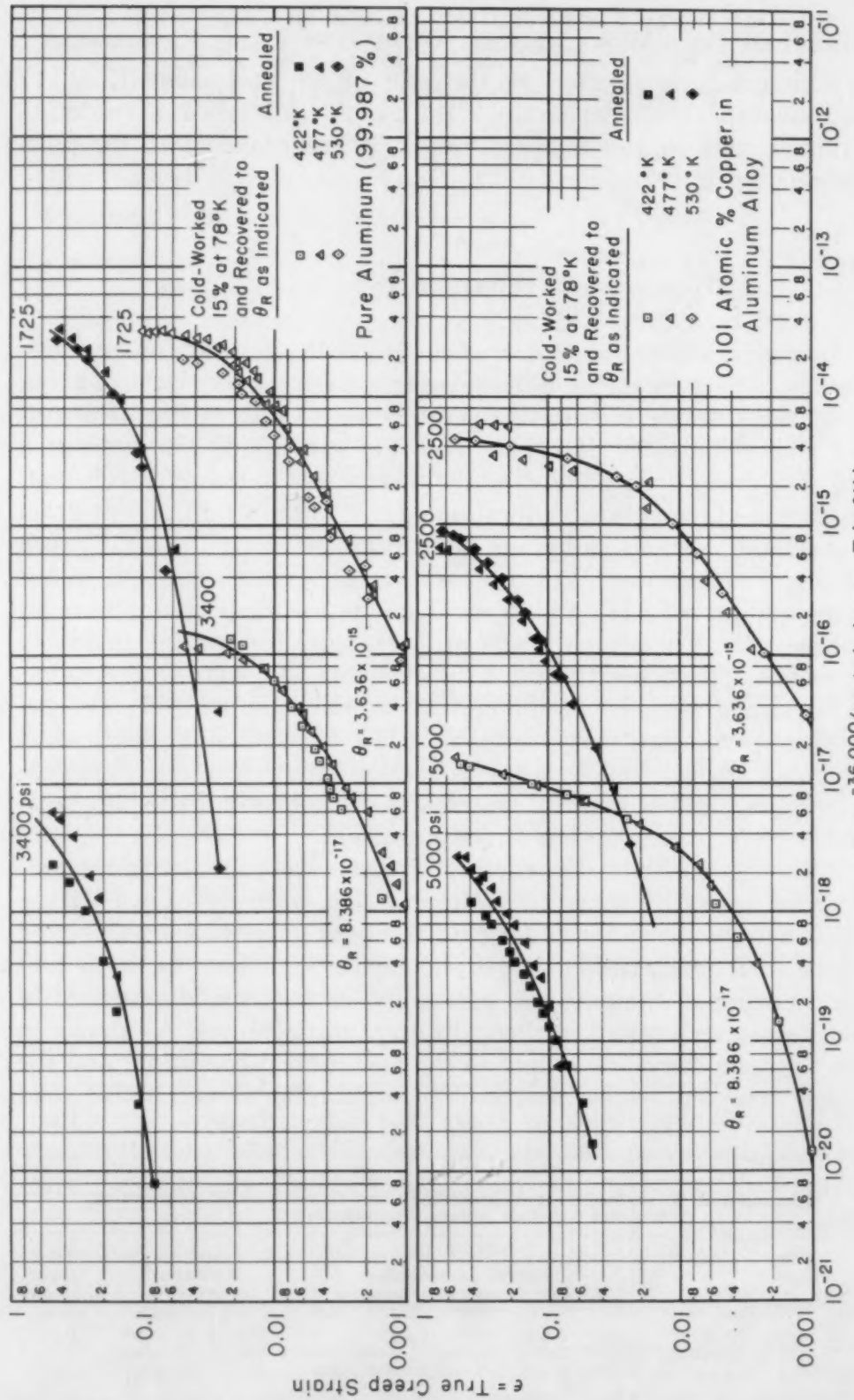


Fig. 1—Correlation of Creep Strain-Time Data for Annealed and Cold-Worked States of Dilute Aluminum Alloys by Means of the Relation $\epsilon = f(\theta, \sigma_c)$.

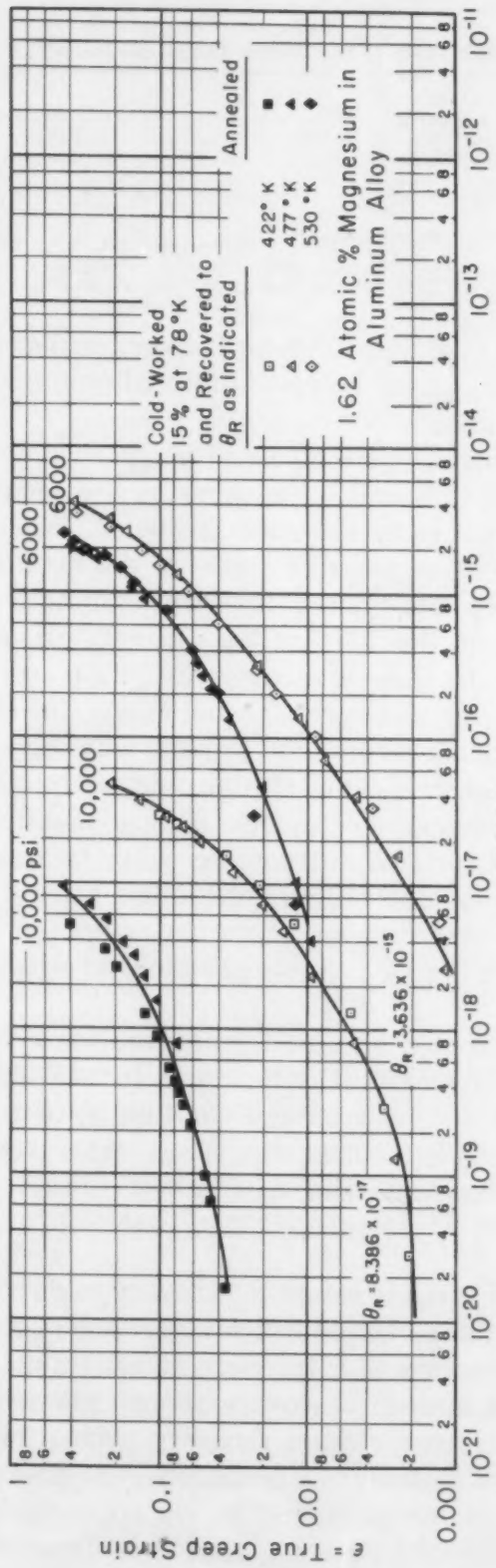


Fig. 1 (cont.)—Correlation of Creep Strain-Time Data for Annealed and Cold-Worked States of Dilute Aluminum Alloys by Means of the Relation $\epsilon = f(\theta, \sigma_c)$.

Table II
Initial State of the Alloys Tested in Creep

Creep Temp °K	A	B					C				
	Annealed	Annealed, Prestrained 15% at 78 °K and recovered as follows:					Annealed, Prestrained 15% at 78 °K and recovered as follows:				
		T_1 °K	t_1 Hrs.	T_2 °K	t_2 Hrs.	θ_R	T_1	t_1 Hrs.	T_2 °K	t_2 Hrs.	θ_R
422											
477		530	1.95	477	2.00	3.636×10^{-15}	477	1.98	422	2.00	8.386×10^{-17}
530		530	2.00	—	—	3.636×10^{-15}	477	2.00	—	—	8.386×10^{-17}

symbols of Fig. 1. These data confirm the earlier observations (7–9) that the activation energy for creep of dilute aluminum alloys is about 36,000 calories per mole.

Initial states B and C were obtained by prestraining the annealed alloys 15% at 78 °K followed by an appropriate recovery treatment for each of the two states as shown in Table II. Such consistent recovery treatments were necessary to provide the same initial state for each alloy at the creep test temperatures investigated. It was reasonsonable to expect that the amount of recovery depended on $\theta_R = te^{-\Delta H_R/RT}$ where t is the time of recovery at temperature T, and ΔH_R, the activation energy for recovery, is equal to ΔH_c for creep. This concept is verified by the data recorded in Fig. 2 which represent the tensile stress-strain curves for cold-worked high purity aluminum at 298 °K following various recovery treatments. Almost identical stress-strain curves were obtained for two different recovery treatments, one after 1750 hours recovery at 530 °K and the other after 117.5 hours recovery at 572 °K. These data prescribe an activation energy for recovery equal to about 36,000 calories per mole which is identical with that for creep.

In order to achieve a standard recovered state in a reasonable period of time, it was occasionally desirable to recover for time t_1 at temperature T_1 followed by recovery for time t_2 at temperature T_2. Under these conditions equivalent recovered states were presumed to be established at constant values of θ_R, where

$$\theta_R = t_1 e^{-\Delta H_R/RT_1} + t_2 e^{-\Delta H_R/RT_2} \qquad \text{Equation 3}$$

As shown in Table II, state B refers to recovery to $\theta_R = 3.636 \times 10^{-15}$ whereas state C is that obtained following recovery to $\theta_R = 8.386 \times 10^{-17}$. In Fig. 2 the θ concept for recovery of aluminum is again shown to be valid for these multiple recovery treatments wherein the activation energy for high temperature recovery equals the activation energy for creep. Fig. 2 also reveals that the stress-strain curves at 298 °K for the two recovered states are yet appreciably greater than that for the annealed state, showing that considerable effects of the previous cold working were retained following recovery. Additional confirmation of the retention of the effects of cold work following re-

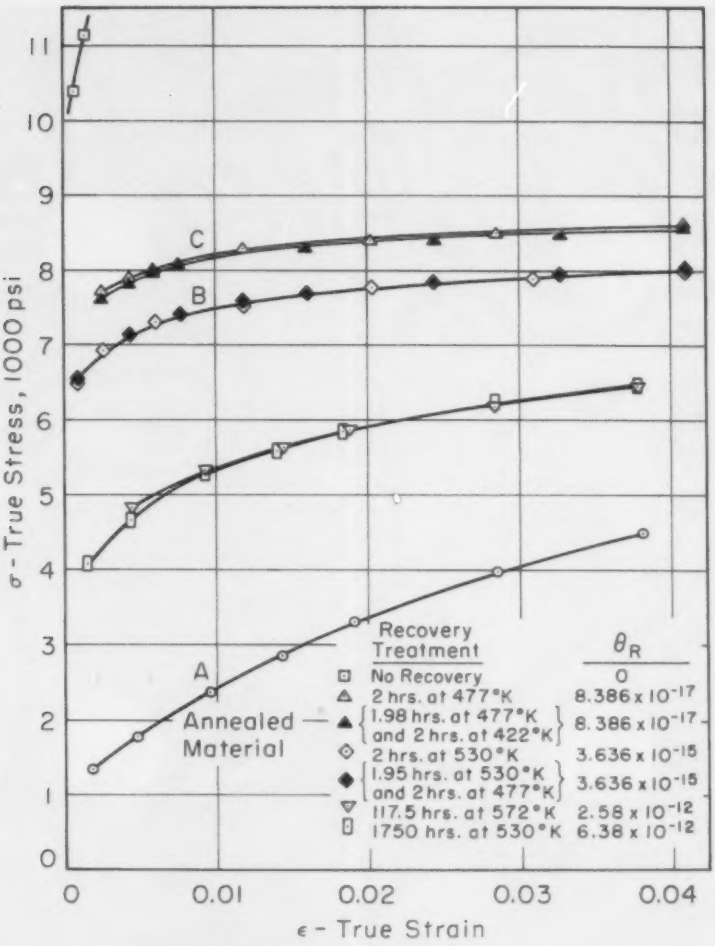


Fig. 2—Effect of Recovery on the Tensile Curves at 298 °K of High Purity Aluminum Prestrained 15% at 78 °K.

covery to $\theta_R = 8.386 \times 10^{-17}$ is shown by the back-reflection Debye-Scherrer X-ray photograms reproduced in Fig. 3. The annealed coarse-grained structure reveals only relatively few grains so oriented to satisfy Bragg angles. After cold working and recovery broad short diffuse arcs were obtained indicative of the retention of some of the cold working effects.

The creep curves following cold work and recovery are recorded in Fig. 1. Although the creep resistance of each of the alloys was appreciably increased following the cold working and recovery treatments, the activation energy for creep remained about 36,000 calories per mole. Therefore the activation energy for creep is presumed to be a constant independent of the structural changes induced by cold work.

Effect of Cold Work on the Stress Parameter

As shown in Fig. 1 cold work improves the creep resistance, but the activation energy for creep appears to be independent of the struc-

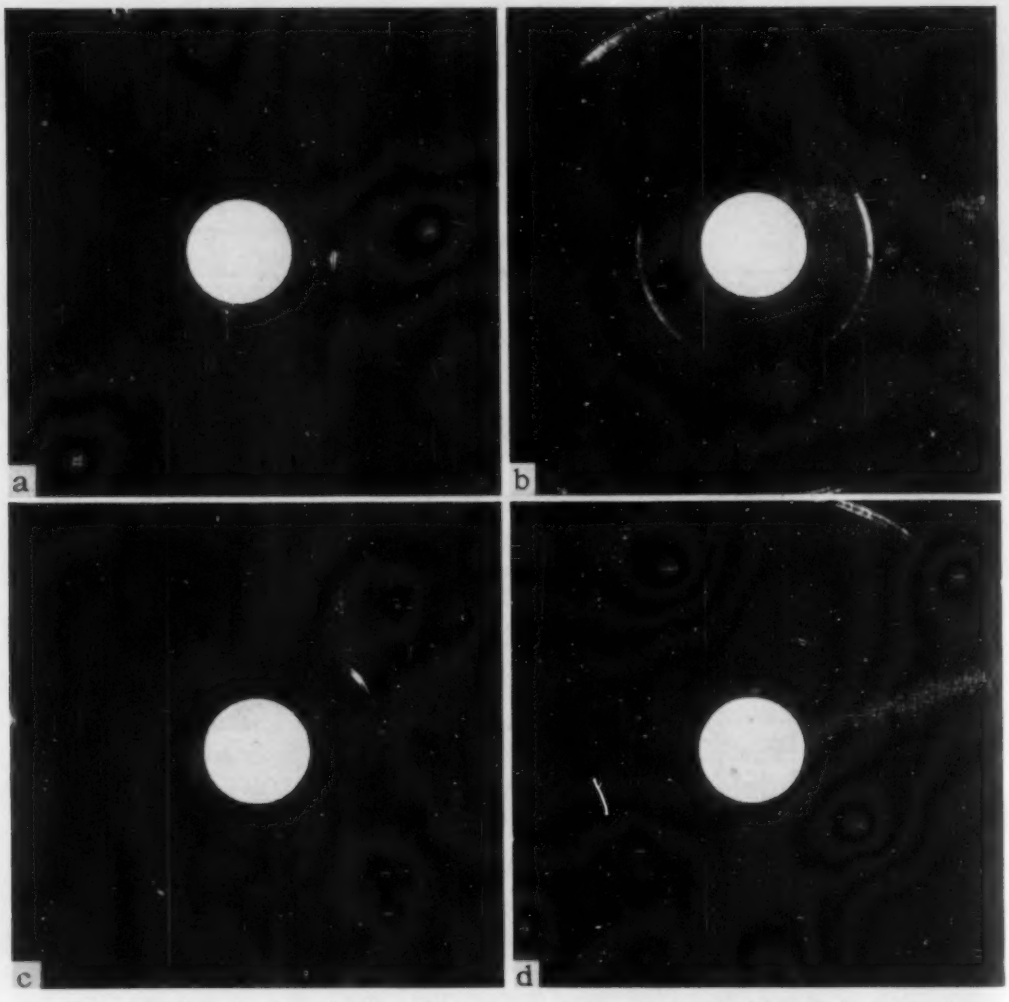


Fig. 3—X-Ray Back Reflection Photograms of Annealed and Cold Worked Aluminum Before and After Creep Testing. a and b—Annealed aluminum; a—Before creep testing, b—At fracture after creep under $\sigma_e = 3400$ psi at 477 °K. c and d—Annealed aluminum prestrained 15% at 78 °K and recovered to $\Theta_R = 8.386 \times 10^{-17}$; c—Before creep testing, d—At fracture after creep under $\sigma_e = 3400$ psi at 477 °K.

tural changes attending cold working. Consequently cold work must affect some other parameter of the creep equation. Previous investigations (10) have demonstrated that the creep rate of initially annealed metals is given by

$$\dot{\epsilon} = S\, e^{-\Delta H_e/RT} e^{B\sigma} \qquad \text{Equation } 4^2$$

where B, the stress parameter, was observed to be a constant independent of the instantaneous temperature or the previous creep history of the alloy. Consequently all effects of structural changes attending creep on the instantaneous creep rate were found to arise from changes in the parameter S. The reciprocal of B, however, increased practically linearly with atomic percent of small additions of solute elements (10).

[2] Equation 4 is valid for values of $B\sigma >> 0$. As $B\sigma$ approaches zero the creep rate must also approach zero. For low stresses therefore, $e^{B\sigma}$ must be replaced by some function that vanishes as $B\sigma$ vanishes such as sinh $B\sigma$, $(e^{B\sigma}-1)$ or $B\sigma e^{B\sigma}$.

Because ΔH_c is unaffected by cold work and yet the creep resistance is improved, either B or S or both of these parameters must be affected by the structural changes attending low temperature straining. In order to study the effect of pretreatment on S it is first necessary to determine whether the structural changes subsequent to cold work and partial recovery affect B. Since the stress parameter B might change with changes in the cold-worked state during creep it was necessary to evaluate B for various creep strains. The procedure adopted in evaluating B during creep of a cold-worked and recovered metal was as follows: Annealed high purity aluminum was prestrained 15% at 78 °K, held for two hours at the creep temperature of 477 °K and then precrept under $\sigma_c = 4{,}000$ psi to a prescribed strain, following which the stress was reduced and the new instantaneous creep rate was determined. It was assumed that the structural changes attending the precrept condition would remain unaltered immediately following a reduction in stress.[3] The instantaneous creep rate at the lower stress would thus be characteristic of the particular cold worked, recovered and precrept structure. This procedure was repeated on a new sample for each new value of the reduced stress. The relationship between the instantaneous creep rate and the true stress for the various reduced stresses would therefore pertain to a specific structure. The results for four precrept states of the cold-worked and partially recovered metal are shown in Fig. 4. The linear relationship between the stress and the logarithm of the strain rate exhibited by the data of Fig. 4 further confirm the earlier validity of the stress term in Equation 4. Cut A of Fig. 4 reveals that 1/B is about 535 following a precreep strain of $\epsilon = 0.0017$ whereas the remaining cuts show that 1/B decreases as the precreep strain increases. Since previous tests on annealed high purity aluminum (10) gave 1/B equal to about 191 for all creep strains, it follows that cold work results in an increase in 1/B. As shown in Fig. 5 the value of 1/B for the cold-worked aluminum decreases with increasing creep strain and appears to approach the value of 1/B for the creep of aluminum in the annealed state. This suggests that the structural modifications induced by cold working are gradually eliminated during high temperature creep. Partial confirmation of this suggestion is contained in the x-ray photograms of Fig. 3, which reveal extensive polygonization for the fractured specimen initially in the annealed state as well as for the ruptured specimen initially cold worked.

Effect of Cold Work on the Structure Parameter

During creep of annealed aluminum ΔH_c and 1/B remain constant independent of the creep strain (10). This fact implies that the param-

[3] This, of course, would not be true upon increasing the stress because the instantaneous increase in strain due to the increase in stress would result in an instantaneous change in the structural state.

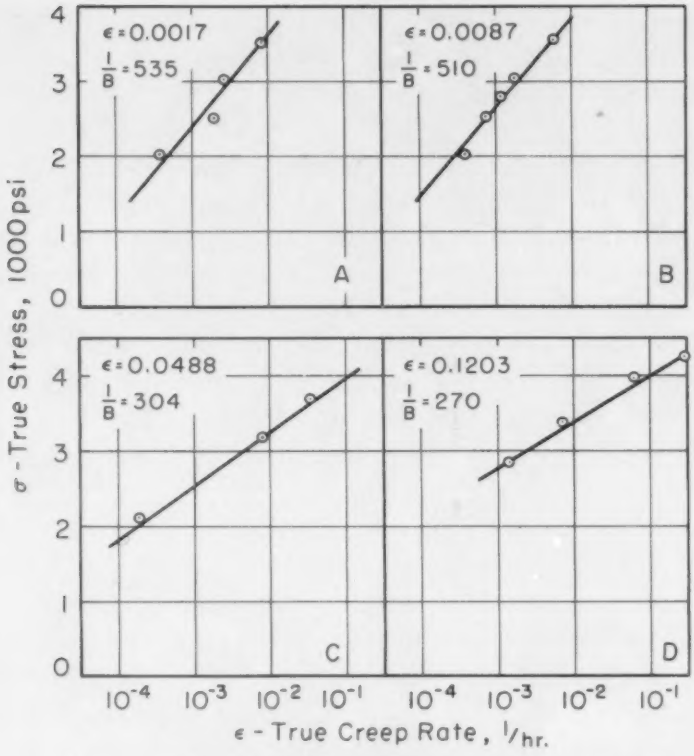


Fig. 4—Effect of True Stress on the True Creep Rate at Various Cold-Worked Structures of Aluminum. (Structures developed by prestraining 15% at 78 °K followed by creep under $\sigma_e = 4000$ psi at 477 °K to creep strains indicated above.)

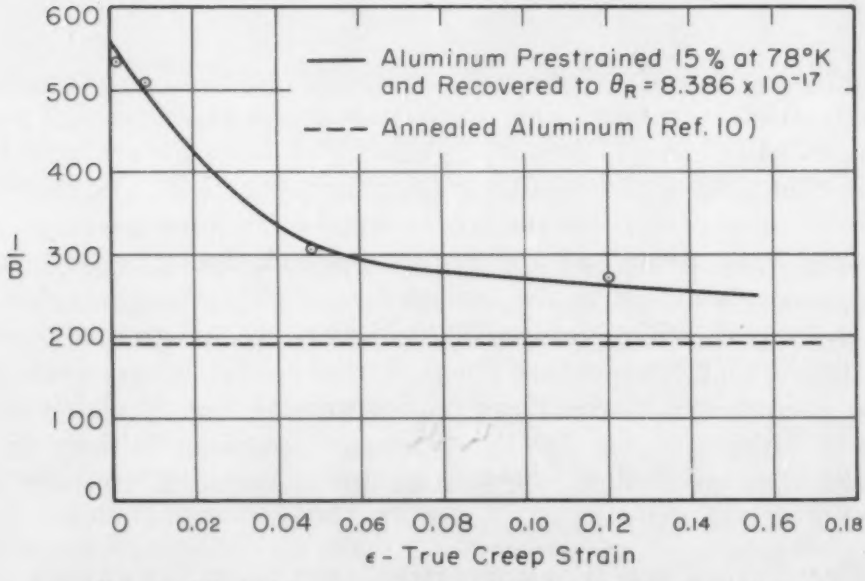


Fig. 5—Effect of Creep on 1/B for Cold-Worked Aluminum Under a Creep Stress of $\sigma_e = 4000$ psi at 477 °K.

eters ΔH_c and 1/B are insensitive to the structural changes that attend the creep of initially annealed aluminum. Consequently the great changes in the creep rate of initially annealed specimens with creep

strain are attributable to the effect of structural changes that are induced by creep on S. A typical example of the effect of creep strain for a constant load creep test on S for $\sigma_c = 4000$ psi is shown by curve (b) in Fig. 6. The values of S were calculated by means of Equation 4 using the instantaneous true creep rate, the instantaneous true stress, $\Delta H_c = 36{,}000$ calories per mole, and $1/B = 191$.

The effect of creep strain on S was calculated in an analogous way for the initially cold-worked and partially recovered aluminum under the same constant load condition of $\sigma_c = 4000$ psi. Here however, the instantaneous values of 1/B given in Fig. 5 were introduced in Equation 4. As shown in Fig. 6, S for the cold-worked material also appears to decrease with the creep strain. Unfortunately a direct comparison between the annealed and cold-worked aluminum cannot be made because of the high initial strain upon initial loading of the annealed aluminum and the early fracture of the cold-worked aluminum. The extrapolated curves, however, suggest that when comparisons are made at the same creep strain, S appears to be increased merely by about an order of magnitude for the various cold-worked states developed in this investigation.

Discussion

Although it is somewhat premature to attempt a complete analysis of the data reported here at this time, some interesting deductions might nevertheless be made. The data for cold-worked and partially recovered aluminum are consistent with the previously reported data in that the high temperature creep rate of metals is given by

$$\dot{\epsilon} = S\, e^{-\Delta H_c/RT} e^{B\sigma} \qquad \text{Equation 4}$$

These results demand that the usual models for creep, consisting either of thermal activation of dislocations over barriers (13) or local fluctuations of strain energy (14), be discarded since they all require that the stress parameter B be proportional to the reciprocal of the absolute temperature. An alternate model for creep has been suggested (15) which is based on the hypothesis that the rate-controlling process consists of the recovery of barriers and that dislocations migrate to the next barrier whenever the barrier strengths recover to the value of the applied stress. Since the barriers themselves are often considered as dislocations or patterns of dislocations, the unit recovery process can be self-diffusion, consisting of vacancy-atom exchanges at the center of the dislocations.

According to the usual models for creep (13,14), cold work would be expected to increase the barrier heights and thus the activation energy for creep. This prediction is contrary to the reported observation that ΔH_c is independent of the initial state of the metal. On the basis of the recovery model, however, the ΔH_c for the creep of an initially

cold-worked metal should remain equal to that for self-diffusion in complete harmony with the facts reported here.

On the basis of the model of thermal activation of dislocations over a barrier, B is proportional to the so-called volume of a dislocation divided by the absolute temperature. It is possible that an entire dislocation could not be activated at one time but that it loops over the barriers in segments. If the length of each loop were determined by the spacing of the barriers it is possible that cold work, which might introduce more closely spaced barriers, would result in the looping of smaller segments of the dislocation, causing B to be smaller than that for an annealed material. But the previously proven fact that B is independent of temperature (10) disqualifies the usual model for creep based on the thermal activation of dislocations over a potential barrier. On the other hand the recovery model for creep does not yet permit an unqualified conclusion as to why 1/B is greater for the cold-worked state. As is known, alloying increases 1/B, apparently by increasing the barrier strengths. It would therefore be expected that vacancies, interstitials and dislocations introduced during cold work could well cause 1/B to increase in a manner analogous to the effect of solid solution alloying. But the high temperature recovery annealing treatment following cold work and preliminary to the application of the creep stress, should have restored the vacancy and interstitial patterns to their equilibrium states. Perhaps the high 1/B values for the cold-worked and partially recovered aluminum are attributable to the nonequilibrium retention of some vacancies and interstitials in low energy states in appropriate strain centers or to the greater interaction forces arising from an overall increase in the number of dislocations. The gradual approach of 1/B with creep from that of the cold-worked and partially recovered metal to that for an initially annealed metal suggests the rather gradual approach to a steady state structure. Even though the picture on how 1/B is increased by cold work is yet very incomplete the experimental results do not disqualify the recovery model for creep.

The effect of structural changes during creep on the S-parameter can be incorporated into both the activation-over-barrier models (13, 14) and the recovery model for high temperature creep. On the basis of the more acceptable recovery model for creep, cold working should increase the density of barriers and also increase the number of dislocations present. Whereas the first factor would decrease S, the second would increase S. Since there is as yet no apriori justification for assuming which of these two factors might predominate, the probable increase in S following cold work and partial recovery as suggested by the results in Fig. 6 is not a critical observation. The increase in S due to cold working, however, does not appear to have nearly as important an effect on the creep rate as the exponential effect of an increase in 1/B due to cold working.

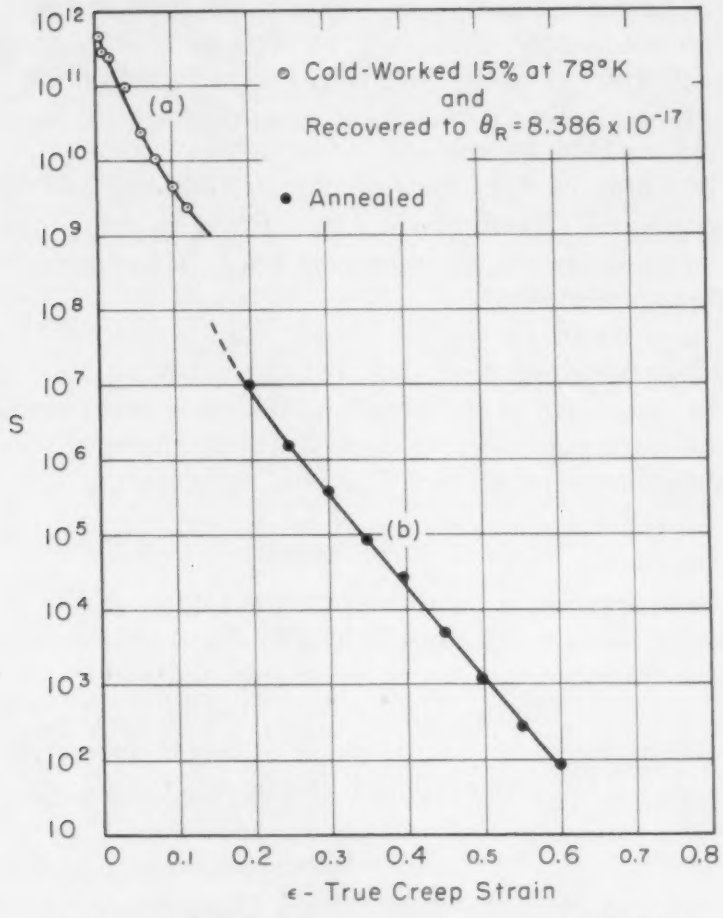


Fig. 6—Effect of Creep on S-Parameter for (a) Cold-Worked Pure Aluminum and (b) Annealed Aluminum Under a Creep Stress of $\sigma_c = 4000$ psi at 477 °K.

High values of ΔH_c and low values of B and S are conducive to high creep resistance at elevated temperatures. The principal effect of cold working on the creep resistance appears to be primarily attributable to the effect of cold work on decreasing B. Additional investigations, covering a wider range of cold-worked states, however, will have to be made in order to ascertain more completely the effect of cold work on S.

Conclusions

1. The high temperature creep of cold-worked as well as annealed aluminum can be represented by the equation

$$\dot{\epsilon} = S\, e^{-\Delta H_c/RT} e^{B\sigma}$$

where $\dot{\epsilon}$ = creep rate
ΔH_c = activation energy for creep
R = gas constant
T = absolute temperature
σ = applied stress
B = stress parameter
and S = structure parameter

2. The activation energy for high temperature creep is unaffected by previous cold work. This fact, as well as others, disqualifies the commonly postulated model for creep that is based on the assumption that the rate-controlling process for creep consists of thermal activation of dislocations over barriers.

3. The value of 1/B for initially cold-worked and partially recovered aluminum is greater than that for aluminum initially in the annealed state. However, as creep continues 1/B appears to approach that for the annealed metal.

4. S appears to be slightly larger for the initially cold-worked and partially recovered state than for the annealed state when compared at the same total creep strain and the same creep stress.

5. The principal effect of cold work on the creep resistance of aluminum appears to arise from its effect on increasing 1/B.

ACKNOWLEDGMENTS

This investigation is sponsored by the Office of Naval Research. The authors wish to thank the ONR staff for their continued interest and full cooperation throughout this and related studies on the plastic properties of metals. The authors wish to also thank Mr. R. L. Orr for his assistance in the experimental phase of this investigation and Mrs. G. Pelatowski for her preparation of the figures to this report.

References

1. A. I. Blank and H. L. Burghoff, "Creep Characteristics of Phosphorized Copper (0.019% Phosphorus) at 300, 400, and 500 °F," *Proceedings*, American Society for Testing Materials, Vol. 51, 1951, p. 981.
2. W. D. Jenkins and T. G. Digges, "Creep of Annealed and Cold-Drawn High Purity Copper," *Journal of Research*, National Bureau of Standards, Vol. 47, No. 4, October 1951, p. 272.
3. D. N. Frey and J. W. Freeman, "Fundamental Effects of Cold Working on the Creep Resistance of an Austenitic Alloy," *Transactions*, American Institute of Mining and Metallurgical Engineers, Vol. 191, 1951, p. 755.
4. H. R. Zschokke and K. H. Niehus, "Requirements of Steel for Gas Turbines," *Journal*, Iron and Steel Institute, Vol. 156, 1947, p. 271.
5. J. N. Greenwood and H. K. Worner, "Types of Creep Curve Obtained with Lead and Its Dilute Alloys," *Journal*, Institute of Metals, Vol. 64, No. 1, 1939, p. 135.
6. O. D. Sherby and J. E. Dorn, "The Effect of Cold-Rolling on the Creep Properties of Several Aluminum Alloys," TRANSACTIONS, American Society for Metals, Vol. 43, 1951, p. 611.
7. O. D. Sherby and J. E. Dorn, "Creep Correlations in Alpha Solid Solutions of Aluminum," *Transactions*, American Institute of Mining and Metallurgical Engineers, Vol. 194, 1952, p. 959.
8. O. D. Sherby and J. E. Dorn, "Some Observations on Correlations Between the Creep Behavior and the Resulting Structures in Alpha Solid Solutions," *Transactions*, American Institute of Mining and Metallurgical Engineers, Vol. 197, 1953, p. 324.
9. W. H. Giedt, O. D. Sherby and J. E. Dorn, "The Effect of Dispersions on the Creep Properties of Aluminum-Copper Alloys," *Transactions*, Amer-

ican Society of Mechanical Engineers, Vol. 77, No. 1, January 1955, p. 57.

10. O. D. Sherby, R. E. Frenkel, J. Nadeau and John E. Dorn, "Effect of Stress on the Creep Rates of Polycrystalline Aluminum Alloys under Constant Structure," *Journal of Metals,* American Institute of Mining and Metallurgical Engineers, Vol. 6, February 1954, p. 275.
11. O. D. Sherby, R. L. Orr and John E. Dorn, "Creep Correlations of Metals at Elevated Temperatures," *Journal of Metals,* American Institute of Mining and Metallurgical Engineers, Vol. 6, January 1954, p. 71.
12. R. L. Orr, O. D. Sherby and J. E. Dorn, "Correlations of Rupture Data for Metals at Elevated Temperatures," TRANSACTIONS, American Society for Metals, Vol. 46, 1954, p. 113.
13. W. Kauzmann, "Flow of Solid Metals from the Standpoint of the Chemical-Rate Theory," *Transactions,* American Institute of Mining and Metallurgical Engineers, Vol. 143, 1941, p. 57.
14. R. Becker, "Uber Plastizität, Verfestigung und Rekrystallization," *Zeitschrift für Technische Physik,* Vol. 7, 1926, p. 547.
15. O. D. Sherby and J. E. Dorn, "A Recovery Model for the High Temperature Creep Process," Institute of Engineering Research Report, University of California, Berkeley, Series No. 22, Issue No. 30, August 15, 1953.

DISCUSSION

Written Discussion: By C. O. Smith, research engineer, Mechanical Testing Division, Aluminum Company of America, New Kensington, Pa.

The authors are to be congratulated on their presentation of a very interesting proposed recovery model for creep. The data presented appear to support the proposal but it is unfortunate that these data apply only for a stress of 4000 psi at a temperature of 400 °F.

As the authors point out "Additional investigations, covering a wider range of cold-worked states, however, will have to be made in order to ascertain more completely the effect of cold work on S." It appears to us that additional work is also required to better delineate the behavior of the stress parameter, B.

We wonder whether this proposed recovery model and the proposed creep rate equation will work for more highly alloyed aluminum and for cold-worked material which has not been given a recovery treatment. We have used the values of the parameters and the creep rate equation given in this paper to compare with measured creep rate at a stress of 4000 psi at 400 °F for data previously published by Messrs. Sherby and Dorn.[4] Four examples were considered: two samples of 1100-0 (2S-0) with different annealing treatments, one sample of 1160-H18 (99.6-H18) and one sample of 1100-H18 (2S-H18). For the samples of 1100-0 (2S-0) the measured creep rates were 100 x 10^{-3} and 2 x 10^{-3} in/in/hr. while the calculated creep rate for both samples was 10 in/in/hr. or about 100 and 5000 times as great, respectively. In the case of 1160-H18 (99.6-H18) the measured creep rate was 1 x 10^{-3} in/in/hr. while the calculated creep rate was 200 x 10^{-3} in/in/hr. or about 200 times as great. Similarly, for 1100-H18 (2S-H18) the measured creep rate was 1.2 x 10^{-3} in/in/hr. and the calculated creep rate was 600 x 10^{-3} in/in/hr. or about 500 times

[4] O. D. Sherby and J. E. Dorn, "The Effect of Cold-Rolling on the Creep Properties of Several Aluminum Alloys," TRANSACTIONS, American Society for Metals, Vol. 43, 1951, p. 611.
O. D. Sherby and J. E. Dorn, "Effect of Annealing on the Creep Properties of 2S-O Alloy," *Proceedings,* American Society for Testing Materials, Vol. 51, 1951, p. 954.

as great. (In all cases it is assumed that the units of S, the structure parameter, are in/in/hr. as they do not appear to be specified in the paper.)

To us, this large difference between measured and calculated creep rate emphasizes that much more work is needed to determine if the proposed recovery creep model and creep rate equation are workable, and if so, to determine the proper values of the parameters for various conditions of cold work.

Written Discussion: By R. P. Carreker and R. W. Guard, Metallurgy Research Department, General Electric Co., Research Laboratory, Schenectady, N. Y.

Before discussing the technical aspects of the paper we would like to make several comments on the format. Although this paper represents one of a continuing series by the same group of authors, a brief summary of the experimental techniques used to obtain the data would be very desirable. The task of the reader is also rendered more difficult because five important references, including the description of the "Recovery Model" of creep, are privately distributed reports.

While we do not fully agree with all of the premises made by the authors based on previous work, the following discussion will generally be confined to the present paper. In this paper the authors have attempted the difficult task of reasoning from phenomenology to mechanism. Our criticisms are directed at places in this reasoning process where we feel that the data are not conclusive.

The data of Fig. 1 indicate that the scatter in plots of θ versus ϵ is larger than might be expected from sample to sample variation. Our experience in using this parameter on our own data is that ΔH_ϵ for aluminum is not very clearly defined but may vary from 28,000 to 42,000, depending on the exact details of how it is determined. While it is obviously a useful tool for engineering approximation, the θ parameter leaves much to be desired as a scientific law. Likewise, it is not appropriate to reason from equivalency of ΔH_{Creep} to $\Delta H_{Diffusion}$ to equivalency of processes.

We feel that Fig. 2 does not represent a proper test of the validity of Equation 3. Differences in minutes between the two treatments for States B and C could hardly be altered by two hours at 50 °K less in view of the temperature dependence indicated by the data shown. Equation 3 may be correct, but more strenuous tests are necessary.

In justifying Equation 4, the authors put forth the argument that B is independent of temperature. Such an argument is valid only if the term related to the "volume" of a dislocation is completely independent of prior history. The data in Reference 10 do not prove whether this is true or not.

We are disappointed that neither the effect of cold work on B or on S can be explained by the proposed "recovery" model. It is hoped that more work on the details of the model in the future will allow one to make predictions using it.

Written Discussion: By William D. Jenkins, National Bureau of Standards, Washington, D. C.

This paper represents an excellent attempt, by the authors, to formulate a basic law of high temperature creep of metals.

The fact that the authors' observations do not appear to conform to the usual models may be attributed to the structural changes induced by temperature prior to and during the creep or tensile test. Additional information regarding the hardness and the microstructure of the material in the initial condition,

as affected by the test temperature only, and as affected by the test conditions would be most helpful.

The nonexistence of the recovery model for creep was not a deterring factor in the interpretation of the data, obtained in the laboratories of the National Bureau of Standards, for high purity copper tested within the temperature range 110 to 300 °F (less than 0.45 of the melting point of copper). It was shown, within the range of test conditions used, that the barrier heights were definitely increased by cold working. Confirmation of this observation has been made from both creep tests and short-time constant-strain rate tensile tests on both copper, nickel and alloys of these two elements.

The low temperature creep and tensile results indicate the necessity of the application of the Becker or Kauzmann concept. The data, obtained by the writer on two 70% nickel — 30% copper type alloys, indicate that the activation energy and the mechanical properties were unaffected by small variations in alloy content (initial grain size constant) within the temperature range 1200 to 1700 °F. Moreover, within this temperature range, the activation energy of a 70% copper — 30% nickel alloy was apparently unaffected by cold drawing the material 25%, 40% or 70% reduction in area before testing in tension at the same strain rate.

It appears to the writer that the complete abandonment of accepted and partially proven concepts in favor of a theory admittedly limited to a small range of test conditions, would be unwise at this time.

Authors' Reply

The authors wish to thank Dr. C. O. Smith for his contribution to their paper. They heartily agree with Dr. Smith concerning the need for more definitive investigations not only on the β and s parameters that the authors have introduced but equally on all phases of the phenomenon of high temperature creep.

As shown in the text as well as by extensive earlier publications and more recent unpublished data, Equation 1 of the text has rather broad ranges of applicability. Of course it is not universally applicable inasmuch as it applies only to high temperature creep and simple alloy systems which are structurally stable. As shown in the text, however, it appears to be valid for cold-worked metals.

The authors' comments that s of Equation 4 appeared to be insensitive to cold work did not mean that it depended only on the creep strain. As shown in the text, for the single example investigated, the s value for the cold-worked metal was only about 15 times greater than that for the annealed state when the data were extrapolated to the same creep strain. This is indeed small in contrast to the 10,000 times decrease in s during primary creep of the annealed metal. It was therefore suggested that 15 times is a small change when compared to a change of 10,000 times.

Evidently the authors did not outline in sufficient detail why their cold-worked specimens were recovered to the same state before creep testing. In the usual procedure the specimens are heated to the creep testing temperature and held for a fixed period of time before the load is applied. Consequently cold-worked specimens will have recovered more extensively during the hold at higher temperatures preceding application of the load. Such procedures were

used for obtaining the creep data for the cold-worked alloys 2S-H18 etc. which Smith describes in his discussion. Under these conditions the cold-worked alloys were not at the same state at the beginning of each creep test. But as shown by the data of Fig. 2, the recovery treatments used in this study did provide the same initial state for all cold-worked specimens. One factor, therefore, that was responsible for the lack of correlation obtained in Dr. Smith's analyses arose from the fact that this issue was neglected. But other factors also contributed to the lack of correlation Smith obtained. The parameters quoted in the text of this paper apply only to the alloys that were tested. Furthermore the variations of β and s for the cold-worked metal was evaluated for only one stress and temperature. These parameters might well be quite different for creep of the alloys that Smith considered in his analyses.

The authors wish to express their appreciation to Drs. Carreker and Guard for their contribution to this paper. The desirability of reducing the context of the paper precluded the opportunity of summarizing again the experimental techniques which had been announced previously. Furthermore almost all references to "privately distributed reports" have been modified upon proof of the galley sheets to actual publications in the open literature. They will therefore be available to the general reader.

The authors must agree that some scatter exists in the ΔH that is calculated for creep, dependent on the technique that is used. In general, however, the $\epsilon - \theta$ and correlated methods of measuring ΔH give "reasonably" reproducible values. As analyses of the extensive data by Carreker on the creep of Pt reveal[5] (Ref. 11), the scatter upon $\epsilon - \theta$ analysis appear to be essentially random. As a matter of fact Carreker's data show that such scatter is also obtained when duplicate or triplicate tests are run under identical conditions of stress and temperatures. Such scatter cannot be used to imply "that ΔH_c for aluminum is not very clearly defined." Obviously the $\epsilon - \theta$ technique of evaluating ΔH results in accumulating all scatter in β and s in the estimated value of ΔH. In addition, the authors would like to state that we are now using a new technique[6] that avoids this difficulty. Here ΔH was found to be insensitive to stress and strain. The variation among the various ΔHs being less than 10%. Additional tests now in progress on aluminum and its dilute alloys also confirm the nominal validity of previous studies except perhaps that a slightly lower ΔH is being obtained by the new technique.

The authors cannot agree that the equivalency of ΔH for high temperature creep and ΔH for self-diffusion is without meaning as inferred by Carreker and Guard. This equivalency does not and should not be inferred to mean identity of processes. But it is reasonable in view of this equivalency to assume that high temperature creep is somehow *controlled* by a self-diffusion process.

In general the authors agree with the comments of Carreker and Guard concerning whether the data recorded in Fig. 2 prove that ΔH for recovery is identical with that for creep except perhaps for the 117.5 hour recovery at 572 °K and the 1750 hour recovery at 530 °K where this statement appears to be valid. But these data were not obtained primarily for this purpose; rather they were obtained to illustrate that these alternate treatments preceding creep of the cold-worked metal does lead to approximately the same recovered state at the time the creep load was applied. And these data do reveal nominal validity of this fact.

The justification for β of Equation 4 being insensitive to the temperature was clearly shown for the case of annealed alloys in a series of previous investigations. This justification does not rest, as Carreker and Guard suggest, on some assumptions concerning a Kauzmann model for creep where β is presumed theoretically to be proportional to the area of a dislocation times the distance it must be moved for activation (in terms Carreker and Guard's terminology the volume of the dislocation loop that is activated) divided by the absolute temperature. Actually β is insensitive to the temperature because experiment shows this to be true. And conversely all theories yielding contrary results appear to be inaccurate and consequently are ineffectual arguments against the experimental facts. In the current paper, however, no attempt was made to ascertain how β of a cold-worked metal varies as the creep test temperature is changed. Perhaps as suggested by Carreker and Guard such studies as well as additional studies on s should be made. The $\epsilon - \theta$ correlations obtained for the cold work state revealed in this report, however, suggest that β is a function of θ.

The authors wish to express their appreciation to Dr. Jenkins for his interesting contribution to their paper. His observations that the high temperature activation energy for plastic flow of 70% nickel—30% copper alloys is insensitive to minor changes in composition and cold work further confirm the authors' thesis. But the authors cannot agree that their observations regarding the insensitivity of the activation energy to stress and to strain does not invalidate the Becker-Orowan or the Kauzmann types of creep models for the high temperature region of creep. Of course these models might be valid at low temperatures and should not therefore be completely discarded as yet. Dr. Jenkins' observations on the intermediate temperature creep of copper are interesting. It is indeed unfortunate, however, that he did not present his original data and the methods of analysis by which he deduced that the activation energy for low temperature creep increased with strain, especially since they are contrary to results obtained recently for the creep of copper from 348 to 468 °K.[6] In this investigation the temperature was cycled ± 15 °C abruptly throughout the course of creep. Consequently an unambiguous evaluation of the activation energy for creep was obtained showing that ΔH for these tests was 37,000 $\pm$ 3,000 cal/mole for strains up to 0.38 and for stresses ranging from 9,900 to 38,300 psi. Thus in this intermediate range of temperatures, the same laws of creep were observed as are obtained at elevated temperatures; the only significant difference concerned the fact that the activation energy was less than that for self-diffusion at the intermediate temperatures.

[5] R. P. Carreker, "Plastic Flow of Platinum Wires," *Journal of Applied Physics*, 1950, Vol. 21, p. 1289.

[6] T. E. Tietz and J. E. Dorn, "Creep of Copper at Intermediate Temperatures," Institute of Engineering Research Report, University of California, Berkeley, Series No. 22, Issue No. 38, September 15, 1954.

CREEP-TEMPERING RELATIONSHIPS IN HARDENED 4.5% CHROMIUM STEELS

By E. C. Roberts, N. J. Grant and Morris Cohen

Abstract

The behavior of three hardened 4.5% chromium steels has been studied from the standpoint of tempering phenomena and creep-rupture properties in the temperature range of 800 to 1300 °F (425 to 705 °C). By interrelating the information obtained on the time dependency of the tempering reactions and the creep characteristics of these steels, it has been possible to show that the application of stress during the fourth stage of tempering, formation of $(Cr,Fe)_7C_3$, produces no consistent change in the tempering reaction rate from that found in unstressed specimens.

Hardness and electrical resistance measurements have been employed to delineate the second, third and fourth stages of tempering in the hardened steels and to evaluate the effect of stress on the fourth stage. Carbide isolation has been used to follow the development of $(Cr,Fe)_7C_3$ and the disappearance of $(Fe,Cr)_3C$.

Microscopic evidence for the accelerated loss of strength at 1200 and 1300 °F (650 and 705 °C) in the highest carbon steel is presented. The increased rate of softening of the stressed specimens at 1300 °F (705 °C) compared to the unstressed specimens tempered at the same temperature is discussed.

Introduction

IMPORTANT among the many factors affecting the creep-rupture properties of alloys is the occurrence of phase changes. However, not much is known about the possible effect of stress and strain on the phase changes that may take place during creep-rupture measurements.

The complexity of the so-called "high temperature alloys" makes the diagnosis of the reactions and the determination of their rates in these alloys quite difficult (1).[1] On the other hand, low alloy steels,

[1] The figures appearing in parentheses pertain to the references appended to this paper.

Based on a thesis submitted in partial fulfillment of the requirements for the degree of Doctor of Science in Metallurgy.

A paper presented before the Thirty-sixth Annual Convention of the Society, held in Chicago, November 1 to 5, 1954. Of the authors, E. C. Roberts was formerly research assistant, Department of Metallurgy, Massachusetts Institute of Technology, and is now assistant professor of metallurgy, Montana School of Mines, Butte, Montana, N. J. Grant is associate professor of metallurgy and Morris Cohen is professor of metallurgy, Massachusetts Institute of Technology, Cambridge, Mass. Manuscript received December 29, 1953.

Table I
Chemical Composition of Steels

Steel	% C	% Cr	% Mn	% Si
A	0.16	4.58	0.33	0.19
B	0.40	4.32	0.25	0.19
C	0.68	4.55	0.30	0.28

which are used for certain limited-temperature applications (2), are considerably simpler in composition and far better understood with regard to the identity and kinetics of the reactions that occur.

A common phase transformation in such steels is the formation of an alloy carbide from one or more of its less stable predecessors (3,4). Certain low chromium steels, for example, ultimately develop $(Cr,Fe)_7C_3$ as the stable carbide but, preliminary to the nucleation and growth of this phase, cementite, $(Fe,Cr)_3C$, is precipitated (5). In the first stage of tempering the original martensite decomposes into a hexagonal carbide (ϵ carbide) and another martensite containing about 0.25% carbon. The second stage of tempering involves the decomposition of the retained austenite into bainite. The formation of cementite constitutes the third stage of tempering, while the development of $(Cr,Fe)_7C_3$ and the concurrent disappearance of the cementite comprise the fourth stage of tempering in these chromium steels. These latter two stages of tempering have been carefully evaluated in low chromium steels in a previous investigation (5), thus providing the basis for the steel compositions selected in the present studies.

The overall objective here was to determine the effect of stress and strain on the rate of formation of $(Cr,Fe)_7C_3$, and simultaneously, to ascertain the influence of this tempering reaction on the concomitant creep-rupture properties. The test temperatures were chosen primarily in the fourth stage of tempering (800–1300 °F).

Experimental Procedure

Materials—Three steels were selected from within the composition range where $(Cr,Fe)_7C_3$ is the stable carbide phase (5,6); their analyses are given in Table I. These materials are fairly representative of the low, the medium, and the high carbon ranges of 4.5% chromium steel.

The steels were received in the form of $\frac{3}{8}$ inch diameter rods which had been hot-rolled, spheroidized, and then centerless ground. The creep specimen gage dimensions were set at 0.250 inch in diameter and 2 inches long. Hardening studies showed that these specimens could be oil-quenched and then refrigerated in liquid nitrogen without cracking. The austenitizing temperature was adjusted to obtain complete carbide solution without incipient melting at the grain boundaries. Holding for 30 to 40 minutes at 2100 ± 10 °F (1150 ± 5 °C) not

only satisfied these two requirements, but did not cause excessive grain growth from the standpoint of creep-rupture properties (ASTM Nos. 3–4). An atmosphere of prepurified nitrogen was used during austenitizing to avoid undue decarburization and oxidation.

In order to minimize retained austenite as a possible variable in the creep-rupture measurements, the test specimens were cooled in liquid nitrogen immediately after the hardening treatment. This reduced the retained austenite to well below 10% in the highest carbon steel, and the retained austenite decreased noticeably with decreasing carbon content.

Tempering Studies—The tempering treatments (except for those conducted as a part of the creep-rupture tests) were carried out in molten alloy or salt baths, controlled to ± 5 °F. Bare specimens were used for the short tempering times, but the specimens were sealed in evacuated pyrex tubes for the longer runs.

The reaction kinetics in both the unstressed and stressed states were followed by hardness and electrical resistance measurements. Because of the wide range of hardness values encountered, the Rockwell A scale (brale indentor with 60 kilogram load) was adopted. The electrical resistance was measured between fixed knife-edges (1½ inches apart) with a Kelvin double bridge. These measurements were all made in liquid nitrogen (−320 °F) in order to minimize the thermal component of the resistance and thus accentuate the changes due to structural transformations. The values reported here have been corrected to a standard cross section of 0.250 inch diameter, and are accurate to within ± 1 microhm.

Previous work (5) had shown that it was possible to determine the amount of $(Cr,Fe)_7C_3$ in low chromium steels as a function of the tempering treatment by chemical analysis of the electrolytically extracted carbides. However, in the present investigation the extracted carbides, consisting of mixtures of $(Fe,Cr)_3C$ and $(Cr,Fe)_7C_3$, were subjected to X-ray analysis, and the respective fractions of these two phases were found from the integrated intensities of a pair of prominent diffraction lines. Calibration of the method was obtained from synthetic mixtures of the two carbides. The specimens used for the electrolytic extraction were the same ones that provided the hardness and electrical resistance data and, in certain cases, the creep-rupture data.

Creep Studies—Because a preliminary check showed that excessive oxidation of the specimens might be expected if the usual type of creep-rupture furnace were employed, a special furnace arrangement was designed to allow the specimens to be tested in a purified helium atmosphere. The applied stresses were adjusted to permit the specimens to undergo first and second stage creep within reasonable periods of time (about 500 hours max.). Third stage creep, where necking

ensues, was generally avoided for the concomitant tempering studies in order that the effective stress could be regarded as uniaxial.

Creep-rupture curves for hardened specimens could only be obtained, however, on testing at 1200 and 1300 °F (650 and 705 °C). When tested at the two lower temperatures (800 and 1000 °F), the specimens invariably fractured in a brittle fashion by cracking along the austenitic grain boundaries before appreciable creep occurred. Prior tempering for extended periods at the testing temperatures before the application of stress was of no avail in the prevention of this brittle grain boundary failure. Nevertheless, loads below a certain level could be sustained without creep by the hardened steels at 800 and 1000 °F (425 and 540 °C), and such loads were used. On the other hand, brittle fractures were not encountered even at these low testing temperatures if the steels were either annealed or hardened and tempered at 1350 °F (730 °C).

Because of the great dependency of the tempering rate on temperature, it was necessary to bring the hardened specimens to the testing temperature as rapidly as possible. This was done by superheating the furnace to a predetermined temperature, then inserting the specimen and its holding apparatus and allowing the assembly to reach the desired testing temperature. This usually occurred in about 20 minutes. The specimen was then held at the testing temperature for a full hour in the unstressed condition before the load was applied for the creep-rupture run.

The load was applied as carefully as possible in order to avoid shock by the use of a hydraulic jack. The creep extensions were measured with a dial gage having 0.001 inch divisions.

One set of test specimens was used to determine the creep-rupture curves, and hence was run to fracture. Tests on additional specimens were interrupted at intermediate periods of time so that the course of the tempering reactions could be traced.

Discussion

Creep-Rupture Behavior—The creep-rupture curves for the three hardened steels at 1200 and 1300 °F (650 and 705 °C) are presented in Fig. 1. There is the usual linear relationship between log stress and log rupture time. It is noteworthy that the lines for the highest carbon steel C have the steepest slope, and designate an accelerated loss of strength with long times of testing. The most plausible explanation for this behavior is that preferential carbide precipitation takes place along the austenitic boundaries (Fig. 2) as the tempering proceeds under stress, but this does not occur in the unstressed condition, nor in the lower carbon steels. As a result, steel C fails in creep with an intergranular fracture, while the lower carbon steels have transgranular fractures.

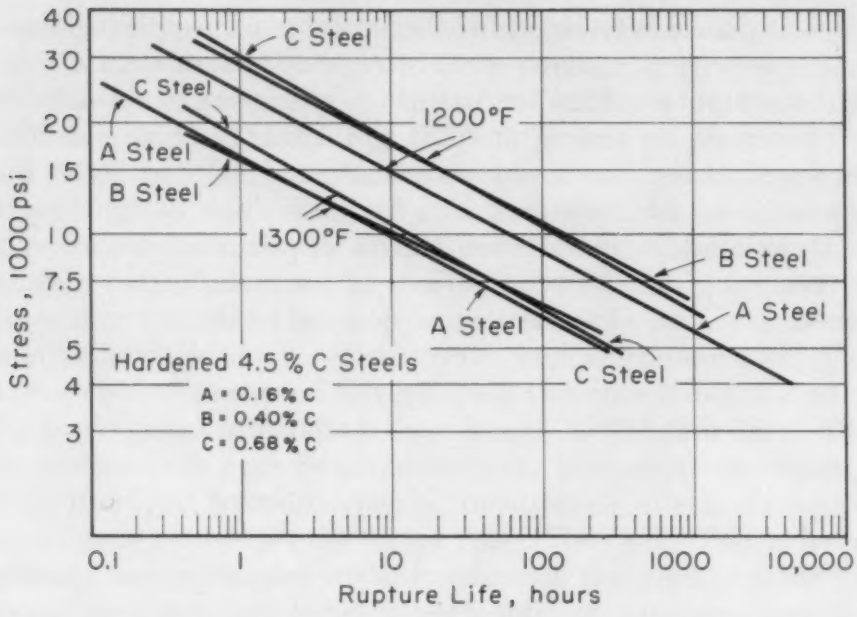


Fig. 1—Creep-Rupture Curves for Hardened 4.5% Chromium Steels at 1200 and 1300 °F.

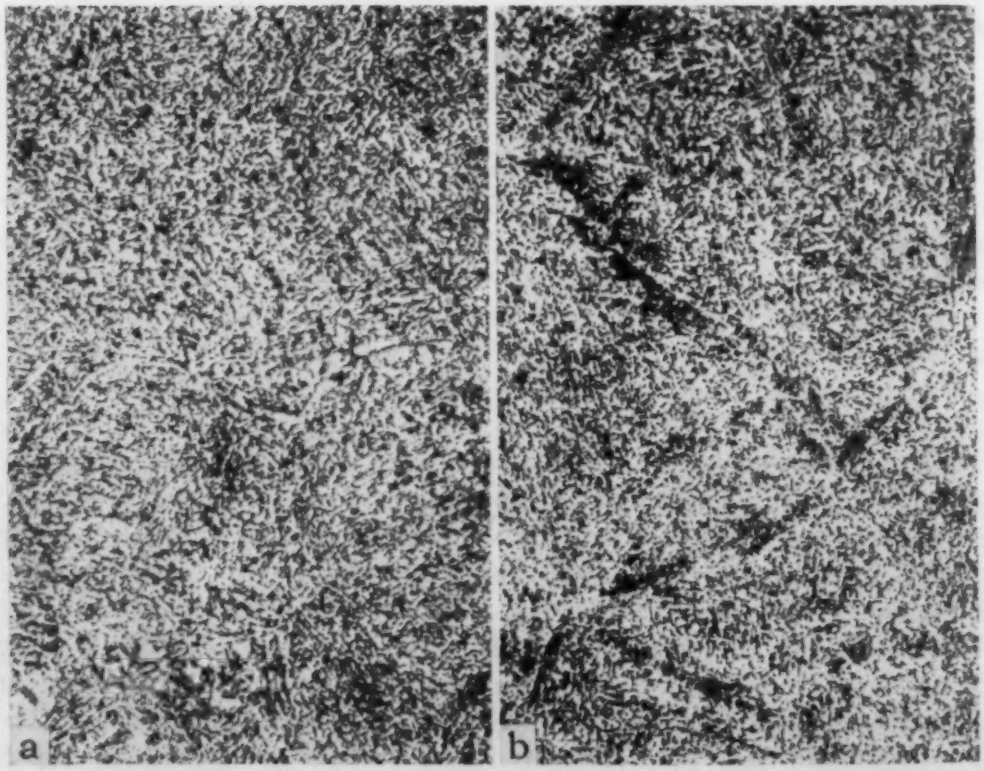


Fig. 2—Photomicrographs of (a) Unstressed and (b) Stressed Sections of Hardened 4.5% Chromium Steel C (0.68% Carbon) Tested at 1300 °F and 5500 psi. (Rupture Life—189 hours). Etched with 4% nital, 1% zephiran chloride. X 500

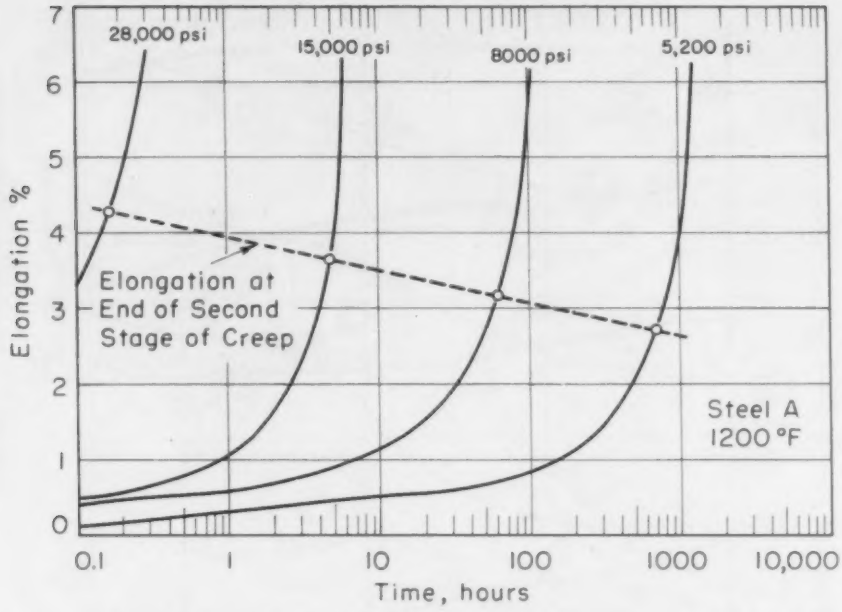


Fig. 3—Creep Curves for Hardened 4.5% Chromium Steel A (0.16% Carbon) at 1200 °F.

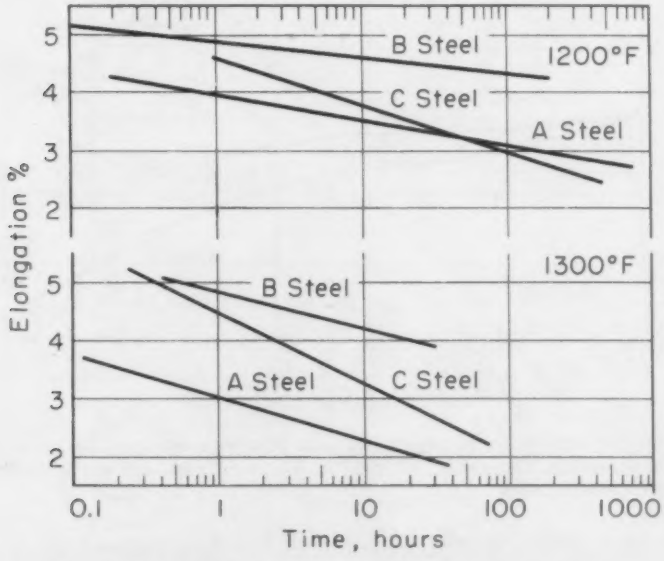


Fig. 4—Elongation at the End of the Second Stage of Creep as a Function of Time at 1200 and 1300 °F for Hardened 4.5% Chromium Steels. A = 0.16% carbon, B = 0.40% carbon, C = 0.68% Carbon.

This difference in behavior is also illustrated by the magnitude of the per cent elongation at the end of the second stage of creep (sometimes called the "true elongation" (7)). An example of the variation of "true elongation" is given in Fig. 3 for steel A at 1200 °F (650 °C). Similar plots for the three steels at the two test temperatures of 1200 and 1300 °F (650 and 705 °C) permitted the drawing of Fig. 4, from which it is evident that the elongation at the end of the second stage of creep decreases with increasing time much more rapidly for the C steel

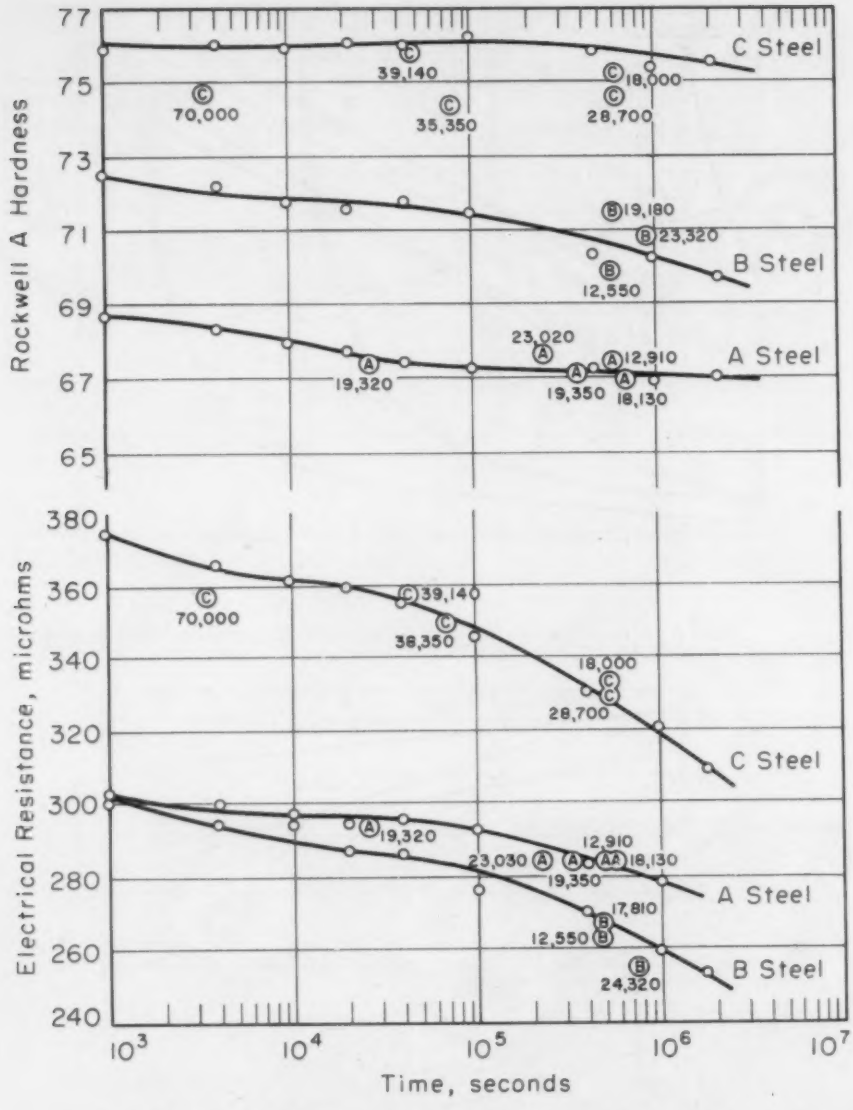


Fig. 5—Changes in Hardness and Electrical Resistance of 4.5% Chromium Steels on Tempering at 800 °F. Inserted numbers show applied stress for indicated points.

than for the two lower carbon steels. This is a consequence of the difference in the mode of fracture as previously discussed.

Analysis of Tempering Phenomena—Hardness and electrical resistance changes during tempering at 800 to 1300 °F (425 and 705 °C), with and without stress, are plotted in Figs. 5 through 8. The curves are drawn through the points for the unstressed specimens, while the data for the stressed specimens are shown as individual points with the applied stress indicated. The effect of stress on the tempering process is discussed in the next section.

The stages of tempering represented by the data in Figs. 5 through 8 are conveniently analyzed in terms of the composite resistance curves in Fig. 9. These curves were obtained by translating the 1000, 1200,

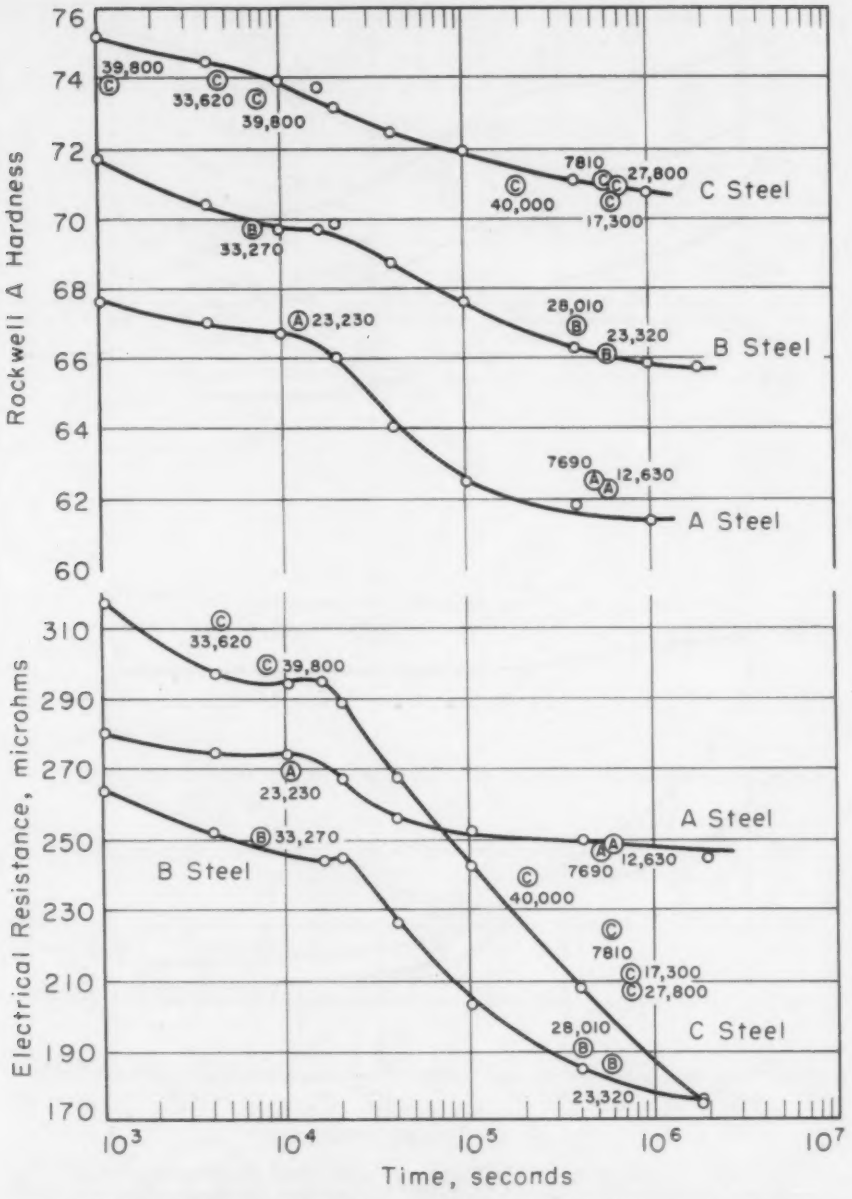


Fig. 6—Changes in Hardness and Electrical Resistance of 4.5% Chromium Steels on Tempering at 1000 °F. Inserted numbers show the applied stress for indicated points.

and 1300 °F (540, 650 and 705 °C) curves of the three steels along the log time axis of the respective 800 °F (425 °C) curves until the best match between overlapping portions of the curves was ascertained. This gave an effective time scale at 800 °F (425 °C) ranging from 10^3 seconds (17 minutes) to 10^{11} seconds (32 centuries), and comprised the end of the third stage of tempering followed by the fourth stage of tempering. In order to delineate the third stage more clearly by introducing at least a part of the second stage, additional data were taken at 800 °F (425 °C) for short tempering times down to one second.

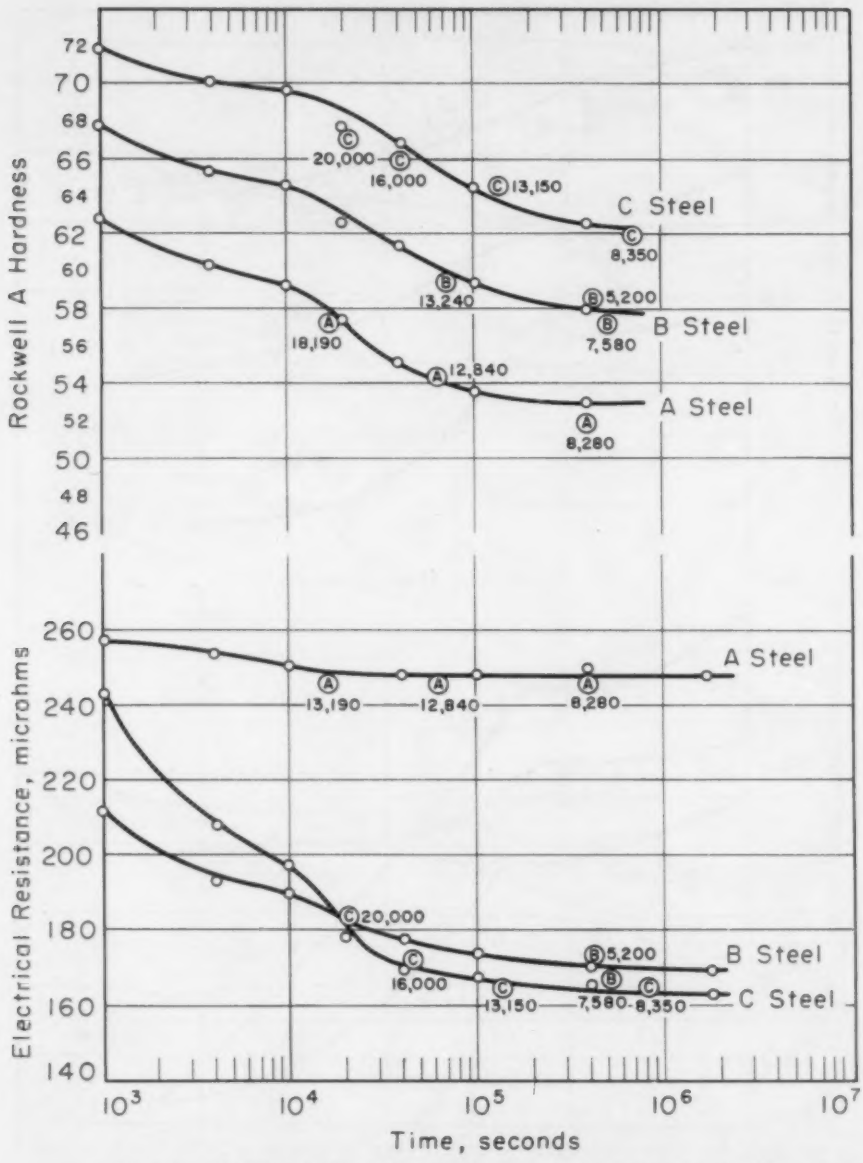


Fig. 7—Changes in Hardness and Electrical Resistance of 4.5% Chromium Steels on Tempering at 1200 °F. Inserted numbers show the applied stress for indicated points.

The generalized curves in Fig. 9 tend to smooth out some of the details[2] revealed by the individual curves in Figs. 5 through 8, but permit an instructive overall picture of the tempering process. The initial increase in electrical resistance is caused by the decomposition of the retained austenite during the second stage of tempering. This change is relatively small because:

(a) the amount of austenite present was deliberately reduced by the prior refrigeration treatment,

[2] One of these details is the slight increase in electrical resistance after about 10^4 seconds at 1000 °F (Fig. 6). This may be due to coherency strains involved in the early precipitation of $(Cr,Fe)_7C_3$. However, it was not observed at the other tempering temperatures, and so was averaged out in the composite curves of Fig. 9.

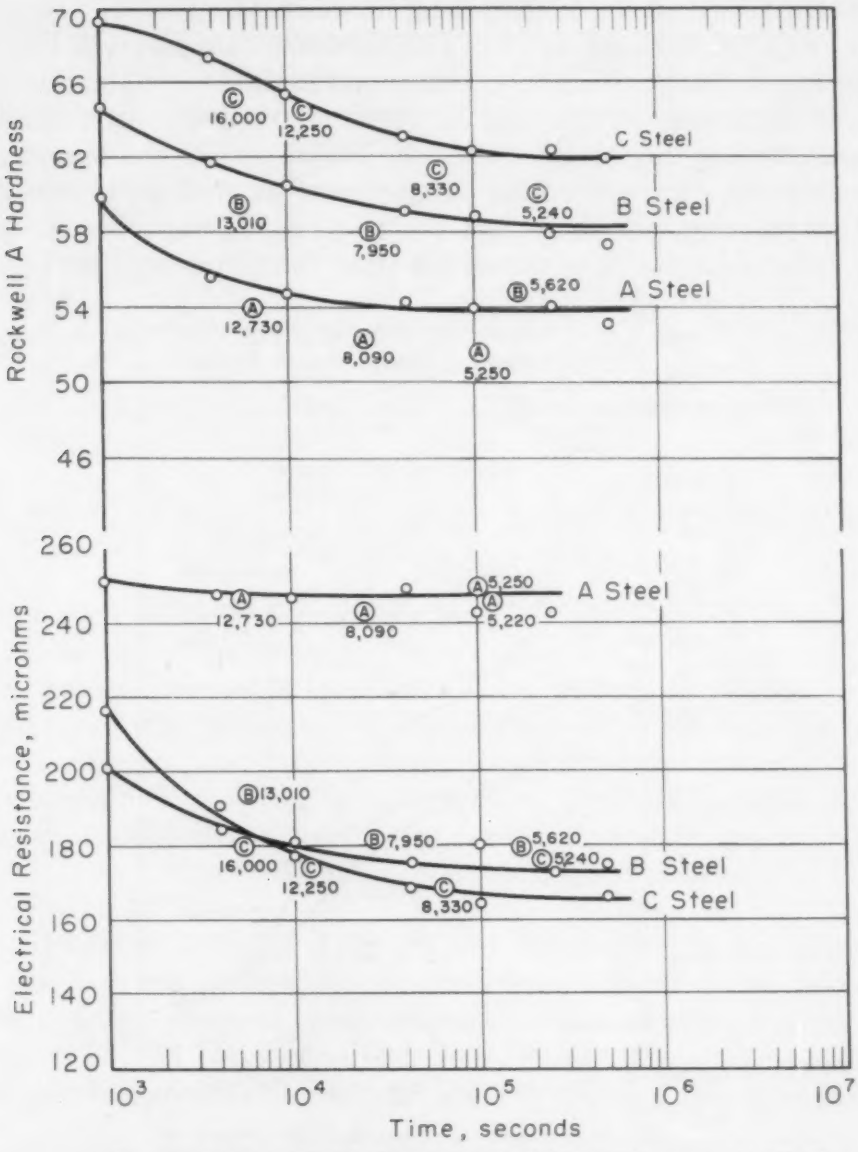


Fig. 8—Changes in Hardness and Electrical Resistance of 4.5% Chromium Steels on Tempering at 1300 °F. Inserted numbers show the applied stress for indicated points.

(b) the austenite conversion during tempering at 800 °F (425 °C) occurs too quickly to be studied in detail. Nevertheless, it is worth noting that the second stage of tempering produces an increase in electrical resistance whereas the opposite is true in plain carbon and most other alloy steels. Chromium appears to increase the electrical resistance of austenite less rapidly than that of its decomposition products, and hence the usual change in resistivity on transformation reverses sign in the presence of sufficient chromium.

The marked drop in resistance, after the initial increase, denotes the formation of cementite in the third stage of tempering. The further decrease in resistance beyond about 10^4 seconds at 800 °F (425 °C) is

due to the fourth stage of tempering in which $(Cr,Fe)_7C_3$ precipitates and $(Fe,Cr)_3C$ redissolves (5). The hardness data given in Fig. 5 for tempering at 800 °F (425 °C) correspond to the end of the third stage and the beginning of the fourth; there is relatively little change in hardness during this period. After the initial part of the fourth stage, a pronounced decrease occurs in hardness as well as in resistance. Electron micrographs show that the $(Cr,Fe)_7C_3$ particles are larger, more spheroidal and less numerous than the cementite particles that

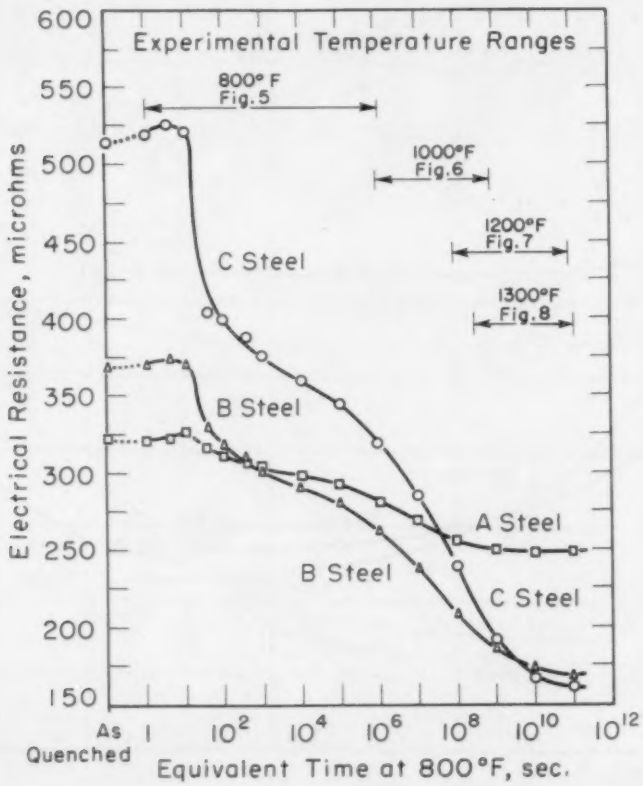


Fig. 9—Changes in Electrical Resistance of 4.5% Chromium Steels on Tempering at 800, 1000, 1200, and 1300 °F, all Referred to Equivalent Times at 800 °F.

are replaced (5). This difference, together with the removal of chromium from the solid solution matrix to form the chromium-rich carbide, results in appreciable softening during the fourth stage. The chromium depletion from the matrix is evidenced by the cross-over of the resistance curves in Figs. 6,7,8, and 9. The highest carbon steel ultimately attains the lowest resistance because the amount of chromium removed from the matrix, when $(Cr,Fe)_7C_3$ precipitates, increases with the carbon content.

By means of electrolytic extraction and X-ray diffraction studies the carbide precipitated during the third stage of tempering was identified as $(Fe,Cr)_3C$, and that of the fourth stage as $(Cr,Fe)_7C_3$. Fig. 10

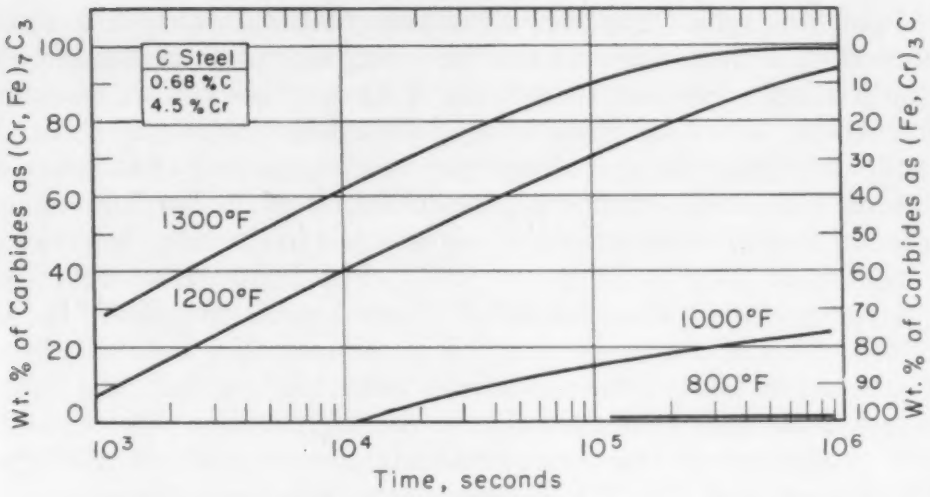


Fig. 10—Changes in $(Fe, Cr)_3C$ and $(Cr, Fe)_7C_3$ in 0.68% Carbon, 4.5% Chromium Steel as a Function of Time and Temperature of Tempering. Determined by X-ray diffraction measurements on extracted carbides.

shows how the $(Cr,Fe)_7C_3$ replaces the $(Fe,Cr)_3C$ in steel C as a function of time and temperature.

Effect of Stress—In general, the experimental points for the stressed specimens, as plotted in Figs. 5 through 8, fall near the hardness and electrical resistance curves drawn for the unstressed specimens, although there is considerable scatter. The data are indicative of the fourth stage of tempering. Except for the hardness curve at 1300 °F (705 °C), no consistent variations due to stress are evident. The results are compared in Table II.

At 1300 °F (705 °C) (Fig. 8), the hardness values of the three steels decrease more rapidly under stress than without stress. However, a corresponding effect of stress on the electrical resistance changes at 1300 °F (705 °C) is not observed. Accordingly, it must be concluded that the applied stress influences the state of aggregation of the precipi-

Table II

Effect of Stress on Changes in Hardness and Electrical Resistance During Tempering

	800 °F	1000 °F	1200 °F	1300 °F
	Displacement from Hardness Curve for Unstressed Specimens *			
Steel A	None	Slightly Above	None	Below
Steel B	None	None	None	Below
Steel C	Below	None	None	Below
	Displacement from Electrical Resistance Curve for Unstressed Specimens *			
Steel A	None	Slightly Below	Slightly Below	None
Steel B	None	Slightly Above	None	Slightly Above
Steel C	None	Above	None	None

* In view of the downward trend of the hardness and electrical resistance curves, "below" signifies acceleration by stress and "above" signifies retardation by stress.

tated carbides, rather than the rate of precipitation. Microscopic examination does, in fact, show a more rapid agglomeration of the carbides in the stressed specimens than in the unstressed ones. This would account for the faster softening of the stressed specimens.

These experimental findings may be summarized as follows: because of the various tempering reactions latent in hardened steels, structural instability assumes a prominent role in the creep behavior of the chromium (7) steels under study. The brittle fracture of the hardened specimens when subjected to stress at 800 and 1000 °F (425 and 540 °C) is a consequence of a high temperature instability, such as has been previously observed in other steels (8,9) and alloys (10,11). The grain boundary precipitation in the high carbon steel C under stress, which results in intergranular fractures even at 1200 and 1300 °F (650 and 705 °C), is also a manifestation of structural instability. The accelerated rate of agglomeration at 1300 °F (705 °C) under stress is likewise an instability effect, leading to reduced hardness and strength.

It is significant that neither applied stress nor the associated strain, at least within the limits investigated here, increases the rate of the fourth stage of tempering. Evidently, the precipitation of $(Cr,Fe)_7C_3$ or the accompanying solution of $(Cr,Fe)_3C$ is diffusion-controlled (5), and the rate of diffusion is not materially affected by the creep process. It has been shown (12) that the self-diffusion rate of iron under uniaxial compression is a function of the strain rate, rather than of the strain itself. Presumably, the creep rates encountered in the present work were too small to exert a measurable influence on the overall kinetics of the fourth stage of tempering. The conditions of creep testing do lead to localized precipitation at the grain boundaries in the high carbon steel C at 1200 and 1300 °F (650 and 705 °C), but there is no corresponding effect on the bulk reaction rate as revealed by the electrical resistance measurements.

Conclusions

1. Hardened 4.5% chromium steels are not amenable to creep testing at 800 and 1000 °F (425 and 540 °C) because they undergo intergranular fracture before appreciable creep takes place.

2. On testing and tempering at 1200 and 1300 °F (650 and 705 °C), the high carbon, 4.5% chromium steel (0.68% carbon) has higher strength than the lower carbon steels (0.16 and 0.40% carbon) only for short testing times. As the time of testing is increased, the strength of the high carbon steel decreases more rapidly than that of the lower carbon steels. This is due to the intergranular type of failure found in the high carbon steel, which is initiated under stress by preferential carbide precipitation at the grain boundaries during the fourth stage of tempering.

3. The second, third and fourth stages of tempering in 4.5% chromium steels can be readily followed by electrical resistance measurements. The second stage of tempering is attended by an increase in resistance, unlike the case in plain carbon and most other alloy steels. The third and fourth stages are accompanied by successive decreases in resistance. Electrolytic extraction studies show that the $(Fe,Cr)_3C$ formed during the third stage of tempering is replaced by $(Cr,Fe)_7C_3$ during the fourth stage.

4. The application of stress, as in creep runs, during tempering has no consistent effect on the overall kinetics of the fourth stage. This is also true for the associated hardness changes, except at 1300 °F (705 °C) where the hardness is found to decrease more rapidly under stress than without stress. The latter phenomenon appears to result from an increased rate of agglomeration of the carbides on tempering under stress.

5. The insensitivity of the fourth-stage kinetics to applied stress is attributed to the fact that the underlying reaction is diffusion-controlled, and the rate of diffusion is not affected much by stress unless the corresponding strain rate is considerably higher than is encountered in the usual creep studies.

Acknowledgments

The authors wish to thank the U. S. Navy Bureau of Ships for sponsoring this research. They are also indebted to S. G. Fletcher of the Latrobe Steel Company for furnishing the steels, and to Ralph P. Kimble for his help with the creep tests.

References

1. J. R. Lane and N. J. Grant, "Carbide Reactions in High Temperature Alloys," Transactions, American Society for Metals, Vol. 44, 1953, p. 113.
2. The Book of Stainless Steels, Edition 2, 1953, American Society for Metals, Cleveland.
3. E. C. Bain and Z. Jeffries, "Cause of Red Hardness of High-Speed Steel," *Iron Age,* Vol. 112, 1923, p. 805.
4. E. Houdremont, H. Bennek and H. Schrader, "Hardening and Tempering of Steels Containing Carbides of Low Solubility, Especially Vanadium Steels," *Transactions,* American Institute of Mining and Metallurgical Engineers, Vol. 116, 1953, p. 260.
5. R. W. Balluffi, M. Cohen and B. L. Averbach, "The Tempering of Chromium Steels," Transactions, American Society for Metals, Vol. 43, 1951, p. 497.
6. W. Crafts and C. N. Offenhauer, "Carbides in Low Chromium Steel," *Transactions,* American Institute of Mining and Metallurgical Engineers, vol. 150, 1942, p. 275.
7. N. J. Grant and A. G. Bucklin, "On the Extrapolation of Short-Time Stress-Rupture Data," Transactions, American Society for Metals, Vol. 42, 1950, p. 720.

8. G. V. Smith, W. B. Seens, H. S. Link, P. R. Malenock, "Microstructural Instability of Steels for Elevated Temperature Service," *Proceedings,* American Society for Testing Materials, Vol. 51, 1951, p. 895.

9. A. J. Lena and M. F. Hawkes, "Embrittlement of High Chromium Ferritic Steels at 475 °C," *Journal of Metals,* February 1952, p. 146.

10. A. G. Guy, C. S. Barrett and R. F. Mehl, "Mechanism of Precipitation in Alloys of Beryllium in Copper," *Transactions,* American Institute of Mining and Metallurgical Engineers, Vol. 175, 1948, p. 216.

11. A. H. Geisler, "Property Changes During Aging," *Transactions,* American Institute of Mining and Metallurgical Engineers, Vol. 180, 1949, p. 230.

12. F. S. Buffington and M. Cohen, "Self-Diffusion in Alpha Iron Under Uniaxial Compressive Stress," *Transactions,* American Institute of Mining and Metallurgical Engineers, Vol. 194, 1952, p. 859.

THE STRENGTH OF WROUGHT ZIRCONIUM-BASE BINARY ALLOYS AT 1800 TO 2200 °F

By H. A. Saller, J. T. Stacy and S. W. Porembka

Abstract

The effects of binary additions of chromium, columbium, molybdenum, tantalum, tungsten, and vanadium on the workability, hardness, and high-temperature strength of zirconium were investigated. Alloys of tantalum or tungsten were the most easily worked. At 1600 °F (870 °C), maximum hardness was obtained with a tungsten addition. Metals of Group 6 were more effective strengtheners than metals of Group 5, tungsten being the most effective strengthener for zirconium at 1800 to 2200 °F (980 to 1205 °C). The 100-hour creep-rupture strength at 1800 °F (980 °C) of a zirconium — 8wt % tungsten alloy was 1700 psi. None of the alloys studied were superior in strength to Inconel or Type 310 stainless steel over the range 1800 to 2200 °F (980 to 1205 °C).

Introduction

BECAUSE of its high melting point (3325 °F), zirconium is potentially an attractive material for high temperature service, either in non-corrosive media or with suitable protective cladding. At elevated temperatures, however, zirconium has relatively poor mechanical properties. The possibility of improvement by alloying is of considerable interest. The present investigation was undertaken to determine the effectiveness of alloying in increasing the strength of zirconium at 1800 to 2200 °F (980 to 1205 °C).

The development of zirconium-base alloys for use at elevated temperatures has been reported previously by both Battelle Memorial Institute and the General Electric Research Laboratory; however, in both instances, testing was carried out at lower temperatures. In the earlier Battelle investigations, strengths were obtained at 930 °F (500 °C) and hardness values were measured at temperatures up to 1470 °F (800 °C) (1,2).[1] In the General Electric work, tensile strengths were measured at temperatures up to 930 °F (500 °C) (3,4,5,6). The Battelle studies differed from those of General Electric in that they were concerned with the maintenance of low neutron

[1] The figures appearing in parentheses pertain to the references appended to this paper.

Work performed under AEC Contract W-7405-end-92.

A paper presented before the Thirty-sixth Annual Convention of the Society, held in Chicago, November 1 to 5, 1954. The authors, H. A. Saller, J. T. Stacy and S. W. Porembka, are associated with the Battelle Memorial Institute, Columbus, Ohio. Manuscript received May 14, 1954.

absorption in the alloys. In the present work, nuclear cross section was of secondary interest, although its importance in reactor application was recognized.

At temperatures of 1800 to 2200 °F (980 to 1205 °C), it appeared unlikely that much precipitation hardening could be expected and that strengthening would have to be of the solid-solution type. Selection of the zirconium-binary alloy systems for initial investigation was based on: known solid-solution alloying characteristics, solid-solution alloy theory, the results of zirconium-alloy tests at lower temperatures, and such pertinent elemental properties as melting points and high temperature strength. Elements selected for alloying additions to zirconium were the transition metals of Groups 5 and 6: chromium, columbium, molybdenum, tantalum, tungsten, and vanadium.

The investigative program consisted of five phases: preparation of the binary alloys by melting; rolling the alloys to sheet at 1850 and 2200 °F (1010 and 1205 °C); hardness testing at room temperature and 1600 °F (870 °C); short-time rupture-strength determinations at 1800, 2000, and 2200 °F (980, 1095 and 1205 °C) in helium; and creep-rupture testing of the most promising alloy at 1800 °F (980 °C) in vacuum.

Experimental Procedure

Materials and Melting

All alloys were made with low hafnium crystal-bar zirconium obtained from the Foote Mineral Company. The following alloying elements, of commercial purity, were used:

Chromium, Union Carbide and Carbon electrolytic;
Columbium, Fansteel sheet and partially sintered bar;
Molybdenum, Fansteel wire and sheet;
Tantalum, Fansteel sheet;
Tungsten, Fansteel rod and powder; and
Vanadium, Union Carbide and Carbon ductile chips.

Nonconsumable (tungsten)-electrode-arc furnaces with power sources of about 500 and 1000 amp were used to melt the zirconium-base alloys in a helium atmosphere. Water-cooled copper-block crucibles of 7.5- and 32-cm^3 capacity permitted the melting of small rectangular ingots in two sizes for rolling and hardness tests, and for short-time stress-rupture tests, respectively. Charges of 50 to 75 grams were generally melted four to six times to attain homogeneity, and then melted together where larger rectangular ingots were needed, as in the fabrication of short-time rupture specimens. Alloys of zirconium-molybdenum and zirconium-tungsten were the most difficult to produce. Increasing the current and the number of remelts resulted in increased homogeneity of the zirconium-molybdenum alloys. Alloying of zirconium and tungsten was improved by charging tungsten powder and stacking pieces of nibbled zirconium around it in the crucible. On

partial melting at relatively low current, the powder was gathered by the molten zirconium. Homogeneous alloys were obtained after several remelts.

Test Methods

All alloys were tested for workability by rolling at 1850 and 2200 °F (1010 and 1205 °C). The specimens, unjacketed halves of 50-gram rectangular arc melts, were reduced 50% by reductions of 10% per pass. A reheat time of 15 minutes, in a helium-atmosphere furnace, was allowed between passes, and the alloys were examined for surface and edge cracks after each pass.

An increase in gas content, which might affect subsequent hardness and strength determinations, appeared likely to result from rolling the zirconium-base alloys bare at 1850 to 2200 °F (1010 to 1205 °C). To check this possibility, gas determinations were made on arc-melted zirconium after each of three stages in the processing. The results of these analyses are tabulated below for metal which had been surface ground to remove the heavy oxide. No increase in gas content is indicated.

Condition of Zirconium	Analysis, w/o		
	Oxygen (a)	Hydrogen (a)	Nitrogen (b)
Arc melted	0.071	0.0062	0.002
Arc melted, rolled at 1850 °F	0.053	0.0053	0.002
Arc melted, rolled at 2200 °F	0.046	0.0054	0.002

(a) Vacuum-fusion analysis, accuracy ± 10 to 20%
(b) Chemical analysis.

Hardness measurements were taken at room temperature and at 1600 °F (870 °C) on all workable alloys. Although it was desirable to determine hardnesses in the range 1800 to 2200 °F (980 to 1205 °C) for purposes of comparison and selection for strength tests, determinations above 1600 °F (870 °C) were not possible with existing equipment. While this temperature is slightly above the allotropic-transformation temperature of zirconium, 1585 °F (865 °C), and considerably above the reported transformation temperatures of some of the alloys,[2] it was recognized that the alpha-beta transformation may occur over a temperature range. In such cases, the hardnesses obtained at 1600 °F (870 °C) would not be true approximations of the hardnesses of the beta phases of the alloy systems.

At room temperature, hardness tests were made with a Vickers-Armstrong tester using a 5-kilogram load. At 1600 °F (870 °C), an apparatus employing a Vickers-type indenter was used (2). In these hot tests, the specimens and indenter were heated together in vacuum and held at 1600 °F (870 °C) for 15 minutes, and four or five indentations were made in each specimen under a load of 0.870 kilogram. When the specimens had cooled to room temperature, the impressions

[2] All of the alloying elements tested lower the alpha-beta-transformation temperature; e.g., chromium lowers it to 1535 °F, columbium to 1200 °F, molybdenum to 1435 °F, and tungsten to 1560 °F.

were measured and converted to Diamond Pyramid Hardness Numbers, and the numbers averaged. In each case, values for the same specimen did not differ by more than 10%.

To determine rapidly the relative strengths of the zirconium-base alloys from 1800 to 2200 °F (980 to 1205 °C) in a neutral atmosphere, a short-time stress-rupture testing apparatus was constructed. A description of the construction and operation of this equipment is given below. Alloys for stress-rupture tests were fabricated from 225-gram arc-melted rectangular ingots. These were rolled to strip at 2200 °F (1205 °C) from a helium-atmosphere furnace, surface ground, and machined. Spectrographic analyses were made on material from the gage length of each alloy. To provide a basis for comparison and to check the testing procedure, the strengths of several commercially available alloys were evaluated also.

The short-time rupture-test apparatus is shown in Fig. 1. It consists essentially of a wire-wound resistance furnace, suitable adapters and expansion bellows, and a 1½-inch-bore pneumatic cylinder for applying a load. The furnace and cylinder are swivel mounted to facilitate specimen handling and alignment. To protect the O-ring seals between the ceramic furnace tube and flanges, the flanges are water-cooled. To obtain a relationship between air pressure in the cylinder and load on the specimen, the pneumatic cylinder was calibrated with a beam balance prior to testing. These values were corrected for the effects of the bellows and neutral-gas pressure.

Test specimens were 10½ inches long and 0.030 inches thick, and had a gage length of 2 inches. Temperatures were measured in the center and at each end of the gage length with three platinum-platinum 10 per cent rhodium thermocouples; uniform temperatures being obtained by the appropriate shunting of the furnace winding. A slight positive pressure of helium was maintained in the furnace at all times. After heating, a specimen was held at temperature for 15 minutes before applying a load. In loading, compressed air was introduced into the cylinder in steps of 1 psi, equivalent to about a 1.5-pound load in the specimen. After each step, 1½ minutes were allowed before checking for elongation, which was shown by a pointer on the piston shaft. Loading was continued in this manner until sustained elongation was noted. Then the specimen was allowed to elongate to rupture without further loading. The time of elongation ranged from 0.3 to 0.5 hours. The accuracy of the stress measurement was about ± 50 psi. Temperature was controlled to ± 10 °F.

A series of creep-rupture tests were made on a zirconium-tungsten alloy at 1800 °F (980 °C) in vacuum. These tests were made in a vacuum resistance furnace mounted on a standard creep frame. The furnace consisted essentially of a Chromel-wound central tube shielded from an exterior water-cooled brass shell by concentric stainless steel

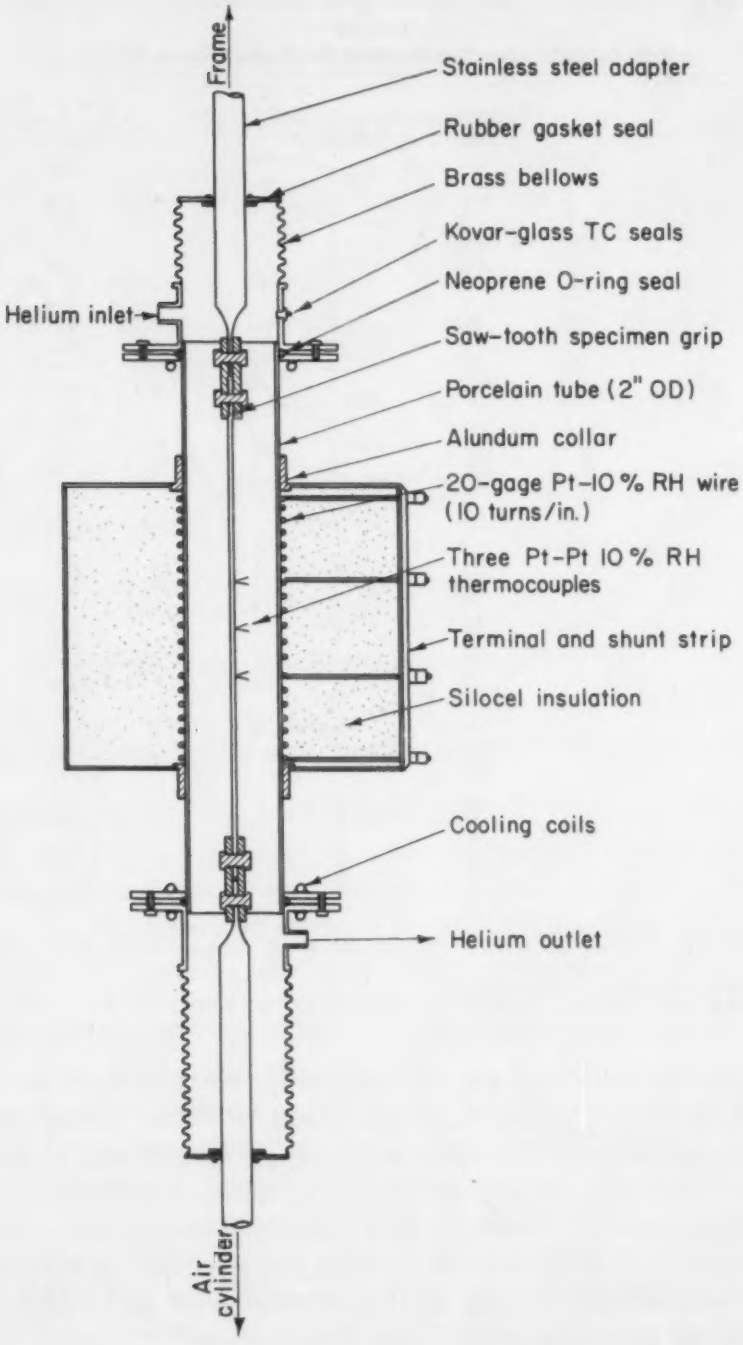


Fig. 1—Sketch of Short-Time Stress-Rupture Apparatus.

baffles. Metal expansion bellows provided for the movement of the specimen adapters for transmitting the load, while suitable windows permitted observation of the heated specimen. A vacuum of 1 to 5 microns was maintained during test and the specimen temperature was controlled to within ± 3 °F.

Table I
Workability and Hardness of Zirconium-Base Alloys

Nominal Alloy Addition, Wt %	Workability[a] at 1850 °F	Workability[a] at 2200 °F	Diamond Pyramid Hardness Number 70 °F	Diamond Pyramid Hardness Number 1600 °F
0(100 Zr)	—	—	121	12.6
4Cr	P	F	329	20
10Cr	P	F	440	14.6
20Cr	NG	P	—	—
30Cr	NG	F	587	18.1
5Cb	F	F	299	8.0
10Cb	E	F	343	12.6
20Cb	F	E	234	29
30Cb	P	F	295	36.5
40Cb	NG	F	314	56.2
7.5Mo	E	E	359	16.8
15Mo	F	F	492	36
20Mo	NG	P	341	37.4
22Mo	NG	F	502	25.6
30Mo	F	F	—	—
40Mo	NG	F	532	19.6
5Ta	E	E	297	8.8
10Ta	F	E	264	7.8
20Ta	E	E	331	18.0
40Ta	E	E	279	23.0
50Ta	E	E	410	16.1
5V	F	F	298	9.4
10V	F	F	313	12.5
15V	P	E[b]	556	19.6
20V	NG	F	500	43.6
40V	NG	NG	—	—
4W	E	F	320	78.3
8W[c]	E	E	414	22.0
10W[c]	E	E	418	16.6
12W	E	E	362	31.6
15W[c]	E	E	490	17.6
20W	E	E	509	12.5

[a] Workability is based on rolling characteristics: E = no cracks; F = small cracks, essentially sound; P = large cracks; and NG = broken.
[b] Results could not be reproduced.
[c] Prepared with tungsten powder.

Two arc-melted ingots of the alloy were rolled at 2200 °F (1205 °C), surface ground, and machined to form specimens 0.050-inches thick and 5½-inches long with a gage length of 1½ inches. In testing, the stress was applied within 2 or 3 hours after the specimen had reached temperature. Extensometer readings were taken on ruled platinum reference strips attached to the gage section of the specimen; a filar micrometer microscope with a sensitivity of 0.00005 inches being used for the measurements.

Results

Workability and Hardness

The data obtained from workability and hardness tests of the arc-melted zirconium-base alloys are listed in Table I. Of the alloys rolled at 1850 and 2200 °F (1010 and 1205 °C), tantalum and tungsten alloys were the most workable and vanadium and chromium alloys the least workable. Workability ratings given in Table I indicate that

Table II
Short-Time Rupture Strengths of Zirconium-Base Alloys

Nominal Alloy Addition, Wt %	Short-Time Rupture Strength[a] 1800 °F Analysis[b], Wt %	1800 °F Stress, psi	1800 °F Elongation in 2 In., %	2000 °F Analysis[b], Wt %	2000 °F Stress, psi	2000 °F Elongation in 2 In., %	2200 °F Analysis[b], Wt %	2200 °F Stress, psi	2200 °F Elongation in 2 In., %
0(100Zr)	—	740	30	—	270[c]	62.5	—	79[c]	106
4Cr	3.7Cr	3010	32	3.9Cr	1440[c]	37.5	3.4Cr	430	78
20Cb	20.4Cb	2350	81	19.8Cb	1810	124	19.7Cb	1650	126
7.5Mo	7.1Mo	3030	65	7.1Mo	1230	62.5	6.8Mo	750	116
15Mo	14.9Mo	3310	61	—	2220	104	14.7Mo	1330	125
20Mo	—	—	—	20.5Mo	1800	102	—	—	—
10Ta	—	1790	56	10.4Ta	1050	56	—	820[c]	97
20Ta	—	3680[c]	36	—	2320[c]	44	19.7Ta	1200	114
40Ta	39.3Ta	3510	44	—	2320	50	40.3Ta	1960	81
15V	—	—	—	—	—	—	14.5V	150	130+
20V	—	—	—	—	—	—	18.6V	160	130+
4W	4.4W	4660	11	3.9W	1870	24	3.6W	1460	29
8W[d]	8.1W	3950	11	8.1W	2280	28	7.3W	2180	18
12W	—	—	—	12.2W	2550	31	—	—	—

[a] Data are for two specimens, except as otherwise indicated.
[b] Spectrographic analysis of gage section.
[c] Single specimen.
[d] Powdered tungsten used to lower segregation.

better rolling results were obtained at 2200 °F (1205 °C) than at 1850 °F (1010 °C). However, considerably more oxidation occurred at the higher temperature and, to secure clean metal for subsequent testing, it was necessary to remove about 0.015 inches of the surface by grinding.

Hardness tests at room temperature and at 1600 °F (870 °C) gave quite dissimilar results, as would be anticipated from knowledge of the solubility changes and the intervening allotropic transformation. At room temperature, additions of equal weight percentages of chromium, molybdenum, tungsten, or vanadium had roughly equivalent hardening effects on zirconium. In this regard, all were superior to columbium or tantalum. At the 5wt % addition level, however, the hardnesses of all the binary alloys were within a 10% spread. At 1600 °F (870 °C), maximum hardness was developed by an addition of 4wt % tungsten, the hardness decreasing with increasing tungsten content. This behavior appeared to be a transformation-temperature effect. A similar decrease with increasing tungsten content was also noted in short-time stress-rupture tests at 1800 °F (980 °C), but did not occur at 2000 or 2200 °F (1095 or 1205 °C). At 1600 °F (870 °C), the zirconium-binary alloys containing 30 to 40wt % columbium, 15 to 20wt % molybdenum, and 20wt % vanadium showed relatively high hardnesses, whereas binary alloys containing chromium and tantalum were comparatively soft.

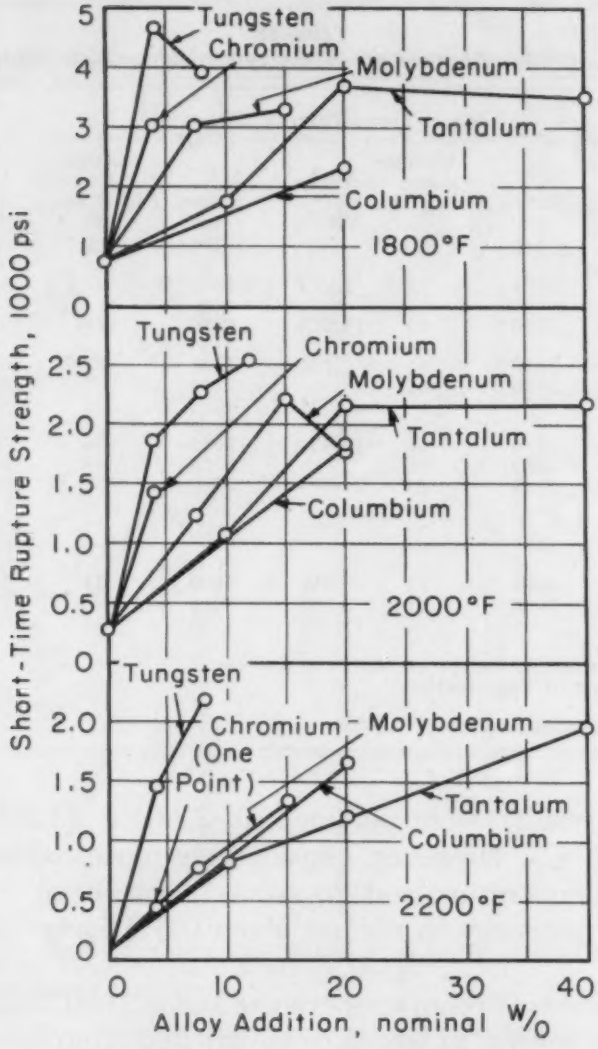


Fig. 2—Short-Time Rupture Strengths of Zirconium-Base Alloys at 1800, 2000, and 2200 °F in Helium.

Short-Time Rupture Strengths

The short-time rupture strengths obtained for the zirconium-base alloys at 1800, 2000, and 2200 °F (980, 1095 and 1205 °C) in helium are listed in Table II and are shown graphically in Fig. 2. These alloys were all arc melted and hot rolled. Tungsten is by far the most effective strengthener at these temperatures, on either a weight or an atom basis. Although a quite comparable strength at 2200 °F (1205 °C) can be obtained with an addition of 40wt % tantalum, the thermal-neutron cross section of such an alloy is excessively high and the principal advantage of zirconium for any high temperature reactor application is nullified. Of the alloys tested, the 20wt % columbium alloy showed the least loss of strength over the 1800 to 2200 °F (980 to 1205 °C)

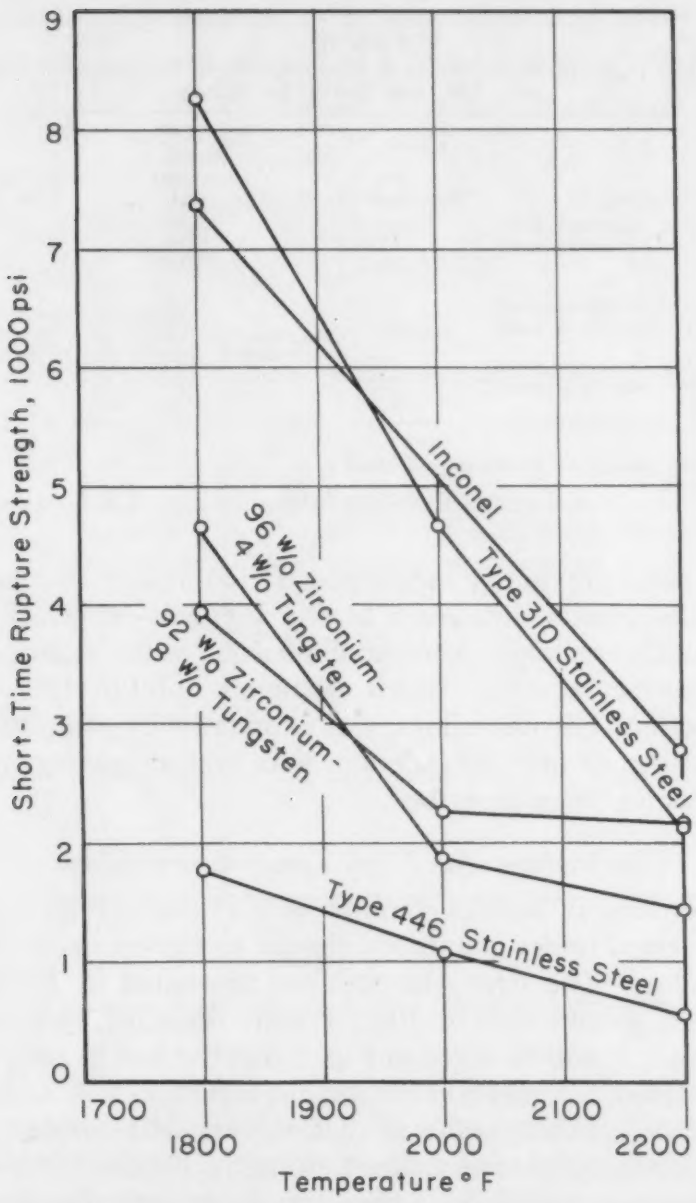


Fig. 3—Strength Comparison of Zirconium-Tungsten Alloys and Commercial High-Temperature Alloys.

temperature range. However, this alloy was relatively weak at 1800 °F (980 °C).

No good correlation could be obtained between results of hardness tests at 1600 °F (870 °C) and the short-time stress-rupture strengths obtained at 1800, 2000, and 2200 °F (980, 1095 and 1205 °C). Plots of hardness at 1600 °F (870 °C) versus high temperature strength were erratic, and even showed a decrease in strength with increase in hardness for tungsten alloys at 2000 and 2200 °F (1095 and 1205 °C). These inconsistencies are probably attributable to the proximity of the hardness-testing temperature to the alpha-beta-transformation tempera-

Table III
Short-Time Rupture Strengths of Commercial High Temperature Alloys at 1800, 2000, and 2200 °F in Helium

Alloy	Temperature, °F	Short-Time Rupture Strength(a), psi	Elongation in 2 In., %
Type 310 stainless steel	1800	8280	40
Type 446 stainless steel	1800	1780	75
Inconel	1800	7380	39
Type 310 stainless steel	2000	4690	31
Type 446 stainless steel	2000	1090(b)	62.5
Type 310 stainless steel	2200	2140	20
Type 446 stainless steel	2200	580	68
Inconel	2200	2780	53
Timken 16-25-6	2200	2350	18.5

(a) Two tests, except as otherwise indicated.
(b) Single test.

ture as has been previously mentioned. It is unlikely that segregation influenced the results, inasmuch as the surfaces on which hardness measurements were taken were homogeneous when examined metallographically. Segregation, which occurred only in the arc-melted tungsten and molybdenum alloys, was eliminated by using additions of tungsten powder or fine molybdenum wire and increasing the number of remelts, as has been described.

Comparison with High Temperature Alloys

For comparison, several commercially available high temperature alloys were tested under conditions similar to those used in testing the zirconium alloys. The strengths obtained are listed in Table III and are compared graphically in Fig. 3 with those of two zirconium-tungsten alloys. It will be noted in Fig. 3 that the 8wt % tungsten alloy, although decidedly weaker at 1800 °F (980 °C), has a strength at 2200 °F (1205 °C) comparable to that of Type 310 stainless steel.

To relate the short-time rupture strengths obtained in this investigation to the more usual short-time tensile-strength figure, duplicate sheet specimens of Type 310 stainless steel were tensile tested at 1800 °F (980 °C) in air at a strain rate of 0.02 per minute. Tensile strengths of 9550 and 9380 psi were obtained. These values are about 1000 psi greater than short-time rupture strengths of the same material at 1800 °F (980 °C), as noted in Table III. This difference is ascribable to the sensitivity of the elevated-temperature tensile strength to the time required to complete the test (7).

Creep-Rupture Tests

On the basis of its strength in the short-time stress-rupture tests, the arc-melted zirconium—8wt % tungsten alloy was selected for creep-rupture testing at 1800 °F (980 °C) in vacuum. Test results are given

Table IV
Creep-Rupture Tests of a Zirconium—8 wt% Tungsten Alloy at 1800 °F in Vacuum

Arc-Melt Ingot	Stress, psi	Rupture Time, hr	Elongation in 1.5 In., %	Minimum Creep Rate, %/hr
1	[a]	—	—	—
1	2000	192.0	[b]	0.0014
2	2500	0.1	2.8[c]	—
2	2500	0.2	6.9[c]	8.5
2	2000	18.4	6.4	1.6
2	1500	74.9	14.8	0.10

[a] Failed during assembly.
[b] Broken in removal from furnace; badly oxidized.
[c] Ruptured at end of gage length.

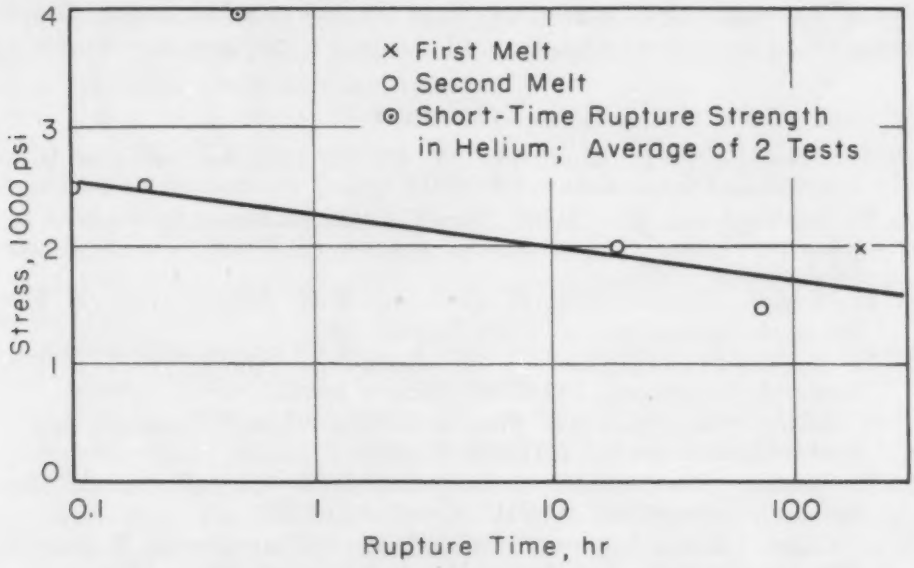


Fig. 4—Stress-Rupture Strength of a Zirconium—8Wt% Tungsten Alloy at 1800 °F in Vacuum.

in Table IV. A plot of the stress-rupture strength, shown in Fig. 4, indicates that the alloy has a 100-hour rupture strength of about 1700 psi at 1800 °F (980 °C). It will be noted that the melts differ somewhat in strength and that there is considerable discrepancy between the stress-rupture strength obtained in vacuum and the short-time rupture strength previously observed in helium.

Although additional tests would be necessary for a more accurate 100-hour rupture-strength determination, the zirconium—8wt % tungsten alloy appears to be somewhat weaker at 1800 °F (980 °C) than the better wrought austenitic stainless steels. At this temperature, the 100-hour rupture strengths of Type 310 and 309 stainless steels are 3200 and 2200 psi, respectively (8).

Conclusions

Tungsten was found to be a very effective strengthener for zirconium in the temperature range 1800 to 2200 °F (980 to 1205 °C).

Zirconium-tungsten alloys can be readily hot-worked, but care is required to produce homogeneous alloys by arc melting. Comparison with commercial alloys in this temperature range shows that zirconium-tungsten alloys approach the strength of Inconel or Type 310 stainless steel at 2200 °F (1205 °C).

Binary additions of chromium, columbium, molybdenum, and tantalum also strengthen zirconium at 1800 to 2200 °F (980 to 1205 °C), but to a less extent than does tungsten. With the exception of tantalum, these elements and vanadium markedly reduce workability.

In conclusion, the metals of Group 6 are more effective in strengthening zirconium at 1800 to 2200 °F (980 to 1205 °C) than are those of Group 5. For a given group, the heavier the metal, the more effective it is as a strengthener, and the less it reduces hot workability.

References

1. A. D. Schwope, L. L. Marsh and W. Chubb, Battelle Memorial Institute, Unpublished Information, 1951–1953.
2. A. D. Schwope and W. Chubb, "Small Additions Raise Strength of Zirconium at Elevated Temperatures," *Journal of Metals*, Vol. 4, November, 1952, p. 1138–1140.
3. J. H. Keeler, "Development of Zirconium-Base Alloys," General Electric Research Laboratory, SO-2506, July 5, 1952.
4. J. H. Keeler, "Development of Zirconium-Base Alloys," General Electric Research Laboratory, SO-2508, January 5, 1953.
5. J. H. Keeler, "Development of Zirconium-Base Alloys," General Electric Research Laboratory, SO-2511, July 5, 1953.
6. J. H. Keeler, "Development of Zirconium-Base Alloys," General Electric Research Laboratory, SO-2512, October 5, 1953.
7. N. J. Grant, "Stress Rupture Testing," HIGH-TEMPERATURE PROPERTIES OF METALS, American Society for Metals, Cleveland, Ohio, 1951, p. 41.
8. "Digest of Steels for High-Temperature Service," 5th Edition, Timken Roller Bearing Company, Canton, Ohio, 1946.

DISCUSSION

Written Discussion: By J. H. Keeler, General Electric Research Laboratory, Schenectady, N. Y.

The authors, like others working with zirconium-base alloys, are handicapped by the lack of constitution diagrams for some of the seemingly interesting alloy systems. For this paper, it would have been advantageous to have diagrams for the zirconium-columbium,[3] zirconium-tantalum, and zirconium-vanadium[3] systems readily available so that more detailed conclusions could be drawn from the data. Even though constitution diagrams for the systems zirconium-chromium, zirconium-molybdenum, and zirconium-tungsten have been determined by the Armour Research Foundation, these other diagrams would be useful for comparison purposes.

It is of interest, as might be anticipated, that for the alloys containing

[3] The Zr-Cb and Zr-V systems have recently been investigated by the Ames Laboratory of the Atomic Energy Commission, but as yet have not been placed in the readily available metallurgical literature.

tungsten, chromium, and molybdenum, the short-time rupture strengths shown in Fig. 2 can be roughly correlated to the maximum solid solubility in beta zirconium at the test temperature. Estimates of the amount of solubility of tungsten, chromium, and molybdenum in beta zirconium from their constitution diagrams,[4, 5] are shown in Table V.

Table V
Amount of Solubility of Tungsten, Chromium and Molybdenum in Beta Zirconium

Element	1800 °F	2000 °F	2200 °F
W	1 %	2 %	2.5%
Cr	1.7	2.6	3.7
Mo	11.5	13	15

The rate of increase of rupture strength with per cent alloying element is greater with smaller solubility values since the slopes in Fig. 2 are in increasing order, molybdenum, chromium, and tungsten.

It is also to be noted that the slopes of these curves in Fig. 2 decrease after the solid solubility limit is exceeded. This seems to indicate that second-phase hardening by these elements is less effective per unit amount of element added, than is solid-solution hardening.

In addition to the present value of this paper, greater importance will accrue as additional constitution diagrams become available to aid in the interpretation of the data.

Written Discussion: By J. A. McGurty, Aircraft Nuclear Propulsion Project, General Electric Co., Cincinnati.

The authors are to be commended for a concise report which clearly defines the high temperature strength properties of the binary zirconium-base alloys studied. The preparation of high alloy zirconium-base compositions of satisfactory uniformity is a difficult problem as is their testing at temperature levels at which zirconium is highly reactive with air. The authors report no contamination of their alloys by oxygen, nitrogen, or hydrogen, as a result of hot working in air, but one wonders if surface effects (oxidation) could have had an effect on the work properties of these alloys (described in Table I). In further work of this type there might be some merit to hot working under an inert atmosphere. In their widely distributed film on the hot forging of molybdenum, the Knolls Research Laboratory of the General Electric Company has demonstrated the value of this means of processing reactive metals.

The higher strength of the 4.4% tungsten alloys in comparison to the 8.1% tungsten alloy at 1800 °F is certainly interesting, and one wonders at what tungsten content below 4.4% that maximum strength might be achieved. From a thermal neutron absorption cross section viewpoint, tungsten is one of the least desirable materials for reactor applications; however, zirconium alloys containing columbium additions for strength above 1800 °F might also be strengthened appreciably at temperatures below 1800 °F by the addition of only 1 or 2% tungsten.

The main use of zirconium and its alloys at the present time is in the

[4] R. F. Domagala, D. J. McPherson and M. Hansen, "Systems Zirconium-Molybdenum and Zirconium-Wolfram," *Journal of Metals*, Vol. 5, January 1953; *Transactions*, American Institute of Mining and Metallurgical Engineers, Vol. 197, 1953, p. 73.

[5] R. F. Domagala, D. J. McPherson and M. Hansen, "System Zirconium-Chromium," *Journal of Metals*, Vol. 5, Sec. 2, February 1953; *Transactions*, American Institute of Mining and Metallurgical Engineers, Vol. 197, 1953, p. 279.

atomic energy field because of the excellent nuclear properties of this element for reactor applications. Of the alloys studied in this paper, those containing columbium are of the most interest for this purpose since next to zirconium, columbium possesses the best nuclear properties of the addition elements studied. It is unfortunate that the authors were unable to carry their strength evaluation studies of these columbium-containing alloys to compositions above 20%. From the hardness data presented for these alloys in Table I (to 40% columbium) and from the short time tensile strength data presented graphically in Fig. 2 for alloys containing up to 30% columbium, one might expect that alloys containing up to 30% columbium might be as good as 8% tungsten alloy or even better especially in the high temperature range.

The poor workability reported for the 30% columbium alloy is surprising since B. A. Rogers and D. F. Atkins of Iowa State College in their investigation of the zirconium-columbium phase diagram (Document ISC 500) report that alloys containing 20 to 30% columbium can be readily fabricated hot or cold. As a matter of fact, they report that the 20 to 30% columbium alloys are more readily workable than the 10 to 20% compositions which in the BMI investigations were found to have fair to excellent workability properties at 1850 and 2200 °F.

Although the high temperature strength of these alloys is not as high as those of type 310 stainless steel and Inconel, it does appear that alloys of adequate high strength may be obtained for some high temperature structural applications where zirconium is a preferred element. It is probable that further work using the excellent techniques developed by the authors may well result in the development of alloys more closely competitive with 310 stainless steel and Inconel.

Authors' Reply

The authors thank Dr. Keeler and Mr. McGurty for their very interesting and very pertinent comments. As Dr. Keeler points out for the chromium, molybdenum, and tungsten alloys, the rate of strengthening with added alloying element is greater with smaller solubility values. In regard to the zirconium-columbium alloys, the constitution diagram[6] shows that at 2000 and 2200 °F (1095 and 1205 °C), there is complete solid solubility. In the present work, the rate of hardening with added columbium is lower than with chromium, molybdenum, or tungsten and Dr. Keeler's observations are, consequently, further confirmed. The zirconium-vanadium constitution diagram[7] shows that the solubility of vanadium in zirconium falls between the solubilities of chromium and molybdenum in zirconium. However, only two zirconium-vanadium alloys were tested for strength. Both of these alloys contained a considerable excess of vanadium from the standpoint of solid solubility and both were very weak at 2200 °F (1205 °C). Further testing would be necessary to correlate strength data with solid solubility in the case of the zirconium-vanadium alloys.

The authors agree with Mr. McGurty that it would be desirable to hot work the zirconium-base alloys in an inert atmosphere. With regard to ternary zirconium-base alloys, none were investigated. Certainly, zirconium-columbium-tungsten alloys should be examined in any future work in this field. The differ-

[6] Rogers, B. A., and Atkins, D. F., "Zirconium-Columbium Diagram," Report ISC-500, Ames Laboratory, Iowa State College, June 29, 1954.

[7] Williams, J. T., "The Vanadium-Zirconium Alloy System," Report ISC-491, Ames Laboratory, Iowa State College, June 15, 1954.

ence in workability of the zirconium-columbium alloys observed in the present study and that observed by B. A. Rogers and D. F. Atkins may be ascribable to several causes. In recent work with columbium-base alloys, the authors have found that the purity of the columbium affects the workability very markedly. Rogers and Atkins used wrought columbium sheet for their alloys, while the authors used both sheet and partially sintered bar. The presumed lesser purity of the partially sintered bar may have rendered the alloys less workable. Also, Rogers and Atkins hot swaged jacketed alloys only, while in the present work all alloys were hot rolled unjacketed. In the case of the 10–20 w/o columbium-zirconium alloys, which Rogers and Atkins found somewhat less workable than the higher columbium alloys, it must be remembered that in the present work the alloys were rolled in the gamma field, or at considerably higher temperatures than those employed by Rogers and Atkins, where no two-phase field would be encountered.

THE INFLUENCE OF CHEMICAL COMPOSITION ON THE MACHINABILITY OF REPHOSPHORIZED OPEN HEARTH SCREW STEEL

By E. J. Paliwoda

Abstract

Uniformity of machining quality is particularly important in steels which are subjected to mass production in automatic screw machines. Minor differences in chemical composition appear to be responsible for appreciable machinability variations. Modified tool life tests indicate that increased carbon and silicon contents are markedly detrimental to the cutting quality of C-1213 steels. The machinability advantages of sulphur depend on both the nature of the sulphide inclusions and the amount present. As in Bessemer screw stock, oval sulphides are desirable for maximum machinability and the formation of this type of sulphide is favored by low carbon and silicon contents.

Results were not conclusive regarding the significance of manganese, phosphorus and nitrogen differences. It is possible, however, that tool life tests do not accurately define the principal machinability benefits derived from nitrogen and phosphorus.

The machining quality of a number of C-1213 steels evaluated in automatic screw machines was calculated in terms of the effects of carbon, silicon and sulphur observed in laboratory tests. The correlation between calculated ratings and automatic screw machine performance suggests that carbon, silicon and sulphur contents can be employed as an approximation of machinability and that improved uniformity may be realized through strict control of these elements.

Introduction

PRODUCTION of rephosphorized open hearth screw steels has increased substantially during recent years. These steels are generally similar in chemical composition to standard Bessemer grades, although some producers have modified the base analyses in order to improve other metallurgical characteristics (1).[1] Adjustment of phosphorus and nitrogen contents, for example, may be utilized to ob-

[1] The figures appearing in parentheses pertain to the references appended to this paper.

A paper presented before the Thirty-sixth Annual Convention of the Society, held in Chicago, November 1 to 5, 1954. The author, E. J. Paliwoda, is research engineer in the Metallurgical Research Division, Jones and Laughlin Steel Corp., Pittsburgh. Manuscript received May 10, 1954.

tain a screw steel for specialized applications in which cold working is an important consideration.

Despite the similarity in chemical composition, there appear to be some subtle differences between Bessemer and open hearth screw steels. Specifically, oxysulphide inclusions, frequently found in Bessemer, are not generally present in open-hearth screw stock. The inclusions of the latter vary from oval, bulky nonmetallics to elongated stringer-like sulphides. Differences favoring open hearth screw steel have been noted in cold working properties, case hardening response and rolling performance.

Bessemer and open hearth screw steels are subjected to mass cutting operations in automatic screw machines and the machinability problems are essentially similar. Due to the economic penalties involved in tool changes, machining uniformity as well as overall quality are of paramount interest. Data have been published regarding factors governing machinability variations within Bessemer grades (2,3,4). On the other hand, little information is available concerning the machining variations in open hearth screw stock.

In the present work, efforts were made to isolate the influence of minor differences in the amounts of common elements on the machinability of rephosphorized open hearth screw stock. Machinability measurements were made by means of special turning tests and by evaluation in automatic screw machines.

Machinability Testing Procedure

Machinability has frequently been described as the ease or satisfaction with which a material can be cut in various machining operations (5,6,7). Rate of cutting or tool life, machined finish, chip character, and power required are some of the many factors involved in the measurement of machinability.

Experience has shown that the primary considerations in the production of premium screw steels are rate of machining (tool life) and as-machined finish. The machinability test employed in this work is a modified method of ascertaining the cutting speed-tool life relationship. Briefly, moderately alloyed and comparatively soft cutting tools are used to turn screw steel at progressively increased speeds (usually 10 surface feet per minute increments). The highest speed at which two cubic inches of metal can be turned without exceeding a prescribed tool wear is termed the machinability index or rating. Specific details of the test procedure have been described previously (8).

After each test run, a 50 diameter image of the cutting tool is projected on the screen of an optical comparator as shown in Fig. 1. Extensions of the comparatively unaffected edges of the tool are employed to gage the amount of tool tip wear. Acceptable test runs are

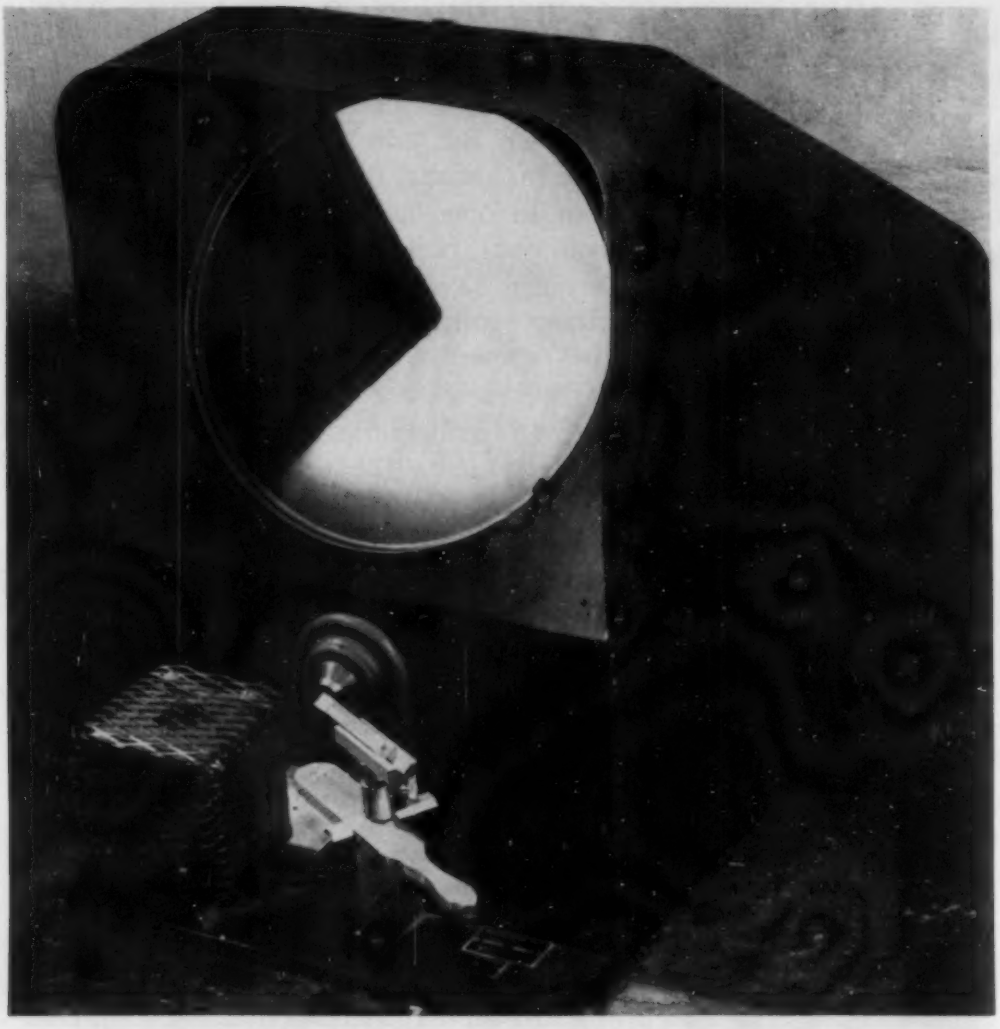


Fig. 1—Method of Determining Tool Wear. Following each turning test, a magnified image (X50) of the cutting tool is projected on the screen of an optical comparator. Extensions of the relatively unaffected edges of the test tool are employed to gage tool tip wear. The highest speed of turning two cubic inches of metal that produces a 1/16 inch or less tool tip wear is termed the machinability rating or index.

obtained when $\frac{1}{16}$-inch or less tool tip wear is noted on the projected profile. The machinability rating or index is expressed as turning speed in surface feet per minute calculated on the basis of the final diameter of the bar.

The Effect of Various Elements on Cutting Quality

Machinability ratings were obtained on a series of 27 experimental and production heats which represented a wide range of chemical compositions as shown in Table I.

Multiple correlation methods were employed in an attempt to isolate the effects of minor variations of the common elements on the machinability rating. These findings indicated that carbon, silicon and sulphur variations are particularly significant. The combined influence

Table I
Chemical Composition and Machinability Data *

Sample No.	Chemical Composition						Machinability Index—S.F.M.
	C	Mn	P	S	Si	N	
1	0.08	0.95	0.09	0.31	0.02	0.009	100
2	0.09	0.81	0.10	0.36	0.02	0.007	90
3	0.08	0.90	0.10	0.28	0.01	0.006	130
4	0.11	0.93	0.08	0.30	0.01	0.007	90
5	0.09	0.82	0.09	0.37	0.01	0.008	120
6	0.10	0.79	0.10	0.38	0.01	0.008	120
7	0.14	0.93	0.11	0.28	0.01	0.012	70
8	0.07	1.06	0.14	0.24	0.01	0.014	105**
9	0.09	0.80	0.10	0.35	0.02	0.007	80
10	0.08	0.83	0.09	0.33	0.03	0.007	80
11	0.09	0.81	0.10	0.35	0.01	0.008	120
12	0.09	0.82	0.10	0.29	0.04	0.012	below 50
13	0.08	0.94	0.09	0.32	0.01	0.006	100
14	0.13	0.88	0.07	0.25	0.01	0.006	80
15	0.11	0.87	0.08	0.26	0.01	0.009	90
16	0.11	0.86	0.09	0.31	0.01	0.006	80
17	0.10	0.91	0.08	0.26	0.01	0.006	90
18	0.12	0.86	0.09	0.30	0.01	0.008	80
19	0.12	0.86	0.09	0.29	0.02	0.008	70
20	0.08	0.78	0.10	0.32	0.01	0.007	120
21	0.08	0.81	0.10	0.33	0.01	0.007	120
22	0.12	0.94	0.09	0.28	0.02	0.012	65**
23	0.09	0.79	0.11	0.35	0.01	0.007	120
24	0.13	0.92	0.08	0.28	0.01	0.007	80
25	0.12	0.80	0.11	0.29	0.02	0.011	80
26	0.13	0.95	0.11	0.28	0.01	0.011	70
27	0.09	0.93	0.10	0.34	0.01	0.010	110

*All steels were 1 to 1.5 inch cold drawn rounds.
**Average of two tests.

of these elements will be discussed later in the report. For purposes of clarity, observations regarding each of the elements will be treated separately.

Carbon

The relationship between carbon content and machinability ratings of rephosphorized open hearth screw steels containing 0.01% silicon is shown in Fig. 2. The least squares correlation indicates that an 0.01% increase in carbon is equivalent to a loss of about 8 index points. The standard deviation for the relationship is approximately ± 10 index points. In this investigation, steels containing high carbon contents generally exhibited stringer-like sulphides, while the non-metallics in low carbon material were usually oval, bulky sulphides (Fig. 3). A similar observation has been made in Bessemer screw stock (9).

Silicon

As a rule, the action of silicon in C-1213 steels parallels that noted in Bessemer screw stock (3,10). Fig. 4 illustrates the marked detrimental effect of increased silicon on the cutting quality of open hearth screw steels containing 0.08 to 0.09% carbon. An increase of 0.01% silicon is accompanied by a loss of about 20 index points. Steels with relatively high silicon contents contained stringer-like sulphides (Fig. 5). Exceptions to the effect of silicon on inclusions and ma-

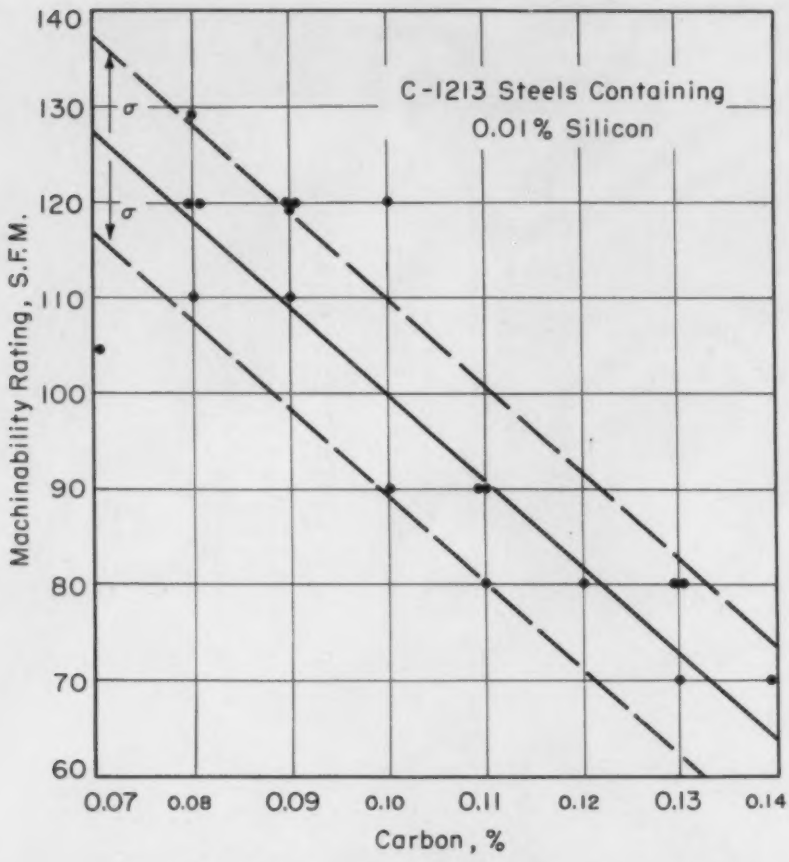


Fig. 2—The Influence of Carbon Content on the Machinability Ratings of C-1213 Steels. It can be noted that for C-1213 steels containing 0.01% silicon, an increase of 0.01% carbon is equivalent to a machinability loss of about 8 index points.

chinability similar to those observed in Bessemer steels were not encountered in this group of steels (4).

Sulphur

The influence of sulphur in rephosphorized open-hearth screw steels is illustrated in Fig. 6. This correlation is based on the effect of sulphur on the machinability rating of a series of steels containing 0.01% silicon. The ordinate, in this instance, represents the deviation from the least squares correlation between carbon content and machinability shown in Fig. 2. The deviation is the difference between the actual machinability index and the average value expected from the carbon content. An increase of 0.01% sulphur is equivalent to a machinability rating change of + 1.5 index points. It is interesting to note that machinability tests, in the past, indicated a 20 index point difference between B-1112 and B-1113 steels or that an 0.01% increase in sulphur resulted in a gain of about 2 index points.

From the standpoint of machinability, both the total sulphur content and the sulphide inclusion nature are important factors. As in

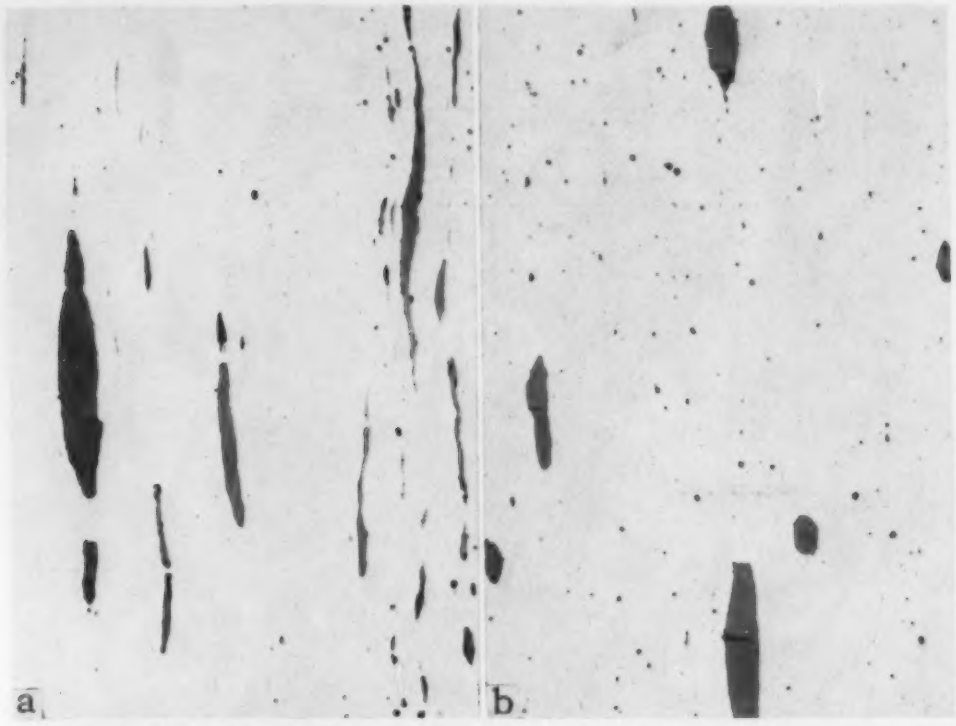


Fig. 3—The Effect of Carbon Content on Sulphide Inclusion Nature. X 200. (a) 0.14% carbon-0.01% silicon. (b) 0.07% carbon-0.01% silicon. In this work, steels containing higher carbon contents generally exhibited more elongated sulphide inclusions. Low carbon material possessed oval, bulky sulphides.

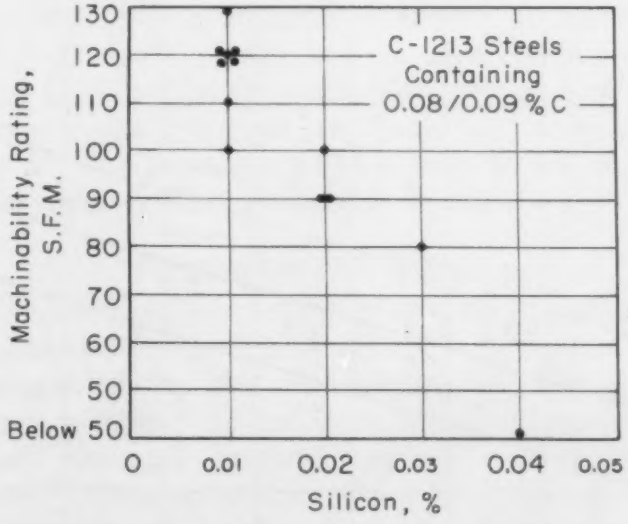


Fig. 4—Machinability Ratings Versus Silicon Contents for C-1213 Steels Containing 0.08 to 0.09% Carbon. Increased silicon is markedly detrimental to the cutting quality of C-1213 steels with an 0.01% increase resulting in average loss of 20 surface feet per minute in the machinability rating.

Bessemer steels (10), oval rather than stringer-like sulphides are desirable. Oval inclusions are associated with low silicon and carbon contents. Since these elements are strong deoxidizers in screw steel, it

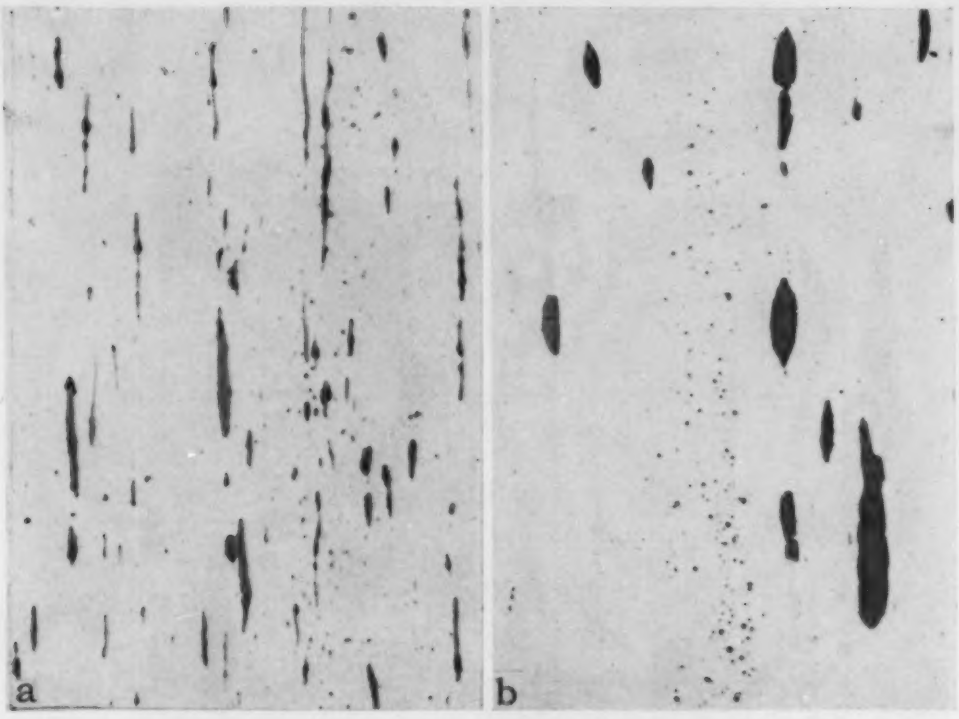


Fig. 5—The Influence of Silicon on Sulphides in C-1213 Steels. X 200. (a) 0.09% carbon-0.04% silicon. (b) 0.08% carbon-0.01% silicon. Increased silicon contents appear to favor the formation of stringer-like sulphides. These observations are similar to those made by Van Vlack (10) and Boulger, Moorhead and Garvey (4).

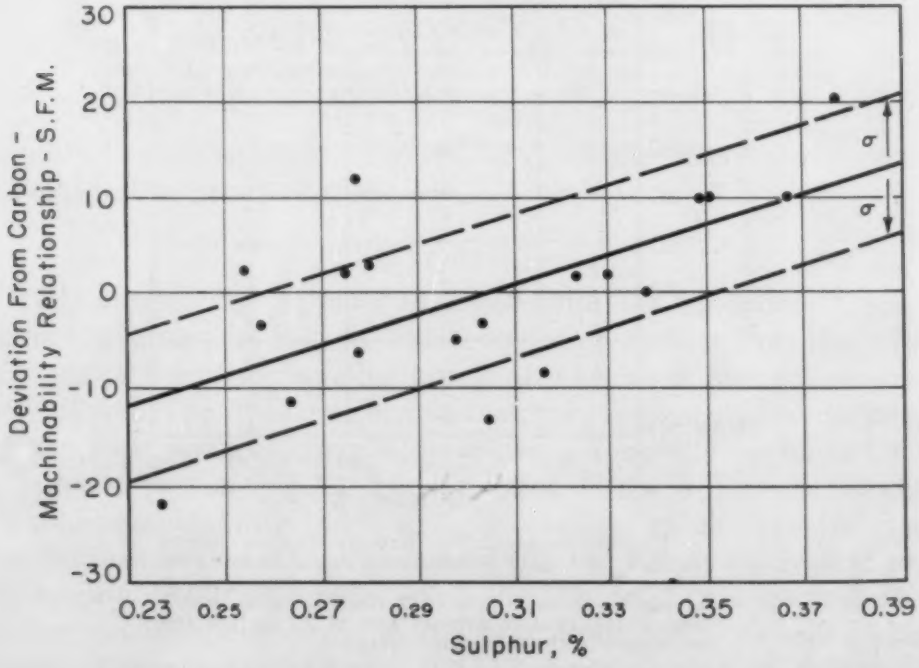


Fig. 6—The Influence of Sulphur Variations on the Machinability of Rephosphorized Open Hearth Screw Steels. The ordinate represents the deviation from the least squares relationship between carbon content and machinability shown in Fig. 2. A difference of 0.10% sulphur is equivalent to 15 index points which compares favorably with the 20 point difference in average machinability ratings of B-1112 and B-1113 grades.

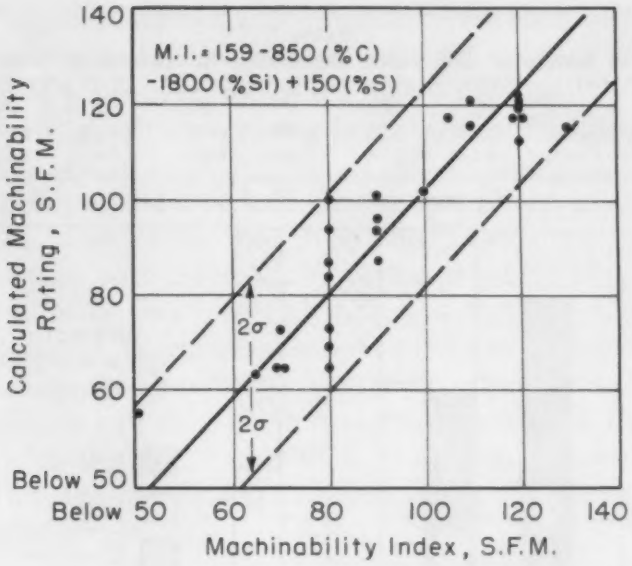


Fig. 7—Calculated Versus Actual Machinability Ratings. It can be observed that machinability ratings of the first series of steels can be approximated in terms of the measured effects of carbon, silicon and sulphur contents.

appears logical to assume that a high state of oxidation favors the formation of oval sulphides and hence contributes to cutting quality.

Manganese

The significance of manganese variations in screw stock, either Bessemer or open hearth grades, has not been completely established. In the present work, no pronounced effect of manganese on the machinability rating was observed. It should be recognized, however, that the amount of manganese present may be an important factor in the formation of oval, bulky sulphide inclusions.

Phosphorus and Nitrogen

Variations in these elements did not appear to influence cutting quality as measured by the machinability test. Enzian observed that the effects of phosphorus and nitrogen are, to some extent, complementary in contributing to the work-embrittlement of steel (11). These elements may act to promote "cleaner" cutting with its inherent advantages to finish, chip characteristics and dimensional accuracy. Simple turning tests may not accurately define the benefits derived from nitrogen and phosphorus. Past experience has indicated that the 0.090% minimum phosphorus limit stipulated by Graham is important in the production of premium free-cutting steels (12).

Further Studies of Carbon, Silicon and Sulphur

By means of multiple correlation analysis, it was possible to determine the effects of carbon, silicon and sulphur variations on the

Table II
Composition Range of the Steels Evaluated in Automatic Screw Machines

	C	Mn	P	S	Si	N
Minimum	0.06	0.68	0.08	0.24	Trace	0.005
Maximum	0.14	1.16	0.13	0.44	0.03	0.021

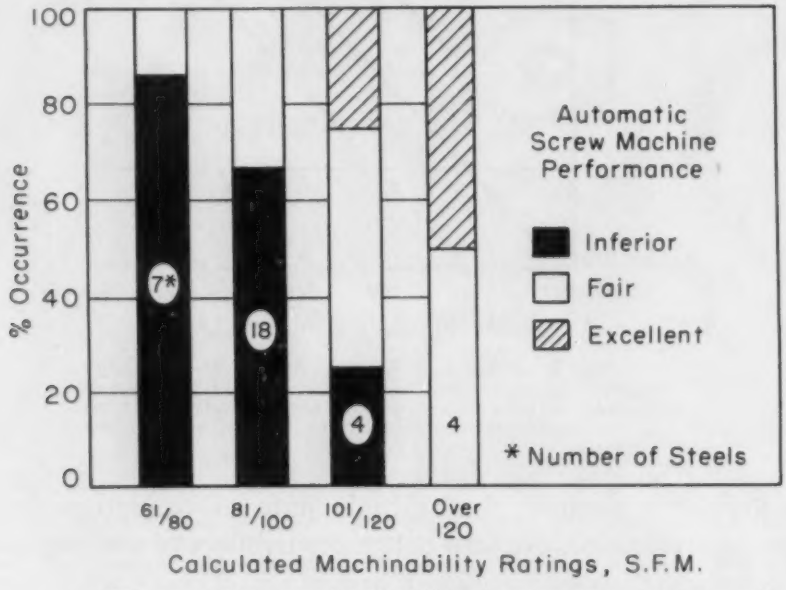


Fig. 8—Calculated Machinability Ratings Versus Automatic Screw Machine Performance. The correlation suggests that carbon, silicon and sulphur contents can be used as an approximation of the machining quality of C-1213 steels.

machinability ratings of all steels tested. The mathematical expression is as follows;

$$\text{Machinability Index} = 159 - 850(\%C) - 1800(\%Si) + 150(\%S)$$

The correlation between actual and calculated ratings for the first series of steels (1 to 1.5 inch cold drawn rounds) is shown in Fig. 7. The standard deviation of the relationship is approximately 11 index points which indicates that about 95% of the calculated ratings should fall within limits of $\pm$ 22 index points of the actual rating. It can be noted that carbon, silicon and sulphur contents may be used as an approximation of the machinability rating of cold drawn C-1213 material.

During the course of the investigation, thirty-three free cutting steels were evaluated in commercial cutting operations in automatic screw machines. The steels were rated as inferior, fair, or excellent in terms of tool life and/or as-machined finish. Table II contains the composition limits for this material.

The steels involved were not of a bar size suitable for machinability testing, and a comparison was made between calculated machinability ratings based on the measured effects of carbon, silicon and sulphur

and automatic screw machine performance. The relationship is shown in Fig. 8. It can be noted that carbon, silicon and sulphur contents may be employed as an approximation of the machining quality. In addition, improved machining uniformity may be realized through close control of these elements.

One exception to the effect of silicon was observed in this phase of the work. One steel termed fair in an automatic screw machine contained 0.03% silicon with a resultant calculated rating of 65. Metallographic examination of this material indicated that the silicon did not promote formation of undesirable thin stringer-like sulphides. Boulger, Moorhead and Garvey found that Bessemer screw steels with higher than normal silicon contents machined satisfactorily if the steels exhibited oval sulphides (4). A similar condition probably exists in C-1213 steels, but further data are needed since only one exception was observed in sixty steels.

Summary

In C-1213 steels, carbon and silicon exert a pronounced influence on cutting quality. Increased carbon and silicon contents are markedly detrimental to machinability, as measured by tool life tests, and favor formation of elongated sulphide inclusions. Higher sulphur contents have a mild beneficial effect on machining performance of rephosphorized open-hearth screw stock. The principal machinability advantages of sulphur may be determined by the nature of the sulphide inclusions. As in Bessemer screw steels, oval inclusions appear desirable.

Minor variations in manganese, phosphorus and nitrogen contents did not appear to influence cutting quality as measured by tool life tests.

An expression based on the effects of carbon, silicon and sulphur was developed as an approximation of the machinability rating of cold drawn C-1213 steels. A relationship was noted between calculated machinability ratings and automatic screw machine performance which suggests that these elements can be employed as a gage of the machining quality. Within practical limits, control of carbon, silicon and sulphur contents appears to be an effective means of improving the machining uniformity of rephosphorized open-hearth screw steel.

References

1. S. Feigenbaum, "Open Hearth Screw Steels Replacing Bessemer," *Journal of Metals,* Vol. 5, No. 6, June 1953, p. 796.
2. H. W. Graham, "What the User Should Know About Free-Cutting Steels," *Iron Age,* Vol. 131, No. 23, June 8, 1933, p. 303.
3. S. L. Case, U. S. Patent No. 2,485,358 (October 18, 1949).
4. F. W. Boulger, H. A. Moorhead and T. M. Garvey, "Superior Machinability of MX Explained," *Iron Age,* Vol. 167, No. 20, May 17, 1951.
5. O. W. Boston, "Machinability of Steel," ASM Handbook, 1948, p. 360.

6. N. E. Woldman and R. C. Gibbons, *Machinability and Machining of Metals,* 1951, p. 1, McGraw-Hill Book Company Inc.
7. F. W. Boulger, "Materials and Machinability," 1950, MACHINING-THEORY AND PRACTICE, 1950, p. 69, American Society for Metals.
8. A. C. Cruickshank, U. S. Patent No. 2,269,360 (Jan. 6, 1942).
9. F. T. Kent, "E Steel," *Iron Age,* Vol. 165, No. 5, Feb. 2, 1950, p. 79.
10. L. H. Van Vlack, "Correlation of Machinability with Inclusion Characteristics in Resulphurized Bessemer Steels," TRANSACTIONS, American Society for Metals, Vol. 45, 1953, p. 741.
11. G. H. Enzian, "Some Effects of Phosphorus and Nitrogen on the Properties of Low Carbon Steel," *Journal of Metals,* Feb. 1950, p. 346.
12. H. W. Graham, "Machinability from the Viewpoint of Metal Being Cut," *Machinability of Metals Symposium,* Pittsburgh Chapter ASM, April 29, 1938.

DISCUSSION

Written Discussion: By R. F. Harvey, Chief Metallurgist, Brown and Sharpe Mfg. Co., Providence, R. I.

The author is to be commended for a comprehensive investigation of the machining characteristics of 27 different compositions of screw stock. The many recent efforts of steel suppliers to improve the machinability of screw stock should result in advantages to users in increased production, longer tool life and better finishes.

The author concludes that steels having oval or thick inclusions were better machining than long, stringer type sulphides. L. H. Van Vlack and other investigators have also reported this. In recent years there has been somewhat of a trend towards lower carbon screw stock and the author reports that decreased carbon favors the formation of the more desirable oval or globular inclusions.

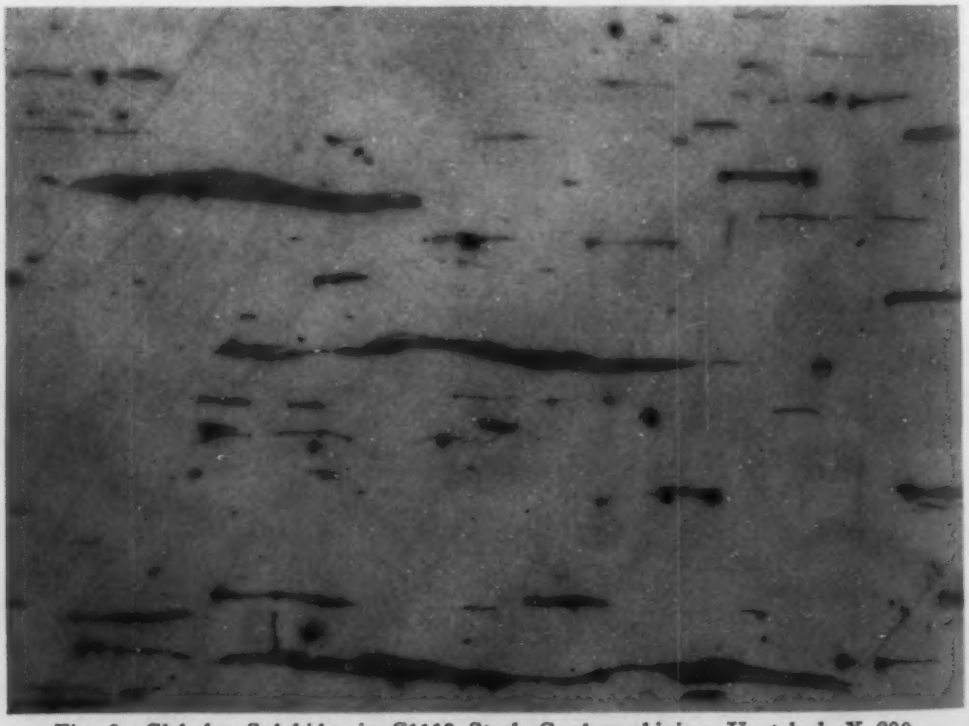


Fig. 9—Globular Sulphides in C1119 Steel. Good machining. Unetched. X 200.

We have found that this is not always true, at least not in the presence of higher manganese. For example, C 1119 steel, higher in carbon than any of the compositions listed in Table I of the author's paper, was observed to have thick, globular inclusions. These characteristics of sulphides, found to impart good machining qualities to C 1119 steel, are illustrated in Fig. 9. This tends to substantiate the observations of the author and others that thick sulphides are desirable but also indicates the need for a more detailed investigation into the influence of carbon.

The C1119 steel was found to turn at higher surface speeds than B1113 or C1213. A limited amount of testing done on screw machine parts also indicates better machinability for C1119 steel than the standard nonleaded screw stocks. While these results are insufficient to be considered other than indicative, it does appear that the standard machinability ratings based on turning B1113 or C1213 and C1119 should be reviewed.

In view of the increased popularity of leaded screw stock it would be of interest to know how this type compares with other screw stocks reported. While leaded C1119 has not been made insofar as it is known, there are indications that such a grade may have very excellent cutting qualities.

Authors' Reply

The author wishes to express his appreciation to Mr. Harvey for his discussion. The observation that C-1119 material can be turned at faster rates than B-1113 or C-1213 stock is interesting. In a limited number of tool life tests, we have encountered a somewhat similar condition in which cutting rates for several C-1117 heats were higher than expected and approached those for C-1213 steel. It seems likely that established turning rates for low phosphorus screw steels could well be reviewed in the light of changes in steelmaking practices during the past few years. For example, furnace blocking with silicon has been eliminated in the production of C-1100 series steels at Jones and Laughlin; this has resulted in an overall improvement in the quality of these grades.[2]

It appears difficult, at present, to evaluate the significance of sulphide inclusion differences between grades, since other variables such as chemical composition may also be important. Sulphide inclusions of the type shown in Figs. 3b and 5b are not usually found in C-1119 or other similar grades. This is consistent with the observed trend between carbon content and sulphide nature of rephosphorized open hearth screw stock.

[2] J. H. Flaherty, "Quality Control in the Production of High Sulpher Steels," *Open Hearth Proceedings*, Vol. 36, 1953, pp. 13–19.

THE INFLUENCE OF THE GRINDING PROCESS ON THE STRUCTURE OF HARDENED STEEL

By Walter E. Littmann and John Wulff

Abstract

The temperature distribution within hardened SAE 52100 steel has been measured, using a thermocouple formed by welding a constantan wire to the bottom of a hole which extends nearly to the ground surface. The observed temperature history within ground samples was correlated with structural changes and with the energy expended in grinding. The heating rates in grinding were reproduced by electrical heating of thin strips to determine the peak temperature required to form a rehardened surface layer in grinding. The peak temperature required for surface rehardening in grinding is about 1550 °F (845 °C). A peak temperature of about 650 °F (345 °C) is required to cause additional tempering in a prior structure of 52100 steel hardened and tempered to Rockwell C-64.

Introduction

THE effect of the heat which is generated in the grinding process has long been a subject of interest for those who make machine parts of hardened steel. If such heat is excessive, the structure and the state of residual stress in the material beneath the ground surface can be altered to the detriment of the product.

One of the characteristics of the grinding operation is the high energy required per unit volume of metal removed. Almost all of this energy is dissipated as heat and much of it enters the work, causing a momentary rise in temperature as the grinding contact passes a given point in the work.

Several investigators (1–6)[1] have made metallographic observations of structural changes resulting from grinding and have shown that grinding damage may alter the fatigue properties of hardened steels. Their research has shown that when the steel just beneath the ground surface is heated sufficiently a thin layer may be austenitized as the grinding wheel passes. The cooler material in the bulk of the work promptly quenches and thus rehardens the austenitized layer. Beneath such a rehardened layer the steel, heated to temperatures approaching

[1] The figures appearing in parentheses pertain to the references appended to this paper.

A paper presented before the Thirty-sixth Annual Convention of the Society, held in Chicago, November 1 to 5, 1954. Of the authors, Walter E. Littmann is research metallurgical engineer, The Timken Roller Bearing Co., Canton, Ohio, and John Wulff is professor of metallurgy, Massachusetts Institute of Technology, Cambridge, Mass. Manuscript received April 6, 1954.

that required to form austenite, is tempered to a degree depending upon the peak temperatures reached. The depth to which these structural changes extend is a function of the grinding severity.

The mechanics of grinding have been studied with quantitative measurement of grinding forces (7,8,9). Outwater attempted to measure surface temperatures in grinding and compared his results with temperature calculations based on grinding forces.

Some information concerning the extent of penetration of grinding heat was obtained by Wulff (10) in the grinding of 18-8 stainless steel. Detection of ferrite by electron diffraction at various depths below the ground surface gave an indication of the penetration of plastic deformation and of the maximum temperatures reached beneath the ground surface.

Because the damage produced by grinding in hardened steel should be related to the thermal history of the steel beneath the ground surface, it seemed worthwhile to measure the temperature distribution in ground steel samples and to relate such data to corresponding structural changes.

Experimental Work

The temperature distribution in space and time was measured for points at various depths below the ground surface by placing a thermocouple at a known distance below the surface to be ground. The temperature was recorded as a function of time for each grinding pass, the thermocouple moving a known incremental distance closer to the surface with each pass until the thermocouple was ground through. The thermocouple was formed by spot welding a constantan wire (0.010-inch diameter) to the bottom of a hole which extended nearly to the surface to be ground as shown in Fig. 1. The diameter of the small hole was 0.021 or 0.026 inch, depending upon the thickness of the insulation on the wire. An iron wire was welded to the back side of the sample and was connected, with the constantan wire, to an oscilloscope which permitted the accurate recording of the extremely rapid changes in temperature within the ground samples. The horizontal sweep on the oscilloscope was synchronized with the motion of the sample, relative to the grinding wheel, so that each sweep of the spot on the oscilloscope photographed on 35-millimeter film recorded the thermocouple emf as a function of time for a point at a given depth below the ground surface.

Because the heat flow to the measuring junction was entirely by metallic conduction the observed trace of emf versus time was a true measure of the temperature history beneath the ground surface. An example of the record obtained for two successive passes of intermittent grinding is shown in Fig. 2 with a typical record obtained in continuous grinding.

The emf values were converted to temperatures by using a cali-

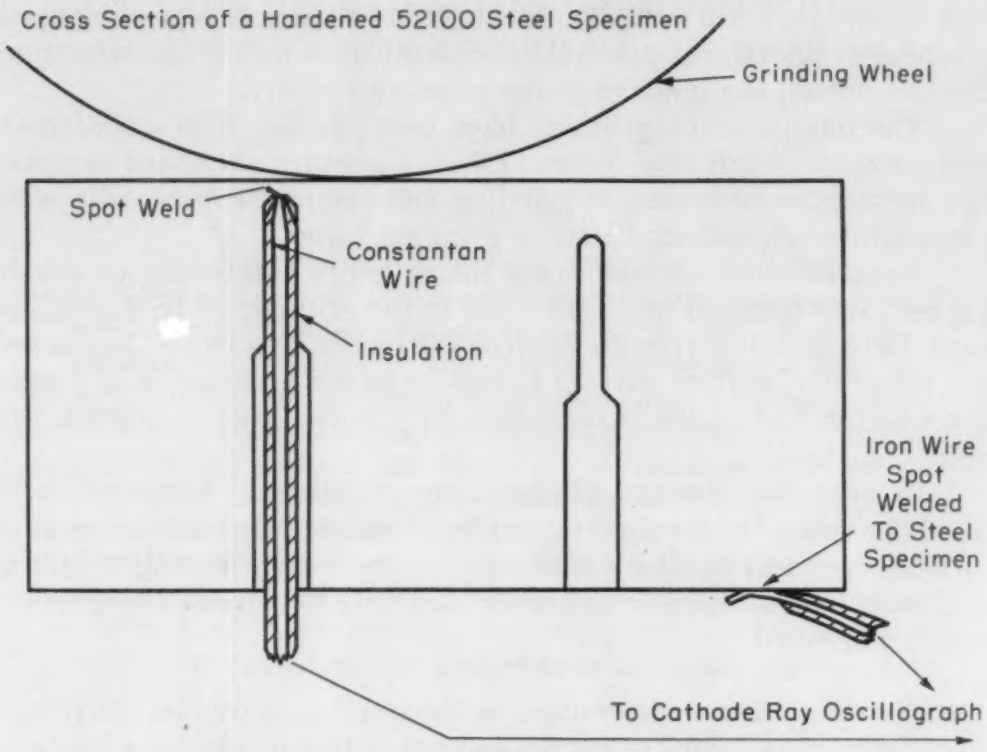


Fig. 1—A Diagrammatic Longitudinal Section of a Sample Used for Measurement of Temperatures Beneath the Ground Surface. One thermocouple is shown in the hole at the left. A second constantan wire would be welded into the hole at the right for use after grinding through the first thermocouple.

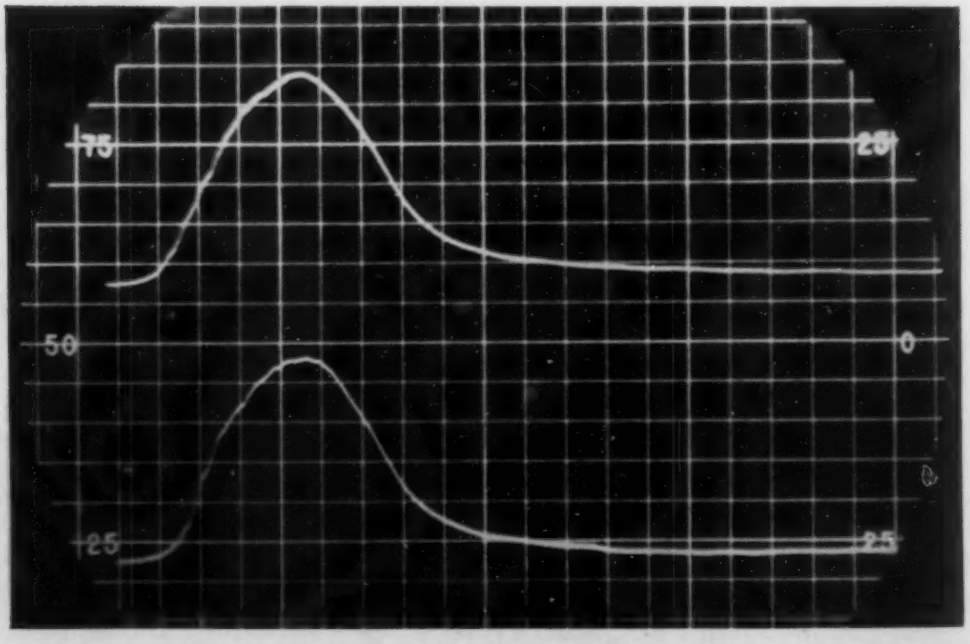


Fig. 2a—A Photograph of the Oscilloscope screen Showing the Trace of emf Versus Time for Two Successive Grinding Passes on an Intermittently Ground Sample. One division horizontally is 0.005 second; one division vertically is 5 millivolts. The work speed was 20 fpm.

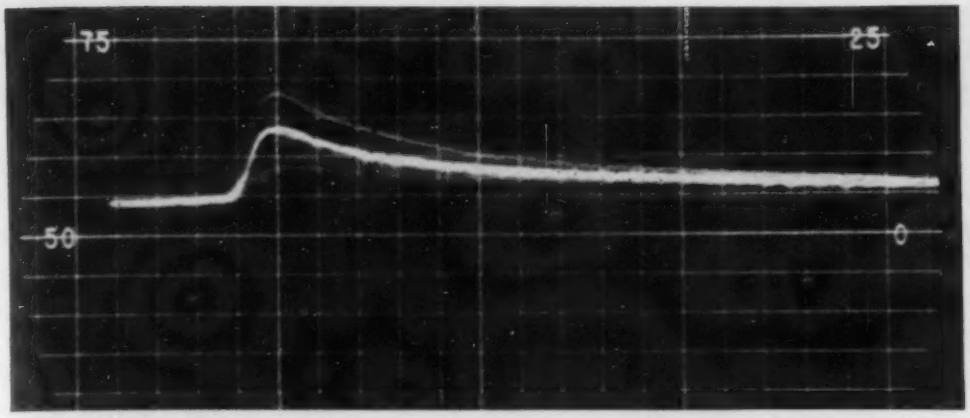


Fig. 2b—A Similar Photograph for a Continuously Ground Sample. One division horizontally is 0.00083 second; one division vertically is 0.45 millivolts. The work speed was 250 fpm. The traces for several revolutions of the work are superimposed in the photograph.

bration curve which was determined experimentally for the hardened 52100 steel-constantan thermocouple. This curve was similar to the standard (I.C.) iron-constantan curve but displaced from it by 50 °F or less.

Samples for intermittent grinding $\frac{7}{16}$ by $\frac{1}{2}$ inches in cross section and of various lengths were machined from $\frac{3}{4}$-inch square bars of annealed AISI 52100 steel. The samples for continuous grinding were short cylinders, $1\frac{1}{4}$ inches high, $4\frac{3}{4}$ inches O.D. with a $\frac{3}{8}$ inch wall thickness. Before hardening, holes for the thermocouples were drilled in all specimens. Each hole was shorter than the one preceding it. Thus, as soon as one thermocouple was ground through, the next was used, etc.

The samples were austenitized at 1550 °F (845 °C) for one hour, oil-quenched, and tempered one hour at 300 °F (150 °C) to give a hardness of Rockwell C-64. After hardening, the bottoms of the holes were cleaned and the thermocouple welds were made. By gaging the depth of each hole before making the welds, the distances of the measuring junctions below the ground surface were always known.

The intermittent grinding was carried out on a reciprocating table surface grinder so that the grinding direction coincided with the long dimension of the sample. The continuous grinding was done on a 6-inch rotary surface grinder, the grinding wheel being in continuous contact with the cylindrical specimen. In the latter case, the downfeed was driven at a constant rate by a low speed electric motor; in the former, the downfeed was made manually at the end of each pass when the wheel was out of contact with the work.

In all cases, the grinding wheel was $\frac{1}{2}$ inch wide, 6 to 7 inches in diameter and was rotated at a speed which maintained the peripheral speed between 5500 to 6500 fpm. The wheel face in all cases was wide enough to overlap the work width and no crossfeed was used.

The grinding wheel was dressed by passing a pyramidal diamond across the face of the wheel at a constant speed, feeding the wheel down

0.001 inch after each crossfeed of the diamond. Thus, a reproducible dress was obtained, but it should be noted that for a given wheel specification the condition of the wheel was influenced by the grinding conditions as well as the dress.

The principal variables used to control the severity of grinding were: (a) the abrasive used, aluminum oxide or silicon carbide, (b) the downfeed per pass or per revolution designated as d, in inches, and (c) the work speed, v, in feet per minute.

Force measurements were made for the same grinding conditions under which temperature measurements were made to permit correlation of grinding energies with temperature distributions. The force measurements were made, using strain gage dynamometers in the Metal Cutting Laboratory at the Massachusetts Institute of Technology.

The structural changes resulting from grinding heat were evaluated by examining taper sections of the ground samples, using the optical microscope and by making microhardness traverses on the same taper sections. A Reichert microhardness tester was employed, using a 20-gram load with a Vickers type diamond indenter.

In order to obtain a quantitative relationship between the temperature distribution and changes in structure, it was necessary to grind several samples under reproducibly severe conditions. The resulting gradient in structure was gradual enough so that microhardness measurements made on taper sections were not in error because of the hardness of underlying material. The grinding conditions used for specific samples referred to in this paper are given in Table I. Sample G-19 showed perceptible tempering to a depth of 0.015 inch with a hardness gradient gradual enough to permit an accurate evaluation of the degree of tempering as a function of depth except for the region 0.0005 inch or less below the ground surface.

Even under the very severe grinding conditions of sample G-19, the depth of the rehardened layer was only 0.0001 inch. For very small values of depth below the ground surface, the thermocouple results become less accurate; therefore, an indirect method was used to confirm the peak temperature required to form austenite under the

Table I
Grinding Conditions For Several Intermittently Ground Samples

Sample No.	Wheel* Specification	Peripheral Wheel Speed V Ft./Min.	Work Speed v Ft./Min.	Downfeed d In./Pass	Coolant
G-12	38A60H8VG	6500	60	0.001	Soluble Oil
M-1	38A60H8VG	6000	60	0.0005	Soluble Oil
G-19	37C36P5V	5700	15	0.0005	Soluble Oil

*38A indicates aluminum oxide abrasive
37C indicates silicon carbide abrasive

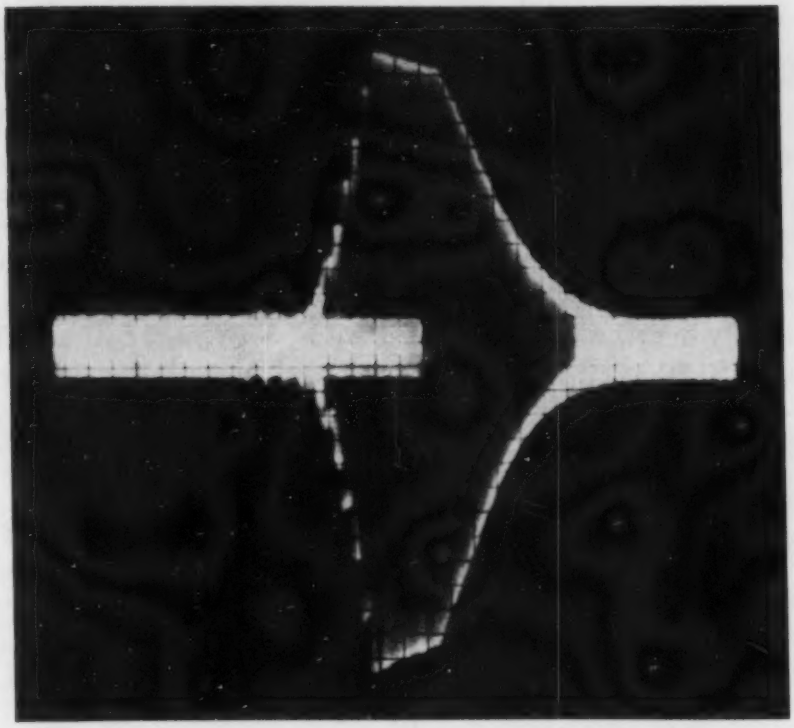


Fig. 3—A Photograph of the Oscilloscope Trace Obtained From the Lead Sulphide Cell in the Rapid Heating of a Thin Strip of Steel by Passage of Electric Current. The horizontal sweep of the pattern represents about one-half second and the vertical amplitude is proportional to the temperature at any time.

conditions of grinding. The rapid heating rates of grinding were reproduced by heating strips of hardened 52100 steel $\frac{3}{8}$ inch wide, 0.007 inch thick, and about 2 inches long by passage of electric current. This was done by clamping the strips between the electrodes of a spot welder in an evacuated chamber and using the welding cycle controller to regulate the duration of the current pulse and to turn on a hydrogen quench immediately after shutting off the electric current. The temperature history of the heated portion of the strip was recorded by sighting an infra-red sensitive lead sulphide cell on the strip and photographing the oscilloscope which was connected to the cell output. The use of the lead sulphide cell to measure rapidly changing temperatures produced in this fashion has been described in a paper by Huggins, Roll, and Udin (11).[2]

A series of thin strips were thus heated to peak temperatures from 1350 to 1650 °F (730 to 900 °C) and a record of the heating and cooling obtained from each. A typical photograph of the oscilloscope trace obtained for one of these samples is shown in Fig. 3. The calibration between the cell signal and temperature is not linear, but the shape of the actual heating and cooling curve is quite similar to the trace shown.

[2] The equipment described in Reference 11 was used for this phase of the investigation and Robert A. Huggins assisted in obtaining the data on the thin strips heated electrically.

Discussion of Results

The results obtained from the electrically heated strips are reported in Table II which shows the peak temperature reached for each specimen. The heating rates obtained are shown with the resulting structural changes as indicated by microhardness measurements and metallographic observations. The results show that for heating rates of the order of 11,000 °F per second, austenite appears between 1510 and 1540 °F (820 and 840 °C) and a completely rehardened structure is obtained when the peak temperature is between 1540 and 1560 °F (840 and 850 °C). Heating rates measured beneath the surfaces being

Table II
Results from Electrical Heating

Sample No.	Peak Temperature °F	Heating Rate °F/Second	Hardness Kg/mm² (20 g Load)	Structure
S-14	1650	10,700	1150-1200	Rehardened
S-15	1560	11,000	1150-1200	Rehardened
S-20	1540	10,500	—	Partly Rehardened
S-18	1510	10,100	500-550	Tempered
S-17	1470	9,570	540-580	Tempered
S-16	1350	9,300	605-635	Tempered

ground ranged from 3×10^4 °F per second to 5×10^5 °F per second, depending on work speed and the magnitude of the peak temperatures. The heating rates in grinding decreased as the peak temperatures were approached, so that the heating rates obtained in the electrically heated strips were of the same order or somewhat lower than those in the severely ground samples.

The effect of heating rates up to 2400 °F (1315 °C) per second on the critical temperatures for several steels has been reported by Feuerstein and Smith (12). Extrapolation of their data indicates that the peak temperature required to form austenite should not exceed 1650 °F (900 °C) for a heating rate of 5×10^5 °F per second in hardened 52100 steel.

Since the time in the vicinity of the peak temperature was extremely short and the heating rates were similar for the ground samples and the electrically heated strips, it was concluded that the peak temperature of about 1550 °F (845 °C) which was required to form austenite in the electrically heated strips is the same as the peak temperature reached at the lower boundary of a rehardened zone formed in grinding.

The tempering which occurred beneath the rehardened zone in grinding and in the electrically heated samples should likewise be a function of the peak temperature reached in each case because of the very rapid heating and cooling. By comparing the hardness corresponding to several subcritical peak temperatures in the electrically heated

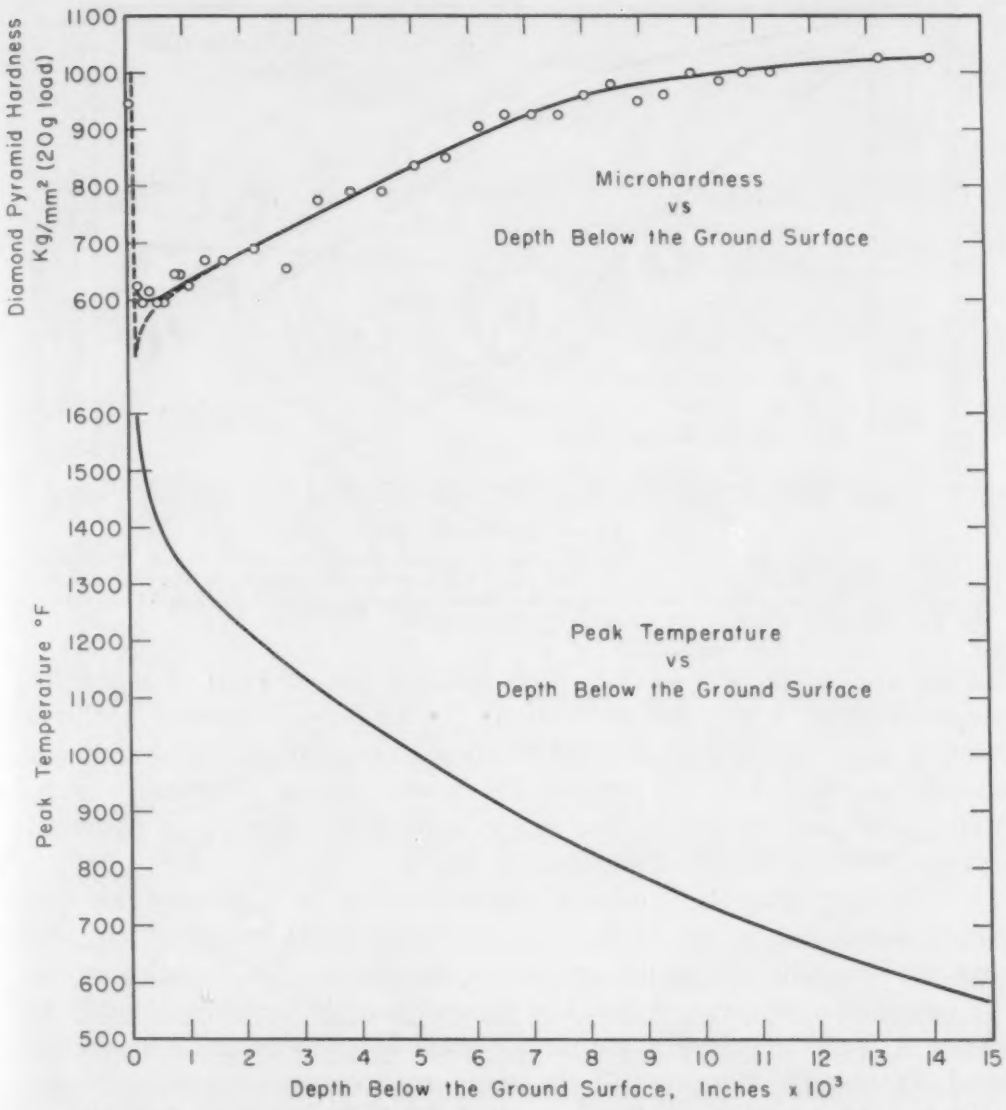


Fig. 4—Summary of Results Obtained from Sample G-19, Severely Ground. The peak temperature distribution is compared with the corresponding microhardness distribution made on a taper section of the sample after grinding. The dotted line shows the probable hardness distribution near the surface where the steep hardness gradient made values inaccurate.

samples with the microhardness variation with peak temperature in the severely ground samples a check on the accuracy of the grinding temperature measurements was obtained.

The peak temperature and microhardness are shown in Fig. 4 as a function of depth for sample G-19. By cross plotting the data of Fig. 4, the variation of hardness with peak temperature was found and is shown in Fig. 5 and the normal tempering curve for one hour at temperature is included for comparison. The hardness gradient shown in Fig. 4 is the cumulative result of about forty successive grinding passes, each pass removing 0.0005 inch of material. It should be noted that the curve of hardness versus peak temperature would be somewhat

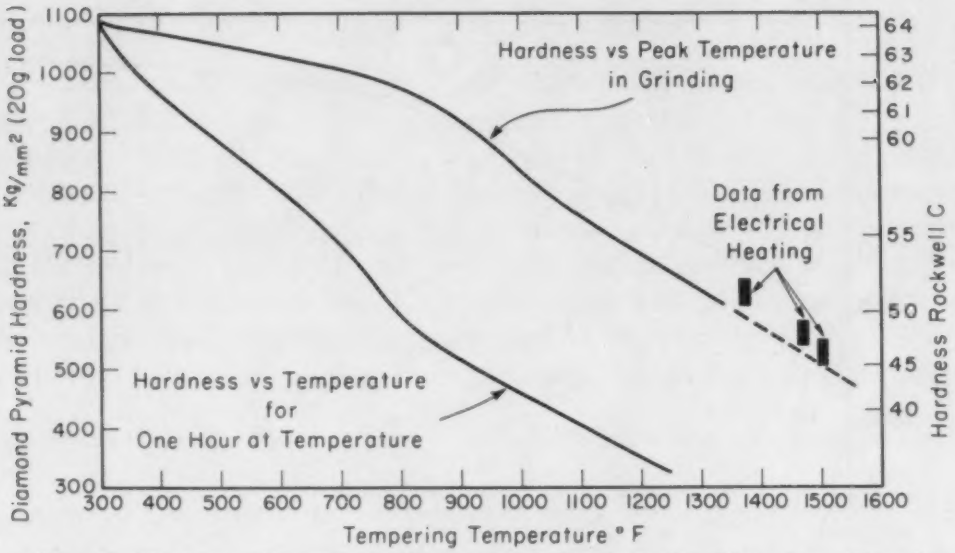


Fig. 5—Hardness Changes in Hardened 52100 Steel Resulting from Transient Grinding Heat Obtained from Fig. 4. The curve for one hour at temperature is included for comparison. The microhardness measurements were calibrated against Rockwell C hardness for the steel used to obtain the scale shown at the right.

higher for a single grinding pass because the degree of tempering shown in Fig. 4 at a given depth is the result of repeated cycles of heating and cooling with a small increase in peak temperature for each successive cycle. For this reason, the points for the electrically heated strips which are the result of a single heating and cooling lie above the extrapolation of the grinding data in Fig. 5.

The fact that the hardness corresponding to a given peak temperature reached in the electrically heated strips is in agreement with that predicted by the grinding data as shown in Fig. 5 indicates that the temperatures measured in the ground sample were reasonably accurate. When the grinding conditions were less severe, the temperature gradient became steeper and the temperature measurements became less accurate for very small values of depth below the ground surface.

An overall picture of the temperature distribution beneath the ground surface for moderately severe grinding is shown in Fig. 6. This diagram was prepared from the data for sample G-12. The diameter of the thermocouple weld area is seen to be small compared to the length of the arc of contact between wheel and work and relative to the variation of temperature in the grinding direction. Temperatures above 900 °F (480 °C) were present just beneath the surface, but could not be accurately measured. The transverse variation in temperature was appreciable at small depths below the ground surface as shown in Fig. 7 by the structural variation in that direction. For distances less than 0.001 inch below the ground surface, the recorded temperatures were somewhat lower than the actual peak temperatures because only an average temperature over the area of the measuring junction of the thermocouple was recorded.

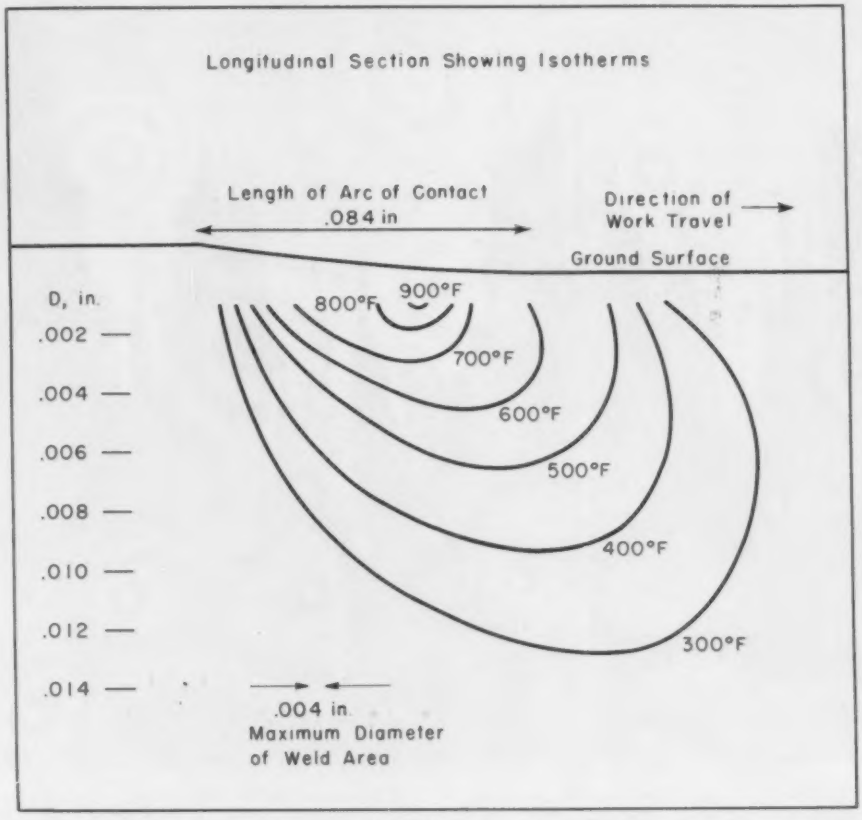


Fig. 6—The Temperature Distribution in a Longitudinal Section of Sample G-12. The work speed was 60 fpm and the downfeed was 0.001 inch at the end of each intermittent grinding pass.

For identical grinding conditions, the measured temperature distributions were reproducible within 50 °F or less. The scatter of data for a single thermocouple is shown in curve (a) of Fig. 8. For very light feed rates the condition of the grinding wheel became more critical and slight variations in dressing technique were reflected in differences in grinding forces and temperature distribution.

The data shown in Fig. 5 may be used with the knowledge of the peak temperature required to form austenite in grinding to deduce the temperature gradient in samples ground under conditions where direct measurement is impossible. In Fig. 7, for example, point (a) at the lower boundary of the rehardened region must have reached a peak temperature of 1500 to 1550 °F (815 to 845 °C). Since the prior structure of sample M-1 was 52100 hardened and tempered to Rockwell C-64, a perceptible difference in etching should be produced by a decrease in hardness beyond Rockwell C-63. From Fig. 5 it is seen that a peak temperature of 650 to 700 °F (345 to 370 °C) is required to cause tempering to Rockwell C-63 in grinding. Thus, point (b) in Fig. 7 must have reached above 700 °F (370 °C). Since (b) was about 64 x 10^{-6} inches below point (a) the average temperature gradient between (a) and (b) was 12.5 x 10^{6} °F per inch. Extrapo-

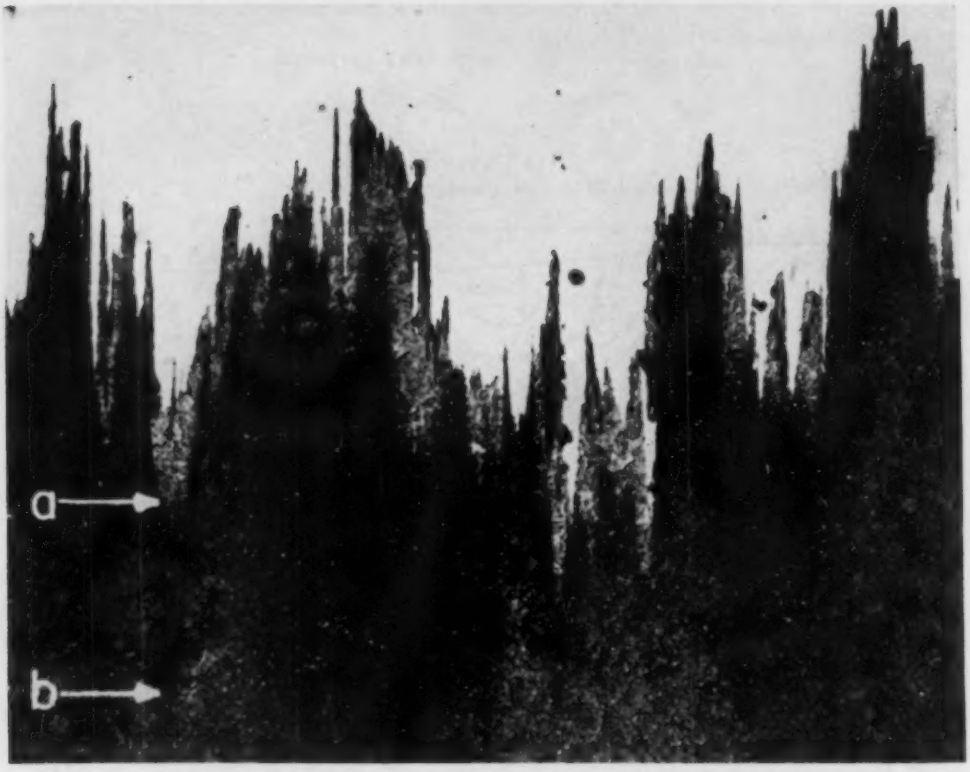


Fig. 7—A Taper Section of Sample M-1. The superficial rehardened layer appears as a light etching area just beneath the chromium plating used to preserve the surface profile. The optical magnification is X 250, vertical magnification of distance is X 12,500 because of the 1/50 taper section. Etch: 4% nital with Zephiran Chloride.

lating this gradient linearly to the surface gives a surface temperature estimate of 1900 °F (1040 °C). The actual surface temperature must be even higher since the temperature gradient is even steeper nearer the surface. The steep temperature gradients near the ground surface for conditions approaching good commercial practice must result in steep gradients of structure so that microhardness measurements must be interpreted with due regard to the effect of steep hardness gradients. For example, the Vickers microhardness measured just under the rehardened zone in the sample of Fig. 7 was 850 kilograms per square millimeter (Rockwell C-58) whereas the actual value at that point should be about 500 kilograms per square millimeter (Rockwell C-43) according to Fig. 5.

Effect of Mechanical Variables

The temperature distributions resulting from various grinding conditions are summarized in Fig. 8. As the work speed, v, is increased or downfeed, d, is decreased the peak temperature reached at any depth is lowered. The grinding forces are likewise decreased and a relation is to be expected between temperature distribution and energy expended in grinding. By the combination of data from Fig. 8 with force

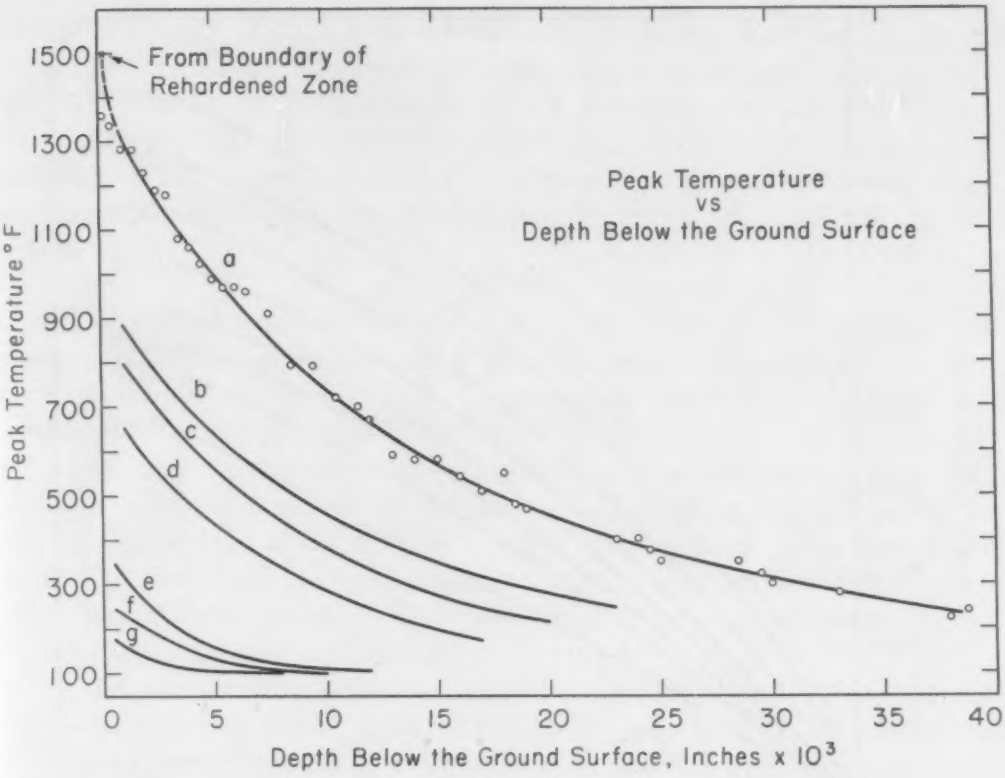


Fig. 8—Peak Temperature Distribution for Various Grinding Conditions.

Curve	Downfeed, d, In./Pass	Work Speed, v, Ft./Min.	Wheel Specification	Type of Grinding
a	0.0005	15	37C36P5V (SiC)	Intermittent
b	0.0010	30	38A60H8VG (Al_2O_3)	Intermittent
c	0.0010	60	38A60H8VG (Al_2O_3)	Intermittent
d	0.0005	60	38A60H8VG (Al_2O_3)	Intermittent
e, f, g	0.000011	250	38A60H8VG (Al_2O_3)	Continuous

The actual points are shown only for curve a. The scatter became less for the less severe grinding conditions and points are omitted for clarity.

measurements made for the same grinding conditions the relationship indicated in Fig. 9 was obtained. Q_A is the total grinding energy per square inch of work area ground in a plunge cut (no crossfeed) obtained from the following equation:

$$Q_A = \frac{F_H(V + v)}{12bv}$$

where: F_H = horizontal force component in pounds,
V = surface speed of grinding grits $\left(\frac{\pi D'N}{12}\right)$ in fpm,
D' = wheel diameter in inches,
v = work speed in fpm,
b = width of contact between wheel and work in inches,
Q_A = total grinding energy per square inch of work area ground in a plunge cut in foot pounds per square inch.

It is not implied that all of the grinding energy enters the work as heat, but merely that the fraction of the total grinding energy which

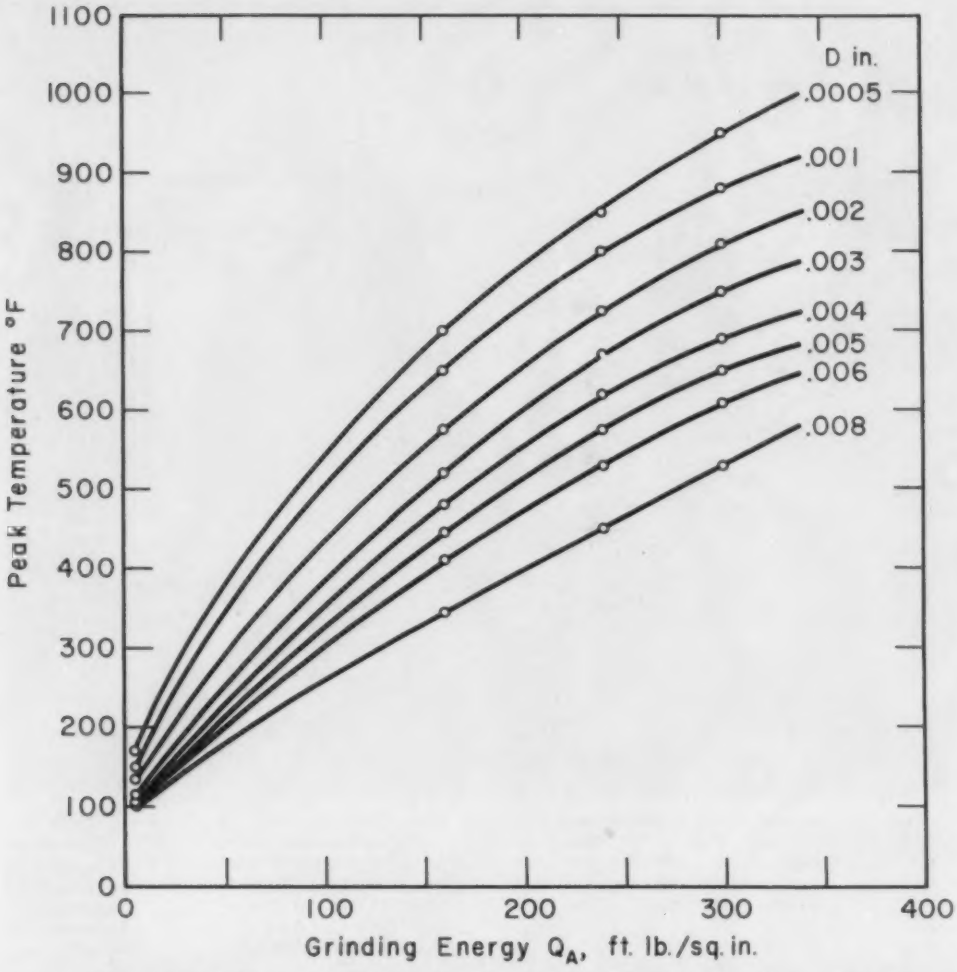


Fig. 9—Peak Temperature Plotted Versus Q_A for Various Values of D Obtained from Force Measurements and the Curves of Fig. 8. D indicates depth below the ground surface in inches.

enters the work as heat does not vary widely. The depth at which a given peak temperature occurs can be estimated from the relationship between peak temperature distribution and grinding energy shown in Fig. 9 and measurement of the energy consumed in grinding. Such a measurement may be made by comparing the power input to a grinder when it is grinding, with the power input when it is idling at the normal operating speed. Thus, Q_A is a semi-quantitative measure of grinding severity and can be used to estimate the temperature rise beneath the ground surface during a plunge cut.

The effect of wheel condition is difficult to express quantitatively. The grinding operation tends to establish a given condition for a wheel of given specification which is somewhat dependent on the type of dressing technique used. The variation in wheel condition is most significant for light feed rates where attritious wear glazes the wheel quickly. For example, in Fig. 8, curves (e), (f), and (g) show the variation in temperature distribution for grinding conditions identical

except for slight variations in wheel condition. Curve (e) was obtained with a wheel which had been grinding at the same feed rate for ten minutes. Curve (g) was obtained with a freshly dressed wheel, and curve (f) with a wheel in a condition between these extremes. Force measurements showed that the condition of the wheel changes as grinding proceeds until the glazing is sufficient to cause wheel breakdown.

Summary

The temperature distribution has been measured within hardened steel samples during the surface grinding operation. Structural changes corresponding to the observed temperature histories have been determined from metallographic observation and microhardness surveys.

The peak temperature required to cause tempering to Rockwell C-63 in a prior structure of 52100 steel, hardened and tempered to Rockwell C-64, is about 650 °F (345 °C). The peak temperature required to reaustenitize and, thus, reharden a surface layer in such a prior structure is about 1550 °F (845 °C) for the rapid heating produced by grinding at commercial work speeds.

One temperature gradient near the surface deduced from structural changes was found to be 12.5×10^6 °F per inch for a work speed of 60 feet per minute and a downfeed of 0.0005 inch per pass with soluble oil coolant. The extrapolated surface temperature for these conditions was in excess of 1900 °F (1040 °C).

An approximate relationship was found between the grinding energy input and the peak temperatures reached within the work.

The mechanical factors which minimize the heat generated in grinding are decreased downfeed per pass, increased work speed, lubrication by the coolant, and a dressing technique which yields the sharpest wheel conditions consistent with finish requirements.

Acknowledgment

We are indebted to The Timken Roller Bearing Company for the financial support of the research reported in this paper.

References

1. L. P. Tarasov, "Detection, Causes and Prevention of Injury in Ground Surfaces," Transactions, American Society for Metals, Vol. 36, 1946, p. 389.
2. L. P. Tarasov, "Some Metallurgical Aspects of Grinding," Machining—Theory and Practice, American Society for Metals, 1950, p. 409.
3. L. P. Tarasov, "Grindability of Tool Steels," Transactions, American Society for Metals, Vol. 43, 1951, p. 1144.
4. L. P. Tarasov and C. O. Lundberg, "Nature and Detection of Grinding Burn in Steel," Transactions, American Society for Metals, Vol. 41, 1949, p. 893.
5. L. P. Tarasov and H. J. Grover, "Effects of Grinding and Other Finishing Processes on the Fatigue Strength of Hardened Steel," *Proceedings*, American Society for Testing Materials, Vol. 50, 1950, p. 668.

6. H. E. Boyer, "Effects of Grinding on Physical Properties of Hardened Steel Parts," TRANSACTIONS, American Society for Metals, Vol. 40, 1948, p. 491.
7. J. O. Outwater and M. C. Shaw, "Surface Temperatures in Grinding," *Transactions,* American Society of Mechanical Engineers, January, 1952, p. 73.
8. E. R. Marshall and M. C. Shaw, "Forces in Dry Surface Grinding," *Transactions,* American Society of Mechanical Engineers, January, 1952, p. 51.
9. W. R. Backer, E. R. Marshall and M. C. Shaw, "The Size Effect in Metal Cutting," *Transactions,* American Society of Mechanical Engineers, January, 1952, p. 61.
10. John Wulff, "Surface Finish and Structure," *Transactions,* American Society of Mechanical Engineers, Vol. 145, 1941, p. 295.
11. R. A. Huggins, I. B. Roll and H. Udin, "Measurement of Transient Surface Temperatures," *Review of Scientific Instruments,* Vol. 23, No. 9, September, 1952, p. 467.
12. W. J. Feuerstein and W. K. Smith, "Elevation of Critical Temperatures in Steel by High Heating Rates," TRANSACTIONS, American Society for Metals, Vol. 46, p. 1270.

DISCUSSION

Written Discussion: By D. Niconoff, Canton Metallurgical Laboratory, Republic Steel Corp., Canton, Ohio.

The authors succeeded in filling a blank space in the existing knowledge of some important details of the grinding operation, which are of considerable interest not only to a relatively small group of metallurgists engaged in surface finishing of their products by grinding, but also to a much greater number of laboratory workers employing this process as an intermediate step in the preparation of their test pieces.

It is generally agreed, for instance, that grinding of flats on E. Q. hardenability specimens is one of the least amenable to standardization steps involved in the preparation of these pieces, and therefore one most likely to be responsible for abnormal scatter of the hardenability data encountered occasionally. But because the "burning" or overheating by grinding can occur at the point of maximum hardness as well as at any other spot along the specimen, the knowledge also of the peak temperature distribution for intermediate hardness levels would be helpful for this application.

While referring frequently to the severity of grinding, the authors somehow omitted giving a definition of this concept. What constitutes the severity of grinding? It would be logical to define it as the rate of removal of the material subjected to grinding. The authors were probably thinking in these terms when they said that "as the work speed and/or downfeed is decreased, the peak temperature reached at any depth is lowered." In such a case the severity of the grinding operations corresponding to the curves reproduced in Fig. 8 could be evaluated thus:

Curve	Downfeed In./Pass	Work Speed Ft./Min.	Severity Sq.in./Pass/Min.
A (high)	0.0005	20	0.012
B	0.0010	30	0.036
C	0.0010	60	0.072
D (low)	0.0005	60	0.036

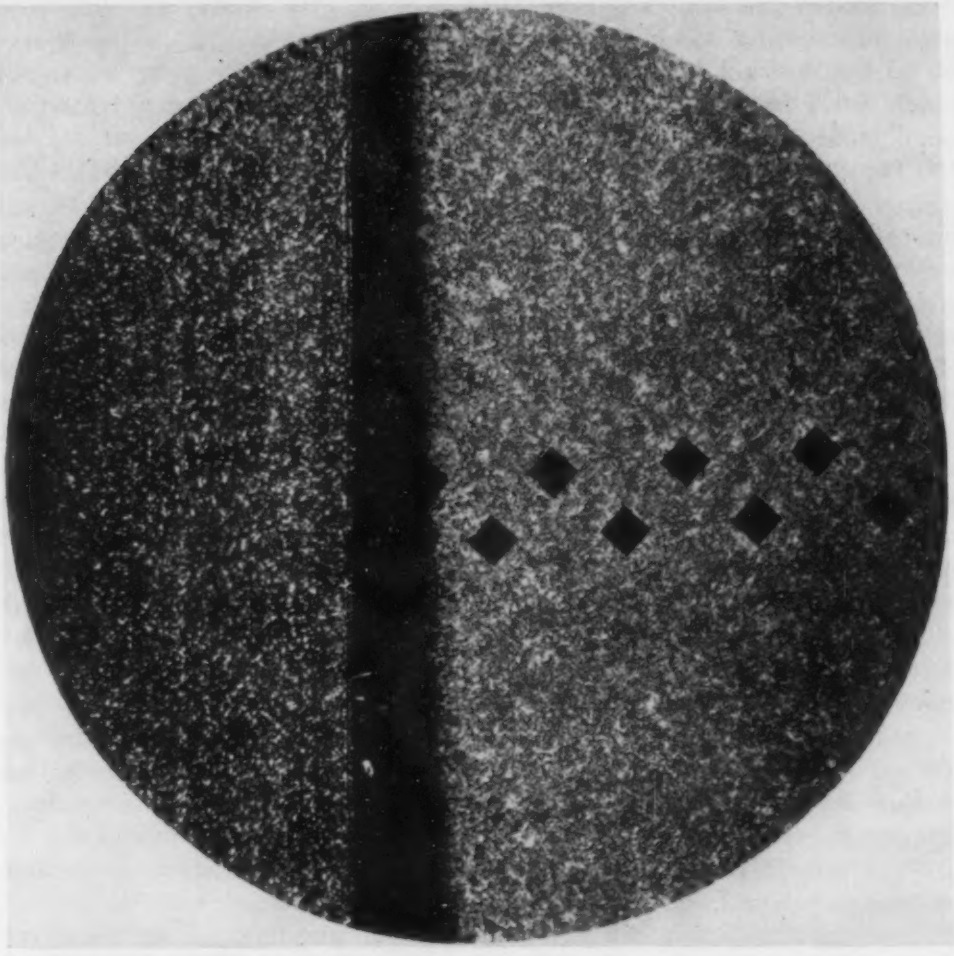


Fig. 10—Cross-Section of the Ground Bearing Surface of a Camshaft of Carburized and Hardened SAE 8617 Steel on Which Heavy Grinding Checks Were Indicated by Magnaflux Inspection. 4% picral etch. Original Magnification X 100, reduced ⅓.

But instead of the expected direct relation between severity of grinding and the resulting overheating, we find conditions of almost inverse proportionality. Here appears to be a powerful factor, probably burnishing, which has been overlooked in this study and which assumes predominant role under conditions of lower severity of grinding.

It was probably the consideration of this burnishing effect that prompted the authors to say in their summary: "The mechanical factors which minimize the heat generated in grinding are decreased downfeed per pass, (and) increased work speed. . . ."

Do the authors refer to the same work speed when they say one time that the decreased work speed lowers the peak temperature, and next time that increased work speed has the effect of minimizing the heat generated in grinding?

Written Discussion: By R. B. Boswell, research metallurgist, Chrysler Corp., Detroit.

It should be pointed out that structural changes of the type described in this paper can often be observed on metallographic examination of the cross-sections of heat treated parts which have been ground. For example, Fig. 10 shows the cross-section at X 100 of the ground bearing surface of a camshaft

of carburized and hardened SAE 8617 steel on which heavy grinding checks were indicated by Magnaflux inspection. It is apparent that the structure of the carburized and hardened case has been affected to a depth of approximately 0.004 inch as evidenced by the darkened area of tempered martensite found immediately below the surface.

The Vickers hardness impressions (10 kg. load) shown in this photomicrograph are taken every 0.004 inch inward from the surface. The hardness impression nearest the surface at the boundary of the heat affected zone gave a reading of 627 V.D.P. (Rockwell C-56.5), whereas the next reading inward gave a reading of 698 V.D.P. (Rockwell C-60). Using a microhardness tester with Vickers penetrator (100 gm. load), the hardness at 0.001 inch below the surface was measured at 589 V.D.P. (Rockwell C-54.5), increasing to 695 V.D.P. (Rockwell C-60) at 0.004 inch depth, and reaching a maximum of 716 V.D.P. (Rockwell C-61) at 0.006 inch below the surface. Specification hardness for the bearing surfaces was Rockwell C-58 minimum. No evidence of a white reformed martensitic layer was found either on metallographic examination of the cross-section or on visual examination of the ground bearing surfaces after etching with a 4% solution of nitric acid in water followed by a 2% solution of concentrated hydrochloric acid in acetone. The grinding checks and soft surface condition described were subsequently completely eliminated on such parts through a 25% reduction in the downfeed rate during semi-finish grinding of the bearings.

The authors are to be congratulated for presenting a paper which not only substantially furthers our understanding of the grinding process, but also contains important information of practical value for those who are confronted with grinding problems in practice.

Written Discussion: By Robert A. Huggins, assistant professor of metallurgy, School of Mineral Sciences, Stanford University.

The metallurgical problems resulting from grinding are of great commercial importance, and the authors are to be congratulated upon their fundamental approach to the problem.

Recent work[3] on the formation of austenite at heating rates of 2000 to 20,000 °C per second has shown that the austenitizing behavior is quite dependent upon the prior structure. The prior structure had considerable influence on both the temperature of the onset of austenite formation and the rate at which it transformed, finer structures transforming more rapidly and at lower temperatures. This would mean that the depth of the rehardened zone under identical grinding conditions would be somewhat different for different prior structures of the same steel.

The authors stated that they converted emf values to temperatures by using a calibration curve for a hardened 52100-constantan couple. The structure of the 52100 would certainly be changed upon exposure to the calibration temperatures. Did the authors find that metallurgical structure had any effect on thermoelectric behavior?

One might expect a slightly different temperature distribution just under the grinding wheel for uphill grinding compared to downhill grinding. Have the authors any information on this?

---

[3] Huggins, Udin, and Wulff, "The Formation of Austenite in Plain Carbon Steels at High Heating Rates," to be published.

Finally, we know that the state of stress has an effect upon the temperature at which some phase transformations occur. I would like to ask the authors if they would care to comment on the probable state of stress at the time of austenite formation just below a ground surface, and what effects that might have upon the transformation kinetics.

Written Discussion: By L. P. Tarasov, Research and Development Department, Norton Co., Worcester, Mass.

This is the first paper on the quantitative evaluation of grinding temperatures that is based on first-rate experimental work and that does not involve the questionable assumptions characteristic of what little has been previously published on grinding temperatures. The authors are to be congratulated for having developed an experimental technique whose validity it will be most difficult to dispute.

Several comments should be made about the ground surface illustrated by Fig. 7. While it is true that the extreme shallowness of the burned layer in this particular instance caused the indenter to penetrate into the underlying steel that reached a lower peak temperature and hence was harder than the taper section surface at that point, there is another factor that may contribute to the greater measured hardness than would be expected from the instantaneous tempering curve of Fig. 5. This is the transition structure between the fully rehardened and the fully overtempered region, in which the pre-existing austenitic grain boundaries become reaustenitized at the same temperature at which austenite does not have time to form in the grain interiors. The writer has observed the resultant formation of martensitic grain boundaries surrounding overtempered grain interiors in heat treated and severely ground 18-4-1 high speed steel, high-carbon high-chromium die steel, and 52100 steel. In order to observe this transition structure, it is generally necessary to burn the steel sufficiently to get a much deeper heat-affected layer and perhaps to use a higher taper magnification, such as 100 to 1. The grain boundary rehardening just below the fully rehardened surface can result in a considerably greater hardness than that of the fully overtempered grain interiors, as has been shown in the authors' Ref. 4. Perhaps grain-boundary rehardening was negligible under the authors' experimental conditions, but the possibility of its existence and effect upon the microhardness measurements should be kept in mind in other studies that may be made along this line.

To return to the increase in hardness caused by the presence of less overtempered steel directly underneath the surface of the taper section, this can be reduced to some extent by the use of a Knoop indenter instead of a Vickers type indenter because the former produces a shallower and longer indentation for the same load than does the latter.

A very interesting feature of the burn pattern in Fig. 7 is that while the depth of rehardening is roughly the same in the greater portion of the taper section, the depth of softening is far greater for the principal peaks of the grinding scratches than it is for the adjoining valleys. The substantially equal depth of rehardening indicates a corresponding degree of equality in the temperature gradient in the rehardened layer and presumably below it. Would the large differences observed in the depth of softening be due to a time effect, in which the peaks were heated for a longer time to the same maximum temperature than were the valleys?

Now that the experimental technique has been developed, it is to be hoped

that it will be possible to continue this work so as to obtain similar information for a far wider range of significant grinding variables.

Written Discussion: By Milton C. Shaw, professor of mechanical engineering and John E. Mayer, assistant in mechanical engineering, Massachusetts Institute of Technology, Cambridge, Mass.

The grinding of hardened steel surfaces of members designed to operate in sliding contact is an important production problem. If care is not exercised a thin softened surface layer may result from phase transformation or overtempering near the surface. The authors have presented a valuable discussion of the variables that influence the subsurface temperature, which is one of the important items pertaining to surface softening.

Other items of interest to this problem are the temperature and stress **at the surface** during grinding and the time during which the surface and subsurface material is at temperature.

It has been reasoned by the authors that the maximum temperature at any interval point in a ground surface (Θi) will be proportional to the grinding energy per unit of ground surface (Q_A)

$$\text{i.e., } \Theta \sim Q_A \qquad \text{Equation 1}$$

The quantity Q_A may also be expressed in terms of the energy required to grind a unit volume of metal (u) as follows:

$$Q_A = \frac{u\,v\,b\,d}{v\,b} = u\,d \qquad \text{Equation 2}$$

where v is the work speed
b is the width of grind
d is the wheel downfeed per pass.

It is convenient to express Q_A in terms of u since the energy per unit volume has been shown to be a very important quantity in grinding (8) and quite a bit is known about the influence the several grinding variables have on u. The

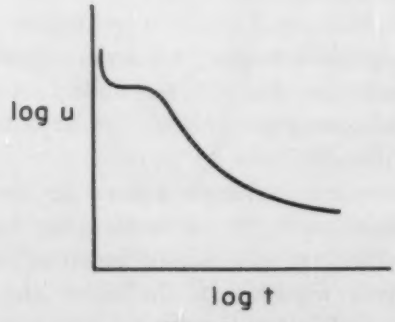


Fig. 11

quantities which influence u are work material, abrasive material and sharpness and the mean size of the individual chips produced. Only the mean chip size will vary when a given material is ground with a given wheel, and the manner in which u varies with chip size (t) is shown in Fig. 11 of this discussion. Here, the mean chip size is taken to be the maximum undeformed chip thickness which is approximately (9)

$$t = \sqrt{\frac{4v}{VCr}\sqrt{\frac{d}{D}}} \qquad \text{Equation 3}$$

where D is the wheel diameter
C is the number of cutting points per square inch of wheel surface
r is the mean ratio of width to depth of an individual scratch.

From Equations 1 to 3 and Fig. 11 we have a convenient means for estimating the influence of any grinding variable upon the subsurface temperature at any point.

The mean surface temperature (Θ_s) has been discussed in reference (7) and it may be shown that

$$\Theta_s \sim u \qquad \text{Equation 4}$$

to about the same approximation as the subsurface temperature (Θ_i) may be taken to be proportional to Q_A:

$$\text{i.e., } \Theta_i \sim u\,d \qquad \text{Equation 5}$$

The surface and subsurface temperatures are thus seen to be related to the wheel depth of cut (d) in an entirely different way. While the surface temperature will decrease slightly with an increase in d (since $t \sim d^{1/4}$ in Equation 3), the subsurface temperature will increase significantly with an increase in d.

In addition to the surface and subsurface temperatures, the time the metal is at temperature is also important. Negligible over-tempering or phase change will occur even at high temperature if the time is short enough. The time any given point on the workpiece will be subjected to grinding action during a single pass of the wheel is a measure of the time at temperature. This grinding time per pass (T) will be

$$T = \frac{l}{v} = \frac{\sqrt{Dd}}{v} \qquad \text{Equation 6}$$

where l is the mean undeformed chip length $= \sqrt{Dd}$.

In order to avoid grinding damage, surface and subsurface temperatures should be as low as possible and the time at temperature as short as possible. This may be best achieved in the following ways:

1. By use of sharp cutting points chosen to give low u. Points are sharpened by proper dressing and an aluminum oxide wheel will give lower u on steel than a similar silicon carbide wheel.

2. By use of a good fluid that removes heat and decreases u particularly in the fine grinding region. In general oils provide better lubrication and hence lower u while water base fluids provide better cooling. Both of these actions are important in practice.

3. By use of a small wheel depth of cut (d) in finishing operations. While giving slightly higher surface temperatures (Equations 3, 4) this will give lower subsurface temperatures for shorter periods of time (by Equations 5 and 6). The net effect of a decrease in d should in all cases be a decrease in the extent of surface damage.

4. Use of a small diameter wheel in finishing operations is very attractive since it will reduce the time at temperature (Equation 6) and simultaneously decrease surface and subsurface temperatures by increasing t (Equation 3) and hence decreasing u (Fig. 11). The disadvantage of using a small wheel lies in the fact that more frequent dressing is required which results in increased labor and wheel costs.

5. Use of a large table speed (v) will not only decrease time at

Table III

Test	Abrasive	d, ipp	V, fpm	v, fpm	t, in.	u, psi	ud lb/in	Measured Temp, ° F Θ_s	Measured Temp, ° F Θ_i ** at 0.001" depth	l, in	T, sec
a	36 grit-SiC	.0005	5700	15	52×10^{-6}	12×10^{6}**	6000	4000*	1320	.059	20×10^{-3}
b	60 grit-Al_2O_3	.0010	6000	30	73×10^{-6}	3.6×10^{6}	3600	1700	880	.084	14×10^{-3}
c	60 grit-Al_2O_3	.0010	6000	60	103×10^{-6}	2.9×10^{6}	2900	1100	800	.084	7×10^{-3}
d	60 grit-Al_2O_3	.0005	6000	60	87×10^{-6}	3.8×10^{6}	1900	1400	650	.059	5×10^{-3}
g	60 grit-Al_2O_3	.00011	6000	250	11×10^{-6}	6.9×10^{6}	76	3200	160	.0088	0.17×10^{-3}

Notes

* 1. Estimated from other work on SiC.

** 2. Θ_s measured by method to be described in forthcoming paper.

3. In computing t, C was taken equal to 3000 grains per square inch, r = 15, and wheel diameter D = 7 in.

4. A soluble oil was used in all tests.

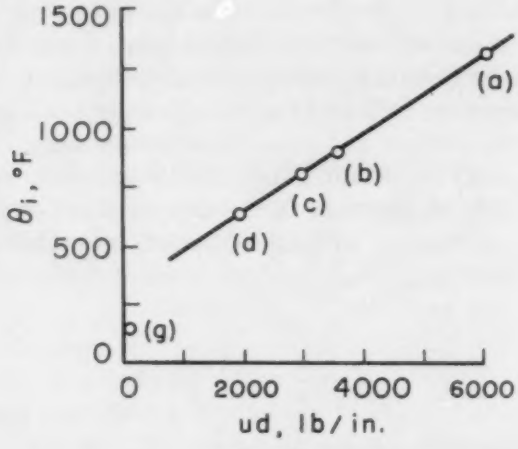


Fig. 12

temperature (T, see Equation 6) but also decrease Θ_i and Θ_s since t will increase (Equation 3) and hence u will decrease (Fig. 11).

6. A decrease in wheel speed will increase t, decrease u and hence cause a decrease in both the surface and subsurface temperatures.

7. A decrease in C, the number of cutting points per square inch, will likewise cause an increase in t, a decrease in u and hence a decrease in Θ_s or Θ_i. The quantity C can be increased by a fast dressing feed and use of a wheel of fairly large grain size. Contrary to what might be expected a 60 grit finishing wheel is much less likely to cause grinding damage than an 80 or 120 grit wheel.

The last three quantities (v) (V) and (C) can be adjusted only within the limits of the finish required, for as v is increased or C and V are decreased, the finished surface will become rougher.

In conclusion the data of the authors' Fig. 8 may be reconsidered to illustrate the foregoing points. Additional quantities needed for this purpose are given in Table III. While an attempt will not be made to illustrate all of the foregoing points the reader can readily verify that the quantities in Table III are in good agreement with the foregoing discussion of the surface and subsurface temperatures and time at temperature.

The measured values of Θ_i at a distance 0.001 inch below the surface are seen to vary directly with the quantity u d (Fig. 12). Likewise, the surface

temperature Θ_s is seen to be approximately proportional with u. In test (g) we have a case where the surface temperature is very high (due to u being large) while the subsurface temperature is very low (due to u d being small). The time T is seen to be very small and hence it is expected that this would be a good grinding condition from the point of view of grinding damage despite the high surface temperature obtained. It is significant to note that test (g) corresponds to a very small d and very large v. The temperatures for case (a) are so very high due to the fact that SiC always gives a much larger u than Al_2O_3 when grinding steel. The aluminum oxide tests in Table III (tests b to g) are arranged in order of decreasing tendency for grinding damage to occur. The improvement is again achieved by increasing v and decreasing d. Further improvement could be obtained if necessary by decreasing wheel diameter (D), using a more effective grinding fluid than the soluble oil used and by decreasing the wheel speed V (if permissible, considering the surface finish required).

Authors' Reply

The authors are grateful to Mr. Niconoff and others who pointed out the error on page 11–13 of the preprint. The phrase "as the work speed and/or down-feed is increased," should read "as the work speed is increased or down-feed is decreased." The standardization of a grinding technique for end quench hardenability specimens is practical, but the dressing technique will be the operation most difficult to reproduce from one laboratory to another. However, a standard wheel specification and schedule of downfeeds could be used which would leave a margin of safety so that no softening would be produced by the grinding despite variations in wheel condition. The temperature distribution should not vary with hardness for a given steel, but the softer structures which are less susceptible to structural damage are probably more susceptible to the introduction of residual tensile stresses by grinding.

The severity of grinding is defined in a semi-quantitative fashion by Q_A. Certainly more data are required to confirm the usefulness of this parameter, but for plunge grinding it seems to correlate well with temperature distribution within the work piece.

Mr. Boswell has given us an excellent example of the type of structural damage which can occur in practice. The absence of any rehardened layer would indicate that this layer was removed in finish grinding, but the tempered region formed in rough grinding penetrated beyond the finish grinding stock. The powerful effect of downfeed is emphasized since a 25% decrease eliminated the damage.

The transition region which Dr. Tarasov mentioned was extremely narrow for the steel and grinding conditions used. Grain boundary rehardening has been observed in 52100 hardened from 1900 °F, having a prior austenite grain size of 3–4 when severe grinding produces a low temperature gradient.

The Vickers indenter with a 20 gram load was used because it gave more reproducible results than a Knoop indenter using the same load.

The increased penetration of tempering beneath the peaks shown in Fig. 7 is probably due to a focussing of heat from the sides of the peaks, whereas the heat generated at the bottom of the scratches can be dissipated over a wide range of directions. Thus, a point beneath a peak probably does spend a longer time in the vicinity of the peak temperature than a point at the same depth below the bottom of a scratch.

We will look forward to Dr. Huggins' publication on the effect of prior structure and heating rate on the formation of austenite. In answer to the question on calibration of the 52100 constantan thermocouple, an irreversible change did occur in the samples heated for calibration. The curve of emf versus temperature for the 52100 constantan couple ran parallel to the standard I.C. curve, but approached it at higher temperatures. The displacement was extrapolated for this work because of the rapid heating and cooling, but in no case could an error larger than 50 °F have been due to calibration error.

We have no reliable data on uphill versus downhill grinding. All the results reported in this paper were for uphill grinding.

We would expect strong compressive stress at the time austenite is formed in grinding. The Claussius Clapeyron equation and the data of Ref. 12 would lead us to believe that austenite should form at a lower temperature under compressive stress than under no stress at a given heating rate. Thus, we may over estimate the peak temperature reached at the lower boundary of the rehardened region since the electrically heated strips were under essentially zero stress in the determination of the temperature required to form austenite at high heating rates.

Messrs. Mayer and Shaw have related the measurable grinding parameters to give a coherent picture of the manner in which they affect temperatures at the surface and within the work. Because of an error in the original data of Fig. 8, the work speed and grit size for Test a are incorrect. A 36 grit SiC wheel was used and v was 15 feet per minute. T will thus be 20×10^{-3} seconds, but since both C and v are decreased, the effect on t and the other data will be negligible. The analysis of grinding mechanics as related to grinding damage provides valuable information. Quantitative data is still needed, however, on the partition of grinding energy between chips, coolant, work and wheel. This partition may vary widely with downfeed, coolant, and wheel condition. It is hoped that the technique described in this paper can be used with the recently developed analysis of grinding mechanics to provide a better understanding of the grinding process.

The authors wish to thank all the discussers for the interest demonstrated by their comments.

THE ZONAL ROLLING TEXTURE OF LOW CARBON STEEL COLD-ROLLED AT VARIOUS TEMPERATURES

By C. Nusbaum and William Brenner, Jr.

Abstract

Most of the factors which influence the texture of cold-rolled steel strip are well recognized and have been adequately studied. In a recent publication it was shown that when such strip is rolled at higher temperatures a new type of rolling texture was developed. However, the samples examined were prepared in the laboratory and the X-ray study made only on the surface.

In view of these conditions, it seemed desirable to extend the investigation to samples taken from several production rolled conditions; (a) when the mill was cold, (b) when the mill was warm and (c) when the mill was hot (operated with the maximum temperature above 500 °F); also to determine the extent of this new type of texture which is developed during "warm rolling."

X-ray examinations were made not only at (a) the surface of the samples but also (b) after 25% of the sample had been removed by etching and (c) after 50% of the sample had been similarly removed. The results indicate quite clearly that the "warm rolling" texture (110) [001] exists primarily in the outer layers of a sample; that at the middle portion of the strip (50% etch) the (001) [110] texture is present though the orientation is not of such a high degree as for cold or normal rolling; that at the intermediate region (25% etch) there is for "warm rolling" a transition stage between the two types of orientation.

Introduction

THE texture developed at ordinary temperatures by a rolling operation has for most metals been quite thoroughly investigated (1)[1] and presented in the literature. Perhaps of all the metals, the rolling texture of iron has been most extensively studied, both as produced at ordinary temperatures and also by hot rolling (2,3). The

[1] The figures appearing in parentheses pertain to the references appended to this paper.

A paper presented before the Thirty-sixth Annual Convention of the Society, held in Chicago, November 1 to 5, 1954. Of the authors, C. Nusbaum is associate professor of physics, Emeritus, Case Institute of Technology, Cleveland, and consultant, The Cold Metal Products Company Laboratory, Canfield, Ohio, and William Brenner, Jr., is metallurgist, The Cold Metal Products Company Laboratory, Canfield, Ohio. Manuscript received March 31, 1953.

textures of several metals rolled at higher temperatures has also been described (4,5).

In a recent publication of work done by Goss (6), in this laboratory, he has shown that when low carbon steel strip is rolled at temperatures above 500 °F (260 °C), a new type of texture is developed. In this texture the diagonal plane of the elementary cube is in the rolling plane and the edge of the cube is in the rolling direction. This texture is designated by (110) [001]. The texture of the low carbon steel as developed by rolling at ordinary temperatures is of the type (001) [110] in which the cube face is in the plane of rolling and the diagonal of the cube face in the rolling direction. At intermediate temperatures (300 to 500 °F) there is a transition from one texture to the other during which random orientation is simulated.

In molybdenum, according to Tsien and Chow (7), the effective slip planes are the (112) planes at lower temperatures (15–300 °C) while at 1830 °F (1000 °C) the (110) planes become the effective slip planes. If the effective slip planes for iron change with temperature on account of the change in elastic constants due to temperature, a new type of texture might well be expected at higher temperatures.

In the present day rolling practice of using the 4 high mill, either in tandem or as a single stand, the strip may easily reach a temperature of 500 °F (260 °C) or higher, depending on the speed of the strip, the amount of reduction per pass, and the manner of cooling. It thus seemed desirable to investigate the degree and extent to which these types of textures existed under various temperature conditions of rolling as actually performed in the mill. This was especially important since in his experiment Goss had examined only the surface texture of the samples prepared in the laboratory.

Experimental Procedure

Preparation of Samples

In order that the chemical composition and the initial microstructure of all the samples should be as nearly the same as possible, the original hot strip of 6.5 inches in width was slit into three strips, each 2 inches wide. Each of the strips was then rolled on a single stand 4 high mill. One of these strips was rolled at a low temperature such as would be encountered when rolling the first strip on a cold mill—one which had been idle overnight. The second rolling was performed after the mill had been in operation for some time, and the housing and the back-up rolls had become quite warm. The third and last rolling was performed after the mill had been in operation for a considerably longer time, and the rolls and mill stand were quite hot. In this rolling no water was circulating through the cooling drums; however, the speed of the mill was increased as well as the percentage of reduction per pass.

Table I
Cold Rolling

Hot Strip 6½ Inches by 0.0985 Inch Total Reduction 75.9%

Pass No.	Strip Thickness	Reduction	% Reduction	Strip Speed F.P.M.	Temperature (°F.) of Strip Enter	Strip Leave	B.U.* Rolls	Remarks
0	0.0985	—	—	—	—	—	—	
1	0.084	0.0145	14.75	150	R.T.	120	80	Loading Pass
2	0.0755	0.0085	10.1	200	90	120	90	
3	0.068	0.0075	9.9	180	100	130	90	
4	0.061	0.007	10.3	200	100	140	100	
5	0.055	0.006	9.8	200	110	150	100	
6	0.0495	0.0055	10.0	200	110	150	100	
7	0.0445	0.005	10.1	200	110	140	100	
8	0.040	0.0045	10.1	250	100	140	100	
9	0.036	0.004	10.0	200	100	140	100	
10	0.0325	0.0035	9.7	250	100	140	100	
11	0.029	0.0035	10.8	250	100	140	100	
12	0.026	0.003	10.3	250	90	130	100	
13	0.0235	0.0025	9.65	300	90	130	100	
				Average	100	135		

(*) Back-up Rolls

The samples taken from the first of these strips may be designated as "cold-rolled" samples, the second as "normal-rolled" samples, and the third as "warm-rolled" samples. These terms "cold," "normal," and "warm" are used in this sense so as to properly differentiate these conditions of cold rolling from the term "hot rolling" which correctly designates rolling at temperatures above 1300°F (705°C). The conditions of rolling are presented in Tables I, II, and III. They include the initial and final thickness of each strip for each pass, the number of passes, and the per cent reduction per pass, the temperature of the strip for each pass, and also the temperature of the back-up rolls. The relationship between the strip thickness-temperature for cold, normal and warm rolling is shown in Fig. 1.

Table II
Normal Rolling

Hot Strip 6½ Inches by 0.0985 Inch Total Reduction 75.9%

Pass No.	Strip Thickness	Reduction	% Reduction	Strip Speed F.P.M.	Temperature (°F.) of Strip Enter	Strip Leave	B.U.* Rolls	Remarks
0	0.0985	—	—	—	—	—	—	
1	0.0865	0.012	12.2	500 1200	R.T.	110	130	Loading Pass
2	0.0735	0.013	15	1300 1000	120	150	130	
3	0.0625	0.011	15	1200 900	130	190	140	
4	0.053	0.0095	15.2	1100 800	170	250	160	
5	0.045	0.008	15.1	1000 800	180	250	160	
6	0.0383	0.0067	14.9	1000 800	210	270	180	
7	0.0325	0.0058	15.1	1000 900	280	280	180	
8	0.0277	0.0048	14.8	1150 1000	260	300	200	
9	0.0235	0.0042	15.1	1200	230	260	180	
				Average	185	230		

(*) Back-up Rolls

Table III
Warm Rolling

Hot Strip 6½ Inches by 0.0985 Inch Total Reduction 75.9%

Pass No.	Strip Thickness	Reduction	% Reduction	Strip Speed F.P.M.	Temperature (°F.) of Strip Enter	Temperature (°F.) of Strip Leave	Temperature (°F.) of B.U.* Rolls	Remarks
0	0.0985	—	—	—	—	—	—	
				300				
1	0.072	0.0265	26.9	400	R.T.	180	150	Loading Pass
				1100				
2	0.057	0.015	20.9	1200	140	240	160	
				1200				
3	0.046	0.011	19.4	1300	220	270	170	
				1100				
4	0.037	0.009	19.5	1200	250	340	190	
				1200				
5	0.0295	0.0075	20.3	1300	260	360	200	
				1600				
6	0.0235	0.006	20.3	1700	360	620	210	
				Average	220	335		

(*) Back-up Rolls

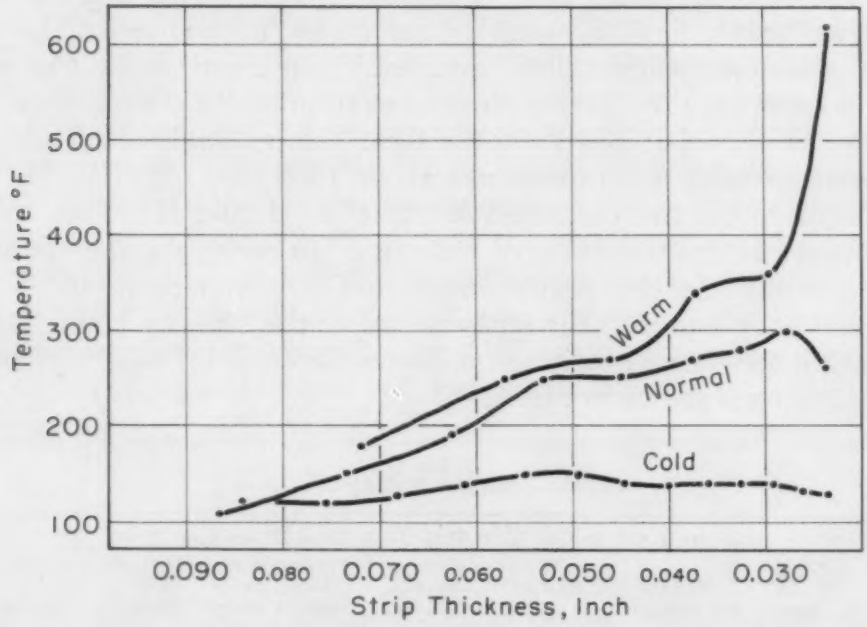


Fig. 1—Strip Thickness-Temperature Curves for Cold, Normal and Warm-Rolled Strip.

The temperatures of the strip during rolling were measured by means of an Alnor Pyrocon portable contact pyrometer. On each strip were placed special "markers" separated initially by several feet. As these "markers" passed the observer for each pass, the temperature between each of them was recorded along with the other data. The rolling operation was at no time interfered with by the observer.

The total reduction for each of the strips was the same. However, to attain the higher temperatures the number of passes for the separate strips was decreased, and the per cent of reduction per pass as well as

the speed of the strip was increased. The mean temperatures for the strips entering and leaving the rolls are summarized in the table below:

Condition of Rolling	Mean Speed Ft/Min.	Number of Passes	Average Reduction Per Pass	Mean Temperature °F Strip Enter	Strip Leave	Increase	Back-up Rolls Ave. °F
Cold	220	13	10.4%	100	135	35	180
Normal	1000	9	14.7%	185	230	45	95
Warm	1300	6	21.2%	220	335	115	165

The temperature attained in the warm rolling at the last pass was 620°F (325°C).

X-ray Samples and Technique

Several samples were taken from that portion of the strip between the "markers" and were distributed along its length. None of the samples for X-ray analysis were taken from the edge of a strip, but only from its central section. The samples taken from a given strip were placed into three groups. In one of these groups the surface of the sample for X-ray analysis was used in the "as-rolled" (unetched) condition. The second group was etched in warm dilute nitric acid until its thickness had been reduced by 25%, and the third group was similarly etched to 50% of its original thickness. In the preparation of the latter two groups, one surface was adequately protected against acid attack by a coating of hard DeKhotinsky cement. The surfaces of the respective groups thus used for X-ray examination were (a) the untreated surfaces, (b) surfaces 25% below the original surface of the sample, and (c) the surface in the central plane or 50% below the original surface of the sample.

X-raygrams

The "reflection" method of analysis in which the X-ray beam is incident at a definite angle on the surface of the sample was used. The angle used was 10 degrees as this is the Bragg angle for Mo $K\alpha$ radiation for the (110) planes of iron. The most important advantage of this method is that it does not necessitate the preparation of a sample of a definite thickness, but rather the depth of penetration of the X-rays determines the effective thickness of the sample examined. The only disadvantage of the "reflection" method is that it does not give the entire diffraction ring. All X-raygrams were taken with the plane of the beam perpendicular (transverse "T") to the rolling direction, and parallel (P) to the rolling direction. These conditions are designated respectively by the notation T-10 and P-10.

In Fig. 2 are shown a set of X-raygrams taken in the transverse (T) direction, in which the diffraction patterns for the cold-rolled samples are compared with the patterns for the warm-rolled samples

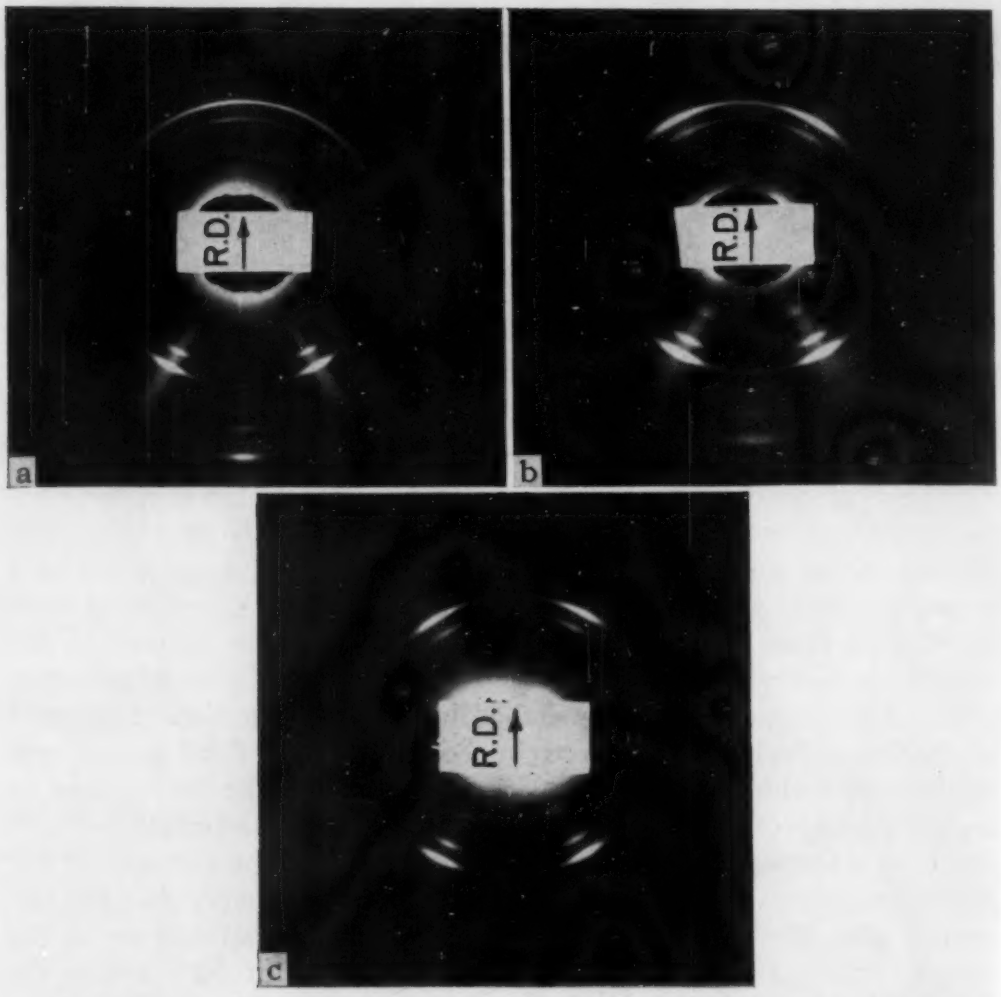


Fig. 2—X-ray Diffraction Patterns of Warm and Cold-Rolled Samples. All patterns were taken in the transverse (T) direction with the surface of the specimen set at an angle of 10 degrees with the X-Ray beam using Mo Kα radiation. (a) X-ray pattern of warm-rolled sample (upper half of print) and cold-rolled sample (lower half) of the unetched surface. (b) Same arrangement as (a) but etched to 25% below the surface. (c) Same arrangement as (a) but etched to 50% below the surface. The comparison patterns were made on the same pin-hole and film to obviate differences in exposure, film, and developing.

at the surface, 25%, and 50% etch. The diffraction ring (110) of the X-ray patterns taken at the surface of the warm-rolled samples have their maximum intensities in the vertical position of the arc. All the cold-rolled samples have the conventional cold-rolled diffraction pattern of iron in which the maximum of the diffraction ring (110) makes an angle of 30 degrees with the vertical. The intensity maximums of the diffraction patterns for the warm-rolled samples are less sharply defined for the 25% etch and 50% etch, than for the cold-rolled samples.

In Fig. 3 are presented the diffraction patterns taken in the parallel (P) direction in which the patterns for the warm and cold-rolled samples are compared at the surface, 25% etch, and 50% etch. For the warm-rolled samples at the surface, the maximum of intensity

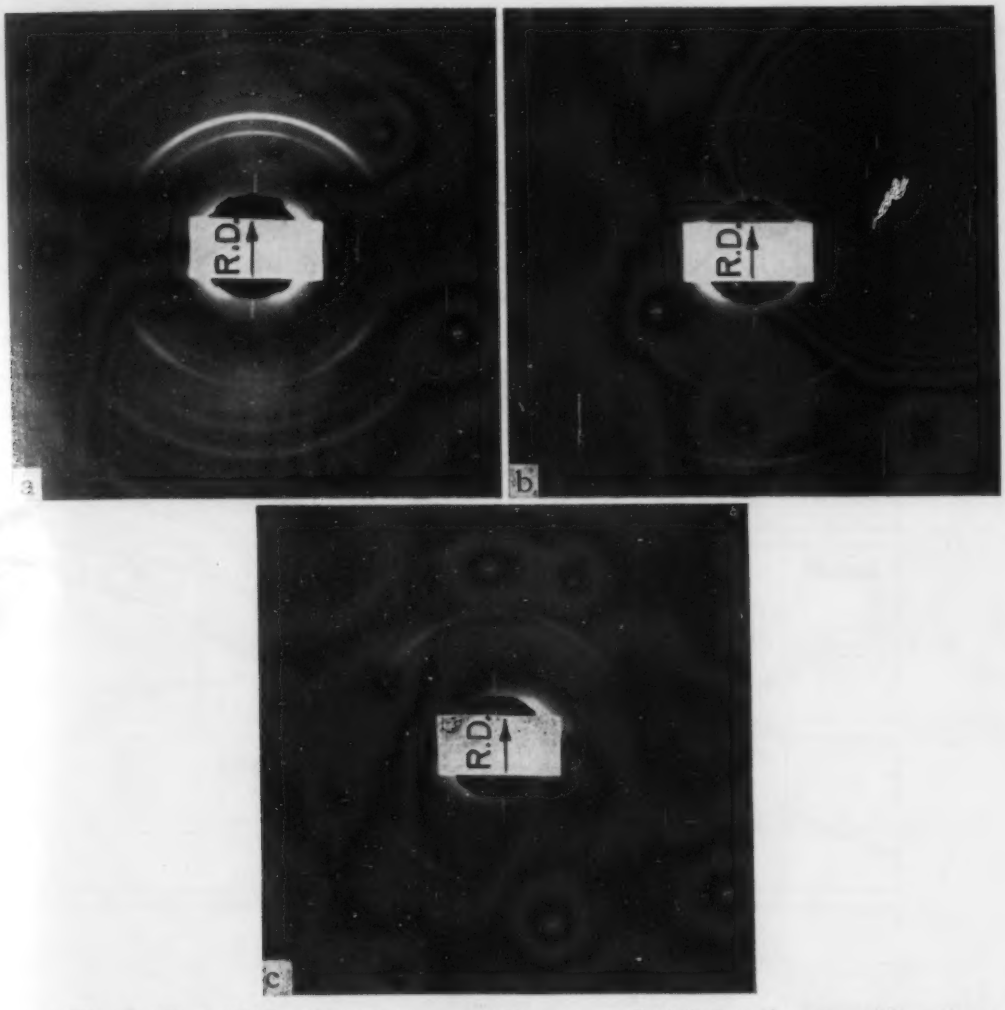


Fig. 3—X-ray Diffraction Patterns of Warm and Cold-Rolled Samples. All patterns were taken in the parallel (P) direction with the surface of the specimen set at an angle of 10 degrees with the X-ray beam using Mo Kα radiation. (a) X-ray pattern of warm-rolled samples (upper half of print) and cold-rolled samples (lower half) of the unetched surface. (b) Same arrangement as (a) but etched to 25% below the surface. (c) Same arrangement as (a) but etched to 50% below the surface. The comparison patterns were made on the same pin-hole and film to obviate differences in exposure, film, and developing.

of the diffraction ring (110) is again in the vertical position of the arc while the cold-rolled samples show the conventional pattern in which the maximums are at an angle of 45 degrees from the vertical. The maximums for the warm-rolled samples are less sharply defined for the 25% and 50% etch than for the corresponding cold-rolled samples. Similar X-raygrams were also taken in which the diffraction patterns for warm and normal-rolled samples were compared. No X-raygrams are presented but the intensity curves of such patterns are submitted.

Intensity Curves

Visual examination of the diffraction patterns gives only a qualitative comparison of their relative intensity. In order that such com-

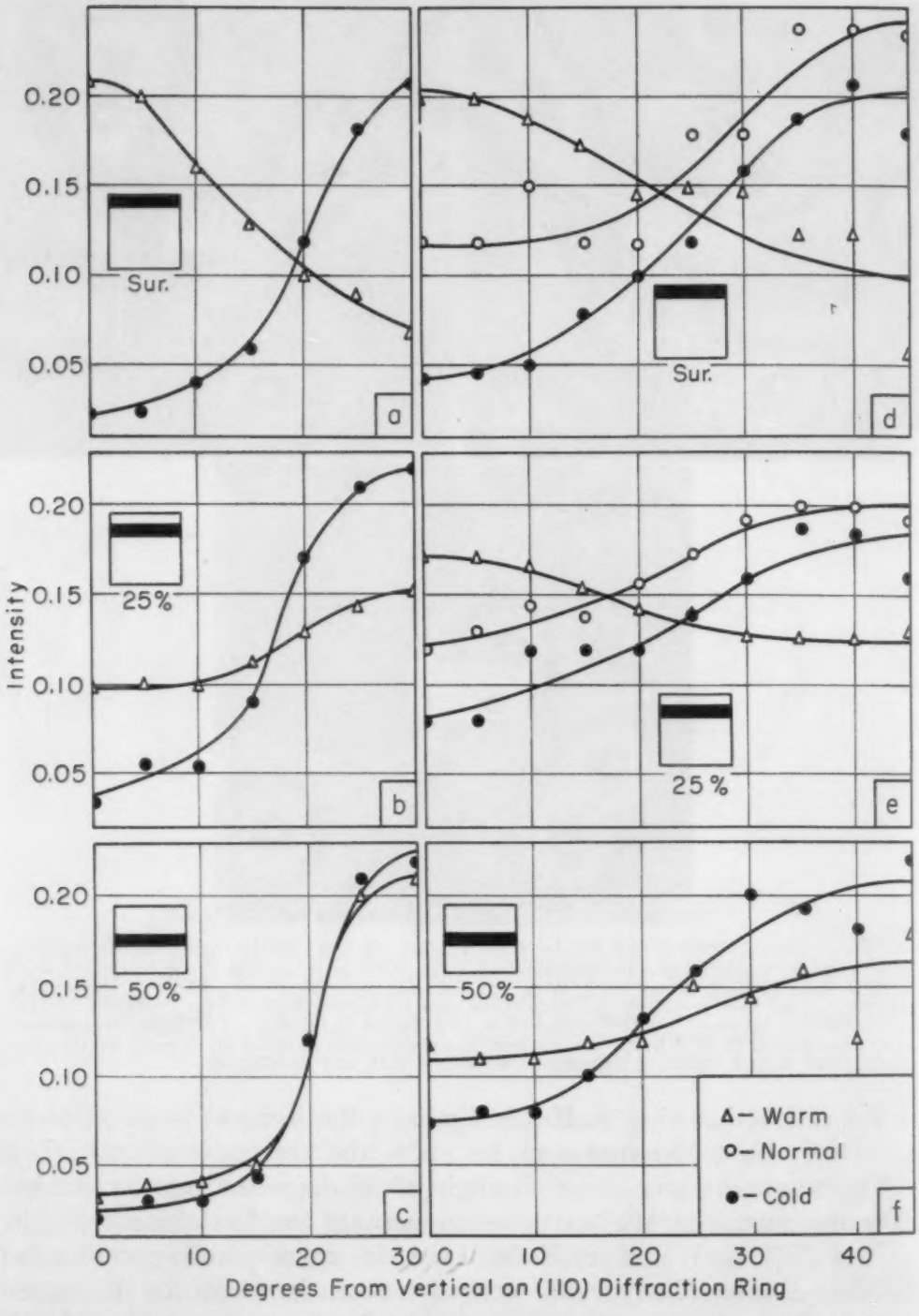


Fig. 4—Intensity of the (110) Diffraction Pattern Measured in Degrees From the Vertical. Comparison of intensities for warm and cold-rolled sample. (a) at the surface, (b) 25% etch, and (c) 50% etch. X-raygrams taken in the transverse (T) direction. Comparison of intensities for warm, normal, and cold-rolled sample (d) at the surface, (e) 25% etch, and (f), 50% etch. X-raygrams taken in the parallel (P) direction.

parison may be quantitative in nature, microphotometer measurements were made at 5 degree intervals from a vertical line through the diffraction patterns, for all the rolled samples cold, normal, and warm,

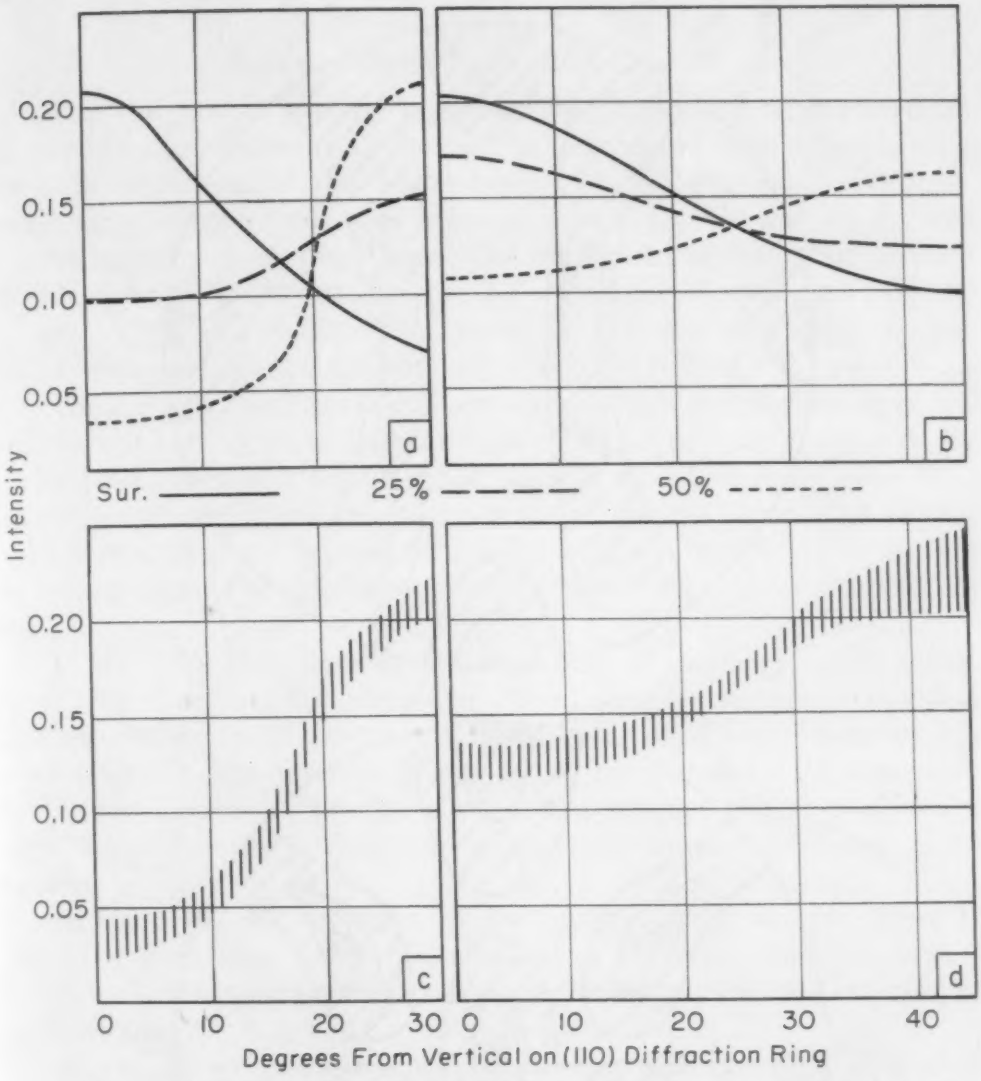
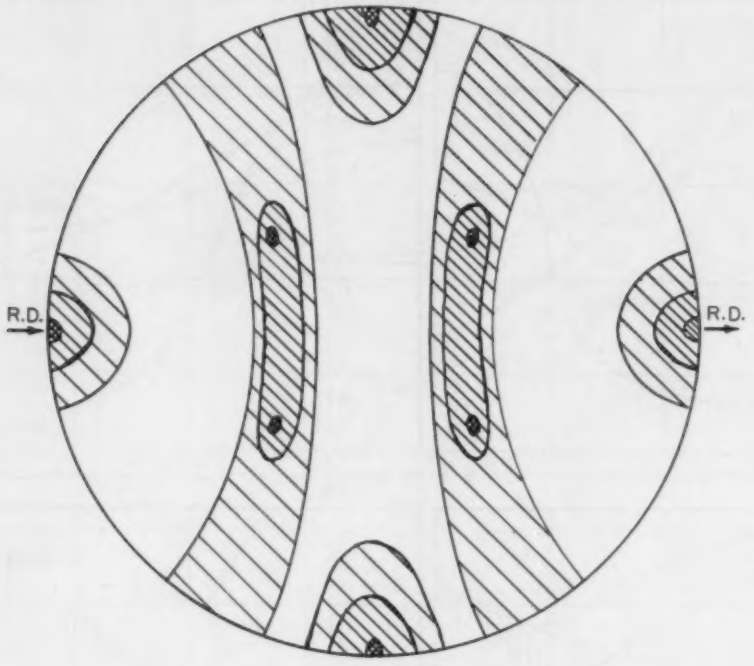


Fig. 5—Intensity of the (110) Diffraction Pattern Measured in Degrees From the Vertical. (a) Comparison of the intensities for the warm-rolled samples at the surface, 25% etch, and 50% etch. X-raygrams taken in the transverse (T) direction. (b) Similar comparisons for the warm-rolled samples, with X-raygrams taken in the parallel (P) direction. (c) Broad band indicating the range of intersities for normal and cold-rolled samples at the surface, 25% etch, and 50% etch. X-raygrams taken in the transverse (T) direction. (d) Similar to (c) with the X-raygrams taken in the parallel (P) direction.

and at the surface, 25 and 50% etch. Intensity curves in which the intensity of the diffraction ring as ordinate is plotted against the angular co-ordinate in degrees as abscissa are presented in Figs. 4 and 5. In Fig. 4a, 4b and 4c, the intensity curves for the cold and warm-rolled samples taken in the transverse (T) direction are compared at the surface, 25% etch, and 50% etch. The curves for the normal-rolled samples are not included since they agree closely with the cold-rolled samples. In Fig. 4d, 4e and 4f, similar comparisons are made for the parallel (P) direction. The curves for the normal-rolled samples are included in Fig. 4d and 4e, but not in 4f. In Fig. 5a and 5b, comparison of the intensities are made for the warm-rolled samples at the surface,



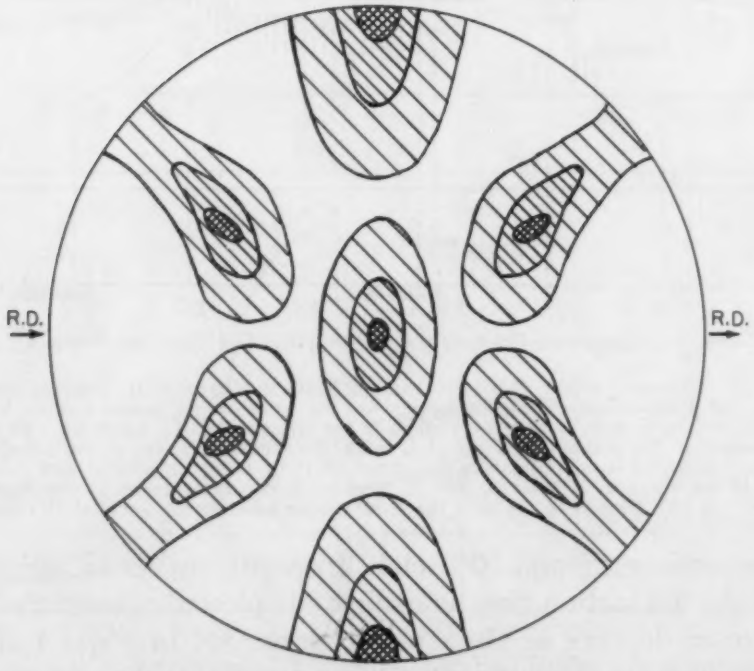


Fig. 6a—110 Pole Figure for the Conventional Cold-Rolled (001) [110] Texture of Strip Steel.

Fig. 6b—110 Pole Figure for (110) [001] Texture Developed at the Surface by Warm Rolling of Strip Steel.

25% etch, and 50% etch, for both the transverse (T) and parallel (P) directions. Similar comparisons are also made for the normal-rolled samples in Fig. 5c and 5d, where the intensity curves for surface, 25 and 50% etch fall within a broad band.

Discussion of Intensity Curves

The diffraction pattern taken at the surface of a warm-rolled sample has its maximum of intensity at zero degrees angular reading for both directions of the X-ray beam, while the normal and cold-rolled samples have their maximum of intensity at 30 and 45 degrees respectively, for both directions. The maximum of intensity is more sharply defined for the transverse (T) than for the parallel (P) direction. Also, the maximum of intensity for normal rolling is less sharply defined than the maximum for the cold rolling.

The first of these surface textures in which the maximum of intensity is at zero degrees angular reading is the texture designated by (110) [001] in which the diagonal plane of the elementary cube is in the rolling plane and the cube edge in the rolling direction. The second texture described by the notation (001) [110] has the cube face in the rolling plane and the diagonal of the cube face in the rolling direction.

In the 25% etch samples the maximum of intensity in the transverse (T) direction for the warm-rolled samples agrees in position with the maximum of intensity for the cold-rolled samples though it is considerably less intense. However, in the parallel (P) direction maximum of intensity for the warm-rolled samples occurs at zero degrees, while for the normal and cold-rolled samples it occurs at 45 degrees.

In the 50% etch samples, or the middle of the sample, there is very little difference in the distribution of the intensities. However, the cold-rolled samples always show a more sharply defined maximum, and thus a higher degree of preferred orientation.

In Fig. 5a and 5b, the intensity curves for the surface, 25% etch and 50% etch, are compared for the warm-rolled samples. These curves show that the (110) [001] texture in which the maximum of intensity occurs at zero angle, is primarily a surface effect. For the 25% etch the maximum of intensity occurs in the transverse (T) direction at 30 degrees, while in the parallel (P) direction the maximum still occurs at zero degrees. This difference between the two types of textures is due to the partial rotation of the grain fragments around the axis normal to the rolling direction and in the rolling plane.

The normal-rolled samples as well as the cold-rolled samples at all levels examined gives the first type of texture (001) [110], though the intensity maxima are more sharply defined at the central plane than at the surface. This is indicated by the curves of Fig. 5c and 5d, in which the curves cross but fall within a broad band.

In Fig. 6a and 6b, are presented the pole figures for the two types of textures. These figures were constructed according to a method of analysis due to Wood (8), and DeBarr and Roberts (9).

Conclusions

An analysis of the experimental results presented justifies certain conclusions:

1. That the texture developed in the warm rolled samples is zonal in nature.

2. That at the surface of a low carbon steel strip when rolled at a temperature above 400°F (205°C), the texture existing at the surface is of the type (110) [001].

3. That at the center of the strip the texture is of the type (001) [110], which is the conventional cold rolling texture.

4. That in a plane 25% below the surface of the strip, the texture represents a transition from that of the first to the second type. This transition may be considered as a rotation of the crystal planes around an axis in the plane of rolling, and normal to the direction of rolling.

References

1. C. S. Barrett, *Structure of Metals,* 2nd edition, 1952, McGraw-Hill Book Company, New York City.
   a—Face-Centered Cubic Rolling Textures, p. 457–459.
   b—Body-Centered Cubic Rolling Textures, p. 465–469.
   c—Close Packed Hexagonal Rolling Textures, p. 473.
2. N. P. Goss, "Hot Working, Cold Working and Recrystallization Structures," Transactions, American Society for Metals, Vol. 24, 1936, p. 967.
3. M. Gensamer and P. A. Vukmanic, *Transactions,* American Institute of Mining and Metallurgical Engineers, Vol. 125, 1937, p. 507.
4. L. G. Morrell and J. D. Hanawalt, *Journal of Applied Physics,* Vol. 3, 1932, p. 161.
5. R. L. Dietrich, "Surface Orientation and Rolling of Magnesium Sheet," *Transactions,* American Institute of Mining and Metallurgical Engineers, Vol. 185, 1949, p. 621.
6. N. P. Goss, "The Effect of Temperature on the Rolling Texture of Plastically Deformed Low Carbon Steel Strip," Transactions, American Society for Metals, Vol. 45, 1953, p. 333.
7. L. C. Tsien and Y. S. Chow, *Proceedings,* Royal Society, (London), Vol. A 163, 1937, p. 14.
8. J. K. Wood, "An Analytical Discussion of the Construction of Pole Figures," *Journal of Applied Physics,* Vol. 19, 1948, p. 784.
9. A. E. DeBarr and B. Roberts, "The Determination of the Texture of Rolled Sheet," *Journal,* Iron and Steel Institute, Vol. 164, 1950, p. 285.

AN ELECTRON METALLOGRAPHIC STUDY OF THE DEPENDANCE OF MICROSTRUCTURE ON HARDENABILITY

By S. T. Ross, R. P. Sernka and W. E. Jominy

Abstract

The nature of nonmartensitic transformation products in six 0.40% carbon steels is predicted from cooling transformation diagrams and identified by electron microscopy. Incompletely transformed martensitic areas of end quench hardenability bars are studied. Three shallow hardening steels (SAE 1040, 1340 and 4040) contain carbide-free ferrite, pearlite and upper bainite in martensite. Three deeper hardening steels (SAE 4340, 5140 and 8640) contain carbide-free ferrite, upper bainite and lower bainite in martensite. The physical appearance of the phases comprising the constituents of transformation products is similar for all steels investigated. A martensite subgrain structure is also reported. The accuracy of the proeutectoid ferrite area of the SAE 4340 steel cooling transformation diagram is questioned on the basis of current data. An estimated revision of the area is included.

Introduction

THE hardenability of steels is commonly determined through use of the end quench test. Such hardenability specimens contain structures present as a result of continuous cooling conditions which vary from the drastic water quench to an air cool. These structures are martensite, proeutectoid ferrite (or carbide), upper bainite, lower bainite, pearlite and a constituent associated with martensite which cannot be classified by optical microscopy.

Early researchers such as Portevin (1)[1] called this unknown structure troostite or primary troostite. More recently (2,3) the name has become transformation products or intermediate transformation products. Hollomon and Jaffe (4) refer to a nonmartensitic product and establish a need for its identification on the basis that it could enable more accurate determination of the effect of alloying elements on hardenability.

[1] The figures appearing in parentheses pertain to the references appended to this paper.

A paper presented before the Thirty-sixth Annual Convention of the Society, held in Chicago, November 1 to 5, 1954. Of the authors, S. T. Ross is project engineer, Metallurgical Research, R. P. Sernka is research metallurgist, and W. E. Jominy is chief metallurgist-research, Chrysler Corp., Detroit. Manuscript received April 12, 1954.

Table I
Steel Analyses and Grain Size Measurements

Type	ASTM Grain Size	Percent Alloying Elements C	Mn	P	S	Si	Ni	Cr	Mo	Quenching Temp., °F
SAE 1040	7–8	0.42	0.71	0.017	0.026	0.24	0.08	0.16	0.01	1550
SAE 1340	8–9	0.41	1.88	0.019	0.024	0.29	0.02	0.04	0.03	1550
SAE 4040	7–8	0.45	0.84	0.011	0.028	0.25	0.03	0.04	0.24	1500
SAE 4340	8–9	0.41	0.70	0.012	0.022	0.26	1.82	0.99	0.21	1500
SAE 5140	7–8	0.42	0.82	0.020	0.030	0.28	0.10	0.86	0.06	1500
SAE 8640	8–9	0.42	0.86	0.024	0.030	0.23	0.50	0.45	0.20	1550

Occurrence of the other structures resulting from heat treatment of steels can be predicted from such relationships as isothermal or cooling transformation diagrams. Since transformation products are a result of an austenite change, it should also be possible to predict their nature from some time temperature relationship. Thus, the purpose of this investigation was twofold: To identify and to predict the nature of transformation products associated with martensite in incompletely hardened steels.

Hardenability Bars

Six common hypoeutectoid steels of the 0.40 carbon range were chosen for this investigation: SAE 1040, 1340, 4040, 4340, 5140 and 8640. The first three are shallow hardening, while the final three may be regarded as relatively deep hardening steels. End quench hardenability bars were machined from cold-rolled rods of each steel which had been normalized previously for 4 hours at 1650 °F (900 °C). With the exception of the SAE 4340 bar, each was of the standard dimensions: 3 inches long by 1 inch in diameter. The SAE 4340 bar was made 4 inches long since, because of its extremely deep hardening characteristics, it was not possible to obtain a 50% martensitic area within 3 inches from the quenched end. Analyses and grain size measurements of the steels investigated are given in Table I.

Hardenability data were recorded on standard forms (5). These forms indicate the relationships between Rockwell C hardness, distance from the quenched end in $\frac{1}{16}$ inch and cooling rate as measured at 1300 °F (705 °C). Also, notation was made of the location of the 90, 70 and 50% martensitic areas of each bar. These data were condensed and are presented in Table II. The hardenability data are in agreement with those obtained by U. S. Steel (6) and the SAE (7).

The per cent martensite was rated by optical microscopy at X 500 on polished and etched surfaces. Fig. 1 is given in example. It shows an area rated as 90% martensite on the SAE 5140 hardenability bar, at $\frac{3}{16}$ inch from its quenched end. Fig. 2 is a photograph of the same area taken near the limit of optical microscopic magnification at X 2000. It will be noted that the black transformation products are incapable of resolution at both X 500 and X 2000.

Table II
Hardenability Data

Type	Per cent Martensite	Distance from Quenched End, 1/16 Inch	Cooling Rate at 1300 °F °F per Second
SAE 1040	90	2.1	190
SAE 1040	70	2.8	120
SAE 1040	50	3.1	100
SAE 1340	90	4.0	75
SAE 1340	70	5.5	50
SAE 1340	50	7.0	36
SAE 4040	90	3.0	100
SAE 4040	70	3.5	85
SAE 4040	50	4.5	60
SAE 4340	90	18.0	8
SAE 4340	70	54.0	3 (Est.)
SAE 4340	50	63.0	0.2 (Est.)
SAE 5140	90	3.0	100
SAE 5140	70	4.5	60
SAE 5140	50	6.5	40
SAE 8640	90	4.5	60
SAE 8640	70	6.0	45
SAE 8640	50	8.0	30

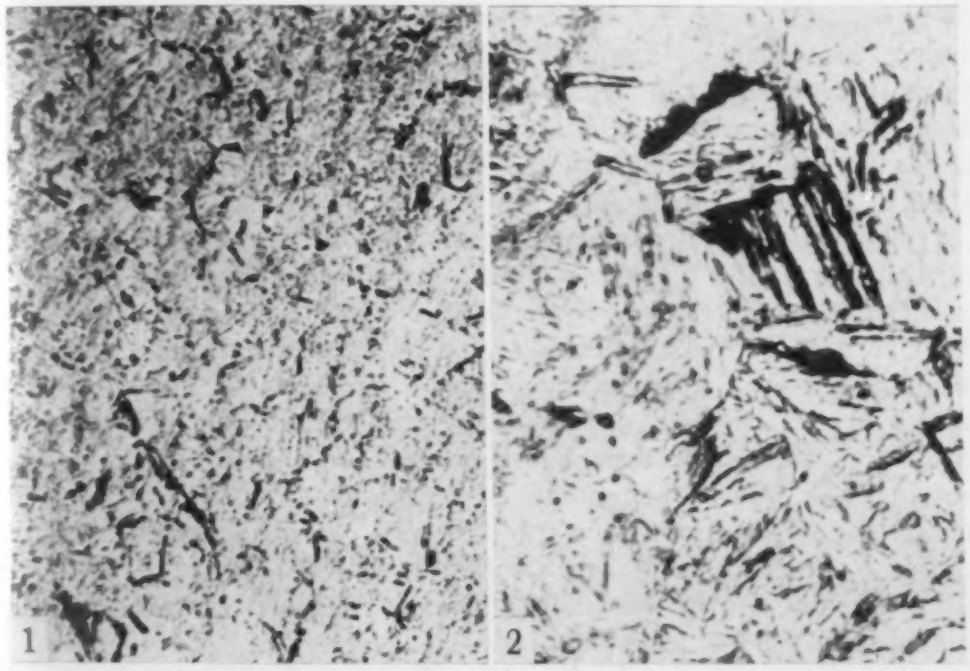


Fig. 1—Micrograph of SAE 5140. The Area Shown was Judged to Contain 90% Martensite. Similar Ratings on Each Hardenability Bar of the Six Steels Investigated Were Made at this Magnification for 90%, 70% and 50% Martensite. 4% Picral Etch. X 500.

Fig. 2—Micrograph of SAE 5140. The Area Shown is 90% Martensite. At This Higher Magnification, Which is Nearing the Practical Limit of the Light Microscope, the Transformation Products are Still Unresolved. 4% Picral Etch. X 2000.

Cooling rates at 1300 °F (705 °C) for each 90, 70 and 50% martensitic area were determined from the hardenability data and are listed in Table II. Areas of lower martensite content were not included. Slack quenching is not often done deliberately, and few such areas are of critical significance in commercial production. It was recognized that the cooling rate of a given area on a hardenability bar varies at

lower temperatures from that determined at 1300 °F (705 °C). However, it was believed that such variation would not be so significant as to destroy the qualitative nature of the investigation.

Cooling Transformation Diagrams

A time temperature relationship for the decomposition of austenite and its transformation to martensite is recorded for a steel by its isothermal transformation diagram. The data required for construction of these diagrams are gathered under constant temperature, or isothermal, conditions. However, the end quench hardenability bar is subjected to an infinite number of rates of cooling. Thus, its austenite cannot be considered as undergoing isothermal change.

According to Grange and Kiefer (9) and Liedholm (10), the isothermal transformation diagram does not reflect the course of austenite decomposition or transformation under conditions of continuous cooling. Moreover, cooling rate curves cannot be constructed on it without contradiction of the principle of constant temperature change. However, a diagram can be constructed from an isothermal transformation diagram which will allow prediction of the course of athermal austenite change. It is referred to as a cooling transformation diagram. Cooling curves may be plotted on this diagram without violation of underlying principles.

The method of Grange and Kiefer (9) was used to construct cooling transformation diagrams for the steels considered in this report. Isothermal data were not available for SAE 1040 and 8640 steels. However, Grange (11) recommended that their isothermal diagrams be estimated from data published on other steels of the same alloy type. Thus, the isothermal transformation diagram for SAE 8640 steel was estimated from data published on SAE 8630 and 8660 steels, and that for SAE 1040 was estimated from data on SAE 1050 and 1060 steels. The Ms temperatures for the steels were calculated from the data of Republic Steel (12) after the method of Grange and Stewart (13). The balance of the cooling transformation diagrams were calculated from the isothermal data of U. S. Steel (6).

In construction, two basic assumptions are made:

1. The condition of continuously cooled austenite at the instant it cools to the temperature at which its cooling curve intersects the line signifying the beginning of austenite decomposition on the isothermal transformation diagram is not substantially different than if the austenite had been quenched instantly to that temperature. Thus, some additional cooling time will be required before any measurable decomposition occurs.

2. The amount of decomposition of austenite cooled through a limited temperature range (T_1 to T_2) in a given time (I_1 to I_2) is approximately equal to the amount indicated by the isothermal diagram

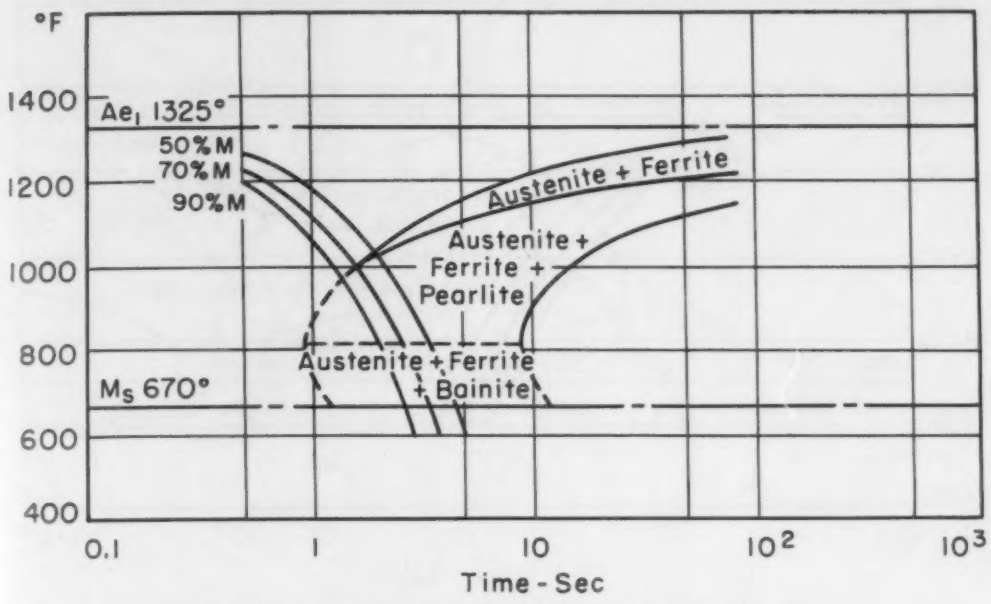


Fig. 3—Cooling Transformation Diagram of SAE 1040 Steel.

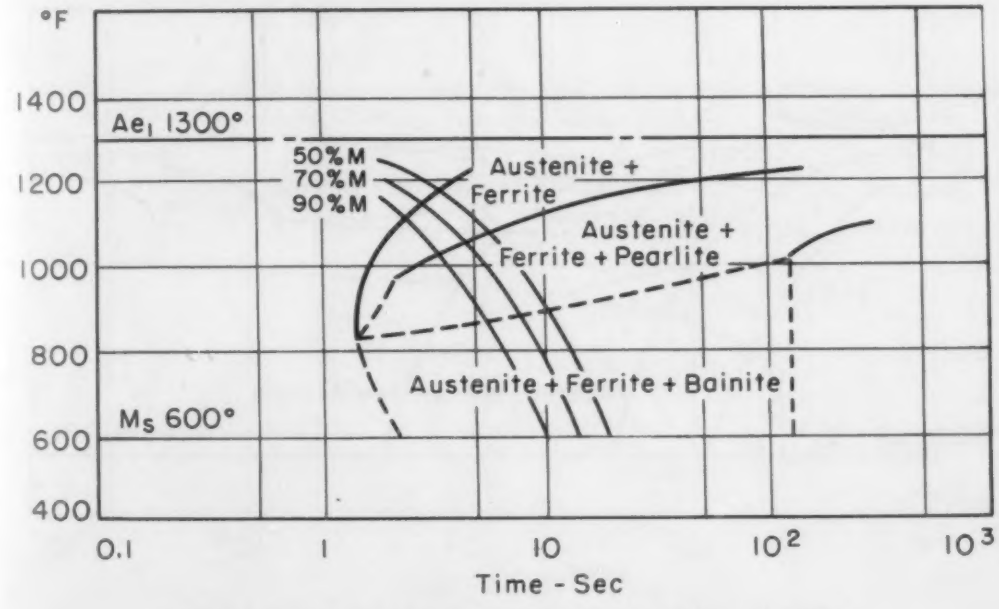


Fig. 4—Cooling Transformation Diagram of SAE 1340 Steel.

at the mean temperature $\frac{1}{2}$ $(T_1 + T_2)$ after a time interval of $(I_2 - I_1)$.

Cooling transformation diagrams so determined are given in Figs. 3 through 8. Those for SAE 1040, 1340 and 4040 steels contain areas wherein austenite decomposes to ferrite and pearlite directly over areas wherein austenite decomposes to ferrite and bainite. Most authors generalize by describing both of these areas as one large region representing the decomposition of austenite to ferrite and carbide. Since prediction of the nature of decomposition products is desired, it

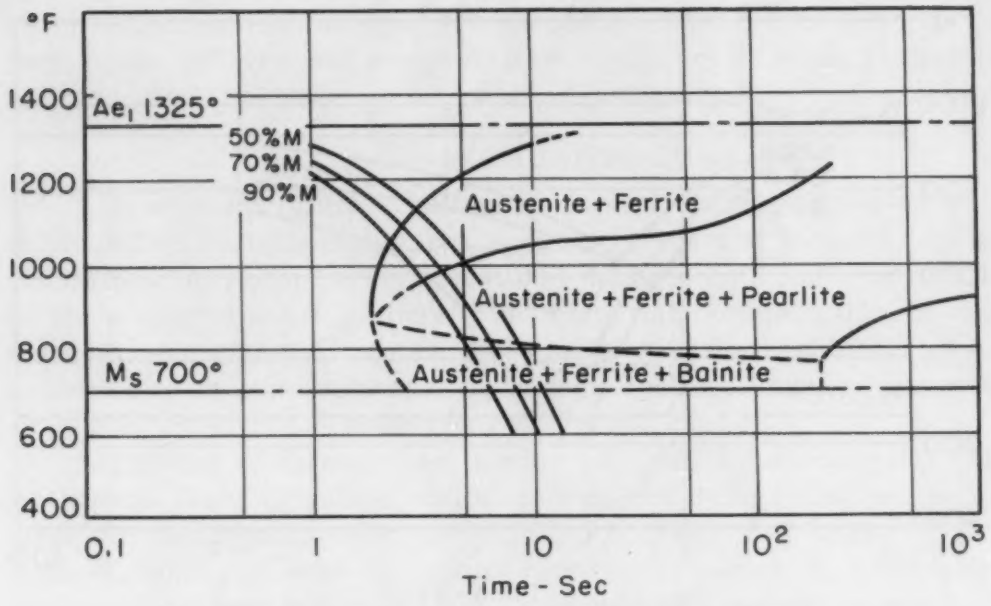


Fig. 5—Cooling Transformation Diagram of SAE 4040 Steel.

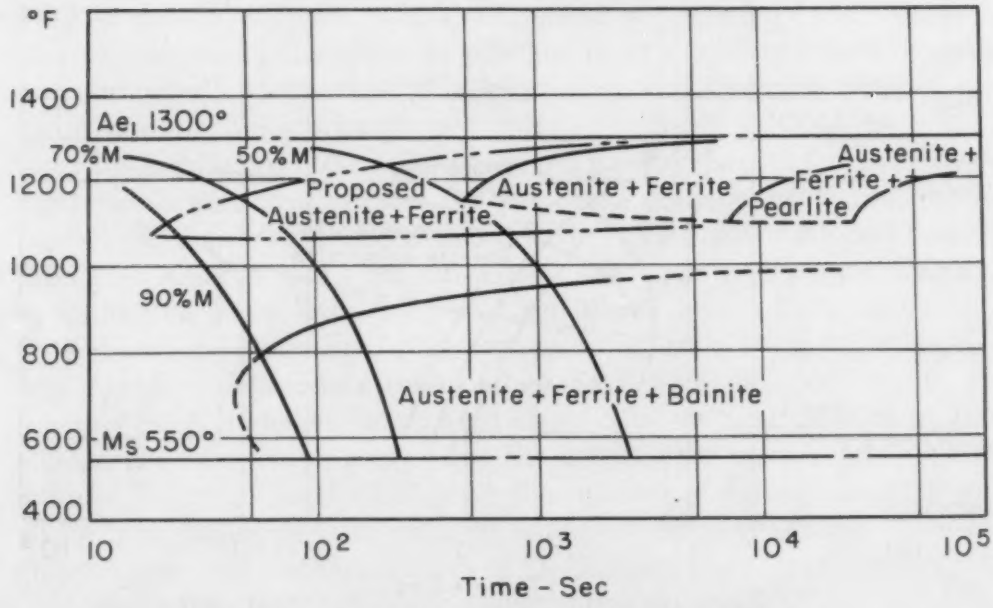


Fig. 6—Cooling Transformation Diagram of SAE 4340 Steel.

is necessary to divide this region into pearlitic and bainitic areas according to the temperatures and configurations of the diagrams involved. Therefore, the dashed line dividing these areas extends from the pearlite nose of the cooling transformation diagram to the lowest inflection point of the end-of-transformation line. Each is a point of inflection showing different rates of change at both higher and lower temperatures. Thus, the effects of two reactions are indicated. The higher temperature decomposition is to pearlite and the lower is to bainite. Insufficient data were available to allow distinction between

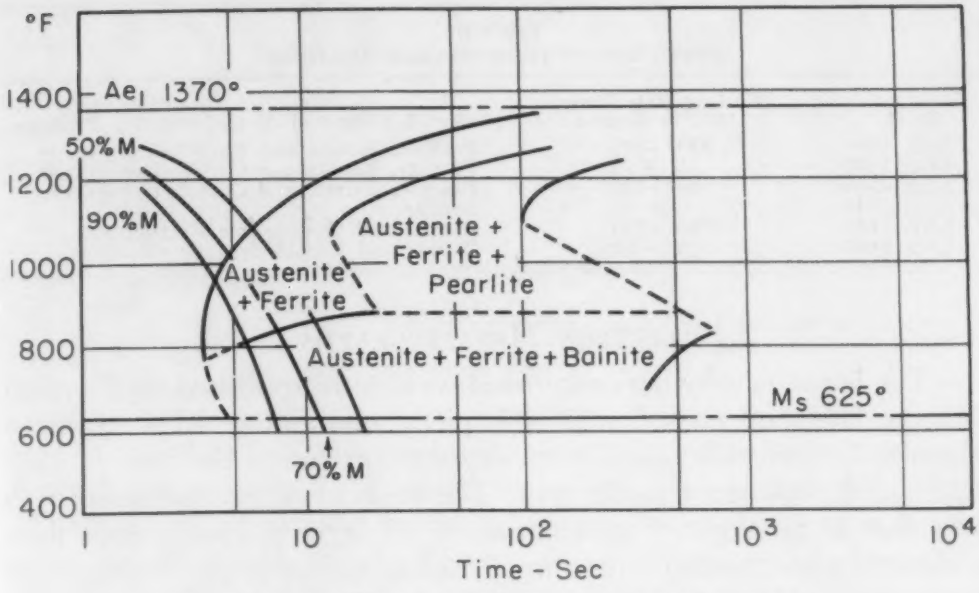


Fig. 7—Cooling Transformation Diagram of SAE 5140 Steel.

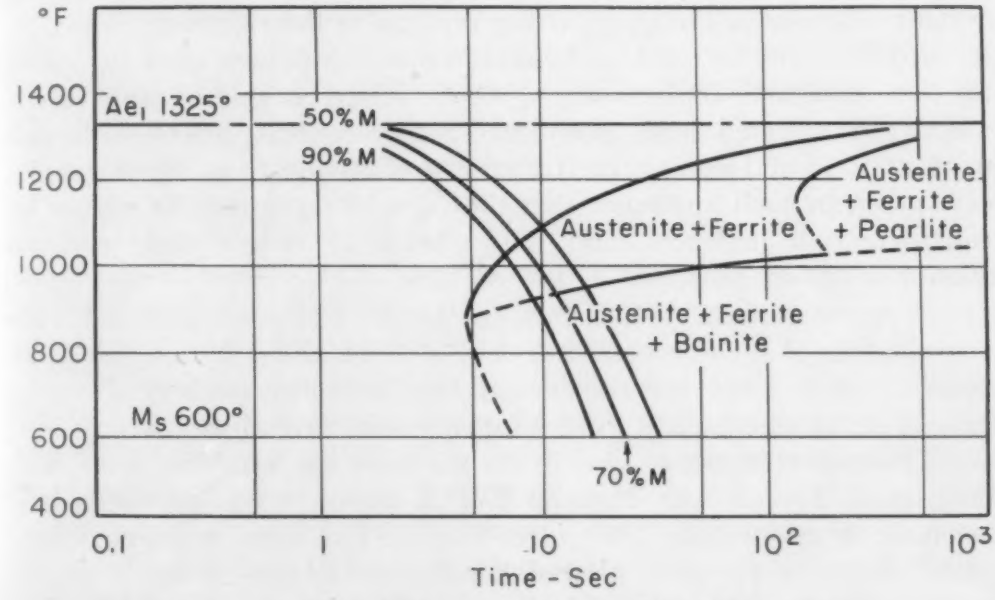


Fig. 8—Cooling Transformation Diagram of SAE 8640 Steel.

areas of upper and lower bainite. Differentiation between these products could be made only on the basis of microstructure.

Curves indicating the cooling rates for 90, 70 and 50% martensitic areas as determined from hardenability data were plotted from the Ae_1 temperature on the cooling transformation diagram of each steel. The nature of their transformation products was then predicted from consideration of the mode of intersection of the cooling curves with the diagrams. Table III lists the predictions made from consideration of Figs. 3 through 8.

Table III
Predictions of Transformation Products

Steel	Cooling Rate Range °F Per Second	Predicted Nature of Transformation Products
SAE 1040	130 –240	Pearlite, Bainite and Carbide-free Ferrite
SAE 1340	36 – 75	Pearlite, Bainite and Carbide-free Ferrite
SAE 4040	60 –100	Pearlite, Bainite and Carbide-free Ferrite
SAE 4340	0.2– 8	Bainite
SAE 5140	40 –100	Bainite and Carbide-free Ferrite
SAE 8640	30 – 60	Bainite and Carbide-free Ferrite

Electron Metallography

The hardenability bars examined were finish-polished on diamond abrasive laps and etched with 4% picral containing 0.1% zephiran chloride. Parlodion replicas were dry-stripped from the bars at each 90, 70 and 50% martensitic area. The replicas were shadowed with chromium at an angle of approximately 45 degrees. Impressions used in obtaining hardenability data were used as guides in positioning 200-mesh nickel grids at the proper areas for stripping of the replicas. Grids served the dual purpose of delineating rated areas for study in the electron microscope, and supporting replicas in the electron stream.

An RCA model EMU-2B electron microscope was used for viewing the shadowed replicas at × 4000. Electron micrographs were taken at the selected areas using lantern slide contrast plates. Enlarged prints at × 15,000 were made from the × 4000 negatives. Micrographs were taken in such a manner that they would represent the nature of transformation products, and not necessarily reflect their relative amount at a given position.

Progress reports (14, 15) issued by ASTM are concerned with identification of the microstructures of steel obtained through electron metallography. They are considered standards for isothermal work, and can serve as excellent guides for athermal investigations.

This report concerns 0.40% carbon steel hardenability bars, and the published work was done on 0.87% carbon steel specimens isothermally transformed. Therefore, the ASTM data must be interpreted to apply to these altered conditions. Since all steels under investigation are hypoeutectoid, they can contain proeutectoid ferrite, a structure not studied by the ASTM Committee.

Some of the transformation products in martensite were underdeveloped in nature. Thus, differentiation between embryonic upper bainite and pearlite was difficult. Comparison of these structures in the ASTM papers was made on the basis of carbide size and orientation. Since randomness, or order, of carbide distribution and relative size could not always be determined, another criterion of comparison was used in this investigation.

The acicular nature of bainite has been well established in both light and electron metallography. Likewise, the equiaxed grain struc-

Table IV
Identification of Transformation Products

Fig. No.	Steel	Percent Martensite	Identity of Transformation Products
9	SAE 1040	90	Ferrite in Martensite (Pearlitic)
10	SAE 1040	70	Pearlite, Upper Bainite and Carbide-free Ferrite
11	SAE 1340	50	Upper Bainite and Carbide-free Ferrite
12	SAE 1340	90	Pearlite and Carbide-free Ferrite
13	SAE 4040	50	Pearlite and Upper Bainite
14	SAE 4040	70	Pearlite and Upper Bainite
15	SAE 8640	50	Lower Bainite
16	SAE 8640	50	Upper Bainite
17	SAE 5140	70	Lower Bainite
18	SAE 5140	50	Carbide-free Ferrite, Upper and Lower Bainite
19	SAE 4340	90	Carbide-free Ferrite and Upper and Lower Bainite
20	SAE 4340	50	Lower Bainite

ture of pearlite has also been established. In this report, areas of electron micrographs in question were identified as upper bainite if they displayed an acicular habit and as pearlite if they were rhombohedral or equiaxed in nature. The typical cross-striated structure found in lower bainite needles was considered as readily identifiable in transformation products as in the ASTM specimens.

The embryonic nature of transformation products also became apparent in some wholly pearlitic areas. Incomplete decomposition apparently resulted in lamellae of ferrite and martensite rather than ferrite and carbide. Such areas, although not pearlite in the strict sense were regarded as pearlitic in habit for the purposes of classification.

Identification of Transformation Products

Figs. 9 through 20 are representative electron micrographs taken at the rated areas of each steel. All photomicrographs are captioned, and a summary of their structures is given in Table IV.

Transformation products in the shallow hardening steels exhibited a marked pearlitic tendency. However, in these steels (SAE 1040, 1340 and 4040) areas of carbide-free ferrite and upper bainite were found to coexist with pearlite in martensite. The deeper hardening steels contained upper and lower bainite and carbide-free ferrite as transformation products. The occurrence of proeutectoid ferrite in the martensite of SAE 4340 steel was not predicted from consideration of the cooling transformation diagram. However, carbide-free ferrite was found in transformation products of SAE 4340 steel to the same relative extent as it was found in SAE 5140 and 8640 steels. The possibility that retained austenite could have been mistaken for carbide-free ferrite was investigated by X-ray diffraction methods. A G.E. XRD-3 direct-reading unit using chromium Kα radiation at a tube voltage of 35 KV and 22 milliamperes was employed. This diffraction study revealed that no austenite was present in the investigated areas of the SAE 4340 sample. The martensite matrices appeared roughened and to have a subgrain structure. No lower bainite was found in the marten-

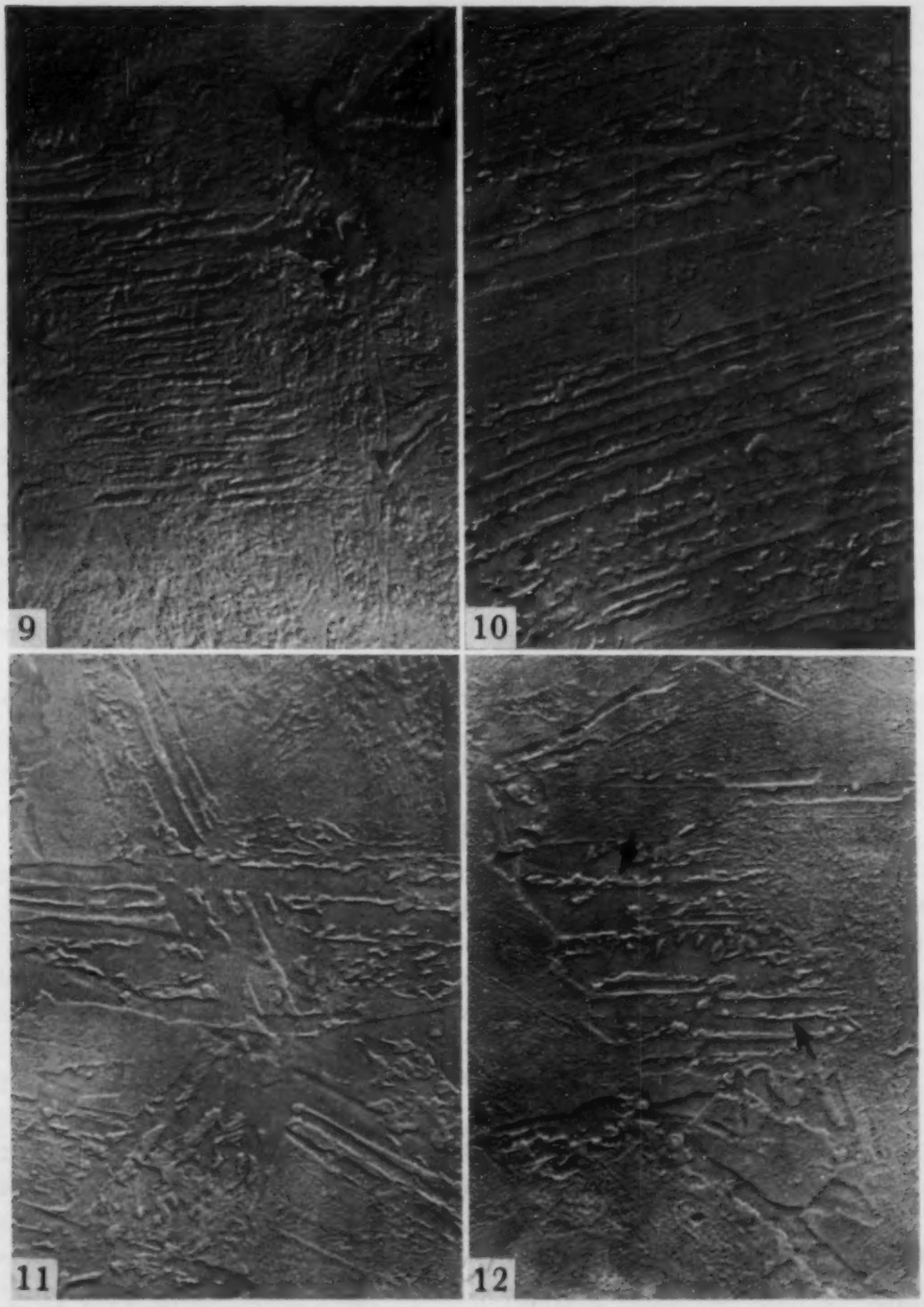


Fig. 9—SAE 1040 at an Area of 90% Martensite. Ferrite has Precipitated Along Preferred Planes Retained from the Prior Austenite and Displays the Pearlitic Habit within the Martensite Matrix. The Arrow Points to an Area of Pro-eutectoid Ferrite. X 15,000.

Fig. 10—SAE 1040 at an Area of 70% Martensite. The Area Shown is Largely Pearlitic in Nature, But Contains Some Carbides Oriented in the Manner of Upper Bainite as May be Seen at the Bottom of the Micrograph. X 15,000.

Fig. 11—SAE 1340 at an Area of 50% Martensite. The Intersection of Several Needles Containing Ferrite and Carbides Oriented as Upper Bainite is shown. X 15,000.

Fig. 12—SAE 1340 at an area of 90% Martensite. Some Carbide-free ferrite areas Exist, and the Arrows Indicate an Area Containing Ferrite and Carbides in the Pearlitic Habit. X 15,000.

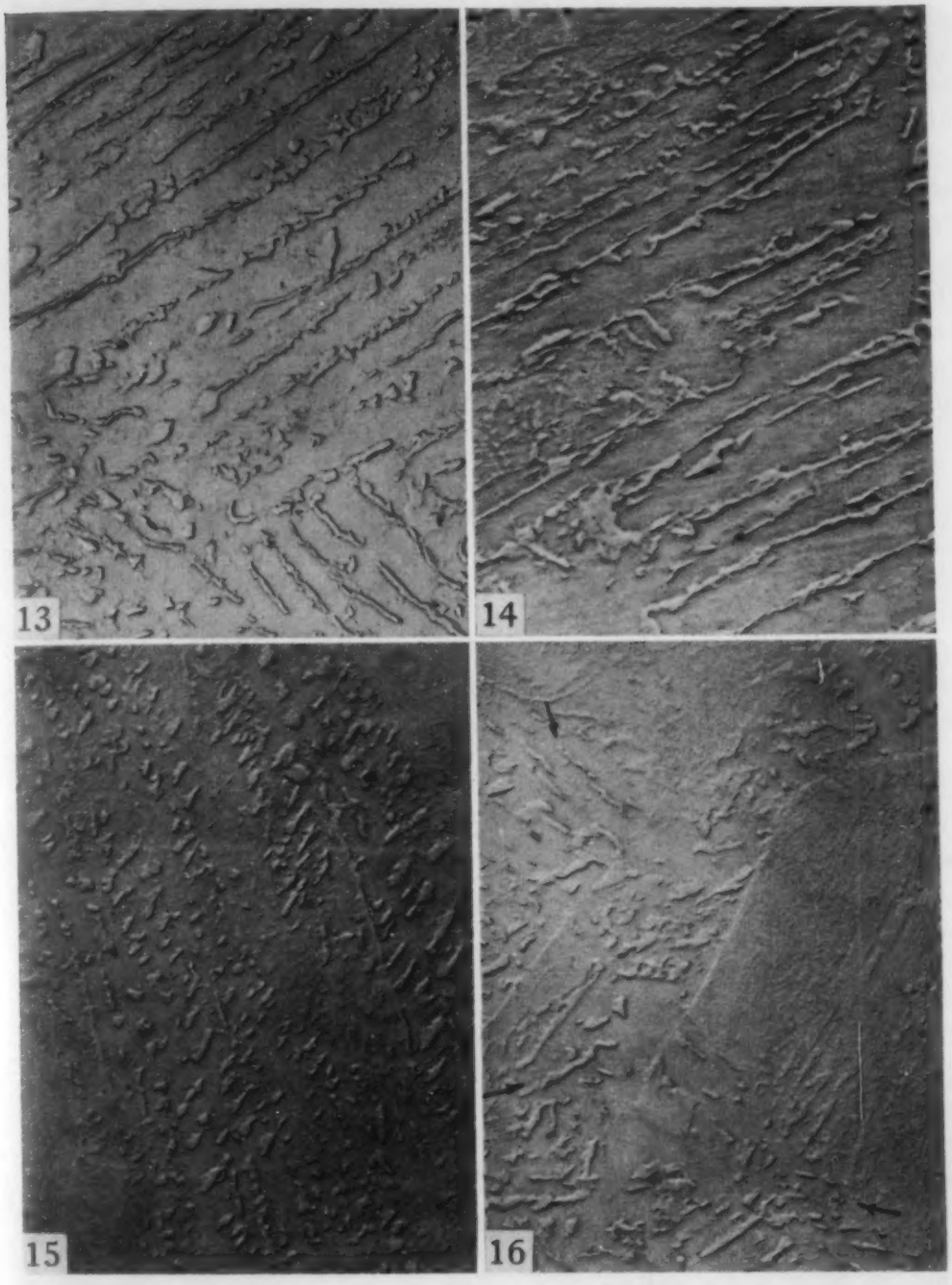


Fig. 13—SAE 4040 at an Area of 50% Martensite. The Area is Predominately Pearlitic with Some Carbides Oriented in the Manner of Upper Bainite. No Martensite is Present in the Micrograph. X 15,000.

Fig. 14—SAE 4040 at an Area of 70% Martensite. The Long Carbides Are Oriented in a Pearlitic Manner, while Those at the Right Appear as Upper Bainite. X 15,000.

Fig. 15—SAE 8640 at an Area of 50% Martensite. Several Needles of Lower Bainite are Oriented so that Their Axes are Nearly Vertical. A Cross-striated Habit is evident, which is Typical of Carbides in Lower Bainite. X 15,000.

Fig. 16—SAE 8640 at an Area of 50% Martensite. The Electron Micrograph Shows an Area of Upper Bainite Containing Carbides Oriented in Several Directions as Shown by the Arrows. This Indicates the Intersection of Several Upper Bainite Needles. X 15,000.

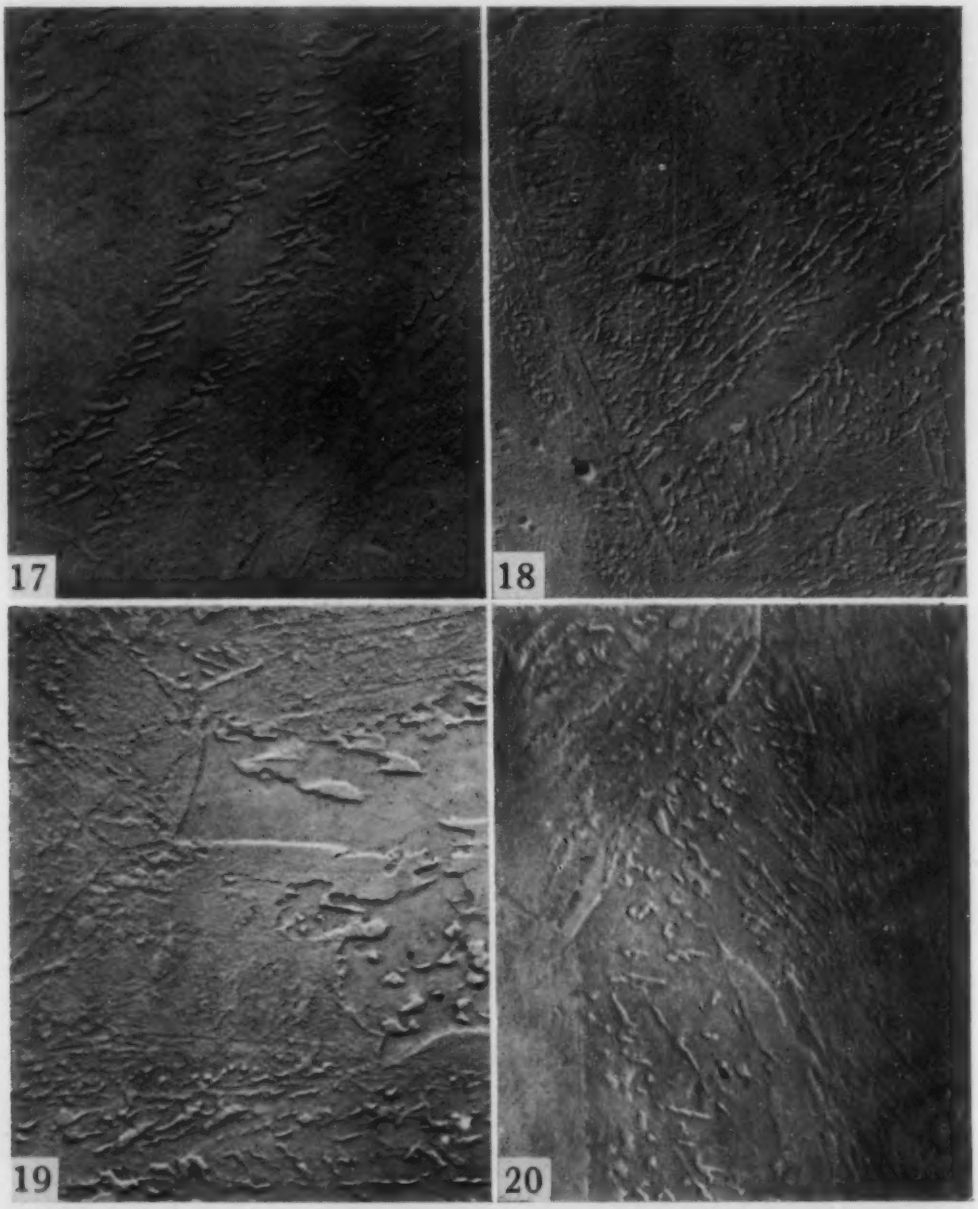


Fig. 17—SAE 5140 at an Area of 70% Martensite. A Long Needle of Lower Bainite is Shown, Containing Cross-striated Carbides at Angles of About 60 degrees to its Axis. X 15,000.

Fig. 18—SAE 5140 at an Area of 50% Martensite. A Bainitic Area is Shown Containing Carbides Oriented Both Parallel to its Axis in the Manner of Upper Bainite, and at 60 degree Angles to its Axis in the Manner of Lower Bainite. The arrow points to the Region of Upper Bainite. X 15,000.

Fig. 19—SAE 4340 at an Area of 70% Martensite. A Needle of Lower Bainite Appears at the Bottom of the Micrograph. A Large Area of Ferrite at the Upper Right is Relatively Carbide-free. X 15,000.

Fig. 20—SAE 4340 at an Area of 50% Martensite. A Portion of a Large Needle Containing Carbides Oriented in the Manner of Lower Bainite is Shown. X 15,000.

site of the shallow hardening steels, nor was any pearlite found in the martensite of the deeper hardening steels.

Discussion

It is now evident that the transformation products which could

not be resolved with the light microscope are finely divided products of austenite decomposition, or ferrite, pearlite, upper bainite and lower bainite. The martensite subgrain structure requires further investigation, and may well be explained as being intermediate in the austenite decomposition when improved metallographic techniques enable resolution at levels greater than × 15,000. The electron microscope, itself, is capable of higher magnification and greater resolution. However, electron metallographic technique is limited by both the resolving power of the etchant and the resolving power of the plastic replica (16). In this investigation, it was experienced that exposure of negatives at levels much greater than × 4000 resulted in empty magnification and loss in definition. Correspondingly, very little was gained by enlarging final prints to magnifications beyond × 15,000.

Consideration of the electron micrographs corroborates the concept that pearlite and upper and lower bainite are carbide-ferrite agglomerates differing only in the mode of their carbide precipitation. A corrolary to this concept may also be drawn: Pearlite or upper bainite or lower bainite will be of the same configuration in the martensite of all incompletely transformed steels. The amount of proeutectoid constituent may vary with the carbon content, but the arrangement of carbides within any given type of ferrite-carbide agglomerate in martensite is the same.

For example, pearlite in SAE 1340 steel is similar to pearlite in SAE 4040 steel as shown by Figs. 12 and 14. Likewise, lower bainite in SAE 8640 steel is similar to that in the martensite of SAE 4340 steel as illustrated by Figs. 15 and 19. Thus, there is a lack of direct correlation between the chemical content (exclusive of carbon) and the microstructure of alloy steels that have been incompletely hardened. However, correlation has been established between chemical content and the hardenability of alloy steels. This report indicates that the nature of decomposition products in martensite is dependant on the hardenability of a given steel. Therefore, it may be summarized that alloy content will not influence the configuration of the ferrite and carbides in each decomposition product, but it will be a factor in determining which decomposition products will be present in the martensite of an incompletely hardened steel.

Interpretation of the electron micrographs also indicates that the same transformation products have been found in all rated areas of each given steel whether they contain 90 or 50% martensite. Thus, the suggestion of Hollomon and Jaffe (4) that the first nonmartensitic product is bainite does not appear to hold true for shallow hardening steels. Upper bainite was found only in conjunction with pearlite in SAE 1040, 1340 and 4040 steels, even at 90% martensitic areas. It seems much more likely that the first nonmartensitic product will be a proeutectoid constituent rather than a carbide-ferrite agglomerate;

either carbide-free ferrite or cementite, depending on the carbon content of the alloy in question.

Analysis of the cooling transformation diagram of SAE 4340 steel did not lead to prediction of the carbide-free ferrite that was found in the electron micrographs. Recent unpublished work (17) on the magnetic determination of the SAE 4340 steel cooling transformation diagram agrees with this electron micrographic evidence. Thus, the accuracy of the published isothermal transformation diagram (6) upon which Fig. 6 was based can be questioned. It is believed that reinvestigation of this diagram will disclose an enlarged proeutectoid ferrite region. An estimated revision of the cooling transformation diagram of SAE 4340 steel based on current data is indicated by dashed lines in Fig. 6. Since one in six of these steels investigated revealed discrepancies in isothermal data, other steels may require reinvestigation. Isothermal transformation diagrams for many steels were obtained before current techniques attained their present stage of development.

Consideration of Figs. 3 through 8 resulted in accurate prediction of the nature of decomposition products found in the martensite of the steels investigated. These predictions also emphasize dependance on hardenability. Deep hardening steels do not contain pearlite in martensite, because, due to retarded initial decomposition, their austenite does not begin to change until such low temperatures are reached that pearlite is unable to form. Conversely, the austenite decomposition in shallow-hardening steels is initiated at such high temperatures that pearlite must form.

From the thermodynamic concept, in end-quenched shallow hardening steels the free energy of formation of pearlite is greater than that of the formation of upper bainite over a range of temperature from the beginning of austenite decomposition to the pearlite nose of the cooling transformation diagram as indicated in Fig. 21. Below the nose and extending to the Ms temperature, the free energy of upper bainite formation is greater than that of pearlite formation. Below the Ms the free energy of formation of martensite is greater than either that of pearlite or upper bainite. Likewise, in end-quenched deep hardening steels, the free energy of upper bainite formation is the greater over the higher range of temperature, and that of lower bainite is the greater from some intermediate temperature down to the Ms temperature. It is understood that at rates faster than the critical cooling rate, these relationships are still valid, but that insufficient time is available for the proper amount of carbon diffusion to satisfy the several conditions of equilibrium.

It should be emphasized that the three reactions: austenite → pearlite; austenite → upper bainite and austenite → lower bainite are similar in that all may be written: austenite → ferrite + carbide. The electron micrographs show that the differences among ferrite-carbide

agglomerates lie in the mode of carbide precipitation in ferrite. For example, the long carbide plates of pearlite are the most stable (possess the greatest free energy of formation) at higher temperatures in shallow hardening steels as they are cooled toward the pearlite nose, while the shorter and cross-striating carbides of lower bainite are the most stable of all carbide configurations in deep hardening steels at temperatures near the Ms temperature. The fact that upper bainite and either pearlite or lower bainite can coexist in martensite indicates that,

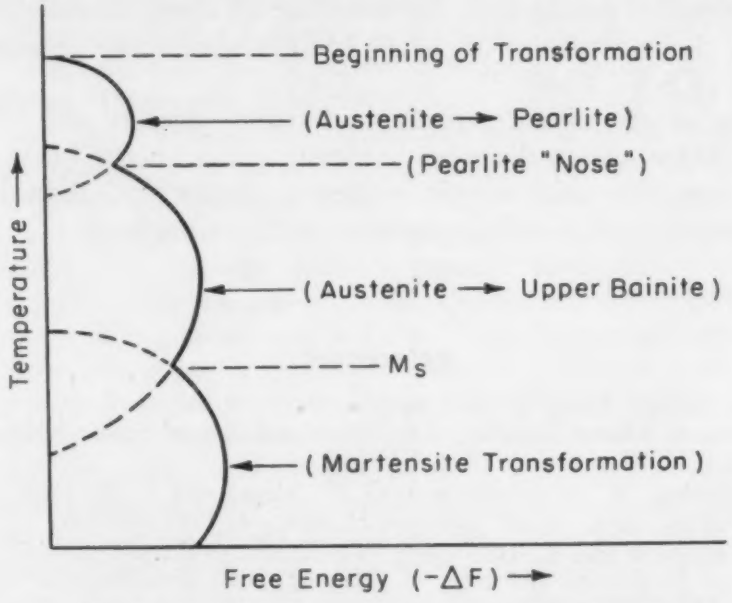


Fig. 21—Relation Between Temperature, Free Energy and Austenite Decomposition in a Shallow-Hardening Steel.

once formed, a decomposition product possesses a sufficiently large energy of activation that it does not undergo further change. If this were not the case, then transformation products would have been identified as consisting of only lower bainite and no steel would contain pearlite no matter how slowly it was cooled.

The following conclusions have been drawn from consideration of the results of this investigation:

1. The transformation products associated with martensite in incompletely hardened steels can be resolved and identified by electron microscopy.

2. The transformation products in the incompletely hardened shallow hardening steels (SAE 1040, 1340 and 4040) consist of ferrite and ferrite-carbide agglomerates identified as pearlite and upper bainite.

3. The transformation products in the incompletely hardened deeper hardening steels (SAE 4340, 5140 and 8640) consist of ferrite and ferrite-carbide agglomerates identified as upper and lower bainite.

4. The nature of transformation products in incompletely

hardened alloy steels can be predicted from consideration of applicable hardenability data and cooling transformation diagrams.

5. With each individual steel investigated it was found that the same transformation products were always present whether that steel contained 90, 70 or 50% martensite. Between grades of steel these products can vary.

6. The physical appearance of the phases (ferrite and carbide) comprising the constituents (pearlite, upper bainite or lower bainite) of transformation products is the same for all steels investigated, (e.g. pearlite in the martensite of SAE 1340 is similar to pearlite in the martensite of SAE 4040).

7. The extent of the proeutectoid ferrite area of the SAE 4340 cooling transformation diagram is questionable on the basis of magnetic and electron microscopic evidence. Isothermal data on other steels may also require reinvestigation by these methods.

References

1. Albert Portevin, *Revue de Metallurgie,* 1917.
2. H. J. French, "Some Aspects of the Hardenability of Steels," METAL PROGRESS, Vol. 59, April, 1949, p. 505–515.
3. W. E. Jominy, M. A. Grossmann, G. C. Riegel and C. B. Post, "Hardenability of Steel," ASM METALS HANDBOOK, 1948 Edition.
4. J. H. Hollomon and L. D. Jaffee, "The Hardenability Concept," *Transactions,* American Institute of Mining and Metallurgical Engineers, Vol. 167, 1946, p. 601.
5. Chrysler Engineering Form 684S, revised.
6. U. S. Steel, *Atlas of Isothermal Diagrams,* 1951, Supplement 1953.
7. SAE-AISI, "Hardenability of Alloy Steels—Contributions to the Metallurgy of Steels," No. 11, June, 1947.
8. J. M. Hodge and M. A. Orehoski, "Relationship Between Hardenability and Per cent of Martensite in Some Alloy Steels," *Transactions,* American Institute of Mining and Metallurgical Engineers, Vol. 167, 1946, p. 627.
9. R. A. Grange and J. M. Kiefer, "Transformation of Austenite on Continuous Cooling and Its Relationship to Transformation at Constant Temperature," TRANSACTIONS, American Society for Metals, Vol. 29, 1941, p. 85.
10. C. A. Liedholm, "Continuous Cooling Diagram—From Modified End-Quench Method," METAL PROGRESS, Vol. 45, 1944, p. 94.
11. R. A. Grange, personal communication.
12. "Republic Alloy Steels," 166, 1949.
13. R. A. Grange and H. M. Stewart, *Metals Technology,* June, 1946.
14. ASTM, "Electron Microstructure of Bainite in Steels," *Proceedings,* American Society for Testing Materials, Vol. 52, 1952.
15. ASTM, "Electron Microstructure of Steels," *Proceedings,* American Society for Testing Materials, Vol. 50, 1950.
16. ASTM, "Techniques for Ferrous Electron Metallography," *Proceedings,* American Society for Testing Materials, Vol. 53, 1953.
17. R. D. Chapman and W. E. Jominy, "A Method for Determining the Continuous Cooling Transformations in Steel," TRANSACTIONS, American Society for Metals, Vol. 47, 1955.

DISCUSSION

Written Discussion: By Bernard S. Lement, Research Staff (Division of Industrial Co operation), Massachusetts Institute of Technology, Cambridge, Mass.

I would like to point out that Fig. 21 does not properly show the variation of free energy of formation ($-\Delta F$) with temperature for the pearlite, bainite, and martensite reactions. The free energy of formation for each of these reactions should be shown as continually increasing with decrease in temperature rather than first increasing and then decreasing to a zero value.

The authors imply that it is necessary for the free energy of formation of bainite to be greater than that of pearlite in order for bainite to form; and for the free energy of formation of martensite to be greater than that of bainite in order for martensite to form. This is doubtful since at any temperature below $A\gamma_1$, the free energy of formation of pearlite would be expected to be greater than that of either bainite or martensite.

From a thermodynamic point of view, a given reaction has the possibility of occurring if the free energy change is negative. However, whether the reaction will actually occur depends on rates of nucleation and growth. The principal factor controlling these rates is the activation energy associated with each process. The activation energy for the reaction as a whole is some combination of the activation energies for nucleation and growth. At a given temperature, the reaction that actually occurs is the one with the lowest activation energy. Thus, below the pearlite nose, bainite forms in preference to pearlite because the bainite reaction has a lower activation energy. Even though the free energy of formation may be lower than that of pearlite, the factors controlling kinetics are in favor of bainite formation.

Written Discussion: By Subrata Bhattacharyya, research associate, Columbia University, New York.

The authors have proposed that the appearance of a relatively carbide-free ferrite area in Fig. 19 indicates the presence of proeutectoid ferrite in their 70% martensitic structure of SAE 4340 steel. They have also checked that no retained austenite is present in the resulting structure.

Some electron-micrographic investigation has been carried out at Columbia University on isothermal transformation products of AISI 4340 steel, both at the lower and upper bainite temperature levels. At a transformation temperature of 845 °F, electron-micrograph of a partially transformed bainitic structure, as shown in Fig. 22, indicates many large ferrite areas free of carbide. At this temperature and under isothermal transformation condition no proeutectoid ferrite could be present in the structure. The large carbide-free ferrite areas could very well result from the fact that the orientation of the plane of polish was such that in those areas carbide particles were not intersected by the plane of polish. Also, this could be explained if we consider that for some reason, in these alloy steels carbide precipitation does not take place absolutely at random. It is also to be noticed in your Fig. 19 and in the given Fig. 22 that these relatively large carbide free areas are present in close proximity to the martensitic areas. With complete transformation and with time for far more uniform distribution of diffusing elements, appearance of such relatively large carbide-free areas will be insignificant. This has been verified in our investigation. Thus, it seems, that the ferrite in Fig. 19 may not be proeutectoid ferrite but is similar to what is

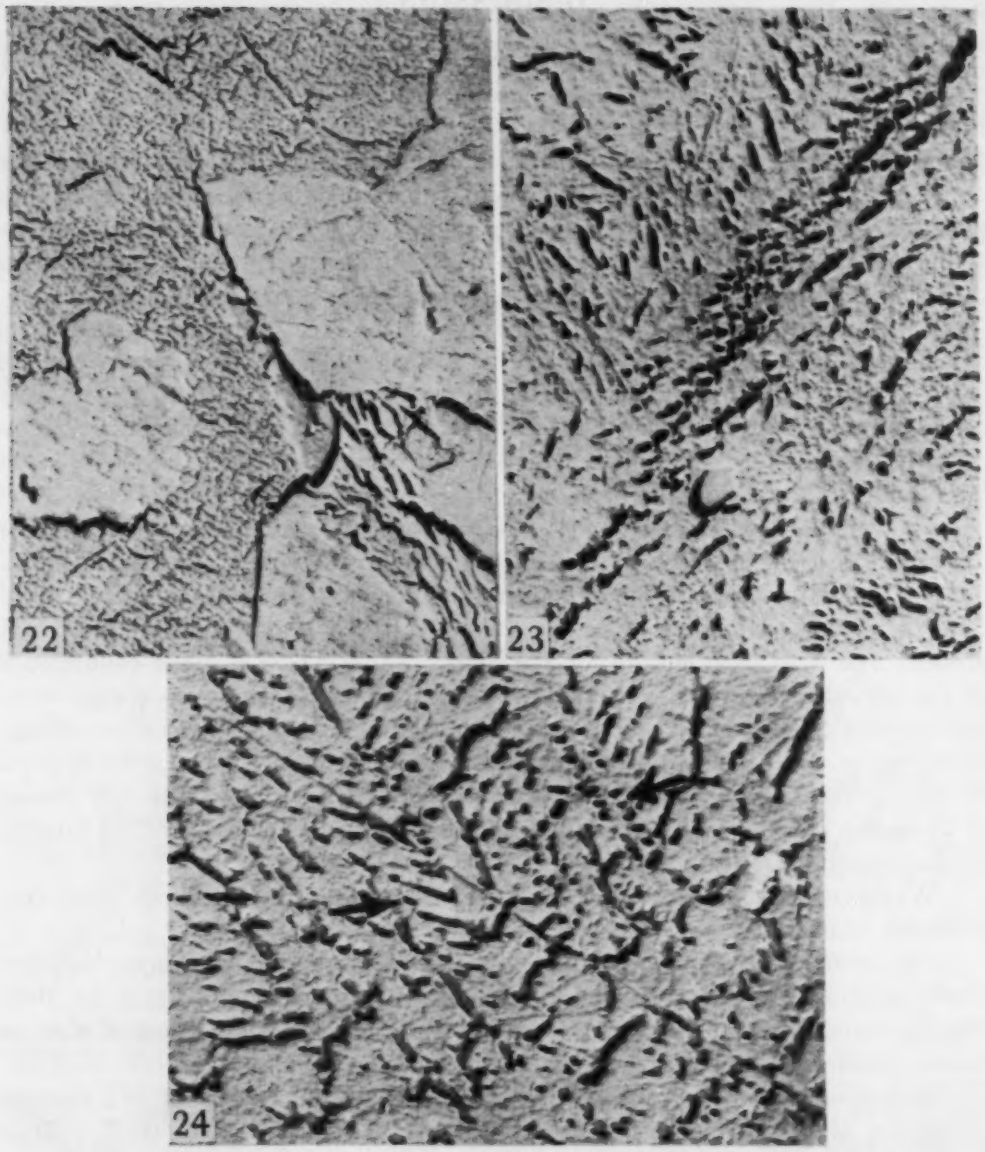


Fig. 22—Electron Photomicrographs of Upper Bainite Isothermally Formed at 845 °F for 100,000 seconds in AISI 4340 Steel. X 21,000. Etched in Saturated Picral. Ferrite areas can be seen within martensitic area and adjacent to it. Fine, short, black wavy lines in martensite are shadows of cracks in the replica. This is a reverse print.

Fig. 23—Electron Phontomicrograph of Lower Bainite Isothermally Formed at 650 °F for 1200 seconds in AISI 4340 Steel. X 12,000. Etched in Saturated Picral. Cross-striated appearance of carbide particles indicative of lower bainite structure. This is a reverse print.

Fig. 24—Electron Photomicrograph of Upper Bainite Isothermally Formed at 845 °F for 10,000 seconds under 60,000 psi stress in AISI 4340 Steel. X 12,000. Etched in Saturated Picral. Arrows indicate oriented appearance of some carbide particles indicative of lower bainite structure. This is a reverse print.

indicated in Fig. 22. It therefore appears that more clear evidence of proeutectoid ferrite formation is necessary before any alteration in the present T-T-T diagram of AISI 4340 steel can be suggested.

Table IV of the paper under discussion, indicates that in SAE 4340 steel, when 50% of austenite is transformed under continuous cooling, the transformation product is lower bainite and an electron-micrograph of such a structure is

shown in Fig. 20. Table IV also indicates that at a faster cooling rate, when only 10% of austenite is transformed, the transformed structure is carbide-free ferrite, upper and lower bainite. Fig. 6 of this paper, however, indicates that with a slower cooling rate (50% martensite), the structure that is first formed will be in the upper bainite transformation range and thus one would expect more upper bainite in 50% martensitic structure in comparison to that in either 70% or 90% martensitic structure.

At 650 °F, the isothermal transformation product is lower bainite, as expected, and cross-striated appearance of the bainite is shown in Fig. 23. At 845 °F, such cross-striated appearance is very seldom observed in the distribution of carbide particles in the microstructure, but occasionally such is observed, and is shown in Fig. 24 as indicated by arrows. Possibly, lower to upper bainitic structural transition under isothermal condition begins around 800 °F and is completed not much above 850 °F.

Written Discussion: By R. A. Grange, United States Steel Corp., Fundamental Research Laboratory, Kearny, N. J.

Reliable classification of the ferrite-carbide aggregate structures which are developed in steel continuously cooled from the austenitic state is often difficult, if not impossible, using the optical microscope; the authors are to be complimented for undertaking a pioneering study which applied the electron microscope to this problem.

Using the electron microscope, the authors observed proeutectoid ferrite in specimens of 4340 steel cooled considerably faster than the critical cooling rate for proeutectoid ferrite according to a cooling transformation diagram estimated from isothermal data for a different heat of 4340 steel (Fig. 6). This led them to question the accuracy of the isothermal transformation diagram. If the following factors are considered, this apparent discrepancy demonstrates a limitation rather than an inaccuracy in isothermal transformation data.

First, no single isothermal transformation diagram can precisely represent all heats of the grade of steel to which it applies. This is particularly true in the case of 4340 steel which, with elements on the high side of the permissible chemical composition range, will develop almost no proeutectoid ferrite and yet, with elements on the low side, is decidedly hypoeutectoid. Add to this the possibility of chemical segregation in any particular sample, and it is to be expected that the amount of proeutectoid ferrite formed and, especially, the time required for proeutectoid ferrite to begin to form from austenite under either isothermal or continuous cooling conditions will vary appreciably among different heats of 4340 steel.

Secondly, in common with most other isothermal transformation diagrams, the line representing the beginning of transformation in the 4340 isothermal transformation diagram referred to by the authors is based upon some arbitrary but definite amount of transformation rather than upon the first minute trace detectable anywhere in a specimen by means of the optical microscope. In this particular diagram, the beginning lines are based upon nominally 0.1% of transformation. A proeutectoid ferrite beginning line based upon the first trace of ferrite detectable with the optical microscope would be to the left of that shown in the published 4340 isothermal transformation diagram, and there would hence be less difference between it and the authors' results using the electron microscope. It is pertinent to inquire of the authors as to the amount

of proeutectoid ferrite upon which the beginning line, as constructed in their Fig. 6, is based.

Authors' Reply

The authors appreciate the comments and suggestions of Messrs. Lement, Bhattacharyya, and Grange.

Dr. Lement has commented on Fig. 21 from the viewpoint of classical thermodynamics. His views agree with current writings. However, we think they are not entirely applicable to the problem at hand. We believe that two of the assumptions on which they are based are not entirely correct: (a) that equilibrium conditions exist and (b) that austenite decomposition can be represented by a single equation.

Table III of the paper indicates estimated cooling rates of areas of the end quench bars that were investigated. The rapidity with which these areas were cooled from Ae_1 to the M_s temperatures precluded establishment of equilibrium during formation of nonmartensitic transformation products. We have also shown that although the austenite change can be represented by the equation: austenite $\longrightarrow$ ferrite + carbide, we consider that more accurate representation may be gained by use of the three relations: austenite $\longrightarrow$ pearlite, austenite $\longrightarrow$ upper bainite and austenite $\longrightarrow$ lower bainite. For the purpose of this treatment, the formation of pro-eutectoid ferrite was not considered.

Concerning equilibrium conditions, we believe that the systems: austenite $\longrightarrow$ pearlite and austenite $\longrightarrow$ upper bainite are approaching a form of equilibrium with each other in the region of the pearlite nose. A similar situation exists between the system austenite $\longrightarrow$ lower bainite and the martensite transformation at M_s temperature. If the austenite change to nonmartensite decomposition products was thought to be represented by a single relation, the points of intersection of the curve in Fig. 21 at the pearlite nose and M_s temperatures could be considered as possible points on the free-energy temperature curve. It will be noted that these two points are indicative of constantly increasing free energy ($-\Delta F$) with decreasing temperature. Rapid cooling of the end quench bars prevented consideration of single-reaction equilibrium at other temperatures.

Passage of the separate curves through maxima is not considered contrary to current concepts, and it will be noted that the position of zero free energy has not been indicated on the abcissa of Fig. 21. The three curves were drawn to indicate the role of each reaction during austenite change to the nonmartensitic transformation products. Obviously, there was no need to represent them in their entirety. We are conscious of the importance of activation energy in consideration of reaction kinetics. We are also familiar with the concepts of pearlite nucleation by cementite and bainite nucleation by ferrite. Further, we know that two forms of bainite have been identified and that coarse pearlite may be differentiated from fine pearlite as a separate structure. Reconciliation of the structures of these three, and possibly four, products of austenite decomposition with the two proposed mechanisms of nucleation appeared exceedingly complex. Therefore, we employed the concept of the free energy-temperature diagram of Fig. 21. It was used to illustrate our concept of the relative importance of the separate reactions associated with austenite change to transformation products under the nonequilibrium conditions produced by continuous cooling.

Mr. Bhattacharyya has suggested that the carbide-free ferrite areas in SAE 4340 steel, as illustrated in Fig. 19, are the result of the mode of intersection of the cutting plane with the microconstituent. Further, he compares these areas with those of his Fig. 22.

The interpretation of Fig. 22 is difficult. Consideration of the highlights produced by shadowing discloses several etched levels. The few scratches present do not vary in appearance from martensite to what is described as ferrite, leaving doubt whether the so-called ferrite areas are etched in the expected manner. The probability of the cutting plane exposing such large areas free of carbide is remote. Although the cracks in the replica obscure the structure, it is believed the only ferrite present in Fig. 22 are the small depressed areas near the center and at one edge of the micrograph. The ferrite in Fig. 19 is a proeutectoid ferrite, in that it formed before and did not take part in the decomposition of austenite to the two-phase mixture of ferrite + carbide.

Bhattacharyya has also compared the structures listed in Table IV with those which he has anticipated on the basis of Fig. 6. It must be emphasized that Table IV is a summary of structures appearing in the micrographs as stated on page 735 of our paper; it is not a description of overall microstructures for the given rated areas. It is repeated that the micrographs do not represent the relative amounts of the decomposition products, rather, only their nature. The relative amounts of microconstituents at any particular rated area is not a consideration of this paper. It is not believed that Fig. 6, or any of the cooling transformation diagrams indicates any more or less of one product than another at any rated area for a given steel. The cooling transformation diagrams are used in the qualitative sense only.

It is agreed that Bhattacharyya's Fig. 23 is representative of lower bainite and his Fig. 24 is representative of upper bainite. However, conjecture concerning the transition range of lower to upper bainite under isothermal conditions is beyond the scope of this paper.

In answer to the question of Mr. Grange, the line indicating the beginning of proeutectoid ferrite formation in Fig. 6 is an approximation based upon the appearance of carbide-free ferrite in areas of the SAE 4340 hardenability bar studied. We established no criterion as to the amount present. It should be emphasized that quantitative determination of microconstituents by electron microscopy is greatly complicated by the difficulty of obtaining pictures representative of the entire sample under consideration.

We agree that consideration of this factor and those of heat-to-heat variation and chemical segregation reconcile much of the disagreement between our results and isothermal transformation data.

CALCULATION OF HARDENABILITY IN HIGH CARBON ALLOY STEELS

By C. F. Jatczak and R. W. Devine, Jr.

Abstract

Hardenability effects of manganese, silicon, chromium, nickel and molybdenum, singly and in combination, were studied in 1.0% carbon steels by the end-quench test at quenching temperatures of 1475 to 1575 °F (800 to 855 °C) and from normalized and spheroidize annealed prior structures. An empirical procedure for calculation of hardenability, based upon multiplying factors, was devised which predicts hardenability from composition within about ±10% for normalized steels and ±15% for annealed steels.

Introduction

OUR interest in the effects of alloying elements on the hardenability of high carbon steels stems from necessity. Twice in the last ten years drastic curtailment of nickel has forced us to use other alloying elements as substitutes for part of the nickel contained in the AISI 4620 steel used in automotive bearing races. From the core hardenability standpoint, this substitution could be made readily from time-tested information. However, in considering case hardenability, a literature survey disclosed that what data were available at hypereutectoid carbon levels (1,2)[1] applied to austenitizing conditions designed to promote complete solution. Since our bearing races are quenched from the carburizing temperature and reheated to relatively low austenitizing temperatures for subsequent oil quenching, we were originally without worthwhile information relating to case hardenability. At normal hardening temperatures for double quenched cases of carburized steels and high carbon tool steels, carbide solution is incomplete and the excess carbide not only affects hardenability by robbing the austenite of alloy but also serves to nucleate subcritical transformation. Our own concern over case hardenability results from the fact that most races are quenched on a cold serrated plug with the hot race in contact with the plug lands. The consequent reduction of cooling rates of the surface layers, particularly in the subcritical temperature region, makes the subject of case hardenability one of real importance to us.

[1] The figures appearing in parentheses pertain to the references appended to this paper.

A paper presented before the Thirty-sixth Annual Convention of the Society, held in Chicago, November 1 to 5, 1954. The authors, C. F. Jatczak and R. W. Devine, Jr., are research metallurgists, Steel and Tube Division, The Timken Roller Bearing Co., Canton, Ohio. Manuscript received April 29, 1954.

As a result, a large amount of hardenability information has been amassed in our laboratory over a period of years. The approach has been largely unsystematic, but completely practical. The present paper is the result of an attempt to organize the available data into a form suitable for study of the effects of individual alloying elements. A completely empirical but, we believe, workable method of predicting hardenability from chemical composition under the conditions of testing imposed has resulted and will be described.

Procedure

At the outset, it was decided to use only 1.0% carbon steels as material for end-quench hardenability testing rather than carburized cases of low carbon steels because of the greater precision of the former and the fact that the maximum surface carbon of our carburized cases corresponds closely to this value.

Preliminary tests indicated complete agreement between the hardenability of 1.0% carbon alloy steels when end-quenched from a normalized prior structure and the 1.0% carbon level of the carburized end-quench bars when reheated to the same temperature and end-quenched. Limited data were obtained from annealed prior structures to compare with alloy tool steel practice.

Table I lists the chemical compositions of the steels used. The four digit heat numbers designate thirty pound induction heats while the five digit numbers correspond to basic electric production heats. All heats were forged or rolled to 1¼-inch diameter bars and spheroidize annealed before machining. After machining, the specimens designated for the normalized prior structure were heated to 1700 °F (925 °C) in salt for two hours and air-cooled. Those heat numbers followed by an "A" indicate that they were tested from the spheroidize annealed prior structure, while "N" designates the normalized condition. Where available, the production annealed hardness is given.

The standard ASTM end-quench procedure was used throughout except that final austenitization was accomplished in a neutral salt bath. Duplicate specimens were subjected to a 45-minute austenitizing treatment (35 to 40 minutes at temperature) at each of three temperatures, 1475, 1525, and 1575 °F (800, 830 and 855 °C). The criterion of hardenability used was the distance to Rockwell C-60, a value close to the acceptable minimum for bearing components and most tool steel applications. Microscopic examination of the structure of many of the specimens indicated a close agreement between the Rockwell C-60 point and 10% transformation for all but those quenched from the highest austenitizing temperature and some of the highly alloyed types where the presence of bainite began to interfere with the otherwise simple pearlitic transformation behavior.

The hardenability data are contained in Tables II and III for the

Table I
Chemistry of 1.00% Carbon Steels
Quenched From Normalized (N) and/or Annealed (A) Prior Structures

Heat No.	Chemistry C	Mn	Si	Cr	Ni	Mo	Annealed Hardness (B.H.N.)
BASE REFERENCE ANALYSIS (Values Based On Average of Seven Heats)							
Various Production Heats	1.00	0.39	0.27	0.16	0.16	0.02	—
SINGLE ALLOY STEELS							
Manganese Series							
Unknown N	0.99	0.32	0.26	0.24	0.20	0.01	—
Unknown N	1.00	0.46	0.14	0.25	0.30	0.01	—
Unknown N	1.02	0.50	0.26	0.23	0.24	0.02	—
10542 N	1.00	1.04	0.28	0.11	0.20	0.04	—
2790 N	1.06	1.14	0.17	0.37	0.33	0.01	—
Nickel Series							
2424 NA	0.99	0.32	0.32	0.02	0.34	0.01	179
2425 NA	0.99	0.31	0.34	0.03	0.58	0.01	179
2428 NA	0.98	0.32	0.33	0.02	1.06	0.01	187
2429 N	0.99	0.32	0.31	0.03	1.54	0.01	—
2430 NA	0.97	0.32	0.34	0.02	2.04	0.01	192
Chromium Series							
2434 NA	0.96	0.32	0.34	0.53	0.06	0.01	179
2435 NA	0.98	0.29	0.31	1.07	0.06	0.01	179
2436 NA	0.99	0.33	0.35	1.58	0.05	0.01	179
2437 NA	0.99	0.34	0.34	2.10	0.05	0.01	187
Molybdenum Series							
02330 N	1.00	0.28	0.14	0.31	0.30	0.12	—
02787 N	1.03	0.27	0.14	0.36	0.30	0.16	—
02698 N	1.00	0.28	0.28	0.12	0.40	0.20	—
02788 N	1.06	0.24	0.12	0.33	0.31	0.43	—
Silicon Series							
Unknown	1.00	0.32	0.26	0.24	0.20	0.01	—
2761 N	1.02	0.33	0.50	0.20	0.15	0.01	—
2762 N	0.99	0.30	0.66	0.20	0.27	0.02	—
MULTI-ALLOY (NICKEL-CHROMIUM-MOLYBDENUM) STEELS							
Standard 46100 Type (1.75% Nickel)							
1728 N	0.98	0.57	0.27	0.17	1.78	0.22	—
1735 N	0.97	0.71	0.24	0.17	1.75	0.24	—
1736 N	0.99	0.87	0.27	0.16	1.73	0.22	—
1733 N	0.98	0.41	0.23	0.32	1.77	0.22	—
1729 N	0.96	0.57	0.25	0.32	1.76	0.23	—
1734 N	1.00	0.71	0.24	0.32	1.73	0.23	—
1732 N	0.99	0.39	0.23	0.48	1.76	0.22	—
1731 N	0.96	0.46	0.25	0.48	1.77	0.23	—
1730 N	0.96	0.58	0.23	0.48	1.74	0.23	—
2123 N	0.98	0.46	0.28	0.46	1.76	0.22	—
2124 N	1.02	0.57	0.29	0.34	1.78	0.22	—
2125 N	0.98	0.71	0.30	0.20	1.78	0.23	—
2126 N	0.96	0.46	0.29	0.27	1.79	0.23	—
2127 N	0.98	0.63	0.27	0.31	1.78	0.22	—
Modified 46100 Type (1.50% Nickel)							
2062 N	1.01	0.55	0.28	0.17	1.48	0.23	—
2063 N	1.02	0.70	0.29	0.17	1.48	0.23	—
2064 N	1.01	0.95	0.29	0.16	1.47	0.23	—
2065 NA	0.99	0.45	0.30	0.31	1.50	0.23	—
2067 NA	1.04	0.65	0.29	0.32	1.51	0.22	—
2068 NA	1.01	0.76	0.28	0.28	1.51	0.20	—
2069 N	1.00	0.34	0.27	0.45	1.49	0.23	—
2070 N	1.03	0.48	0.27	0.45	1.50	0.24	—
2071 N	1.03	0.62	0.27	0.46	1.50	0.23	—
47100 Type (1.20% Nickel)							
2054 N	1.00	0.64	0.28	0.17	1.17	0.21	—
2055 N	1.00	0.85	0.28	0.17	1.19	0.22	—
2051 N	1.02	0.99	0.26	0.17	1.19	0.22	—
2056 NA	0.97	0.49	0.28	0.31	1.21	0.22	—
2057 NA	1.01	0.72	0.28	0.32	1.21	0.22	—
2058 NA	1.00	0.83	0.28	0.32	1.20	0.22	—
2059 N	1.01	0.38	0.29	0.44	1.21	0.22	—
2060 N	1.02	0.57	0.31	0.42	1.20	0.23	—
2061 N	1.02	0.67	0.31	0.43	1.21	0.22	—

Table I—(Continued)
Chemistry of 1.00% Carbon Steels
Quenched From Normalized (N) and/or Annealed (A) Prior Structures

Heat No.	Chemistry C	Mn	Si	Cr	Ni	Mo	Annealed Hardness (B.H.N.)
Modified 47100 Type (0.90% Nickel)							
2039 NA	0.97	0.62	0.30	0.32	0.89	0.22	—
2040 NA	1.02	0.77	0.28	0.32	0.87	0.22	—
2053 NA	1.00	0.84	0.26	0.31	0.89	0.23	—
2038 N	0.99	0.45	0.28	0.47	0.88	0.22	—
2037 N	0.98	0.65	0.30	0.47	0.88	0.23	—
2052 N	1.01	0.77	0.28	0.47	0.89	0.23	—
2043 N	1.01	0.32	0.28	0.62	0.89	0.24	—
2044 N	0.94	0.49	0.30	0.60	0.89	0.23	—
2045 N	0.95	0.63	0.30	0.61	0.89	0.21	—
94100 and 97100 Types (0.50% Nickel)							
2559 N	0.95	0.50	0.32	0.31	0.52	0.16	—
2560 N	0.99	0.75	0.32	0.30	0.52	0.16	—
2561 N	0.99	0.94	0.32	0.30	0.51	0.14	—
2562 N	1.03	1.15	0.31	0.30	0.51	0.15	—
2563 N	1.04	1.30	0.33	0.30	0.53	0.14	—
97100 Type (Varying Silicon)							
2564 N	1.01	0.51	0.30	0.28	0.51	0.10	—
2565 N	1.06	0.54	0.64	0.32	0.54	0.11	—
2566 N	1.01	0.85	0.67	0.31	0.52	0.10	—
2567 N	1.05	0.55	0.52	0.32	0.53	0.10	—
Various Nickel-Chromium-Molybdenum Types (Varying Molybdenum)							
2271 N	1.05	0.60	0.27	0.54	1.05	0.12	—
2272 N	1.06	0.59	0.30	0.54	1.29	0.10	—
2274 N	0.98	0.66	0.26	0.34	1.10	0.25	—
2275 N	1.00	0.63	0.24	0.34	1.29	0.27	—
2467 NA	1.02	0.62	0.35	0.37	1.06	0.36	—
2468 NA	1.07	0.59	0.35	0.35	1.32	0.35	—
2469 NA	1.05	0.63	0.33	0.34	1.32	0.30	—
2470 NA	1.03	0.61	0.33	0.31	1.05	0.32	—
41100 Type (High Manganese, Chromium, Molybdenum—Low Nickel)							
27235 NA	1.03	0.82	0.34	1.43	0.23	0.25	—
27331 NA	1.01	0.77	0.31	1.40	0.15	0.28	—
Miscellaneous Nickel-Chromium-Molybdenum Series, Annealed Data Only							
2099 A	1.00	0.31		0.31	0.56	0.10	192
2101 A	0.97	0.30		0.30	1.01	0.09	197
2102 A	0.98	0.29		0.29	1.48	0.09	201
2104 A	0.97	0.57		0.32	0.52	0.09	201
2106 A	1.02	0.58		0.32	1.02	0.10	207
2105 A	1.02	0.60		0.32	1.48	0.10	212
2134 A	0.97	0.91		0.31	1.02	0.10	212
2140 A	0.93	0.87		0.31	1.53	0.10	223
2193 A	0.96	0.45		0.40	1.32	0.13	207
2271 A	1.01	0.61		0.53	1.05	0.10	204
2272 A	1.04	0.59		0.51	1.30	0.09	215
2273 A	1.01	0.59		0.51	1.50	0.11	219
2274 A	0.96	0.66		0.33	1.11	0.27	209
2275 A	0.98	0.63		0.32	1.31	0.27	209
2276 A	0.97	0.63		0.31	1.53	0.26	223
2195 A	0.98	0.59		0.39	1.21	0.23	217
2197 A	1.00	0.77		0.44	1.30	0.22	217
2130 A	0.94	0.59		0.52	1.03	0.24	217
2196 A	0.98	0.61		0.51	1.30	0.24	212
2131 A	0.95	0.61		0.52	1.51	0.26	223

Normal Range — .25/.35

normalized and annealed prior structures, respectively. The D_I values were obtained from the Jominy distances by using the accepted conversion curve (3,5) of Fig. 1 relating the two. The D_I values of Table II were subsequently corrected for deviations from 1.0% carbon by means of the curves of Fig. 2. The carbon multiplying factors were derived from data previously published from this laboratory (4,6). Corresponding values of D_I in Table III were not corrected for carbon

Table II
Measured and Calculated Hardenability of 1.00% Carbon Steels Normalized Prior Structure

Heat No.	AUSTENITIZING TEMPERATURE 1475 °F: Measured J Distance to Rc 60 (16's)	1475 °F: Corresponding D_I to Rc 60 (In.)	1475 °F: Calculated D_I	1525 °F: Measured J Distance to Rc 60 (16's)	1525 °F: Corresponding D_I to Rc 60 (In.)	1525 °F: Calculated D_I	1575 °F: Measured J Distance to Rc 60 (16's)	1575 °F: Corresponding D_I to Rc 60 (In.)	1575 °F: Calculated D_I	FRACTURE GRAIN SIZE 1475 °F	1525 °F	1575 °F
BASE REFERENCE ANALYSIS (Values Based on Average of Seven Heats)												
Various Production Heats	2.13	1.10/ 1.05	—	2.30	1.18/ 1.13	—	2.90	1.40/ 1.35	—	8.0	7.5	7.0
SINGLE ALLOY STEELS												
Manganese Series												
Unknown	2.10	1.05	1.10	2.30	1.18	1.20	2.70	1.35	1.40	8.0	8.0	7.0
Unknown	2.45	1.25	1.26	2.70	1.35	1.37	3.30	1.65	1.68	8.0	7.0	7.0
Unknown	2.55	1.28	1.29	2.90	1.45	1.40	3.50	1.72	1.75	7.0	7.0	7.0
10542	3.20	1.55	1.52	4.00	1.83	1.78	5.30	2.25	2.32	8.0	7.5	7.0
2790	3.45	1.68	1.73	—	—	—	6.00	2.40	2.52	8.0	—	7.5
Nickel Series												
2424	—	—	—	2.40	1.20	1.19	2.70	1.35	1.43	—	6.0	6.5
2425	—	—	—	2.50	1.27	1.24	2.90	1.45	1.48	—	6.0	6.0
2428	—	—	—	2.70	1.35	1.34	3.20	1.55	1.60	—	6.0	6.0
2429	—	—	—	3.10	1.50	1.47	3.60	1.70	1.73	—	6.5	6.5
2430	—	—	—	3.40	1.65	1.65	4.20	1.90	1.94	—	6.0	6.0
Chromium Series												
2434	2.45	1.23	1.27	2.70	1.35	1.38	3.10	1.52	1.68	9.0	8.5	8.0
2435	2.55	1.32	1.31	2.95	1.45	1.50	3.50	1.68	1.78	9.0	9.0	9.0
2436	2.70	1.37	1.38	3.20	1.55	1.58	4.30	1.95	1.90	9.5	10.0	9.0
2437	3.00	1.48	1.57	3.80	1.80	1.79	4.60	2.02	2.15	9.5	9.0	9.0
Molybdenum Series												
02330	2.45	1.23	1.25	2.70	1.35	1.37	3.20	1.55	1.64	7.0	7.0	7.0
2787	2.45	1.27	1.30	—	—	—	3.40	1.65	1.69	7.0	—	6.5
2698	2.70	1.35	1.36	3.00	1.45	1.46	4.00	1.83	1.75	8.0	7.0	7.0
2788	3.00	1.45	1.45	—	—	—	5.10	2.18	2.26	8.0	—	7.0
Silicon Series												
Unknown	2.10	1.05	1.05	2.20	1.18	1.18	2.70	1.35	1.35	8.0	—	—
2761	2.30	1.22	1.20	—	—	—	—	—	—	8.0	—	—
2762	2.50	1.32	1.30	—	—	—	—	—	—	8.5	—	—
MULTI-ALLOY (NICKEL-CHROMIUM-MOLYBDENUM) STEELS												
Standard 46100 Type (1.75% Nickel)												
1728	10.5	3.50	3.53	—	—	—	—	—	—	8.0	—	—
1735	13.2	4.05	4.05	—	—	—	—	—	—	8.0	—	—
1736	18.0	4.85	—	—	—	—	—	—	—	8.0	—	—
1733	8.0	2.90	2.78	—	—	—	—	—	—	8.0	—	—
1729	11.8	3.78	3.42	—	—	—	—	—	—	8.0	—	—
1734	14.0	4.20	4.32	—	—	—	—	—	—	8.0	—	—
1732	8.2	2.95	2.85	—	—	—	—	—	—	7.5	—	—
1731	10.5	3.50	3.10	—	—	—	—	—	—	8.0	—	—
1730	13.0	4.00	3.70	—	—	—	—	—	—	8.0	—	—
2123	9.5	3.28	3.06	—	—	—	—	—	—	8.0	—	—
2124	10.0	3.40	3.50	—	—	—	—	—	—	7.5	—	—
2125	12.0	3.80	4.20	—	—	—	—	—	—	8.0	—	—
2126	9.5	3.28	2.86	—	—	—	—	—	—	8.0	—	—
2127	12.5	3.90	3.50	—	—	—	—	—	—	8.0	—	—
Modified 46100 Type (1.50% Nickel)												
2062	6.2	2.42	2.50	6.4	2.50	2.70	9.0	3.15	3.40	8.0	8.0	6.5
2063	8.0	2.90	2.90	9.2	3.18	3.82	12.1	3.82	4.22	8.0	7.5	6.5
2064	11.0	3.60	—	13.0	4.00	—	19.0	5.00	—	8.0	8.0	7.0
2065	6.2	2.42	2.34	7.2	2.67	2.70	9.0	3.15	3.26	8.5	9.0	8.0
2067	8.3	3.00	2.96	9.5	3.25	3.18	13.5	4.10	4.28	8.5	8.0	8.0
2068	10.0	3.40	3.38	11.0	3.55	3.48	17.0	4.70	4.80	8.5	8.5	8.0
2069	5.5	2.30	2.30	6.2	2.45	2.64	8.1	2.90	2.95	8.0	7.5	7.0
2070	7.0	2.65	2.60	8.2	2.95	3.00	11.5	3.70	3.72	8.0	8.0	7.5
2071	8.2	2.95	3.00	9.9	3.35	3.46	14.0	4.20	4.42	8.5	8.0	8.0

Table II—(Continued)

Heat No.	AUSTENITIZING TEMPERATURE 1475 °F: Measured J Distance to Rc 60 (16's)	1475 °F: Corresponding D_I to Rc 60 (In.)	1475 °F: Calculated D_I	1525 °F: Measured J Distance to Rc 60 (16's)	1525 °F: Corresponding D_I to Rc 60 (In.)	1525 °F: Calculated D_I	1575 °F: Measured J Distance to Rc 60 (16's)	1575 °F: Corresponding D_I to Rc 60 (In.)	1575 °F: Calculated D_I	FRACTURE GRAIN SIZE 1475 °F	1525 °F	1575 °F
47100 Type (1.20% Nickel)												
2054	5.0	2.15	2.18	5.9	2.38	2.46	7.9	2.85	2.96	8.0	7.0	6.5
2055	6.7	2.55	—	8.2	2.93	—	11.4	3.70	—	8.0	8.0	6.5
2051	8.0	2.87	—	9.4	3.22	—	15.0	4.38	—	8.0	8.0	6.5
2056	5.0	2.15	2.08	6.1	2.40	2.46	8.5	3.00	2.94	8.0	8.0	7.5
2057	6.5	2.50	2.46	8.0	2.90	2.95	12.0	3.80	3.75	8.0	8.0	7.5
2058	7.8	2.85	—	9.0	3.15	—	13.3	4.10	—	8.0	8.0	7.5
2059	4.5	2.00	2.02	5.1	2.20	2.35	7.1	2.65	2.78	8.0	8.0	7.0
2060	5.5	2.30	2.28	6.8	2.60	2.75	10.2	3.45	3.35	8.0	7.5	7.0
2061	6.5	2.50	2.48	8.0	2.90	2.98	11.5	3.70	3.72	8.0	8.0	7.0
Modified 47100 Type (0.90% Nickel)												
2039	4.6	2.05	2.00	5.5	2.30	2.32	8.0	2.90	2.95	8.0	8.0	8.0
2040	5.2	2.20	2.15	5.75	2.32	2.45	8.5	3.02	3.16	8.0	8.0	7.5
2053	6.2	2.40	2.20	7.0	2.65	2.60	10.0	3.30	3.30	8.0	8.0	8.0
2038	4.5	2.00	1.95	4.6	2.02	2.14	6.6	2.38	2.58	8.0	8.0	7.5
2037	5.3	2.22	2.15	5.1	2.20	2.50	8.2	2.95	3.14	8.0	8.0	7.5
2052	6.0	2.38	2.28	6.8	2.58	2.66	8.5	3.00	3.37	8.0	8.0	7.5
2043	4.5	2.00	1.83	—	—	—	—	—	—	8.0	8.0	7.5
2044	5.3	2.22	2.00	—	—	—	—	—	—	8.0	8.0	7.5
2045	6.1	2.40	2.26	—	—	—	—	—	—	8.0	8.0	7.5
94100 and 97100 Types (0.50% Nickel)												
2559	3.6	1.65	1.70	3.6	1.70	1.86	5.0	2.15	2.35	8.0	8.0	7.0
2560	4.4	1.92	1.90	4.6	2.03	2.14	6.8	2.60	2.72	8.0	8.0	7.0
2561	4.8	2.10	2.05	5.4	2.25	2.31	8.25	2.95	2.98	8.5	8.5	7.5
2562	5.5	2.22	2.14	5.9	2.35	2.42	9.4	3.25	3.12	9.5	8.5	7.0
2563	7.3	2.70	—	—	—	—	—	—	—	8.5	8.5	7.0
97100 Types (Varying Silicon)												
2564	3.4	1.60	1.60	—	—	—	—	—	—	8.5	—	—
2565	3.85	1.78	1.75	—	—	—	—	—	—	9.0	—	—
2566	4.95	2.15	1.98	—	—	—	—	—	—	8.5	—	—
2567	3.45	1.65	1.63	—	—	—	—	—	—	9.0	—	—
Various Nickel-Chromium-Molybdenum Types (Varying Molybdenum)												
2271	4.45	2.00	2.05	5.5	2.25	2.34	6.7	2.50	2.98	8.0	8.0	6.5
2272	4.6	2.02	2.06	6.1	2.35	2.37	7.3	2.75	3.00	8.0	7.5	7.0
2274	5.6	2.30	2.13	—	—	—	8.4	3.05	3.15	8.5	8.0	7.5
2275	6.75	2.52	2.54	8.2	3.00	3.10	11.9	3.78	3.83	8.0	7.5	7.5
2467	7.6	2.78	2.68	8.75	3.10	3.05	13.8	4.18	3.85	8.0	8.0	7.5
2468	8.0	2.88	2.88	10.2	3.40	3.42	16.2	4.55	4.20	8.0	8.0	7.5
2469	7.5	2.75	2.79	9.5	3.25	3.38	15.4	4.45	4.35	8.0	8.0	7.5
2470	6.25	2.50	2.42	7.2	2.70	2.75	10.9	3.58	3.50	8.0	7.0	7.0
41100 Type (High Manganese, Chromium, Molybdenum and Low Nickel)												
27235	6.5	2.50	2.47	9.3	3.10	3.00	12.0	3.80	3.74	9.5	9.0	9.0
27331	6.0	2.40	2.30	8.5	3.02	2.94	11.5	3.68	3.82	9.5	9.0	8.5

deviation since comparable data from annealed prior structures were lacking. The fracture grain size values were obtained by comparing the fractures of thin slices cut from the quenched end of the Jominy bars with Shepherd standards.

Also given in Tables II and III are the calculated hardenability values for each quenching temperature. Comparison with the measured D_I values reveals reasonable agreement over a fairly wide range of composition. The development of the method of computation will now be considered.

Table III
Measured and Calculated Hardenability of 1.00% Carbon Steels Annealed Prior Structure

Heat No.	AUSTENITIZING TEMPERATURE 1475 °F: Measured J Distance to Rc 60 (16's)	Corresponding D_I to Rc 60 (In.)	Calculated D_I	1525 °F: Measured J Distance to Rc 60 (16's)	Corresponding D_I to Rc 60 (In.)	Calculated D_I	1575 °F: Measured J Distance to Rc 60 (16's)	Corresponding D_I to Rc 60 (In.)	Calculated D_I	FRACTURE GRAIN SIZE 1475 °F	1525 °F	1575 °F
MULTI-ALLOY STEELS												
2099	3.0	1.45	1.27	—	—	—	—	—	—	6.5	—	—
2101	3.7	1.75	1.45	4.4	2.00	1.65	5.5	2.30	2.22	7.0	—	—
2102	4.4	2.00	1.95	4.8	2.10	2.35	6.2	2.40	2.70	7.0	—	—
2104	3.3	1.60	1.65	—	—	—	—	—	—	6.5	6.5	6.0
2106	5.2	2.20	1.88	5.8	2.35	2.12	6.6	2.45	2.65	7.0	6.5	5.5
2105	7.2	2.70	2.80	8.0	2.90	3.20	8.8	3.10	3.83	7.0	6.5	6.0
2134	7.0	2.63	—	8.3	2.97	—	10.8	3.55	—	7.0	6.5	5.5
2140	9.8	3.35	—	11.5	3.70	—	15.3	4.43	—	7.0	6.5	5.5
2193	5.6	2.30	2.20	7.7	2.80	2.88	8.8	3.10	3.35	7.0	6.5	5.5
2271	6.6	2.45	2.05	7.2	2.70	2.63	8.4	3.00	3.40	—	7.0	6.0
2272	7.5	2.75	2.42	7.8	2.80	2.95	10.3	3.45	3.50	—	7.5	7.5
2273	8.7	3.05	3.00	12.3	3.80	3.74	13.3	4.08	4.40	—	8.0	7.5
2274	9.1	3.15	2.85	11.5	3.70	3.50	13.8	4.18	4.68	—	7.5	7.0
2275	9.0	3.10	3.05	11.6	3.70	3.75	12.6	3.90	5.10	—	8.0	7.5
2276	11.9	3.78	3.62	15.3	4.43	4.38	17.0	4.70	5.20	—	8.0	7.5
2195	8.8	3.00	2.82	9.6	3.28	3.28	11.6	3.70	4.50	—	8.0	7.0
2197	11.5	3.70	3.50	13.5	4.10	4.30	19.2	5.03	5.15	—	8.0	7.0
2130	7.7	2.80	2.80	11.2	3.65	3.60	14.6	4.30	4.50	—	—	—
2196	9.5	3.25	3.20	14.2	4.23	3.95	20.0	5.18	5.15	—	8.0	7.0
2131	12.4	3.90	3.95	17.8	4.85	4.95	25.8	5.90	6.20	—	8.0	7.0
2039	—	—	—	6.2	2.45	2.52	—	—	—	—	7.5	—
2040	—	—	—	7.7	2.80	2.72	—	—	—	—	7.5	—
2053	—	—	—	8.2	2.90	2.92	—	—	—	—	8.0	—
2056	—	—	—	6.8	2.60	2.74	—	—	—	—	8.0	—
2057	—	—	—	10.5	3.45	3.42	—	—	—	—	7.5	—
2058	—	—	—	11.2	3.63	3.82	—	—	—	—	8.0	—
2065	—	—	—	8.0	2.87	3.05	—	—	—	—	7.5	—
2067	—	—	—	11.0	3.57	3.70	—	—	—	—	8.0	—
2068	—	—	—	13.6	4.10	4.12	—	—	—	—	8.0	—
2467	9.8	3.35	3.02	—	—	—	—	—	—	—	—	—
2468	10.0	3.35	3.35	—	—	—	—	—	—	—	—	—
2469	9.0	3.13	3.18	—	—	—	—	—	—	—	—	—
2470	8.5	3.00	2.70	—	—	—	—	—	—	—	—	—
27235	9.2	3.10	2.80	12.0	3.80	3.60	16.5	4.60	4.60	10.0	9.0	9.0
27331	7.5	2.78	2.65	10.0	3.35	3.46	14.5	4.25	4.40	9.5	9.5	9.0
SINGLE ALLOY STEELS												
Nickel Series												
2424	—	—	—	1.75	1.00	1.00	2.20	1.18	1.30	—	6.0	5.5
2425	—	—	—	2.00	1.10	1.06	2.40	1.25	1.35	—	6.0	5.5
2428	—	—	—	2.50	1.30	1.25	2.70	1.35	1.50	—	6.5	5.5
2429	—	—	—	3.50	1.68	1.62	4.30	1.95	1.72	—	6.5	5.5
Chromium Series												
2434	2.20	1.13	1.11	2.70	1.35	1.28	3.20	1.53	1.66	7.5	7.0	6.5
2435	2.40	1.18	1.18	3.10	1.52	1.45	3.50	1.70	1.75	9.0	8.5	8.0
2436	2.50	1.25	1.28	3.45	1.60	1.55	4.80	2.05	1.95	9.0	9.0	8.0
2437	3.00	1.45	1.48	4.00	1.82	1.81	5.70	2.28	2.28	9.0	9.0	9.0

Computation of Hardenability

A group of seven representative 1.0% carbon tool steel heats was chosen as the hardenability base line for this work. The average composition is shown in Table I, while Table II gives the average measured hardenability. The lower of the two D_I values represents a later

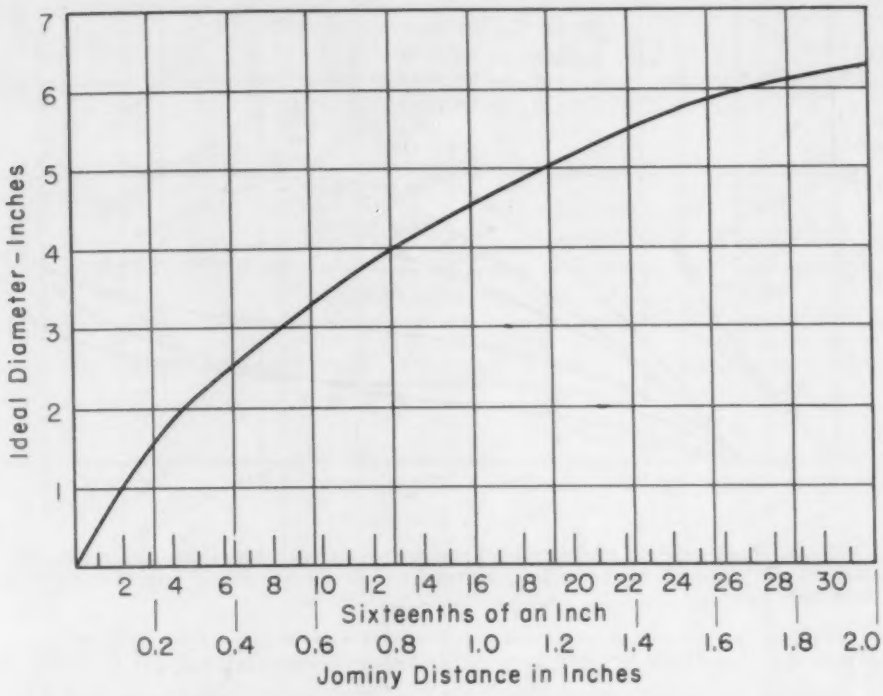


Fig. 1—Jominy Distance Versus Ideal Diameter (Taken From Kramer, Toleman and Hafner (3), and Carney (5)).

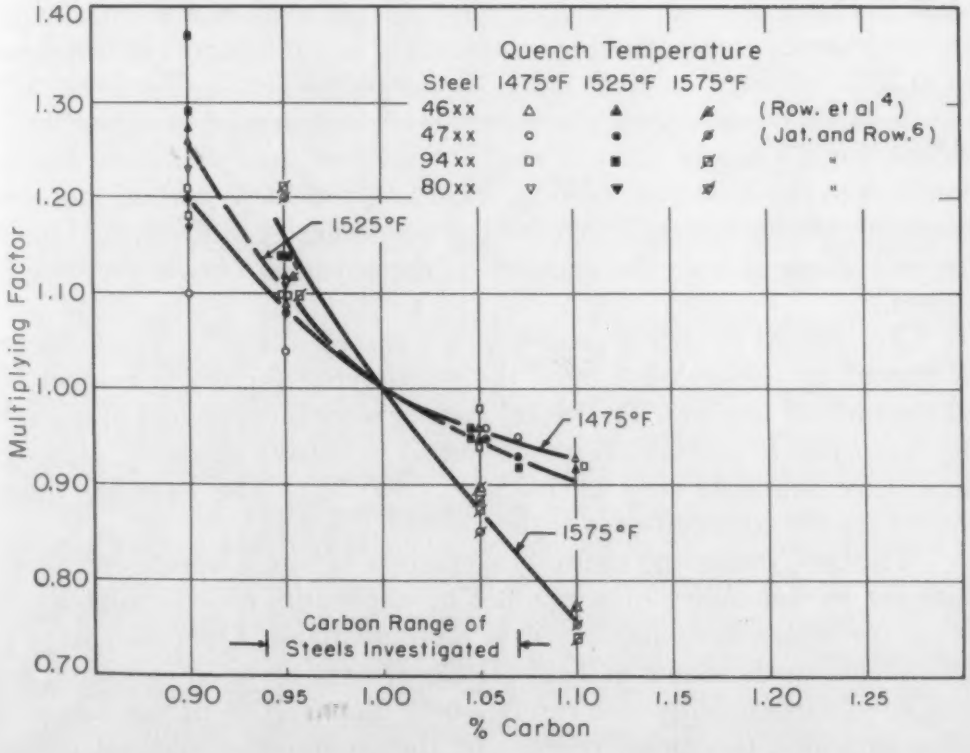


Fig. 2—Average Carbon Correction Factor for Normalized Nickel-Chromium-Molybdenum 1.0% Carbon Steels at Three Austenitizing Temperatures.

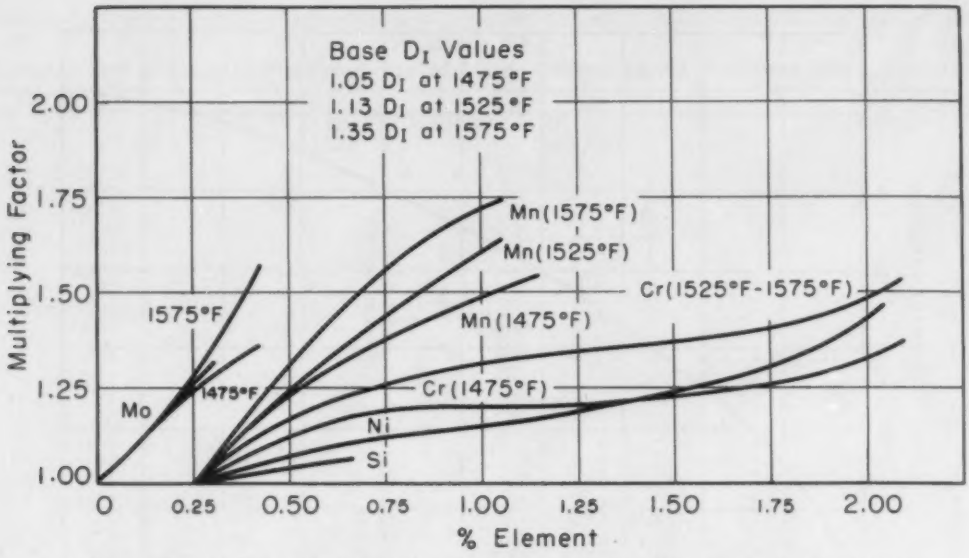


Fig. 3—Hardenability Multiplying Factors for Various Elements Limited to Normalized Single Alloyed Steels and to Normalized Multi-Alloyed Steels of Less than 1.0% Nickel.

correction of the base to a more adaptable composition of 0.25% each of manganese, silicon, chromium and nickel and zero% molybdenum.

The series of singly alloyed steels of Table II provided the first approximation of the effects each of the common alloying elements, manganese, silicon, chromium, nickel and molybdenum on hardenability. The measured D_I values were plotted against element content for each series and quenching temperature and the curves extrapolated to 0.25% element content (0% for molybdenum), the arbitrarily selected base composition. These curves were then used to adjust the D_I values for all singly alloyed steels whose residual elements did not conform to the base composition, including the 1.0% carbon tool steel heats referred to above. The final step was to derive multiplying factors for each element from the quotient of the adjusted D_I and the base D_I values.

The results of such a procedure are shown in Fig. 3. The influence of quenching temperature upon the multiplying factors is evident for all the carbide formers. The nickel factors were independent of quenching temperature and silicon was assumed to behave similarly, although data were available only at 1475 °F (800 °C). The base D_I values shown are the adjusted ones at the head of Table II.

The base values and multiplying factors of Fig. 3 were used to compute the hardenability of a number of chromium-nickel-molybdenum steels for which hardenability data were available. Over the range of normalized steels shown in Table II, agreement between measured and computed hardenability was rarely worse than ±10% of the measured value provided the nickel content of the composition did not exceed 1.0%. At higher nickel levels, the computed hardenability value was always low and the divergence increased with nickel content.

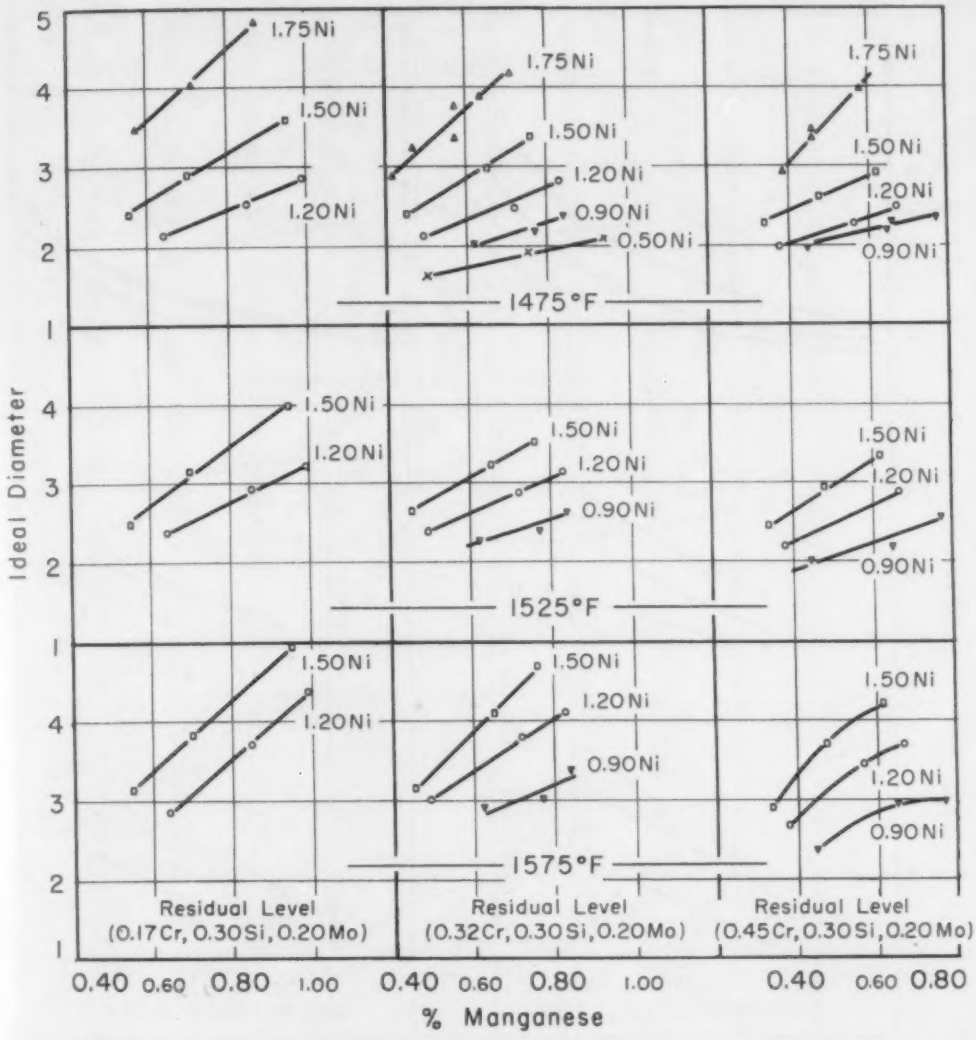


Fig. 4—Effects of Manganese on the Hardenability of Normalized Nickel-Chromium-Molybdenum 1.0% Carbon Steels at Several Base Chromium and Nickel Levels and Hardening Temperatures.

The data of Table II involving chromium-nickel-molybdenum steels are plotted in Figs. 4,5 and 6 in which D_I is shown as a function of each of the alloying elements—manganese, nickel, chromium and molybdenum—at each temperature in turn at several increments of the other three elements. Analysis of these data led to the conclusion that the major cause of disagreement between measured and computed hardenability at the higher nickel levels lay in an interdependence of the effects of manganese and nickel on each other, in which the combined effect was far larger than consideration of their single effects indicated. This interaction, of course, precluded the use of multiplying factors for each element since independence of alloying element effects is implicit in the multiplying factor approach. In this case, however, the difficulty was surmounted by the expedient of computing combined nickel-manganese multiplying factors as shown in Fig. 7. Each nickel-manganese factor was obtained by dividing the D_I of the steel by the

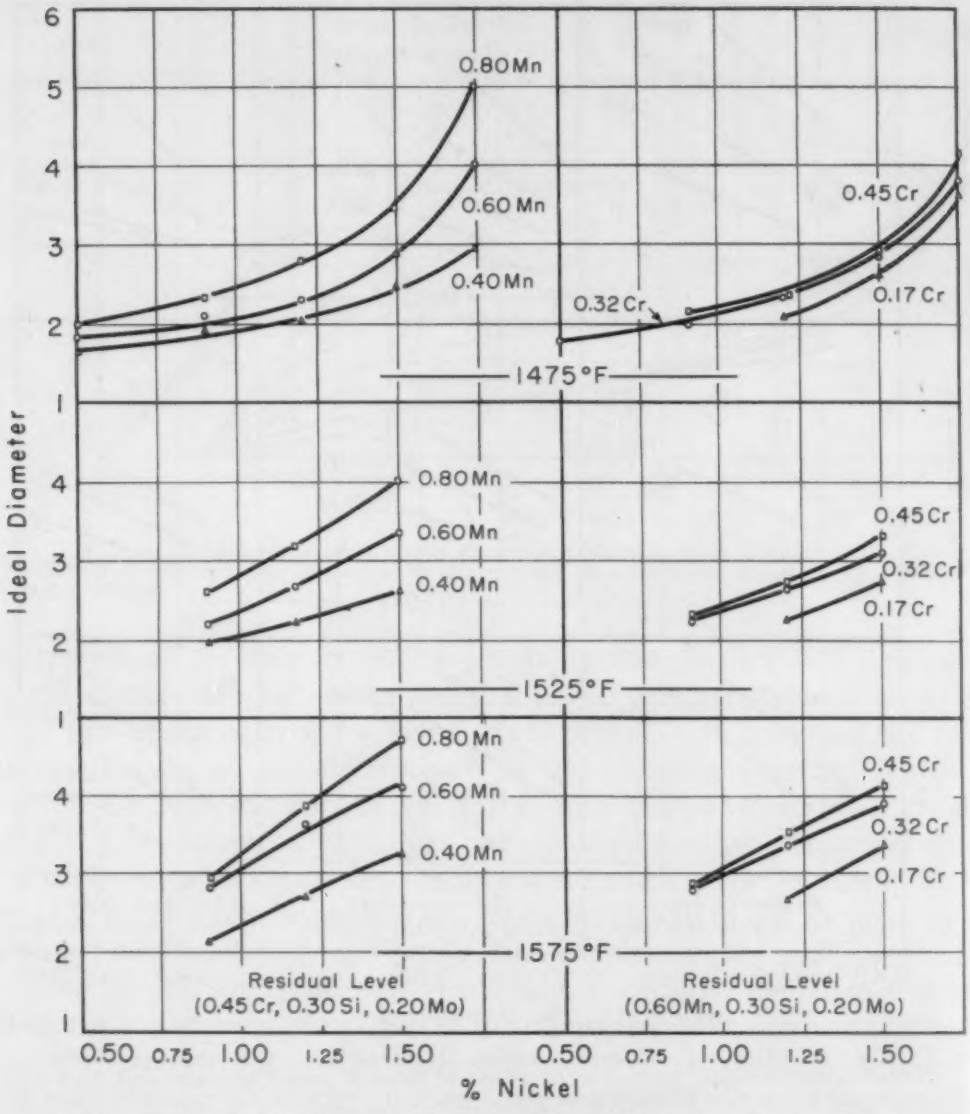


Fig. 5—Effect of Nickel on the Hardenability of Normalized Nickel-Chromium-Molybdenum 1.0% Carbon Steels at Several Base Manganese and Chromium Levels and Hardening Temperatures.

product of the appropriate factors for silicon, chromium, molybdenum and the D_I of the base analysis. For any specific nickel value, the combined factor may be found by interpolating between the curves of the manganese increments at the desired hardening temperature.

In addition, it was found that while the molybdenum contribution to hardenability in the high nickel multi-alloy steels was apparently independent of other alloying elements, the specific effect was noticeably greater above 0.20% molybdenum than in molybdenum steels alone or in low nickel, chromium-nickel-molybdenum compositions. The chromium and silicon multiplying factors were found to be unchanged. Fig. 8 gives the multiplying factors for these three elements appropriate for normalized chromium-nickel-molybdenum steels of

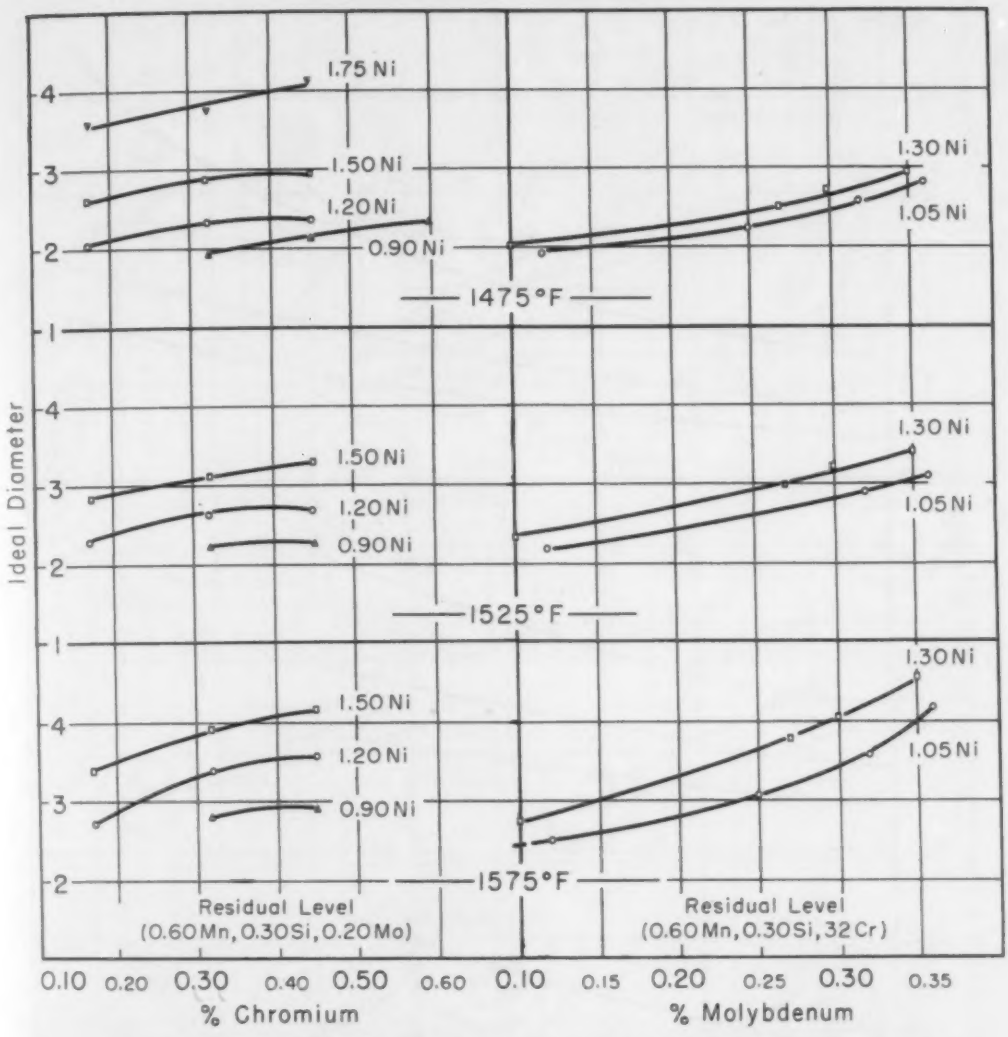


Fig. 6—Effect of Chromium and Molybdenum on the Hardenability of Normalized Nickel-Chromium-Molybdenum 1.0% Carbon Steels at Several Base Nickel Levels and Hardening Temperatures.

greater than 1.0% nickel content. Within these limitations and the range of steels studied, hardenability values computed from Figs. 7 and 8 compared with the measured values within about ±10% of the measured value.

The problem of hardenability calculation for steels end-quenched from spheroidize annealed prior structures proved to be a more difficult task. In the first place, a far smaller amount of data was available for analysis (Table III) and secondly, inspection of the plots of Figs. 9 and 10 disclosed almost complete dependence of each element upon the others for the value of its hardenability effect. Furthermore, some combinations such as nickel and molybdenum had a combined effect significantly greater than expected from their individual factors while others, chromium and molybdenum, yielded a combined value less than expected from their individual contributions. After several trials, the

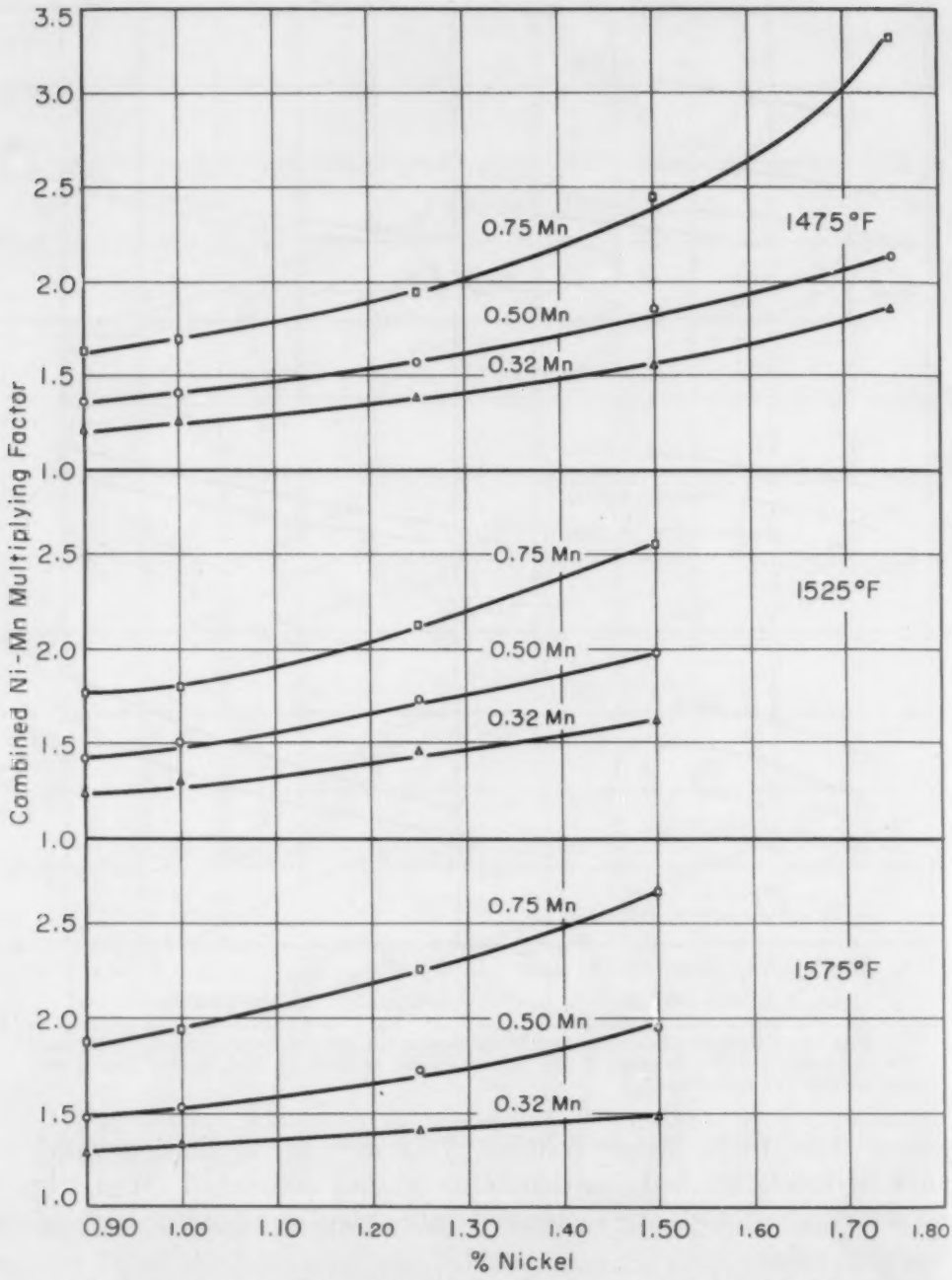


Fig. 7—Combined Hardenability Multiplying Factors for Nickel and Manganese in Normalized Nickel-Chromium-Molybdenum 1.0% Carbon Steels at Several Hardening Temperatures.

conclusion was reached that the multiplying factor approach could not be applied to these data.

Recourse was made to a simple correlation, shown in Fig. 11, between the D_I from a normalized prior structure and the corresponding value from the spheroidized condition on all heats for which both values were available regardless of type. Besides showing the definite hardenability advantage of the annealed over the normalized prior structure

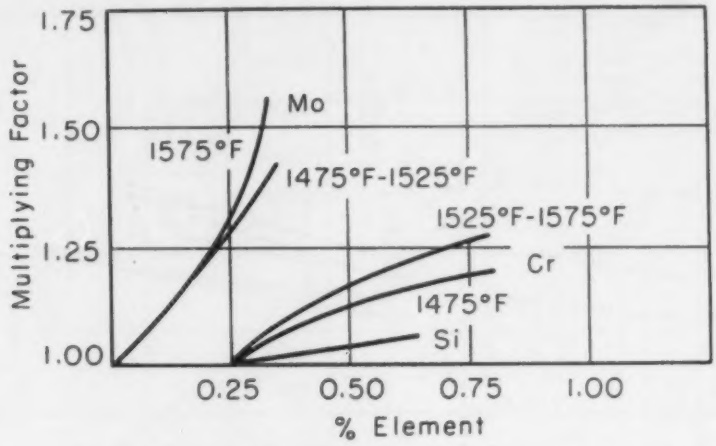


Fig. 8—Hardenability Factors for Molybdenum, Chromium and Silicon to be used with Normalized Multi-Alloyed Compositions Containing More than 1.0% Nickel.

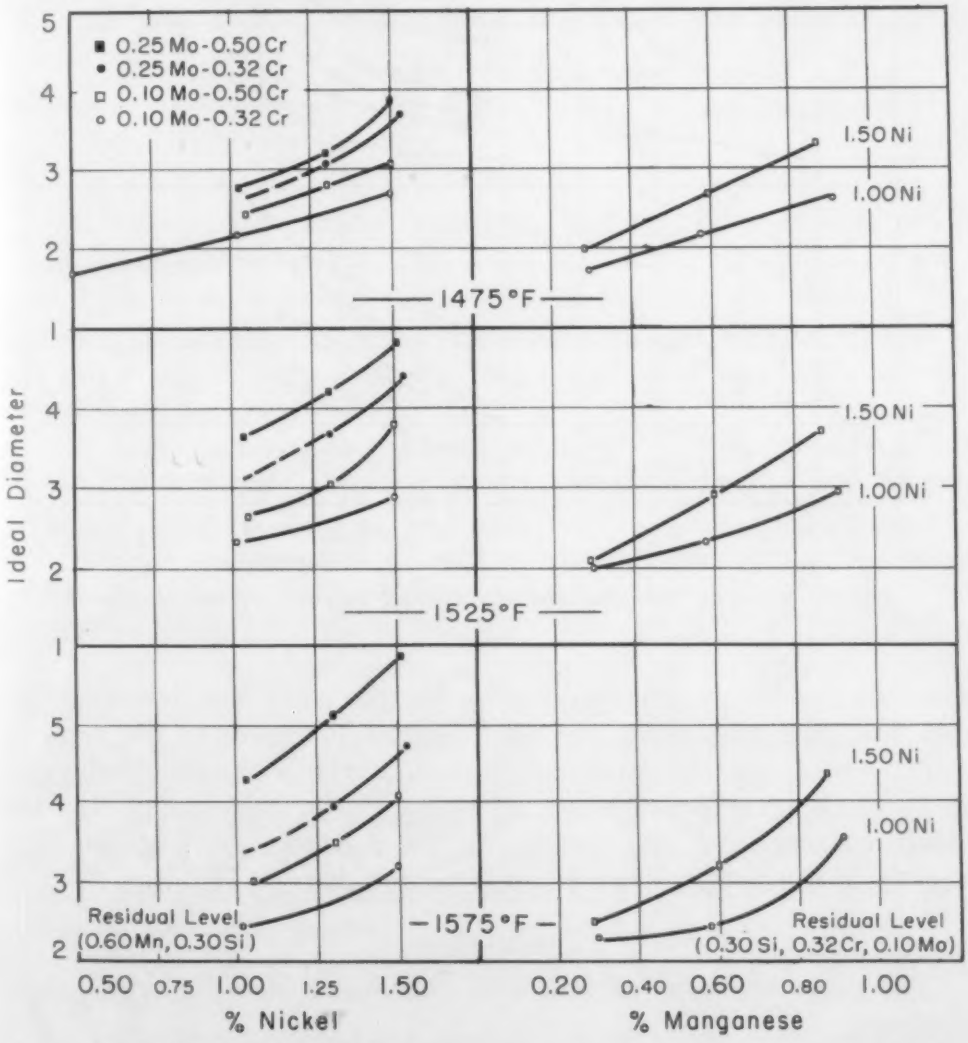


Fig. 9—Effect of Nickel and Manganese on Hardenability of Annealed Nickel-Chromium-Molybdenum 1.0% Carbon Steels at Several Base Chromium and Molybdenum Levels and Hardening Temperatures.

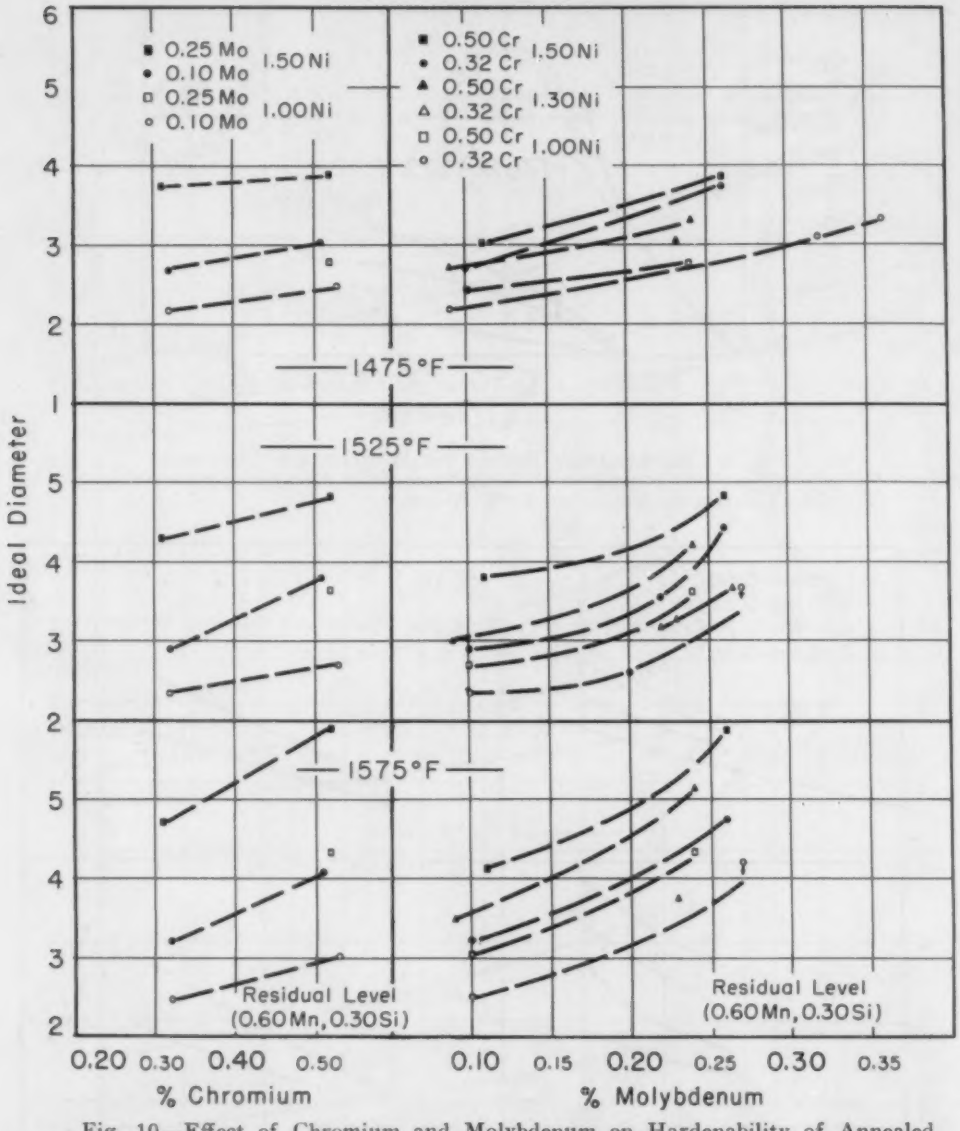


Fig. 10—Effect of Chromium and Molybdenum on Hardenability of Annealed Nickel-Chromium-Molybdenum 1.0% Carbon Steels at Several Base Nickel Levels and Hardening Temperatures.

under the conditions of test, except for the very low hardenability steels, this plot emphasizes the small degree of scatter of the data. In order to compute the hardenability of steels with annealed prior structures, it is only necessary to perform the calculations for the normalized condition and convert to the annealed by Fig. 11. The precision of the computation is rarely poorer than ± 15%.

Discussion

The procedure for hardenability calculation may be summarized as follows:

1. Select the base D_I value corresponding to desired quenching temperature at top of Fig. 3.

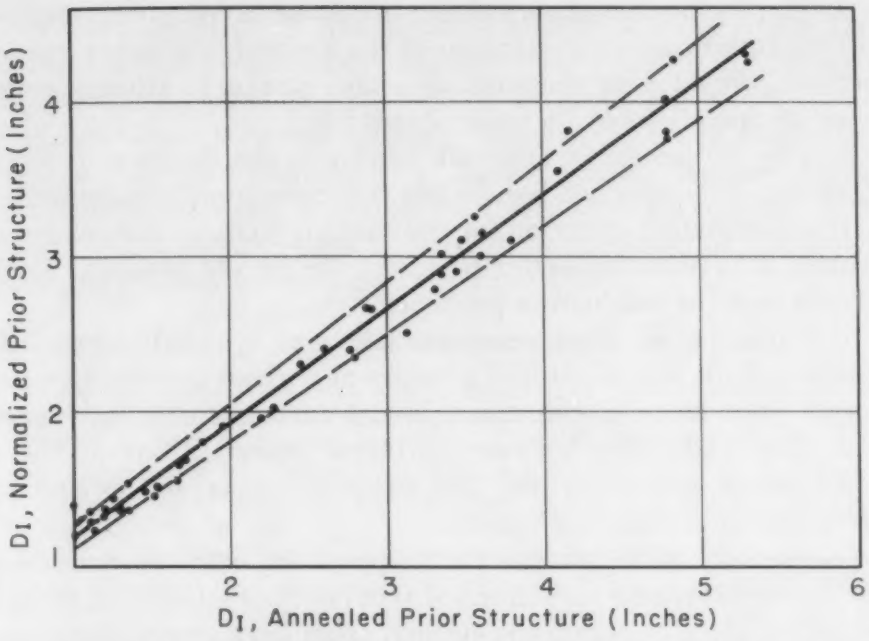


Fig. 11—Correlation Between Hardenability Based on Normalized and Annealed Prior Structures in Alloyed 1.0% Carbon Steels.

2. Correct for carbon deviation from the 1.0% base by use of multiplying factors of Fig. 2.

3. If the nickel content of multi-alloyed steels is below 1.0% or the composition is a nickel steel in which the other alloying elements do not differ significantly from the base composition, apply the appropriate multiplying factors of Fig. 3.

4. If the composition is a multi-alloyed steel of more than 1.0% nickel content, apply the multiplying factors of Figs. 7 and 8 instead of Fig. 3.

5. If it is desired to know the hardenability from the annealed rather than the normalized prior condition, convert the final D_I value by the use of the solid line of Fig. 11.

6. Fig. 1 may be used to convert the final D_I value to the more familiar distance to Rockwell C-60 on the end-quench bar.

The use of this method of calculation is subject to several important limitations which must be recognized. These are:

1. The quenching temperature must be within the range of 1475 to 1575 °F (800 to 855 °C) and some discretion needs to be used in interpolating between the multiplying factor curves at other than the three temperatures shown.

2. The time at the austenitizing temperature must be between 35 and 40 minutes.

3. Only normalized and spheroidize annealed prior structures may be applied.

4. Experience has shown that it is unwise to compute compositions requiring significant extrapolation of the multiplying factor curves for carbon and the alloying elements. It is also unwise to attempt computation for compositions of D_I value above 5.0.

5. The hardenability criterion used was the distance to Rockwell C-60 on the end-quenched bar. While this corresponds quite well to the 10% transformation criterion for the vast majority of the compositions examined, it is probably better to accept the purely practical Rockwell C-60 criterion for calculation purposes.

6. Variation in fracture grain size was ignored. Much of this variation is built into the base D_I values at a given quenching temperature and even more is contained in the carbon correction curves of Fig. 2. The variability between different compositions at the same carbon content and quenching temperature is accepted as one of the errors inherent in the computation.

It is readily admitted that the scope of the work described in this paper leaves something to be desired from both practical and theoretical standpoints. Data are certainly needed from high quenching temperatures to correlate with single quenched carburizing practice. From a theoretical standpoint, the empirical nature of the approach employed makes a fundamental appraisal of the effects of the alloying elements difficult. Under constant austenitizing and prior structure conditions the amounts of the various alloying elements in solution are obviously not the same, nor is the carbon solution equivalent as the composition is changed. It is recognized that a more fundamental criterion of the condition of the austenite just before quenching is needed for a true appraisal of the effects of the common alloying elements on hardenability. Furthermore, the effects of changing transformation characteristics need to be taken into account in establishing a hardenability criterion based on structure rather than hardness and the interdependence of the alloying elements in their hardenability effects needs to be better understood. Some work is underway on these problems and, if fruitful, will be reported in due course.

Nevertheless, from a standpoint of practical treatment of double quenched carburized cases and annealed tool steels, the hardenability predictions arrived at by this procedure have been of definite usefulness in our operations.

Summary and Conclusions

The effects of manganese, silicon, chromium, nickel and molybdenum, both singly and in combination, on the hardenability of 1.0% carbon steels were studied by means of the end-quench test. The tests were run from both normalized and spheroidize annealed prior structures at commercial hardening temperatures of 1475, 1525 and 1575 °F (800, 830 and 855 °C) after thirty-five to forty minutes at temperature.

For normalized prior structures, a system of multiplying factors was devised which predicted the hardenability from compositions with a precision rarely poorer than ± 10% of the measured value. While the inter-relationships between alloying elements were apparently too complex to express by multiplying factors when quenched from annealed prior structures, a simple hardenability correlation between annealed and normalized data allowed the calculation of hardenability for annealed prior structures within about ±15%.

References

1. C. R. Austin, W. G. Van Note and T. A. Prater, "Third Element Effects on Hardenability of a Pure Hypereutectoid Iron Carbon Alloy," TRANSACTIONS, American Society for Metals, Vol. 31, 1943, p. 517.
2. T. G. Digges and L. Jordan, "Hardening Characteristics of 1.00 Per Cent Carbon Tool Steels," TRANSACTIONS, American Society for Metals, Vol. 23, 1935, p. 839.
3. J. R. Kramer, R. H. Hafner and S. L. Toleman, "Effect of Sixteen Alloying Elements on Hardenability of Steel," TRANSACTIONS, American Institute of Mining and Metallurgical Engineers, Vol. 158, 1944, p. 138.
4. E. S. Rowland, J. Welchner, R. G. Hill and J. J. Russ, "The Effect of Carbon Content on Hardenability," TRANSACTIONS, American Society for Metals, Vol. 35, 1945, p. 46.
5. D. J. Carney, "Another Look at Quenchants, Cooling Rates and Hardenability," TRANSACTIONS, American Society for Metals, Vol. 46, 1954, p. 882.
6. C. F. Jatczak and E. S. Rowland, "The Influence of Boron on Case Hardenability in Alloy Carburizing Steels," TRANSACTIONS, American Society for Metals, Vol. 45, 1953, p. 771.

DISCUSSION

Written Discussion: By John C. Hamaker, Jr., research metallurgist, Vanadium-Alloys Steel Co., Latrobe, Pa.

Although many investigations have been devoted to hardenability calculations in the past fifteen years, very few have involved high carbon steels and even fewer have employed normal austenitizing temperatures rather than temperatures of complete carbide solution. The authors are to be congratulated on their systematic approach to this problem, and, particularly, for the determination of numerical values to indicate the very important effects of austenitizing temperature and prior structure on the hardenability of hypereutectoid steels.

In the tool steel industry, the hardenability of high carbon steel is of considerable interest because many die applications require closely controlled depths of hardened case and tough core for satisfactory performance. Because of the precision required at low hardenabilities, the Shepherd PF, PV, and Disk tests have been preferred over the end quench test for routine inspection and experimental work. A number of years ago, this Laboratory ran a series of PF tests to compare the effects of 1.00% additions of various alloys on the hardenability of 1.00% carbon tool steel.[2] Since the conditions of this experiment were similar

[2] Refer to TOOL STEELS by Gill, Roberts, Johnstin, and George, American Society for Metals, 1946; Tables XXV and XXVI, p. 282.

to those given in the paper, it was felt that a comparison of D_I values and multiplying factors calculated from the two methods might prove interesting.

The PF specimens, 1-¼ inches in diameter and 3 inches long, were machined from forged bars 1-⅜ inches square, pretreated by oil quenching after 40 minutes at 1600 °F, and then brine-quenched in a standard PF fixture after 12 minutes at 1450 °F. The severity of the quench, determined in a separate experiment involving ⅜, ½, ¾, 1, 1-½, 2, and 2-½ inch rounds of three different steel compositions, gave H values of 4.5, 4.9, and 5.5 for an average of 5.0. In Table IV are assembled the PF readings and corresponding ideal diameters for the 1.00% carbon, 1.00% alloy compositions tested. In order to obtain data which could be compared with that in the paper, each D_I value was then adjusted to correspond with the base composition selected by the authors, using the 1475 °F curves in Figs. 2 and 3 of the paper. Fortunately, at these low D_I values, the difference between the PF, D_I for 50% martensite at the center and the 90% martensite criterion used in the paper is believed to be quite small. Since the analyses of the carbon tool steels ran much lower in residual alloys than the selected base composition of the authors, rather large corrections were required to obtain the adjusted D_I values shown in Table IV. The multiplying factors derived from these values could then be directly compared with the factors given at the 1.00% element level in Fig. 3.

The "adjusted D_I" of 0.87 from the PF test of carbon tool steel quenched from 1450 °F is considerably smaller than the authors' value of 1.05 from the end quench test of high carbon production steel quenched from 1475 °F. The 25 °F difference in austenitizing temperature can account for only a portion of this discrepancy, since other data in our files indicates a maximum effect of only 1/64 inch penetration or about 0.05 D_I for carbon tool steel in this range. The lower pretreatment temperature which resulted in a finer grain size (9 vs 8) and the shorter austenitizing time (12 vs 35 minutes) would also contribute to a smaller D_I in the tool steel. Any remaining differences might be attributed to errors introduced in adjusting the D_I values to a common base. However, in view of the relatively high residuals in the alloys studied in the paper, the presence of another relatively potent hardenability agent like copper must also be considered. Did the authors analyze for this element in any of their steels?

A comparison of the multiplying factors derived from the PF tests with the curves in Fig. 3 shows a remarkably good check for the elements manganese, chromium, and nickel—probably within 5%. A very rough extrapolation of the molybdenum curve suggests that it might also fall in the vicinity of the PF value (2.05), but the effect of silicon indicated by the two methods appears to be at considerable variance. The PF tests show silicon to be about equally as potent as manganese, whereas the end quench tests indicate it to be only ¼ to ⅕ as effective. The data of previous investigators show similar large discrepancies for silicon, but all tend toward higher multiplying factors per unit of added silicon than indicated by its slope in Fig. 3. However, considering the two vastly different methods of testing and the extensive conversions and adjustments involved, the correlation between the two sets of data is generally very good.

A comparison between the slopes of the multiplying factor curves for these hypereutectoid steels and those reported for lower carbon steels provides a point of theoretical interest. It will be noted that the stronger carbide-formers, chromium and molybdenum have relatively less potency in the high carbon steels because they are partially tied up in undissolved carbide, while nickel and manganese appear to behave about the same in both high and low carbon steels.

As shown in Table IV, the very strong carbide-formers like tungsten or vanadium may actually reduce hardenability by decreasing the amount of carbon which dissolves in the austenite.

Table IV

Effect of 1.00% Alloy Content on the Hardenability of 1.00% Carbon Tool Steel as Determined by the PF Test

Base Analysis: 1.00% C, 0.25 Mn, 0.25 Si, 0.05 Cr, 0.03 Ni, 0.02 Mo
Treatment: (1) 40 minutes at 1600 °F., oil quench (pretreatment)
(2) 12 minutes at 1450 °F., agitated brine quench (H=5.0)

Steel	Penetration 64ths Inch in 1¼" Round	Corresponding D_I	Adjusted* D_I	Multiplying** Factor	Fracture Grain Size
Base	5½	0.67	0.87		9
1.00% Si	18	1.16	1.29	1.48	9
1.00% Mn	16	1.09	1.27	1.46	8¾
1.00% Cr	16	1.09	1.06	1.22	10
1.00% Ni	10	0.89	1.02	1.17	9¼
1.00% Mo	22	1.45	1.78	2.05	9¾
1.00% W	4½	0.62	0.75	0.86	9¾
1.00% V	5½	0.67	0.80	0.92	9¾

* Adjusted to "selected base composition" of 1.00% C, 0.25% Mn, 0.25% Si, 0.25% Cr, 0.25% Ni, 0.00% Mo; and 1.00% of alloying element.
** For addition of 0.75% Si, Mn, Cr, or Ni; or 1.00% Mo, W, or V to "selected base composition."

Authors' Reply

We would like to thank Mr. Hamaker for his very constructive discussion of our paper. It is a pleasure to consider his comments and observations.

First of all, we would like to state that copper was present in our 10100 reference base analysis. In our zealous efforts to cut the original text to publication size, we completely neglected to insert into the text or into the composition table, the full residual content of our 10100 base steels. We would like to make this correction for record and list now that in addition to the manganese, silicon, chromium, nickel, and molybdenum contents listed, our base composition contained 0.019% sulphur, 0.013% phosphorus, and 0.15% copper. Residual contents of other steels were similar, with copper about 0.08 to 0.15%, 0.13% average. It is obvious that 0.15% copper will contribute appreciably to the hardenability of the 10100 base analysis. Assuming the effect of copper to be closely similar to that of nickel, which is not an unreasonable assumption, this amount of copper can be expected to increase hardenability about 0.07 to 0.09 D_I units. Adding to this, the necessary adjustments of base D_I values for the difference in hardening temperature, holding time, and grain size between Mr. Hamaker's PF hardening conditions and ours, the value of 1.05 inch D_I obtained by end quench means for our base analysis can reasonably be obtained from Mr. Hamaker's value of 0.87. A correction of 0.05 D_I units apiece, for the difference in temperature and for the difference in holding times is not unreasonable, while a correction of about 0.02 to 0.03 D_I units for grain size would likewise not be excessive. Adding these corrections to the copper contributions to hardenability, a value of 1.08 is obtained, which agrees well with our measured value of 1.05. Actually, the 1.08 value can be brought even closer, if the difference in hardenability criteria between our tests and Mr. Hamaker's tests are considered.

In Fig. 12 is shown a correlation of hardenability data based on the Rockwell C-60 hardness criterion and the 50% martensite criterion obtained during the course of this hardenability study.

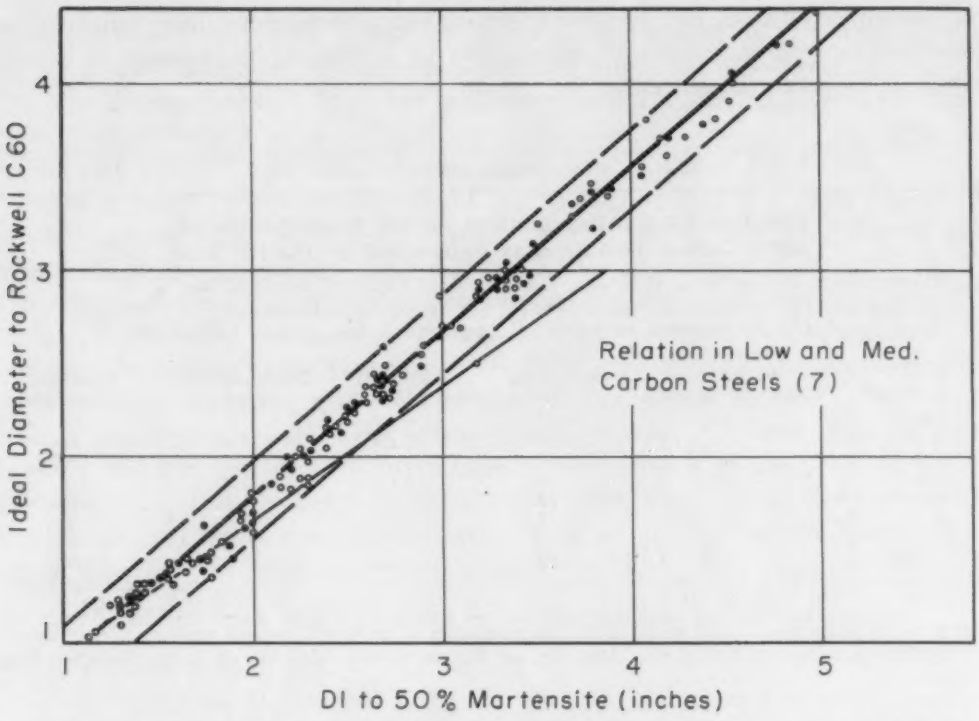


Fig. 12—Correlation Between Hardenability Based On 50% Martensite And Rockwell C-60 Criteria In 1.00% Carbon Steels.

This relationship was not included in the paper because of the fact that a structure and a hardness criteria, two different animals, were being correlated, and an explanation might unduly lengthen the paper. The use of this conversion proves interesting herein, however, and is thus shown. It is obvious that a D_I value of 1.08 based on the 50% martensite criterion, corresponds to a value of about 1.04 or 1.05 based on the Rc 60 criterion. Thus, when all factors are accounted for, Mr. Hamaker's D_I of 0.87 actually converts to 1.05. Referring again to Fig. 12, it is obvious that this correlation may be employed to convert data computed to the Rockwell C-60 criterion, to the 50% martensite criterion with equal facility at higher D_I values. The accuracy of such conversions has not been determined, but is believed to be more than satisfactory.

Commenting now on the hardenability effects of the various elements, we are extremely pleased that the PF test data checks so closely with our factors for manganese, chromium, nickel, and molybdenum. Why the effect of silicon should vary so radically, is however, quite disturbing. Not so much from the fact that our results are low, because these have been satisfactorily rechecked, but because on occasion under other alloying conditions, we have noted the effects of silicon to be considerably larger than shown in this paper. We do not feel that the method of hardenability testing was a factor, since the end-quench method was used in both cases. We are presently attempting to determine the cause for this apparently erratic behavior of silicon. In closing, we appreciate the addition of data on tungsten and vanadium, and have no constructive criticism to add on this point except to reiterate Mr. Hamaker's words that strong carbide formers may actually decrease hardenability in hypereutectoid steels by decreasing the amount of carbon which dissolves in the austenite.

HARDENABILITY OF CARBON TOOL STEEL

By Neil J. Culp

Abstract

A series of hardness-penetration curves has been developed for hypereutectoid carbon tool steels, annealed to a fully spheroidized structure, which permit prediction, to a first approximation, of the depth to which a given steel will harden in a cylinder of specified diameter. Rigid application of these curves to steels with a carbon content in excess of 0.90% necessitates a pretreatment of 40 minutes at 1600 °F (870 °C), followed by oil quenching prior to treating at 1450 °F (790 °C), and quenching into a well agitated brine solution at room temperature. This pretreatment, of course, may be omitted for steels with a carbon content of 0.90% or lower. In order to utilize these curves, it is necessary only to ascertain the critical cooling velocity or the depth of hardness penetration in a given cylinder size of the steel in question, using the aforementioned heat treatment.

The construction of these curves is based on the calculations of Scott (1,2),[1] employing as a fundamental parameter to designate hardenability, the cooling rate in degrees Fahrenheit per second at 1300 °F (705 °C) with which the steel must be cooled to attain the critical hardness, or a 50% martensite —50% pearlite structure.

Calculated hardness-penetration curves are compared with experimentally determined hardness penetrations on 1-inch, 1½-inch, 2-inch, and 2½-inch diameter cylinders from heats of five well known types of carbon tool steel. The experimental data thus obtained indicate that these curves are sufficiently accurate for practical applications.

THE hardenability concept in recent years has acquired an increasingly fundamental and quantitative aspect. Primarily, this is due to the work of Grossmann (3), Shepherd (4), Jominy and Boegehold (5), Post, Greene and Fenstermacher (6), and Carney (7), to mention just a few. Today, the end quench test of Jominy (5) has been generally accepted as a basis for ordering alloy steel of specified hardenability. Correlation curves are available to predict hardness contours in finite sections on the basis of the Jominy end quench test (8,9), and the critical bar diameter of Grossmann (3).

[1] The figures appearing in parentheses pertain to references appended to this paper.

A paper presented before the Thirty-sixth Annual Convention of the Society, held in Chicago, November 1 to 5, 1954. The author, Neil J. Culp, is associated with the Metallurgical Department, The Carpenter Steel Co., Reading, Pa. Manuscript received April 12, 1954.

It is the purpose of this paper to introduce a series of curves for predicting hardness penetration in rounds of relatively shallow hardening carbon tool steel in terms of a fundamental parameter. The parameter chosen to designate hardenability is the rate in degrees Fahrenheit per second at 1300 °F (705 °C) with which the steel must be cooled to attain the critical hardness which is associated with the 50% martensite—50% pearlite structure. For the hypereutectoid steels with which this paper is concerned, the critical hardness is Rockwell C-55, marking the boundary between case and core.

Calculated Cooling Rates and Hardness Penetration Curves:

A prediction of hardness contours in steel cylinders based upon a cooling rate parameter necessitates, of course, a determination of cooling rates at various positions in these sections during quenching. However, to obtain these requisite cooling rates, either experimentally, or through solutions of the classical heat conduction equation, is both difficult and time consuming. Fortunately, Scott (1,2) and Russell (10) have considered solutions of this equation and have calculated comprehensive tables of temperature functions for the quenching of infinite slabs and cylinders. Briefly, their solutions are based upon the assumption that Newton's "Law of Cooling" is followed during the quenching operation and that the thermal constants of the metal are independent of temperature.[2]

By simple graphical analysis, Scott's calculations (1) may be readily adapted to the conditions under which the steels in question are treated. Hereinafter, the austenitizing temperature for these steels is stipulated as 1450 °F (790 °C). The quenchant is a well agitated 10% brine solution for which the quenching constant determined by the method of Grossmann (3) from the experimental work in this project equals $4.00^{-1/in.}$ ($H = 4.00^{-1/in.}$) These conditions are thought to be typical of the heat treatment of carbon tool steels.

With but scant attention to the mathematics involved, the necessary definitions, variables, and relations are as follows:

(a) T = Temperature at a given position and time after start of quench, hereinafter = 1300 °F (705 °C).

(b) T_i = The initial or quenching temperature—1450 °F (788 °C).

(c) T_o = Temperature of quenching medium—77 °F (25 °C).

(d) By substitution of one variable for the above three in the usual manner:

$$U = \frac{T - T_o}{T_i - T_o}, \text{ or } \frac{(705\,^\circ C - 25\,^\circ C)}{(788\,^\circ C - 25\,^\circ C)} = 0.89, \text{ or } 0.90 \text{ for this work.}$$

(e) a^2 = Thermal diffusivity of steel, and from previous work, it is taken to be 0.040 square centimeters per second.[3] (This value was first deter-

[2] We would like to emphasize the fact that the pretreatment of the hardenability specimen and the steel sections, such as rounds, in which the penetration is desired must be identical. See Reference (6) for a detailed investigation of the effects of pretreatment on the hardenability of carbon steel.

[3] Units are in c.g.s. system to permit the use of Scott's calculated values. (All units are converted to the English system to obtain Figs. 2 and 3.)

mined by Scott in his work, and later redetermined by Post and Fenstermacher (11) in The Carpenter Steel Laboratory.

(f) b = Half diameter or radius of cylinder in centimeters.

(g) r = Distance from axis of cylinder to point at temperature T, in centimeters.

(h) t = Time at which temperature has fallen to T-degrees in seconds after start of quench.

(i) h = Quenching constant of the quenching medium based on cylinder radius, in reciprocal centimeters (note that the quenching constant of Grossmann as determined for the well agitated brine quench, $H = 4.00^{-1n.}$ is one-half of this constant.) Thus, for the agitated brine quench

$$h = 2 \times H = 8^{-1n.}, \text{ or}$$
$$h = 3.15 \text{ cm}^{-1}.$$

(j) Critical cooling velocity is the cooling rate at 1300 °F (705 °C) which is necessary to produce a critical hardness of Rockwell C-55 in hypereutectoid steels.

With these definitions in mind, the cooling rate at temperature, T, on the basis of Newton's law may be written:

$$\frac{d\,T}{d\,t} = (T_i - T_o)\frac{d\,u}{d\,t}, \qquad \text{Equation 1}$$

or

$$\frac{d\,T}{d\,t} = \frac{c\,a^2}{b^2}(T_i - T_o), \qquad \text{Equation 2}$$

where c (cooling rate term) $= \frac{b^2}{a^2} \cdot \frac{d\,u}{d\,t}$,

and is to be evaluated for U = 0.90.

More detailed information concerning the actual mathematics involved may be found in the original work of Scott (1,2) or Russell (10).

Scott's tabulated values for a temperature ratio (U) of 0.90, however, are incomplete, as they are calculated from a rapidly converging series. This necessitates extrapolation and interpolation of the original calculations into the region of large cylinder radius and high quenching power. Simple calculations of reciprocal values of the basic cooling rate term (c) and the product of cylinder radius and quenching power (hb) as listed in Table I permits construction of Fig. 1, to evaluate the cooling rate term (c) under the desired conditions. Values of c obtained by this method are tabulated in Table II.

These values substituted in Equation 2 in turn enable construction of Fig. 2, which is a plot of calculated cooling rates at 1300 °F (705 °C) at various positions along the radii of cylinders up to and including 5 inches in diameter. The information available in Fig. 2 may be used quite simply to determine the case depth (depth of hardness penetration) on a given size cylinder, providing the critical cooling velocity at 1300 °F (705 °C) of the steel has been determined. For example, if the critical cooling velocity at 1300 °F (705 °C) of a par-

Table I
Reciprocal of Cooling Term and hb Product For U = 0.90

Reciprocal Values of hb	VALUES OF $\frac{a^2}{b^2} \cdot \frac{dt}{du}$ for r/b:					
Product	0	0.5	0.7	0.8	0.9	1.0
0.000	0.296	0.198	0.071	0.026	—	—
0.100	0.364	0.262	0.132	0.064	0.028	—
0.200	0.417	0.321	0.184	0.115	0.054	—
0.333	0.500	0.412	0.250	0.167	0.087	—
0.625	0.649	Not Determined	0.394	Not Determined	0.182	—
1.000	0.840	Not Determined	0.595	Not Determined	0.331	0.200
1.250	0.972	Not Determined	"	Not Determined	Not Determined	0.278
2.000	1.351	"	Not Determined	"	"	0.625

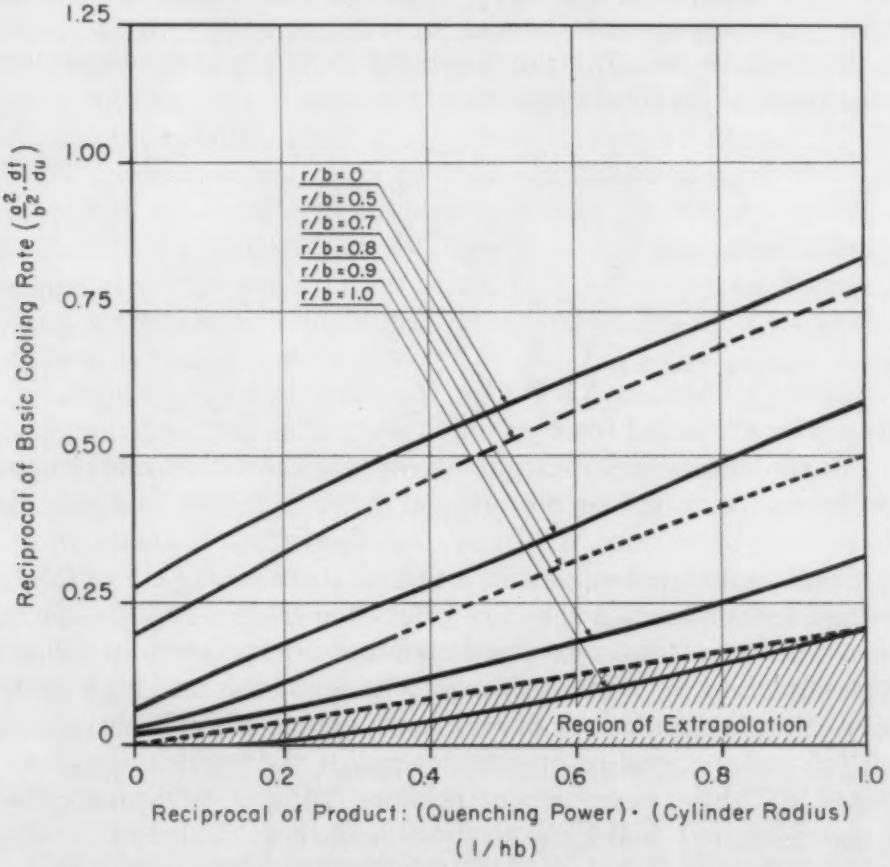


Fig. 1—Basic Cooling Rate Term for Several Positions in Various Sized Cylinders as a Function of Quenching Power. Reciprocal functions plotted to permit extrapolations into the region of high quenching power and large cylinder radius. Broken lines represent extensions of Scott's calculated values.

ticular steel is known to be 200 °F (95 °C) per second, and the case depth of a 1.5 inch diameter cylinder is desired, one finds 200 °F (95 °C) per second on the vertical axis of Fig. 2 and proceeds across to the curves marked 1.5 inch diameter, and then observes on the horizontal axis the position 0.84 on the radius of the cylinder (0.75 inch).

Table II
Cooling Rate Term For Various Positions in Cylinders Up to 5.00 inches in Diameter Under Conditions Stipulated in Part I

Radius of Cylinder inches	b cms:	hb h=3.15 cm^{-1}	Values of $\frac{b^2}{a^2}\frac{du}{dt}$ (c.g.s. units) U=0.90 for r/b =					
			0	0.5	0.7	0.8	0.9	1.0
0.50	1.27	4.00	2.30	3.00	4.96	8.25	19.70	106
0.75	1.91	6.00	2.50	3.52	5.26	9.40	21.00	144
1.00	2.54	8.00	2.65	3.70	6.22	9.86	22.50	170
1.25	3.18	10.00	2.80	3.87	6.30	9.96	23.30	200
1.50	3.81	12.00	2.93	3.97	6.62	10.10	23.50	210
1.75	4.45	14.00	2.96	4.08	6.70	10.50	23.60	252
2.00	5.08	16.00	2.99	4.16	6.79	10.80	23.71	293
2.25	5.72	18.00	3.09	4.20	6.95	10.84	23.80	333
2.50	6.35	20.00	3.10	4.28	7.05	11.00	24.00	382

Thus, at a distance of 0.84 × 0.75, or 0.63 inches from the center of the cylinder, the cooling rate at 1300 °F (705 °C) will be 200 °F (95 °C) per second, providing the steel has been treated according to the previously stipulated conditions. The value 0.63 inch, of course, is the calculated radius of the unhardened core of the particular cylinder under discussion. By simple subtraction of this value from the actual cylinder radius, one then may calculate the desired case depth of the cylinder to be 0.75–0.63, or 0.12 inches.

Selection of a wide range of cooling rates at 1300 °F (705 °C) to embrace all possible cooling rates given in Fig. 2, and the arbitrary designation of these selected cooling rates as critical cooling velocities at 1300 °F (705 °C), yields a sufficient number of values to construct Fig. 3, using the simple arithmetical calculations previously outlined. In essence, Fig. 3 is a plot of critical cooling velocity at 1300 °F (705 °C) versus radius of unhardened core, employing as a parameter, cylinder diameter. Direct plots of cooling velocity versus case depth would result in a prohibitively narrow spread of the curves. However, due to the arrangement of the step-like scales of Fig. 3, (which read from right to left), it is possible to read directly the case depth of a given diameter cylinder when either the critical cooling velocity at 1300 °F (705 °C), or the case depth of a given size cylinder is known. This is accomplished simply by following the critical cooling velocity of interest to its point of intersection with the curve of the cylinder size desired, and then dropping to the horizontal axis pertaining to this particular cylinder and reading the case depth directly. Alternately, one may determine the depth to which a given size cylinder will harden and then locate this value on the horizontal scale of Fig. 3, which pertains to the diameter of the test cylinder, then proceed vertically to the intersection of this value with the curve of the cylinder in question, and read on the vertical axis, the critical cooling velocity of the steel.

Actually, from the viewpoint of case depth, Fig. 3 is made up of a series of curves, each with its own horizontal axis (case depth) which is read from right to left, but all with a common vertical axis of critical

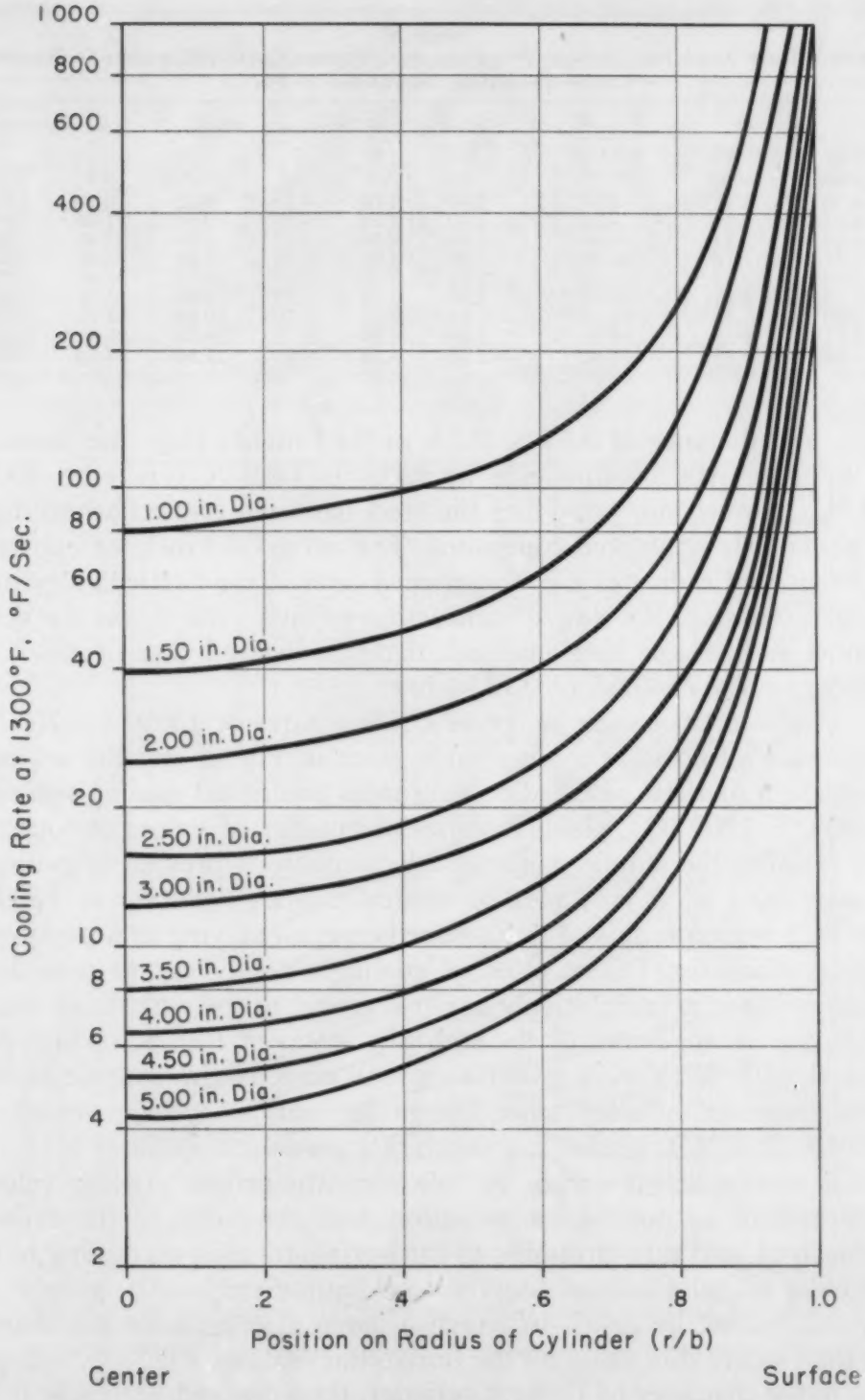


Fig. 2—Calculated Cooling Rates at 1300 °F (705 °C) In Various Sized Cylinders. Quenching temperature = 1450 °F (790 °C). Agitated brine quench $H = 4.00$ inch^{-1}.

cooling velocity at 1300 °F (705 °C). The critical cooling velocity may be experimentally determined by the cone test of Post, Greene and

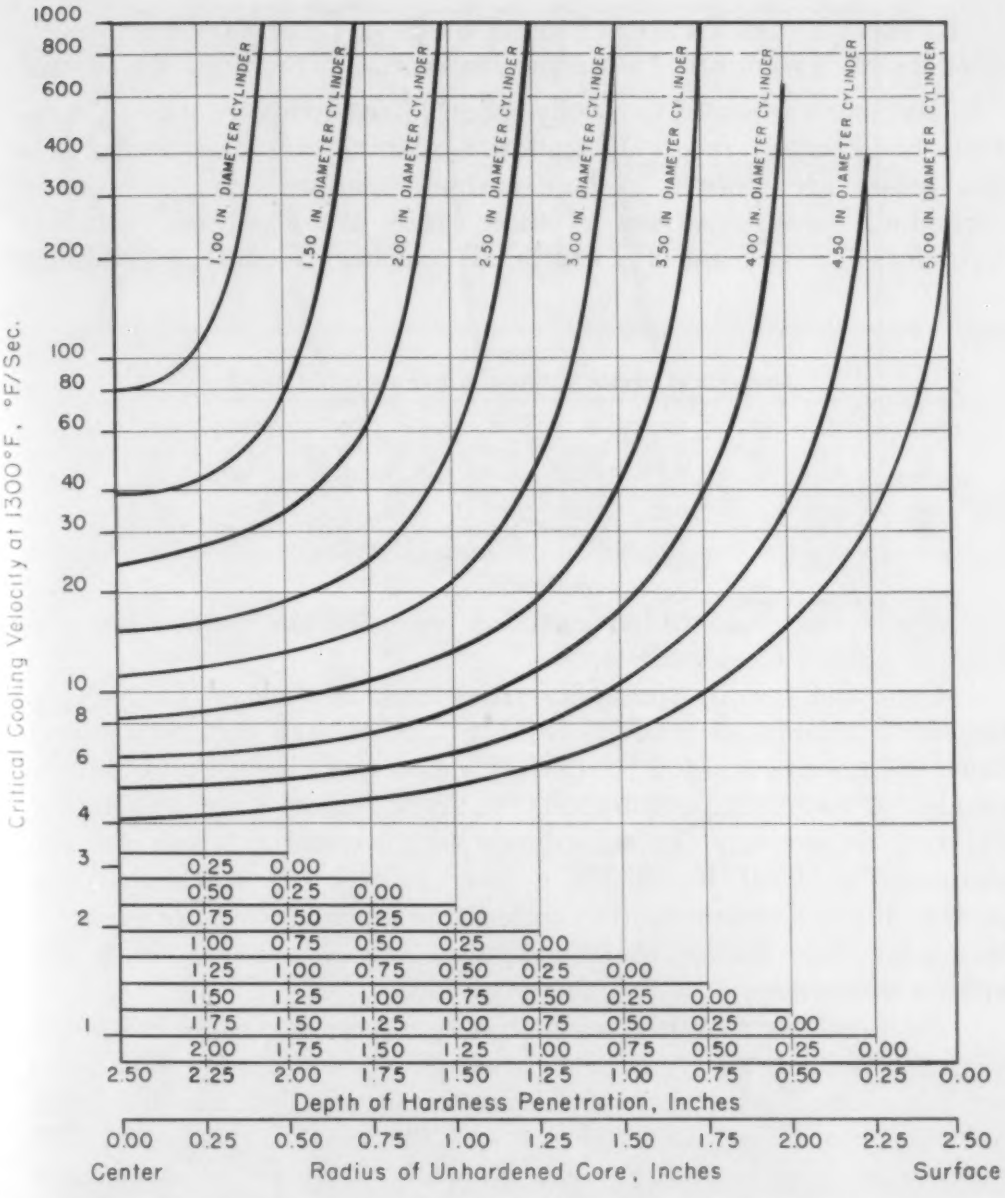


Fig. 3—Calculated Hardness Penetration Curves. Hardness penetration as a function of cooling velocity at 1300 °F (705 °C). Quenching temperature = 1450 °F (790 °C) Agitated brine quench; H = 4.00 inch^{-1}.

Fenstermacher (6) or by the standard end quench test, although the accuracy of the latter test for these shallow hardening steels is rather questionable. It is thus possible by means of a simple test, e.g., the cone test, the end quench test, or by simply quenching a given size round, to ascertain quantitatively with the use of Fig. 3, the hardenability of shallow hardening tool steels. It is, of course, essential that the pretreatment and hardening procedure employed for the hardenability specimen and the rounds be exactly identical.

Experimental Determination of Case Depth on Rounds, One Inch Through Two-and-One-Half Inches in Diameter.

Bar stock annealed to a fully spheroidized structure was procured from five heats of relatively shallow hardening tool steel. Included in this group are straight carbon, carbon-vanadium, and carbon low chromium steels. Analyses of these steels are listed in Table III. Cylinders 1, 1½, 2 and 2½ inches, all 6 inches in length, to minimize

Table III
Analyses of Steels Utilized in Experimental Work

Steel	C	Mn	Si	P	S	Cr	Ni	Mo	Cu	V
A	1.08	0.20	0.17	0.010	0.011	0.06	0.12	0.02	0.11	0.20
B	1.04	0.24	0.27	0.011	0.014	0.15	0.10	0.02	0.12	—
C	0.94	0.20	0.37	0.025	0.016	0.18	0.07	0.02	0.16	—
D	0.99	0.33	0.32	0.020	0.013	0.44	0.28	0.07	0.15	—
E	0.88	0.37	0.44	0.012	0.009	0.13	0.06	0.02	0.14	—

end effects, one standard hardenability cone, and one Jominy specimen were machined from each steel.

Cone and Jominy specimens from steels A through D were pretreated 40 minutes at 1600 °F (870 °C), oil-treated, and then austenitized 10 minutes at 1450 °F (790 °C) and quenched in a 10% brine solution at room temperature (80 °F, 25 °C) from Cone and Jominy fixtures, respectively. In accordance with normal practice, the pretreatment at 1600 °F (870 °C) was omitted for specimens from Steel E due to a carbon content under 0.90%. The furnace employed to heat treat these hardenability specimens was an electric muffle type with an atmosphere of approximately 4% 0_2.

Heat treatment of the various cylinders from each steel was identical with that of the respective hardenability specimens save for a variable austenitizing time of 5 minutes per diameter inch of each cylinder. The quenchant employed was the usual well agitated 10% brine solution with an "H" value of $4.00^{-in.}$. In order to eliminate surface conditions, and thus facilitate subsequent hardness measurements, the various cylinders were heat treated in a neutral salt bath.

After hardening, the cones were tested magnetically (12) and then split longitudinally, and etched in a 1:1 HCl solution for three minutes at 180 °F (80 °C) to determine the critical cooling velocity visually. Jominy specimens, of course, were tested in the conventional manner. Hardenability ratings, including Shepherd Disk Number Conversions are tabulated with all other significant experimental data in Table IV.

Following heat treatment, the various size rounds were nicked and fractured to determine the fracture grain size (Table IV). A disk ½ inch thick was then cut from one of the fractured surfaces of each round and surface ground. In the case of each 2.5 inch diameter disk,

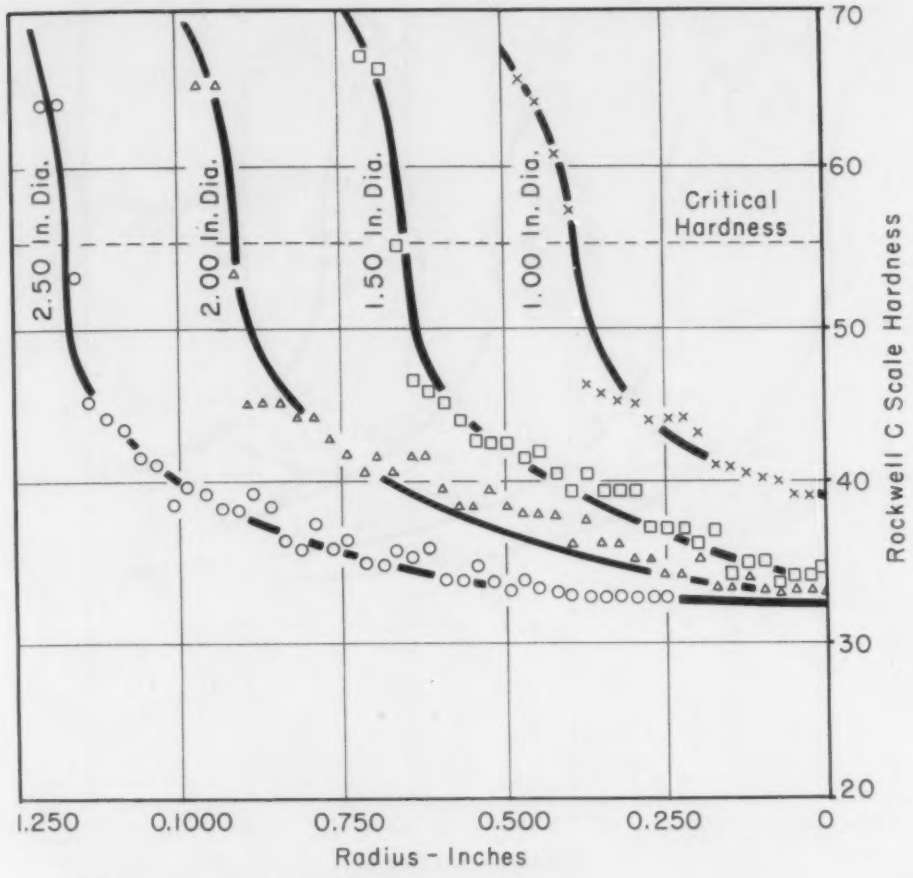


Fig. 4a—Rockwell Contour Curves Steel A.
Hardness penetrations:
1.00 inch diameter cylinder = 0.113 inch
1.50 inch diameter cylinder = 0.088 inch
2.00 inch diameter cylinder = 0.075 inch
2.50 inch diameter cylinder = 0.062 inch

only a one-quarter section of the disk was so prepared in order to facilitate fitting the specimen in the micrometer stage employed for determining hardness profiles of the rounds. With the use of the micrometer stage, Rockwell N-30 readings were taken every 0.025 inch from surface to center, traversing four separate radii on each specimen. The four Rockwell N-30 profiles were then averaged, converted to Rockwell C scale, and plotted against distance from surface to center of the round as in Figs. 4a to 4e, inclusive.

Measurement of the case depth of the various rounds was obtained directly from Figs. 4a to 4e by determining the point at which the critical hardness line, Rockwell C-55, intersected each particular hardness contour curve (Table IV). One should note that the third figure in these measurements is merely an approximation obtained by the use of the micrometer stage. Following these measurements, each disk was etched with the same technique employed for the cones, and coated with lacquer to preserve the etched case and core. It should

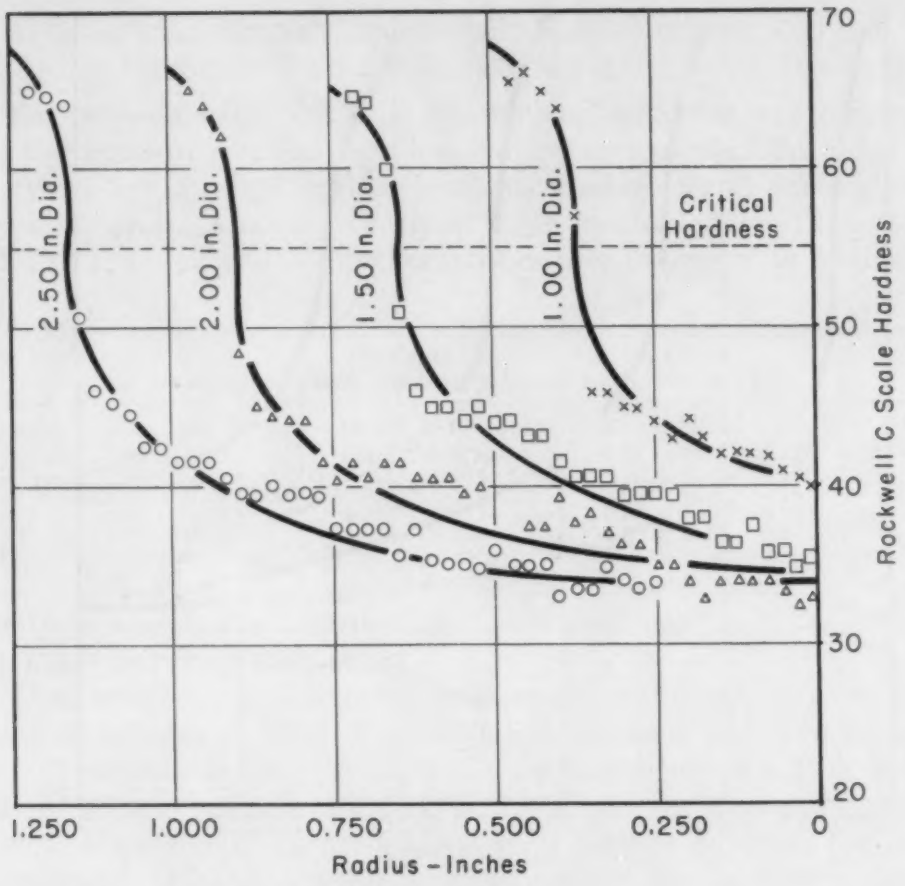


Fig. 4b—Rockwell Contour Curves Steel B.
Hardness Penetrations:
1.00 inch diameter cylinder = 0.125 inch
1.50 inch diameter cylinder = 0.100 inch
2.00 inch diameter cylinder = 0.090 inch
2.50 inch diameter cylinder = 0.077 inch

be noted here that the etched appearance of the disk consisted of three regions; a gray outer case, a dark inner ring (the width of which increased with hardenability), and a light core. Visual measurements were made to the inner rim of this gray outer case, as hardness tests and metallographic examinations established the location of the critical hardness (Rockwell C-55) at this point. Visual measurements thus obtained compared favorably with those obtained graphically, as is shown in Table IV.

The work of Heindlhofer (13), and more recently, that of Carney and Janulionis (7,14) has demonstrated that the application of Newton's Law to quenching problems is not strictly valid. This is due in general to the variation of the thermal constants of the steel during quenching, and in particular to the variation of the quenching constant, (H or h), of the quenching medium with cylinder diameter and temperature. However, determination of an average H value after the manner of Grossmann appears to permit calculation of hardness pene-

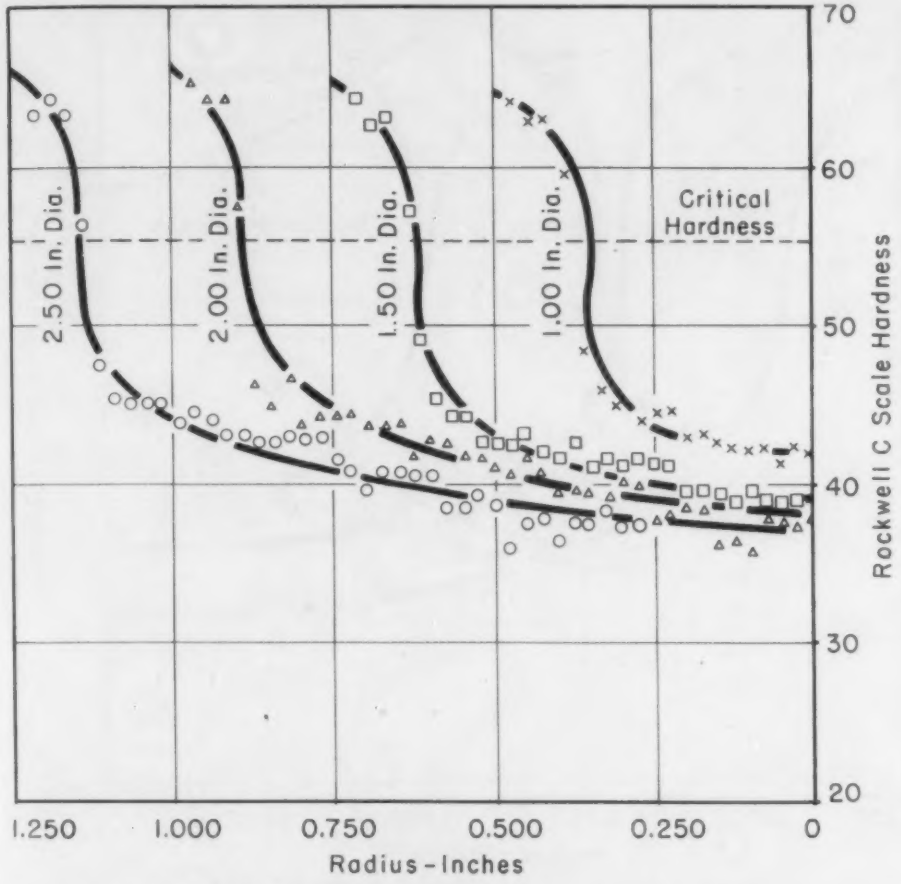


Fig. 4c—Rockwell Contour Curves Steel C.
Hardness Penetrations:
1.00 inch diameter cylinder = 0.133 inch
1.50 inch diameter cylinder = 0.113 inch
2.00 inch diameter cylinder = 0.100 inch
2.50 inch diameter cylinder = 0.085 inch

trations which are sufficiently compatible with experimental results for practical applications.

A comparison of experimental data with the calculated curves of Fig. 3 is presented in Fig. 5. This comparison appears to be satisfactory, and in many cases, the deviation is zero, notably on larger diameter rounds. Actually, this deviation substantiates the conclusion of Carney and Janulionis (7,14), since they have established that the quenching constant increases with decreasing bar diameter, and conversely. This, of course, would produce deeper hardening on small diameter cylinders, and shallower hardening on large diameter cylinders than would be expected from calculated values based on an average constant value for the quenching power of the bath. Fig. 5 definitely illustrates this trend.

Summary

The favorable comparison of calculated values with experimentally determined hardness penetration presented in Fig. 5 appears to justify

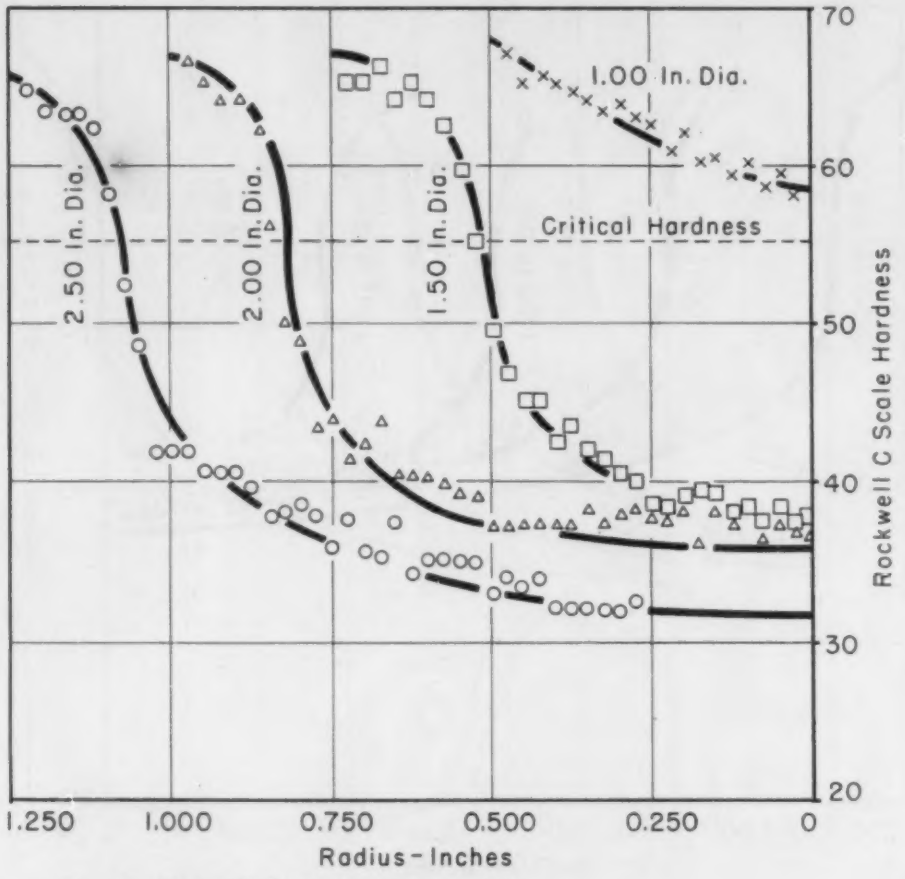


Fig. 4d—Rockwell Contour Curves Steel D.
Hardness Penetrations:
1.00 inch diameter cylinder = Hardened through
1.50 inch diameter cylinder = 0.225 inch
2.00 inch diameter cylinder = 0.181 inch
2.50 inch diameter cylinder = 0.163 inch

Table IV
Experimental Data

Identification	Critical Cooling Velocity at 1300 °F From Cone Test and Shepherd Hardenability Number	Critical Cooling Velocity at 1300 °F From Jominy End Quench Test	Diameter of bar (Inches)	Diameter of Unhardened Core (Inches)	Case Depth (Inches) From Hardness Profiles	Case Depth (Inches) Visual	Fracture Grain Size
Steel A	332 °F/sec. No. 9	350 °F/sec.	1.000	0.774	0.113	0.109	9-¼
			1.500	1.324	0.088	0.085	9-¼
			2.000	1.850	0.075	0.077	9
			2.500	2.376	0.062	0.063	9-¼
Steel B	277 °F/sec. No. 11	260 °F/sec.	1.000	0.750	0.125	0.110	9
			1.500	1.300	0.100	0.097	9
			2.000	1.820	0.090	0.086	9
			2.500	2.346	0.077	0.078	9-¼
Steel C	196 °F/sec. No. 13	200 °F/sec.	1.000	0.734	0.133	0.117	8-½
			1.500	1.274	0.113	0.110	8
			2.000	1.800	0.100	0.101	8
			2.500	2.330	0.085	0.086	8
Steel D	Hardened Through	85 °F/sec. No. 17	1.000	No Core	Thru	Thru	9-¼
			1.500	1.050	0.225	0.219	9-¼
			2.000	1.638	0.181	0.180	9-¼
			2.500	2.174	0.163	0.164	9-¼
Steel E	175 °F/sec. No. 14	180 °F/sec.	1.000	0.700	0.150	0.156	8-½
			1.500	1.250	0.125	0.136	8-½
			2.000	1.758	0.121	0.118	8-½
			2.500	2.274	0.113	0.114	8-½

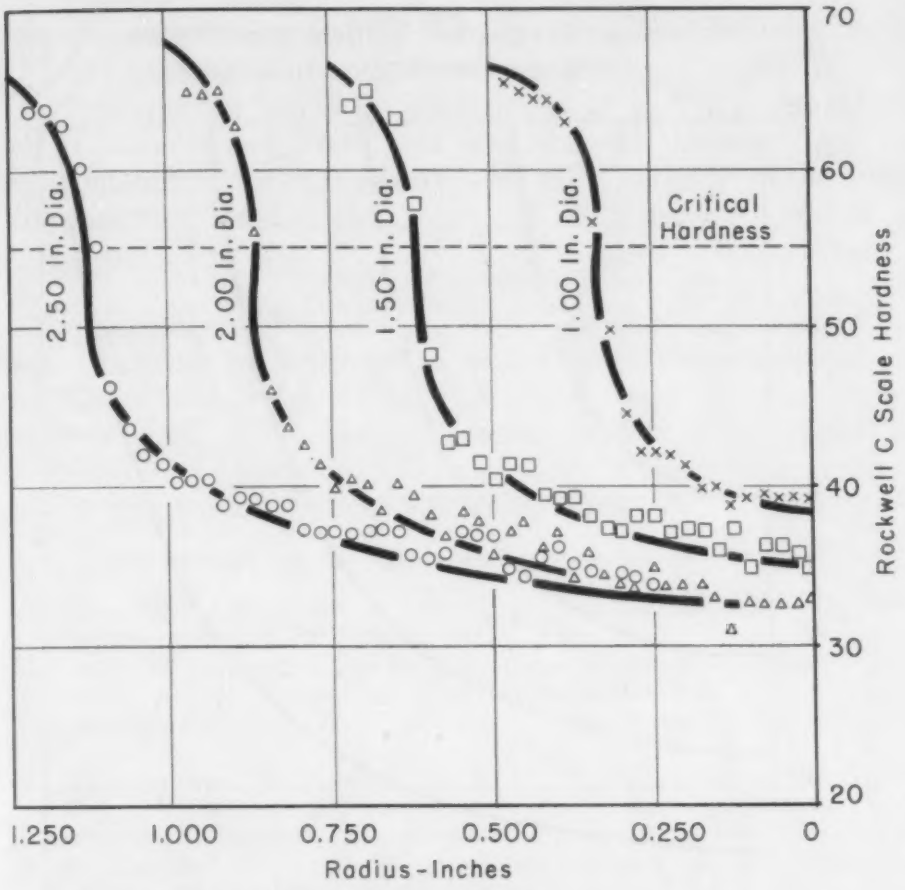


Fig. 4c—Rockwell Contour Curves Steel E.
Hardness Penetrations:
1.00 inch diameter cylinder = 0.150 inch
1.50 inch diameter cylinder = 0.125 inch
2.00 inch diameter cylinder = 0.121 inch
2.50 inch diameter cylinder = 0.113 inch

the application of Fig. 3 to practical heat treating problems. Furthermore, these curves have been successfully applied to various hardenability problems at The Carpenter Steel Company arising from specifications concerned with a specific case to core ratio. It seems probable that the curves of Fig. 3 dealing with cylinders 3 inches through 5 inches in diameter, though they lack experimental verification, do not deviate very greatly from the actual behavior of these larger size cylinders, as all curves conform to a similar pattern. At the very least, Fig. 3 should serve as a valuable guide to the practical heat treater.

However, several precautions should be noted in any rigid application of the curves in Fig. 3:

1. Heat treatment of the cylinders, including pretreatment, must be identical with that employed for the hardenability specimen.

2. Cylinders must be hardened from, or in the vicinity of 1450 °F (790 °C), with a resulting fracture grain size in the range of 8 to 9.

3. Values of case depth determined by these curves apply only to cylinders which are quenched into a well agitated 10% brine solution

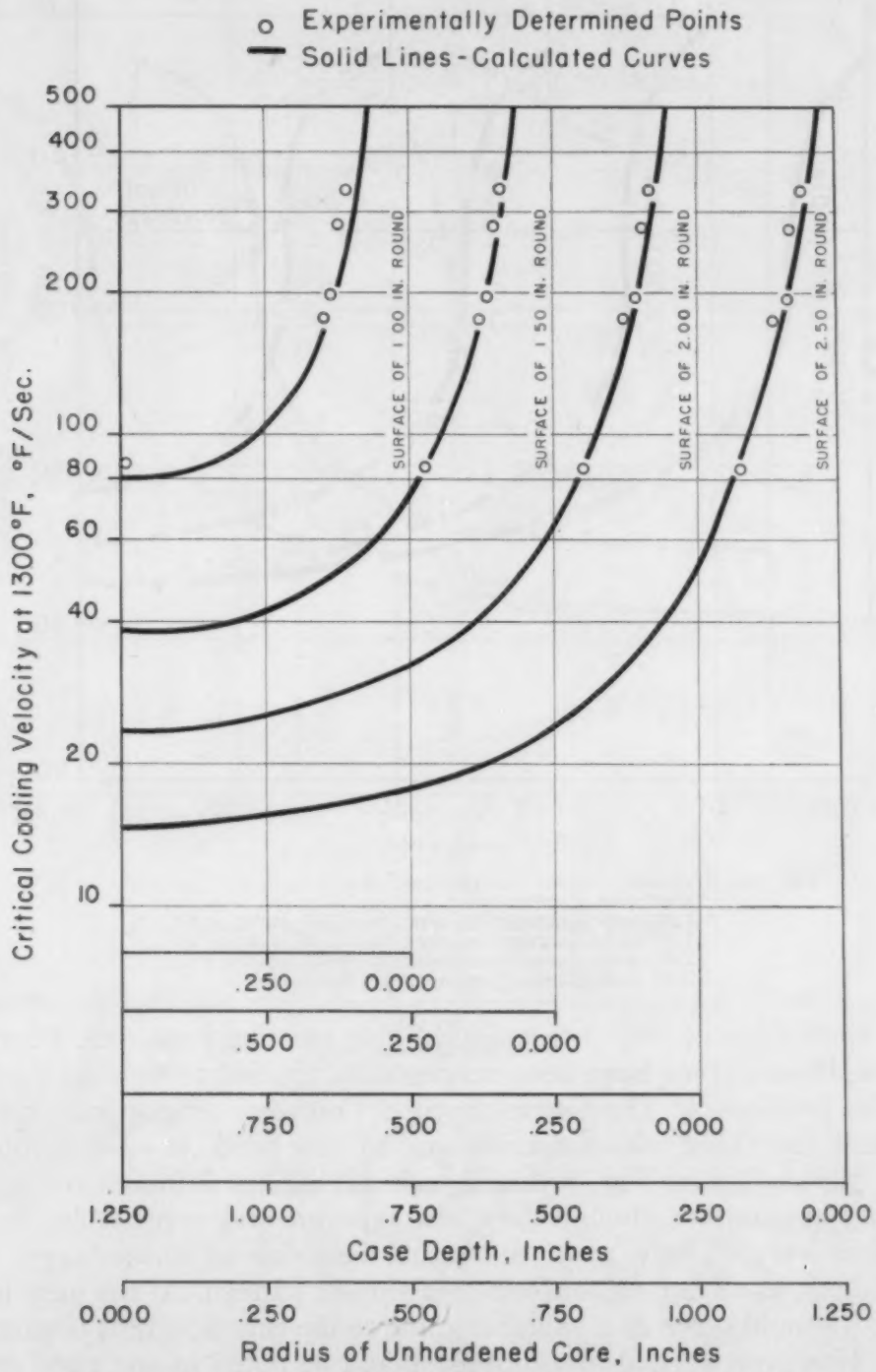


Fig. 5—Comparison of Calculated Hardness Penetrations with Experimentally Determined Penetrations. Quenching temperature = 1450 °F (790 °C) Agitated Brine Quench (H = 4.00 inch^{-1}).

($H = 4.00^{-in.}$).

4. Curves are valid only for hypereutectoid steels with a critical hardness of Rockwell C-55.

5. If a pretreatment, consisting of 40 minutes at 1600 °F (870 °C), followed by oil quenching, is not employed for steels with

carbon contents in excess of 0.90%, penetrations obtained on such steels will be somewhat deeper than those predicted by Fig. 3.

6. Penetrations which are determined from Fig. 3 on cylinders 1 inch in diameter and under, will very likely be shallower than those actually obtainable due to the afore-mentioned variation of the quenching constant with bar diameter.

ACKNOWLEDGMENT

The author gratefully acknowledges the encouragement of J. H. Parker, Chairman of the Board, Frank Palmer, President, and C. B. Post, Chief Metallurgist, of The Carpenter Steel Company, without which this work would not have been possible. The assistance of R. J. Ebbert of the Metallurgical Laboratory in the experimental work of this investigation is especially acknowledged.

References

1. H. Scott, "Some Problems of Quenching Steel Cylinders," TRANSACTIONS, American Society for Metals, Vol. 22, 1934, p. 68.
2. H. Scott, Discussion of Paper by B. R. Quereau and W. H. Mayo, "Hardenability and Its Designation, The Hardenability Line," from Symposium, "HARDENABILITY OF ALLOY STEELS," American Society for Metals, 1939, p. 251.
3. M. A. Grossmann, M. Asimow and S. F. Urban, "Hardenability, Its Relation to Quenching, and Some Quantitative Data," Symposium, HARDENABILITY OF ALLOY STEELS, American Society for Metals, 1939, p. 124.
4. B. F. Shepherd, "Inherent Hardenability Characteristics of Tool Steel," TRANSACTIONS, American Society for Metals, Vol. 17, 1930, p. 90.
5. W. E. Jominy and A. L. Boegehold, TRANSACTIONS, American Society for Metals, Vol. 26, 1938, p. 579; Ibid. Vol. 27, 1939, p. 1072.
6. C. B. Post, O. V. Greene, W. H. Fenstermacher, "Hardenability of Shallow Hardening Steels," TRANSACTIONS, American Society for Metals, Vol. 30, 1942, p. 1202.
7. D. J. Carney, "Another Look at Quenchants, Cooling Rates and Hardenability," TRANSACTIONS, American Society for Metals, Vol. 46, 1954, p. 882.
8. J. L. Lamont, "How to Estimate Hardening Depth in Bars," *Iron Age,* Oct. 14, 1943.
9. M. Asimow, W. F. Craig and M. A. Grossmann, "Correlation Between Jominy Test and Quenched Round Bars," *Journal,* Society of Automotive Engineers, Vol. 49, 1941, p. 283.
10. T. F. Russell, "Some Mathematical Considerations on the Heating and Cooling of Steel," *Iron and Steel Institute, Special Report No. 14,* 1936, p. 149.
11. C. B. Post and W. H. Fenstermacher, "Rates of Cooling in Blocks and Cylinders," TRANSACTIONS, American Society for Metals, Vol. 33, 1944, p. 19.
12. C. B. Post and W. H. Fenstermacher, "Magnetic Measurement of the Hardenability of Carbon Tool Steels," METALS PROGRESS, American Society for Metals, February 1945, p. 286.
13. K. Heindlhofer, *Physical Review,* Vol. 20, 1922, p. 221.
14. D. J. Carney and A. D. Janulionis, "An Examination of the Quenching Constant, 'H'," TRANSACTIONS, American Society for Metals, Vol. 43, 1951, p. 480.

DISCUSSION

Written Discussion: By D. Niconoff, Canton Metallurgical Laboratory, Republic Steel Corp., Canton, Ohio.

The author is to be congratulated upon the ingenious application of the Scott's and Russell's solution of the heat flow equation to calculation of hardenability of carbon tool steels.

The degree of agreement between the empirical and calculated hardenabilities obtained by the new method is almost phenomenal in comparison with the same relation existing for alloy steels, where the calculated values not uncommonly are found to be 10 to 15% off the experimental data.

This remarkable agreement is probably due to uniformity of the position of critical points in this rather restricted by its composition group of steels, which permitted selection of the cooling rate through 1300 °F as the parameter for designation of hardenability. In case of alloy steels the conditions are far from being so ideal since the presence of alloying elements might elevate or depress the transformation temperature considerably, depending whether the elements are ferrite or austenite promoters.

The low alloy content of the carbon tool steels is likely to assure also a relative freedom from chemical segregation, at least in the elements exercising a profound effect upon the transformation temperature.

In view of the above considerations it would be interesting to know whether the presence of alloying elements in the hypereutectoid steels, similar to the ones used in this investigation, would interfere with the applicability of this new method.

Does the author possess any information as to how great a concentration of alloys could be tolerated in this type of steel before the unusually good agreement between the calculated and the experimental results ceases to exist?

Author's Reply

The comments by Mr. D. Niconoff are greatly appreciated. It is true that the low alloy content of carbon tool steels results in relatively uncomplicated transformations; however, some work has been previously published in Reference 11 to this paper in which the same cooling rate parameter is employed to predict hardenability in finite sections of a 0.90% carbon, 1.60% manganese oil hardening tool steel. The degree of correlation between experimental and calculated values was found to be quite satisfactory. With respect to other alloy additions, it is thought that elements such as silicon and chromium would probably not influence the degree of correlation very greatly; whereas an element such as molybdenum very likely would.

Although some work is in progress in The Carpenter Steel Company laboratories correlating analysis and hardenability, the author cannot state with any exactness what maximum alloy content could be tolerated in hypereutectoid carbon steels before the agreement between calculated and experimental results would be materially affected.

EFFECT OF CARBON AND NITROGEN ON THE ATTAINABLE HARDNESS OF MARTENSITIC STEELS

By A. E. Nehrenberg, Peter Payson and Peter Lillys

Abstract

The maximum hardness which can be obtained in steels containing 0.035 to 0.15% carbon heat treated to have fully martensitic structures free from residual carbides and residual nitrides is shown to be a function of nitrogen as well as carbon content. The following empirical logarithmic equation satisfactorily describes the relationships among attainable hardness, carbon and nitrogen contents and is applicable to a carbon range of 0.035 to 0.50% when the nitrogen is low and to a nitrogen range of 0.01 to 0.30% when the carbon is 0.05 to 0.15%:

$$\log \text{Rockwell C hardness} = 2.182 + 0.469\ (\log C) + 0.108\ (\log C)^2 + 0.164\ (\log N) + 0.025\ (\log N)^2$$

where C = carbon content in weight per cent
and N = nitrogen content in weight per cent.

Although the chromium content was varied from 0.5 to 15.5% in steels containing 0.035 to 0.16% carbon there was no evidence to suggest that there was any effect of this variation in chromium content on the attainable hardness.

Introduction

IT IS commonly observed that the attainable hardness of low carbon high alloy steels, such as the martensitic stainless steels for example, is somewhat greater than would be predicted from the Burns, Moore and Archer relationship (1)[1] between carbon content and maximum hardness of martensite. There are several possible explanations for this discrepancy. In the first place, the Burns, Moore and Archer relationship may not be accurate when the carbon content is lower than about 0.12%. In their work these authors obtained hardness data for only three steels of such low carbon content, and these steels were carbon steels which may not have hardened fully even when drastically quenched. Burns, Moore and Archer realized that their relationship between carbon content and martensite hardness for carbon contents

[1] The figures appearing in parentheses pertain to the references appended to this paper.

A paper presented before the Thirty-sixth Annual Convention of the Society, held in Chicago, November 1 to 5, 1954. The authors, A. E. Nehrenberg, Peter Payson and Peter Lillys, are associated with the Research Laboratory, Crucible Steel Company of America, Harrison, N. J. Manuscript received April 19, 1954.

less than about 0.12% is uncertain and consequently drew a dashed line through the points for these three very low carbon steels. In the second place, the martensitic stainless steels are sometimes found to contain almost, if not as much, nitrogen as carbon. There is some evidence that additions of nitrogen increase the hardness of high chromium martensitic steels (2). In the third place, the high chromium content of the martensitic stainless steels may be partly responsible for such steels having a higher attainable hardness by providing some solid solution hardening. Bain (3) showed that drastically quenched iron-chromium alloys containing about 0.02% carbon increased in hardness with increasing chromium and concluded that this indicated that chromium affects the maximum hardness at a given low carbon level.

The present paper is the result of work carried out for the purpose of evaluating the relative importance of these possible explanations for the discrepancy between the attainable hardness of low carbon high alloy martensitic steels and the Burns, Moore and Archer relationship.

Material

Altogether 54 experimental steels were used during the course of this investigation. Of this number 12 were ordered explicitly for this study whereas the remaining 42 steels had been originally obtained for other projects. All of the steels were induction melted, deoxidized with aluminum cast into 15-pound ingots and were forged to $\frac{5}{8}$ inch square bars. The check analyses for the forged bars are shown in Table I. The carbon contents of these steels vary from 0.035 to 0.16% and the chromium from about 0.5 to about 15.5%. In the steels of lower chromium content additions of up to 6% nickel and up to 3% manganese were made. The steels containing 12 to 15.5% chromium contain only residual nickel and molybdenum together with normal amounts of silicon and up to 2% manganese. The nitrogen was varied from about 0.030 to about 0.30% in the steels containing 12 to 15.5% chromium.

Procedure

All of the steels were annealed by a sub-critical temper. Then, test specimens $\frac{1}{4}$-inch thick were cut from each bar, austenitized in duplicate at temperatures of 1800, 1900 and 2000 °F (980, 1040 and 1095 °C), water-quenched and immediately refrigerated in liquid nitrogen at minus 320 °F (195 °C) to minimize the retained austenite. The specimens were subjected to metallographic examination and those containing any residual carbides or residual nitrides were discarded. Five hardness determinations were made on each specimen which passed the metallographic examination, and the average for each specimen was computed. The Rockwell C hardness value shown in Table I is the grand average for either four or six specimens for each steel.

The standard error for the grand average was determined to be 0.25 in Rockwell C units.

The data obtained were analyzed by employing conventional statistical procedures (4).

Table I
Analyses and Attainable Hardnesses of Experimental Steels

Bar	C	Mn	Si	Ni	Cr	Mo	N	Observed Rockwell C Hardness	log Observed Rockwell C Hardness	Computed * Rockwell C Hardness (in logarithms)	Deviation ** (in logarithms)	Computed Rockwell C Hardness
5256	0.160	1.26	1.36	1.80	0.43	0.44	0.013	43.6	1.6395	1.6556	−0.0161	45.2
5463	0.090	1.37	0.91	1.76	0.73	0.23	0.007	37.7	1.5763	1.5711	+0.0052	37.2
5259	0.142	1.19	1.19	2.17	0.88	0.25	0.015	42.3	1.6263	1.6449	−0.0186	44.1
3804	0.044	3.32	0.20	3.20	3.35	0.01	0.033	36.8	1.5658	1.5557	+0.0101	36.0
3805	0.054	3.28	0.18	3.19	3.31	0.01	0.020	34.8	1.5416	1.5537	−0.0121	35.8
3806	0.116	3.41	0.21	3.17	3.41	0.01	0.023	41.8	1.6212	1.6351	−0.0139	43.2
3807	0.054	1.72	0.21	6.17	3.33	0.01	0.023	36.5	1.5623	1.5586	+0.0037	36.2
3808	0.052	1.74	0.21	6.28	3.31	0.01	0.019	35.8	1.5539	1.5488	+0.0051	35.4
3809	0.091	1.79	0.19	6.22	3.33	0.01	0.021	39.8	1.5999	1.6052	−0.0053	40.3
3810	0.114	1.76	0.20	6.20	3.31	0.01	0.022	42.0	1.6232	1.6317	−0.0085	42.8
3803	0.064	3.26	0.20	3.23	4.22	0.01	0.037	39.1	1.5922	1.5916	+0.0006	39.0
5448	0.035	0.33	0.17	0.11	4.76	0.55	0.013	29.6	1.4713	1.5069	−0.0356	32.1
5452	0.080	0.44	0.27	0.10	5.13	0.56	0.018	37.8	1.5775	1.5865	−0.0090	38.6
3811	0.038	1.77	0.21	3.18	6.71	0.01	0.029	35.6	1.5514	1.5401	+0.0113	34.7
3812	0.045	1.65	0.19	3.17	6.70	0.01	0.031	36.6	1.5635	1.5550	+0.0085	35.9
3813	0.107	1.72	0.21	3.16	6.71	0.01	0.028	43.1	1.6345	1.6331	+0.0014	43.0
3814	0.118	1.78	0.22	3.16	6.70	0.01	0.026	45.3	1.6561	1.6418	+0.0143	43.8
5456	0.079	0.45	0.13	0.11	8.37	0.55	0.024	39.1	1.5922	1.5953	−0.0031	39.4
3745	0.087	0.56	0.31	0.14	12.01	0.05	0.034	41.4	1.6170	1.6183	−0.0013	41.5
3746	0.103	0.58	0.29	0.14	12.01	0.05	0.038	43.4	1.6375	1.6410	−0.0035	43.8
3747	0.147	0.51	0.26	0.13	11.88	0.04	0.043	49.8	1.6972	1.6879	+0.0093	48.7
3750	0.122	0.55	0.28	0.14	12.88	0.05	0.045	45.7	1.6599	1.6673	−0.0074	46.5
3751	0.140	0.45	0.26	0.14	12.73	0.02	0.029	47.2	1.6739	1.6662	+0.0077	46.4
3755	0.091	0.61	0.20	0.14	12.55	0.01	0.050	44.1	1.6444	1.6390	+0.0054	43.6
3760	0.102	0.54	0.30	0.14	12.81	0.17	0.055	45.3	1.6561	1.6556	+0.0005	45.2
3764	0.116	0.61	0.32	0.14	12.85	0.01	0.036	44.8	1.6513	1.6521	−0.0008	44.9
3765	0.148	0.60	0.30	0.14	12.35	0.10	0.044	50.1	1.6998	1.6897	+0.0101	48.9
3766	0.069	0.56	0.31	0.14	12.75	0.01	0.097	43.7	1.6405	1.6420	−0.0015	43.9
3767	0.108	0.60	0.31	0.14	12.68	0.01	0.075	45.7	1.6599	1.6760	−0.0161	47.4
3768	0.131	0.59	0.32	0.14	12.88	0.01	0.090	49.4	1.6937	1.7071	−0.0134	50.9
3769	0.147	0.56	0.26	0.14	12.27	0.01	0.115	52.1	1.7168	1.7336	−0.0168	54.2
3771	0.081	0.83	0.18	0.45	11.76	0.01	0.097	45.6	1.6590	1.6576	+0.0014	45.5
3773	0.133	0.55	0.27	0.27	12.26	0.19	0.041	46.2	1.6646	1.6738	−0.0092	47.2
4267	0.060	0.40	0.46	0.13	12.55	0.01	0.13	44.5	1.6484	1.6440	+0.0044	44.1
4270	0.097	0.43	0.31	0.13	12.17	0.01	0.14	49.5	1.6946	1.6953	−0.0007	49.6
3919	0.085	0.71	0.31	0.21	11.98	0.01	0.074	45.0	1.6532	1.6494	+0.0038	44.6
3920	0.096	0.77	0.37	0.14	12.49	0.01	0.13	48.0	1.6812	1.6902	−0.0090	49.0
3921	0.082	0.80	0.34	0.14	12.60	0.02	0.22	50.0	1.6990	1.7024	−0.0034	50.4
4030	0.065	0.76	0.34	0.14	13.46	0.01	0.11	44.0	1.6434	1.6425	+0.0009	43.9
4032	0.075	0.80	0.35	0.14	13.68	0.02	0.19	47.5	1.6767	1.6853	−0.0086	48.5
4269	0.098	0.44	0.38	0.13	13.74	0.01	0.13	49.5	1.6946	1.6925	+0.0021	49.3
3629	0.071	1.96	0.14	0.14	13.79	0.07	0.12	47.5	1.6767	1.6554	+0.0213	45.2
3631	0.063	2.03	0.15	0.13	13.49	0.05	0.15	46.5	1.6674	1.6559	+0.0115	45.3
4268	0.081	0.42	0.36	0.14	14.91	0.01	0.14	48.0	1.6812	1.6763	+0.0049	47.4
4029	0.062	0.80	0.39	0.14	15.53	0.01	0.16	45.5	1.6580	1.6579	+0.0001	45.5
4033	0.071	0.78	0.40	0.15	15.41	0.01	0.21	49.0	1.6902	1.6856	+0.0046	48.5
4035	0.064	0.77	0.32	0.14	15.66	0.01	0.28	48.7	1.6875	1.6924	−0.0049	49.2
4037	0.068	1.63	0.41	0.15	15.34	0.01	0.19	48.0	1.6812	1.6760	+0.0052	47.4
4038	0.066	1.60	0.31	0.14	15.72	0.01	0.22	50.0	1.6990	1.6814	+0.0176	48.0
4039	0.064	1.65	0.29	0.15	15.77	0.01	0.30	50.0	1.6990	1.6966	+0.0024	49.7
3923	0.090	1.67	0.35	0.14	15.24	0.01	0.19	51.0	1.7076	1.7038	+0.0038	50.6
3924	0.087	1.71	0.36	0.15	15.49	0.01	0.27	51.0	1.7076	1.7205	−0.0129	52.5
3926	0.083	1.59	0.31	0.17	15.20	0.01	0.17	50.0	1.6990	1.6893	+0.0097	48.9
3927	0.097	1.66	0.36	0.16	15.48	0.02	0.26	51.0	1.7076	1.7298	−0.0222	53.7

* $\log Rc = 2.182 + 0.469 (\log C) + 0.108 (\log C)^2 + 0.164 (\log N) + 0.025 (\log N)^2$

** Standard error of estimate equals 0.0107 (in logarithms). In terms of Rockwell C units this amounts to 1.5 at Rc 60, 1.2 at Rc 50 and 1.0 at Rc 40.

Results and Discussion

Effect of Carbon and Nitrogen—In the preliminary analysis graphical methods were used. It was established that the relationship between carbon or nitrogen and attainable hardness is approximately linear when the data of Table I are plotted on log-log coordinates. This indicated that an empirical equation of the form

$$\log \text{Rockwell C hardness} = a + b\,(\log C) + C\,(\log N) \qquad \text{Equation 1}$$

where C = carbon content in weight per cent
and N = nitrogen content in weight per cent

might be useful in describing the relationships among these variables. The preliminary equation of this form which was evolved was found to provide reliable hardness estimates for the data of Table I, but it gave low estimates when the carbon content was higher, such as for the bulk of the Burns, Moore and Archer data.

It was considered that an equation which would conform to the Burns, Moore and Archer data as well as our own data, and thus be applicable over a wider range of carbon content, would be more useful. Consequently, the Burns, Moore and Archer data for steels containing up to 0.50% carbon were incorporated with the data of Table I and a new regression equation was determined. The nitrogen content of the steels used for the Burns, Moore and Archer relationship was not known, so it was assumed that those steels contained 0.01% nitrogen.

The relationship between carbon content and Rockwell C hardness on log-log coordinates was found to exhibit a definite upward curvature when the carbon content increases above about 0.15%, hence a logarithmic equation involving log C to the second as well as the first power was indicated as being required to describe this parabolic relationship. Since log-log plots of per cent nitrogen versus Rockwell C hardness at constant carbon levels also exhibited some tendency to curve upward when the nitrogen content exceeded about 0.1% the regression equation should also involve log N to the first and second powers. Thus, the graphical analysis indicated that an equation of the following type would be appropriate for the combined data:

$$\log \text{Rockwell C hardness} = a + b\,(\log C) + c\,(\log C)^2 + d\,(\log N) + e\,(\log N)^2 \qquad \text{Equation 2}$$

The constants in Equation 2 were evaluated mathematically and the following empirical equation was thereby obtained:

$$\log \text{Rockwell C hardness} = 2.182 + 0.469\,(\log C) + 0.108\,(\log C)^2 + 0.164\,(\log N) + 0.025\,(\log N)^2 \qquad \text{Equation 3}$$

The standard error of estimate expressed in logarithms for this multiple regression equation was found to be 0.0107. In two cases out of three, therefore, the logarithm of the actual Rockwell C hardness can be expected to deviate by no more than ± 0.0107 from the estimated

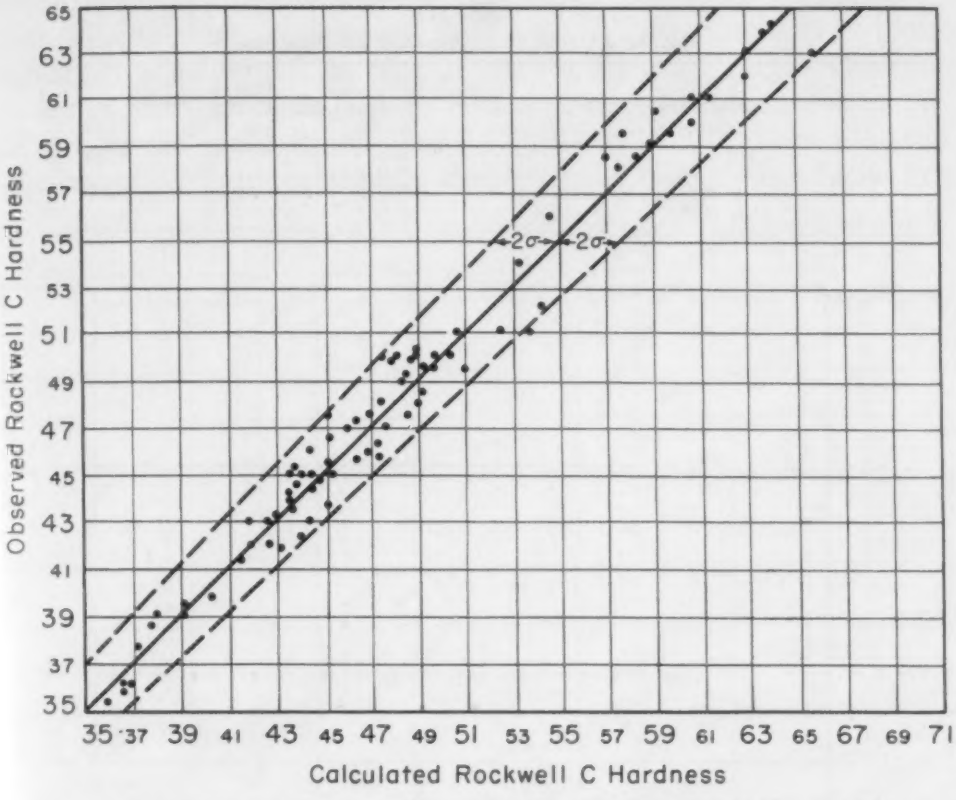


Fig. 1—Correlation Between Observed Rockwell C Hardness Values and Values Estimated from the Carbon and Nitrogen Contents by Means of the Empirical Equation, Log Rockwell C Hardness = 2.182 + 0.469 (log C) + 0.108 (log C)^2 + 0.164 (log N) + 0.025 (log N)^2.

value. In terms of actual Rockwell C hardness values the standard error amounts to 1.0 at Rockwell C-40, 1.2 at Rockwell C-50 and 1.5 at Rockwell C-60.

Equation 3 was used for estimating the attainable hardness of martensite from the carbon and nitrogen contents for each of the steels used in developing the regression equation. The computed hardness values are compared in Table I with our observed hardness values, and these data together with similar data for the higher carbon steels of the Burns, Moore and Archer investigation are plotted in Fig. 1. The dashed lines in this figure denote the 2-sigma, or 95% confidence limits, for the estimated values. Fig. 1 serves to illustrate graphically that there is quite good agreement between the observed and computed values.

The standard error of each of the four regression coefficients in Equation 3 was computed and the results obtained are summarized in Table II. The standard error of the regression coefficients for log C, (log C)^2 and log N amounts to only 12% or less, and hence these coefficients can be considered to be quite reliable. Percentage-wise, the standard error of the regression coefficient for (log N)^2 is rather high, but this is not serious since the coefficient is numerically small.

Table II
Standard Error of Regression Coefficients

Independent Variable	Regression Coefficient	Standard Error	Standard Error in Per Cent
(log C)	0.469	0.024	5.1
$(\log C)^2$	0.108	0.013	12.0
(log N)	0.164	0.018	11.0
$(\log N)^2$	0.025	0.007	28.0

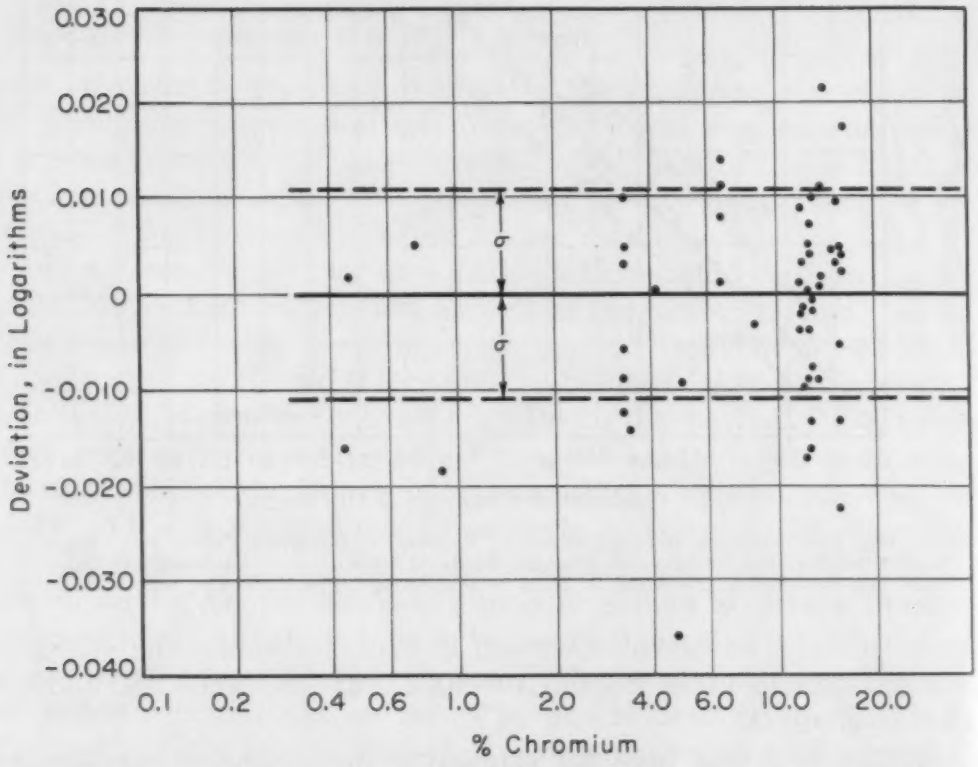


Fig. 2—Chromium Content Versus Difference Between Observed and Estimated Rockwell C Hardesses, Expressed in Logarithms.

The coefficient of multiple determination for Equation 3 was computed to be 0.975. In other words, it is estimated that about 97.5% of the total variability in log Rockwell C hardness is explained or accounted for by the regression equation. Like other statistics the coefficient of multiple determination is subject to chance variation so that the true value may be either higher or lower than the value estimated from the sample. When allowance is made for this possible chance variation it can be concluded that the regression equation accounts for at least 96% of the total variability in log Rockwell C hardness.

Effect of Alloying Elements—In order to determine whether any of the unexplained variability in log Rockwell C hardness might be attributed to the variations in alloy content of the various steels

used in this investigation, the deviations of the observed hardnesses from the computed hardnesses, expressed in logarithms, were plotted against alloy content. The plot of these deviations versus chromium content is reproduced in Fig. 2. Although the chromium content was varied over the range from about 0.5 to about 15.5%, there is no indication that this wide variation in chromium in these steels which varied

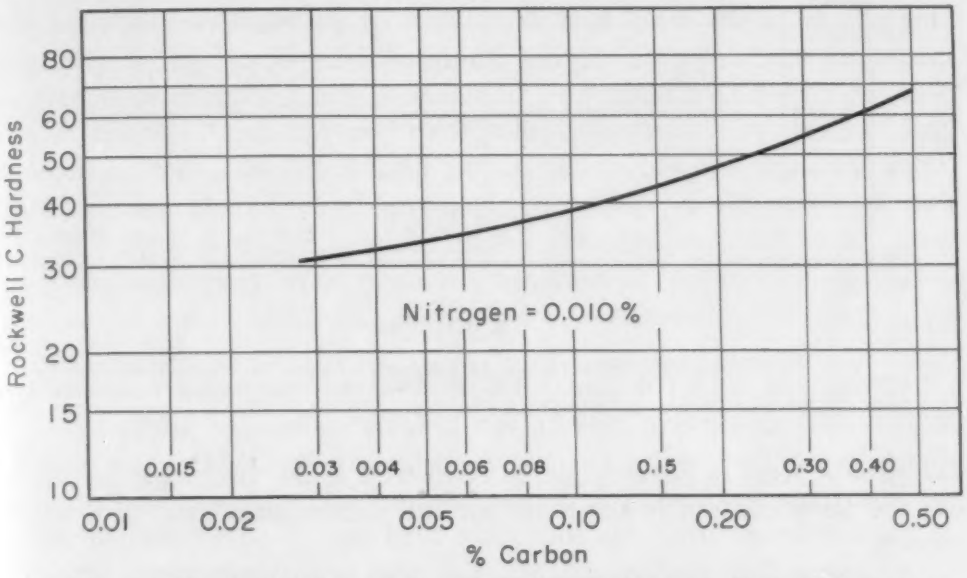


Fig. 3—Effect of Carbon on the Attainable Hardness of Steels Quenched to Produce Fully Martensitic Structures Free from Residual Carbides.

in carbon from 0.035 to 0.16%, had had any significant effect on the attainable hardness. Similarly, no correlation was found with any of the other alloying elements.

Our results are in disagreement with the work of Bain (3) which showed that the maximum hardness of 0.02% carbon, iron-chromium alloys increased with increasing chromium. However, since the nitrogen content of the alloys studied by Bain was not indicated, it is possible that the effect he observed might be attributable to nitrogen which tends to increase with increasing chromium, rather than to the actual chromium variation.

Curves of Hardness Versus Carbon and Nitrogen—Equation 3 was used as the basis for constructing the curves shown in Figs. 3 and 4 which describe the relationships between carbon and nitrogen content and attainable hardness. Fig. 3 serves to extend the Burns, Moore and Archer relationship to lower carbon contents and is in agreement with the original relationship when the carbon is above 0.10%. When the carbon content is less than 0.10% somewhat higher hardnesses are attainable than were indicated by the earlier relationship. For example, the original Burns, Moore and Archer relationship indicated that the maximum hardness obtainable in a steel containing 0.05% carbon would be expected to be about Rockwell C-28 whereas Fig. 3 indicates

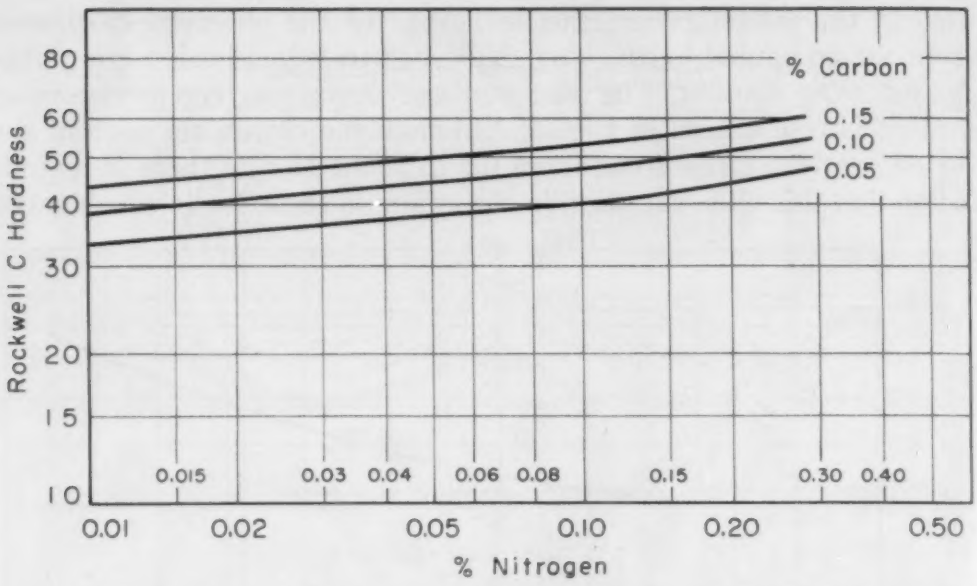


Fig. 4—Effect of Nitrogen on the Attainable Hardness of Steels at Carbon Levels of 0.05, 0.10 and 0.15% Quenched to Produce Fully Martensitic Structures Free from Residual Carbides and Residual Nitrides.

that such a steel is hardenable to Rockwell C-34, provided, of course that the alloy content is adequate for full martensitic hardening on the quench.

Fig. 4 shows the relationship between nitrogen in the range 0.01 to 0.30% and attainable hardness for carbon levels of 0.05, 0.10 and 0.15%. The effect of nitrogen on attainable hardness is not as great as that of carbon, yet it is of a rather high order of magnitude. For example, in a steel containing 0.10% carbon an increase in nitrogen from 0.01 to 0.05% increases the attainable hardness from Rockwell C-39 to 44.5, an increase of 5.5 Rockwell C units. The nitrogen content of the 12% chromium martensitic stainless steels normally varies in this range of values, thus the attainable hardness at a given carbon level is subject to a rather wide variation depending upon the actual nitrogen content. Nitrogen is therefore largely responsible for the observation that higher attainable hardnesses are obtained in the martensitic stainless steels containing about 0.10% or more carbon than would be expected from the Burns, Moore and Archer relationship.

Summary

The present paper indicates that the maximum hardness which can be obtained in steels heat treated to have fully martensitic structures free from residual carbides and residual nitrides can be considered to be a logarithmic function of the carbon and nitrogen contents. A variation in chromium from 0.5 to 15.5% in steels containing 0.035 to 0.16% carbon appeared to have no significant effect on the attainable hardness.

The following equation describes an empirical logarithmic relationship between the attainable hardness and the carbon and nitrogen content:

$$\log \text{Rockwell C hardness} = 2.182 + 0.469\ (\log C) + 0.108\ (\log C)^2 + 0.164\ (\log N) + 0.025\ (\log N)^2$$

where C = carbon content in weight per cent
and N = nitrogen content in weight per cent

This equation was shown to account for at least 96% of the total variability in log Rockwell C hardness and reliably predicts the attainable hardness when applied to steels having carbon and nitrogen contents within the limits covered by this investigation. The steels of high nitrogen content contained 0.05 to 0.15% carbon. It was not established whether the effect of nitrogen would be the same as that indicated by the above equation when the carbon content is at a higher level.

The standard error of estimate, in terms of Rockwell C units, was found to be 1.0 at Rockwell C-40, 1.2 at Rockwell C-50, and 1.5 at Rockwell C-60.

Conclusions

This paper has indicated that two factors are responsible for the fact that higher attainable hardnesses are often observed in martensitic stainless steels than would be expected from the Burns, Moore and Archer relationship. In the first place, higher hardnesses can be obtained in steels containing less than 0.10% carbon and about 0.01% nitrogen than the Burns, Moore and Archer relationship would indicate. Secondly, nitrogen has a rather marked effect on the attainable hardness and this effect is generally ignored. In the martensitic chromium stainless steels containing 0.10% carbon an increase in nitrogen from 0.01 to 0.05% will increase the attainable hardness 5.5 points Rockwell C.

Acknowledgment

The authors are grateful to the management of Crucible Steel Company of America for giving us permission to publish the results of the work described in the paper and are indebted to G. A. Stefanelli, F. Baureis, Mrs. A. Holcomb and other associates in the Research Laboratory who assisted us in various phases of the work.

References

1. J. L. Burns, T. L. Moore and R. S. Archer, "Quantitative Hardenability," Transactions, American Society for Metals, Vol. 26, 1938, p. 1.
2. Data sheets published by Electro Metallurgical Company. See Metal Progress, April 1952, p. 105, for example.
3. E. C. Bain, Functions of the Alloying Elements in Steel, American Society for Metals, 1939.
4. Mordecai Ezekiel, *Methods of Correlation Analysis*, John Wiley & Sons, Inc., New York, 1950.

THE ROLE OF WATER VAPOR AND AMMONIA IN CASE HARDENING ATMOSPHERES

By P. A. Clarkin and M. B. Bever

Abstract

Specimens of low carbon steel (AISI 1020) were case hardened four hours at 1475, 1550 and 1625 °F (800, 845 and 885 °C), respectively, in various atmospheres. The ammonia concentration in the inlet gas was varied from zero to 5% and the dew point ranged from —37 to 85 °F (—35 to 30 °C); the inlet gas also contained 5% CH_4, the balance was carrier gas. Surface hardness, microhardness and case depths were determined on oil-quenched specimens; the amounts of retained austenite in the cases were measured by lineal analysis. Other specimens were air-cooled after case hardening at 1550 °F (845 °C) and the cases were analyzed for carbon and nitrogen. The effects of variations in the concentration of ammonia and water vapor in the inlet gas were determined. The results extend previously published data in the direction of lower ammonia concentrations and provide new information on the role of water vapor in case hardening atmospheres.

Introduction

ONE OF the advantages claimed for the carbonitriding process of case hardening steel is the satisfactory performance of furnace atmospheres containing larger concentrations of water vapor than can be tolerated in gas carburizing. The literature, however, contains little experimental evidence in support of this claim. Any difference in the action of water vapor in gas carburizing and carbonitriding atmospheres undoubtedly can be attributed to the presence of ammonia in the latter.

Most of the earlier experimental work on carbonitriding was carried out with ammonia concentrations in the inlet gas of 10% or more, but lower concentrations are currently also used in industrial

This paper is based in part on a thesis submitted by P. A. Clarkin in February 1954 to the Department of Metallurgy at the Massachusetts Institute of Technology in partial fulfillment of the requirements for the degree of Master of Science.

A paper presented before the Thirty-sixth Annual Convention of the Society, held in Chicago, November 1 to 5, 1954. Of the authors, P. A. Clarkin was formerly graduate student and research assistant, Department of Metallurgy, Massachusetts Institute of Technology and is now associated with the Lewis Flight Propulsion Laboratory, National Advisory Committee for Aeronautics, Cleveland, and M. B. Bever is associated with the Department of Metallurgy, Massachusetts Institute of Technology, Cambridge, Mass. Manuscript received April 9, 1954.

practice (1)[1]. The present paper reports the results of an experimental investigation of the effects of variations in the concentration of water vapor and ammonia on the carbonitriding process. Tests with water vapor as a variable were also made in the absence of ammonia and, although the temperature range did not include the most common carburizing temperature of 1700 °F (925 °C), the results are significant for gas carburizing. This investigation supplements earlier papers from this laboratory (2–6) and in large measure was stimulated by discussions of this work (7).

Review of Previous Work—It is well known that water vapor tends to decarburize steel at elevated temperatures (8–11). In the simplest case, water vapor and carbon present in the steel react to form carbon monoxide and hydrogen (12). Similarly, water vapor, by the water gas reaction, tends to decrease the ratio of carbon monoxide to carbon dioxide and thus reduces the carburizing potential of an atmosphere containing carbon monoxide. Quantitative information on the carbon contents of steels in equilibrium with various atmospheres containing water vapor is available and systems of carbon control based on the dew point of a furnace atmosphere are of considerable current interest (13–15). At the same time, the literature contains evidence that over a limited range of low concentrations water vapor has a beneficial effect on the carburizing process and specifically on the rate of carburizing (11,16,17,18); this seems to be especially true for strongly carburizing atmospheres containing hydrocarbons. This beneficial effect of water vapor has been attributed to the control of the dissociation of hydrocarbons and of sooting or to the activation of the surface of the steel (19), but the true nature of this phenomenon is not definitely known.

The behavior of water vapor in carbonitriding atmospheres is also not well understood (20). An early investigation of the process suggested that water vapor gives unsatisfactory results (21). Later research led to the conclusion that water vapor in the entering gas has no appreciable effect on the case produced (2) but discussions of this paper attributed this finding to the high concentration of hydrocarbons and ammonia used in this research (7). A recent survey of industrial carbonitriding practice shows that high dew points are found in some commercial installations in which carbonitriding is carried out successfully (1).

Experimental Procedures

Specimens of AISI 1020 were prepared by normalizing, machining to dimensions of ¾ by ¾ by 4 inches and surface grinding. They were case hardened in a muffle furnace for four hours at 1475, 1550 and 1625 °F (800, 845 and 885 °C) and quenched into oil at 110 °F. Cylindrical specimens for carbon and nitrogen analysis (1

[1] The figures appearing in parentheses pertain to the references appended to this paper.

inch diameter by 5 inches) were case hardened at 1550 °F (845 °C) and cooled in still air. The case hardening atmospheres consisted of carrier gas, methane and varying amounts of ammonia and water vapor; the total flow of gases was kept the same in all experiments.

The carrier gas was prepared by combining carefully measured streams of tank hydrogen, carbon monoxide and nitrogen in the proportions corresponding to the gas which would result from the complete reaction of propane with air in a gas generator. Such a gas analyses is nominally 23.8% carbon monoxide, 31.6% hydrogen and 44.6%

Table I
Conditions of Casehardening

Temperature (°F)	Composition of Inlet Gas — NH_3	CH_4	Carrier Gas	Dew Point (°F) of Inlet Gas
1475	5%	5%	90%	−12, 32, 78
1475	3%	5%	92%	−13, 32, 78
1475	1%	5%	94%	−16, 32, 78
1550	5%	5%	90%	−32, 12, 32, 60, 85
				−15* 32* 74*
1550	3%	5%	92%	−32, 12, 32, 62, 83
1550	1%	5%	94%	−32, 10, 32, 62, 85
				−20* 32* 72*
1550	0%	5%	95%	−37, 8, 42, 60, 76
1625	5%	5%	90%	−16, 10, 32, 60, 79
1625	3%	5%	92%	−12, 3, 32, 60, 77
1625	1%	5%	94%	−12, 0, 32, 60, 79
1625	0%	5%	95%	−30, 32, 64

* Specimens for chemical analysis and other tests. Indicated by circled symbols in Figs. 1, 3, 4 and 5.

nitrogen. A synthetic carrier gas was used because of its greater uniformity and convenience. The ammonia was the anhydrous grade; the bottled methane contained not more than 2% ethane plus propane.

The compositions of the inlet gases used in the various runs are given in Table I. The carrier gas, methane and ammonia were passed through flowmeters and combined in the desired proportions. Carbon dioxide was removed by absorption in alkali solution. The water vapor concentration in the inlet gas was controlled by using the tank gases as received, by drying or by saturating them with moisture. When the gases were used as received or dried, dew points ranging from −37 to −12 °F (−38 to −24 °C) resulted. For higher water vapor concentrations the methane was passed through a saturator immersed in a thermostated bath and then mixed with the carrier gas. The mixture was passed through a thermostated condenser which reduced the concentration of water vapor to the desired level. Ammonia, if used, was added to the mixture at this point.

The concentration of water vapor in the inlet gas was measured by a dew point meter. In the operation of this meter condensation of moisture on a chilled disk of highly polished nickel was observed, while

the temperature of the disk was measured with a thermocouple. Repeated readings indicated a reproducibility of ±2 °F and no serious errors due to undercooling are believed to have occurred. The degree of control of the dew point is shown by the measured variation which during an entire run was never more than 5 °F and in most runs no more than 3 °F.

Surface hardness was determined by Rockwell 15-N readings; the reported values are averages of about twelve readings made on several faces of each specimen. Microhardness was measured on a transverse section at known distances below the surface with a Knoop indenter using a load of 500 grams; the reported values are averages of two or more traverses, which were always taken below the side which had faced upward in the furnace. The case depth was determined as the point at which the maximum slope of the curve of microhardness versus depth reached the value of the core hardness. The amounts of retained austenite at various depths below the surface of the specimens were measured by lineal analysis after darkening the martensite by tempering for one minute at 600 °F (315 °C).

Samples for chemical analysis were prepared by removing layers 0.003 or 0.005 inches thick on a lathe from the cylindrical specimens. These specimens had been air-cooled because faster cooling would have resulted in a case too difficult to machine. Air cooling, however, had the undesirable result of producing an oxidized surface layer, which had to be rejected; also loss of nitrogen beyond the depths of the oxidized surface layer is suspected.

Experimental Results

The surface hardness as a function of concentration of water vapor in the inlet gas, as measured by the dew point, is shown in Fig. 1 for a case hardening temperature of 1550 °F (845 °C) and concentrations of ammonia ranging from 0 to 5%. With atmospheres containing ammonia, the surface hardness decreases markedly above intermediate dew points, the exact value of which depends on the ammonia concentration; the rate of this decrease becomes greater as the concentration of ammonia is reduced. In the presence of ammonia, there is evidence that the surface hardness also decreases slightly in the region of low dew points. When ammonia is reduced from 1% to zero, all surface hardness values attained are lower and the hardness decreases continuously with increasing dew points. The results for 1475 and 1625 °F (800 and 885 °C) resemble those for 1550 °F (845 °C). Values for 1625 °F (885 °C) and other additional data may be found in reference 22.

Fig. 2 shows microhardness values at various depths below the surface of specimens case hardened at 1550 °F (845 °C) in atmos-

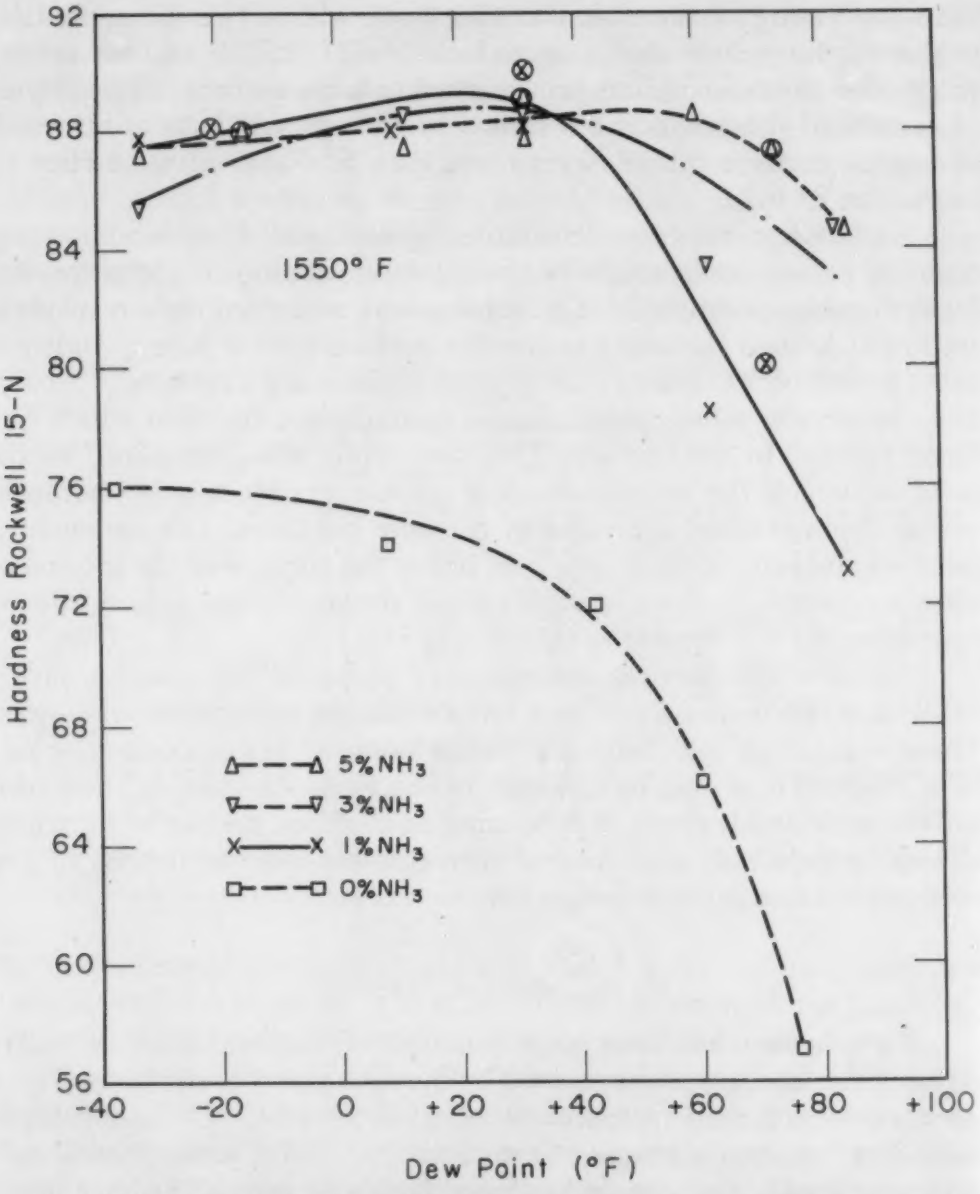


Fig. 1—Surface Hardness as a Function of Water Vapor Concentration (Dew Point) For Different Concentrations of Ammonia in Inlet Gas, Containing also 5% Methane, Balance Carrier Gas. Specimens casehardened four hours at 1550 °F and oil-quenched. Circled symbols refer to runs in which specimens for chemical analysis were also prepared.

pheres containing various concentrations of water vapor and ammonia as indicated by analyses of the inlet gas. The microhardness values are lower in specimens case hardened in atmospheres with high dew points, especially as the concentration of ammonia is reduced. At all ammonia levels represented, intermediate dew points (10 to 32 °F) in the inlet gas yield the best microhardness profiles, while the lowest dew point (—32 °F) results in inferior microhardness with respect to absolute level, distribution of hardness or both. Curves for 0% ammonia and 1550 °F (not included in Fig. 2) have rather flat and shallow hardness

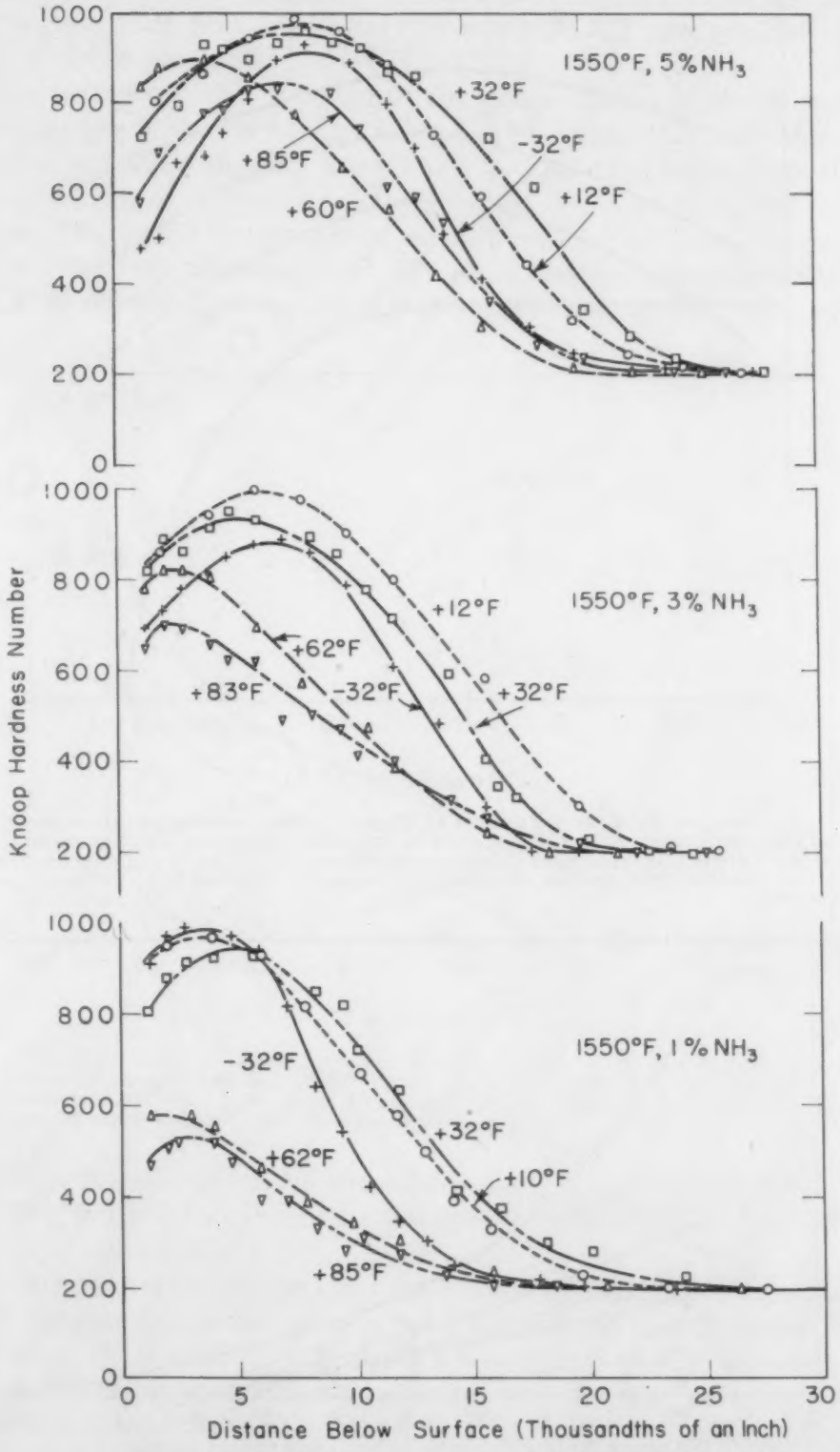


Fig. 2—Microhardness Across the Case of Specimens Carbonitrided Four Hours at 1550 °F in Atmospheres Containing Various Concentrations of Ammonia and Water Vapor and Oil-quenched. Temperatures indicate dew point in inlet gas.

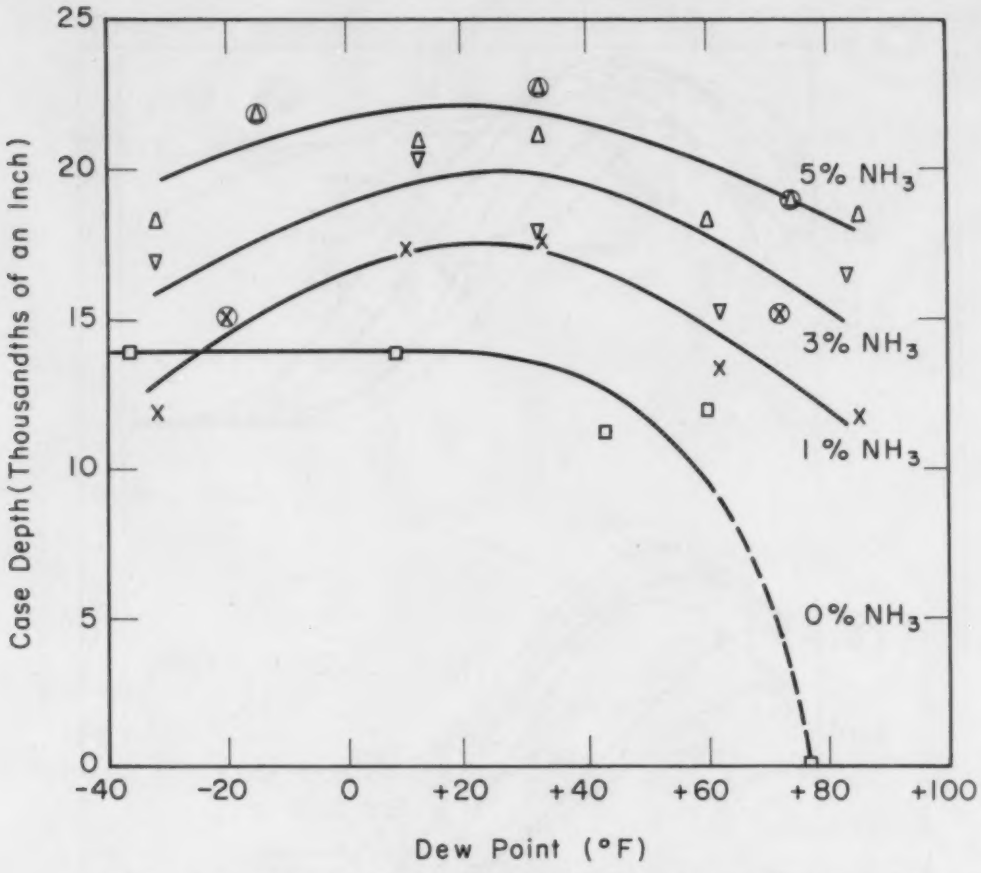


Fig. 3—Case Depth as a Function of Water Vapor Concentration (Dew Point) For Different Concentrations of Ammonia in Inlet Gas, Containing also 5% Methane, Balance Carrier Gas. Specimens Casehardened four hours at 1550 °F and oil-quenched. Circled symbols refer to runs in which specimens for chemical analysis were also prepared.

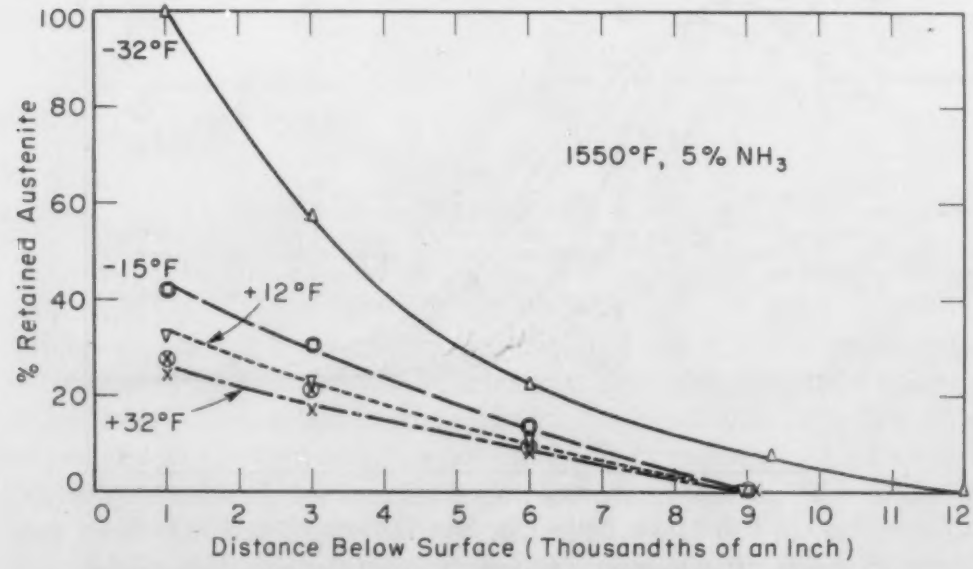


Fig. 4—Percent Retained Austenite Across the Case for Specimens Carbonitrided Four Hours at 1550 °F in Atmospheres Containing 5% Ammonia and Various Concentrations of Water Vapor and Oil-quenched Temperatures indicate dew points in inlet gas. Circled symbols refer to runs in which specimens for chemical analysis were also prepared.

profiles. The general features of the microhardness traverses for case hardening at 1625 and 1475 °F (885 and 800 °C) are qualitatively similar to those for 1550 °F (845 °C) (22).

The case depth as a function of the concentration of water vapor in the inlet gas is shown in Fig. 3 for 1550 °F (845 °C) and concentrations of ammonia ranging from 0 to 5%. These curves indicate that in the presence of ammonia maximum case depth is produced with atmospheres having intermediate dew points. The case depth at 1550 °F (845 °C) increases with ammonia concentration. In the absence of ammonia, case depth decreases continuously with increasing

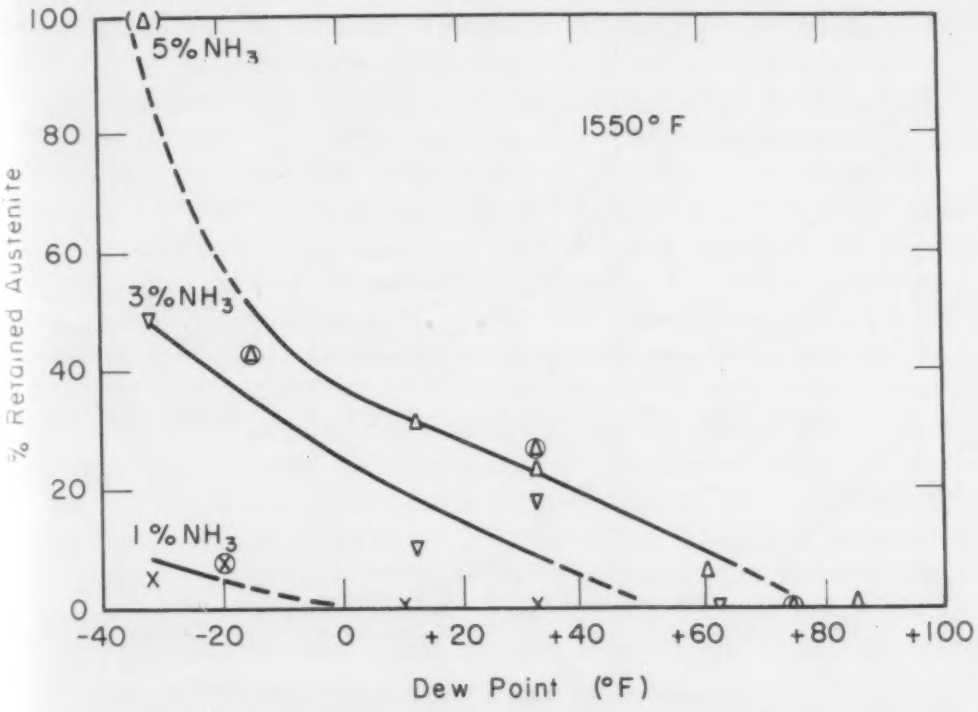


Fig. 5—Percent Retained Austenite at 0.001 Inches Below the Surface as a Function of Concentration of Water Vapor (Dew Point) in Inlet Gas. Specimens Carbonitrided at 1550 °F for Four Hours and Oil-quenched. Circled symbols refer to runs in which specimens for chemical analysis were also prepared.

dew point. A comparison of the results for 1475, 1550 and 1625 °F (800, 845 and 885 °C) confirms the expected increase in case depth with temperature (22).

The amounts of retained austenite are shown in Fig. 4 as a function of distance below the surface for 5% ammonia and different dew points at 1550 °F (845 °C). Fig. 5 is a plot of the retained austenite at 0.001 inches below the surface as a function of the dew point for three ammonia concentrations at 1550 °F (845 °C). Figs. 4 and 5 indicate a marked decrease in retained austenite with increasing dew point in the inlet gas. At 1475 °F (800 °C) retained austenite showed a similar decrease with increasing dew points: approximately 20% and 5% of

retained austenite occurred at a depth of 0.001 inches with ammonia concentrations of 5% and 3%, respectively, and a dew point at 78 °F; it should be noted that at 1550 °F (845 °C) these gas compositions would not result in the retention of austenite. Much smaller amounts of retained austenite are produced by case hardening at 1625 °F (885 °C) than at 1550 °F (845 °C) (22).

Fig. 6 shows the concentration gradients of carbon and nitrogen for six specimens carbonitrided at 1550 °F (845 °C) at two ammonia concentrations and three different dew points in the inlet gas. The outer layer of all of these specimens was rejected because it had become oxidized during air cooling. The thickness of this oxidized layer differed between samples for unknown reasons in spite of identical

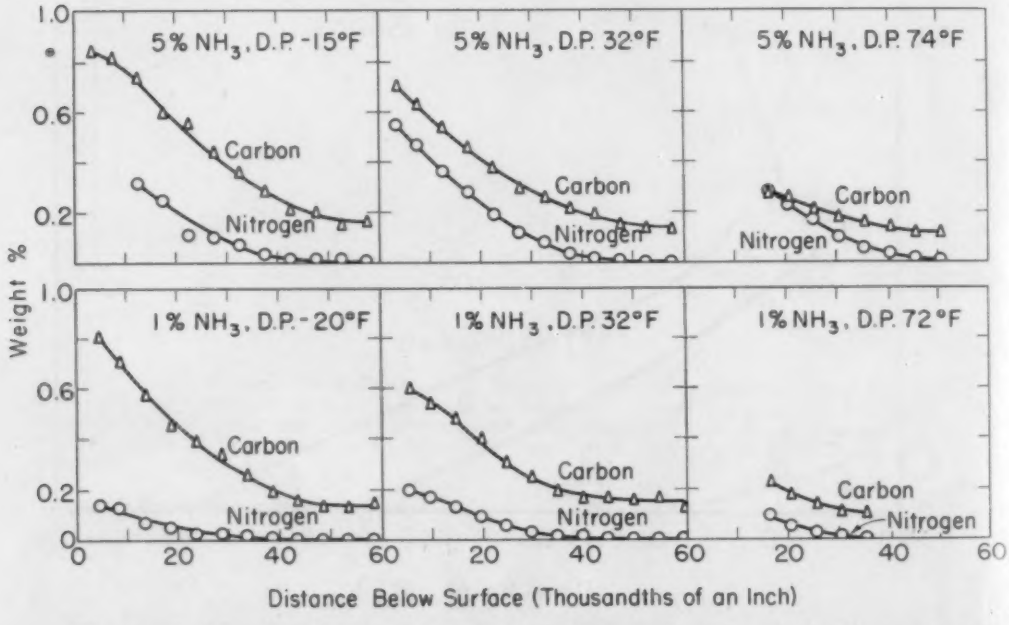


Fig. 6—Carbon and Nitrogen Concentrations Across the Case of Specimens Carbonitrided Four Hours at 1550 °F in Atmospheres Containing Various Concentrations of Ammonia and Water Vapor in Inlet Gas. Specimens were air cooled after casehardening; other data for oil-quenched specimens casehardened in same runs are indicated in Figs. 1, 3, 4 and 5 by circled symbols.

cooling conditions. The nitrogen contents of the two outer layers of the specimen carbonitrided with a gas containing 5% ammonia and having a dew point of —15 °F were unreasonably low and are omitted from the figure. It is also possible that other nitrogen values for layers near the surface are in error because of loss of nitrogen after removal of the specimens from the furnace. The carbon analysis of the core showed some spread, which is attributed to segregation in the commercially produced rods, but is believed not to affect the conclusions of this investigation. An analysis of a sample of the untreated steel gave a value of 0.004% nitrogen.

Discussion of Results

Effects of Variations in Water Vapor Concentration—With increasing water vapor concentrations in the inlet gas at the two levels of ammonia investigated the profiles of carbon concentration become lower while the nitrogen concentrations are not affected appreciably (Fig. 6). The decrease in carbon values is paralleled by a decrease in the amounts of retained austenite with increasing water vapor concentration (Figs. 4 and 5). These data confirm the expectation that carbon and nitrogen promote the retention of austenite in carbonitrided cases. Inasmuch as high water vapor concentrations, at constant ammonia of 5% or less and 5% methane, lower the carbon in the steel, a decrease in retained austenite with increasing dew point is reasonable.

The finding that variations in water vapor content affect the carbonitriding process, if it is conducted with these relatively low concentrations of ammonia and methane, supplements, but does not contradict, an earlier statement (2) according to which in richer atmospheres variations of the concentration of water vapor in the inlet gas over wide limits had no appreciable effect. As suggested by the discussions of this paper (7), differences in the concentrations of ammonia and methane are responsible for this difference in the behavior of water vapor.

Effects of Variations in Ammonia Concentration—For essentially identical water vapor concentrations, a decrease in ammonia content in the inlet gas from 5% to 1% is accompanied by a substantial reduction in nitrogen content of the steel (Fig. 6). There is also some decrease in carbon concentration with decreasing ammonia, especially at higher dew points. This may in part be attributed to reactions in the gas phase, whereby increasing ammonia tends to counteract the effects of increasing water vapor contents in the inlet gas. Also, the absorption of carbon in the steel is promoted by the lowering of the transformation range due to the presence of nitrogen.

A comparison of the present results with the carbon and nitrogen concentrations found in an earlier investigation using higher concentrations of ammonia and methane (3) is not meaningful. In the latter an outer layer of carbon-nitrogen-iron compounds was present and produced constant nitrogen and carbon concentrations at the boundary between this outer layer and the inner case.

The Pattern of Hardness Distribution—The decrease in surface hardness with increasing concentrations of water vapor above intermediate dew points (Fig. 1) can be explained by decreasing carbon contents in the austenite, while the decrease in surface hardness at low dew points in the presence of ammonia is attributed to increasing amounts of retained austenite. The value of the dew point at which this reversal takes place increases with ammonia concentration, which is

consistent with the foregoing argument involving the retention of austenite. In the absence of ammonia, the surface hardness continues to increase with decreasing water vapor concentration since not enough austenite is retained to lower the hardness.

The lower surface hardness after case hardening at 1550 °F (895 °C) without ammonia compared to the hardness resulting with ammonia (Fig. 1) is due to the effect of nitrogen on the transformation range. It is consistent with this reasoning that the surface hardness produced at 1625 °F (885 °C) with low water vapor concentrations in the absence of ammonia is comparable with that produced with 1% ammonia.

A significant feature of the profiles of microhardness (Fig. 2) is the marked maximum occurring below the surface with intermediate and low dew points. In the ascending branch of the curves, the hardness increases because of the decreasing amounts of retained austenite; the descending branch of the hardness curves is caused by the lowering of carbon and nitrogen with increasing depth in the case. It is significant in this connection that the maximum tends to disappear with increasing dew points, which are associated with a reduction in the retained austenite (Figs. 4 and 5). The lowering of the absolute values with increasing dew point and decreasing ammonia is mainly due to lower carbon contents of the cases.

Case Depth—The marked decrease in case depth at high concentrations of water vapor (Fig. 3) is attributed to decreased carbon absorption. The decrease in case depth at low concentrations of water vapor, however, may be apparent rather than real and may be due to the manner in which the case depth was derived from the microhardness traverses. Metallographic examination indicated essentially a constant case depth based on structure for specimens carbonitrided in atmospheres having dew points below about 32 °F (*22*).

General Comments—Some general comments may be made on the procedures used and the results obtained in this investigation. All data concerning atmosphere compositions refer to the inlet gas and do not necessarily give the composition of the furnace atmosphere in contact with the specimens. This experimental arrangement would not be appropriate for investigating the equilibria of case hardening reactions, but it is suitable for investigating the effects of process variables on the rate of case hardening and the nature of the case produced.

In interpreting the effects of variations of water vapor and ammonia, it should be recognized that conditions yielding superior hardness and case depth in a laboratory investigation are also likely to result in freedom from soft spots and uniformity of the cases generally in industrial production. A similar explanation can be given for the beneficial effects which have been attributed to the use of small amounts

of ammonia for carburizing in concentrations below the level required for carbonitriding (2).

Conclusions

The following major conclusions may be drawn from this investigation concerning the role of water vapor in case hardening atmospheres.

1. Variations in water vapor concentration in the inlet gas affect the results of case hardening with atmospheres containing 5% methane, 5% or less of ammonia, balance carrier gas at 1550 °F (845 °C). The effects of water vapor at 1475 and 1625 °F (800 and 885 °C) are in general similar to those at 1550 °F (845 °C).

2. The effects of increasing water vapor concentrations in the inlet gas consist chiefly in lowering the carbon concentration in the case produced, the case depth and the amounts of retained austenite.

3. The decrease in carbon concentration results in lower surface hardness.

4. In the presence of ammonia in the case hardening atmosphere a decrease in water vapor concentration below intermediate values is accompanied by a slight decrease in hardness, which is due to an increase in the amount of retained austenite.

5. Within the concentration limits of these experiments, the nitrogen absorption due to the presence of ammonia is not appreciably affected by variations in water vapor concentration in the inlet gas.

The following major conclusions may be drawn concerning the role of ammonia in case hardening atmospheres.

1. Decreasing concentrations of ammonia in the range of 5% to zero are accompanied by a substantial reduction in nitrogen content of the case.

2. Decreasing concentrations of ammonia are accompanied by some decrease in carbon content of the cases produced, especially at higher dew points.

Acknowledgments

The investigation reported in this paper was made possible through a fellowship sponsored by the Ammonia Division of Armour and Company of Chicago. The authors wish to express their sincere appreciation of this support. They also acknowledge gratefully their indebtedness to Professor C. F. Floe, who was responsible for the initiation of this entire research program.

References

1. M. B. Bever, C. F. Floe and W. G. Zaruba, "A Survey of Industrial Carbonitriding Practice," *Industrial Heating*, Vol. 20, 1953, p. 256, 650, 872 (Also Iron Age, Vol. 168, No. 11, September 13, 1951, p. 151).

2. G. W. P. Rengstorff, M. B. Bever and C. F. Floe, "The Carbonitriding Process of Case Hardening Steel," TRANSACTIONS, American Society for Metals, Vol. 43, 1951, p. 342.
3. G. W. P. Rengstorff, M. B. Bever and C. F. Floe, "Constitution of Carbonitrided Cases," TRANSACTIONS, American Society for Metals, Vol. 43, 1951, p. 378.
4. H. C. Fiedler, M. B. Bever and C. F. Floe, "Investigations into the Carbonitriding of Plain Carbon Steel," TRANSACTIONS, American Society for Metals, Vol. 44, 1952, p. 410.
5. H. C. Fiedler, M. B. Bever and C. F. Floe, "The Carbonitriding of Alloy Steels," TRANSACTIONS, American Society for Metals, Vol. 44, 1952, p. 420.
6. G. W. Powell, M. B. Bever and C. F. Floe, "The Carbonitriding of Plain Carbon and Boron Steels," TRANSACTIONS, American Society for Metals, Vol. 46, 1954, p. 1359.
7. Discussions by W. H. Holcroft and O. E. Cullen of Reference 2.
8. W. E. Jominy, "The Surface Decarburization of Steel at Heat Treating Temperatures," University of Michigan Engineering Research Bulletin, No. 18, 1931.
9. A. Johansson, R. von Seth and N. Elfstrom, "The Decarburization of Steel," *Jernkontorets Annaler,* Vol. 116, 1932, p. 565 (quoted after Ref. 16, p. 268).
10. C. R. Austin, "Heat Treatment in Controlled Atmospheres Including Gaseous Carburizing," TRANSACTIONS, American Society for Metals, Vol. 23, 1935, p. 157.
11. E. E. Slowter and B. W. Gonser, "An Experimental Study of Gases for Controlled Atmospheres in the Heat Treatment of Steel," *Metals and Alloys,* Vol. 8, 1937, p. 159, 195.
12. A. Bramley and Co-workers, Iron and Steel Institute, *Carnegie Scholarship Memoirs,* Vol. 15, 1926, p. 17; Vol. 16, 1927, p. 35; Vol. 17, 1928, p. 23; Vol. 18, 1929, p. 1.
13. W. T. Groves, "Dew Point vs. $\%CO_2$ as Furnace Atmosphere Control Check," *Industrial Heating,* Vol. 16, No. 6, 1949, p. 966.
14. O. E. Cullen, "Controlled Atmospheres—Their Generation and Utilization," METAL PROGRESS, Vol. 64, No. 6, December 1953, p. 101.
15. N. K. Koebel, "Dew Point—a Means of Measuring the Carbon Potential of Prepared Atmospheres," METAL PROGRESS, Vol. 65, No. 2, February 1954, p. 90.
16. I. Jenkins, *Controlled Atmospheres for the Heat Treatment of Metals,* Chapman and Hall, London 1946.
17. R. J. Cowan, "Notes on Continuous Gas Carburizing," TRANSACTIONS, American Society for Metals, Vol. 25, 1937, p. 843.
18. R. G. Guthrie and O. Wozasek, "Gas Carburization of Steel," TRANSACTIONS, American Society for Steel Treating, Vol. 12, 1927, p. 853.
19. C. R. McCloskey and J. H. Loux, "A Theory of the Mechanics of Carburization," *Steel Processing,* Vol. 32, No. 1, 1946, p. 53.
20. S. Tour, "Facts and Fancies About Ammonia Carburizing," METAL PROGRESS, Vol. 55, 1949, p. 495.
21. R. J. Cowan and J. T. Bryce, "The Process of Dry Cyaniding," TRANSACTIONS, American Society for Metals, Vol. 26, 1938, p. 766.
22. P. A. Clarkin, "Investigations into the Carbonitriding Process of Case Hardening Steel," S. M. Thesis, Massachusetts Institute of Technology, 1954.

DISCUSSION

Written Discussion: By Norbert K. Koebel, director of research, Lindberg Engineering Company, Chicago.

The authors, Messrs. Clarkin and Bever, show in a quantitative way, some very interesting data which has been known in a general qualitative way in commercial carbonitriding practice for the past few years. It is indeed gratifying to see that water vapor (dew point) is being given careful consideration in research studies on controlled atmosphere heat treating processes. So much research work in the past has been meaningless because water vapor has been overlooked. The more data presented by research studies on the role of water vapor, the more accurately and scientifically the control of atmosphere processes will become.

Commercial operating tolerances for dew point control of the carbonitriding processes have been observed by the writer and put into practice by his company for the past five years. We have found for bright carbonitriding, the furnace dew point should not exceed 50 °F if high hardness is to be obtained on the case. If the dew point exceeds 50 °F, then a danger point is reached where excessive hydrocarbon, which will cause sooting and blackening of the work, will have to be used to obtain the carbon for high hardness.

A healthy furnace condition is to have a furnace dew point between 30 and 40 °F. This bears out the authors' laboratory results. A dew point of 40 °F at 1550 °F will give approximately 0.80% carbon at the surface with the usual 5 to 10% NH_3 and 5% natural gas hydrocarbon.

Inasmuch as an endothermic generator is most efficiently operated from a +10 to +20 °F, we are not concerned by getting too low a dew point in the furnace. In commercial batch or continuous type furnaces, the dew point in the furnace will always be somewhat higher than the generator dew point. The differential depends upon many factors, such as infiltration during charging and discharging, entrained air in the charge of work, full muffle construction or open brickwork type of furnace, size of furnace, thermal gas reactions, and flow of carrier gas being used.

This brings up an important point that should be discussed before attempting to apply the authors' findings to a commercial carbonitriding furnace. The dew point should be checked in the furnace chamber for control purposes. As discussed above, there are many factors that have a bearing on the furnace dew point, and it is, therefore, essential to check the dew point of the gases in the furnace as well as before the gases enter the furnace for control and trouble-shooting.

Written Discussion: By W. H. Holcroft, executive vice president, Holcroft & Company, Detroit.

I have read the article by Messrs. Clarkin and Bever with much interest and feel that it discloses a great deal of hard work as was true of the past work along similar lines with which Dr. Bever was associated.

Our own laboratory work and experience in carbonitriding production (reports of which have been published in the past in METAL PROGRESS for September 1947, February 1948, December 1950 and April 1952) indicate that some results shown in this paper (Fig. 6) may be inaccurate.

In the report published in December 1950 we stated "the amount of carbon

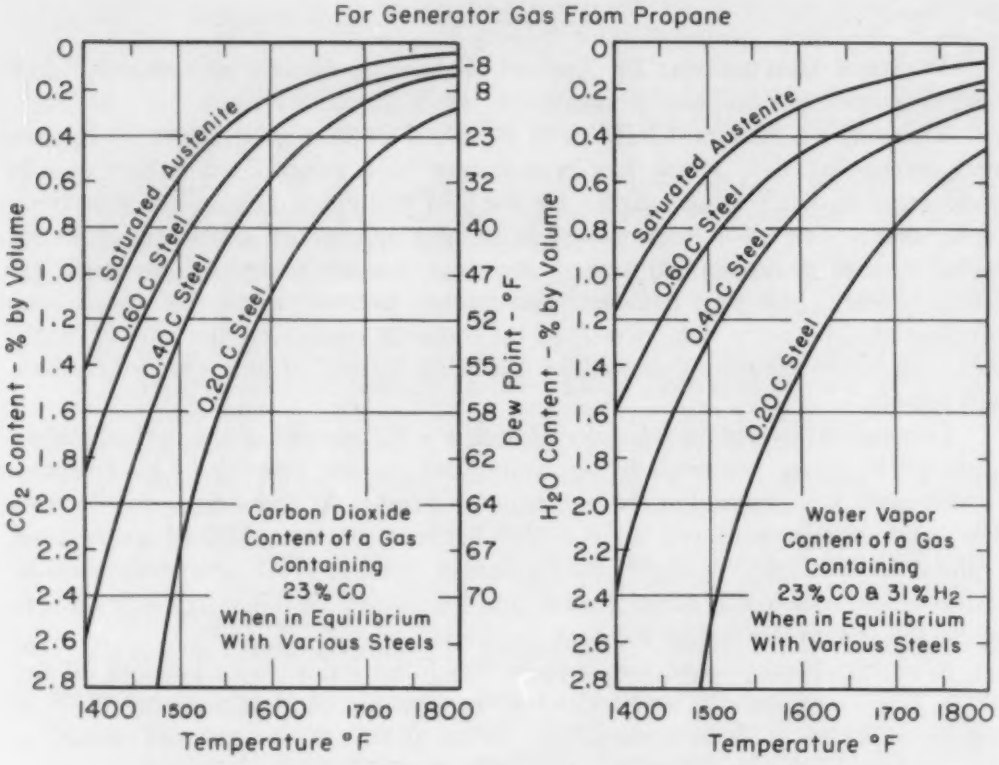


Fig. 7—Equilibrium Curves for Steels in Contact with Atmospheres Containing Carbon Dioxide or Water Vapor.

in the very surface of the steel is the amount which is called for at that temperature by equilibrium between the iron and the existing mixture of carburizing gases (such as CO and CH_4) and decarburizing gases (such as CO_2 and H_2O)." We, therefore, take issue with the introductory paragraph and cannot see that any attempt has been made to analyze the gases surrounding the work.

We agree with the conclusion that air cooling of the samples for chemical analysis probably resulted in loss of nitrogen and quite possibly of carbon. In connection with Figs. 1 and 2, it is our belief that had samples of the gas surrounding the work been obtained the dew point or CO_2 readings would have shown equilibrium values for the results obtained and would tie in with our published equilibrium curves attached (Fig. 7). At 1550 °F a dew point of approximately 25 degrees would be in equilibrium with saturated austenite which is about the point of maximum hardness shown in Fig. 1. The slight lowering of hardness in the region of low dew points may well be due to the formation of a thin white layer of nitrogenous austenite under these conditions.

This is borne out by Figs. 4 and 5 and the discussion of the patterns of hardness distribution.

We would agree with the conclusions reached in Fig. 3 if we consider the case depth shown as hardenable case depth. We have repeatedly stated that while hardenable case depth may be increased by the addition of ammonia we see no difference in total case depths when measured to core carbon, except that inherent in lowering the critical temperature. The diffusion curves may vary greatly with variations in carbon potential of the gas and consequently an end

point of core carbon may be hard to find. Inasmuch as four hours at 1550 °F should give a total case depth of 0.030 inch we are at a loss to determine what went wrong in Fig. 6. Further quoting from the article of December 1950 "the amount of ammonia or nitrogen in the atmosphere—within limits—does not affect its carburizing action or interfere notably with the diffusion of carbon in the hot steel." That is to say, in carbonitrided cases the depth of case and the carbon content at various depths below the surface are what would be expected from a carburized case of equivalent thermal history. However, the thermal decomposition of ammonia, making two volumes from one, rapidly decreases the partial pressures of the other gases considered above when ammonia is used in high percentages. From the equation $K = \frac{(CO)^2}{CO_2}$ it may be seen that if the partial pressure of CO is halved (by dilution), the tolerable amount of CO_2 must be divided by four. This means that if the CO_2 in the furnace is as high as may be permitted, simple dilution of the atmosphere by hydrogen and nitrogen will tend to reduce the carburizing potential.

Two important exceptions should be made here: Nitrogen in solution in iron reduces the critical temperature, so that austenite—and therefore rapid carburization—starts at a lower temperature. Likewise, nitrogen-bearing austenite does not transform to martensite as easily as normal austenite. Quenched carbonitrided cases retain more austenite, and while they usually are file-hard, Rockwell hardness may drop noticeably.

"The above remarks depend upon the premise that enough carbon and nitrogen is brought into the furnace continually to replace that portion which is absorbed by the steel being treated plus any leakage which may occur."

CO_2 will be formed in the furnace by the reaction $CO + H_2O \rightleftarrows CO_2 + H_2$. This reduces the dew point of the entering gases at the same time the carbon dioxide is forming. The extent to which the above reaction reaches equilibrium is of course a function of time and temperature and inasmuch as no analyses were made of effluent gases or those surrounding the work the progress of this reaction is unknown.

We believe the nitrogen contents shown for 32 degrees dew point in Fig. 6 agree with results published in our article of September 1947. However, while surface carbons are definitely low, total case depth here shown is greater than possible. Some samples also show abnormally low base carbons.

Written Discussion: By F. E. Harris, consultant, The Dow Furnace Co., Detroit.

The authors should be commended for the clarity with which the experimental data and the conclusions are presented. It may not be amiss to make brief analyses for two of their conclusions, one referring to the role of ammonia and the other to that of water vapor.

The authors state that ammonia additions to a high dew point carrier gas may increase the rate of carbon additions to steel. It may be interesting to consider the role of the water gas and producer gas reactions in this respect. Beginning with a carrier gas composition which the authors could well have approximated as an equilibrium mixture at 1500 °F, composition (1) in Table II, the effect of a 5% ammonia addition on the equilibrium mixture is given by composition (4). Here for simplicity the ammonia is considered as completely dissociated and the hydrocarbon additive is neglected. Applying the producer

gas reaction where $K_{PG} = \frac{100 \times \%CO_2}{(\%CO)^2}$, the constant for composition (1) is 94/484 or 0.194 while for composition (4) it becomes 75/404 or 0.185. Since the lower value indicates a higher carbon potential of the carrier gas, moderate additions of ammonia may favor the addition of carbon from the methane when the retort temperature favors these intermediate reactions.

The role of increasing water vapor concentrations which limit the addition of carbon while having little effect on nitrogen contents may present metallurgical problems aside from poor hardness characteristics. The low temperature nitriding process illustrates this point by the surface condition found when decarburized parts are processed. Perhaps the authors will agree that the role of carrier gas reactions with respect to carbon potentials demands careful consideration for satisfactory processing even if ammonia is added to the atmosphere.

Table II
Effect of Ammonia Addition To A Carrier Gas

	Composition			
	1	2	3	4
CO	22.00	22.00	20.00	20.10
H_2O	1.32	1.32	1.20	1.30
H_2	31.00	38.50	35.00	34.90
CO_2	0.94	0.94	0.85	0.75
N_2	44.74	47.24	42.95	42.95
	100.00	110.00	100.00	100.00
Kwg	1.00	0.80	0.80	1.00

1. Equilibrium composition at 1500 °F., $K_{WG} = \frac{H_2O \times CO}{H_2 \times CO_2} = 1.00$
2. Composition (1) plus H_2 and N_2 furnished by dissociation of 5% NH_3 addition
3. Composition (2) divided by 1.10
4. Equilibrium composition of (3) at 1500 °F.

Written Discussion: By C. O. Sundberg, chief metallurgist, Diamond Chain Co., Inc., Indianapolis.

The continued study by the authors of the role played by the various factors in case hardening operations is commendable and has provided increased knowledge of practical usefulness to those of us in industry who are concerned with operating problems.

In order to prevent misconceptions which may arise concerning the importance of water vapor, I would like to present some data on this subject which we obtained in our preliminary studies of the major variables involved in carbonitriding. These data are shown in the form of a Latin square since this experiment was designed for statistical analysis by the analysis of variance techniques. Nonetheless, they do show the influence not only of water vapor, but also of ammonia and propane in an endothermic carrier gas atmosphere used for carbonitriding. The data are for AISI 8615 material treated in a standard #1F American Gas revolving retort furnace at 1600 °F for 40 minutes at temperature with a total gas flow of 120 cfh. The carbon and nitrogen data are extrapolated to the surface of parts based upon results obtained by turning 0.004 inch off the diameter of parts chosen at random from furnace loads.

From these data it may be seen that the surface carbon content of the case varies with the dew point of the gas when a 1% propane enrichment is used. However, the carbon content is not affected by the water vapor present in the range of + 10 to + 30 °F when 3% or greater propane enrichment is used.

Furthermore, our data indicate that the carbon content is seemingly not affected by ammonia additions ranging from 5 to 15%.

Carbonitrided at 1600 °F—Latin Square Design

DEW POINT			% NH_3 A — 5%	B — 10%	C — 15%
		I	a)	b)	c)
a) 10 °F			% C 0.95	% C 0.84	% C 0.77
b) 20 °F	% C_3H_8	1%	% N 0.196	% N 0.202	% N 0.296
c) 30 °F		II	b)	c)	a)
±2 °F			% C 0.97	% C 0.99	% C 0.97
		3%	% N 0.159	% N 0.230	% N 0.384
		III	c)	a)	b)
			% C 1.24	% C 1.15	% C 1.21
		5%	% N 0.16	% N 0.208	% N 0.431

Although there may be some indication that water vapor influences the surface nitrogen content of the case, our data show that the nitrogen concentration is primarily dependent upon the percentage of ammonia used.

Statistical analysis of these data indicates that variations in dew point between + 10 and + 30 °F (normal limits of control on commercial generators) are not significant in the control of carbon and nitrogen gradients in carbonitrided case hardening. The percentage of propane enrichment was found to be statistically significant in the control of the carbon gradient. Similarly, the percentage of ammonia addition was shown to be statistically significant in the control of the nitrogen gradient. Our added experience has shown this to be the case.

Although we have no experience with the use of methane as the enrichment, it is apparent to us from data shown in Fig. 6 that insufficient carburizing potential is available from the 5% CH_4 addition to produce saturated austenite. As such, it is probable that this corresponds to the 1% propane enrichment level which we used that shows an influence of water vapor on the carbon gradient.

It was noted that the flow rate of gases used was not shown in the paper. Although it is likely that this is not important where only one or two samples are being treated, it is obvious that the ratio of gas flow to surface area of parts treated is important under nonequilibrium conditions which exist in the case hardening operation. Perhaps this could be a subject for further study.

Similarly, the use of shorter cycles to produce lighter case depths normally used commercially present complications which need further study. Obviously, the initially high rate of carbon absorption and diffusion at the start of a carburizing cycle cannot be satisfied unless large volumes of gas are used or higher potential gases are provided.

Written Discussion: By T. A. Frischman, chief metallurgist, Eaton Manufacturing Co., Axle Division, Cleveland.

The authors' findings on the role of water vapor in the carbonitriding process are a welcome contribution to the existing information on this method of heat treatment. Beyond the aspect of water vapor, it is advantageous to have data which show that additions as low as 1% ammonia significantly increase surface hardness and case depth over nonammonia bearing atmospheres.

From the viewpoint of commercial application of these data, it is fortuitous

that both the hardness and case depth peak at intermediate dew points. These findings are important, because in many large heat treating departments the tendency is to manifold the generators together to give a common supply of carrier gas used for both the carburizing and carbonitriding atmospheres. Thus, by standardizing the carrier gas composition and dew point, the problem of atmosphere generation is simplified for either process without conceding an advantage to one over the other.

Written Discussion: By E. E. Staples, executive vice president, Hevi Duty Electric Co., Milwaukee.

This paper fills a need of long standing for factual data in regard to the practical use of ammonia in improving carburizing of steels. While it has been general knowledge that additions of ammonia permitted more uniform case penetration and hardening with better surface condition when carburizing with gases of high dew point, the exact relationships have not heretofore been published.

The obtaining of maximum hardness from quenched specimens, heat treated in an atmosphere of 10 to 32 °F dew point, follows quite closely the experience in hardening steels heated in neutral atmospheres.

Of particular interest is Fig. 6 which shows the weight per cent of carbon and nitrogen in the cases at various depths. It would be of value to know what per cent of nitrogen would be found in the case of similar samples heat treated at 1700 °F and 5% ammonia.

Another interesting observation may be made from Fig. 6. At 32 °F dew point of the atmosphere, the carbon content of the case is less and the nitrogen content greater than at the lower dew point, —15 °F. Could one draw the conclusion that a dew point of 32 degrees in a nitriding atmosphere would be better than a dry ammonia of the same per cent dissociation?

Authors' Reply

The authors wish to express their thanks to Messrs. Koebel, Holcroft, Harris, Sundberg, Frischman and Staples for their discussions and contributions to the subject of this paper.

Mr. Koebel's remarks on the atmosphere conditions in industrial furnaces supplement this paper in an important respect. The authors agree that the dew point is likely to be higher in the furnace chamber of production equipment than in the inlet gas. As Mr. Koebel suggests, this tendency should be kept in mind in applying the findings of this paper to an industrial installation. In the small laboratory furnace used, however, the atmosphere in the muffle depended only on the composition of the inlet gas, and changes in the composition of the latter must have caused corresponding changes in the former.

The comments immediately preceding also apply to Mr. Holcroft's remarks concerning the lack of analyses of the gases surrounding the work. In further reply to Mr. Holcroft, Figs. 1 and 2 are directly concerned only with the effects of variations in the composition of the inlet gas on surface hardness and microhardness gradients. While inferences can be drawn from the hardness to the structure and composition of the case and even to the composition of the furnace atmosphere, the reasoning becomes increasingly indirect and uncertain. Also, Mr. Holcroft's otherwise interesting curves apply to generator gas and must be modified for atmospheres containing hydrocarbons.

Mr. Holcroft's comments on case depth and its measurement bring out the importance of defining case depth in a manner appropriate for a given problem. The intersection of the maximum gradient of the microhardness with the core hardness is only one possible definition, but it gives consistent and reasonable results as used here (Fig. 3).

The authors believe that the chemical analyses of the cases (Fig. 6) correctly represent the compositions of the samples of various subsurface layers. Errors in the position of the samples (which were machined from cylindrical specimens) are not likely to have had a significant effect on the composition gradients. This view is supported by the curves for nitrogen on which full agreement seems to prevail. The accuracy of the values for carbon, especially in the lowest layer of the case, may have been affected adversely by variations in the carbon content of the steel before case hardening. These variations, which are mentioned in the paper, may be somewhat more important than the authors had assumed. Except for any slight errors in the position of the sample and the effects of variations in core carbon, however, the authors know of no reason why the carbon values should be inaccurate. While some of the carbon and nitrogen profiles (Fig. 6) show a somewhat deeper penetration than might be expected, it is significant that this tendency increases with decreasing dew point and increasing ammonia; the tendency toward deeper penetration thus seems to be related to gas composition in a reasonable manner.

Mr. Harris points out the dilution effect of ammonia. This is unquestionably of importance from the standpoint of gas-metal equilibria, especially with relatively large concentrations of ammonia. However, ammonia probably also has a direct chemical action, the nature of which can at present be only the subject of speculation. Mr. Harris is correct in stating that there might be conditions under which the nitrogen content of the case would become relatively more important than the carbon content; these conditions, however, are not likely to occur in carbonitriding. The authors agree with Mr. Harris that the carbon potential of the atmosphere retains its fundamental importance even in the presence of ammonia, but it must be recognized that ammonia affects this potential.

The data contributed by Mr. Sundberg are of considerable interest. While the range of dew points is more limited than in this paper, the ammonia concentrations extend to higher values (which were covered in previous papers from this laboratory) and propane is used in place of methane. Mr. Sundberg's successful use of the Latin square suggests that this method of experimental design may merit more attention in the investigation of heat treating problems. The completion and publication of his investigation may be awaited with interest. His remarks concerning the importance of flow rates, especially in producing thin cases, are well founded; in all experiments reported here the flow rate was the same.

Mr. Frischman's remarks on the role of the dew point in the carrier gas may serve as a reminder that the right composition of the inlet gas, though not sufficient in itself, is nevertheless necessary for good results in carburizing and carbonitriding.

In answer to Mr. Staples' question concerning the role of water vapor in atmospheres for nitriding (as distinguished from carbonitriding), the authors would hesitate to extrapolate their results over so large a range of gas composition, even if the differences in nitrogen content of the cases could definitely be

considered to exceed the experimental error. The question as to the probable nitrogen content of samples of plain carbon steel carbonitrided at 1700 °F with 5% ammonia requires extrapolation over a rather large temperature interval. The nitrogen content may be expected to be lower, mainly because of an increase in the wasteful dissociation of ammonia in the furnace chamber. This argument is supported by a comparison of the amounts of retained austenite in cases carbonitrided at 1550 °F and at 1625 °F with 5% ammonia: data reported in Ref. 22 show a marked decrease in retained austenite at the higher temperature and this points to a decrease in nitrogen content of the case.

As Mr. Staples states, small concentrations of ammonia have been used to cure difficulties in gas carburizing. The present investigation may be considered to supply a quantitative explanation of the basis of this practice. The question arises as to how carbonitriding can be distinguished from carburizing with additions of small amounts of ammonia. The authors suggest that an essential criterion of carbonitriding is the action of nitrogen as an alloying element which raises the hardenability. This factor is not a consideration in the carburizing practice using small additions of ammonia.

EFFECT OF HEAT TREATMENT UPON MICROSTRUCTURES, MICROCONSTITUENTS, AND HARDNESS OF A WROUGHT COBALT BASE ALLOY

By J. W. Weeton and R. A. Signorelli

Abstract

This investigation was conducted to determine the response of wrought Stellite 21, a typical cobalt base alloy, to heat treatment in an effort to better understand the fundamental metallurgical behavior of this type of alloy. Metallographic hardness, and X-ray diffraction studies were made of the alloy in various conditions of heat treatment. Specimens were solution treated, and transformed both by aging and isothermal transformation at temperatures of 1200 to 1950 °F (650 to 1065 °C) for periods of 5 minutes to 72 hours in order to relate the manner and extent of precipitation with time, temperature, and type of heat treatment. The results presented herein may be considered preliminary to a study of relations of microstructures to the high temperature properties of wrought Stellite 21.

A period of 72 hours at 2250 °F (1230 °C) was sufficient for effective solution-treatment of the material so that little or no residual precipitate was visible. Pearlitic structures were formed at grain boundaries of solution-treated specimens after isothermal transformation at 1950, 1750, and 1500 °F (1065, 955 and 815 °C). In addition to pearlite, a star-shaped Widmanstätten structure occurred in specimens transformed at 1750 and 1500 °F (955 and 815 °C). Little visible precipitate was formed by isothermal transformation at 1200 °F (650 °C) for times up to 72 hours. The aging treatments resulted in the formation of scattered precipitates along slip lines and twin boundaries. Spheroidization and agglomeration of precipitates occurred at temperatures as low as 1500 °F (815 °C) and were initiated more rapidly in aged specimens than in isothermally transformed specimens.

The hardness of the solution-treated specimens was Rockwell C-20 to C-22. Isothermal or aging treatments above 1200 °F (650 °C) appreciably increased the hardness of specimens. A maximum hardness of Rockwell C-42 was de-

---

A paper presented before the Thirty-sixth Annual Convention of the Society, held in Chicago, November 1 to 5, 1954. The authors, J. W. Weeton and R. A. Signorelli, are associated with the Lewis Flight Propulsion Laboratory, National Advisory Committee for Aeronautics, Cleveland. Manuscript received May 21, 1954.

veloped by aging 72 hours at the temperature range from 1400 to 1500 °F (760 to 815 °C). Overaging or softening occurred within 72 hours at temperatures of 1750 °F (955 °C) and above for aging, and 1950 °F (1065 °C) for isothermal transformation. The specimens aged or isothermally transformed at 1200 °F (650 °C) did not increase in hardness. Specimens aged at 1500 °F (815 °C) and those isothermally transformed at 1750 and 1500 °F (955 and 815 °C) continued to increase in hardness up to 72 hours at respective temperatures.

The X-ray diffraction results coupled with metallographic studies indicated that $Cr_{23}C_6$ was the most prevalent carbide in the alloy. M_6C types of carbides and the sigma phase were detected in almost all of the specimens studied by X-ray diffraction methods. Other types of carbides indicated to form in the alloy are Cr_7C_3 and Cr_3C_2, although the X-ray indications for these phases were very weak. The sigma phase was thought to form in conjunction with or subsequent to the formation of $Cr_{23}C_6$.

The relative quantities of the matrix phases, either the high-temperature phase, alpha (a face-centered cubic solid solution) or the lower temperature phase, beta (a hexagonal close-packed solid solution), were estimated from the X-ray diffraction patterns in each alloy in various conditions of heat treatment.

Particular attention was given to the pearlitic structures which form from the high temperature face-centered cubic phase upon furnace cooling or isothermal transformation.

Introduction

THE investigation reported herein was undertaken as part of a fundamental program concerned with the general metallurgical improvement of turbine-blade alloys to provide a basis for proper selection and heat treatment of alloy materials. Previous work (1 to 3) [1] had demonstrated that improvement in the life of turbosupercharger blades of Stellite 21 could be obtained by suitable heat treatment. For example, it was found that a heat treatment which produced a lamellar type of precipitation in the microstructure, resembling pearlite in steel (3), approximately doubled the average blade life. (Pearlite, in this report, refers to the lamellar-type structure.)

Wrought Stellite 21 was used in the present study rather than the cast alloy in an effort to avoid grain-size variables and to permit a more thorough homogenization by solution-treatment.

Badger and Sweeney (4) observed pearlitic structures in such cobalt-base alloys as Stellite 21, 61, 6059, and X-40 (Stellites 21, 23, 27, and 31, respectively) and the carbides $M_{23}C_6$, M_6C, and Cr_7C_3 in

[1] The figures appearing in parentheses pertain to the references appended to this paper.

Stellite 21 (where M represents any carbide-forming element). Reference 5 reports $M_{23}C_6$ and MC carbides in cobalt-base alloys; $M_{23}C_6$, M_6C, Cr_7C_3, and the sigma phase were found in Stellite 21 and Stellite 21 type alloys (6). Such carbides as Cr_3C_2, $Cr_{23}C_6$, M_6C, Cr_7C_3, and MC were observed in one or more alloys such as Stellite 21 type alloys, 422–19, and J (7). Also introduced in Reference 7 is a concept of carbide decomposition: Cr_7C_3, which is rich in carbon, was believed to undergo the following decomposition upon aging:

$$Cr_7C_3 \longrightarrow Cr_{23}C_6 + \text{free carbon}$$
$$\text{Free carbon} + Cr \longrightarrow \text{additional } Cr_{23}C_6$$

The matrix phases of several of these alloys are known (refs. 4,6, and 8) to be either face-centered cubic (alpha) or hexagonal close-packed (beta). In pure cobalt, transformation of the face-centered cubic to the hexagonal close-packed structure was shown to occur by a martensitic type of reaction (9), and this type of reaction has been assumed to apply to the similar transformation in the cobalt-rich solid solution which makes up the matrix of Stellite 21.

In the present investigation, a systematic study of the microstructural and hardness changes produced in wrought Stellite 21 by heat treatment has been made in order to relate the amount and type of precipitation with the time, temperature, and manner of heat treatment.

In addition, X-ray diffraction studies were made to determine what minor phases precipitated from the alloy matrix. Particular emphasis was placed upon identifying the phases that made up the pearlitic structures.

Procedure

Wrought Stellite 21 of the following chemical analysis was employed in this investigation:

C	Cr	Ni	Co	Mo	Fe	Si	Mn
0.29	28.75	3.01	Bal. (61.10)	5.52	0.33	0.44	0.56

The material was fine-grained, with an ASTM grain size of 7–8. The microstructure of the as-wrought material is shown in Fig. 1.

Slugs of this material were cut from ¾-inch-diameter bar stock supplied by the manufacturer and heat treated in electric furnaces using Globar heating elements. The metal slugs were placed inside a 2.25-inch-inside-diameter tube of Inconel X in the heating zone of the furnace. Temperatures, which were measured by a platinum-platinum plus 13% rhodium thermocouple located immediately above the samples, were controlled to ±10 °F of the nominal temperatures. Argon was circulated through the tube to provide an inert atmosphere during heat treatment. The gas was originally 99.6% pure argon and was further

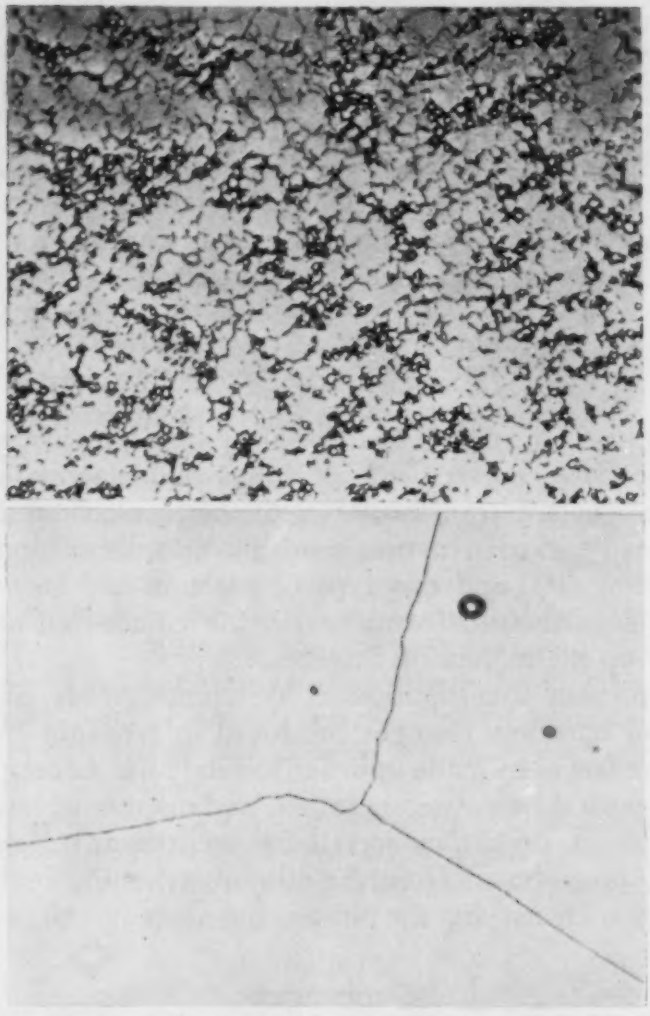


Fig. 1—Microstructures of As-Rolled and Solution-Treated Stellite 21. Upper—As-rolled condition. Electrolytically etched in 5% aqua regia. X 750. Lower—Solution-treated 72 hours at 2250 °F and water-quenched. Electrolytically etched in 5% aqua regia. X 750.

purified before entering the specimen tube by passing over shavings of titanium metal at 1300 to 1400 °F (705 to 760 °C).

The metal slugs were placed in the furnace at a temperature of approximately 2000 °F (1095 °C) and held at this temperature for 1 to 2 hours. The purpose of holding at this temperature was to effect some preliminary homogenization of the structure and to minimize any tendencies towards eutectic melting at higher temperatures. The temperature was then raised to a solution treating temperature of 2250 °F (1230 °C) and held for 72 hours to produce a homogeneous solid solution of carbon in the face-centered cubic matrix of the alloying metals.

At the end of the solution treatments, the specimens were either water-quenched and aged or transferred directly to furnaces held at

Table I
X-Ray Diffraction Pattern Standards Used For Comparison

Compounds checked (standards)	Number of standards checked	Source or reference
$FeO \cdot Cr_2O_3$ (spinel)	2	ASTM card index
$CoOCr_2O_3$ (spinel)	1	ASTM card index
Cr_2O_3	3	ASTM card index
Cr_3C_2	2	ASTM card index
Cr_7C_3 or Mn_7C_3	1	ASTM card index
Co_4W_2C (M_6C)	1	ASTM card index
Fe_3W_2C or Fe_3Mo_3C or $Fe_4W_2C \cdot (M_6C)$	1	ASTM card index
M_6C	1	Ref. 5
Sigma (or gamma) Co_2Cr_3	1	Diffraction standard obtained from specimen given NACA by Battelle Memorial Institute
Sigma (Co–Cr–Mo)[a]	1	Ref. 19
Sigma (Co–Cr–Ni)[a]	1	Ref. 19
Sigma (FeCr)	1	Ref. 20
Sigma (CoCr)	1	Ref. 21
Sigma (Fe–Cr–Ni)	1	Ref. 20
Co_7W_6	1	ASTM card index
Co_3W	1	ASTM card index
$Cr_{23}C_6$	2	ASTM card index
Mo_2C	2	ASTM card index
Cr_2N and βCr_2N	2	ASTM card index
Co_3C	1	ASTM card index
Fe_3C	1	ASTM card index
WC	2	ASTM card index
αW_2C	1	ASTM card index
βW_2C	1	ASTM card index

[a] Either one pattern or the other was checked.

lower temperatures for isothermal transformations. The nominal transformation temperatures were 1200, 1500, 1750, and 1950 °F (650, 815, 955 and 1065 °C), and times at each of these temperatures were 5 minutes and 2,4,25, and 72 hours. In order to obtain sufficient data for drawing representative hardening curves, additional heat treatments were carried out at intermediate temperatures and times, as indicated subsequently. All specimens were water-quenched after the transformation treatments.

The use of salt baths for the isothermal transformation treatments was found impractical because of the severe corrosion of the specimens, especially at high temperatures and long transformation times.

Rockwell hardness measurements were made on the heat treated specimens after outer surfaces had been removed by sanding or grinding. A minimum of three hardness measurements were made on each specimen. The specimens were then mounted, polished, and etched with 5% aqua regia in water for metallographic study.

To identify the crystal structures of matrix and minor phases, X-ray diffraction patterns were obtained from as-received specimens and specimens heat-treated as shown in Table II. Powder specimens given heat treatments C, E, F, H and I, were obtained from heat treated metallic slugs. Specimens given heat treatments B, D and G, were solution-treated as slugs, and powders were ground from the solution-treated slugs, sealed in evacuated quartz tubes and again

Table II
X-Ray Diffraction Identification of Matrix and Minor Phases

Heat treatment	Solution treatment	Isothermal transformation		Aging treatment		Percentages of Matrix Phases-determined by		Minor phases indicated [a]							
		Temp. °F	Time Hrs.	Temp. °F	Time Hrs.	X-ray diffraction (Percentages visually estimated)		Cr_3C_2	Cr_7C_3	$Cr_{23}C_6$	M_6C	Sigma	Cr_2O_3	Spinels	Cr_2N
						Alpha	Beta								
A	None as-rolled	—	—	—	—	30	70			W		W		W	
B	(1) 2250 °F; 16 Hrs. water quench (2) Grind X-ray powders (3) Heat treat powders 2250; ¼ Hr.; water quench					100	0			VW	VW				
C	2250 °F; 69 Hrs.	1950	¼			100	0			S	W	M	S		M
D	(1) 2250 °F; 16 Hrs. water quench (2) Grind X-ray powders (3) Heat treat powders 2250 °F; ¼ Hr.	1950	2			100	0			S	S				M
E	2250 °F; 69 Hrs.	1950	72			10	90		VW	S	W	M	W		S
F	2250° F; 72 Hrs.	1500	¼			50	50			S		M			W
G	(1) 2250 °F; 16 Hrs. water quench (2) Grind X-ray powders (3) Heat treat powders 2250 °F; ¼ Hr.	1500	2			95	5			M	W	S	W	W	
H	2250 °F; 72 Hrs.	1500	72			Trace	>90		VW	S	W	W	W	VW	S
I	2250 °F; 46 Hrs.	1850	1½	1500	2	50	50	W		S		S	W	S	S

[a] Indications of the presence of minor phases in these alloys are as follows:
S Good indication of presence
M Fairly good indication of presence
W Possible
VW Minimum indication considered

solution-treated and isothermally transformed in the powdered form.

Powders for the X-ray diffraction studies were ground from specimens with a small tungsten carbide burr mounted in a high speed drill press and with the exception of specimens B, D and G, were stress-relief annealed at 1500 °F (815 °C) for ½ hour in evacuated quartz tubes (0.5 micron pressure). A temperature of 1500 °F (815 °C) would appear high; however, this stress relieving treatment was of such duration that the X-ray results were found to be unchanged. The annealed powders were mounted on a fine quartz fiber and patterns were obtained with a 143.2-millimeter-diameter Debye-Scherrer powder camera and chromium radiation. Exposure times of 25 to 40 hours were used and one third of the width of each pattern was filtered with a vanadium oxide coated paper strip. The patterns were measured with a vernier scale to the nearest 0.1 millimeter. The Straumanis technique (10) was used to compensate for film shrinkage.

Identifications of minor phases were made by comparing the patterns obtained with standard patterns of carbides and intermetallic compounds that appeared reasonable on the basis of composition and which are listed in the ASTM card index or in the literature (see Table I). Only the stronger lines of the standard patterns were used for the comparisons. The analysis of the patterns were difficult because of the weakness, the great number, and the overlapping of the diffraction lines. These difficulties prohibit positive statements that every minor phase listed in the results (Table II) actually was present.

Concentration techniques attempted—Attempts to strengthen the minor-phase lines relative to matrix-phase lines in order to permit more positive identifications were made but, in general, the patterns were not improved.

Stain etching and heat tinting—To supplement the X-ray data, an attempt was made to verify metallographically the presence of different carbides and the sigma phase. Three types of stain etchant were selected from the literature (Table III). The first etchant was intended to color the sigma phase; the second to differentiate between carbides and the sigma phase; and the third to differentiate among and to identify the carbides. Heat tinting as described in Reference 7 but more nearly approaching the method described in Reference 6 was also used.

Two specimens selected for stain etching and heat tinting were as follows: An as-rolled specimen and a specimen solution treated for 41 hours at 2250 °F (1230 °C) and furnace-cooled in stepwise fashion (holding 2 hours at temperatures of 2000, 1900 and 4 hours at 1800 °F) to develop a large quantity of both fine and coarse pearlite.

Results

Microstructures—Microstructures of as-received and heat treated specimens, are shown in Figs. 1 to 3. The as-received specimen of

Table III
Stain Etchants and Heat Tinting

Coloring process	Method	Purpose	Source of methods	First etchant		Staining method		Colors of minor phases obtained by previous investigators
				Solution	Method	Solution	Method	
1	Etch	To stain sigma	Rideout and Beck (ref. 19) (Cr, Ni, Mo alloys)	8 Percent oxalic acid; 92 percent water	Electrolytic etch; 8-10 sec; 6 volts; room temperature	5 g $KMnO_4$; 5 g NaOH; 90 ml water	Immerse 10-20 sec; room temperature	Sigma: bright green or red to purple
2	Etch	To differentiate between carbides and sigmaphase	Batelle (ref. 6) for Stellite 21 type alloy	10 percent NaCN; 90 percent water	Electrolytic etch; 10-20 sec; 1.5 volts	Murakami's 10 g $K_3Fe(CN)_6$; 10 g KOH; 100 ml water	Immerse 2-4 sec; room temperature	Carbides: straw to yellow brown or buff Gamma (sigma): grey to blue or greenish grey $Cr_{23}C_6$: brown Cr_7C_3: pale yellow to light tan M_6C: red, green, yellow, blue (also reticulation)
3	Etch	To identify carbides	Badger and Sweeney (ref. 4) for Stellite 21 and Co-Cr base alloys	2 percent chromic acid; 98 percent water	Light electrolytic etch	1 part (20 percent $KMnO_4$, 80 percent water) + 1 part (8% NaOH 92% water)	Immerse 7 sec; room temperature	
4	Heat Tint	To identify carbides and sigmaphase	Batelle (ref. 6) Also see Lane and Grant (ref. 7)	5 percent HCl; 95 percent H_2O	Electrolytic (light); 1 sec; 5 volts	(1) Heat polished specimen to dull red (2) Held at temperature until surface becomes colored (3) Air-cooled or Hg quenched		Sigma: dark-medium brown $Cr_{23}C_6$: white M_6C: dark Note: M_6C and sigma cannot be differentiated in same structure

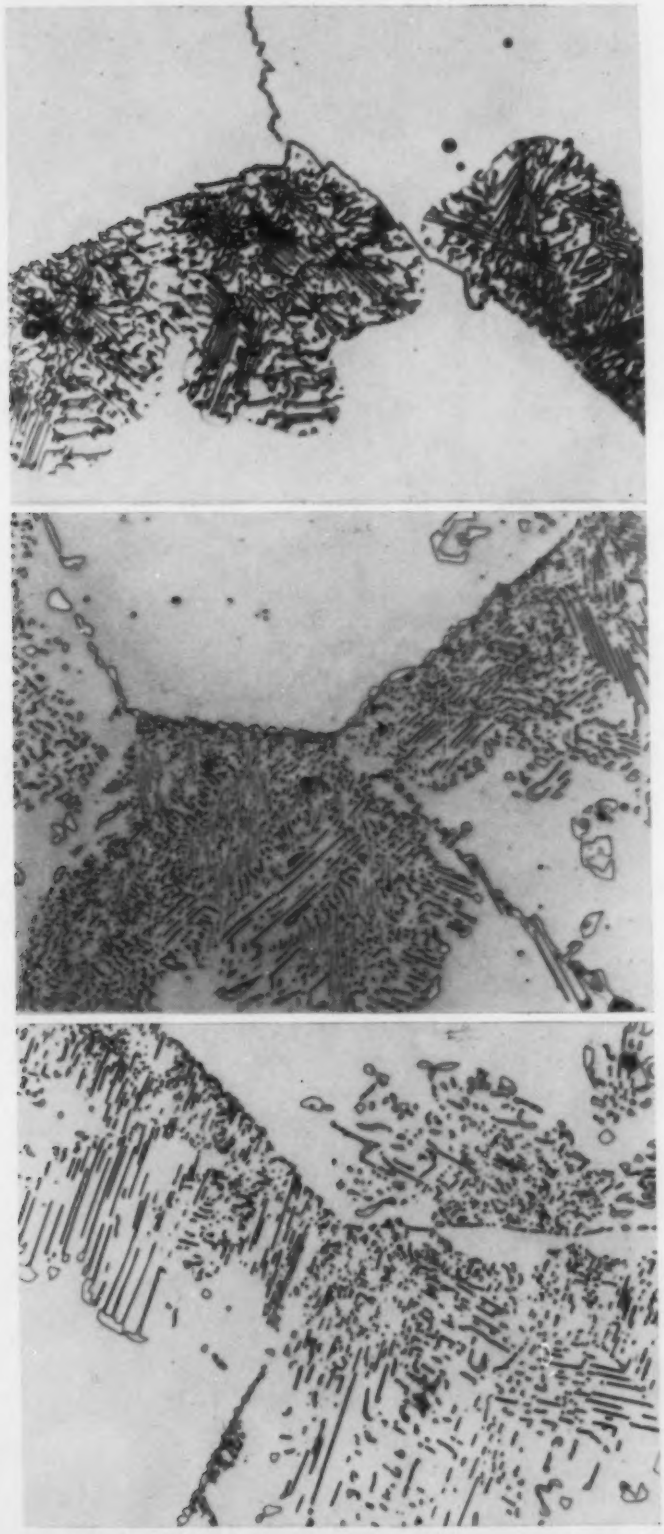


Fig. 2a—Microstructure of Stellite 21 after Isothermal Transformation. Original magnification X 750, reduced 40% in reproduction. Temperature of transformation 1950 °F. Top—5 minutes; middle—25 hours; bottom—72 hours.

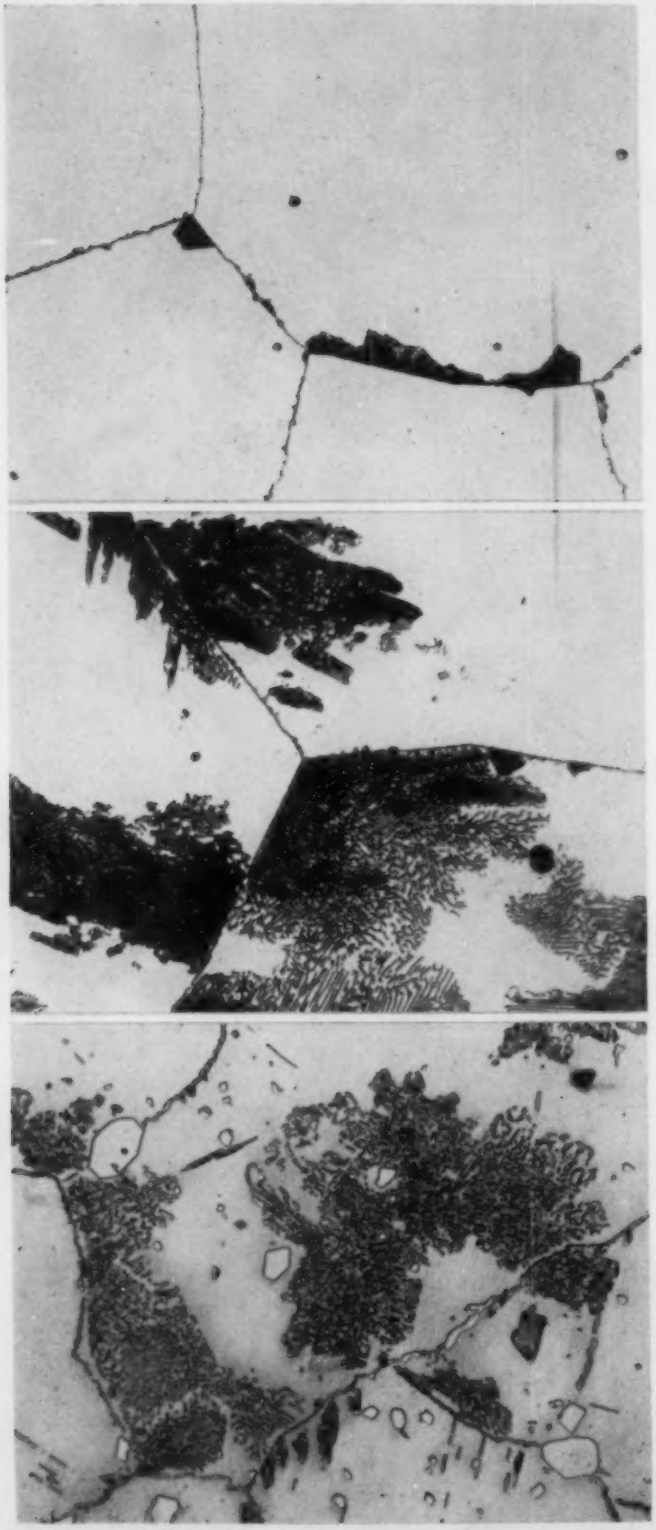


Fig. 2b—Microstructure of Stellite 21 After Isothermal Transformation. Original magnification X 750, reduced 40% in reproduction. Temperature of transformation 1750 °F. Top—5 minutes; middle—4 hours; bottom—72 hours.

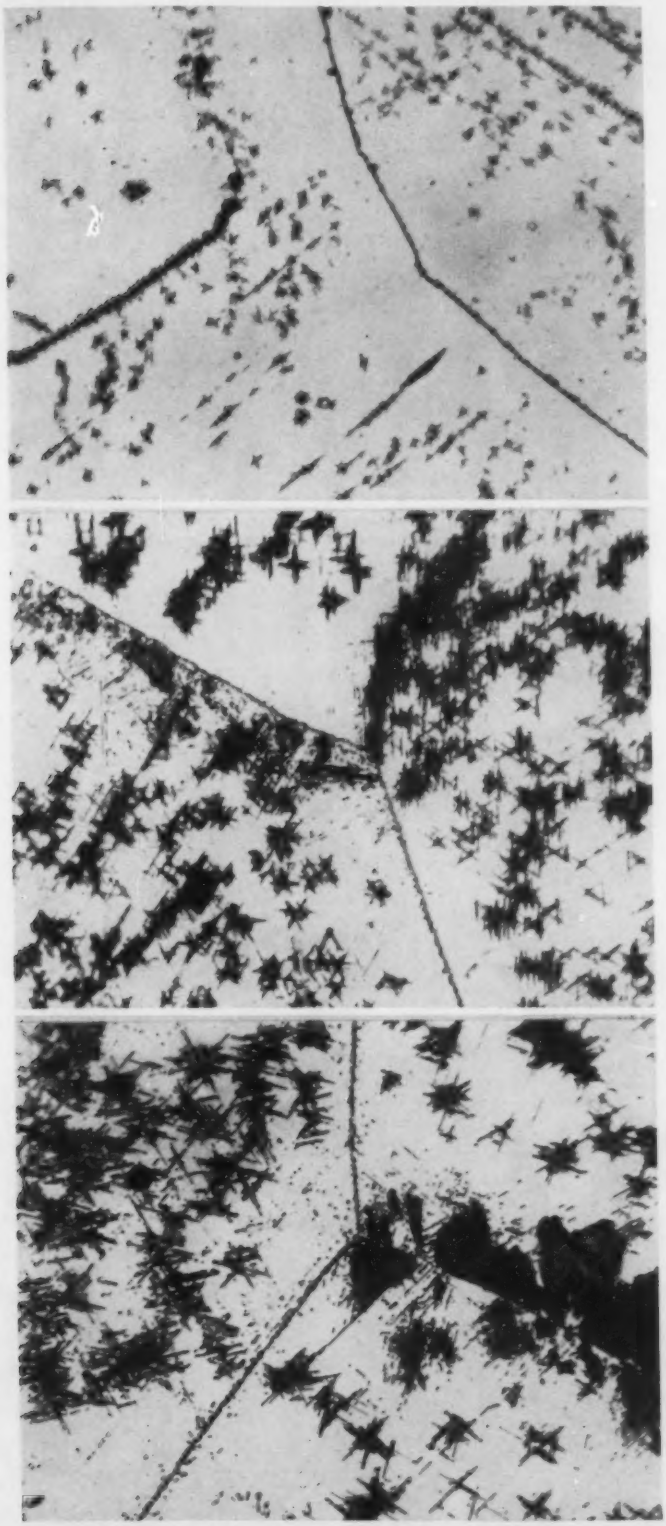


Fig. 2c—Microstructure of Stellite 21 After Isothermal Transformation. Original magnification X 750, reduced 40% in reproduction. Temperature of transformation 1500 °F. Top—2 hours; middle—25 hours; bottom—72 hours.

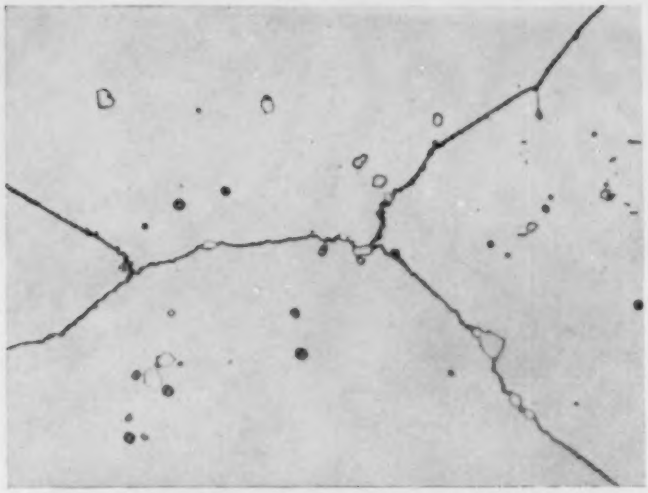


Fig. 2d—Microstructure of Stellite 21 After Isothermal Transformation. Original magnification X 750, reduced 40% in reproduction. Temperature of transformation 1200 °F, 72 hours.

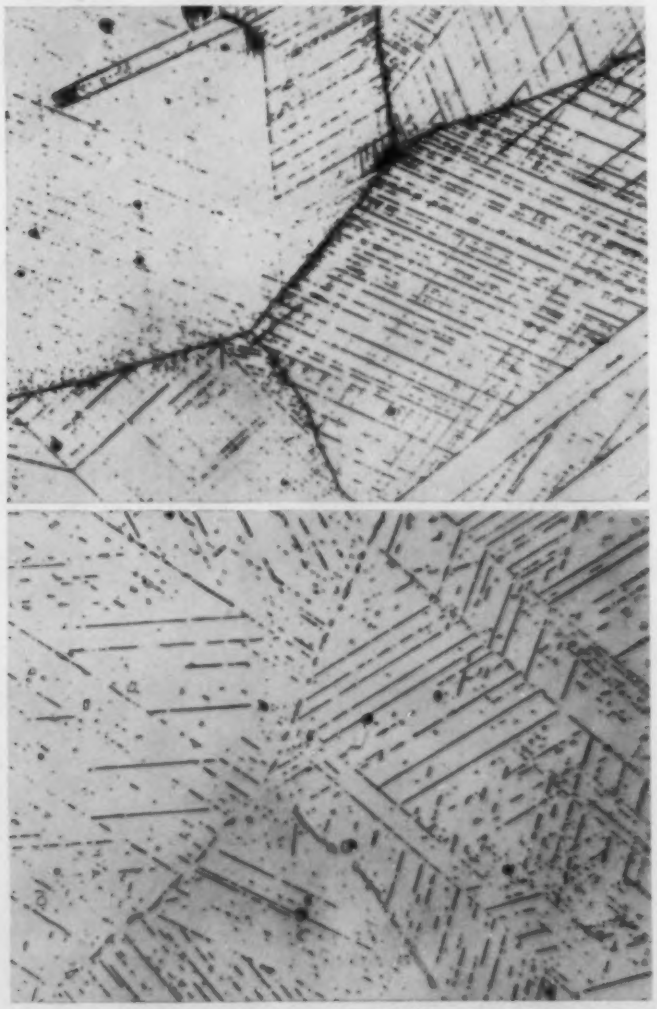


Fig. 3a—Microstructure of Stellite 21 After Aging. Original magnification X 750, reduced 40% in reproduction. Aged at 1950 °F. Upper—5 minues; lower—72 hours.

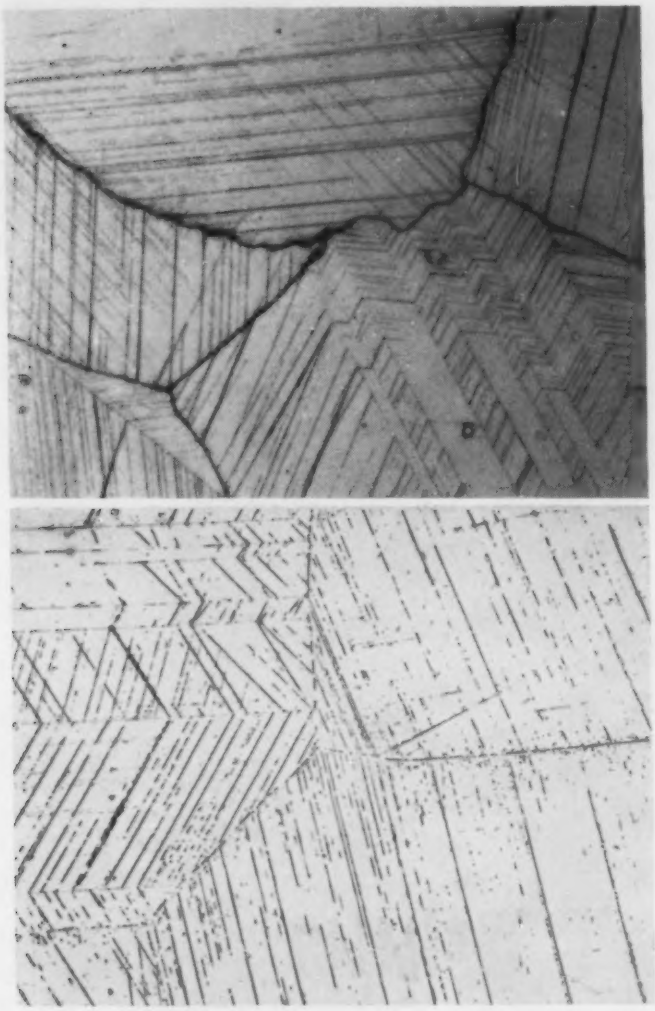


Fig. 3b.—Microstructure of Stellite 21 After Aging. Original magnification X 750, reduced 40% in reproduction. Aged at 1750 °F. Upper—5 minutes; lower—72 hours.

Stellite 21 in the as-rolled condition was found to be extremely fine grained (ASTM 7–8) as was previously noted and to consist of equiaxed grains, massive carbides, and fine, difficult-to-resolve precipitates in the grain boundaries.

Solution-treated structure—The solution treatment was sufficiently complete to produce a solid solution showing little or no residual precipitate in the microstructure, as shown in Fig. lb. While considerable grain growth occurred during solution treating, the final grain size was still less than that of cast Stellite 21. Little further grain growth was evident during subsequent aging or isothermal transformation.

Precipitation by isothermal transformation—Isothermal transformation of the solution-treated material at a temperature of 1950 °F (1065 °C) resulted in the formation of a lamellar, pearlitic type of

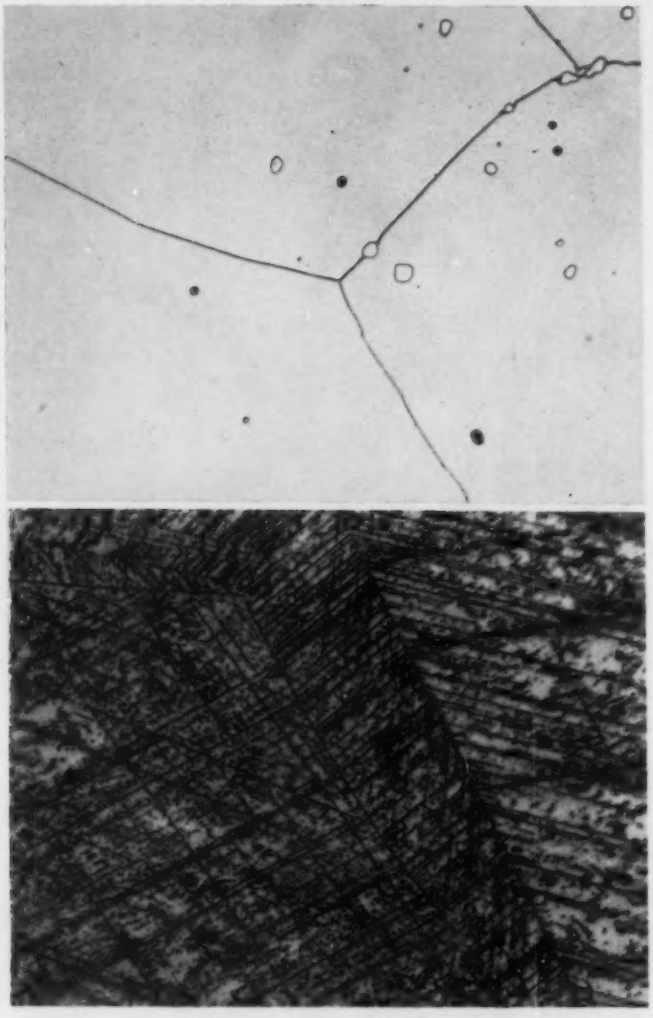


Fig. 3c—Microstructure of Stellite 21 After Aging. Original magnification X 750, reduced 40% in reproduction. Aged at 1500 °F. Upper—5 minutes; lower—72 hours.

structure along the grain boundaries as shown in Fig. 2a. Pearlitic precipitation has started in less than 5 minutes and appears to be complete after 2 hours at 1950 °F (1065 °C). "Divorcing" of the pearlite, or the tendency of the lamellae to break up and agglomerate into small spheroidized particles, is evident as the time of transformation increases, which is analogous to the behavior of steels.

Isothermal transformation at 1750 °F (955 °C) (Fig. 2b) was largely by pearlitic formation along the grain boundaries, as at 1950 °F (1065 °C), with some scattered precipitation within the grains. The rate of pearlitic growth was less at 1750 °F (955 °C) than at 1950 °F (1065 °C), and the interlamellar distance in the pearlite was reduced by the lowering of the temperature. There was an increase in the amount of precipitate for times up to 72 hours. Spheroidization was noted in the microstructure after 25 and 72 hours.

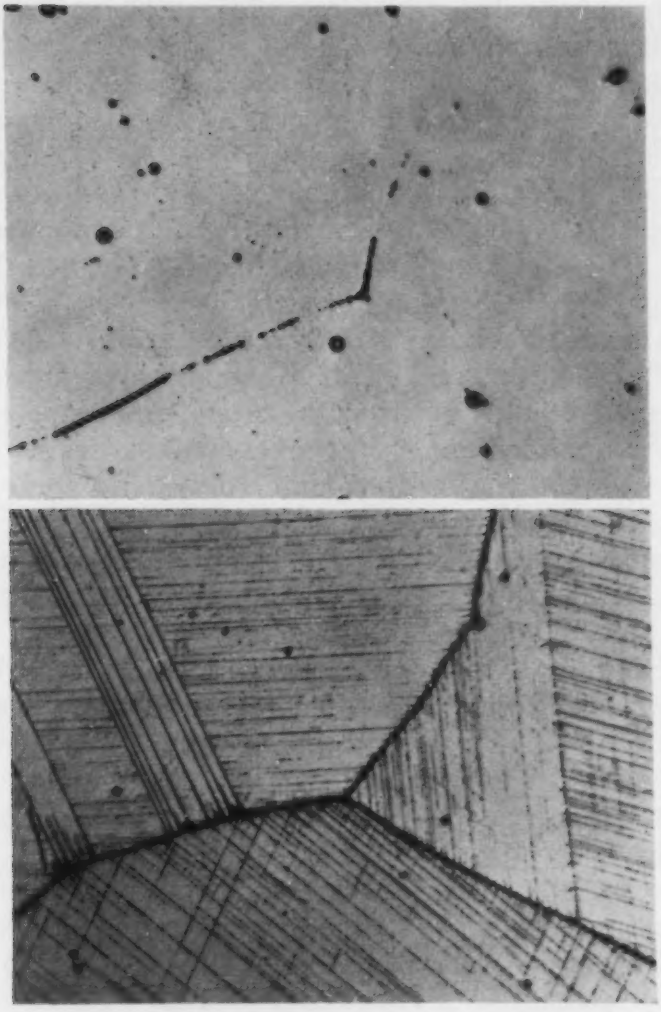


Fig. 3d—Microstructure of Stellite 21 After Aging. Original magnification X 750, reduced 40% in reproduction. Aged at 1200 °F. Upper—5 minutes; lower—72 hours.

Unlike specimens transformed at 1750 and 1950 °F (955 and 1065 °C), those transformed at 1500 °F (815 °C) have only a small amount of pearlite (Fig. 2c). The precipitate formed at this temperature was almost entirely of a star-shape (Widmanstätten type) distributed throughout the grains. The amount of visible precipitate increases with the time of transformation up to 72 hours. Although it is not evident from the photomicrographs shown, there is a distinct layer of precipitate-free matrix along most of the grain boundaries. As in other alloys, this effect is probably the result of the agglomeration of precipitate in the grain boundaries (11). The few small patches of pearlite appearing at some grain boundaries consist of very closely packed lamellae, unresolved at × 750 magnification.

At 1200 °F (650 °C), little visible precipitate was formed by isothermal transformation for periods up to 72 hours (Fig. 2d). Traces of

pearlite were observed in specimens transformed for 25 and 72 hours, although this is apparent in the photomicrograph.

Precipitation by aging—In sharp contrast to the precipitate formed by isothermal transformation, no pearlite was formed by any of the aging treatments. Aging at temperatures of 1950, 1750, and 1500 °F (1065, 955 and 815 °C) resulted in precipitation almost entirely along slip lines and twin boundaries through the grains as shown in Figs. 3a, 3b, and 3c. These slip lines and twin boundaries are the result of thermal stresses set up by water quenching from the solution treating temperature prior to aging. Precipitation by aging was very rapid at 1950 and 1750 °F (1065 and 955 °C) and appeared to be complete in 1 to 2 hours. Continued aging at these temperatures resulted in the agglomeration or coalescence of the precipitate particles.

The amount of visible precipitate formed by aging at 1500 °F (815 °C) continued to increase up to 72 hours.

Short-time aging at 1200 °F (650 °C) (Fig. 3d) gave no visible precipitate, while longer times (25 to 72 hours) at 1200 °F (650 °C) developed a small amount of precipitate along slip lines.

Grain boundary behavior—Agglomeration of the precipitates in the grain boundaries occurred with increasing time. This was particularly evident at the higher temperatures of isothermal transformation, and could be observed down to 1500 °F (815 °C). At 1200 °F (650 °C) the grain boundaries remained fine and continuous with increasing time of aging or isothermal transformation.

For specimens aged at 1200 °F (650 °C), the grain boundaries were very fine and difficult to show clearly by the etching technique. In the case of the specimen aged 5 minutes, it was necessary to substitute a more corrosive etchant (1 :1 HCl, electrolytically) than 5% aqua regia in order to attack the grain boundaries, since the specimen was still essentially in the solution-treated condition.

Hardness—The hardness of the specimens after solution treatment lay in the range from Rockwell C-20 to C-24. Subsequent hardening during aging or isothermal transformation at temperatures below the solution treating range is shown in Figs. 4 to 7. These figures present the data in both the conventional type of hardening curve (hardness against the logarithm of time of aging or isothermal transformation at constant temperature, Figs. 4 and 5) and in cross plots to show the effect of temperature (hardness against temperature at constant time, Figs. 6 and 7). In constructing these hardness curves, the experimental points were first plotted on both types of figure. Trial curves were next drawn to "average out" the experimental deviations on each separate type of plot. Values were read from the trial curves of one type of figure and cross-plotted on the other. New curves were then drawn to best approximate both the experimental points and the values obtained from the trial curves. The process was repeated

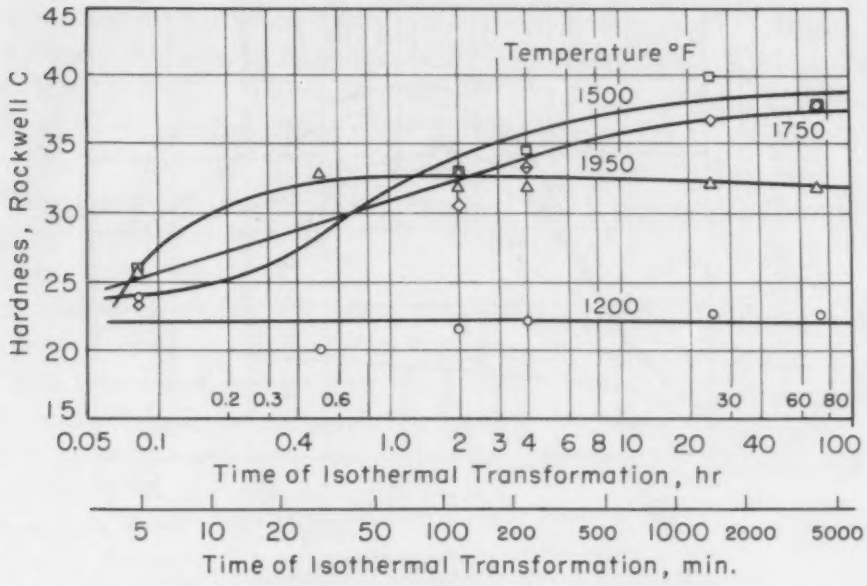


Fig. 4—Effect of Time on Hardness for Isothermal Transformation of Solution-Treated Wrought Stellite 21 at Various Temperatures.

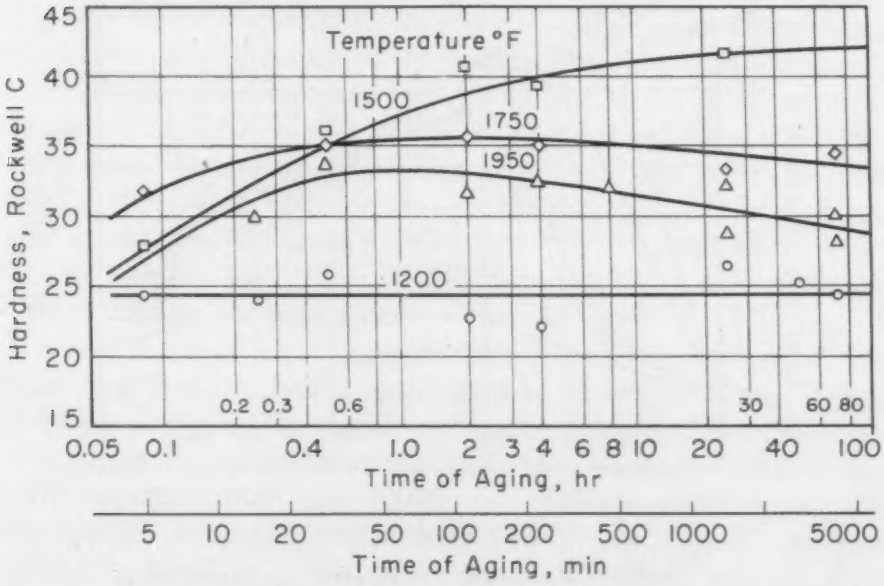


Fig. 5—Effect of Time on Hardness for Aging Solution-Treated Wrought Stellite 21 at Various Temperatures.

until the final curves on both sets of figures were consistent and gave the best representation of the general trend within the limits of experimental error.

At 1950 °F (1065 °C), both aged and isothermally transformed specimens hardened to a maximum hardness of about Rockwell C-33 in a matter of several minutes, after which some overaging and softening took place. This softening is related to the agglomeration or coalescence of the precipitate in the microstructure, as noted previously.

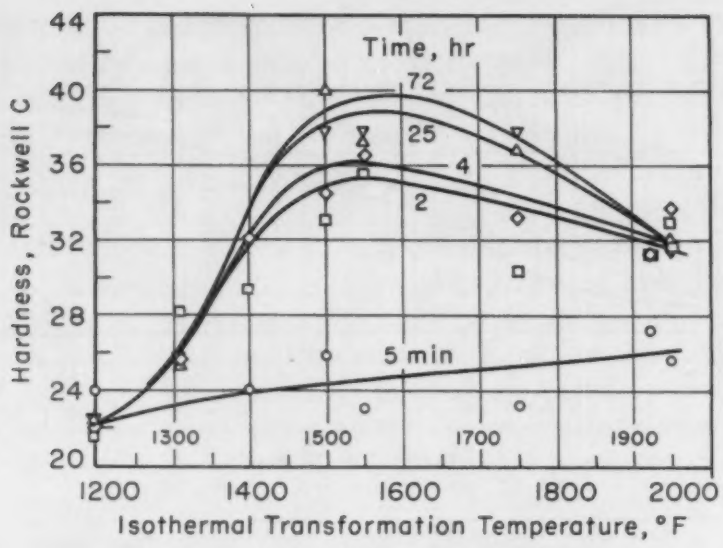


Fig. 6—Effect of Temperature of Isothermal Transformation on Hardness of Wrought Stellite 21 for Various Times of Isothermal Transformation.

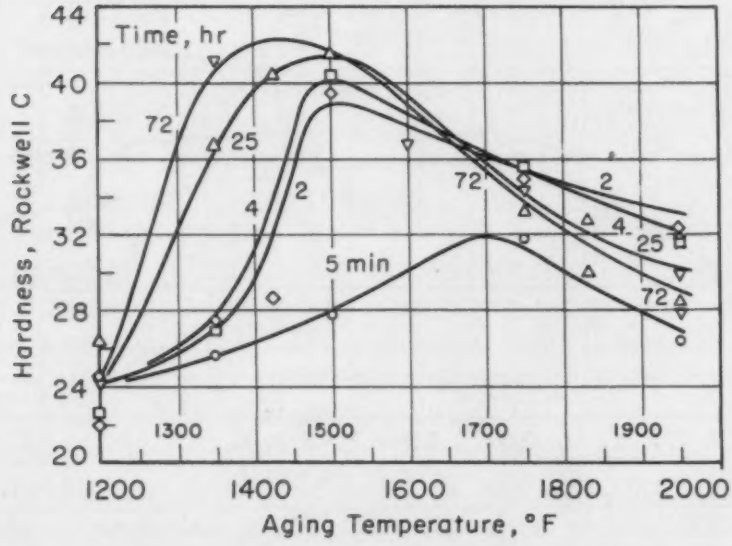


Fig. 7—Effect of Aging Temperature on Hardness of Wrought Stellite 21 for Various Times of Aging.

At 1750°F (955°C), the aged specimens hardened more rapidly than those isothermally transformed, reaching a maximum hardness of Rockwell C-36 after 2 hours of aging. Softening of the aged specimens after 2 hours was presumably due to the coalescence of the fine carbides precipitated along the slip lines. The isothermally transformed specimens continued to harden to 72 hours, when their hardness was Rockwell C-38.

At 1500°F (815°C), the aged specimens again hardened more rapidly than those isothermally transformed, but there was no evidence

of overaging or softening within the time investigated. Instead there was a steady increase in hardness with time for both types of heat treatment. Aging for 72 hours at 1500 °F (815 °C) gave a hardness of Rockwell C-42, while isothermal transformation for the same time resulted in a hardness of Rockwell C-39. Little further increase in hardness due to aging could be obtained by changing the temperature of aging, and 1500 °F (815 °C) appeared to be the temperature for maximum hardness.

At 1200 °F (650 °C), there was no measurable increase in hardness with the time of aging or isothermal transformation, and the hardness was constant at about Rockwell C-24 for the aged specimens and Rockwell C-22 for the isothermally transformed specimens. This is as would be expected from the microstructural behavior at this temperature, which showed little change in microstructure from that of the solution treated condition.

X-Ray Diffraction Results

Matrix phases—The percentages of the alpha (face centered cubic) and beta (hexagonal close packed) matrix phases were visually estimated from the intensities of the diffraction lines and are shown in Table II. The matrix consisted entirely of the alpha phase after solution treatment at 2250 °F (1230 °C). No beta formed upon isothermal transformation for short time periods of ¼ hour or 2 hours at 1950 °F (1065 °C) whereas these same transformation times produced a considerable quantity of beta at 1500 °F (815 °C). The longer time period 72 hours at both 1950 and 1500 °F (1065 and 815 °C) converted almost all of the matrix to the beta phase.

Minor phases—The results of the X-ray identification of minor phases in as-rolled and heat treated Stellite 21 are shown in Table II.

Indications of $Cr_{23}C_6$, sigma, and a spinel-type oxide were obtained from the diffraction pattern of the as-rolled specimen (treatment A). No certain evidence of any minor constituents were found in the solution-treated specimen (treatment B) but some of the diffraction lines found in the X-ray pattern indicated that M_6C and $Cr_{23}C_6$ may not have completely dissolved during the 16-hour solution treatment. Evidence of the formation of $Cr_{23}C_6$ and sigma phase were found in the specimens isothermally transformed for very short periods of time (15 minutes) at 1950 and 1500 °F (1065 and 815 °C) (treatments C and G). The carbide M_6C possibly was present in the specimen heat treated at 1950 °F (1065 °C). The specimens given the long-time isothermal-transformation treatments of 72 hours at 1950 and 1500 °F (1065 and 815 °C) (treatments E and H) appeared to contain the same minor constituents as the specimens heat treated at these temperatures for 15 minutes. However, some evidence of the presence of the high carbon carbide Cr_7C_3 was found. The specimens which were solution-

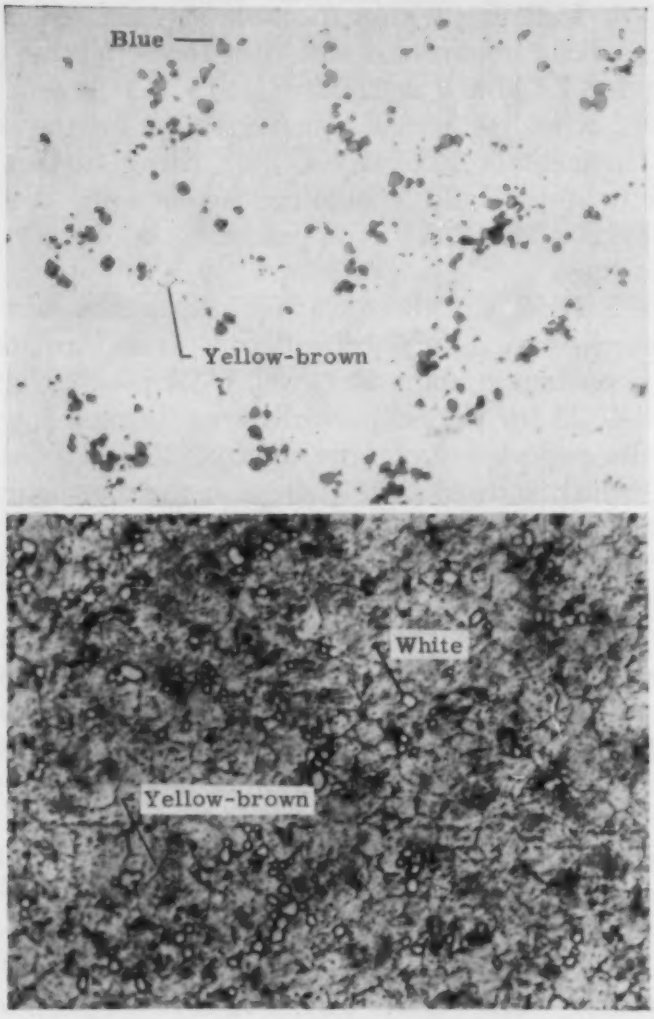


Fig. 8a—Microstructures of Various Stain-Etched and Heat-Tinted Specimens. Rolled Stellite 21. Upper—Stain etchant 3; X 1000; blue-M_6C, yellow-brown-$Cr_{23}C_6$. Lower—Heat-tinted; X 1500; white-$Cr_{23}C_6$, yellow-brown-sigma. (Reduced 40% in reproduction).

treated and isothermally transformed in the powdered state (treatments D and G) appeared to contain the same carbides as the specimens heat treated prior to obtaining powdered specimens (treatments C, E, F, and H). The X-ray pattern from the specimen isothermally transformed at 1500 °F (815 °C) for 2 hours (treatment G) contained evidence of the presence of sigma phase but no evidence was found in the specimen transformed 2 hours at 1950 °F (1065 °C) (treatment D). The pattern from the specimen given heat treatment I (selected because of the unusually large quantity of pearlite in the microstructure) gave strong indications of $Cr_{23}C_6$ and sigma and a possible indication of Cr_3C_2.

Stain-etching and heat-tinting results—Photomicrographs of stain-etched and heat-tinted specimens of rolled, and heat treated Stel-

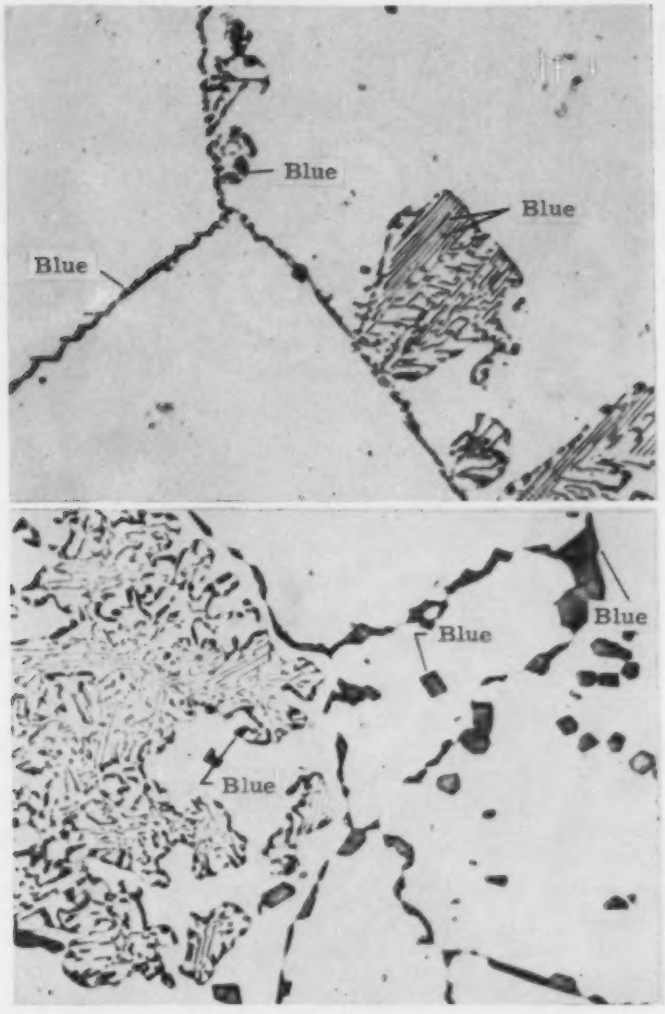


Fig. 8b—Microstructures of Various Stain-Etched and Heat-Tinted Specimens. Rolled Stellite 21 (furnace-cooled from 2250 °F to develop large quantity of pearlite). Upper—Stain etchant 1; X 1000; blue-sigma. Lower—Stain etchant 3; X 1000; blue-M_6C. (Reduced 40% in reproduction).

lite 21, are shown in Fig. 8. In this figure the colors and their interpretations for different microstructures have been recorded. The colors have been reported in the literature to represent particular minor phases but these color identifications need not necessarily apply to this alloy.

Discussion of Results

After a 72-hour solution treatment of 2250 °F (1230 °C), wrought Stellite 21 is essentially a homogeneous solid solution. This has been shown to have a face-centered cubic structure (see Table II, treatment B and references 6 and 12). Subsequent transformation at lower temperatures occurs both with changes in the crystal structure of the matrix and with the formation of minor phases. The matrix transformation from face-centered cubic (alpha phase) to hexagonal close-

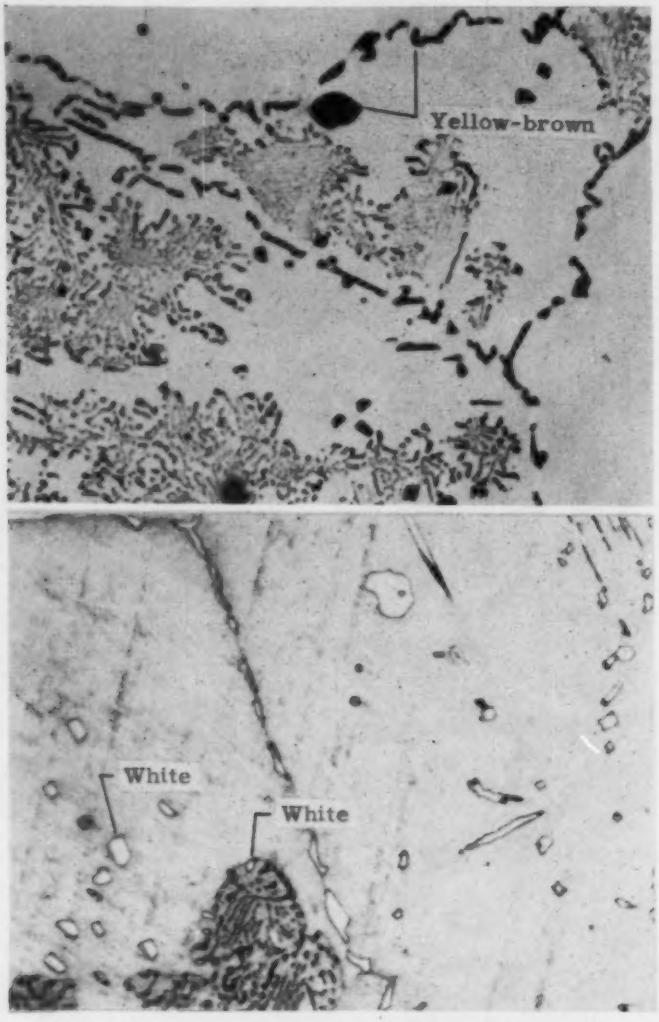


Fig. 8c—Microstructures of Various Stain-Etched and Heat-Tinted Specimens. Rolled Stellite 21 (furnace-cooled from 2250 °F to develop large quantity of pearlite). Upper—Stain etchant 2; X 750; yellow-brown carbides. Lower—Heat-tinted; X 1500; white-$Cr_{23}C_6$. (Reduced 40% in reproduction).

packed (beta phase) structures has already been described as taking place by a martensitic type of reaction (6 and 12). The formation of the minor phases may occur by precipitation directly from a single-phase solution, by a eutectoid decomposition, and/or by the transformation from one type of carbide to a second type; in any case, a nucleation and growth involving diffusion of atoms through the lattice is the most likely mechanism.

Precipitation of minor constituents is nucleated almost entirely at grain boundaries in the case of specimens isothermally transformed at 1750 and 1950 °F (955 and 1065 °C). Pearlitic growth increases with time at these temperatures and occurs with the diffusion of carbon from within the grains to the grain boundary where it reacts with the

carbide forming elements to form the carbide lamellae (largely $Cr_{23}C_6$ as will be discussed subsequently.)

This results in a localized depletion of chromium in the solid-solution lamellae alternating with the carbide lamellae and in adjacent areas, which therefore have less resistance to attack by the etchant. The depleted zones appear to have a definite and distinct border between the solid-solution lamellae in the pearlite and the matrix in the main body of the grains (Fig. 9), as has been noted previously with other

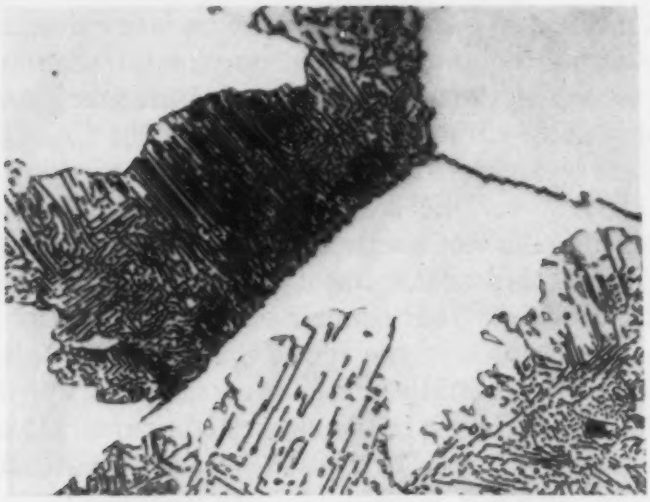


Fig. 9—Microstructure of Heat Treated Wrought Stellite 21 (16 Hours at 2250 °F, Isothermally Transformed 2 Hours at 1950 °F), Showing Pearlite Surrounded by Border. Electrolytically etched in 5% aqua regia. Original magnification X 750, reduced 40% in reproduction.

lamellar precipitates (11). A similar observation was made by DeVries and Mohling (13) in the case of a high temperature alloy having the following composition:

C	Cr	Co	Ni	Si	Mn	Mo	W	Fe
0.51	20.02	27.76	19.08	0.40	0.86	2.11	6.83	22.26

Slightly lighter areas were observed to surround the carbide precipitates in the microstructure of this alloy, and it was felt by the authors that this was due to concentration gradients rather than to a fully developed second phase. These areas were reasoned to be areas impoverished of austenite strengtheners by the formation of the precipitates and thereby weakened, which would account for the lower stress-rupture properties obtained for this alloy as compared with other alloys studied by these investigators. No direct proof is offered for the correctness of this view, and others (14) have explained the same effect as being due to the difference in orientation between the two matrix

areas brought about by recrystallization. A third possibility is that the differently etched areas are due to the presence of beta phase in the lamellae as distinct from the alpha phase of the remaining matrix (15). (As will also be discussed).

The starlike Widmanstätten structure of the carbide particles which appear as the main precipitate formed by isothermal transformation at 1500 °F (815 °C) strongly suggests that this type of precipitate forms on the (111) octahedral planes of the face-centered cubic matrix. This type of precipitate also occurs by isothermal transformation at 1750 °F (955 °C), where it forms a minor part of the total.

Precipitation is, in general, known to be favored on those crystallographic planes of the parent matrix on which the atomic spacing is nearly equal to that on the adjoining plane of the precipitant. This condition is readily shown for the precipitation of the $Cr_{23}C_6$ type of carbide on the (111) plane of the face-centered cubic matrix; thus, using a value of 3.566 A for the lattice parameter of face-centered cubic Stellite 21, which is the value reported by Rosenbaum (8), the distance between the metal atoms on the (111) plane is calculated to be $0.707 \times 3.566 = 2.52$ A. The distance of closest approach between the metal atoms for a carbide of the type $(Cr, Fe)_{23}C_6$ is given by Goldschmidt (16) as 2.45 to 2.51 A. This is a satisfactorily close match to favor precipitation of $Cr_{23}C_6$ in the suggested manner. It might also be noted that the close structural relation between this carbide and the austenitic matrix makes it possible that, in its initial stages of formation, the carbide forms from the austenite by a spontaneous transformation of the lattice, not involving atomic diffusion, as Goldschmidt points out.

In the case of the aged specimens, carbide precipitation is almost entirely along slip lines, or twin boundaries, with little or no tendency towards pearlitic or Widmanstätten type formations. Nucleation sites for this type of precipitation are provided by thermal stresses set up by water quenching from the solution treating temperature prior to aging. These slip planes are the (111) planes in the face-centered cubic matrix.

Constitution of various microstructures—The microstructure of as-rolled Stellite 21 etched conventionally or stain etched and heat tinted is shown in Figs. 1a and 8a. The large spheroidized microconstituents which are evident in the photomicrographs could be either $Cr_{23}C_6$ or sigma from the weak X-ray indications of both as shown in Table II. The appearance of the structure upon heat tinting indicates that the large particles are probably $Cr_{23}C_6$. Additional unpublished work with concentrated powders (the carbides were segregated by electrolytic digestion in a nonacidic solution) revealed only $Cr_{23}C_6$. This at least partially confirms the X-ray results obtained from the powdered alloy. The matrix of this structure consisted of both the face-

centered cubic and hexagonal close-packed structures. (Table II, treatment A).

Upon solution treatment of rolled Stellite 21 at 2250 °F (1230 °C) for 72 hours, most of these particles dissolve in the matrix (Fig. 1) and, therefore, no X-ray patterns were made of the specimen. An X-ray diffraction pattern obtained from a specimen which was solution-treated for 16 hours at 2250 °F (1230 °C) indicated that $Cr_{23}C_6$ and M_6C may have been residual carbides, although the indications were extremely weak. Of course, the matrix was 100% face-centered cubic.

The presence of $Cr_{23}C_6$ was indicated in all the rolled Stellite 21 specimens transformed at 1950 and 1500 °F (1065 and 815 °C) Table II. Both M_6C and sigma were indicated in almost every specimen, and Cr_7C_3 was indicated in the specimens transformed for 72 hours at 1950 and 1500 °F (1065 and 815 °C). The strength of the X-ray indications for $Cr_{23}C_6$ indicate that this phase is the predominant minor constituent in heat treated Stellite 21. The M_6C may, of course, precipitate directly from the face-centered cubic solid solution, but on the other hand, it may be, in part, a residual carbide or a transformation product of $Cr_{23}C_6$ (more correctly $M_{23}C_6$). The latter change would involve the diffusion of only a few atoms of molybdenum or other carbide formers (16). Sigma precipitation may have occurred in conjunction with, or subsequent to, carbide precipitation.

The chromium nitride gamma' CrN, M_2C (W_2C or Mo_2C), and M_3C type carbides might have been present in some of the specimens; however, there were too few significant lines in the standard patterns to list the phases in the tables. The Co_7W_6 (which could have an isomorph of the approximate stoichiometric composition Co_7Mo_6 in the molybdenum bearing alloys) has few strong lines and these coincide with sigma lines; Co_3W (or possibly Co_3Mo) has one d-value which appeared unique, but this value is in a range in which the accuracy of the d-value measurements is poor.

On the basis of X-ray diffraction patterns, the possibility existed that WC (or MoC) was present in almost every specimen. The numerous indications of this carbide suggested that the powders were being contaminated by the tungsten carbide burr, but the use of a diamond burr instead of the tungsten carbide burr did not affect the results. Also, the strong lines of standard WC patterns overlapped standard spinel patterns and, therefore, the two phases could not be differentiated.

It was observed that X-ray indications of the sigma phase were found in almost every specimen investigated, and since sigma as a precipitant could significantly affect the physical properties of this class of alloys it is worthy of further consideration. Precipitation of carbides would tend to deplete alloys of the cobalt-base type of chromium and molybdenum (or tungsten). However, in spite of chromium deple-

tion by carbide precipitation in high-chromium steels, the precipitation of carbides promote the formation of sigma phase (17). In the discussion following this article, Foley and the authors indicated their belief that the straining of the matrix lattice by precipitation of carbides promoted sigma precipitation in the vicinity of the carbides. The results of this investigation indicate that sigma is associated with large quantities of carbides.

Pearlitic structures—Previously Badger and Sweeney showed that the pearlitic structures in as-cast Stellite 21 may be dissolved by solution-treating at 2375 °F (1300 °C) and subsequently reformed by furnace cooling (4); the time of the solution treatment was not given, however. In addition, this structure was previously produced during an investigation (3) with Stellite 21 turbine blades at the Lewis laboratory, by solution-treating for 1½ hours at 2250 °F (1230 °C) and furnace cooling. In either case, it is uncertain whether reasonably complete homogenization took place and, therefore, it was not known whether an alloy of Stellite 21 composition would decompose and form similar lamellar structures upon cooling if it were originally thoroughly homogenized. In reference 15 it was shown that the bar stock from which the specimens for this investigation were obtained was homogenized thoroughly at 2250 °F (1230 °C) for 41 hours and that large quantities of lamellar structures (pearlitic and feathery structures) were obtained upon stepwise furnace cooling from the solution treating temperature.

In this investigation, it was shown that the matrix was entirely alpha or face-centered cubic after a 16-hour solution treatment (Table II) and thus the 72-hour solution treatment used for most of the specimens of this report, was selected principally to remove any possible chemical heterogeneity prior to producing the pearlitic or other structures. Changes in the crystal structure of the matrix of the alloy occurs at lower temperatures and often occurs simultaneously with the precipitation of minor phases.

In Reference 4 it was reported that pearlitic structures grew near areas of beta. However, in reference 15, it was found that this was not always the case. Several cobalt-base specimens, including a cast Stellite 21 specimen solution treated and isothermally transformed at 2000 °F (1095 °C) for 2 hours, contained considerable pearlite but no beta (hexagonal close packed phase) although little or no pearlite was found in alloys that did not form detectable quantities of the beta phase with most of the heat treatments employed. Furthermore, beta formed in alloys where no pearlitic structures were found. Therefore it was not possible to conclude that the solid solution lamellae of the pearlite consisted of the beta phase or that the pearlitic structure is a eutectoid.

Specimens given heat treatments C, E, F, H, and I Table II were

known to contain considerable quantities of pearlite. All of these specimens were indicated to contain M_6C and/or sigma in addition to $Cr_{23}C_6$ which previously was noted to be the predominant carbide which formed in this alloy. Thus, the carbide portion of the pearlitic lamellae could also contain M_6C. It is not known whether M_6C precipitates along with the carbides $Cr_{23}C_6$, whether it is a residual carbide following solution treatment, or whether it forms from $Cr_{23}C_6$ by diffusion of alloying elements to the $Cr_{23}C_6$ precipitants. Stain etching and heat tinting results indicated that when the pearlite is formed from face-centered cubic solid solution, $Cr_{23}C_6$ is the carbide constituent. These observations partially confirm the work of Reference 18 which reports that the pearlite consisted of lamellae of Cr_4C ($Cr_{23}C_6$) and a cobalt-rich solid solution.

With regard to the formation of the sigma phase, in the cast and heat treated cobalt-base alloys investigated in reference 15, X-ray diffraction evidence indicated that sigma was not always found in specimens containing large quantities of pearlite and the carbides $Cr_{23}C_6$ and M_6C.

Metallographic examinations made of numerous specimens of Stellite 21 have indicated that the solid-solution phase of the pearlitic lamellae does not consist of a phase such as sigma, nor do stain-etchant and heat tinting results. From observations of the paths of growth of pearlitic lamellae, from stain etching characteristics, and from microhardness tests made over a period of time, the phase other than the carbide in the pearlitic structure is not believed to be sigma but one of the matrix phases.

Hardness changes with heat treatment—The hardening behavior of Stellite 21 may be termed normal. Initial increases in hardness upon aging specimens at temperatures above 1200 °F (650 °C) may be observed. Prolonged aging or heat treating at 1750 and 1950 °F (955 and 1065 °C) causes the hardness to decrease after relatively short times. The softening that then occurs may be associated with spheroidization and agglomeration of the precipitate. The initial rate of hardening is greater for specimens transformed by aging than for those isothermally transformed at the same temperature, as would be expected from the greater number of nucleation sites provided by water quenching in the first case.

X-ray diffraction techniques—The difficulties of detection of minor phases by the X-ray diffraction techniques used in this investigation has been mentioned and has also been discussed in more detail in reference 15.

In spite of the inherent difficulties of the methods, most of the diffraction results compare favorably with results of other investigators of cast Stellite 21 some of whom used electrolytic digestion techniques to concentrate minor phases, Table IV. It was interesting to note that

Table IV
Minor Phases Detected in Cast Stellite 21 by Other Investigators [a]

Alloy	Phases found	References
Stellite 21	Cr_7C_3	4, 6
	$M_{23}C_6$ (or $Cr_{23}C_6$)	4, 5, 6
	M_6C	4, 6
	Sigma	6
Stellite 21 - Type 0.1-0.90% C	Cr_7C_3	7
	$Cr_{23}C_6$	7
	M_6C	7
Stellite 21 - Type 3.21% C	Cr_3C_2 + above carbides	7

[a] Phases found in one or more specimens, cast or heat treated or both.

indications of the sigma phases were found in almost all of the specimens transformed at temperatures below the solution treating temperature. In the investigations where digestion techniques were used to concentrate the minor phases, no sigma phase was found presumably because sigma would dissolve in the electrolytes.

Stain etching and heat tinting—The results of stain etching and heat tinting are helpful but not easily evaluated, because of several inherent difficulties. The colors of fine precipitates or thin pearlitic lamellae are not discernible. The colors of large phases depend upon the chemical composition, which, in turn, depends upon the heat treatment given the specimen. For example, a chromium-rich carbide of the $Cr_{23}C_6$ type would be expected to react to chemical attack differently from chromium-poor $Cr_{23}C_6$. Coring of carbides was sometimes observed and, in addition, minor phases frequently seemed to be surrounded with a band of different material which was visible either under oblique light at high magnification or polarized light. However, such banding may have been the result of optical effects.

In order to discuss more readily the stain etching and heat tinting results previously presented, reference may again be made to Fig. 8. In the case of rolled Stellite 21, Badger and Sweeney's etchant indicated M_6C to be present although X-ray diffraction results indicated the carbide to be $Cr_{23}C_6$. In the furnace cooled specimen, Beck's etchant showed a few blue dots indicating sigma phase, but such a small quantity of sigma phase could not have shown up in X-ray patterns. The etchant to differentiate between carbides and the sigma-phase showed only one color (yellow brown) indicating carbides, and similarly Badger and Sweeney's etchant showed only one color (blue) indicating M_6C. This tendency to stain or heat tint everything one color seemed fairly evident in the case of the Stellite 21 alloys.

Although the stain etching and heat tinting results were not completely satisfactory, these methods did leave the impression that grain boundary precipitates and many massive constituents were $Cr_{23}C_6$.

Summary of Results

The results of this investigation of microstructural and hardness

changes produced in wrought Stellite 21 by heat treatment and the studies of minor phases which form in the alloy upon heat treatment, are as follows:

1. Solution treatment of 72 hours at 2250 °F (1230 °C) was sufficient to produce a solid solution showing few or no residual precipitates in the microstructure. Grain growth occurred during solution treatment at 2250 °F (1230 °C), and after 72 hours the grain size increased from ASTM 7–8 (as wrought) to a mixed grain size with some grains 10 to 20 times larger than ASTM 1.

2. Isothermal transformation of the solution-treated material at temperatures of 1950, 1750, and 1500 °F (1065, 955 and 815 °C) resulted in the formation of pearlite along grain boundaries. Both the quantities of pearlite and the interlamellar spacing decreased with decreasing temperature.

3. Widmanstätten structures formed by isothermal transformation at temperatures as high as 1750 °F (955 °C). At 1500 °F (815 °C), Widmanstätten precipitation predominated over pearlitic precipitation.

4. Little visible precipitate was formed by isothermal transformation at 1200 °F (650 °C) for times up to 72 hours.

5. Aging the solution-treated and water-quenched material at temperatures from 1200 to 1950 °F (650 to 1065 °C) resulted in precipitation principally along slip lines and twin boundaries.

6. With sufficiently prolonged times of aging or isothermal transformation, spheroidization and agglomeration of the precipitated carbide particles occurred at temperatures as low as 1500 °F (815 °C). This occurred more rapidly in the structures formed by aging than in those formed by isothermal transformation.

7. The hardness of the material after solution treatment for 72 hours at 2250 °F (1230 °C) and water quenching was Rockwell C-20 to C-22. The temperature for developing maximum hardness in the solution-treated material was between 1400 and 1500 °F (760 and 815 °C). Aging for 72 hours in this temperature range produced a hardness of Rockwell C-42. The maximum hardness for isothermal transformation was about Rockwell C-40 and was developed between 1500 and 1600 °F (815 and 870 °C).

8. Hardness was not increased by aging or isothermal transformation at 1200 °F (650 °C). Specimens aged at 1500 °F (815 °C) and those isothermally transformed at 1500 and 1750 °F (815 and 955 °C) continued to harden up to 72 hours. Overaging or softening occurred within 72 hours at temperatures of 1750 °F (955 °C) and above for aging and at 1950 °F (1065 °C) for isothermal transformation.

9. Aging the solution-treated and water-quenched material generally resulted in a more rapid increase in hardness than isothermal transformation at the same temperature.

10. X-ray diffraction methods indicated that $Cr_{23}C_6$ was the residual carbide in the as-rolled alloy. In heat treated, rolled, specimens $Cr_{23}C_6$ appeared to be the most prevalent carbide, although M_6C was almost as frequently indicated. Sigma found in the heat treated specimens, was thought to form in conjunction with, or subsequent to the formation of the carbide $Cr_{23}C_6$.

11. X-ray diffraction results coupled with metallographic examinations of stain-etched and heat-tinted specimens indicated that one of the two phases of the pearlite (one of the two lamellae) consisted predominantly of $Cr_{23}C_6$. The other phase of the lamellae was indicated to be one of the matrix solid solution phases. This would confirm results obtained by others in their studies of cast Stellite-21. The M_6C carbide was also detected in many specimens and possibly formed from the transformation of the $Cr_{23}C_6$ lamellae.

12. The relative quantities of the matrix phases of each alloy studied, in various conditions of heat treatment, were estimated from the X-ray diffraction patterns. The matrix consisted of the face-centered cubic structure after solution treatment at 2250 °F (1230 °C). At 1950 °F (1065 °C), short transformation times of ¼ to 2 hours did not result in transformation of the face-centered cubic matrix to the hexagonal close packed structure. At 1500 °F (815 °C), short transformation times produced large quantities of this structure. Long time transformation of 72 hours at 1500 and 1950 °F (815 and 1065 °C) converted almost all of the matrix to the hexagonal phase.

Acknowledgment

The authors are greatful to the Lewis Flight Propulsion Laboratory of the NACA for permission to publish results of this investigation. The assistance of members of the Lewis staff is greatfully acknowledged and special thanks should be given to Miss Patricia Boyd for her untiring assistance in evaluating the many X-ray diffraction patterns, and Mr. Wm. J. Waters for his metallographic work.

References

1. Charles A. Hoffman and Charles Yaker, "Effects of an Aging Treatment on Life of Small Cast Vitallium Gas-Turbine Blades," NACA TN 2052, 1950.
2. C. Yaker and C. A. Hoffman, "Effects of Some Solution Treatments Followed by an Aging Treatment on the Life of Small Cast Gas-Turbine Blades of a Cobalt-Chromium-Base Alloy. I—Effect of Solution-Treating Temperature," NACA TN 2320, 1951.
3. C. A. Hoffman and C. F. Robards, "Effects of Some Solution Treatments Followed by an Aging Treatment on the Life of Small Cast-Gas-Turbine Blades of a Cobalt-Chromium-Base Alloy. II—Effect of Selected Combinations of Soaking Time, Temperature, and Cooling Rate," NACA TN 2513, 1951.

4. F. S. Badger, Jr. and W. O. Sweeney, Jr., "Metallurgy of High-Temperature Alloys Used on Current Gas Turbine Designs," *Symposium on Materials for Gas Turbines,* ASTM, June 1946, p. 99–112.

5. B. M. Rosenbaum, "X-ray Diffraction Investigation of Minor Phases of 20 High-Temperature Alloys," NACA TN 1580, 1948.

6. E. E. Fletcher, et al., "Alloys for High-Temperature Service (Investigation of the Fundamental Factors Promoting High-Temperature Strength to Alloys)," Summary Report to Office Naval Research, Batelle Memorial Institute, March 31, 1952. (Navy Dept. Contract No. N5ori-111, Task Order 1, Proj. NR 031-003.)

7. J. R. Lane and N. J. Grant, "Carbide Reactions in High Temperature Alloys," TRANSACTIONS, American Society for Metals, Vol. 44, 1952, p. 113; discussion, p. 134–137.

8. Burt M. Rosenbaum, "The Crystal Structures at Room Temperatures of Six Cast Heat-Resisting Alloys," NACA RM E7D23, 1947.

9. A. R. Troiano and J. L. Tokich, "The Transformation of Cobalt," *Transactions,* American Institute of Mining and Metallurgical Engineers, Vol. 175, 1948, p. 728; discussion p. 739–741.

10. N. F. M. Henry, H. Lipson and W. A. Wooster, "The Interpretation of X-ray Diffraction Photographs," D. Van Nostrand Co., Inc., 1951, p. 171.

11. A. H. Geisler, "Precipitation from Solid Solutions of Metals. Phase Transformation in Solids," 1951, p. 387; discussion, p. 541–544, John Wiley Sons, Inc., New York.

12. R. L. Beck, et al., "Alloys for High-Temperature Service." Final Report to Office Naval Research, Battelle Memorial Institute, April 30, 1952. (Navy Dept. Contract No. N5ori-111, Task Order 1, Proj. NR 031-003.)

13. Ralph P. DeVries, Jr. and Gunther Mohling, "The Development of Forging and Casting Alloys for Turbine Buckets," AF Technical Report No. 6615, Allegheny Ludlum Steel Corp., United States Air Force, Wright Air Development Center, Wright-Patterson Air Force Base, Dayton (Ohio), August 1951. (Contract No. AF 33(o38)-11669, E. O. No. R605-227.)

14. R. M. Brick and Arthur Phillips, *Structure and Properties of Alloys,* 1949, Second edition, McGraw-Hill Book Co., Inc., New York.

15. J. W. Weeton and R. A. Signorelli, "The Investigation of Lamellar Structures and Minor Phases in 11 Cobalt Base Alloys Before and After Heat Treating," NACA TN 3109, 1954.

16. H. J. Goldschmidt, "The Structure of Carbides in Alloy Steels," Pt. I—General Survey, *Journal,* Iron and Steel Institute, (London), December 1948, p. 345.

17. F. J. Shortsleeve and M. E. Nicholson, "Transformation in Ferritic Chromium Steels Between 1100 and 1500 °F (595 aand 815 °C)," TRANSACTIONS, American Society for Metals, Vol. 43, 1951, p. 142.

18. F. S. Badger, Jr. and F. C. Kroft, Jr., "Cobalt-Base and Nickel-Base Alloys for Ultrahigh Temperature," METAL PROGRESS, Vol. 52, No. 3, 1947, p. 394.

19. Sheldon Paul Rideout and Paul A. Beck, "Survey of Portions of the Chromium-Nickel-Molybdenum Quaternary System at 1200 °C," NACA TN 2683, 1952.

20. Ahmed El Bindari, P. K. Koh and Otto Zmeskal, "Sigma-Phase Formation in a Wrought Heat Resistant Steel," TRANSACTIONS, American Society for Metals, Vol. 43, 1951, p. 226.

21. Paul Pietrokowsky and Pol Duwez, "Crystallography of the Sigma Phase," *Transactions,* American Institute of Mining and Metallurgical Engineers, Vol. 188, 1950, p. 1283.

DISCUSSION

Written Discussion: By Arthur G. Metcalfe, research metallurgist, Armour Research Foundation, Chicago.

In an investigation[2] of a cast alloy of similar composition (carbon—0.32%; chromium—27.26%; nickel—2.36%; iron—1.34%; silicon—0.64%; manganese—0.25% and cobalt—62.28% by analysis) similar results in many respects were obtained. The hardness of quenched specimens fell from Rockwell C-30.4 at 2190 °F (1200 °C) to Rockwell C-26.2 at 2250.°F (1230 °C), but rose when quenching temperatures above 2290 °F (1255 °C) were used, due to the appearance of liquid melt in the boundaries. Holes appeared in specimens quenched from 2250 °F (1230 °C) due to transient melting unless slow heating was used.

Specimens were water-quenched after 6 hours at 2250 °F (1230 °C) and subsequently aged at temperatures of 1290, 1520, 1700, 1790, 1920 and 2100 °F (700, 825, 925, 975, 1050, and 1150 °C). Hardening occurred at all temperatures, reaching a maximum in 3 hours at 2100 °F (1150 °C) with a hardness of about Rockwell C-37. This peak hardness occurred at longer times at lower temperatures, but a higher hardness was reached, e.g. in 12 hours at 1790 °F (975 °C) when the hardness was Rockwell C-40. A plot of log time against the reciprocal of the temperature gave an approximate straight line. At 1700 and 1520 °F (925 and 825 °C) peaks occurred at times which fell approximately on this curve (20 hours and 35 hours), but peaks were also observed at shorter times. These peaks were observed to be at 50 minutes and 100 minutes respectively for these temperatures. At 1700 °F (925 °C) the hardness reached Rockwell C-42.5 after 50 minutes, fell to Rockwell C-40 after 120 minutes, but rose to reach Rockwell C-41 after 20 hours.

The structures showed that the first peak was associated with the formation of a pearlitic type of product. This seemed to form by a eutectoid reaction between 1750 and 1815 °F (955 and 990 °C) involving the decomposition,

$$\alpha \longrightarrow \beta + \text{chromium-rich phase}$$

where α is the high temperature face-centered cubic lattice and β the hexagonal close-packed matrix.

Similar behaviour can be observed in the authors' results in Fig. 5. The hardness values have been recorded in Table V together with the hardness values from work discussed above.

Table V

Time	Hardness after aging, Rockwell—C	
	Authors' — 1500 °F (815 °C)	A.G.M. — 825 °C
5 minutes	28	32
30 minutes	36	42
2 hours	41	46
4 hours	39	44.5
25 hours	42	46

The higher carbon content and lower nickel content of the alloy used by the writer is believed to be enough to account for the higher hardnesses.

Another reason to suppose that a different mechanism occurs at lower

[2] Investigation performed at the Deloro Smelting and Refining Co. Ltd., Deloro, Ontario, Canada.

temperatures is that the authors' show that the initial hardening is more rapid at 1500 and 1750 °F than at 1950 °F, whereas raising the temperature would be expected to increase the rate of precipitation (Fig. 5).

On the other hand, the authors' microstructures do not show the formation of pearlitic products on aging. It would be interesting to have the authors' opinion on the cause of the double peak at 1500 °F and the slower initial rate of hardening at 1950 °F than at 1750 °F.

Written Discussion: By F. L. VerSnyder, supervisor, Metallography and High Temperature Testing Unit, Small Aircraft Engine Laboratory, and H. J. Beattie, Jr., physicist, Thomson Laboratory, General Electric Co., West Lynn, Mass.

Considering the complexities of the metallurgy of cobalt base-alloys, this paper presents additional information which is most welcome. Perhaps the authors could offer some clarification on the following items:

1. In the paper the authors did not mention either the type of chromium used in the alloy or the nitrogen analysis of the alloy; however, it is noted in Table II that a chromium nitride phase is listed. Knowing the nitrogen content of the alloy would aid in determining the possibilities of such a nitride being present; furthermore, it is noted (if one assumes that an indication of presence may also be interpreted as an indication of quantity) that the chromium nitride appears to be present to an equal or greater extent after isothermal transformation than every phase with the exception of $M_{23}C_6$.

A most interesting observation may be made by comparing the "indication of presence" for heat treatments C and E—also, for heat treatments F and H. It will be noted from Table VI that, in the first case, with an increase in isothermal holding time from ¼ of an hour to 72 hours that the "indication of presence" changed from M, (i.e. fairly good indication) to S, (i.e. good indication). The same observation may be made for isothermal holding at the 1500 °F temperature where at ¼ of an hour there was a "possibility of the presence" of the phase while at the end of 72 hours, there was a "good indication" of the presence of the phase. Both the presence of the chromium nitride, as well as these observations on changes with isothermal holding time, appear from the authors' data to be significant. In addition, in what manner can microstructural observations be correlated with the X-ray diffraction evidence of the presence and changes of the Cr_2N. Do the authors have any comment?

2. The lattice parameters of the complex cubic carbides $M_{23}C_6$ and M_6C often indicate differences in composition, particularly in the molybdenum content. For instance, if the $M_{23}C_6$ is $Cr_{23}C_6$ as the authors indicate, the lattice parameter should be 10.64Å. The amount of molybdenum in this alloy may be favorable for its substitution in the carbide to the saturation composition of $Cr_{21}Mo_2C_6$, in which case the lattice parameter should be around 10.7Å. Variation in molybdenum content of the M_6C can also cause a pronounced variation in lattice parameter. We have observed it to vary from 10.8Å to 11.0Å in nickel-base alloys. In view of the fact that the authors indicated at one point in their discussion that the $Cr_{23}C_6$ might be more properly called $M_{23}C_6$, we wonder if the authors have lattice parameter data which might indicate the extent of molybdenum substitution in the carbides.

3. The authors give as a supporting fact to the precipitation of the $M_{23}C_6$ on the (111) planes of the face-centered cubic matrix the close match in interatomic distances of the metal atoms in the two phases. This is actually an in-

Table VI

Heat Treatment	Solution Treatment	Isothermal Transformation Temp °F	Isothermal Transformation Time, Hrs.	Minor Phases Indicated * Cr_3C_2	Cr_7C_3	$Cr_{23}C_6$	M_6C	Sigma	Cr_2N
C	2250 °F; 69 Hrs.	1950	¼			S	W	M	M
D	(1) 2250 °F; 16 Hrs. Water Quench (2) Grind X-Ray Powders (3) Heat Treat Powders 2250 °F; ¼ Hrs.	1950	2			S	S		M
E	2250 °F; 69 Hrs.	1950	72		VW	S	W	M	S
F	2250 °F; 72 Hrs.	1500	¼			S		M	W
G	(1) 2250 °F; 16 Hrs. Water Quench (2) Grind X-Ray Powders (3) Heat Treat Powders 2250 °F; ¼ Hrs.	1500	2			M	W	S	
H	2250 °F; 72 Hrs.	1500	72		VW	S	W	W	S
I	2250 °F; 46 Hrs.	1850	1½	W		S		S	S

* Indications of the presence of minor phases in these alloys are as follows:
S Good indication of presence
M Fairly good indication of presence
W Possible
VW Minimum indication considered

evitable result of the relatively fixed atomic radii of metal atoms in configurations of high co-ordination number. What really needs to be shown is that some two-dimensional network in the carbide lattice is similar to the (111) planes of the matrix. Since the 48(h) + 4(a) positions of the $M_{23}C_6$ lattice are 13-atom clusters of cubic close-packing, perhaps this would be possible.

4. Bigelow and Brockway of the University of Michigan have made electron diffraction studies of the iron-base 16-25-6 alloy.[3] They have found strong indications that the aging of this alloy after solution treatment proceeds by the initial appearance of $M_{23}C_6$ as a transition phase from the face-centered cubic matrix to the equilibrium carbide M_6C. We have observed similar indications in nickel-base alloys containing molybdenum. What holds for both iron- and nickel-base alloys one would expect might hold also for cobalt-base alloys. Would the authors have any further comment on this possibility?

Written Discussion: By Joseph R. Lane, Naval Research Laboratory, Washington, D. C.

In view of the well-known influence of cold work on the cobalt transformation, a question might be raised concerning the authors' technique for determining the crystallographic structure of the matrix. Their specimen material was apparently the powder produced by grinding, but it was not clear if this was true in all cases (Table II). It is realized that the grain-size problem makes difficult the determination on solid material.

The observations of various isothermal decomposition products, as described in the paper, are an original and valuable contribution. Have the authors any data on high temperature mechanical properties of such microstructures?

Authors' Reply

The authors would like to thank Messrs. VerSnyder and Beattie, and Drs. Metcalf and Lane for their comments and questions. In answer to the questions

[3] W. C. Bigelow and L. O. Brockway, "An Electron Metallographic Investigation of the Minor Phases of 16-25-6 Alloy," presented at the International Conference on Electron Microscopy, London, 1954.

by Messrs. VerSnyder and Beattie about the type of chromium (which is related to the N_2 content) and about the N_2 content of the alloy, the authors have no way of determining what type of chromium was used in the ingots from which the bar stock was rolled. The stock purchased conformed to the composition specified by the AMS specifications for cast Stellite 21. From past analyses of similar alloys, it could be assumed that the nitrogen content would be between 0.09 to 0.17%. In regard to the comments on the presence of the Cr_2N phase, it should be noted that the X-ray diffraction variables inherent to the methods used, make it impossible to consider the results quantitative. The indications of the presence of phases are indications of certainty and it is felt that the results should not be interpreted more rigorously.

For similar reasons, lattice parameter measurements were not made of the $Cr_{23}C_6$ ($M_{23}C_6$) diffraction lines.

In answer to the question as to whether $M_{23}C_6$ types of carbides transform to a more stable structure in cobalt base alloys as well as in iron and nickel base alloys, it should be observed that the Goldschmidt atomic diameters for face-centered cubic structures for iron, nickel and cobalt are very nearly the same. Therefore, $M_{23}C_6$ carbides in cobalt base alloys would be expected to transform to M_6C types of carbides with time at elevated temperatures, as was noted in the paper. The authors agree that the carbide $M_{23}C_6$ would tend to increase in molybdenum content, as aging or isothermal transformation time is increased, for the transformation of $M_{23}C_6$ would be likely only if molybdenum diffused. In addition to the recent work of Brockway and Bigelow [4] in which this transformation was observed in an iron base alloy, Goldschmidt [5] had noted sometime ago that such a transformation would occur as Mo replaces carbon in specific lattice points of $M_{23}C_6$.

Dr. Metcalf has described hardness peaks in an almost identical material which formed at times as low as 50 and 120 minutes at temperatures of 1695 and 1515 °F (925 and 825 °C). Such hardness peaks were not observed by the authors in any of the present work or subsequent work. It is believed that the pearlite observed by Dr. Metcalf after short transformation times was not responsible for the early high hardness of his specimens. Rather it is felt that coherent matrix precipitation, invisible upon etching, caused the high hardness. The pearlitic structure observed on aging by Dr. Metcalf is believed to have resulted because the quenching was not drastic enough to strain his material. Fig. 10 shows the microstructure of a water-quenched and aged specimen of this investigation compared with an air-cooled and aged specimen. Large quantities of pearlite have developed in the structure which was cooled slowly.

As far as the dips which occurred in Dr. Metcalf's data, the authors feel that the magnitude of the dip is too slight to be considered significant. The generally higher hardness of the material may be attributed to the higher carbon content but may also have been the result of hot working variables coupled with the short solution time of 6 hours.

The slower initial hardening rate of the specimens aged at 1950 °F (1065 °C)

---

[4] L. O. Brockway and W. C. Bigelow, "Development of Procedures for the Identification of Minor Phases in Heat Resistant Alloys by Electron Diffraction," Annual Summary Rep., January 15, 1952—January 15, 1953, Engineering Research Institute, University of Michigan, May 1953 (Wright Air Development Center, Wright-Patterson Air Force Base Contract AF-33 (616), E. O. No. R 463 Br-1).

[5] H. J. Goldschmidt, "The Structure of Carbides in Alloy Steels. Pt. I—General Survey," *Journal*, Iron and Steel Institute (London), December 1948, p. 142.

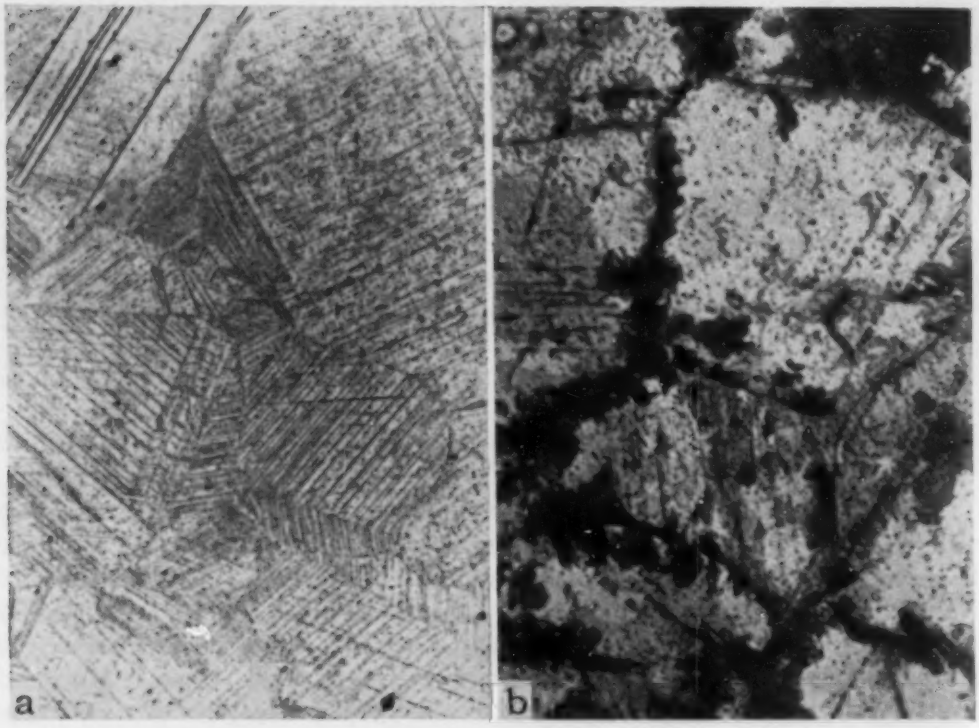


Fig. 10—Effect of Different Quenching Methods on Microstructure and Hardness of Aged Specimens. Solution treated at 2250 °F, aged 72 hours at 1950 °F. X 100. (a) Water-quenched. (Present investigation.) Rockwell C-29. (b) Air-cooled. (Another investigation.) Rockwell C-32.

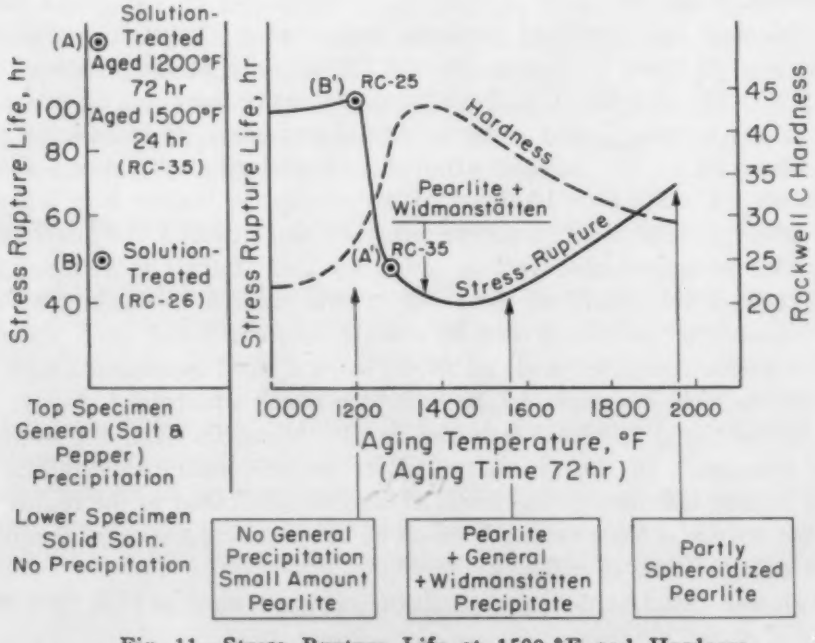


Fig. 11—Stress Rupture Life at 1500 °F and Hardness, Versus Aging Temperatures and Related Microstructures. (Specimens solution treated at 2250 °F aged at various temperatures.)

relative to the specimens aged at 1750 °F (955 °C) may not be explained by a different mechanism since the forms of the precipitate in both cases are the

same. The 1950 °F (1065 °C) treatment would be expected to erase some of the coherency stresses almost at the time of precipitation.

Dr. Lane suggested that, in view of the effects which cold work could have upon the transformation of the alpha to the beta phase, the technique for determining the crystal structure of the matrix phases might be questioned. The authors agree that the transformation could have been influenced somewhat by the grinding of the powders and subsequent annealing. However, evidence was obtained in the early stages of the investigation that indicated that grinding and annealing the powders did not cause the transformation of the alpha to the beta phase. An example may be seen in Table II of the paper. The specimen given heat treatment C (a solution treatment followed by isothermal transformation at 1950 °F for ¼ hrs.) which was powdered with the burr and subsequently annealed for 30 minutes at 1500 °F (815 °C) did not contain detectable quantities of beta phase but did contain minor phases, as revealed by metallographic means and X-ray diffraction.

Dr. Lane has also asked whether any properties have been obtained for the alloy in question for various conditions of heat treatment or microstructure. Fig. 11 shows some of the results obtained from a subsequent investigation.[6] The solid curve represents the 20,000 psi stress rupture life of wrought Stellite 21 (from the same stock used in the present investigation) tested at 1500 °F (815 °C). The dashed curve represents the hardness of these specimens prior to testing. All of the specimens represented by the curves were solution treated at 2250 °F (1230 °C), air-cooled and aged 72 hours at temperatures indicated on the abscissa.

Maximum stress rupture lives were obtained after heat treatment at temperatures of 1000 to 1200 °F (540 to 650 °C). These specimens had the lowest hardnesses, of the order Rockwell C-22-25. As the aging temperature was raised, the stress rupture life dropped and the hardness reached a maximum at about 1350 °F (730 °C). As the aging temperature was raised still further, the quantities of pearlite increased along with general matrix precipitation and the stress rupture life rose to a fairly high value at 1950 °F (1065 °C). Again the hardness dropped as the rupture life increased. The 1950 °F (1065 °C) temperature caused partial solution treatment of the structure as well as the formation of partially spheroidized pearlite.

From these curves alone, it could be concluded that high hardness was associated with low life and low hardness with high life.

This relationship was found to be secondary to the importance of microstructures, however. The values plotted on the left will help illustrate the latter point. The top data point (A) represents a group of specimens given a double age of 72 hours at 1200 °F (650 °C) and 24 hours at 1500 °F (815 °C), after solution treatment at 2250 °F (1230 °C). For a stress of 20,000 psi, the stress rupture life was 160 hours. The hardness prior to testing was Rockwell C-35. A group of specimens with comparable hardness, as shown by point (A′) on the stress rupture curve, had a much lower stress rupture life—50 hours. The bottom point on the left, (B), represents a group of specimens given a solution treatment and no aging treatment prior to testing. In this case the hardness was RC 26. It may be seen that the properties of this specimen were very low in

[6] F. J. Clauss and J. W. Weeton, "Relation of Microstructure to High Temperature Properties of a Wrought Cobalt Base Alloy, Stellite 21 (AMS 5385)," NACA TN 3108, 1954.

contrast to specimens represented by point (B′) in the rupture curve at the right, which also had a comparable hardness Rockwell C-25.

The excellent properties of the specimen given the double age, (A), was associated with a fine, well dispersed, well developed precipitate which strengthened the matrix of the alloy prior to the test. In direct contrast, the specimens aged at temperatures of 1000 to 1200 °F (540 to 650 °C) did not contain any appreciable visible precipitates prior to the 1500 °F (815 °C) tests. The high strength of these specimens, (B′), may be attributed to rapid precipitation during the test in nucleation sites that were formed at the low aging temperatures of 1000 to 1200 °F (540 to 650 °C). The poor properties of the solution treated specimens, (B), relative to the specimens aged at 1200 °F (650 °C) (B′), were no doubt due to the fact that precipitation during testing was too slow to strengthen the matrix of the alloy. The low strength of the specimen transformed at 1350 °F (730 °C) was associated with a star-like Widmanstatten structure.

It was noted that air cooling permitted the formation of some pearlite in the aged specimens whereas in the investigation just presented, no pearlite formed in the aged specimens. Pearlite was found to increase ductility but reduce strength (relative to the general types of precipitation just described).

SECONDARY GRAPHITIZATION OF QUENCHED AND TEMPERED DUCTILE CAST IRON

By J. C. Danko and J. F. Libsch

Abstract

The mechanism of secondary graphitization of quenched and tempered structures of ductile iron was investigated by metallographic studies. Secondary graphitization proceeds by the decomposition of martensite to ferrite and some silicon rich carbides which rapidly decompose or graphitize to fine graphite spheroids. Increase in the silicon content in the ductile iron results in greater quantities of secondary graphite, whereas carbide forming elements appear to reduce the amount of fine graphite spheroids.

Introduction

QUENCHED structures of fully austenitized ductile cast iron consist of primary spheroids of graphite dispersed in a matrix of martensite. Subsequent tempering treatments that decompose the martensite produce a large quantity of secondary graphite in the form of fine graphite spheroids. Secondary graphite was observed by Rehder (1)[1] during his investigation on the mechanical properties of quenched and tempered structures of ductile iron. Schwartz (2) et al, reported an increase in the number of graphite spheroids by quench and temper treatments. Aside from these observations on secondary graphite, no known theory has been advanced to explain the actual mechanism of secondary graphitization in quenched and tempered ductile iron. The purpose of this paper, therefore, is to report metallographic observations on the formation of secondary graphite and to propose a mechanism for its formation.

Occurrence of Secondary Graphite

Secondary graphitization was investigated in six different heats of ductile cast iron. Their chemical compositions are presented in Table I.

Specimens for metallographic observations were cut from the legs of one-inch keel blocks after annealing at 1700 °F (925 °C) for 2

[1] The figures in parentheses pertain to the references at the end of this paper.

A paper presented before the Thirty-sixth Annual Convention of the Society, held in Chicago, November 1 to 5, 1954. Of the authors, J. C. Danko is instructor, Lehigh University, Bethlehem, Pa., and formerly a research fellow for International Nickel Co.; J. F. Libsch is professor of metallurgy, Lehigh University and consulting metallurgist, Lepel High Frequency Laboratories, Inc., New York. Manuscript received April 9, 1954.

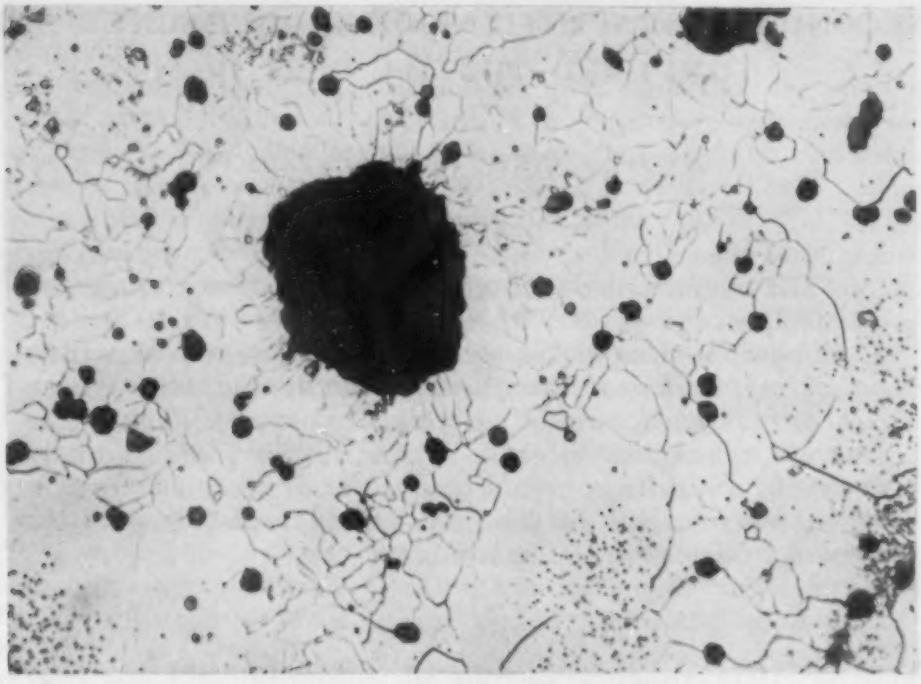


Fig. 1—Heat A Quenched and Tempered 2 Hours at 1300 °F (705 °C). Small graphite spheroids are secondary graphite. Nital Picral Etch, X 500

hours. Specimens were then austenitized at 1650 °F (900 °C) for 1 hour, oil-quenched, and then tempered at 800 °F (425 °C) to 1300 °F (705 °C) in 100 °F (38 °C) intervals for tempering times of 30 to 120 minutes.

Metallographic observations on the quenched and tempered structures of the ductile iron revealed several important features in the formation of the secondary graphite. At tempering temperatures below 1000 °F (540 °C) and for times up to 2 hours, no secondary graphite was evident in the tempered structures. However, at 1100 °F (595 °C), secondary graphite appeared in small quantities in all six heats of ductile iron. At 1200 °F (650 °C) and 1300 °F (705 °C), the secondary graphite became more abundant and larger. Secondary graphite occurred only in the dendritic cores. While some carbides remained in the dendritic cores, the majority were concentrated in the interdendritic areas after tempering at 1300 °F (705 °C). Secondary graphite is shown in the quenched and tempered structure of heat A in Fig. 1.

Table I
Chemical Analysis—Percentage

Heat	T.C.	Si	Mn	Ni	P	S	Mg	Cr
A	3.42	1.87	0.32	0.75	0.034	0.01	0.076	
B	3.24	2.06	0.73	0.63	0.020	0.016	0.063	
C	3.47	3.10	0.78	0.83	0.034	0.01	0.062	
D	3.49	2.98	0.34	0.83	0.034	0.01	0.056	
E	3.39	2.25	0.67	0.70	0.020	0.014	0.051	0.23
F	3.00	2.20	0.43	3.43	0.021	0.017	0.061	

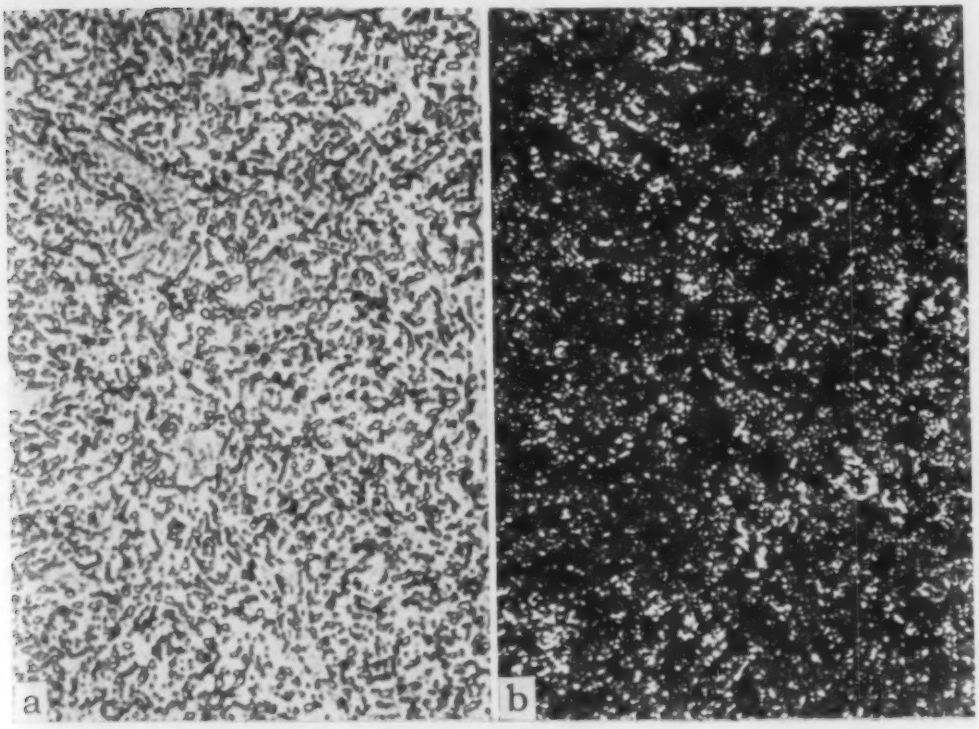


Fig. 2—1080 Steel Quenched and Tempered at 1250 °F (675 °C). (a) Spheroidal carbides-bright light; (b) Same field under polarized light. Picral Etch, X 1000

Polarized Light Observations

When viewed under polarized light (3), the dendritic carbides generally had a distinctly different appearance from the carbides located in the interdendritic areas, i.e., the dendritic carbides exhibited a characteristic cross which was absent in the interdendritic carbides. Such an optical cross has been observed in globular inclusions possessing transparent optical properties (4). The polarized light penetrates such inclusions and causes reflection at the hemispherical interface between the inclusions and the matrix to produce an optical cross. Since the dendritic carbides exhibited the optical cross while the interdendritic carbides did not, it appears that the dendritic carbides may be of different composition.

To determine the nature of the dendritic and interdendritic carbides, bright and polarized light observations were made on normal iron carbide (Fe_3C) produced in quenched and tempered 1080 steel. Although the carbides produced in the steel were spheroidal, they did not produce an optical cross. This is illustrated in Fig. 2, a quenched and tempered 1080 steel viewed under bright and polarized light. It may therefore be concluded that the carbides situated in the dendritic cores of the quenched and tempered ductile iron are not normal iron carbide (Fe_3C), but of a different composition.

In summary, bright field and polarized light observations on quenched and tempered ductile iron disclosed the following information: (a) Secondary graphite occurs only in the dendritic cores; (b) The dendritic carbides exhibited an optical cross under polarized light; and (c) Few dendritic carbides remained after secondary graphitization, whereas a multitude of interdendritic carbides that differed from the dendritic carbides were present.

For the short tempering cycles employed, namely two hours, normal iron carbide (Fe_3C) which is fairly stable would not be expected to decompose to graphite and iron. In order to account for the rapid graphitization of the carbides, a very unstable carbide must therefore be produced by the martensite decomposition. Since silicon, a powerful graphitizer, is present in large percentages in ductile iron, there is a likelihood for silicon to replace some iron in the normal iron carbide and thereby enhance graphitization of the carbides to secondary graphite. In addition, the presence of silicon in the dendritic carbides may be responsible for the optical cross under polarized light, and it is interesting to note in this connection that silicon carbide (SiC) (5) is non-opaque.

Existence of Silicon-Rich Carbides

The existence of silicon in carbides was illustrated by Stead (6) as early as 1910. Stead noted that increasing silicon contents in iron-carbon-silicon alloys resulted in a carbo-silicide of iron. Gontermann (7) in his work on the iron-carbon-silicon system considered silicon to be found in the carbide and austenite. Honda and Murakami (8) reported two types of carbides in iron-silicon alloys high in carbon; one was the ordinary Fe_3C and the other a silico-iron carbide. Hatfield (9) also found that some silicon crystallizes with the carbide in white cast irons. These carbides were separated electrolytically and chemically analyzed. The results show that silicon may replace some of the iron in the carbide and that the amount of silicon in the carbide depends upon the silicon present in the cast iron as well as the presence of manganese and sulphur. Silicon was also found to render the carbides less stable at elevated temperatures.

Marles (10) investigated silicon-rich carbides in iron-carbon-silicon alloys by heat tinting techniques. Normal iron carbide (Fe_3C) was darkened, whereas silicon-rich carbides did not respond to heat tinting. Marles found that the silicon-iron carbide phase increased with greater amounts of silicon until at 6.7% silicon, the normal iron carbide (Fe_3C) was completely displaced by the silicon-rich carbides. The silicon-rich carbides decomposed to graphite upon annealing at 1290 °F (700 °C), while the iron carbide (Fe_3C) remained. Harry (11) also found that silicon-rich carbides are markedly unstable and readily decompose to graphite.





Fig. 3—As-Quenched Martensite. Picral Etch, X 500

Fig. 4—Martensite Tempered 5 Minutes at 1200 °F (650 °C). Picral Etch, X 2000

Owen and Street (12) recently examined by X-ray diffraction high purity iron-carbon-silicon alloys. Their evidence indicates the presence of a microconstituent termed the x-constituent contains silicon, and therefore can be described as an iron-silicon carbide. Moreover, their observations indicate that this iron-silicon carbide can be precipitated from austenite. Further evidence of the existence of iron-silicon carbides was obtained by Morrogh and Williams (13) during their investigation of undercooled graphite in cast irons. The carbide

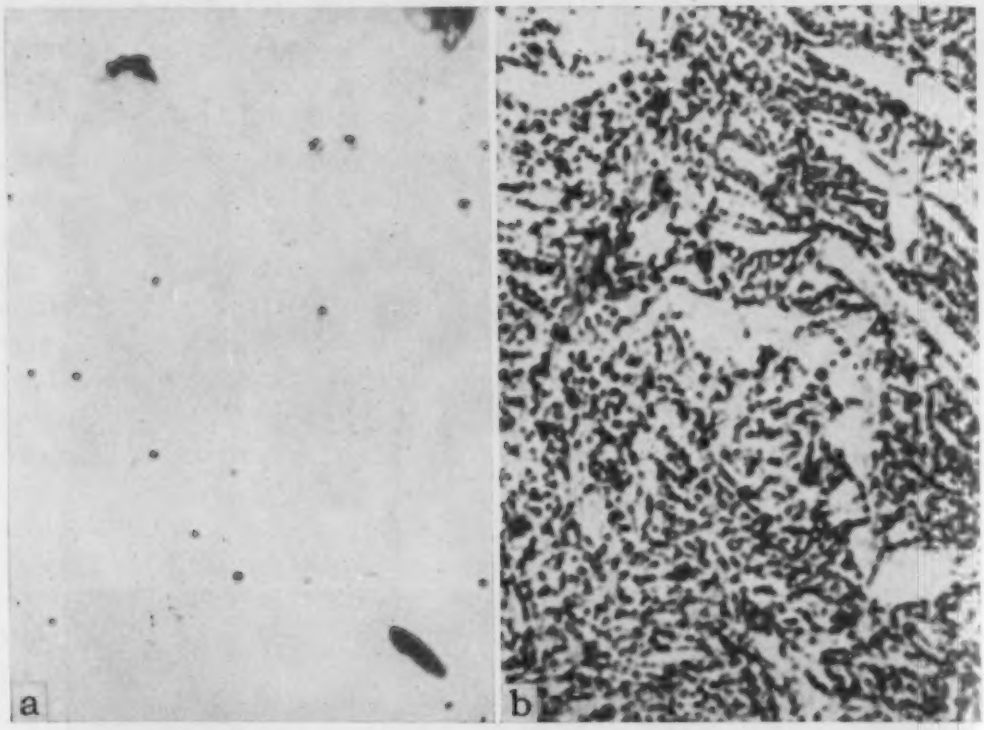


Fig. 5—Martensite Tempered 15 Minutes at 1200 °F (650 °C). (a) Unetched; (b) Picral Etch, X 2000

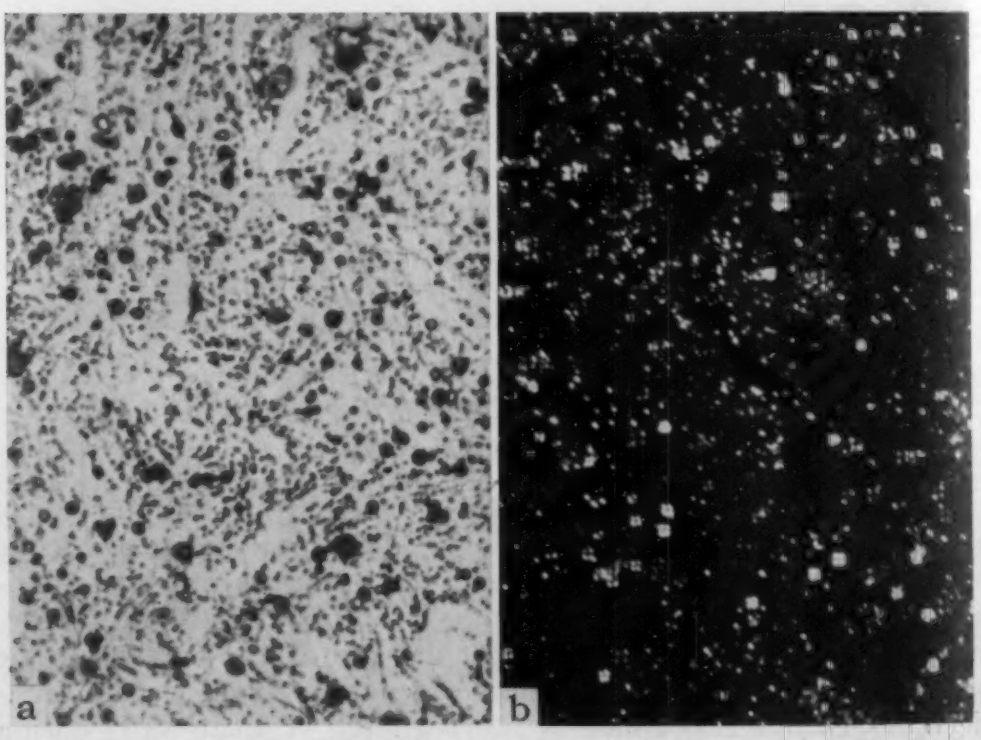


Fig. 6—Quenched and Tempered 2 Hours at 1100 °F (595 °C). (a) Bright Field; (b) Polarized Light. Picral Etch, X 1000

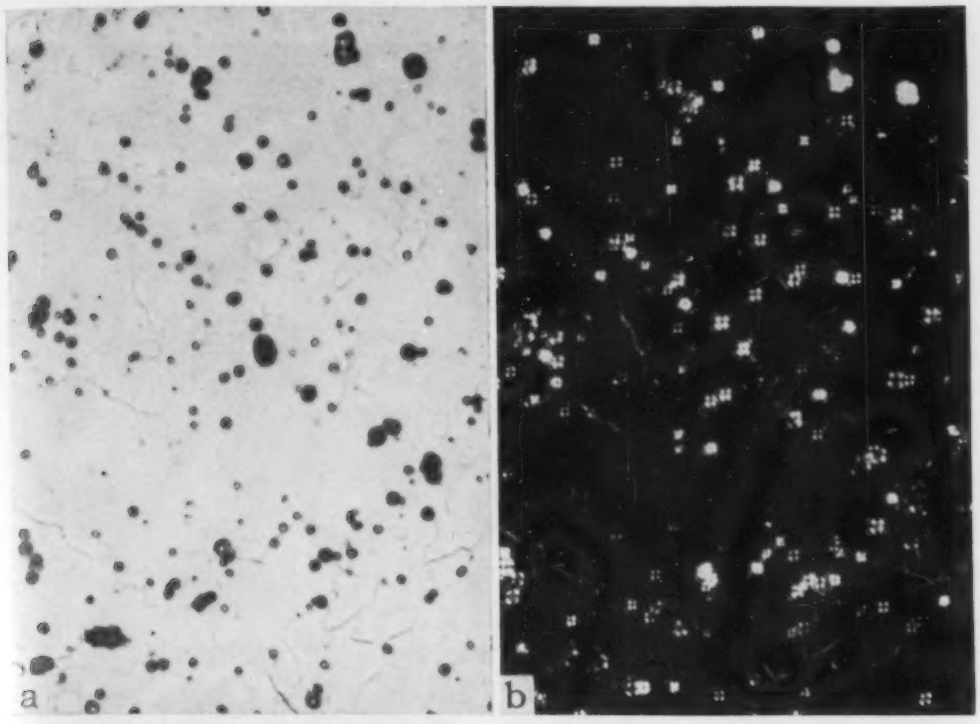


Fig. 7—Quenched and Tempered 2 Hours at 1200 °F (650 °C). (a) Bright Field; (b) Polarized Light. Picral Etch, X 1000

phase in a number of iron-carbon-silicon alloys was extracted chemically, and the analysis of the residue revealed that the amount of silicon in the residue increased with the amount of silicon. This was attributed to the presence of an iron-silicon carbide.

Heat tinting techniques that were originally used by Stead were employed on quenched and tempered structures of several heats of ductile iron to differentiate the carbides. The dendritic carbides did not respond to heat tinting and remained light, while the interdendritic carbides were darkened.

Hence, the presence of silicon-rich carbides in the quenched and tempered structures of ductile iron may readily account for the following observations: (a) the occurrence of an optical cross in the dendritic carbides under polarized light; (b) failure of the dendritic carbides to respond to heat tinting; and (c) rapid graphitization of the dendritic carbides during tempering.

Metamorphosis of Secondary Graphite

The metamorphosis of secondary graphite commences with the decomposition of martensite. As-quenched martensite is shown in Fig. 3. During the initial stages of tempering, 5 minutes at 1200 °F (650 °C), extremely fine spheroidal carbides are produced from the martensite decomposition. These carbides are exemplified in Fig. 4

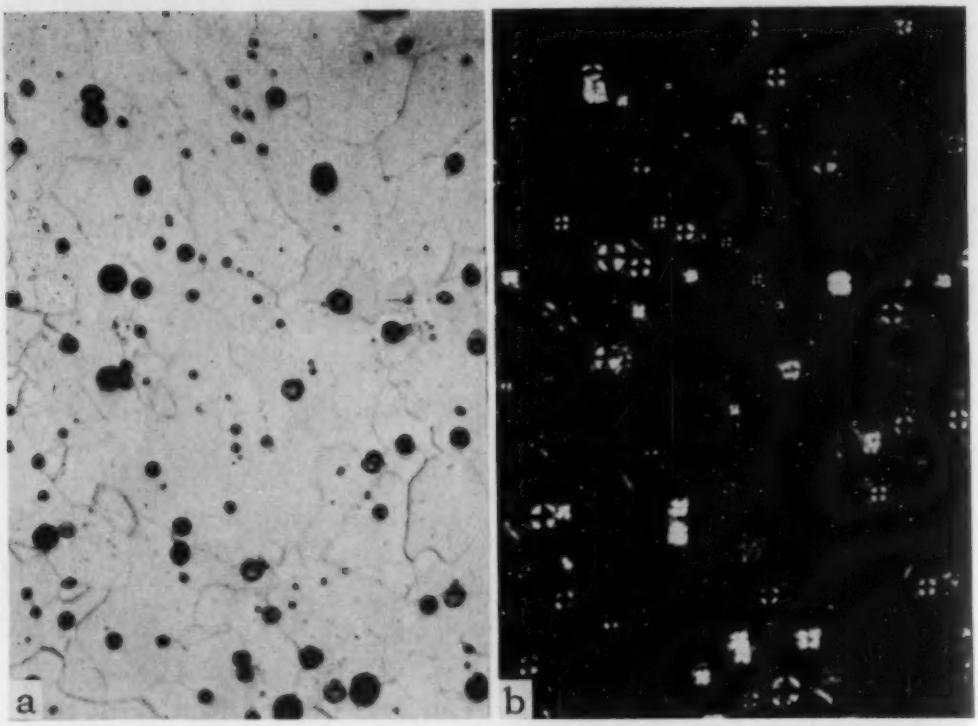


Fig. 8—Quenched and Tempered for 2 Hours at 1300 °F (705 °C). (a) Bright Field; (b) Polarized Light. Picral Etch, X 1000

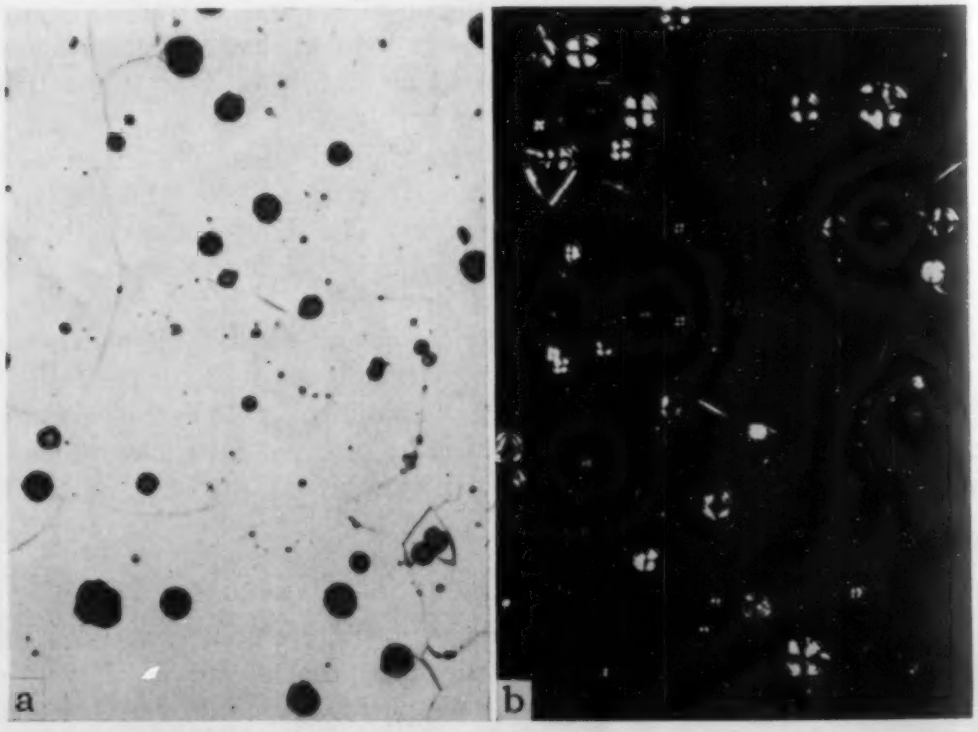
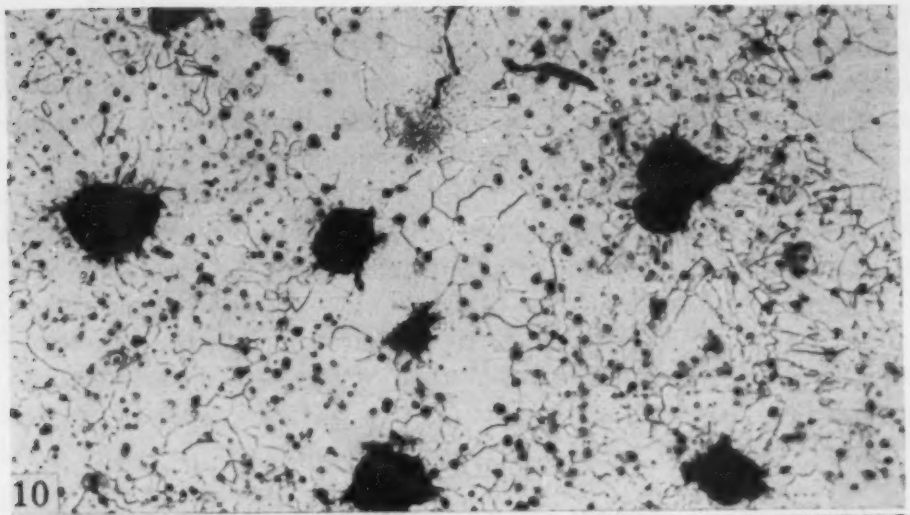
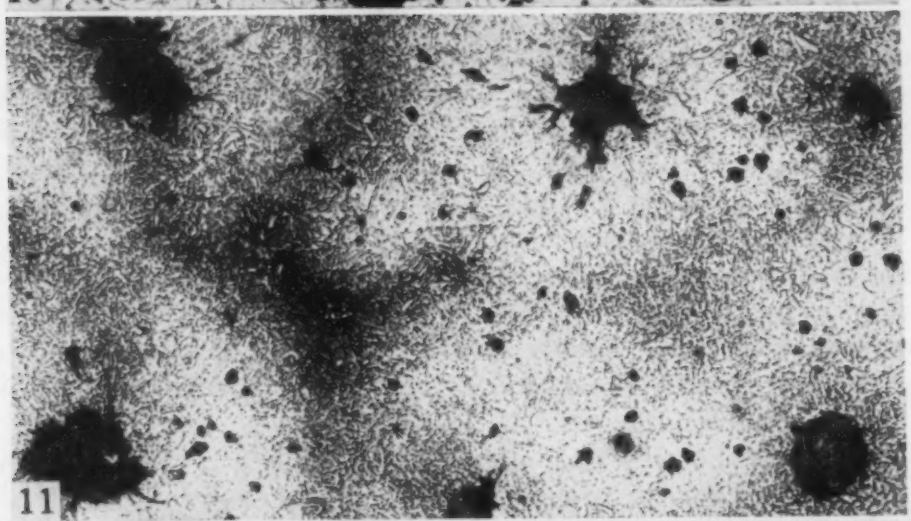


Fig. 9—Quenched and Tempered for 2 Hours at 1400 °F (760 °C). (a) Bright Field; (b) Polarized Light. Picral Etch, X 1000





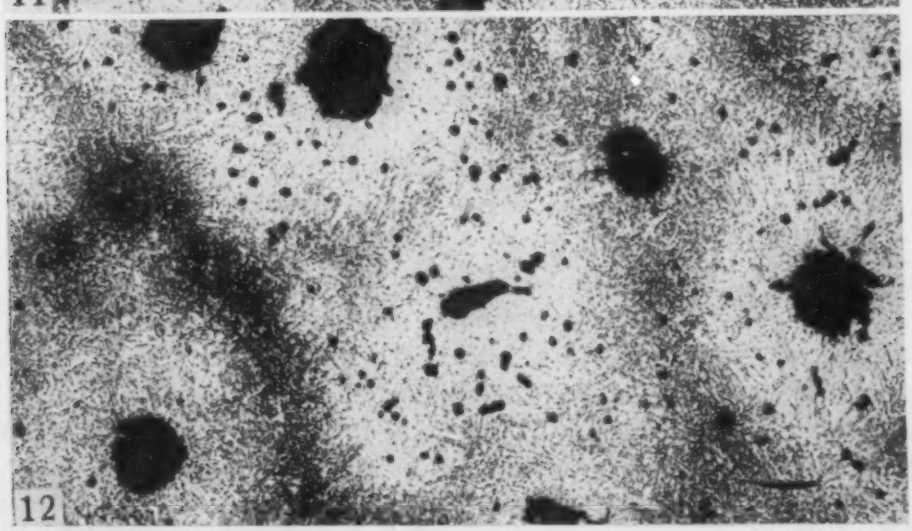


Fig. 10—Heat D Quenched and Tempered 2 Hours at 1300 °F (705 °C). Nital-Picral Etch, X 250

Fig. 11—Heat B Quenched and Tempered 2 Hours at 1300 °F (705 °C). Nital-Picral Etch, X 250

Fig. 12—Heat E Quenched and Tempered 2 Hours at 1300 °F (705 °C). Nital-Picral Etch, X 250

and the former martensite platelets are still discernible. In general carbides are first precipitated in the dendrite areas and are silicon-rich carbides. The carbides located interdendritically are precipitated later, since these areas are segregated and usually high in alloying elements. After 15 minutes at 1200 °F (650 °C) some of the silicon-rich carbides are graphitized to produce fine spheroids of secondary graphite as shown in Fig. 5 in the etched and unetched conditions. However, the vast majority of the carbides remain unaffected. At 1100 °F (595 °C) for 2 hours a multitude of fine carbides and secondary graphite is discernible, as illustrated in Fig. 6. In the same figure, the identical field is shown under polarized light. Both the silicon-rich carbides and the secondary graphite exhibit an optical cross. After tempering treatments at 1200 °F (650 °C) for 2 hours, the secondary graphite and carbides are much larger, as shown in Fig. 7. A polarized light view reveals the optical cross in the carbides and secondary graphite. With increasing tempering temperatures the secondary graphite spheroids increase in size and fewer silicon-rich carbides remain, for more of the carbides undergo decomposition at the higher temperatures. This is well illustrated in Figs. 8 and 9, the structures quenched and tempered for 2 hours at 1300 °F (705 °C) and 1400 °F (760 °C), respectively.

From the previous microstructures, it appears that the precipitation of silicon-rich carbides is the first stage of the secondary graphitization process. Decomposition or graphitization of the silicon-rich carbides that is enhanced by the silicon constitutes the second stage. Finally, growth of the secondary graphite completes the process of secondary graphitization.

Although the secondary graphite spheroids are very fine, nevertheless, they exhibit remarkable stability. After tempering for 50 hours at 1300 °F (705 °C), the secondary graphite was apparently unaltered. Austenitizing treatments as high as 1800 °F (980 °C) for times up to 30 seconds used in surface hardening experiments did not completely redissolve the secondary graphite.

Influence of Composition on Secondary Graphitization

Since increasing silicon content appears to increase the ratio of silicon in the carbides, the addition of silicon to ductile iron will undoubtedly influence the quantity of secondary graphite. On the other hand, the addition of strong carbide forming elements may produce the opposite effect, i.e., the carbides may be impoverished in silicon and may therefore become more stable. Hence, less secondary graphite would be expected in the quenched and tempered structures.

These views were confirmed by the observations of the various heats of ductile iron investigated. For example, heat D high silicon and low manganese (2.98% Si and 0.34% Mn) appeared to contain the greatest quantity of secondary graphite, as shown in Fig. 10. High

silicon contents and low percentages of carbide formers favor large amounts of secondary graphite. A low silicon and high manganese heat (2.06% Si and 0.73% Mn), heat B, produced small amounts of secondary graphite, as illustrated in Fig. 11. Strong carbide formers also reduce the amount of secondary graphite. Heat E, a chromium heat (2.25% Si, 0.67% Mn and 0.23% Cr) is shown in Fig. 12 and it is obvious that less secondary graphite is present compared to the high silicon heat (Fig. 10).

Summary and Conclusions

1. Secondary graphitization in quenched and tempered ductile iron proceeds as follows:

   (a) The decomposition of martensite to ferrite and carbides. Dendritic carbides are silicon-rich.
   (b) Rapid graphitization or decomposition of the silicon-rich carbides.
   (c) Growth of secondary graphite.

2. Secondary graphite spheroids are quite stable.

3. An increase in the silicon content results in greater quantities of secondary graphite, while the addition of carbide forming elements retards its formation.

Acknowledgment

The authors are grateful to the International Nickel Company of New York for sponsoring the experimental work reported herein.

References

1. J. E. Rehder, "Quench-Temper Treatments Improve Nodular Irons," *Iron Age,* Vol. 169, January 17, 1952, p. 89.
2. H. A. Schwartz, J. D. Hedberg and R. Eriksen, "Subcritical Isothermal Graphitization," *Transactions,* American Foundrymen's Association, Vol. 58, 1950, p. 578–583.
3. L. V. Foster and J. E. Wilson, "The Examination of Metals in Polarized Light," *Proceedings,* American Society for Testing Materials, Vol. 38, 1938, p. 315.
4. R. W. Dayton, "Theory and Use of the Metallurgical Polarization Microscope," *Transactions,* American Institute of Mining and Metallurgical Engineers, Vol. 117, 1935, p. 119.
5. E. Larsen and H. Berman, "The Microscopic Determination of Non-opaque Minerals," *Geological Survey Bulletin 848,* United States Dept. of Interior, 1934, p. 77.
6. J. E. Stead, "Report of the 80th Meeting of British Association for Advancement of Science," 1910, p. 549–561.
7. W. Gontermann, "Iron-Silicon-Carbon Alloys," *Journal,* Iron and Steel Institute, 1911, No. 1, p. 421–475.
8. Honda and Murakami, "On the Structural Constitution of Iron-Carbon-Silicon Alloys," *Journal,* Iron and Steel Institute, 1923, No. 1, p. 545–583.
9. W. H. Hatfield, *Cast Iron in the Light of Recent Research,* Charles Griffin and Company, Limited, 1928, Third Edition, p. 213.

10. D. Marles, "The Carbides in Iron-Carbon-Silicon Alloys and Cast Irons," *Journal,* Iron and Steel Institute, Vol. 158, April 1948, No. 1, p. 433–436.
11. E. D. Harry, "Metallography of Carbon in Silicon-Iron Alloys Containing 4% Si," *Journal,* Iron and Steel Institute, Vol. 167, Part 3, March 1951, p. 241–246.
12. W. S. Owen and B. G. Street, "Identification of Certain Iron-Silicon Carbides," *Journal,* Iron and Steel Institute, Vol. 172, September 1952, p. 15.
13. H. Morrogh and W. J. Williams, "Undercooled Graphite in Cast Irons and Related Alloys," *Journal,* Iron and Steel Institute, Vol. 176, April 1954, p. 375.

DISCUSSION

Written Discussion: By R. W. Kraft, University of Michigan, Department of Production Engineering, Ann Arbor, Mich.

The authors are to be congratulated for a comprehensive study of the factors influencing secondary graphitization in quenched ductile irons. It would be interesting if the authors would present some data on fully ferritized irons, with and without secondary graphite nodules, in the same analysis, to illustrate the effect, if any, of the secondary graphite particles on mechanical properties.

Written Discussion: By H. Morrogh, British Cast Iron Research Association, Alvechurch, Birmingham, England.

It appears that the authors' conclusions are based on a misinterpretation of their observations with the polarizing microscope. The optical cross phenomenon is shown by any approximately spheroidal particle which has a marked convexity or concavity of surface and which exhibits specular metallic reflection. The optical cross developed in hemispherical transparent inclusions represents the case of reflection of polarized light from a concave surface—the inclusion/metal interface. The occurrence of the optical cross does not indicate anything of the composition or structure of the particle but only gives information about geometry of the reflecting surface. This was explained in great detail by Dayton,[2] and Portevin and Castro [3] have also dealt with the dangers of misinterpreting such elliptical polarization effects and have illustrated the optical cross effect in glycerine droplets. More recently [4] the present writer has illustrated these spurious optical effects with particular reference to hard titanium carbide particles.

The carbide particles in tempered steels and nodular cast irons are relatively hard spheroids in a relatively soft matrix and as a result, particularly when etched, they stand in relief from the matrix and they tend to have convex surfaces. This is an ideal condition for the production of the optical cross. The apparent brightening and darkening of etched pearlite on rotating between crossed nicols is a special case of the optical cross effect for a lamellar constituent standing in relief and is due entirely to the surface geometry. Exactly the same result is given by a series of finely ruled lines on a metallic surface.

If some spheroidal carbides show no optical cross whereas others of the same size show the effect, it may only be deduced that the former stand in greater re-

[2] R. W. Dayton, *Transactions,* American Institute of Mining and Metallurgical Engineers Vol. 117, 1935, p. 119.
[3] A. M. Portevin and R. Castro, *Journal,* Iron and Steel Institute, Vol. 135, 1937, p. 223.
[4] H. Morrogh, "The Examination and Identification of Inclusions in Metals and Alloys' —Chapter 5 of "Polarized Light in Metallography" edited by G. K. T. Conn and F. J. Bradshaw, Butterworths Scientific Publications, London 1952.

lief from the matrix than the latter. This difference may be due to variations in matrix hardness and also to variations in depth of etching. It is not necessary to invoke differences in carbide composition.

When the particles are very small it may be below the resolving power of the optical system to reveal the optical cross. In this case each particle will appear bright as in Fig. 2b of the authors' paper. When the stage is rotated such fine particles remain bright for all positions of the stage, indicating the effect to be one of elliptical polarization and not of crystal anisotropy.

It should be a golden rule for metallographists using polarized light that examinations of small particles be made on unetched specimens in order to avoid the confusion of elliptical polarization effects with those produced by crystal anisotropy.

When polished spherulites of an anisotropic substance are examined under polarized light a form of dark cross can be seen which owes its origin to the radial disposition of anisotropic fibers. This dark cross must not be confused with that obtained on convex metallic reflecting surfaces. The dark cross is obtained on spherulites with perfectly flat surfaces.

I submit that if these facts are appreciated the authors are not entitled to draw the conclusions set out.

If the dendritic carbides exhibited the optical cross while the interdendritic carbides did not, then all that may be deduced is that the latter are either smaller than the former or that they are not standing in such pronounced relief. It is quite conceivable that the matrix hardness is different in the interdendritic regions and this would explain a different degree of relief. The conclusion that the dendritic carbides are not normal Fe_3C is untenable on this evidence. Similarly, the suggestion that the optical cross in the dendritic carbides is due to their containing silicon is without foundation. I can assure the authors that optical cross effects can be produced quite easily in the spheroidized carbides of pure iron-carbon alloys.

If you will accept this argument the authors' reasoning becomes supposition without foundation.

The authors have stated that the dendritic carbides did not respond to heat tinting. It is a pity they gave no proof of this, particularly for the irons having less than 2.7% silicon. I have been unable to find evidence of the silico-carbide in irons having less than 2.7% silicon. If the authors had produced micrographic evidence of the occurrence of a non heat tinting carbide in the dendritic positions and a heat tinting carbide in the interdendritic positions their argument would have been worthy of more attention.

Finally, the authors might find the observations of Grant[5] on this subject to be of some interest.

Written Discussion: By Albert De Sy, Metallurgical Laboratory, University of Ghent, Ghent, Belgium.

We have read the paper of J. C. Danko and J. F. Libsch on secondary graphitization of quenched and tempered ductile cast iron with great interest because a couple of years ago similar phenomena were observed in our laboratory by Dr. Vidts and J. van Eeghem during their work on isothermal transformation and comparison of direct isothermal transformation products with structures obtained by martensite tempering.

[5] J. W. Grant, *Journal of Research and Development*, British Cast Iron Research Association, Vol. 4, August 1952, p. 366.

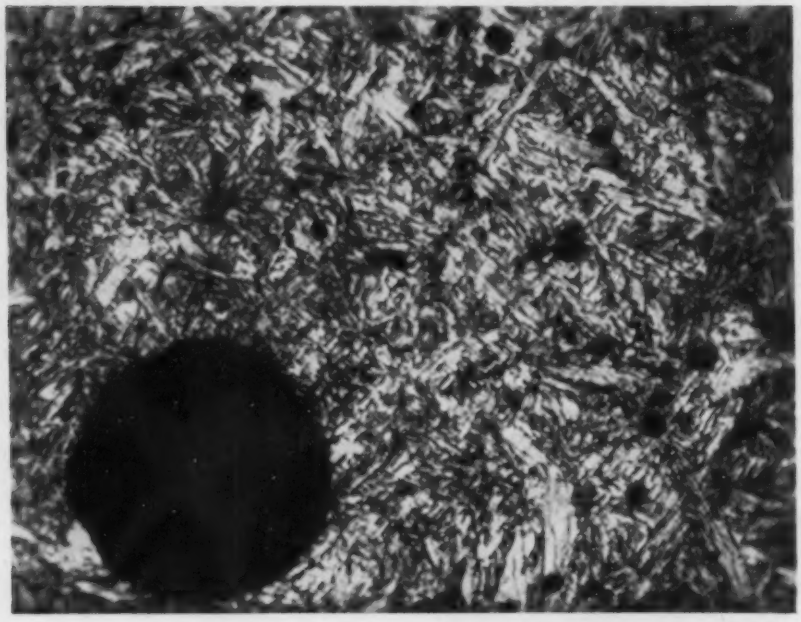


Fig. 13—Austenitized 1 Hour at 900 °C, Water-Quenched; Tempered 4 Hours at 703 °C, Water-Quenched; Austenitized 2 Hours at 900 °C, Water-Quenched. X 1000.

On receiving, two weeks ago, a copy of the preprint together with a letter from Dr. J. B. Austin, president of the A.S.M., in which we were kindly invited to prepare a discussion of the paper, we took one of the old specimens and prepared a photomicrograph at magnification 1000.

This micrograph is reproduced in Fig. 13; the heat treatment story is rather complicated, as indicated under Fig. 13.

After martensite tempering for 4 hours at 703 °C, we observed a great many small black spots, approximately 1 micron in diameter, at the limit of the resolving power of the optical microscope.

By etching, both number and dimensions of these spots increase, and it is not at all easy to determine the exact nature of these spots; they may be secondary graphite or holes (diffusion holes?).

After a second austenitizing treatment (2 hours at 900 °C) followed by a water quench, we obtained the result shown in Fig. 13.

This treatment, as proven by martensitic matrix, was able to dissolve secondary graphite that might have been present. But after this treatment the black spots remained and their dimensions were increased to permit their identification as holes.

We are still in doubt about the nature of the black spots after martensite tempering treatment, and would like to ask some questions:

1. Is there any proof, other than the optical cross under polarized light, that permits the identification of the black spots?
2. How do the authors explain the increase of the number of black spots, that they consider as graphite particles, by etching?
3. Did they also experiment with normal flake graphite iron; we know that the same treatment gives similar black spots, perhaps less well rounded.

Finally, would it not be interesting to examine the black spots with the electron microscope?

Authors' Reply

The authors welcome Mr. Morrogh's comments on the polarized light observations described in the paper. We agree that the size, geometry and degree of relief of the carbides by etching may have an important influence on the appearance of the optical cross. However, as pointed out in the presentation of the paper, the carbides in the dendritic areas appear similar in size to those developed in the interdendritic areas and in the 1080 steel, and yet the optical cross was uniformly observed in the dendritic carbides and not in the interdendritic areas of the ductile iron or in the steel. Furthermore, deep etching to place the carbides of the steel in greater relief did not develop the optical cross. Thus, we believe that there is a difference in the optical characteristics of the dendritic and interdendritic carbides. On the basis of the other observations made, we believe this difference may be the presence of silicon. Ultimate confirmation of the presence of silicon must await some technique which will allow selective separation of the dendritic and interdendritic carbides and X-ray or chemical analysis.

Mr. Morrogh mentions the development of an optical cross in normal iron carbides. Recent observations by the authors on spheroidized carbides resulting from isothermal transformation of a eutectoid steel did show the optical cross. Furthermore, large carbides developed by extended tempering in a 1080 steel have shown evidence of the cross. However, we have not been able to develop the optical cross in numerous other tempered steel specimens which showed resolvable carbides.

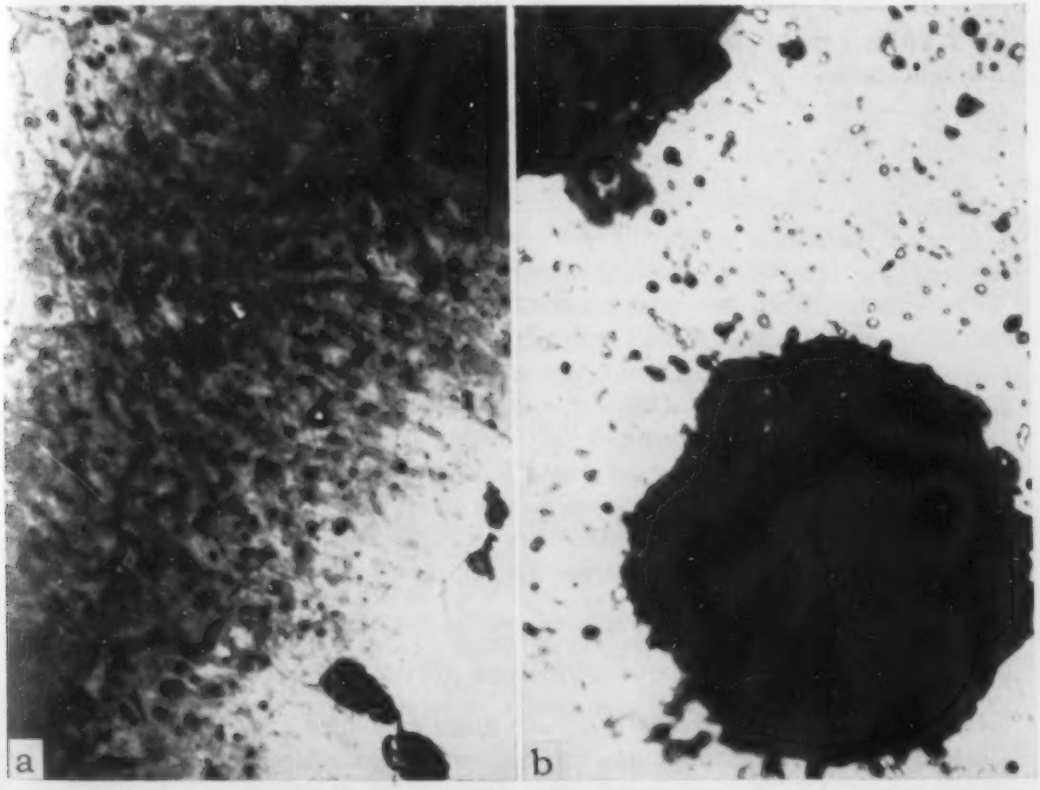


Fig. 14—Picral Etch and Heat-Tinted 15 Minutes at 600 °F (315 °C). X 1500. (a) Interdendritic carbides are darkened. (b) Dendritic carbides are unaffected.

In regard to Mr. Morrogh's comment on heat tinting, the photomicrographs of Fig. 14 are presented. The heat tinted specimens of Heat D (3.49% carbon, 2.98% silicon and 0.34% manganese) reveal darkening of the interdendritic carbides (Fig. 14a), while the dendritic carbides remain unaffected. (Fig. 14b). Similar results were obtained for Heat A, the lowest silicon heat investigated (3.42% carbon, 1.87% silicon and 0.32% manganese).

Finally, it is stressed that the primary objective of this paper, aside from the observations relating to the development of secondary graphite was to point out a difference between the carbides which form in the dendritic areas and are very unstable, and those which form in the interdendritic areas and appear relatively stable. In this connection, an attempt to summarize the evidence has been made in Table II. We submit that the evidence supports a reasonable mechanism of secondary graphite formation.

Table II
Nature of Carbides

Characteristics	Dendritic	Interdendritic
Time of formation	First to form	Last to form
Response to heat tinting	Unaffected	Darkened
Boiling alkaline sodium picrate etch	Unaffected	Colored
Boiling ferricyanide etch	Unaffected	Darkened
Polarized light effects	Optical cross	No cross
Effect of tempering	Decompose or graphitize to secondary graphite	Tend to remain Stable
Analysis effects	Silicon enhances formation	

The black spots that Mr. De Sy refers to are not truly cavities although some of the reproductions may indicate this. On the contrary, the spots at high magnification, × 500 to × 1000 have the same radial characteristics as the primary graphite when viewed under polarized light. This is well illustrated in Fig. 9a and 9b.

The number of black spots (secondary graphite) do not increase by etching. However, the secondary graphite nodules decrease in numbers and increase in size with increasing tempering temperature. It would be very interesting to observe the secondary graphite under the electron microscope but such an investigation has not as yet been made.

In regard to Mr. Kraft's question on the mechanical properties of fully ferritized ductile iron with and without the presence of secondary graphite, Heat D (3.49% carbon, 2.98% silicon, 0.34% manganese) was investigated. Secondary graphite was produced by the normal quench and temper treatments. Secondary graphite was not observed in the specimens fully ferritized by an isothermal heat treatment. The microstructures were essentially the same, although the specimens with the secondary graphite had a somewhat finer ferritic grain size. The mechanical properties are listed below:

	T.S.	Y.S.	% El.	% R.A.	Unnotched Charpy	R_a Hardness
Quench and Temper	71,700	59,000	10.5	10.4	40	52
Ferritized Isothermally	71,750	58,500	17.5	26.3	110	52

(Results reported are average of 2 tests made on 1 inch gage length 0.252 inch diameter tensile bars and 2 unnotched, Charpy impact specimens.)

The low ductility associated with the quenched and tempered specimens may be the result of the presence of secondary graphite; however, embrittlement during tempering may also influence the results.

A METHOD FOR DETERMINING THE CONTINUOUS COOLING TRANSFORMATIONS IN STEEL

By R. D. Chapman and W. E. Jominy

Abstract

Equipment was designed and built to determine transformation in steel by a magnetic method. This equipment is simply an electrical transformer in which the specimen acts as a core. As transformation takes place in the steel specimen the permeability is increased producing an emf in the secondary winding of the transformer. Four commercial alloy steels, SAE 4340, 8642, 4140 and 52100, were studied to determine the Ms point by the magnetic method. Good agreement was found between the metallographic and magnetic determinations.

The equipment was also used to develop continuous cooling diagrams for SAE 4340 and 4063 steels. It was found that the magnetic method can better define the bainite areas than the metallographic method.

Introduction

SINCE the time Tchernoff first observed a transformation in iron, scientists have studied the mode of austenite decomposition in steel. From these studies have evolved the iron-carbon diagram, the isothermal diagram and the continuous cooling diagram. In conjunction with these latter diagrams, the temperature for the beginning of martensite formation (Ms) has been studied. All these investigations have resulted in useful information for the heat treatment of steel and have produced such processes as austempering, martempering, as well as developing a better understanding for the heat treatment of steel.

The development of these diagrams have in the main been done with the use of metallographic samples or by dialatometric analyses. Such procedures have been very time consuming and tedious to employ. Since these determinations were so difficult to carry out, it was decided to investigate these transformations by use of magnetic changes accompanying them.

Development of Equipment

It was reasoned that if a steel specimen were made the core of an electric transformer when transformation takes place and the

A paper presented before the Thirty-sixth Annual Convention of the Society, held in Chicago, November 1 to 5, 1954. Of the authors, R. D. Chapman is research metallurgist and W. E. Jominy is chief metallurgist-research, Engineering Division, Chrysler Corp., Detroit. Manuscript received April 12, 1954.

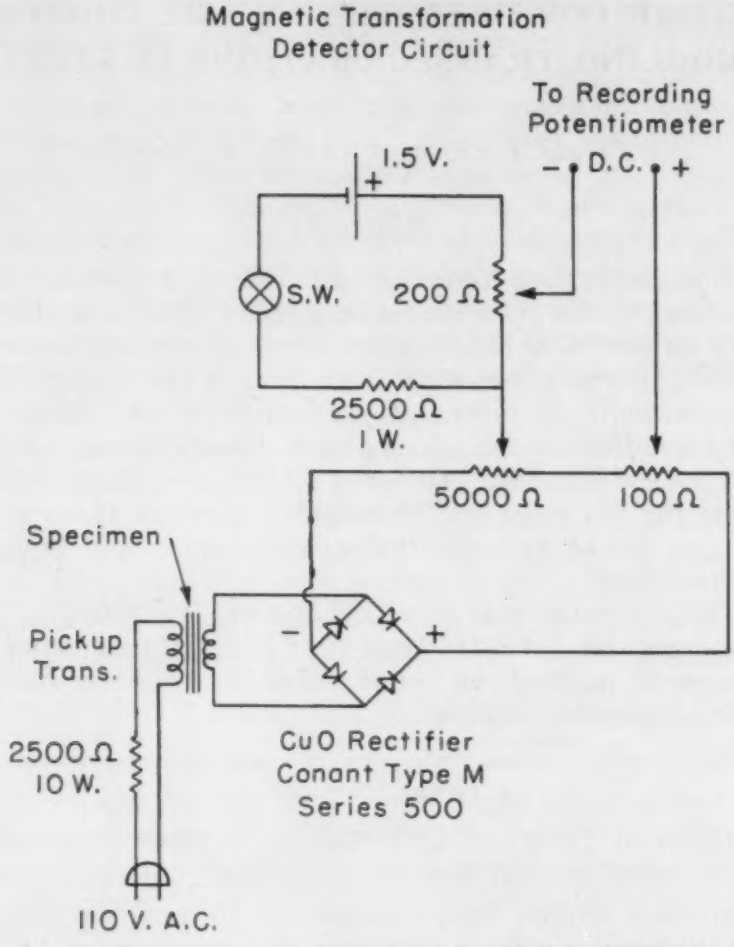


Fig. 1—Schematic Diagram for the Magnetic Detecting of Transformation Points in Steel.

sample becomes magnetic, an emf should be developed in the secondary winding. The magnetic principle has been employed by Nagler and Wood (10) for the measurement of constant temperature transformation and has been discussed by Chandler (11)[1] in his work with Upthegrove for continuous cooling. Fig. 1 shows the schematic drawing of the detector circuit used in these studies. The pick-up transformer or coil consists of two windings which are the primary and secondary of a transformer. The primary winding is attached to a 110 volt A.C. line. When a ferro-magnetic material is inserted in this coil an A.C. current is produced in the secondary winding which in turn is connected to a copper oxide rectifier. The D.C. output of this rectifier is fed through the windings of two variable resistances connected in series, and the desired potential is tapped off for connection to the recording potentiometer. Without a specimen in the detector circuit there is a slight electrical coupling effect which must be neutralized by an auxiliary circuit

[1] The figures appearing in parentheses pertain to the references appended to this paper.

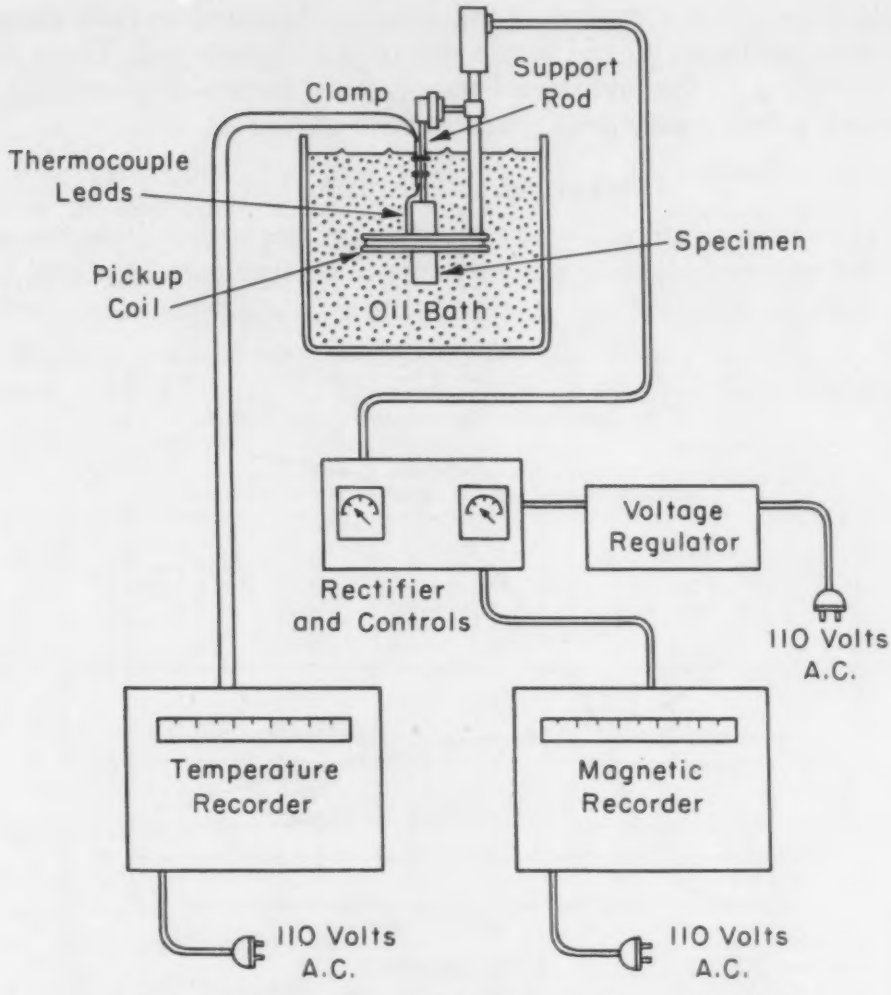


Fig. 2—Schematic Drawing of the Apparatus used in Making Magnetic Transformation Measurements.

producing a back emf. The current in this circuit is supplied by two 1.5 volt dry cell batteries connected in parallel as shown on the diagram. By properly balancing the circuit the couple can be nullified. The auxiliary circuit also compensates for electrical changes in the copper oxide rectifier. The variable resistances in series with the output of the rectifier are varied to provide the desired deflection of the recording potentiometer when the sample is in the coil. The deflection amounted to about 6 inches on the recorder chart between 0 and 100% permeability of the specimen in the coil when connected to the recording potentiometer. It should be pointed out that only nonmagnetic materials were used in the construction of the pick-up coil.

The specimen of steel on which measurements are to be made is a solid bar ¾ inch in diameter by 3 inches long. A tapped hole is provided in one end to attach the supporting rod (18-8 stainless steel). Midway along the length of the specimen a chromel-alumel thermo-

couple is percussion welded to the outer surface and in turn through porcelain insulators affixed to the side of the support rod. These leads are connected to the high speed temperature recording potentiometer as shown schematically in Fig. 2.

Operating the Equipment

The temperature and magnetic recorder are both adjusted to provide the proper balancing and settings. The specimen is placed in a tube furnace for heating. A dried nitrogen atmosphere is used to

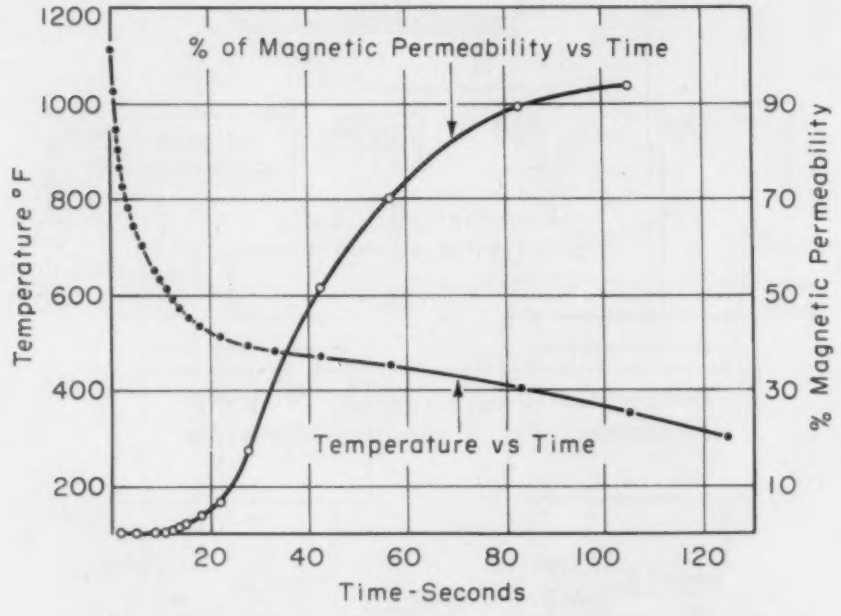


Fig. 3—Typical Cooling Curve (time vs. temperature) and Magnetic Transformation (time vs. permeability) for an SAE 4340 Steel oil-quenched.

prevent decarburization and scaling during heating. After austenitizing the sample is removed and quickly placed in the magnetic pick-up coil. The temperature recorder and magnetic recorder chart drives are turned on simultaneously and the pick-up coil with sample is submerged in the quenching media. By this method changes in magnetic permeability versus time, and temperature in degrees Fahrenheit versus time are simultaneously recorded as the sample cools to room temperature.

Fig. 3 shows a typical cooling chart and magnetic permeability chart obtained during a test on an SAE 4340 steel when oil-quenched. In these determinations the liquid quenching medium was contained in a large glass receptacle in order not to influence the magnetic pick-up coil. It is apparent from this chart that there is no significant change in magnetic permeability in this material until a temperature of approximately 575 °F (300 °C) is reached at the surface. At this tem-

perature the surface becomes ferro-magnetic and produces an increase in magnetic permeability until ultimately the bar becomes 100% ferro-magnetic.

The Determination of Ms Points

The procedure just described was used to determine the beginning of martensite transformation for four different SAE alloy steels. The analysis of the steels used is shown in Table I. All this hot-rolled bar stock except SAE 52100 was normalized at 1600 °F (870 °C) for 1 hour per inch of thickness prior to machining.

Results from these determinations are shown in Fig. 4. This figure is plotted from data as shown in Fig. 3 except time is omitted.

Table I
Analysis of Steels Used for Ms Determinations

Steel	C	Mn	P	S	Si	Ni	Cr	Mo	Aust. Temp.
SAE 4340	0.40%	0.80%	0.013%	0.017%	0.31%	1.85%	0.78%	0.24%	1600 °F
SAE 4140	0.38	0.86	0.027	0.028	0.26	0.19	0.98	0.21	1600
SAE 8642	0.39	0.83	0.019	0.020	0.24	0.57	0.58	0.21	1600
SAE 52100	1.00	0.33	0.025	0.018	0.30	—	1.28	—	1950

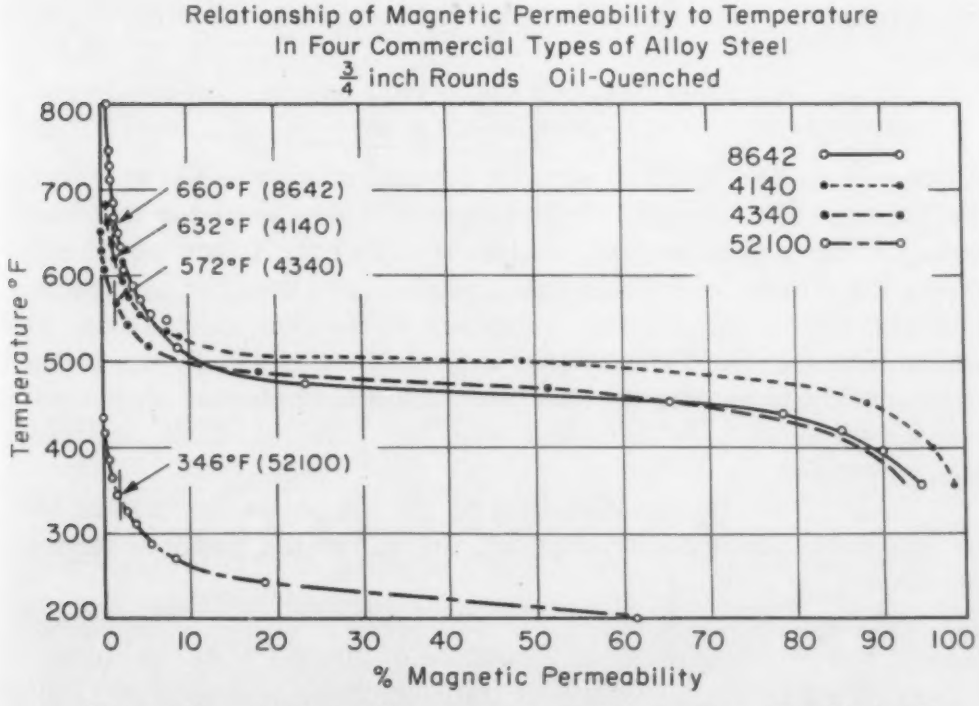


Fig. 4—Magnetic Permeability versus Temperature for Four Alloy Steels Oil-quenched with their Respective Ms Points Using 1% Permeability for Measurement.

It will be noted that the permeability curve approaches the abscissa or temperature scale asymptotically, making it difficult to determine exactly the temperature at which transformation on the surface begins. Consequently a point on the curve corresponding to 1% magnetic perme-

Table II
Ms Temperature from Three Methods

Steel	Magnetic Ms	Metallographic Ms	Calculated Ms	
			Payson & Savage	Grange & Stewart
	°F	°F	°F	°F
SAE 4340	572	560	568	553
SAE 52100	345	330	313	*—
SAE 4140	632	633	627	607
SAE 8642	660	628	621	618

* Grange and Stewart claim no accuracy for their formula at this high carbon level.

ability was arbitrarily selected. Other considerations for choosing this value are discussed later in this paper. The values so determined are indicated in Fig. 4.

In order to check these temperatures the formula developed by Grange and Stewart (1) was employed. This formula is:

$$\text{Ms } (°\text{F}) = 1000 - 650 \times \%\text{C} - 70 \times \%\text{Mn} - 35 \times \%\text{Ni} - 70 \times \%\text{Cr} - 50 \times \%\text{Mo}$$

Also, in calculating these temperatures the revised formula of Payson and Savage (2) was used. Their revised formula as shown by Nehrenberg is:

$$\text{Ms } (°\text{F}) = 930 - 540 \times \text{C} - 60 \times \text{Mn} - 40 \times \text{Cr} - 30 \times \text{Ni} - 20 \times \text{Si} - 20 \times \text{Mo}$$

As an added check a metallographic determination was likewise run on the material. The method of Greninger (3) was used for this metallographic determination and consists briefly of the following: Austenitizing the sample, quenching into a molten bath near the Ms at a temperature of T_1, immediately reheating in another molten bath at a higher temperature T_2 to temper any martensite which was formed, and quenching immediately into brine. These samples are then studied metallographically to determine the per cent of dark martensite needles present.

Table II lists the temperatures of the Ms points determined from the magnetic permeability method, the calculated methods and the metallographic method.

Our determination of the Ms temperature by the metallographic method was based on the transformation of about 1% of the austenite. This criterion of the beginning of transformation was used by Grange and Stewart and has been generally accepted. It will be noted that the 1% magnetic permeability values for Ms correspond approximately to the metallographic values. Further, to obtain 1% magnetic permeability we believe there must be 1% magnetic material in the affected area. For these reasons it seems logical to use the 1% magnetic permeability condition as the Ms point.

The results reported here are taking place almost entirely at the surface of the specimen. Calculations were made as to the flux density distribution in a ¾ inch round bar. For these calculations it was assumed that permeability was a constant across the bar and room temperature was also assumed. This calculation showed that the flux density at the surface was approximately four times as great as it was in the core. This value is conservative because the core will cool more slowly and hence have a greater resistance to magnetic lines of flux as a result of its higher temperature. This in turn would mean that the lines of flux would be concentrated at an even higher level at the surface.

Determination of Continuous Cooling Diagrams

In all the steels studied during the Ms determination, there was sufficient delay to cause very slow or sluggish transformation. The slow

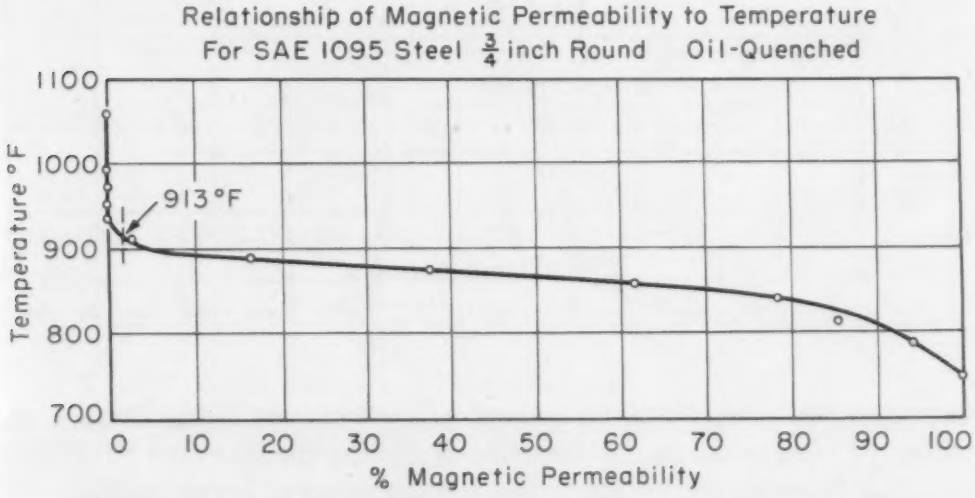


Fig. 5—Magnetic Transformation Diagram for Water Hardening SAE 1095 when Oil-quenched Showing Beginning of Transformation at 913 °F.

transformation allowed the steel to be quenched in oil whose cooling rate was fast enough to avoid the beginning of the pearlite or bainite transformation. These steels in the size employed for the specimen, contained sufficient hardenability to be fully martensitic on the completion of the quench. Therefore, a material, namely SAE 1095, was selected whose hardenability would not be great enough to be fully martensitic when oil-quenched. The analysis of this water hardening type steel was as follows:

C 0.92%, Mn 0.36%, P 0.012%, S 0.023%, Si 0.25%, Cr 0.06%

The material was austenitized at 1600 °F (870 °C) and quenched in oil comparable to the alloy steels. The temperature versus permeability curve is shown in Fig. 5. A temperature corresponding to 1% magnetic

permeability in this steel was found to be 913 °F (490 °C). This could only be a pearlitic or bainitic transformation. It is interesting to note that at 750 °F (400 °C) the permeability has reached 100% indicating no austenite remains to transform to martensite.

As a result of this test it was felt that the magnetic method might be used to determine a continuous cooling curve. The following dia-

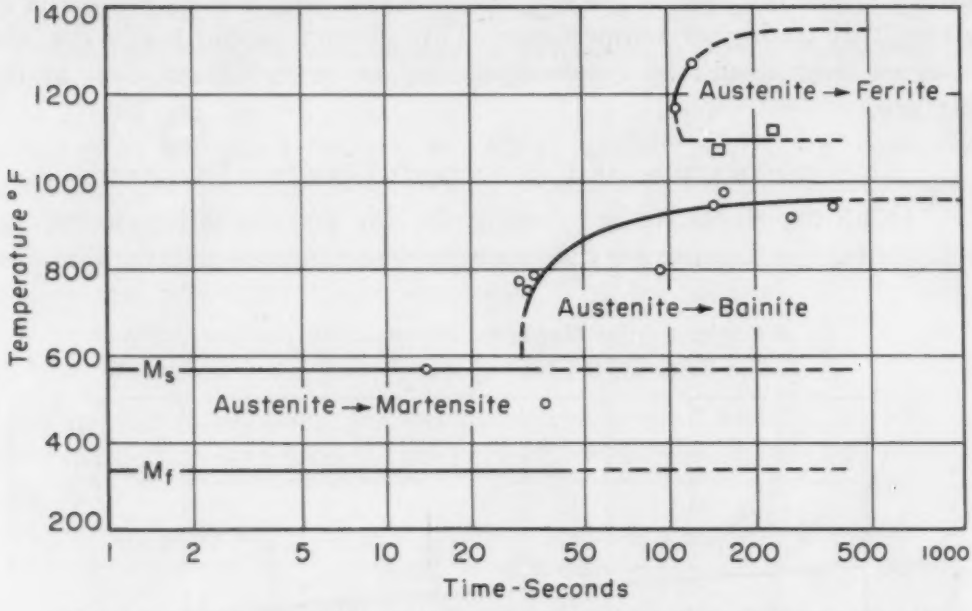


Fig. 6—Continuous Cooling Diagram for SAE 4340 Steel Determined by the Magnetic Permeability Method.

gram then describes the development of such curves. Since Grange and Kiefer (4) had published a continuous cooling diagram for SAE 4340 steel, this type of steel was selected for the original investigation.

By varying the cooling rates of the specimen and determining the magnetic transformation such a curve was developed as shown in Fig. 6. By using such quenchants as oil, carbon tetrachloride, forced air and still air, a variety of cooling rates can be obtained. Several of these rates are plotted in Fig. 7. The quenching oil which is a 100 viscosity oil at 100 °F, was rapid enough to avoid any austenite decomposition products other than martensite. Quenching into carbon tetrachloride was not too reproducible. It appeared that on subsequent quenches into this medium that a chemical change took place in the carbon tetrachloride giving a different cooling curve. It was noted that a reddish precipitate formed in the solution which was probably ferric chloride. However, since the cooling curve was obtained with each quench the data are plotted and should be valid. The forced air cooling was accomplished by means of a small automotive heater-sirocco type blower discharging the air longitudinally along the specimen. The

cooling rate of still air was likewise used and to obtain a still slower cooling rate a small cylinder of asbestos was made to fit inside the pick-up coil. This container was lined with 0.002-inch austenitic type stainless steel to minimize radiation losses. It was during this test that it was first noted that an unusual phenomenon took place. Here on cooling in the asbestos lined cylinder the beginning of ferrite formation

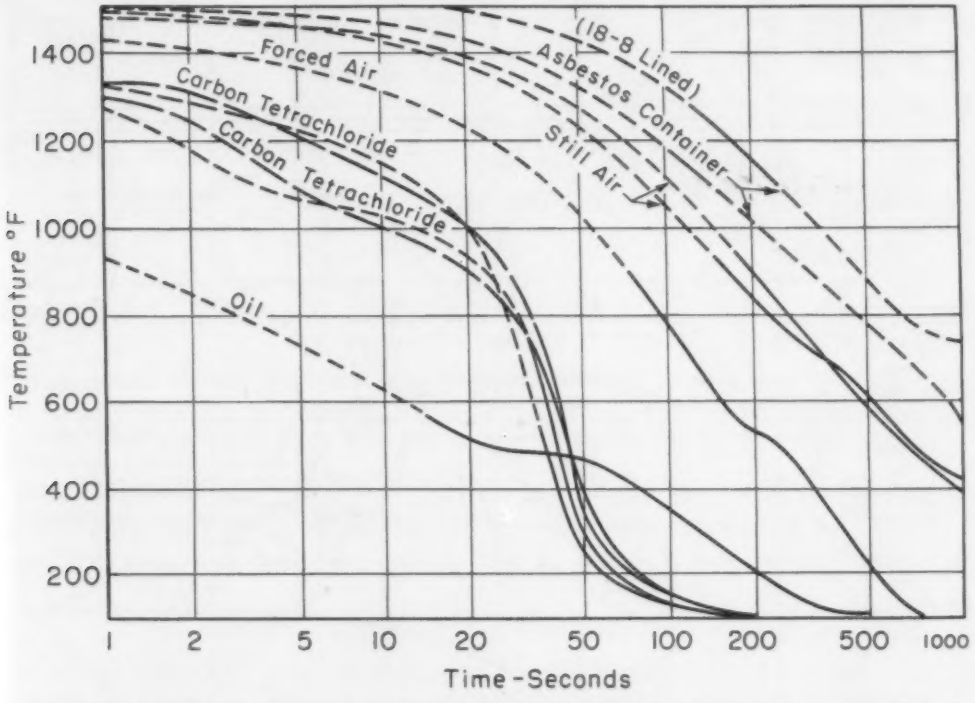


Fig. 7—Cooling Curves for Several Quenching Media Employed in Developing Continuous Cooling Diagram of SAE 4340 Steel.

was noted on the magnetic permeability curve. This produced a certain amount of deflection on the curve which remained constant for a period of time and then with further cooling of the specimen another deflection was noted. This point will be covered more fully in the discussion.

Since Grange and Kiefer (4) have published a calculated curve for SAE 4340 steel, the data obtained by the magnetic permeability method is superimposed upon their findings and shown in Fig. 8. The agreement between the two methods is rather good as far as the austenite to bainite reaction is concerned. The magnetic method which yielded higher temperatures for the Ms point determinations likewise was higher for the continuous cooling determinations. However, a large difference existed between the beginning of the austenite-ferrite reaction which will be covered in the discussion.

The same procedure was used to obtain the cooling diagram shown

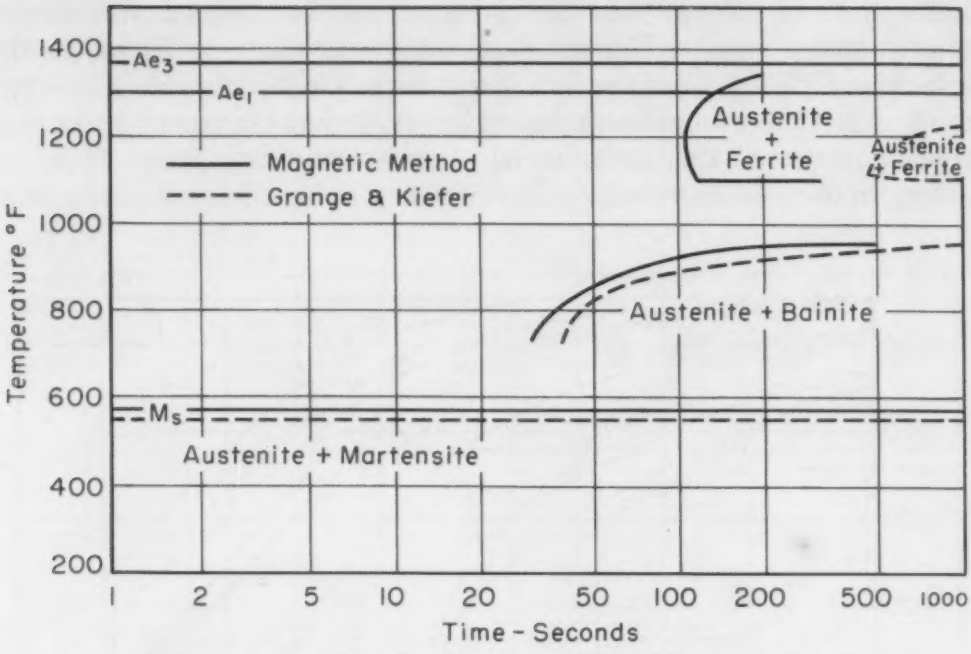


Fig. 8—Comparison of Magnetic Continuous Cooling Curve and the Grange and Kiefer Continuous Cooling Diagram for SAE 4340 Steel.

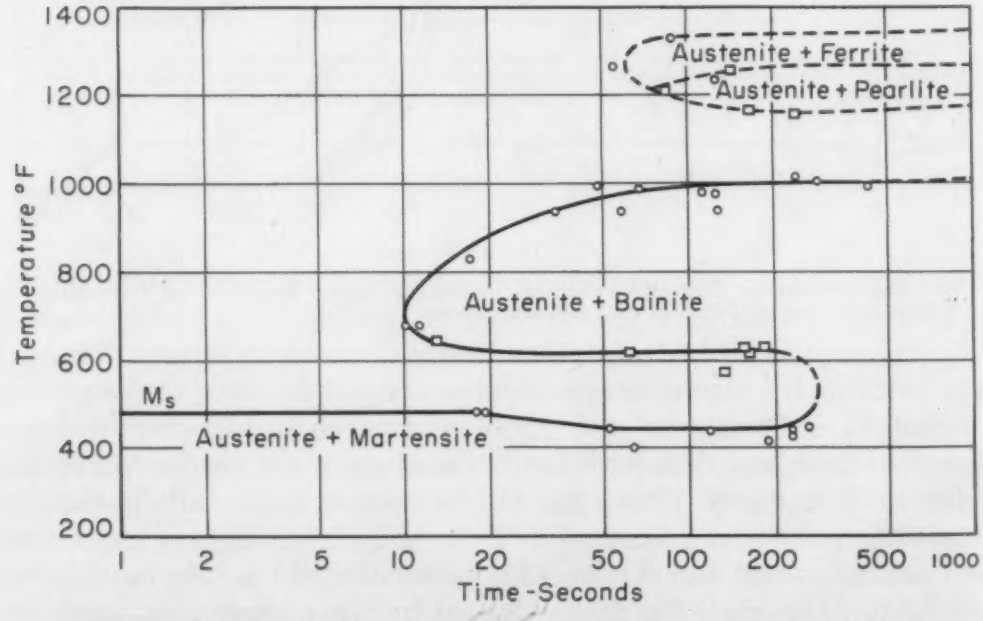


Fig. 9—Continuous Cooling Diagram for SAE 4063 Steel Determined by the Magnetic Method.

in Fig. 9. This was obtained with an off analysis SAE 4063 steel of the following analysis:

	C	Mn	P	S	Si	Ni	Cr	Mo
SAE 4063	0.62	1.20	0.030	0.034	0.30	0.13	0.17	0.27

This material was normalized at 1600 °F (870 °C) for 1 hour prior to machining and was austenitized in the dried nitrogen atmosphere for

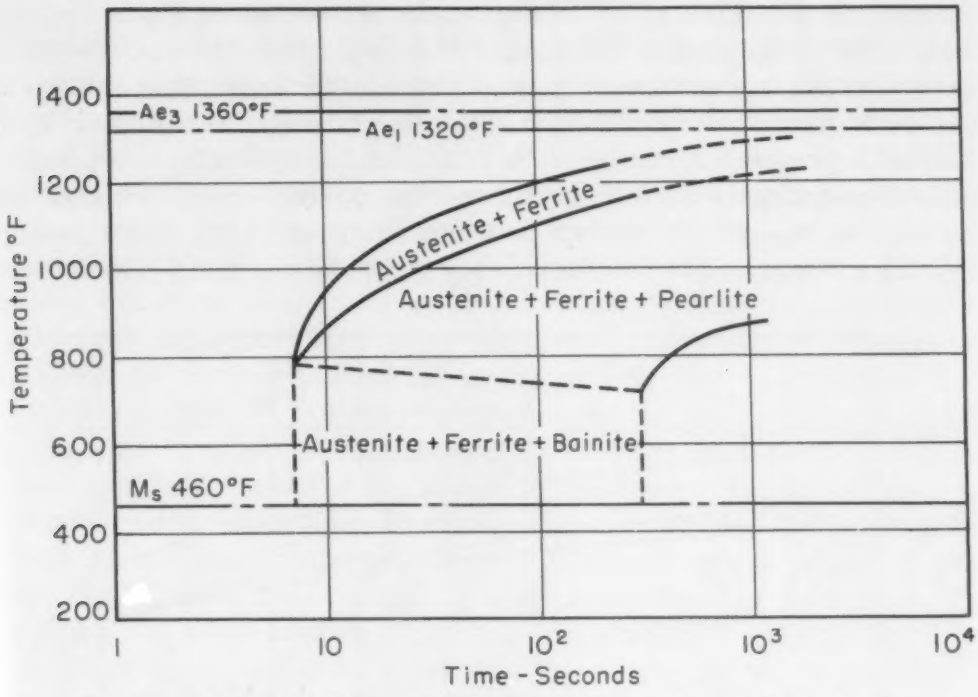


Fig. 10—Calculated Continuous Cooling Diagram for SAE 4063 Steel after Grange and Kiefer.

quenching at 1600 °F (870 °C). The calculated curve derived from the method of Grange and Kiefer (4) is also incorporated as shown in Fig. 10. There appears very little similarity in these two diagrams.

Discussion of Results

In Table III good agreement in Ms temperature exists between the three methods of determination in the SAE 4340 and 4140 steels. However, some discrepancy does exist between the magnetic and metallographic method for the SAE 8642 steel. In determining the Ms point by the metallographic method it was found that this particular steel was badly banded. This chemical segregation could account for the temperature difference between the two methods.

By using the two formulae (Grange and Stewart, and Payson and Savage) and calculating back, the per cent carbon was determined that would yield the Ms temperature found by the magnetic method. Only the carbon factor was considered and all other alloying element

Table III

Steel	% C Chem. Analysis	%C to give Ms temp. determined magnetically	
		Payson & Savage	Grange & Stewart
SAE 8642	0.39	0.316	0.32
SAE 4340	0.40	0.39	0.37
SAE 4140	0.38	0.37	0.34

factors remained the same. These results are shown in Table III. It is rather obvious that the SAE 8642 steel which shows 7 points of carbon variation is not very good. On the other hand, this amount of carbon segregation could well exist in the particular heat of steel used. Using the revised formula of Payson and Savage only one point of carbon variation is found for the remaining two steels. This is well within the accuracy of carbon determinations and thus could be considered a check. A greater discrepancy exists between the values found

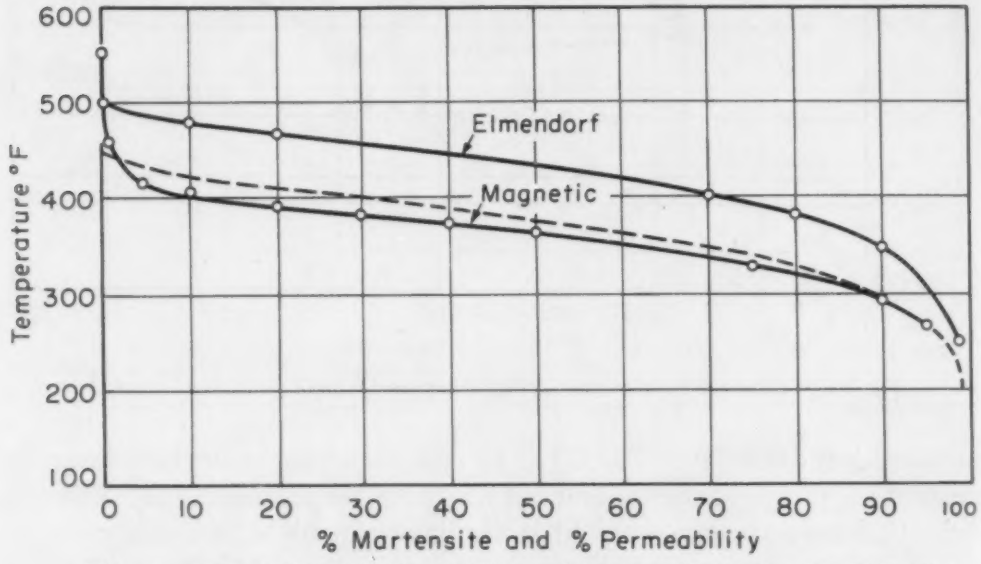


Fig. 11—Percent Magnetic Permeability and Percent Martensite for SAE 4063 Steel. Dashed line represents Elmendorf curve corrected for composition difference.

by the Grange and Stewart method. Thus from these tests it appears the Payson formula approaches the values found by magnetic permeability more closely. Payson's work also appears closer to the metallographic determination Ms point for the three steels studied in this investigation.

In most cases the magnetic determination has produced a slightly higher Ms temperature than either the metallographic or calculated values. One of the reasons that can be postulated for these higher temperatures is the result of carbon segregation. It is known that carbon is nine times as potent on the Ms temperature as any single element. Therefore a slight amount of banding or carbon segregation would definitely produce a higher Ms temperature by the magnetic method. Grange and Stewart claim that the Ms temperature determined metallographically is to the nearest 5 to 10 °F. From the two methods the Ms temperature is probably well bracketed.

In order to determine whether there might be a relationship between per cent martensite and permeability, Fig. 11 is shown. The per cent martensite versus temperature is taken from the work of

Elmendorf (5) who worked on an SAE 4063 steel of lower manganese content than our material and did not report the presence of nickel and chromium. Except for the beginning of transformation, these curves are very comparable being displaced only on the temperature scale. Using the Grange factor of 70 X %Mn and multiplying by the Mn difference of 0.6% between the two steels (0.61 Elmendorf and 1.20 for our steel) the Elmendorf curve is lowered 42 °F. Likewise, the chromium difference will lower the Elmendorf curve another 12 °F. Plotting his curve then for these lower temperatures, the two curves at 50% martensite and 50% permeability are only about 15 °F apart. The modified curve corrected for chemical difference is shown as the dashed line in Fig. 11. An interesting observation can be made regarding the austenite-martensite reaction from these curves. One of the postulated mechanisms for the austenite-martensite reaction proposed by Fisher, Hollomon, and Turnbull (6) assumes a nucleation and growth of the martensitic plates. Another mechanism proposed by Cohen (7) assumes a nucleation and shear for the formation of martensite. In both theories nucleation is a portion of the theory. Referring to Fig. 11 it will be noted that the beginning of the magnetic curve is very comparable to a nucleation and growth curve or similar to the type of curve for the nucleation and growth curve of the austenite to pearlite reaction. The curve of Elmendorf, however, does not show this type of nucleation. Since Elmendorf used isothermal transformation methods, there is a possibility of austenite conditioning taking place. As pointed out by Cohen (8) if conditioning takes place the austenite will transform to a greater degree on cooling than if conditioning had not occurred. Likewise, he explains that this conditioning raises the temperature of the martensitic range and the material behaves as a lower carbon steel. This fact could account for the difference in the Elmendorf curve and our curve. From the above discussion it is apparent that a relationship between per cent permeability and per cent transformation probably exists but further work needs to be done to actually establish this premise.

Discussing the continuous cooling curve of SAE 4340, it should be pointed out that the beginning of ferrite precipitation starts much sooner than indicated by the work of Grange and Kiefer. Some independent work done in our laboratories by Ross, Sernka and Jominy (9) using the electron microscope, has likewise shown this condition. Minute amounts of ferrite first precipitated are difficult to determine metallographically, because of the shape and etching characteristic of the ferrite. This then could account for the difference found between the magnetic diagram and the Grange and Kiefer diagram.

The discrepancies between the continuous cooling diagram calculated by Grange and Kiefer and by our magnetic method for the SAE 4063 steel in Figs. 9 and 10 may be due in part to three factors: (a) the

difference in chemical composition of the two steels, (b) the conditions of the experiment, the one being continuously cooled, the other calculated from isothermal conditions, and (c) possible error in the original isothermal diagram. This indicates that more work of this type should be done. We recognize that the magnetic transformations do not indicate whether the transformation products are pearlite, ferrite, bainite or martensite. We have assumed in Fig. 9 that bainite is formed when the transformation takes place at 800 to 1000 °F (425 to 540 °C).

It will be noted by the points plotted by squares in both the continuous cooling diagrams in Figs. 8 and 9, that transformation was arrested at these points. From the time versus magnetic permeability curve it was observed that a certain amount of deflection occurred during the initial quench, this deflection then remained constant over a period of time and then again started deflecting. From this type of curve it was concluded that transformation started during the initial quench and then stopped. Although the steel sample continued cooling; no further magnetic permeability change occurred for some finite time. On further cooling, the transformation again started. This was interpreted to mean that in the SAE 4340 steel ferrite started forming during this particular cooling condition and formed a certain percentage of ferrite in the austenite. Thus the austenite was enriched in carbon and transformation halted even though the material was still cooling. A temperature was then reached at which this higher carbon austenite started transforming, deepening the bainitic area of the continuous cooling diagram.

In the continuous cooling curve for SAE 4063 it will be seen that the austenite to bainite reaction stops at 620 °F (330 °C). By the magnetic method, therefore, these areas can be defined more closely than by the metallographic method. Another interesting observation from this curve is that the Ms point seems to be a little lower with slower rates of cooling.

Conclusions

Equipment has been designed and used for determining the mode of transformation of steel employing the Curie point. This has been employed for ascertaining the beginning of the austenite to martensite reaction in four alloy steels and appears to be as reliable as the metallographic method. However, like the metallographic method, the magnetic method is sensitive to inhomogenieties in the steel. In addition, by varying the cooling rate of the specimen, a continuous cooling diagram can be determined by the use of this equipment and diagrams for SAE 4340 and 4063 steel have been developed.

The method presented herein is much less time consuming than other known procedures.

ACKNOWLEDGMENT

The authors would like to thank the Chrysler Physics Research Department and in particular C. R. Lewis for building the apparatus described in this paper. Acknowledgment is also due to R. B. Boswell who made the start of martensite transformation determinations and H. M. Luehmann who did the work on continuous cooling, both associated with the Chrysler Metallurgical Research Department.

References

1. R. A. Grange and H. M. Stewart, "The Temperature Range of Martensite Formation," *Transactions*, American Institute of Mining and Metallurgical Engineers, Vol. 167, 1946, p. 467.
2. A. E. Nehrenberg—discussion of Reference (1) p. 495.
3. A. B. Greninger, "The Martensite Thermal Arrest in Iron-Carbon Alloys and Plain Carbon Steels," TRANSACTIONS, American Society for Metals, Vol. 30, 1942, p. 1.
4. R. A. Grange and J. M. Kiefer, "Transformation of Austenite on Continuous Cooling and Its Relation to Transformation at Constant Temperature," TRANSACTIONS, American Society for Metals, Vol. 29, 1941, p. 85.
5. H. J. Elmendorf, "Effect of Varying Amounts of Martensite Upon the Isothermal Transformation of Austenite Remaining after Controlled Quenching," TRANSACTIONS, American Society for Metals, 1944, Vol. 33, p. 236.
6. J. C. Fisher, J. H. Holloman and D. Turnbull, "Kinetics of the Austenite-Martensite Transformation," *Transactions*, American Institute of Mining and Metallurgical Engineers, Vol. 185, 1949, p. 691.
7. M. Cohen, "Retained Austenite," TRANSACTIONS, American Society for Metals, Vol. 41, 1949, p. 35.
8. M. Cohen, E. S. Machlin and V. G. Paranjke, "Thermodynamics of the Martensite Transformation," TRANSACTIONS, American Society for Metals, Vol. 42, 1950, p. 242.
9. S. T. Ross, R. P. Sernka and W. E. Jominy, "Electron Metallographic Study of the Dependence of Microstructure on Hardenability," TRANSACTIONS, American Society for Metals, Vol. 47, 1955, p. 727.
10. Charles Nagler and William Wood, "The Effect of Normal Elements and Alloy Elements on the Rate of Austenite Transformation in Cast Iron at Constant Temperature," TRANSACTIONS, American Society for Metals, Vol. 30, 1942, p. 491.
11. Henry T. Chandler, discussion, R. A. Grange and T. M. Garvey, "Boron Treated Steel," TRANSACTIONS, American Society for Metals, Vol. 37, 1946, p. 179.

DISCUSSION

Written Discussion: By D. J. Blickwede, research engineer, Bethlehem Steel Co., Bethlehem, Pa.

In recent years, especially in Europe, there has been a general awakening to the limitations of both the hardenability concept and the isothermal transformation diagram as methods for describing the course of austenite transformation during continuous cooling. So it is good to see the experimental results of this

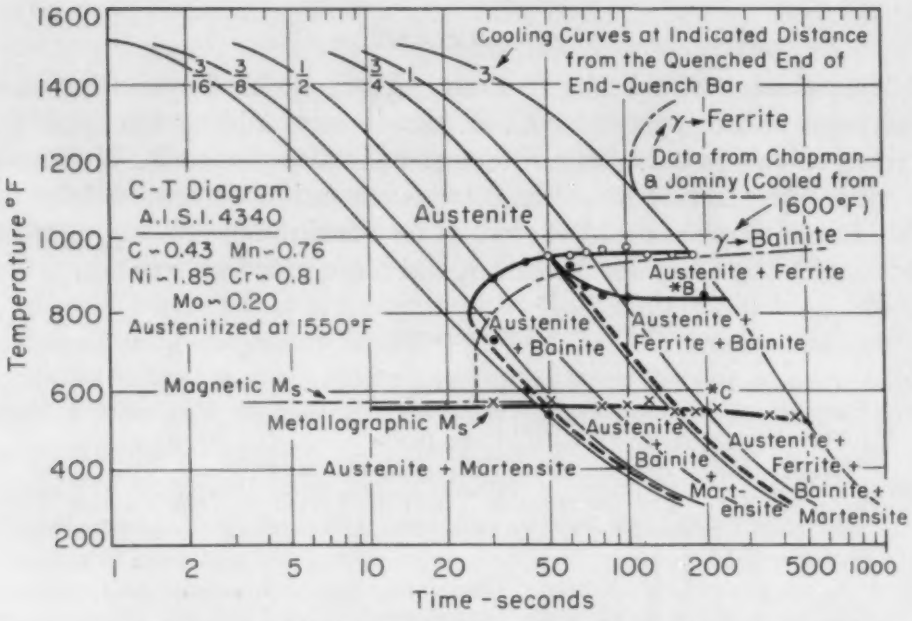


Fig. 12—Cooling Transformation Diagram for AISI 4340 Austenitized at 1550 °F. Heavy lines are data obtained metallographically; light, broken lines are from data of Chapman and Jominy obtained by magnetic method. Note the intermediate transformation to ferrite precedes that to bainite at slow cooling rates. Also note the depression of M_S at slow cooling rates. Asterisks indicate locations at which the photomicrographs in Figs. 13 and 14 were taken.

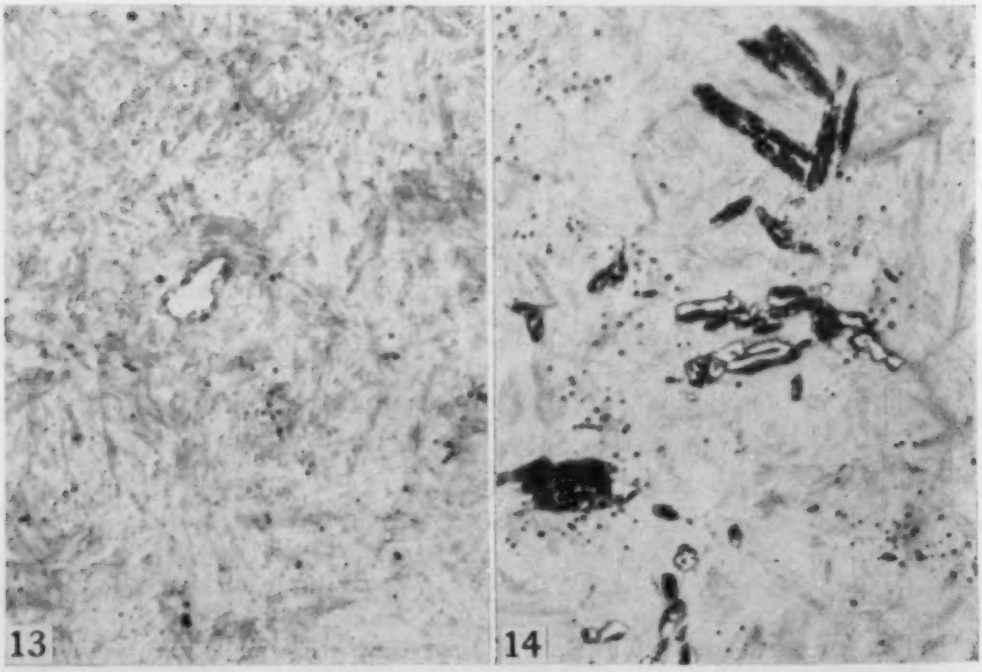


Fig. 13—Ferrite 1.5 Inches from End of Specimen Delay-Quenched 150 Seconds (see Fig. 12). Etched in picral. X 1000.

Fig. 14—Ferrite and Bainite 1.25 Inches from End of a Specimen Delay-Quenched 210 Seconds (see Fig. 12). Etched in picral. X 1000. Note that some of the ferrite needles have degenerated and are surrounded by carbide particles. In other areas new bainite appears to have been formed.

paper, not only for their intrinsic value, but also because they point up a useful method for acquiring information of this sort.

At Bethlehem Steel we have also been making studies of the cooling transformation behavior of steels. Our method has been the metallographic examination of delay-quenched end-quench bars, in the manner described by Liedholm.[2] In this we have also included a determination of the M_s temperature by merely observing the distance from the quenched end at which dark etching tempered martensite appears in the various delay-quenched specimens. The effect of cooling rate on M_s is described by transposing the time-distance measurements to the appropriate location on the cooling curves.

Although the metallographic method for determining cooling transformation diagrams is more laborious than the magnetic method used by the authors, it has the advantage of revealing somewhat more detail. A good example is shown in Fig. 12, where the 4340 diagram of the paper is compared to one that we have determined. The heavy lines through the experimental points describe the beginning of austenite transformation to various products, and the curves running diagonally across the diagram are the actual cooling curves at various locations along a 4340 end-quench bar. For clarity all cooling curves were not drawn on the diagram.

There are some differences in the two diagrams that perhaps may be attributed to slight differences in the steel compositions or austenitizing temperature. Most noteworthy is the shorter time and higher temperature at which bainite was found to appear in our experiments. Also no high temperature transformation to ferrite was found in the range of cooling rates that we studied, but the authors' diagram indicates that we may have just missed it with our slowest cooling rate.

At the same time, there are some gratifying similarities in the two diagrams. The temperature at which the intermediate reaction starts is about 950 °F in both of them. Also the observed M_s temperatures for the rapid cooling rates are virtually the same (572 °F in the authors' diagram and 560 °F in ours).

Of particular interest is the information obtained by the metallographic method about the nature of the transformation products. We have found that bainite is the first transformation product to form only if the cooling rate is rapid. When the cooling rate is slower than that equivalent to the ¾ inch station on the end-quench bar, acicular ferrite forms. (See Fig. 13). This forms in increasing amounts down to 850 °F but at this temperature some of it begins to degenerate into lower bainite by precipitation of carbides within and at the boundaries of the needles. This mechanism agrees with the idea that bainite is formed through an intermediate stage of martensite, i.e. supersaturated ferrite. Not all the ferrite breaks down to bainite though, because as cooling proceeds the reaction eventually stops. At the same time new bainite needles are formed which differ in appearance from the degenerate ferrite by the presence of more carbides, as shown in Fig. 14.

It is also interesting to see how the ferrite and bainite reactions at slow cooling rates cause the M_s temperature to be depressed. Such an effect has been observed by Cameron[3] to result from prior ferrite and pearlite transformation

---

[2] C. A. Liedholm, "Continuous Cooling Diagram from Modified End-Quench Methods," METAL PROGRESS, Vol. 45, 1944, p. 94.

[3] J. A. Cameron, "Application of Isothermal Transformation Diagram to the Normalizing of En 40C Steel," *Journal*, Iron and Steel Institute, Vol. 170, 1952, p. 313.

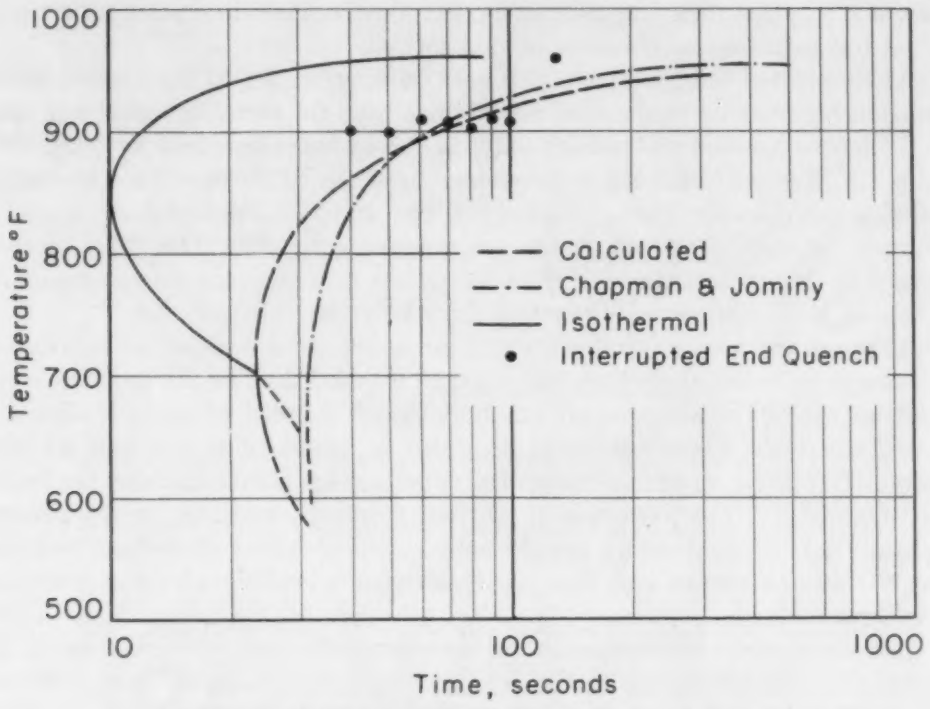


Fig. 15—Isothermal and Continuous Cooling Diagrams for the Bainite Region of SAE 4340.

in the very slow-cooled center sections of large forgings made from a 0.4% carbon, 3% chromium steel. Cameron found that the net result of this was the retention of large amounts of high carbon austenite in the steel. However, in this case it seems unlikely that either the low temperature austenite-ferrite reaction or the formation of bainite should cause changes in the remaining austenite composition that would depress the martensite start temperature 40 °F (equivalent to an increase of about 0.06% carbon). Instead it may be possible that the formation of either acicular ferrite or bainite uses up potential sites for later martensite formation. If this is so, the M_f would be unaffected. Perhaps the authors would comment on the possibility that the magnetic measurement might help resolve the question by giving a reliable indication of the M_f temperature.

So it seems that both methods for determining cooling transformations have particular advantages. Indeed there are many cases where it might be desirable to employ both of them to get the full story of continuous cooling.

Written Discussion: By C. R. Simcoe, principal metallurgist Battelle Memorial Institute, Columbus, Ohio.

The magnetic permeability test on ¾-inch-diameter bars, as described by Chapman and Jominy, is a rapid method for obtaining continuous cooling transformation data. However, as recognized by these authors, the test does not allow distinction among the possible transformation structures. Furthermore, the test is strictly qualitative and does not furnish information on the basic decomposition reactions.

The time and temperature at which transformation starts on continuous cooling depend largely on the nucleation characteristics of the steel. These characteristics are determined from the isothermal transformation curves, the

cooling curves, and a knowledge of the temperature ranges over which fractional nucleation times are additive. It was determined recently that for SAE 4340 fractional nucleation times are additive from the critical temperature to approximately 1100 °F. A second temperature range where fractional nucleation times were additive overlapped the first temperature range slightly and started at 1200 °F. This second temperature range extended down to the M_s temperature.

With the knowledge of the temperature ranges where fractional nucleation times were additive, the isothermal transformation curve, and the cooling curves, a continuous cooling transformation curve was calculated for 1% transformation product. This calculated curve is shown in Fig. 15 where it is compared with experimental data on the time to produce 1% transformation from interrupted end-quench tests. It is compared also with the experimental curve shown in Fig. 6 of this paper and the isothermal transformation curve.

In spite of the many objections to the magnetic permeability tests, there is good agreement between the curve obtained from this test and the calculated curve. Both curves exhibit good agreement with the interrupted end-quench data. Comparison of the continuous cooling curves with the isothermal curve shows the futility of using isothermal curves to predict continuous cooling transformation.

Unfortunately, data are not available for comparison with the magnetic permeability data for the austenite to ferrite reaction. However, the published isothermal transformation curves and the curve determined in an investigation at Battelle Memorial Institute would be on the right of the continuous cooling curve of Fig. 6. This discrepancy suggests that the upper portion of the diagram determined by Chapman and Jominy may not be valid.

Written Discussion: By Paul L. Jackson, Metallurgy Department, Scientific Laboratory, Ford Motor Co., Dearborn, Mich.

The authors state that they believe that there must be 1% transformation in order to obtain a permeability equal to 1% of the room temperature permeability of their steels. The description of the experimental equipment is not complete enough to permit a calculation of the value of the field strength within the pickup coil. However, it seems reasonable to suppose that the sample was not magnetically saturated. In unsaturated iron the value of the permeability increases with rising temperature.[4] This writer recognizes that there are no direct data to show that this holds true for the steels which the authors investigated, but undoubtedly the general shape of the permeability-temperature curve would not be greatly altered from that of pure iron by the small amounts of alloying elements present in these steels. The discrepancies in the locations of the ferrite plus austenite regions of the continuous cooling transformation diagrams of the authors and of Grange and Kieffer can be explained if less than 1% ferrite produces a permeability value equal to 1% of the room temperature permeability. If the authors' reported 1% transformation line actually represents smaller amounts of ferrite, their diagram should not match that of Grange and Kieffer.

Written Discussion: By Charles Arthur Nagler, associate Professor, Department of Chemical and Metallurgical Engineering, Wayne University, Detroit.

---

[4] R. M. Bozorth, *Ferromagnetism*, 1951, p. 59. D. Van Nostrand.

I want to thank the authors for this opportunity afforded me to discuss their paper regarding the application of a magnetic method for determining the transformation on continuous cooling of austenite in steels.[5]

Quoting from the paper: "In order to avoid the use of metallography in the determination of austenite transformation rates, a method has been devised, based on the magnetic changes which accompany the transformation. This method makes it possible to determine a transformation curve in a much shorter time and with greater accuracy than is possible with the metallographic method which was developed by Davenport and Bain."

A further quotation from the paper, under the heading, "Theoretical Basis," states: "When steel or cast iron transform from the austenitic to the pearlitic, acicular or martensitic state, one of the important properties that is radically changed is the magnetic permeability. Although the permeability is somewhat different among the products of the austenitic transformation, the order of magnitude of the permeability of austenite is entirely different from that of its decomposition products. This change in permeability is, in reality, a measure of the degree of transformation."

It goes on to say, under the heading, "Development of the Transformer Apparatus": "With this phenomenon as a basis, the authors devised an apparatus in which the sample, after being quenched for a few seconds in the lead bath, was placed between the poles of a specially designed alternating current transformer. As the transformation took place, the permeability of the sample increased, causing an increase in the emf generated in the secondary coil. The changes in the secondary current were read on an ammeter, and the results were plotted as ammeter readings against time. On the basis of the assumption that the secondary current is a measure of the amount of austenite in the sample, this plot was the same as a plot of per cent austenite against time."

Fig. 3 in the paper, by the authors Chapman and Jominy, indicates the typical cooling curve and magnetic transformation curve for an SAE 4340 steel, oil-quenched, for a section ¾ inch in diameter and 3 inches long.

I would like to inquire of the authors if they are able to reproduce the same time and transformation based on magnetic permeability for a bar of a section size of ¼ inch. Were there any metallographic determinations made to determine if any transformation products, other than martensite, formed during oil quenching, due to no agitation of the specimen, or the quenching medium during determination of the cooling curve?

Normally, on still quenching of a ¾ inch diameter round, in oil, there would be formed a vapor interface along the surface of the bar, which would materially reduce the cooling rate and tend to cause the formation of a small amount of a transformation product, other than martensite, on continuous cooling at Ar_1.

Using a specimen ¾ inch diameter and 3 inches long, does the exact position of the specimen in the secondary coil influence the initial permeability reading while the sample is in the austenitic condition?

Again referring to Fig. 3, on the initial portion of the plot of per cent of magnetic permeability vs. time, the incubation, or initial increase in permeability,

---

[5] W. P. Wood and C. Nagler, "The Effect of Normal Elements and Alloy Elements on the Rate of Austenite Transformation in Cast Iron at Constant Temperature," TRANSACTIONS, American Society for Metals, Vol. 30, 1942, p. 491.

possibly can be attributed to the formation of an extremely fine pearlite, the result of the intersection of the Ar_1.

In reference to Fig. 3, it was stated that at the temperature of 575 °F, the surface becomes ferromagnetic and produces an increase in magnetic permeability until ultimately the bar becomes 100% ferromagnetic. Relative to this statement, were any metallographic determinations made utilizing temperature tests to determine the retention of small amounts of austenite during the oil quenching of the SAE 4340 steel?

In closing I want to refer to a publication by R. L. Dowdell and C. Nagler,[6] which further utilized the original magnetic method described in the paper of 1942, by Wood and Nagler, in determining a family of isothermal transformation curves for various molybdenum-bearing cast irons.

Written Discussion: By R. A. Grange, United States Steel Corp., Fundamental Research Laboratory, Kearny, N. J.

The authors have described a relatively rapid and convenient method of measuring the progress of austenite transformation during continuous cooling. Like other methods that have been used for this purpose, this magnetic method would appear to be more reliable when the steel studied is of high hardenability and there is not too great a difference in microstructure from surface to center of the 0.75 inch diameter specimen at any instant during cooling. Thus, the 4340 cooling transformation diagram developed by the authors is in reasonably satisfactory agreement with one estimated from the isothermal transformation diagram when allowance is made for differences which must be expected among different heats of 4340 steel.

In 4063 steel, however, very poor agreement exists between the diagram determined by the magnetic method and one estimated from an isothermal transformation diagram. In this more rapidly transforming steel, a considerable difference in microstructure throughout the cross-section of the 0.75 inch diameter specimen may have existed during some portion of the cooling cycle. The authors' Fig. 9 implies that the microstructure of an end-quenched bar of 4063 steel will be bainitic and nowhere contain proeutectoid ferrite or pearlite; this is implied because the slowest cooling rate curve in the standard end-quenched bar will not intersect the austenite + ferrite and austenite + pearlite zones in Fig. 9. On the other hand, the diagram for 4063 estimated from an isothermal diagram, authors' Fig. 10, tells us that microstructures in an end-quenched bar will consist in part of ferrite and pearlite. Fortunately, this discrepancy can be easily resolved by examination of microstructure in an end-quenched hardenability test specimen. We have done this and observed both ferrite and pearlite in what we consider to be a reasonably typical heat of 4063, and suggest that the authors similarly examine an end-quenched specimen of their 4063 steel.

Finally, we would like to ask the authors why they chose a specimen having a diameter of 0.75 inches. It is our thought that for steels of moderate and low hardenability a smaller cylinder or possibly a thin-walled tubular specimen might prove more satisfactory in order to minimize the thermal and consequent structural gradient across the section.

Authors' Reply

The authors would like to thank the various discussers of this paper and

[6] R. L. Dowdell and C. Nagler, "Isothermal Transformation of Molybdenum Cast Iron," Transactions, American Foundrymen's Society, Vol. 55, 1947.

appreciate the data submitted by Blickwede and Simcoe. We were unable to determine the bainite formation data shown by Blickwede by our transformation method. However, an electron microscope study made at Chrysler on a hardenability bar of SAE 4340 steel and reported by Ross, Sernka and Jominy,[7] shows carbide free ferrite grains unresolved by the light microscope existing in very small percentages of non-martensitic decomposition products. Unfortunately, they did not determine the temperature at which this ferrite formed but it might have been in that temperature region shown by Blickwede. As for the magnetic method resolving the question raised by Mr. Blickwede concerning martensite formation by the enrichment in carbon of austenite or the potential loss of martensite sites, we doubt that the equipment could be used for such a measurement. This would necessitate the measuring of the Mf temperature and no degree of accuracy would be obtained. Without a doubt the ending of the martensite transformation would approach the 100% permeability asymptotically making the temperature determination rather difficult.

It is gratifying to see the good agreement that exists between the curves of Grange, Simcoe and Blickwede and our magnetic method in the bainitic region. It may be fortuitous but the ideal critical diameter calculated by the Grossmann method shows that the hardenability of Blickwede's material was the lowest, followed by our material, and Grange's material had the highest hardenability and we note that the beginning of transformation of these three steels is in the order of their critical diameters. As Mr. Simcoe points out, the continuous cooling curves certainly show the futility of using isothermal curves to predict continuous cooling transformation.

The authors regret having overlooked the work of Nagler and Wood and have inserted their reference in the paper. The title of their paper does not indicate that a magnetic method was used for their determinations. In reply to Mr. Nagler's questions, we did not use bar sections as small as ¼ inch in diameter but we did make metallographic determinations on the SAE 4063 steel in the bainitic region to ascertain whether we were getting bainite or pearlite. As for the location of the specimen in the pick-up coil, we attempted to center the specimen in all cases inasmuch as we wanted the temperature recording thermocouple to be in the same area in which the permeability was being measured. No metallographic determinations were made on SAE 4340 to determine the retention of small amounts of austenite. However, it would not be at all surprising to find the existence of austenite in this high hardenability steel.

Mr. Grange's point regarding the formation of pearlite and ferrite at the slowest cooling rate of the end quench bar is well taken. We quite agree that these microstructures will exist in the bar, but do not think that they can be used to predict the location of transformation diagram areas. The published cooling rates for the end quench bar as shown by the SAE were established on lower carbon steels. The higher carbon in the SAE 4063 steel causes this material to require a longer time before transformation; therefore, austenite will be present for a greater length of time during end quenching and being a poorer conductor of heat will retard the cooling of the upper portion of the bar considerably. We believe that as long as round bars are compared to the end

[7] S. T. Ross, R. P. Sernka and W. E. Jominy, "An Electron Metallographic Study of the Dependance of Microstructure on Hardenability," TRANSACTIONS, American Society for Metals, Vol. 47, 1955.

quench bar the comparison is valid since the differences in cooling rates cancels out at least in large measure. We have experienced on sluggish transforming steels the air-cooled end of the bar remains hotter for a much greater length of time than do the shallow hardening steels. In effect, this means that the position that should be compared for decomposition products with the transformation diagram on a hardenability bar of an SAE 4063 steel should be considerably closer to the quenched end of the bar than indicated by the SAE chart.

In an effort to further check the validity of our diagram the following experiment was carried out: We noted that a still air quench possessed such a cooling rate in a ¾ inch round section that it entirely missed that portion of the diagram we called the austenite + ferrite and the austenite + pearlite region. Therefore, we air-cooled a sample with an attached thermocouple to 1100 °F in air and then water-quenched. The time elapsed to cool to 1100 °F was found to be 85 seconds. The microstructure of this sample was entirely martensitic and showed no pearlite, ferrite or bainite. We do not have the data as to at what location on the end-quenched bar we obtain this cooling rate. Another sample was then air-cooled in 110 seconds to 1000 °F followed by a water quench. The microstructure of this specimen contained a minute amount (less than 1%) of decomposition product, showing transformation had just started. This agrees very favorably with the beginning of transformation as shown on our diagram and could be used as a further proof for the validity of the magnetically determined diagram.

The idea of using a tubular specimen as recommended by Mr. Grange sounds very good for shallow hardening steels and we will attempt to employ such a specimen.

Regarding Mr. Jackson's discussion, we agree and have pointed out in the paper that more work need be done on the relationship between permeability and amount of transformation. It was interesting to have this discussion and we hope that sufficient interest has been aroused to increase the amount of work to determine continuous cooling diagrams on other alloy constructional steels. From such work more information of the austenite decomposition on continuous cooling should add to our knowledge of the thermal behavior of steel.

DELAYED FAILURE AND HYDROGEN EMBRITTLEMENT IN STEEL

By R. P. Frohmberg, W. J. Barnett and A. R. Troiano

Abstract

The phenomenon of delayed failure in steel has been correlated with the presence of electrolytically introduced hydrogen. Delayed failure may occur over a wide range of relatively low applied stresses depending upon strength level, notch acuity and aging time after the introduction of hydrogen. The sensitivity to delayed failure may persist even though conventional tensile results indicate full ductility. The observed reductions in ductility are a function of both the depth of hydrogen penetration and the degree or severity of hydrogen embrittlement. Aging with and without load has demonstrated the necessity of exceeding some minimum critical stress in the presence of hydrogen to embrittle steel. This value of stress can be made to vary with notch acuity and aging time and may be associated with the initiation of plastic flow. The effects of aging under load depend upon the magnitude of the load and permit the production of a wide variety of failure times. A bainitic structure behaved in a fashion similar to that of tempered martensite, except that the overall embrittlement appeared less severe. Delayed failure cannot be attributed solely to retained austenite since the bainitic structure contained no trace of austenite.

Introduction

MANY problems associated with embrittlement have been encountered in the increased use of alloy steels heat treated to high strength levels. In recent years, particularly in aircraft, engineers have been working towards higher strength levels which makes an understanding of the various forms of embrittlement of increasingly greater importance (1)[1]. One of the phenomena encountered when steels are heat treated to high strength levels is the occurrence of brittle delayed failures in service. This is a particularly insidious type of failure in that spontaneous brittle fracture will occur at loads substantially below those that may have been previously successfully sustained, and in material which shows good ductility in conventional laboratory evaluation.

[1] The figures appearing in parentheses pertain to the references appended to this paper.

This paper presents a portion of the results from investigations sponsored by the Aeronautical Research Laboratory, Wright Air Development Center.

Of the authors, R. P. Frohmberg and W. J. Barnett are research associates, and A. R. Troiano is head, Department of Metallurgical Engineering, Case Institute of Technology, Cleveland. Manuscript received July 21, 1954.

Thus a "proof stress" type of test is of little value. For example, electroplated steel bolts heat treated to high strength levels have shown delayed failure at the root of threads or in the head fillet; similarly other plated or pickled parts have been known to fail in a brittle manner under the influence of relatively mild static loads.

Previous Experimental Work

The published literature actually contains relatively little on the subject of delayed failure *per se*, but many studies have been made of the effects of hydrogen on the ductility of steel. An explanation of delayed failure based on the presence of hydrogen must be consistent with the other embrittling effects of hydrogen. The following is a cursory review of some of the many observations of the effects of hydrogen. An exhaustive literature survey has been made by Buzzard and Cleaves (2) and other work includes summaries of previous information together with relatively abridged bibliographies (3,4,5 and 6).

Hydrogen may be introduced into steel from a variety of sources which might be divided into natural and artificial origins. Considering first the congenital sources, the steelmaking process itself is one major origin of hydrogen (7,8) and it is particularly troublesome in large section sizes (9,10). Here the presence of hydrogen is manifest as flakes or substantial reductions in ductility (11). Other processing operations such as pickling (12,13) and electroplating (14,15,16) are recognized sources which have been studied. Welded sections sometimes show loss of ductility and flakes, both of which have been attributed to the presence of hydrogen.

There are several laboratory techniques for the deliberate introduction of controlled amounts of hydrogen into steel. Specimens may be heated in the vicinity of 2000 °F (1095 °C) in hydrogen at or near one atmosphere pressure. Some investigators heat to lower temperatures in hydrogen under pressure. Electrolytic charging is also commonly used, sometimes with a "poison" to enhance the pickup of hydrogen by the specimen. Pickling in solutions of various concentrations has been shown to be effective in charging specimens with hydrogen. One investigator has shown (17) that electrolytic charging and the introduction of hydrogen under pressure at 600 °C both gave the same embrittling effect, as measured by reduction in area.

The equilibrium solubility of hydrogen in ferritic steel at room temperature is thought to be extremely small. However, large amounts of hydrogen may be introduced and retained in steel. In one instance, for example, a concentration of 65 cubic centimeters per 100 grams[2] (18) was attained by electrolytic charging, while in another case a 5 by 5-inch steel billet retained up to 5 cubic centimeters per 100 grams

[2] The concentration of hydrogen in steel may be stated in several ways. The designation used here will be cc of hydrogen at standard pressure and temperature per 100 grams of steel (cc/100 gm). One cc/100 gm = 0.0787 relative volumes = 0.00009 weight per cent = 0.9 parts per million.

eight months after fabrication (9). Thus, relatively large quantities of hydrogen, well in excess of equilibrium solubilities, may be retained in steel. A curious feature of this problem is the fact that austenitic steels are relatively immune to the embrittling effects of hydrogen (19,20) when compared with ferritic steels of proportionate hydrogen contents (17,21,22).

Darken and Smith (23) showed that the maximum amount of hydrogen absorbed in pickling steel increased linearly with the amount of prior cold work. They also found that the rate of absorption demonstrated a similar dependence on the degree of deformation. The evolution of hydrogen is accelerated during cold working (24,25). Bend tests have shown that steel when cold-worked is more susceptible to embrittlement than when annealed (16,26).

Several experiments have been reported in which hydrogen appears to have opened passageways through steel (27,28). A vivid demonstration has been given (18) in which molten brass permeated to a considerable depth below the surface of a charged steel wire. When the charged hydrogen was removed by aging 10 hours at 750 °C, penetration upon immersion in brass was not observed. When subjected to severe electrolytic charging (21,24), surface bursts, presumably the result of hydrogen pressure build up, have been found.

It appears that the elastic behavior of steel during tensile testing is unaffected by the presence of hydrogen, but some changes do occur in the plastic region of the stress-strain curve. Several investigators (17,21,29) have clearly demonstrated that increasing amounts of hydrogen reduce the fracture strain. More detailed studies (30) have revealed a slight lowering of the upper and lower yield points and a decrease in the strain hardening exponent of a pickled low carbon steel. The strong dependence of hydrogen embrittlement on strain rate and testing temperature has been verified by a number of investigations (20,30,31,32). The strength level to which steel is heat treated also has a strong effect on the susceptibility to hydrogen embrittlement (17,33).

Numerous studies have been made in which recovery from the embrittled state has been observed on aging, usually at room temperature (19,21,22,24,34,35). In general, the degree of embrittlement decreased with increasing aging time and complete recovery of ductility was eventually attained if the charging conditions were not too severe. Occasionally, a minimum has been observed in the aging curve at short aging times, i.e., an initial decrease in ductility prior to recovery. Aging at elevated temperatures accelerates the recovery process while for all practical intents and purposes the aging process may be stopped completely if the temperature is low enough. The evolution of hydrogen during aging has also been studied (36).

Studies on the delayed failure of electroplated lockwashers (15,33) have indicated a strong dependence of propensity towards de-

layed failure on strength level. It was also shown that delayed failures could be minimized or eliminated by baking at 400 °F (205 °C) after plating. In conical disk tests (37), a strong dependence of test life under static load on hardness was apparent. A number of heats of steel were studied and no mention was made of the addition of hydrogen. Thus, delayed failure was observed in the absence of artificially introduced hydrogen.

Review of Proposed Mechanisms

One of the most popular explanations for hydrogen embrittlement has been developed by Zapffe and co-workers over the past ten or twelve years and is known as the "planar pressure theory." A succinct statement of this concept is that, "Hydrogen embrittlement is nothing other than the result of an aging action in which the precipitate is a gas" (19). This theory is attractive in that it can explain many (though not all) of the observed phenomena in connection with the presence of hydrogen in steel. For example, the appearance of surface blisters in severely charged specimens seems readily explicable on the basis of the relief of internal gas pressure by the disruption of surface layers of metal. Detailed applications of the planar pressure theory of hydrogen embrittlement may be found in the literature (3,6,19,26).

There are several questions pertaining to the planar pressure concept which might be raised. For one, the proposed precipitation sites (mosaic disjunctions or lattice rifts) are of the order of magnitude of interatomic spacings in size, hence it is difficult to visualize the development of pressure by applying the classic kinetic theory of gases. Another consideration is the calculation of the pressures developed by hydrogen in voids. This was first done in 1932 (38) and subsequently extended in an attempt to show that very high pressures are developed by the hydrogen present in steel. It has been pointed out (39) that these calculations give fugacity,[3] and the difference between fugacity and pressure may become quite considerable. If the planar pressure concept is correct, the precipitation of gas and subsequent embrittlement should occur in austenitic as well as in ferritic structures. The solubility of hydrogen in austenite is greater than in ferrite, however, inordinately large quantities of hydrogen are required to produce even a slight embrittlement in austenitic steels.

The relationship between testing temperature and ductility provides an interesting test for the planar pressure theory. It has been shown (30,32) that for a given charging condition the ductility first decreases, then increases, passing through a minimum as the testing temperature is increased. The first portion of the curve is readily explicable. As the temperature is increased, the diffusion of hydrogen

[3] The ratio of fugacity to pressure is called the activity coefficient and is a measure of the deviation of a gas from ideality. For hydrogen, the fugacity may be considerably greater than the pressure.

is accelerated and precipitation in voids is facilitated. One encounters considerable difficulty in attempting to visualize how the planar pressure concepts or extensions of it might explain the minimum and subsequent increase in ductility with increasing temperature. Brown and Baldwin (32) have considered this point in some detail, and clearly demonstrated that a mechanism fundamentally different from the planar pressure theory or allied concepts must be operative under certain conditions of embrittlement.

Consideration has been given to the possibility of applying the concept of a Cottrell atmosphere surrounding a dislocation to the case of hydrogen embrittlement in steel (30,32). The essential feature of this concept is that the presence of the interstitial solute atoms reduces the elastic strain energy in the vicinity of a dislocation by reducing the degree of distortion (46). Under applied stress, the movement of the dislocation is restrained by the atmosphere, and the dislocation may break free, remain fixed, or move through the lattice "dragging" the atmosphere with it.

Little if any lattice distention has been observed with the addition of hydrogen to steel (47,48). For a steel containing 10 cubic centimeters hydrogen per 100 grams, the atomic percentage is 0.005 which corresponds to one atom of hydrogen for every 20,000 iron atoms. In contrast to this, a 0.1% carbon steel contains 0.5 atomic percentage carbon or one carbon atom for every 200 iron atoms. Thus, the atomic concentration of hydrogen is only 1/100 that of carbon. This then leads one to question whether a restraining Cottrell atmosphere could be formed by the solute hydrogen atoms by an elastic strain mechanism.

It has been shown (49) however, that a yield point attributable to hydrogen exists in a charged 1020 steel. The author states that, "Preliminary experiments also indicate that this yield point is not observed above about —120°C." Thus, a Cottrell atmosphere due to hydrogen is presumably responsible for the yield point phenomenon. If a Cottrell atmosphere based on distortion is rejected by the size argument given above, one might consider that some other mechanism (possibly electrostatic) might be operative in reducing the energy around a dislocation.

Although the metallurgical literature on delayed failure under static load is meager, the problem has been studied in some detail in glasses. It is well known that a relatively high static load may be sustained by glass for only a short time but that a lesser load may be tolerated without fracture for a much longer time. The Griffith crack theory has been employed with reasonable success in an attempt to explain this behavior (40,41).

The concept of the presence of microcracks arose out of the large disparity between the theoretical fracture strength (based on attractive forces between atoms) and the observed fracture strengths in brittle solids. Experimentally, it was found that theoretical strengths could

be approached in some instances by prolonged annealing, by minimizing surface scratches and by testing thin fibers. Griffith (42,43) provided a mathematical treatment for a two dimensional model which resulted in the following expression for the breaking strength of a *brittle isotropic solid:*

$$R = \sqrt{\frac{2ET}{\pi C}}$$

where R = stress applied normal to a crack in a thin plate
E = Young's Modulus
T = surface energy of the material
2C = length of crack

This equation has been used by Orowan (40) to explain the phenomenon of delayed failure in glasses. The surface energy of mica was 4,500 erg/per square centimeter in vacuum and 375 erg/per square centimeter in air as determined experimentally, and the ratio of these two values was presumed to be preserved for glasses. This means that two values may then be considered for R, R_v corresponds to the strength where cracks grow in a vacuum, while R_a corresponds to some lower strength value where the cracks grow in an atmosphere. If a stressed specimen is exposed to a suitable atmosphere and adsorption occurs, the surface energy of the crack is reduced and the crack may then readily propagate. This propagation is limited by the fact that if a crack grows too rapidly, the vacuum value for surface energy must be considered together with the higher unit breaking stress R_v. Once crack propagation has proceeded to a point where the unit stress is greater than R_v, cataclysmic failure results.

Two interesting features of this concept follow. First, this predicts that there is some critical value of stress, associated with R_a, below which delayed failure should not occur. Secondly, a specimen subjected to a static load between values of the load corresponding to R_a and R_v, then subsequently unloaded short of the time necessary for failure, should have a breaking strength less than that of a specimen without the prior stress.

The work of Gurney and Pearson (41) and others (44,45) provides experimental confirmation of this model. In one series of experiments (41) it was shown that the phenomenon of delayed failure could be eliminated by annealing glass rods in vacuum and testing them in vacuum. When tested in air, the familiar pattern of delayed failure was encountered. On the other hand, when tested in air from which both CO_2 and H_2O were removed, delayed failure was again eliminated. In those cases where delayed failure was not observed, the breaking strength of the glass rods was far above that normally obtained and approached the theoretical value.

The application of these concepts to the case of hydrogen embrittlement and delayed failure in steels has been considered (31). In the case of steels, the atmosphere adsorbed on crack surfaces would be the

hydrogen present in metastable solution, and the previous reasoning could be applied. The time delay would be due to the fact that time is required for hydrogen to diffuse into the immediate vicinity of the crack and deposit as an adsorbed layer on the growing crack surface, thereby reducing the energy of that surface. However, caution should be used in extending the Griffith crack theory from the case of delayed failure in glasses to delayed failure in metals. The Griffith relationship was developed for brittle materials, in terms of the elastic stress required to separate atoms, while even the most brittle fracture in metals is accompanied by some plastic flow.

There are certain appealing features of each of the three theories outlined above, however, it is difficult to accept any one of these mechanisms for hydrogen embrittlement without reservation. It is quite possible that combinations or modifications of these concepts will ultimately come to be accepted as the cause of hydrogen embrittlement and delayed failure in steel.

Materials and Procedure

The material used was taken from a commercial heat of SAE-AISI 4340 steel, the chemical analysis of which is given in Table I. Specimens were heat treated to three different strength levels, 200,000, 230,000 and 270,000 psi by austenitizing at 1550 °F (790 °C) for 45 minutes, followed by an oil quench, and tempering one hour at 850, 700, and 450 °F (455, 370 and 230 °C).

Table I
Composition of 4340 Steel Used in This Investigation

C	Mn	Si	Ni	Cr	Mo
0.39%	0.76%	0.28%	1.80%	0.75%	0.24%

Two types of specimens were employed. A specimen with a two inch radius test section was used for much of the tensile testing. The sharp notch specimen had a 50%, 60 degree notch whose root radius was less than 0.001 inches. In both cases the diameter at the minimum section was 0.212 inches.

Tensile testing was performed at room temperature with the cross-head feed maintained at a constant rate. A dead weight horizontal lever arm type of creep rupture machine was employed for testing under static load. In both cases, especially designed concentric test fixtures were used to assure a high degree of concentricity. Calibrating runs indicated a maximum eccentricity of 0.001 inches.

Hydrogen was introduced by cathodic charging and the procedure used almost exclusively will be referred to as charging condition A. The specimen was first thoroughly cleaned in carbon tetrachloride. Unnotched specimens were coated with glyptal under the heads in those cases where head failures were likely to occur. Specimens were charged

for 5 minutes in an aqueous 4% sulphuric acid electrolyte without poison. The current density was 0.02 amps per square inch. After charging, specimens were first rinsed in water, then alcohol, and dried. The time between the end of charging and beginning of a test was taken as the aging time. A five minute aging time was convenient to allow rinsing, drying, and locating the specimen in the concentric test fixtures. All aging and testing was performed at room temperature.

Results and Discussion

Effects of Charging Conditions

The reduction in area at fracture in the tensile test was one of the properties used as an index of hydrogen embrittlement. Charging

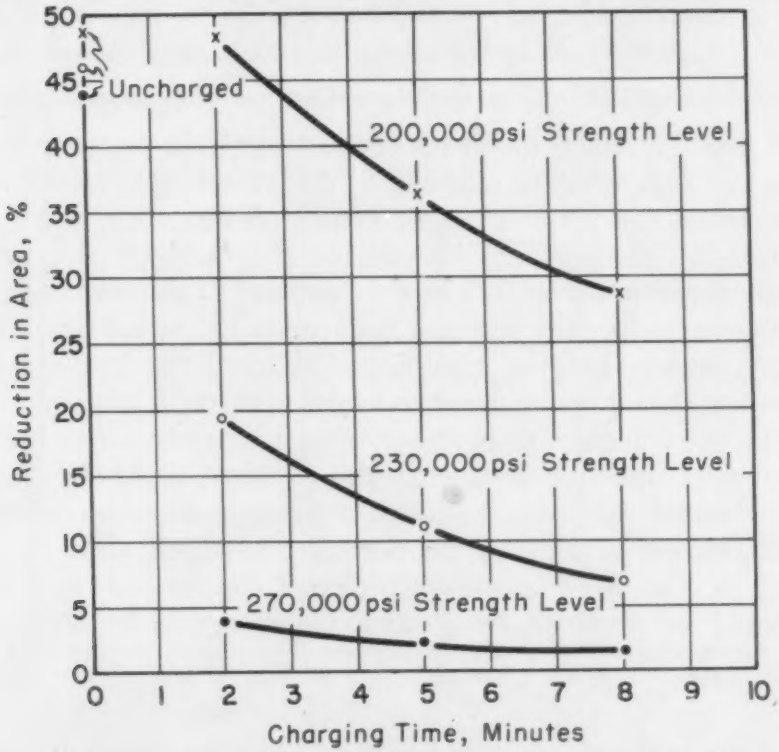


Fig. 1—Effect of Charging Time on Ductility of 4340 Steel Heat Treated to Various Strength Levels. (4% H_2SO_4, 0.02 amps/sq. in. aged 5 minutes at room temperature before tensile testing).

conditions were selected such that the ductility was reduced to a low value, but not zero. If the steel were embrittled to the point where fracture occurred with no visible evidence of ductility, treatments which produced improvements might be difficult to evaluate. The effects of varying the charging time, for three different strength levels, are shown in Fig. 1. The strong dependence of embrittlement on strength level is apparent. In addition, the ductility is less sensitive to charging times at the 270,000 psi strength level than for the lower strength levels

The results of the standard charging condition A on mechanical properties are summarized in Table II for the conventional tensile

Table II
Effect of Charging Condition "A" on Some Mechanical Properties of 4340 Steel Heat Treated to Several Strength Levels

	Tempered Martensite			Bainite
Nominal Strength Level, psi	200,000	230,000	270,000	230,000
Uncharged				
Tensile Strength, psi	205,000	236,000	279,000	238,000
Yield Strength, psi *	195,000	220,000	235,000	210,000
Reduction in Area at Fracture, Percent	49	46	44	49
Fracture Strength, psi	321,000	345,000	388,000	351,000
Hardness, Rockwell C Scale *	43	48	53	45
Notch Tensile Strength, psi	292,000	315,000	330,000	336,000
Charging Condition "A" (5 Minute Age)				
Tensile Strength, psi	205,000	236,000	255,000	238,000
Reduction in Area at Fracture, Percent	36	11	3	24
Fracture Strength, psi	265,000	261,000	265,000	260,000
Notch Tensile Strength, psi	266,000	300,000	207,000	314,000

* Yield Strength (0.2% offset) and hardness were unaffected by the charging condition used.

test and for the sharp notch specimens tested in tension. Note that charging with hydrogen influenced the properties associated with ductility while the yield strength remained relatively unaffected. A comparison of stress-strain curves for the charged and uncharged conditions is given in Fig. 2. The only apparent effect of charging with hydrogen is to reduce the strain at fracture in the stress-strain curve.

More severe charging conditions [4] reduced the fracture strain to values so low that it was difficult to evaluate them. It may be seen from Fig. 2 that the fracture strength serves as a more sensitive measure of the severity of embrittlement when this is the case. At the 270,000 psi strength level for example, the fracture strength could be reduced to as low as 60,000 psi or 25% of the normal uncharged yield strength, as indicated in Fig. 3. The widely different degrees of embrittlement which could be obtained by electrolytic charging are illustrated by Figs. 1 and 3.

Effect of Aging on Ductility

The effect of aging on the recovery from the embrittled state, for three strength levels, is shown in Fig. 4. Unnotched specimens, after charging and aging as indicated, were tested in tension and the reduction in area at fracture was plotted as the index of embrittlement. The initial ductility (for the shortest aging times) varied inversely with strength level. On the other hand, the time for recovery did not appear to follow a consistent trend. At all strength levels, the return to full ductility as measured by reduction in area was evident after aging for 100 hours.

Aging curves were determined for sharp notch specimens tested in tension. The relationship between the aging time and notch tensile

[4] Charging conditions of this order have been commonly employed in studying the effects of hydrogen in steel at lower strength levels.

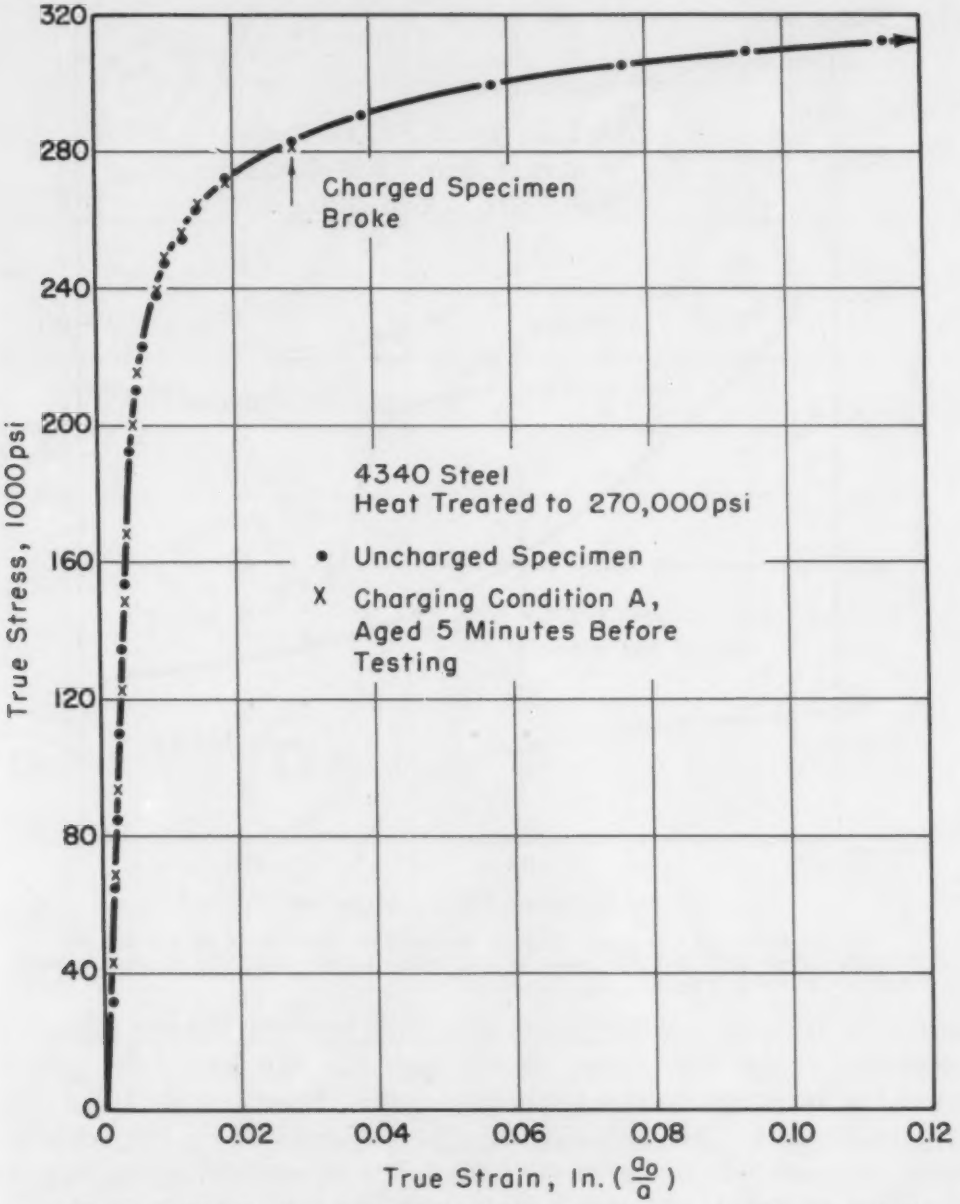


Fig. 2—Initial Portion of True Stress-True Strain Curve for Charged and Uncharged Specimens.

strength at the 230,000 and 270,000 psi strength levels is illustrated in Fig. 5. The change in notch ductility was small for the sharp notch specimens and was not as sensitive to recovery as the notch tensile strength. The latter property, then, was taken as an index of embrittlement.

Certain differences in form are evident in a comparison of Fig. 5 with Fig. 4. The aging curve for the sharp notch specimens exhibited a marked minimum at approximately two hours while unnotched specimens for the corresponding strength levels showed a more or less continuous increase in ductility. A second feature of this comparison is that the unnotched ductility has recovered to its full uncharged value after

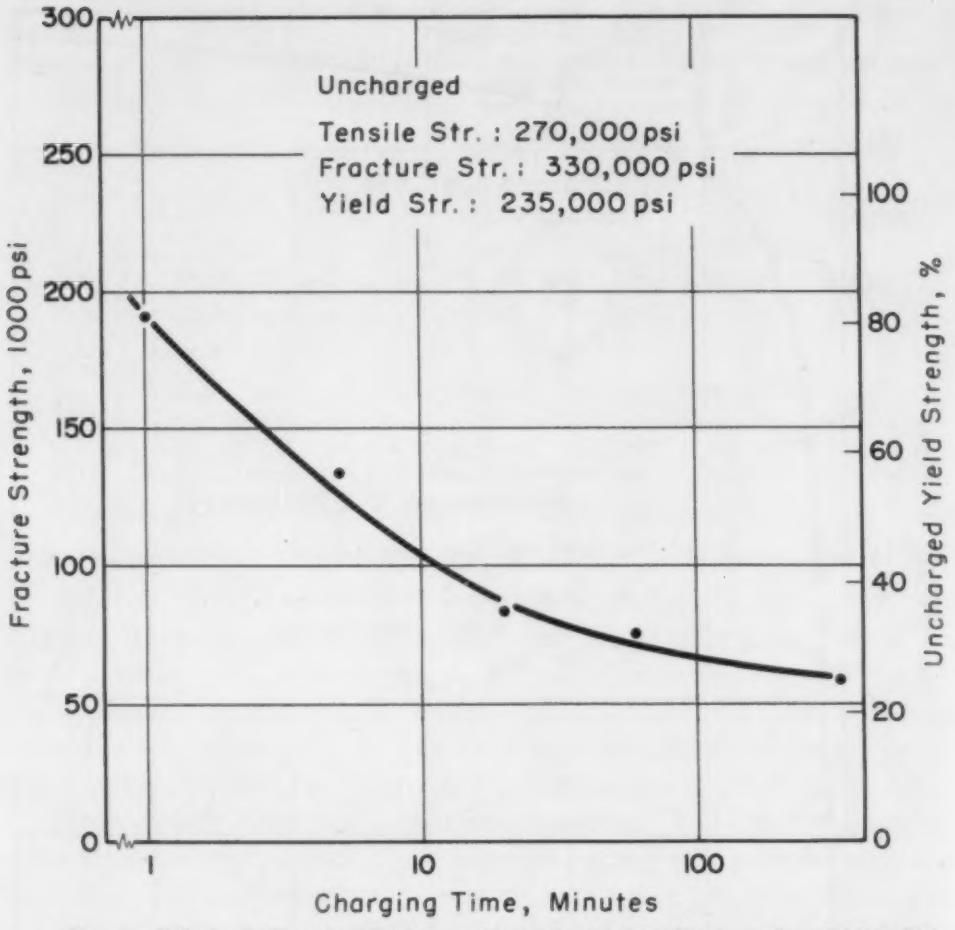


Fig. 3—Effect of Charging Time on Strength of 4340 Steel at the 270,000 Psi Strength Level. (4% H_2SO_4, 1 amp/sq. in., poison added. Aged five minutes at room temperature before testing.

aging for 100 hours, while the notch tensile strength has not completely recovered in the same aging time. From this, one may infer that the notch test is more sensitive to the presence of hydrogen than the standard tensile test. This behavior may be rationalized on the basis that hydrogen merely constitutes the addition of an embrittling agent to one already present, that is, the sharp notch.

Distribution Studies

During the course of this work several instances were observed in which the fracture surfaces of charged specimens displayed a concentric ring, i.e., a change in luster across the fractured area. This has also been observed by others (6) and raised the question of how hydrogen was distributed in the test piece after charging.

Distribution studies are made difficult by the fugitive nature of hydrogen. The conventional techniques for measuring the distribution of solutes in alloys, such as in diffusion studies, seem impractical if not impossible. Since the ductility of steels varies with hydrogen content, if only the outer layer were impregnated with hydrogen, removal of

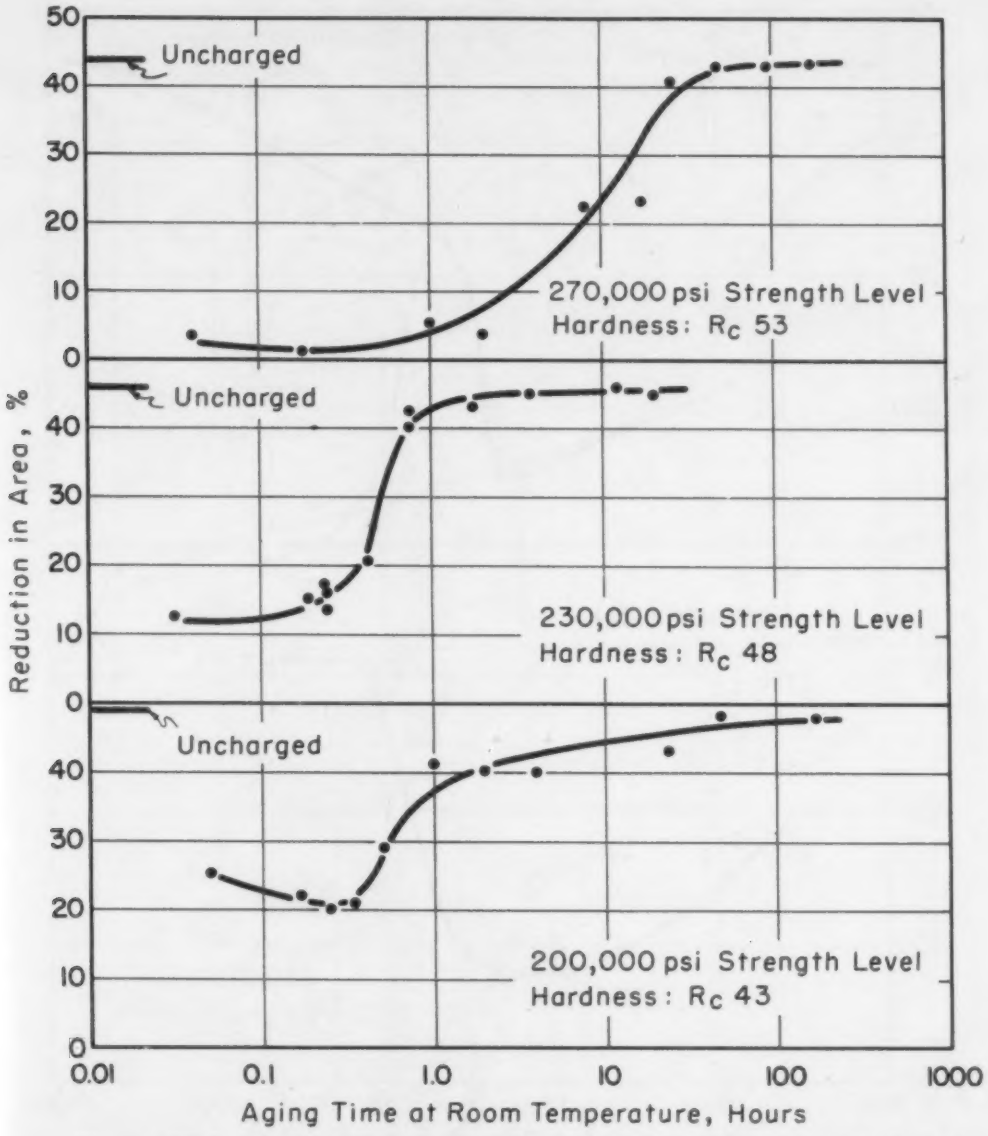


Fig. 4—Effect of Aging Time on Ductility of 4340 Steel Heat Treated to Several Strength Levels. (Unnotched tensile tests, charging condition A).

that brittle layer by machining or grinding should result in the restoration of the ductility of the specimen.

The technique consisted of charging the unnotched specimens with hydrogen and then aging at room temperature. Upon expiration of the aging time, a portion of the specimen surface was removed by grinding, during which the specimen surface was flooded with coolant. The specimen was finally finish polished and immediately tested.

The results, for three different aging times, are plotted in Fig. 6, which illustrates how the ductility was increased by removing surface layers from the test specimens. The abscissa is radial distance, i.e., the thickness of metal removed from the surface. It is evident from this figure that the penetration of hydrogen into the test specimen during charging must have been relatively small, as the removal of the outer

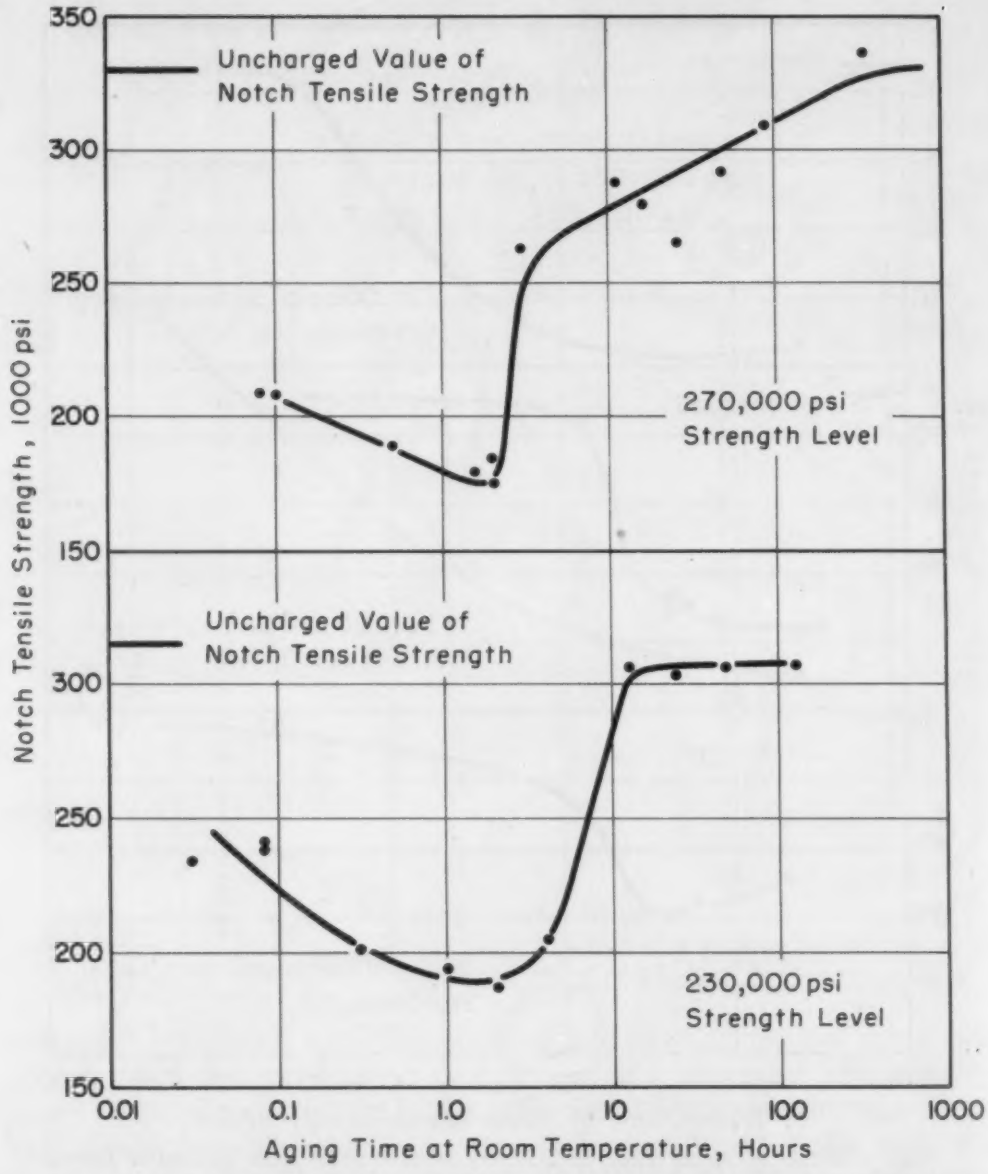


Fig. 5—Effect of Aging Time on Notch Tensile Strength of 4340 Steel Heat Treated to Two Strength Levels. (Charging condition A).

0.020 inches of surface permitted the return to full ductility at the shortest aging time. Upon aging, as indicated in Fig. 6, the embrittled zone was displaced inward.

An interesting feature of the relationships shown in Fig. 6 is that specimens aged four hours exhibited a considerably greater depth of the embrittled zone than specimens aged five minutes. This was true despite the fact that the charged ductility (without removal of stock) after aging four hours was greater than after aging five minutes. Thus, it is evident that two factors are operative; one, the depth of embrittlement and two, the degree or severity of embrittlement.

A comparison of the hydrogen distribution for two different strength levels at an aging time of five minutes is presented in Fig. 7.

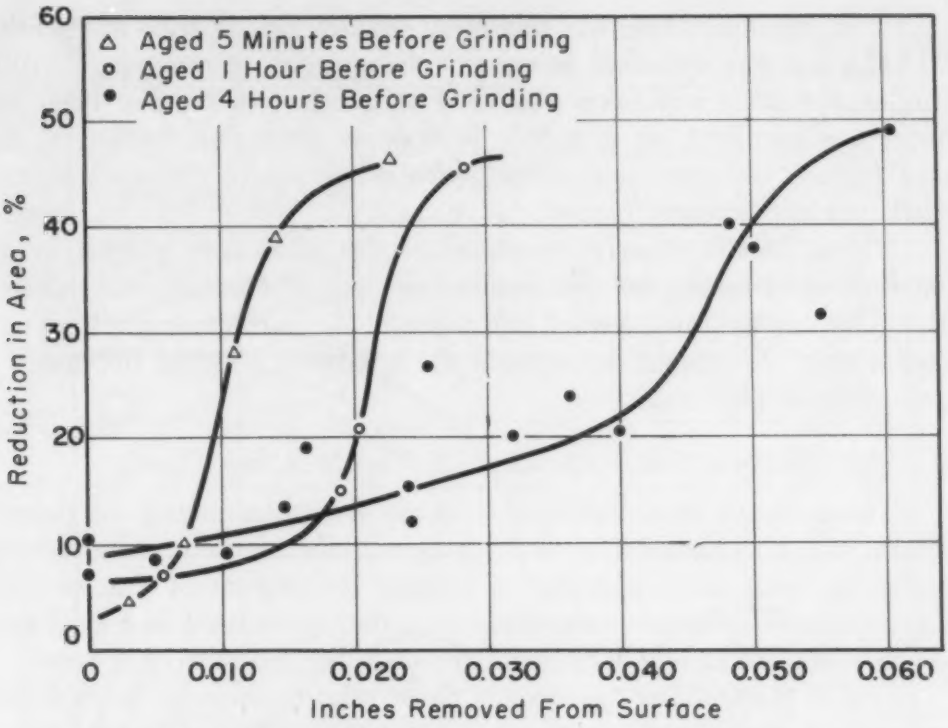


Fig. 6—Effect of Removing Surface Layers of Metal From Charged Specimens. Unnotched tensile specimens, 270,000 psi. Strength level, charging condition A, aged as indicated.

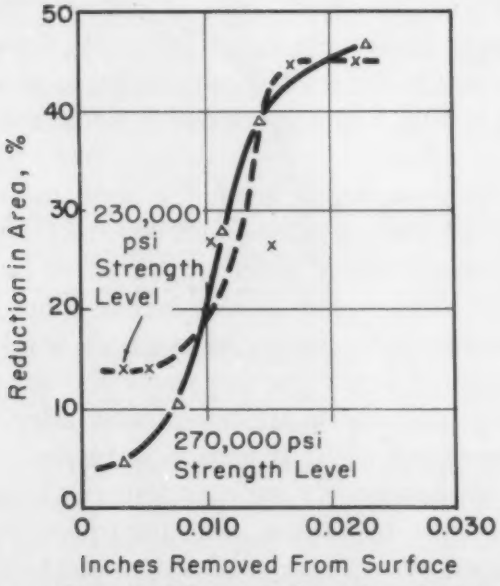


Fig. 7—Effect of Removing Surface Layers of Metal from Charged Specimens Heat Treated to Two Different Strength Levels. Unnotched tensile specimens, aged 5 minutes before grinding. (Charging condition A).

The same amount of hydrogen, (identical charging conditions) and the same depth of embrittlement penetration have a more deleterious effect on steel treated to a 270,000 psi strength level than at a 230,000 psi strength level.

It is significant that the relatively shallow brittle zone of less than 0.020 inches was sufficient to cause a substantial decrease in ductility. Similar behavior has been observed in steels which have been carburized, siliconized, or nitrided. It appears then that hydrogen may have certain features in common with other solute elements when a brittle surface layer is formed.

These results clearly demonstrate the vital role played by the distribution of hydrogen. Delayed failure, loss of ductility, etc., all were caused by the shallow layer of hydrogen at the surface, and a high concentration of hydrogen throughout the specimen was not necessary to produce these phenomena.

Delayed Failure Studies (5 Minute Aging Time)

The primary objective was to study the phenomenon of delayed failure and its relationship to hydrogen embrittlement. Sharp notch specimens were used in order to localize the region of fracture and to provide a multiaxial stress state. The data presented in Fig. 8 indicate that delayed failure will occur in steels charged with hydrogen.

One of the striking features of these relationships is the relatively low applied stresses that were sufficient to produce delayed failure. When compared with the yield strengths given in Table II, it may be seen that applied stresses of as little as 40% of the yield strength [5] (270,000 psi strength level) can cause failure in several hours. Identical notched specimens in the uncharged condition were stressed at high loads as indicated in Fig. 8 and remained unbroken after times of over 250 hours.

Regardless of the strength level, the time to failure was always of the same order of magnitude—from approximately 1 to 8 hours. Within a given strength level, there appeared to be only a slight dependence of failure time on the applied stress. Thus, the delay in time for failure is evidently independent of strength level and only slightly dependent upon applied stress for the particular set of test conditions employed. Varying the test conditions may alter the relationships cited. Since the mobility of hydrogen is a factor which may be expected to remain approximately independent of the strength level and applied stress, the time to failure appears to be associated with the diffusion of hydrogen, which may well represent the time to accomplish a critical redistribution of hydrogen.

The plateau of the stress-rupture curves at high applied stresses coincided with the notch tensile strength for a given strength level. It seems axiomatic that if a static load were applied which was in excess of this value, failure would occur on loading. In those cases where this was tested by applying static loads just above and below the value of the

[5] This does not mean to imply that there is no flow, since the unit stress at the root of the notch is considerably greater than the applied stress. This will be considered in detail later.

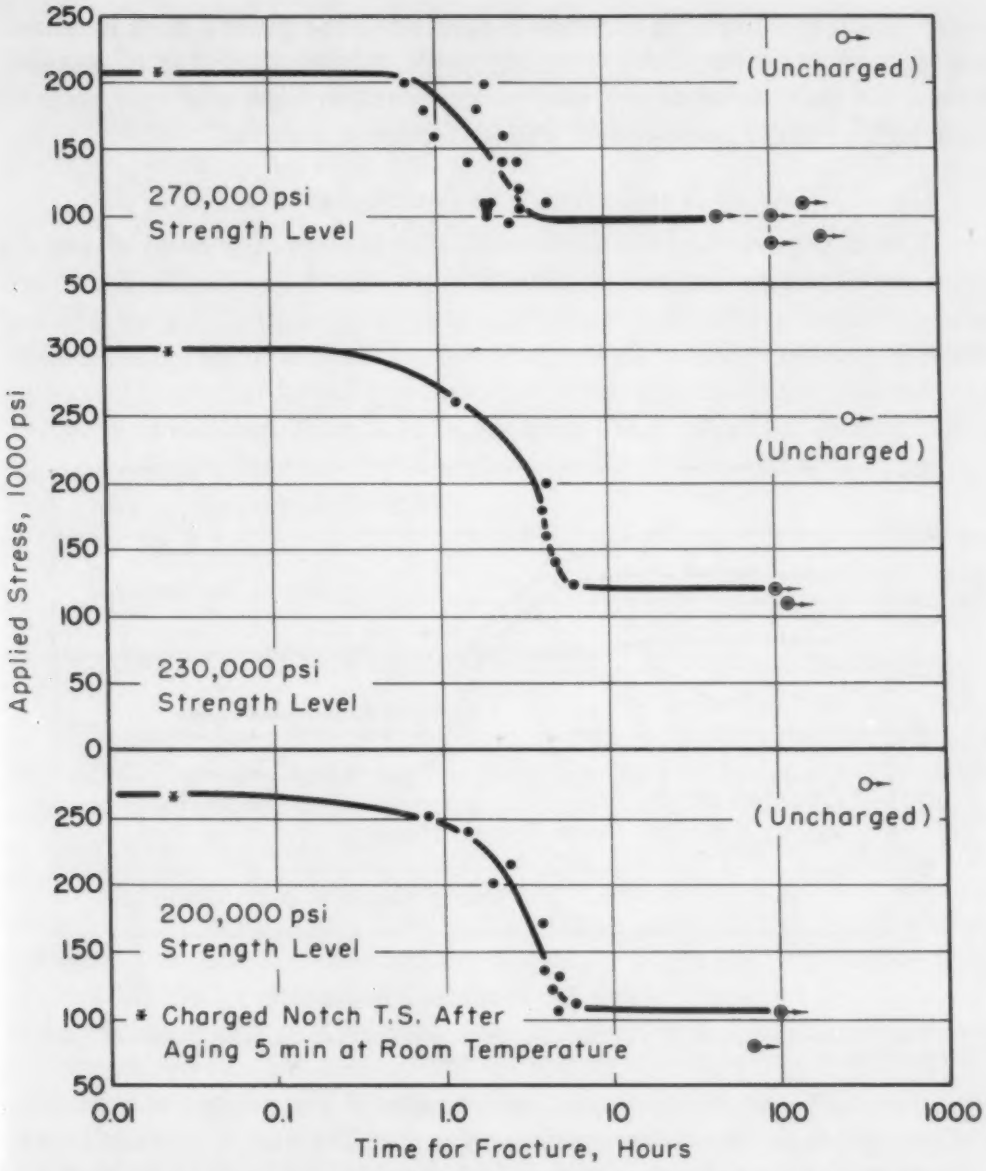


Fig. 8—Stress Rupture Tests on 4340 Steel Heat Treated to Several Strength Levels. (Charging condition A, aged 5 minutes, sharp notch specimens).

notch tensile strength, the correlation was justified. It should be noted, however, that the tensile test represents continuously increasing applied loads over a finite period of time, and as such, may mask short delayed failure times. The upper critical stress value at the 270,000 psi strength level was less than that of the other two strength levels. Presumably this is due to the fact that the embrittlement caused by hydrogen was sufficient to give the marked decrease in notch strength observed at the 270,000 psi strength level.

A most significant characteristic of the stress-rupture relationships is the fact that there was a minimum critical value of applied stress below which delayed failure did not occur.[7] It is evident that for a

[7] The test was generally discontinued if a specimen remained unbroken after 100 hours, although times as long as 2160 hours without failure were observed.

sharp notch specimen an externally applied stress gives a high localized stress concentration. By exceeding some minimum value of applied stress, the unit stress at the root of the notch is high and may well be sufficient to cause plastic flow and subsequent failure.

Effect of Notch Acuity on Stress Rupture Tests

The dependence of the minimum critical stress for delayed failure upon the necessity for plastic flow may be tested by varying the notch acuity. A specimen with a milder notch should require a higher applied stress to produce plastic flow at the root of the notch and thus exhibit a higher minimum critical stress to produce delayed failure. The radius at the root of the notch was increased to 1/32 inch and also to 2 inches,

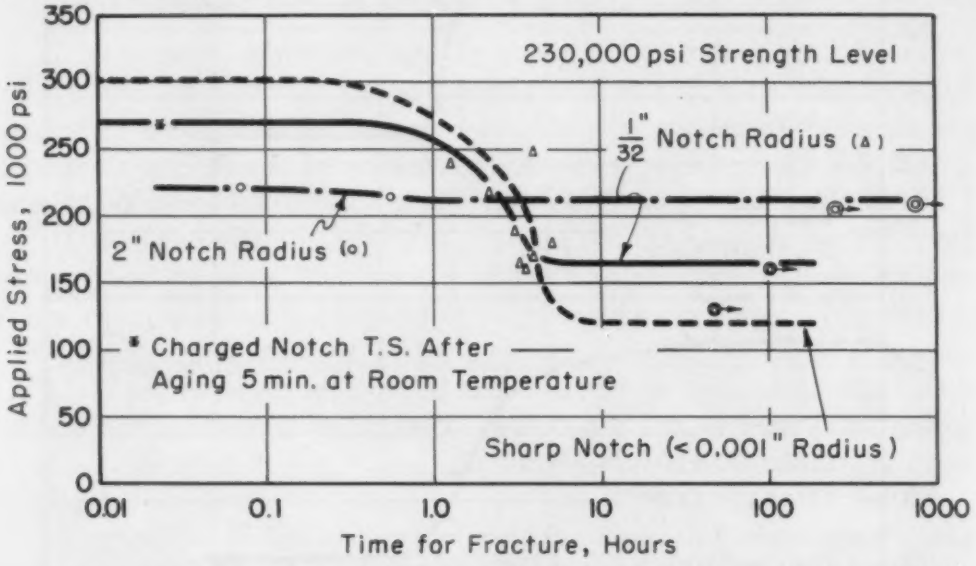


Fig. 9—Comparison of Stress Rupture Properties for Specimens of Different Notch Sharpnesses. (Charging condition A, aged 5 minutes).

while the 50% notch depth was held constant. Fig. 9 is a comparison of stress-rupture curves for specimens at the 230,000 psi strength level with three different notch acuities. It is immediately apparent that the lower critical stress value was raised as the notch acuity was decreased.

A similar comparison was made at the 270,000 psi strength level by conducting stress rupture tests on 2-inch radius specimens, as summarized in Table III. Again, failure occurred either immediately or not at all, depending upon the applied stress. The critical stress, in this case 225,000 psi, falls between the yield point and proportional limit of the material (cf. Fig. 2 and Table II).

An interesting set of relationships may be developed by a comparison of the upper and lower critical stress values given in Fig. 9. As the notch acuity was increased, the spread between the upper and lower critical stress values also increased and the ratio between the two is summarized in Table IV.[8]

[8] These ratios closely match the stress concentration factors for the respective notch geometries, although the precise quantitative physical significance of the ratio is not apparent.

Table III
Stress Rupture Tests on Charged 2-Inch Radius Specimens at the 270,000 Psi Strength Level

Applied Stress psi	Time to Fracture Hours	Reduction in Area at Fracture — %
240,000	0.3	2.3
230,000	0.2	2.9
230,000	0.55	2.3
220,000	Unbroken - 140 hours	—
220,000	Unbroken - 236 hours	—
200,000	Unbroken - 146 hours	—
200,000	1.6	*

* Fracture occurred away from minimum section. See Text.

Table IV
Comparison of Critical Load Values in Stress Rupture Tests

(Data from Fig. 9)

Notch Radius	Notch Tensile Strength - psi (A)	Minimum Critical Stress For Delayed Failure-psi (B)	Ratio A/B
<0.001 Inch	300,000	120,000	2.5
1/32 Inch	270,000	165,000	1.6
2 Inches	220,000	215,000	1.0

The necessity for exceeding some critical stress value to produce delayed failure has been clearly demonstrated by varying the notch acuity of the test specimen. For the sharp notch, with the highest degree of stress concentration, delayed failure was produced by the smallest load. The milder notch (1/32-inch radius) required a greater applied stress for flow at the root of the notch to take place. In the 2-inch radius specimen the stress concentration was very slight so that plastic flow was not highly localized.

On the other hand, in some abnormal cases fracture occurred at a point removed from the minimum section of the test piece (Table III), while in other instances, fracture took place under the head of the specimen at the 0.030 inch fillet. Some cases were even observed where the delayed failure took place in the shank of the specimen. This was traced to the presence of almost imperceptible circumferential grinding scratches and the seemingly anomolous behavior is readily understandable in the light of the previous discussion on the effect of stress raisers in the presence of hydrogen.

Effect of Aging Time on Stress Rupture Tests

Since the embrittlement characteristics indicate a strong dependence on aging, the effect of varying the room temperature aging time before applying a static load was examined. The procedure was to charge with hydrogen, age various times at room temperature, then apply a static load until failure.

At the 230,000 psi strength level (Fig. 10), the time to fracture was plotted as a function of the aging time for several values of applied

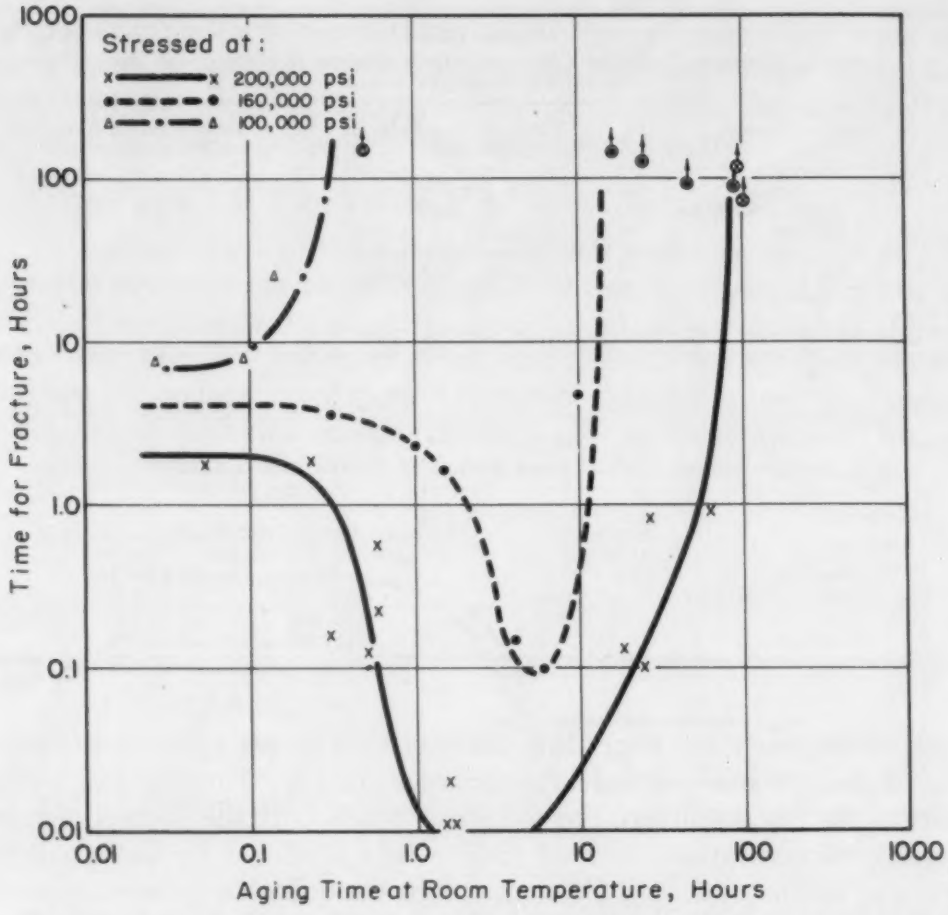


Fig. 10—Effect of Aging Time at Room Temperature on Time to Fracture for 4340 Steel Heat Treated to 230,000 Psi. (Charging condition A, sharp notch specimens).

stress. Note that these curves are of the same form as the aging curves previously discussed. At low values of applied stress, the sensitivity to delayed failure was lost in less than an hour, while for higher stresses, delayed failure occurred in specimens aged for a considerably longer time.

The same relationship may be examined by determining stress-rupture curves for various aging times. This approach was employed in studies at the 270,000 psi strength level, see Figs. 11 and 12. The stress dependence of time to failure was previously noted to be small for the five minute aging time, but at longer aging times (48 to 96 hours) a rather strong dependence was observed. It is instructive to present the relationships between aging time, applied stress and time to failure on a three-dimensional graph. The data of Figs. 10,11 and 12 are so treated in Figs. 13 and 14.

Aging 100 hours at room temperature subsequent to charging did not eliminate the phenomenon of delayed failure. However, after the same aging time of 100 hours, the reduction in area has recovered to its full uncharged value (Fig. 4). This means that delayed failure may

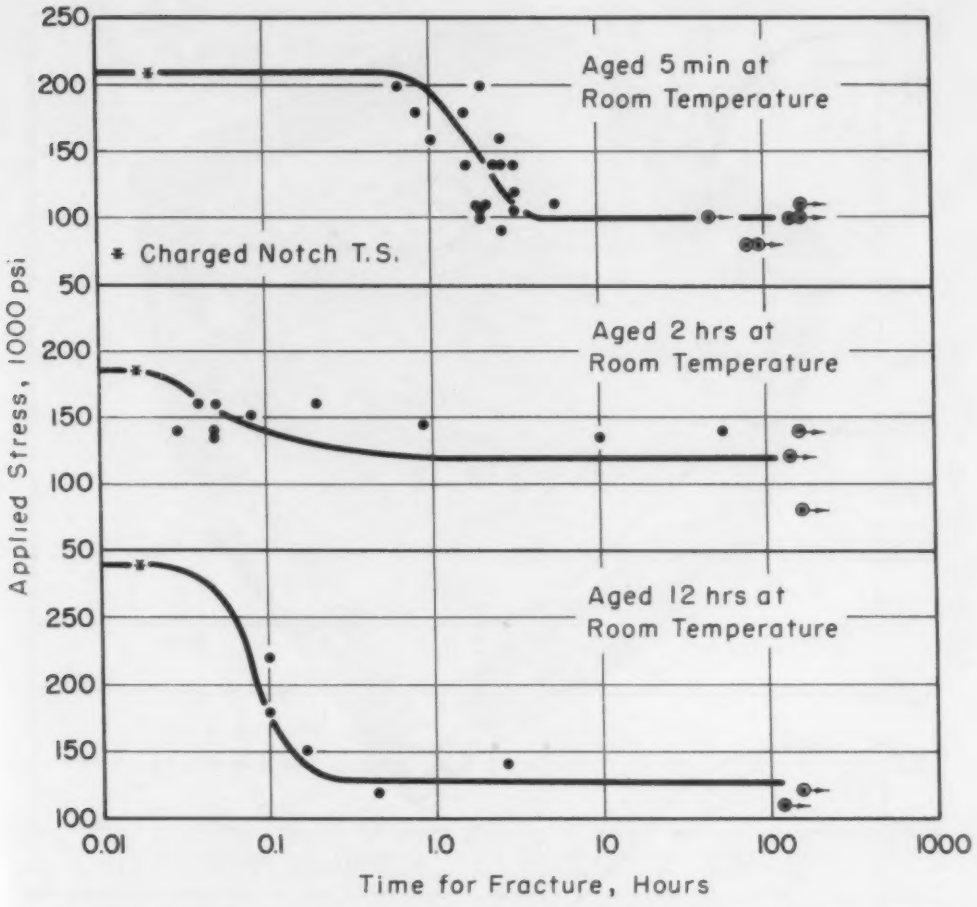


Fig. 11—Stress Rupture Tests on 4340 Steel Heat Treated to 270,000 Psi and Aged as Indicated. (Charging condition A, sharp notch specimens).

occur in a high strength steel which exhibits full ductility as determined by conventional tensile tests. Hence a normal value of reduction in area is no guarantee that delayed failure cannot occur. On the other hand, the notch tensile strength after an aging period of 100 hours still fell short of the uncharged value (Fig. 5) and may be a better measure of the recovery insofar as delayed failure is concerned. The lower critical stress, below which delayed failure did not occur, increased continuously with aging time. It is evident in both Figs. 13 and 14 that at longer times this value must increase quite rapidly.

Aging With and Without Applied Stress

Further examination of the stress rupture data broadens the picture of the role of flow which has already been considered in the discussion of the effects of notch acuity. In the delayed failure curves previously presented (Fig. 8, for example), it is evident that the time to failure is essentially aging time under load. This may be considered analogous to the aging curves for sharp notch specimens (as in Fig. 5) except for the fact that it is impossible to get data for times beyond the (minimum) inflection point, as the specimen would fracture.

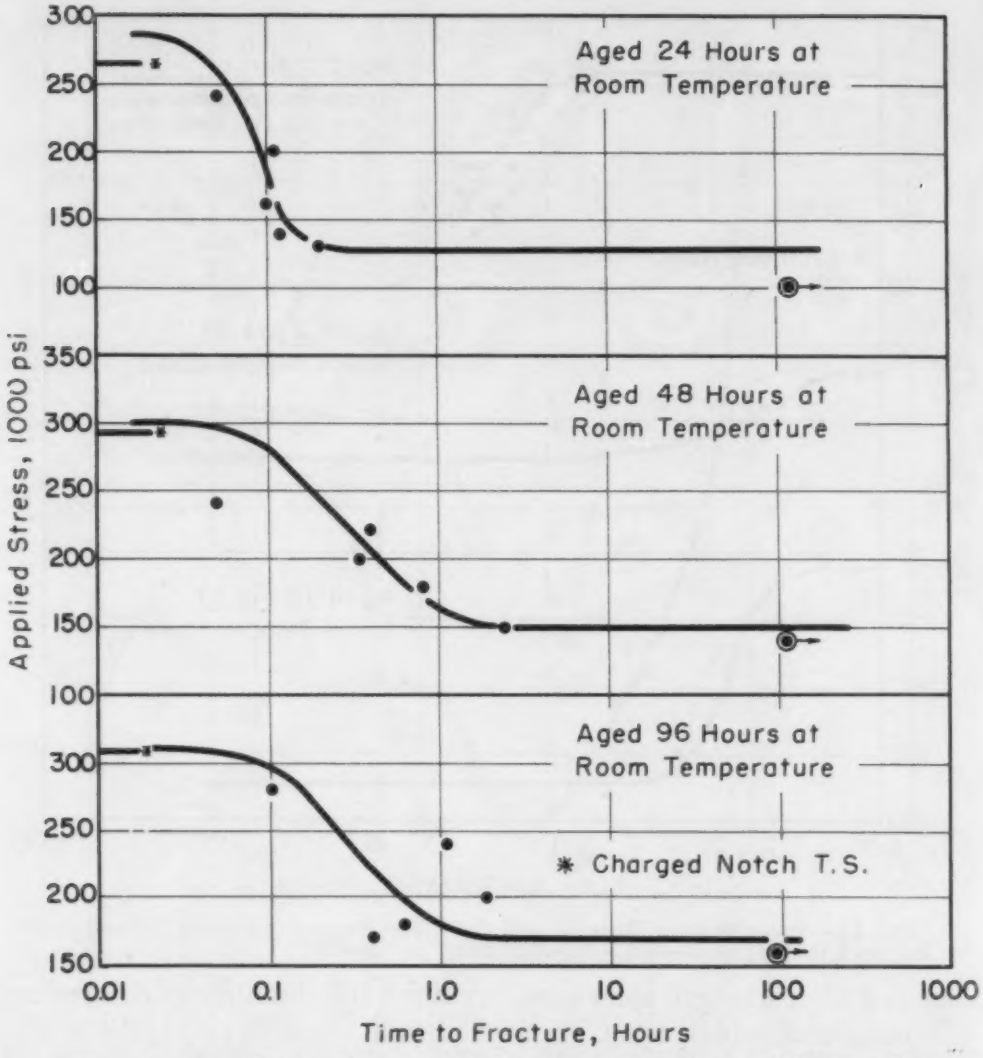


Fig. 12—Stress Rupture Tests on 4340 Steel Heat Treated to 270,000 Psi and Aged as Indicated. (Charging condition A, sharp notch specimens).

In order to determine the influence of aging under load on the recovery of ductility, unnotched tensile specimens (230,000 psi strength level) were aged for various times at an applied stress of 200,000 psi, then subjected to conventional tensile tests. There was no apparent difference in the reduction in area in the tensile test between specimens aged without load and those aged at a stress of 200,000 psi (Fig. 15). The applied stress of 200,000 psi was not capable of producing the minimum amount of plastic deformation which was required, since failure under static load did not occur. (Cf. Fig. 9).

Consider, however, the behavior of notched specimens at the 270,000 psi strength level as shown in Fig. 16. Aging at a stress of 140,000 psi, which was sufficient to produce delayed failure (Fig. 8) lowered the notch tensile strength below the value obtained by aging without load. The stress applied during aging was in excess of the critical value of stress associated with flow at the root of the notch. If a

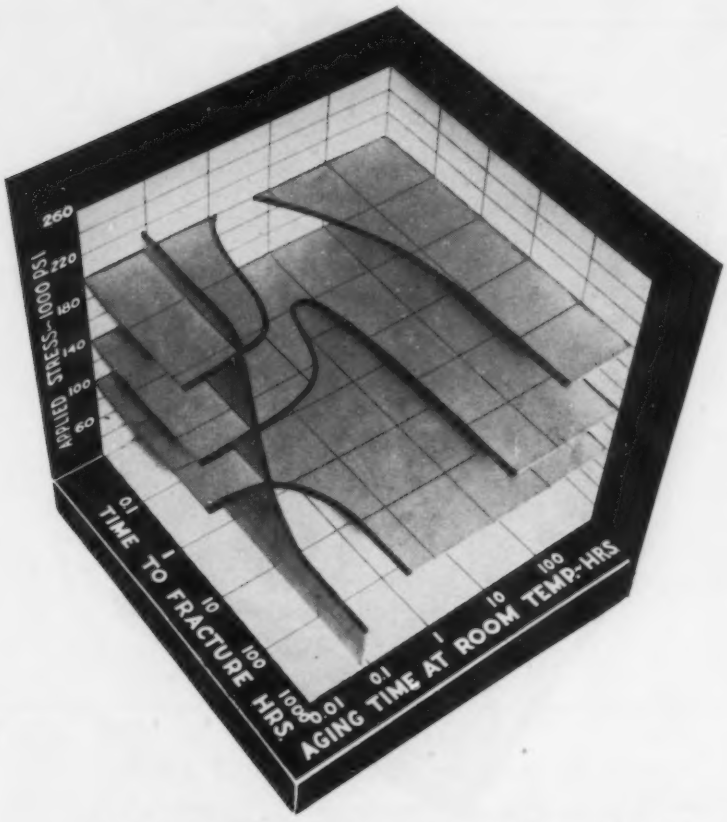


Fig. 13—Relationship Between Applied Stress, Aging Time at Room Temperature and Time to Failure. 230,000 psi strength level. (Charging condition A, sharp notch specimens).

line is drawn through the three solid points (aged at 140,000 psi) and extrapolated to short times, it tends toward convergence with an extension of the curve for aging without load. The increment of embrittlement, due to aging at a stress value in excess of the lower critical stress, increases as the aging time under load is prolonged.

At the applied stress of 140,000 psi failure resulted in several hours aging time. Longer aging times under load were attained at a stress below the lower critical value, this is also shown in Fig. 16. It is apparent that once again there is no difference between aging without load and aging at some stress, below a critical value, which is presumably associated with the initiation of plastic flow.

Further experiments were conducted in which notched specimens at the 230,000 psi strength level were aged alternately without load and at a stress in excess of the lower critical value. This is illustrated schematically in Fig. 17, for five different aging treatments. In all cases the specimens were charged, aged at no load, then a static stress of 160,000 psi was applied for the times indicated. Note that the applied stress of 160,000 psi is greater than the lower critical value of stress for the five minute aging time (Fig. 8).

In the first case (A), the conventional stress rupture test after

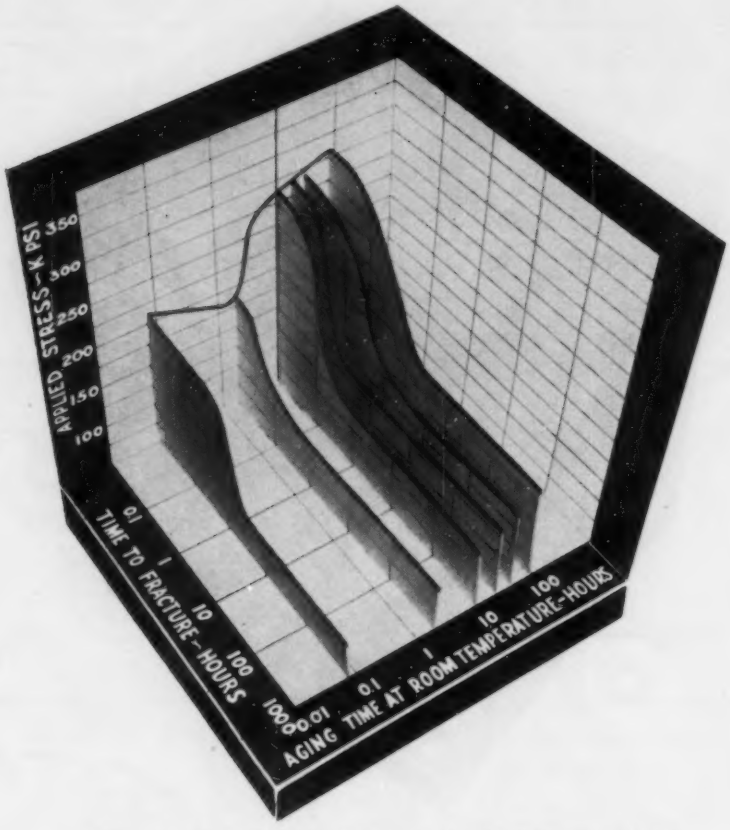


Fig. 14—Relationship Between Applied Stress, Aging Time at Room Temperature and Time to Failure. 270,000 psi strength level. (Charging condition A, sharp notch specimens).

a 3.6 hour aging period at no load, the specimen remained unbroken after 94 hours at an applied stress of 160,000 psi. Here the 3.6 hour age was sufficient to raise the lower critical stress value above the static stress which was applied, and the specimen did not break. In the second case (B), the load was immediately applied for 0.1 hours, then released for 3.5 hours. The specimen subsequently broke after aging 2.8 hours at the applied stress of 160,000 psi. This behavior illustrates the significance of the increase in the lower critical stress value with aging time at no load. These two treatments also confirm the deleterious effects of even a short time age at a stress greater than the lower critical stress value.

If a specimen was stressed at 160,000 psi for only 0.1 hours, aged at no load for 100 hours and subsequently subjected to the stress rupture test, delayed failure at an applied stress of 160,000 psi was not observed after 69 hours (Fig. 17, (C)).[9] If the initial aging under load was carried out for 3.5 hours (just short of failure) and then aged without load for 100 hours, the time to failure after reloading was 0.9

[9] The specimen was tested after aging an additional 800 hours at no load and had a notch tensile strength of 275,000 psi. This is substantially below the uncharged notch tensile strength as shown in Fig. 5 (230,000 psi strength level).

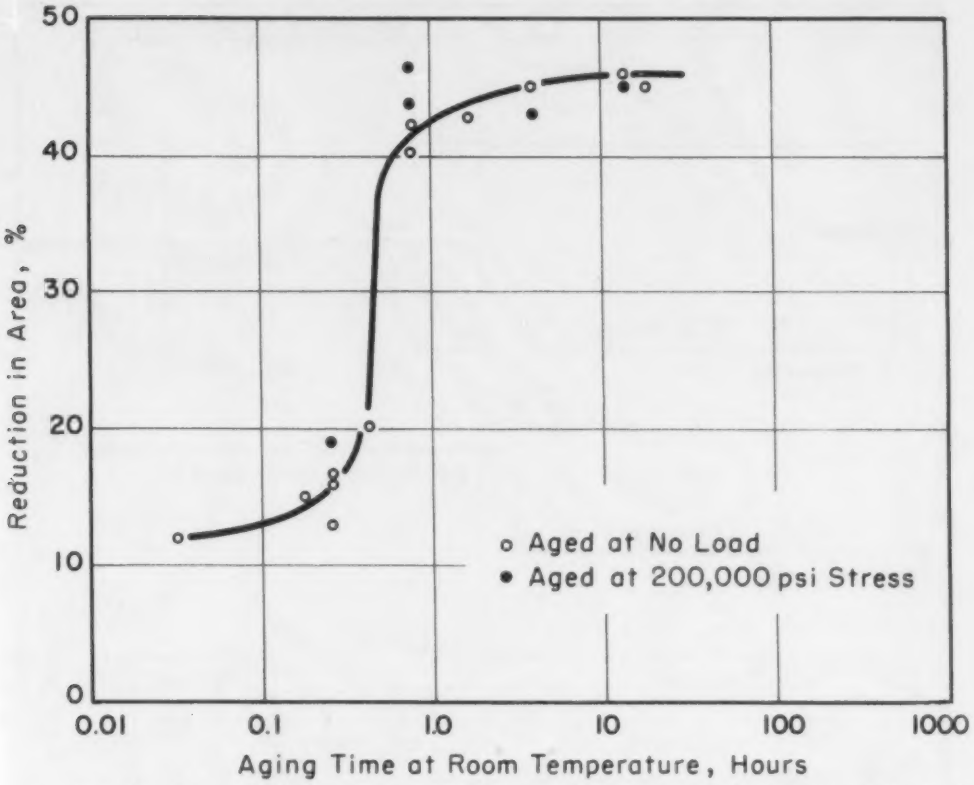


Fig. 15—Effect of Aging Charged Specimens at No Load and at 200,000 Psi Applied Stress. Unnotched specimens, 230,000 psi strength level. (Charging condition A).

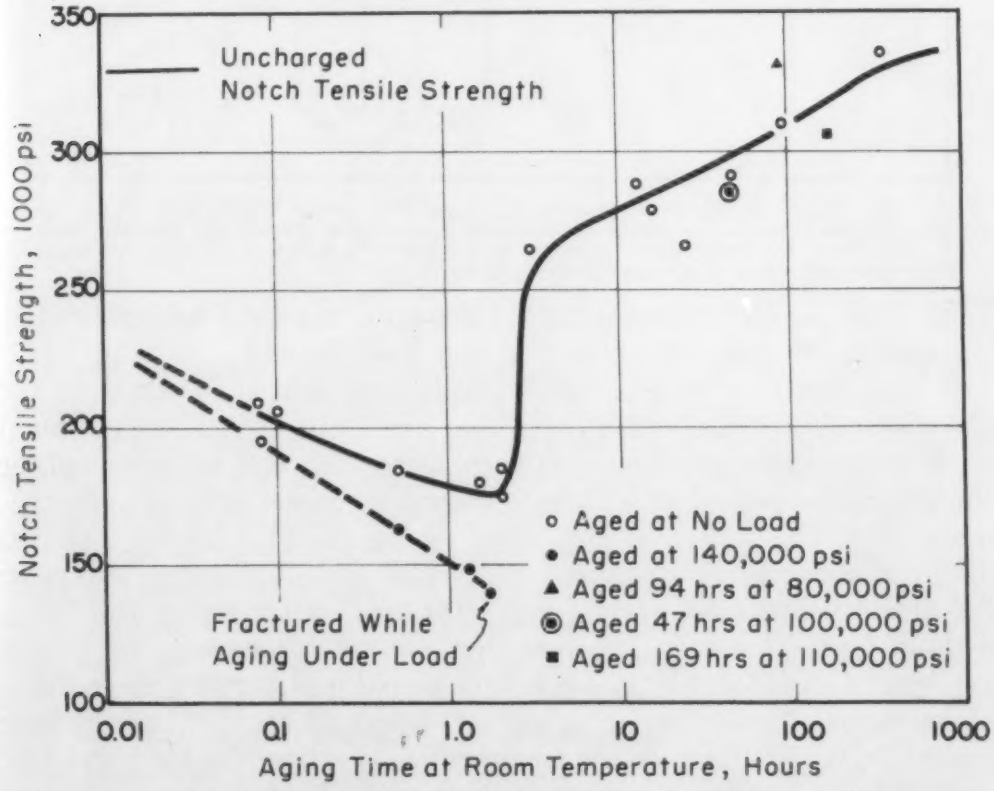


Fig. 16—Effect of Aging Charged Specimens With and Without Applied Stress. Sharp notch specimens heat treated to 270,000 psi. (Charging condition A).

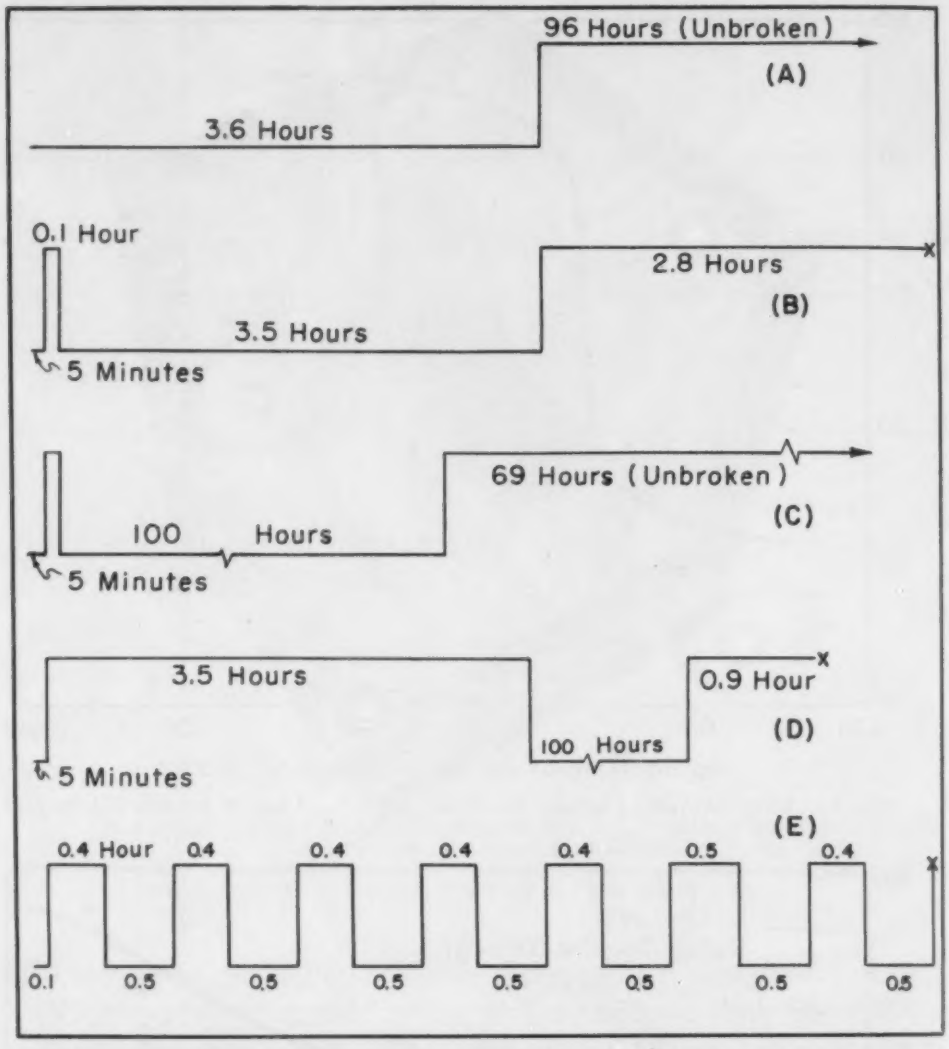


Fig. 17—Schematic Representation of Aging Treatments With and Without Applied Stress. Charging condition A, sharp notch specimens, 230,000 psi strength level. In each case, the lower line represents aging without applied stress and the upper line represents aging at an applied stress of 160,000 psi.

hours (D). The total time at load in this latter case was 4.4 hours while the total aging time after charging was 104.5 hours.

This behavior may be qualitatively rationalized in terms of the observations on aging with and without load (Fig. 16). There appeared to be only a slight difference between aging with and without load for the short time period of 0.1 hours according to the previous observations (Fig. 16). This was confirmed in Fig. 17 (C) by the fact that the brief initial aging treatment under load had no apparent effect on the stress rupture behavior (at 160,000 psi) after aging 100 hours without load. However, the fact that the notch tensile strength still exhibited a significant lack of recovery would lead one to believe that a higher applied stress, after aging 100 hours at no load, would have caused delayed failure. In the treatment (D) where the load was first applied for 3.5 hours, the effect of aging under load was severe enough

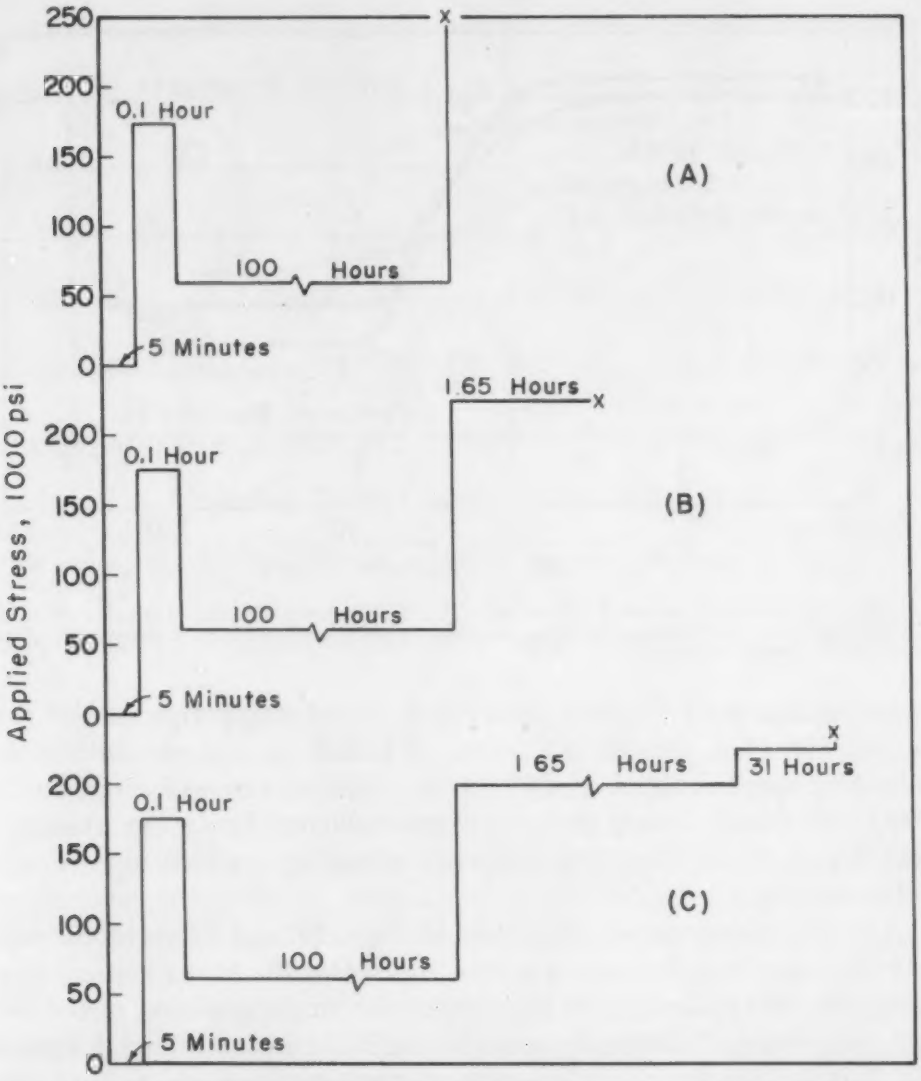


Fig. 18—Schematic Representation of Aging Treatments at Various Values of Applied Stress. Sharp notch specimens, 230,000 psi strength level, charging condition A.

to inhibit the loss of embrittlement (as measured by the stress-rupture test) after aging for 100 hours at no load.

The final treatment, Fig. 17 (E) consisted simply of cyclic aging between no load and an applied stress of 160,000 psi. The total elapsed time to failure was identical with that of treatment B.

Instead of aging at no load, other experiments were performed in which specimens were aged at applied stresses above and below the lower critical stress value. As illustrated in Fig. 18, three specimens were stressed 0.1 hours at 175,000 psi (above the critical stress), then aged 100 hours at 60,000 psi (below the critical stress value). The applied stress was then increased to the various values indicated. The initial treatment at 175,000 psi was sufficient to cause failure on loading to 250,000 psi (A), while in the second case (B) a stress of 225,000

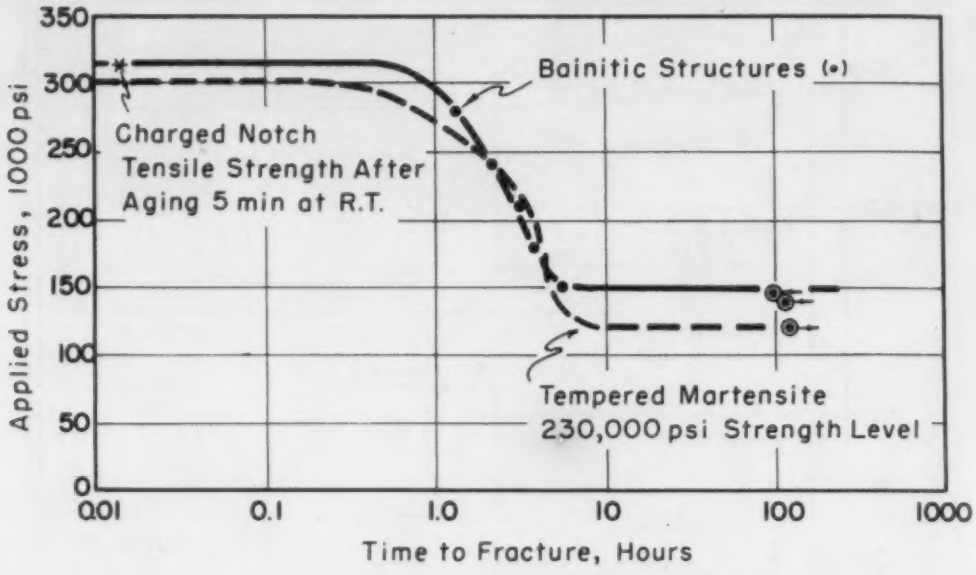


Fig. 19—Stress Rupture Tests on 4340 Steel. Tempered bainitic structure, 230,000 psi strength level. (Charging condition A, sharp notch specimens aged 5 minutes at room temperature before testing).

psi was sustained 1.65 hours after the initial treatment. In the third case, Fig. 18 (C), the static stress of 200,000 psi was not sufficient to produce delayed failure in 165 hours. The stress was increased to 225,000 psi for 31 hours and the specimen then broke on loading to 235,000 psi. Thus, the time between charging and failure is some 296 hours.

The aging treatments described in Figs. 17 and 18 vividly demonstrate the significance of aging above and below the lower critical stress value. This also makes possible a qualitative understanding of the wide range in times to failure reported in the field in commercial applications. For the charging conditions employed in this work, failure times have been produced which range from several minutes to several hundred hours between charging and failure. It is apparent that sequences of varying loads and times could be devised to produce failure at virtually any predetermined length of time.

Bainitic Structures

A fully bainitic structure tempered to 230,000 psi was produced for comparison with tempered martensite heat treated to the same strength level. The charged specimens with a bainitic structure followed basically the same behavior as the tempered martensite (Fig. 19) and the stress rupture curve was displaced slightly upward when compared with that of the tempered martensite. This displacement may be attributed to the fact that the residual stress state in an austempered structure is inherently less severe than that of a quenched and tempered structure. In other words, the martensite with its higher residual stress

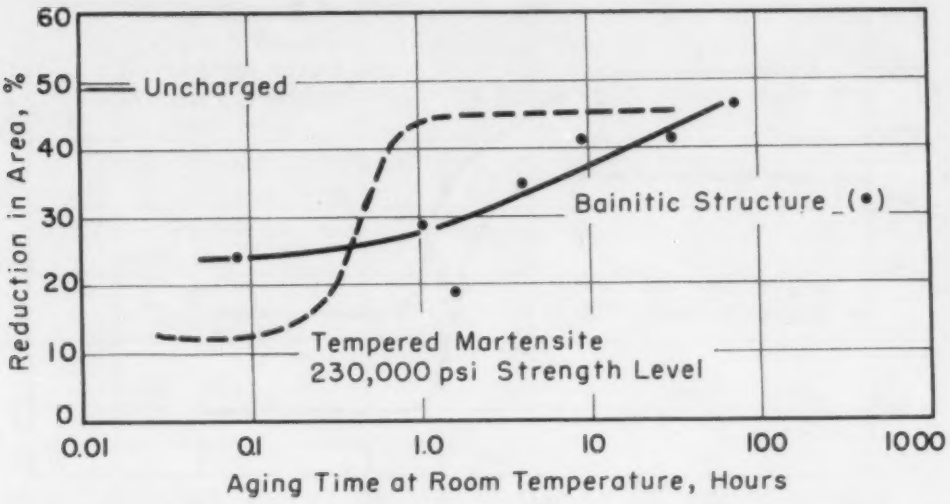


Fig. 20—Effect of Aging Time on Ductility of 4340 Steel Heat Treated to a 230,000 psi, Strength Level. Tempered bainitic structure. (Charging condition A, unnotched tensile tests).

state, required a smaller externally applied stress to cause delayed failure.

The room temperature aging characteristics of specimens with a bainitic structure are shown in Fig. 20. Again, the corresponding curve for tempered martensite has been superimposed. It is immediately apparent that the initial embrittlement is less severe for the bainite than for the martensite. In specimens with a bainitic structure, the recovery of ductility with aging time appeared markedly slower than the recovery of ductility for specimens with a tempered martensite structure.

It has been suggested that the decomposition of retained austenite under an applied stress in the presence of hydrogen may play a significant role in hydrogen embrittlement and delayed failure. The bainitic structure gave no indication of retained austenite when examined by X-ray diffraction, thus retained austenite does not play a primary role in hydrogen embrittlement and delayed failure.

Evaluation of Variables

One of the difficulties encountered in this work was the sporadic occurrence of scatter in the experimental data. This has been observed by others, and in some instances electrolytic charging has been abandoned in favor of thermal charging for this and other reasons. Zapffe and Haslem (13) for example, found two different charging curves (plot of bend angle versus charging time) for specimens taken from the two ends of a 50-foot coil of wire. Both chemical and metallographic analyses yielded no clue to the origin of this difference. A somewhat similar behavior was observed in this study and is shown in Fig. 21. The two series of specimens came from the same bar, but each series was

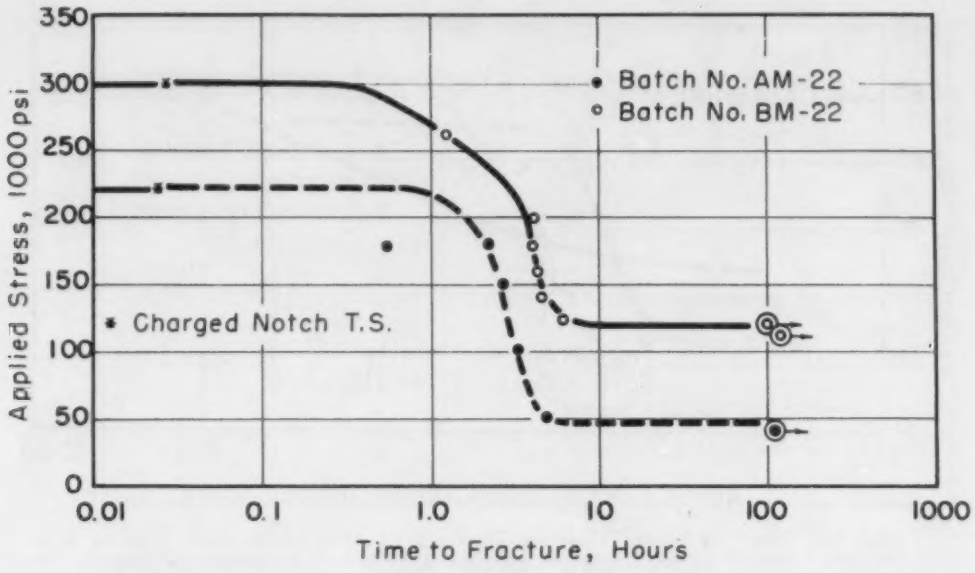


Fig. 21—Stress Rupture Tests on 4340 Steel Heat Treated to 230,000 Psi. (Charging condition A, sharp notch specimens). See text for details.

prepared separately. It is apparent that despite all the precautions to maintain uniformity between batches, some factor was different and gave the behavior observed in Fig. 21. The two curves, however, are internally consistent.

There are many factors which could affect the amount of hydrogen absorbed by the specimen; the obvious variables, current density, charging time, bath temperature, etc., were readily controllable. Every attempt was made to prevent the entrance of impurities into the electrolyte, as the presence of only minute amounts of substances which act as a "poison" would be sufficient to alter substantially the quantity of hydrogen absorbed by the specimen. A case has been cited in connection with Table V, where an apparently polished surface showed delayed failure away from the minimum section. This was subsequently traced to almost imperceptible circumferential scratches which had not been removed in the final polishing operation. The strain rate, aging temperature and testing temperature are also variables which could affect the results but which were held constant.

Perhaps the most difficult variables to evaluate would be those associated with the quenching operation, where any cooling rate greater than the critical cooling velocity would yield the same structure and the same properties by most testing standards. However, a considerable difference may exist in the residual stress state after quenching, and this might be manifest in some test such as the stress rupture tests performed here. The behavior reported in Fig. 21 is a case in point. The specimens from which the lower curve was obtained may have had a more severe concentration of residual stress than the specimens from which the upper curve was determined. In other words, the specimens

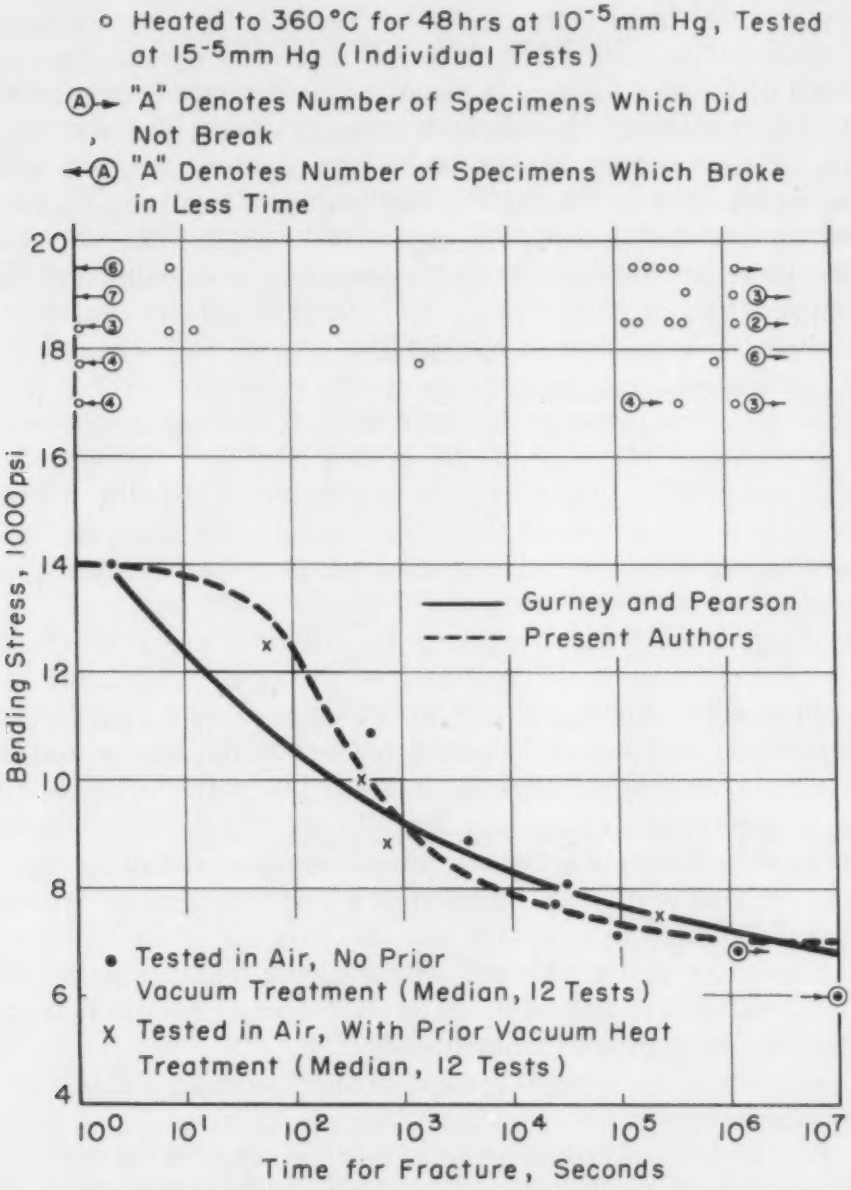


Fig. 22—Relationship Between Bending Stress and Time for Fracture for Annealed Glass Rods Tested in Air and in Vacuum. (Gurney and Pearson, Ref. 41).

were in essence preloaded and required a smaller applied stress to give delayed failure. This concept is further strengthened by the observations reported for specimens with a bainitic structure (Fig. 19). The upper curve then, gives a more nearly correct picture of the effect of an externally applied stress on time to failure, and was used previously in Fig. 8.

It was felt that the scatter encountered in this work did not have any serious effect on the validity of the data reported. It simply meant that care and judgment had to be exercised in the acceptance of data taken from each batch of specimens.

Summary and Conclusions

Each of the three concepts discussed in the introduction might be capable of explaining the observations reported. The questionable features of each theory have already been pointed out, but a model similar to that used in the Griffith crack concept is attractive, particularly when considering the data on delayed failure. The strong similarity between data obtained for glasses and steel is striking, and Fig. 22 has been reproduced from Gurney and Pearson (41) to illustrate this. The dashed curve has been added by the present authors, and the essential features of the stress-rupture curves as determined for steel are evident in this interpretation of their data. A hydrogen charged steel would correspond to glass in the atmosphere and uncharged steel would be comparable to glass tested in vacuum. Thus, the upper and lower critical stress values of the stress rupture test and the observed effects of aging with and without load would seem readily explicable by following the same line of argument as given for glass.

In summarizing, the foregoing investigation has resulted in the opening of three avenues of approach to the study of delayed failure and the presence of hydrogen in steel. Stress rupture curves have been determined and the effects of strength level, notch acuity and aging time at room temperature were considered. The patterns of the effects of these major variables have been established. The distribution studies are particularly interesting because they show that the distribution of hydrogen in steel is of major importance and that a small amount of hydrogen distributed in a certain way can produce drastic embrittling effects. Studies on aging with and without load, together with varying the notch acuity, have helped to clarify the role of plastic flow in delayed failure and hydrogen embrittlement.

As a result of the foregoing experimental work, a number of conclusions may be drawn:

1. Brittle delayed failure at relatively low applied stresses can be made to occur in steels electrolytically charged with hydrogen.

2. The sensitivity to delayed failure may persist after aging long enough for "full recovery" as measured by the reduction in area in tensile testing. Under certain conditions, the notch tensile strength may be a better index of the recovery.

3. Delayed failure under static load is attributed to the application of some minimum critical amount of stress in the presence of hydrogen. If stressed below this critical value which appears to be associated with plastic flow, delayed failure will not occur.

4. The minimum critical stress value is influenced by notch acuity, hydrogen distribution and aging time. This stress value exhibited only slight dependence upon strength level over the range studied.

5. The effects of aging under load depend upon the magnitude of

the load. If the applied stress is above some critical value, cumulative permanent damage occurs. If below the critical value, there appears to be no difference between aging with and without load.

6. Delayed failure occurs in the absence of retained austenite and therefore cannot be attributed to austenite decomposition.

7. Distribution studies have shown that there are two factors to consider, one the depth of hydrogen penetration and two, an intensity factor or the degree of embrittlement, associated with concentration.

References

1. L. J. Klingler, W. J. Barnett, R. P. Frohmberg and A. R. Troiano, "The Embrittlement of Alloy Steel at High Strength Levels," TRANSACTIONS, American Society for Metals, Vol. 46, 1954, p. 1557.
2. R. W. Buzzard, H. E. Cleaves, "Hydrogen Embrittlement of Steel Review of the Literature," National Bureau of Standards Circular 511, 1951, 29 pages.
3. C. E. Sims, "The Behavior of Gases in Solid Iron and Steel," GASES IN METALS, American Society for Metals, Symposium, 1952.
4. D. P. Smith, "Fundamental Metallurgical Thermodynamic Principles of Gas-Metal Behavior," GASES IN METALS, American Society for Metals, Symposium, 1952.
5. D. P. Smith, "Hydrogen in Metals," The University of Chicago Press, 1948.
6. C. A. Zapffe, C. E. Sims, "Hydrogen Embrittlement and Defects in Steel," *Transactions,* American Institute of Mining and Metallurgical Engineers, Vol. 145, 1941, p. 225.
7. S. F. Carter, "Effect of Melting Practice on Hydrogen," *Journal of Metals* American Institute of Mining and Metallurgical Engineers, Vol. 188, January 1950, p. 30 and *Journal of Metals* American Institute of Mining and Metallurgical Engineers, Vol. 188, February 1950, p. 245.
8. C. Sykes, H. H. Burton, C. C. Geggs, "Hydrogen in Steel Manufacture," *Journal,* Iron and Steel Institute, Vol. 156, 1947, p. 155.
9. S. Marshall, T. M. Garvey and D. S. Llewelyn, "Relationship Between Hydrogen Content and Ductility of Steels," *Electric Furnace Steel Proceedings,* American Institute of Mining and Metallurgical Engineers, Vol. 6, 1948, p. 59.
10. F. B. Foley, "Flakes and Cooling Cracks in Forgings," *Metals and Alloys,* Vol. 12, 1940, p. 442.
11. F. J. Shortsleeve, A. R. Troiano, "A Literature Survey on the Mechanism of Flake Formation," Interim Technical Report No. 1, Contract No. DA 33-019-ORD-897.
12. C. A. Edwards, "Pickling or the Action of Acid Solution on Mild Steel and the Diffusion of Hydrogen Through the Metal," *Journal,* Iron and Steel Institute, Vol. 110, 1924, p. 9.
13. C. A. Zapffe, M. E. Haslem, "Acid Composition, Concentration, Temperature and Pickling Time as Factors in the Hydrogen Embrittlement of Mild Steel and Stainless Steel Wire," TRANSACTIONS, American Society for Metals, Vol. 39, 1947, p. 213.
14. J. R. Gustafson, "Some of the Effects of Cadmium, Zinc, and Tin Plating on Springs," *Proceedings,* American Society for Testing Materials, Vol. 47, 1947, p. 782.
15. K. B. Valentine, "Stress Cracking of Electroplated Lockwashers," TRANSACTIONS, American Society for Metals, Vol. 38, 1947, p. 488.
16. C. A. Zapffe, M. E. Haslem, "Measurement of Embrittlement During Chromium and Cadmium Electroplating and the Nature of Recovery of

Plated Articles," TRANSACTIONS, American Society for Metals, Vol. 39, 1947, p. 241.

17. J. D. Hobson, C. Sykes, "Effect of Hydrogen on the Properties of Low Alloy Steels," *Journal,* Iron and Steel Institute, Vol. 169, 1951, p. 209.
18. P. Bardenheuer, H. Ploum, "Das Eindringen von Messinglot in den Stahl als Folge der Wasserstoffaufnahme beim Beisen," *Mitt Kais-Wilh-Inst fur Eisenforsch,* Vol. 16, 1934, p. 137.
19. C. A. Zapffe, M. E. Haslem, "A Test for Hydrogen Embrittlement and its Application to 17 Percent Chromium, 1 Percent Carbon Stainless Steel Wire," *Transactions,* American Institute of Mining and Metallurgical Engineers, Vol. 167, 1946, p. 281.
20. J. D. Hobson, J. Hewitt, "The Effect of Hydrogen on the Tensile Properties of Steel," *Journal,* Iron and Steel Institute, Vol. 173, 1953, p. 131.
21. J. B. Seabrook, N. J. Grant, D. Carney, "Hydrogen Embrittlement of SAE 1020 Steel," *Transactions,* American Institute of Mining and Metallurgical Engineers, Vol. 188, 1950, p. 1317. Discussion, *Journal of Metals,* July 1951, p. 588.
22. C. E. Sims, "Hydrogen Elimination of Aging," *Transactions,* American Institute of Mining and Metallurgical Engineers, Vol. 188, 1950, p. 1321.
23. L. S. Darken and R. P. Smith, "Behavior of Hydrogen in Steel During and After Immersion in Acid," *Corrosion,* Vol. 5, 1948, p. 1.
24. P. Bardenheuer, H. Ploum, "Die Wasserstoffbruchigkeit des Stahles in Abhangeigkeit von der aufgenommenen Wasserstoffmenge," *Mitt Kais-Wilh-Inst fur Eisenforsch,* Vol. 16, 1934, p. 129.
25. D. J. Murphy, "Metallurgical Activities in Japan," METAL PROGRESS, Vol. 65, No. 1, January 1954, p. 67.
26. C. A. Zapffe, O. G. Specht, "Effect of Composition, Heat Treatment, and Cold Work on the Hydrogen Embrittlement of Stainless Steel Wire During Cathodic Pickling," TRANSACTIONS, American Society for Metals, Vol. 39, 1947, p. 193.
27. T. C. Poulter, L. Uffelman, "The Penetration of Hydrogen Through Steel at 4000 Atmospheres," *Physics,* Vol. 3, 1932, p. 147.
28. P. W. Bridgman, "The Physics of High Pressure," G. Bell & Sons, Ltd. (London), (1949), p. 96.
29. P. Bastien, P. Azou, "Discussion on Hydrogen Embrittlement of SAE 1020 Steel," by Seabrook, Grant and Carney, *Transactions,* American Institute of Mining and Metallurgical Engineers, Vol. 191 (1951), pp. 559–560.
30. P. Bastien, P. Azou, "Effect of Hydrogen on the Deformation and Fracture of Iron and Steel in Simple Tension," PROCEEDINGS OF FIRST WORLD METALLURGICAL CONGRESS 1951, p. 535, American Society for Metals.
31. N. J. Petch, P. Stables, "Delayed Fracture of Metals Under Static Load," *Nature,* Vol. 169, No. 4307, May 17, 1952, p. 842.
32. J. T. Brown, W. M. Baldwin, Jr., "Hydrogen Embrittlement of Steels," *Journal of Metals,* American Institute of Mining and Metallurgical Engineers, February 1954, p. 298.
33. V. Stefanides, Discussion to reference 15 (Valentine), TRANSACTIONS, American Society for Metals, Vol. 38, 1947, p. 495.
34. S. C. Langdon, M. A. Grossmann, "The Embrittling Effects of Cleaning and Pickling upon Carbon Steels," *Transactions,* American Electrochemical Society, Vol. 37, 1920, p. 543.
35. C. T. Eakin, H. W. Lownie, Jr., "Reducing Embrittlement in Electro Plating," *The Iron Age,* November 21, 1946, p. 69.
36. G. A. Moore, D. P. Smith, "Occlusion and Evolution of Hydrogen by Pure Iron," *Transactions,* American Institute of Mining and Metallurgical Engineers, Vol. 135, 1939, p. 255.

37. E. H. Bucknall, W. Nicholls, L. H. Toft, "Delayed Cracking in Alloy Steel Plates," *Symposium on Internal Stresses in Metals and Alloys,* Institute of Metals, 1948, (Institute of Metals Monograph and Report Series No. 5).

38. L. Luckemeyer-Hasse, H. Schenck, "Solubility of Hydrogen in Several Metals and Alloys," *Archiv, Eisenhuttenwesen,* Vol. 6, 1932, p. 209.

39. D. J. Carney, J. Chipman, N. Grant, "An Introduction to Gases in Steel," Electric Furnace Steel *Proceedings,* American Institute of Mining and Metallurgical Engineers, Vol. 6, 1948, p. 34.

40. E. Orowan, "The Fatigue of Glass Under Stress," *Nature,* Vol. 154, No. 3906, September 9, 1944, p. 341.

41. C. Gurney, S. Pearson, "The Effect of Surrounding Atmosphere on the Delayed Fracture of Glass," *Proceedings,* Physical Society, Vol. 62, No. 8 August 1, 1949, p. 469.

42. A. A. Griffith, "The Phenomena of Rupture and Flow in Solids," *Philosophical Transactions,* Royal Society, Series A, Vol. 221, 1920, p. 163.

43. A. A. Griffith, "The Theory of Rupture," *Proceedings,* First International Congress for Applied Mechanics, Delft, 1924, p. 55.

44. F. W. Preston, "The Mechanical Properties of Glass," *Journal of Applied Physics,* Vol. 13, October 1942, p. 623.

45. T. C. Baker, F. W. Preston, "Fatigue of Glass Under Static Loads," *Journal of Applied Physics,* Vol. 17, March 1946, p. 170.

46. A. H. Cottrell, *Dislocations and Plastic Flow in Crystals,* Oxford, 1953.

47. F. Wever, B. Pfarr, "Uber die Gitterparameteranderung Des a-Eisens Bei der Wasserstoffbaldung," *Mitt Kaiser-Wilhelm Inst.* Vol. 15, 1933, p. 147.

48. C. A. Zapffe, "The Iron Hydrogen Binary System," METALS HANDBOOK, 1948, p. 1208, American Society for Metals.

49. H. C. Rogers, "A Yield Point in Steel Due to Hydrogen," ACTA METALLURGICA, Vol. 2, No. 1, January 1954, p. 167.

EFFECTS OF VARIATION IN NORMALIZING AND TEMPERING PROCEDURE ON STRESS RUPTURE STRENGTH, CREEP EMBRITTLEMENT AND NOTCH SENSITIVITY FOR A Cr-Mo-V AND A 17 Cr-4Ni-Cu STEEL

By M. H. Jones, D. P. Newman, G. Sachs, and W. F. Brown, Jr.

Abstract

The paper describes a systematic investigation of the influence of several heat treating variables on the notch and smooth stress rupture strength and smooth ductility of a Cr-Mo-V and a 17Cr-4Ni-4Cu steel. For the Cr-Mo-V steel the variables were the normalizing temperature, the tempering temperature and the tempering time. All tests on this steel were conducted at 1000 °F. For the 17Cr steel the variables were tempering temperature and test temperature.

It is shown that both notch sensitivity and smooth ductility for both alloys are greatly influenced by the heat treatment. High normalizing temperatures are particularly damaging to the ductility and the notch strength of the Cr-Mo-V steel. This effect appears to be independent of the grain size at least below the temperature of rapid austenite grain coarsening. Optimum tempering treatments can be found for either alloy which greatly reduce notch sensitivity at a given testing temperature and involve only a relatively small reduction in the smooth strength.

Loss of stress rupture ductility and notch sensitivity in a normalized Cr-Mo-V steel is apparently associated with a carbide precipitation which can occur either during tempering or during testing. If the precipitate occurs during testing, its embrittling effects are much more severe than if it occurs during tempering. An analysis is presented which indicates the smooth rupture strength is not increased by precipitation during testing at 1000 °F but is reduced by the presence of the embrittling precipitate.

Introduction

NUMEROUS investigations have shown the creep strength of low alloy steel to be sensitive to heat treating procedure. However, only a comparatively small amount of published data relates to

The authors, M. H. Jones, D. P. Newman and W. F. Brown, Jr., are associated with the National Advisory Committee for Aeronautics, Lewis Flight Propulsion Laboratory, Cleveland and G. Sachs is associated with Syracuse University, Syracuse, New York and is a Consultant to NACA. Manuscript received May 11, 1954.

such effects on high-temperature stress-rupture properties and particularly to creep embrittlement associated with variations in heat treatment.

According to a survey by Bennek and Bandel (1)[1] covering the period to 1943, the creep properties are influenced both by type and distribution of carbides present and also by grain size. In the case of low alloy steels a structure consisting of a mixture of pearlite and bainite (such as is often formed by normalizing) was generally found to yield superior creep strength compared to structures obtained by quenching and tempering. For most alloys an increase in grain size appeared to increase creep resistance.

More recently the influence of a number of interrelated structural variables on creep resistance of low alloy chromium-molybdenum steels has been investigated by Delbart and Ravery (2,3,4). The data is not easily interpreted because the structures produced by various heat treatments were difficult to define and because there is considerable scattering associated with low creep rate data. It was found that no particular heat treatment (structure) could be considered optimum for all test conditions investigated. However, structures produced by normalizing, particularly from high austenitizing temperatures and tempering at 112 °F (600 °C) (mixture of bainites and pearlite) yielded consistently high creep resistance. The properties of isothermally transformed structures were strongly dependent on the test conditions. Structures consisting of tempered martensite possessed low creep resistance except in the case of a low carbon steel where the resulting structure also contained lower bainite.

An investigation now in progress (5) compares the stress rupture properties of isothermally transformed structures of a chromium-molybdenum-vanadium steel with those obtained by normalizing and tempering. The results indicate that normalized and tempered structures yield consistently high stress-rupture strengths at test temperatures between 900 and 1200 °F (480 and 650 °C).

The above described investigations which attempt to use structure as the independent variable are open to the objection that it is difficult to clearly define the structures. Small, undetectable changes in carbide distribution can produce considerable variations in creep properties (6).

In several investigations Glen (7), (8) varied both the normalizing and the tempering procedure for a series of molybdenum, chromium-molybdenum and molybdenum-vanadium steels. It was shown that increasing normalizing temperature from 1560 to 1830 °F (850 to 1000 °C) of subsequently tempered specimens of a molybdenum-vanadium steel increased the creep resistance and that this increase became more pronounced as testing time increased. It

[1] The figures appearing in parentheses pertain to the references appended to this paper.

also was shown that the effect of increasing tempering time is to first increase and then to decrease creep strength. The optimum time depended on alloy composition, tempering temperature and test temperature.

Glen (7) also investigated the effect of normalizing and tempering procedures on the stress-rupture strength of these steels. The data indicates the effects of variation in normalizing temperature to be within the limits of scattering. Regarding the effect of tempering, long time rupture tests (in excess of 1000 hours) at 1105 and 1200 °F (595 and 650 °C) showed a 0.12% carbon, 0.54% molybdenum, 0.27% vanadium steel to be weakened with an increase in the tempering time (up to 40 hours). However, at short times to rupture the effect of tempering time was greatly reduced. In general, it appears that conditions yielding the highest stress rupture strength resulted in the lowest elongations.

As pointed out previously by the authors (11) there is insufficient published data to define the effects of heat treatment on creep notch sensitivity. However, a few tests by Clark (9) and Thum and Richard (10) showed that the rupture ductility of low alloy steels decreased rapidly as normalizing temperature increased above a certain temperature and it might be expected that such structures would be notch sensitive.

Based on the above evidence and on the authors previous work relating to notch sensitivity (11,12,13), the following general conclusions are proposed:

1. Normalizing and tempering of low alloy chromium-molybdenum and chromium-molybdenum-vanadium steels yields high creep resistance and high rupture strength under most conditions of testing. This heat treatment is preferred in this country and in Europe where section size permits sufficiently rapid cooling rates. However, only very limited systematic data relates stress rupture properties to variations in normalizing and tempering procedures.

2. Both creep resistance and rupture strength can be raised by increasing normalizing temperature and in some cases, by reducing tempering temperature. However, these improvements may be accompanied by low ductilities.

3. There are indications that loss in rupture ductility is frequently associated with high notch sensitivity. Therefore, a heat treatment yielding high strength but low ductility may be unsuitable for severe service applications.

For the present investigation two alloys have been selected, a low alloy chromium-molybdenum-vanadium steel and the precipitation-hardenable ferritic stainless steel 17–4PH. The general objective of the present work was to obtain more detailed information regarding conclusions 2 and 3 stated above. Specifically the investigation was

directed toward a determination of: (a) influence of normalizing temperature on both conventional (smooth) rupture properties and on notch-rupture properties, (b) influence of tempering temperature and time on smooth and notch rupture properties, (c) possible relationships between time-temperature dependent embrittlement observed in stress rupture tests and that produced by variations in heat treating procedure, and (d) heat treatment conditions yielding optimum combinations of smooth strength and notch properties for severe service applications.

Material and Procedure

The composition of 17–22A(S) and 17–4PH is reported in Table I. Specimen blanks were cut from one inch diameter hot-rolled

Table I
Composition of Alloys Investigated

Alloy	Composition, percent								
	C	Cr	Ni	Mo	Mn	Si	Fe	Cu	Others
17-22 A(S)	0.33	1.23	0.23	0.53	0.57	0.68	Bal.	0.16	0.24 V
17-4PH	0.05	17.86	4.43		0.64	0.33	Bal.	3.91	0.36 Cb

Table II
Heat Treating Schedule

Alloy	Austenitizing temperature, °F (½ hr)	Tempering temperature, °F	Tempering time, hr
1722 A(S)	1650	1200	6
	1725 *	1200	6
	1850	1200	6
	1975	1200	6
	2075	1200	6
	2075→1725 **	1200	6
	1850→1725 **	1200	6
	1725	Room	
	1725	800	6
	1725	1100	6
	1725	1100	20
	1725	1200	2
	1725	1200	6
	1725	1200	20
	1725	1300	0.5
	1725	1300	2
	1725	1300	6
	1725	1300	20
17-4PH	1900	1000	0.5
	1900	1100	0.5

* Conventional heat treatment
** Double normalizing

and annealed bar stock and heat treated before machining. For each alloy all specimens were made from the same heat. The heat treating schedule is shown in Table II.[2] Normalizing was done in a circulating air furnace and specimens were air-cooled by scattering on the floor. It will be noted that two series of 17-22A(S) blanks were given

[2] The conventional heat treatment (1725 °F, ½ hour; 1200 °F, 6 hours) referred to in this table is that used previously by the authors and is considered to be normal practice for 17-22A(S).

"double normalizing" treatments which consisted of holding ½ hour at either 2075 or 1850 °F (1135 or 1010 °C) and then furnace cooling to 1725 °F (940 °C) and holding again for ½ hour. Tempering was also done in a circulating air furnace, the blanks being air-cooled from the tempering temperature. An additional series of tests not shown in Table II performed on 17-22A(S) consisted of a complete reheat treatment (1725 °F, ½ hour; 1200 °F, 6 hours) after normalizing at 2075 (1135 °C) and at 1850 °F (1010 °C).

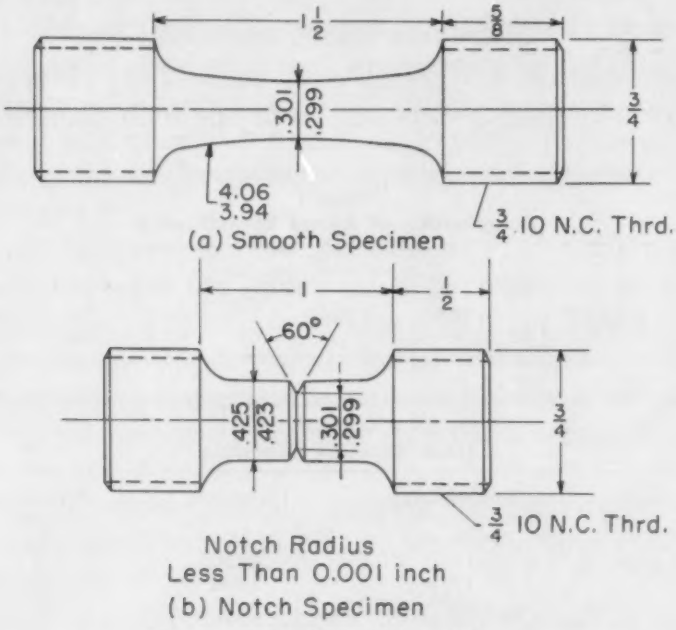


Fig. 1—Stress Rupture Specimens.

Notch and smooth specimens, Fig. 1, were tested for each condition of heat treatment to establish the stress rupture strength over the time range from approximately 0.1 to 1000 hours. All specimens of 17-22A(S) alloy were tested at 1000 °F (540 °C), a temperature of practical importance for many applications. A series of test temperatures, namely, 300, 450, 600, 700 and 800 °F (150, 230, 315, 370 and 425 °C) were employed for 17-4PH. Details of testing technique have been adequately described elsewhere (12). Hardness values reported are the average of at least five readings taken on the ends of specimen blanks or on blanks of similar size after removal of the decarburized layer by flood grinding. Photomicrographs were obtained on sections cut from these blanks.

The reduction of area after fracture was determined for both smooth and notch specimens and the values reported are referred to as smooth and notch ductility respectively.

Results For 17-22A(S)

The data relating to hardness and rupture strength of 17-22A(S) are assembled in Figs. 2 to 8. In representations of effects of either

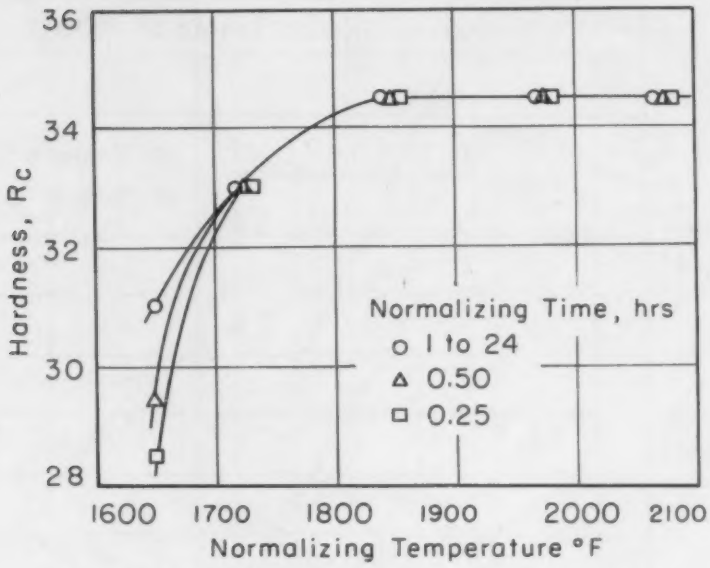


Fig. 2—Hardness as a Function of Normalizing Temperature and Time for 17-22A (S) Tempered 1200 °F for 6 Hours.

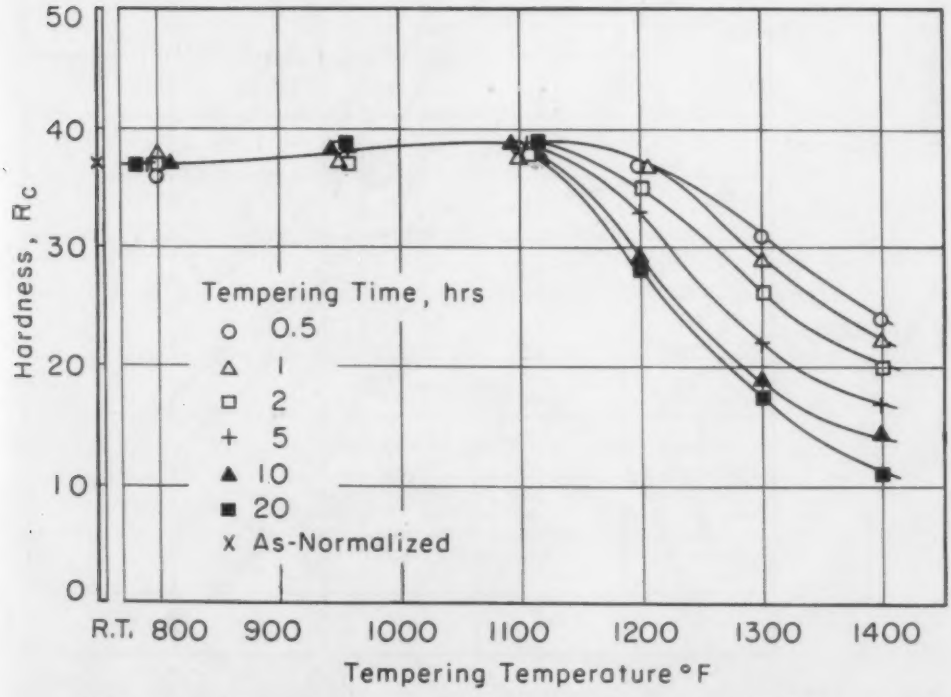


Fig. 3—Hardness as a Function of Tempering Temperature and Time for 17-22A (S) Normalized 1725 °F for ½ Hour.

tempering temperature or tempering time, the as normalized properties are plotted at room temperature or zero time, respectively. The effects of the heat treating variables on embrittlement as revealed by the notch test and the ductilities will be presented later.

Hardness:—The influence of normalizing temperature and time on the hardness of specimens tempered 6 hours at 1200 °F (650 °C) is shown in Fig. 2. The hardness increases with normalizing temperature

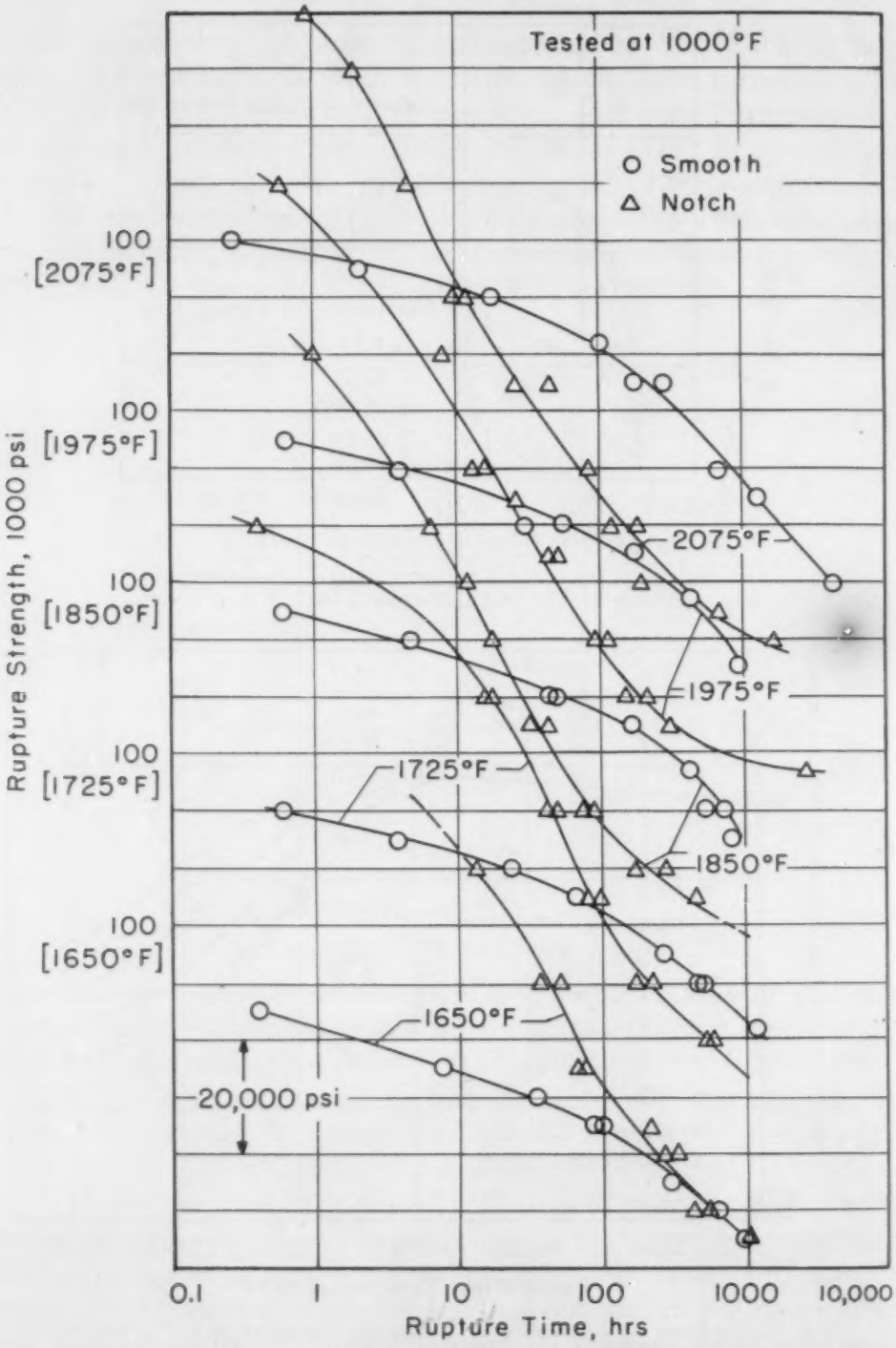


Fig. 4—Smooth and Notch Rupture Strength for 17-22A (S) Normalized ½ Hour at Several Temperatures and Tempered at 1200 °F for 6 Hours.

up to a temperature of 1850 °F (1010 °C) after which it remains constant. An increase in hardness with increasing normalizing time is noticeable only at a normalizing temperature of 1650 °F (900 °C).

The influence of tempering temperature and time on the hardness of specimens normalized for ½ hour at 1725 °F (940 °C) is shown in Fig. 3. For temperatures between 800 and 1100 °F (425 and

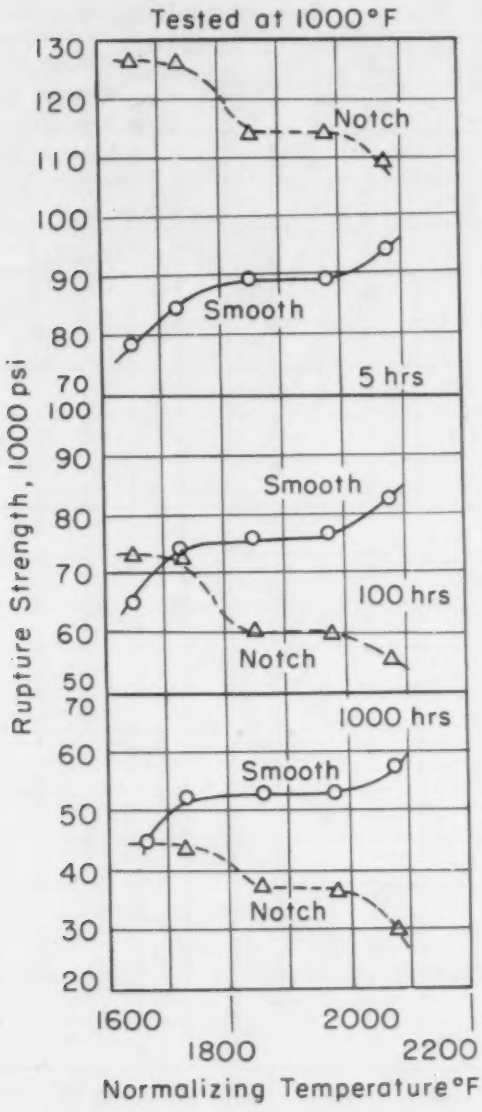


Fig. 5—Smooth and Notch Rupture Strength as a Function of Normalizing Temperature at Various Rupture Times for 17-22A (S) Tempered at 1200 °F for 6 Hours.

595 °C) the hardness is not affected by the time of tempering within the limits of test accuracy. In this temperature range there is a slight increase in hardness with increasing tempering temperature to a value of 39 Rockwell C at 1100 °F (595 °C). Above 1100 °F (595 °C) the hardness decreases rapidly with both increasing temperature and time.

Effect of Normalizing Temperature on Rupture Strength:—The influence of normalizing temperature on smooth and notch rupture strength of specimens tempered at 1200 °F (650 °C) for 6 hours is shown in Fig. 4. In general, the time dependence of the notch effect is fundamentally similar to that reported previously for a number of alloys (12). At 1650 °F (900 °C) apparently no notch sensitivity

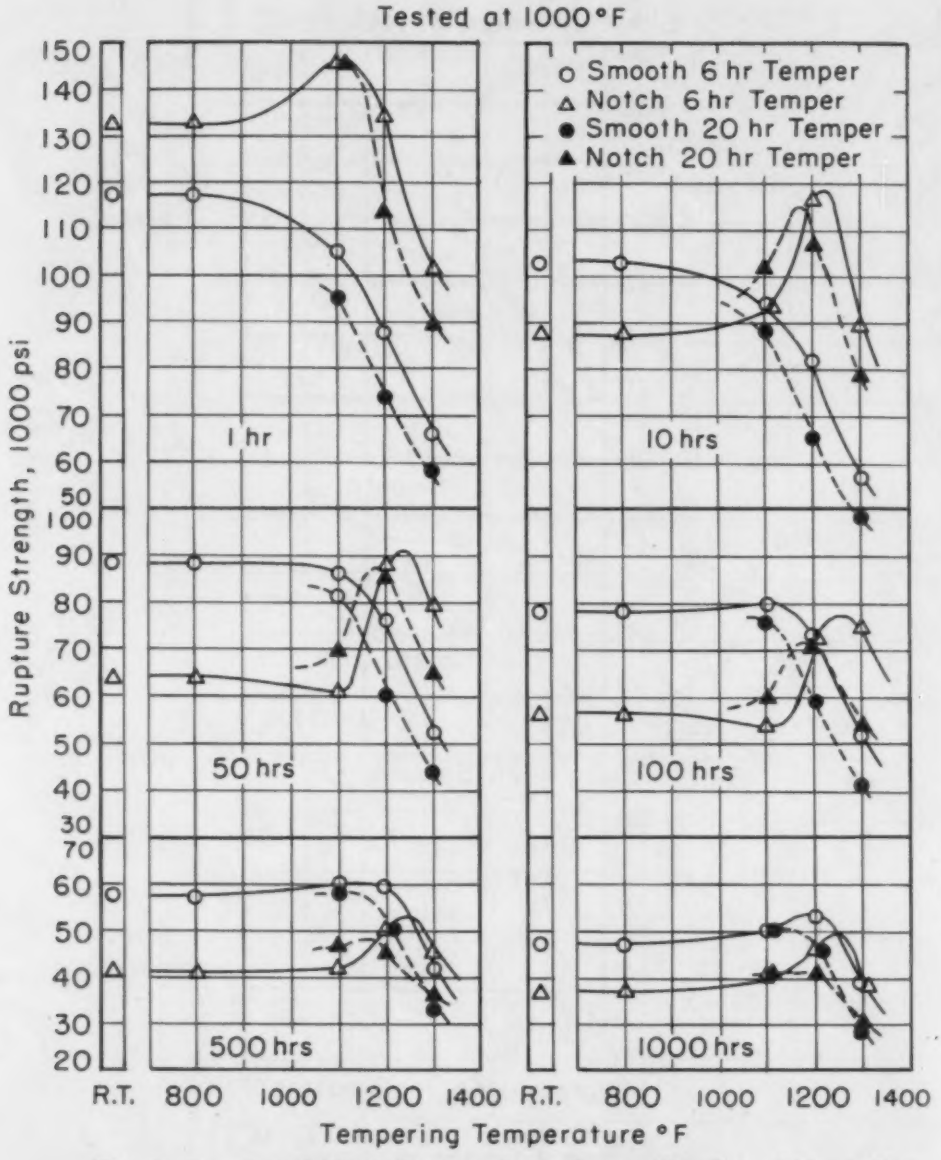


Fig. 6—Smooth and Notch Rupture Strength as a Function of Tempering Temperature at Various Times to Rupture for 17-22A (S) Tempered 6 and 20 Hours Following Normalizing at 1725 °F for ½ Hour.

would be observed at any time to rupture, since the strength curves for the smooth and notched specimens become identical at rupture times longer than approximately 500 hours. At the higher normalizing temperatures a notch sensitivity is observed which increases in magnitude and extends to shorter rupture times as the normalizing temperature is increased.

The data of Fig. 4 have been replotted in Fig. 5 against normalizing temperature for several rupture times. This representation reveals several interesting facts. (a) At temperatures between 1650 and 1725 °F (900 and 940 °C) the notch strength remains practically constant while the smooth strength increases rapidly. (b) With further increase in normalizing temperature the notch strength decreases con-

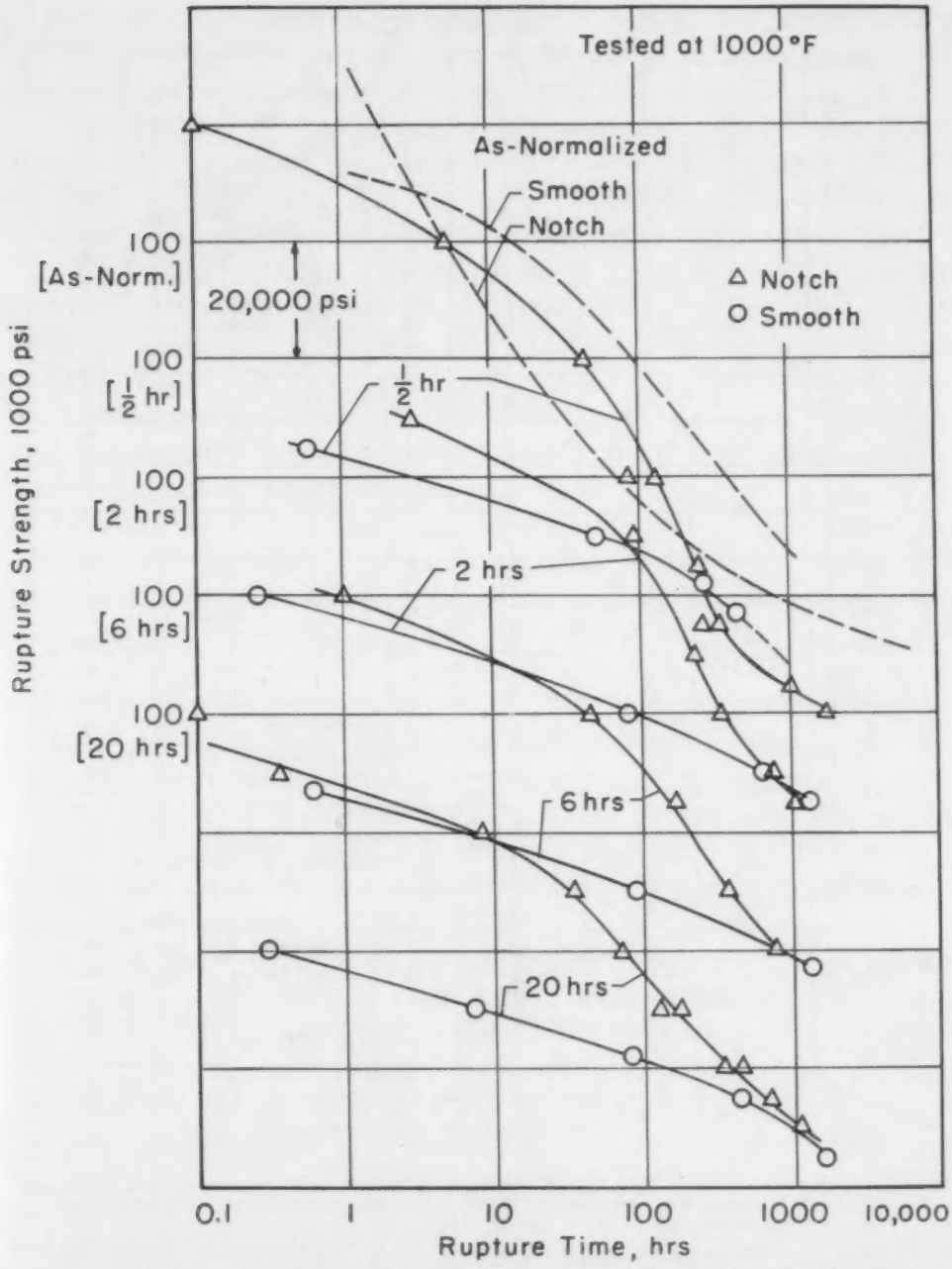


Fig. 7—Smooth and Notch Rupture Strength for 17-22A (S) Tempered at 1300 °F for Various Times After Normalizing at 1725 °F for ½ Hour.

siderably to assume a constant value at normalizing temperatures between 1850 and 1975 °F (1010 and 1080 °C). In this temperature range the smooth strength also remains practically constant. (c) If the normalizing temperature is further increased the smooth strength again increases and the notch strength decreases.

Effect of Tempering on Rupture Strength:—The influence of tempering temperature on smooth and notch rupture strength of specimens normalized ½ hour at 1725 °F (940 °C) and tempered for 6 and 20 hours respectively is shown in Fig. 6. The general trend of

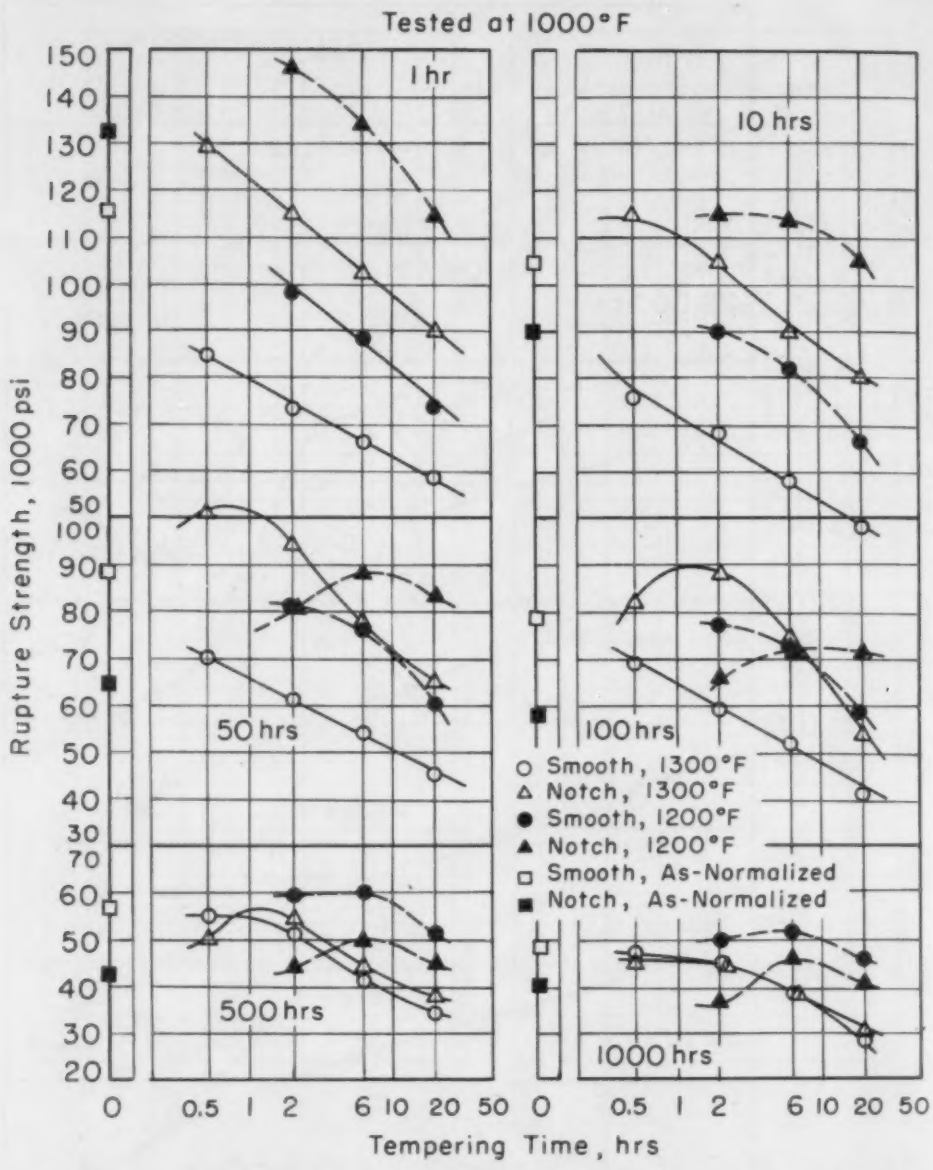


Fig. 8—Smooth and Notch Rupture Strength as a Function of Tempering Time at Various Rupture Times for 17-22A (S) Tempered at 1200 and 1300 °F After Normalizing at 1725 °F for ½ Hour.

these curves is essentially the same for the two tempering times. With an increase in tempering time the curves are generally displaced to lower temperatures by approximately 70 °F. In addition, the maximum in the notch strength becomes somewhat less pronounced.

With increasing tempering temperature up to about 1200 °F (650 °C) the smooth strength decreases at short rupture times but appears to increase slightly at longer rupture times. At tempering temperatures above 1200 °F (650 °C) the values decrease rapidly at all times to rupture.

At times to rupture of 10 hours or longer the notch strength exhibits a maximum which appears to occur at a tempering temperature

of approximately 1250 °F (675 °C) for a 6-hour tempering and at 1180 °F (640 °C) for 20 hour tempering. These maxima become less pronounced as the rupture time approaches 1000 hours.

The influence of tempering time was systematically investigated for material normalized ½ hour at 1725 °F (940 °C) tempered at 1200 and 1300 °F (650 and 705 °C). The notch and smooth rupture strengths are shown in Fig. 7 for a tempering temperature of 1300 °F (705 °C), with tempering time as parameter. Notch sensitivity at this tempering temperature is observed only if the tempering time is short (2 hours). At longer tempering times the notch strength becomes approximately equal to the smooth strength at extended rupture times. This is distinctly different from the behavior at the 1200 °F (650 °C) tempering temperature where notch sensitivity was encountered at all tempering times investigated (see Fig. 8).

In order to more clearly define the influence of tempering time data for 1300 °F (705 °C) tempering, Fig. 7, has been replotted in Fig. 8 as a function of tempering time for several times to rupture. Added to this representation are the results obtained for 1200 °F (650 °C) tempering at times between 2 and 20 hours. In general, the smooth strength decreases continuously with increasing tempering time at either tempering temperature, with the exception that at 500 and 1000 hours to rupture a slight maximum occurs for approximately 6-hour tempering at 1200 °F (650 °C). In every case the smooth strength is higher at 1200 °F (650 °C) than at 1300 °F (705 °C), although this difference is rather small for short tempering times at long times to rupture.

The notch strength at rupture times of 10 hours and over exhibits a maximum which occurs at approximately 6 hours tempering at 1200 °F (650 °C) and at approximately one hour tempering at 1300 °F (705 °C). The notch strength associated with short tempering times is higher for 1300 °F (705 °C) than for 1200 °F (650 °C) tempering at rupture times over 10 hours.

Results For 17-4PH

The test results for 17-4PH have been assembled in Fig. 9. In order to more completely define the trend of the curves, room temperature tensile data has been appended. The effect of testing and tempering temperature on the embrittlement will be discussed later.

Smooth and notch rupture strengths for specimens tempered at 1000 and 1100 °F (540 and 595 °C) are shown in Fig. 9 as a function of testing temperature for several times to rupture. In contrast to the behavior of 17-22A(S) (12) the smooth strength of this alloy decreases only slightly with increasing test temperature or rupture time in a temperature range, below 600 °F (315 °C) where the notch effects are observed.

The smooth rupture strength also differs only slightly for the two

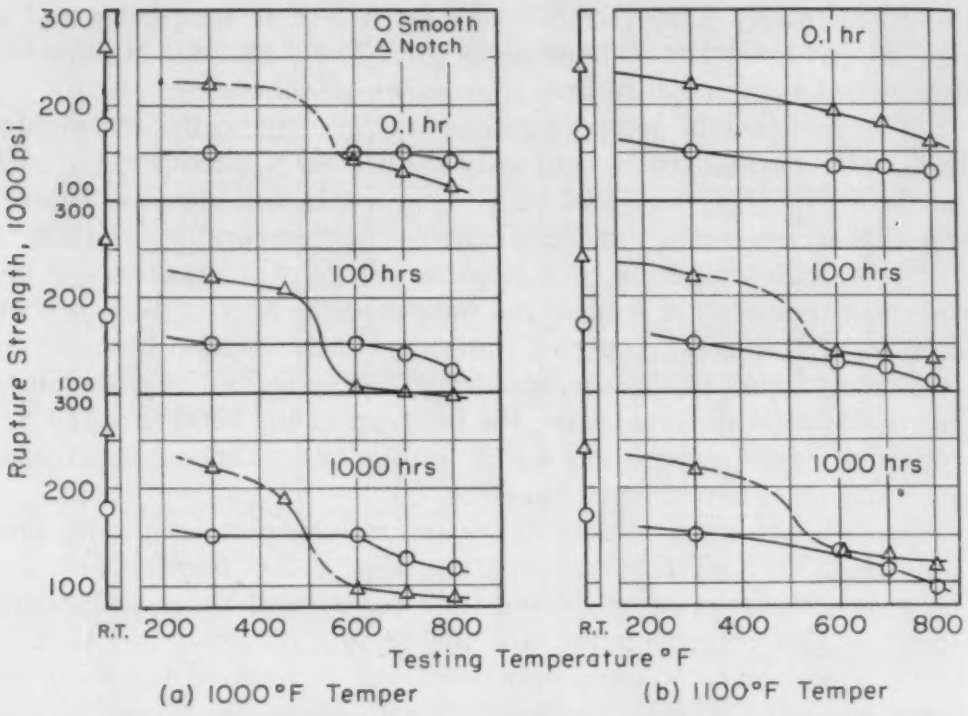


Fig. 9—Smooth and Notch Rupture Strength as a Function of Testing Temperature at Several Rupture Times for 17-4 PH Tempered at 1000 and 1100 °F.

tempering temperatures investigated. However, on tempering at 1000 °F (540 °C) this alloy becomes very notch sensitive while for 1100 °F (595 °C) tempering the notch strength always remains higher than the smooth strength.

Embrittlement and Notch Sensitivity

It has been shown previously (11,14) that smooth ductility is not always an indicator of embrittlement which may be encountered under severe service conditions. Therefore, in the following discussion both the ratio between the notch and smooth rupture strength (notch strength ratio) and the notch ductilities are presented. For the purposes of this discussion the alloy is said to be notch sensitive when the notch strength ratio is less than unity.

Effect of Normalizing Temperature for 17-22A(S):—Smooth and notch ductilities and notch strength ratio are shown in Fig. 10. The smooth and notch ductilities, Fig. 10a, exhibit distinctly different trends at low normalizing temperatures and at short rupture times. Thus, smooth ductility decreases only slightly between normalizing temperatures of 1650 and 1975 °F (900 and 1080 °C), while notch ductility decreases rapidly in this temperature range. At longer rupture times both the smooth and notch ductilities exhibit essentially parallel trends remaining practically constant between normalizing temperatures of 1850 and 1975 °F (1010 and 1080 °C) and then decreasing rapidly to extremely low values at 2075 °F (1135 °C). The trend of the

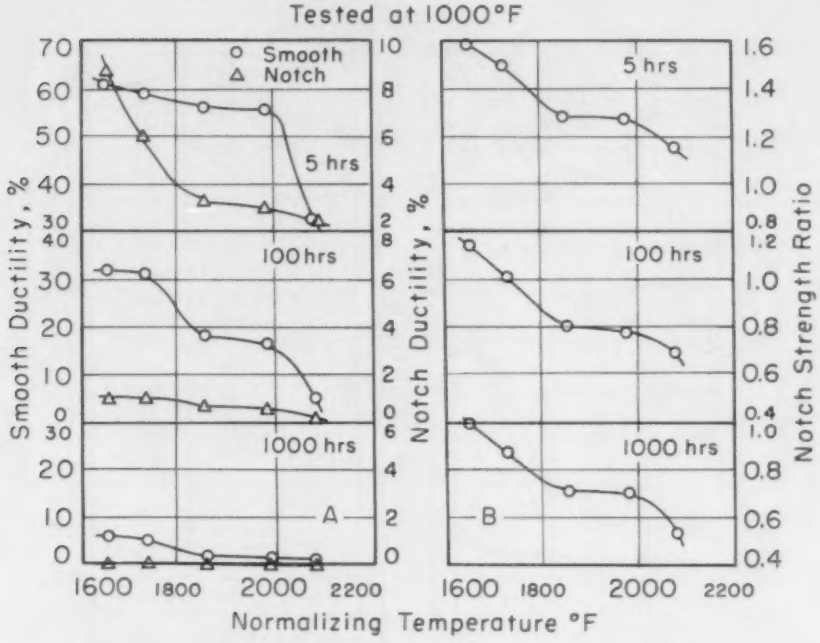


Fig. 10—Smooth and Notch Ductility and Notch Strength Ratio as a Function of Normalizing Temperature at Several Times to Rupture for 17-22A (S) Tempered at 1200 °F for 6 Hours.

notch strength ratio agrees with that of the notch ductility and indicates that severe notch sensitivity is associated with normalizing temperatures above 1725 °F (940 °C) even at 100 hours to rupture.

Effect of Tempering Temperature for 17-22A(S):—Smooth and notch ductilities and notch strength ratio are shown in Fig. 11 as a function of tempering temperature for tempering times of 6 and 20 hours.

Both notch and smooth ductilities, Fig. 11a, exhibit essentially identical trends over the range of tempering temperatures investigated. Tempering for 6 hours at temperatures up to 1100 °F (595 °C) produces only a slight increase in ductility compared with the quite brittle as normalized condition. Between 1100 and 1200 °F (595 °C and 650 °C) the ductilities increase rapidly, the curve for 20-hour tempering being displaced to lower temperatures. It is of interest to note that in the intermediate rupture time range the ductilities of the 1300 °F (705 °C) temper are somewhat lower at the longer tempering time. However, at the longest rupture times the longer tempering time yields the highest ductility.

The notch strength ratio, Fig. 11b follows the same general trend as the ductilities with the exception that a slight minimum appears at intermediate rupture times for 1100 °F (595 °C) tempering. In general, notch sensitivity is quite pronounced for tempering temperatures below 1100 °F (595 °C). Only the 1300 °F (705 °C) temper yields notch strength ratios of unity or above at the longest rupture times.

Effect of Tempering Time for 17-22A(S):—Smooth and notch

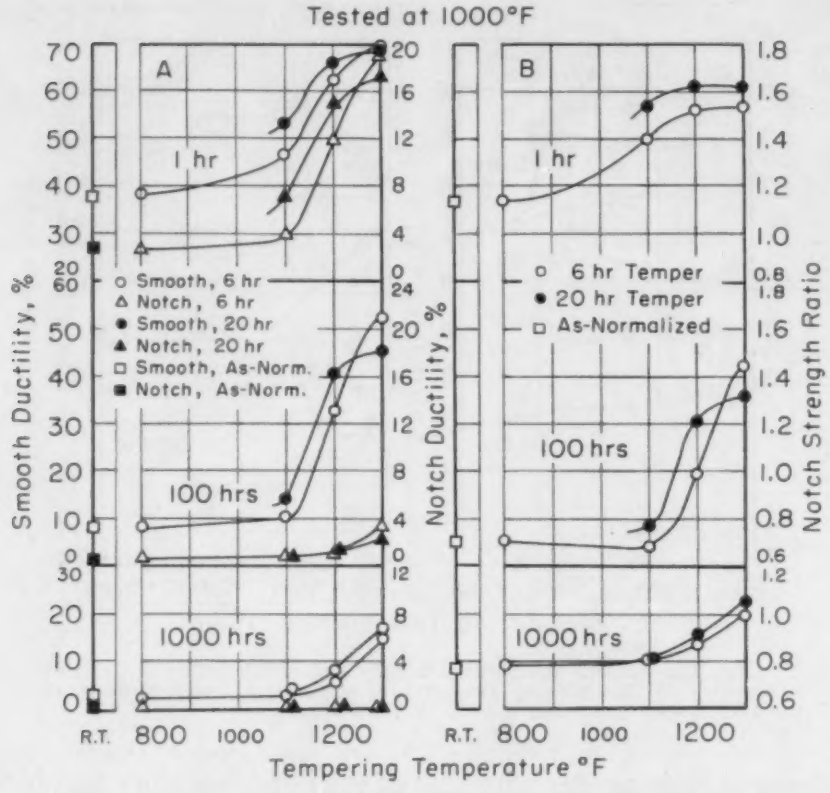


Fig. 11—Smooth and Notch Ductilities, and Notch Strength Ratio as a Function of Tempering Temperature at Several Rupture Times for 17-22A (S) Tempered for 6 and 20 Hours After Normalizing at 1725 °F for ½ Hour.

ductilities and notch strength ratio are shown in Fig. 12 as functions of tempering time for tempering temperatures of 1200 and 1300 °F (650 and 705 °C). At either tempering temperature the notch and smooth ductilities, Fig. 12(a), exhibit essentially the same trends. For 1200 °F (650 °C) tempering the ductilities continuously increase with increasing tempering time. For 1300 °F (705 °C) tempering the ductilities reach maxima at a tempering time of approximately 2 hours. These maxima fade out with increasing time to rupture and at 1000 hours to rupture the ductility of the 2 hour temper is considerably below that obtained by either 6 or 20 hours tempering. In general, the data reveal that pronounced improvements in ductility can be obtained by tempering for a relatively short time at 1300 °F (705 °C).

The notch strength ratios, Fig. 12b, essentially parallel the ductilities. A great reduction in notch sensitivity with increasing tempering time is evident at a rupture time of 100 hours. However, at the longest rupture time only small gains in notch strength ratio can be obtained by increasing the tempering time over ½ hour for 1300 °F (705 °C) tempering and over 6 hours for 1200 °F (650 °C) tempering.

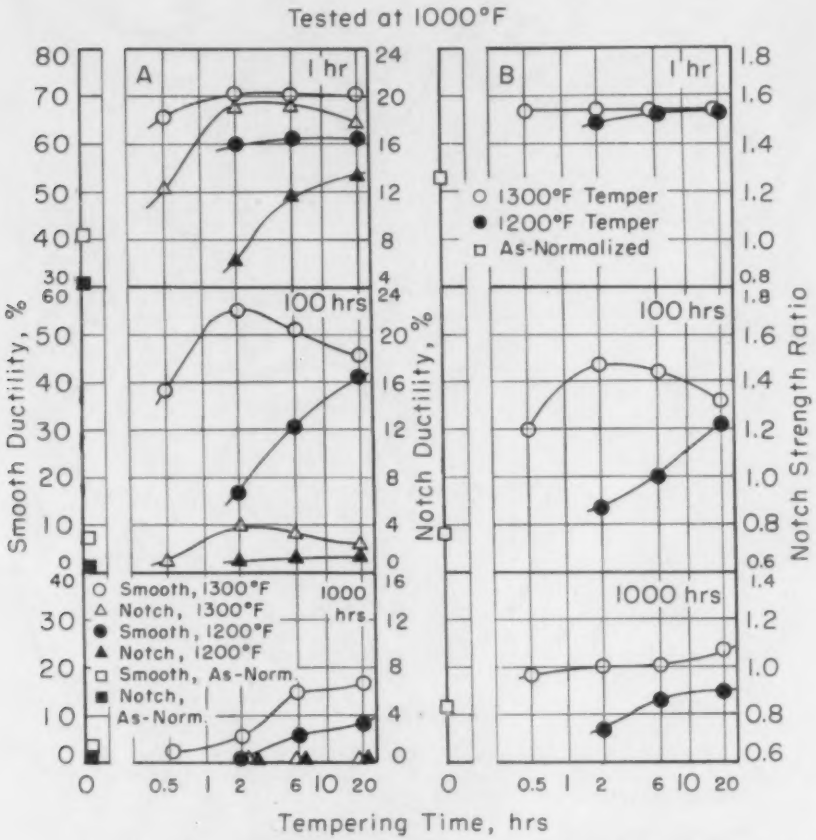


Fig. 12—Smooth and Notch Ductilities, and Notch Strength Ratio as a Function of Tempering Time at Several Times to Rupture for 17-22A (S) Tempered at 1200 and 1300 °F Following Normalizing at 1725 °F for ½ Hour.

Effect of Tempering Temperature and Test Temperature for 17-4PH:—The smooth ductilities[3] and the notch strength ratios of 17-4PH are shown in Fig. 13 as a function of testing temperature for tempering temperatures of 1000 and 1100 °F (540 and 595 °C). In general at either tempering temperature the smooth ductility decreases rapidly in a restricted range of test temperatures. While the data for 1000 °F (540 °C) tempering is insufficient to clearly define the limits of this range, it is apparently displaced to higher testing temperatures when the tempering temperature is raised to 1100 °F (595 °C). At either tempering temperature the ductility exhibits a minimum which becomes more pronounced and shifts to lower test temperatures as the rupture time increases tempering at 1100 °F (595 °C) results in a more ductile condition than tempering at 1000 °F (540 °C).

The notch strength ratios, Fig. 13b, follow the general trend of the smooth ductilities and clearly illustrate the high notch sensitivity associated with 1000 °F (540 °C) tempering.

The general behavior of the smooth ductility and notch strength

[3] The notch ductilities are not shown because in many cases the values are extremely low and therefore do not define curve trends as well as the smooth ductilities.

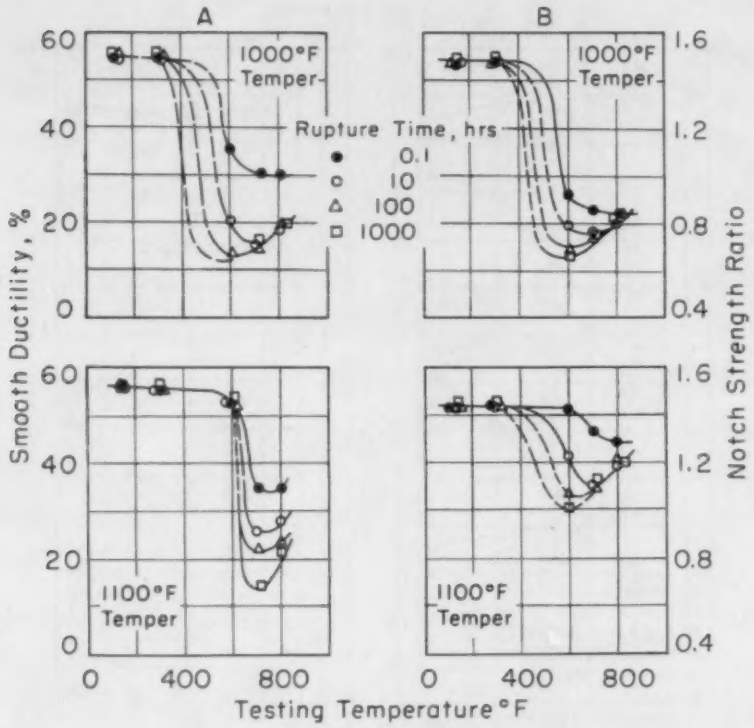


Fig. 13—Smooth Ductility and Notch Strength Ratio as a Function of Testing Temperature at Several Rupture Times for 17-4PH Tempered at 1000 and 1100 °F.

ratios discussed above is essentially similar to those observed for 17-22A(S) tested at temperatures between 600 and 1300 °F (315 and 705 °C) (13) and indicate a precipitation reaction is associated with the notch weakening. However, 17-4PH differs from 17-22A(S) in that notch sensitivity is observed at considerably lower test temperatures and at a temperature (600 °F) where the smooth strength is practically time independent.

Discussion of Results

In the following discussion an attempt will be made to analyze those structural factors dependent on heat treating which influence ductility and notch sensitivity of 17-22A(S).

Normalizing:—In order to determine grain size and observe the carbide structure, metallographic examinations were made of the as received (annealed) material and tempered structures produced after normalizing at various temperatures. It is recognized that small changes in carbide structure can influence creep properties and that such changes are difficult to detect using conventional metallographic procedures. However the photomicrographs in Fig. 14, reveal the following: (a) The annealed structure consists of agglomerated carbides which are primarily concentrated in the grain boundaries (b) A continuous increase in the austenitic grain size occurs with increasing

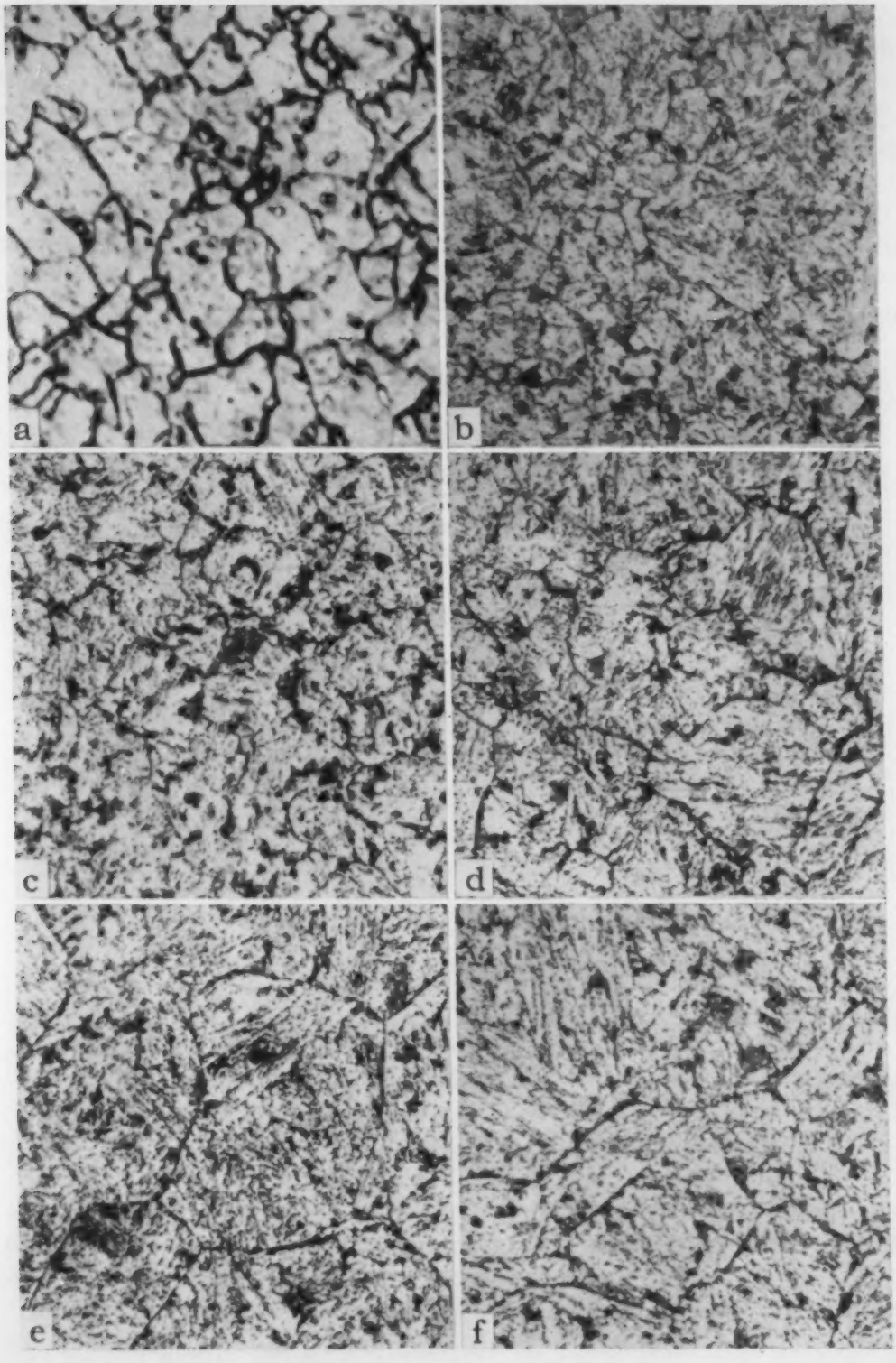


Fig. 14—Structures for 17-22A (S) as Received and Those Obtained by Normalizing at Various Temperatures for One-Half Hour and Tempering 1200 °F for 6 Hours. (a) As received annealed. X 1500; (b) Normalized 1650 °F. X 500. ASTM No. 8; (c) Normalized 1725 °F. X 500. ASTM No. 8; (d) Normalized 1850 °F. X 500. ASTM No. 7; (e) Normalized 1975 °F. X 500. ASTM No. 5 and >1; (f) Normalized 2075 °F. X 500. ASTM No. 3 and >1.

normalizing temperature above 1725 °F (940 °C) (c) Exaggerated austenite grain growth begins, at 1975 °F (1080 °C) and is quite pronounced at 2075 °F (1135 °C) (d) The carbide particles become smaller and more uniformly distributed as normalizing temperature is increased.

It does not seem likely that the rather complex shape of the curves for the smooth strength, ductility and notch strength ratio, Figs. 5 and 10, could be explained solely by the changes in austenitic grain size associated with increasing the normalizing temperature. Referring to

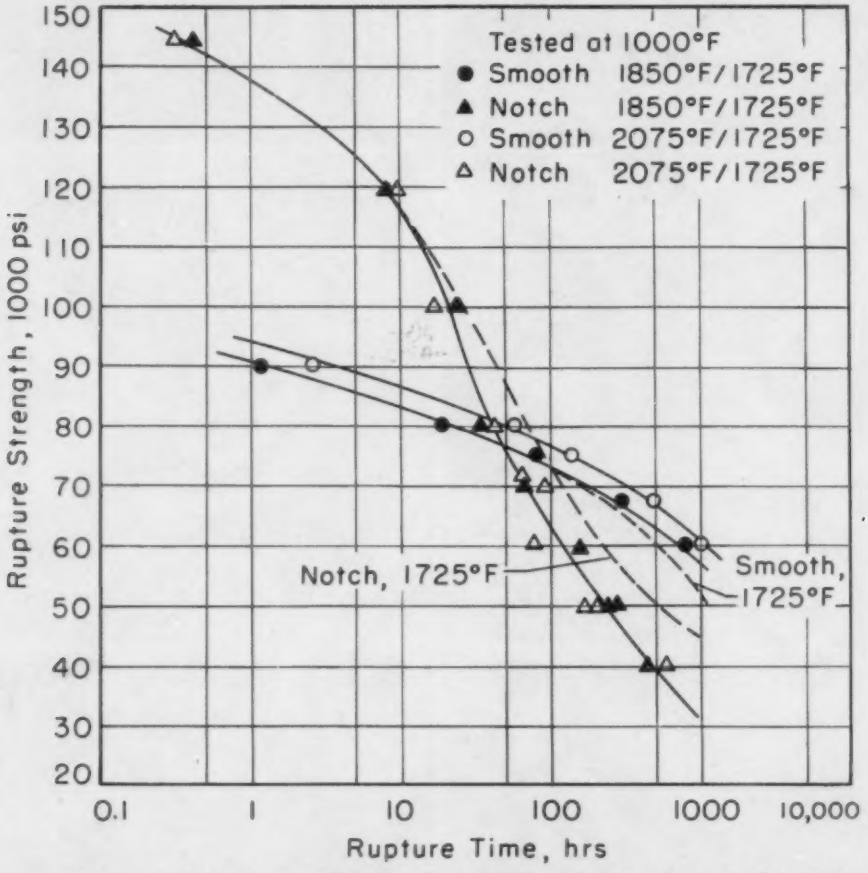


Fig. 15—Smooth and Notch Rupture Strength for 17-22A (S) Heat Treated at 1850 or 2075 °F for ½ Hour, Furnace Cooled to 1725 °F and Held for ½ Hour and then Air Cooled. All specimens tempered 1200 °F for 6 hours.

Fig. 5 the smooth strength at long times to rupture is practically independent of normalizing temperature between 1725 and 1975 °F (940 and 1080 °C), even though the structures exhibit a large difference in grain size. However, the increase in smooth strength at 2075 °F (1135 °C) may be associated with exaggerated austenite grain growth which is very pronounced at this temperature. Regarding the ductilities and the notch strength ratios, Fig. 10, it is likewise observed that these values remain constant over a range of normalizing temperatures (1850 to 1975 °F) which yield appreciable changes in grain size.

In an attempt to further evaluate the role of grain size, two addi-

tional series of tests were made in which specimens were held at 2075 or 1850 °F (1135 or 1010 °C) for one half hour, furnace-cooled to 1725 °F (940 °C), held for one half hour, air-cooled, and tempered at 1200 °F (650 °C) for 6 hours. This double normalizing was designed to produce the same grain size, but different carbide structures than obtained by single normalizing at 1850 or 2075 °F (1010 or 1135 °C). These results, Fig. 15, show the 2075 °F/1725 °F (1135 °C/940 °C) normalizing yields higher smooth strength than obtained by either the conventional treatment or the 1850 °F/1725 °F (1010 °C/940 °C) normalizing. This might be explained in part by exaggerated austenitic

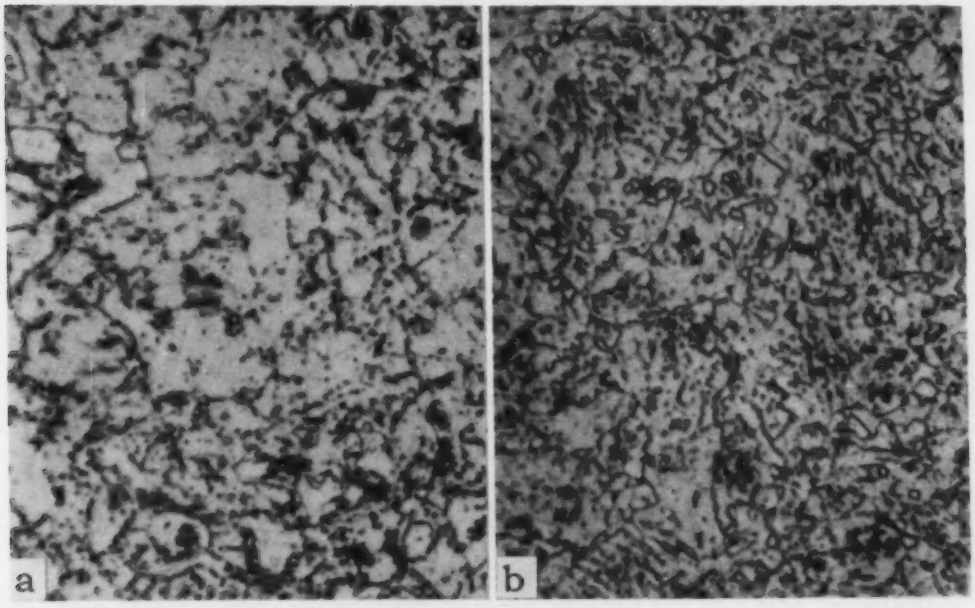


Fig. 16a—Structures for 17-22A (S) normalized 1725 °F for ½ Hour and Tempered at 1300 °F for 2 Hours.

Fig. 16b—Structures for 17-22A (S) Normalized 1725 °F for ½ Hour and Tempered at 1300 °F for 20 Hours.

grain growth at 2075 °F (1135 °C). The notch strength of the two double normalized structures is identical within the limits of scatter in spite of large grain size differences. Generally, the values are lower than those obtained by the conventional treatment and this difference may be associated with differences in carbide structure.

It is felt that grain size plays a minor role in determining rupture strength and ductility except where exaggerated austenite grain coarsening occurs. It is assumed that the carbide structure is of prime importance at normalizing temperatures below which there is incomplete carbide solution. According to Fig. 14, the solution of carbides present in the annealed structure does not approach completion until normalizing temperatures are reached which produce rapid austenite grain coarsening. Regarding the influence of the carbide structure, it is assumed that the strength of the grains is increased with increasing normalizing temperature due to better carbide solution and distribu-

tion. This increase in the strength of grains surrounded by relatively brittle carbides should result in decreased ductility. Superimposed to this effect is solution of these brittle grain boundary carbides with increasing normalizing temperature which would be expected to raise the ductility. These counteracting effects should be considered in an explanation of the rather complex trends of the curves shown in Figs. 5 and 10.

Tempering:—Metallographic examination was made of structures produced by tempering for various lengths of time at 1300 °F (705 °C)

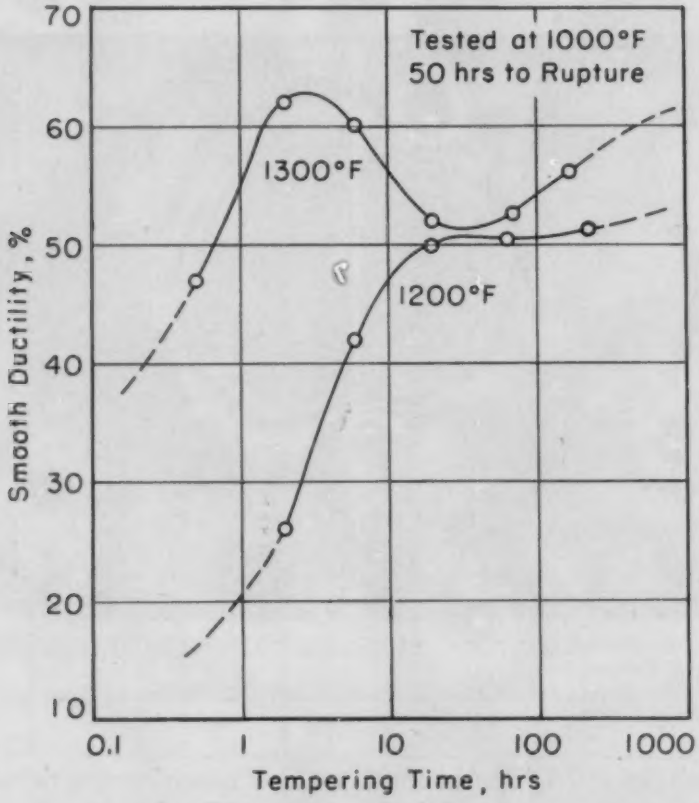


Fig. 17—Smooth Ductility as a Function of Tempering Time for 17-22A (S) Tempered at Various Temperatures Following Normalizing at 1725 °F for ½ Hour.

following normalizing at 1725 °F (940 °C) for one-half hour. The only definite effect of tempering time was a progressive spheroidization of the matrix carbides. Thus, the structure tempered for only 2 hours, Fig. 16a appears to show very little spheroidization compared with that tempered for 20 hours, Fig. 16b. It might be expected that if this were the only structural change the ductility would increase continuously (to some limiting value) with increasing tempering time. However, referring to Fig. 12 at intermediate rupture times the more completely spheroidized structures show decreasing notch and smooth ductility and decreasing notch strength ratio. The conclusion therefore can be reached that some additional structural change occurs during

tempering which reduces the ductility and decreases the notch strength ratio.

According to previous investigations (12,13) a time-temperature dependent notch sensitivity is developed in this alloy given the conventional heat treatment when tested over a wide range of temperatures. It was postulated that this phenomena is associated with a precipitation of carbide from ferrite which occurs during the creep test. Further evidence for carbide instability in molybdenum steels was furnished by Bowman (15). It was shown that after quenching followed by tempering at low temperatures molybdenum is mostly in solid solution but reverts to carbide on raising the tempering temperature. This observation further indicates a precipitation may occur during the tempering of 17-22A(S).

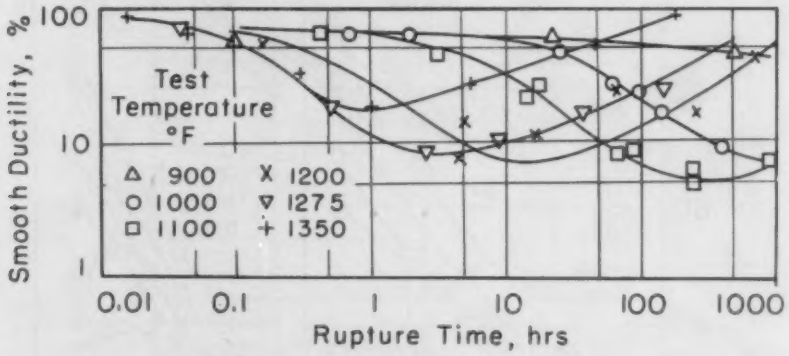


Fig. 18—Smooth Ductility as a Function of Rupture Time at Several Test Temperatures for 17-22A (S) Conventionally Heat Treated.

In this connection it is interesting to compare the data obtained by tempering various lengths of time at 1200 and 1300 °F (650 and 705 °C) and testing at 1000 °F (540 °C) with that obtained by rupture testing the conventionally heat treated material in the same range of temperature. For the purposes of this comparison the smooth ductility has been selected since it is subject to considerably less scatter than the notch ductility but has been shown (in this case) to follow closely the trend of the notch ductility and notch strength ratio.

The smooth ductility at 50 hours to rupture is shown in Fig. 17, as a function of tempering time for 1200 and 1300 °F (650 and 705 °C) tempering temperatures.[4] Results of additional tests for extended tempering times have been added to these curves. The smooth ductility as a function of rupture time with testing temperature as a parameter is shown in Fig. 18 for conventionally heat treated material. It can be seen from Fig. 17 that ductility minima develope on tempering the alloy at either 1200 or 1300 °F (650 or 705 °C) and that the minima shift to longer times with a decrease in tempering temperature. Corresponding minima also occur if the alloy is tested in stress rupture at these temperatures, Fig. 18. The presence of such minima can be

[4] For these tempering temperatures the effects of subsequently testing for 50 hours at 1000 °F should negligibly influence the structure.

taken to indicate that an embrittling precipitate takes place during either tempering or rupture testing. Comparing Figs. 17 and 18 it is seen that the presence of stress accelerates the precipitation and increases the magnitude of embrittlement. At sufficiently long testing or tempering times agglomeration of the precipitate occurs and the ductility recovers.

Some insight into the effects of this precipitation on the smooth strength may be gained from an examination of the relation between smooth strength and the hardness of structures produced by temper-

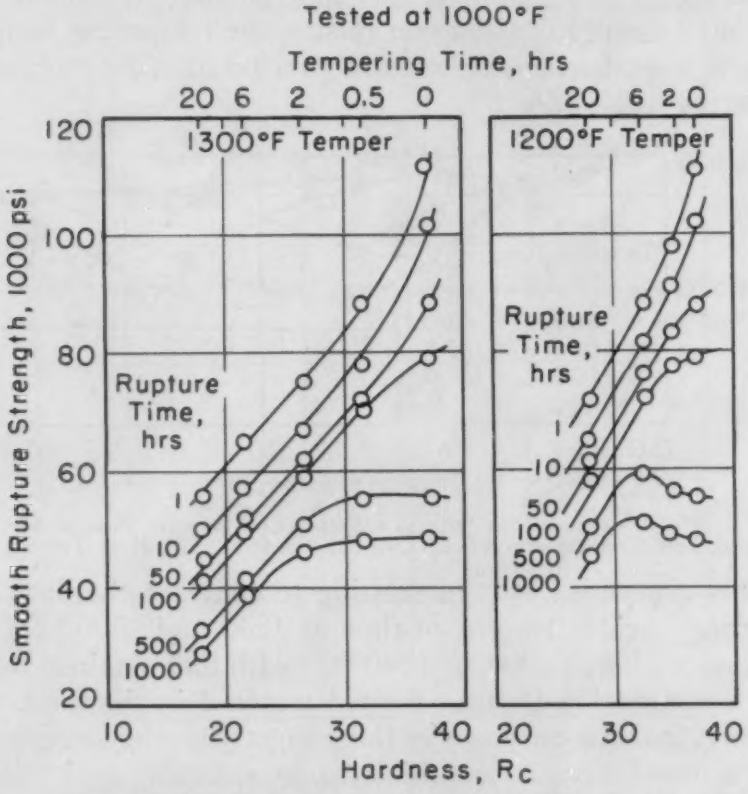


Fig. 19—Smooth Strength as a Function of Hardness at Several Rupture Times for 17-22A (S) Normalized at 1725 °F and Tempered at 1200 and 1300 °F.

ing for various times at 1200 and 1300 °F (650 and 705 °C). This relation is shown in Fig. 19 with time to rupture as a parameter. It is assumed that the hardness is influenced only by the progressive spheroidization of the carbides formed on normalizing and that little spheroidization of these carbides occurs during rupture testing at 1000 °F (540 °C). This latter assumption is supported by metallographic evidence and by hardness data previously presented (13). It will be noted, Fig. 19, that the smooth strength increases continuously with increasing hardness for times to rupture up to 100 hours. In this range it can be assumed that changes in the strength are due to the same factors affecting the hardness, namely the degree of spheroidization of the carbide structure due to tempering. At longer rupture

times (500 and 1000 hours) the curves level out at high hardnesses. This behavior may be associated with appearance of the previously discussed embrittling precipitate. Such a precipitation would be expected to occur at long rupture times at 1000 °F (540 °C) (see Fig. 18), for those structures tempered for short times and therefore incompletely precipitated during tempering. Also, as might be expected the effects of the precipitate are more pronounced for the lower tempering temperature.

Apparently the embrittling precipitate does not influence the smooth strength when it occurs during tempering but adversely affects the rupture life when it occurs during the creep test.

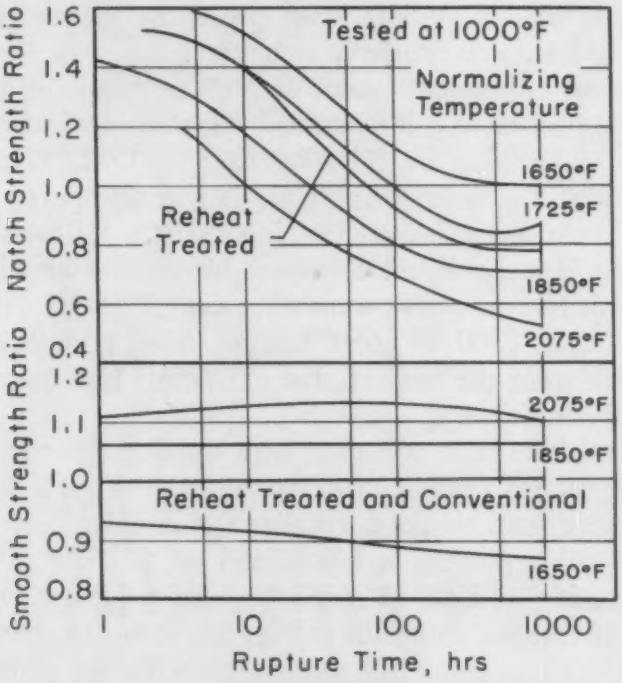


Fig. 20—Comparison of Smooth Strength and Notch Sensitivity Developed by Various Normalizing Temperatures for 17-22A (S) Tempered 1200 °F, 6 Hours.

Significance of Results

The results presented in this paper indicate that rather small variations in the normalizing and tempering procedure considerably influence the creep embrittlement and notch sensitivity of both 17-22A(S) and 17-4PH. Notch sensitive structures, even though possessing high smooth strength, may not be suitable for severe service applications which involve embrittling factors such as high stress concentrations, vibratory stresses, etc.

It now appears possible to arrive at recommendations (for rupture times up to 1000 hours) regarding optimum heat treatment procedures designed to reduce embrittlement and notch sensitivity and involving a minimum sacrifice in smooth strength. In the following section the

various heat treatments will be compared regarding their effects on smooth strength and notch strength ratio and an attempt will be made to indicate the practical significance of the results.

Normalizing of 17-22A(S):—Notch strength ratios are plotted against the rupture time in Fig. 20 for several normalizing temperatures. Added to this representation is the ratio of the smooth strength produced by a given normalizing temperature to that obtained with the conventional heat treatment (smooth strength ratio). This representation indicates that while an appreciable improvement in smooth strength can be obtained by raising the normalizing temperature, this is accompanied by very low notch strength ratios. On the other hand, lowering the normalizing temperature to 1650 °F (900 °C) results in from 11 to 13% loss in smooth strength at the longer rupture times but does not yield a notch sensitive structure.

The problem of embrittlement at high normalizing temperatures was found to be particularly important in certain fabricating operations involving copper brazing or Nicrobrazing of 17-22A(S). Standard production procedures often involve air (or atmosphere) cooling (i.e. normalizing) from a continuous brazing furnace followed by tempering. For example, experimental hollow blades for an air-cooled gas turbine brazed at temperatures somewhat over 2000 °F (1095 °C) and tempered 6 hours at 1200 °F (650 °C) possessed poor operating characteristics which were attributed to the extremely high notch sensitivity of this material condition.

In order to determine whether high brazing (normalizing) temperatures alone would permanently damage the alloy, a series of tests were made on specimen blanks normalized at 2075 or 1850 °F (1135 or 1010 °C) and subsequently renormalized at 1725 °F (940 °C) followed by tempering at 1200 °F (650 °C) for 6 hours. Data obtained for these reheat treated conditions, Fig. 20, indicate that the smooth strength is reduced to the value associated with the commercial heat treatment. On the other hand, the notch sensitivity is considerably reduced by reheat treatment and identical notch strength ratios are obtained for either 1850 or 2075 °F (1010 or 1135 °C) normalizing. However, the trend of the notch strength ratio curve for the reheated condition in Fig. 20 indicates some permanent damage is associated with normalizing at these high temperatures, the magnitude of which increases with increasing rupture time. As might be expected turbine blades reheat treated in this manner show improved engine performance.

Tempering of 17-22A(S):—For the purposes of comparison the notch strength ratio and the ratio of the smooth strength of the as-normalized condition to the smooth strength obtained by several tempering treatments (referred to as the smooth strength ratio) for 17-22A(S) is shown in Fig. 21 as a function of rupture time. From this representation it is seen that the as-normalized material possesses the

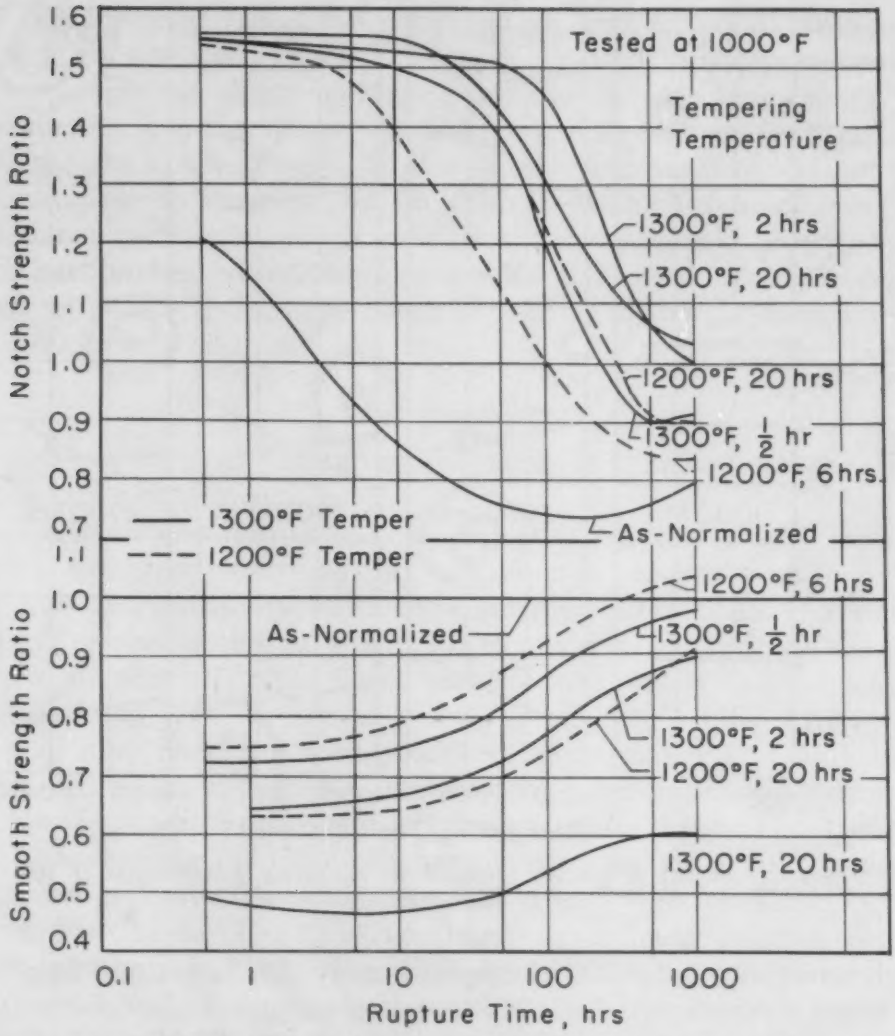


Fig. 21—Comparison of Smooth Strength and Notch Sensitivity Developed by Various Tempering Treatments for 17-22A (S) Normalized at 1725 °F, ½ Hour.

highest smooth strength except at the longest rupture times where the conventionally heat treated specimens are slightly stronger. The as-normalized condition, however, is extremely notch sensitive even at 10 hours to rupture.

Increasing the tempering temperature or the tempering time compared with the conventional heat treatment results in a decrease in the smooth strength but reduces notch sensitivity. If the tempering time at 1200 °F (650 °C) is increased from 6 to 20 hours the smooth strength decreases on the average approximately 17%. The 1000 hour notch strength ratio increases from 0.84 to 0.90.

By short time tempering at 1300 °F (705 °C) structures can be produced which have reduced notch sensitivity and suffer relatively small losses in smooth strength compared with the conventional heat treatment. Thus, tempering one-half hour at 1300 °F (705 °C) yields a 5 to 6% decrease in smooth strength but shifts the time of onset of

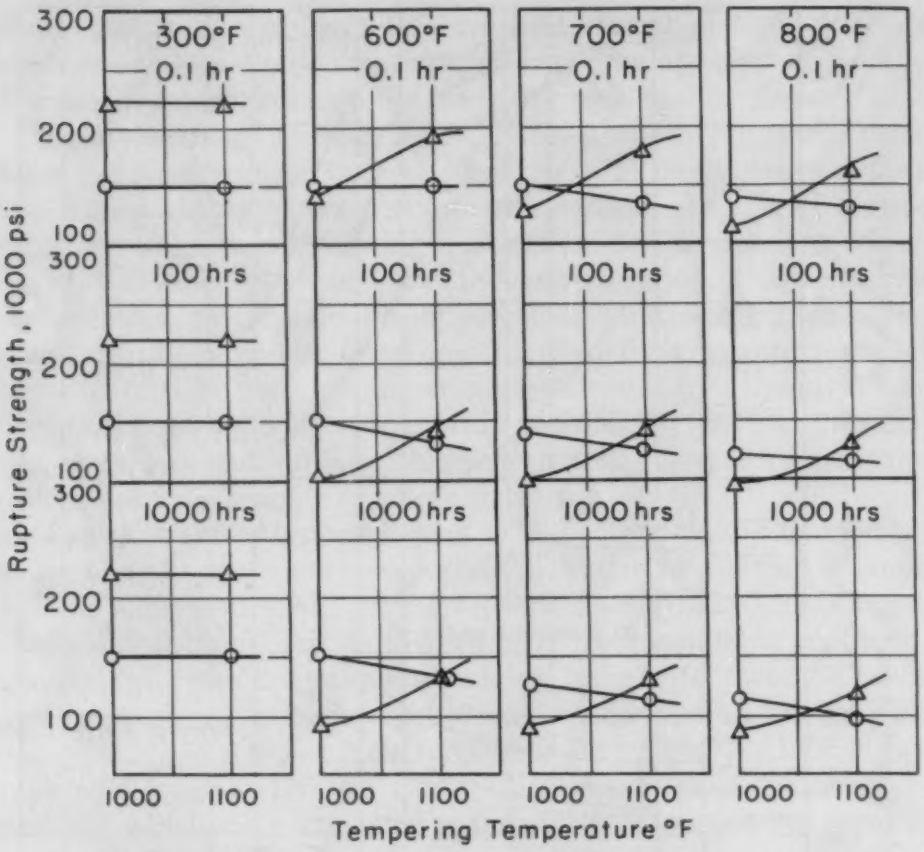


Fig. 22—Smooth and Notch Strength for Tempering Temperatures of 1000 and 1100 °F at Various Times to Rupture and at Several Testing Temperatures for 17-4 PH.

notch sensitivity from 100 to approximately 250 hours and increases the notch strength ratio at 1000 hours to rupture from 0.84 to 0.92.

Increasing the tempering time to 2 hours at 1300 °F (705 °C) results in smooth strengths approximately 15% lower than the conventionally heat treated material but no notch sensitivity at any of the rupture times investigated. Tempering for 20 hours at 1300 °F (705 °C) greatly reduces the smooth strength compared with the conventional treatment and results in lower notch strength ratios at intermediate rupture times than obtained for a tempering time of 2 hours.

From consideration of this data it appears complete freedom from notch sensitivity cannot be obtained without some sacrifice in smooth strength. Minimum notch sensitivity coupled with minimum reduction in smooth strength is associated with short tempering times at 1300 °F (705 °C).

A practical example of the beneficial effects of raising the tempering temperature is furnished by tests on the previously mentioned experimental hollow turbine blades. Due to permanent damage introduced by brazing and to the severity of operating conditions it was found extremely beneficial to raise the tempering temperature to 1300 °F (705 °C) in order to obtain maximum ductility.

Tempering of 17-4PH:—Surprisingly large effects of tempering temperature are noted in Fig. 22 for 17-4PH. In this representation the notch and smooth strength are plotted against the tempering temperature for several rupture times. At test temperatures over 300 °F (150 °C) the notch strength is considerably increased by raising the tempering temperature to 1100 °F (595 °C). This increase is accompanied by some loss in smooth strength but the structures produced are much less notch sensitive. For example the 1000-hour smooth strength at 800 °F (425 °C) decreases about 17% while the notch strength ratio increases from 0.80 to 1.2.

Conclusions

On the basis of this investigation the following tentative conclusions may be drawn:

1. Notch sensitivity and creep embrittlement of 17-22A(S) and 17-4PH are greatly influenced by variations in heat treatment.
2. Notch sensitivity and creep embrittlement of 17-22A(S) is increased by normalizing at temperatures above 1725 °F (940 °C) and reduced by normalizing at lower temperatures, but with some loss in smooth strength.
3. Embrittled structures produced by normalizing at high temperatures may be appreciably improved by a renormalizing treatment at a lower temperature without adverse effects on the smooth strength.
4. Increasing the tempering temperature for either alloy reduces notch sensitivity with an attendant loss in smooth strength.
5. For 17-22A(S), the tempering treatments yielding lowest notch sensitivity and involving minimum reduction in smooth strength may be obtained by tempering at relatively high temperatures for short times.
6. Creep embrittlement and notch sensitivity of 17-22A(S) normalized at high temperatures are primarily associated with the carbide structure.
7. Carbide precipitation from ferrite can occur either during tempering or during creep testing. If the precipitate occurs during testing its effects on the embrittlement and notch sensitivity are considerably larger than if it occurs during tempering.
8. The smooth strength is affected only if the precipitate occurs during testing.

Acknowledgments

The authors wish to thank B. Pinkel of the Lewis Laboratory of NACA for his interest and encouragement. Appreciation is expressed to J. Sessler of Syracuse University, and J. L. Shannon, S. P. Barnosky and O. T. Hickey of NACA for their assistance with the tests. Thanks are also due Miss Anne Kendra for the metallographic preparations.

References

1. H. Bennek and G. Bandel, "Influence of the Structure as Determined by Heat Treatment and Composition on the Creep Strength of Steel," *Stahl and Eisen,* Vol. 63, 1943, p. 653.
2. G. Delbart and M. Ravery, "Influence of Microstructure on the Hot Strength of Steel," *Metal Treatment and Drop Forging,* Vol. 17, no. 63, Autumn 1950, p. 171.
3. G. Delbart and M. Ravery, "Les Ñecherches sur la trempe esotherme en France et á létranger," *Revue de Métàllurgie,* Vol. 6 and 7, June 1949, p. 394, July 1949, p. 475.
4. G. Delbart and M. Ravery, "Influence of Microstructure on the Hot Strength of Steel," *Metal Treatment and Drop Forging,* Vol. 20, December, 1953, p. 579.
5. R. L. Jones, A. I. Rush and J. W. Freeman, "Four Low Alloy Steels for Rotor Disks of Gas Turbines in Jet Engines," Eleventh Progress Report, University of Michigan, Air Force Contract No. AF33(038)-13496, Project M 903, Sept. 30, 1953.
6. H. Esser, S. Eckhardt and G. Lautenbusch, "Relationship Between the Creep Strength, Heat Treatment, and Cold Work of Thin-Walled Tubes," *Archiv für das Eisenhuttenwesen,* Vol. 16, 1942, p. 131.
7. J. Glen, "Abnormal Creep of Chromium Steels," *Journal,* Iron and Steel Institute, Vol. 155, 1947, p. 501.
8. J. Glen, "The Creep Properties of Mo, Cr-Mo, and Mo-V steels," *Journal,* Iron and Steel Institute, Vol. 158, 1948, p. 37.
9. C. L. Clark, "Lower Alloys Developed for High Temperature Use," *Iron Age,* Vol. 169, Feb. 21, 1952, p. 98.
10. A. Thum and K. Richard: "Strength of Steels in Creep Loading," *Mitt. Verein Grosskesselbesitzer,* No. 85, Dec. 1941, p. 171.
11. G. Sachs and W. F. Brown, Jr., "A Survey of Embrittlement and Notch Sensitivity of Heat Resisting Steels. Symposium on Strength and Ductility of Metals at Elevated Temperatures," American Society for Testing Materials, Special Technical Publication No. 128, 1952, p. 6.
12. W. F. Brown, Jr., M. H. Jones and D. P. Newman, "Influence of Sharp Notches on the Stress Rupture Characteristics of Several Heat Resisting Alloys, Symposium on Strength and Ductility of Metals at Elevated Temperatures," American Society for Testing Materials, Special Technical Publication No. 128, 1952, p. 25, Part II, *Proceedings,* American Society for Testing Materials, Vol. 53, 1953, p. 661.
13. D. P. Newman, M. H. Jones and W. F. Brown, Jr., "Time-Temperature Dependence of the Notch Effect and Influence of Notch Depth in Stress Rupture Tests on a Cr-Mo-V Steel," *Proceedings,* American Society for Testing Materials, Vol. 53, 1953, p. 677.
14. G. Sachs, L. J. Ebert and W. F. Brown, Jr., "Comparison of Various Structural Low Alloy Steels by Means of the Static Notch Bar Tensile Test," T. P. 2110, *Metals Technology,* Vol. 13, no. 8, Dec. 1946.
15. F. E. Bowman: "Partition of Molybdenum in Hypoeutectoid Iron-Carbon-Molybdenum Alloys," TRANSACTIONS, American Society for Metals, Vol. 36, 1946, p. 61.

DISCUSSION

Written Discussion: By A. J. Herzog, Materials Laboratory, Wright Air Development Center, Wright-Patterson Air Force Base, Ohio.

This investigation is considered an unusually valuable contribution toward the solution of embrittlement problems in materials. Embrittlement is caused by two primary influences, first the problem of the metallurgical variations and

second the analytical mechanics problem of stress-strain-time relationships. Important metallurgical changes occur when materials are exposed to temperature and time and within a rather narrow range of heat treatment temperatures and times these variations have a marked effect on mechanical properties, although previous microstructure investigations have shown little evidence of metallurgical changes. The metallurgical investigation presented shows that optimum mechanical properties can be obtained by proper heat treatment. It is apparent from the information presented that when these optimum properties were obtained metallurgical changes were effectively reduced and the material remained stable for the test times and temperatures investigated.

If the authors' method of approach to the selection of heat treating procedures can be extended for a wide range of material types, more definitive materials could be obtained which in turn would justify the selection of more accurate design factors. The method of approach presented in this paper is considered to be a guide for the determination of optimum properties for all heat treatable alloys. The possibility of defining detailed heat treatments for aircraft and engine structural materials, to reduce load-time dependent failures as indicated by the experimental data presented, is considered a significant contribution in the advancement of materials science.

Present stress analysis methods assume that a material remains stable during test. Although this stability may not be required for structural applications, stability for a given test time is essential for the solution of the stress analysis problems encountered in all time dependent tests. Although the notched specimen geometry adopted for this investigation was satisfactory for definition of optimum metallurgical treatment, it is recommended that future work be done on specimens which are more suitable for stress analysis purposes. According to the Davis and Manjoine, ASTM Preprint 78, 1952, a root radius of 0.005 inches is considered a minimum value for very carefully machined notches. Machining variations are magnified in the preparation of sharp notches, resulting in varied amounts of cold working and residual stresses. These undesirable machining variables are aggravated by unavoidable misalignment during test. Therefore a minimum root radius of 0.020 inches is recommended for general use. If the specimen used in this investigation were changed to a specimen with 0.020 inch root radius maintaining the same unnotched to notched area relationship, an outside diameter of about 0.600 inches would be required to give a theoretical notch factor greater than 3.0. A theoretical notch factor of 3.0 to 3.5 is considered to be high enough to produce severe notch conditions and very little difference in trends of test results is likely to occur with higher notch factors. Also, the stress concentration effect of the specimen shoulders will influence test results with a specimen having a short gage length. It is desirable to have a distance of at least four times the root diameter between the edge of the notch and the beginning of the shoulder fillet.

It is expected that the solution of metallurgical problems as presented in the paper will also contribute to a better understanding of creep and relaxation, especially for notched material, and will help in the investigation of fatigue at elevated temperatures. Generally the stress analysis problems involved in all these fields are basically similar and their solution will probably be attacked with success from a common physical base such as the one presented by the authors. The presentation shows also that the recommendations for the heat treatment of materials should be made carefully when the application in air-

craft design is involved where the safety factors have to be kept extremely small for weight saving purposes. These heat treatment recommendations for the various cases of application should be based on more elaborate investigations to cover accurately the behavior of the materials for the variations in normalizing, tempering and other heat treatment procedures.

Authors' Reply

The authors wish to thank Dr. Herzog for his valuable discussion which clearly recognizes that high temperature embrittlement of steels is often associated with structural factors that may be subject to control through proper heat treating technique.

Dr. Herzog recommends that the notch radius be increased to 0.020 inch and the outside specimen diameter to 0.600 inch. This would result in a decrease in the notch sharpness (ratio of one-half the notch diameter to the root radius) from the present value of 150 to approximately 11 and a consequent reduction in the stress concentration factor. The authors agree that such a change would assist in the analysis of the stress distribution. However, previous experience[1,2], indicates that a specimen having a notch sharpness of 11 would not reveal inherent notch sensitivity in many high temperature alloys. In order to obtain an indication of material stability and notch sensitivity in service, the most severe stress concentration possible must be incorporated into the laboratory test. This is necessary because often the material in service is subject to a combination of loading conditions resulting in even more severe embrittlement than introduced by the sharpest notch in a test specimen.

The authors recognize that unintentional variations in machining practice will introduce variations in the notch properties. However, the notch radius in these investigations has been held within close limits, and it should be remembered that the notch strength varies progressively more slowly with increasing notch sharpness as the notch sharpness increases beyond that value producing maximum notch strength. Variations in the residual stresses, the amount of cold at the notch root, or for that matter in the notch radius if significant, would be expected to result in scatter of the notch strength values. However, in these investigations, the scatter of the notch strength has been very little more than that encountered for the smooth strength.

It appears that the necessity for a sharp notch has been emphasized by only a few investigators, but that the problem of producing such a specimen has been emphasized by many. In the authors' experience the production of sharp notches having close tolerances is no more costly or difficult than the production of mild notches in the same material.

---

[1] W. F. Brown, Jr. and G. Sachs, "Notch Sensitivity at High Temperatures Evaluated," *Iron Age*, March 20, 1952, p. 91–95.

[2] G. Sachs, W. F. Brown, Jr. and D. P. Newman, "Die Wirkung von Spannungskonzentrationen auf die Zeitstandfestigkeit der Werkstoffe," *Zeitschrift fur Metallkunde*, Vol. 44, 1953, p. 233–239.

THE EFFECT OF TIME AND TEMPERATURE ON VARIOUS MECHANICAL PROPERTIES DURING STRAIN AGING OF NORMALIZED LOW CARBON STEELS

By F. Garofalo and G. V. Smith

Abstract

The effect of aging time and temperature after plastic straining in tension or compression on the notch-impact transition temperature range, yield strength, tensile strength and hardness has been investigated for three low carbon steels in the normalized condition.

The notch-impact results, which include aging times up to several years and exposure temperatures between 75 and 1200 °F, reveal little difference between a steel made by the liquid metal practice and deoxidized with silicon and aluminum and a capped open hearth steel in the maximum shift of the transition temperature range after straining in tension and aging at 75 or 450 °F, whereas a capped bessemer steel shows an appreciably greater shift. Stress relief treatment at 900 or 1200 °F has little effect on the transition temperature range of strain-aged steels. Prestraining in compression followed by aging at 75 or 450 °F has an effect on the transition temperature range similar to that of prestrain in tension followed by aging at these temperatures.

After prestraining in tension and aging at 75 °F the changes in yield and tensile strength indicate that the steel made by the liquid metal process deoxidized with silicon and aluminum ages less rapidly and to a lesser degree than open hearth and bessemer capped steels. The change in yield strength is found to increase at a faster rate than the change in tensile strength.

Following prestraining in compression and aging at 75 °F, an upward shift in the tensile flow curve is found, indicating a hardening effect, without the return of discontinuous yielding. The yield point behavior returns upon aging at 450 °F.

The effect of prestraining in tension and aging at 75 and 450 °F on hardness has been studied and it is found that no over aging is encountered even when exposure is extended to over two years. The change in hot hardness with temperature between 75 and 500 °F and the change in hardness

---

The authors, F. Garofalo and G. V. Smith, are associated with the United States Steel Corp., Research Laboratory, Kearny, N. J. Manuscript received September 16, 1954.

at temperature with aging time at 200, 250 and 300 °F have been investigated.

Various theories of strain aging and the effect of recovery during strain aging are discussed.

Introduction

With reference to mild steel, the term "strain aging" designates any change in properties which occurs after deformation and upon aging at temperatures ranging from approximately 500 °F (260 °C) to subatmospheric. Above 500 °F the changes caused by relaxation or recovery, carbide spheroidization, and possibly recrystallization, may mask, if not actually overshadow changes caused by strain aging. For practical reasons, however, it is important to investigate the effect of temperature beyond 500 °F to ascertain the usefulness of initial or interim stress relief in eliminating strain aging effects.

The changes in mechanical properties caused by straining and aging at temperatures in the neighborhood of 500 °F, or below, have been studied extensively (1–15).[1] The results indicate that the effects of strain aging on the various mechanical properties may differ widely, depending upon such variables as chemical composition, metallurgical structure and prior thermal history, aging time and temperature, and type of prestrain. It would seem, therefore, that a better understanding of the mechanism of strain aging requires a comprehensive investigation which will clearly show the effect of these, and possibly other variables, upon many different mechanical properties during aging.

In the present investigation, a study has been made of the strain aging characteristics, following both tensile and compressive prestrains, of three low carbon steels in the normalized condition. Notch-impact tests covering the transition range, tensile tests at room temperature, and hardness tests at room and at elevated temperatures were included in the testing program. Aging at 75 and 450 °F (24 and 230 °C) was extended to several years. Hot hardness measurements (16) were made up to 500 °F (260 °C). The effect of stress relief at 900 and 1200 °F (480 and 650 °C) was also investigated.

Materials

The identification, type, chemical composition, and grain size after normalizing of the three steels investigated are presented in Table I. Steel A was made by the liquid metal practice and was deoxidized with silicon and aluminum. Steels B and C are capped open-hearth and bessemer steels, respectively, and are essentially not

[1] The figures appearing in parentheses pertain to the references appended to this paper.

Table I
Description of Steels

Steel	Melting Practice	Chemical Composition Per Cent							Grains
		C	Mn	P	S	Si	Al(a)	N (a	/mm²
A	Liquid Metal-Deoxidized with Silicon and Aluminum	0.25	0.56	0.017	0.028	0.13	0.013	0.011	75.0×10^2
B	Open-Hearth-Capped	0.07	0.43	0.006	0.026	0.007	0.005	0.005	34.5×10^2
C	Bessemer-Capped	0.08	0.47	0.075	0.032	0.012	0.006	0.016	29.5×10^2

(a) Acid Soluble

deoxidized. In addition to the differences in extent of deoxidation, and the differences in phosphorus and nitrogen contents related to steelmaking practice, there is a considerable difference in carbon content of these steels.

Steel A was received in the form of hot-rolled seamless pipe of 0.377 inch wall thickness and 4.5 inch outside diameter. Steels B and C were received in the form of hot-rolled buttwelded pipe of 0.300 inch wall thickness and 3.0 inch outside diameter. In order to provide a comparable initial structure these steels were normalized by heating to 1650 °F (900 °C), holding for ½ hour at temperature and air cooling.

Test Procedures

Prestraining and Aging of Test Steels

For each of the three steels, strips were cut from 21 inch long pipe sections and normalized as described above. These strips were subsequently machined to a width of 1 inch and a thickness of ¼ inch. Gage marks at 1 inch intervals were scribed along the length of each strip; the distance between marks was then measured to the nearest 0.01 inch. These strips were loaded in tension until a permanent strain of 10% was obtained. After straining, a survey of the distances between gage marks revealed that the maximum variation from 10% strain for any strip was ± 1.0%. These strips were held at 75, 450, 900 and 1200 °F (24, 230, 480 and 650 °C) for various intervals up to a maximum of 25×10^3 hours at both 75 and 450 °F, and for 10 hours at 900 °F (480 °C) and 2 hours at 1200 °F (650 °C). Longer times at the latter two temperatures could not be studied owing to exhaustion of the test stock.

To study the effect of prestraining in compression, several normalized pipe sections 9 inches in length were compressed 10% and subsequently aged at 75 and 450 °F. The compression tube specimens were machined with parallel, surface-ground ends. Gage marks at 1 inch intervals were placed along the length at three positions around the circumference at 120-degree intervals. Although bulging was en-

countered during prestraining, notch-impact and tensile specimens were machined from wall sections which were essentially straight and exhibited between 9 and 11% strain in compression.

To determine the change in hardness, measured at 75 °F, during aging of prestrained normalized material, tensile bars with a 4 inch long, ½ inch wide and 3/16 inch thick reduced section were polished on one face. Diamond pyramid hardness was determined on one end, the specimen then strained 10% in tension, repolished and the hardness determined within the reduced section. These specimens were then aged for various periods at 75 and 450 °F and hardness determinations made again within the reduced section. At least five hardness impressions using a 20-kilogram load were made initially and after each aging interval.

To determine the effect of straining in tension on tensile properties, specimens were machined from normalized stock and strained 10% in tension before aging. Exposure of these specimens at 450 °F (230 °C) for periods up to 10^3 hours was carried out in air, but at 900 and 1200 °F (480 and 650 °C) the specimens were placed in a closed container packed with cast iron chips. Upon removal from the container the specimens exhibited a bright surface. For aging times greater than 10^3 hours, at both 75 and 450 °F (24 and 230 °C), tensile specimens were machined from the 21 inch long, prestrained strips.

Impact Tests

Because of the thin pipe wall it was impossible to obtain an impact specimen of standard ASTM dimensions. All dimensions of the specimen employed were the same as those of the standard V-notch specimen, except in the width direction (parallel to the notch axis) which was ½ that of the standard dimension. These specimens were obtained from all blanks so that the specimen axis was parallel to the axis of the original pipe and the notch axis was normal to the pipe surface.

In determining the impact transition temperature range, three specimens were tested at each test temperature. In most cases six temperatures were employed, although on a few occasions five different temperatures adequately bracketed the transition range. The specimens were held at the test temperature at least 15 minutes. The transition temperature was taken arbitrarily as the temperature corresponding to 10 ft-lb energy absorption as read from the curve through averages of the triplicate test results, and is thus a measure of the so-called ductility transition.

Tensile Tests

Two tensile specimens were tested for each aging time investigated. These specimens were machined with a reduced section 1.88

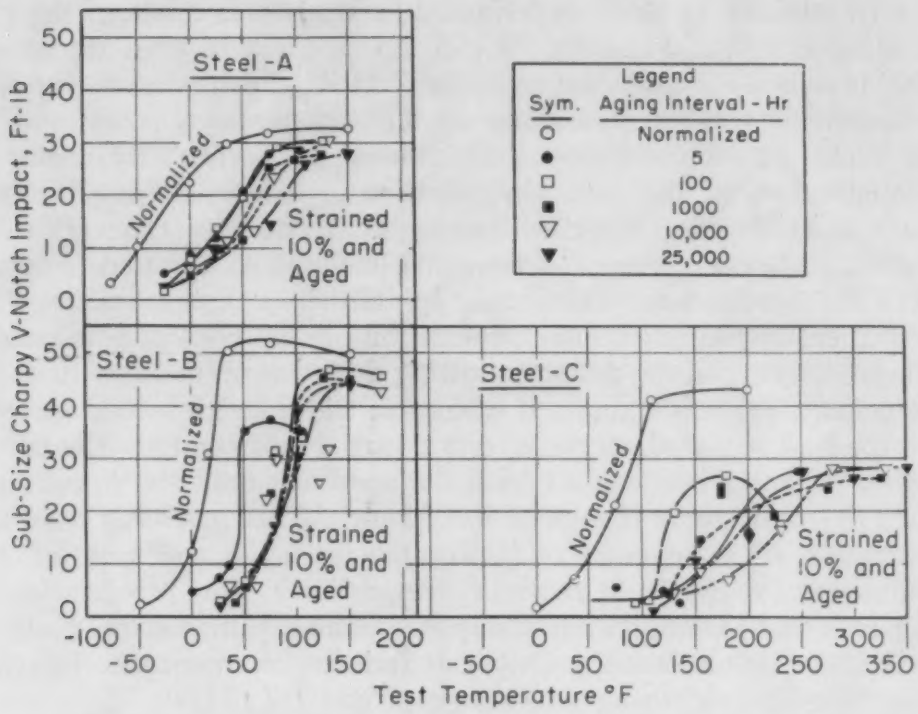


Fig. 1—Effect of Straining in Tension and Aging at 75 °F on Impact Resistance-Temperature Curves.

inch long and 0.1250 inch in diameter and threaded ends ½ inch long and ¼ inch in diameter. A load-extension record was obtained using a Selsyn motor, one inch gage length, averaging extensometer giving a X40 magnification in extension on the recorder. Autographic records during prestraining were made as well as during retesting after aging. Values of the load at the end of the prestrain and after a 0.2% strain on subsequent retesting were determined from the autographic record. The maximum load of retest was also obtained from the autographic record.

Measurement of Hardness at Temperature

By means of a recently designed hot hardness tester (16), a number of measurements were made to determine the change in hardness of the normalized steels with temperature between 75 and 500 °F (24 and 260 °C). The hot hardness specimens used in these experiments were ⅜ inch square and 1/16 to 3/16 inch thick. As previously described (16), hot hardness specimens are polished to a degree suitable for metallographic examination. Moreover, the polished surface is kept parallel to the surface which is in contact with the anvil of the tester. In these tests at least three indentations were made at each temperature: A load of 10 kilograms was used at room temperature and a 5-kilogram load at all other temperatures.

In addition to these experiments, a study was made of the rate of aging at 200, 250 and 300°F (95, 120 and 150°C). In accordance with previously established procedure (16), the hardness was first measured at room temperature on the hot hardness tester and on the Vickers hardness tester as a check on the former. By means of manual operation, the cycle of application of load in the hot hardness tester was reduced to less than 2 seconds. The loading is, nevertheless, gradual and does not approach impact loading. At elevated temperatures the hardness was measured initially in a similar manner. In subsequent measurements the penetration of the indenter was carried to a predetermined depth and following a predetermined time interval the penetration was completed within an additional 2-second interval and the load removed. In these tests a partial load is applied by bringing the indenter into contact with the specimen until the penetration dial (16) indicates a change of 0.0035 inch. This results in a partial impression with diagonals of approximately 0.310, 0.375, and 0.330 millimeters for Steels A, B, and C, respectively. For these steels, the diagonals for an impression completed under full load range from 0.350 to 0.500 millimeters. Only one indentation was made for each aging time interval, using a 10-kilogram load for all tests.

Results and Discussion

Effect of Straining and Aging on Impact Transition Temperature Range After Prestraining in Tension

The effect of straining in tension (10%) and aging between 5 and 25×10^3 hours at 75°F on the notch-impact transition temperature range is shown for the three steels in Fig. 1. In these, as well as all impact resistance-temperature curves that follow, the points shown represent the average of three impact values. A considerable shift in transition range to higher temperatures occurred for Steel A upon straining and aging 5 hours, and a much smaller additional shift occurred when aging was continued to 25×10^3 hours. For Steel B a small increase is noted upon straining and aging for 5 hours, but a somewhat more noticeable shift than was the case for Steel A is found for longer aging times. For this steel, the curves for aging times between 10^2 and 25×10^3 hours show higher impact values at temperatures above the transition range than after aging for 5 hours. No explanation can be offered for this unusual behavior. Steel C also behaves in an unusual manner. The only curve for this steel which indicates normal behavior is that for material aged 10^4 hours. It should be noted in connection with this steel that the transition temperature range after straining and aging lies completely above room temperature. Thus additional aging may have been introduced during the holding period at each test temperature.

By comparing the results of Fig. 1 with those of Fig. 2 it is found that upon aging at 450 °F (230 °C) the transition temperature range of the steels tested is shifted with few exceptions to temperatures higher than those observed after equivalent aging times at 75 °F (24 °C). Steel A exhibits a transition temperature of 64 °F (18 °C) (at a 10 ft-lb level) upon straining and aging 5 hours[2] at 450 °F (230 °C), but upon additional aging the transition temperature decreases until for an aging interval of 10^4 hours the transition temperature is the same as that found after the same aging period at 75 °F. A further slight decrease, perhaps not significant, is found after aging 25×10^3 hours. However, the total decrease in transition temperature for aging intervals between 5 and 25×10^3 hours is relatively small, amounting to only 34 °F.

For Steel B the shift in transition temperature is greater after aging at 450 °F (230 °C) than after aging for equivalent intervals at 75 °F. The effect of aging time at 450 °F on the transition temperature of Steel B is small. The behavior of Steel C again differs from that of the other steels. The transition temperature shows an overall trend to higher temperature with increasing time (with a maximum difference of 85 °F), but with inconsistent variations at intermediate aging times. It seems doubtful, however, that these variations with aging time are significant.

It should be pointed out that for Steels A and B the impact results obtained after straining and aging at 75 °F, Fig. 1, or after aging at 450 °F for Steel B, Fig. 2, indicate no tendency to over-age or a return to original impact transition temperature range. Slight tendencies for recovery of the transition temperature range in the case of Steel A are found upon aging at 450 °F, Fig. 2.

In terms of maximum shift in transition temperature (10 ft-lb level), Table II, it is found upon aging at 75 or 450 °F that Steels A and B show a similar maximum increase. Steel C shows a much greater maximum shift than the other two steels.

Effect of Straining and Aging on Transition Temperature Range After Prestraining in Compression

The results on the effect of prestraining in compression (10%) on the notch impact behavior after aging at 75 or 450 °F (24 or 230 °C) are shown in Fig. 3. The transition temperature ranges for the Steels B and C aged at 75 °F lie for the most part above the aging temperature; thus, as mentioned previously, additional aging may have occurred at the test temperature during the holding period.

The effect of straining Steel A in compression and aging at 75 or 450 °F is very similar, in terms of shift of transition range, to prestraining in tension followed by a comparable aging treatment. This

[2] As indicated in Fig. 2, all the steels were held 5 hours at 75 °F before aging at 450 °F.

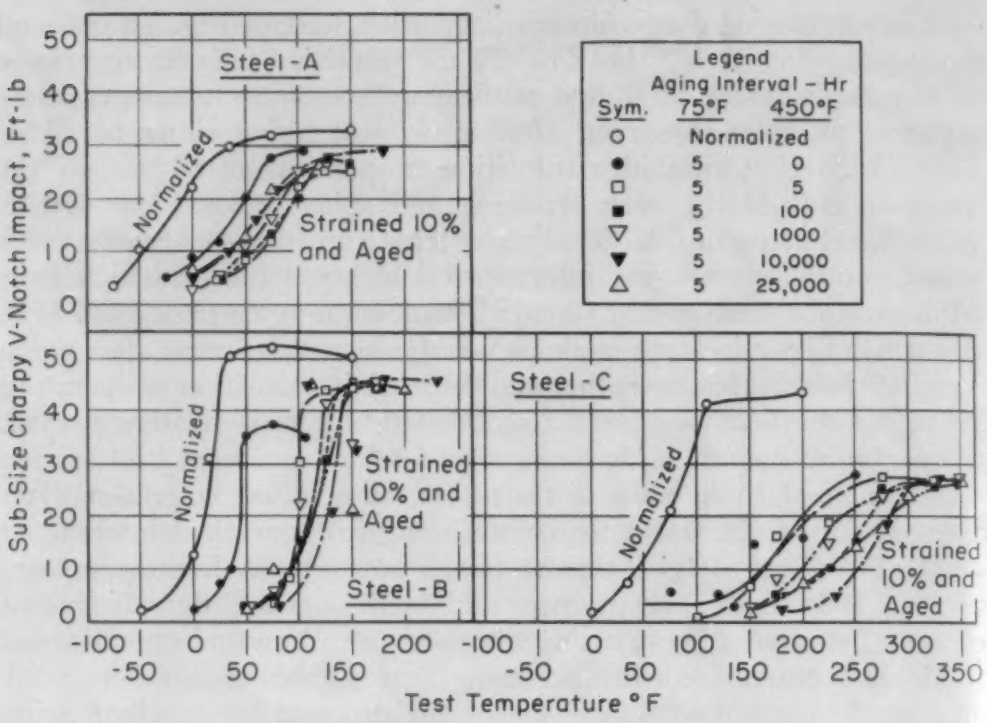


Fig. 2—Effect of Straining in Tension at 75 °F and Aging at 450 °F on Impact Resistance-Temperature Curves.

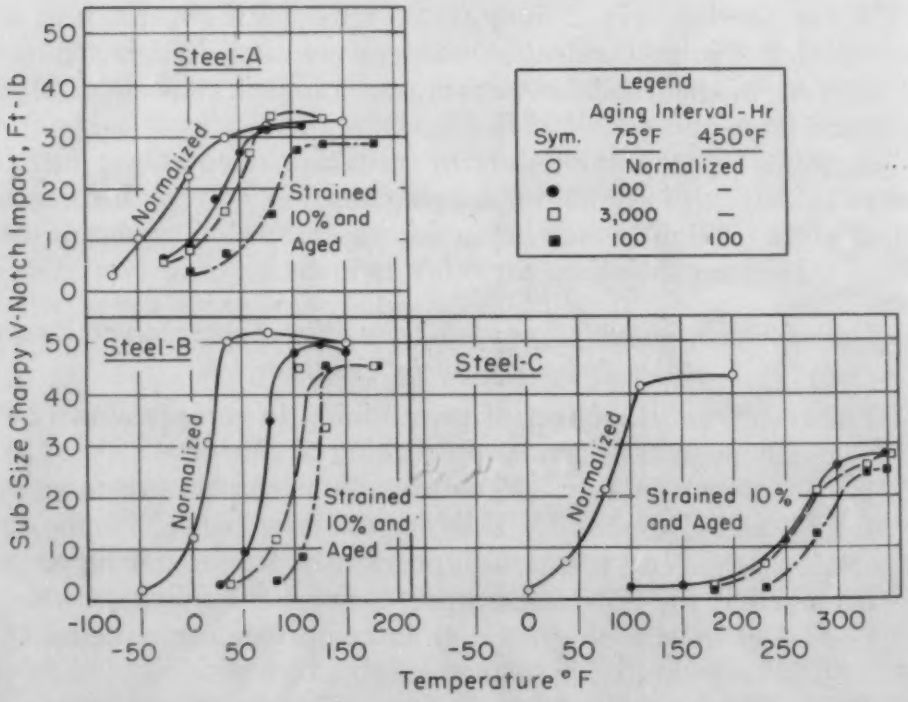


Fig. 3—Effect of Straining in Compression at 75 °F and Aging at 75 °F or 450 °F on Impact Resistance-Temperature Curves.

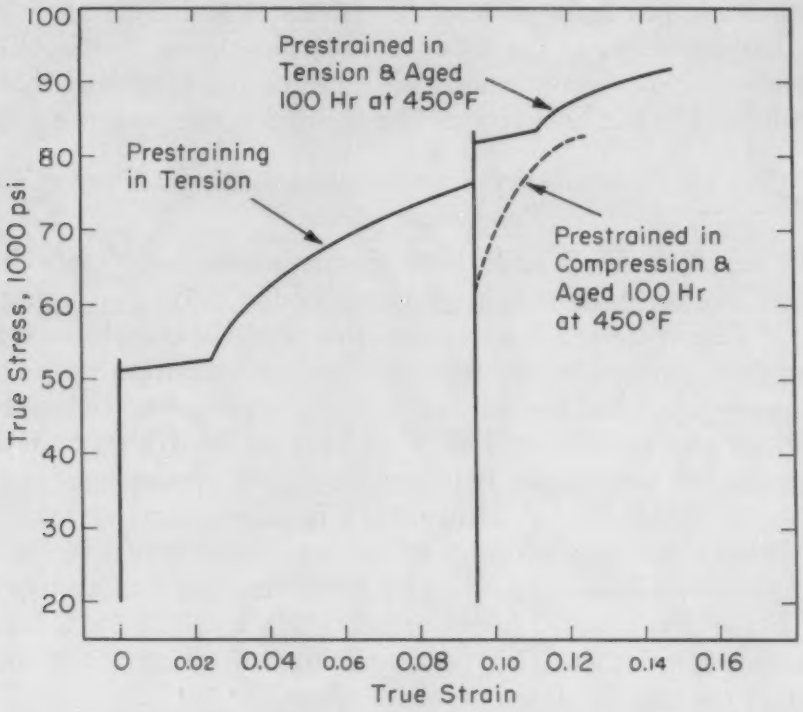


Fig. 4—Tensile True Stress-Strain Curves for Steel A During Prestraining in Tension, After Prestraining in Tension and Aging 100 Hours at 450 °F and After Prestraining in Compression and Aging 100 Hours at 450 °F.

is also true for Steel B. Steel C shows a greater shift after compression and aging at 75 and 450 °F than after straining in tension and aging, although it must be remembered that the 75 °F aging tests are of uncertain validity, since the transition temperature is greater than the aging temperature.

Because of the Bauschinger effect in these steels, prestraining in compression changes remarkably the behavior in subsequent tension. This is shown in Fig. 4, in which are included the tensile true stress-strain curves for Steel A, upon prestraining in tension, after prestraining in tension and aging 10^2 hours at 450 °F (230 °C) and after prestraining in compression and aging 10^2 hours at 450 °F. Since the impact properties are affected to about the same degree by tensile

Table II
Maximum Increase in Notch-Impact Transition Temperature (10 Ft-Lb Level) After Straining in Tension (10%) and Aging at 75 or 450 °F

Steel	Transition Temperature Before Straining and Aging — °F	Maximum Increase in Transition Temperature After Straining and Aging — °F	
		75	450
A	−48	86	112
B	− 8	73	116
C	+43	147	209

or compressive prestrain, at least for Steels A and B, it must be concluded that the shape of the true stress-strain curve, that is, the presence or absence of discontinuous yielding, or the height of this curve is not reflected in the behavior of the transition temperature range.

Effect of Stress-Relief Treatments on Impact Transition Temperature Range

The results which have been discussed so far clearly indicate that upon straining in tension or compression and upon aging at 75 or 450 °F (24 or 230 °C) an appreciable shift in transition temperature occurs. Recovery or return of the impact transition range toward the range observed for normalized material is not observed even after long periods of exposure at 450 °F (230 °C). Recovery of the impact transition range seemingly requires exposure of the aged steels at temperatures above 450 °F. However, it is quite clear from the results in Fig. 5 that essentially no recovery of the impact transition temperature range is obtained after aging at room temperature and exposing at 900 °F (480 °C) for 10 hours or 1200 °F (650 °C) for 2 hours.

As shown by others (15), normalizing will bring about complete recovery of the transition temperature range.

Effect of Strain Aging on Tensile Properties Following Prestraining in Tension

The changes in yield or tensile strength for the three steels tested after prestraining in tension and aging at 75 or 450 °F (24 or 230 °C) are shown in Figs. 6 and 7. Each experimental point is the average of two tests. The flow stress at 0.2% strain offset (the yield strength), at 10% strain, and the tensile strength were computed from load values obtained from autographic load-extension records. The change in yield strength is the difference between the true stress after a 10% strain in tension and the stress at 0.2% strain offset upon retesting after aging. The change in tensile strength is taken as the difference between the original tensile strength after normalizing and the value observed after straining and aging; both of these quantities for purposes of comparison are related to an original area (A_o) computed after 10% strain in tension.

Upon aging prestrained material at 75 °F, Fig. 6, the change in tensile strength is small for Steel A and without evidence of over aging, whereas the change in yield strength increases to a maximum after 10^3 hours and decreases somewhat upon further aging. These results clearly show that the rates of change in yield and tensile strengths upon aging at 75 °F are not the same. This is also evident in the results for Steels B and C, where an appreciable increase in the change in tensile strength is found, Fig. 6. In these latter steels the change in tensile strength also goes through a maximum which is

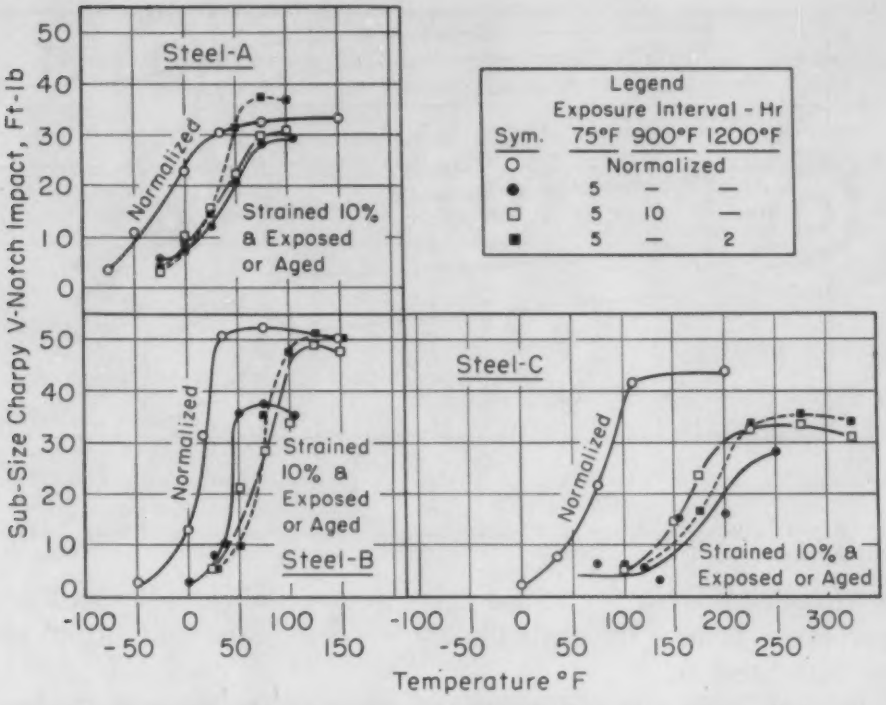


Fig. 5—Effect of Exposure at 900 °F and 1200 °F on Impact Resistance-Temperature Curves After Straining in Tension and Aging 5 Hours at 75 °F.

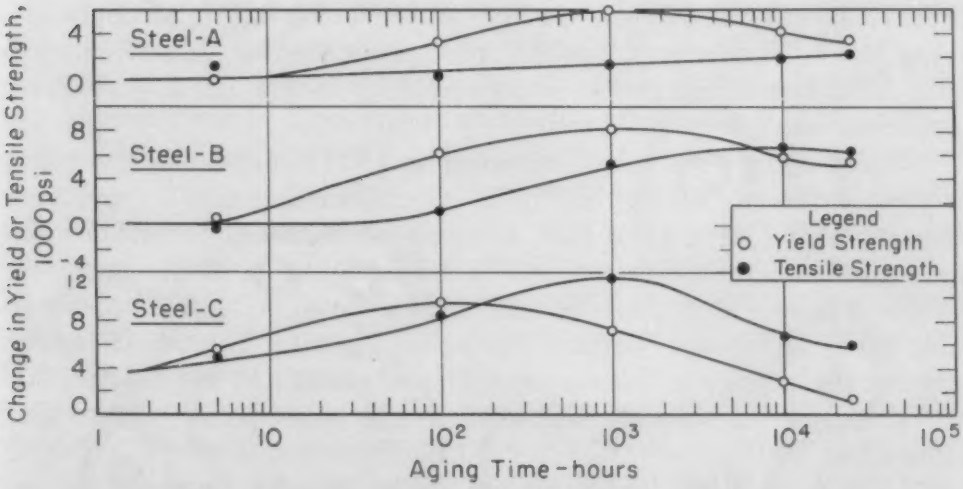


Fig. 6—Change in Yield or Tensile Strength After Prestraining 10% in Tension and Aging at 75 °F.

reached after greater aging times than the maximum in change in yield strength.

The two capped steels age faster and to a greater degree than Steel A. After aging only 5 hours at 75 °F, Steel C exhibits a degree of aging similar to the maximum amount exhibited by Steel A.

In terms of percentage change in yield strength, the maximum increase is 6.4, 16.2 and 14.6% for Steels A, B and C, respectively. This

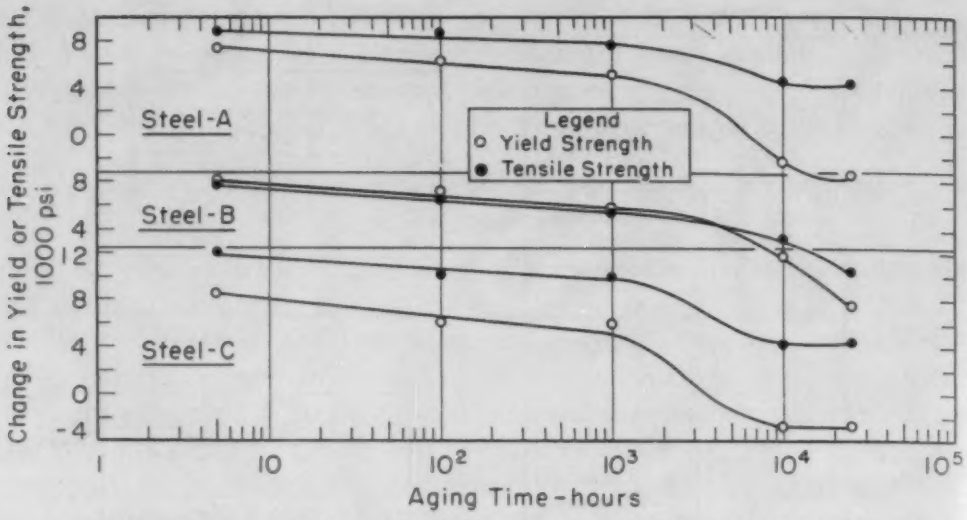


Fig. 7—Change in Yield or Tensile Strength After Prestraining 10% in Tension and Aging at 450 °F.

type of measurement for strain aging susceptibility indicates that the capped steels behave the same but show greater susceptibility to strain aging than Steel A.

In evaluating test results on the effect of straining and aging on tensile or other mechanical properties, it is felt that these properties are not only affected by aging but also by the concurrent crystal recovery. As indicated by the changes in yield and tensile strength after aging at 75 °F, it seems that different properties are not affected the same by strain aging and as determined by others (25,26), different properties are affected differently by recovery.

Upon aging prestrained material at 450 °F (230 °C) the change in yield or tensile strength, Fig. 7, as expected is much more rapid than at 75 °F (24 °C). In fact, as aging is continued beyond 5 hours, a continuous decrease in strength is evident. The rates of decrease of yield and tensile strengths for each steel seem to be approximately the same up to 10^3 hours; beyond this point a greater spread is observed between the change in tensile strength and change in yield strength.

Exposure of initially normalized and subsequently prestrained material at 900 °F (480 °C) for 10 hours and at 1200 °F (650 °C) for 2 hours resulted, Table III, in an appreciable decrease in yield strength when compared to the maximum stress reached during prestraining. After 2 hours at 1200 °F (650 °C), recovery of the yield strength is complete for Steel B; in fact, the yield strength after this treatment is lower than that after normalizing. Appreciable recovery is also observed for the other two steels. Exposure at 900 °F (480 °C) for 10 hours has little effect on the tensile strength of all steels. After exposure at 1200 °F (650 °C), however, the tensile strength of each steel is lower than the value after straining and aging 5 hours at 75 °F and even lower than the value after normalizing, Table III.

Table III
Effect of Prestraining in Tension (10%) and Aging 5 hours at 75 °F on Yield and Tensile Strength in Tension After Exposure at 900 and 1200 °F

Steel	Exposure Temperature—°F	Exposure Interval—Hr.	True Stress at 10% Strain Before Exposure 1000 Psi	Yield Strength (True Stress at 0.2% Offset) Before or After Exposure 1000 Psi	Tensile[a] Strength 1000 Psi	
					Not[b] Exposed	Exposed
A	900	10	76.9	65.1	79.5	81.2
A	1200	2	74.7	54.9	79.5	70.0
B	900	10	49.9	45.1	54.2	54.5
B	1200	2	49.8	31.5	54.2	48.4
C	900	10	65.9	57.4	73.4	72.8
C	1200	2	66.3	51.4	73.4	68.3
A	Initial Properties before Prestraining or Exposure			49.8	78.4	
B	" " "		"	35.5	54.7	
C	" " "		"	41.3	68.6	

(a)—Computed from relation $\frac{P_{max}}{A_o}$ where Ao is area after 10% strain in tension including prestrain.
(b)—After aging 5 hours at 75 °F.

Effect of Strain Aging on Tensile Properties Following Prestraining in Compression

The results of tensile tests of precompressed material aged at 75 or 450 °F (24 or 230 °C) are given in Table IV. Because of the Bauschinger effect, the tensile flow stress after 10% strain in tension is greater for the steels tested than the yield strength in tension after 10% strain in compression and aging 10^3 hours at 75 °F. Any strengthening of the precompressed material during the 10^3 hours aging period would tend to minimize this effect. Such is the case for Steels B and C which exhibit comparatively little difference between these two stress values. This finding is attributed to the rapid rate and relatively large magnitude of aging which is characteristic of these two steels even at 75 °F. In contrast, the tensile yield strength of Steel A after prestraining in compression and then aging is considerably below the tensile flow stress after 10% tensile strain, even after prolonged aging.[3]

Upon further aging at 75 °F an increase in yield strength is observed followed by a softening or recovery of the yield strength except for Steel C which was not aged beyond 3×10^3 hours. No relaxation in the tensile strength is found following aging at 75 °F. The decreasing trend in yield and tensile strength for Steel A upon aging at 450 °F (230 °C) is similar to that observed after prestraining in tension, Fig. 7. Additional aging intervals beyond those indicated in Table IV were not investigated because of lack of material.

An interesting observation is the finding that, whereas appreciable aging occurred at 75 °F in all steels prestrained in compression, no

[3] It is also possible, of course, that the magnitude of the Bauschinger effect, in the absence of aging effects, is greater in Steel A than in Steels B and C for inherent reasons such as finer grain size.

Table IV
Effect of Prestraining in Compression (10%) on Yield and Tensile Strength in Tension After Aging at 75 and 450 °F (a)

Steel	Aging Temperature—°F	Aging Interval—Hr.	Yield Strength in Tension (True Stress at 0.2% Offset) or True Stress at 10% Strain 1000 Psi	Tensile Strength (b 1000 Psi
A	Normalized Condition		49.8	78.4
A	Normalized and Strained 10% in Tension		75.4	—
A	75	1,000	44.0	67.9
A	75	3,000	52.8	72.8
A	75	9,000	48.4	73.8
A	450	100	64.7	80.4
A	450	9,000	59.6 (c)	77.1
B	Normalized Condition		35.5	54.7
B	Normalized and Strained 10% in Tension		49.8	—
B	75	1,000	44.8	53.8
B	75	3,000	50.6	60.1
B	75	9,000	45.8	60.7
B	450	100	50.2 (c)	59.4
C	Normalized Condition		41.3	68.6
C	Normalized and Strained 10% in Tension		64.9	—
C	75	1,000	56.9	70.8
C	75	3,000	59.0	75.3
C	450	100	54.6	74.1

(a) Aging at 450 °F was preceded by an aging period of 100 hours at 75 °F.
(b) Computed from relation $\frac{P_{max}}{A_o}$, where Ao is the area after 10% strain in tension including the prestrain for the normalized samples and 10% in compression for the aged samples.
(c) A return of the yield point behavior after aging was observed for these specimens.

return of discontinuous yielding is found. This is in agreement with similar observations (12,13) in which the direction of the principal strains was changed after the prestrain. Load-elongation curves obtained in the present study after aging 3×10^3 hours at 75 °F, showing the maximum amount of aging, are reproduced in Fig. 8. None of the curves shows discontinuous yielding. Return of a defined yield point in tension after prestraining in compression was found after aging 100 hours for Steel B and 9×10^3 hours for Steel A at 450 °F (230 °C). Steel C did not show a return of the yield point after aging 100 hours at 450 °F.

The role of recovery on the return of discontinuous yielding in tension after prestrain in compression and aging at 75 or 450 °F may be of importance. It seems likely that after prestraining in compression the residual stresses, which are believed to cause the Bauschinger effect, may oppose the return of the yield point behavior (13). Thus, elimination of these residual stresses through recovery at 75 °F and return of discontinuous yielding require extremely long times, and as may be inferred from the results in Table IV, longer than 9×10^3 hours. But as shown in Table IV, by increasing the aging temperature to 450 °F a return of the yield point behavior may be found after an exposure of only 100 hours as shown for Steel B.

As in the case after prestraining in tension, the yield and tensile strengths are not shifted by equal amounts during aging at 75 °F. It

is found in Table IV that the tensile strength is still increasing while the yield strength has begun to decrease.

Effect of Strain Aging on Hardness Measured at Room Temperature

The effect of straining on the hardness of mild steels when measured at room temperature is well established. As the amount of strain is increased the hardness increases at a decreasing rate. The hardness of mild steel, as is generally known, increases with time if

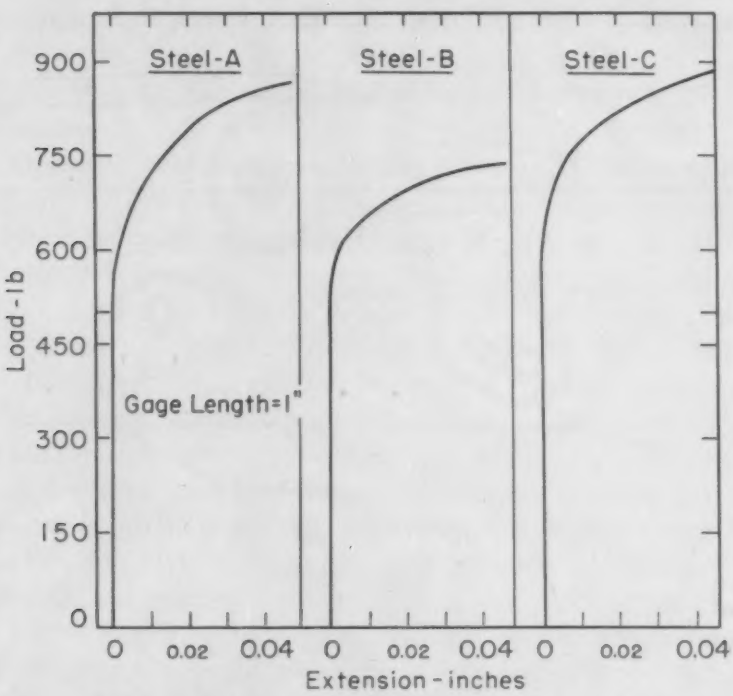


Fig. 8—Effect of 10% Compressive Strain and Aging 3000 Hours at 75 °F on Yield Point Behavior in Tension.

the strained material is held at a moderate temperature. This of course constitutes hardening by strain aging.

The effect of aging time at 75 or 450 °F after 10% tensile strain on hardness at room temperature was investigated and the results obtained are shown in Fig. 9. The change in hardness is the difference between the hardness immediately after straining and the hardness after the indicated aging time. Each experimental point represents the average of at least five impressions.

The trend exhibited by the curves upon aging at 75 °F is very similar to that indicated by the change in yield strength except that very little recovery, even for Steel C, is found by measuring the change in hardness. Steel A ages at a slower rate than Steel B or C. Steel C ages more rapidly than the other two steels. The maximum increase in hardness for all steels is essentially the same (approximately 20

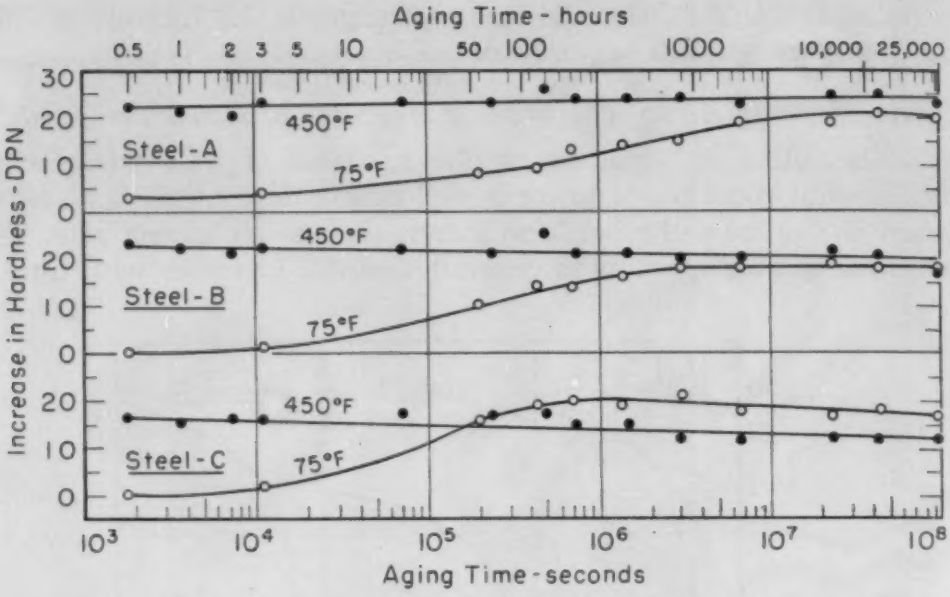


Fig. 9—Increase in Hardness After Straining 10% in Tension and Aging at 75 °F or 450 °F.

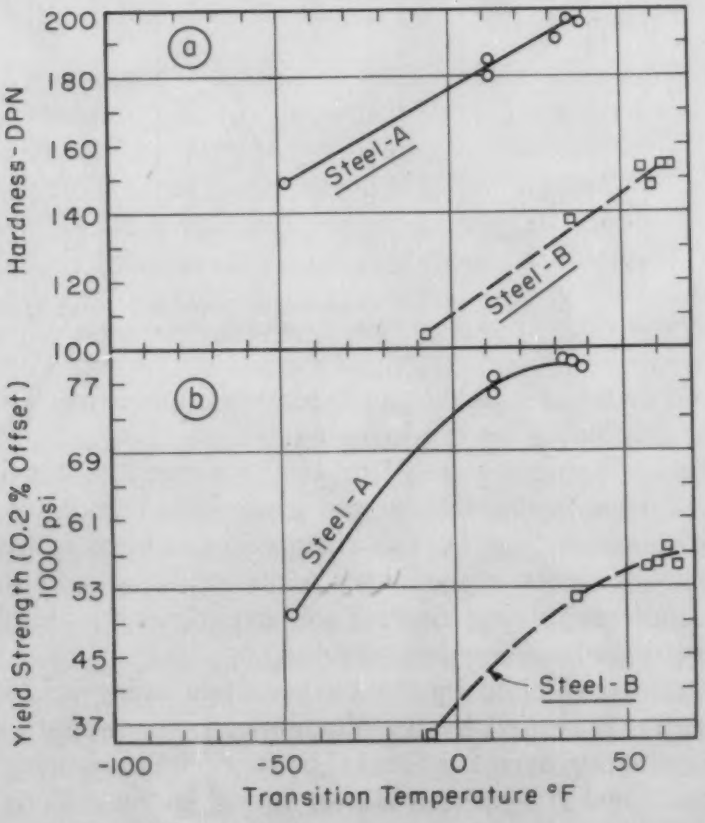


Fig. 10—Relationship Between Hardness or Yield Strength and Transition Temperature (10 ft-lb Level) After Normalizing, Straining and Aging 5 to 25,000 Hours at 75 °F.

DPN). Thus, except for differences in rate of aging, hardness changes indicate these steels to be equally susceptible to strain aging at 75 °F.

At 450 °F, Steel A aged to nearly its maximum extent after the first aging time (½ hour); thereafter this steel shows a very slight increase in hardness, whereas Steels B and C show a definite softening beyond the first aging time.

An important factor revealed by these hardness results is that hardening by strain aging at 75 or 450 °F (24 or 230 °C) persists for long periods of time and there is no evidence of overaging, although a certain amount of recovery is in evidence at 75 °F in Steel C and at 450 °F in Steels B and C, Fig. 9. As mentioned previously, the impact results also indicated that a true overaging effect during strain aging was not observed.

As mentioned earlier, strain aging as well as the concurrent recovery seem to affect various mechanical properties differently. Additional evidence substantiating this finding is given in Fig. 10 in which is shown the relationship between hardness or yield strength and transition temperature of Steels A and B after normalizing, prestraining in tension and aging at 75 °F up to 25×10^3 hours. The linear relationship observed between hardness and transition temperature, Fig. 10a, indicates that the combined effects on hardness of straining and aging and of any recovery which may occur at 75 °F is similar to the combined effect on transition temperature. This is not the case when comparing yield strength and transition temperature at 75 °F. As revealed in Fig. 10b the relationship between these two properties is not linear. Since evidence of an appreciable amount of recovery is found in the yield strength, Fig. 6, and not in the impact results, the concave downward curves were to be expected. No relationships similar to those found in Fig. 10 were expected for Steel C, which, after prestraining, exhibited a transition range above room temperature.

Effect of Temperature and Aging Time on Hot Hardness Measurements

The change in hardness of the three steels tested as temperature is increased is shown in Fig. 11. Each experimental point represents the average of two impressions. The change in hardness is the difference between room temperature hardness and hardness at the indicated temperatures. The loading and unloading cycle of the hot hardness tester used is 2 minutes long. However, total penetration is essentially completed during the initial 25 seconds of the loading cycle. Thus any hardening caused by aging and any softening caused by recovery must occur as deformation proceeds during this initial period. Creep is not found to be a factor in the range of temperatures covered during the 2 minute cycle.

For Steel C, the hardness increases sharply with temperature, goes through a maximum between 350 and 400 °F (175 and 205 °C), and then decreases sharply. Steel B exhibits a sharp increase in hardness beyond 200 °F (95 °C), a maximum between 350 and 400 °F and a sharp decrease beyond the maximum. Steel A shows an initial decrease in hardness with a minimum at about 250 °F (120 °C) followed by an increase in hardness, a maximum at about 400 °F and a decrease beyond the maximum.

Several factors are involved when measuring the hardness of mild steels at temperatures above 75 °F; therefore the results are not

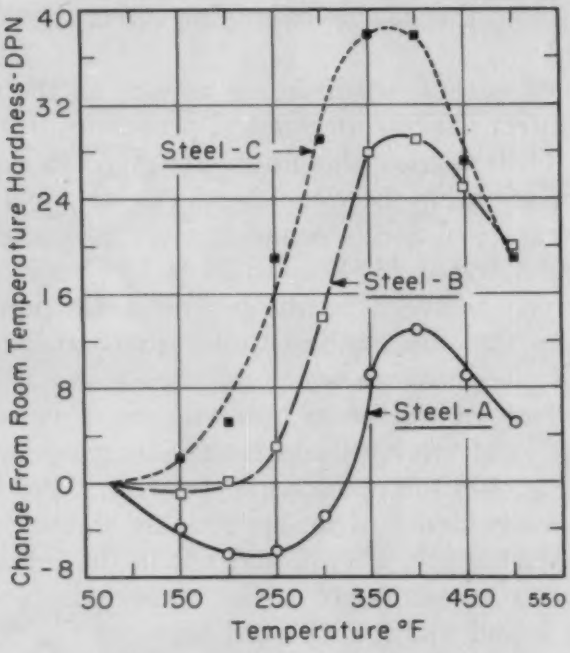


Fig. 11—Change in Hardness Between Room Temperature and Various Temperatures up to 500 °F.

easily interpreted. It would seem that the change in hardness from 75 °F as the temperature is raised depends, up to moderate temperatures, on at least three factors, namely, strain aging, recovery or relaxation, and the normal decrease in resistance to penetration as temperature is increased. The first two factors are affected by time and therefore rate considerations are involved. From the present results it may be concluded that for Steels B and C strain aging is the predominant factor up to the maximum hardness change; the other factors become more dominant at higher temperatures. For Steel A strain aging is predominant only for a short range in temperature, between 300 and 400 °F (150 and 205 °C).

The change in hardness with aging time intervals of short duration at 200, 250 and 300 °F (95, 120 and 150 °C) is shown in Fig. 12. As

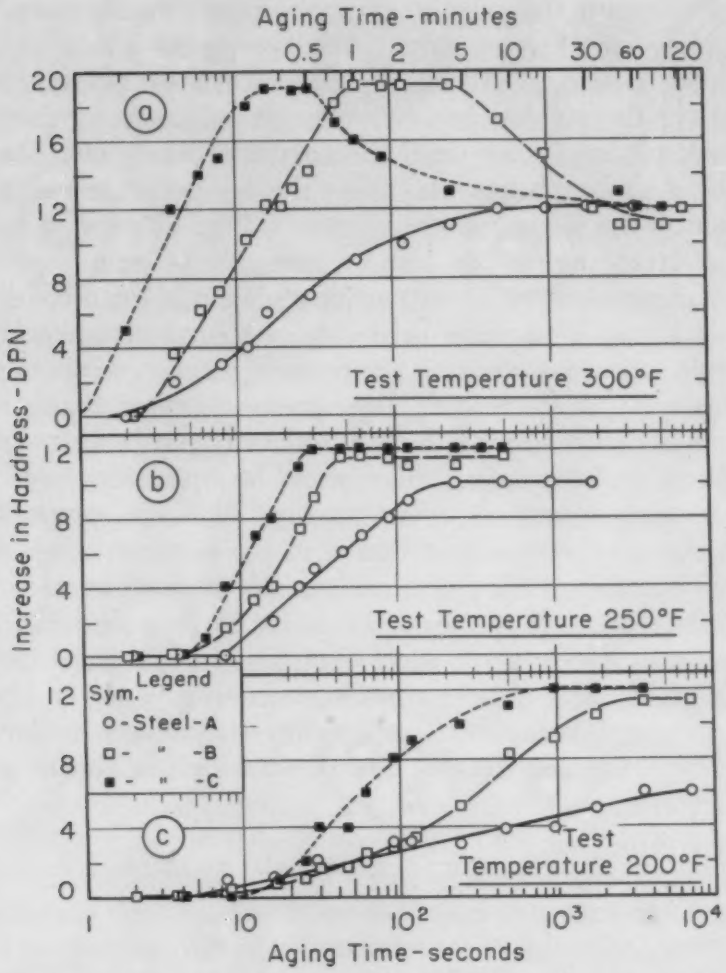


Fig. 12—Increase in Hardness at 200, 250 or 300 °F Upon Interrupting Hardness Test for Various Time Intervals.

mentioned previously, these results were obtained by making a partial impression, constituting the prestrain, aging for a prescribed interval and completing the impression. The initial hardness which is used as a base for computing the increase in hardness is determined by applying the total load within 2 seconds at a constant rate to preclude impact loading. However, at 300 °F (150 °C) Fig. 12a, some aging may occur within a loading cycle of 2 seconds. For ferritic steels, good agreement is found at room temperature between values determined by the standard loading cycle and a loading cycle of 2 seconds. Because of strain aging and other effects, the results at higher temperatures are in agreement only after equivalent aging times.

As aging is continued two factors are affecting the hardness. Strain aging tends to increase the hardness, whereas recovery tends to lower it. The net result of these effects determines the hardness observed. As temperature is increased from 200 °F (95 °C) in Fig. 12c to 300 °F (150 °C) in Fig. 12a, the curves are shifted to

the left, indicating that strain aging becomes much more rapid. At 300 °F (150 °C) recovery apparently overtakes strain aging in the case of Steels B and C. At this temperature, a maximum in hardness is reached for these steels and recovery, at a decreasing rate, seems to be the predominant factor until the hardness levels off. Steel A does not exhibit a similar behavior within the temperature range covered.

Evidently the slopes of the curves in Fig. 12 depend not only on the rate of strain aging but also on the rate of recovery. Thus, the point of maximum increase in hardness depends on recovery as well as on strain aging. This point is of some importance when attempting, for example, to compute activation energies for strain aging from data of this type. Since it is now generally accepted that strain aging depends on the diffusion of carbon and nitrogen in iron (6,11), the activation energy for strain aging should be equivalent to that for the diffusion of carbon and nitrogen, namely, 20 K cal. per mol. (17,18, 19,21). Although the results obtained in the present investigation are too limited for accurate determinations of the activation energy, the values which were computed on the basis of time for half of maximum aging differ widely for each steel, ranging from 18 to 28 K cal. per mol. This finding should not be surprising, since in the present study, as presumably in other strain aging studies in which mechanical properties have been measured, the effect which is observed includes that of recovery.

Effect of Strain Aging Treatments on Microstructure

Careful microscopic examination was made of various samples after straining and aging to detect changes in microstructure associated with the changes in properties upon aging. No change could be detected in any steel upon exposure at room temperature or at 450 °F (230 °C). Exposure at 900 °F (480 °C) caused slight spheroidization, and at 1200 °F (650 °C) extensive spheroidization was found in all steels. No graphitization was noted in any instance.

A detailed study using the electron microscope revealed no appearance of a precipitate or other structural change within the ferrite grains during aging, although the samples investigated had been strained and aged at 75 or 450 °F for at least 2 years and appreciable changes in mechanical properties resulted.

Mechanism of Strain Aging

Until recently the mechanism of strain aging has been considered to be due to precipitation hardening (2,6,9). However, it was not known whether the process is a solution and precipitation effect or a change in solubility caused by the strain, or something altogether different.

Several attempts (6) have been made to identify the elements

which cause strain aging in mild steel. In general, three elements, carbon, nitrogen and oxygen, have been suspected of being responsible and have been investigated extensively. The results obtained have been generally accepted as showing that strain aging may be eliminated, or at least greatly diminished, by removing the carbon and nitrogen by means of hydrogen, by the addition of strong deoxidizers (2,3,7), or by the addition of strong carbide formers, which generally are also strong nitride formers (4,5,7).

It is difficult at first to rationalize the differences implied by these methods. For example, the addition of such elements as titanium, vanadium, columbium or possibly chromium, which are carbide and nitride-formers as well as strong deoxidizers should eliminate strain aging. But, strain aging is also thought by some to be suppressed by complete deoxidation with aluminum (3), a nitride but not a carbide forming element. Yet in steels heavily deoxidized with aluminum, aging, especially at the higher aging temperatures, cannot be completely suppressed though it may be minimized by proper heat treatment (14). The results in the literature indicate that, although carbon and nitrogen bring about aging, the role of oxygen is not completely clarified, and oxygen may have a secondary influence on the amount of carbon necessary to cause strain aging. It has been pointed out that the rate of strain aging depends on the permeability (product of diffusivity and concentration) of the solute atoms, carbon and nitrogen (11). Because of the greater solubility of nitrogen in α-iron, this element is more effective than carbon in causing strain aging.

Strain aging was believed by some to involve the precipitation of a compound (carbide, nitride and possibly an oxide) on the slip planes set up by prior strain, and at the grain boundaries. The grain boundary precipitate has been associated with the stress-corrosion cracking of strained and aged mild steel (22) and discontinuous yielding (13). On the other hand, the precipitate on the slip planes was believed to cause the hardening effect observed during aging, for it is generally accepted that grain boundary precipitate will bring about little over-all hardening (2).

The belief that strain aging is due to a precipitation hardening, similar to quench aging, leads, however, to several conclusions which are not in agreement with test results. It is generally accepted that in quench aging of mild steel, or other alloys such as duralumin, if the hardness of a quenched sample is found to increase fairly rapidly with time, then during over aging it decreases again rapidly towards its original level. A second characteristic of quench aging is that the maximum hardness increases with decreasing aging temperature. At the same time, the rate of change of hardness decreases. Such behavior differs from that observed during strain aging in mild steel, which is characterized, as shown in the present investigation and by others (2),

neither by an over aging effect nor by an increase in maximum hardness with decreasing aging temperature. Instead, a wide range of temperatures will cause an appreciable amount of hardening with no visible evidence of softening during extended periods of time. An indication of softening is found in the yield and tensile strength at 75 °F; however, no such recovery is found in the hardness. Unlike quench aging, hardening in strain aging is extremely rapid even at temperatures where no indication of eventual softening is observed. These differences indicate that strain and quench aging are essentially different.

Recently, Cottrell (20) has advanced a mechanism of strain aging and discontinuous yielding in ferrite containing carbon or nitrogen atoms in solution. From the interactions between solute atoms and dislocations, Cottrell concluded that migration of interstitial atoms, such as carbon or nitrogen, to the vicinity of dislocations partly relieves local internal stress. This leads to the formation of "atmospheres" of carbon or nitrogen atoms around existing dislocations.

Accordingly, when an external force is applied each dislocation tends to move and leave its "atmosphere" behind. However, the force necessary to move each dislocation depends not only on the force needed to propagate each dislocation through the lattice, but also on the anchoring force of the "atmosphere." When the external force is large enough to overcome the anchoring force, each dislocation will move through the lattice at high speed. Moreover, since the force necessary to overcome the anchoring force is greater than that needed to keep them in motion (21), the dislocations accelerate. This results in rapid deformation at a stress smaller than the initial stress. In other words, this constitutes a sharp upper yield point followed by yielding under relatively constant load at a lower yield point.

Discontinuous yielding is completely eliminated by over-strain. Upon aging, however, it is proposed by Cottrell that the carbon or nitrogen atoms diffuse to the vicinity of dislocations forming new traps and therefore discontinuous yielding returns. This is the mechanism proposed to account for strain aging.

Cottrell's mechanism explains satisfactorily discontinuous yielding both before and after strain aging, but deals only with the early stages of aging and does not, in its present form, explain other events which occur as aging progresses. For example, the present theory is not intended to deal with the appreciable strengthening observed during extended aging. That is to say, it does not explain the increase in the lower yield or tensile strength or the difference in rate of increase of these quantities, Figs. 6 and 7.

After aging it seems clear that during the lower yield extension the propagation of each dislocation through the lattice should be impeded only by the interactions between the moving dislocations and

newly formed "atmospheres" after the anchoring force is overcome. However, this may mean, in part, even at 75 °F that moving dislocations may drag along with them, at least over a very short distance, parts of the "atmospheres" around them. This mechanism is believed to operate at much higher temperatures and at slow strain rates where more rapid diffusion of solute atoms is possible (23). Such a mechanism may explain the increase in the lower yield strength during extended aging but does not explain the effect on the remainder of the stress strain curve.

It is very likely, however, that migration of interstitial atoms occurs to places of less internal stress than around well defined dislocations [4] or in other words it may be possible that the rate of migration is controlled by the length of edge dislocation per unit volume (24). If this assumption is true, it may well be that upon aging interstitial atoms tend to migrate initially to the vicinity of well defined dislocations because of the greater magnitude of local internal stresses at these locations. However, upon further aging a general migration occurs to other points of less internal stress. It is thus possible in this manner to explain the difference in rate of increase of yield and tensile strengths upon aging, Fig. 6. The greater rate of migration to the vicinity of well defined dislocations leads to a faster rate of increase in yield strength since these are probably the dislocations set in motion during discontinuous yielding. The tensile strength, however, is affected by the more general migration which takes place at a slower rate to points of potential initiation of dislocations or at least around less well defined dislocations whose propagation requires further plastic deformation or greater applied loads. An explanation of the eventual decrease in yield or tensile strength as well as the difference in rate of decrease, Fig. 6, will have to await a better understanding of the mechanism of recovery. It is unlikely that the recovery of these properties is caused by over aging, that is, precipitate agglomeration, since the change in hardness, Fig. 9, does not indicate any such occurrence.

However, selective migration of solute atoms to locations of internal stress may be interpreted as causing the formation of a special type of precipitate. Thus, it is possible to think of the "clouds" around the well defined dislocations as a selective type of a special precipitate, while the less extensive "clouds" near the other lattice distortions may be described as a general precipitate of the same type. The characteristics of such a special precipitate, as might be expected, differ from those of the precipitate obtained during quench aging.

Although, by the Cottrell mechanism, the return of discontinuous yield upon strain aging is mandatory, the pattern of residual stresses

[4] It is of interest to note that work on recovery of prestrained 2S-0 aluminum (25) indicates that in the work-hardened state at least two different types of imperfections having different interaction energies may exist.

formed during the prestrain can completely mask the return of the yield point behavior. This seems to be the case when tension is preceded by prestrain in compression. However, as shown in Table IV, the strengthening caused by strain aging is still in evidence. Thus, if it is assumed that a general migration of the interstitial atoms, as mentioned previously, accompanies the selective migration, it is reasonable to expect that although the residual stress pattern may completely eliminate discontinuous yielding, an upward shift of the entire flow curve is not precluded. An explanation of the return of the yield point after extensive aging at 450 °F (230 °C), Table IV, must await a more complete knowledge of recovery which is associated with the removal of residual stresses.

Summary and Conclusions

The effects of time and temperature on the strain aging characteristics of three low carbon steels in the normalized condition have been investigated. After prestraining 10% in tension, the material was exposed at 75, 450, 900 or 1200 °F (24, 230, 480 or 650 °C) for various predetermined time intervals. Following 10% prestrain in compression, the material was exposed at 75 or 450 °F (24 or 230 °C). The effects of exposure time and temperature on the notch-impact transition temperature range, yield strength and tensile strength were investigated.

The effect of prestraining in tension and aging at 75 or 450 °F on hardness determined at room temperature was studied. The change in hardness with temperature between 75 and 500 °F (24 and 260 °C) was also determined. The effect of aging intervals of short duration at 200, 250 and 300 °F (95, 120 and 150 °C) was investigated.

The following conclusions are drawn from the results obtained in this investigation.

A. *Effect of Straining and Strain Aging on Impact Transition Temperature Range*

1. In terms of maximum shift in transition temperature (chosen at a level of 10 ft-lb) after straining in tension and aging at 75 °F, Steels A and B show a similar shift, Table II. Steel C shows a much greater shift; however, it should be noted that for Steel C the transition temperatures after straining and aging are above the aging temperature.

2. Upon aging at 450 °F, Steels A and B again exhibit a similar maximum shift in transition temperature. Steel C shows again a much greater maximum shift. No real overaging effect after aging at 75 or 450 °F was noted.

3. Results obtained on material prestrained in compression (10%) and aged at 75 or 450 °F show essentially that the effect on

notch-impact transition temperature range is the same as prestrain in tension.

4. Impact tests on material strained in tension and aged 5 hours at 75 °F and exposed at 900 and 1200 °F (480 and 650 °C) show that very little effect on the transition temperature range is found.

B. *Tensile Results*

1. As measured by the increase of yield and tensile strengths of initially normalized material with time after straining 10% in tension, Steels B and C aged more rapidly and to a greater degree at 75 °F than did Steel A. The yield and tensile strengths change at different rates, the yield strength increasing at a faster rate and reaching a maximum at a shorter time.

2. The maximum increase in yield or tensile strength upon aging at 450 °F is followed by a recovery upon further aging. The effect of this recovery or relaxation, which is also observed when aging at 75 °F, in particular in Steels B and C, is different from a true overaging effect like that found during quench aging. The experimental results obtained in this investigation indicate that recovery plays an important role in the effects observed during strain aging at 450 °F or even at 75 °F.

3. Following prestraining in compression, aging at 75 °F, and testing in tension, appreciable aging is found without a return of the yield point behavior. Discontinuous yielding returns after aging at 450 °F. The absence of the yield point behavior after aging at 75 °F is believed to be related to the pattern of residual stresses resulting during the prestrain in compression.

4. Exposure at 900 or 1200 °F (480 or 650 °C) of all steels strained in tension (10%) and aged at 75 °F caused appreciable recovery in yield and tensile strengths, the recovery in the yield strength being, however, much the greater.

C. *Hardness Results*

1. After straining in tension and aging at 75 °F, the maximum increase in hardness is essentially the same for all steels, however, the increase is most rapid for Steels B and C. A slight softening beyond the aging time of 1000 hours is found for Steel C; the other steels show no softening up to 25,000 hours aging time. Upon aging at 450 °F (230 °C), the hardness of Steel A increases slightly with time; for Steels B and C the hardness decreases continually with aging time.

2. The variation in hardness with temperature differs widely for the three steels. Steels B and C show hardness peaks of much greater magnitude than Steel A. Moreover, in this hot-hardness test, Steel A, which is deoxidized with silicon and aluminum, shows little indication

of strain aging below a temperature of 300 °F (150 °C). By this method Steels B and C indicate strain aging tendencies at temperatures just above room temperature.

3. Strain aging in the steels studied is extremely rapid at temperatures above 250 °F (120 °C), as revealed by the increase in hardness upon making a partial impression at temperature, aging for short-time intervals, and completing the impression. These results again indicate that Steels B and C age at a faster rate and to a greater degree than Steel A.

D. *Mechanism of Strain Aging*

The return of discontinuous yielding during the early stages of strain aging is explained adequately by the Cottrell mechanism. However, amplification of this mechanism becomes necessary in order to explain other results such as the increase in yield strength or difference in rate of increase of yield and tensile strengths during extended aging.

It is proposed here that the increase in lower yield strength as aging proceeds is related to the possible interaction between moving dislocations and newly formed "atmospheres."

The difference in rate of increase in yield and tensile strengths is perhaps related to the difference in rate of migration of carbon or nitrogen atoms to a number of sites of differing degrees of internal stress. Interstitial atoms tend to migrate most rapidly to regions of great internal stress around well defined dislocations, whereas migration to regions of lattice disturbances having less internal stress occurs at a slower rate.

Acknowledgments

Grateful acknowledgment is made to W. B. Seens, W. L. Jensen and E. K. Lynn for conducting all mechanical tests. We are also indebted to the National Tube Division of United States Steel Corporation for the test steels.

References

1. H. V. Kockritz, "The Progress of Aging with Time of Soft Steel and the Aging of Steel from Various Sources," M. H. Forsch *Inst. Ver. Stahleverke,* Vol. 2, 1932, p. 193.
2. E. S. Davenport and E. C. Bain, "The Strain Aging of Steel," TRANSACTIONS, American Society for Metals, Vol. 23, 1935, p. 1047.
3. B. N. Daniloff, R. F. Mehl and C. H. Herty, Jr., "The Influence of Deoxidation on the Aging of Mild Steels," TRANSACTIONS, American Society for Metals, Vol. 24, 1936, p. 595.
4. C. A. Edwards, H. J. Jones and B. Walters, "A Study of Strain-Age-Hardening of Mild Steel," *Journal, Iron and Steel Institute,* Vol. 139, 1939, p. 341.
5. C. A. Edwards, D. L. Phillips and H. N. Jones, "The Influence of Some Special Elements Upon the Strain-Aging and Yield-Point Characteristics of Low-Carbon Steels," *Journal, Iron and Steel Institute,* Vol. 142, 1940, p. 199.

6. J. R. Low, Jr. and M. Gensamer, "Aging and the Yield Point in Steel," *Transactions,* American Institute of Mining and Metallurgical Engineers, Vol. 158, 1944, p. 207.
7. G. F. Comstock and J. R. Lewis, "A Comparison of Aluminum and Titanium Deoxidation for Preventing Strain Aging Embrittlement in Low Carbon Steels," TRANSACTIONS, American Society for Metals, Vol. 34, 1945, p. 425.
8. W. H. Bruckner and W. E. Ellis, "Strain Aging in Welding Low Carbon Structural Steel," *Welding Journal,* Vol. 27, 1948, p. 4415.
9. G. Sachs, "Strain Aging Criteria," *Iron and Steel,* Vol. 21, August 1948.
10. H. Schwartzbart and J. R. Low, Jr., "The Yielding and Strain Aging of Carburized and Nitrided Single Crystals of Iron," *Transactions,* American Institute of Mining and Metallurgical Engineers, Vol. 185, 1949, p. 637.
11. J. D. Fast, "Aging of Iron and Steel," Iron and Coal Trades Review, Vol. 160, 1950, p. 837.
12. C. F. Tipper, "Effect of Direction of Rolling, Direction of Straining, and Aging on the Mechanical Properties of Mild-Steel Plate," *Journal, Iron and Steel Institute,* Vol. 172, October 1952, p. 173.
13. N. H. Polakowski, "Effect of Residual Stresses on Yielding and Strain-Aging of Carbon Steel," *Journal, Iron and Steel Institute,* Vol. 172, 1952, p. 369.
14. W. C. Leslie and R. L. Rickett, "Influence of Aluminum and Silicon Deoxidation on the Strain Aging of Low-Carbon Steels," *Journal of Metals,* August 1953.
15. C. T. Osborn, A. F. Scotchbrook, R. D. Stout and G. B. Johnston, "Effect of Plastic Strain and Heat Treatment," *Welding Journal,* Vol. 28, 1949, p. 337.
16. F. Garofalo, P. R. Malenock and G. V. Smith, "Hardness of Various Steels at Elevated Temperatures," TRANSACTIONS, American Society for Metals, Vol. 45, 1953, p. 377.
17. J. L. Snoek, "Effect of Small Quantities of Carbon and Nitrogen on the Elastic and Plastic Properties of Iron," *Physica,* Vol. 8, 1941, p. 711.
18. W. A. West, "Elastic After-Effects in Iron Wires from 20C to 550C," *Transactions,* American Institute of Mining and Metallurgical Engineers, Vol. 167, 1946, p. 192.
19. Ting-Sui Ke, "Anelastic Properties of Iron," *Transactions,* American Institute of Mining and Metallurgical Engineers, Vol. 176, 1948, p. 448.
20. A. H. Cottrell and B. A. Bilby, "Dislocation Theory of Yielding and Strain Aging in Iron," *Proceedings, Physical Society,* Sec. A, Vol. 62, 1949, p. 49.
21. A. H. Cottrell and A. T. Churchman, "Changes of Electrical Resistance During the Strain Aging of Iron," *Journal, Iron and Steel Institute,* Vol. 162, 1949, p. 271.
22. J. T. Waber and H. T. McDonald, "Relation of Strain Aging to the Stress Corrosion Cracking of Mild Steel," *Welding Journal,* Vol. 25, 1946, p. 2235.
23. A. H. Cottrell, "Dislocations and Plastic Flow in Crystals," Oxford University Press (1953).
24. S. Harper, "Precipitation of Carbon and Nitrogen in Cold-Worked Alpha-Iron," *Physical Review,* Vol. 83, Series 2, p. 709 (1951).
25. T. V. Cherian, P. Pietrokowsky and J. E. Dorn, "Some Observations on the Recovery of Cold Worked Aluminum," *Transactions,* American Institute of Mining and Metallurgical Engineers, Vol. 185, 1949, p. 948.
26. J. E. Wilson and L. Thormassen, "X-ray Line Broadness of Metals and Alloys and Its Relation to High Temperature Stability," TRANSACTIONS, American Society for Metals, Vol. 22, 1934, p. 769.

THE TENSILE PROPERTIES OF MOLYBDENUM AT ELEVATED TEMPERATURES

By J. W. Pugh

Abstract

A detailed analysis has been made of the tensile properties of molybdenum as a function of temperature. It is concluded that the excellent high temperature strength of this metal is due to strain aging.

Introduction

INCREASED interest in molybdenum during the last few years has resulted in the accumulation of a vast amount of technical data (1).[1] Perhaps the most remarkable single property of molybdenum is its high strength at temperatures in the range 1600 to 2000 °F (870 to 1095 °C). The work reported in this paper was undertaken to obtain more detailed information about the high temperature strength on the basis of short-time constant-rate tests and long-time creep tests.

Preparation of Material

Molybdenum was prepared by arc melting sintered bar ends in a furnace similar to that described by Pugh, Hadley, and Hennig (2). Melting was accomplished using 2500 amperes and 30 volts in a 4-inch diameter water-cooled copper crucible. The crushed melting stock was fed into the crucible continuously as a water-cooled, tungsten-tipped electrode rotated over the molten metal. This operation took place in a vacuum-tight shell filled with argon at one atmosphere pressure.

The ingot was scalped to 3.5 inches in diameter and extruded to one inch in two passes at 3000 °F (1650 °C) using molten glass for a die lubricant. Swaging at 1830 °F (1000 °C) reduced the extruded rod to 0.345 inch in diameter. This produced a cold-worked or fibrous structure having 88% cold reduction. Annealing at 2550 °F (1400 °C) for 4 hours produced a recrystallized structure having an average of 500 grains per square millimeter.

A chemical analysis was made on one of the ruptured tensile bars. The results of this analysis are shown in Table I.

[1] The figures appearing in parentheses pertain to the references appended to this paper.

The author, J. W. Pugh, is associated with the Metallurgy Research Department, General Electric Company, Research Laboratory, Schenectady, N. Y.
Manuscript received July 27, 1954.

Table I
Chemical Analysis of Molybdenum

Element	Weight Per Cent Found
O	0.003
H	0.0003
N	0.001
C	0.05

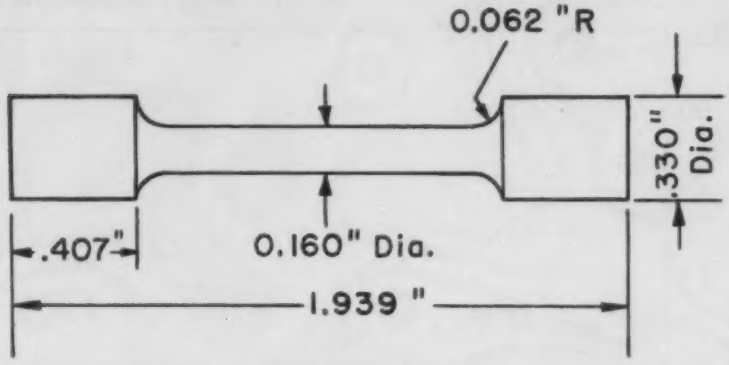


Fig. 1—Tensile Test Specimen.

Testing Procedure

Short-time constant-rate tests were made at two strain rates, 0.2 and 0.02 inches per inch per minute on an Instron testing machine. With the exception of the room temperature test, all tests were made in vacuum. The specimen used is illustrated in Fig. 1. Data were recorded autographically on load-time charts where time is a measure of extension. Temperature readings were made by means of a platinum-platinum rhodium thermocouple resting on top of the test sample.

Constant-load creep-rupture tests were conducted in an argon atmosphere at 1600, 1800, and 2000 °F (870, 980 and 1095 °C). The testing machine used employs a pulling string which includes strain measuring devices and is almost completely enclosed in a vacuum-tight capsule. This string is loaded by means of a lever arm, from which calculated weights are balanced against a specified pulling load. Pull rods enter the capsule through "O" ring seals. Strain is measured inside the capsule by concentric extension tubes linked to the specimen itself. Extension is read through a window in the capsule by means of a strain gage which is acted on by the extension tubes.

Temperatures were controlled and measured by thermocouples inside the capsule in the vicinity of the specimen. Four couples were used: one for controlling the temperature, the other three for measuring the temperature through the vicinity of the specimen. Three Nichrome heating coils provided uniform heat distribution at each temperature.

Specimens used for these tests were identical to those used for

the constant-strain-rate tests, except that the button heads were threaded, so that extension rods could be attached.

Results and Discussion

Constant-rate Tensile Properties

True-stress, true-strain curves for the as-swaged material are shown in Figs. 2 and 3, while the curves for recrystallized molybdenum

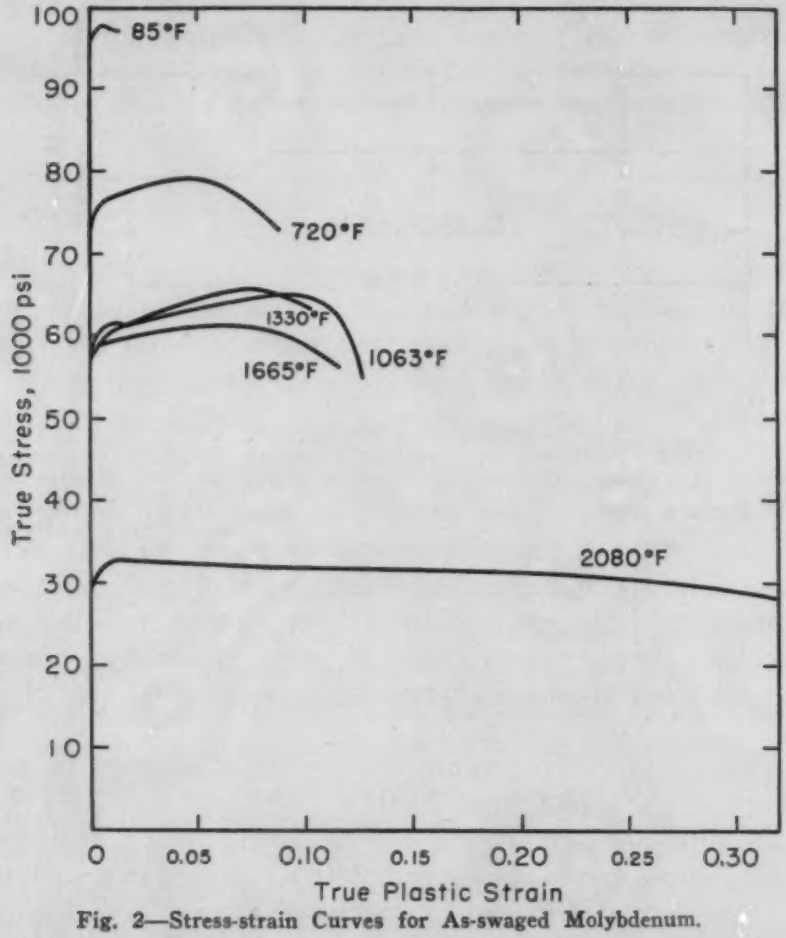


Fig. 2—Stress-strain Curves for As-swaged Molybdenum.

are represented in Figs. 4 and 5. The logarithmic stress-strain relationships are linear over most of the plastic range. Deviations at low strain are associated with initial yielding. The most extreme deviations result from the yield-point phenomenon which was observed for recrystallized molybdenum in tests from room temperature to about 1200 °F (650 °C). The slopes of the curves for as-swaged molybdenum are all nearly horizontal, and in some cases negative.

Evaluation of the plastic flow curves has been made by assuming that the mechanical equation of state (3) is applicable to these tests and by using the expressions:

$$\sigma = A\epsilon^m|\dot{\epsilon},T \qquad \text{Equation 1}$$

and

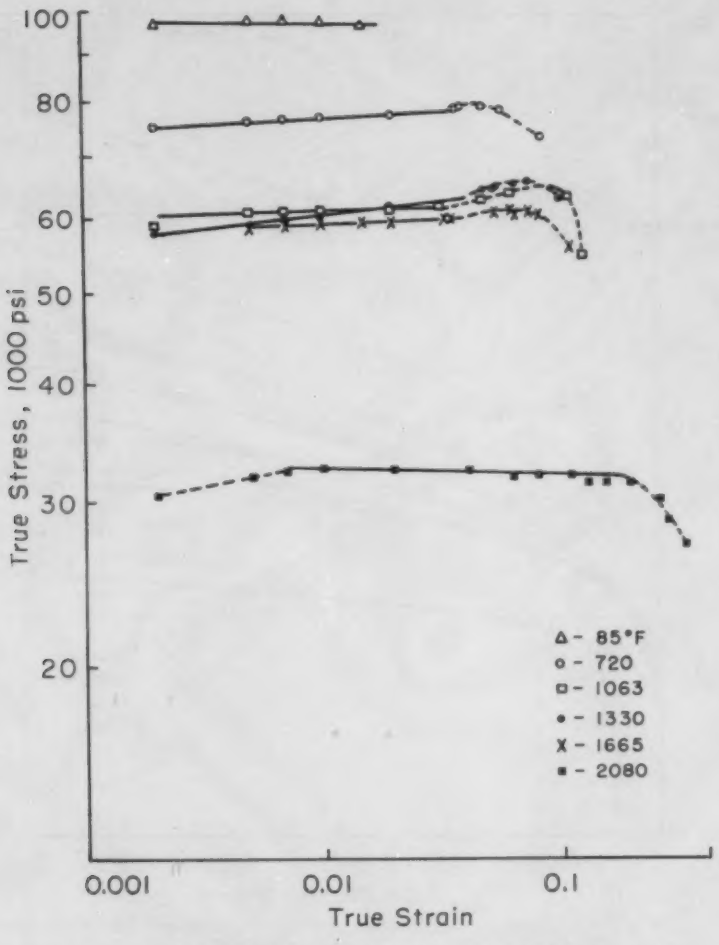


Fig. 3—Logarithmic Stress-strain Relationships for As-swaged Molybdenum. Strain rate equals 0.2 inch per inch per minute.

$$\sigma = B\dot{\epsilon}^{n}|\epsilon,T \qquad \text{Equation 2}$$

where:

σ = true flow stress
ϵ = true strain
m = strain-hardening coefficient
n = strain-rate sensitivity
A = stress at unit strain
B = stress at unit strain-rate
T = temperature

The validity of Equation 1 is supported by the linear character of the logarithmic relationship of true stress and true strain.

Figs. 6 and 7 show A, m, and n plotted against temperature for the as-swaged and the recrystallized molybdenum, respectively. For as-swaged material, A has a slight maximum at about 1400 °F (760 °C), m is negative at room temperature and at 2080 °F (1140 °C), but has a positive maximum at 1300 °F (705 °C), and n apparently has a minimum at about 1100 °F (595 °C). The temperature dependence for these coefficients is similar for the recrystallized molybdenum but the absolute values are considerably different, as

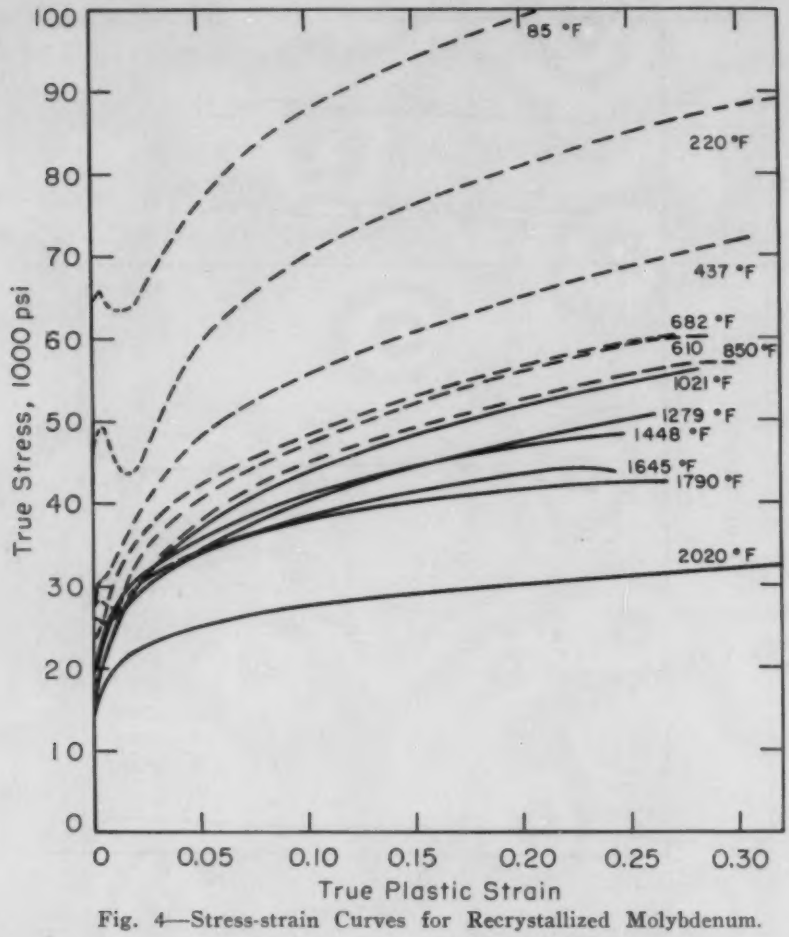


Fig. 4—Stress-strain Curves for Recrystallized Molybdenum.

shown in Fig. 7. If the coefficients for the two structures are compared, it is observed that m is much larger, the magnitude of the change in n is greater, and the low temperature value of A is greater for recrystallized metal.

The observation of a maximum for the strain hardening coefficient plotted versus temperature has also been made by Bechtold (4). His data show the maximum at about 300 °F (150 °C) instead of 1300 °F (705 °C), but this difference is attributable to the fact that his strain rate was about one-tenth as fast. These maxima suggest a temperature-dependent metallurgical change. Ordinarily, a continuous diminuation of m with temperature is observed.

If the logarithm of m is plotted as a function of reciprocal absolute temperature, the relationship shown in Fig. 8 is obtained. This plot consists of two straight-line segments having slopes of different sign and intersecting at a temperature between 1200 and 1300 °F (650 and 705 °C).

The temperature dependence of n in Figs. 6 and 7 also suggests a metallurgical change. Strain-rate sensitivity normally rises continuously with temperature. The minimum for n can be observed to occur

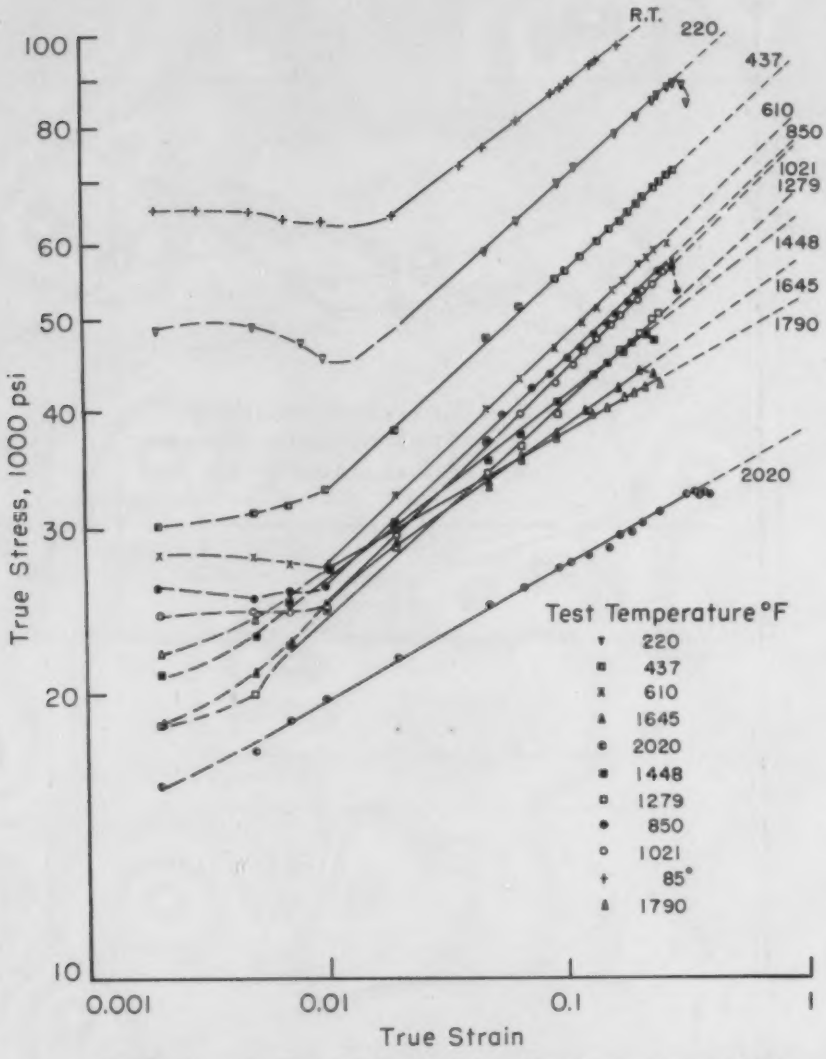


Fig. 5—Logarithmic Stress-strain Curves for Recrystallized Molybdenum 113. Strain rate equals 0.2 inch per inch per minute.

at roughly the same temperature as the maximum for m. Fig. 9 shows log n plotted as a function of reciprocal absolute temperature. The straight-line segments intersect at approximately the same temperature observed for the intersection of the m segments in Fig. 8. These plots suggest a hardening mechanism which has an increasing effect with increasing temperature to about 1200 °F (650 °C), and a diminishing effect thereafter.

Yield points have been observed previously in molybdenum. In one case, wires heated in nitrogen for 1 minute at 2370 °F (1300 °C) had yield points at room temperature which were not observed for similar material annealed in hydrogen (5). Bechtold found yield points in molybdenum between 1100 °F (595 °C) and —320 °F (—196 °C) (4). Cottrell has interpreted the yield point phenomenon

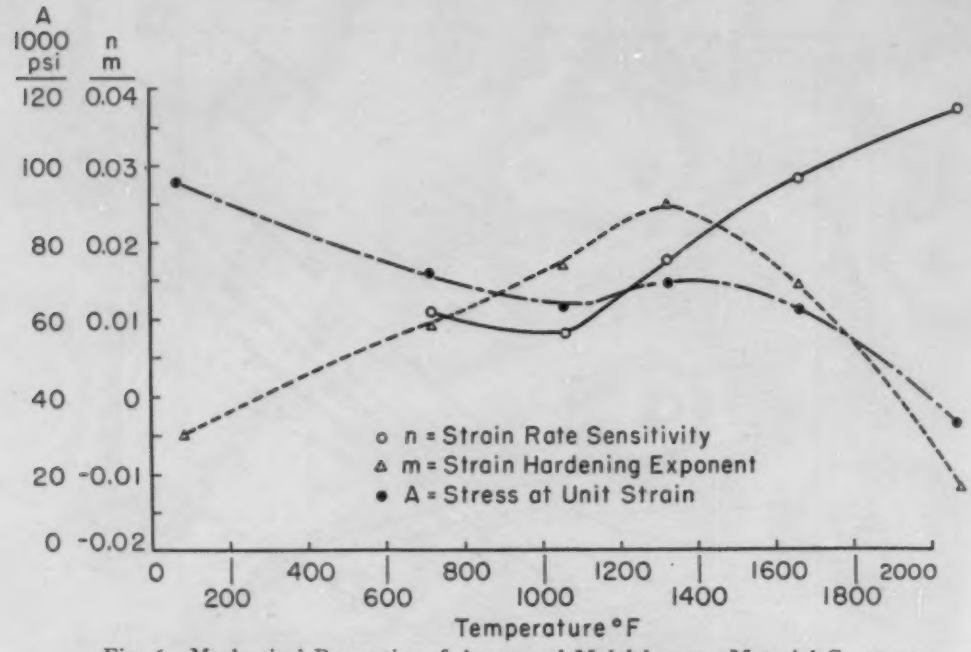


Fig. 6—Mechanical Properties of As-swaged Molybdenum—Material Constants Versus Temperature.

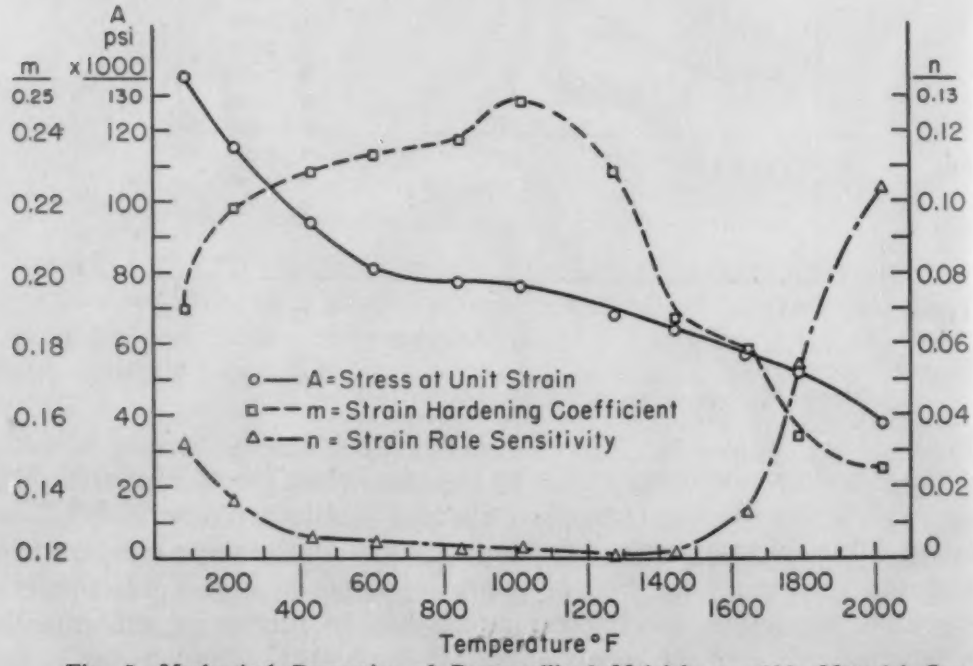


Fig. 7—Mechanical Properties of Recrystallized Molybdenum 113—Material Constants Versus Temperature.

as a result of interstitial solute atoms pinning dislocations which finally break loose during the period of discontinuous yielding in the tensile test (6). This mechanism suggests that an internal friction peak should be produced at some critical temperature. Peaks for molybdenum have tentatively been located by work at Battelle Memorial Institute (7).

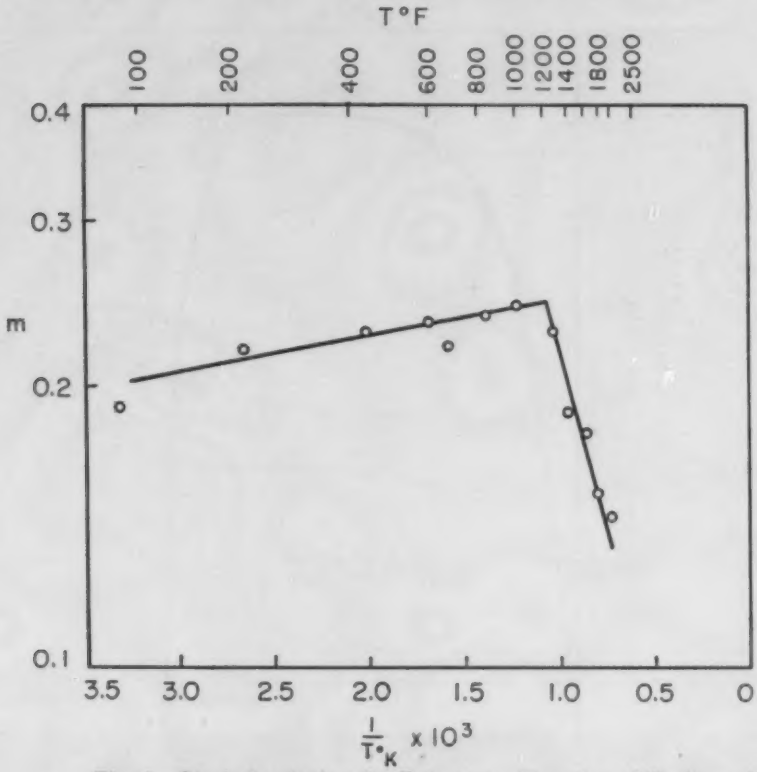


Fig. 8—Strain-hardening Coefficient as a Function of Reciprocal Absolute Temperature.

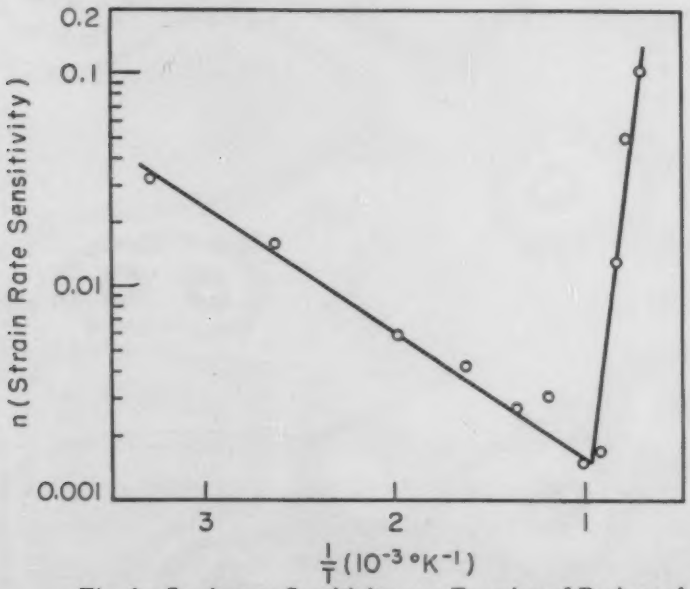


Fig. 9—Strain-rate Sensitivity as a Function of Reciprocal Absolute Temperature for Recrystallized Molybdenum.

These are expected to result from carbon, nitrogen, or oxygen impurities.

Another observation of discontinuous yielding has been made. In the temperature range 1000 to 2000 °F (540 to 1095 °C), serrated loadtime curves were produced by the autographic record. Fig. 10 is

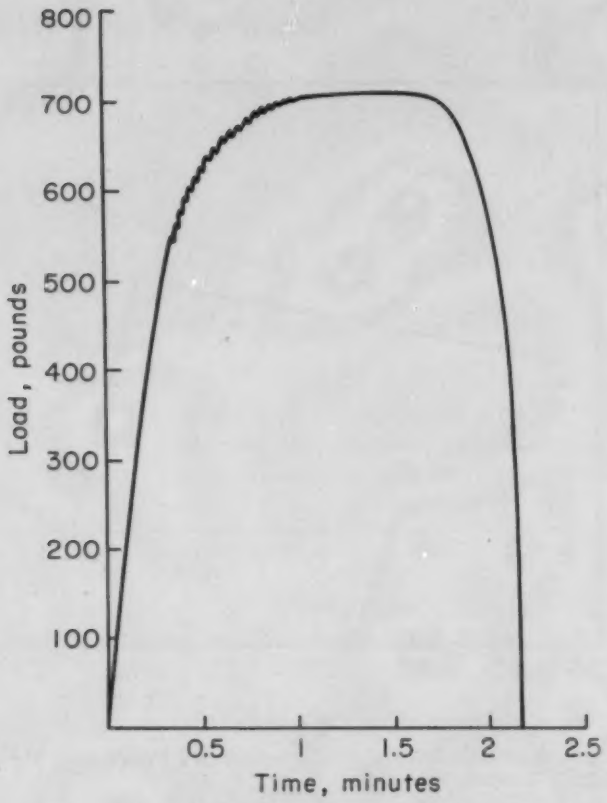


Fig. 10—Autographic Record of a Tensile Test of Recrystallized Molybdenum. Extension rate equals 0.2 inch per minute. Chart speed 2 inches per minute. Temperature 1645 °F.

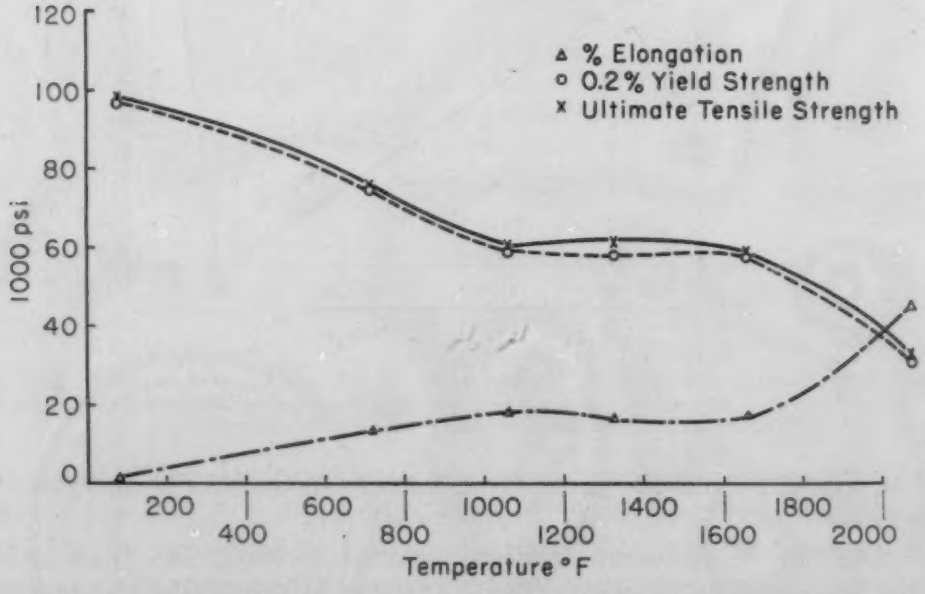


Fig. 11—Mechanical Properties of As-swaged Molybdenum—Strength and Ductility Versus Temperature.

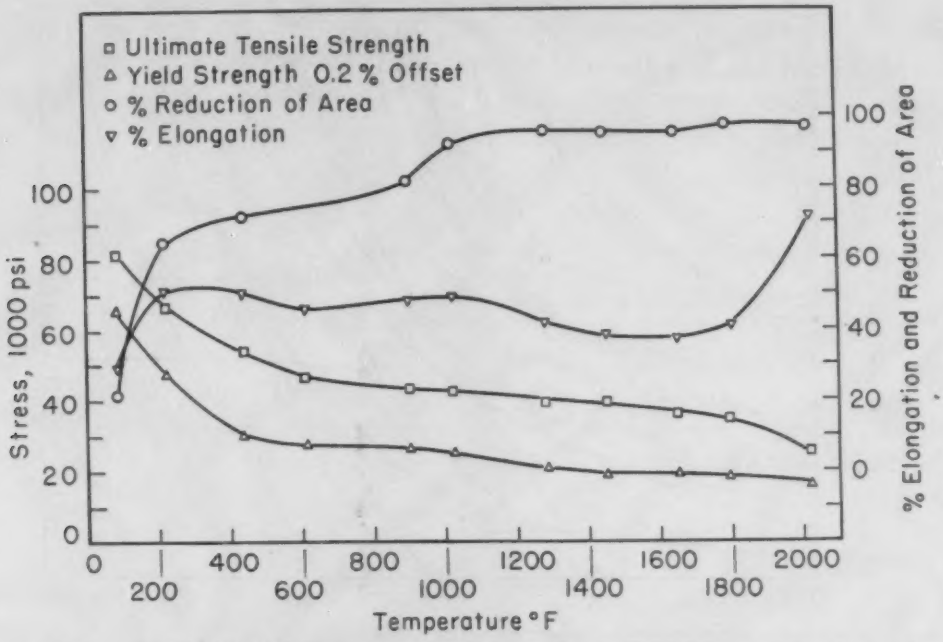


Fig. 12—Mechanical Properties of Recrystallized Molybdenum 113—Strength and Ductility Versus Temperature.

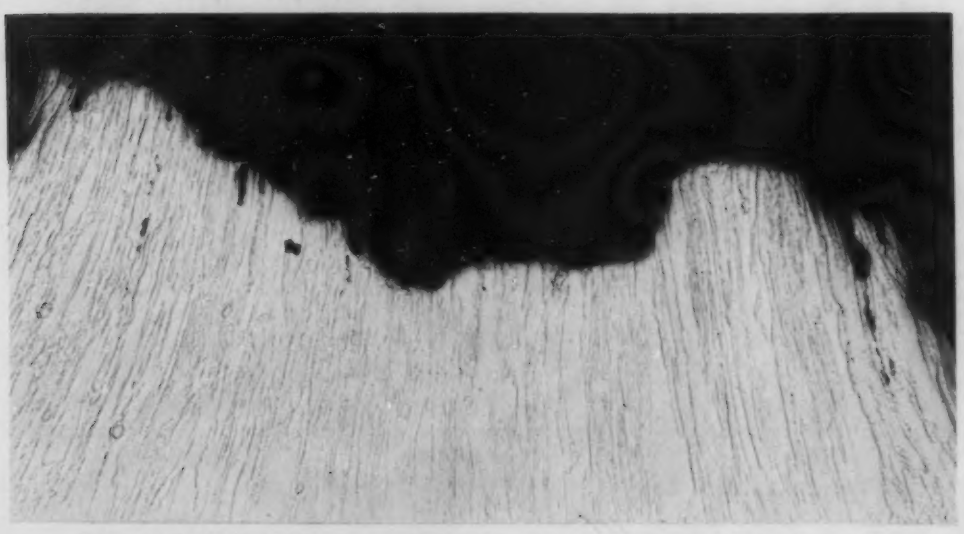


Fig. 13—Tensile Fracture of Recrystallized Molybdenum at 1645 °F. × 100.

a reproduction of a typical example of a serrated record. Prior to this, serrated stress-strain relationships have been discovered for steel, aluminum, brass, phosphor bronze, and nickel (8). They have been described as a series of small yield points and are expected to be caused by successive pinning of dislocations as a result of strain-induced diffusion. The wide temperature range for this observation in molybdenum is unusual.

Figs. 11 and 12 show strength and ductility plotted as a function of temperature. Strength diminishes with increasing temperature more rapidly at low temperatures than at high temperature. At intermediate

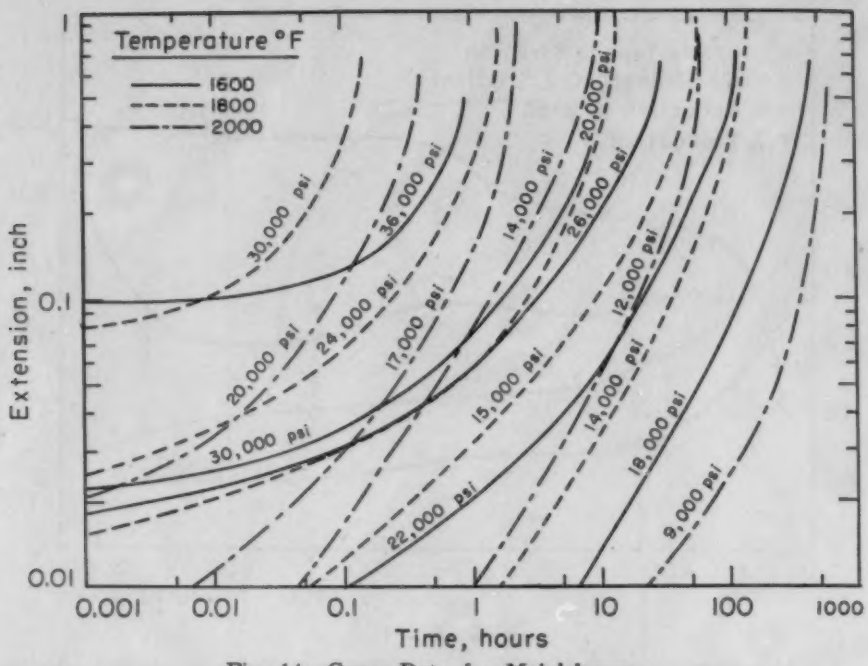


Fig. 14—Creep Data for Molybdenum.

Table II
Tensile Properties of Recrystallized Molybdenum

Test	Temp. °F	Yield Strength 0.2% Offset	Ultimate Tensile Strength	% Elongation	% Reduction of Area	m, Strain Hardening Coef.	n, Strain Rate Sensitivity
2358	85	65,250	81,250	28.96	21.5	0.190	0.0321
2298	220	47,000	66,250	50.49	64.5	0.218	0.0161
2297	437	30,250	53,500	50.09	71.5	0.228	0.0059
2296	610	28,100	46,000	46.0	—	0.233	0.0043
2299	850	26,000	43,000	48.09	81.5	0.237	0.0027
2300	1021	24,250	42,600	48.98	92.0	0.243	0.0031
2360	1279	20,000	39,050	42.95	96.0	0.228	0.0015
2363	1448	19,000	38,500	38.44	95.5	0.187	0.0017
2362	1645	18,500	35,500	37.54	95.5	0.178	0.01315
2364	1790	18,000	34,500	41.47	97.5	0.154	0.05021
2365	2020	16,000	24,950	71.86	97.0	0.145	0.10371

Table III
Tensile Properties of Molybdenum After 88 Per Cent Cold-Swaging

Test	Temp. °F	Yield Strength 0.02% Offset	Ultimate Tensile Strength	% Elongation	m, Strain-Hardening Coef.	n, Strain-Rate Sensitivity
2518	85	95,000	97,150	1.8	–0.005	—
2517	720	73,000	75,500	13.4	0.010	0.01099
2516	1063	58,000	60,750	18.1	0.017	.00802
2515	1330	57,000	61,500	16.6	0.025	.01767
2514	1665	57,000	58,800	17.6	0.014	.02803
2367	2080	30,500	32,250	44.7	–0.012	.03715

temperatures the strength is maintained almost constant over a substantial temperature range. Also significant, perhaps, is the elongation minimum in the temperature range 1000 to 1800 °F (540 to 980 °C).

The anomalous behavior described above for the temperature de-

pendence of n, m, strength, and ductility, together with the discontinuous yielding evidenced in the yield points and serrated load curves, indicates that molybdenum of the purity investigated is subject to strain aging. Similar effects have frequently been observed for other strain aging materials; for example, copper, aluminum, and steel (9,10).

Table IV
Stress-rupture Properties of Molybdenum

Temperature, °F	10 Hours	100 Hours	1000 Hours
1600	28,000 psi	22,000 psi	17,000 psi
1800	19,000	15,000	12,000
2000	14,500	11,500	9,000

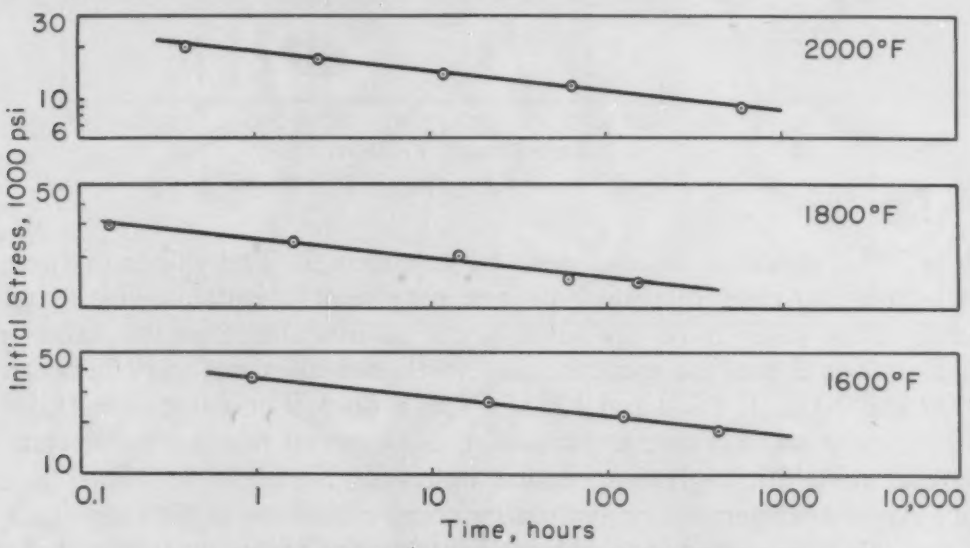


Fig. 15—Stress-rupture Life of Molybdenum.

Fractures produced in these tests were all transgranular and, with the exception of the room-temperature tests, appeared to be fibrous. Fig. 13 is an example of these fractures.

Tables II and III summarize the data obtained from tensile tests.

Creep-rupture Properties

The creep curves obtained on recrystallized molybdenum appear in Fig. 14 in logarithmic form, so that they might all be presented on a single set of coordinates.

Fig. 15 shows the stress-rupture life correlations for these tests, and Table IV summarizes the rupture properties obtained. These straight-line plots can be described by the equation

$$S = Ct^{-N}\Big|_{T} \qquad \text{Equation 3}$$

where C is a constant, S is the initial stress, t is time, and N is the

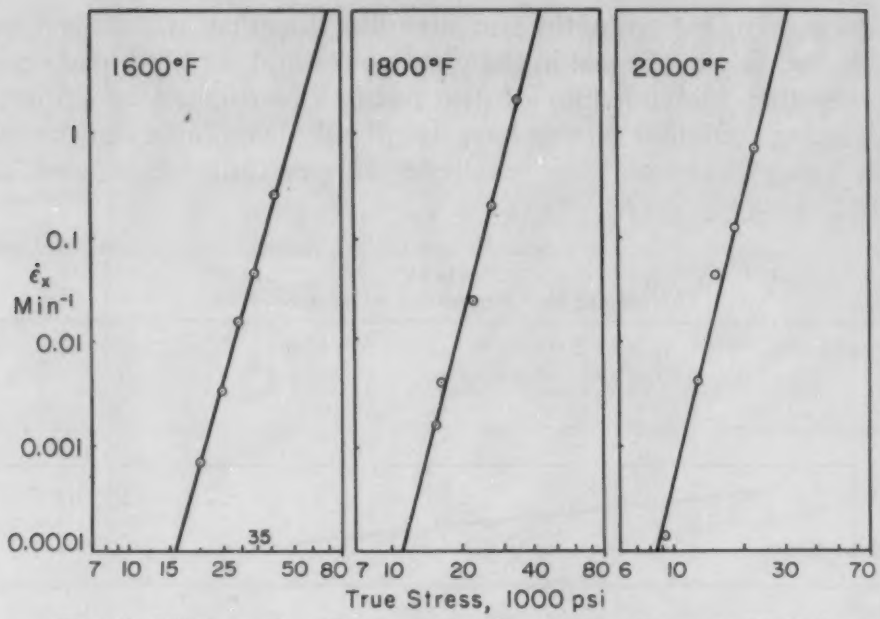


Fig. 16—Minimum Creep Rate as a Function of True Stress for Molybdenum Creep Tests.

slope. This equation is analogous to Equation 2. The slopes of these log-stress log-time relationships are very nearly equal, being about 0.108. This value is of the same order of magnitude as the value n in Equation 2 for the constant-rate tests, but does not vary between 1600 and 2000 °F (870 and 1095 °C) as n does. The value $N = 0.108$ is relatively small. For comparison, it is observed that for most commercial austenitic high temperature materials $N = 0.18$ to 0.20.

Another criterion for evaluating creep resistance is the magnitude of the minimum creep rate obtained during the creep-rupture test. In Fig. 16, the logarithm of the minimum creep rate, indicated here as log $\dot{\epsilon}_x$, is plotted versus the logarithm of the true stress caused by the test load.

In Fig. 17, the logarithm of minimum creep rate for several constant true stresses taken from Fig. 16 is plotted against reciprocal absolute temperature. This plot is, for the three temperatures considered, a linear relationship. It is then possible to apply the Zener-Hollomon suggestion (11) that

$$\sigma = f\left(\dot{\epsilon} e^{\Delta H/RT}\right) \qquad \text{Equation 4}$$

If $\dot{\epsilon}_x$ is substituted for $\dot{\epsilon}$ in this expression, the ΔH may be termed activation energy for creep at the minimum creep rate. It has been found to vary somewhat with stress as follows:

Stress (psi)	*(Cal.)*
15,000	78,500
20,000	83,000
25,000	87,500
30,000	88,500

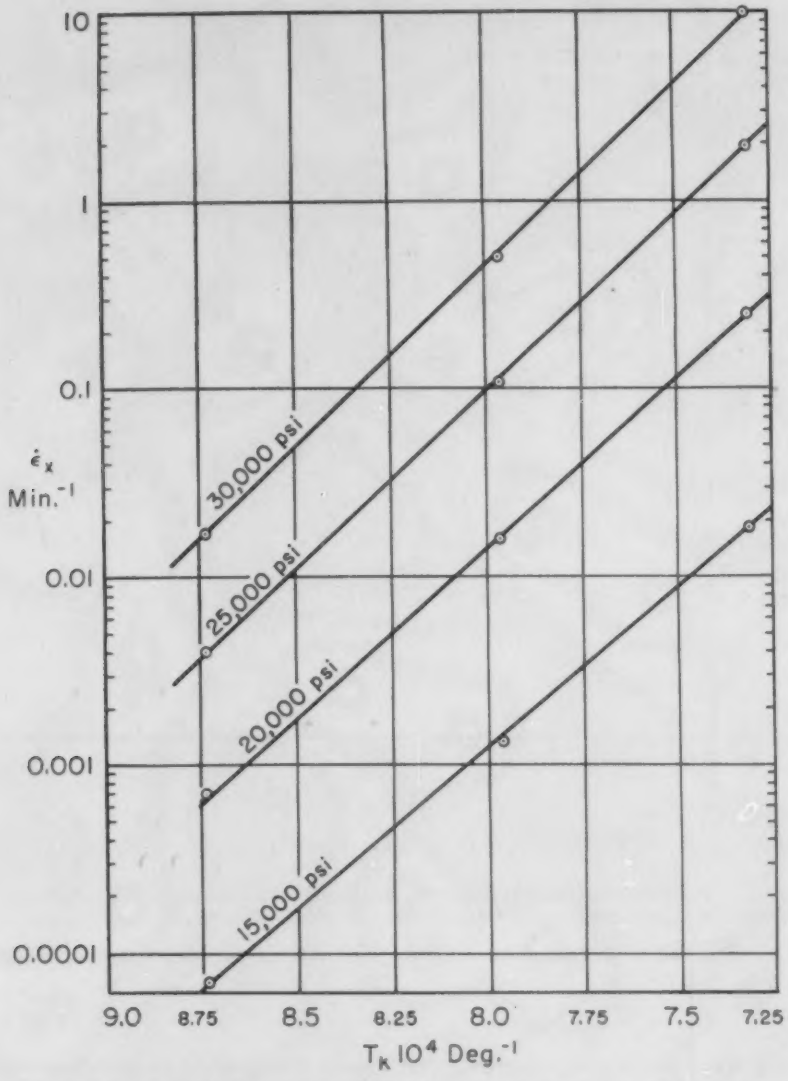


Fig. 17—Minimum Creep Rate as a Function of Reciprocal Absolute Temperature.

This trend toward higher activation energies for higher stresses can, perhaps, be rationalized by attributing it to the variation in strain aging as a function of strain and temperature.

An activation energy of 86,400 calories was obtained by plotting stress versus ΔH and selecting a value for activation energy corresponding to the average of the true stresses acting in all tests made. This value was used in the Zener-Hollomon type parameter

$$\ln\dot{\epsilon}_x + \frac{\Delta H}{RT},$$

and it was plotted as a function of the logarithm of true creep stress. This relationship is shown in Fig. 18. A similar plot for maximum true stress versus this parameter for the constant-rate test results does not compare well with these results, nor is it a linear relationship.

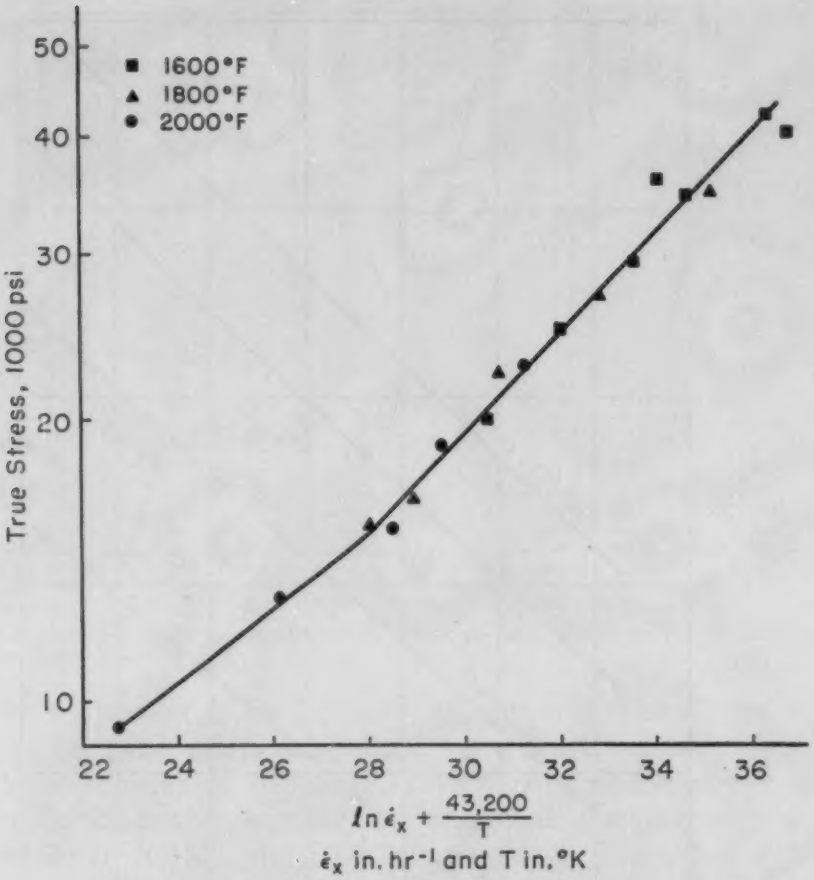


Fig. 18—Zener-Hollomon Parameter as a Function of True Stress for Molybdenum Creep Data.

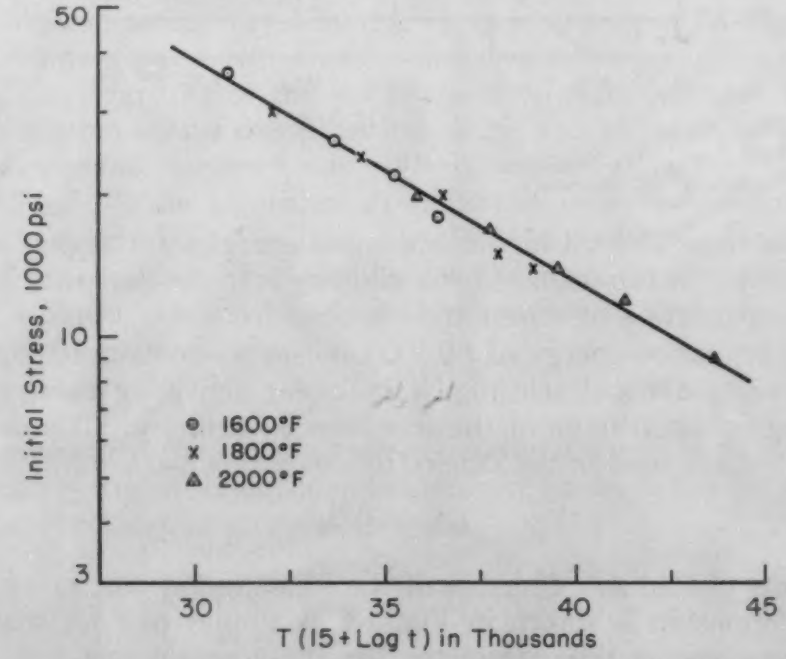


Fig. 19—Larson-Miller Parameter Versus Stress for Molybdenum.

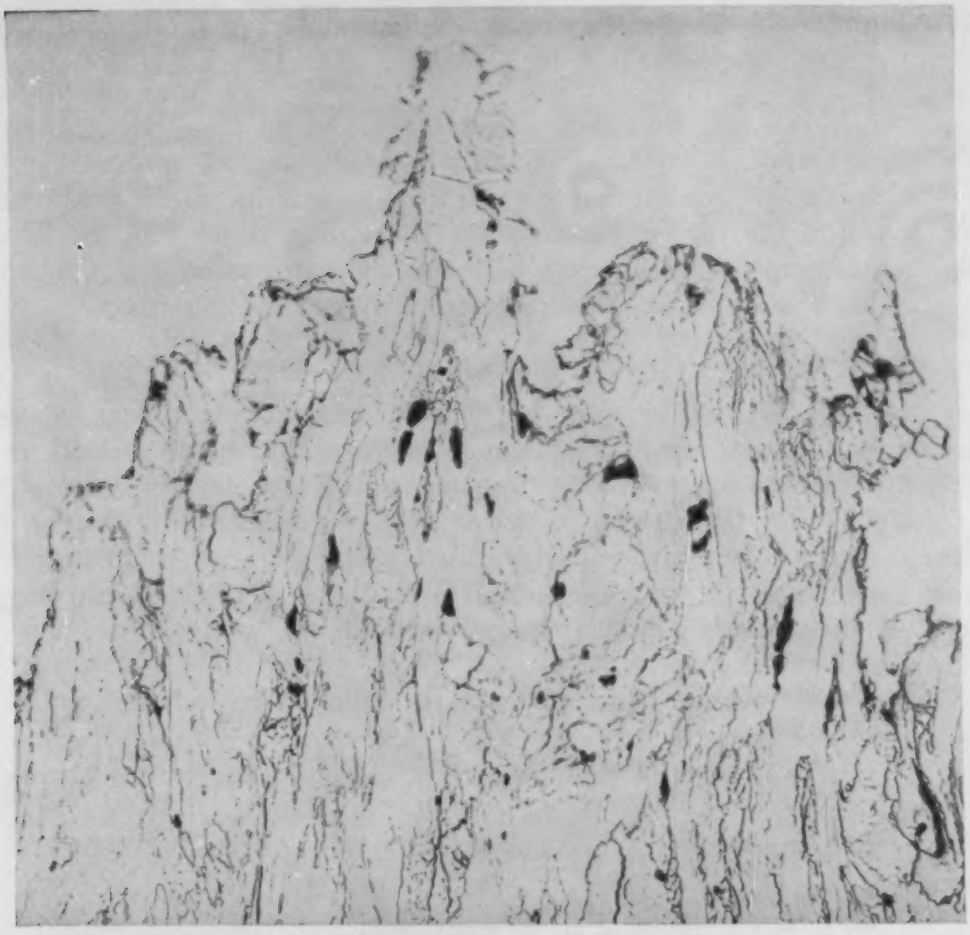


Fig. 20—Creep-rupture Fracture for Recrystallized Molybdenum at 2000 °F × 250.

Table V
Creep-rupture Data for Molybdenum

Temp. °F	Nom. Stress (psi)	Rupture Life (hours)	Time to Inflection Point (hours)	Minimum Creep Rate $\dot{\epsilon}_x$ (min^{-1})	True Stress at $\dot{\epsilon}_x$ (psi)	Strain at $\dot{\epsilon}_x$	Total Strain	Z-H Parameter $\ln\dot{\epsilon}_x + 43{,}200/T$	Stress Rupture Parameter (all values × 10^{-3})
2000	20,000	0.41	0.13	0.711	22,680	0.1340	0.620	31.2847	35.9
	17,000	2.33	0.61	0.124	18,675	0.0985	0.915	29.5393	37.8
	14,000	11.8	1.25	0.0437	15,225	0.0875	1.250	28.4948	39.6
	12,000	63.6	14.4	0.00427	12,894	0.0745	0.824	26.1621	41.3
	9,000	595.5	156.0	0.000139	9,306	0.0340	0.672	22.7441	43.7
1800	30,000	0.15	0.0336	2.1893	34,815	0.1605	0.715	35.2059	32.1
	24,000	1.69	0.348	0.2074	26,940	0.1225	0.880	32.8492	34.4
	20,000	14.5	3.31	0.0258	22,320	0.1160	1.050	30.7645	36.6
	15,000	60.0	7.92	0.00417	16,425	0.095	0.945	28.9424	38.0
	14,000	151	33.0	0.00164	15,330	0.095	1.105	28.0091	38.9
1600	36,000	0.930	0.222	0.256	41,886	0.1635	0.500	36.3992	30.9
	34,000	—	0.145	0.3872	40,154	0.1810	—	36.8134	—
	30,000	—	2.05	0.0458	34,410	0.1470	—	34.6787	—
	26,000	20.5	5.52	0.0153	29,354	0.1290	0.675	33.5823	33.7
	22,000	120	30.0	0.0033	24,723	0.12375	0.725	32.0484	35.3
	18,000	444	136	0.0007	19,980	0.1100	0.670	30.4978	36.4

The Larson-Miller stress-rupture parameter (12) was applied with the result shown in Fig. 19. The value C = 15 fits best in the expression

$$P = T(C + \log t) \qquad \text{Equation 5}$$

for molybdenum.

The fractures obtained for these tests were similar in appearance to those for the higher temperature short-time tests. Fig. 20 is a photomicrograph representative of these fracture sections.

Table V summarizes the creep-rupture data.

Conclusion

An investigation into the tensile properties of molybdenum under conditions of constant rate for short times and constant load for long times has characterized the remarkable high temperature strength of molybdenum. There is evidence in this analysis to indicate that a strengthening phenomenon depending on temperature and strain, such as strain aging, is responsible for the very attractive high temperature properties of molybdenum. The following observations summarize this evidence.

1. The maximum in temperature dependence of the strain-hardening coefficient.
2. The minimum in the temperature dependence of the strain-rate sensitivity.
3. The persistence of low temperature strength to high temperatures.
4. The minimum in the temperature dependence of per cent elongation.
5. The yield point phenomena in the range room temperature to 1200 °F (650 °C).
6. The occurrence of serrated load curves in the range 1000 to 2000 °F (540 to 1095 °C).
7. The small slope associated with the stress-rupture life correlations in the range 1600 to 2000 °F (870 to 1095 °C).

It is suggested that this strain aging phenomenon which appears to be responsible for the outstanding high temperature strength of molybdenum may occur in molybdenum-base alloys. Furthermore, it is possible that a properly-adjusted combination of purity, deformation, and heat treatment would be of great value in enhancing the properties of such alloys.

References

1. Parke, R. M., "Molybdenum, A New High Temperature Metal," Metal Progress, Vol. 60, (July 1951), p. 81.
2. Pugh, J. W., R. L. Hadley, and R. W. Hennig, "An Arc Furnace for Melting Refractory Metals," Metal Progress, Vol. 63 (March 1953), p. 70.
3. Hollomon, J. H., "The Mechanical Equation of State," *Transactions*, American Institute of Mining and Metallurgical Engineers, Vol. 162, 1945, p. 268.

4. Bechtold, J. H., "Effects of Temperature on the Flow and Fracture Characteristics of Molybdenum," *Journal of Metals,* (Nov. 1953), 1469.
5. Turey, P. and S. Krauz, "Effect of Molecular Nitrogen on Molybdenum at High Temperatures," *Nature,* Vol. 138, 1936, p. 331; Vol. 139, 1937, p. 30. Turey, P., "Effect of Nitrogen Dissolved in Molybdenum," Math. naturw. Anz. ungar. Akad. Wiss., Vol. 57 (1938); C. A., Vol. 33, 1939, p. 8156.
6. Cottrell, A. H., "Dislocations and Plastic Flow in Crystals," Oxford Press, 1953, p. 140.
7. Battelle Memorial Institute, "A Metallurgical Study of Molybdenum," 13th Quarterly Rept. to ONR, Sept. 1, 1952.
8. McReynolds, A. W., "Plastic Deformation Waves in Aluminum," *Transactions,* American Institute of Mining and Metallurgical Engineers, Vol. 185, 1949, p. 32.
9. Holloman, J. H. and L. D. Jaffee, *Ferrous Metallurgical Design,* John Wiley and Sons, Inc., New York, N. Y., 1947, p. 76–121.
10. Lubahn, J. D., TRANSACTIONS, American Society for Metals, Vol. 44, 1952, p. 643–666.
11. Zener, C. and J. H. Hollomon, "Effect of Strain Rate on the Plastic Flow of Steel," *Journal of Applied Physics,* (Jan. 1944), p. 22.
12. Larson, F. R. and J. Miller, "A Time-temperature Relationship for Rupture and Creep Stresses," American Society of Mechanical Engineers, Paper No. 51–A–36, Ann. Meeting, Nov. 1951.

A CONTRIBUTION TO THE VANADIUM-OXYGEN PHASE DIAGRAM

By W. Rostoker and A. S. Yamamoto

Abstract

A partial diagram in the range 0–26 wt. % oxygen was constructed on the basis of metallographic, X-ray diffraction and resistometric studies. The body-centered tetragonal beta phase is hypothesized as a stabilization of a low temperature allotrope of vanadium. The beta phase is shown to form by a peritectic reaction between VO and the melt. A new delta phase is shown to derive from a peritectoid reaction between beta and VO. The terminal solid solubility, the $\alpha + \beta/\beta$, $\beta/\beta + VO$, *and* $\beta + VO/VO$ *boundaries are approximately established. Accessory information on powder pattern lines, lattice parameters and hardness are given.*

Introduction

IN LINE with a general objective of developing useful vanadium-base alloys, it was felt desirable to undertake limited studies on the system vanadium-oxygen to understand some of the origins of embrittlement in alloys of that metal. Information about this system had been very limited until the recent publication of the work of Seybolt and Sumsion (1).[1] Earlier investigation of the lower vanadium oxides by Klemm and Grimm (2) indicated that the solubility of oxygen in vanadium was about 11.2%[2] and that the lattice was distorted tetragonally. Allen, Kubaschewski and von Goldbeck (3) reported a very much lower solubility at lower temperatures i.e. about 0.25%. Seybolt and Sumsion resolved the apparent contradiction by demonstrating that there was not a continuous transition from body-centered cubic to body-centered tetragonal lattice but that in the temperature range 600 to 1400 °C (1110 to 2550 °F), a mixed phase field exists between the body-centered cubic phase and the body-centered tetragonal phase. Accordingly, Klemm and Grimm's solubility limit referred to the beta phase while Allen, Kubaschewski and von Goldbeck's work actually did pertain to the terminal solid solubility or alpha solubility limit.

Seybolt and Sumsion set the terminal solubility limit at 0.95% with no apparent temperature dependence and the existence range of

[1] The figures appearing in parentheses pertain to the references appended to this paper.
[2] All compositions refer to weight percentages.

Of the authors, W. Rostoker is supervisor, Physical Metallurgy Research, and A. S. Yamamoto is associate metallurgist, Metals Research Department, Armour Research Foundation of Illinois Institute of Technology, Chicago. Manuscript received August 27, 1954.

beta as between 5.3 and 8.3%. They further cited evidence for a high temperature allotrope of pure vanadium deriving by a transformation at 1550 ± 10 °C. The new phase was deduced as decomposing eutectoidally to the alpha and VO phases which necessitated the assumption that the beta phase formed by a peritectoid reaction: $\alpha + VO \rightleftharpoons \beta$. A limited number of measurements indicated a minimum in the solidus curve at about 6.2% oxygen and 1650 °C (3000 °F). A recent paper by McCalden and Duwez (4) reports on experiments which do not support the existence of the high temperature modification of vanadium.

The present paper contributes further information on the $\alpha - \beta$ equilibrium, on the solidification reactions and on phase relationships in the composition region between β and VO.

Experimental Procedures

Materials—Calcium-reduced vanadium was obtained from the Electro-Metallurgical Division of the Union Carbide and Carbon Corporation. A typical analysis is as follows:

Carbon	— 0.06%
Oxygen	— 0.07%
Nitrogen	— 0.10%
Hydrogen	— 0.002%
Iron	— —

Vanadium pentoxide powder, chemically pure and air-dried, supplied by Vanadium Corporation of America, New York, was used as a source of oxygen.

Melting Procedure—A non-consumable electrode arc melting furnace identical to that described in detail in a previous paper (5) was used in preparing all alloys. Specific components included a water-cooled tungsten electrode and a water-cooled copper crucible. The furnace atmosphere was high purity argon.

Since the vanadium-pentoxide was in powder form, it was not convenient to use it directly in charges. Two vanadium-oxygen master alloys analyzing 23.4 and 26% oxygen were prepared.

Ingots weighing 8 to 20 grams were then melted by combining vanadium metal and calculated amounts of the master alloy. Sixteen alloys in all were made having nominal compositions: 0.09, 0.25, 1, 2, 3, 4, 5, 7, 9, 11, 13, 15, 17, 19, 21 and 23.9% oxygen.

Most alloys were breakable with hammer and cold chisel indicating extreme brittleness associated with oxygen contents. Pieces of proper size for heat treatments were thus easily obtained.

Heat Treatments—Isothermal heat treatments of samples up to 1500 °C (2730 °F) were conducted in Vycor or quartz bulbs and using conventional tube furnaces. Vycor bulbs were used for annealing at temperatures up to 1100 °C (2010 °F), quartz for higher temperatures. Below 950 °C (1740 °F), the bulbs were evacuated, while

above this temperature a reduced pressure of argon was introduced to maintain approximately one atmosphere at the annealing temperature. At the conclusion of heat treatments all bulbs were broken under water at the instant of quenching.

Table I
Analyses of Vanadium-Oxygen Alloys

Alloy No.	Oxygen, Wt. %
VO-5-2444	5.04
VO-7-2920	8.2
VO-9-3281	10.3
VO-11-2921	11.8
VO-13-3282	15.3
VO-15-2922	14.5
VO-17-3374	17.8
VO-19-3375	20.5
VO-21-3376	21.4
VO-23.9-2357	26.02
VO-23.9-2944	23.4

Note: The oxygen contents were determined by difference after analyzing for vanadium. The alloys containing less than 5 wt. % oxygen did not yield reproducible results and their nominal compositions were employed for construction of the phase diagram.

Table II
Schedule of Heat Treatments for V-O Alloys

Annealing Temperature, °C	Annealing Time, Hrs.	Alloys, % Oxygen
1800	1/12	1, 2, 3, 4, 5
1700	1/12	1, 4, 7, 9
1600	1/6	1, 4, 9, 11, 13
1500	1/3	5
1425	1/2	7, 9, 11, 13, 15
1400	1/2	4, 5
1300	1	5, 7, 9, 11, 13, 15, 17, 19, 21
1200	4	2, 4
1200	17	9, 11, 13, 17, 19, 21
1100	24	1, 2, 3, 4, 5, 7, 9, 11, 13, 15
1100	168	13, 15, 17, 19, 21
1000	24	2, 3, 4, 5, 7, 9, 11, 13, 15
900	170	0.09, 0.25, 1, 2, 3, 4, 5, 7, 9, 11, 13, 15, 17, 19, 21, 23.9
800	195	2
750	170	2
400	285	1, 2, 3

For temperatures above 1500 °C (2730 °F), a specially designed furnace for high temperature heat treatments was available. Basically, it is a vacuum resistance furnace, a split cylinder of thin molybdenum sheet being the heating element. The detailed description of the furnace can be found in a publication (6). Specimens were hung vertically in the furnace in tungsten wire baskets and dropped onto the water-cooled brass bottom to accomplish quenching.

Solidus curves were determined by using a vacuum induction heating furnace and by employing metallographic examination for detection of incipient melting in the quenched specimens. Details of the furnace and its operation may be found in the literature (5).

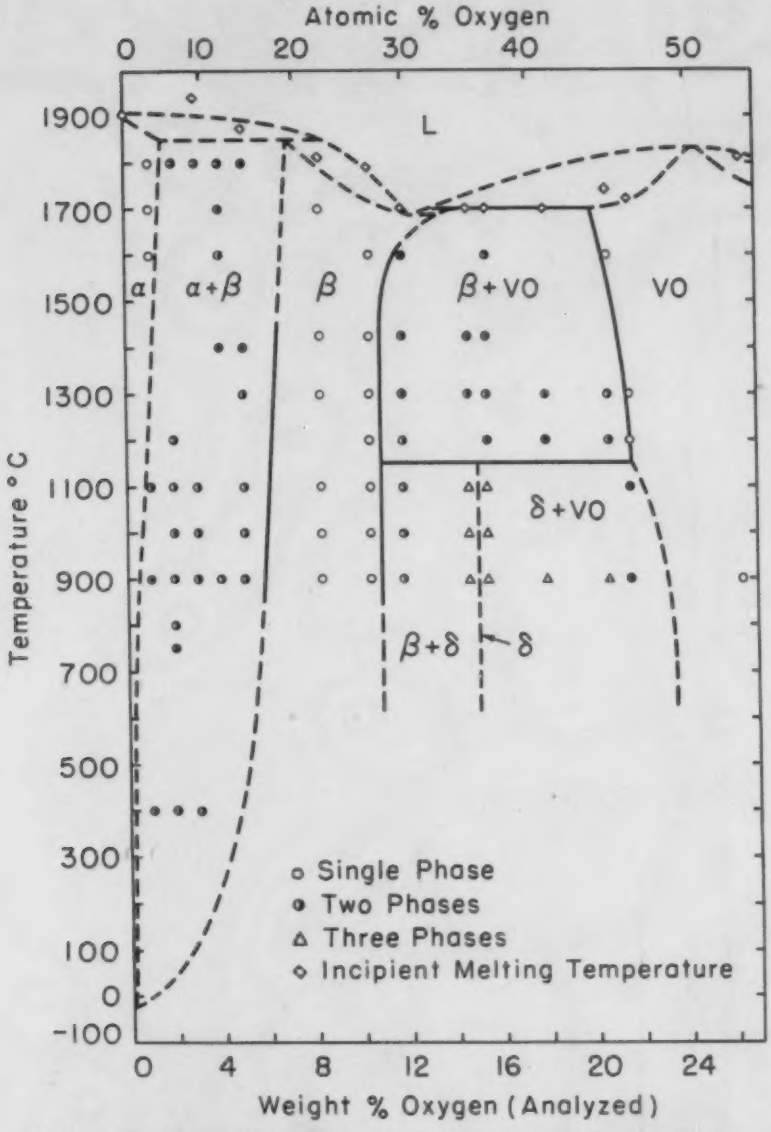


Fig. 1—Tentative Phase Diagram of the Vanadium-Oxygen System

X-ray Analyses—X-ray studies were made concurrently on many samples to assist metallographic interpretation of structures under examination. Powder samples (minus 200 mesh) were exposed to filtered CuK_α radiation ($CuK_{\alpha 1} = 1.527295$ kX) in a 14-centimeter diameter Debye-Scherrer camera. Exposure times varied from 4 to 8 hours.

Results and Discussion

The tentative partial phase diagram of the vanadium-oxygen system is shown in Fig. 1, based on a weight per cent scale. The diagram is constructed as far as possible on the basis of analyzed compositions which are listed in Tab[illegible] alloys containing less than 5% oxygen could not be satisfactorily analyzed. Table II tabulates all heat treatments employed for the studies.

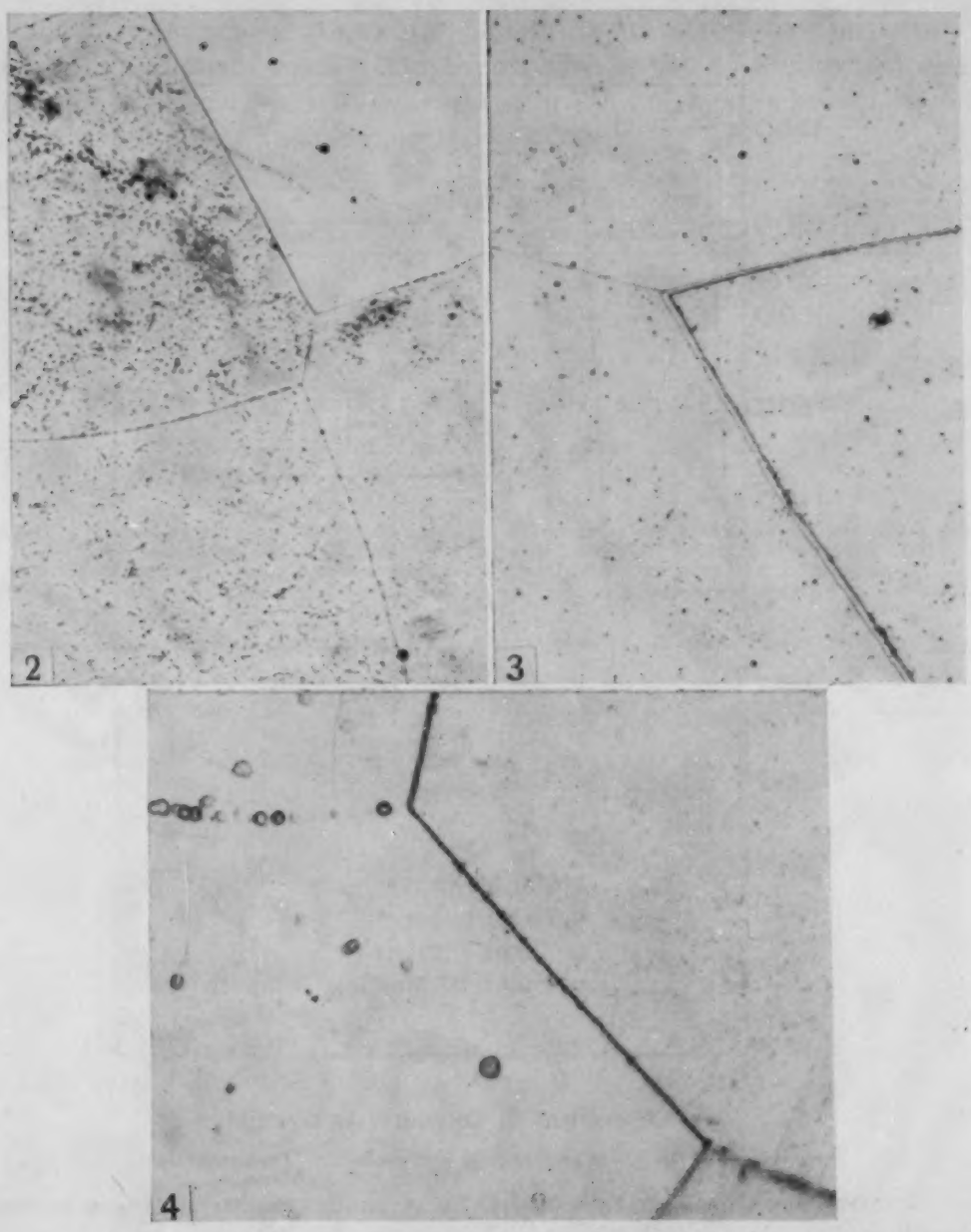


Fig. 2—As-Cast 0.25% Oxygen Alloy. Dispersed phase. Etched. X 250.
Fig. 3—0.25% Oxygen Alloy Quenched from 900 °C. Coagulation of dispersed phase at grain boundaries. Etched. X 250.
Fig. 4—1.00% Oxygen Alloy (Nominal) Quenched from 1100 °C. Alpha plus a second phase. Etched. X 500.
Etchant: 60 glycerine; 20 HNO_3; 20 HF.

The Terminal Solubility Limit—The oxygen content of the unalloyed vanadium was about 0.07%. The microstructure of this material showed a single phase. An alloy containing 0.25% oxygen in the as-cast form showed a fine dispersion of particles (Fig. 2). After annealing at 900 °C (1650 °F) for 170 hours, the dispersed phase coagulated at the grain boundaries as seen in Fig. 3. The solubility limit at this temperature must be between 0.07 and 0.25%. An alloy con-

taining 1% oxygen annealed at 1100 °C (2010 °F) for 24 hours shows a small amount of second phase (Fig. 4). The same alloy annealed above 1600 °C (2910 °F) appears to be single phase. The solubility boundary, therefore, appears to decrease from about 1% to less than 0.25%.

The Beta Phase—X-ray diffraction patterns on alloys containing

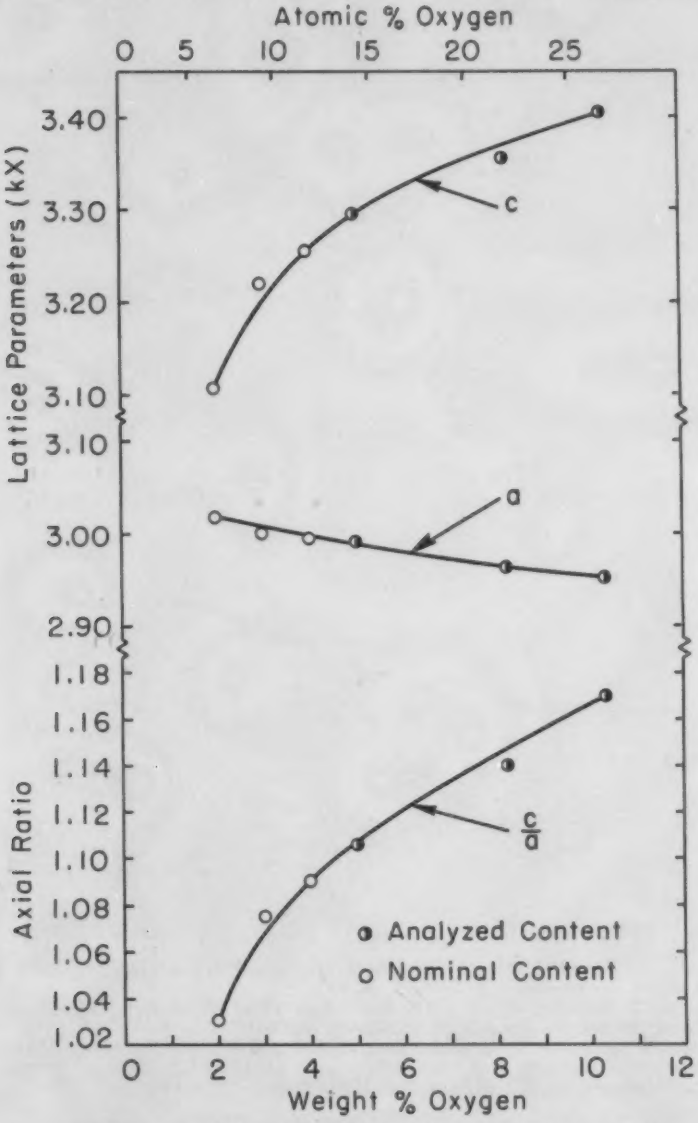


Fig. 5—Lattice Parameters of the Beta Phase in the Vanadium-Oxygen System.

from 2 to 10.3% oxygen showed the existence of only the body-centered tetragonal phase called beta by Seybolt and Sumsion. The lattice parameters and axial ratios are summarized in Fig. 5. The continuity of parameters establishes that the beta phase at room temperature is homogeneous over the range 2 to 10.3% oxygen. Whether this could be said to be true also of the elevated temperatures from which

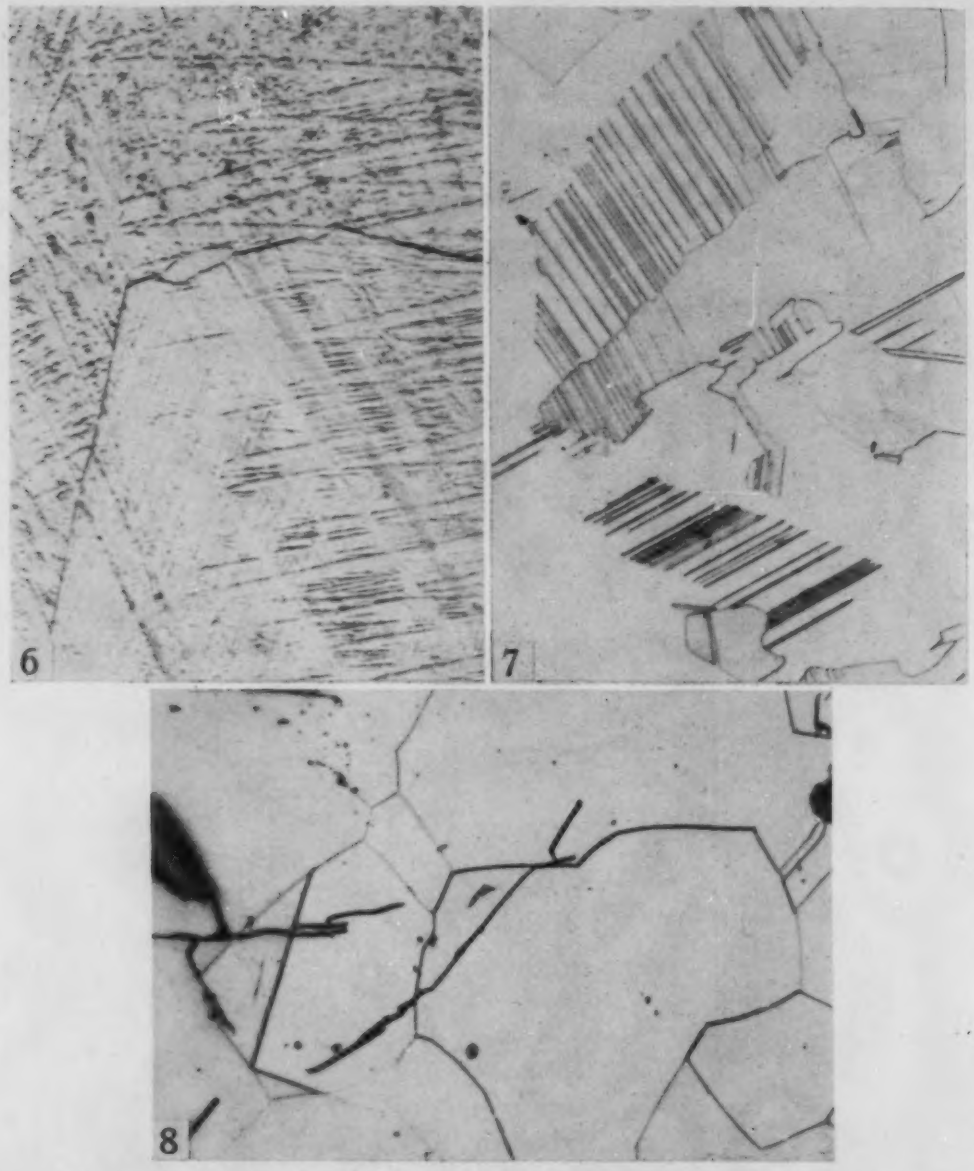


Fig. 6—3.00% Oxygen Alloy (Nominal) Quenched from 1100 °C. Beta phase transformed from alpha on quenching. Etched. X 500.

Fig. 7—5.00% Oxygen Alloy Quenched from 1100 °C. Beta phase showing evidence of some transformation on quenching. Etched. X 500.

Fig. 8—8.2% Oxygen Alloy Quenched from 1100 °C. Beta phase. Absence of transformation structure indicates that beta was stable at 1100 °C. Etched. X 500.
Etchant: 60 glycerine; 20 HNO_3; 20 HF.

the specimens were quenched depends on whether all transformations were suppressible by quenching.

Examination of microstructures in the range 2 to 5% oxygen revealed structures which appeared acicular (Fig. 6) or banded (Fig. 7). At the lower oxygen contents the whole structure was populated with these configurations while at the higher contents, they occurred only in patches. At greater than 5% oxygen contents, there is no evidence of these structures at all and the 8.2 and 10.3% oxygen alloys show

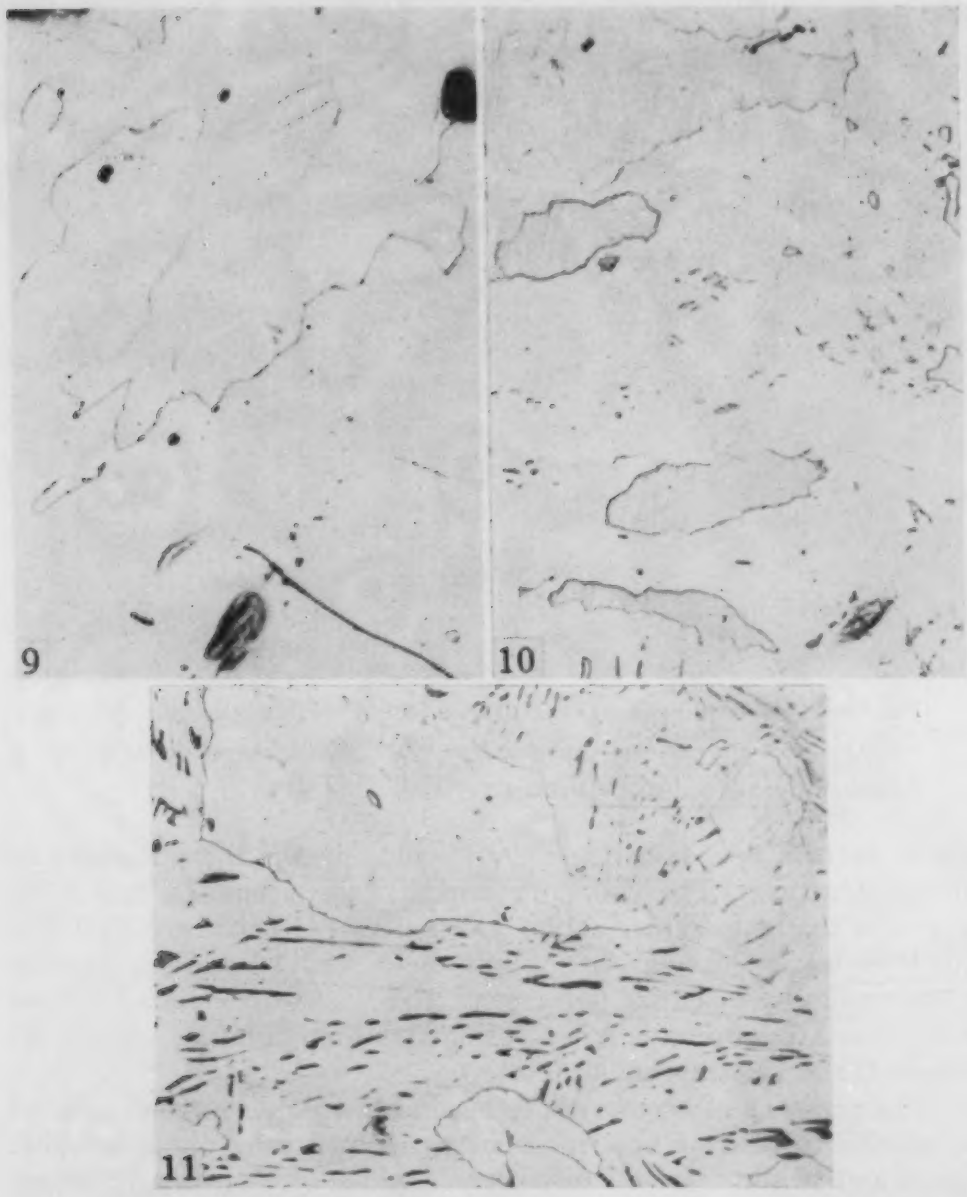


Fig. 9—10.3% Oxygen Alloy Quenched from 1100 °C. Beta phase. Absence of transformation structure indicates that beta was stable at the temperature. Etched. X 500.
Fig. 10—11.8% Oxygen Alloy Quenched from 1100 °C. Two phase structure of beta plus another phase. Etched. X 250.
Fig. 11—11.8% Oxygen Alloy Quenched from 1600 °C. Two phases, beta plus VO. Etched. X 250.
Etchant: 60 glycerine; 20 HNO_3; 20 HF.

(except in special instances to be later referred to) single phase microstructures (Figs. 8 and 9). The presence of banded or acicular type structures have frequently been correlated with insuppressible type transformations. In this particular instance, the interpretation has been made that metastable alpha transforms insuppressibly to beta. Accordingly, the microstructures which show areas of banding were in a two phase field of $(\alpha + \beta)$ at the annealing temperature. It is relatively



Fig. 12—14.5% Oxygen Alloy Quenched from 1425 °C. Primary dendrite of VO and interdendritic beta. Etched. X 500.
Fig. 13—14.5% Oxygen Alloy Quenched from 900 °C. Peritectoid reaction in progress: VO + $\beta \rightleftharpoons \delta$. Etched. X 500.
Etchant: 60 glycerine; 20 HNO_3; 20 HF.

easy to set the $\beta/\alpha + \beta$ boundary by judging the disappearance of banded structures. The boundary must fall between 5.04 and 8.2% oxygen in the temperature range 900 to 1800 °C (1650 to 3270 °F). This is in fairly close agreement with Seybolt and Sumsion. Because of the continuity of lattice parameters, the $\beta/\alpha + \beta$ boundaries must bend toward the ordinate axis crossing room temperature somewhere between 0 and 2% oxygen.

The presence of second phase beyond the higher oxygen limit of the miscibility field of beta is easier to recognize by metallography. Figs. 9 and 10 illustrate microstructures which bracket this boundary at 1100 °C (2010 °F).

The Delta Phase—Above 1200 °C (2190 °F), microstructures show a phase mixture of (β + VO). Fig. 11 presents the structure of an 11.8% oxygen alloy as quenched from 1600 °C (2910 °F), occurring just beyond the solubility limit of the beta phase. The identification of the phases was confirmed by X-ray diffraction analysis. The Widmanstätten pattern in the beta matrix indicates a reduced solid solubility boundary for that phase.

Below 1100 °C (2010 °F), the 14.5 and 15.3% oxygen alloys give microstructural evidence of a peritectoid reaction producing a new phase which is designated delta (δ). Figs. 12 and 13, for a 14.5% oxygen alloy, exhibit structures above and below the peritectoid

temperature. X-ray diffraction analysis shows the appearance of new lines in the 1100 °C (2010 °F) pattern which were not present in the 1300 °C (2370 °F) pattern.

Specimens of 14.5 and 15.3% oxygen alloys were annealed in a second series at 900, 1100, 1200 (except 14.5% oxygen alloy), 1300 and 1425 °C (1650, 2010, 2190, 2370 and 2600 °F), respectively. X-ray diffraction patterns gave evidence of the new delta phase in the 1100 °C (2010 °F) anneal, whereas the 1200 °C (2190 °F) anneal produced no evidence of this phase. The peritectoid temperature, therefore, may be set between 1100 and 1200 °C (2010 and 2190 °F). It was not possible to develop a predominant X-ray diffraction pattern of the delta phase. By subtracting the known lines of β and VO from the patterns obtained from alloys annealed below 1100 °C (2010 °F), a group of 12 lines was left which appeared consistently, and were therefore assigned to delta.

Table III
Diffraction Lines of the δ Phase*
and Tentative Indexings on a Hexagonal Lattice

I	d (kX)	c/a = 1.7 hkl	c/a = 2.15 hkl
vw	1.886		004
vw	1.786	102	110
vft	1.589	003	112
w	1.456	110	113
vw	1.355	103	105
ft	1.219	201	
vft	1.209	004	
w	1.168		106
vft	1.138		121
vft	1.114	202	
vft	1.098	104	122
vft	1.072	113	205

* Taken from pattern for 20.5%, oxygen alloy annealed at 900 °C for 170 hours. w = weak, vw = very weak, ft = faint, vft = very faint.

Some attempts have been made to identify the structure of delta and to indicate its formula by isomorphy with other intermediate phases in metal-oxygen, -nitrogen and -carbon systems. Among the transition metals the M_2X phase is common, where M is a transition metal and X is oxygen, nitrogen or carbon. These phases are most commonly hexagonal with an axial ratio of about 1.6. It was found that 9 of the 12 lines of the delta group could be fitted to such a lattice giving approximately the normal c and a values. However, one of the three lines unaccounted for was consistently present in all patterns and relatively strong in intensity. Another system of indexing could be made at c/a = 2.15, by which nine lines could also be accounted for. In this case the unaccounted lines were all very faint. The two tentative indexings are shown in Table III. There is insufficient evidence to identify delta as V_2O_5.

The VO Phase—The master alloy containing 26% oxygen was found to be almost single-phase which was identified as the VO phase

with the NaCl structure and lattice parameter $a = 4.08$ kX. Klemm and Grimm (2) reported a homogeneity range of VO being between $VO_{0.9}$ and $VO_{1.3}$ (22 and 29% oxygen). No accurate determination of the homogeneity limit of VO on the vanadium-rich side was made in the present work.

Inconclusive evidence of VO decomposing at a low temperature was presented by Klemm and Grimm. It was purported to decompose to the terminal vanadium solid solution and an undefined phase (presumably higher oxide) in the same manner as FeO does. The VO lines appeared in their X-ray diffraction film as low as at the composition of $VO_{0.4}$ (11.2% oxygen). In the present work, no indication of a eutectoid transformation of this type was encountered. In Fig. 1, VO is shown to melt congruently. This is a supposition, there being no evidence in the as-cast structures for a peritectic reaction.

Table IV
Incipient Melting Results on V-O Alloys

Alloy, Wt. %	Incipient Melting Point, °C
3	1940
5.04	1865
8.2	1810
10.3	1785
11.8	1690
14.5	1690
15.3	1690
17.8	1700
20.5	1730-1750
21.4	1710
26.02	1800

Solidification Characteristics—Adenstedt and his collaborators (7) determined the melting point of the same vanadium metal used for the present study. They reported a melting point of 1900 ± 25 °C, the value being confirmed by D. J. McPherson of the Foundation in the contributed discussion to their paper. Table IV tabulates the results of incipient melting measurements on the vanadium-oxygen alloys. As can be seen, there is a minimum in the solidus boundary at about 12% oxygen. The data confirm the trend reported by Seybolt and Sumsion.

An examination of as-cast microstructures of all alloys prepared gave no evidence of a eutectic structure. It was assumed that peritectic reactions only would be involved in the solidification on either side of a minimum at 12% oxygen. The metallographic appearance of a 14.5% oxygen alloy after incipient melting study gives direct evidence of a peritectic reaction on the VO phase side of the minimum in the solidus curve (Fig. 14). The invariant peritectic horizontal was approximately located at 1690 °C (3075 °F), involving the reaction: Liquid + VO $\rightleftharpoons$ X. The minimum in the incipient melting curve must be rationalized as the azeotropic solidification of a phase X, where X is either α or β, depending upon which phase enters into the above







Fig. 14—14.5% Oxygen Alloy Heated to Incipient Melting at 1690 °C. Structure indicates incomplete peritectic reaction: VO + liquid $\rightleftharpoons \beta$. Etched X 500.

Fig. 15—8.2% Oxygen Alloy Quenched from 1700 °C. Structure indicates that beta phase was stable at the annealing temperature. Etched. X 500.

Fig. 16—5.00% Oxygen Alloy Heated to Incipient Melting at 1865 °C. Structure indicates that a solid state transformation has occurred, probably of the type $\alpha \rightarrow \beta$. Etched. X 250.

Etchant: 60 glycerine; 20 HNO_3; 20 HF.

mentioned peritectic reaction. The γ phase or high temperature allotropic modification was suggested by Seybolt and Sumsion and denied by McCalden and Duwez. According to Seybolt and Sumsion the gamma phase is thought to solidify azeotropically and decompose eutectoidally into alpha and VO. However, in our opinion, the structures presented in their paper as evidence cannot be interpreted as

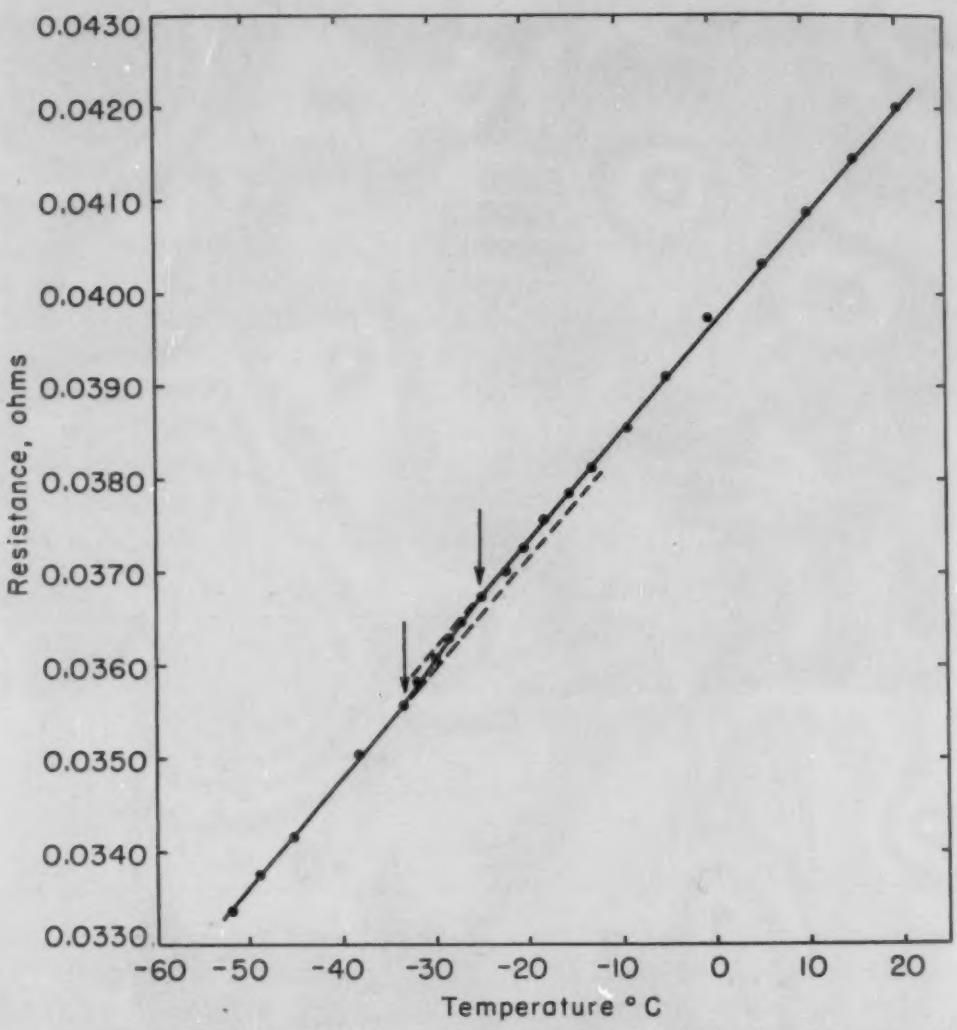


Fig. 17—Temperature Versus Electrical Resistance of Vanadium Wire. (Arrows indicate start and finish of transformation).

eutectoidal. In view of the conflict of evidence on the existence of gamma, we have omitted it from the diagram. It might be further pointed out that none of the structures encountered in as-cast or heat treated states required the assumption of a gamma phase to be explained.

Two critical specimens indicate that the β phase is the proper selection out of the two, α or β. Fig. 15 shows a 8.2% oxygen alloy annealed at 1700 °C (3090 °F) for 5 minutes. The structure is clearly one of untransformed beta. On the other hand, a 5% oxygen alloy quenched from 1850 °C (3360 °F), gives definite indication of having undergone a transformation of the type $\alpha \rightarrow \beta$ (Fig. 16).

Summarizing this information, it would appear that the solidification over the composition range of 0 to 23.9% oxygen involves two peritectic reactions:

$$\text{Liquid} + \alpha \rightleftharpoons \beta \text{ (indirect evidence)}$$
$$\text{Liquid} + \text{VO} \rightleftharpoons \beta \text{ (direct evidence)}$$

Allotropy in the Metal Vanadium—At room temperature and above, the first intermediate phase appears to have a body-centered tetragonal structure. It is quite unusual that the homogeneous field of a true intermediate phase persists to as low as 6.4 atomic % (2 wt. %) of a solute element because this involves an average interaction distance between solute atoms in this case of about 10 Å. This range of effective interaction is rare. It appeared that a more reasonable alter-

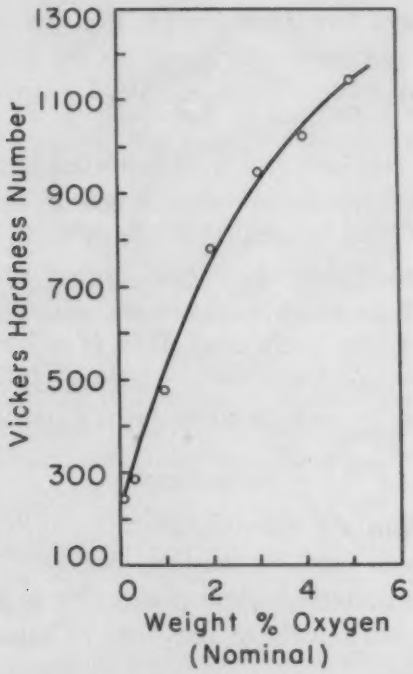


Fig. 18—Hardness Versus Oxygen Content.

native was to assume that the beta field was the stabilization by oxygen of a low temperature allotropic modification of vanadium.

To test this hypothesis, an unalloyed vanadium bar was swaged to 0.050-inch wire. Rather than anneal and risk contamination, the cold-worked wire was wound around an insulated bar to provide a convenient resistivity specimen. The arrangement was immersed in a Dewar flask with dry ice and acetone, and the resistivity was measured with a very accurate Kelvin double bridge as the bath warmed up to room temperature. The temperature was measured both with a copper-constantan thermocouple and a low temperature thermometer capable of measurements to within 0.5 °C. The bath temperature was raised by using a heating coil immersed in the medium. The bath warmed so slowly that there was no measurable temperature change during the period of any resistivity measurement. A plot of measured resistance versus temperature is shown in Fig. 17. There is a clearly indicated change in resistivity occurring between —33 and —25 °C. This result is taken as supporting evidence that a low temperature modification in

vanadium does exist. In the vanadium-oxygen system, the low temperature modification would have a body-centered tetragonal lattice with an axial ratio of 1.04 or less (as extrapolated from the parameter data for the beta phase).

Hardness Measurements on Alloys of Low Oxygen Contents—Hardness measurements were made on all alloys containing less than 5% (nominal) oxygen which were annealed at 900 °C (1650 °F) for 170 hours, and followed by water quenching. A 5 kilogram load was employed on a Vickers hardness tester. Fig. 18 shows the results obtained. The smooth hardness curve seems to indicate that deviations of these low oxygen alloys from nominal compositions are at least systematic.

McKechnie and Seybolt (8) first reported hardness versus oxygen content data. Beatty (9) reported a relation between hardness and lattice parameter of high purity vanadium with various contents of oxygen and nitrogen. However, it was found impossible to compare the results inasmuch as all the alloys examined by different people were varying in nitrogen contents. Beatty reported that small additions of both oxygen and nitrogen resulted in a sharp increase in hardness of vanadium as well as in its lattice parameter.

Summary

A partial diagram of the vanadium-oxygen system was constructed on the basis of limited studies. Melting and heat treating of the alloys were conducted under protective conditions to prevent contamination. The characteristic features of the diagram are as follows:

(a) The limit of solubility of oxygen in alpha vanadium at temperatures below 900 °C is somewhere between 0.07 and 0.25% oxygen. At very high temperatures the maximum solubility reaches nearly 1%.

(b) The solidus curve has a minimum where the beta phase solidifies azeotropically. The phase has a body-centered tetragonal lattice and is considered as a stabilized phase of the low temperature allotrope. It has a large range of homogeneity.

(c) A peritectic reaction occurs at 1690 °C (3075 °F) between VO and vanadium-rich liquid of about 14% oxygen to form the beta phase.

(d) The delta phase is formed by a peritectoid reaction between β and VO phases at approximately 1100 °C (2010 °F). There is insufficient evidence to identify delta as V_2O.

(e) A low temperature allotropy in vanadium was found by temperature versus resistivity measurement in the temperature range between —33 and —25 °C.

ACKNOWLEDGMENTS

The authors are grateful for the sponsorship of this project by the Wright Air Development Center, Wright-Patterson Air Force Base, Ohio, and for their permission to publish the paper.

Special thanks are due R. F. Domagala (heat treatment and incipient melting), C. A. Johnson (Metallography) and R. J. Van Thyne (melting of alloys) who rendered their assistance during various phases of this work.

References

1. A. U. Seybolt and H. T. Sumsion, "Vanadium-Oxygen Solid Solutions," *Transactions,* American Institute of Mining and Metallurgical Engineers, Vol. 5, 1953, p. 292.
2. W. Klemm and L. Grimm, "On the Knowledge of the Lower Vanadium Oxides," *Zeitschrift fur anorganische und allgemeine Chemie,* Vol. 150, 1942–43, p. 42.
3. N. P. Allen, O. Kubaschewski and O. von Goldbeck, "The Free Energy Diagram of the Vanadium-Oxygen System," *Journal,* Electrochemical Society, Vol. 98, No. 11, 1951, p. 417.
4. J. O. McCalden and P. Duwez, "Allotropic Transformations at High Temperature," TN 215E, *Journal of Metals,* Vol. 6, No. 5, 1954, p. 619.
5. M. Hansen, H. D. Kessler and D. J. McPherson, "The Titanium-Silicon System," TRANSACTIONS, American Society for Metals, Vol. 44, 1952, p. 518.
6. R. F. Domagala and D. J. McPherson, "System Zirconium-Oxygen," *Journal of Metals,* February 1954, p. 238.
7. H. K. Adenstedt, J. R. Pequignot, and J. M. Raymer, "The Titanium-Vanadium System," TRANSACTIONS, American Society for Metals, Vol. 44, 1952, p. 990.
8. R. K. McKechnie and A. U. Seybolt, "Preparation of Ductile Vanadium by Calcium Reduction," *Journal,* Electrochemical Society, Vol. 97, No. 10, 1950, p. 311.
9. S. Beatty, "Note on the Effect of Oxygen and Nitrogen on the Hardness and Lattice Parameter of High Purity Vanadium," TN 121E, *Transactions,* American Institute of Mining and Metallurgical Engineers, Vol. 194, 1952, p. 987.

INDEX OF AUTHORS

VOLUME XLVII

TRANSACTIONS OF AMERICAN SOCIETY FOR METALS

1955

A

Averbach, B. L.....267, 291, 380

B

Barnett, W. J..... 892
Beattie, H. J., Jr..... 211
Beck, F. H..... 473
Bever, M. G..... 794
Bhattacharyya, Subrata 351
Binder, W. O..... 231
Bond, W. E..... 578
Brenner, William, Jr..... 715
Brown, W. F., Jr..... 926
Busby, C. C..... 135
Busby, Paul E..... 408

C

Carlson, O. N..... 520
Chapman, R. D..... 869
Clarkin, P. A..... 794
Cochardt, A. W..... 440
Cohen, Morris 267, 291, 380, 650
Culp, Neil J..... 769
Curry, W. E..... 193

D

Danko, J. C..... 853
Davis, Moss V..... 605
Devine, R. W., Jr..... 748
Dieter, G. E..... 423
Domagala, R. F..... 565
Dorn, John E.....102, 632
Duwez, Pol 543

F

Fiedler, H. C..... 267
Fisher, John C..... 451
Fishel, W. P..... 605
Fontana, M. G.....473, 554
Franks, Russell 231
Frenkel, Robert E..... 632
Frohmberg, R. P..... 892
Fukutomi, Takeo 599

G

Garofalo, F. 957
Grant, N. J..... 650

H

Hansen, Rosa D..... 508
Hauser, F. E..... 102
Hawkes, M. F..... 135
Hazlett, Thomas H..... 508
Horne, G. T..... 423

J

Jatczak, C. F..... 748
Jepson, James O..... 543
Jominy, W. E.....727, 869
Jones, M. H..... 926

K

Keeler, J. H..... 157
Kehl, George L..... 351
Kenney, D. J..... 520
Kraft, R. Wayne, Jr..... 611

L

Lement, B. S..... 291
Lena, A. J..... 193
Libsch, J. F..... 853
Lillys, Peter 785
Littmann, Walter E..... 692

M

Matthews, Norman A..... 611
Mehl, R. F..... 423
Morris, W. 463
Muir, Hugh 380

N

Nehrenberg, A. E..... 785
Newman, D. P..... 926
Nusbaum, C. 715

O

Orrell, F. L., Jr..... 554

P

Paliwoda, E. J. 680
Paxton, H. W..... 135
Payson, Peter 785
Porembka, S. W..... 665
Priest, D. K..... 473
Pugh, J. W. 984

R

Rhines, F. N..... 578
Roberts, E. C..... 650
Ross, S. T..... 727
Rostoker, W. 565, 1002
Rozalsky, I. 77
Rummel, R. A..... 578
Rutter, J. W..... 463

S

Sachs, G. 926
Saller, H. A. 665
Sernka, R. P. 727
Sherby, Oleg D. 632
Signorelli, R. A. 815
Smith, G. V. 957
Speiser, Rudolph 493
Spretnak, J. W. 493
Stacy, J. T. 665
Starr, C. D. 102

T

Thompson, James 231
Tietz, L. 102
Tiller, W. A. 463
Troiano, A. R. 892

V

Vajda, John 408
VanHorn, Kent R. 38
VerSnyder, F. L. 211

W

Weeton, J. W. 815
Wilhelm, H. A. 520
Wilks, Charles R. 611
Wilson, D. V. 321
Winegard, W. C. 463
Wulff, John 692

Y

Yamamoto, A. S. 1002

SUBJECT INDEX

Activation energy

for creep 633–637
for recovery 636

Alloy formation

thermodynamic expressions .. 494

Alloy steels, high carbon

hardenability. See under Hardenability.

Aluminum

hardness traverses 85–87
tensile specimens prestrained in biaxial tension 85–87
wrought products 38–75
factors affecting directional properties 38–75

Aluminum alloy bar

directional properties 66–74
correlation with preferred orientation 69–72

Aluminum alloys, dilute

effect of cold work on creep. See Cold work.

Aluminum-copper-magnesium alloy

pole figures 67–68
illustrating duplex type of preferred orientation in extruded bar 67–68
tensile properties 68–69, 72–74
after recrystallization 72–74
effect of preferred orientation 72

Aluminum plate

compressive prestrain 81–82, 96
dependence of strain anisotropy upon 81–82, 96
flow properties 94–99
effect of prestraining under different stress states ..94–99
fracture properties 77–93, 96–99
effect of prestraining under different stress states 77–93, 96–99

Aluminum plate (cont.)

longitudinal and transverse strain distributions 82–85, 96
for hydraulic cicular bulges 82–85, 96
effect of bulging pressure 83–85
retained tensile ductility 86–93, 96–97
effect of biaxial tension and biaxial compression 88–89, 97
effect of prestrain in simple compression or simple tension 89–91, 97
effect of prestrain stress state 90–91, 97
effect of tensile and compressive prestrain 86–89, 96
tensile fracture stress ..91–93, 97–98
comparison of compressive effects 93, 97–98
for various prestrain states and prestrain directions 93, 97–98
effect of various prestrain stress states 91–93, 97–98
yield strength 94–96, 98
comparison of compressive prestrain effects upon 94, 96, 98
for various prestrains stress states and directions 94, 96, 98
effect of various stress states 94–95, 98

Aluminum sheet

deep drawing 47–48, 50, 63–66
effect of preferred orientations 47–48, 50
drawing capacity 62–65
effects of preferred orientation 62–65
ear formation 60–62
earing 42, 47–48, 60–65
pole figures .....
..40–41, 45–49, 52–54, 58–63, 65

Aluminum sheet (cont.)
mixture of rolling and recrystallization textures 48, 62–63, 65
rolling texture 40, 47, 58–60
recrystallization texture 46, 49, 60–62
tensile tests 46–47, 49
effect of preferred orientation 46–47,49
yield strength 53–55
effect of rolling direction ...53–55

Aluminum-vanadium system
alloy examination 522–523
aluminum rich alloys 523–529
microstructures 525–527
solid solubility of vanadium. 524
aluminum rich diagram 539
phase diagram 524
phases 536
previous investigations 520
vanadium rich alloys 529–534
lattice constant – composition 531
microstructures 530, 532–533
solid solubility of aluminum. 529

Annealing
hardened steels
effect on elastic limit.392–393, 396

Annual Address of the President 8

Annual Dinner of ASM..... 32

Annual Meeting of ASM 7

Annual Report – ASM Foundation for Education and Research..... 29

Annual Report of the Secretary 15

Annual Report of the Treasurer 11

Arc-melting
Zirconium 179–192

ASM Foundation for Education and Research – Annual Report 29

Austenite
decomposition products 727–746
isothermal transformation of
under applied tensile stress.
See Isothermal transformation of austenite.

Austenitic ductile cast irons
creep and stress rupture data 615–623
hot tensile properties 625–627
structural stability and growth 623–625

Austenitic steels
See Chromium-Manganese Steel.
See Stainless Steels, Austintic.

Bainite
effect of stress on formation.359–366
character of bainite formed 367–371
mechanism of formation 351–354
structural nature 739

Banitic structures
SAE 4340 steel 918–919
room temperature aging characteristics 918–919

Bauschinger Effect 96

Bend planes
in magnesium .....
.....109–110, 112–113, 117–118
associated with twinning.117–118
schematic illustration 117

Boron
effect on hardenability.....410–413
in end-quenched steel sections
effect on tensile and impact properties 413–416

Carbide morphology
effect on fatigue properties of eutectoid steel 434–438

Carbides
distribution in iron-carbon-titanium-vanadium alloys 605–610
in 4.5% chromium steels
changes during tempering.660–661

Carbon
content of steel
effect on elastic limit.....
.....387–390, 395–397
distribution in iron-carbon-titanium-vanadium alloys 605–610
effect on creep-rupture behavior of 4.5% chromium steels 653–654
effect on hardenability 411
effect on machinability of steel 683, 687–689
effect on transformation temperatures of iron 504, 506
in end-quenched steel sections
effect on tensile and impact properties 417
solubility in ferrite 306–310
in titanium
effect on beta-alpha transformation 506–507

Carbonitriding
steel AISI 1020 794–814
case depth 800–801, 804
effect of water vapor..800–801
effect of ammonia concentration 800–801
carbon concentrations .....
....802–803, 807–808, 810–813
effect of ammonia 802–803
effect of water vapor ..802–803
microhardness 797–799, 804
effect of water vapor ..797–799
effect of ammonia concentration 797–799
nitrogen concentrations ....
....802–803, 807–808, 810–813
effect of ammonia 802–803
effect of water vapor...802–803
retained austenite 800–802
effect of water vapor...800–801
effect of ammonia concentration 801
role of water vapor and ammonia 794–814
surface hardness.797–798, 803–805
effect of water vapor 797–798, 803–805
effect of ammonia concentrations ...797–798, 803–805

Carbon tool steel
hardenability of cylinders. See under Hardenability.

Case depth
determinations for carbon tool steel cylinders 776–782

Case hardening atmospheres
role of water vapor and ammonia 794–814

Cathodic protection
of magnesium alloy J 1 from stress-corrosion.....483–485

Cementite
solubility in gamma iron ...504–505

Cementite in steel
effect of cold work
changes in magnetic intensity 343–344
displacement of Curie point 340–343
on magnetic intensity 325–330
mechanical reversibility.330–334
solonoid studies 334–335
tectural stress evidence...344–345
thermal-magnetic analysis 322–325
x-ray results 336–340

Cementite particles
minimum stable size 304–306
solubility in ferrite
effect of carbon form..... 310
effect of size 306–309
effect of strain 309–310

Cerium
in iron alloys. See Iron—cerium system.

Chi Phase
in 12% Cr–4% Mo stainless alloy 211–230
effect of titanium .....
....213–215, 223–224, 226–230

Chi Phase (cont.)
identification 219–223
chemical analysis 222
lattice parameters.220, 222, 229
photomicrographs 221
structure 220–223

Chromium
in binary zirconium alloys
effect on elevated temperature strength 671–674
effect on workability and hardness 670–671
in high carbon alloy steels
effect on hardenability ...759, 762

Chromium-manganese-nickel steels
corrosion resistance 255–258
effect of chromium 256–257
effect of manganese 255–257
effect of nickel 255–257
intergranular corrosion ..256–258
effect of carbon 256–258
effect of nitrogen 256–258
izod impact.....241, 249–254
influence of composition ..249–252
effect of carbon.....251, 253
effect of chromium 251
effect of manganese 251–252
effect of nickel 251
effect of nitrogen 251, 253
influence of temperature..252–254
effect of aging 253–254
mechanical properties .....
.....239–241, 243–254
elongation 241, 244–246
effect of cold working 246
effect of manganese ...241, 245
Erichsen values 241, 245
izod impact.....241, 249–254
tensile strength..240–241, 244–246
effect of carbon.....241, 244
effect of chromium.240–241, 244
effect of cold working...245–246
effect of manganese.241, 244–245
effect of nickel....240–241, 244
effect of nitrogen.....241, 244

Chromium-manganese-nickel steels (cont.)
work hardening..239, 243, 247–250
effect of manganese....239, 243
yield strength.....241, 244, 246
oxidation tests 264–265
phases present.....233–240, 242–243
after heating at 1075 °C and air cooling 233–239
effect of carbon.....236–238
effect of chromium.....234-239
effect of manganese.....234–239
effect of nickel.....234–239
effect of nitrogen.....236–238
in chill cast samples at various temperatures .....
.....239–240, 242–243
relative magnetism.239–240, 242
stress – rupture strength....262–265
true stress – strain curves...247–250
welding characteristics 254–255
charpy impact 254
effect of nickel..... 254
tensile properties of weld... 254

Chromium-manganese steel
photomicrographs 207–208
showing sigma formation.207–208
rate of sigma formation..... 207
effect of cold work..... 207
effect of recrystallization... 207

Chromium-molybdenum-vanadium steel
17-22A (S) steel.....926–956
effect of variation in normalizing and tempering procedure 926–956
creep embrittlement 926–956
notch sensitivity 926–956
stress rupture strength..926–956

Chromium-nickel-copper steel
17-4PH steel 926–956
effect of variation in normalizing and tempering procedure
creep embrittlement 926–956
notch sensitivity 926–956
stress rupture strength..926–956

Chromium steel

hardened 4.5 chromium steels
creep-tempering relationships. See creep-tempering relationships.

Cobalt base alloy

See stellite 21

Cold-rolled steel, low carbon

effect of rolling temperature on zonal texture
experimental procedure ..716–719
previous investigations ...715–716
rolling conditions 717–718
strip thickness vs. temperature 717–719
x-ray diffraction study....719–726
intensity curves 721–726
pale figures 724

Cold work

chromium-manganese steel ... 207
effect on sigma formation... 207
effect on cementite in steel. See Cementite in steel.
effect on creep properties of dilute aluminum alloys
activation energy for creep 633–637
activation energy for recovery 636
alloys tested 633
creep curves 634–635
creep strain equation 633
effect of recovery on tensile curves 636–637
initial state of alloys.....633, 636
recovery model 641–643
stress parameter relation..637–640
to creep strain.....639–640
structure parameter relation 639–641
to creep strain.....641, 643
true stress vs. true creep..639–640
stainless steels, type 310
effect on sigma formation... .....195–196, 198–207

Columbium

in binary zirconium alloys
effect on elevated temperature strength 671–674
effect on workability and hardness 670–671

Constitution diagrams

See Phase Diagrams.

Continuous cooling diagrams

.....876–879, 881–887
determined by magnetic permeability method 876–879
Grange and Kiefer diagram.877–879

Continuous cooling transformations

magnetic method for determining 869–891

Cooling curves

SAE 4340 steel.....876–877
for several quenching media 876–877

Cooling rate

calculation for carbon tool steel cylinders 770–775
versus percent martensite...729–730

Cooling transformation curves

SAE 4340 steel..... 872

Cooling transformation diagrams 730–733, 884–887

Bainite region 886–887
transformation products 884–885

Copper-gold system

constitution of ordering alloys
alloys investigated 581
equilibrium results 584
experimental procedure ..583–584
phase diagrams 579, 587
phases 595–596
rates of approach to equilibrium 589–595

Corrosion resistance
chromium-manganese-nickel steels 255–258

Corrugations
formation during solidification 464, 469

Cottrell mechanism ...978–980, 982

Cottrell's theory 451

Crack formation
magnesium 125–129, 132–134

Creep curves
molybdenum 994–995
substructure influence in nickel and nickel alloys
alloys tested 510
constant creep rate region.514–515
formula for initial curve..513–514
nickel-cobalt 515
effect of alloy content..... 515
nickel-iron 514
nickel titanium 514
prestrain for linear curve 515–516
prestraining substructure treatment 508–510
effect of amount of prestrain 508–509, 511, 516
effect on tensile properties 508–511, 513
pure nickel curves.....511–513
relation to flow stress....509, 512
test procedure 509–510

Creep embrittlement
Cr – Mo – V and 17 Cr – 4 Ni – 4 Cu steels.....926–956
effects of variation in normalizing and tempering procedure 926–956

Creep properties
of dilute aluminum alloys
effect of cold work on. See Cold work.
of ductile or modular cast irons 613–623

Creep properties (cont.)
of 4.5% chromium steels..... 655
of steel isothermally transformed under applied tensile stress 362–365

Creep-rupture curves
for 4.5% chromium steels...653–656
effect of carbon content..653–654
microstructures 654

Creep-rupture data
molybdenum 999–1000

Creep-rupture fracture
molybdenum 999–1000

Creep-rupture properties
molybdenum 995–1000
of zirconium – 8% tungsten alloy at 1800 °F.....674–675

Creep-rupture test
molybdenum 996–997
minimum creep rate.....996–997
activation energy 996
as a function of reciprocal absolute temperature 996–997
as a function of true stress. 996

Creep strain
in dilute aluminum alloys
equation 633
relation to stress parameter 637–640
relation to structure parameter 639–641

Creep-tempering relationships
in hardened 4.5% chromium steels
analysis of tempering phenomena 656–661
changes in carbides.....660–661
hardness and electrical resistance data 656–660
creep-rupture behavior...653–656
effect of carbon content.653–654
microstructures 654

Creep-tempering relationships (cont.)
effect of stress during tempering 661–662
on hardness and electrical resistance 661
effect of structural instability 662
experimental procedure
phases formed during tempering 651
steels tested 651

Critical cooling velocity
in hardening carbon tool steels 774–782

Critical stress range
for isothermal transformation of austenite.....360–362

Crystallographic orientation
zirconium 173, 175–176, 178
relation to plastic strain 173, 175–176, 178

Curie paints
effect of cold work on.....328–343

Damping of some engineering alloys
effect of static stress
cause in ferromagnetic materials 447
compositions of alloys..... 443
experimental procedure...441–443
formula for 442
importance of damping...440–441
magneto-mechanical damping of Fe-40% Co.....447–449
on AISI 403 steel.....444–447
effect of temperature..... 445
on Refractory 26.....445–446
effect of temperature..... 446
plastic flow damping.....447–449

Deep drawing
aluminum sheet....47–48, 50, 63–66
effect of preferred orientations 47–48, 50
cylindrical cup
schematic representation 55

Deformation
effect on cementite in steel. See Cementite in steel.
of iron-carbon alloys
effect on carbon solubility.309–310

Deformation mechanisms
in polycrystalline magnesium.102–129

Delayed failure
steel 892-922
from hydrogen embrittlement 892–922

Delayed yield
dislocation theory. See Dislocation theory.

Dendritic growth in alloys
constitutional supercooling... 469
corrugations 464, 469
critical conditions for.....467–470
dentritic transition.....466–470
distribution coefficient..463, 465, 470
experimental procedure.....465–466
solute concentration.....463–464
solute temperature distribution. 464
supercooling gradient 469

Detwinning
magnesium 112, 115–116

Directional properties
aluminum alloy bar.....66–74
correlation with preferred orientation 69–72
aluminum wrought products..38–75

Dislocation theory
application to delayed yield in steel
Cottrell's theory 451
delay time equations and results 453–458
effect of strain aging..... 457
exceptions 456–457
relation to shear modulus 454–458
relation to temperature.454–458

Dislocation theory (cont.)
energy to initiate slip....452–453
rate of thermal nucleation.. 453
yield stress vs. temperature 458–461
for iron 461
for molybdenum 460

Drawing capacity
aluminum alloy sheet.....62–65
effects of preferred orientation 62–65

Ductile cast iron
bright field observations....855–856
elevated temperature properties
alloys tested 612–615
advantages of ductile irons.. 611
austenitic ductile iron
creep and stress rupture data 615, 617, 620–623
creep curves 619, 622
residual tensile properties. 615
stress rupture curves...621, 623
experimental procedure...612–619
ferritic ductile iron
creep and stress rupture data 613, 617, 620, 623
creep curves 618, 622
residual tensile properties. 613
stress rupture curves...620, 623
heat treatments 613–614
hot tensile properties.....625–627
limiting creep stress vs. temperature 617, 620–623
comparative data for low carbon steel 620
limiting rupture stress vs. temperature 617, 620–623
comparative data for low carbon steel 623
metallography 616, 626
pearlitic ductile iron
creep and stress rupture data 614, 617, 620–623
creep curves 618, 622
residual tensile properties. 614
stress rupture curves...620, 623
structural stability and growth 623–625

Ductile cast iron (cont.)
microstructures 857–863
secondary graphite 854
showing influence of composition on secondary graphite 861–863
showing metamorphosis of secondary graphite ...857–862
polarized light observations.855–856
quenched and tempered.....853–868
secondary graphitization..853–868
secondary graphite 857–863
influence of composition..861–863
metamorphosis of 857–862
silicon-rich carbides 856–857, 859

Ductility
molybdenum 992–995
as a function of temperature 992–995
SAE 4340 steel.....899–906
effect of hydrogen embrittlement 899–906
17-22A(S) steel...938–941, 946–947
effect of normalizing temperature 938–939
at several times to rupture 938–939
effect of rupture time..... 947
at several test temperatures 947
effect of tempering temperature
at several rupture times.939–940
effect of tempering time..946–947
at various tempering temperatures 946–947
effect of tempering time..939–941
at several times to rupture 940–941
17-4 PH steel.....940–942
effect of tempering temperature 940–942
at several rupture times.941–942
effect of test temperature..940–942
at several rupture times.941–942
various steels 137–144
brine quenched and refrigerated 140–141

Ductility (cont.)
effect of refrigeration....140–141
effect of specimen size.....
.....142–144, 154–155
quenched in iced brine....137–140
quenched in oil.....141–142

Ear formation
aluminum sheet 60–62

Earing 42, 47–48, 60–65
aluminum sheet 47–48, 60–65

Elastic limit and yield behavior
of hardened steels
apparatus and procedure..381–386
definition 380–381
effect of isothermal annealing 392–393, 396
effect of quench and transformation stresses .....
.....394–395, 403
effect of rate of cooling from tempering temperature..
..... 390–397
effect of tempering temperature 384–386, 405–407
effect of tempering temperature on hardness and strength 384–387
effect of tempering temperature on yield strength.384–391
influence of carbon content..
.....387–390, 395–397
mechanical properties vs. hardness .....
....387–388, 391–392, 405–407
mechanical test results....385–389
relation to strength and hardness 393–394
relation to yield strength..391, 394
steels tested 381–382
stress residual strain curves
.....384, 386
temper embrittlement 397

Election of officers 31

Electrical resistance
of tempered 4.5% chromium steels 656–660
effect of stress during tempering 661–662
vanadium 1014–1015
as a function of temperature
..... 1014–1015

Electron metallography
of dependence of microstructure on hardenability 727–746

Electron micrographs
of iron-carbon alloys tempered at 700–1000 °F....
.....294, 297–299, 314–316
of steel isothermally transformed 374–375

Elevated temperature properties
of ductile or nodular cast irons. See Ductile cast irons.
of wrought binary zirconium alloys. See zirconium alloys.

Elmendorf curve
SAE 4063 steel 880–881

Elongation
chromium – manganese – nickel steels 241, 244–246
molybdenum 992–995
as a function of temperature
..... 992–995
zirconium .161–162, 170–172, 180–181
effect of annealing temperature 170–172
effect of test temperature...
.....161–162, 180–181

Embrittlement
17-22A(S) steel 938–941
effect of normalizing temperature 938–939
at several times to rupture
..... 938–939
effect of tempering temperature 939–940
at several rupture times.939–940

Embrittlement (cont.)
effect of tempering time..939–941
at several times to rupture 940–941
17-4 PH steel.....940–942
effect of tempering temperature 940–942
at several rupture times.941–942
effect of test temperature..940–942
at several rupture times.941–942

End-quenching
of heavy steel sections
transverse properties. See Slack-quenched steel.

Enthalpy
of binary interstitial solid solutions 494–507

Erichsen values
chromium – manganese – nickel steels 241, 245

Fatigue properties
of lamellar and spheroidal eutectoid steel
crack location 432–433
effect of carbide morphology 434–438
effect of inclusions..425, 433, 436
factors affecting 433–438
fatigue statistics 430–432
material and testing.....426–427
mechanical properties 426
microstructures 433–435
statistical analysis methods 423–425, 427–430

Ferritic ductile cast irons
creep and stress rupture data 613–623
hot tensile properties.....625–627
structural stability and growth 623–625

Ferroboron
compared with Grainal No. 79
for effect on hardenability.412–413
for effect on tensile and impact properties 412–414

Ferromagnetic materials
damping characteristics 444–447

Flow properties
aluminum plate 94–99
effect of prestraining under different stress states...94–99

Fracture properties
aluminum plate 77–93, 96–99
effect of prestraining under different stress states... .....77–93, 96–99

Flow stress
relation to substructure of nickel alloys 509, 512

Free energy
of binary interstitial solid solutions 495–507
relation for decomposition of austenite 740–741

Gamma iron
solubility of cementite in....504–505

Glass rods, annealed
relationship between bending stress and time for fracture 921–922

Grain boundary shear
magnesium 122–126

Grain orientation
aluminum wrought products..39–42
correlation with directional properties 39–42

Grains
magnesium
orientation 104, 106–107

Grain size
of iron-carbon alloys
effect of tempering temperature on 296–302
zirconium 170–172, 174–175
effect of annealing temperature 170–172, 174–175

Grinding

influence on structure of hardened steel
effect of mechanical variables 702–705
effect of wheel condition..704–705
electrical simulation of...696–697
experimental work 693–697
grinding conditions 696
grinding energy relation.... .....703–704, 710–713
peak temperature vs. microhardness 699–700
reason for investigating..692–693
results from electrical heating 698
temperature distribution beneath surface 700–701
temperature for rehardening 698–700
temperature for tempering.698–702
temperature vs. grinding conditions 702–703
transverse temperature variations 700–702

Hardenability

of carbon tool steel cylinders
calculated cooling rates...770–775
calculated hardness penetration curves 775
case depth determinations.776–782
comparison with calculated values 779, 782
critical cooling velocity...774–775
hardness penetration curves 771–775
steels used 776
dependance on microstructure
character of bainite 739
character of pearlite 739
cooling rates vs. percent martensite 729–730
cooling transformation diagrams 730–733
method of constructing..730–731
method of using.....733–734

Hardenability (cont.)

electron metallography..... .....734–742, 744
identification of transformation products ...735–738
free energy, temperature, decomposition relation..740–741
hardenability data 728–729
microstructures 728–729
steels tested 728
of heavy steel sections
effect of boron.....410–413
effect of carbon..... 411
effect of nickel..... 412
effect of rare earth meals... 410
effect of silicon.....410–412
of high carbon alloy steels
composition of steels.....750–751
computation of hardenability 754–764
effect of chromium.....759, 762
effect of manganese.....757, 761
effect of molybdenum....759, 762
effect of nickel.....758, 761
effect of nickel plus manganese 760
effect of silicon.....752–753
hardenability data 749–754
reason for interest.....748–749

Hardenability data

for 0.4% carbon steels.....728–729

Hardened steels

elastic limit and yield behavior. See Elastic limit and yield behavior.

Hardness

18% Cr–8% Ni stainless steel. 273
austenite 273
martensite 273
17-22A(S) steel 930–937
as a function of normalizing temperature and time.931–932
as a function of tempering temperature and time.931–933

Hardness (cont.)
of hardened steels
relation to elastic limit....393–394
relation to mechanical properties .....
....387–388, 391–392, 405–407
of iron-carbon alloys
effect of tempering temperature on 293, 304
low carbon steels...971–973, 981–982
effect of strain aging.....971–973
effect of aging time....971–973
relationship to transition temperatures 972–973
martensitic steels 785–793
effect of alloying elements.790–791
effect of carbon..788–789, 791–793
effect of chromium..... 790
effect of nitrogen.788–789, 791–793
stainless steels, type 310....208–209
effect of sigma formation.208–209
stellite 21 ....830–833, 841, 849–851
aging 830–833
effect of aging temperature for various times 832, 850–851
effect of time at various temperatures 831
changes with heat treatment. 841
effect of different quenching methods 849–850
isothermal transformation.830–833
effect of temperature for various times 832
effect of time at various temperatures 831
of tempered 4.5% chromium steels 656–660
effect of stress during tempering 661–662
of titanium-cobalt alloys..... 562
vanadium-oxygen alloys..1015–1016
as a function of oxygen content 1015–1016
of wrought binary zirconium alloys
at room temperature and 1600°F 670–671

Hardness (cont.)
zirconium 172
annealed for various time–temperature combinations 172

Hardness penetration curves
for carbon tool steel cylinders 771–775

Hardness traverses
aluminum tensile specimens...85–87
prestrained in biaxial tension 85–87

Heat tinting
stellite 21 .....821–822, 834–836, 842

Heat treatment
effect on stress-corrosion of magnesium alloy J1.... 479

High carbon alloy steels
hardenability. See under Hardenability.

Hot hardness
low carbon steels.....
.....961–962, 973–976, 981–982
effect of aging time.....974–976
effect of temperature.....973–974

Hydrogen embrittlement
proposed mechanisms 895–898
Cottrell atmosphere surrounding a dislocation 896
Griffith crack theory.....896–898
planar pressure theory....895–896
SAE 4340 steel 892–922
bainitic structures 918–919
room temperature aging characteristics 918–919
ductility 899–900, 903–906
effect of charging conditions 899–900
effect of charging time... 899
effect of removing surface layers of metal from charged specimens .903–906
at two strength levels.904–905
effect of aging.....904–905

Hydrogen embrittlement (cont.)
effect of aging time.....900, 904
on ductility 900–903
on notch tensile strength..
.....900–902, 904
hydrogen distribution 902–906
mechanical properties 899–900
effect of charging conditions 899–900
relationship to delayed failure 906–908
strength 900, 902
effect of charging time 900, 902
stress rupture tests.....906–921
critical load values.....908–909
effect of aging with and without applied stress 911–918
sharp notched specimens 912–913
unnotched specimens..912, 915
effect of aging time....909–914
relationships between aging time, applied stress and time to failure 910–914
effect of notch acuity...908–909
evaluation of variables.919–921
tempered martensite 918–919
room temperature aging characteristics 918–919
true stress-true strain curves 900–901
charged and uncharged specimens 900–901

Impact properties
of end-quenched heavy steel sections
effect of boron 413–416
effect of carbon 417
effect of mass 418–420
effect of nickel 415
effect of rare earth metals.414–416
effect of silicon 414–417
low carbon martensites 135–152
steels 144–148, 150–151
effect of alloying elements 146–148, 151

Impact properties (cont.)
effect of carbon 146–148, 153
effect of chromium ..147–148, 153
effect of manganese 148
effect of nickel 147, 151, 153
effect of strain aging 150–151
effect of testing temperature 145–147, 151

Impact transition temperature range
low carbon steels ..961–967, 980–981
effect of prestraining in compression and aging...963–965
effect of aging temperature 963–965
effect of prestraining in tension and aging....961–963
effect of aging temperature 963
effect of straining and strain aging 980–981
effect of stress – relief treatments 966–967

Inclusions
in steel
effect on fatigue properties 425, 433, 436

Intergranular corrosion
chromium-manganese-nickel steels 256–258

Interstitial solid solutions
thermodynamics. See Thermodynamics.

Iron
yield stress vs. temperature .. 461

Iron-carbon alloys
microstructural changes on tempering. See Tempering of iron-carbon alloys.

Iron-cerium system
determination of cerium....552–553
diffraction data 550–551

Iron-cerium system (cont.)
effect of cerium on transformation 546
experimental procedure ...543–545
phase boundary determinations 546–548
phase diagram 544, 548
partial 547
structure of intermediate phases 548–551
$Co Fe_3$ phase 552

Iron-cobalt alloys
damping 447–449

Isothermal transformation of austenite under applied tensile stress
applied stress relation to percent transformed 359–360
character of banite formed..367–371
creep behavior 362–365
critical stress range 360–362
critical true strain 366
during a portion of transformation time 368
effect on beginning and ending times 357–359
effect on rate of decomposition. 367
electron micrographs 374–375
experimental procedure 354–357
previous results 351–354
true strain vs. banite formed.363, 366
true strain vs. time 362–365
true stress – true strain relation
of unstable austenite prior to banite formation 366
of unstable austenite transformed to banite 366–367
typical microstructures 361

Izod impact
chromium-manganese-nickel steels 241, 249–254

Larson-Miller parameter
as a function of stress 997–998
for molybdenum 997–998

Lattice parameters
18% Cr – 8% Ni type
austenite 269
martensite 269
stellite 21 838
vanadium-oxygen system .1007, 1011
beta phase 1007
VO phase 1011

Laves phase
in 12% Cr – 4% Mo stainless alloy 211–230
effect of titanium.....
....213–215, 233–224, 226–230
identification 215–220
chemical analysis 216–217
internuclear distances ..218–220
latice, parameters 220, 226
structure 216–220

Lead-tin alloys
dendritic growth 463–470

Low carbon steels
creep and rupture stress vs. temperature 617, 620–623
effect of rolling temperature on texture. See Cold-rolled steel, low carbon
impact transition temperature range 960–967, 980–981
effect of prestraining in compression and aging ..963–965
effect of aging temperature 963–965
effect of prestraining in tension and aging 961–963
effect of aging temperature.963
effects of straining and strain aging 980–981
effect of stress-relief treatments 966–967
microstructure 976
effect of strain aging treatments 976
hardness 971–973, 981–982
effect of strain aging....971–973
effect of aging time 971–973

Low carbon steels (cont.)
hot hardness 973–976, 981–982
effect of aging time 974–976
effect of temperature 973–974
tensile properties 966–971
effect of prestraining in compression and aging ..969–971
effect of prestraining in tension and aging 966–969
tensile strength 966–971
effect of prestraining in compression and aging ..969–971
effect of prestraining in tension and aging 966–969
effect of aging time 966–967
transition temperatures 972–973
relationship to hardness ..972–973
relationship to yield strength 972–973
time stress-strain curves....965–966
prestrained in compression and aged 965–966
prestrained in tension and aged 965–966
yield point behavior 970–971
effect of prestraining and aging 970–971
yield strength 966–971
effect of prestraining in compression and aging ..969–971
effect of prestraining in tension and aging 966–969
effect of aging time.....966–969

Machinability
of rephosphorized open hearth screw steel
effect of composition. See Rephosphorized open hearth screw steel

Machinability index 689

Magnesium
bend planes .....
.....109–110, 112–113, 117–118
associated with twinning..117–118
schematic illustration..... 117
crack formation ...125–129, 132–134
deformation mechanisms in..102–129

Magnesium (cont.)
detwinning 112, 115–116
grain boundary shear 122–126
grains 104–107
method of identification...104–105
orientation 104, 106–107
noncrystallographic low angle boundaries 117–122
crossing grain boundary ..120–121
effect of stress on displacement of 121–122
formation and movement..118–120
noncrystallographic surface traces 127–128
rupturing 125–129
slip 110–111
critical stress for 110–111
slip-bands 108–111
stress-strain curves 105, 107–108
twinning 111–117, 125
bending planes associated with 117
bilateral growth 112–113
detwinning 112, 115–116
unilateral growth 112, 114

Magnesium alloys
stress-corrosion. See Stress-corrosion

Magnetic intensity
of cold worked steel 325–344

Magnetic transformation curves
SAE 4340 steel..... 872

Magnetic transformation diagram
SAE 4340 steel
relation of magnetic permeability to temperature.875–876

Magneto-mechanical damping 447–449

Manganese
effect on machinability of steel. 687
in high carbon alloy steels
effect on hardenability ...757, 760–761

Manganese steels
martensitic transformation..286–288

Martensite
18% Cr–8% Ni stainless steel
relationship to electrical resistance 269–270
isothermal formation 272–275, 282–284
18% Cr–8% Ni stainless steel 272–275
effect of carbon 272–275
effect of holding temperature 272–275
effect of plastic deformation 282–283
mechanical stabilization.282–284
mechanism of formation ...352–354
SAE 4340 steel 918–919
hydrogen embrittlement...918–919
room temperature aging characteristics 918–919

Martensitic steels
attainable hardness 785–793
effect of alloying elements.790–791
effect of carbon..788–789, 791–793
effect of chromium 790
effect of nitrogen.788–789, 791–793

Martensitic transformation
18% Cr–8% Ni stainless steel 267–290
effect of carbon..270, 272, 285–286
effect of deformation 267–290
effect of plastic strain on subsequent transformation 279–280
martensite produced by plastic deformation 273–277
for a range of temperatures 273–276
for various elongations .276–277
nature of martensitic product 271–273
manganese steel 286–288

Mechanical properties
chromium-manganese-nickel steels 239–241, 243–254

Mechanical properties (cont.)
of hardened steels 385–389
relation to hardness 387–388, 391–392, 405–407
of lamellar and spheroidal eutectoid steel 426
molybdenum 987–995
material constants vs. temperature 987–991
strength and ductility vs. temperature 992–995
SAE 4340 steel 899–900
effect of hydrogen embrittlement 899–900

Melting points
of titanium-aluminum-manganese alloys 576

Microstructure
of Al-V alloys.525–527, 530, 532–533
of 4.5% chromium steels 654
of cold-worked steel
relationship to magnetic intensity 325–345
ductile cast iron.....854, 857–863
showing influence of composition on secondary graphite 861–863
showing metamorphsis of secondary graphite...857–862
secondary graphite 854
of ductile or nodular cast irons 616, 626
of fatigue cracks in eutectoid steel 433–435
of iron-carbon alloys 293–304
changes during tempering. See Tempering of iron carbon alloys
low carbon steels 976
effect of strain aging treatments 976
relationship to hardenability.727–746
17-22A(S) steel ..942–943, 945–947
normalized at various temperatures 942–943
tempered for various lengths of time 945–947

Microstructure (cont.)
of steel during transformation. 361
Stellite 21.818, 821, 823–830, 835–841
as rolled 818, 821, 827, 838
effect of different quenching methods 849–850
heat treated and isothermally transformed 837
showing pearlite surrounded by border 837
pearlitic structures 840–841
precipitation by aging.....826–830
precipitation by isothermal transformation 823–830
solution-treated 818, 827
of stress-corrosion
in magnesium alloy J 1.....479–480, 483
of titanium-aluminum-manganese alloys 572–573
of titanium-cobalt alloys....556–560
vanadium-oxygen alloys .....
.....1006, 1008–1010, 1013

Minimum creep rate
molybdenum 996–997
activation energy 996
as a function of reciprocal absolute temperature.996–997
as a function of true stress.. 996

Molybdenum
in binary zirconium alloys
effect on elevated temperature strength 671–674
effect on workability and hardness 670–671
creep curves 994–995
creep-rupture data 999–1000
creep-rupture fracture 999–1000
creep-rupture properties...995–1000
ductility
as a function of temperature 992–995
elongation 992–995
as a function of temperature 992–995
in high carbon alloy steels
effect on hardenability ..759, 762

Molybdenum (cont.)
Larson-Miller parameter ...997–998
as a function of stress 997–998
mechanical properties 987–995
material constants vs. temperature 987–991
strength and ductility vs. temperature 992–995
minimum creep rate.....996–997
activation energy 996
as a function of reciprocal absolute temperature ..996–997
as a function of true stress.. 996
reduction of area 993–995
as a function of temperature 993–995
strain hardening coefficient ...
.....987–991, 993–995
as a function of reciprocal absolute temperature.988, 991
strain rate sensitivity.....
.....987–991, 993–995
as a function of reciprocal absolute temperature.988, 991
stress at unit strain....987–988, 990
stress-rupture life 995
equation 995
tensile fracture 993, 995
tensile properties 984–1000
at elevated temperatures.984–1000
tensile strength 990–995
as a function of temperature 992–995
true stress-true strain curves 986–989
yield points 989–992
yield strength 992–995
as a function of temperature 992–995
yield stress vs. temperature .. 460
Zener-Hollomon parameter.996–998
as a function of true stress.996–998

M, Temperatures..873–875, 879–880
equation for 874

Nickel
creep curves vs. prestrain...511–513
effect on hardenability 412

Nickel (cont.)
in end-quenched steel sections
effect on tensile and impact properties 415
in high carbon alloy steels
effect on hardenability 758, 760–761

Nickel-cobalt alloys
creep curves vs. prestrain 515
effect of alloy content 515

Nickel-iron alloys
creep curves vs. prestrain.... 514

Nickel-titanium alloys
creep curves vs. prestrain 514

Nitrogen
effect on machinability of steel. 687
effect on transformation temperatures of iron ..504, 506
in titanium
effect on beta to alpha transformation 506–507

Nodular cast irons
elevated temperature properties. See Ductile cast irons

Noncrystallographic low angle boundaries
magnesium 117–122
crossing grain boundary ..120–121
effect of stress on displacement of 121–122
formation and movement .118–120

Noncrystallographic surface traces
magnesium 127–128

Notch sensitivity
Cr–Mo–V and 17 Cr–4 Ni–4 cu steels.....926–956
effects of variation in normalizing and tempering procedure 926–956

Notch strength ratio
17–22A(S) steel..938–941, 949–952
as a function of rupture time 949–952
for several normalizing temperatures 949–950
for various tempering treatments 950–952
effect of normalizing temperature 938–939
at several times to rupture 938–939
effect of tempering temperature 939–940
at several rupture times.939–940
effect of tempering time ..939–941
at several times to rupture 940–941
17–4PH 940–942
effect of tempering temperature 940–942
at several rupture times.941–942
effect of test temperature 940–942
at several rupture times.941–942

Oxygen
in titanium
effect on beta to alpha transformation 506–507

Pearlite
effect on fatigue crack propagation 435–438
structural nature 739

Pearlitic ductile cast irons
creep and stress rupture data 614–623
hot tensile properties 625–627
structural stability 623–625

Phase diagrams
aluminum-vanadium 524, 539
copper-gold 579, 587
iron-cerium 544, 547–548
titanium-aluminum-manganese 566–576
titanium-cobalt 557
vanadium-oxygen 1005

Phase transformations
during tempering of 4.5% Cr steels 651–664

Phosphorus
effect on machinability of steel. 687

Photomicrographs
chromium-manganese steel
showing sigma formation.207–208
18% Cr – 8% Ni stainless steel.
.....271–273, 278–282, 289
showing change in martensite on cooling after deformation 280–282
showing martensite produced by deformation 278–280
showing nature of martensitic product 271–273
stainless steels, 12% Cr – 4% Mo 213–215, 221
effect of titanium 213–215
stainless steels, type 310....179–203
showing sigma formation.197–203
zirconium 170, 174–175

Plain carbon eutectoid steel
fatigue properties 423–439

Plain carbon steel
solubility of carbon 306–310

Planar Pressure Theory..... 895

Plastic flow
aluminum sheet 53–55
effect of rolling direction ..53–55

Plastic flow damping.....447–449

Plastic strains
types 77–79
zirconium 173, 175–176, 178
relation to crystallographic orientation ..173, 175–176, 178

Pole figures
aluminum-copper-magnesium alloy bar 67–68
illustrating duplex type of preferred orientation ..67–68

Pole figures (cont.)
aluminum sheet 40, 46–49, 58–65
mixture of rolling and recrystallization textures.48, 62–63, 65
recrystallization texture ....
.....46, 49, 60–62
rolling texture.....40, 47, 58–60

Preferred orientation
aluminum alloy bar.....69–72
correlation with directional properties 69–72
aluminum-copper-magnesium bar 67–68
aluminum sheet 46–50, 62–65
effect on deep drawing.47–48, 50
effects on drawing capacity.62–65
effect on tensile tests 46–47, 49

President's Annual Address. 8

Prestrains
effect on substructure 508–510
types 77–79

Probit analysis
of fatigue properties .....
.....424–425, 429–430

Rare earth metals
in end-quenched steel sections
effect on hardenability 410
effect on tensile and impact properties 414–416

Rate sensitivity
definition 167
equations 167–168
zirconium 166–170, 182
effect of amount of strain... 168
effect of grain size 168
relation to test temperature 168–170

Recovery
in cold worked aluminum
activation energy 636
effect on tensile curves at 298°K 636–637

Recrystallization
chromium-manganese steel ... 207
effect on sigma formation... 207
stainless steels, type 310....200–207
effect on sigma formation.200–207

Reduction of area
molybdenum 993–995
as a function of temperature 993–995

Refractaloy 26
damping under static stress..445–446

Rephosphorized open hearth screw steel
influence of composition on machinability
advantages of open hearth steel 681
effect of carbon.....683, 687–689
effect of manganese..... 687
effect of nitrogen..... 687
effect of phosphorus..... 687
effect of silicon..683–685, 687–689
effect of sulphur.....684–689
machinability index 689
machinability testing procedure 681–682

Retained tensile ductility
aluminum plate.....86–93, 96–97
effect of biaxial tension and biaxial compression.88–89, 97
effect of prestrain in simple compression or simple tension 89–91, 97
effect of prestrain stress state 90–91, 97
effect of tensile and compressive prestrain.....86–89, 96
steel, SAE 1340.....89–91
effect of prestrain in simple compression or simple tension 89–91

Rolling texture
of cold-rolled steel
effect of rolling temperature. See Cold-rolled steel, low carbon

Screw steel
machinability vs. composition.. 680–691

Secondary graphite
ductile cast iron.....854, 857–863
influence of composition..861–863
metamorphosis of 857–862
microstructure 854

Secondary graphitization
ductile cast iron.....853–868
quenched and tempered...853–868

Secretary's annual report... 15

Shear modulus
relation to delayed yield time.. 454–458

Sigma formation
austenitic stainless steels
effect of cold work and recrystallization 193–209
chromium-manganese steel .207–208
effect of cold work..... 207
effect of recrystallization.... 207
stainless steels, type 310....195–207
effect of aging temperature 195–196, 198–207
effect of aging time..... .....195–196, 198–207
effect on bend angle.....208–209
effect of cold working..... .....195–196, 198–207
effect on hardness.....208–209
photomicrographs showing.. 197–203
relation to recrystallization.. 200–207

Silicon
effect on hardenability.....410–412
effect on machinability of steel 683–685, 687–689
in end-quenched steel sections
effect on tensile and impact properties 414–417
in high carbon alloy steels
effect on hardenability...752–753

Slack-quenched steel

transverse properties of heavy sections
effect of mass.....418–420
hardenability results 409–413
previous results 408–409
procedure 409
tensile and impact properties 413–419

Slip

energy to initiate.....452–453
magnesium 110–111
critical stress for.....110–111

Slip-bands

magnesium 108–111

Smooth strength ratio

17–22A(S) steel.....949–952
as a function of rupture time 949–950
for several normalizing temperatures 949–950
as a function of rupture time 950–952
for various tempering treatments 950–952

Solid solubility limits

thermodynamic expressions.501–507
cementite in gamma iron..504–505

Solid solutions

thermodynamics of binary interstitial. See Thermodynamics

Solidification

deutritic growth 463–470

Solonoid

use in studying cold worked steel 334–335

Solute

concentration during solidification 463–464
temperature distribution during solidification 464

Specific volumes

18% Cr–8% Ni stainless steel. 269
austenite 269
martensite 269

Stain etching

Stellite 21.....821–822, 834–836, 842

Stainless steels

AISI 403
damping under static stress 444–447
12% Cr–4% Mo steels....211–230
Chi phase 211–230
effect of titanium..... ..213–215, 223–224, 226–230
Laves phase 211–230
effect of titanium..... ..213–215, 223–224, 226–230
photomicrographs ...213–215, 221
effect of titanium.....213–215

Stainless steels, austenitic

chrominum-manganese-nickel steels .239–241, 243–258, 262–265
corrosion resistance 255–258
intergranular corrosion.256–258
elongation 241, 244–246
Ericksen values.....241, 245
izod impact 241, 249–254
mechanical properties 239–241, 243–254
oxidation tests 264–265
stress-rupture strength ...262–265
tensile strength..240–241, 244–246
true stress-strain curves..247–250
yield strength 241, 244, 246
welding characteristics ...254–255
work hardening..239, 243, 247–250
18% Cr–8% Ni type.....267–290
electrical resistance 269–270
relationship to percent martensite 269–270
hardness 273
austenite 273
martensite 273
isothermal formation of martensite 272–275, 282–284
effect of carbon.....272–275

Stainless steels, austenitic (cont.)
effect of holding temperature 272–275
effect of plastic deformation 282–283
mechanical stabilization.282–284
lattice parameters 269
austenite 269
martensite 269
martensite transformation.267–290
comparison of measured and calculated values of M_s 270
effect of carbon..... .....270, 272, 285–286
effect of deformation...267–290
effect of plastic strain on subsequent transformation 279–280
martensite produced by plastic deformation... 273–277
for a range of temperatures 273–276
for various elongations.. 276–277
nature of martensitic product 271–273
photomicrographs 271–273, 278–282, 289
showing change in martensite on cooling after deformation 280–282
showing martensite produced by deformation 278–280
showing martensite 271–273
specific volumes 269
austenite 269
martensite 269
type 310 193–209
bend angle 208–209
effect of sigma formation.. 208–209
hardness 208–209
effect of sigma formation 208–209

Stainless steels, austenitic (cont.)
rate of sigma formation...193–207
effect of aging temperature 195–196, 198–207
effect of aging time..... .....195–196, 198–207
effect of cold working..... .....195–196, 198–207
effect of recrystallization 200–207
sigma formation 193–209
effect of cold work and recrystallization 193–209

Static stress
effect on damping. See Damping of some engineering alloys.

Statistical analysis
of fatigue properties..... .....423–425, 427–432

Steels
See Low Carbon steels.
delayed yield. See Dislocation theory.
effect of cold work on cementite. See Cementite in steel.
effect of grinding on structure. See Grinding.
impact properties ..144–148, 150–151
effect of alloying elements.. .....146–148, 151, 153
effect of strain aging.....150–151
effect of testing temperature 145–147, 151
magnetic permeability versus temperature 873–874
magnetic transformation diagram 875–876
relationship of magnetic permeability to temperature.. 875–876
martensite 880–881
relationship to magnetic permeability 880–881
versus temperature 880
M_s temperatures ..873–875, 879–880
equation for 874

Steels (cont.)
tensile properties ..137–144, 148–150
effect of strain aging.....148–150
transformation points.....869–875
magnetic detection 869–875
determination of M_s points 873–875
operation of equipment... 872
schematic diagram of apparatus 871
schematic diagram of circuit 870
typical cooling and magnetic transformation curves. 872
SAE 4063
Elmendorf curve 880–881
SAE 4340 .....872, 876–877
cooling curves for several quenching media 876–877
cooling and magnetic transformation curves 872

Steel, trade designations
AISI 403
damping under static stress.. 444–447
AISI 1020
elastic limit and yield behavior 384–398
AISI 1040
elastic limit and yield behavior 384–398
AISI 1045
isothermal transformation curves 359
AISI 1080
elastic limit and yield behavior 384–398
AISI 1085
isothermal transformation curves 356–357
AISI 4340
isothermal transformation curves 358
SAE 1040
hardenability vs. microstructure 727–746
SAE 1090
electron micrographs 314–316

Steel, trade designations (cont.)
SAE 1340
hardenability vs. microstructure 727–746
SAE 4040
hardenability vs. microstructure 727–746
SAE 4340
hardenability vs. microstructure 727–746
SAE 5140
hardenability vs. microstructure 727–746
SAE 8640
hardenability vs. microstructure 727–746

Stellite 21
grain boundary behavior..... 830
hardness 830–833, 841, 849–851
aging 830–833
effect of aging temperature for various times.... 832
effect of time at various temperatures 831
changes with heat treatment. 841
effect of different quenching methods 849–850
isothermal transformation 830–833
effect of temperature for various times 832
effect of time at various temperatures 831
versus aging temperatures.850–851
heat tinting....821–822, 834–836, 842
lattice parameter 838
microstructure 818, 821, 823–830, 835–841, 849–850
as-rolled 818, 821, 827, 838
effect of different quenching methods 849–850
heat treated and isothermally transformed 837
showing pearlite surrounded by border 837
pearlite structures 840–841
precipitation by aging....826–830

Stellite 21 (cont.)
precipitation by isothermal transformation 823–830
solution treated 818, 827
stain-etching..821–822, 834–836, 842
stress rupture life.....850–851
versus aging temperature.850–851
X-ray diffraction 819–821, 833–834, 841–842
matrix phases 819–821, 833
minor phases 819–821, 833–834, 842

Stereographic projections 51–53, 56–59, 70–71

Strain aging
effect on delayed yield time.... 457
relation to solute segregation.. 451
mechanism of.....976–980, 982
of steel
effect on carbon diffusion.. 347

Strain energy
of binary interstitial solid solutions 500–507

Strain-hardening coefficient
molybdenum 987–991, 993–995
as a function of reciprocal absolute temperature.988, 991

Strain-hardening exponent
zirconium.160, 162, 170–172, 176–179
effect of annealing temperature 170–172
effect of testing temperatures 160, 162, 180–181
relation to texture.....176–179

Strain rate sensitivity
molybdenum 987–991, 993–995
as a function of reciprocal absolute temperature.988, 991

Stress
effect on creep-tempering of 4.5% chromium steels.661–662
effect on elastic limit of steel.. .....394–395, 403

Stress (cont.)
effect on isothermal transformation of austenite. See Isothermal transformation of austenite.

Stress at unit strain
molybdenum 987–988, 990

Stress-corrosion
of magnesium alloy J 1
apparatus and procedure..475–479
cathodic protection 483–485
direction of cracking....482–483
effect of heat treatment..... 479
mechanism of 485–486
microstructures 479–480, 483
nature of stress corrosion... 474
previous observations 475

Stress-residual strain curves
for hardened steels.....384, 386

Stress rupture life
molybdenum 995
equation 995
Stellite 21 850–851
versus aging temperatures.850–851

Stress-rupture properties
of ductile or nodular cast irons 613–623

Stress-rupture strength
chromium-manganese-nickel steels 262–265
Cr – Mo – V and 17 Cr – 4 Ni – 4 Cu steel.....926–956
effects of variation in normalizing and tempering procedure 926–956
17-22A(S) steel 932–937, 944–945, 948–949
as a function of hardness... 948
at several rupture times.. 948
effect of carbide structure.944–945
effect of grain size..... 945
effect of tempering temperature 934–937

Stress-rupture strength (cont.)
effect of tempering time...936–937
at various rupture times.. 936–937
effect of normalizing temperature 932–935
at various rupture times.. 933–935
17-4 PH steel.....937–938, 952–953
as a function of tempering temperatures 952–953
for several ruptures times. 952–953
as a function of testing temperature 937–938
at several rupture times.937–938

Stress rupture tests
specimen 930
SAE 4340 steel.....906–921
hydrogen embrittlement ..906–921
aging with and without applied stress 911–918
critical load values.....908–909
effect of aging time....909–914
effect of notch acuity..908–909
evaluation of variables influencing 919–921

Stress-strain curves
magnesium 105, 107–108
zirconium 162–163, 165–166
load-elongation curve..... 163
yield point indication.....165–166

Structure
of hardened steel
effect of grinding. See Grinding.

Substructure
effect on creep in nickel and nickel alloys. See Creep curves.

Sulphur
effect on machinability of steel 684–689

Supercooling
during solidification 469

Tantalum
in binary zirconium alloys
effect on elevated temperature properties 671–674
effect on workability and hardness 670–671

Technical program and reports of officers, American Society for Metals–36th Annual Convention, Chicago, November 1 to 5, 1954 1

Temper embrittlement
of hardened steels..... 397

Temperature
during cold-rolling of steel
effect on texture.....715–726
effect on damping
of AISI 403 steel..... 445
of Refractaloy 26..... 446
effect on limiting creep and stress rupture
for ductile or nodular cast irons 617, 620–623
effect on yield stress produced by grinding
effect on structure of hardened steel 692–714
relation to delayed yield time 454–458

Tempering
hardened 4.5% chromium steels
effect on creep. See Creep-tempering relationships.

Tempering of iron-carbon alloys
cementite particles
effect of carbon form on solubility 310
effect of size on solubility.306–309
effect of strain on solubility 309–310
minimum stable size..... .....304–306, 311–312
compositions of alloys tested... 292
effect on ferritic grain size..296–302

Tempering of iron-carbon alloys (cont.)
effect on hardness.....293, 304
effect of temperature up to 700 °F 291–292
electron micrographs..... .....294, 297–299, 314–316
microstructural changes at 700-1000 °F 293–304
relationship to hardness..... 294

Tempering temperature
of steel
effect on elastic limit..... .....384–386, 405–407
effect on hardness and strength 384–387
effect of rate of cooling from 390–397
effect on yield strength....384–391

Tensile characteristics
zirconium 157–192
effect of annealing temperature 170–172
effect of oxygen and nitrogen impurities 179–182, 184, 186–192
influence of texture..... ....172–173, 175–176, 178–179

Tensile fracture
molybdenum 993, 995

Tensile fracture stress
aluminum plate.....91–93, 97–98
comparison of compressive effects 93
for various prestrain states and prestrain directions 93, 97–98
effect of various prestrain stress states.....91–93, 97–98

Tensile properties
aluminum-copper-magnesium alloy
extruded bar.....68–69, 72–74
after recrystallization.....72–74
effect of preferred orientation 72

Tensile properties (cont.)
of end-quenched heavy steel sections
effect of boron.....413–416
effect of carbon..... 417
effect of mass.....418–420
effect of nickel..... 415
effect of rare earth metals.. 414–416
effect of silicon.....414–417
low carbon martensites.....135–152
low carbon steels.....966–971, 981
effect of prestraining in compression and aging....969–971
effect of prestraining in tension and aging.....966–969
molybdenum 984–1000
at elevated temperatures.984–1000
of nickel and nickel alloys
effect of prestrain on.508–511, 513
steels 137–144, 148–150, 154–155
brine quenched and refrigerated 140–141
effect of refrigeration.....140–141
effect of specimen size..... .....142–144, 154–155
effect of strain aging....148–150
load-extension curves..148, 150
quenched in iced brine....137–140
quenched in oil.....141–142
zirconium 180–182

Tensile strength
chromium-manganese-nickel steels 240–241, 244–246
of hardened steels
relation to elastic limit...393–394
low carbon steels.....966–969, 981
effect of prestraining in compression and aging...969–971
effect of prestraining in tension and aging.....966–969
effect of aging time....966–969
molybdenum 992–995
as a function of temperature 992–995

Tensile strength (cont.)
zirconium
effect of annealing temperature 170–172
effect of test temperature... ....161–162, 180–181

Tensile stress
effect on isothermal transformation of austenite. See Isothermal transformation of austenite.

Tensile tests
aluminum sheet 46–47, 49
effect of preferred orientations 46–47, 49
molybdenum 990–993
autographic record 992

Texture
zirconium 173, 175–179
influence on tensile characteristics 172–173, 175–176, 178–179
relation to strain-hardening exponent 176–179

Thermal nucleation
rate for steel..... 453

Thermodynamics
of binary interstitical solid solutions
beta to alpha transformation in titanium
effect of carbon, oxygen and nitrogen 506–507
energies for formation....494–507
enthalpy 494–507
expressions for alloy formation 494
influence of carbon and nitrogen in iron on gamma-alpha transformation temperatures 504–506
solid solubility limit.....501–507
of cementite in gamma iron 504–505
strain energies 500–507

Thermo-magnetic balance... 322–325

Titanium
beta to alpha transformation
effect of carbon, oxygen and nitrogen on 506–507
carbide forming tendencies in steel 605–610

Titanium-aluminum-manganese system
contour projection of the beta space 569
examination of alloys..... 571
isothermal section at 750 °C... 566
isothermal section at 800 °C... 567
isothermal section at 900 °C... 567
isothermal section at 1000 °C.. 568
isothermal section at 1100 °C.. 568
isothermal section at 1200 °C.. 569
literature review 565–568
melting point contour projection 576
microstructures 572–573
phase equilibria 571–576
procedure 569–571
vertical sections 574–576

Titanium-cobalt system
beta decomposition 559
eutectic composition 558
hardness values 562
intermediate phases.....559–562
literature review 554–555
melting range determinations.. 562
metallographic studies 556–560
phase diagram 557
procedure 555–556

Tool steels
hardenability of carbon steel cylinders. See under Hardenability.

Torsional deformation
of tungsten wires.....602–604

Transformation of austenite
See Isothermal transformation of austenite.

Transformation in titanium
effect of carbon, oxygen and nitrogen on 506–507

Transformation points
magnetic detection 869–875
determination of M_s points.. 873–875
operation of equipment..... 872
schematic diagram of apparatus 871
schematic diagram of circuit. 870
typical cooling and magnetic transformation curves ..872

Transformation temperatures
of iron
effect of carbon and nitrogen on 504, 506
of iron-carbon-titanium-vanadium alloys 606–610
alloys containing pearlite..606–607
alloys having titanium and vanadium alloyed with ferrite 609–610
alloys having vanadium alloyed with ferrite..607–609
distribution of carbon....605–606

Transition temperatures
low carbon steels.....972–973
relationship to hardness..972–973
relationship to yield strength 972–973

Transverse properties
of slack-quenched heavy steel sections
effect of mass.....418–420
hardenability results 409–413
previous results 408–409
procedure 409
tensile and impact properties 413–419

Treasurer's Report 11

True strain
effect on isothermal transformation of austenite.....362–366

True stress
true creep relation
for cold worked aluminum.. 639–640

True stress-true strain
of unstable austenite
before and during transformation 366–367

True stress-true strain curves
chromium-manganese-nickel steels 247–250
low carbon steels.....965–966
prestrained in compression and aged 965–966
prestrained in tension and aged 965–966
molybdenum 986–989
SAE 4340 steel.....900–901
effect of hydrogen embrittlement 900–901
zirconium .....
159–164, 166, 168, 171, 173, 175–176, 178, 180–181, 183–184
effect of annealing temperature and grain size...171, 176
influence of strain rate...166, 168
logarithmic plot 159, 161
showing range of values resulting from changes in test variables.....183–184
strong and weak texture.... .....173, 175–176, 178

Tungsten
in binary zirconium alloys
effect on creep-rupture at 1800 °F 674–675
effect on elevated temperature properties 671–674
effect on workability and hardness 670–671

Tungsten wires
effect of twisting at high temperatures 599–604
apparatus and procedure..600–602
importance of sagging resistance 599

Tungsten wires (cont.)
resistance to torsional deformation 602–604
effect of grain structure... 604

Twinning
magnesium 111–117, 125
bending planes associated with 117
bilateral growth 112–113
detwinning 112, 115–116
unilateral growth 112, 114

Vanadium
allotropy in 1014–1016
carbide forming tendencies in steel 605–610
electrical resistance 1014–1015
as a function of temperature 1014–1015
in binary zirconium alloys
effect on elevated temperature properties 671–674
effect on workability and hardness 670–671

Vanadium-Oxygen
phase diagram 1005

Vanadium-Oxygen alloys
hardness
as a function of oxygen content 1015–1016
melting points 1012
microstructures .....
.....1006, 1008–1010, 1013
solidification characteristics...
.....1012–1014

Vanadium-Oxygen System
beta phase 1007–1010
axial ratios 1007
lattice parameters 1007
delta phase 1010–1011
x-ray diffraction lines ..1010–1011
solubility limit of oxygen..1006–1007
VO phase 1011–1012
lattice parameter 1011

Welding characteristics
chromium-manganese-nickel steels 254–255

Workability
of binary zirconium alloys...670–671

Work hardening
chromium-manganese-nickel steels 239, 243, 247–250

X-Ray diffraction
Stellite 21.819–821, 833–834, 841–842
matrix phases 819–821, 833
minor phases .....
.....819–821, 833–834, 842

X-Ray diffraction camera
"structure integrating" 44

X-Ray diffraction lines
vanadium-oxygen system .1010–1011
delta phase 1010–1011

X-Ray diffraction patterns
standards 819

X-Ray diffraction study
of iron-cerium system 550–551
of texture of cold-rolled steel
effect of temperature.....719–726
of worked steel 336–340

X-Ray photograms
of cold worked aluminum before and after creep tests.. 638

Yield point behavior
low carbon steels 970–971
effect of prestraining and aging 970–971

Yield points
molybdenum 989–992
relation to solute segregation .. 451
zirconium 165–167

Yield strength

aluminum plate 94–96, 98
comparison of compressive prestrain effects upon for various prestrain stress states and direction.94, 96, 98
effect of various stress states 94–95, 98
aluminum sheet 53–55
effect of rolling direction...53–55
chromium-manganese-nickel steels 241, 244, 246
low carbon steels 966–973, 981
effect of prestraining in compression and aging...969–971
effect of prestraining in tension and aging 966–969
effect of aging time 966–969
relationship to transition temperature 972–973
molybdenum 992–995
as a function of temperature 992–995
relation to elastic limit of steel 391, 394
zirconium
effect of annealing temperature 170–172
effect of testing temperature 161–162, 167, 180

Yield stress

as function of temperature
for iron 461
for molybdenum 460

Zener-Hollomon Parameter

as a function of true stress for molybdenum creep data 996–998

Zirconium

elongation.161–162, 170–172, 180–181
effect of annealing temperature 170–172
elongation
effect of test temperature 161–162, 180–181

Zirconium (cont.)

grain size 170–172, 174–175
effect of annealing temperature 170–172, 174–175
hardness 172
photomicrographs 170, 174–175
rate sensitivity 166–170, 182
effect of amount of strain .. 168
effect of grain size 168
relation to test temperature 168–170
relations between plastic strain and crystallographic orientation 173, 175–176, 178
strain hardening exponent.... .....160, 162, 170–172, 176–181
effect of annealing temperature 170–172
effect of test temperature 160, 162, 180–181
relation to texture 176–179
stress-strain curves.162–163, 165–166
load-elongation curve 163
yield point indication 165–166
tensile characteristics 157–192
effect of oxygen and nitrogen impurities 179–182, 184, 186–192
tensile characteristics
influence of texture..... ....172–173, 175–176, 178–179
tensile properties 180–182
tensile strength 161–162, 170–172, 180, 186
effect of annealing temperature 170–172
effect of test temperature 161–162, 180
texture 176–179
relation to strain-hardening exponent 176–179
true stress – true strain curves. 159–164, 166, 168, 171, 173, 175–176, 178, 180–181, 183–184
effect of annealing temperature and grain size 171, 176
influence of strain rate ..166, 168

Zirconium (cont.)
showing range of values resulting from changes in test variables 183–184
strong and weak texture.... .....173, 175–176, 178
yield point 165–167
yield strength .161–162, 170–172, 180
effect of annealing temperature 170–172
yield strength
effect of testing temperature 161–162, 167, 180

Zirconium alloys
strength of wrought binary alloys at 1800–2200 °F
creep-rupture tests of 8% tungsten alloy..674–675
experimental procedure ..666–670
hardness at 70° and 1600 °F 670–671
rupture strengths 671–674
comparison with high-temperature alloys.673–674
selection of alloying additions 666